COMPOSITE STRUCTURES

Theory and Practice

PETER GRANT
CARL Q. ROUSSEAU
EDITORS



STP 1383

STP 1383

Composite Structures: Theory and Practice

Peter Grant and Carl Q. Rousseau, editors

ASTM Stock Number: STP 1383



ASTM
100 Barr Harbor Drive
PO Box C700
West Conshohocken, PA 19428-2959

Printed in the U.S.A.

Library of Congress Cataloging-in-Publication Data

Composite structures: theory and practice/Peter Grant and Carl Q. Rousseau,
p. cm. — (STP; 1383)
Includes bibliographical references.
ISBN 0-8031-2862-2
1. Composite construction. 2. Structural analysis (Engineering) 3. Fibrous composites.
4. Laminated materials. I. Grant, Peter, 1942. II. Rousseau, Carl Q., 1962. III. ASTM special technical publication; 1383.

TA664.C6375 2000
620.1'18—dc21

00-059356

"ASTM Stock Number: STP1383."

Copyright © 2001 AMERICAN SOCIETY FOR TESTING AND MATERIALS, West Conshohocken, PA. All rights reserved. This material may not be reproduced or copied, in whole or in part, in any printed, mechanical, electronic, film, or other distribution and storage media, without the written consent of the publisher.

Photocopy Rights

Authorization to photocopy items for internal, personal, or educational classroom use, or the internal, personal, or educational classroom use of specific clients, is granted by the American Society for Testing and Materials (ASTM) provided that the appropriate fee is paid to the Copyright Clearance Center, 222 Rosewood Drive, Danvers, MA 01923, Tel: 508-750-8400; online: http://www.copyright.com/.

Peer Review Policy

Each paper published in this volume was evaluated by two peer reviewers and at least one editor. The authors addressed all of the reviewers' comments to the satisfaction of both the technical editor(s) and the ASTM Committee on Publications.

The quality of the papers in this publication reflects not only the obvious efforts of the authors and the technical editor(s), but also the work of the peer reviewers. In keeping with long standing publication practices, ASTM maintains the anonymity of the peer reviewers. The ASTM Committee on Publications acknowledges with appreciation their dedication and contribution of time and effort on behalf of ASTM.

Printed in Philadelphia, PA
Oct. 2000

Foreword

This publication, *Composite Structures: Theory and Practice,* contains papers presented at the symposium of the same name held in Seattle, Washington, on 17–18 May 1999. The symposium was sponsored by ASTM Committee D-30 on Composite Materials. The symposium co-chairmen were Peter Grant and Carl Q. Rousseau. They both served as STP editors.

Contents

Overview vii

STRUCTURAL DAMAGE TOLERANCE

USAF Experience in the Qualification of Composite Structures—J. W. LINCOLN 3
A Review of Some Key Developments in the Analysis of the Effects of Impact Upon Composite Structures—R. OLSSON, L. E. ASP, S. NILSSON, AND A. SJÖGREN 12
Certificate Cost Reduction Using Compression-After-Impact Testing—T. C. ANDERSON . 29

SKIN-STRINGER BEHAVIOR

Mechanisms and Modeling of Delamination Growth and Failure of Carbon-Fiber-Reinforced Skin-Stringer Panels—E. GREENHALGH, S. SINGH, AND K. F. NILSSON 49
Parametric Study of Three-Stringer Panel Compression-After-Impact Strength—C. Q. ROUSSEAU, D. J. BAKER, AND J. DONN HETHCOCK 72
A Method for Calculating Strain Energy Release Rates in Preliminary Design of Composite Skin/Stringer Debonding Under Multiaxial Loading—R. KRUEGER, P. J. MINGUET, AND T. K. O'BRIEN 105

ROTORCRAFT AND PROPELLER STRUCTURAL QUALIFICATION ISSUES

Fail-Safe Approach for the V-22 Composite Proprotor Yoke—L. K. ALTMAN, D. J. REDDY, AND H. MOORE 131
RAH-66 Comanche Building Block Structural Qualification Program—A. DOBYNS, B. BARR, AND J. ADELMANN 140
The Effects of Marcel Defects on Composite Structural Properties—A. CAIAZZO, M. ORLET, H. McSHANE, L. STRAIT, AND C. RACHAU 158
Influence of Ply Waviness on Fatigue Life of Tapered Composite Flexbeam Laminates—G. B. MURRI 188
Structural Qualification of Composite Propeller Blades Fabricated by the Resin Transfer Molding Process—S. L. SMITH, AND J. L. MATTAVI 210

BOLTED JOINT ANALYSIS

Three-Dimensional Stress Analysis and Failure Prediction in Filled Hole Laminates—E. V. IARVE AND D. H. MOLLENHAUER 231
Damage-Tolerance-Based Design of Bolted Composite Joints—X. QING, H.-T. SUN, L. DAGBA, AND F.-K. CHANG 243
Open Hole Compression Strength and Failure Characterization in Carbon/Epoxy Tape Laminates—H. BAU, D. M. HOYT, AND C. Q. ROUSSEAU 273
The Influence of Fastener Clearance Upon the Failure of Compression-Loaded Composite Bolted Joints—A. J. SAWICKI and P. J. MINGUET 293

TEST METHODS

Characterizing Delamination Growth in a 0°/45° Interface—R. H. MARTIN AND C. Q. ROUSSEAU 311
New Experiments Suggest That All Shear and Some Tensile Failure Processes are Inappropriate Subjects for ASTM Standards—M. R. PIGGOTT, K. LIU, AND J. WANG 324
Effect of Friction on the Perceived Mode II Delamination Toughness from Three- and Four-Point Bend End-Notched Flexure Tests—C. SCHUECKER AND B. D. DAVIDSON 334
Finite-Element Analysis of Delamination Growth in a Multidirectional Composite ENF Specimen—M. KÖNIG, R. KRÜGER, AND S. RINDERKNECHT 345
Comparison of Designs of CFRP-Sandwich T-Joints for Surface-Effect Ships Based on Acoustic Emission Analysis from Load Tests—ANDREAS J. BRUNNER AND ROLF PARADIES 366
Development of a Test Method for Closed-Cross-Section Composite Laminates Subjected to Compression Loading—R. B. BUCINELL AND B. ROY 382
Tension Pull-off and Shear Test Methods to Characterize 3-D Textile Reinforced Bonded Composite Tee-Joints—S. D. OWENS, R. P. SCHMIDT, AND J. J. DAVIS 398

STRENGTH PREDICTION

What the Textbooks Won't Teach You About Interactive Composite Failure Criteria—L. J. HART-SMITH 413
Curved Laminated Beams Subjected to Shear Loads, Moments, and Temperature Changes—S. O. PECK 437
Damage, Stiffness Loss, and Failure in Composite Structures—S. N. CHATTERJEE 452
Compressive Strength of Production Parts Without Compression Testing—E. J. BARBERO AND E. A. WEN 470

ENVIRONMENTAL EFFECTS

Environmental Effects on Bonded Graphite/Bismaleimide Structural Joints—K. A. LUBKE, L. M. BUTKUS, AND W. S. JOHNSON 493
Accelerated Tests of Environmental Degradation in Composite Materials—T. G. REYNOLDS AND H. L. McMANUS 513

PLENARY SESSION

The Effects of Initial Imperfections on the Buckling of Composite Cylindrical Shells—J. H. STARNES, JR., M. W. HILBURGER, and M. P. NEMETH 529

Indexes 551

Overview

The Symposium on "Composite Structures: Theory and Practice" sponsored by Committee D-30 on Composite Materials, was held in Seattle on 17th and 18th May 1999. This topic was a departure from the traditional D-30 symposia themes of "Design and Testing" and "Fatigue and Fracture." The reasons for this were to focus more specifically on structural certification/qualification issues, and to garner more interest and participation from government and industry experts. As stated in the Call for Papers, "The objective of this symposium (was) to bring together practitioners and theoreticians in the composite structural mechanics field, to better understand the needs and limitations under which each work."

The Symposium was structured around seven general topics (the various sessions), seven invited speakers on these or more global issues, the Wayne Stinchcomb Memorial Award and Lecture, and a wrap-up panel discussion with the invited speakers. The following paragraphs provide brief overviews of all of the papers included in this STP, as well as comments on the panel discussion and additional oral presentations given during the Symposium.

Professor Paul Lagace opened the Symposium with an invited talk on "Technology Transition in the World of Composites—An Academic's Perspective." Professor Lagace provided the attendees with an insightful and entertaining overview of some of the more popular composite structures research topics over the years, and some of the resulting successes and/or barriers to practical use. No technical publication in this STP was warranted for Prof. Lagace's editorial subject.

Structural Damage Tolerance

Lincoln USAF/ASC, gave an invited talk and related paper that reviews the development of procedures used by the United States Air Force in the qualification of composite structures. He also reviews Navy programs, and the resulting Joint Service Specification Guide. The challenges in future certification initiatives, in particular, the need to reduce cost and address changes in manufacturing processes are discussed. He proposes a re-examination of the building-block process and a critical review of probabilistic methods.

Dr. Larry Ilcewicz, FAA National Resource Specialist for Composites, gave an invited talk on his previously published "Perspectives on Large Flaw Behavior for Composite Aircraft Structure." This presentation gave an authoritative overview of low-velocity impact and discrete source damage threats, certification requirements, and structural response. No technical publication of this work was possible for this STP.

Olsson, Asp, Nilsson, and Sjogren review, in the main work performed at the Aeronautical Research Institute of Sweden (FFA), of studying the effects of impact upon composite structures. Both damage resistance and damage tolerance are studied, along with an assessment of the effects of global buckling.

Anderson presented a practical approach to design-specific compression strength-after-impact certification. The application cited was that of a carbon/thermoplastic light helicopter tailboom.

Skin-Stringer Behavior

Greenhalgh, Singh, and Nilsson investigate the behavior of damaged skin-stringer panels under compressive loading. Analysis and test of delamination growth are compared through the use of fi-

nite element and fractographic analysis. Local delamination and global buckling are modeled through the use of a moving mesh technique. The effects of embedded skin defects, with respect to size and location, are studied. Guidelines for realistic modeling and damage tolerant design are presented.

Rousseau, Baker, and Hethcock perform a parametric study of critical compression-after-impact (CAI) strength variables for three-stringer panels, and demonstrate practical global-local analytical tools to predict initial buckling and CAI strength. A particular benefit to this paper is the large size of the experimental three-stringer CAI panel database (39 specimens), which should be of use to future analysis validation exercises.

Krueger, Minguet, and O'Brien present a simplified method of determining strain energy release rates in composite skin-stringer specimens under combined in-plane and bending loads. In this method, a quadratic expression is derived for the two relevant fracture modes, and three finite element solutions are used to determine the quadratic coefficients. Both linear and geometrically nonlinear problems are evaluated. The resulting quadratic expressions for energy release rates are in excellent agreement with known linear solutions, and satisfactory agreement over a wide range of nonlinear loading conditions.

Dr. Andrew Makeev (co-author Armanios) gave an oral presentation on a global analysis for separating fracture modes in laminated composites. An exact elasticity solution with approximated boundary conditions for self-similar delamination growth was used. The predicted mode ratio was compared with existing results for eight-ply quasi-isotropic laminates under axial extension. No manuscript is published in the STP for this presentation.

Rotorcraft and Propeller Structural Qualification Issues

Altman, Reddy, and Moore in an invited paper, present the rationale for substantiation of the fiberglass/epoxy V-22 proprotor yoke using a "fail safe" methodology. Significant delaminations were observed in fatigue tests on both prototype and production components within the "safe life" goal of 30 000 hours. "Fail safe" qualification of other Bell Helicopter composite yokes is reviewed. In these components delamination is shown to be a benign failure mode. "Fail safe" substantiation methodology results in a lower life cycle cost.

Dobyns, Barr, and Adelmann discuss the RAH-66 Comanche airframe building-block structural qualification program from testing at the coupon level to full scale static test of the complete airframe structure. Testing discussed includes bolted joints, sandwich structure, crippling specimens, fuselage-sections, and design specific tests. The interaction of the building-block test results with detail design is shown to be important.

Caiazzo, Orlet, McShane, Strait, and Rachau develop a method for predicting key properties of composite structures containing ply waviness, several times the ply nominal thickness. These "marcelled" regions have been observed in thick components. This analytical tool is intended to be used to disposition parts containing these defects. The validity of the method is demonstrated in correlation with test data.

Murri studies the effect of ply waviness upon the fatigue life of composite rotor hub flexbeams. Delamination failure of test specimens having these "marcelled" regions occurs at significantly shorter fatigue lives than in similar specimens without marcels. Geometrically, nonlinear analysis addressing interlaminar normal stresses shows the critical influence of the degree of marcelling. A technique is presented for acceptance/rejection criteria of marcels in flexbeams.

Smith and Mattavi show that unique challenges exist in the development of design allowables for a resin-transfer-molded (RTM) propeller blade. They show that coupon level tests successfully provide data for elastic constants, effects of batch variability, effects of adverse environments, and for the shape of fatigue curves, but do not provide enough guidance for the design of full scale structure in the absence of full scale test data. The number of full-scale tests needed is greater for a RTM blade or structure than for a metal blade or standard prepreg structure.

Bolted Joint Analysis

Iarve and Mollenhauer use a 3-D displacement spline approximation method to evaluate an observed stacking sequence effect upon the pin-bearing strength of two quasi-isotropic laminates. A qualitative agreement is obtained between predicted stress distributions and experimental damage observation. The analysis identifies critical transverse shear and normal stresses.

Qing, Sun, Dagba, and Chang propose an approach for the design of bolted composite joints based on a progressive damage model. The computer code, 3DBOLT/ABAQUS, is capable of predicting joint response from initial loading to final failure. The effects of bolt clamping force and area, and joint configuration upon joint response are summarized.

Bau, Hoyt, and Rousseau present work aimed at developing better numerical predictions of open hole compressive strength, a key structural design driver currently determined experimentally. First, experimental results for a wide range of carbon/epoxy laminates are studied and the predominant lamina-level failure modes isolated. Secondly, a progressive damage 2-D finite element code developed by F. K. Chang at Stanford, is evaluated relative to the large set of experimental data. It is concluded that the progressive damage model yields good results for hard laminates exhibiting 0°-ply-dominated failure modes, but improvements to matrix/off-axis-ply-dominated failure modes are required.

Sawicki and Minguet investigate the effects of fastener hole-filling and hole clearance upon the strength of composite bolted joints loaded in compression. Experiments show three primary modes of failure, which vary depending upon the bolt diameter, hole diameter, and bearing-bypass loading ratio. Strength predictions based upon progressive damage finite element analysis demonstrate reasonable agreement with experimental trends.

Test Methods

Mr. Rich Fields, ASTM D-30 Vice-Chair, made an invited oral presentation on "An American Perspective on International Standardization of Composites." This sensitive subject covered recent D-30 experience with ISO TC61 as well as the author's opinions of the relative merits of ASTM versus ISO approaches to consensus standardization. This briefing was well-attended by ASTM leadership, including Jim Thomas, President. No technical publication in this STP was warranted for Mr. Field's editorial subject.

Martin and Rousseau compare mode I delamination growth behavior at a 0°/0° ply interface with that of a 0°/45° ply interface in glass/epoxy tape. The motivation for this work was that most structural delaminations occur at dissimilar ply interfaces, such as 0°/45°, while the ASTM standard coupon delamination test methods all utilize unidirectional coupons (in order to minimize residual and free-edge stresses). Martin and Rousseau observe in their experimental work that fiber-bridging is similar in both lay-ups (unexpected for the 0°/45° configuration), delaminations grow in a self-similar manner (i.e., do not jump to other ply interfaces), and static critical strain energy release rate, G_{Ic}, from the 0°/45° lay-up exhibits a lower mean and higher scatter (on a small sample size) than the unidirectional configuration. Both specimen designs yield similar fatigue delamination onset results. A useful sidelight to this work is the development of a general method of designing multidirectional laminated delamination coupons that minimizes bend-twist coupling, free-edge, and residual stresses.

Piggot reviews several ASTM D-30 standards, concentrating on the aspects of shear dominated failures. He applies his knowledge of the failure of polymers when subjected to shear loading, and shows that these failures are in fact tensile in nature. He presents a case for a re-evaluation of D30 standards, which involve apparent shear failures.

Schuecker and Davidson present a timely study on the effect of friction on the calculated mode II fracture toughness of the proposed ASTM standard four-point end-notch flexure (4ENF) coupon test. This finite element-based study shows that frictional effects, while present, do not fully account for experimentally observed differences in G_{IIc} between the 4ENF and other mode II test methods.

König, Kreüger, and Rinderknecht present both two-dimensional higher-order plate and three-dimensional layered solid-finite element results in a multidirectionally-laminated end-notch flexure test coupon. The results suggest that width-wise variation in both magnitude and mode ratio of strain energy release rates along the crack front contribute to the shape of the delamination front as well as the final unstable delamination growth. Comparison with experimental results shows that global delamination growth in this case of pure shear (combined modes II and III) is correctly predicted by Griffith's criterion.

Brunner and Paradies (in a paper submitted for publication in this STP, but not presented at the Symposium) evaluate several different T-joint sandwich designs, made from balsa-wood cores having carbon fiber reinforced polymer facesheets. In addition to load-displacement and strain gage data, the test program makes extensive use of acoustic-emission techniques. These techniques monitor early onset of damage and accumulation up to final failure. The specimens were subjected to quasi-static tension and compression loads.

Bucinell and Roy develop a test method for evaluating the properties of closed-section composite laminates. Analysis and test demonstrate that the configuration accurately develops compression properties, and that buckling modes are suppressed. The authors suggest that other laminates be evaluated, and a round-robin test program performed to demonstrate reproducibility of the method.

Owens, Schmidt, and Davis present test methods for generating design properties for skin-to-spar type composite bonded joints, loaded in both shear and pull-off. Data acquisition techniques were developed to capture initial and localized failure modes. The use of a 3-D textile reinforcement is shown to provide improvements over typical unreinforced cocured joints.

Strength Prediction

Hart-Smith, in an invited paper, presents a critical review of fiber-reinforced composites unnotched failure criteria both as taught in academia and as used in practical applications. His criticisms center on the use of interactive failure theories in progressive ply-by-ply failure analyses. He shows that the inhomogeneity of fiber reinforced materials invalidates the use of these theories, and makes a strong recommendation that both the use and teaching of these cease. A strong case is made for the use of separate mechanistic models for failures in the fibers, matrix and at the interfaces.

Dr. Christos Chamis (co-authors Patnaik and Coroneos gave an oral presentation on the capability of an integrated computer code entitled Multi-faceted/Engine Structures Optimization, M^P/ESTOP. The discipline modules in this code include: engine cycle analysis, engine weight estimation, fluid mechanics, cost, mission, coupled structural and thermal analysis, various composite property simulators, and probabilistic methods to evaluate uncertainty in all the design parameters. He described the multifaceted analysis and design optimization capability for engine structures. Results illustrated reliability, noise, and cascade optimization strategy. Both weight and engine noise were reduced when metal was replaced by composites in engine rotors. No manuscript is published in the STP for this presentation.

Peck develops closed form 2-D solutions for the displacements, strains, and stresses in curved and laminated orthotropic beams due to both mechanical and thermal loading. The solutions are exact and thus equally applicable to both solid laminates and sandwich structures. Sample calculations for aluminum honeycomb beams having graphite/epoxy facesheets, predict anticipated failure modes.

Chatterjee uses damage mechanics to develop an approach for inelastic analysis of structural elements made from laminated fiber composites of a brittle nature. This method is used to predict behavior beyond initial damage for a pressure vessel and also address the hole size effect. He suggests that use of this approach to address environmental effects still requires material characterization at the appropriate environments.

Barbero and Wen develop a methodology to estimate the strength of fiber-reinforced composite production components, utilizing minimal characterization data. Compression strength is related to

shear strength and stiffness, and fiber misalignment, which is measured from actual production parts. The method is validated through comparisons with test data.

Environmental Effects

Lubke, Butkus, and Johnson study the long-term durability of a toughened epoxy used to bond graphite/bismaleimide composites. Test data are presented addressing the effects of temperature, environmental exposure, and adherend type on the toughness of these bonded joints. The combination of prior environmental exposure and low test temperature resulted in severe degradation of fracture toughness.

Reynolds and McManus present experimental observations of microcracking damage in PETI-5 and PIXA-M composites exposed to realistic hygro-thermal cycling. With these materials moisture cycling is shown to play a critical role in moisture distribution. Levels of moisture near surfaces and free edges exhibit a cyclic pattern, often with a benign level in the laminate interior. Time at moisture is the dominant factor in material degradation. For these materials damage is shown to be limited to the free edges.

Plenary Session

Starnes, Nemeth, and Hilburger in the final invited paper, present the results of an experimental and analytical study of the effects of initial imperfections on the buckling response of thin unstiffened graphite-epoxy cylindrical shells. The nonlinear finite element code is shown to account for accurately both traditional and non-traditional shell imperfections and load variations. It is proposed that the nonlinear analysis procedure can be used as a basis for a shell analysis and design approach.

Stinchcomb Lecture

Dr C. C. Poe (NASA Langley Research Center) who was the recipient of the Wayne Stinchcomb memorial award gave this lecture, which was not published in the STP. He reviewed a test program aimed at developing damage tolerance allowables for a stitched resin-film-infused material. The material was that used on the NASA Advanced Subsonic Technology (AST) Composite Wing Program, and consisted of IM7 and AS4 fibers in the 3501-6 resin, stitched transversely with Kevlar-29 thread. Tests were conducted in the three fiber directions, and on four different thicknesses to replicate the wing skin from tip to root. The configurations included compact, extended compact, and center notched tension specimens. Normal and shear strains were calculated on fracture planes using a William's type series representation of strain fields for plane anisotropic crack problems. A characteristic distance for ultimate tension and shear was calculated, and an interaction equation determined.

Panel Discussion

The panelists were Drs. Chris Chamis (NASA Glenn Research Center), John Hart-Smith (Boeing), Larry Ilcewicz (FAA), Paul Lagace (MIT), Jack Lincoln (USAF), and Jim Starnes (NASA Langley Research Center). The format included introductory remarks, five questions, to which each panelist had three minutes to respond, and one audience comment on each question. The following were the questions and related general comments.

1. Will composite structures experience more widespread aerospace use due to increased: (a) weight savings or (b) cost savings? Why? General consensus was that reduced cost is the one item that would lead to more widespread use of composites. Comment was made that the General Aviation industry was reducing cost relative to traditional aluminum structure through the use of composites.

2. Can the cost/cycle time of aerospace composite structural substantiation be significantly reduced? If so, by how much? If not, why? General response was yes. However, comments were made that there is not enough understanding of failure modes. We need better analysis methods, education of practicing engineers could be improved, and we need to share specifications.
3. What flight safety/damage tolerance issues will dominate composite structural airworthiness debates 20 years from now? What should we do now to address these issues? We have developed methods based on metals behavior and do not recognize the brittle nature of composites. We need a probabilistic approach to design. We need developments in NDE, and need to address the weak bond issue. Long term aging issues may become important.
4. What emerging analytical tools will be in widespread use 20 years from now, and what near-term initiatives should be pursued to enable their development? We need to develop computer stimulation of the fabrication process and couple this with the other issues. We need design/cost models from early design through to the end of lifetime. Knowledge regarding nonlinear effects in structures, and progressive failure analyses need to be developed. Education was again brought up as an issue. Development of artificial intelligence and self-diagnostic structures was mentioned. We need to solve production problems quickly.
5. How much standardization (of design guidance, test methods, material specifications, etc.) is appropriate for high performance composites, and why? We need to be careful when standards are cast in concrete (this was really emphasized), and must understand the standard. We need educated (education again !!) standardization. We need common databases and need to banish multiple purchase specifications (an example was given of 12 different purchase specifications for one material). We need standards for processes.

The session was moderated by C. Rousseau.

Summary

In summary, the editors feel that the papers in this STP reflect a good cross-section of the current state of the art in composite structures technology. The editors would like to thank the following session chairs for their advice and assistance and in seeing that the sessions rain in a smooth and professional manner:

Darwin Moon (The Boeing Co.)
T. Kevin O'Brien (Army Research Lab)
Steve Hooper (Wichita State University)
Steve Ward (The Boeing Co.)
Brian Coxon (Integrated Technologies, Inc.)
Gene Camponeschi (Naval Surface Warfare Center)
Crystal Newton (University of Delaware)

Finally, the editors wish to thank the paper authors, and reviewers, who's collective effort made this publication possible. Special thanks is extended to the ASTM staff. Their combined work is sincerely appreciated. The editors also wish to acknowledge John Masters for his work in the review phase.

Peter Grant
Symposium co-chairman and Editor:
The Boeing Co.

Carl Rousseau
Symposium co-chairman and
Co-Editor; Bell Helicopter/Textron, Inc.

Structural Damage Tolerance

John W. Lincoln[1]

USAF Experience in the Qualification of Composite Structures

REFERENCE: Lincoln, J. W., **"USAF Experience in the Qualification of Composite Structures,"** *Composite Structures: Theory and Practice, ASTM STP 1383,* P. Grant and C. Q. Rousseau, Eds., American Society for Testing and Materials, West Conshohocken, PA, 2000. pp. 3–11.

ABSTRACT: The prospect of significant reduction in aircraft structural mass has motivated the United States Air Force (USAF) and the aerospace industry to incorporate composite structures in their aircraft designs. The USAF found threats to structural integrity such as moisture, temperature, delaminations, and impact damage that made them take a cautious approach for the acquisition of aircraft with composite materials. Each of these threats acted as an inhibitor to using these materials in the design of operational aircraft. However, the USAF has successfully incorporated composites on several aircraft, including the B-2, C-17, and F-22. The challenge is to find new approaches for the qualification of composite structures that will make them more economically viable for future procurements. It is the purpose of this paper to discuss the background for the current qualification program for composites and suggest some possibilities for improvement of the certification process.

KEYWORDS: damage tolerance, moisture, temperature, impact damage, allowables, design development testing, full-scale testing, and technology transition

Composite structural technology has been in the process of maturing for approximately 40 years. From the early days, both the [now] Materials Directorate and the Air Vehicle Directorate of the Air Force Research Laboratory (AFRL) of the United States Air Force (USAF) have been influential in promoting the technology. These early pioneers faced numerous setbacks in the course of development of the technology. The cause of these setbacks was, in reality, the lack of understanding of the threats to structural integrity. Some of the threats discovered were the degradation from temperature and moisture environment, impact damage, and delaminations.

When these threats revealed themselves through test results, the AFRL sponsored numerous programs that have contributed to the understanding of composite behavior. Some that stand out as being influential to understanding the threats to structural integrity are the following:

—Fatigue sensitivity; contract to Northrop.
—Environmental sensitivity of composites; contract to Grumman.
—Wing/fuselage critical components; contract to Northrop.
—Damage tolerance of composites; contract to Boeing and Northrop.

The process for certification of composite structures for USAF aircraft has been evolving for approximately 30 years. Establishment of the requirements for structural integrity of composite structure for an aircraft has long been a challenge for the certification authorities. This challenge is much greater when the aircraft is operated in an environment where heating of the structure is a factor. However, even for structures where heating does not appreciably affect the structural capability, there

[1] Technical advisor for Aircraft Structural Integrity for the United States Air Force, ASC/EN, 2530 Loop Road West, Wright-Patterson AF Base, OH 45433-7101.

Copyright© 2001by ASTM International www.astm.org

are some major considerations. One of these is the scatter in strength and fatigue data. This scatter, which is larger than observed in metals, is not a deficiency in composites, but a fact that one must account for in the certification process. Another consideration is the difficulty in establishing the growth characteristics of manufacturing or service-induced defects due to load application. This difficulty is due to the mathematical problems in simulating this growth and to the apparent inconsistent empirical results from presumably identical damage conditions. Another consideration is the effect of low-energy impact on thin laminates. The authorities must consider this durability issue in establishing requirements for composite structures.

Several organizations have initiated efforts aimed at addressing the issues related to composite certification. The Technical Cooperation Program (TTCP) made such an effort through sponsoring the Subgroup H Action Group (HAG)-5 panel in 1983. This panel brought the major issues into focus and described some alternative approaches that the designer could use. Another contribution was a United States Navy (USN) sponsored effort by Northrop [*1*]. This work concentrated on approaches relating to reliability and made recommendations on probability distributions that could be used for both strength and durability certification.

In 1976, members of the [now] Structures Branch of the Aeronautical Systems Center (ASC/ENFS) wrote a paper [*2*] that reflected the status of the certification process in the Air Force at that time. This paper painted a rather bleak picture, mainly because the technology base for composites had not matured. The value of this paper was that it examined the potential for certification of composites within the guidance of the USAF Aircraft Structural Integrity Program (ASIP). In addition, it cited the need for the technology development required for certification of future aircraft.

By 1981, the USAF laboratories had made sufficient progress in technology to motivate ASC/ENFS to update [*3*] the proposed approach of the 1976 paper. The Fatigue Sensitivity Program and the Environmental Sensitivity of Advanced Composites Program significantly influenced their thinking. In the 1981 paper, the authors suggested an approach on the primary aspects of composite structural certification. However, this paper did not have the benefit of the results of the Wing/Fuselage Critical Components Program [*4*] and the Damage Tolerance of Composites Program [*5*]. Consequently, certain aspects of the 1981 version of the certification process were lacking.

The major turning point in composite certification for the USAF came with the Wing/Fuselage Critical Components Program and the Damage Tolerance of Composites Program. ASC/ENFS closely followed these programs from their inception since they realized that these programs could resolve most of the remaining issues for the certification of composite structures. At the completion of these programs, they incorporated the results in the military specification AFGS-87221A released in 1990.

The USAF used the requirements in AFGS-87221A for establishing the contract for the F-22 in 1990. Tables 1 and 2 summarize the requirements of this specification.

TABLE 1—*Low-energy impact (tool drop).*

Zone	Damage Source	Damage Level	Requirements
1 High probability of impact	12.7 mm diameter solid impactor Low velocity Normal to surface	Impact energy smaller of 8.16 Joules than visible damage (2.54 mm deep) with minimum of 5.44 Joules	No functional impairment or structural repair required for two design lifetime and no water intrusion No visible damage from a single 5.44 Joule impact
2 Low probability of impact	Same as Zone 1	Impact energy smaller of 8.16 Joules than visible damage (2.54 mm deep)	No functional impairment after two design lifetimes and no water intrusion after field repair if dmage is visible

TABLE 2—*Low energy impact (hail and runway debris).*

Zone	Damage Source	Density	Requirements
All vertical and upward facing horizontal surfaces	Hail 20.3 mm diameter Specific gravity = 0.9 27.4 m/s Normal to horizontal surfaces 45 deg angle to vertical surfaces	Uniform density 20.3 mm on center	No functional impairment or structural repair required for two design lifetimes No visible damage
Structure in path of debris	Runway debris 12.7 mm diameter Specific gravity =3.0 Velocity appropriate to system		No functional impairment for two design lifetimes and no water intrusion after field repair if damage is visible

By this time, the USN had completed the certification of composites in the F-18 and the AV-8B aircraft and they were in the process of certifying the composites in the V-22 and the A-6 wing replacement. They adopted the lower of a B-basis allowable or 85% of the mean for an allowable for strength. They required a component test program that included environmentally conditioned static and fatigue test specimens. They loaded the fatigue test components as well as the full-scale fatigue test article with a severe (critical point in the sky) spectrum. The full-scale static test article and the fatigue test articles did not need to be environmentally conditioned. They required an environmental knockdown on the full-scale static test results. The full-scale fatigue test article was cycled for two lifetimes of severe usage. Later, the USN added requirements for damage tolerance. They required that the structure, after being damaged to the point of being readily detectable with an external visual inspection, have an ultimate strength capability fully compensated for the knockdown described above. They did not allow growth of this damage from cyclic loading.

Subsequently, the USAF and the USN came under considerable pressure from the Department of Defense to have a joint specification for certification of all structures, including composites. They initiated this effort in 1994 and completed it in 1996. The product of this effort was a Joint Service Specification Guide named JSSG-2006.

Current Approach to USAF Composites Certification

The USAF had previously qualified several composite structures for flight. Among these are the F-111 horizontal tail, the F-4 rudders, the A-7 outer wing, the F-16 empennage, and the B-1 horizontal tail. Each of these structures was qualified for flight on an ad hoc basis. Consequently, there was little commonality in the qualification processes. For example, the manufacturers subjected the A-7 outer panel to an environmentally conditioned durability test and the F-16 horizontal tail to a proof test to ensure its structural integrity.

Experience in the development of the process for certification has shown that the ASIP, as defined in MIL-HDBK-1530, is flexible enough for qualifying composite structures. MIL-HDBK-1530 is mandated by an Air Force Policy Directive and Instruction for ASIP. The USAF augments MIL-HDBK-1530 with JSSG 2006, which provides the detailed guidance for composite structures. The major difference between the applications for metal aircraft components and composite aircraft components is a change of emphasis in several of the ASIP elements. The five major tasks that comprise ASIP are

I. Design Information
II. Design Analyses and Development Tests

III. Full-Scale Testing
IV. Force Management Data Package
V. Force Management

Each of these major tasks contains elements that are appropriate to the task heading.

Task I addresses several aspects relating to the composites. It provides the guidance in the area of structural design criteria for strength, damage tolerance, durability, flutter, vibration, sonic fatigue, and weapons effects for both the metal and composite structural elements. For composites, the analyst should place particular emphasis on the issue of battle damage from weapons since the containment of this damage may well dictate the design configuration. In addition to a composite design that can survive weapons damage, the design must also be repairable from in-service damage to maintain operation readiness. Another Task I effort that the USAF must consider carefully is the selection of the design usage. They must adequately define the design missions such that they properly represent potentially damaging high load cases.

In Task II of ASIP, there is an element for the establishment of material allowables. The AFGS-87221A guidance is use B-basis allowables from MIL-HDBK-5 for tested structural components. The allowables for other components should be either A-basis or S-basis from MIL-HDBK-5. All allowables should include the effects of the environment. The temperatures are from the design operational envelope of the aircraft and the moisture conditions range from dry to the end of lifetime condition expected from a basing scenario that is representative of the worst expected moisture exposure.

The allowable for a given flight condition should be based on the temperature appropriate for that flight condition combined with the most critical of the range of possible moisture conditions. Since the strength of a composite structure is inherently dependent on the layup of the laminate, geometry, and type of loading, the B-basis allowable should include these factors. However, the cost of a test program involving the number of complex components necessary to determine the B-basis allowable could be prohibitive. An alternative approach could be to determine a B-basis allowable from coupon data generally representative of layup and loading. This allowable divided by the mean strength of the coupons would be the fraction of the strength allowed when interpreting the results of single complex component tests. Kan showed [*1*] that the scatter in strength of composites is greater than that exhibited by metal structure. He quantified this scatter by showing that a Weibull shape number for composite strength is approximately 20. The Weibull shape number for aluminum structure is somewhat larger, indicating a smaller coefficient of variation. It appears that a Weibull shape number of approximately 25 is representative of the aluminum materials. Probabilistic analyses show that the relative risk between the aluminum structure and the composite structure is significant. However, the absolute risk is low enough to support the use of a B-basis allowable for both metals and composites. A factor of safety of 1.5 is appropriate for use with the allowables derived above.

The AFRL programs alluded to earlier demonstrate that composite structures are relatively insensitive to low-cycle fatigue loading for the low stress cycles, but may suffer damage by the higher stress cycles. Unfortunately, the database from which one may derive high stress cycles for a new aircraft is somewhat meager. Consequently, the USAF will need to carefully define the composite structure usage in Task I.

As for metal structures, the strength, durability, and damage tolerance analyses in Task II for composites are interrelated with the design development tests also required in Task II. For support of all three of these analyses it is envisioned that the design development testing will consist of "building blocks" ranging from coupons to elements, to subcomponents and finally to components. These building block tests must include room temperature dry laminates. In addition, if the effects of the environment are significant, then the manufacturer must perform environmentally conditioned tests at each level of the building block process. In addition, they must adequately strain-gage the test articles to obtain data on potentially critical locations and for correlation with the full-scale static test. In

addition, the test program is to be performed so that environmentally induced failure modes (if any) are discovered. The design development tests are complete when the program achieves the following

—The test identifies the failure modes.
—The nonrepresentative portion of the test structure does not significantly affect the critical failure modes in the tests.
—The structural sizing is adequate to meet the design requirements.

For static test components, the USAF adjusts the failure loads to the B-basis environmentally conditioned allowable.

For durability, the relatively large scatter in fatigue test results and the potential of fatigue damage from high stresses make it difficult to establish a test program that will ensure the durability of the composite components. Experience, however, has shown that the durability performance of composites is generally excellent when the structure is adequate to meet its strength requirements. Therefore, the thrust of the durability test should be to locate detrimental stress concentration areas not found in the static tests. An acceptable way to achieve this goal is to test the durability components to two lifetimes with a spectrum that the USAF expects to be the upper bound of loading for the aircraft. One possibility of acquiring this spectrum is to use the "worst point in the sky" approach that has been used extensively by the USN. When the effects are significant, the durability tests for design development tests should include moisture conditioning. In addition to the testing performed to the design usage spectrum, tests should determine the sensitivity to potential usage changes. In addition, it is evident from the approach described above that separate tests may be appropriate for the metallic and mixed metallic and composite structural parts.

Composite structural designs (as well as metal) should minimize the economic burden of repairing damage from low-energy impacts such as tool drops. To accomplish this goal, it is useful to divide the structure into two regions. The first region is where there is a relatively high likelihood of damage from in-service sources such as maintenance. The second region is where there is a relatively low probability of the structure sustaining damage from these sources. Table 1 gives the specific guidance for these two areas. There are two other threats to the structure that may cause an economic burden. These threats are hail damage to parked aircraft and runway debris damage to aircraft from ground operations. The recommended hailstone size for which the structure should not sustain damage was chosen such that this size or smaller was representative of 90% of hailstorms. The USAF chose the runway debris size to include most of the potentially damaging objects found in ground operations. The velocity of these objects is dependent on the weapon system. Table 2 gives details of the hail and runway debris guidance. The loading spectrum and environmental conditioning for the testing associated with the guidance given in Table 1 and Table 2 should be the same as that described above for the durability tests.

In addition to the threats described above, safety of flight structure should be able to meet other damage threats. These threats are those associated with manufacturing and in-service damage from normal usage and battle damage. Table 3 describes the non-battle damage sources for manufacturing

TABLE 3—*Initial flaw/damage assumptions.*

Flaw/Damage Type	Flaw/Damage Size
Scratches	Surface scratch 101.6 mm in length and 0.51 mm deep
Delamination	Interply delamination equivalent to a 50.8-mm-diameter circle with dimensions most critical to its location
Impact damage	Damage from a 25.4-mm-diameter hemispherical impactor with 136 Joules of kinetic energy or with the kinetic energy required to cause a dent 2.54 mm deep, whichever is less

initial flaws and in-service damage. The design development tests to demonstrate that the structure can tolerate these defects for its design life without in-service inspections should utilize the upper-bound spectrum loading and the environmental conditioning developed for the durability tests. These two lifetime tests should show with high confidence that the flawed structure will meet the residual strength guidance in Table 4. This table shows the loads associated with various categories of inspection. For example, for the "Walk Around Visual" category, the load is the maximum load expected in ten magnified by 100 or 1000 flights. The residual strength guidance is the same for both composite and metallic structures. To obtain the desired high confidence in the composite components, the goal is to show that the growth of the initial flaws is insignificant. As for the durability tests, there should be additional testing to assess the sensitivity to changes in the design usage spectrum.

For many composite structures, the design for damage tolerance will establish the allowable strain. However, the design for battle damage requirements will likely influence the composite structural arrangement. For example, the need to contain battle damage to prevent catastrophic loss of the aircraft may dictate the use of fastener systems and/or softening strips. The analyst should consider the battle damage threat in the initial phase of the design. A fallout capability for battle damage based on configurations that meet all other requirements may not be adequate.

Task III of ASIP includes all of the full-scale testing elements. There will normally be a full-scale durability and damage tolerance test in the development of a weapon system; however, verification of the metal structure is the usual goal of these tests. In the cases where the design development tests can confidently establish metallic structure durability and damage tolerance capability, then the full-scale durability and damage tolerance tests may not be required. For example, a structure that is primarily composite with metallic joints proven in design development testing may fall in this category. Normally, the design development tests of Task II will be able to verify the durability and damage tolerance capability of the composite structure. The full-scale static test, however, is essential for the verification of the composite structure. This test is, of course, also essential for the verification of metallic structure. The USAF recommends testing to ultimate without environmental conditioning only if the design development tests demonstrate that environmental conditioning does not introduce a critical failure mode. To provide assurance that the component static tests were representative of the component tests, these articles must be extensively strain gaged. A test of this structure to failure should be a program option; however, a failing load test is useful in the certification process. If the design cannot meet the failure mode criterion above, then the static test should include environmental conditioning.

Tasks IV and V of ASIP relate primarily to the individual tail number tracking programs for ASIP. With one exception, the composite portion of the aircraft will not change the tracking program guid-

TABLE 4—*Residual strength requirements.*

P_{XX}*	Degree of Inspectability	Typical Inspection Interval	Magnification Factor, M
P_{FE}	in-flight evident	one flight**	100
P_{GE}	ground evident	one day (two flights)**	100
P_{WV}	walk-around visual	ten flights**	100
P_{SV}	special visual	one year	50
P_{DM}	depot or base level	¼ lifetime	20
P_{LT}	non-inspectable	one lifetime	20

* P_{XX} = Maximum average internal member load that will occur once in M times the inspection interval. When P_{DM} or P_{LT} is determined to be less than the design limit load, the design limit load should be the required residual strength level. P_{XX} need not be greater than 1.2 times the maximum load in one lifetime if P_{XX} is greater than design limit load.

** Most damaging mission.

ance in these tasks. Since the composites may be critical for the severe loading cases, then care must be exercised that these high-level occurrences are properly recorded.

Future Certification Initiatives

The certification approach described above has led to excellent structural integrity in operational aircraft. The reason is that the process, when properly applied, addresses the threats to structural integrity. However, the cost of the current approach is high. For example, the B-2 program [*6*] moved successfully through the building block process, full-scale testing, and into operational service. In all, composite coupon and more complex specimen tests for the B-2 included 160 000 specimens. The total cost of this effort is not readily obtainable, but an estimate of $1000 per test specimen would be believable. The total cost of these design development tests, therefore, approximates the cost of the full-scale durability test. The USAF now recognizes that they should make significant changes to the process of certification. The building block process as described above may not be viable in some cases. The testing of thousands of coupons has cost so much that some programs were not able to fund testing of the more important representative structural configurations. New processing techniques have made the testing of numerous coupon specimens even more of questionable value. Industry, in an effort to lower the costs of composite structures, has introduced new manufacturing techniques that have made it difficult to use coupon data to predict the performance of the structural components. The various infusion processes are examples of this change in approach. The emphasis in testing should be on deriving the allowables from ten to twenty specimens that are representative of the manufacturing process. If planned properly, this should be less costly than the current approach. Multiple test components would solve this problem, but again the cost would be high.

Another initiative that holds promise of reducing the cost of composite structures is the use of probabilistic methods. The USAF needs to determine if probabilistic methods [*7*] will provide the accuracy and versatility needed for structural integrity calculations. The incentive here is that probabilistic methods will significantly reduce the scope of the test program. These methods also have the virtue that the analyst could include both the environment and the applied loads and determine the risk of structural failure. The USAF laid the foundation for the use of probabilistic methods by incorporating an acceptable failure probability in AFGS-87221A. They made the determination that a single flight probability of failure of 10^{-7} or less was acceptable.

The impact criteria for damage tolerance in many cases determine the allowable strains in the structure. The USAF derived the current guidance for impact energy from the Damage Tolerance of Composites Program performed by Boeing and Northrop. They intended that the impact energy in Table 3 be the once-per-fleet-lifetime magnitude. Experience has shown that the strains consistent with this energy criterion provide good operational performance. The criterion in Table 3 could be too conservative. However, the database to make this judgment is not readily available. The problem is in identifying the least upper bound of the impact energies that the aircraft population could expect to encounter in service. The judgment at the time of the Damage Tolerance of Composites Program was that the impact energy should be limited if the impact caused a dent of 2.54 mm. The use of this concept could be unconservative since it supposes that someone will identify the damage in a walk-around inspection. Although the USAF has not determined that they should change the impact energy criteria, they are open to its reconsideration.

AFGS-87221A was silent on the use of bonding. The USAF earlier believed that manufacturers used adequate quality control measures to ensure that bonds had acceptable structural integrity. They reexamined this view and decided that the experience with bonds may not justify confidence in the quality control procedures.

The threats to structural integrity of bonded structure are many. One of them is environmental degradation. A bond could initially have apparently adequate strength, but could degrade with time. The degradation process is poorly understood, but based on successes of many repairs in the field and

those made in a factory, the use of strict quality controls during the bonding process appears to solve the problem. Another threat to bond integrity is that the bond did not initially have adequate strength. Contamination in the bonding process is one cause for this problem. This is a difficult threat to overcome because there are no known methods to determine the bond strength by a nondestructive inspection. However, there is evidence that a bond made under strict quality control conditions appears to have its intended strength.

To ensure a bond will have the strict quality control conditions required to rely on its initial strength and its resistance to environmental degradation, one could use the five elements in the technology transition process for materials and processes [*8*]. From a study of the successful transitions of structural technologies from the laboratory to engineering and manufacturing development, the USAF found that five factors constituted a common thread among these successes. In addition, they found that these five factors were essential to the successful completion of the tasks of the MIL-HDBK-1530. These five factors are

—Stabilized material and/or material processes
—Producibility
—Characterized mechanical properties
—Predictability of structural performance
—Supportability

The USAF did not attempt to establish a ranking of importance of these factors. A deficiency in any one of the factors could constitute a fatal defect. The manufacturer should address these elements in the qualification of a bonded structure.

The government can go only so far in criteria modification for the development of composite structures. Innovative designs by the manufacturer have the largest potential for both cost and weight savings. They should work on designs that are inherently resistant to battle damage. They could eliminate many concerns of the certification authorities through designs that are fail-safe. The development of fail-safe designs in composite structures could be as important as the use of this concept has been in metal structures. Another initiative is to remove the inherent weaknesses in composite structures, such as interlaminar strength. One approach that appears promising is the use of "Z-pins." This innovation should remove concerns about bonded joints and should enhance battle damage resistance.

Summary

The USAF has found that that they can easily tailor the Aircraft Structural Integrity Program to provide the essentials of a certification program for composite structures. The current program as described will provide a structure that is safe and economical in operational service. However, this program leads to high costs in the engineering and manufacturing phase of development that could discourage the use of composites. Therefore, the USAF could lose the benefits of being virtually free from fatigue cracking and corrosion. The challenge, therefore, is to reexamine the building block process and perform the tests that truly contribute to the process of qualifying the structure. Probabilistic methods may be the key to both cost and weight reduction. They deserve a critical examination to determine if the potential benefits are achievable. The future for composite structures looks promising, but industry and government must work together to ensure that the promise is realized.

References

[*1*] Whitehead, R. S., Kan, H. P., Cordero, R., and Saether, E. S., "Certification Testing Methodology for Composite Structures," Prepared under contract no. N62269-84-C-0243 for the Naval Air Development Center, Warminster, PA, Dec. 1985.

[2] Goodman, J. W., Lincoln, J. W., and Bennett, T. H., "The Air Force Structural Integrity Program," AIAA paper 77-460 presented at the AIAA/ASME Aircraft Composites Symposium, San Diego, CA, 24 March 1977.

[3] Goodman, J. W., Lincoln, J. W., and Petrin, C. L., Jr., "On Certification of Composite Structures for USAF Aircraft," AIAA paper 81-1686 presented at the AIAA Aircraft Systems and Technology Meeting, Dayton, OH, 11 Aug. 1981.

[4] Whitehead, R. S., Kinslow, R. W., and Deo, R. B., "Composite Wing/Fuselage Program," AFWAL-TR-3098, Feb. 1989.

[5] Horton, R. E., Whitehead, R. S., et al., "Damage Tolerance of Composites," AFWAL-TR-87-3030, July 1988.

[6] Grimsley, F. M., "B-2 Structural Integrity Program," 36th AIAA/ASME/ASCE/AHS/ASC Structures, Structural Dynamics and Materials Conference, April 1995.

[7] Chamis, C. C. et al., "Probabilistic Assessment of Fracture Progression in Composite Structures," *Proceedings of the USAF Structural Integrity Conference,* Dec. 1998.

[8] Lincoln, J. W., "Structural Technology Transition to New Aircraft," *Proceedings of the 14th Symposium of the International Committee on Aeronautical Fatigue,* EMAS Publication, West Midlands, UK, 1987, pp. 619–629.

Robin Olsson,[1] *Leif E. Asp,*[1] *Sören Nilsson,*[2] *and Anders Sjögren*[1]

A Review of Some Key Developments in the Analysis of the Effects of Impact Upon Composite Structures

REFERENCE: Olsson, R., Asp, L. E., Nilsson, S., and Sjögren, A., **"A Review of Some Key Developments in the Analysis of the Effects of Impact Upon Composite Structures,"** *Composite Structures: Theory and Practice, ASTM STP 1383*, P. Grant and C. Q. Rousseau, Eds., American Society for Testing and Materials, West Conshohocken, PA, 2000, pp. 12–28.

ABSTRACT: This paper reviews work at the Aeronautical Research Institute of Sweden, and addresses major issues of importance in evaluating the effect of impact on composite structures. Some more extensive reviews of work by other researchers are referenced. The paper addresses impact response and damage formation, damage characterization, and residual strength and stability by combination of experiments and analysis. Studies showing that impact response type depends on impactor-plate mass ratio are presented. Small mass impact is generally more critical at a given configuration and energy. Analytical models for small mass impact and for damage initiation and growth during large mass impact are discussed. Rate dependency of matrix-dominated properties is briefly discussed. Geometric and constitutive characterization of impact damage zones is presented and the influence of degraded properties demonstrated. The use of an FE-based plate model to simulate delamination growth due to sublaminate buckling and panel skin buckling in stiffened panels after impact is described. Skin buckling causes a steep increase in delamination strain energy release rate and should be prevented.

KEYWORDS: buckling, carbon fiber composites, composite materials, composite structures, damage assessment, delamination growth, impact damage, impact resistance, residual strength

Impact damage may cause severe reductions in the strength and stability of laminated composite structures. The reductions in compressive properties are usually the most critical. For this reason extensive studies in many countries have been devoted to impact on composite structures [*1,2*]. A methodology for treating impact events and their effect on the residual strength of laminates was suggested in Ref *3*. The methodology is based on a building block approach, which divides the complex problem into a number of separate subproblems to be addressed sequentially. Most experimental studies have focused on *impact damage resistance*, which deals with the damage caused by an impact, and *impact damage tolerance*, which deals with the effect of the damage on strength and stability of the structure (Fig. 1). A more limited number of studies have focused on *impact response*, i.e., the structural response and formation of damage during impact, which is necessary to fully understand the factors governing impact resistance. Models for analysis of impact response and residual strength have gradually been developed to reduce the large costs of certification tests and to make design more efficient. The ultimate goal of the work on impact is to efficiently combine impact resistance and impact damage tolerance in design to minimize undesired effects of a given impact. This may be termed a strive for *impact tolerance*.

[1] Research engineers, Composite Mechanics Section, Structures Department, The Aeronautical Research Institute of Sweden, Box 110 21, SE-161 11 Bromma, Sweden.

[2] Scientific coordinator, Composite Mechanics Section, Structures Department, The Aeronautical Research Institute of Sweden, Box 110 21, SE-161 11 Bromma, Sweden.

Copyright© 2001by ASTM International www.astm.org

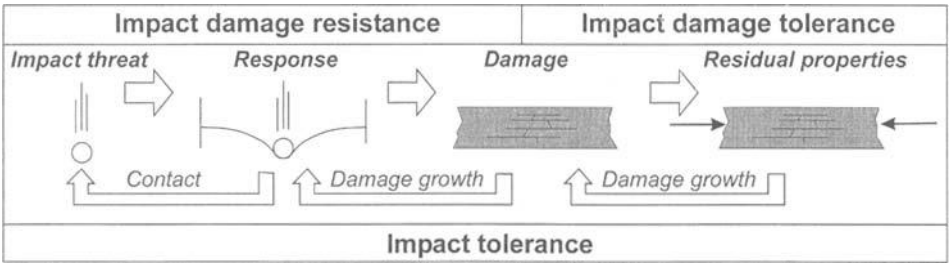


FIG. 1—*Major concepts of interest when considering effects of impact.*

The Aeronautical Research Institute of Sweden (FFA) has extensive experience in experiments and analysis of impact on composites. The work on impact and related subjects, such as contact problems, dynamical material properties, and delamination buckling and growth covers more than 50 scientific papers and reports since 1986 [*4*]. The ultimate goal of our work is to integrate the solution of each subproblem into an efficient building block methodology to model the effects of impact, which will allow prediction of impact criticality and more efficient designs. The present paper reviews work at FFA and addresses major issues of importance to evaluate the effect of impact on composite structures. More extensive reviews of work by other researchers can be found in the papers on analytical response models [*1,5*], damage characterization [*6*], and buckling-induced delamination growth [*7*].

Earlier studies at FFA were aimed at certification and to study the effect of impact on residual strength, and measurements during impact were limited. The development of response models has changed the focus to model validation and for this reason later experiments have been extensively instrumented. The overwhelming majority of impact experiments at FFA and elsewhere have been done with large mass impactors, which cause a "quasi-static" impact response. However, analytical work showed a need to consider the different response caused by small mass impactors [*5,8*]. Models developed for this response type have been validated by several experimental studies, e.g., Refs *9* and *10*. In-house impact response models may be used to predict damage initiation [*11*]. The interaction between moderate damage growth and structural response is also modeled well for sandwich panels, while our present models only provide bounds for the behavior of monolithic panels [*11*]. The goal to improve design of real structures and the importance of impactor mass, geometry, and material motivates surveys of realistic impact threats [*12*].

Comprehensive studies have also been done in *impact damage characterization* by use of thermal deplying to describe delamination shape and fiber fractures in each ply, ultrasonic C-scan and optical microscopy of sections [*6,10,13,14*]. Analytical and computational models of delaminations after impact in this paper are based on the largest delaminated region as obtained from C-scan. Research has recently begun in geometrical and constitutive characterization of the impact damage zone for a range of impact cases [*15*].

The research on *impact damage tolerance* has been focused on compressive failure. Under compression loads, delaminations formed at impact may buckle and grow, causing further decrease in the compressive load carrying capacity of the structure [*1*]. Modeling work has focused on simulation of buckling induced delamination growth, and a program package has gradually been developed to address fracture mode separation, local delamination buckling of sublaminates with contact and interaction with global skin buckling [*7,16–18*]. A recent extension allows analysis of impacted skin-stiffener panesl [*19*]. Previous experiments have demonstrated the need to also consider other failure mechanisms and the change of stiffness properties in the damaged region [*15,19,20*]. Furthermore, the multitude of delaminations, matrix cracks and fiber fracture precludes modeling of each feature and necessitates a degree of simplification. The future development of the program will include consideration of degraded material properties in the damage zone and the competition or interaction be-

tween buckling-induced delamination growth and other failure mechanisms, such as ply failure and in-plane "notch type" failure due to stress concentrations. A review of available notch failure criteria for laminates and various failure criteria for sandwich panels was given in Ref *21*.

The following sections give a more detailed description of the work on impact response and damage formation, impact damage characterization and residual strength and stability. All results and analyses apply for Hexcel HTA/6376C carbon/epoxy prepreg with ply data $E_{11} = 140$ GPa, $E_{22} = E_{33} = 10$ GPa, $G_{12} = G_{13} = 5.2$ GPa, $G_{23} = 3.9$ GPa, $\nu_{12} = \nu_{13} = 0.30$, $\nu_{23} = 0.50$ $t_{ply} = 0.13$ mm, $G_{Ic} = 260$ J/m^2, $G_{IIc} = 600$ J/m^2 [*11*], and $G_c = 450$ J/m^2 for $G_I/G_{II} \approx 1$ [*7*].

Impact Response and Damage Formation

Response Types

In general, an impact initiates elastic waves propagating from the impact point. Material damping and the energy diffusion associated with two- or three-dimensional wave propagation results in a decaying influence of the corresponding waves [*2*]. Thus, for impact times in the order of the transition time for through-the-thickness waves, the response is dominated by three-dimensional wave propagation (Fig. 2*a*). For longer impact times, the response is initially governed by flexural waves and shear waves (Fig. 2*b*). For times much longer than the time needed by these waves to reach the plate boundaries the lowest vibration mode of the impactor-plate system predominates (Fig. 2*c*). The resulting response is quasi-static in the sense that deflection and contact load have the same relation as in a static case.

The response dominated by through-the-thickness waves is typically associated with ballistic impact while accidental impact normally results in impacts of longer duration. Theoretical studies [*5,22,23*], and several experiments [*9*] show that the impact response type is governed by mass ratios and not by impact velocity. Thus, a distinction between large mass impact and small mass impact is more relevant than the common distinction between "high velocity" and "low velocity" impact. As shown in Ref *5*, wave propagation governs the response for impactor masses smaller than one-fifth of the plate mass affected by impact, e.g., hail and runway debris (Fig. 3*a*). The largest plate mass which can remain unaffected of boundaries during a wave controlled impact is determined by the flexural wave speed in different directions and the distance to the first boundary reached by these waves. Impactor masses larger than twice the entire plate mass provide a sufficient condition for quasi-static (large mass) impact [*5,22*], (Fig. 3*b*). Figure 4 shows differences in response and damage due to 10 J impacts with a large and small mass on a clamped 127 × 127 × 6 mm laminate [*10*].

Damage Initiation and Growth

Evidently, response models for undamaged plates may predict damage initiation. Matrix cracks normally initiate first, followed by delamination and eventually fiber fracture. Thus, modeling of im-

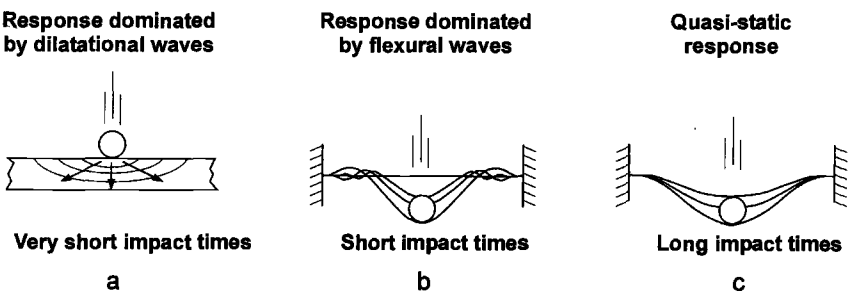


FIG. 2—*Response types during impact on plates* [5].

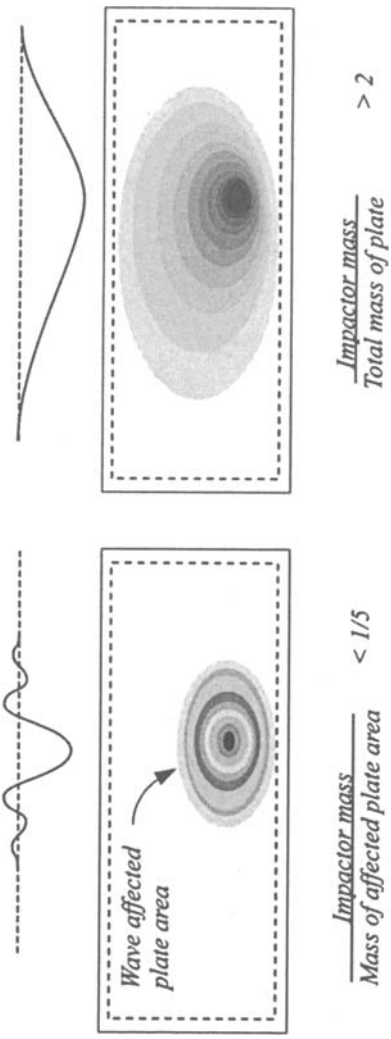


FIG. 3—*Mass criteria for determination of response type* [5].

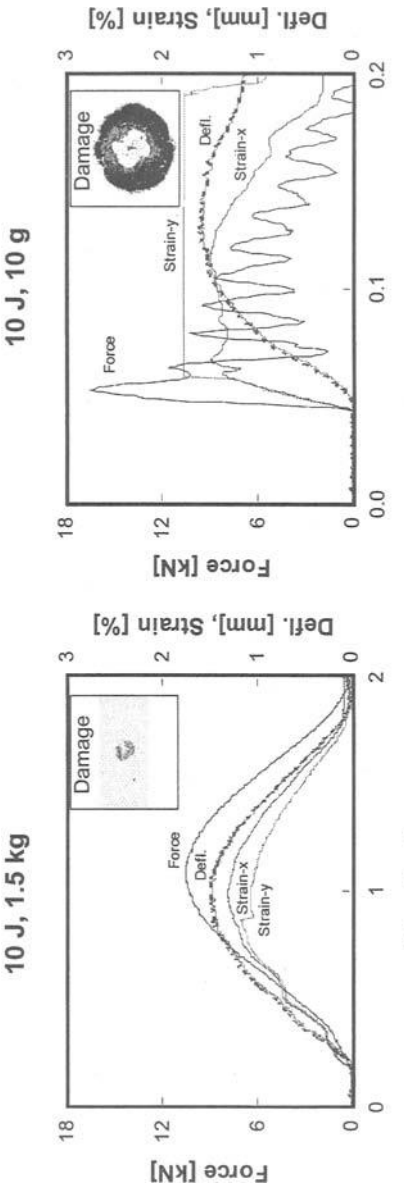


FIG. 4—*Response and damage due to 10 J impact by a large and small mass* [10].

pact damage initiation requires the composite constitutive properties at impact rates of strain. As fiber-dominated properties of CFRP are known to be fairly rate insensitive [*2*], FFA has focused on investigating strain rate dependence of matrix-dominated properties. Dynamic delamination experiments have been done with $+5°/-5°$ interfaces in single-edge notched specimens in a hydraulic load frame [*25*], and with 0°/90° in double-edge notched specimens in a split Hopkinson bar apparatus [*26*]. In both cases the crack velocity influenced the strain energy release rate, which reached peak values at maximum speed (approximately 600 m/s) of about three times the initiation values. The initiation toughness was generally much lower than that for DCB tests which motivates further work to investigate the influence of specimen type and geometry. In contrast to the delamination tests, consistent results were obtained for dynamic out-of-plane tensile properties by use of miniature dogbone specimens in a split Hopkinson bar [*27*]. High-speed Moiré photography was used to study the local strain field at strain rates between 100/s and 800/s and to monitor crack growth. Crack speeds up to 2300 m/s were observed at fracture. An increasing strain rate caused moderate increase in failure stress and strain but no increase in modulus. Therefore, the HTA/6376 material is assumed strain rate independent in our impact models.

At impact, delaminations initiate below the contact region at interfaces with high interlaminar shear stresses. In thin laminates the contact stresses are low and delaminations initiate close to the midplane as predicted from classical plate theory. When the contact stresses are high, such as in thick laminates, delaminations initiate close to the loaded surface. However, the influence of contact stresses vanishes within two contact radii, typically a few millimeters [*2*]. Thus, further growth must occur along the plate midplane after a gradual change of delamination plane. A solution for the axisymmetric problem of a centrally loaded clamped plate with an arbitrary number of symmetrically distributed delaminations was derived in Refs *28* and *29*]. For small deflections the critical load, F_{cr}, for growth of an initial delamination is independent of the delamination radius. The critical load is then given by

$$F_{cr} = \pi\sqrt{32DG_{IIc}/(n+2)} \tag{1}$$

where D is the plate stiffness, G_{IIc} the mode II interlaminar toughness, and n is the number of delaminations. Obviously, a single delamination ($n = 1$) will first appear in the most critical interface close to the midplane. The solution in Refs *28* and *29* was derived for clamped edge conditions. However, an FE-analysis of a plate of 50 mm radius and 2 mm thickness uniformly loaded within 1 mm from the center gave identical results for simply supported conditions [*11*]. For delaminations between 10 and 40% of the plate radius the results from Eq 1 deviated less than 0.3% from results obtained in 3-D FE analysis.

For large mass impact the response may be predicted by a spring mass system involving the impactor mass M, the effective plate mass M_p^*, the contact stiffness k_c, shear stiffness k_s, bending stiffness k_b, and membrane stiffness k_m of the plate under static load (Fig. 5) [*11*]. An elastic version of this model, without a limit on the load carried by shear and membrane action, was suggested for axisymmetric problems [*30*], but may easily be extended to orthotropic rectangular plates [*2*]. A simpler two mass elastic model [*31*] with a linearized contact stiffness yields poor results when the impactor mass and plate mass are of the same order. The latter model, which determines the contact stiffness from the peak contact load on a half space, may be significantly improved by using the average load on a flexible plate [*2*].

A Hertzian contact law gives poor predictions for thin plates, where large deflection effects cause a stiffer contact behavior. However, the plate compliance in such cases is so large that simplifications in the contact model have a negligible effect. The axisymmetric model in Ref *30* was modified for square plates by replacing k_b with the corresponding stiffness of a centrally loaded square plate, and by replacing the plate diameter in k_s and k_m with the geometric average of the width and diagonal of the plates [*11*]. Note that the membrane stiffness provides an *additional* contribution to the critical

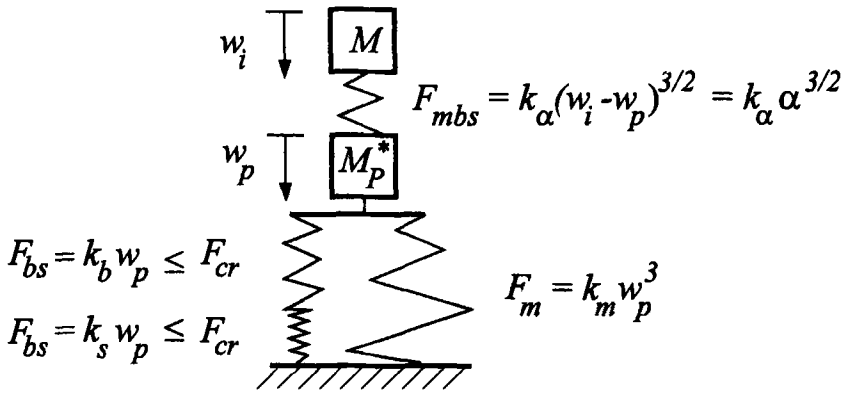


FIG. 5—*Structural model for quasi-static impact response* [11].

load for delamination growth Eq 1. With this modification the response model (Fig. 5) was used to predict critical impact load and impact energy in various quasi-isotropic and cross-ply laminates [*11*], (Figs. 6 and 7). It may be concluded that Eq 1 provides a fairly good conservative prediction of the critical load, which may be further improved by considering membrane effects. Critical impact energies can be significantly improved by considering the energy consumed by indentation and membrane effects as given by the nonlinear solution (Fig. 7).

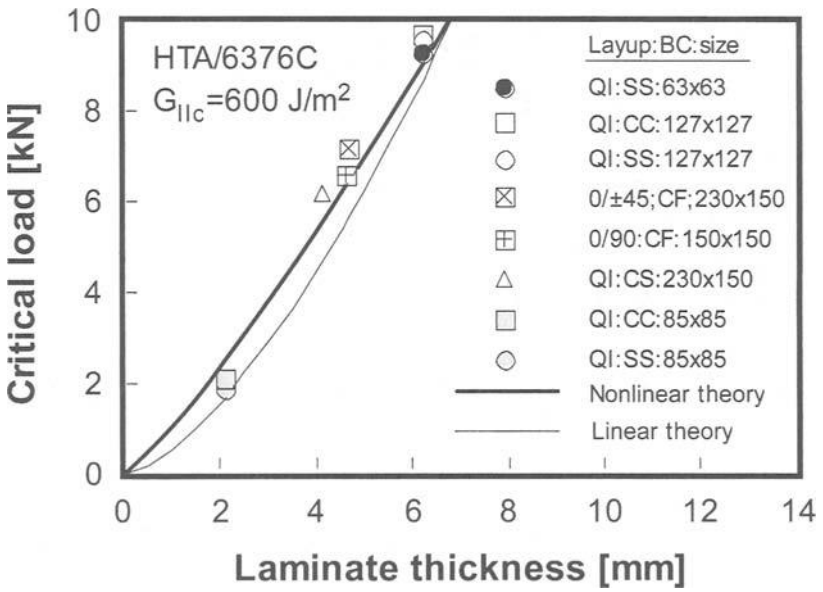


FIG. 6—*Predicted and observed critical load for delamination growth* [11]. *(QI = quasi-isotropic, 0/90 = cross-ply, C = clamped, F = free, S = simply supported).*

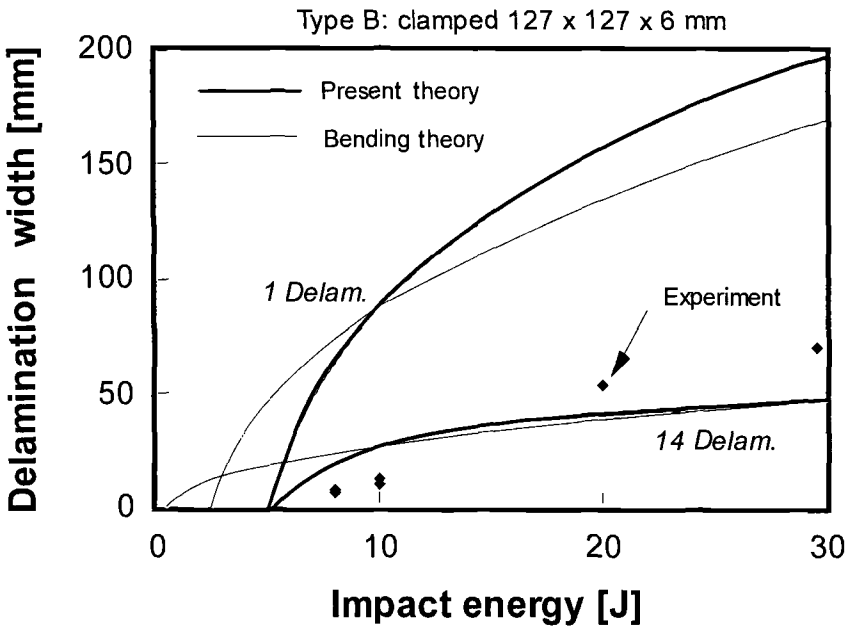


FIG. 7—*Predicted and observed delamination width vs. impact energy in a 127 × 127 × 6 mm clamped laminate* [11].

Further damage growth is highly dependent on the number of delaminations developing after the first delamination. Deplying of a quasi-isotropic layup indicated that the average delamination area per interface was 30% of the base area of a cylinder encompassing all delaminations [*13*]. An extension to orthotropic laminates should replace the circular cylinder by an elliptic cylinder through orthotropic rescaling as outlined in Ref *2*. Figure 7 shows solutions for a single circular delamination and a "saturated" case with delaminations in 30% of the interfaces, i.e., 14 circular delaminations.

Impact Damage Characterization

An impact damage is complex in its features and depends on the geometry and boundary conditions of the structure. A good understanding of the impact, and the resulting damage, is therefore vital for modeling the behavior of a composite structure after impact.

At FFA several experimental studies have been carried out to characterize the impact damage for different geometries and boundary conditions. Early tests were done with the brittle epoxy system T300/914C while in later tests the tougher epoxy system HTA/6376 has been used. Laminate thicknesses have ranged from 2 to 6 mm and layups have usually been quasi-isotropic, although a few studies have been done on orthotropic layups [*4,6*]. Four geometries have mainly been used in the tests: clamped 800 × 200 mm panels to simulate panels common in application [*13,14*], smaller square panels to study the effect of span to thickness ratio and different boundary conditions [*6,10*], rectangular panels, approximately 250 × 150 mm, clamped at the short sides and simply supported at the long sides, and a few tests on clamped square panels with two sides unsupported [*6*].

Our studies show that damage growth normally initiates by matrix cracking, followed by delamination growth, and finally fiber fracture [*6,10*]. Delaminations in thick laminates with span-to-thickness ratios of 10 to 20 typically initiate close to the impacted surface, while delaminations in thin lam-

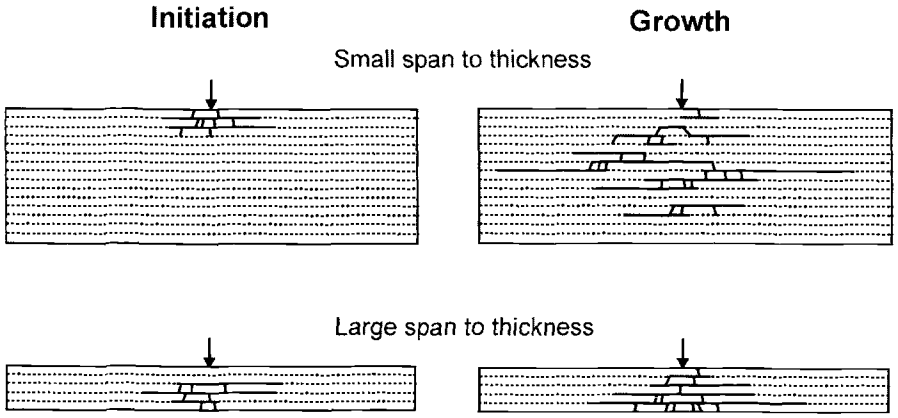


FIG. 8—*Delamination growth sequence in thick and thin laminates* [6].

inates initiate close to the midplane [*6,10*] (Fig. 8). In the following, the "upper face" refers to the impacted surface. Further delamination growth in thick laminates occurs in a "barrel shaped" region by growth of delaminations around the midplane, although a single large delamination may occur at the lowermost interface [*6,10*]. Delamination growth in thin laminates occurs in a conical region by growth of delaminations towards the lower face of the laminate [*6,13*]. Delamination growth in thick laminates may be extensive, while the growth in thin laminates seems to be suppressed by significant membrane effects and the early occurrence of fiber failure and penetration.

Delaminations typically occur between plies of different orientation, and increase in size with thickness and mismatch angle of the plies [*13*]. A characteristic impact damage consists of an array of interconnected matrix cracks and delaminations which separate the laminate into sublaminates [*24*]. The individual delaminations are more or less peanut shaped, extending along the fibers of the neighboring lower ply. In contrast, cracks with fiber failures generally follow the fibers of the neighboring upper ply and appear below delaminations as extensions of a matrix crack [*6,10*]. The width of the zone where fiber fractures are observed generally range from one-third to one-half of the maximum delamination width [*6,10*].

In the stability and residual strength analyses of an impacted composite structure one needs to understand how the impact has changed the constitutive properties of the damaged region. Recent studies of in-plane tensile and compressive properties in impact damage zones prior to sublaminate buckling demonstrated significant differences between thin and thick laminates [*15*]. Delaminations and matrix cracks had a negligible influence on the stiffness and significant stiffness reductions were only observed in a small central region of the thin laminates where fiber failure had occurred. In this region the tensile stiffness was reduced by 80% and the compressive stiffness by 50%. Future work will study flexural properties and the behavior at higher strains.

Residual Strength and Stability

This section concerns damage tolerance of impacted composite structures. The residual strength of an impacted composite plate is governed by delamination growth and/or by the damaged region acting as a stress raiser. The approach taken at FFA is to model the two mechanisms separately at the model development stage. When completed, the models are to be included in a residual strength-modeling package.

Modeling of delamination growth requires data of interlaminar toughness for mixed mode condi-

tions. Several studies have been performed at FFA using the Double Cantilever Beam (DCB), End Notch Flexure (ENF) and Mixed Mode Bending (MMB) tests [*32–34*]. Interpolation of data produces the material failure locus used in modeling to predict delamination growth. Modeling of damage acting as a stress raiser, on the other hand, requires data of stiffness reductions in the damaged area.

Effect of Delamination Growth

Historically, most investigations on delamination growth in laminated composite panels focus on the influence of local delamination buckling only, i.e., adopting the thin film assumption [*16,17*]. A requirement in these studies is prevention of global skin buckling. If, however, global buckling is allowed the panel may buckle in such way that local delamination buckling interacts with global buckling. Such interaction is foreseeable for deep delaminations, i.e., delamination thickness more than one-tenth of the plate thickness. Recent work at FFA has concerned development of models with general nonlinear kinematics to account for interaction of global and local buckling with contact for a panel with a single delamination of arbitrary shape located at the critical ply interface [*7,18*]. The finite-element model developed is based on nonlinear plate theory, using 4-noded mixed interpolation Mindlin/Reissner shell elements. Delaminated plates are represented by two stacked plates representing material above and below the delamination. The plates may be modeled ply by ply using the material properties and ply orientations of the individual layers. Outside the delaminated area the upper and lower segments are coupled by constraint equations to ensure displacement continuity at the plate interface. In the delaminated area, out-of-plane constraints are imposed by spring elements only active at contact. It is assumed that delamination growth is governed by linear elastic fracture mechanics parameters. The strain energy release rate, G, at local delamination growth is computed from the discontinuity in an energy momentum tensor component across the crack front [*7*].

Analysis of a plate or stiffened panel with a delamination is performed in the following steps: (1) Global buckling analysis. (2) Local buckling analysis of the delaminated member. (3) Postbuckling analysis from local buckling with contact iteration and automatic load increase until delamination growth criterion is attained. The growth criterion is currently based on the total critical strain energy release rate. (4) Delamination crack propagation by moving the FE mesh in the growth regions and continued postbuckling analysis.

By this approach, the evolution of delamination propagation is simulated by a large number of crack propagation increments. Note that the moving mesh technique maintains a smooth delamination shape and a suitable mesh at the crack front even at extensive growth. A detailed description of this technique is presented in Ref *17*. The developed model has been validated by experiments on artificially delaminated and impacted plates [*7,19*] and stiffened panels [*18*]. Below, the most important results of these studies are presented.

Numerical and experimental studies of compression loaded plates have been performed using cross-ply laminates with artificial delaminations placed after 3, 5, or 7 layers [*7*]. The loaded edges of the plates were clamped in the test machine, while the two remaining edges were free (Fig. 9). Figure 10 shows the experimental and computed load versus out-of-plane deflection results for two delamination depths. The numerical model is shown to capture the main observations regarding transverse deflections and buckling loads. Furthermore, critical loads, direction, and shape of growth were also well predicted by the model. From a practical point of view the most important result of these studies seems to be that delamination growth for all cases occurred more or less at the global buckling load. Consequently, precaution should be taken in allowing structures with delaminations to buckle globally. Another observation is that, at least for the geometries and materials studied, the so-called thin film assumption is inadequate to predict growth, even for thin delaminated members. This is illustrated in Figs. 10 and 11 where the computed load-deflection and strain energy release rate versus load for the thin film and global bending cases are depicted. In contrast to predictions by the thin film model, the maximum strain energy release rate at the delamination edge predicted by the global

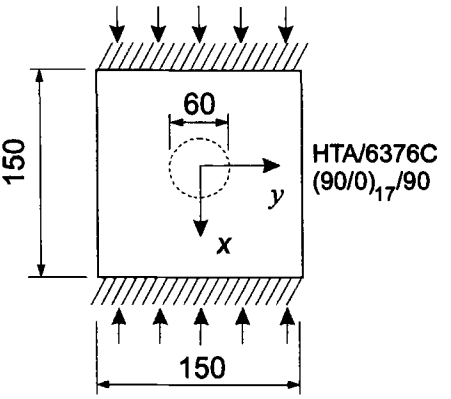


FIG. 9—*Configuration used for studies of buckling in delaminated panels* [7,18,19].

bending model is found to shoot-off as the global buckling load is approached (Fig. 11). In Ref *18* a preliminary analysis of stiffened composite panels is performed. In that study, a scheme for identification of the most critical ply interface is presented.

Test results for artificially delaminated, impacted, and undamaged plates were compared [*19*]. A difference in maximum (global plate buckling) load is conspicuous in the load versus out-of-plane deflections of the plates depicted in Fig. 12. For this particular panel the artificial delamination causes

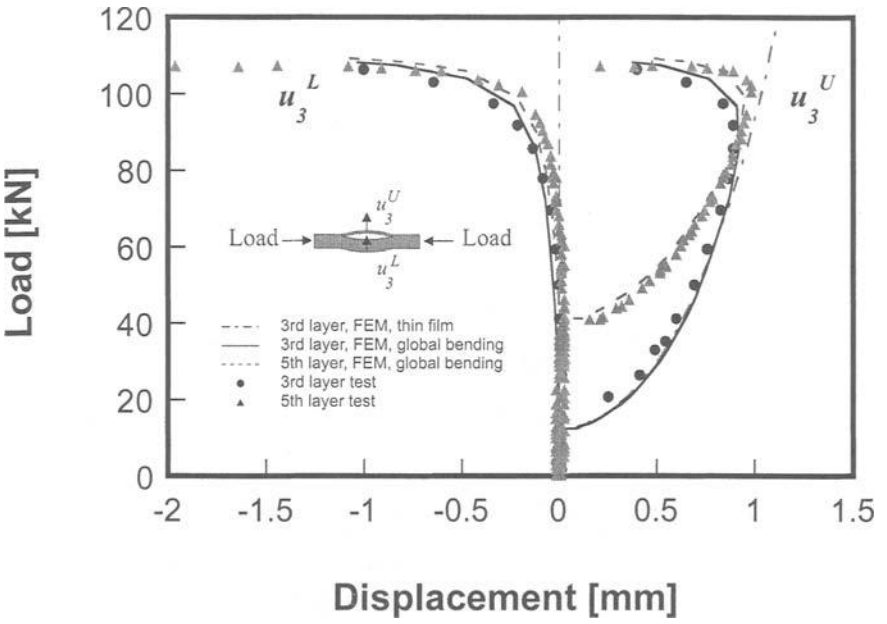


FIG. 10—*Computed and measured out-of-plane displacements for delaminations at two different depths* [7].

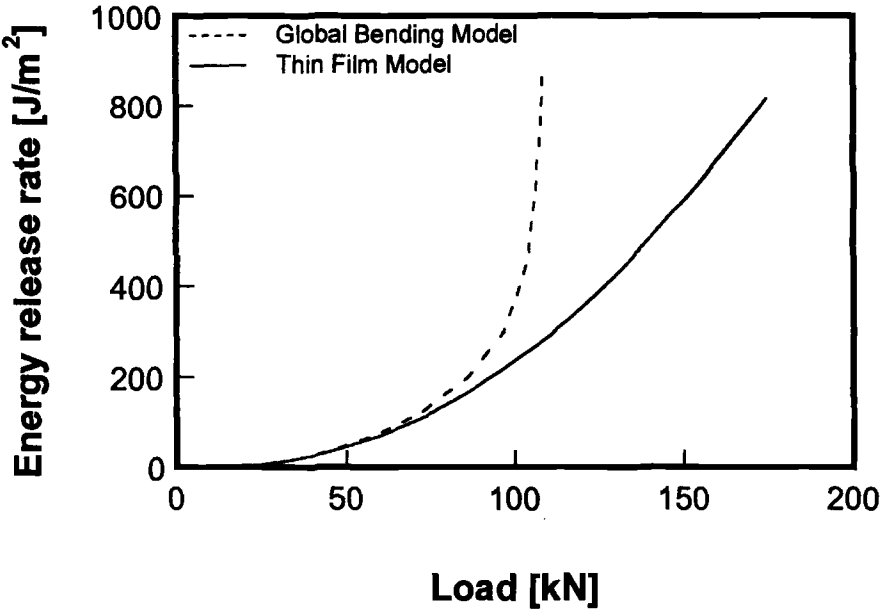


FIG. 11—*Computed out-of-plane displacements for a delamination after three layers* [7].

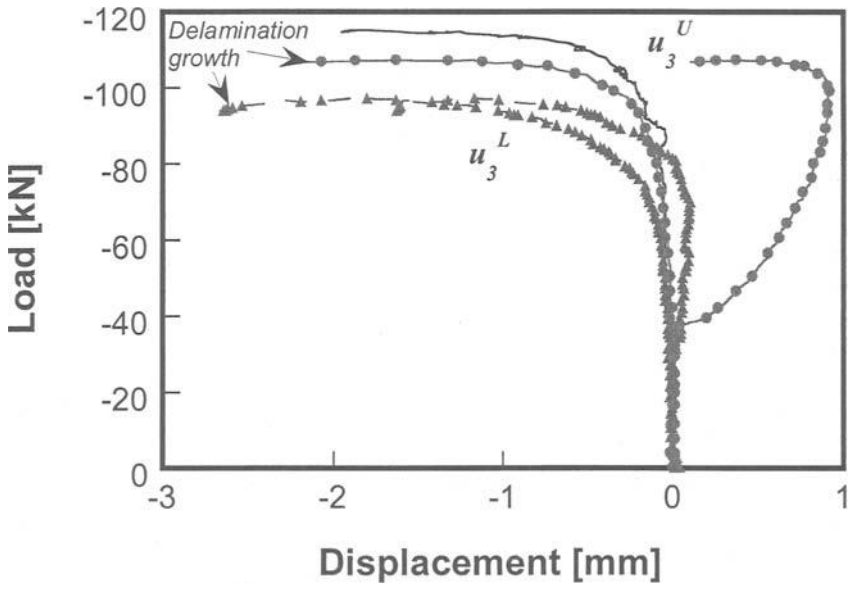


FIG. 12—*Load vs. out-of-plane displacements from experiments* [19].

a 10% reduction in global buckling load, while the reduction caused by impact damage is 20%. These results imply that the reduced stiffness in the impacted zone in some cases may have a fairly large effect on the panel buckling load. Thus, correct prediction of the buckling load of an impacted structure requires methods that consider influence/interaction of the stiffness reduction of the damaged zone. Nevertheless, both the artificially delaminated and impacted plates failed by delamination growth. Hence, the artificially delaminated plate test is appropriate for validation of models developed for residual strength predictions of impacted composite plates of the type investigated.

Effect of Reduced Stiffness in the Impact Damage Zone

In addition to delaminations, which may promote buckling-induced delamination growth, an impact damage may also be associated with local stiffness reductions. Such stiffness reductions affect delamination growth by reducing the buckling loads and cause stress concentrations which may promote in-plane "notch type" failure, as discussed in Ref *21*.

In combination with the experimental study of the constitutive properties of an impact damage a numerical study was carried out to examine how different parameters in the stiffness matrices affect the global buckling load. Figure 13 presents the retained global buckling load of the plate in Fig. 9 as a function of reduction in in-plane stiffness, [*A*]. As expected, the buckling load decreases with reduced [*A*] matrix. A large difference is, however, observed between a symmetric and an unsymmetrical soft inclusion. A 43% reduction in the [*A*] matrix reduces the global buckling load by 2% for a symmetric soft inclusion and by 15% for an unsymmetrical soft inclusion. This highlights the importance of considering thickness-wise stiffness asymmetries of the damage.

As observed in Ref *15* fiber failure in the impact damage zone causes significant local reductions of the tensile and compressive stiffness. For example, damage studies of 230 × 150 × 4 mm speci-

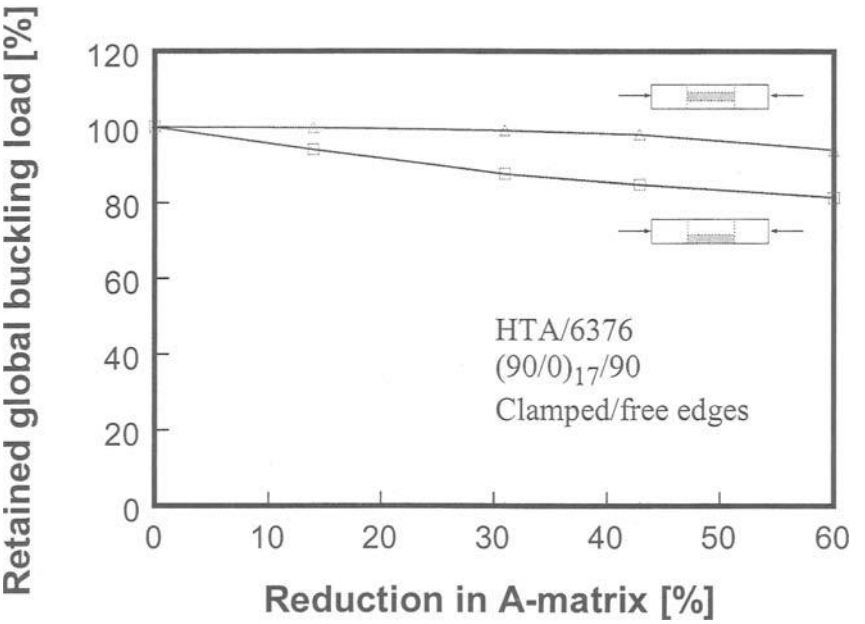


FIG. 13—*Retained global buckling load of the plate in Fig. 9 as a function of reduction in* [A] *matrix.*

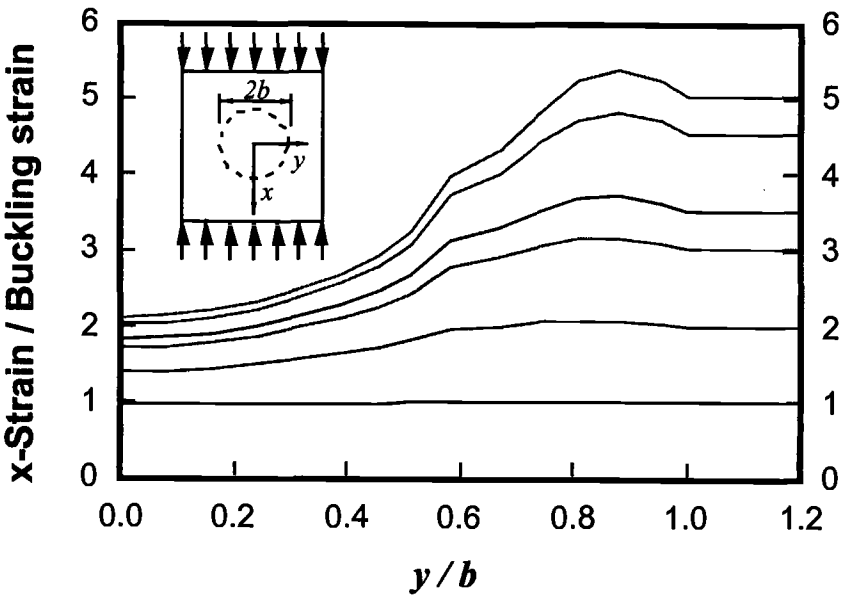


FIG. 14—*Strain distribution in a uniaxially loaded circular buckle at different far-field strains* [21].

mens impacted at 30 J [6] indicated almost complete fiber failure in all plies in about one-third of the total delamination width. Such stiffness losses cause stress concentrations, which in tension may be comparable to the effect of a hole or slit, i.e., stress concentrations of three or more in quasi-isotropic laminates. Appropriate failure criteria for this competing failure mode will be incorporated in future development of the delamination growth FE program.

In the literature it has also been suggested that a buckled sublaminate may act as a stress raiser causing in-plane failure, e.g., Refs *24* and *35*. This effect was studied by analyzing a circular delamination in an isotropic plate with the FE-based buckling delamination model presented in the Effect of Delamination Growth section. The sublaminate thickness was 1.25% of the delamination radius and the parent laminate was 20 times thicker than the sublaminate, i.e., a "thin-film" problem. Figure 14 shows the widthwise distribution of the membrane strain in the load direction normalized with the buckling strain of the sublaminate [*20*]. It is noted that the strain distribution in a postbuckled circular sublaminate differs from the Euler type of behavior of a through-width buckle, assumed in Refs *24* and *35*. Thus, the stresses and strains in the buckle *are not uniform over the width and continue to increase after buckling*. The stress concentration caused by a buckling but undamaged sublaminate is less than 10% of the far field strain, which shows that "notch type" failure primarily is caused by degraded ply properties.

Conclusions

Models and experiments have been presented to address the major issues when determining the effect of impact on composite structures. All models have been validated by extensive experiments. Impact damage resistance involves the response and damage initiation and growth during impact. Impact damage tolerance involves strength and stability due to global buckling, local delamination

buckling, delamination growth, in-plane failure, and interacting failure modes. Necessary input data for models involve damage characterization, interlaminar properties, and strain rate effects. The discussed subjects constitute elements in a building block approach aimed at design of impact tolerant aircraft structures.

The impact response type is shown to depend on the impactor versus plate mass ratio and appropriate models have been suggested for the various response types. A small mass impact on a given laminate results in earlier damage initiation and larger damage if impactor energy and tup remain unchanged. The load for initiation of delamination growth under large mass impact is almost independent of boundary conditions and delamination size if due account is taken for the membrane load contribution. The corresponding initiation energy is obtained by summing contributions due to contact, bending, shear, and membrane deformation. Further delamination growth during impact is highly dependent on the number of delaminations, but reasonable bounds for delamination size have been established.

The damage geometry and degree of fiber fracture depends on the span-to-thickness ratio and on how much the energy for damage initiation has been exceeded. Fiber fracture, which is common in thin laminates, occurs in a small central region of an impact damage and reduces both tensile and compressive stiffness, although the effect in tension is more severe. Such a stiffness asymmetry or a geometrical asymmetry of the damage through the thickness may have a strong influence on the global buckling behavior of the panel.

A finite-element based plate model has been successfully used to model buckling-induced delamination growth in plain laminates and skin-stiffener panels. The model involves an analysis of local delamination buckling and global buckling and a moving mesh routine for treating delamination growth when a growth criterion is satisfied. The most important observation is that the strong interaction between local and global skin buckling causes a catastrophic increase in the delamination strain energy release rate at global buckling. Thus, precaution should be taken in allowing delaminated structures to buckle globally.

Future work will include a more accurate prediction of the impact damage, incorporation of failure criteria for competing failure modes, and an appropriate constitutive model of the damage zone in the model for buckling-induced delamination growth.

References

[1] Abrate, S., "Impact on Laminated Composite Materials," *Applied Mechanics Reviews,* Vol. 44, No. 4, 1991, pp. 155–190.

[2] Olsson, R., "Impact Response of Composite Laminates—A Guide to Closed Form Solutions," FFA TN 1992-33, The Aeronautical Research Institute of Sweden, Bromma, 1993.

[3] Cairns, D. S. and Lagace, P. A., "A Consistent Engineering Methodology for the Treatment of Impact in Composite Materials," *Journal of Reinforced Plastics and Composites,* Vol. 11, No. 4, 1992, pp. 395–412.

[4] Olsson, R., "A Review of Impact Experiments at FFA During 1986 to 1998," FFA TN 1999-08, The Aeronautical Research Institute of Sweden, Bromma, 1999.

[5] Olsson, R., "Mass Criterion for Wave Controlled Impact Response of Composite Plates," to appear in *Composites Part A* (also FFA TN 1999-62).

[6] Sjögren, A., "Fractographic Characterization of Impact Damage in Carbon Fiber/Epoxy Laminates," FFA TN 1999-17, The Aeronautical Research Institute of Sweden, Bromma, 1999.

[7] Nilsson, K.-F., Asp, L. E., Alpman, J. E., and Nystedt, L., "Influence of Delamination Depth on the Behavior of Globally Buckled Composite Laminates," FFA TN 1999-04, The Aeronautical Research Institute of Sweden, Bromma, 1999.

[8] Olsson, R., "Impact Response of Orthotropic Composite Plates Predicted from a One-Parameter Differential Equation," *AIAA Journal,* Vol. 30, No. 6, 1992, pp. 1587–1596.

[9] Olsson, R., "Theory and Experimental Verification of the Impact Response of Composite Plates," *Proceedings, 28th Annual Technical Meeting of the Society of Engineering Science,* Gainesville, FL, Engineering Science Preprint 28.91002, 1991.

[10] Beks, F.-A., "Examination of Impact Response and Damage of Composite Laminates," FFA TN 1996-29, The Aeronautical Research Institute of Sweden, Bromma, 1996.

[11] Olsson, R., "Analytical Prediction of Large Mass Impact Damage in Composite Laminates," *Impact and*

Damage Tolerance Modelling of Composite Materials and Structures, EUROMECH Colloquium 400, London, 1999, pp. 110–117 (also FFA TN 1999-09).

[12] Olsson, R., "DAMOCLES Task 1-Deliverable: A Survey of Impact Conditions Relevant in Aircraft Composite Structures," FFAP H-1353, The Aeronautical Research Institute of Sweden, Bromma, 1998.

[13] Levin, K., "Characterization of Delamination and Fiber Fractures in Carbon Reinforced Plastics Induced from Impact," *Mechanical Behavior of Materials—VI.* Pergamon Press, Oxford, U.K., Vol. 1, 1991, pp. 519–524.

[14] Levin, K. and Östman, P., "On the Character of Neighbouring Low Energy Impact Damages in Carbon Fibre Composites," *Advanced Structural Fiber Composites. Proceedings of Topical Symposium III, 8th CIMTEC-World Ceramics Congress and Forum on New Materials,* Florence, Italy, 1994, Techna, Faenza, 1995, pp. 615–622.

[15] Sjögren, A., Krasnikovs, A., and Varna, J., "Experimental Determination of Constitutive Properties of Impact Damage in Carbon Fibre/Epoxy Laminates," *Impact and Damage Tolerance Modelling of Composite Materials and Structures,* EUROMECH Colloquium 400, London, 1999, pp. 27–34 (also FFA TN 1999-53).

[16] Nilsson, K.-F., Thesken, J. C., Sindelar, P., Giannakopoulus, A. E., and Storåkers, B., "A Theoretical and Experimental Investigation of Buckling Induced Delamination Growth," *Journal of Mechanics and Physics of Solids,* Vol. 41, No. 4, 1993, pp. 749–782.

[17] Nilsson, K.-F. and Giannakopoulus, A. E., "A Finite Element Analysis of Configurational Stability and Finite Growth of Buckling Driven Delamination," *Journal of Mechanics and Physics of Solids,* Vol. 43, No. 12, 1995, pp. 1983–2021.

[18] Singh, S., Asp, L. E., Nilsson, K.-F., and Alpman, J. E., "Development of a Model for Delamination Buckling and Growth in Stiffened Composite Structures," FFA TN 1998-53, The Aeronautical Research Institute of Sweden, Bromma, 1998.

[19] Asp, L. E., Nilsson, S., and Singh, S., "An Experimental Investigation of the Influence of Delamination Growth on the Residual Strength of Impacted Laminates," *Impact and Damage Tolerance Modelling of Composite Materials and Structures,* EUROMECH Colloquium 400, London, 1999, pp. 158–165 (also FFA TN 1999-52).

[20] Nilsson, S., "Static Compressive Strength of Impacted Composite Panels," FFA TN 1996-58, The Aeronautical Research Institute of Sweden, Bromma, 1997.

[21] Olsson, R., "Methodology for Predicting the Residual Strength of Impacted Sandwich Panels," FFA TN 1997-09, The Aeronautical Research Institute of Sweden, Bromma, 1998.

[22] Swanson, S. R., "Limits of Quasi-Static Solutions in Impact of Composite Structures," *Composites Engineering,* Vol. 2, No. 4, 1992, pp. 261–267.

[23] Jackson, W. C. and Poe, C. C., Jr., "The Use of Impact Force as a Scale Parameter for the Impact Response of Composite Laminates," *Journal of Composites Technology and Research,* Vol. 15, No. 4, 1993, pp. 282–289.

[24] Dost, E. F., Ilcewicz, L. B., and Gosse, J. H., "Sublaminate Stability Based Modelling of Impact-Damaged Composite Laminates," *Proceedings of the American Society for Composites,* 3rd Technical Conference, 1988, pp. 354–363.

[25] Thesken, J. C., "A Theoretical and Experimental Investigation of Dynamic Delamination in Carbon Fiber/Epoxy Composites," *Fatigue and Fracture of Engineering Materials and Structures,* Vol. 18, No. 10, 1995, pp. 1133–1154.

[26] Melin, L. G., Thesken, J. C., Nilsson, S., and Benckert, L. R., "Tensile Impact Delamination of a Cross-ply Interface Studied by Moiré Photography," *Fatigue and Fracture of Engineering Materials and Structures,* Vol. 18, No. 10, 1995, pp. 1101–1114.

[27] Melin, L. G. and Asp, L. E., "Effects of Strain Rate on Transverse Tension Properties of a Carbon/Epoxy Composite: Studied by Moiré Photography," *Composites A.,* Vol. 30, No. 3, 1999, pp. 305–316.

[28] Suemasu, H. and Majima, O., "Multiple Delaminations and Their Severity in Circular Axisymmetric Plates Subjected to Transverse Loading," *Journal of Composite Materials,* Vol. 30, No. 4, 1996, pp. 441–453.

[29] Suemasu, H. and Majima, O., "Multiple Delaminations and Their Severity in Nonlinear Circular Plates Subjected to Concentrated Loading," *Journal of Composite Materials,* Vol. 32, No. 2, 1998, pp. 123–140.

[30] Shivakumar, K. N., Elber, W., and Illg, W., "Prediction of Impact Force and Duration Due to Low Velocity Impact on Circular Composite Laminates," *Transactions of ASME, Journal of Applied Mechanics,* Vol. 52, No. 3, 1985, pp. 674–680.

[31] Bucinell, R. B., Nuismer, R. J., and Koury, J. L., "Response of Composite Plates to Quasi-Static Impact Events," *Composite Materials: Fatigue and Fracture (Third Vol.), ASTM STP 1110,* T. K. O'Brien, Ed., American Society for Testing and Materials, 1991, pp. 528–549.

[32] Olsson, R., Thesken, J. C., Brandt, F., Jönsson, N., and Nilsson, S., "Investigations of Delamination Criticality and the Transferability of Growth Criteria," *Composite Structures,* Vol. 36, No. 3/4, 1996, pp. 221–247.

[33] Juntti, M., Asp, L. E., and Olsson, R., "Assessment of Evaluation Methods for the Mixed Mode Bending Test," *Journal of Composites Technology and Research,* Vol. 21, No. 1, 1999, pp. 37–48.

[34] Asp, L. E., "Effects of Moisture and Temperature on the Interlaminar Delamination Toughness of a Carbon/Epoxy Composite," *Composites Science and Technology,* Vol. 58, No. 6, 1998, pp. 967–977.

[35] Xiong, Y., Poon, C., Straznicky, P. V., and Veitinghoff, H., "A Prediction Method for the Compressive Strength of Impact Damaged Composite Laminates," *Composite Structures,* Vol. 30. No. 4, 1995, pp. 357–367.

Timothy C. Anderson[1]

Certification Cost Reduction Using Compression-After-Impact Testing

REFERENCE: Anderson, T. C., **"Certification Cost Reduction Using Compression-After-Impact Testing,"** *Composite Structures: Theory and Practice. ASTM STP 1383,* P. Grant and C. Q. Rousseau, Eds., American Society for Testing and Materials, West Conshohocken, PA, 2000, pp. 29–46.

ABSTRACT: An approach to reduce certification development cost can be accomplished by testing the important strength allowables that make up the primary design drivers. Through a process referred to as a "modified building block approach," these primary design drivers are weighted and selected based on criticality. This approach was used to minimize the development cost of a prototype composite tailboom being considered for a light model helicopter (similar in size to a Bell Model 407). The material system of choice (AS4/APC-2 thermoplastic) and the tailboom's susceptibility to impact damage drove the need to understand impact damage and its effect on strength. Compression after impact (CAI) at barely visible impact damage (BVID) was therefore selected as the critical design parameter. The cost benefit is realized by focusing on the critical design parameters; thus the number of coupon tests necessary to support full aircraft development can be significantly reduced because only limited design aspects have to be considered. The critical design drivers selected would not necessarily be applicable to the fuselage or rotor blades, but they do provide a means to optimize the tailboom design while minimizing the development cost. Certification would still be verified by full-scale testing.

KEYWORDS: compression after impact, barely visible impact damage, composite tailboom, modified building block, thermoplastic, certification

The goal of the Low-Cost Composite Tailboom Program was to develop a lightweight cost-effective tailboom by utilizing a relatively new thermoplastic material and processing system. Specifically, this program was to investigate a PEEK resin system (AS4/APC-2) using an in situ fiber placement process as it applies to thin-walled structure. There were only limited amounts of material properties data available for AS4/APC-2, with most of that data being company proprietary. The available data were more applicable for thick-walled structure. A portion of the data was directly applicable, such as tension and shear data; however, given that the structural design was a thin monocoque shell, it was felt that additional strength data would be necessary for compression. These additional strength data were to guide the design that would eventually be certified by test. However, the cost associated with the development of a full set of material allowables suitable for certification was not acceptable. The problem was to determine what testing would be necessary to develop an optimum design that would be capable of completing certification requirements.

The objective was to eventually certify the tailboom for production. There are several equally acceptable approaches to certification that can be taken. When qualifying a redesigned component on an existing aircraft, such as a tailboom, not all approaches are cost effective. The first approach is to develop a full set of design allowables for the material system, as illustrated in Fig. 1. This option is more applicable for the development of a new aircraft and involves a large capital expense in developing the material allowables, while still requiring a full-scale verification test. The second approach is to build a full-scale component and test to ultimate. If the structure fails to meet strength require-

[1] Principal engineer, Airframe Structures, Bell Helicopter Textron Inc., P.O. Box 482, Fort Worth, TX 76101.

Copyright© 2001by ASTM International www.astm.org

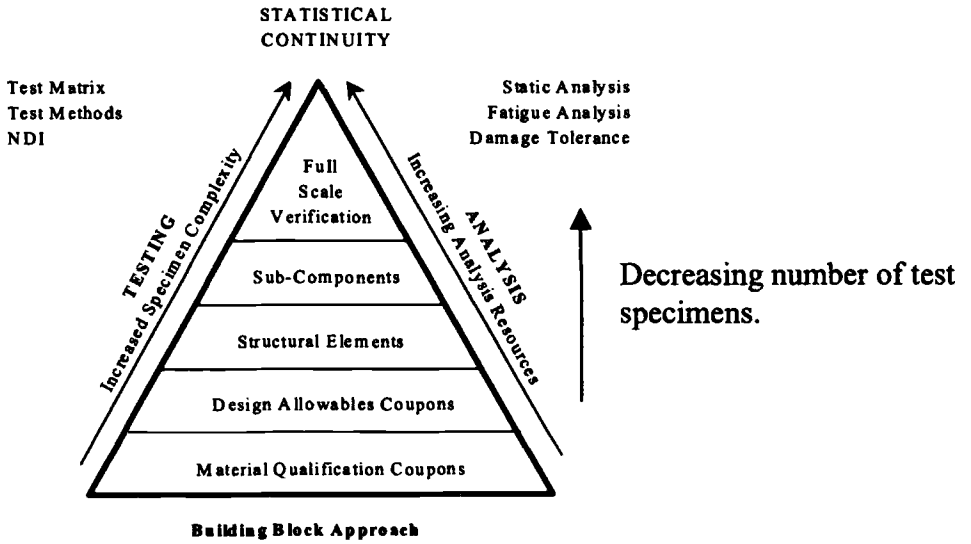


FIG. 1—*Typical building block approach used for full aircraft development.*

ments, then the component is redesigned in the region of failure and retested. This iterative process not only yields an inefficient design; it also is very expensive. The third alternative is to mitigate the design cost by identifying important strength parameters and develop a corresponding strength allowable that is used during the component design. The use and application of this approach is discussed in Ref *1*. This option, which was used in the development of the low-cost composite tailboom, becomes more cost effective because the magnitude of the coupon tests has been minimized. This approach essentially qualifies the component using a full-scale test, but develops only those material allowables that most greatly influence the design.

Approach

A costly and time-consuming full-up building block approach is shown in Fig. 1. This approach requires the development of material and structural allowables ranging from element, to coupon, to component, to full-scale tests. A modified building block approach, as shown in Fig. 2, was used to design the tailboom. This approach eliminated element tests (very costly) and minimized the coupon tests, while relying heavily on the full-scale test to validate the structure. The elimination of element tests and reduction of coupon test has significantly reduced the cost of development, but increased the risk of redesign. To reduce the risk of failure, the modified building block approach must be carefully planned. The process has been divided into four phases.

Phase I establishes a preliminary design concept. It may involve trade studies or may be a proof-of-concept, but it will also always be governed by as set of rules in the form of certification requirements. It is the starting point.

Phase II involves defining those parameters that affect design. Under this phase there are four primary areas from which the design parameters come. First, the design requirements are established by defining strength, stability, and dynamic requirements. Second, the operational environment will establish parameters such as temperature, corrosive resistance, and/or foreign object damage (FOD) damage requirements. Third, the proposed material system may have strengths or weaknesses that must be addressed. Granted, this assumes that there is some level of existing data that can be used to

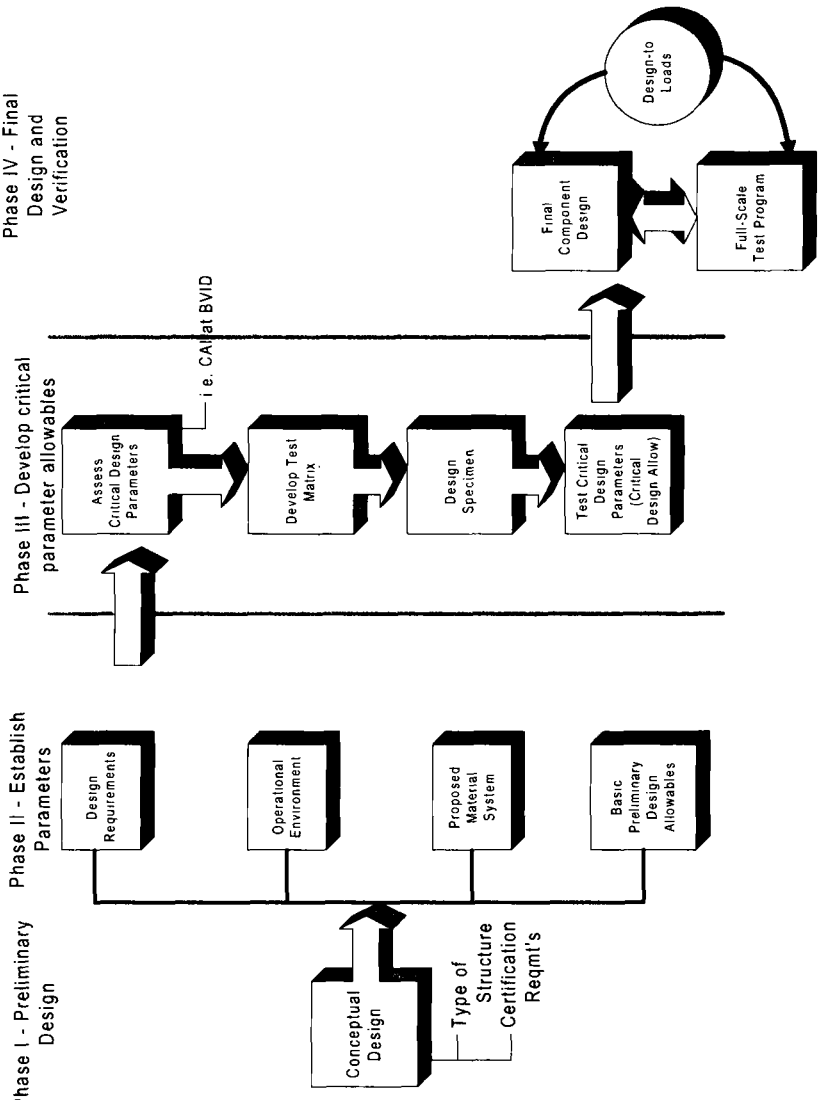


FIG. 2—*Process diagram for a simplified building block approach.*

address the weaknesses. The engineer must make an assessment of those laminate characteristics that need to be evaluated based on a limited knowledge of the material system, loading, environment, etc. As in the case of an APC-2, a thermoplastic material system, laminates constructed of this material system have increased toughness, but poor adhesion capability. Fourth, there may be preliminary material properties available (such as tension, compression, shear, or bearing) from the vendor or some other source that could aid in the design. The use of those material properties must be reviewed relative to the proposed design not only for the type of properties but for the standard and method used in development. Are any or all of the material properties applicable? What properties must be established based on the preliminary design?

During Phase III, the critical design parameters identified under Phase II will be considered and used to determine what tests are necessary to reduce the cost of certification. This phase can be broken down into four steps (as shown in Fig. 2):

1. Establish the critical design parameters.
2. Develop a suitable test matrix that will provide confidence in the resulting laminate allowable.
3. Design the specimen. It is best (where applicable) to use a standardized test and specimen configuration, but that may not always be possible.
4. Test the specimens.

Phase IV is where the final design is completed based on the above-established laminate properties and receives full-scale testing.

Phase I

The objective of the program was to reduce both the cost and weight of a component utilizing a thermoplastic material. The structure to be developed is a thermoplastic monocoque tailboom to be used on a light helicopter model. The basic design of the thermoplastic tailboom is shown in Fig. 3.

Phases II and III

AS4/APC-2 thermoplastic material system was used for the preliminary design of the tailboom. The plies are laid on a metallic mandrel using an in situ fiber placement process. This process allows for the conventional orientation of fibers, that is, 0 deg (along the boom axis), 45 deg (bias), and 90 deg (circumferentially around the boom). The tailboom has a small taper to it as it transitions from the body of the helicopter to the tailrotor gearbox attachment. This taper presented a problem in dropping the plies. That is, the plies being laid on a bond tool, which are only 0.24 in. (6 mm) wide, require a series of laps and gaps. A significant amount of effort was expended in trying to reduce the effect of the lap and gap by compacting the ply as it was laid on the tool; but these laps and gaps provide an inherent crack (or delamination) initiation source. In addition to material processing, and as shown in the design of the tailboom, the boundary conditions (as mentioned above) need also be addressed when trying to determine the material's strength. That is, considering the combined effect of skin thickness and distance between frames, the compression strength allowable was considered inadequate. Material allowables for the most part are generic regardless of where they are used, and therefore rarely would be defined as a function of geometry or boundary conditions. However, to evaluate a specific set of design parameters, as in the case of the tailboom, structural design allowables that consider the uniqueness of the product must be considered. Testing to determine these structural allowables must be considered carefully for every application. The tailboom's thin composite monocoque structure drives the need to understand the effect of stability. In other words, the effect of the boundary conditions must be considered in the test coupons used to establish the structural allowables for the tailboom. In addition, the usage profile shows that the tailboom is more susceptible to impact damage both from natural causes such as hail or human-induced damage such as

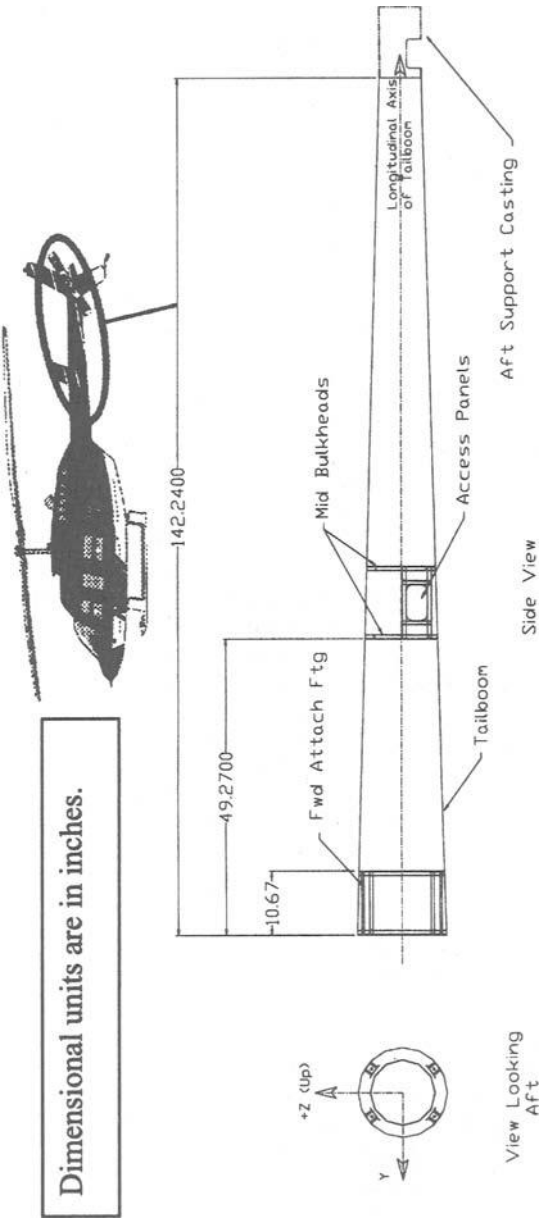


FIG. 3—*Tailboom configuration.*

dropped tools. Given that the design must consider impact damage and that stability of thin structure could be affected by damage, it was evident that compression-after-impact (CAI) at barely visible impact damage (BVID) would be a critical design driver.

From a review of the existing data (shown in Table 1), tension data were considered acceptable, given that tensile strength does not change with thickness and is relatively independent of the matrix system. The in-plane and interlaminar shear data were also considered acceptable since all the shear margins of safety remained positive. The compression strength data, however, were felt to be inadequate, since the test data were developed from thick-walled nonbuckling specimens as opposed to the thin-walled monocoque structure. To consider what type of tests would be required, it is first necessary to review the design requirements from the perspective of certifying safe structure as manifested by the certifying agency. Knowing that compression strength is highly influenced by environment and impact damage (see Table 2 and Fig. 11), and a review of Fig. 4, as interpreted from Refs *2* and *3*, would indicate that the environmentally adjusted compression strength at BVID should be the focus of the material allowables for this design development program. Because the extent of impact damage for thin-walled structure is dependent on the flexibility of the impact site, it can be said that boundary conditions play a primary role in the CAI strength at BVID. The determination of BVID is therefore very crucial. The best way to establish an acceptable BVID threshold is to impact the full-scale structure, rather than removing sections of the structure and then impacting. Therefore, the approach was to determine a CAI allowable that would best reflect the thickness and geometry of the proposed design while also considering possible threats.

To establish BVID, a tailboom was mounted in a fixture simulating attachment to the fuselage and subjected to various impact energies and impactor nose diameters at different locations. The impact sites were sectioned from the tailboom and tested in room temperature ambient (RTA) compression to establish the RTA CAI strength allowable, which is then reduced by an environmental factor based on the ratio of the interlaminar shear RTA to elevated temperature wet (ETW). By systematically impacting at various energies and at various locations multiple times around and along the tailboom and using the minimum data values, a BVID material allowable can be developed such that it would be acceptable for structural sizing. Environmental damage due to hailstones represents a worst-case threat. Tool drop and FOD from rotor wash are not a player due the location of the tailboom with respect to the rest of the airframe. The range of impact energies as illustrated in Fig. 5 (from [*4*]) provided a sanity check on the test matrix. Note that the 0.785-in. (20-mm) diameter hailstone meets a more statistically realistic worst-case size [*4*] based on the probability of storm occurance and associated size of hailstones.

The Test Specimen

Consider that the allowable must cover all design parameters that are transparent to the stress analyst. That is, the stress analyst will determine the stress in a component based on loads and boundary conditions and will check the design against a set of material allowables (that are not themselves a function of boundary conditions). Given this philosophy, the testing to establish a minimum BVID threshold and its associated allowable was completed using a section of the tailboom mounted and supported simulating attachment to an actual helicopter. A stress analysis of the tailboom showed very high compression stresses in the region of tailboom used in the test. This section of the tailboom represents the most conservative configuration relative to thickness and boundary conditions for CAI at BVID. The configuration of the test specimen and test setup is shown in Fig. 6. The location of the impact sites around the circumference is shown in Fig. 7. The test specimen was impacted by dropping a mass normal to the impact site. The impact energy was calculated as $\frac{1}{2} \times \text{mass} \times (\text{velocity})^2$, where the mass was predetermined by the test apparatus, and the velocity was calculated by equating to kinetic energy to potential energy. The test machine measured final velocity to obtain an accurate measure of impact energy. Two different tup diameters were used to assess the influence of diame-

TABLE 1—*AS4/APC-2 material allowables.*

		A-Basis Mechanical Properties				B-Basis Mechanical Properties			
Prestine:		-67F / Dry	Room Temp	180F / Wet	250F / Wet	-67F / Dry	Room Temp	180F / Wet	250F / Wet
	Tension:								
	E11 (Msi)		19.90	20.10	20.30		19.90	20.10	20.30
	E22 (Msi)	1.52	1.44	1.39		1.52	1.44	1.39	
	G12 (Msi)	0.91	0.83	0.74		0.91	0.83	0.74	
	f 11 (Ksi)		288.82	272.12	248.00		298.73	282.78	260.95
	f 22 (Ksi)	10.56	10.12	11.33		12.12	11.17	11.59	
	s 12 (Ksi)	27.05	23.96	21.08		28.28	25.26	22.31	
	e11 (u in/in)		14513.67	13538.11	12216.65		15011.46	14068.86	12854.78
	e22 (u in/in)	6959.93	7020.59	8156.66		7988.15	7749.19	8339.12	
	e12 (u in/in)	29581.27	29009.27	28600.13		30925.78	30587.69	30263.05	
	Compr:								
	E11 (Msi)		17.80	17.70	17.80		17.80	17.70	17.80
	E22 (Msi)	1.47	1.48	1.37		1.47	1.48	1.37	
	G12 (Msi)	0.91	0.83	0.74		0.91	0.83	0.74	
	f 11 (Ksi)		-132.70	-113.12	-104.12		-144.90	-123.78	-114.78
	f 22 (Ksi)	-34.28	-29.86	-24.65		-37.21	-31.42	-26.32	
	s 12 (Ksi)	-27.05	-23.96	-21.08		-28.28	-25.26	-22.31	
	e11 (u in/in)		-7455.28	-6390.73	-5849.21		-8140.22	-6993.45	-6448.54
	e22 (u in/in)	-23388.41	-20179.58	-17940.07		-25385.57	-21236.77	-19154.49	
	e12 (u in/in)	-29581.27	-29009.27	-28600.13		-30925.78	-30587.69	-30263.05	
	ILS Strength								
	Hard	18.55	16.64	14.15		19.26	17.38	14.67	
	Soft	16.39	14.77	11.95		16.84	15.11	12.27	
Open Hole:									
	Tension:								
	F11 (Ksi)		51.60				52.87		
	e11 (u in/in)		2593.17				2656.78		
	Compres:								
	F11 (Ksi)		-39.13	-36.78	-32.10		-40.50	-37.77	-33.40
	e11 (u in/in)		-2198.27	-2078.09	-1803.36		-2275.33	-2134.06	-1876.13

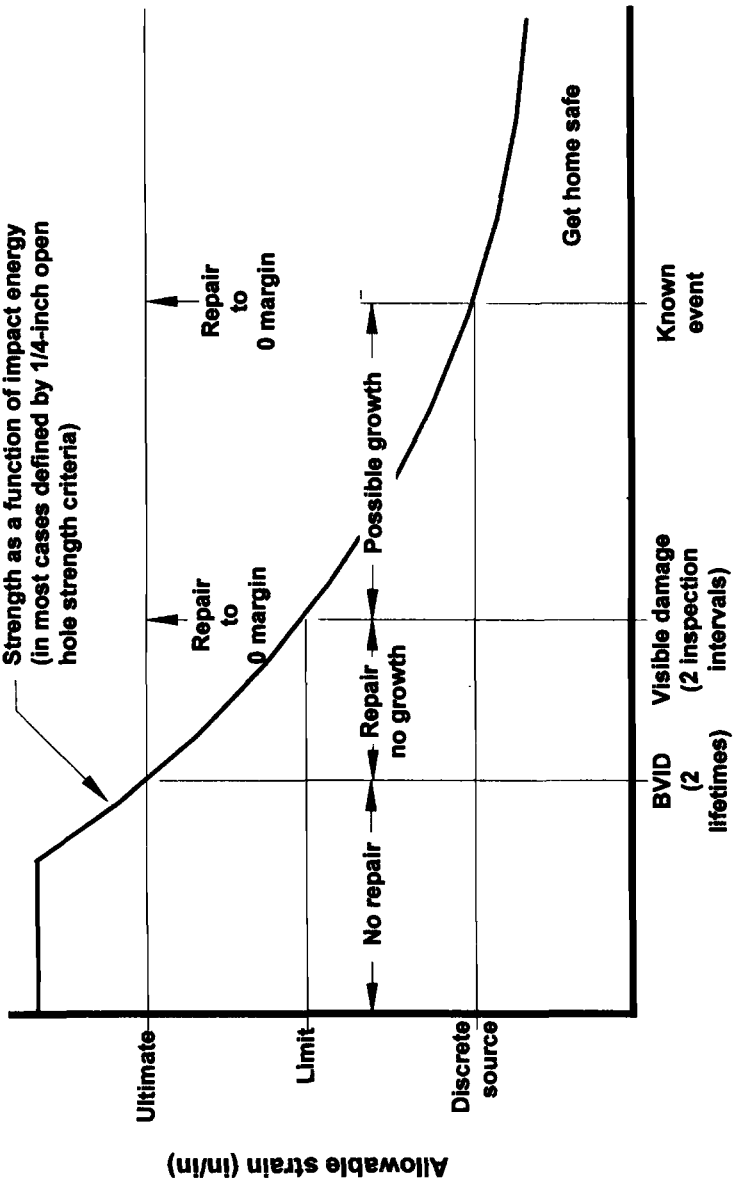


FIG. 4—*Design criteria for impact strength.*

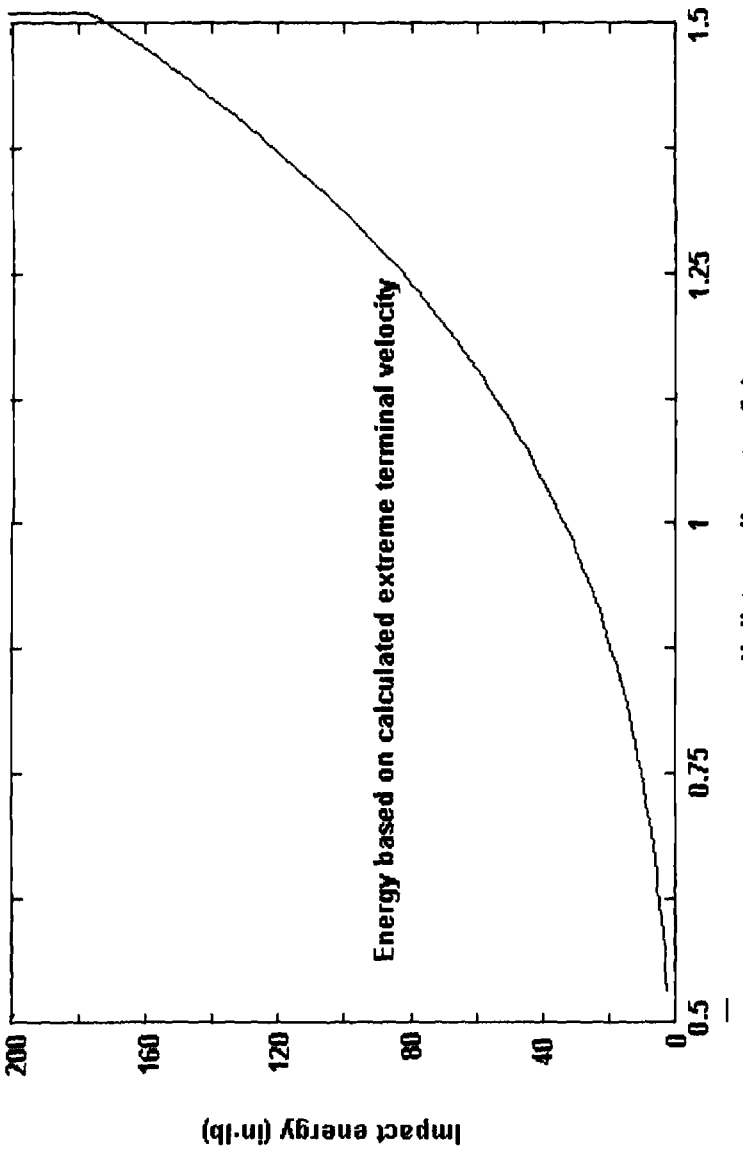


FIG. 5—*Impact energy due to hail (from* [3]).

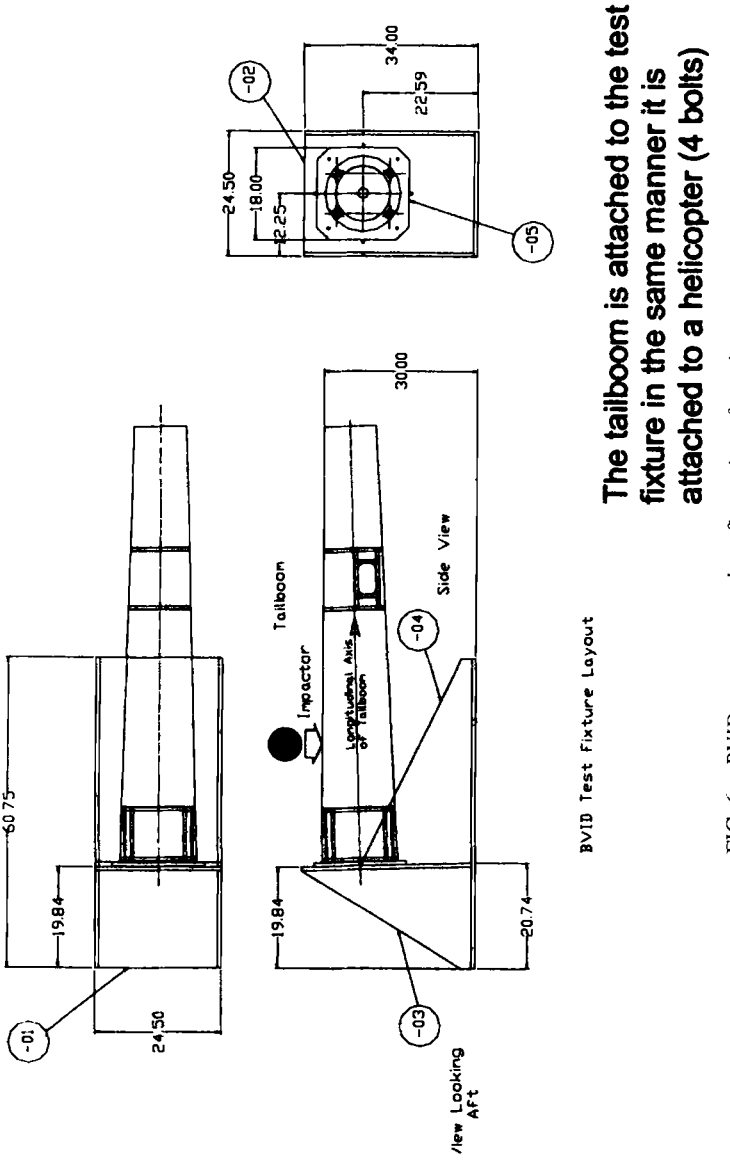


FIG. 6—*BVID test setup and configuration of specimen.*

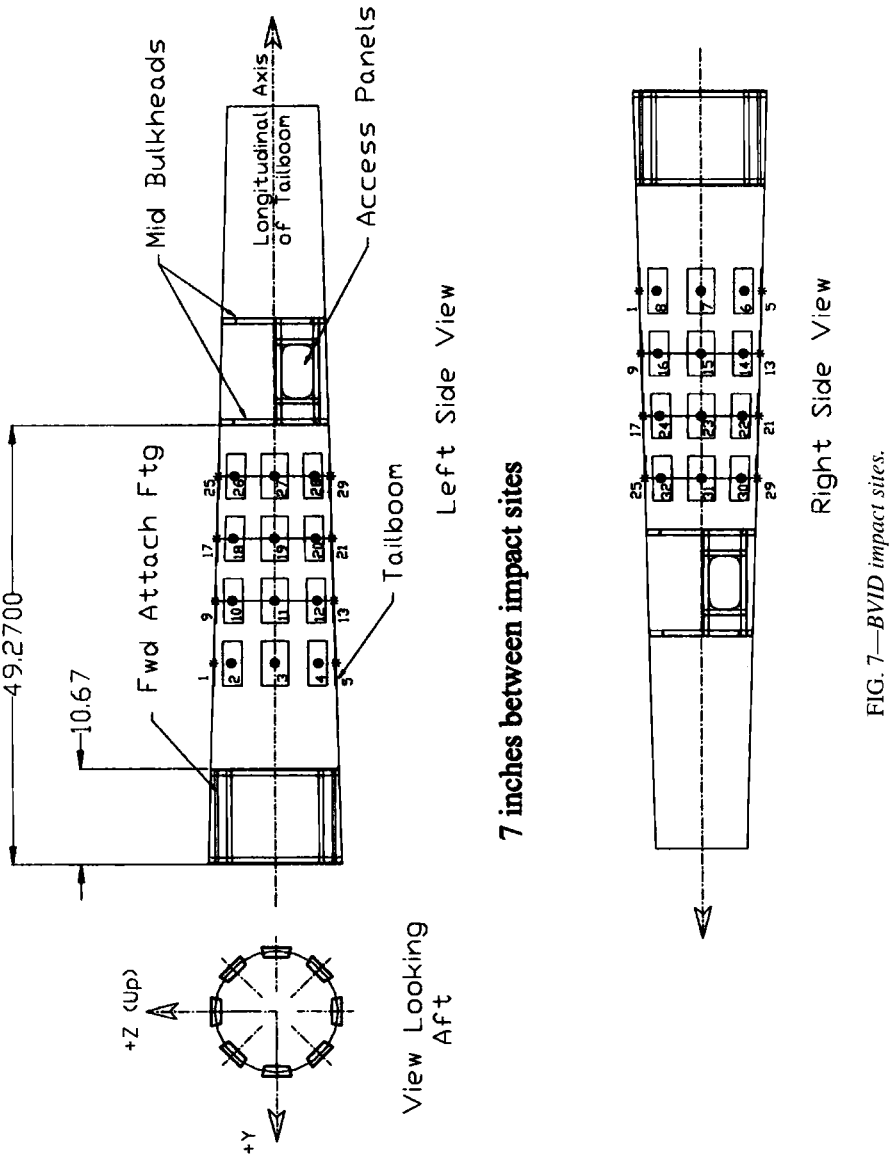


FIG. 7—*BVID impact sites.*

ter, 5/8 in. (15.8 mm) and 2 in. (50.8 mm). The impact sites were spaced so as to ensure that the impact damage from one site would not influence another site, and also to allow sufficient size to cut the CAI specimens (Fig. 7) from the BVID specimen.

The configuration and size of the CAI specimen was predominantly determined by boundary conditions of the specimen. The length of the specimen was predetermined by observations of similar damage from various impact energies from preliminary tests. It was important to ensure both that any internal damage associated with the impact was not imbedded in the potting compound used to clamp the end of the specimen, and that the structural mechanisms from the full-scale structure were captured in the specimen. The width of the specimen was determined by both the width of the impact zone and the length. Consideration was also given to establishing a specimen size that would be free of end or edge effects at the impact site. A common specimen configuration was used for all tests.

The boundary conditions were represented as clamped ends and simply-supported side walls. Potting compound was used to clamp the ends, while back-to-back steel rods clamped to the edges (as seen in Fig. 8) were used to represent the boundary conditions. Without the rods along the edge, an unrealistic failure due to the bending associated with column buckling would occur. In the actual structure, out-of-plane support is inherently provided by the continuous monocoque structure. Some form of verification was done to ensure that the boundary conditions of the test don't influence the strains in the gage region of the specimen. A photoelastic coating on one of the specimens was used to ensure that the edge effects were negligible at the impact site.

BVID Tests and Results

The test matrix shown in Table 2 was designed to establish the onset of BVID and its associated CAI strength. During the course of establishing BVID, an interesting occurrence in the maximum deflection versus impact energy was observed, as seen in Fig. 9. Maximum deflection increased up to penetration, at which point the maximum deflection decreases slightly as the tup penetrates the structure. For thin structure, BVID will occur prior to penetration. Note, backside damage is not considered since this damage is not visible to the maintainer. BVID for this tailboom configuration (material and structural geometry) occurred at approximately 60 in. lb (6780 mN · m). As shown in Fig. 4, visible damage must be capable of taking limit load; for the material used in this tailboom, that equates to approximately 180 in. lb (20 340 nM · m) (onset of penetration), which according to Fig. 5 would be a hailstone approximately 1.5 in. (38.1 mm) in diameter. From the perspective of a global structural response, increasing the steel tup size (impactor diameter) from $\frac{5}{8}$ in. (15.8 mm) to 2 in. (50.8 mm) showed very similar results relative to deflection and impact energy. However, locally within the structure there is a significant difference in maximum contact force between the tup diameters, influenced by the contact area between the tup and the specimen, as demonstrated by the fact that penetration never occurred with a 2-in. (50.8 mm) tup. It should be noted that flexibility of the tup relative to the impact site was not addressed. This damage associated with this energy level is very similar to the bending failures seen in Ref *5*. As the impact energy increases towards penetration the damage area becomes larger. At penetration (Fig. 10*e*), the damage area is dramatically decreased representing more of a shear failure in the matrix system. Figures 10*a* through 10*e* show the progression of internal damage as defined by a TTU ultrasonic inspection for 20, 40, 60, 80, and 180 in. lb (2260, 4520, 6780, 9040, and 20 340 mN · m) impact energy using a $\frac{5}{8}$ in. (15.8 mm) tup. The damage region due to penetration is shown in Fig. 10*e*. The circular region is where the tup penetrated the laminate. There was significant damage localized to the impact site (fiber brooming), but the laminate did not show the same level of damage propagating along the axis of curvature as that seen by lower impact energies. It should be noted that the observed external damage was very consistent in size with internal damage observed from the ultrasonic inspection of the damaged specimens, thus indicating, "What You See Is What You Get" (WYSIWYG). Similar results are shown in Ref *5* for curved surfaces. Although not quite exact, the similarity suggests that geometric curvature of the

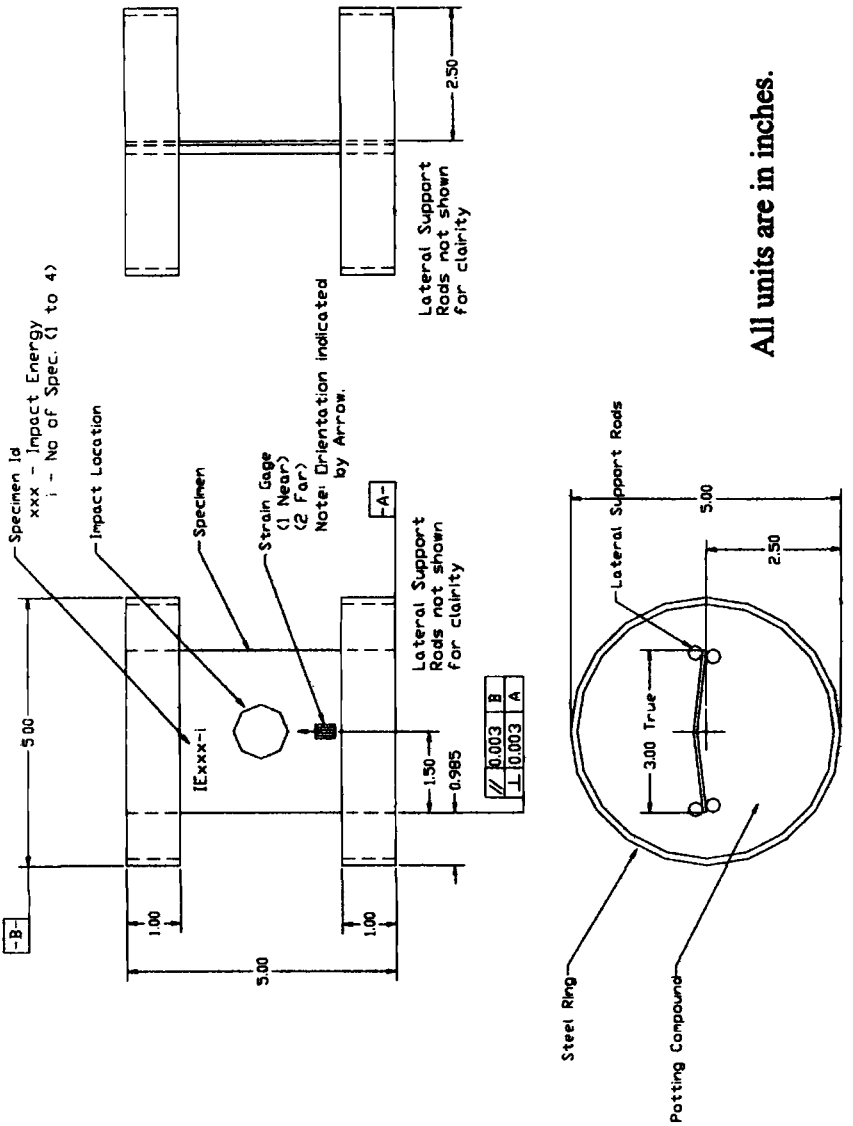


FIG. 8—*CAI specimen configuration.*

TABLE 2—*BVID and CAI test matrix.*

Specimen ID	Impact Energy (in. · lb)*	Number of Tests		
		BVID	CAI	Baseline
1, 10, 19, 28	0	...	...	4
2, 11, 20, 29	60	4	3	...
3, 12, 21, 30	90	4	3	...
4, 13, 22, 31	120	4	3	...
5, 14, 23, 32	150	4	3	...
6, 15, 24, 25	180	4	3	...
7, 16, 17, 26	210	4	3	...
8, 9, 18, 27	240	4	3	...

* 1 in. · lb = 113 mN · m.

component will induce failure along the axis of the curve. The work done in Ref *5* also suggests that layup plays a large role in the orientation of the failure. That is, a highly biased ply orientation will skew the impact damage along the direction of the fibers, and more quasi-isotropic laminates provided symmetric damage response. Unless the ply orientations are highly tailored, the laminate properties will generally be quasi-isotropic, and for impact damage the resulting external damage (crack) would extend along the axis of curvature. The percentage of 0, 45, and 90-deg plies, while not constant along the axis of the boom, is similar in percentage. Therefore the thinner region along the boom was investigated, $t = 0.058$ in. (1.47 mm). The component being evaluated is limited to the laminate percentages and/or thicknesses being tested. Deviations from those laminate percentages or thicknesses would require additional testing. While this appears to be very limiting, the cost associated with developing the same data for other laminate configurations is mitigated.

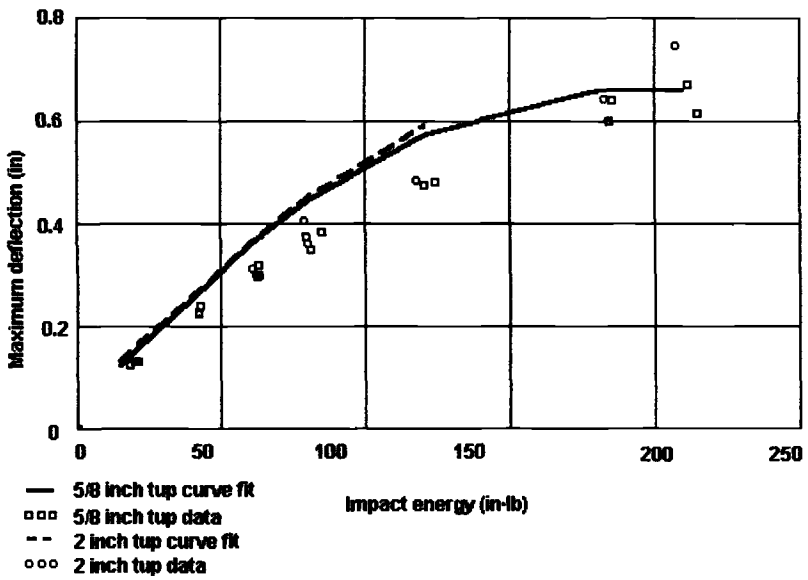
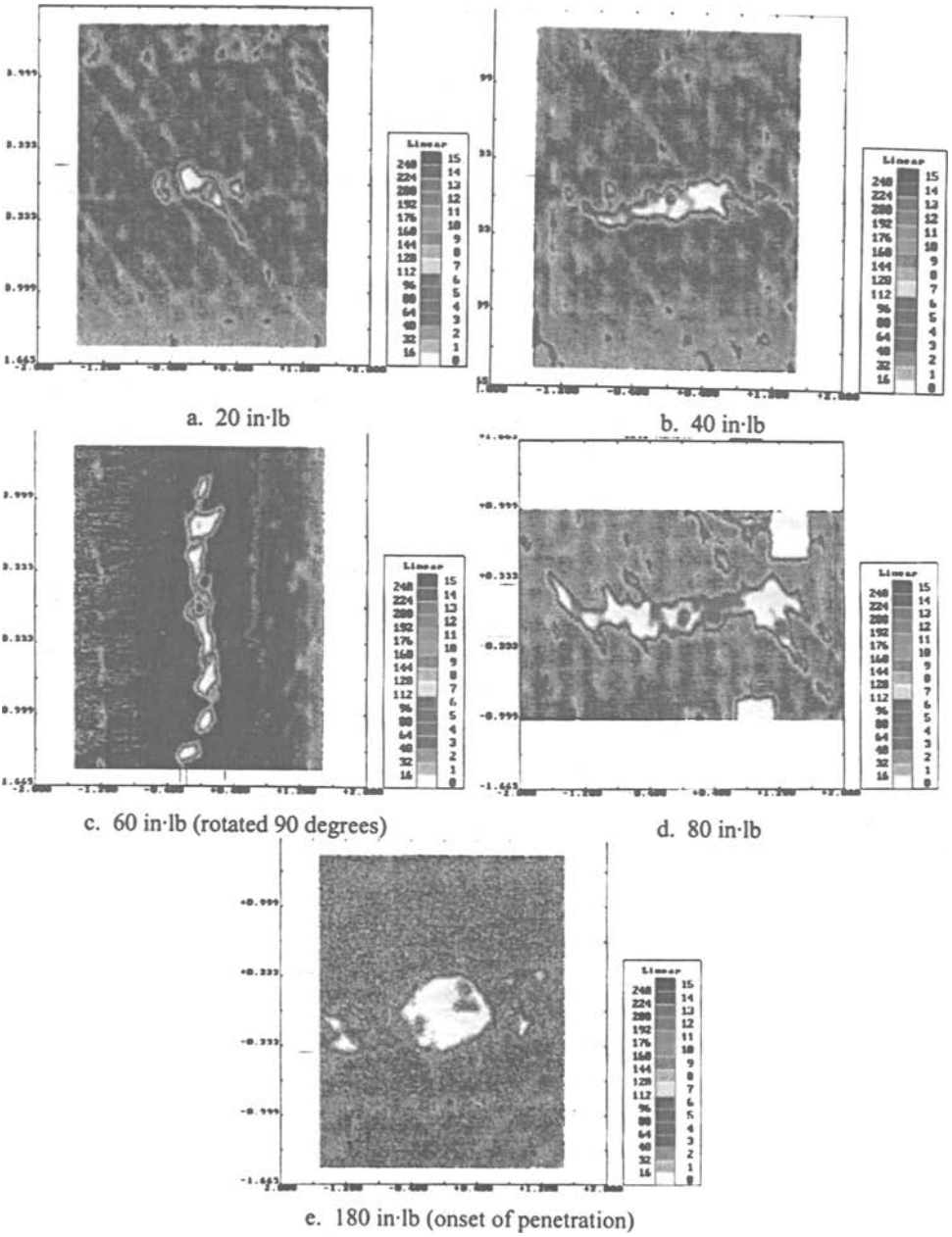


FIG. 9—*BVID impact test results.*



a. 20 in·lb

b. 40 in·lb

c. 60 in·lb (rotated 90 degrees)

d. 80 in·lb

e. 180 in·lb (onset of penetration)

FIG. 10—*NDI TTU scans of impacted specimens.*

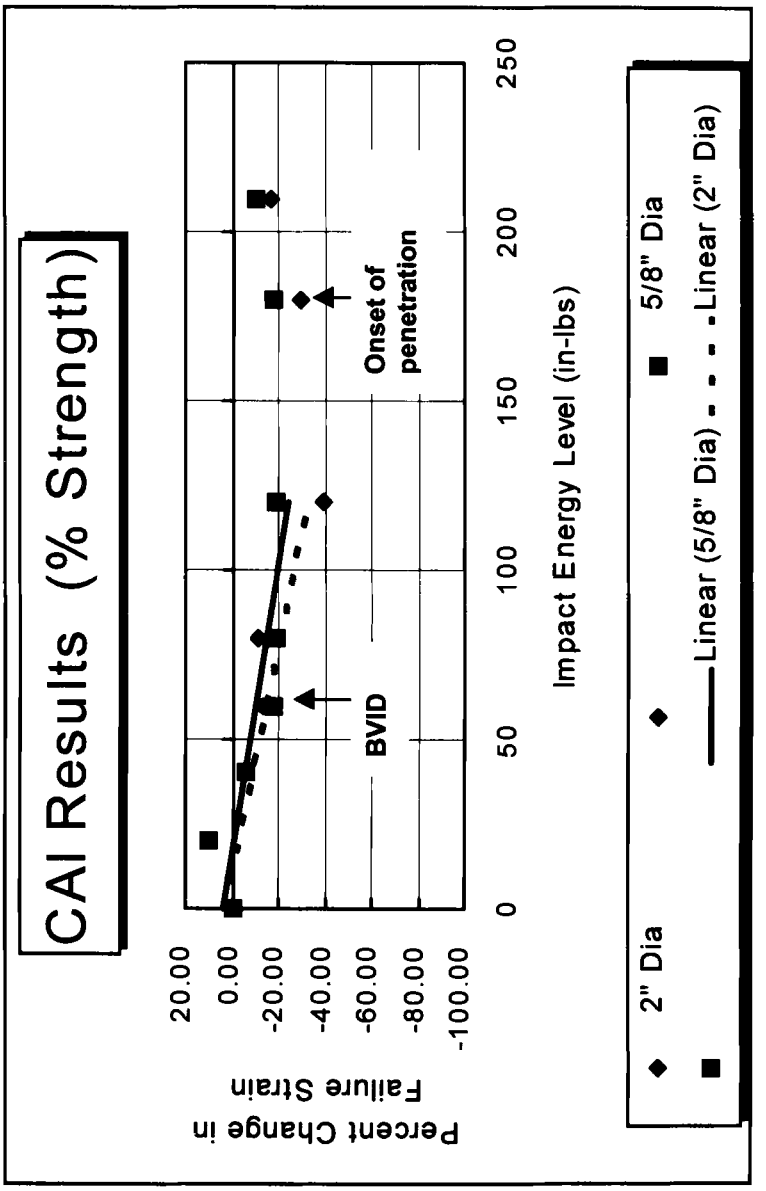


FIG. 11—*Summary of CAI test results.*

Strength Test Results

The strength test results are shown in Fig. 11. While this plot combines the effects of DR (response to the impact event) and DT (response of damaged structure to design loads), they are clearly separate mechanistic issues. The general trend indicated that as impact energy increased, the residual strength decreased as shown in Fig. 9. However, the increase in CAI strength at the higher impact energies is an indication of changing internal failure modes. Internal collateral damage characterized by interlaminar shear failure results in increased CAI strength loss until through penetration occurs. Through penetration is a result of the fibers' inability to support the impact event, minimizing the effect of interlaminar shear. The increase in CAI strength is therefore a result of decreased interlaminar shear damage. However, similar to the condition shown in Fig. 9, as the impact energy approached penetration the slope (strain versus impact energy) changed direction, so in this case an increase in strength was shown. Failure was defined as when the specimen could no longer sustain load, as shown in Fig. 12, where the average bifurcation (shown using back-to-back strain gages) on the strain gages flatten out. As a side note, as instability occurred, the curved specimen would snap through, generally initiating at the impact site. A transverse strength failure, when it occurred, would pass through the center of the impact site. For those specimens that snapped though, no additional propagation of damage was observed. It was suggested that the toughness of the thermoplastic resin system helped prevent further laminate degradation. Failure was defined when load could no longer be applied. For those laminates that failed due to a transverse strength failure, compression or lack of the resin system supporting the compressive loads appeared to be why the laminate fractured normal to the loading direction. Again, failure was defined when load could no longer be applied, but in this case, there was a distinct failure line. As was the case with snap through, the external crack and sublaminate delamination along the axis of the specimen did not change.

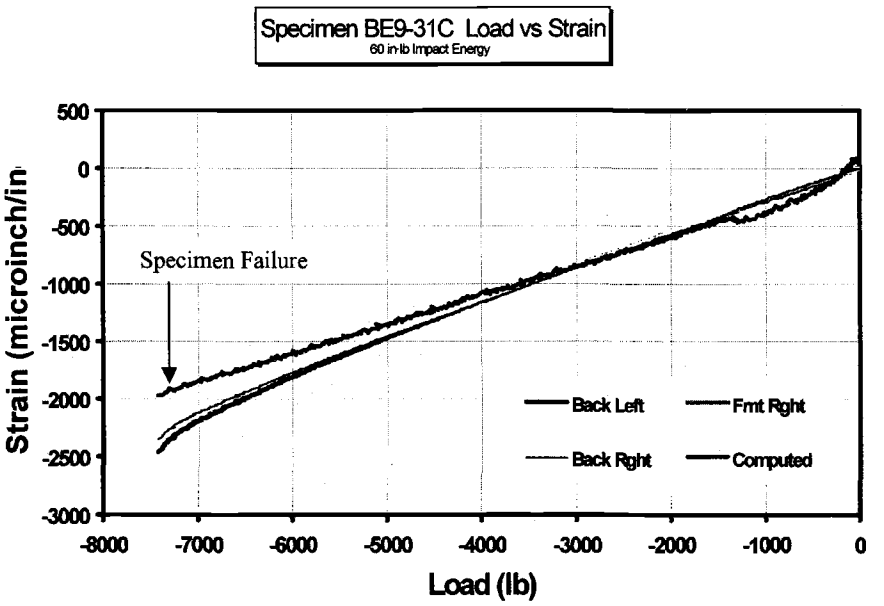


FIG. 12—*CAI typical load vs. strain.*

Discussion of Results

The standard compression specimen as used in the modified ASTM Test Method for Compression Properties of Rigid Plastics (D 695) compression tests are laterally supported from out-of-plane buckling during loading. Laterally supporting the CAI specimen in the region of the impact site would result in overly conservative strength properties relative to the design of the tailboom. As discussed earlier, the circular cross section of the tailboom offers an inherent out-of-plane support for the monocoque skin. The lateral supports, representing simply-supported edge conditions, represents the best approximation at the monocoque geometry of the tailboom. Since the lateral supports are not to be placed at the impact site, the resulting allowable becomes more of a function of stability than it does strength. Realistically this should be considered an accurate structural allowable provided the boundary conditions have been chosen correctly (to be verified by the full-scale test). There will be some regions on the component (near supports) that are nonbuckling in which the allowable will be overly conservative. But in other regions of the component that more closely represent the boundary conditions of the test, the structural allowable will be much more accurate. Since the structural allowable reflects both stability and strength, the critical location becomes sized for the worst case scenario. Therefore the allowable ranges from conservative to accurate, depending on the location of the component being sized. Increased weight due to a conservative allowable would not be an issue, since that would indicate decreased thickness near a support, when in reality the thickness nearly always increases near a support due to other strength requirements. This allowable then becomes transparent to the stress analyst, thus allowing use of traditional strength analysis methodology.

Summary

Using a modified building block approach shows promise in mitigating the dependency on a fully populated test matrix, as defined in a traditional building block approach, to certify a component structurally. This approach is limited to the component under design in that it used those parameters important to that component. In this case, the time and the associated cost of developing a thermoplastic tailboom have been substantially decreased—keeping in mind that it is not cost effective to go through a full-blown design allowables approach for a redesign or improvement of a component. Therefore, this becomes a very viable approach to any development process. However, it is important to note that the design allowables become a part of the geometry evaluated and potentially may not be transferable to other applications.

References

[1] Anderson, T. C., "Low-Cost Composite Tailboom," AIAA/ASME/ASCE/AHS/ASC Structures, Structural Dynamics and Materials (SDM) Conference, St. Louis, MO, 12–15 April 1999.

[2] "Composite Aircraft Structure," Advisory Circular AC 20–107A, para 7.a, Federal Aviation Administration, 25 April 1984.

[3] "Certification Procedures for Products and Parts," FAR AC 27-1, para 27.613 b.4, Federal Aviation Administration, dated 30 July 1997.

[4] "Climatic Information to Determine Design and Test Requirements for Military Systems and Equipment," MIL-STD-210C, Section 5.1.15, 9 Jan. 1987.

[5] Kim, S. J., Goo, N. S., and Kim, T. W., "The Effect of Curvature on Dynamic and Impact-Induced Damage in Composite Laminates," *Composite Science and Technology*, Vol. 57, 1997, pp. 763–773.

Skin-Stringer Behavior

Emile Greenhalgh,[1] *Sunil Singh,*[1] *and Karl-Fredrik Nilsson*[2]

Mechanisms and Modeling of Delamination Growth and Failure of Carbon-Fiber Reinforced Skin-Stringer Panels

REFERENCE: Greenhalgh, E., Singh, S., and Nilsson, K.-F., **"Mechanisms and Modeling of Delamination Growth and Failure of Carbon-Fiber Reinforced Skin-Stringer Panels,"** *Composite Structures: Theory and Practice, ASTM STP 1383*, P. Grant and C. Q. Rousseau, Eds., American Society for Testing and Materials, West Conshohocken, PA, 2000, pp. 49–71.

ABSTRACT: The main objective of this work was to investigate and predict the behavior of damaged structural elements (skin-stringer panels). The study combined characterization through testing with fractographic analysis, and analysis of delamination using the finite-element method. The experimental studies entailed investigation of damage growth from embedded skin defects in panels under compressive load, and the subsequent structural failure. Parameters such as defect size, location with respect to substructure and through-thickness position were studied. Local delamination and global panel buckling were modeled, and the resulting delamination growth was simulated using a moving mesh technique. The results illustrated the importance of the location of the 90° plies to the damage evolution, and the criticality of global buckling and stringer detachment in the structural failure. The understanding gained from both the experimental investigations and numerical simulations has led to guidelines for realistic modeling and rules for designing damage tolerant structures.

KEYWORDS: skin-stringer panels, delamination, fractography, finite-element modeling, moving mesh, structural failure

Introduction

Composites are now widely used in aerospace applications but have not delivered the cost savings expected. This is partly due to the limited success in extrapolating behavior at a material level to structural conditions. Thus, component testing rather than predictive modeling is the required route for certification. In particular, predicting the delamination behavior in composite structures is problematic. There have been many studies into delamination, including a recent one by one of the authors [*1*], but few have investigated the behavior in structures.

The main objectives of this work were to understand and predict the behavior of damaged structural elements (skin-stringer panels) manufactured from a current aerospace material (Hexcel T800/924). For comparison, delaminations in plain laminates under pure compressive (in-plane) loading were also studied, details of which are given elsewhere [*2*]. Delamination initiation and growth were studied using single plane defects between the plies (PTFE inserts). The defects were positioned at three sites: in the bay, partly beneath a stringer foot, and directly beneath the stringer centerline. The finite-element models were constructed using separate layers of shell elements for the two skin sublaminates, linked by constraint equations outside the defect, and further shells repre-

© British Crown Copyright 1999/DERA, published with the permission of the Controller of Her Britannic Majesty's Stationery Office.

[1] Principal scientist and engineer, respectively, Mechanical Sciences Sector, DERA, Farnborough, UK, GU14 OLX.

Senior scientist, FFA, The Aeronautical Research Institute of Sweden, PO Box 11 021, S-16 111 Bromma, Sweden.

Copyright© 2001by ASTM International www.astm.org

sented the stringer feet, webs, and caps. Delamination and global panel buckling were modeled and the damage growth was simulated using a moving mesh technique.

Experimental Details

A plain (i.e., unstiffened) laminate was developed to characterize the effect of purely in-plane loading on the damaged region. A sandwich design (Fig. 1) was used to avoid the complications resulting from using an anti-buckling guide [*3*]. This panel, designed to withstand strains up to $-10\,000$ $\mu\varepsilon$, allowed sizable damage growth; the surface was free from obstructions. These panels had quasi-isotropic skins $[(+45°/-45°/0°/90°)_3]_S$ with 40 mm thick aluminum honeycomb core. The artificial defects were disks cut from 10 μm-thick PTFE film and placed between the plies during manufacture. The panel details are summarized in Table 1. Panels A, B, and I contained defects at the 0°/90° ply interface, three plies deep, while panels E and F contained defects at the +45°/−45° ply interface, five plies deep. Panels B and I were identical so as to characterize the effect of specimen variation. The defects were circular, with diameters typical of damage from 15 J impacts in stiffened panels [*4*].

The skin-stringer panels (Fig. 2) were designed to withstand a strain of -6000 $\mu\varepsilon$ before buckling and had skins of the same stacking sequence as the plain panels $[(+45°/-45°/0°/90°)_4]_S$. The panels each had three I-stringers with tapered feet (Fig. 2) which were co-cured onto the skin. The defects were placed at various locations with respect to the stringers (Table 1); the geometry and depth of these defects were chosen from the results of the plain panel tests. Six skin-stringer panels were tested, two with defects three plies deep at the (0°/90°) ply interface and four with defects five plies deep at the (+45°/−45°) ply interface, counting from the inner face.

All the panels were tested in compression in a 1000 kN servohydraulic test machine at a rate of 0.3 mm/min. Testing of the plain panels was stopped when significant unstable damage growth had occurred; the skin-stringer panels were loaded to failure. Delamination growth was monitored using shadow moiré interferometry [*1*]. After testing, the delaminated surfaces were exposed and examined using optical and electron microscopy.

Modeling Method

Simulation of delamination buckling and growth was carried out using the finite-element based program package DEBUGS (DElamination BUckling Growth and Simulation). DEBUGS, which is based on a shell element formulation, can simulate buckling and growth of in-plane delaminations of quite general contours. The model accounts for the effects of global bending of the structure and contact between the delaminated plies. The development of DEBUGS has been described in a number of papers and reports [*5–11*] and only a synopsis of the main features is given here. DEBUGS uses the commercial FE-code ADINA to generate structural solutions. An FE-mesh of the stiffened panel is depicted in Fig. 3.

Two kinematically nonlinear shear deformable plates model the delaminated skin [*9,10*] as outlined in Fig. 4*a*. In the undelaminated domain, the upper and lower plates are constrained by displacement continuity along the "interface" as illustrated in Fig. 4*b*. In the delaminated domain, Fig. 4*c*, delaminated members are free to deflect from each other but constrained not to penetrate by means of special contact springs [*9,10*]. Stiffeners are also modeled by shell elements connected by constraint equations similar to those used for the undelaminated skin [*12*].

Delamination growth is assumed to take place when the energy release rate attains a critical value. For mixed-mode interface crack growth, the critical energy release rate is usually a function of the pure fracture modes. This is often expressed as $G = G(\psi)$, where ψ is the phase angle defined by $\psi = \text{atan}\,(K_{II}/K_I)$. The energy release rate at local crack growth, G, can be computed from the discontinuity in field variables across the crack front

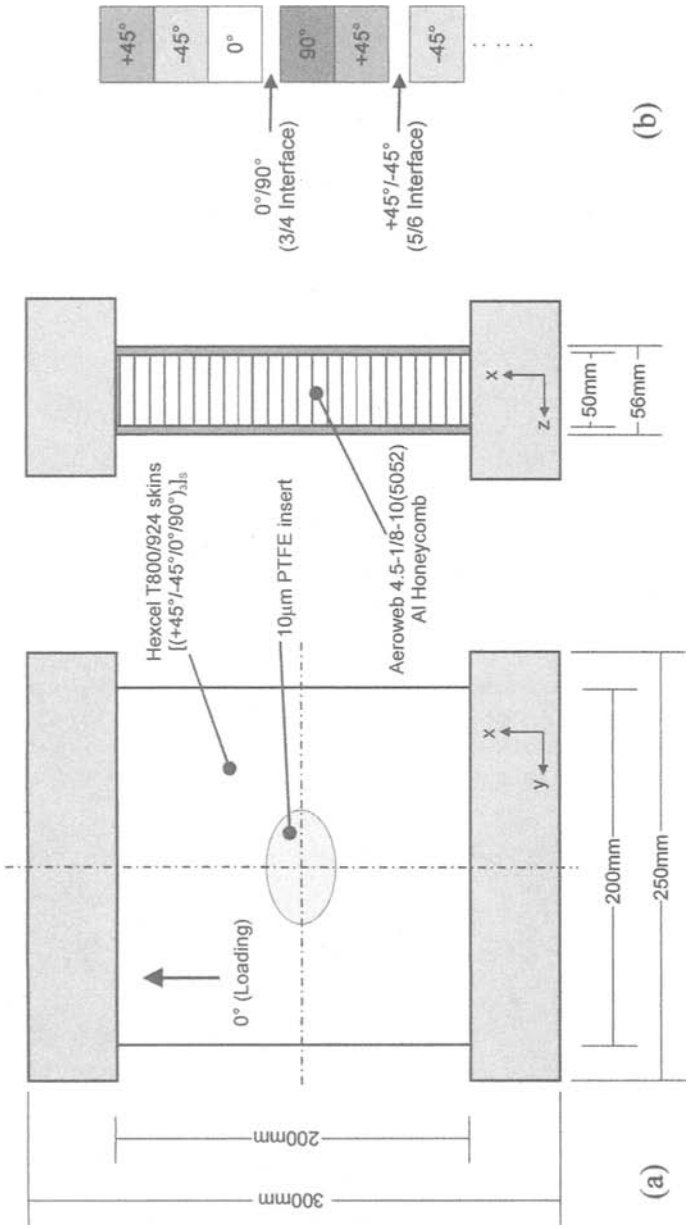


FIG. 1—(a) *Dimensions of plain (unstiffened panels) and* (b) *defect locations.*

TABLE 1—*Insert locations and initiation strains for plain and stiffened panels.*

Panel	Artificial Defect				Delamination Initiation Strain ($\mu\varepsilon$)
	Diameter	Interface	Depth	Site	
A	35 mm	0°/90°	3 Plies	(plain unstiffened panel)	−2400
B	50 mm	0°/90°	3 Plies	(plain unstiffened panel)	−2400
I	50 mm	0°/90°	3 Plies	(plain unstiffened panel)	−1950
SS#6	50 mm	0°/90°	3 Plies	Beneath the stringer foot	−4950
SS#8	35 mm	0°/90°	3 Plies	Center of the bay	−2500
E	35 mm	+45°/−45°	5 Plies	(plain unstiffened panel)	−4150
F	50 mm	+45°/−45°	5 Plies	(plain unstiffened panel)	−3150
SS#1	50 mm	+45°/−45°	5 Plies	Center of the bay	−2850
SS#2	50 mm	+45°/−45°	5 Plies	Beneath the stringer foot	Less than −5250
SS#3	50 mm	+45°/−45°	5 Plies	Beneath the stringer center	In excess of −7174
SS#4	35 mm	+45°/−45°	5 Plies	Center of the bay	−2900

$$G = (P_{nn}^{(1)} - P_{nn}^{(2)}) + (P_{nn}^{(3)} - P_{nn}^{(4)}) \tag{1}$$

The superscript denotes the location of where the tensor, P_{nn}, is evaluated (see Fig. 5*a*) and where

$$P_{nn}^{(h)} = W^{(h)} - N_{n\gamma}^{(h)}\bar{u}_{n,\gamma}^{(h)} - Q_n^{(h)}\bar{u}_{3,n}^{(h)} - M_n^{(h)}\gamma\theta_{n,\gamma}^{(h)} \tag{2}$$

In Eq 2, W is the strain energy function; N, M and Q denote membrane forces, moments and transverse shear force, respectively; $\bar{u}_i$ is the midplane displacement and θ transverse rotation; n denotes the normal direction to the crack front; double Greek indices denote summation of normal and tangential components.

The nonlinear plate problem may locally be reduced to a linear problem if a homogenous strain field is superposed such that the undelaminated region becomes undeformed [*5,13,14*] as outlined in Fig. 5*b*. The number of unknown load resultants is reduced to five but the energy release rate and stress intensity factors are the same as in the nonlinear plate problem. The tensor components, P_{nn}, then become

$$P_{nn}^{(h)} = \frac{\bar{N}_{nn}^{(h)}\bar{\varepsilon}_{nn}^{(h)} + \bar{N}_{nt}^{(h)}\bar{\varepsilon}_{nt}^{(h)}}{2} + \frac{\bar{M}_{nn}^{(h)}\bar{\kappa}_{nn}^{(h)}}{2} + \frac{Q_n^{(h)}\bar{\varepsilon}_{3n}^{(h)}}{2}, \qquad h = 1,2$$

$$P_{nn}^{(h)} = 0, h = 3,4 \tag{3}$$

where ε and κ denote the strain and curvature and where the bar refers to the quantities after superposition.

The fundamental fracture modes are linear functions of the five load resultants

$$\begin{aligned} K_{\mathrm{I}} &= a_1N_{nn} + a_2N_{nn} + a_3Q_n + a_4N_{nt} + a_5N_{nt} \\ K_{\mathrm{II}} &= b_1N_{nn} + b_2N_{nn} + b_3Q_n + b_4N_{nt} + b_5N_{nt} \\ K_{\mathrm{III}} &= c_1N_{nn} + c_2N_{nn} + c_3Q_n + c_4N_{nt} + c_5N_{nt} \end{aligned} \tag{4}$$

The coefficients in Eq 4 may be determined by solving the split beam problem for the material com-

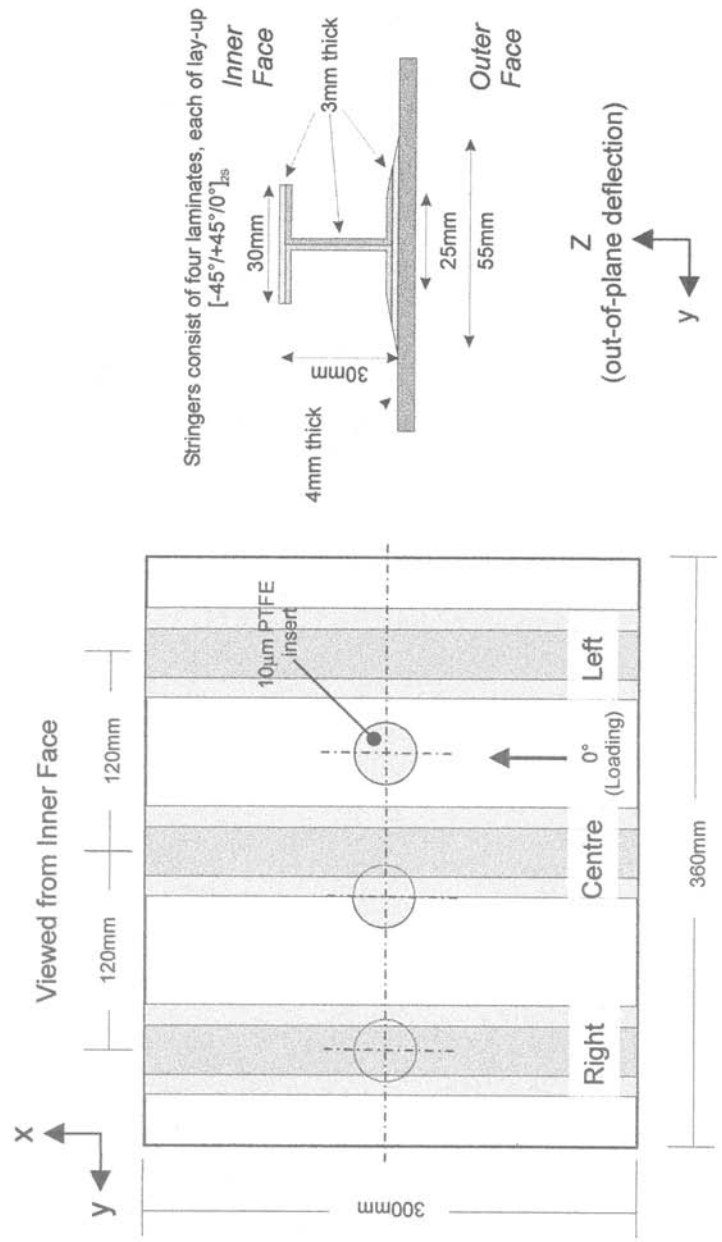


FIG. 2—*Dimensions of skin-stringer panels.*

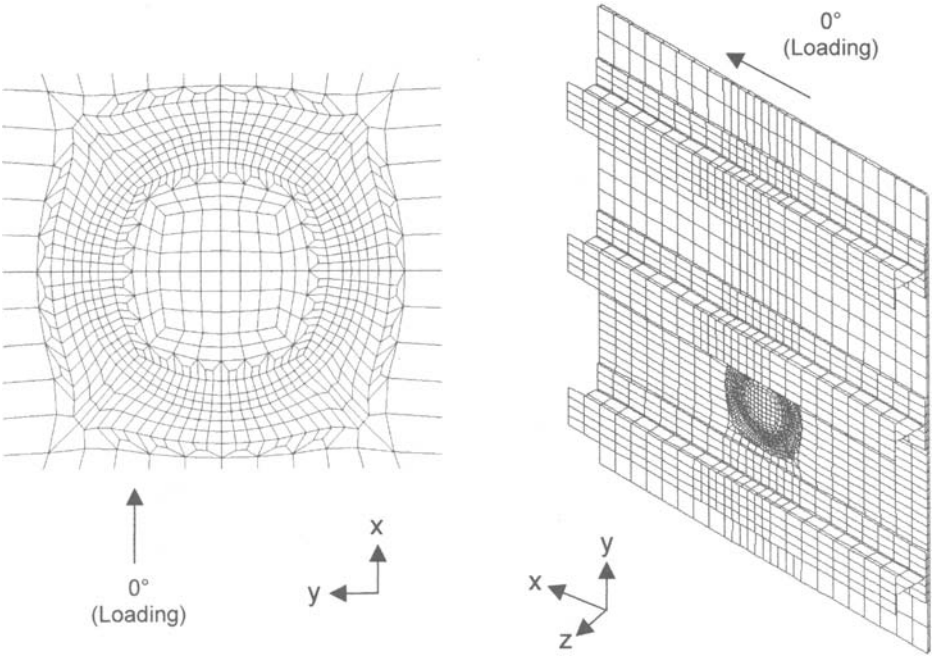


FIG. 3—*Finite-element mesh of skin-stringer panel with a 50-mm-diameter embedded defect.*

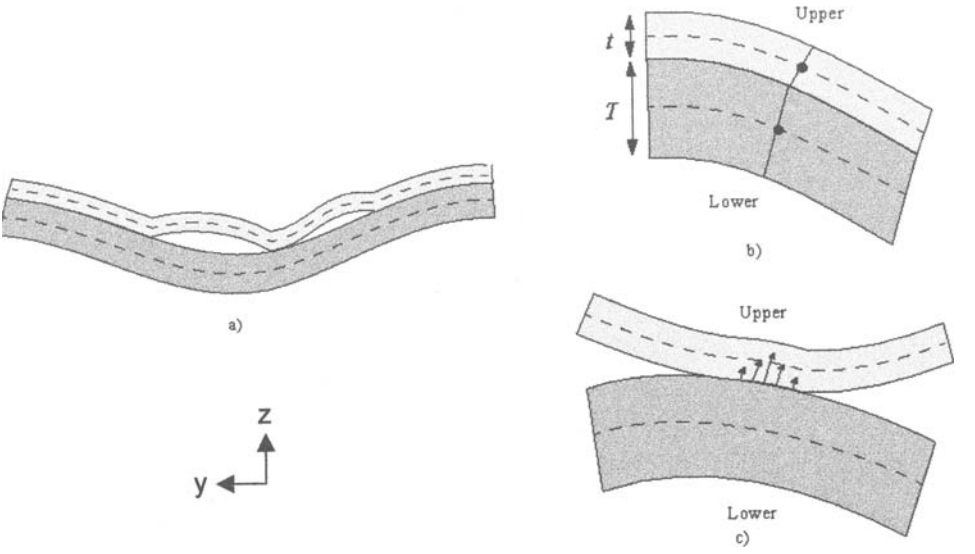


FIG. 4—*Model of delamination skin.*

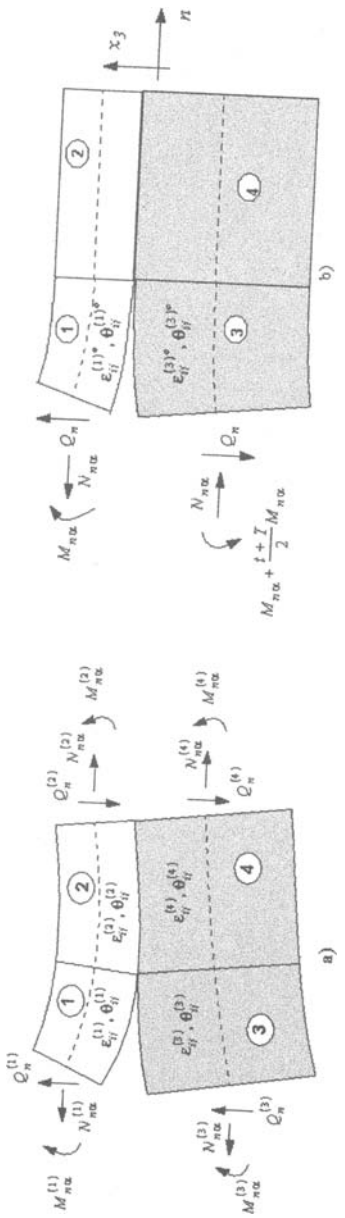


FIG. 5—*Reduction of nonlinear plate problem.*

bination of interest with unit sectional loads one-by-one. This can be a formidable problem for a general layered material. Closed-form solutions for the coefficients have been given in Ref *14* for the isotropic split beam problem and when there is no shear. The only nonvanishing coefficients were then

$$a_1 = \frac{\cos\omega}{\sqrt{2tU}} \qquad a_2 = \frac{\sin(\omega + \gamma)}{\sqrt{2t^3V}}$$

$$b_1 = \frac{\sin\omega}{\sqrt{2tU}} \qquad b_2 = \frac{\cos(\omega + \gamma)}{\sqrt{2t^3V}} \tag{5}$$

$$c_4 = \sqrt{\frac{t + T}{2tT}}$$

and where $\eta = t/(T + t)$ is the thickness ratio, and γ, ω, V, and U geometry functions.

$$1/V = 12(1 + 3\eta^3), \qquad 1/U = 1 + 4\eta + 6\eta^2 + 3\eta^3$$

$$\gamma = a\sin(6\eta^2(1 + \eta)\sqrt{UV}) \qquad \omega = 52.1° - 3°\eta \tag{6}$$

The split-beam problem with the shear force Q_n, was solved using the in-house FE code STRIPE. The loading was virtually pure Mode I for all delamination depths. The very same FE model was also used to confirm the closed-form coefficients given in Eq 5.

In the analysis, energy release rate distribution was calculated along the delamination front using Eqs 1 and 3. Only the "isotropic mode decomposition" was adopted, using Eqs 4 and 5 and assuming that the shear force gives pure Mode I loading. This is obviously a bold simplification. Work is in progress to generate solutions for general layups.

A complete analysis of delamination buckling and growth includes the following steps:

- The global (plate) buckling load is first determined for the structure.
- The delamination buckling load is subsequently determined with due account for contact.
- This is followed by the kinematically nonlinear postbuckling analysis where the full Newton method is adopted and where the contact analysis is performed at each load. Once the contact analysis has converged, the energy release rate is computed along with fracture mode separation (in the present implementation with the isotropic material simplification). Load increments are taken automatically such that load increments are small near the delamination and global buckling loads (where the tangential stiffness may be very low). Load increments are also adjusted such that the crack growth criterion is attained but not significantly exceeded. In the numerical analyses given here, the energy release rate was within 1% of the critical value at crack growth.
- The delamination front may propagate when the crack growth criterion, $G(\Psi) = G_c(\Psi)$, has been attained at some node. The front is then advanced by moving the nodes which have reached the crack growth criterion a small distance in the local normal direction to the front and in the plane of the delamination (see below), followed by a second step where the entire mesh is slightly moved. The postbuckling analysis is then restarted at the previous propagation load, but with the new updated mesh.

By this approach, the evolution of the delamination growth is modeled by performing a large number (typically in the order of a few hundred) of incremental crack propagations. The "small" distance

the nodes are propagated must be finite but sufficiently small. The mesh is moved by solving a two-dimensional finite-element problem using the same mesh as in the shell analysis. Nodes along the delamination front, which have attained the crack growth criterion, have prescribed displacements equal to the crack increments. Nodes along the front, which have not attained the crack growth criterion, and nodes along the outer boundary and stiffeners have zero prescribed displacements. The new nodal coordinates for the shell problem are taken as the nodal coordinates after deformation of this two-dimensional problem.

The following measured properties [*1*] of T800/924 were used: $E_{11} = 155$ GPa, $E_{22} = 8.57$ GPa, $\nu_{12} = 0.33$, $G_{12} = 7.4$ GPa and ply thickness = 0.125 mm. The remaining mechanical properties were assumed: $E_{33} = E_{22} = 8.57$ GPa, $\nu_{13} = \nu_{12} = 0.33$, $\nu_{23} = 0.52$, $G_{13} = G_{23} = 7.4$ GPa.

In the plain panels global buckling was inhibited, which was simulated by making the substrate considerably thicker than the delaminated plies. In the skin-stringer panels (Fig. 3), the loaded edges were locked in all degrees of freedom while the nodes on the opposing edge were joined by rigid links to a master node (free only to move in the loading direction), to which a point load was applied.

Experimental Results

Plain Panels

Examples of the damage growth in the plain panels are shown in Figs. 6 and 7 (50 mm diameter disbonds at 0°/90° and +45°/−45° ply interfaces, respectively); the loading direction was vertical in

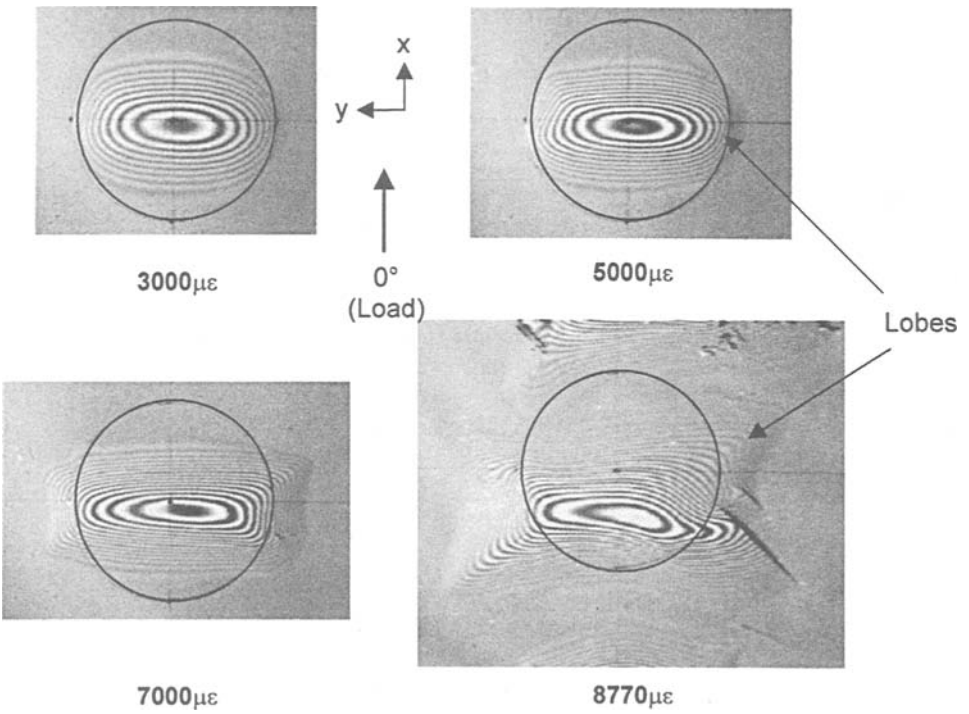


FIG. 6—*Moiré images of damage growth in a plain panel with a 50 mm-diameter defect at 3/4 (0°/90°) ply interface.*

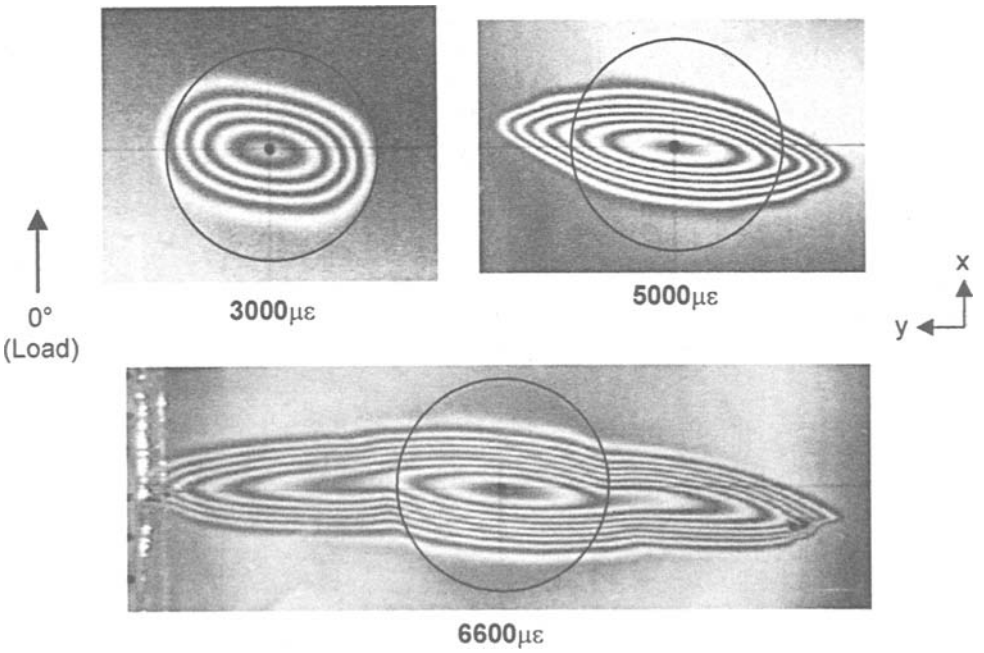


FIG. 7—*Moiré images of damage growth in a plain panel with a 50-mm-diameter defect at 5/6 (+45°/−45°) ply interface.*

these images. The increase in damage width is shown in Figs. 8 and 9 and the delamination initiation strains are given in Table 1.

Damage development from inserts at the 0°/90° ply interface all followed the same pattern (Fig. 6). As the load was increased, the delaminated region became elliptical and growth initiated at the transverse boundaries. The delamination developed into a lozenge shape, with lobes growing on the right side, from just above the major axis of the ellipse and, on the left side, from just below the major axis, almost parallel to the −45° ply. Secondary growth also developed, propagating parallel to the +45° ply, leading to the development of rectangular and ultimately dogbone damage shapes. Finally, there was splitting at the surface and axial damage growth. Comparison between panels B and I (Fig. 8) indicated there was little specimen variation.

The damage development in the panels containing inserts at the +45°/−45° ply interface also followed a pattern (Fig. 7) though not the same as that of the inserts at the 0°/90° ply interface. The delaminated region became elliptical as the load was applied, the major axis of the ellipse was aligned at 105° (clockwise) to the loading direction. Delamination growth initiated from the ends of this elliptical blister and then developed as a flattened ellipse until the test was stopped.

The delamination initiation strains (Table 1) in the plain panels varied considerably, which was attributed to the difficulty in measuring this parameter [*1*]. This was due to the poor resolution of the moiré interferometry at the tip of the defect. There was no trend with insert size, but the initiation strains for the inserts in the 0°/90° ply interfaces were 40% lower than those for the +45°/−45° ply interfaces. However, after initiation, the damage growth from the defects at the 0°/90° ply interface was slower than that from the +45°/−45° ply interface.

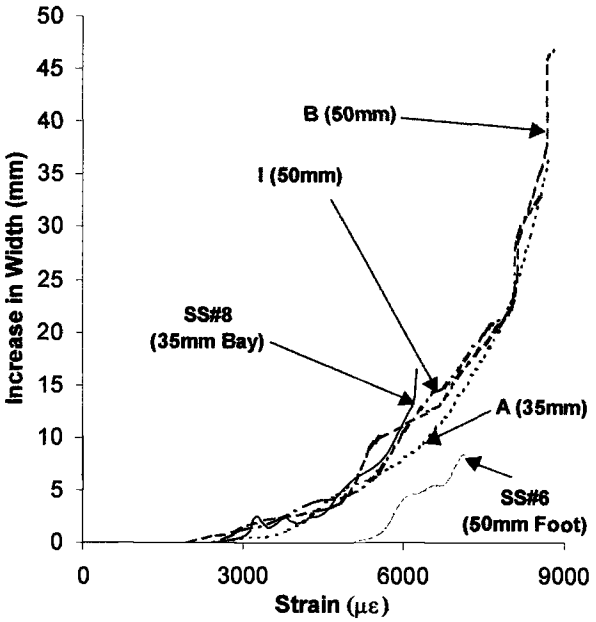


FIG. 8—*Increase in damage width vs. strain at 3/4 (0°/90°) ply interface.*

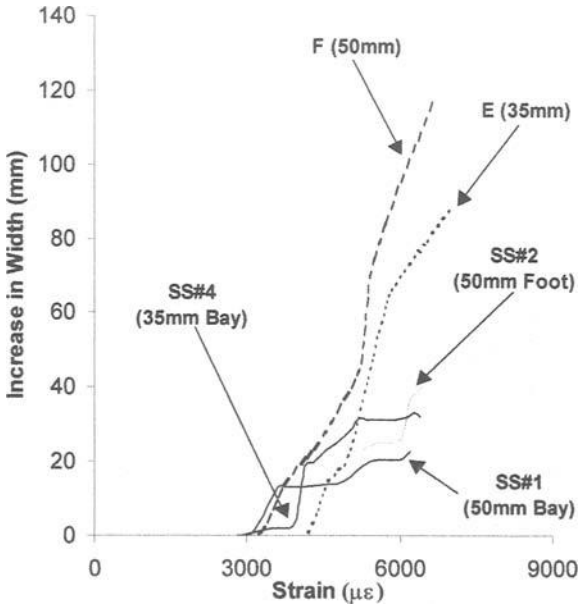


FIG. 9—*Increase in damage width vs. strain at 5/6 (+45°/−45°) ply interface.*

TABLE 2—*Summary of skin-stringer panel test results.*

Parameter	Skin-stringer Panel Number					
	SS#6	SS#8	SS#1	SS#2	SS#3	SS#4
Ply interface	0°/90°	0°/90°	+45°/−45°	+45°/-45°	+45°/−45°	+45°/−45°
Insert diameter	50 mm	35 mm	50 mm	50 mm	50 mm	35 mm
Location	Foot	Bay	Bay	Foot	Centerline	Bay
Buckling strain ($\mu\varepsilon$)	−6600	−5600	−5800	−6000	−6500	−5600
Failure load (kN)	−953	−910	−880	−881	<−987	−924
Failure strain ($\mu\varepsilon$)	−7153	−6261	−6201	−6453	<−7174	−6437
Peak strain ($\mu\varepsilon$)	−9655	−10686	−7686	−7382	−9711	−9233
Peak delamination deflection (mm)	−2.08	−2.35	−1.60	−0.94	+10.17	−2.58

Skin-Stringer Panels with Defects at 0°/90° Ply Interfaces

A summary of the results from the skin-stringer panel tests is given in Table 2. The damage development for the 35 mm defect in the bay (SS#8) was similar to that shown in Fig. 6 for the plain panels. The delamination developed into an ellipse and, at an applied strain of about −2500 $\mu\varepsilon$, there was outward bending (away from the stringers) of the bays. Lateral growth (parallel to the 90° plies) initiated and grew from the right-hand lobe of the delamination, followed by initiation from the left-hand lobe of the delamination at an applied strain of −3500 $\mu\varepsilon$. The damage then extended across the bay and, at an applied strain of −5200 $\mu\varepsilon$, the panel buckled. Although the growth rate increased, the damage had not reached the stringers when failure occurred at an applied strain of −6261 $\mu\varepsilon$.

The damage development for the panel with the 50 mm defect partly beneath the stringer foot (SS#6) is shown in Fig. 10. The delamination formed a bell-shaped blister adjacent to the stringer

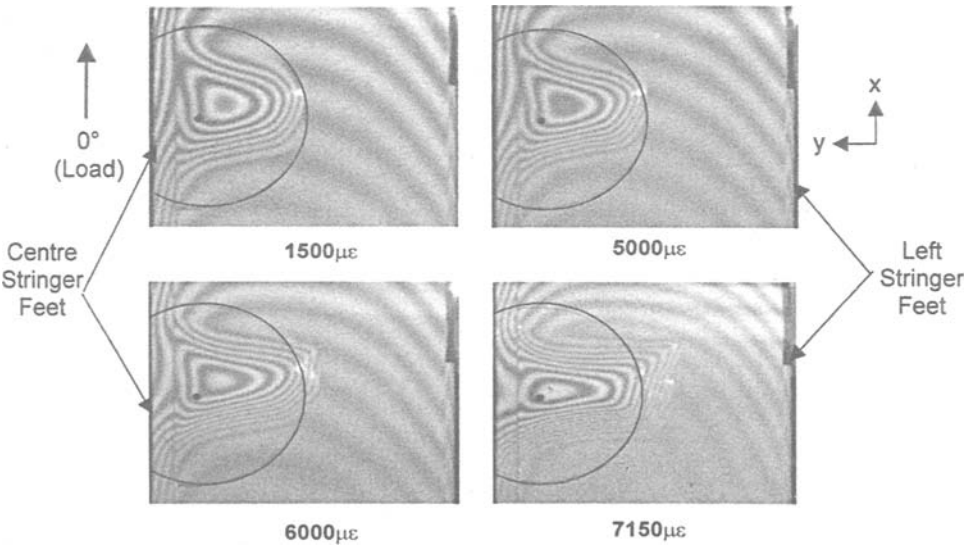


FIG. 10—*Moiré images of damage growth in a skin-stringer panel with a 50 mm-diameter defect at 0°/90° ply interface beneath stringer foot.*

edge and, at an applied strain of $-4950\ \mu\varepsilon$, started to extend across the bay, forming a double-peaked front. At an applied strain of $-6000\ \mu\varepsilon$, the panel started to buckle and the delamination extended along the stringer edge. Failure ($-7153\ \mu\varepsilon$) was preceded by rapid delamination growth and debonding of the central stringer.

The height of the delamination blister from the insert in the bay rose faster and was higher than that partly beneath the foot. In addition, as shown in Fig. 8, the damage growth was dependent on the defect site with respect to the substructure; at a given strain, the damage from the insert beneath the foot (SS#4) had grown less than that in the bay (SS#8). Consequently, the latter failed at a lower strain.

Skin-Stringer Panels with Defects at +45°/−45° Ply Interfaces

Panels SS#1 and SS#4 contained defects in the bay; both exhibited similar damage behavior to that shown in Fig. 7 for the plain panel. An elliptical blister formed at about $-2000\ \mu\varepsilon$ with the major axis aligned in the 105-deg direction. The sublaminate beneath the insert bent outwards as the damage extended along the major axis of the elliptical blister. The delamination grew until it reached the stringers, at which point it flattened and growth was inhibited. The panel buckled at about $-5200\ \mu\varepsilon$ and surface splitting developed within the stringer feet. Eventually, there was massive outward bending of the sublaminate beneath the insert and the panel failed.

The damage development in panel SS#2 (50 mm defect partly beneath the stringer foot) is shown in Fig. 11. There was no visible damage until at $-5274\ \mu\varepsilon$, when there was massive outward deflection beneath the insert and rapid delamination growth across two-thirds of the bay. The panel buckled and the damage continued to extend, reaching the right stringer at $-6200\ \mu\varepsilon$. The damage extended along both stringer feet, forming a horizontal band across the bay. At $-6413\ \mu\varepsilon$ cracking developed at the central stiffener foot and the panel failed.

In panel SS#3 (50 mm defect beneath the stringer centerline) there were no significant nonlinearities in the strain gage responses and no evidence of local buckling from the moiré interferometry.

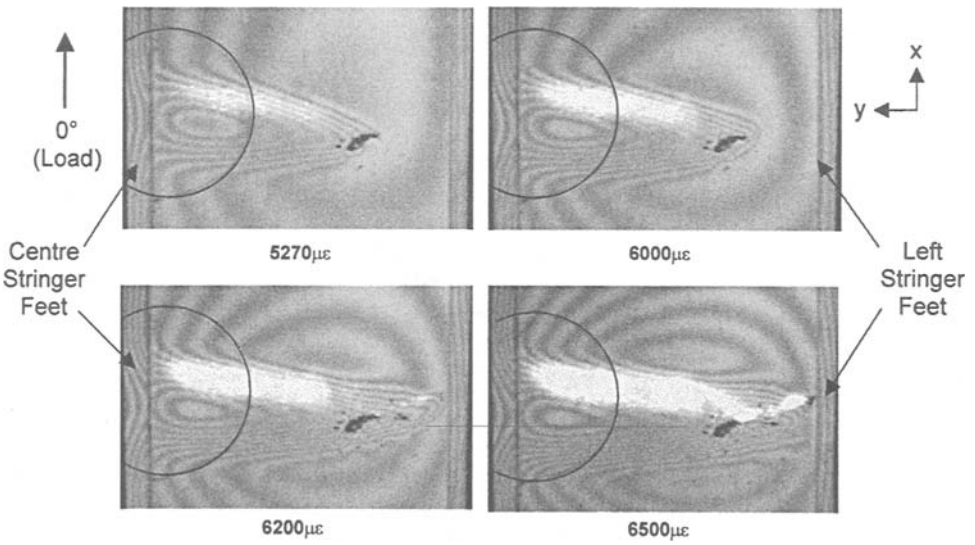


FIG. 11—*Moiré images of damage growth in a skin-stringer panel with a 50 mm-diameter defect at +45°/−45° ply interface beneath stringer foot.*

Global buckling was at $-5800\ \mu\varepsilon$ but, due to test limitations, at $-7174\ \mu\varepsilon$ the test was stopped. Ultrasonic inspection showed that some limited lateral growth had occurred.

There was little difference between the panels in the out-of-plane displacement of the damage, although the delamination from the insert beneath the foot did not start to grow until late in the test. The delamination initiation strains (Table 1) were very dependent on the defect location but all three panels failed at similar applied strains. The damage behavior (Fig. 9) in the two panels containing defects in the bay were relatively similar. However, the damage growth from the defect partly beneath the foot exhibited the same trends in growth as the other panels, but at a higher compressive strain.

Failure Analysis

Plain Panels

In the plain panels the damage mechanisms were governed by the orientation of the delaminated plies. Although the insert was at a single plane, the subsequent damage growth consisted of a number of mechanisms including multiplane delamination growth, ply cracking and fiber fracture. The fracture surfaces exhibited rotational symmetry about the defect center.

The fracture surfaces from a panel containing a defect at the 0°/90° ply interface are shown in Fig. 12. First, splits (marked as white dashed lines), tangential to the defect edge, had developed in the 0° ply directly above the defect plane. Cracks migrated through these splits, forming delaminations at the 2/3 (−45°/0°) ply interface growing parallel to the − 45° ply (zone B in Fig. 12). Splits also developed in the − 45° ply, through which the crack migrated into the 1/2 (+45°/−45°) ply interface, growing parallel to the +45° ply (zone A in Fig. 12). Finally, Mode II delamination had occurred at the defect plane (zone C in Fig. 12). This was all deduced from inspection of the fracture surface morphology.

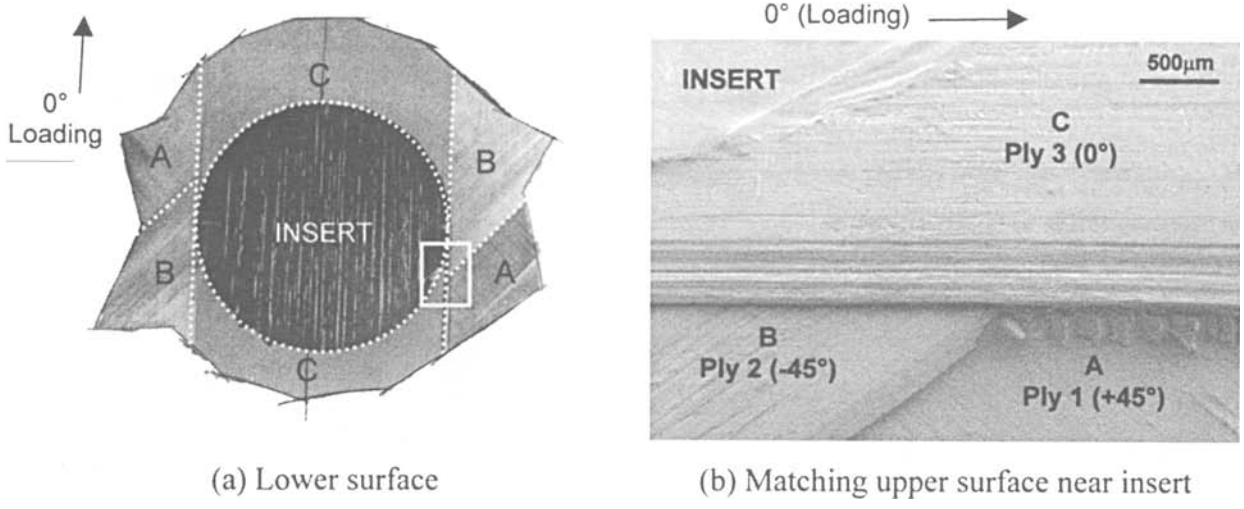
The damage growth at the +45°/−45° (5/6) ply interfaces was quite similar for all the defects (Fig. 13*a*). Unlike the previous panels, the delamination failure initiated at the defect plane and extended as a mixed-mode fracture along the +45° ply. Splits then developed in this ply, through which the delamination migrated and extended along the 90° plies in the adjacent interface (+45°/90°). The delamination continued to grow within this interface, as a Mode I dominated fracture, for the remainder of the test. Splits also developed in the 90° ply, through which the delamination migrated into the 0°/90° layer, where it grew parallel to the 0° ply.

Skin-Stringer Panels Containing Defects at the 0°/90° (3/4) Ply Interface

The fracture which led to the failure in SS#8 (35 mm defect in the bay) remained isolated from the original defect. However, the buckling strain of this panel had been reduced by the presence of the delamination. The failure of the panel with the defect beneath the stringer foot (SS#6) had initiated from splitting and delamination growth in the skin beneath the central stringer. This had led to stringer detachment, followed by local bending and massive skin delamination. The left-hand stringer had then debonded and the inner face of the skin had failed in compression at two sites, initiating from beneath the central and left-hand stringers. Finally, the right-hand stringer had debonded and the outer face of the panel had failed, initiating from the right-hand edge.

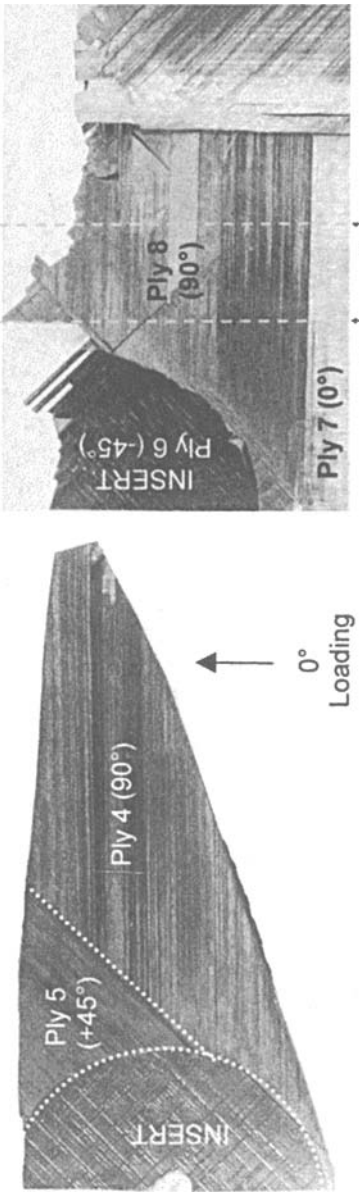
Skin-Stringer Panels Containing Defects at the +45°/−45° (5/6) Ply Interface

In both panels with inserts in the bay (SS#1 and SS#4), the delamination growth had initiated failure from beneath the stringer feet. In panel SS#1, the presence of damage beneath the central stringer foot had promoted detachment from the skin. This had caused compressive failure of the skin which initiated in the delaminated bay and extended across most of the panel width. In SS#4 compressive failure of the skin had initiated from beneath the right stringer after it had partially detached from the



(a) Lower surface (b) Matching upper surface near insert

FIG. 12—*Fracture morphology from a panel with a 50 mm-diameter defect at 0°/90° ply interface.*



(a) Plain (Panel F) – upper surface (b) Stiffened (SS#1) – lower surface

FIG. 13—*Fracture morphology from a 50 mm-diameter defect at +45°/−45° ply interface.*

skin. This mechanism was associated with the damage growth from the defect inducing local splitting and delamination within the foot.

In SS#2 (defect partly beneath the foot), delamination growth had developed from the insert and had extended beneath the central stringer into both bays. This stringer had then debonded from the skin, leading to initiation of compressive failure which had then grown towards the panel edges. The outer stringers had then failed and debonded.

Damage growth in the skin-stringer panels exhibited similarities with that in the plain panels, as can be seen from comparing Fig. 13*a* (Panel F) and Fig. 13*b* (SS#1). In the stiffened panels there had also been massive delamination growth within the 0°/90° (7/8) ply interface (below the defect plane). This had initiated from splits in the sixth (−45°) and seventh (0°) plies with some delamination at the −45°/0° (6/7) ply interface. The damage growth in the skin-stringer panels was not only governed by the orientation of the delaminated plies but also by that of the substrate. The damage growth had also been affected by the stringers; delamination was more extensive in the bays than beneath the stringers.

Modeling Results

Due to time constraints, only plain panels with 35 mm defects (Panels A and E) and skin-stringer panel with a 50 mm defect in the bay (SS#1) were chosen to be analyzed. The algorithm for moving the mesh to simulate growth, previously validated for plain laminates, was adapted for the skin-stringer panel. The models had not been designed to represent the observed crack migration, which had led to the crack front "seeking out" the ply interface with the most favorable fiber orientations for growth. To help account for this behavior, single-plane propagation from circular delaminations was simulated, not only at the 3/4 (0°/90°) and 5/6 (+45°/−45°) ply interfaces, but also at neighboring interfaces, both for plain panels (35 mm defect) and skin-stringer panels (50 mm defect).

Figure 14 shows elliptical contours of out-of-plane deflections for plain panels, prior to the development of any damage (corresponding to the images in Figs. 6 and 7). For the +45°/−45° ply interface the initiation sites (major axis of the ellipse) were at approximately 105 and 285 deg to the loading axis. Figures 15 and 16 show the corresponding maximum strain energy release rate around the circular delamination front for plain and skin-stringer panels, respectively. The maximum value was attained along elliptical axes of the height contour depicted in Fig. 14.

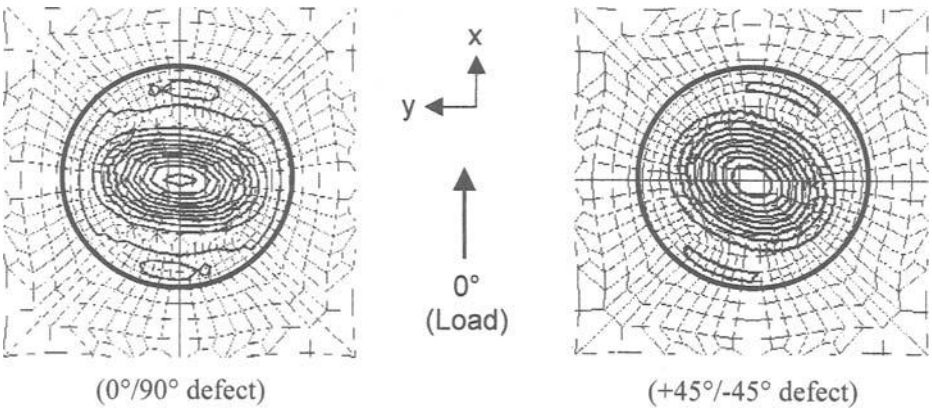


FIG. 14—*Predicted out-of-plane buckling displacement contours prior to delamination growth for a 35-mm-diameter defect.*

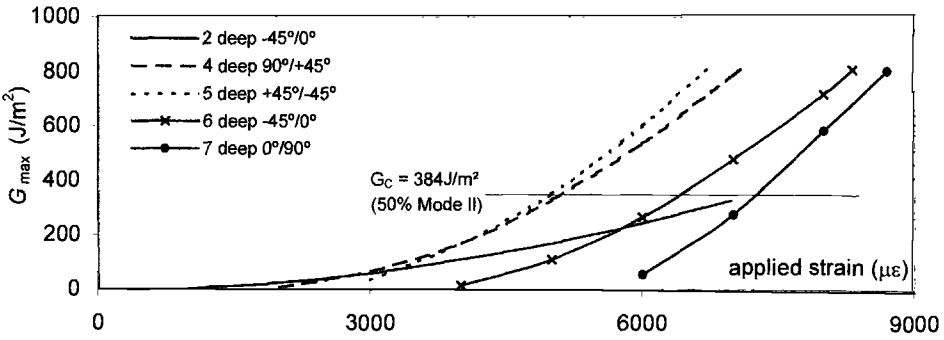


FIG. 15—*Predicted maximum strain energy release rate vs. in-plane strain (plain panels).*

The results shown in Fig. 16 indicate that interface at which growth initiated in both the plain and stiffened panels was the 5/6 (+45°/−45°) ply interface. Calculation of the mode-mixity [*12*] suggested that the delamination growth was about 50% Mode II (G_C = 384 J/m^2, as given in Ref *1*), implying an initiation strain of about −2000 $\mu\varepsilon$ in the stiffened panel (experimental value was −2850 $\mu\varepsilon$), although the fractographic results indicated that Mode I dominated growth at the 4/5 (+45°/90°) ply interface was more relevant. The energy release rate for the strain at which delamination growth initiated for the plain panels in Fig. 15 was below the critical energy release rate, which may be an indication that the sandwich core should not have been modeled as infinite.

Figure 17 shows the buckling behavior of the delaminated plies and the substrate for skin-stringer panels with single-plane delaminations at a number of depths. In this figure the out-of-plane deflection of the delaminated plies (local buckling) is shown as positive values while the out-of-plane deflection of the sublaminate (primarily global buckling) is shown as negative values. As the defect plane became deeper, the strain at which local buckling occurred increased. However, the opening of the delamination blister also became more rapid as the defect got deeper. Figure 18 shows the distribution of G (normalized with respect to G_{max}) around the defect boundary, s, for different defect depths. It can be seen that the strain energy release rate peaked at approximately the s = 0.25 and s = 0.75 positions, i.e., the lateral extents of the defect boundary. The only exception was the peak in the strain energy release rate for the defect five plies deep which was approximately at s = 0.33, as had been observed in the experiments (Fig. 7).

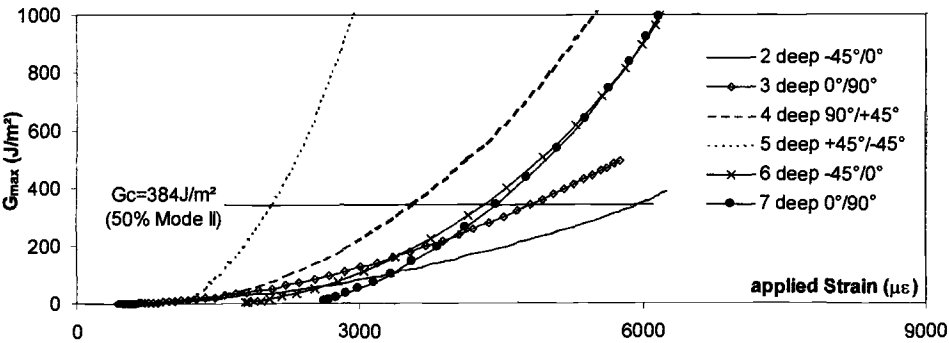


FIG. 16—*Predicted maximum strain energy release rate vs. in-plane strain (stiffened panels).*

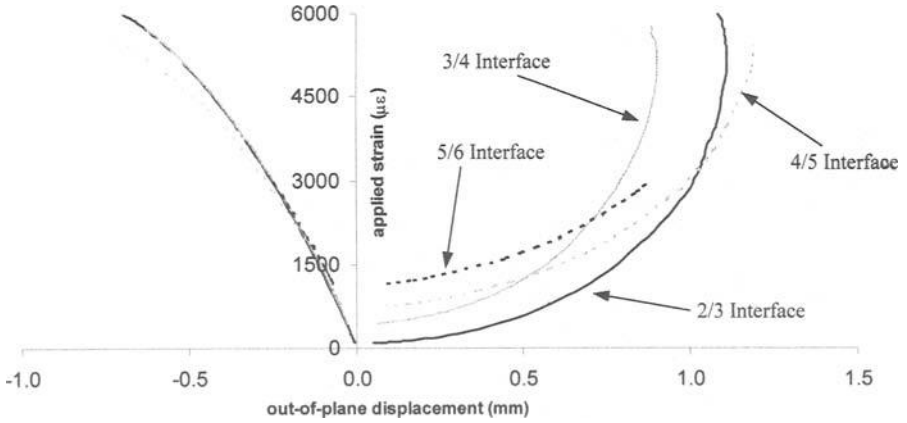


FIG. 17—*Strain vs. out-of-plane displacement for a stiffened panel with 50 mm-diameter defects at different ply interfaces.*

Figures 19*a, b,* and *c* show the predicted damage growth for skin-stringer panel SS#1 for defects three, four, and five plies deep, respectively. As indicated in Fig. 18, the maximum G was at the lateral extents of the defect boundary, and it was from these sites that the damage growth occurred. Models of skin-stringer panels containing bay delaminations predicted global buckling at strains between -6000 $\mu\varepsilon$ and -6500 $\mu\varepsilon$, depending on the defect depth, which was in good agreement with the experimental results.

Discussion

The damage development and structural failure were relatively similar in all the skin-stringer panels, although the detailed processes were affected by defect depth and location with respect to the substructure. Upon loading, the first event was local buckling of the delaminated plies on the stiffened face of the skin. This inward buckling was generally followed by outward bending of the sublaminate beneath the defect, such that the delaminated surfaces moved apart.

As the load increased, delamination initiated from the transverse boundaries of the insert, although the strain at which this occurred was strongly dependent on the surrounding substructure. The subsequent damage growth was similar to that observed in the plain panels. The damage then grew across the bay towards the stringers although, once it was beneath the stringers, growth was inhibited. Panel buckling developed at strains of between -5600 $\mu\varepsilon$ and -6600 $\mu\varepsilon$; damage in the bay promoted buckling. The damage then grew beneath the stringer feet and into the bays. The combination of the damage and large out-of-plane deflections (global buckling) led to stringer detachment, which promoted panel instability and skin failure.

The models were able to represent the local buckling, rotation of the elliptical blister resulting from an unbalanced sublaminate, and the location of the initiation site. It was important that the stacking sequence of delaminated plies was represented explicitly rather than by homogenized orthotropic properties. However, this can generate more complicated local buckling mode shapes than those predicted using homogenized properties, which may cause "snap-through" problems in the analysis. More sensitive time-stepping algorithms than those employed in this study may be required to fully model the behavior. The strong fracture mode dependence of the toughness in conjunction with the indication that the proportion of Mode II was larger in the analyses than in the experiments empha-

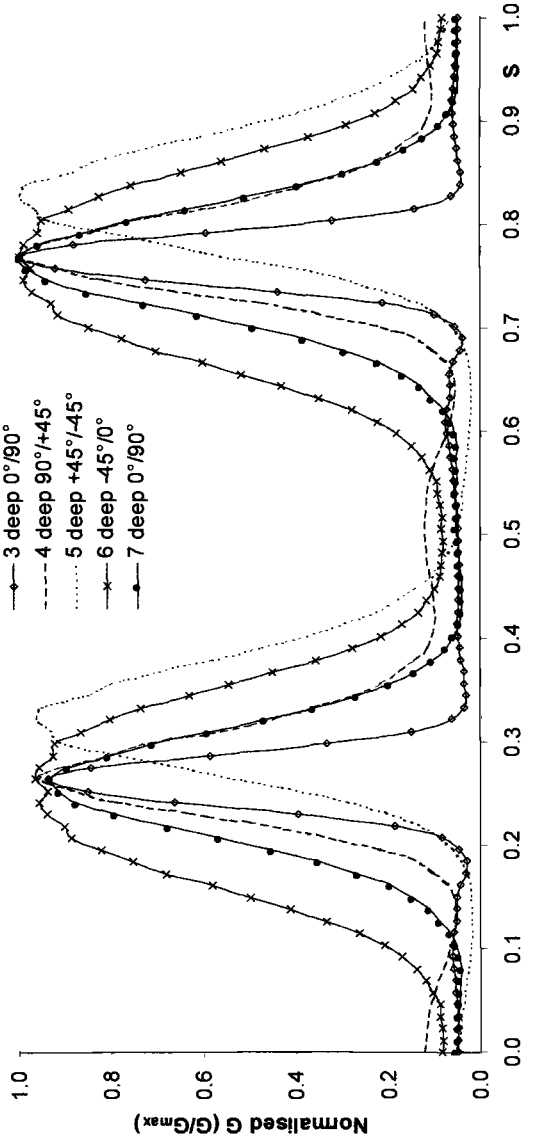


FIG. 18—*Distribution of normalized G (G/G_{max}) at initiation of delamination growth around defect boundaries for a stiffened panel with 50-mm-diameter bay defect at different depths.*

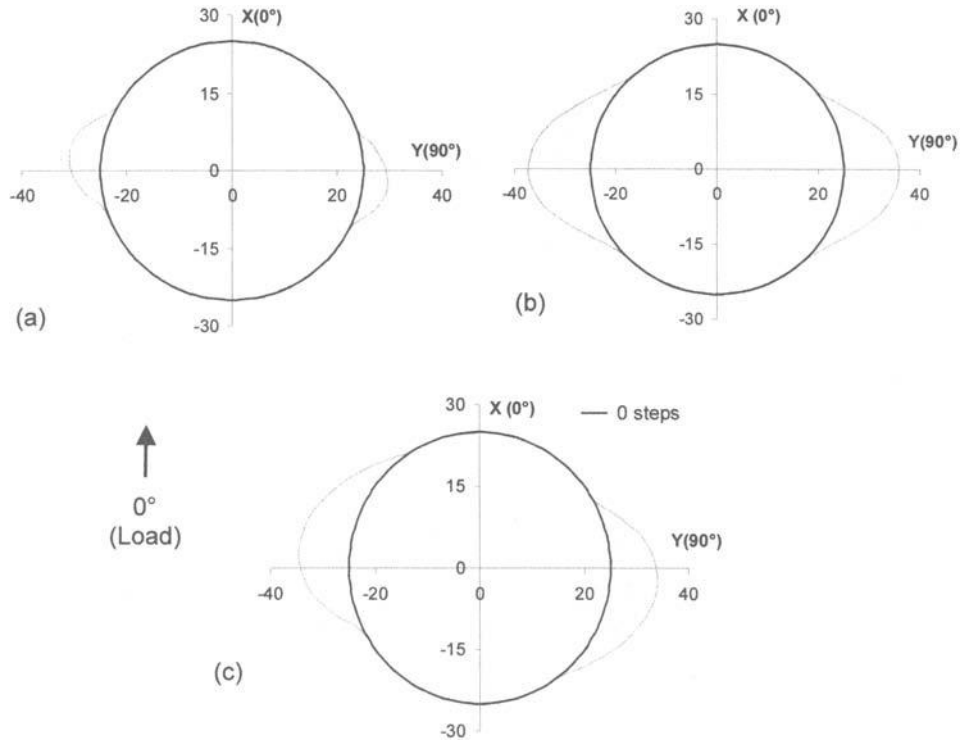


FIG. 19—*Predicted delamination growth in stiffened panel with 50 mm-diameter bay defect between* (a) *plies 3 and 4,* (b) *plies 4 and 5, and* (c) *plies and 5 and 6.*

sizes the importance of accurate mode separation for general layups, although refinement of the analysis (including Q_n term) would reduce the proportion of Mode II.

The damage growth processes and structural failure were affected by a number of factors, the most important of which were the ply interface of the initial defect. The lower thickness and transverse stiffness of the delaminated material for the defects at the 0°/90° ply interface accounted for the lower initiation strain. The subsequent damage growth could be explained by considering the damage mechanisms. Delamination growth did not remain in the defect plane, but migrated towards the free surface, via ply cracks, until it reached an interface in which the driving forces and upper ply directions were approximately coincident. In both instances the main driving force was identified from fractographic evidence as Mode I fracture parallel to the 90° plies [*1*]. For the defect at the 0°/90° ply interface, the upper ply direction was never coincident with this driving force, so growth was inhibited. However, for the defect at the +45°/−45° ply interface, the delamination migrated into the 90°/−45° ply interface, in which it then rapidly grew. This migration mechanism has been previously identified in studies into the fracture toughness of multidirectional laminates [*1*]. To simulate growth from defects and, more importantly, from structural features, it is essential that algorithms are developed to model delamination migration.

The migration mechanism has implications for the strength of the skin-stringer panels. For defects in the bay at the 0°/90° ply interface, the damage didn't reach the stringers before panel failure, so the strength was dictated by other factors such as global buckling. For the defects at the +45°/−45° ply interface, the damage extended up to the stringers before failure which promoted stringer detachment

and catastrophic failure. Delamination migration should be exploited to develop damage tolerant laminates such as by eliminating or reducing the number of 90° plies in the skin. In addition, optimizing the design of the stringer feet to reduce out-of-plane stresses, particularly during global buckling, should significantly enhance the panel strength.

For design, the critical depth for delamination growth under in-service loads should be determined from the predicted Mode I component, and then the stacking sequence of the outer material within this critical depth should be engineered to ensure that none of the ply directions are coincident with the driving forces. For example, in skin-stringer panels under compression this would mean there should be no 90° plies in the outer material up to the critical depth.

Although the early stages of damage growth were similar in the plain and stiffened panels, the local substructure had a significant effect in the later stages. As predicted by the models, the global panel buckling interacted with the damage and increased the Mode I component at the defect boundary. As the damage approached the stringers, the effect of the stress field changed the behavior from that observed in the plain panels; the out-of-plane constraint suppressed the Mode I component and the growth rate was reduced. For defects partly or completely beneath the stringer feet, this constraint led to massive increases in initiation strain.

The moving mesh technique had two distinct advantages over the more common method of simulating crack growth by releasing nodal constraints. First, an initially continuous crack front maintained a continuous profile, thereby avoiding the generation of any mesh-dependent spikes in the strain energy release rate profile. Second, during each growth increment, the connectivities were not changed, and the applied loads and nodal coordinates were only slightly modified. Consequently the stiffness matrix was essentially unchanged, and the previous solution could be used as an approximate solution during the time-stepping, avoiding the need to completely restart the analysis after each increment. Also, this technique simplified tracking of the nodes along the crack front and the evaluation of the energy release rate. However, since the element topology did not change, only moderate crack extension could be modeled, typically 50% of the delamination size [*8,9*]. Larger crack extension would require remeshing.

It should be noted that the approach taken here (evaluating the tendency to grow of cracks at each of a number of ply interfaces) and which was first outlined in Ref *12* is more effective in laminates and structures containing delaminations resulting from impact. It can then be assumed that there exists a sizable delamination at each interface, and one of these will, due to its orientation and depth, be the most favorable for delamination growth. Analysis times could be reduced if an algorithm were developed to automatically identify this critical ply interface, thus removing the need for redundant simulations. Realistic simulation of delamination growth using a fracture mechanics approach depends on representative toughness data in terms of not only the mode mixture but also the ply orientation relative to the loading direction.

Conclusions

The following conclusions have been drawn from the characterization and modeling of delamination growth from implanted defects in CFRP skin-stringer panels under compression.

1. There were similarities between damage growth in plain and skin-stringer panels, particularly for damage in the bay between stringers.
2. The ply interface of the defect and location with respect to the substructure governed the delamination initiation and damage growth processes.
3. Delamination growth from a single plane defect did not occur at one plane, but migrated through the thickness via ply cracks, until it reached an interface in which the driving forces and ply directions were approximately coincident.
4. The substructure (stringer) inhibited delamination buckling which, in turn, increased damage initiation strains and reduced growth rates.

5. Failure of the skin-stringer panels was induced by the interaction between the delaminated material and the stringer foot. The high out-of-plane displacements generated by global buckling then led to stringer detachment and skin compression failure.

6. The moving mesh technique successfully predicted delamination buckling, initiation, and early stages of growth in the skin-stringer panels. This technique is highly efficient at simulating single plane delamination growth. However, further research is required to model crack migration or the damage growth beneath structural features.

7. The delamination migration mechanism could be used to develop damage-tolerant laminates such as by reducing the number of 90° plies. In addition, designing the stringer feet to reduce out-of-plane stresses, particularly during global buckling, will enhance the panel strength.

Acknowledgments

This work was in part funded by the U.K. MOD Applied Research and U.K. DTI CARAD Programmes, and the Swedish Defence Material Administration (FMV). The authors would like to acknowledge the contributions of Johan Alpman, Robin Olsson, Leif Asp, Sarah Bishop, Alison Dewer, and Matthew Hiley.

References

[1] Greenhalgh, E., "Characterisation of Mixed-mode Delamination Growth in Carbon-fiber Composites," Ph.D. thesis, Imperial College, London, 1998.

[2] Greenhalgh, E. and Singh, S., "Investigation of the Failure Mechanisms for Delamination Growth from Embedded Defects," *Proceedings, 12th International Conference for Composite Materials*, T. Massard, Ed., Paris, France, 1999.

[3] Peak, S. and Springer, G., "The Behavior of Delaminations in Composite Plates—Analytical and Experimental Results," *Journal of Composite Materials*, Vol. 25, 1991, pp. 907–929.

[4] Wiggenraad, J., Greenhalgh, E., Gadke, M., Maison, S., Ousset, Y., Roudolff, F., and La Barbera, A., "Damage Propagation in Composite Structural Elements—Structural Experiments and Analyses," *Composites Structures*, Vol. 36, 1997.

[5] Nilsson, K.-F. and Storåkers, B., "On the Interface Crack Growth in Composite Plates," *Journal of Applied Mechanics*, Vol. 59, 1992, pp. 530–538.

[6] Nilsson, K.-F., "On Growth of Crack Fronts in the DCB-Test," *Composites Engineering*, Vol. 3, 1993, pp. 527–546.

[7] Nilsson, K.-F., Thesken, J. C., Sindelar, P., Giannakopoulos, A., and Storåkers, B., "A Theoretical and Experimental Investigation of Buckling Induced Delamination Growth," *Journal of Mechanics of Physical Solids*, Vol. 41, 1993, pp. 749–782.

[8] Nilsson, K.-F. and Giannakopolus, A., "A Finite-Element Analysis of Configurational Stability and Finite Growth of Buckling Driven Delamination," *Journal of Mechanics and Physics of Solids*, Vol. 43, 1995, pp. 1983–2021.

[9] Nilsson, K.-F., Asp, L., and Alpman, J., "Delamination Buckling and Growth at Global Buckling," *Proceedings, 1st International Conference on Damage and Failure of Interfaces*, H.-P. Rossmanith, Ed., Vienna, 1997, pp. 193–202.

[10] Nilsson, K.-F., Asp, L. E., Alpman, J. E., and Nystedt, L., "Delamination Buckling and Growth for Delaminations at Different Depths in a Slender Composite Panel," FFA TN-1999-09, The Aeronautical Research Institute of Sweden, 1999.

[11] Giannakopolous, A., Nilsson, K.-F., and Tsamasphyros, G., "The Contact Problem at Delamination," *Journal of Applied Mechanics*, Vol. 62, 1995, pp. 989–996.

[12] Singh, S., Asp, L., Nilsson, K.-F., and Alpman, J., "Development of a Model for Delamination Buckling and Growth in Stiffened Composite Structures," FFA TN 1998-53, The Aeronautical Research Institute of Sweden, 1998.

[13] Whitcomb, J. D., "Finite Element Analysis of Instability Related Delamination Growth," *Journal of Composite Materials*, Vol. 15, 1981, pp. 403–426.

[14] Hutchinson, J. W. and Suo, Z., "Mixed Mode Cracking in Layered Materials," *Advances in Applied Mechanics*, Vol. 28, Academic Press, New York, 1992, pp. 63–191.

Carl Q. Rousseau,[1] *Donald J. Baker,*[2] *and J. Donn Hethcock*[1]

Parametric Study of Three-Stringer Panel Compression-After-Impact Strength

REFERENCE: Rousseau, C. Q., Baker, D. J., and Hethcock, J. D., **"Parametric Study of Three-Stringer Panel Compression-After-Impact Strength,"** *Composite Structures: Theory and Practice, ASTM STP 1383,* P. Grant and C. Q. Rousseau, Eds., American Society for Testing and Materials, West Conshohocken, PA, 2000, pp. 72–104.

ABSTRACT: Damage tolerance requirements for integrally stiffened composite wing skins are typically met using design allowables generated by testing impact-damaged subcomponents, such as three-stringer stiffened panels. To improve these structures, it is necessary to evaluate the critical design parameters associated with three-stringer stiffened-panel compressive behavior. During recent research and development programs, four structural parameters were identified as sources for strength variation: (*a*) material system, (*b*) stringer configuration, (*c*) skin layup, and (*d*) form of axial reinforcement (tape versus pultruded carbon rods). The relative effects of these parameters on damage resistance and damage tolerance were evaluated numerically and experimentally. Material system and geometric configuration had the largest influence on damage resistance; location and extent of the damage zone influenced the sublaminate buckling behavior, failure initiation site, and compressive ultimate strength. A practical global-local modeling technique captured observed experimental behavior and has the potential to identify critical damage sites and estimate failure loads prior to testing. More careful consideration should be given to accurate simulation of boundary conditions in numerical and experimental studies.

KEYWORDS: composite material, structure, damage tolerance, impact, compression, experimental, numerical, wing, stringer

In the field of applied composite structural mechanics, a great deal of time and effort has been devoted to ensuring the structural integrity of aircraft components in the presence of low velocity impact damage. The low velocity impact threat has long been viewed as the most critical type of in-service damage for laminated composite structures[3]; thus all certifying/specifying agencies have explicit impact damage requirements as part of their more general static strength and/or damage tolerance rules [*1–3*]. Numerous publications have defined the general problem and offered both experimental and analytical studies of various critical variables [e.g., *4–10*]. The purpose of this paper is to add to the current body of knowledge by collecting available compression-after-impact (CAI) data from a variety of sources and attempting to isolate and evaluate several key structural parameters. A brief description of damage resistance, damage tolerance, and the generic three-stringer panel problem is given in the following introductory subsections, followed by a statement of the scope and objective of this parametric study.

Damage Resistance and Damage Tolerance

The framework for this study is set by regulatory static strength and damage tolerance requirements and accepted methods of quantifying damage and assessing its criticality. Specifically, such a regu-

[1] Principal engineer and senior engineering specialist, respectively, Bell Helicopter Textron Inc., Fort Worth, TX 76101.

[2] Research scientist, USA ARL/VTD, NASA Langley Research Center, Hampton, VA 23681.

[3] Discrete source damage (DSD) from ballistic or uncontained engine failure threats is another important damage-tolerant design consideration. While DSD has sized large portions of composite structure in fixed-wing aircraft designs, CAI has proven to be the main design driver in Bell Helicopter military and civil tiltrotor aircraft.

Copyright© 2001by ASTM International www.astm.org

lation is the Federal Aviation Administration (FAA) Advisory Circular AC29-2B, "Certification of Transport Category Rotorcraft," Section (g)(5), which requires that "static strength substantiation should consider . . . impact damage expected during service up to the established threshold of detectability of the field inspection methods to be employed." The field inspection methods are assumed to be visual; thus the established threshold of detectability is commonly defined as "barely visible impact damage" (BVID). BVID is quantified by performing an impact survey on a representative structure and choosing a particular energy level or dent depth, with concurrence of the regulatory or specifying agency. Usually an upper bound energy level of 135 J (1200 in.-lb) is used for thick structure, based on a U.S. Air Force study of impact threats such as tool-drop (some form of through-penetration damage tolerance is required for thin-gage structure).

Note that a structure's *resistance* to damage is not relevant to flight safety. Only the tolerance of undiscovered/unrepaired damage under flight conditions is of concern to the regulator. Nonetheless, for substantiation purposes, as well as for economic durability reasons, the damage resistance of a structure must be separately characterized, at least to the extent of identifying a threshold of detectability. This characterization effort typically takes the form of the above-noted impact damage survey. This survey introduces the first of several parameters, which affects the resulting level of damage tolerance. These parameters are the boundary conditions (in terms of both panel support and location relative to geometric details such as the stringers and ply edges) for the impact events and the energy and tip geometry of the indenter.

The damage tolerance of a structure is determined by imposing the worst-case impact damage (the location on the structure where the BVID energy-level is highest) and testing to failure under the most critical loading condition, usually compression. The resulting strength or strain to failure is then reduced to account for environmental and statistical effects, and used as a special design allowable over the whole expanse of primary structure represented by the tested configuration.

Three-Stringer Panel Problem

In order to realistically simulate the boundary conditions of stiffened panel structures (both for the impact event and subsequent residual strength testing), the common approach is to provide one stringer and two adjacent skin bays for the test region, with a stringer on either side to approximate the proper widthwise and skin-bay constraint. The length of the specimen is determined by the maximum rib or frame spacing (assumed to be the worst case for compressive stability). Panels are often flat rather than curved, in order to simplify specimen fabrication. This simplification is generally assumed to be conservative (for curvature transverse to the loading direction), since it should yield lower results than would a curved panel. Another conservative simplification is in the form of end supports for the impact events. Specimen ends are typically clamped in wooden forms or potted in epoxy casting material (required for subsequent compression testing). Both of these end conditions are assumed to absorb less energy from the impact event than deeper, less stiff rib or frame webs, thus imparting more energy to the test panel than would be seen by the actual on-aircraft fuselage or wing panel.

Scope and Objective of the Parametric Study

The purpose of this paper is to identify and isolate several key parameters controlling the structural efficiency of skin-stringer compressive panels meeting a given level of damage tolerance. This study uses a compilation of available three-stringer compression-after-impact data, and thus is not a designed experiment to isolate particular variables. Nonetheless, a study of the available data combined with limited numerical verification allows certain conclusions to be drawn and improvements in methodology to be discussed. A list of parameters and their studied ranges is given in Table 1. A schematic of a typical I-beam skin-stringer cross section is shown in Fig. 1, and representative tape- and rod-reinforced hat sections are shown in Figs. 2–4. The following sections of this paper describe the experimental and numerical results, and provide a summary discussion and conclusions.

TABLE 1—*Parametric variables.*

Parameter	Initial	Intermediate	Intermediate	Intermediate	Final
Stiffener section	I	...	...	...	Hat
Skin layup	(0/12/0)[a]	(1/16/2)	...	(3/10/2)	(10/10/2)
Plank layup	none	$(4_{RP}/26/4)$[b]	(21/16/2)[c]	(21/16/2)	(35/32/2)
Resin	3501-6	8552	E7T1-2	3900-2	5276-1
Axial reinforcement	Tape	...	...	...	Rodpack

[a] Number of (0/±45/90) plies.

[b] Subscript "RP" denotes rodpack (pultruded carbon rods encapsulated in syntactic adhesive rather than unidirectional tape layers).

[c] Grade 05 FM300 adhesive layers above and below each 0-deg ply pack in plank.

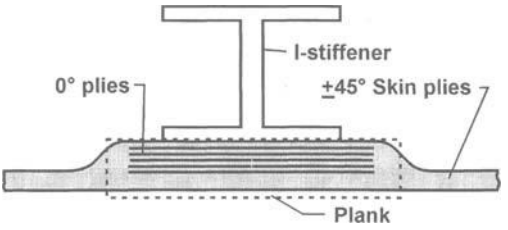


FIG. 1—*Schematic of a typical I-beam/plank/skin configuration.*

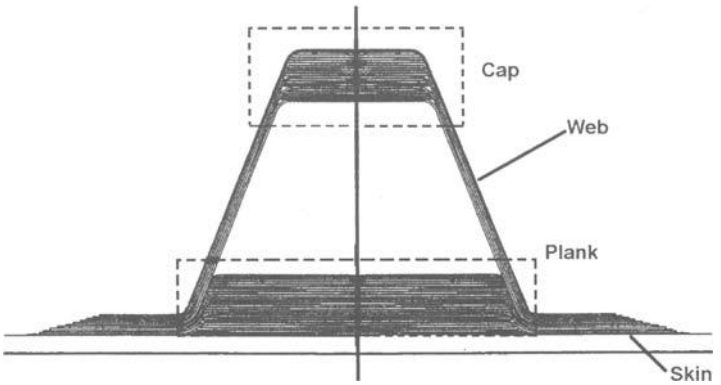


FIG. 2—*Schematic of a typical tape hat/plank/skin configuration.*

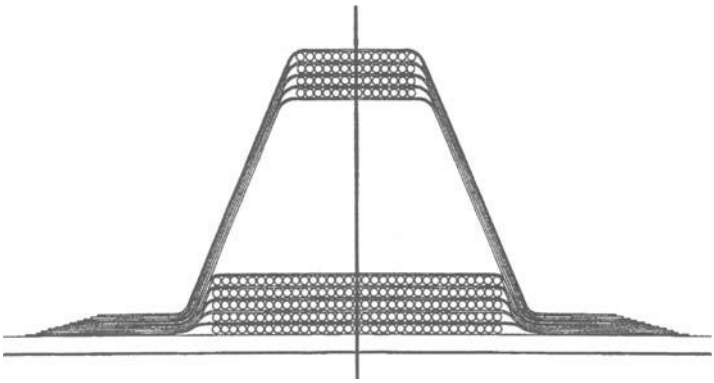


FIG. 3—*Schematic of a typical rod-reinforced hat/plank/skin configuration.*

Experimental Results

This section is separated into discussions of impact survey and compression testing results. The three-stringer panel configurations studied in this paper are described in Table 2. Note that the nomenclature was chosen in order to efficiently capture the state of the parametric variables.

Damage Resistance

Impact surveys were conducted on a variety of three-stringer panels using apparatuses such as that shown in Fig. 5. The drop tower drops a 25-lb (11.3 kg) mass that has a 0.5 in. (0.5 mm) spherical radius on the impactor. The panels are clamped to a table using the potted ends for panels to be tested later or wooden end supports for the damage survey panels. Impact surveys described in this paper were conducted at Bell Helicopter (Fort Worth, TX) and in the NASA Langley Research Center (LaRC) Structural Mechanics Laboratory. These tests were performed without dynamic instrumentation. Impact locations in the surveys were made along the lengths of the specimens without regard to rib support location. During these impact surveys, a number of widthwise locations were hit—typically the skin, mid-stringer, flange termination, plank ramp, and/or web-skin intersection. The results of all impact events were then judged visually by engineering and in some cases by U.S. Government representatives, and a somewhat subjective determination was made of the threshold of visibility. Dent depth was not measured. Future testing would benefit both from instrumentation and careful control of impact location relative to rib spacing, clamping, and stiffness.

Representative examples of survey panels are shown in Figs. 6 and 7. Contact pulse-echo C-scans (color maps of ultrasonic attenuation) were performed on each impact site and the perimeter of the

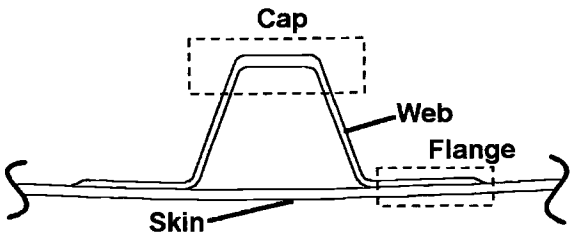


FIG. 4—*Schematic of a typical tape hat/skin configuration.*

TABLE 2—*Panel configurations.*

Nomen.	Stiffener	Skin[a,b]	Web[a]	Flange[a]	Plank[a]	Cap[a]	Resin	Tested
IT1A	I, tape	(1/16/2)	(30/10/4)	(15/5/2)	(21/16/2)	(30/10/4)	3501-6	2
IT1B	I, tape	(1/16/2)	(30/10/4)	(15/5/2)	(21/16/2)[c]	(30/10/4)	3501-6	2
IT2B	I, tape	(1/16/2)	(28/10/4)	(14/5/2)	(28/16/2)[c]	(30/10/3)	3501-6	2
IT1C	I, tape	(1/16/2)	(30/10/4)	(15/5/2)	(21/16/2)	(30/10/4)	8552	3
IT1D	I, tape	(1/16/2)	(30/10/4)	(15/5/2)	(21/16/2)	(30/10/4)	E7T1-2	3
HT1C	Hat, tape	(1/16/2)	(0/10/0)	(0/10/0)	(35/32/2)	(36/30/0)	8552	3
HT1D	Hat, tape	(1/16/2)	(0/10/0)	(0/10/0)	(35/32/2)	(36/30/0)	E7T1-2	1
HR1C	Hat, rod	(1/16/2)	(0/9/1)	(0/9/1)	(4_{RP}/26/4)	(4_{RP}/9/1)	8552	2
HR3D	Hat, rod	(0/12/0)	(0/10/0)	(0/10/0)	(4_{RP}/26/4)	(4_{RP}/10/0)	E7T1-2	4
HT4C	Hat, tape	(3/10/2)	(2_F/8_F/0)	(2_F/8_F/0)	...	(20_T,2_F/8_F/0)	8552	3
HT4E	Hat, tape	(3/10/2)	(2_F/8_F/0)	(2_F/8_F/0)	...	(20_T,2_F/8_F/0)	3900-2	3
HT5C	Hat, tape	(10/10/2)	(2_F/8_F/0)	(2_F/8_F/0)	...	(20_T,2_F/8_F/0)	8552	3
HT5E	Hat, tape	(10/10/2)	(2_F/8_F/0)	(2_F/8_F/0)	...	(20_T,2_F/8_F/0)	3900-2	3
HT5F	Hat, tape	(10/10/2)	(2_F/8_F/0)	(2_F/8_F/0)	...	(20_T,2_F/8_F/0)	5276-1	5

[a] Number of (0/±45/90) plies; tape unless otherwise indicated (RP = rodpack or F = fabric).

[b] One ply of 45-deg fine-grade carbon fabric on IML, and one on OML not shown in layups.

[c] Grade 05 FM300 adhesive layers above and below each 0-deg ply pack in plank.

maximum delaminated area marked in pen. In some cases, the area and aspect ratio of this marked region was measured using a planimeter. The panel descriptions, compression test results, and areal characterization of the impact damage zones (as measured on the impact survey panels, not on the test specimens themselves) are given in Table 3. As a general observation from the survey panels, it is apparent that material system and geometric configuration had the largest influence on damage resistance. The combination of geometric configuration and end support essentially defined the boundary conditions for the impact event.

Finally, for the numerical modeling effort reported later in this paper, additional ultrasonic work was done: time-of-flight (TOF) measurements. These measurements were performed only on the damage sites chosen for analysis in order to discriminate between the individual delaminations. Further discussion of these data is reserved for the subsequent numerical results section.

Compressive Strength-After-Impact

A typical three-stringer compression test specimen is shown in Fig. 8. Carbon/epoxy doublers 4 in. (102 mm) long were bonded to the stringer caps and skin outer mold line (OML) opposite the plank regions, and on the inside of the caps/flanges of the stringers. The ends were potted in RP1220 potting compound, 1 in. (25 mm) thick, by the Bell Helicopter Methods and Materials Lab. The potting was restrained in an aluminum frame made of 1 × 1 in. (25 × 25 mm) bar. The potted ends were then ground flat and parallel to a tolerance of 0.005 in. (0.13 mm). Various configurations of strain gage, transverse LVDT, and moiré interferometry instrumentation were used. The specimens were tested either in the Bell Helicopter Mechanical Test Lab or the NASA Langley Research Center Structural Test Lab. A typical test configuration is shown in Fig. 9.

Compression test results for each specimen are summarized in Table 3. Comparing results for the I-stiffened panels IT1A and IT1B made from Hexcel 3501-6 resin system indicates that interleaving adhesive layers between the local 0-deg plies added to the panels at the stiffeners (see Fig. 1) and the continuous ±45-deg layers in the plank region of the skin increased the failure strain by over 1200 $\mu\varepsilon$. However, a change in plank and stringer configuration (IT1B to IT2B) decreases the failure strain by 1100 $\mu\varepsilon$. Changing from the untoughened 3501-6 resin system to the first-generation toughened 8552 resin (but without adhesive interlayers) resulted in a much higher BVID threshold (500 in. · lb

(56 J) for IT1B versus 1000 in. · lb (113 J) for IT1C), but also a larger damage area (noted by engineers but not quantified in the IT1B data in Table 3). Thus the failure strain for the IT1C panels was 1600 $\mu\varepsilon$ lower than IT1B and also somewhat lower (337 $\mu\varepsilon$) than IT1A. Changing to the E7T1-2 toughened resin system in the panels with an I-stiffener configuration (IT1D versus IT1C) yields somewhat better results (perhaps 620 $\mu\varepsilon$) relative to 8552, but still with a much higher BVID threshold. Note that while higher BVID thresholds are desirable from an operational and supportability standpoint, the toughened resins are penalized due to the visual-inspection-based BVID qualification criterion.

Changing the reinforcement type in the soft skin/plank/hat-section configuration from tape to carbon rod reinforcement (HT to HR) yields mixed results. A detailed examination of the rod-reinforced hat-section panels indicated that the rods in the first layer of the subcomponents made from 8552 resin system (HR1C) were fractured by the 550 in. · lb (62 J) and 1200 in. · lb (136 J) impact events. When

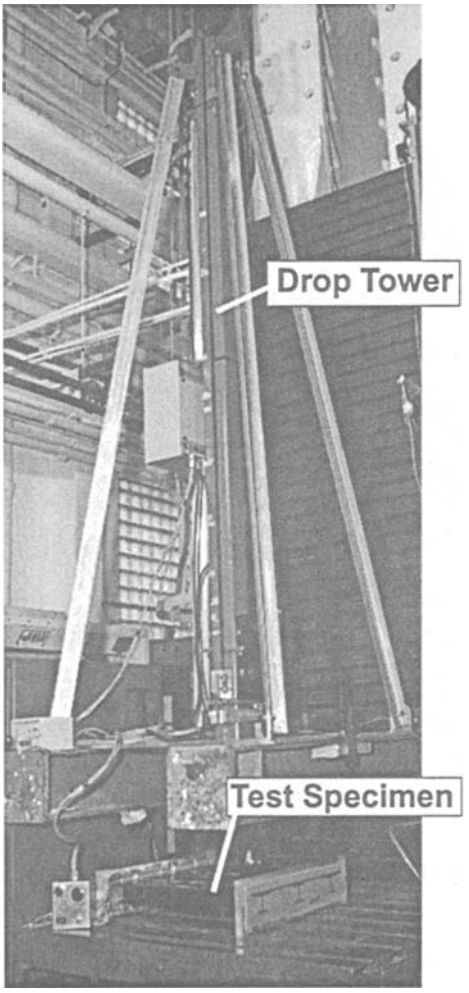


FIG. 5—*NASA Langley low-velocity drop tower.*

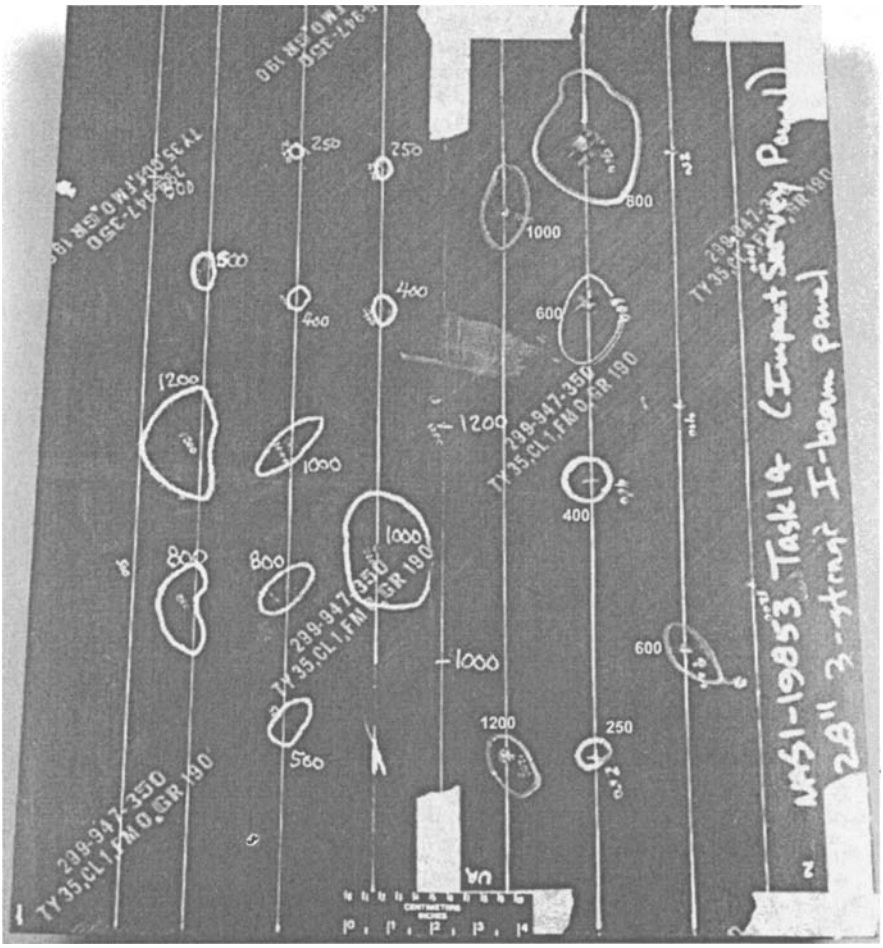


FIG. 6—*Three-stringer IM7/E7T1-2 I-beam impact survey panel.*

impacted with 250 in. · lb (28 J) of energy to obtain BVID, the rod-reinforced hat-section panel made from E7T1-2 resin system and with a (0/12/0) skin layup (HR3D) did not have fractured layers under the impact site. However, when the (1/16/2) skin layup was used (H*1*), both 8552 and E7T1-2 panels generally showed high failure strains when the plank region was not severely impacted, and low strains to failure when it was. Similarly, in the plankless hard-skin/hat configurations (HT4* and HT5*), the harder the skins, the lower the failure strains. Finally, it is noted that the tougher 3900-2 and 5276-1 resins outperformed the less tough 8552 resin system in the hard skin configurations; and the plankless designs, overall, did better than the discretely stiffened soft-skin/plank configurations (i.e., internal ply dropoffs in planks caused pseudo-free-edge/Poisson effects that were detrimental to skin compressive stability).

Typical strain results for the I- and hat-stiffened panels are shown in Fig. 10*a* through 10*f*. Strain gage results for Specimen IT1D0, an undamaged I-stiffened panel, are shown in Fig. 10*a* for the centerline cross section and Fig. 10*b* for a cross section at the quarter point. Figure 10*a* indicates a small

amount of bending in the center and one side stiffener and no bending in the skin. The results shown in Fig. 10*b* for a cross section located at the quarter point indicate bending in the skin and no bending in stiffeners. Strain gage results for Specimen IT1D2, a panel that has been impacted with a 1000 in. · lb (113 J) of energy near the skin and ramp intersection, are shown in Fig. 10*b* and 10*c*. Results shown in Fig. 10*c*, for a cross section located at the center of the specimen, indicate bending in the skin and stiffener adjacent to the impact site. Results shown in Fig. 10*d* for a cross section located at the quarter point indicate some bending in the skin and stiffener in the bay adjacent to the impact site. Strain gage results for a hat-stiffened panel, Specimen HT1D1, are shown in Figs. 10*e* and 10*f*. This panel was impacted with 400 in. · lb (45 J) of energy on the ramp between the hat flange and the skin to give BVID on the skin side. Strain gage results shown in Fig. 10*e* indicate bending in the skin on the impact side and also in the center stiffener. The results at the quarter-point cross section, shown in Fig. 10*f*, indicate bending in the center stiffener and a smaller amount of bending in the outside stiffener. The local moiré fringer pattern at the impact site of specimen IT1D2 at a load of 328 klbf (1.46 MN), with the delamination perimeter superimposed over it, is shown in Fig. 11. Note the high local gradients in out-of-plane displacement due to both fiber damage from the indenter and delaminated sublaminate buckling.

Typical failures for the I- and hat-stiffened panels are shown in Figs. 12*a* through 12*h*. The failure of undamaged Specimen IT1D0 is shown in Figs. 12*a* and 12*b*. Figure 12*a* shows the failure on the skin side of the test specimen, while the opposite side is shown in Fig. 12*b*. The I-stiffeners have failed as shown in Fig. 12*b*. The failure of Specimen IT1D2 is shown in Figs. 12*c* and 12*d*. The failure of the skin side shown in Fig. 12*c* has the same pattern as the undamaged specimen shown in Fig.

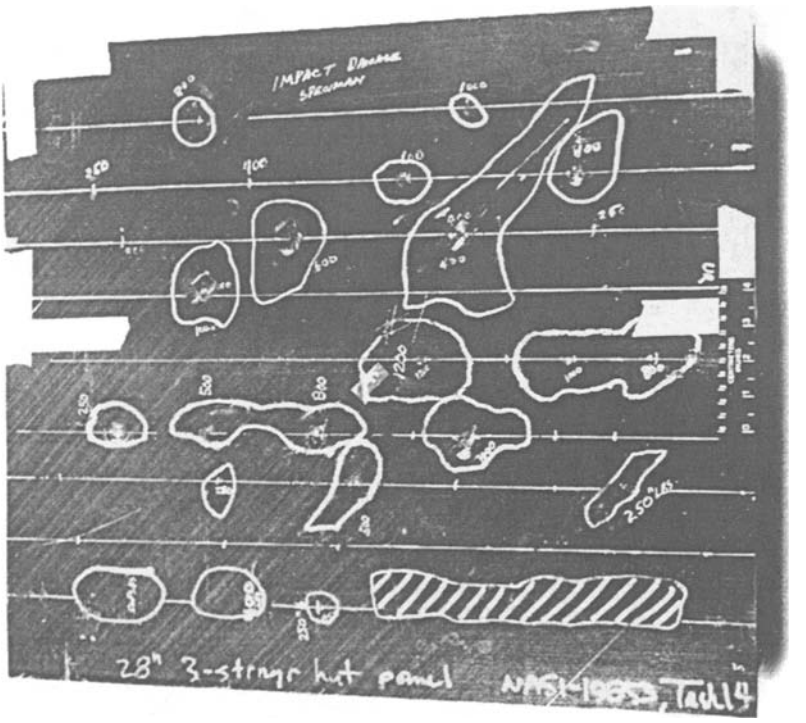


FIG. 7—*Three-stringer IM7/E7T1-2 tape hat impact survey panel.*

TABLE 3—*Compression test results.*

	EA									Damage						P_{max}[c]		
	Skin		Plank[a]		Stringer[a]		Total		Critical	Energy		Area		Orien[b]				*P/EA*
Spec ID	(Msi·in^2)	(MPa·m^2)	(Msi·in^2)	(MPa·m^2)	(Msi·in^2)	(MPa·m^2)	(Msi·in^2)	(MPa·m^2)	location	(in·lb)	(J)	(in^2)	(mm^2)	AR[b]	(deg)	(klbf)	(MN)	(με)
IT1A1	...	...	...	...	...	...	76.03	338	Ramp	550	62.1	...	...	...	...	...	...	3821
IT1A2	...	...	...	...	...	...	76.03	338	Ramp	550	62.1	...	...	...	...	...	...	3538
IT1B1	5.34	23.8	28.83	128	41.86	186	76.03	338	Ramp	500	56.5	...	...	...	...	374.5	1.67	4926
IT1B2	5.34	23.8	28.83	128	41.86	186	76.03	338	Ramp	500	56.5	...	...	...	...	377.4	1.68	4964
IT2B1	4.47	19.9	50.79	226	32.52	145	87.78	390	Ramp	500	56.5	...	...	...	...	348.8	1.55	3974
IT2B2	4.47	19.9	50.79	226	32.52	145	87.78	390	Ramp	500	56.5	...	...	...	...	325.3	1.45	3706
IT1C1	3.65	16.2	44.20	197	35.55	158	83.40	371	Ramp	1000	113	10.62	6852	0.57	0	272.4	1.21	3266
IT1C2	3.65	16.2	44.20	197	35.55	158	83.40	371	Ramp	1000	113	10.62	6852	0.57	0	276.7	1.23	3318
IT1C3	3.65	16.2	44.20	197	35.55	158	83.40	371	Ramp	1000	113	10.62	6852	0.57	0	287.4	1.28	3446
IT1D0	4.68	20.8	15.78	70.2	13.24	58.9	91.75	408	NA	0	0	0	0	NA	NA	431.3	1.92	4700
IT1D1	4.68	20.8	15.78	70.2	13.24	58.9	91.75	408	Ramp	1000	113	2.34	1510	0.80	0	383.4	1.71	4179
IT1D2	4.68	20.8	15.78	70.2	13.24	58.9	91.75	408	Ramp[d]	1000	113	4.00	2581	0.70	0	343.7	1.53	3746
HT1C1	11.29	50.2	47.13	210	27.78	124	86.20	383	Skin	500	56.5	6.64	4284	0.60	45	452.7	2.01	5525
HT1C2	11.29	50.2	47.13	210	27.78	124	86.20	383	Ramp	1200[e]	136	4.64	2994	1.00	0	425.9	1.89	3489
HT1C3	11.29	50.2	47.13	210	27.78	124	86.20	383	Ramp	1200[e]	136	4.64	2994	1.00	0	401.9	1.79	3051
HT1D1	1.17	5.20	23.34	104	9.01	40.1	98.22	437	Ramp	400	45.2	1.28	826	0.88	0	412.5[f]	1.83	4200
HR1C1	...	...	...	...	...	...	72.10	321	Plank	550[g]	62.1	4.70	3032	0.67	0	285.8	1.27	3964
HR1C2	...	...	...	...	...	...	72.10	321	Plank	1200	136	4.70	3032	0.67	0	287.0	1.28	3981
HR3D0	...	...	...	...	...	...	62.50	278	NA	0	0	0	0	NA	NA	420.1	1.87	6722
HR3D1	...	...	...	...	...	...	62.50	278	Plank	250	28.2	...	...	...	0	364.8	1.62	5867
HR3D2	...	...	...	...	...	...	62.50	278	Plank	250	28.2	...	...	...	0	421.5	1.87	6744
HR3D3	...	...	...	...	...	...	62.50	278	Plank	1200	136	...	...	...	0	279.3	1.24	4469
HT4C0	13.35	59.4	...	...	11.73	52.2	25.08	112	NA	0	0	0	0	NA	NA	127.1	0.57	5068
HT4C1	13.35	59.4	...	...	11.73	52.2	25.08	112	Flange	400	45.2	3.80	2452	0.42	0	105.7	0.47	4215
HT4C2	13.35	59.4	...	...	11.73	52.2	25.08	112	Flange	400	45.2	3.80	2452	0.42	0	113.8	0.51	4537
HT4E0	12.65	56.3	...	...	11.27	50.1	23.92	106	NA	0	0	0	0	NA	NA	143.3	0.64	5991
HT4E1	12.65	56.3	...	...	11.27	50.1	23.92	106	Flange	300	33.9	...	...	...	0	138.2	0.61	5778
HT4E2	12.65	56.3	...	...	11.27	50.1	23.92	106	Flange	400	45.2	...	...	...	0	137.4	0.61	5744
HT5C0	32.02	142	...	...	11.73	52.2	43.75	195	NA	0	0	0	0	NA	NA	198.0	0.88	4526
HT5C1	32.02	142	...	...	11.73	52.2	43.75	195	Flange	600	67.8	5.30	3419	0.36	0	145.9	0.65	3335
HT5C2	32.02	142	...	...	11.73	52.2	43.75	195	Flange	500	56.5	...	...	...	0	160.2	0.71	3662
HT5E1	30.92	138	...	...	11.27	50.1	42.19	188	Flange	475	53.7	1.44		0.43	0	191.5	0.85	4539
HT5E2	30.92	138	...	...	11.27	50.1	42.19	188	Hat	450	50.8	...	...	...	0	196.7	0.87	4662
HT5E3	30.92	138	...	...	11.27	50.1	42.19	188	Web	400	45.2	...	...	...	0	190.2	0.85	4508
HT5F1	30.97	138	...	...	11.74	52.2	42.71	190	Flange	500	56.5	2.88	1858	0.38	0	209.0	0.93	4893
HT5F2	30.97	138	...	...	11.74	52.2	42.71	190	Hat	600	67.8	2.82	1819	1.00	0	185.2	0.82	4336
HT5F3	30.97	138	...	...	11.74	52.2	42.71	190	Web	600	67.8	2.18	1406	0.40	0	196.0	0.87	4589
HT5F4	30.97	138	...	...	11.74	52.2	42.71	190	Web	600	67.8	2.18	1406	0.40	0	211.8	0.94	4959
HT5F5	30.97	138	...	...	11.74	52.2	42.71	190	Web	600	67.8	2.18	1406	0.40	0	203.9	0.91	4774

NOTES:

[a] Sum of three planks or stringers.

[b] Aspect ratio (AR) is maximum delamination width/length, with the orientation of the length measurement at an angle denoted "orien" relative to the loading direction.

[c] All tests conducted at room temperature ambient conditions.

[d] Damage mislocated 0.1 inch (2.5 mm) to skin side.

[e] Energy level above BVID using the Air Force 1200 in·lb (136 J) impact energy criterion.

[f] Did not fail through damage area.

[g] Energy level below BVID in order approximate a less severe criterion (the delamination sizes were the same for both 550 in·lb [62 J] and 1200 in·lb [136 J] impact energy levels).

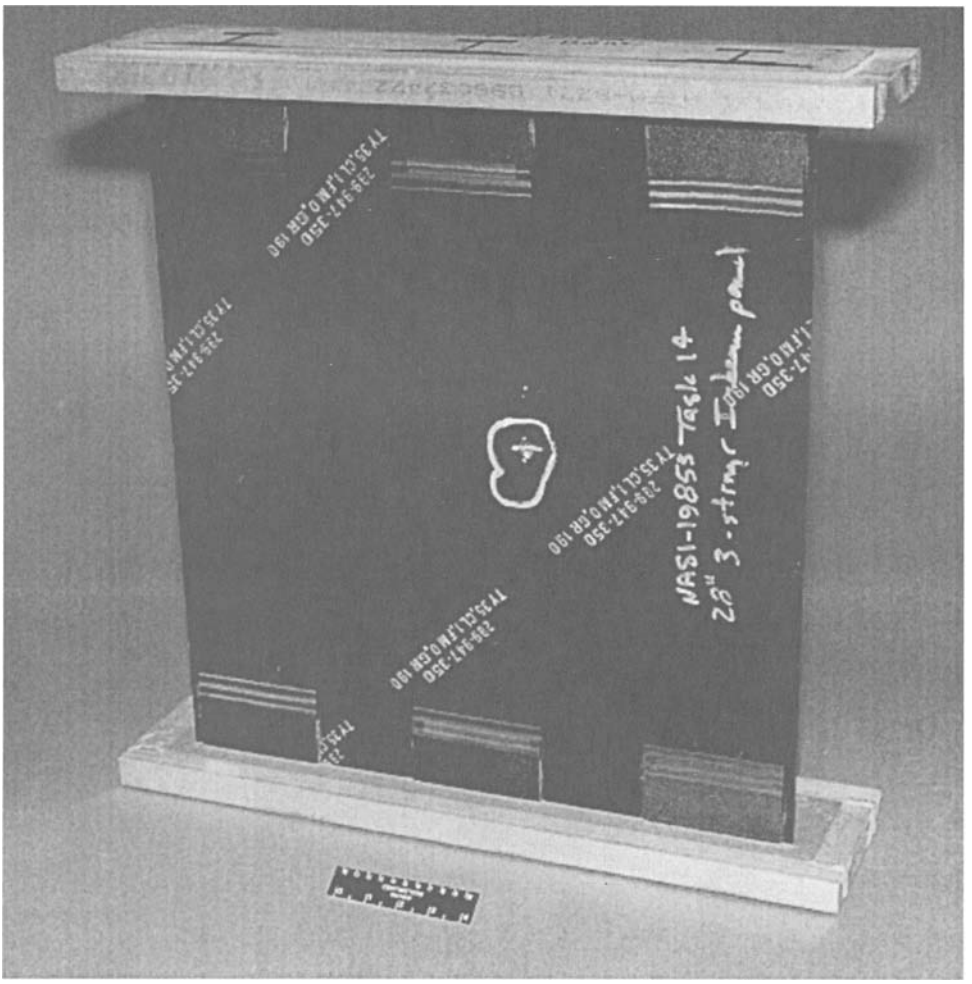


FIG. 8—*Typical three-stringer compression test specimen.*

12*a* of two failure bands or branches merging into a single branch and then extending through the impact site. The failure on the stringer side is shown in Fig. 12*d*. Two stringers have failed at one location while the third stringer failed at two locations and all of the stringers have delaminated from the skin for the full length of the test area. The failure of Specimen IT1D1 is shown in Figs. 12*e* and 12*f*. This specimen was impact damaged with 1000 in. · lb (113 J) of energy at two locations as shown in Fig. 12*e*. The impact sites were on the ramp of the center stiffener at a quarter of the length and on the centerline of the skin, located at the quarter point from the opposite end. The panel failed through the damage on the ramp of the center stiffener. Each stringer failed at one location as shown in Fig. 12*f*. The failure of the damaged hat-stiffener specimen is shown in Figs. 12*g* and 12*h*. Although the skin has many branches to the failure, none of the branches intersect the impact damage. All of the stiffeners failed as shown in Fig. 12*h* and also delaminated at various places between the stiffener flange, the plank runout, and the skin.

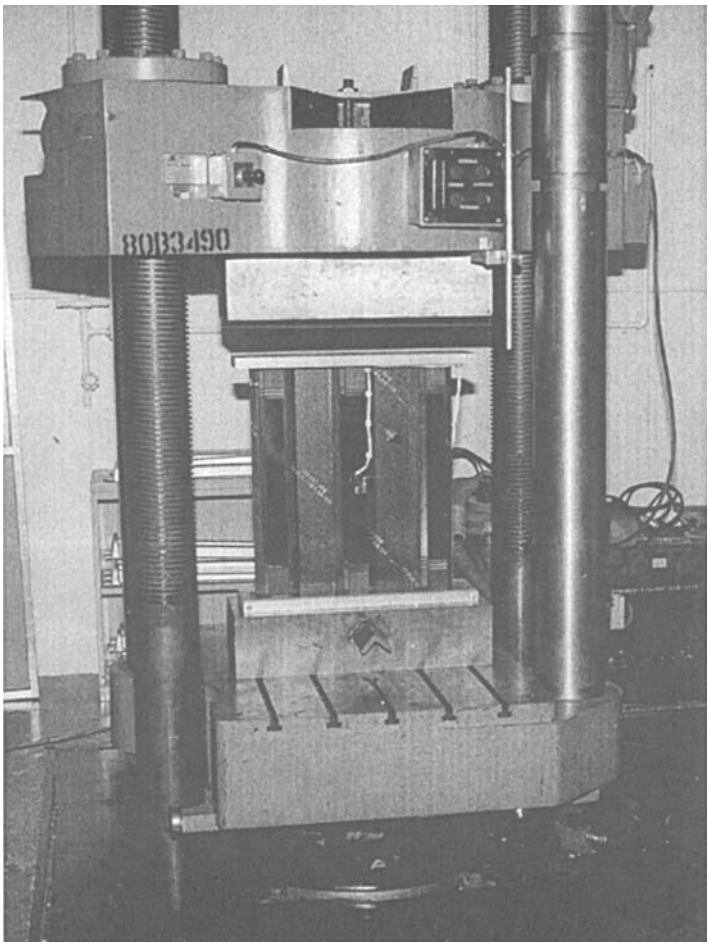


FIG. 9—*Typical three-stringer compression test setup (Bell Helicopter Mechanical Test Lab).*

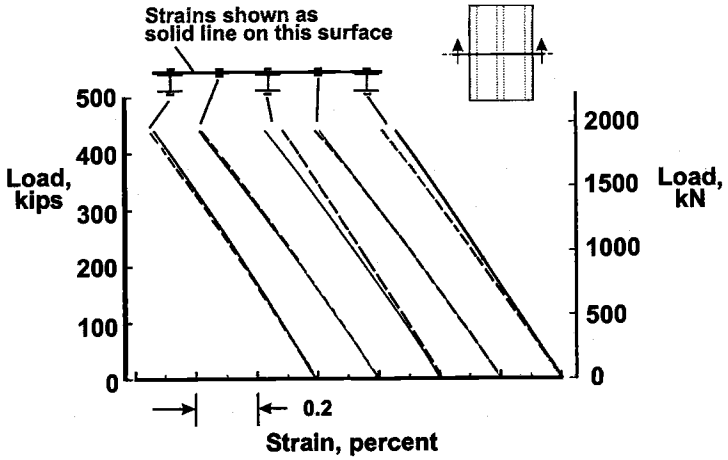


FIG. 10*a*—*Load-strain response at center cross section of (undamaged) Specimen IT1D0.*

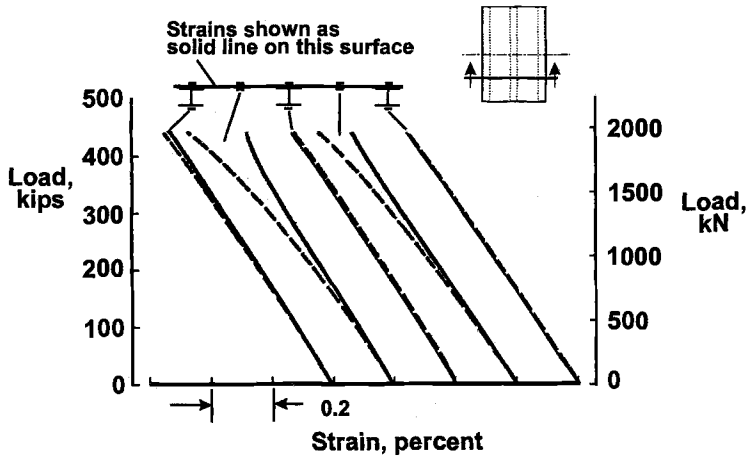


FIG. 10*b*—*Load-strain response at cross section located at quarter point of Specimen IT1D0.*

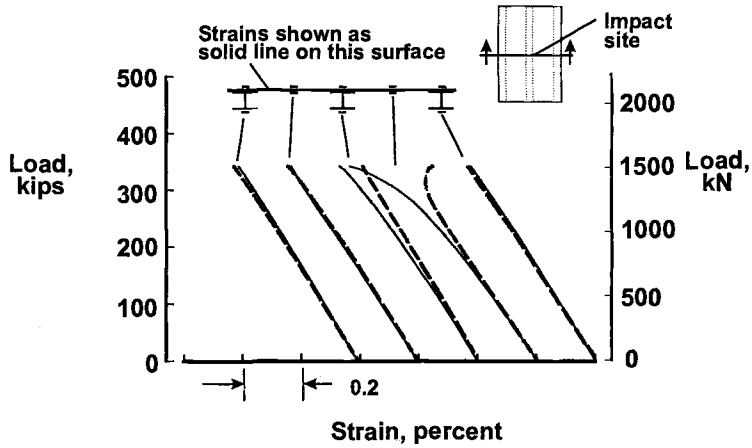


FIG. 10*c*—*Load-strain response at center cross section of Specimen IT1D2.*

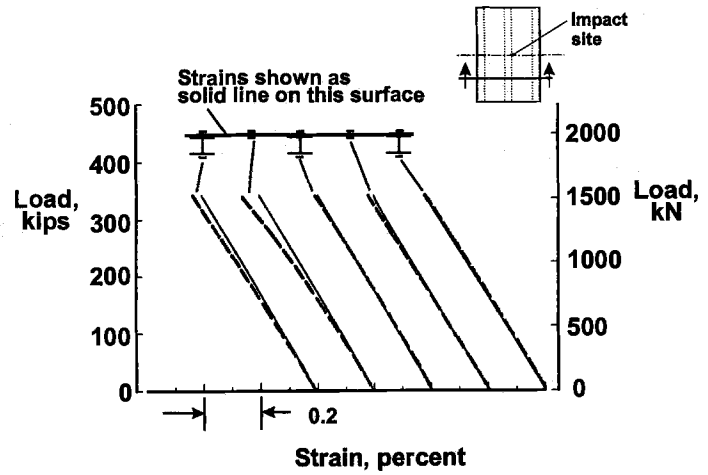


FIG. 10*d*—*Load-strain response at cross section located at quarter point of Specimen IT1D2.*

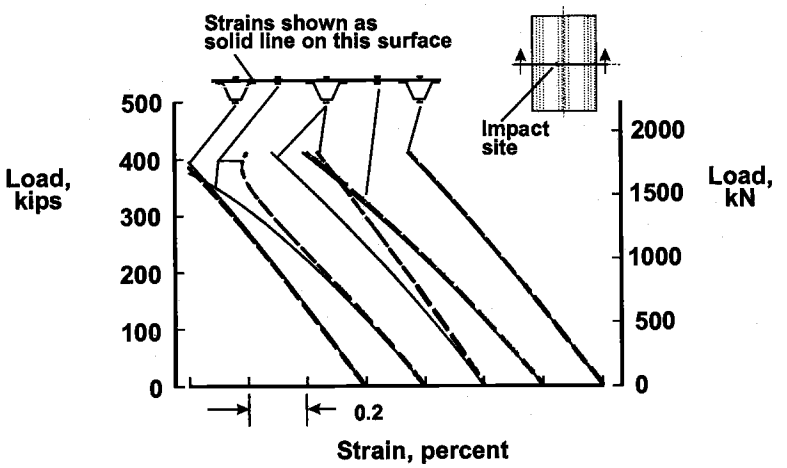


FIG. 10*e*—*Load-strain response at center cross section of Specimen HT1D1.*

Numerical Results

Global finite-element models were built at NASA in order to correlate the observed geometrically nonlinear test results with numerical models that are suitably accurate yet yield efficient elastic response (i.e., strain and displacement) prediction. Global, local, and/or substructured (i.e., fine-grid) models were built at Bell in order to predict ultimate compression strength after impact. The objectives of the NASA and Bell modeling were different, and the results are discussed separately in the two following subsections.

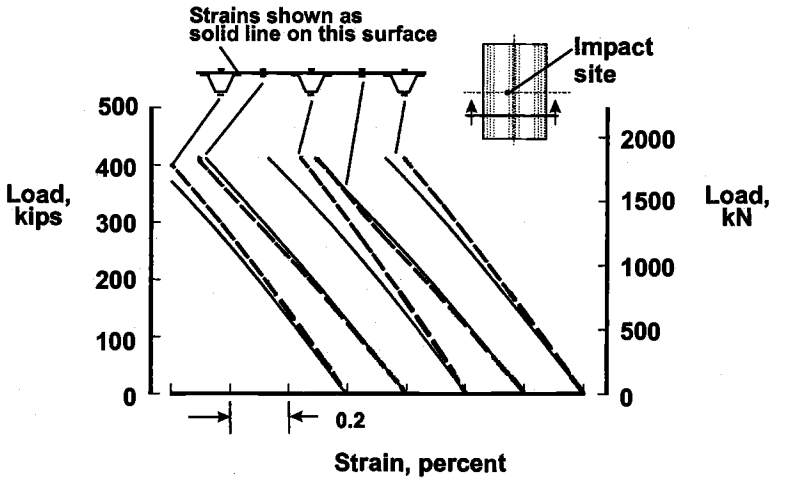


FIG. 10*f*—*Load-strain response at cross section located at quarter point of Specimen HT1D1.*

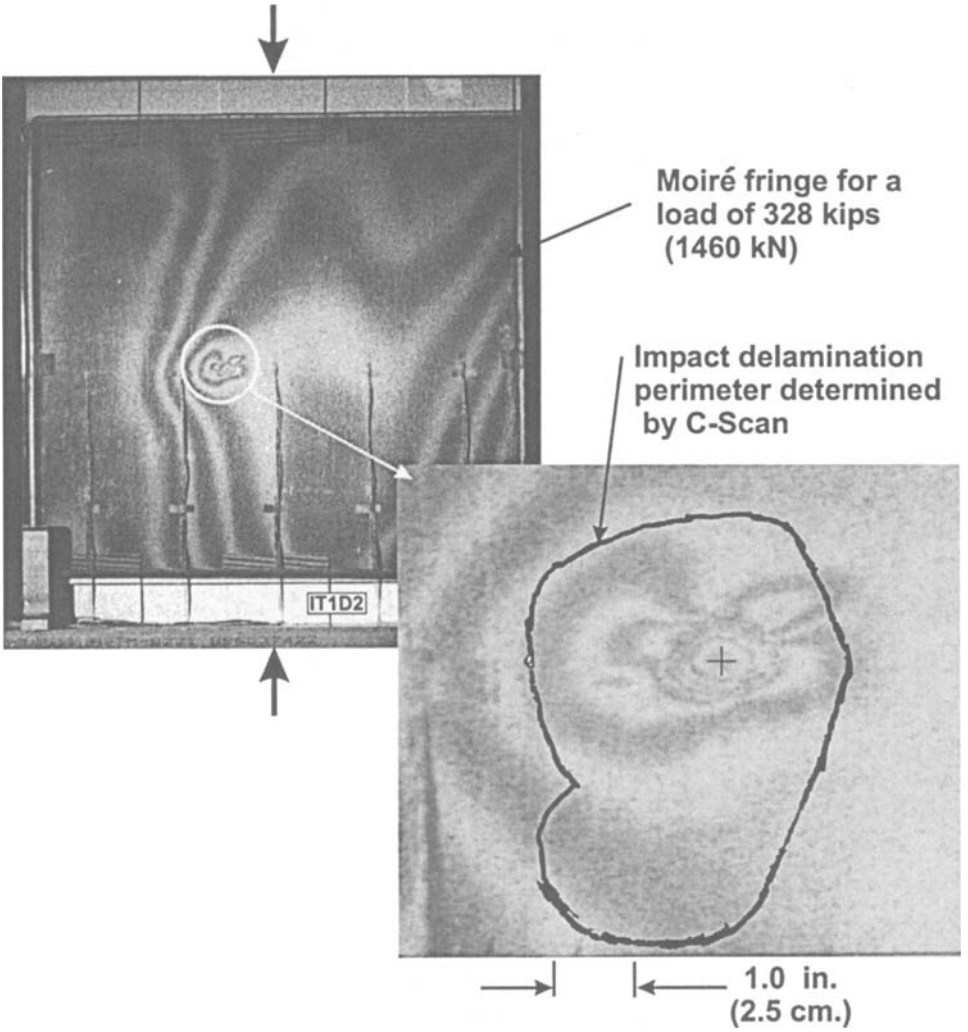


FIG. 11—*Moiré fringe pattern and delamination perimeter of Specimen IT1D2 at 328 kips.*

Global Elastic Response Modeling

The finite-element mesh for an I-stiffened panel (Specimen IT1D0) is shown in Fig. 13, and the mesh for the hat-stiffened panel (Specimen HT1D1) is shown in Fig. 14. The meshes shown in Figs. 13 and 14 reflect the actual panel dimensions. Solutions from NASA were generated using the STAGS (STructural Analysis of General Shells) Version 3.0 finite-element program [*11*]. MSC/PATRAN™[4] was used for pre- and post-processing. The STAGS models used Element 410, a four-node quadrilateral element. The applied boundary conditions for the two global models are shown in Fig. 15.

[4] MSC/PATRAN™ is a trademark of MSC Software Corporation, Los Angeles, CA.

Comparisons of measured response and STAGS predicted displacements and axial strains, for selected locations, are shown in Figs. 16*a* through 16*d* for Specimens IT1D0 and IT1D2 and Fig. 17 for Specimen HT1D1. The end shortening of Specimens IT1D0 and IT1D2 as a function of applied load are shown in Fig. 16*a*. The predicted end shortening is also shown in Fig. 16*a*. The impact damage does not affect the axial stiffness of Specimen IT1D2. Disregarding the offset shown in the experimental results, there is a good comparison between the predicted and experimental results. The out-of-plane displacement at the center of the specimens, on the top of the stiffener, is shown in Fig. 16*b* for Specimens IT1D0 and IT1D2. The predicted displacement at the panel center is also shown in Fig. 16*b*. The out-of-plane displacement (filled squares) for the damaged panel (IT1D2) exceeds the displacement for the undamaged, which would be expected since the impact damage is adjacent to the center stiffener. The out-of-plane displacement for the undamaged panel is less than predicted, as shown in Fig. 16*b*. The predicted and experimental strain on the center stiffener and skin at the quarter point in length is shown in Fig. 16*c*. The experimental strain exceeds the predicted strain at failure by approximately 1000 $\mu\varepsilon$. Very little bending is indicated, at this point in the panel, in either the predicted or the experimental strains. The predicted and experimental strain in the center of the skin at the quarter point in the length is shown in Fig. 16*d*. The test results indicate some bending in the skin at the noted point. The average experimental strain exceeds the predicted strain by approximately 2000 $\mu\varepsilon$. The predicted end shortening for a hat-stiffened panel identical to Specimen IH1D1 is shown in Fig. 17. The experimental results for Specimen HT1D1 are also shown in Fig. 17. The test

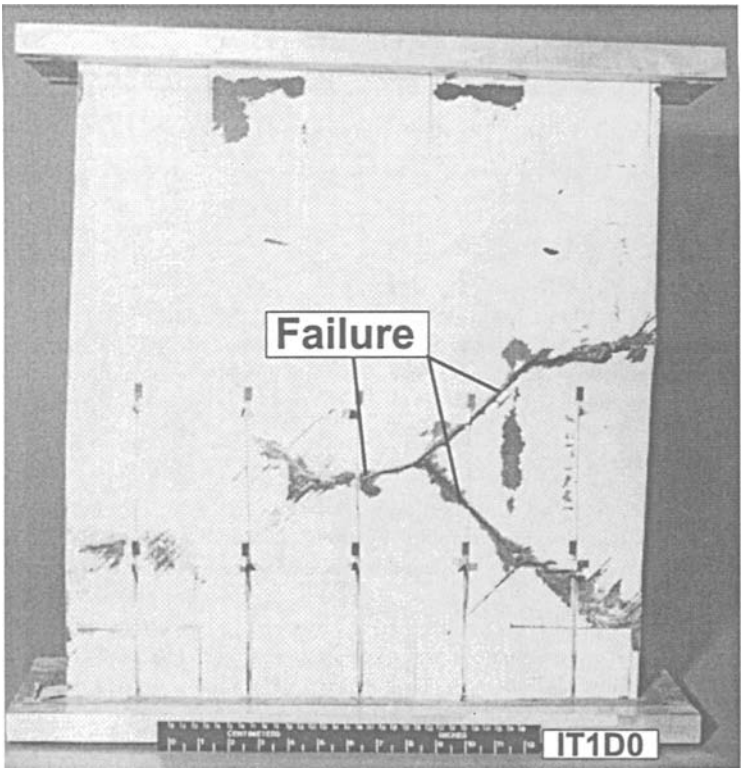


FIG. 12*a*—*Failure location on skin side of Specimen IT1D0.*

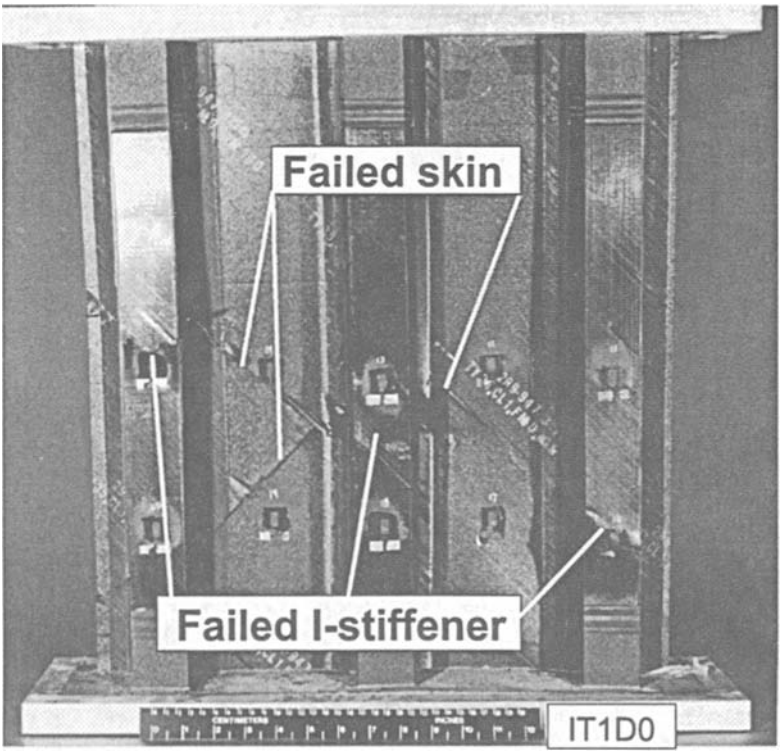


FIG. 12*b*—*Failure location on stiffener side of Specimen IT1D0.*

panel appears to have a lower stiffness than the panel in the analysis, since the predicted values for strain and deflection are less than the test values.

The predicted initial buckling load for an I-stiffened panel, Specimen IT1D0, and a hat-stiffened panel identical to Specimen HT1D1 was 693 klbf (3.08 MN) and 669 klbf (2.98 MN), respectively. Since the predicted buckling load is more than 150% of the failure loads, failure by global buckling was not considered further.

Fine-Grid Strength-After-Impact Modeling

The objective of the fine-grid strength-after-impact modeling was to predict the maximum load carried by the three-stringer panels. The following three subsections will (*a*) overview the general numerical method, (*b*) describe the typically observed behavior for these three-stringer panels, and (*c*) present the numerical results.

General Numerical Method—Finite-element analysis performed at Bell used MSC/NASTRAN™ Version 70.5 solution 106 [*12*]. MSC/PATRAN™ was used for pre- and post-processing. The NASTRAN™ CQUAD4, RBE2, and CGAP elements were the primary elements used. Microsoft® Excel[5] Version 7.0 spreadsheets—developed under a Rotorcraft Industry Technology Association project

[5] Microsoft® Excel is a registered trademark of Microsoft Corp., Redmond, WA.

[*13*]—were used to automate the most labor-intensive aspects of the local modeling and/or substructuring effort. For this CAI study, six different three-stringer panel configurations were modeled. The Excel spreadsheets, collectively referred to as the Structural Laminate Impact Computations (SLIC), automatically build MSC NASTRAN™ geometric nonlinear finite-element models that capture the impact damage state with multiple layered plates tied together with either rigid body or compression-only gap contact elements. This approach makes several assumptions:

1. No delamination growth occurs prior to failure.
2. For damage that occurred directly on plank transition areas such as those shown in Figs. 1–3, open-hole compression (OHC) mean failure strain captures the local pseudo-free-edge effects of ply dropoffs.
3. For panels that do not contain internal ply dropoffs, such as the hat-stiffened uniform skin panels as shown in Fig. 4, an unnotched laminate compression strain allowable was used to establish the point of failure (for these panels, the hat flange drops off abruptly and this geometry was adequately captured in the finite-element model mesh).
4. The state of damage is repeatable (i.e., identical impact energy and location on an identical panel, produces the same state of damage, and the test panels were assumed to have the same damage state as the damage survey panels even though boundary conditions including the proximity and degree of end support most likely varied).
5. Material response is assumed linear to failure, and geometry is the only contributor to nonlinearity.

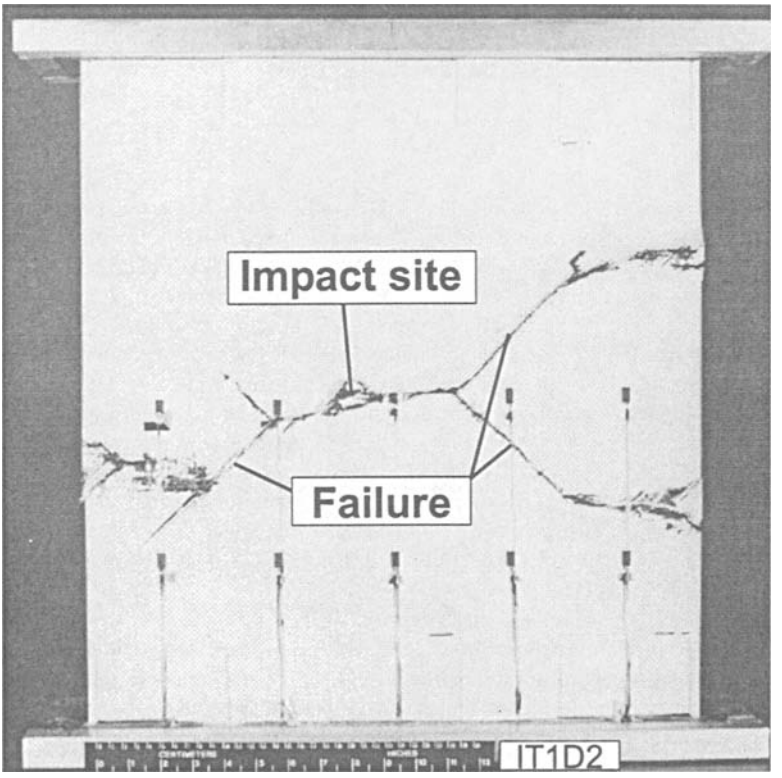


FIG. 12*c*—*Failure location on skin side of Specimen IT1D2.*

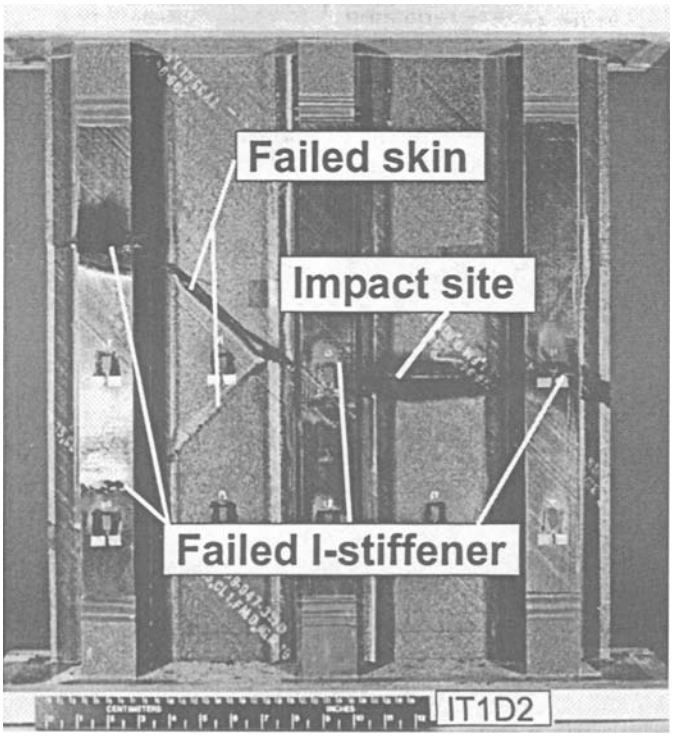


FIG. 12*d*—*Failure location on stiffener side of Specimen IT1D2.*

The local damage state used in the modeling was determined via contact pulse-echo ultrasonic time of flight (TOF) measurements on the appropriate impact energy and location on the damage survey panels. These scans provide data that show the extent and depth of each delamination. Typical TOF scan examples are shown in Figs. 18 and 19. Fig. 18 being a relatively large delamination in an 8552 I-stiffened panel, and Fig. 19 being a much smaller delamination in a tougher 3900-2 resin-system hard-skin/hat configuration. Since the largest delamination is typically on the back side of the panel, one such scan provides all the information required to define the shape, orientation, and depth of all the delaminations. The color scale on the scan is the time required for the ultrasonic wave to bounce off and return from the first interface in the laminate. The scale is proportional to depth or thickness (note that the edges of the dropped 0° plies in Fig. 18 show up as a change in depth as the delamination follows the plank contour). The outer surface on the panel must be smooth in order to provide a consistent reference plane for automated TOF scans. Several damage survey panels had a rough outer surface and could only be hand scanned. Sufficient data was gathered, however, with hand scans to proceed with the SLIC analysis.

As shown in Figs. 20 and 21, the element density for the global portion of the model was typically about 0.4 in. to 0.75 in. (10 mm to 19 mm) using CQUAD4 elements. The global/substructured model of an I-stiffened three-stinger panel is shown in Fig. 20, while Fig. 21 shows a hat-stiffened panel. In the proximity of the impact site, the element density is increased to about 0.10 in. (2.5 mm). This fine-meshed region is duplicated into multiple stacks of plates that align with each other through the thickness and encompass the entire damage region and extend out some distance beyond, as shown in Fig. 22. Each plate layer represents a sublaminate whose boundaries are defined by the delamination in-

terfaces. The extent of damage at each sublaminate interface can be independently defined as a unique ellipse oriented at an alignment angle. SLIC automatically generates a full or truncated ellipse. Any other shape can be transferred from the scans by manual editing. CGAP gap elements are inserted inside the ellipses and transfer only compression forces that prevent the sublaminates from passing through one another. RBE2 rigid body elements are then used to connect the sublaminates in the remaining fine meshed area outside the damage zone.

The models can be set up to run two ways. The first is to run a coarse grid global model with local damage element softening only. A moment fringe plot is then set up in PATRANTM with the fringe bounds set very tightly around zero. A positive moment then plots as one color, while the negative moment region plots as another. The moment inflection lines are then obvious. The local model is then built and run separately using the moment inflection lines as a simplified loading boundary. This method is illustrated in Fig. 23. The total number of elements for a global three-stringer panel model using this technique is around 5000 to 10 000 with around 20 000 to 30 000 degrees of freedom (DOF). The run times are between 30 and 100 central processing unit (CPU) minutes. The local model then contains about 10 000 to 20 000 elements with 20 000 to 80 000 DOF, and the run times go from 100 to 400 CPU minutes. This method requires a careful consideration of local model boundary stiffness, especially for an impact at an edge of a flange or a ramp. It works best for damage isolated in the center of a skin panel.

The second technique is to run the combined local and global model together, i.e., substructuring. This is the technique used in the models shown in Figs. 20–22. The substructuring version of SLIC

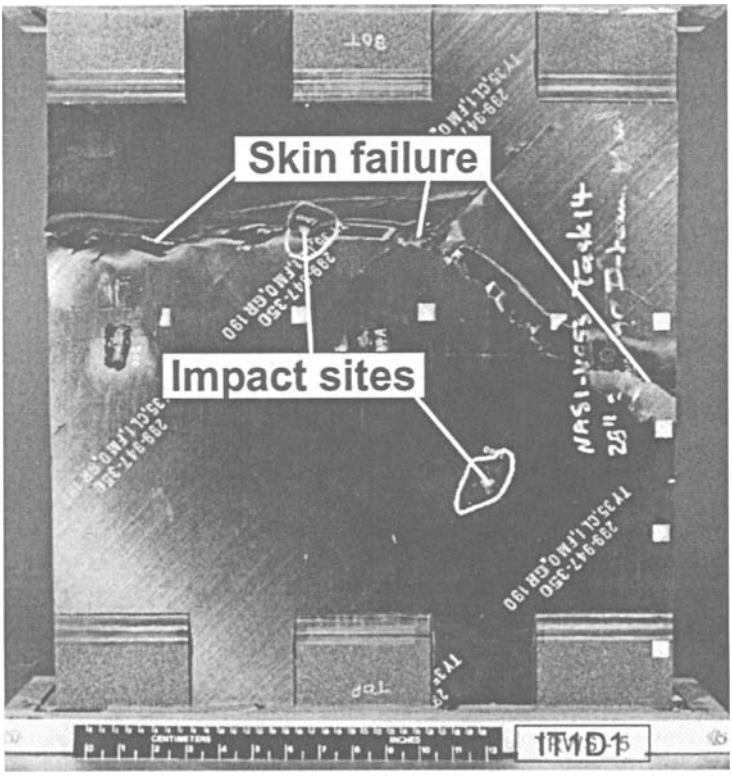


FIG. 12e—*Failure location on skin side of Specimen IT1D1.*

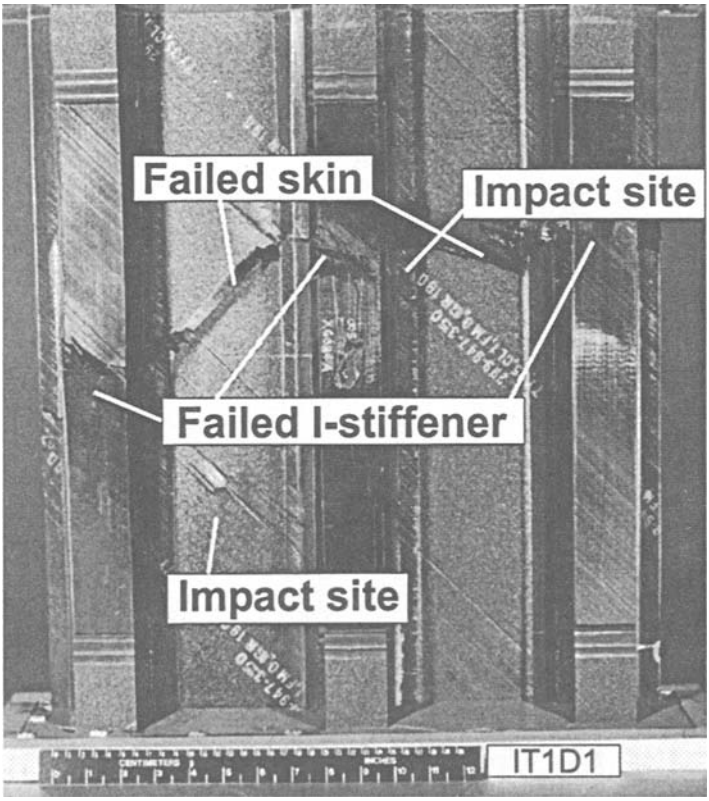


FIG. 12*f*—*Failure location on stiffener side of Specimen IT1D1.*

builds one model and includes a mesh transition region or band between the multilayer fine-grid mesh and the surrounding single-layer coarse elements. SLIC generates a PATRAN™ session file that fully generates the combined model in approximately 10 to 20 min work time. This technique contains between 50 000 to 100 000 elements with 70 000 to 120 000 DOF and runs in about 500 to 1000 CPU min.

In both approaches, the elements at the immediate impact site location are softened to represent local matrix cracking and fiber damage. This local impact damage zone is idealized as a cone that gets progressively larger away from the impact side. The 0.5-in. (13-mm) indenter tip radius and the dent depth, if recorded, determine the impact diameter of the cone. The cone angle is then assumed to be 45 deg. The model now contains two major zones where strain or stress concentrations can develop. The first is along the outside edges of the delaminations where local bending strains can become high, and the second is at the edge of the local impact site where load wants to locally redistribute around the soft spot.

The geometrically nonlinear NASTRAN™ solution 106 is typically set up to run in ten load increments to 100% of the expected failure load and then ten more increments to 150%. The model will usually reach a point where the solution becomes unstable. This point may not be the actual point of final collapse. The next step is to query PATRAN™ for the highest axial strain magnitude (i.e., in the direction of loading). Once the element is identified that has the highest laminate-level axial strain magnitude, the maximum zero degree ply strain is calculated. This strain is then compared to an av-

erage room temperature allowable. If this strain is lower than the allowable, the model must be rerun with either finer load increments or a finer mesh in order to get the model to run stable for a higher load. If the model strain is higher than the allowable, the applied load is reduced by the ratio of worst minimum zero ply model strain over the strain allowable.

Typically Observed Behavior—The typically observed failure modes for these three-stringer panels are various types of buckling and load redistributions leading up to a final compressive strength failure. Pure buckling and strength modes were not found in the three-stringer panels that were evaluated. Three-stringer panels contain multiple load paths. If a web buckles, the stringers can take additional load. If a sublaminate buckles, other parallel sublaminates will also react additional load. As more and more of the redundant load paths become soft from buckling, the remaining strain energy concentrates at an increasing rate into the last stable load paths. Finally, the point of local fiber stability is exceeded and a 0-deg compressive (or "kink-band") failure is initiated. Energy is released by the fiber failure and immediately overloads the adjacent fibers, leading to a sudden collapse. This nonlinear phenomenon is illustrated in Fig. 24 (and captured experimentally in the moiré fringe pattern shown in Fig. 11), and the numbered events may also be related to the exploded view of the substructured model in Fig. 22. The nonlinear NASTRAN analysis will reproduce the progressive sublaminate buckling phenomenon. Numerical instabilities resulting in nonconvergence, and suspicious failure modes (and/or locations) were often encountered, and some judgment was required in recog-

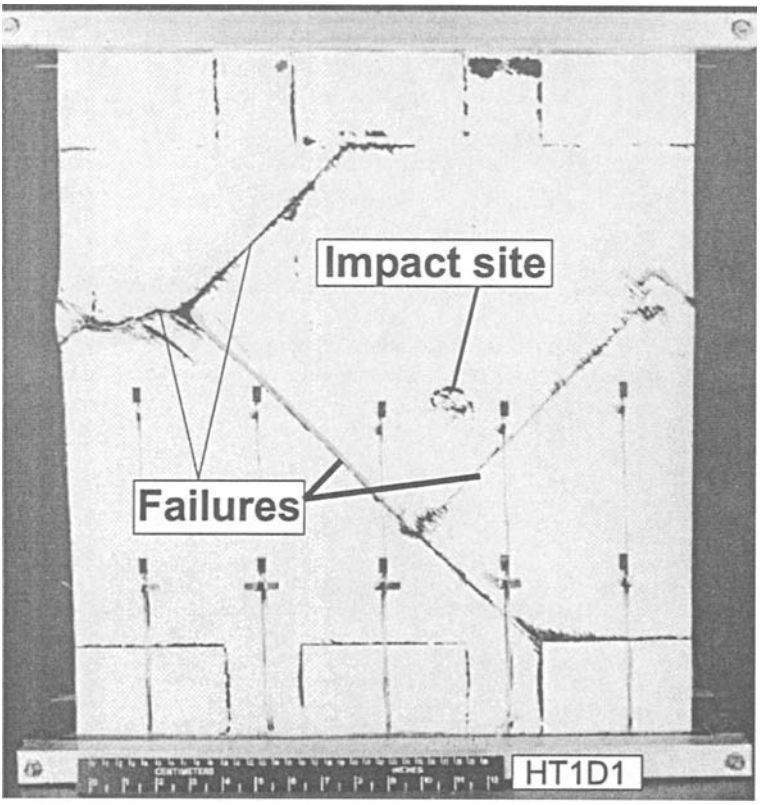


FIG. 12*g*—*Failure location on skin side of Specimen HT1D1.*

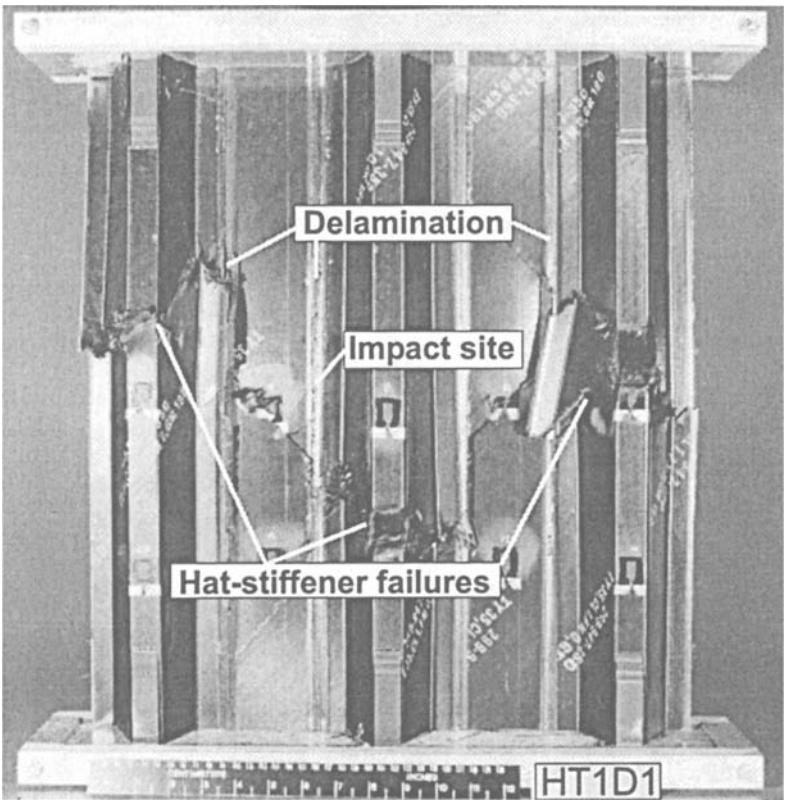


FIG. 12*h*—*Failure location on stiffener side of Specimen HT1D1.*

nizing them and correctly adjusting the solution step size in order to overcome them. By checking the post-processed peak axial strains at the end of a solution, the load and location at which the final kink-band failure occurs may be estimated. The locations of these peak strains, within the unbuckled sublaminate were observed to vary from one configuration to another, but were found either at the center of the impact site or near the edge of a delamination in a successfully converged run.

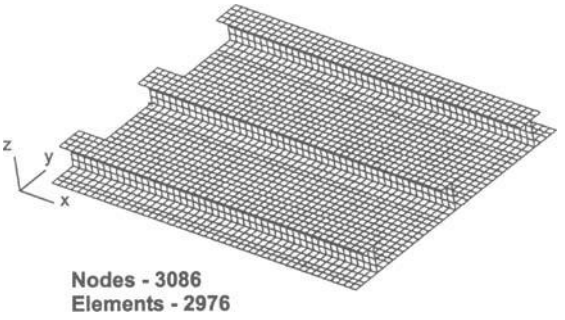


FIG. 13—*Three-stringer I-beam finite-element mesh.*

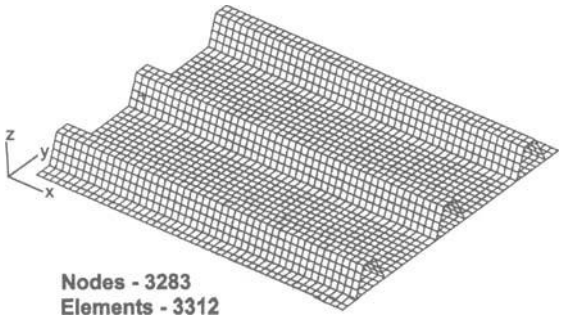


FIG. 14—*Three-stringer hat/plank-stiffened finite-element mesh.*

Detailed Parametric Model Results—Table 4 compares the experimental results to the predicted failure load based on comparing peak local/substructured model axial strains with the noted open hole compression (OHC) or no hole compression (NHC) mean room temperature ambient (RTA) strain allowable. In general, the numerical agreement, within 20% in five of six cases, is considered very good. While a priori knowledge of the experimental results was available for this modeling exercise, it only influenced the overall direction of the model-building in the HT1D case, and blind comparisons with test data will be performed in the near future. The single buckling failure prediction (HT5C) illustrates the caution required in interpreting the nonlinear model results. As mentioned previously, a pure buckling failure is indicative of a poorly converged or too coarsely meshed solution, and thus the tabulated result for case HT5C should actually be discarded (it is only included to illustrate this point) and the model rerun.

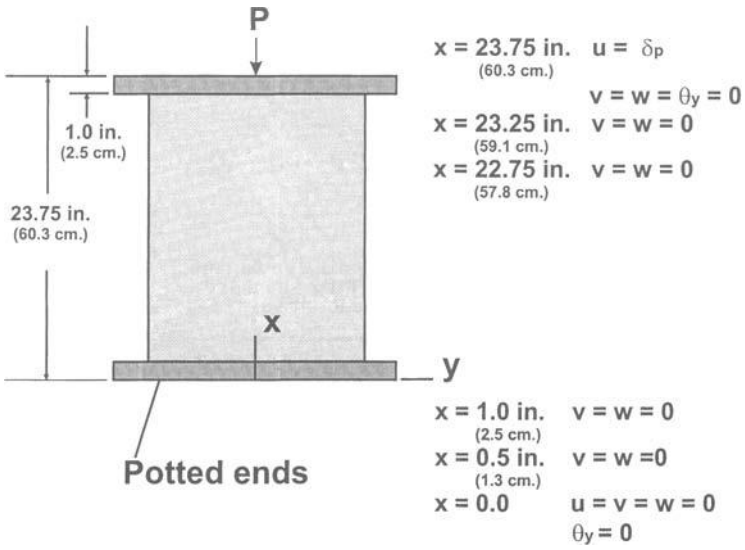


FIG. 15—*Global finite-element boundary conditions.*

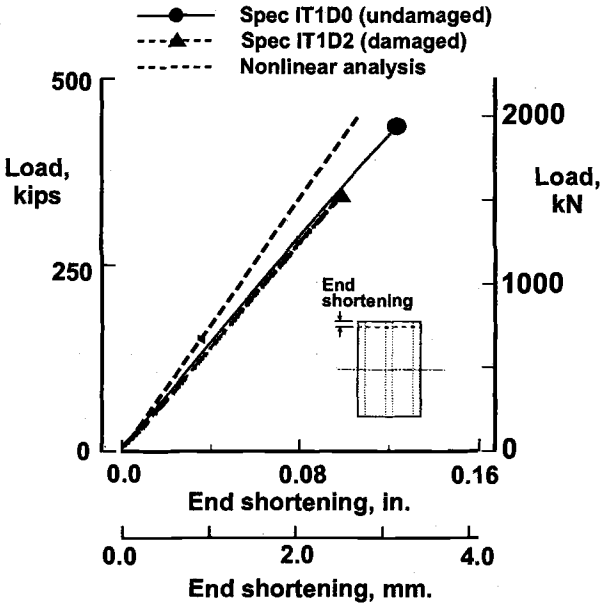


FIG. 16*a*—*Comparison of end shortening of panels with the predicted.*

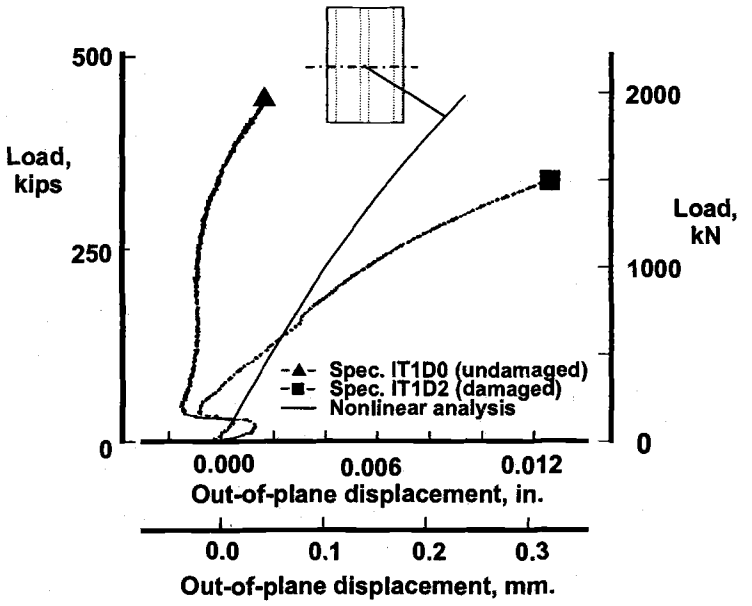


FIG. 16*b*—*Comparison of the out-of-plane displacement.*

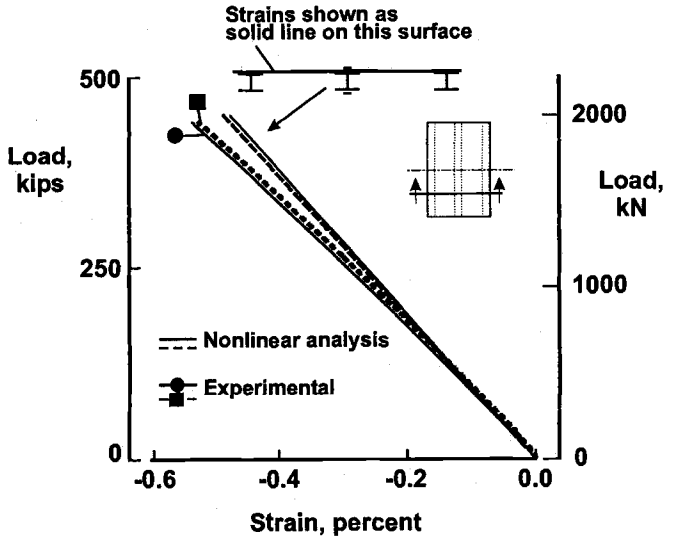


FIG. 16*c*—*Strain results on centerline stiffener.*

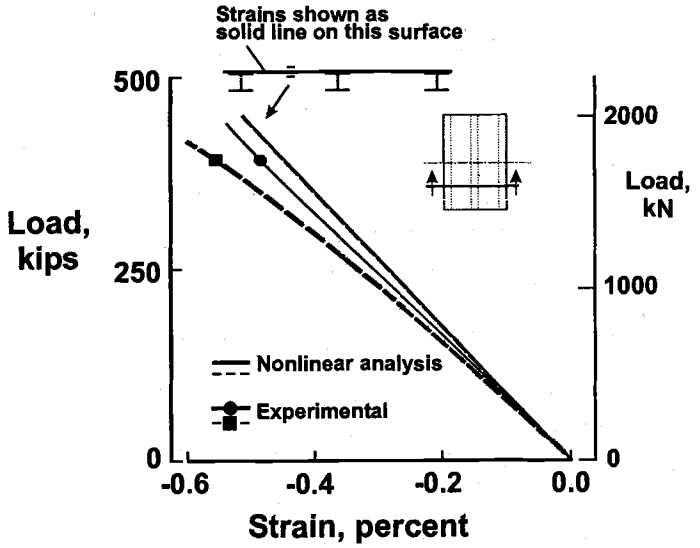


FIG. 16*d*—*Strain results in the skin at the quarter point.*

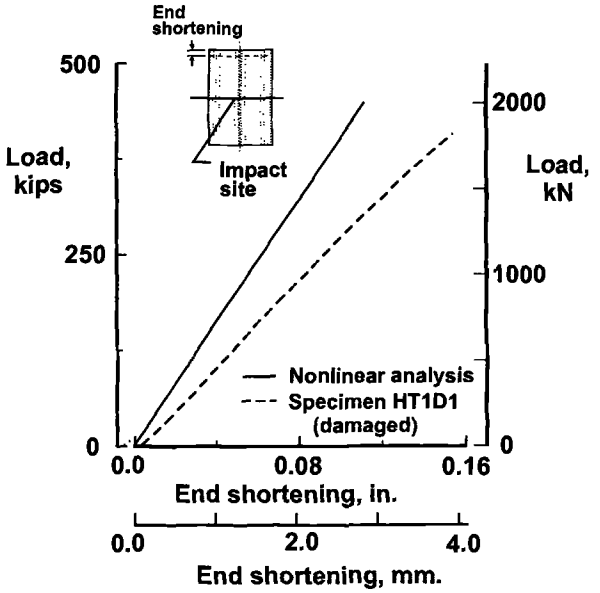


FIG. 17—*Comparison of end shortening for hat-stiffened panels.*

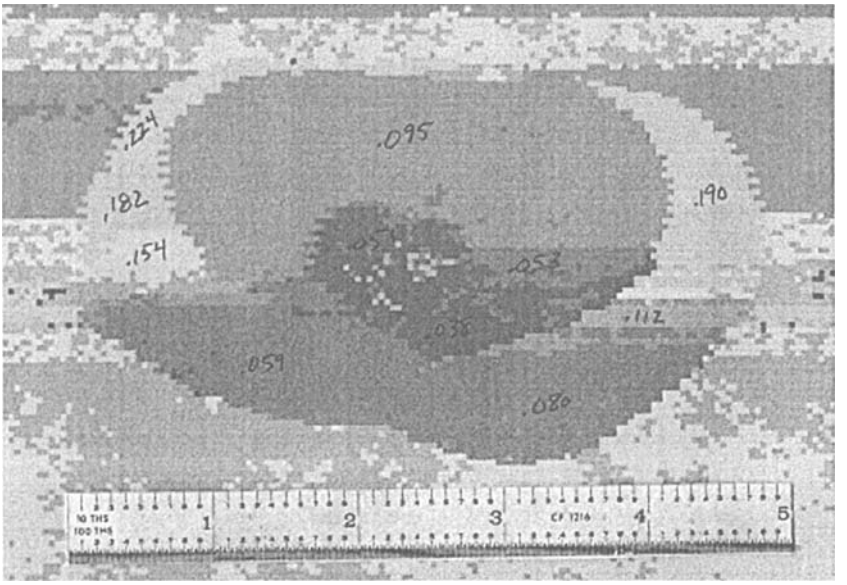


FIG. 18—*Typical TOF image for I-beam/plank/skin delamination.*

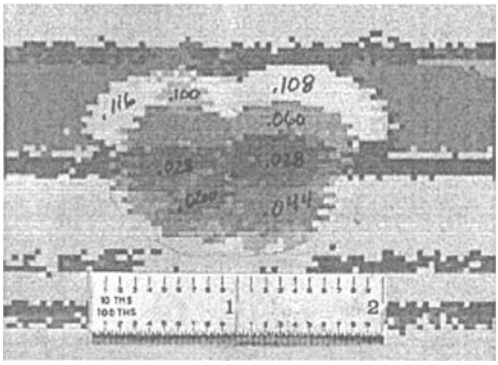


FIG. 19—*Typical TOF image for hard-skin/hat delamination.*

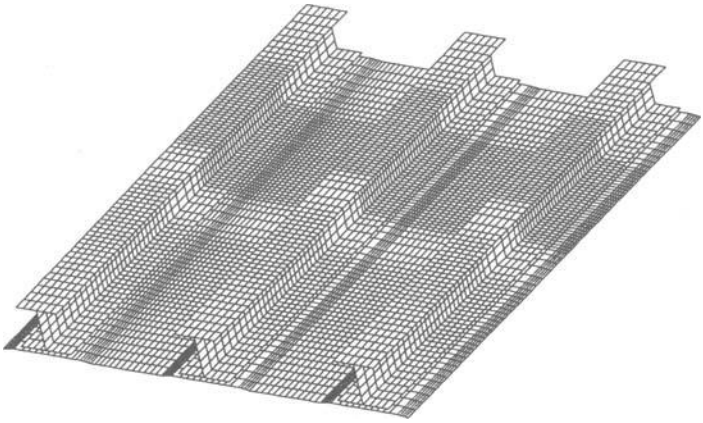


FIG. 20—*Substructured I-beam panel FE mesh.*

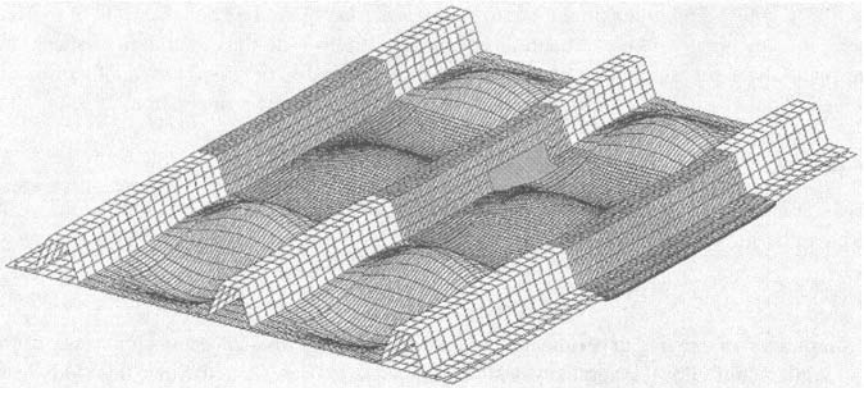


FIG. 21—*Substructured hat-stiffened panel FE mesh.*

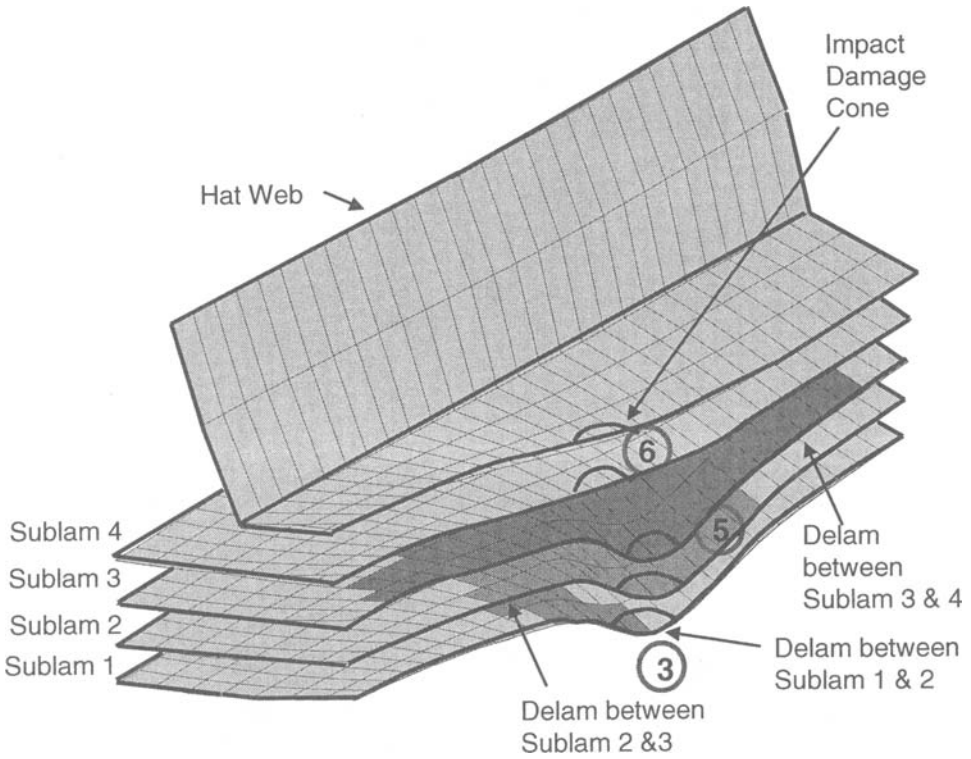


FIG. 22—*Exploded view of multi-layer substructure model (deformed mesh).*

There are several possible ways to improve the accuracy and reliability of this numerical strength prediction method. Certainly characterizing with TOF measurements the delamination actually present in the test panel would be an obvious improvement over the use of survey panel impact sites and the assumption that the test panel damage was identical. A statistically significant study of impact damage variability would also be useful. In addition, a pure compression strain allowable was used in this study with a simple maximum strain failure criterion. This was done in spite of the fact that the critical sublaminate often exhibited large bending strains (and thus interlaminar shear stresses) and in-plane shear stresses as well, depending on local geometric details. Thus, another obvious improvement would be to use a failure criterion with compression-shear interaction.

Summary

This summary is separated into subsections: (*a*) discussing the merits and limitations of the observed results, and (*b*) listing the conclusions.

Discussion

A compilation of existing experimental three-stringer impact resistance and compression after impact strength results allows several key design parameters to be evaluated. Since this study was not a designed experiment, statistically rigorous conclusions were not necessarily possible. Nonetheless, certain useful engineering assessments were able to be made. Most of these conclusions merely con-

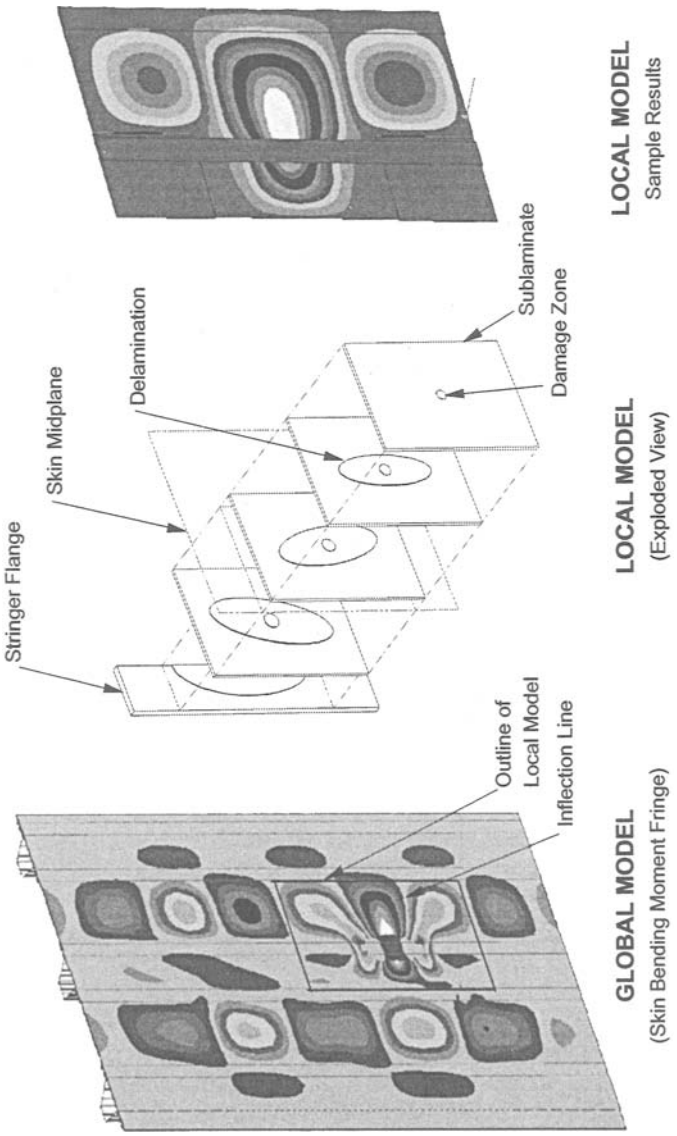
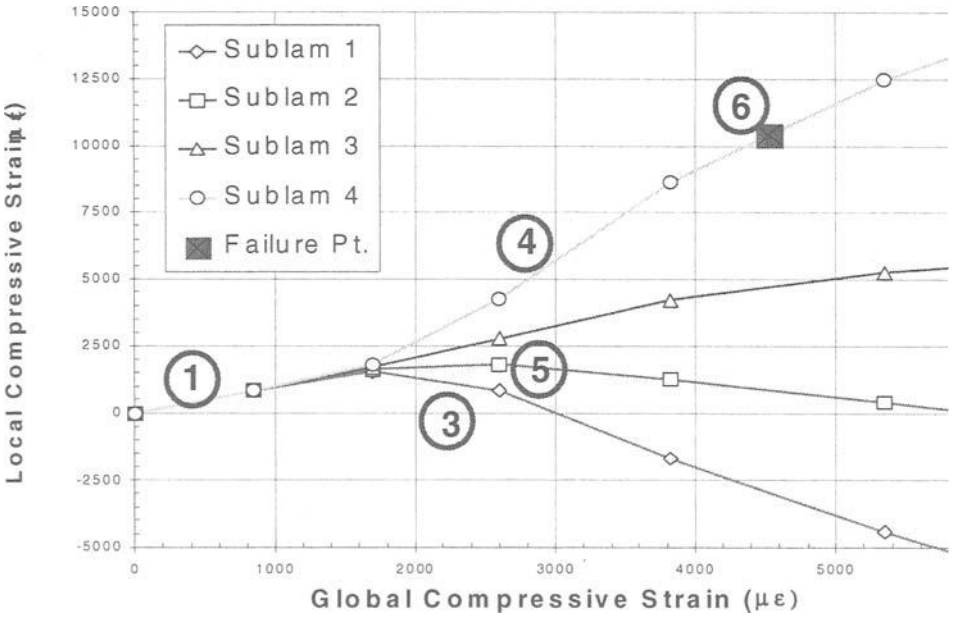


FIG. 23—*Illustration of global-local modeling approach.*



① Initial Linear Response

② Damage Induces Global Lateral Response

③ 1st Sublaminate buckles and unloads

④ Loading rate to remaining Sublaminates Increase

⑤ 2nd Sublaminate buckles etc.

⑥ Kink-Band Compression Failure

FIG. 24—*Nonlinear strain response of delaminated region.*

TABLE 4—*Comparison of FEM and experimental results.*

Panel ID	No. of data points	Material	Critical damage impact energy (in·lb)	Critical damage impact energy (J)	Critical sublam (/tot)	Critical location	Allow local strain (με)	Test global *P/AE* (με)	Predicted failure (% test)	Failure mode
IT1C	3	IM7/8552	1000	136	4/5	plank ramp	–6022	–3343	118	Strength failure at impact site
HT1D	1	IM7/E7T1	none[a]	none[a]	NA	plank	–5794	–4785	109	Strength failure of plank
HT4C	2	IM7/8552	400	45	4/4	skin[b]	–9436	–4376	123	Strength failure at edge of delam
HT5C	1	IM7/8552	600	68	3/4	skin[b]	–9302	–3335	86	Buckling
HT5F.1	1	G40/5276	500	56	3/4	skin[b]	–9061	–4893	114	Strength failure at impact site
HT5F.2	3	G40/5276	600	68	2/4	skin[c]	–8998	–4774	103	Strength failure at edge of delam

NOTES:

[a] Specimen did not fail through impact site; thus, impact damage was not modeled.

[b] Under flange-end

[c] Under web-skin intersection

firmed common existing assumptions, such as the facts that tougher resins yield smaller damage zones and higher detection thresholds, hard laminates have more severe stress concentrations/strength knockdowns, and hat sections are more stable/efficient that I-stiffeners. Since the local details of the damage zone strongly influence strength, careful attention (perhaps in the form of dynamic instrumentation and thorough control of clamping and impact location relative to panel edges) must be paid to boundary conditions for the impact event. Finally, simply compiling and publishing this relatively large experimental data base (39 test panels) for future reference is useful to some extent.

A practical global-local modeling technique was utilized in order to capture observed experimental elastic response and predict structural failure. An obvious improvement to this technique would be a failure criterion with compression-shear interaction. In the future, this numerical technique will allow the user to identify critical damage sites and estimate strength with damage prior to testing.

Finally, a statistically significant study of impact damage variability would be useful from both a certification/qualification support basis, and a confidence-in-modeling standpoint. Another certification/qualification issue highlighted by this study is the strong sensitivity of strength to damage zone size and, thus, to the definition of BVID. Hence, there seems to be merit in considering damage resistance criteria alternatives to BVID.

Conclusions

1. Material system and geometric configuration (i.e., the boundary conditions for the impact event) had the largest influence on damage resistance.
2. Location and extent (relative to critical geometric details such as ply edges) of the damage zone influenced the sublaminate buckling behavior, failure initiation site, and compressive ultimate strength.
3. Skin sublaminate stability and compression strength control structural failure.
4. Planks exhibited detrimental pseudo-edge/Poisson effects on strength.
5. Tougher resin systems had to be hit harder to reach their BVID threshold.
6. Since the tougher resin systems were hit harder, their CAI strength was similar to the more brittle systems.
7. Rodpacks improve structural efficiency only in concert with (0/12/0) skins and webs.
8. Hat stiffeners are more stable than I-stiffeners.
9. The nonlinear global-local finite-element-based strength predictions match the test data fairly well (i.e., within 20%).

Acknowledgments

Bell Helicopter modeling results presented in this paper were generated by Mr. R. Jones and Mr. D. Chin. Ultrasonic measurements were made by Mr. E. Hohman. Panel fabrication, specimen preparation, and testing at Bell were done in the Research Laboratory and the Methods and Materials Laboratory.

Technical tasks described in this document include tasks supported with shared funding by the U.S. rotorcraft industry and government under RITA/NASA Cooperative Agreement No. NCCW-0076, Advanced Rotorcraft Technology, dated August 15, 1995. Additional data were developed under Navy Contract N00019-85-C-0145, USAF Contract F3361-C-5729, NASA Task Order Contract NAS1-19853 and Bell Internal Research and Development funding.

References

[1] USAF Guide Specification for Aircraft Structures, AFGS-87221A. June 1990.
[2] FAA Advisory Circular No. 20-107A, "Composite Aircraft Structure, April 1984.
[3] Jaeb, J. R., "Standardization of Composite Damage Criteria for Military Rotary and Fixed Wing Aircraft," Aerospace Industries Association Material and Structures Committee, Washington, DC, Dec. 1994.
[4] Williams, J. G., Anderson, M. S., Rhodes, M. D., Starnes, J. H., Jr., and Stroud, W. J., "Recent Develop-

ments in the Design, Testing, and Impact-Damage Tolerance of Stiffened Composite Panels," *Fibrous Composites in Structural Design,* E. M. Lenoe, et al., Eds., Conference Proceedings, San Diego, CA, 14–17 Nov. 1978, Plenum Press, 1980, pp. 259–291.

[5] Walker, T. H., Minguet, P. J., Flynn, B. W., Carbery, D. J., Swanson, G. D., and Ilcewicz, L. B., "Advanced Technology Composite Fuselage—Structural Performance," NASA CR 4732, April 1997.

[6] Shyprykevich, P., "Damage Tolerance of Composite Aircraft Structures: Analysis and Certification," *Proceedings, ICCM XI,* Sydney, Australia, 1997.

[7] Wiggenraad, J. F. M., Aoki, R., Gadke, M., Greenhalgh, E., Hachenberg, D., Wolf, K., and Bubl, R., "Damage Propagation in Composite Structural Elements—Analysis and Experiments on Structures," *Composite Structures,* Vol. 36, 1996, pp. 173–187.

[8] Gadke, M., Geier, B., Goetting, H., Klien, H., Rowher, K., and Zimmermann, R., "Damage Influence on the Buckling Load of CFRP Stringer-Stiffened Panels," *Composite Structures,* Vol. 36, 1996, pp. 249–275.

[9] Greenhalgh, E., Bishop, S., Bray, D., Hughes, D., Lahiff, S., and Millson, B., "Characterisation of Impact Damage in Skin-Stringer Composite Structures," *Composite Structures,* Vol. 37, 1997, pp. 187–207.

[10] Falzon, B. and Steven, G., "Buckling Mode Transition in Hat-Stiffened Composite Panels Loaded in Uniaxial Compression," *Composite Structures,* Vol. 37, 1997, pp. 253–267.

[11] Brogan, F. A., Rankin, C. C., and Cabiness, H. D., *STAGS Users Manual,* Lockheed Palo Alto Research Laboratory, Report LMSC P032594, 1994.

[12] *MSC/NASTRAN Quick Reference Guide, Version 70,* MSC Software Corp., Los Angeles, 1998.

[13] Hethcock, J. D., "Strength Determination of Damaged Laminates Using Commercial Finite-Element Model Codes," American Helicopter Society, Stratford, CT, 7–8 Oct. 1998.

Ronald Krueger,[1] *Pierre J. Minguet,*[2] *and T. Kevin O'Brien*[1]

A Method for Calculating Strain Energy Release Rates in Preliminary Design of Composite Skin/Stringer Debonding Under Multiaxial Loading

REFERENCE: Krueger, R., Minguet, P. J., and O'Brien, T. K., "**A Method for Calculating Strain Energy Release Rates in Preliminary Design of Composite Skin/Stringer Debonding Under Multiaxial Loading,**" *Composite Structures: Theory and Practice, ASTM STP 1383,* P. Grant and C. Q. Rousseau, Eds., American Society for Testing and Materials, West Conshohocken, PA, 2000, pp. 105–128.

ABSTRACT: Three simple procedures were developed to determine strain energy release rates, G, in composite skin/stringer specimens for various combinations of uniaxial and biaxial (in-plane/out-of-plane) loading conditions. These procedures may be used for parametric design studies in such a way that only a few finite-element computations will be necessary for a study of many load combinations. The results were compared with mixed-mode strain energy release rates calculated directly from nonlinear two-dimensional plane-strain finite-element analyses using the virtual crack closure technique. The first procedure involved solving three unknown parameters needed to determine the energy release rates. Good agreement was obtained when the external loads were used in the expression derived. This superposition technique, however, is applicable only if the structure exhibits a linear load/deflection behavior. Consequently, a second modified technique was derived which was applicable in the case of nonlinear load/deformation behavior. The technique, however, involved calculating six unknown parameters from a set of six simultaneous linear equations with data from six nonlinear analyses to determine the energy release rates. This procedure was not time efficient, and hence, less appealing.

Finally, a third procedure was developed to calculate mixed-mode energy release rates as a function of delamination lengths. This procedure required only one nonlinear finite-element analysis of the specimen with a single delamination length to obtain a reference solution for the energy release rates and the scale factors. The delamination was subsequently extended in three separate linear models of the local area in the vicinity of the delamination subjected to unit loads to obtain the distribution of G with delamination lengths. This set of subproblems was solved using linear finite-element analyses, which resulted in a considerable reduction in CPU time compared to a series of nonlinear analyses. Although additional modeling effort is required to create the local submodel, this superposition technique is very efficient for large parametric studies, which may occur during preliminary design where multiple load combinations must be considered.

KEYWORDS: composite materials, delamination, fracture mechanics, energy release rate, finite-element analysis, virtual crack closure technique, skin/flange interface

Carbon epoxy composite structures are widely used by today's aircraft manufacturers to reduce weight. Many composite components in aerospace structures consist of flat or curved panels with co-cured or adhesively bonded frames and stiffeners. Testing of stiffened panels designed for pressurized

[1] National Research Council resident research associate and senior research scientist, U.S. Army Research Laboratory, Vehicle Technology Directorate, respectively, NASA Langley Research Center, Mail Stop 188E, Hampton, VA 23681-2199.

[2] Head, Structures Technology Research & Development Group, Boeing, P.O. Box 16858, Mail Stop P38-13, Philadelphia, PA 19142-0858.

Copyright© 2001by ASTM International www.astm.org

aircraft fuselage has shown that bond failure at the tip of the frame flange is an important and very likely failure mode [*1*]. Comparatively simple simulation specimens consisting of a stringer bonded onto a skin were developed and it was shown in experiments that the failure initiated at the tip of the flange, identical to the failure observed in the full-size panels and frame pull-off specimens [*2–7*].

The overall objective of the current work is to develop a simple procedure to calculate the strain energy release rate for delaminations originating from matrix cracks in these skin/stringer simulation coupons for arbitrary load combinations. The total strain energy release rate would then be compared to critical values obtained from an existing mixed-mode failure criterion to predict delamination onset. This procedure could then be used for parametric design studies in such a way that only a few finite-element computations would be necessary to evaluate bonded joint response due to many load combinations. A similar approach based on an approximate superposition analysis technique is described in Ref *8*. Since energy is a quadratic function of the applied loads, simple superposition to add the energy release rates from separate load cases is not valid. Therefore, a simple quadratic expression is developed to calculate the strain energy release rate for any combination of loads [*4*]. To validate this approach, results obtained from the quadratic expression are compared to Mode I and Mode II strain energy release rate components, which are calculated from nonlinear two-dimensional plane-strain finite-element analyses using the virtual crack closure technique [*9,10*].

Three simple procedures are developed to determine strain energy release rates, G, in composite skin/stringer specimens for various combinations of uniaxial and biaxial (in-plane/out-of-plane) loading conditions. The first procedure involved solving three unknown parameters needed to determine the energy release rates. This superposition technique, however, was only applicable if the structure exhibits a linear load/deflection behavior. Consequently, a second modified technique is derived which is applicable in the case of nonlinear load/deformation behavior. A third procedure is developed to calculate mixed-mode energy release rate as a function of delamination length. This procedure requires only one nonlinear finite-element analysis of the specimen with a single delamination length to obtain a reference solution for the energy release rates and the scale factors.

Background

Previous investigations of the failure of secondary bonded structures focused on loading conditions as typically experienced by aircraft crown fuselage panels. Tests were conducted with specimens cut from a full-size panel to verify the integrity of the bondline between the skin and the flange or frame [*1*]. However, these panels were rather expensive to produce and there is a need for a test configuration that would allow detailed observations of the failure mechanism at the skin/flange interface. A simpler specimen configuration was proposed in Ref *2*. The investigations focused on the failure mechanisms of a bonded skin/flange coupon configuration loaded in bending [*2–5*]. In many cases, however, composite structures may experience both bending and membrane loads during in-flight service. Damage mechanisms in composite bonded skin/stringer structures under monotonic tension, three-point bending, and combined tension/bending loading conditions were investigated in Refs *6* and *7*. An analytical methodology was also developed to predict the location and orientation of the first transverse matrix crack based on the principal transverse tension stress distribution in the off-axis plies nearest the bondline in the vicinity of the flange tip. The prediction of delamination onset was based on energy release rate calculations.

The specimens tested in Refs *6* and *7* consisted of a bonded skin and flange assembly as shown in Fig. 1. Both the skin and the flange laminates had a multidirectional layup made from IM6/3501-6 graphite/epoxy prepreg tape with a nominal ply thickness of $h = 0.188$ mm. The skin layup, consisting of 14 plies, was $[0/45/90/-45/45/-45/0]_s$, and the flange layup, consisting of 10 plies, was $[45/90/-45/0/90]_s$. The measured bondline thickness averaged 0.102 mm. Specimens were 25.4 mm wide and 203.2 mm long. Typical material properties for the composite tape and the adhesive material used in the analysis were taken from Ref *2* and are summarized in Table 1.

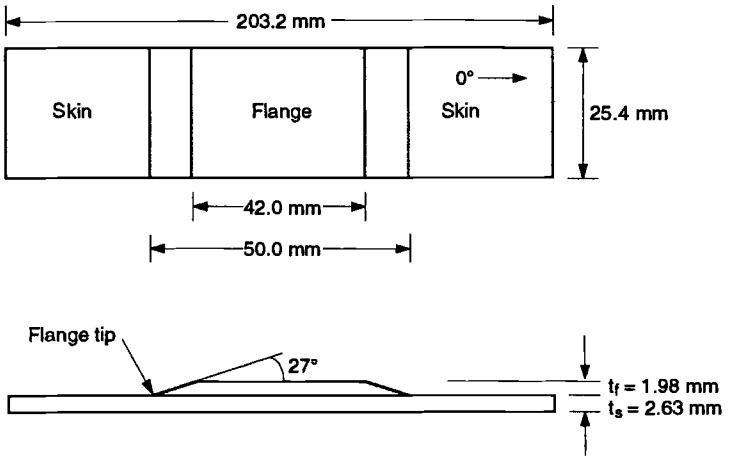


FIG. 1—*Specimen configuration.*

The specimens were subjected to pure tension, three-point bending, and combined axial tension and bending loads. A schematic of the deformed specimen geometries, the boundary conditions, and the loads corresponding to the first damage observed are shown in Fig. 2. In the combined axial tension and bending load case, a constant axial load, P, was applied in a first load step while transverse loads remained zero. In a second load step, the axial load was kept constant while the load orientation rotated with the specimen as it deformed under the transverse load. The tests were terminated when the flange debonded unstably from one of the flange tips. Damage was documented from photographs of the polished specimen edges at each of the four flange corners identified in Fig. 3*a*. Typical damage patterns, which were similar for all three loading configurations, are shown in Figs. 3*b* and *c*. Corners 1 and 4 and corners 2 and 3 had identical damage patterns. At corners 1 and 4, a delamination running in the 90°/45° flange ply interface (delamination A) initiated from a matrix crack in the 90° flange ply as shown in Fig. 3*b*. At longer delamination lengths, new matrix cracks formed and branched into both the 45° ply below the delaminated interface as well as the 90° flange ply above the interface. At corners 2 and 3 a matrix crack formed at the flange tip in the 90° flange ply that subsequently ran through the lower 45° flange ply and the bondline into the skin as shown in Fig. 3*c*. Subsequently, a split (delamination B1) formed from the tip of that matrix crack within the top 0° skin ply and in some cases, a second delamination (delamination B2) was observed below the first in the top 0°/45° skin ply interface.

In previous investigations, stress analyses were used to predict the location and orientation of the first transverse matrix crack based on the principal transverse tension stress distribution in the off axis

TABLE 1—*Material properties.*

IM6/3501-6 Unidirectional Graphite/Epoxy Tape [2]		
E_{11} = 144.7 GPa	E_{22} = 9.65 GPa	E_{33} = 9.65 GPa
ν_{12} = 0.30	ν_{13} = 0.30	ν_{23} = 0.45
G_{12} = 5.2 GPa	G_{13} = 5.2 GPa	G_{23} = 3.4 GPa
CYTEC 1515 Adhesive		
E = 1.72 GPa	ν = 0.30	(assumed isotropic)

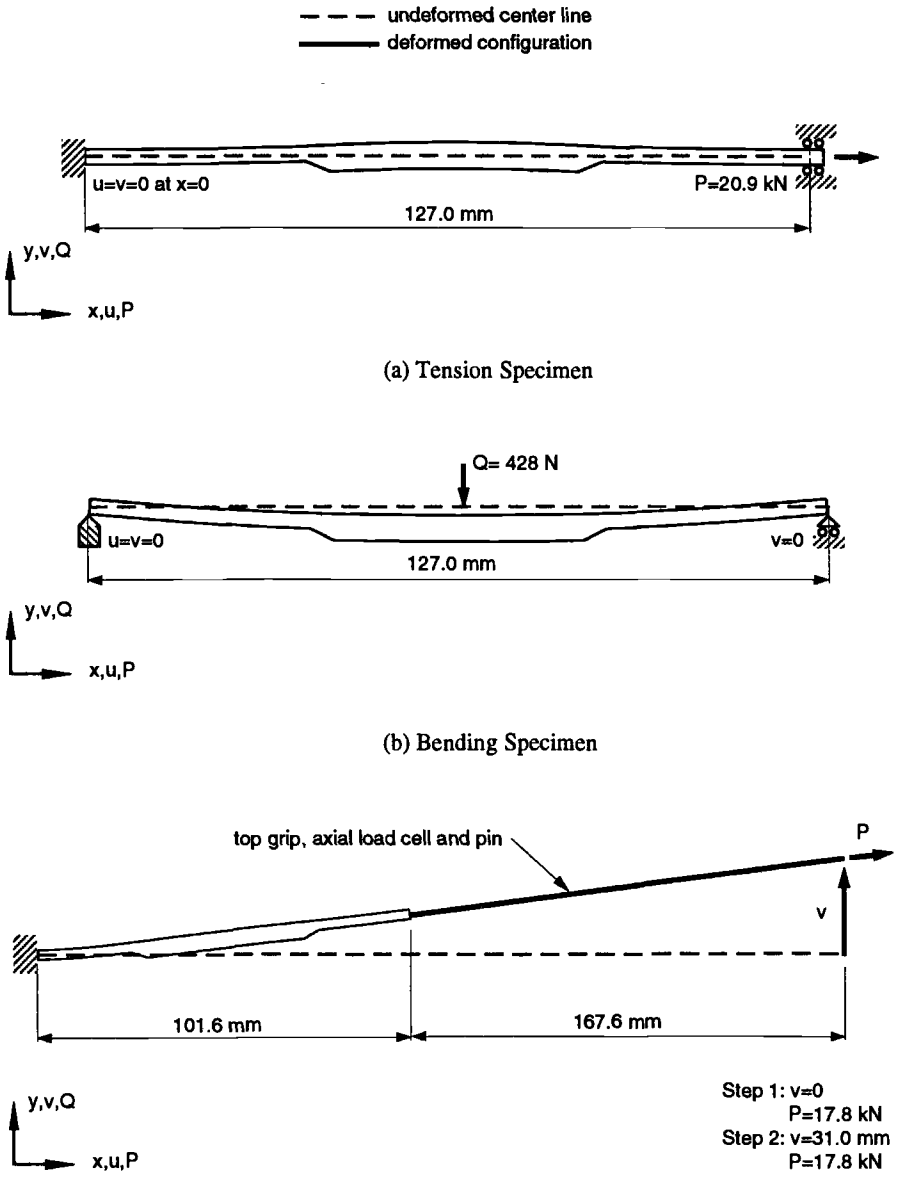
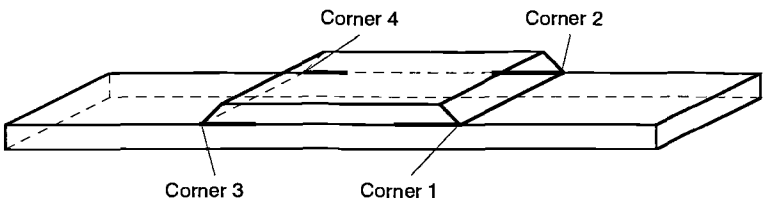
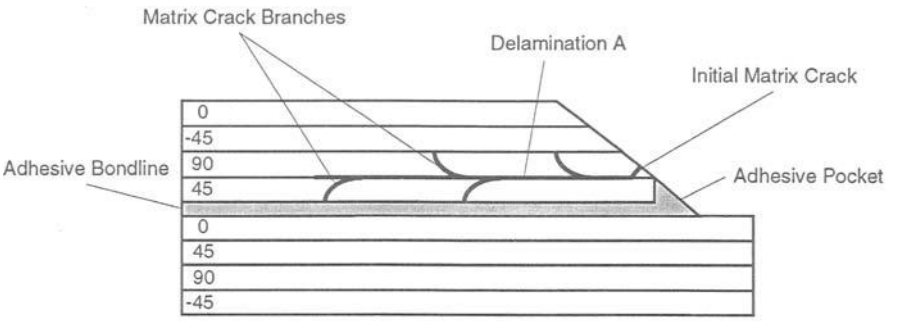


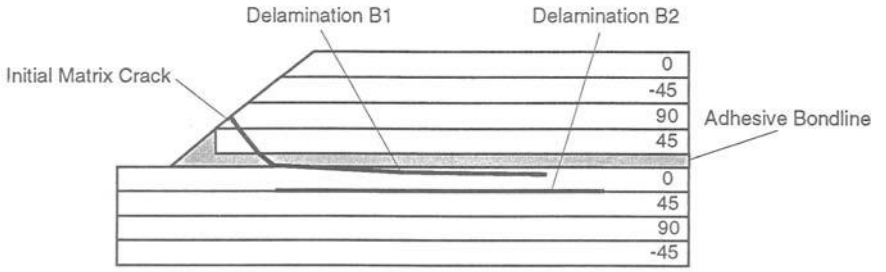
FIG. 2—*Deformed test specimen geometries, load and boundary conditions at damage initiation [6,7].*



(a) Specimen with Crack Locations.



(b) Corners 1 and 4



(c) Corners 2 and 3

FIG. 3—*Typical damage patterns [6,7].*

plies nearest the bondline in the vicinity of the flange tip [*6,7*]. A comparison of the trajectories of the maximum principal tension stress with the damage patterns shown in Figs. 3*b* and *c* indicated that the matrix crack starts to grow perpendicular to the trajectories. For all three loading conditions, maximum principal tensile stresses in the 90° ply closest to the bondline, computed for applied loads at damage onset, were almost identical and exceeded the transverse tension strength of the material. Subsequent finite-element analyses of delamination growth from these matrix cracks were performed using the virtual crack closure technique. However, because the specimen geometry and loadings required nonlinear analyses, this was a computationally intensive process.

Analysis Formulation

Finite-Element Model

In the current investigation the finite-element (FE) method was used to analyze the test specimens for each loading case. The goal of this analysis is to evaluate strain energy release rate components at the delamination tip using the virtual crack closure technique [*9,10*]. To develop a simple procedure to calculate the strain energy release for delaminations originating from matrix cracks, it was reasonable to focus only on one damage pattern during the investigation. Therefore, only a FE model of a specimen with a delamination running in the 90°/45° flange ply interface, corresponding to Fig. 3*b*, was developed and loads and boundary conditions were applied to simulate the three load cases. The two-dimensional cross section of the specimens was modeled using quadratic eight-noded quadrilateral plane strain elements (see Fig. 4) and a reduced (2 × 2) integration scheme was used for these elements. For the entire investigation, the ABAQUS finite-element software was used [*11*].

An outline and two detailed views of the FE model are shown in Fig. 4. A refined mesh was used in the critical area of the 90° flange ply where matrix cracks and delaminations were observed in the test specimens. Outside the refined mesh area, all plies were modeled with one element through the ply thickness. Two elements were used per ply thickness in the refined region, except for the first three individual flange plies above the bondline and the skin ply below the bondline, which were modeled with four elements. Three elements through-the-thickness were used for the adhesive film. Based upon the experimental observations shown in Fig. 3*b*, the model included a discrete matrix crack and a delamination. The initial matrix crack was modeled perpendicular to the flange taper, as suggested by the microscopic investigation as well as the stress analysis, which showed that the matrix crack starts to grow perpendicular to the trajectory of the maximum principle tension stress [*6,7*]. Damage was modeled at one flange tip as shown in Fig. 4. The mesh used to model the undamaged specimen, as discussed in Refs *6* and *7*, was employed at the opposite taper. The model consisted of 6977 elements and 21 486 nodes and had 42 931 degrees of freedom.

For the combined tension and bending load case, performed in NASA Langley's axial tension and bending test frame [*12,13*], the top grip, the load cell, and the load pin were modeled using three-noded quadratic beam elements as shown in Figs. 2*c* and 5, to accurately simulate the combined tension and bending loads applied [*6,7*]. The beams were connected to the two-dimensional plane strain model of the specimen using multipoint constraints to enforce appropriate translations and rotations. As shown in Fig. 5, nodes 1–29 along the edge of the plane strain model (x = 101.6 mm) were constrained to move as a plane with the same rotation as beam node A. To be consistent with the actual tests, a constant axial load, P, was applied in a first load step while transverse loads remained zero. In a second load step, the axial load was kept constant while the load orientation rotated with the specimen as it deformed under the transverse load. During the tests, the maximum specimen deflections under the transverse load were recorded at the top grip contact point. In the FE simulation a prescribed displacement, v, was applied which corresponded to the recorded transverse stroke. For the beam model of the steel parts (top grip, load cell, and load pin), a Young's modulus of 210 GPa and a Poisson's ratio of 0.3 were used as material input data. A rectangular beam cross section was selected to model the square cross section of the top grip ($I = 1.87 \times 10^6$ mm^4) and load pin ($I = 1.4 \times 10^6$ mm^4) and a circular beam cross section was used to model the cylindrical load cell ($I = 8.37 \times 10^3$ mm^4).

When applying two-dimensional plane strain FE models it is assumed that the geometry, boundary conditions and other properties are constant across the entire width of the specimen. The current model, thus, may not always capture the true nature of the problem. As shown in Fig. 3, the delamination pattern changed from corner 3 to corner 4 from a delamination running in the 90°/45° interface to a delamination propagating between the adhesive film and the top 0° ply of the skin. This is a three-dimensional effect and cannot be accounted for in the current plane strain model.

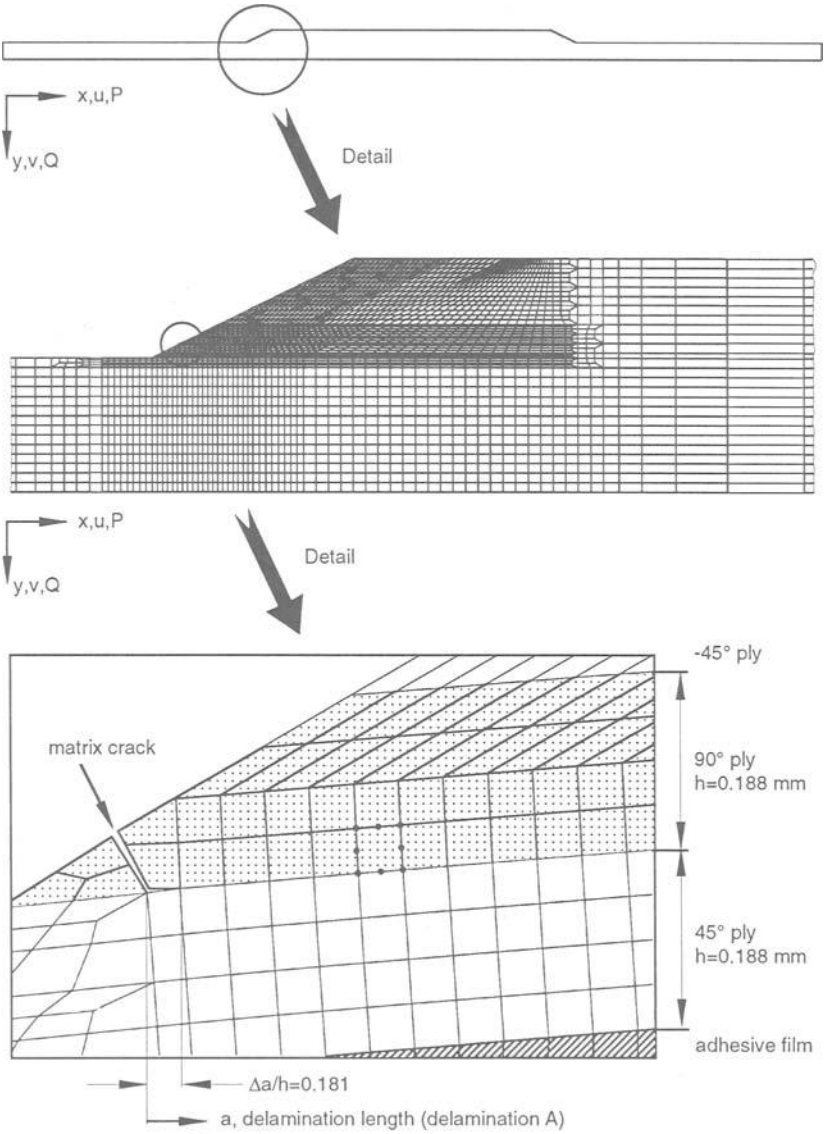


FIG. 4—*Finite-element model of a damaged specimen.*

Virtual Crack Closure Technique

The virtual crack closure technique (VCCT) described in Refs *9* and *10* was used to calculate strain energy release rates for the delaminations. The Mode I and Mode II components of the strain energy release rate, G_I and G_{II}, were calculated as (see Fig. 6)

$$G_I = -\frac{1}{2\Delta a}\left[Y_i'(v_m' - v_{m*}') + Y_j'(v_\ell' - v_{\ell*}')\right] \quad (1)$$

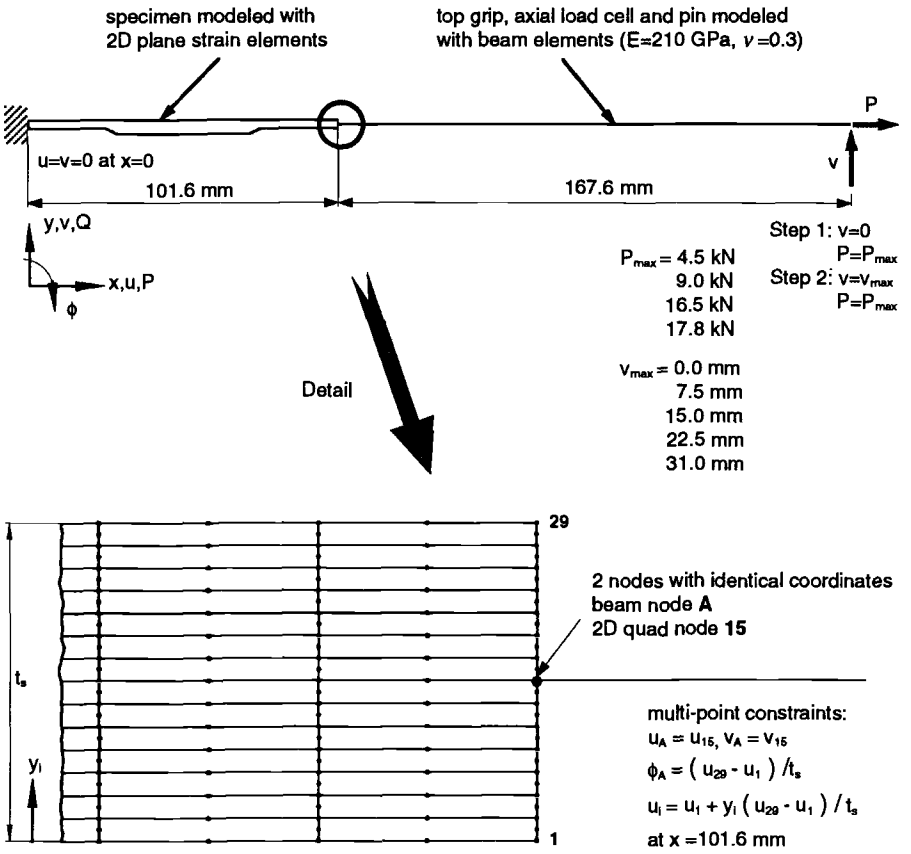


FIG. 5—*Loads and boundary conditions for the combined axial tension and bending test.*

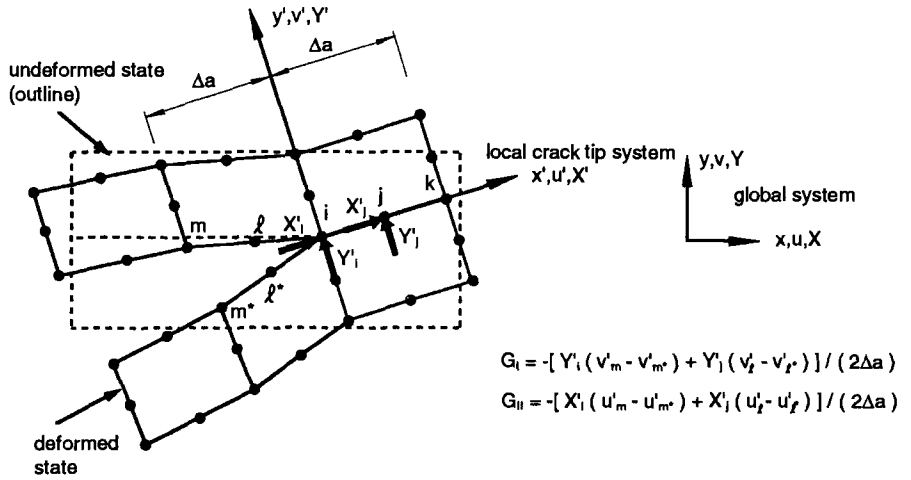


FIG. 6—*Virtual crack closure technique (VCCT).*

and

$$G_{II} = -\frac{1}{2\Delta a}[X'_i(u'_m - u'_{m^*}) + X'_j(u'_\ell - u'_{\ell^*})] \tag{2}$$

where Δa is the length of the elements at the delamination tip, X'_i and Y'_i are the forces at the delamination tip at node i, and u'_m and v'_m are the relative displacements at the corresponding node m behind the delamination tip as shown in Fig. 6. Similar definitions are applicable for the forces at node j and displacements at node ℓ. For geometrically nonlinear analysis, both forces and displacements were transformed into a local coordinate system (x', y'), that defined the normal and tangential coordinate directions at the delamination tip in the deformed configuration. The Mode III component is identically zero for the plane strain case. Therefore, the total strain energy release rate, G_T, was obtained by summing the individual mode components as

$$G_T = G_I + G_{II} \tag{3}$$

The data required to perform the VCCT in Eqs 1 to 3 were accessed directly from the ABAQUS binary result file to get better accuracy. The calculations were performed in a separate post-processing step using nodal displacements and nodal forces at the local elements in the vicinity of the delamination front.

Care must be exercised in interpreting the values for G_I and G_{II} obtained using the virtual crack closure technique for interfacial delaminations between two orthotropic solids [*14,15*]. For the current investigation, the element length Δa was chosen to be about $\frac{1}{4}$ of the ply thickness, h, for the delamination in the 90°/45° flange ply interface. Note that for the FE model shown in Fig. 4 $\Delta a/h = 0.181$ for the element behind and $\Delta a/h = 0.25$ for the element in front of the delamination tip. Therefore, the technique suggested in Ref 9 was used to estimate the forces X'_i and Y'_i for the case of unequal element lengths at the delamination tip. For the further delamination growth a value of $\Delta a/h = 0.25$ was used.

Analytical Investigation

Superposition Technique for Linear Deformation Behavior

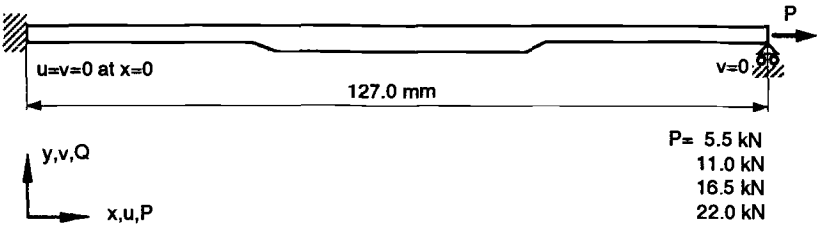
The schematics of the specimen, boundary conditions, and three load cases (tension, bending and combined tension and bending) considered in this part of the study are shown in Fig. 7. These boundary conditions and loads, however, do not represent the conditions applied during the experiments as given in Fig. 2 of the previous section. This new set of boundary conditions was chosen to simplify the derivation of the superposition technique for linear deformation behavior. It was postulated that the specimen exhibits a linear load deflection behavior for the three load cases shown. Only linear finite-element analyses were used. The boundary conditions applied were the same for all load cases.

For a specimen subjected to a pure tension load P as shown in Fig. 7*a*, the energy release rate G_P at the delamination tip can be calculated as

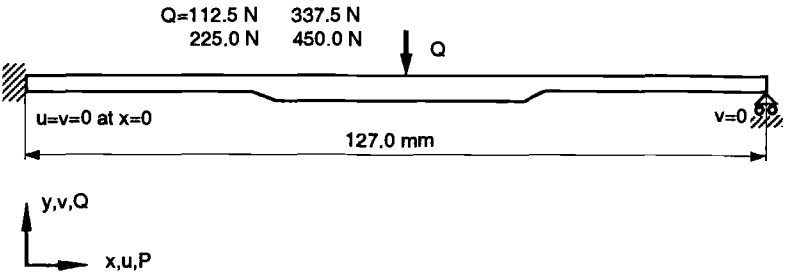
$$G_P = \frac{P^2}{2} \cdot \frac{\partial C_P}{\partial A} \tag{4}$$

where C_P is the compliance of the specimen and ∂A is the increase in surface area corresponding to an incremental increase in load or displacement at fracture [*16*]. For a specimen subjected to a bending load Q, as shown in Fig. 7*b*, the energy release rate G_Q at the delamination tip can be calculated accordingly as

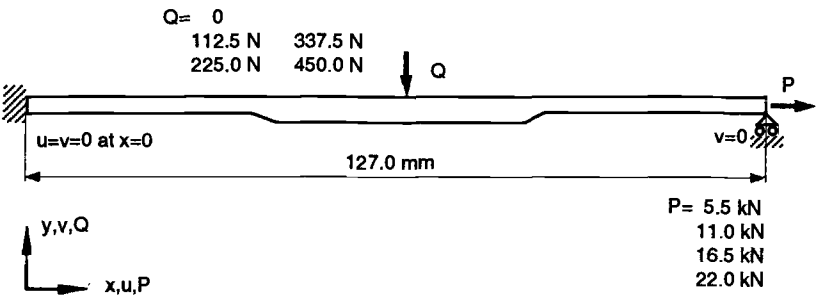
$$G_Q = \frac{Q^2}{2} \cdot \frac{\partial C_Q}{\partial A} \tag{5}$$



(a) Tension Load Case



(b) Bending Load Case



(c) Combined Load Condition

FIG. 7—*Loads and boundary conditions for tension, three-point bending and combined loading case.*

If the external load, R, applied in the linear analysis is simply a fraction or multiple of the tension load P, $R = nP$, or the bending load Q, $R = mQ$, the energy release rate G_R for the new load case may be obtained from the known values using

$$G_R = n^2 G_P \qquad \text{or} \qquad G_R = m^2 G_Q \tag{6}$$

In the case of a combined tension/bending load case as shown in Fig. 7*c*, where the external load is a combination of a fraction or multiple n of the tension load P and a different fraction or multiple m

of the bending load Q, $R = nP + mQ$, we obtain

$$G_R = \frac{(nP + mQ)^2}{2} \cdot \frac{\partial C_R}{\partial A} = \frac{(n^2P^2 + 2mnPQ + m^2Q^2)}{2} \cdot \frac{\partial C_R}{\partial A} \tag{7}$$

Note that for a tension load, P, only, $\frac{\partial C_R}{\partial A} = \frac{\partial C_P}{\partial A}$ and for a bending load, Q, only, $\frac{\partial C_R}{\partial A} = \frac{\partial C_Q}{\partial A}$. For the combined load case Eq 7 can then be approximated by

$$G_R \cong \frac{n^2P^2}{2} \cdot \frac{\partial C_P}{\partial A} + 2mn \frac{PQ}{2} \frac{\partial C_R}{\partial A} + \frac{m^2Q^2}{2} \cdot \frac{\partial C_Q}{\partial A} \tag{8}$$

Using Eqs 4 and 5 yields

$$G_R \cong n^2G_P + 2mn \cdot \underbrace{\frac{PQ}{2} \cdot \frac{\partial C_R}{\partial A}}_{G_{PQ}} + m^2G_Q \tag{9}$$

where G_{PQ} is a coupling term which has the dimension of an energy release rate.

First, linear FE analyses of a simple tension and simple bending case are performed using VCCT to determine G_{I}, G_{II} and G_T. This allows calculation of the G_P and G_Q parameters in Eq 9 for total G, and the G_{I} and G_{II} components. Then a single linear FE analysis of a combined tension and bending load case is performed using VCCT to obtain the G_R parameter in Eq 9 for G_{I}, G_{II} and G_T. Once these parameters are determined, then G_{PQ} may be calculated for G_{I}, G_{II} and G_T. The parameters G_P, G_Q and G_{PQ} may now be used to calculate G_R for G_{I}, G_{II} and G_T for other tension and bending load combinations.

Mode I and Mode II values were computed using VCCT for a delamination running in the 90°/45° flange ply interface with a length equal to the length of the first element ($a/h = 0.181$) as shown in Fig. 4. For the pure tension and bending loads shown in Figs. 7*a* and *b*, energy release rates were also calculated using the analytical expressions of Eq 6. In the example shown in Fig. 8 for the tension load case, the parameter G_P in Eq 6 was computed for $P = 5.5$ kN. The total energy release rate G_T computed using VCCT and the superposed results are identical, since Eq 6 is an exact closed form solution. Minor differences for the individual modes, that cannot be explained, are observed. For all permutations of P and Q loads, as shown in Fig. 7*c*, energy release rates for the combined load case were calculated using Eq 9. In this investigation the parameter G_P in Eq 9 was calculated for a tension load $P = 5.5$ kN, G_Q was determined for a bending load $Q = 112.5$ kN and G_{PQ} was obtained from one analysis of the combined tension and bending load. Energy release rates obtained from Eq 9 were compared to Mode I and Mode II values calculated using VCCT as shown in Fig. 9 for the case where a tension load $P = 11.0$ kN was applied and Q was varied. For the other permutations of loads the comparisons of only the total energy release rates, G_T, are shown in Fig. 10. The good agreement of results confirms that the superposition technique derived in Eq 9 is applicable, in combination with linear finite-element analysis and VCCT to determine the unknown parameters, provided the structure shows a linear load/deflection behavior.

A Modified Technique for Nonlinear Deformation Behavior

For the investigation of the combined axial tension and bending load case as shown in Figs. 2*c* and 5, nonlinear finite analyses were used since this allowed the axial load to rotate with the specimen as it deformed under the transverse load and accounted for the membrane stiffening effect caused by the axial load. In this case the superposition technique derived for the linear case in the previous section Eqs 8 and 9 is no longer applicable and a modified method needs to be developed.

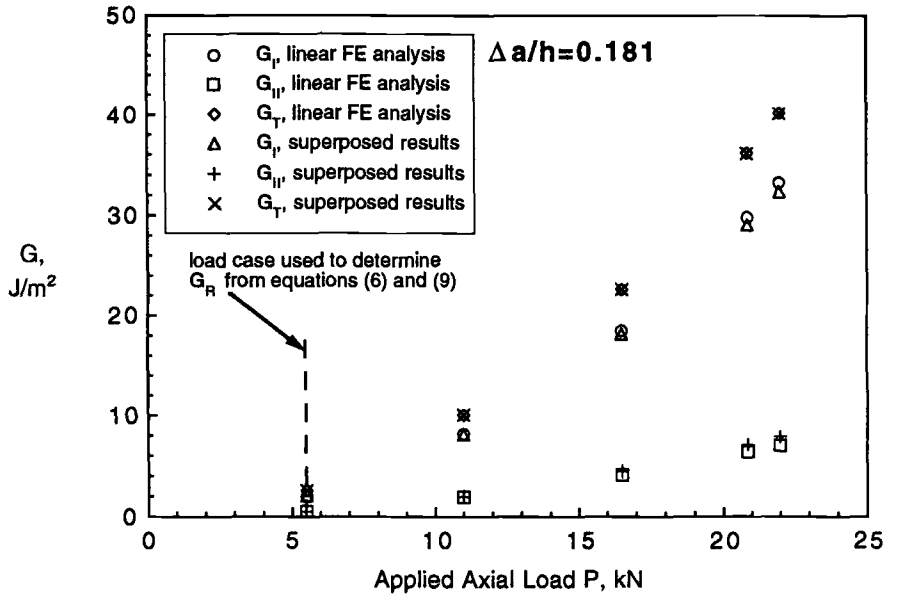


FIG. 8—*Comparison of computed strain energy release rates with superposed values for tension load case.*

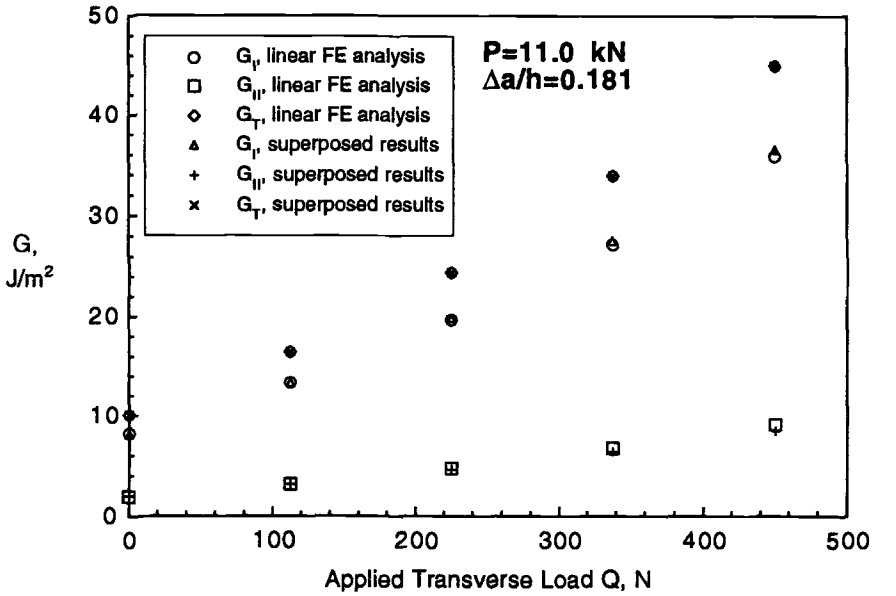


FIG. 9—*Comparison of computed strain energy release rate components with superposed values for combined tension and bending load case.*

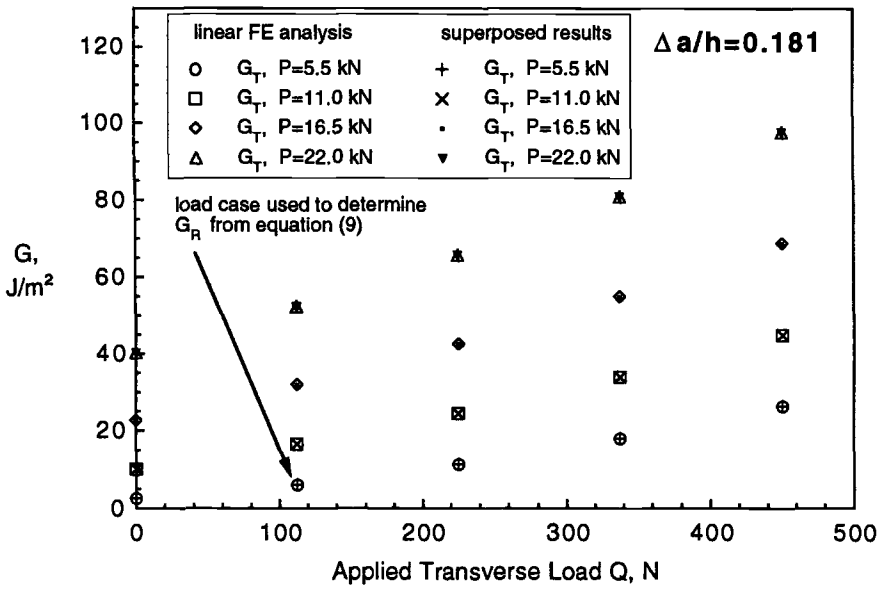


FIG. 10—*Comparison of computed total strain energy release rates with superposed values for combined tension and bending load cases.*

An analytical expression was suggested in Ref *4* that is primarily a modification of Eq 8 derived in the previous section. The external tension load, P, and bending load, Q, in the analytical expression were replaced with the local force resultant N_{xx} and moment resultant M_{xx}, yielding.

$$G = G_{mm}M_{xx}^2 + 2G_{mn}M_{xx}N_{xx} + G_{nn}N_{xx}^2 \tag{10}$$

where G_{mm} and G_{nn} are unknown parameters determined from a pure tension and a pure bending load case and G_{mn} is an unknown combined tension and bending parameter. The local force and moment resultants are calculated at the flange tip as shown in Fig. 11. For improved accuracy, the terms related to the transverse shear force resultant, Q_{xy}, were also included in Eq 10, yielding

$$G = G_{mm}M_{xx}^2 + 2G_{mn}M_{xx}N_{xx} + G_{nn}N_{xx}^2 + 2G_{mq}M_{xx}Q_{xy} + 2G_{nq}N_{xx}Q_{xy} + G_{qq}Q_{xy}^2 \tag{11}$$

Equation 11 may be written in matrix from as

$$G = [M_{xx}^2\ 2M_{xx}N_{xx}\ N_{xx}^2\ 2M_{xx}Q_{xy}\ 2N_{xx}Q_{xy}\ Q_{xy}^2] \cdot \begin{bmatrix} G_{mm} \\ G_{mn} \\ G_{nn} \\ G_{mq} \\ G_{nq} \\ G_{qq} \end{bmatrix} \tag{12}$$

Unlike the linear case where a pure tension or a pure bending load case alone may be used to determine one of the unknown parameters, nonlinear analysis of the pure tension and pure bending load case yielded a combination of M_{xx} and N_{xx} at the flange tip due to the load eccentricity (tension load) and large displacements (bending load). Therefore, the constants G_{ij} $(i,j = m,n,q)$ could not be deter-

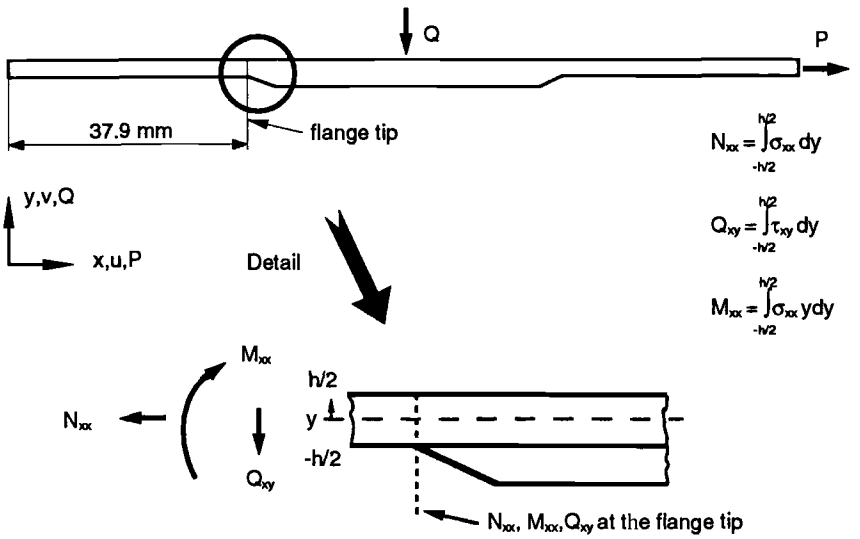


FIG. 11—*Calculation of force and moments resultants.*

mined simply from the pure tension and bending load cases. Consequently, all six constants were calculated from a set of six simultaneous linear equations corresponding to six unique loading combinations solved previously, using nonlinear FE analyses. This yields G_k ($k = 1, \ldots, 6$)

$$\begin{bmatrix} G_1 \\ G_2 \\ G_3 \\ G_4 \\ G_5 \\ G_6 \end{bmatrix} = \begin{bmatrix} M_1^2 & 2M_1N_1 & N_1^2 & 2M_1Q_1 & 2N_1Q_1 & Q_1^2 \\ M_2^2 & 2M_2N_2 & N_2^2 & 2M_2Q_2 & 2N_2Q_2 & Q_2^2 \\ M_3^2 & 2M_3N_3 & N_3^2 & 2M_3Q_3 & 2N_3Q_3 & Q_3^2 \\ M_4^2 & 2M_4N_4 & N_4^2 & 2M_4Q_4 & 2N_4Q_4 & Q_4^2 \\ M_5^2 & 2M_5N_5 & N_5^2 & 2M_5Q_5 & 2N_5Q_5 & Q_5^2 \\ M_6^2 & 2M_6N_6 & N_6^2 & 2M_6Q_6 & 2N_6Q_6 & Q_6^2 \end{bmatrix} \cdot \begin{bmatrix} G_{mm} \\ G_{mn} \\ G_{nn} \\ G_{mq} \\ G_{nq} \\ G_{qq} \end{bmatrix} \tag{13}$$

Further, the local force and moment resultants N_{xx}, M_{xx} and Q_{xy} for all six unique loading combinations were calculated at the flange tip using the equations shown in Fig. 11 by integrating stresses determined in the nonlinear FE analyses yielding N_k, M_k and Q_k ($k = 1, \ldots, 6$). The system of six equations was then solved for the unknown G_{ij} values. With the constants G_{ij} known, G could then be calculated from the force and moment resultants N_{xx}, Q_{xy} and M_{xx} for any combined tension/bending load case using the technique described by Eq 11. The term G is used here for the total energy release rate or for a mixed mode energy release rate component. Hence, the calculation of each of the individual modes G_{I}, G_{II} or G_T requires a unique set of G_{ij} constants each. This means that Eq 13 needs to be solved individually for each fracture mode (I,II) before Eq 11 is used to obtain the individual modes G_{I}, G_{II} or G_T.

The analytical Eqs 10 and 11 were derived with the objective of developing a simple procedure to calculate the strain energy release rate if the specimen shows a nonlinear load/deflection behavior. The expressions may also be used if the specimen exhibits a linear load/deflection behavior. Calculating the force and moment resultants and solving Eq 13 to obtain a unique set of constants G_{ij} for each fracture mode, however, appears to be cumbersome in this case because FE analysis needs to be performed for six unique combined load cases to determine the unknown parameters G_{ij}. In contrast, the use of Eq 8 is simpler, because the external loads are known and only three load cases need to be analyzed to determine G_P, G_Q and G_{PQ}.

The matrix Eq 13, which contains the terms of local force and moment resultants N_k, M_k and Q_k, may become singular. For linear load/deflection behavior this will occur if at least one of the six load cases selected to calculate N_k, M_k, Q_k and G_k is not independent from the other cases, but simply a linear combination of any of them. For nonlinear load/deflection behavior it is not easily predictable under which circumstances the matrix might become singular. In both cases, however, six unique load cases need to be selected to avoid matrix singularity and solve Eq 13 for the unknown parameters.

The energy release rates were calculated using the modified method (Eq 11) for all permutations of axial loads, P, and transverse displacements, v_{max}, shown in Fig. 5. The unknown parameters G_{ij} in Eq 13 were obtained from nonlinear finite-element analyses of six different unique load cases (P_1 = 0.0, v_1 = 30.9 mm; P_2 = 4.5 kN, v_2 = 7.5 mm; P_3 = 4.5 kN, v_3 = 30.9 mm; P_4 = 9.0 kN, v_4 = 7.5 mm; P_5 = 9.0 kN, v_5 = 30.9 mm; P_6 = 17.8 kN, v_6 = 30.9 mm). Calculated mixed-mode results were compared with the energy release rates obtained directly from nonlinear finite-element analyses using VCCT as shown in Fig. 12 for a case where only one axial load of P = 4.5 kN and multiple transverse displacements, v_{max}, were applied. As expected, the results were identical for the two cases which had been selected to determine the unknown parameters G_{ij}. For the other load combinations, G_I, G_{II} and G_T were in excellent agreement. Total energy release rates calculated for all axial load and transverse displacement permutations are shown in Fig. 13. For the remaining load combinations, calculated strain energy release rates differed by less than 5% when compared to results computed directly from nonlinear finite-element analysis using VCCT. Good results, however, were only obtained if the six unique load combinations to determine the unknown parameters G_{ij} include the upper and lower limits of load combinations as shown in Fig. 13. The modified method should be used to interpolate results for different load combinations. Extrapolation may lead to inaccurate results.

Hence, it was possible to derive a technique which was applicable for nonlinear deformation of the specimen. The expression derived for the linear case was modified such that terms of the external

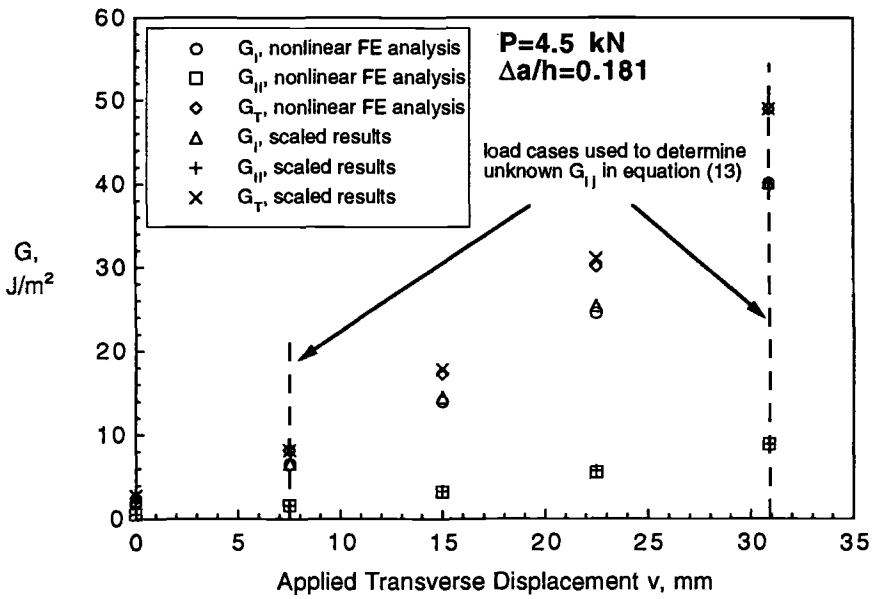


FIG. 12—*Comparison of computed strain energy release rate components with scaled values for combined tension and bending load case.*

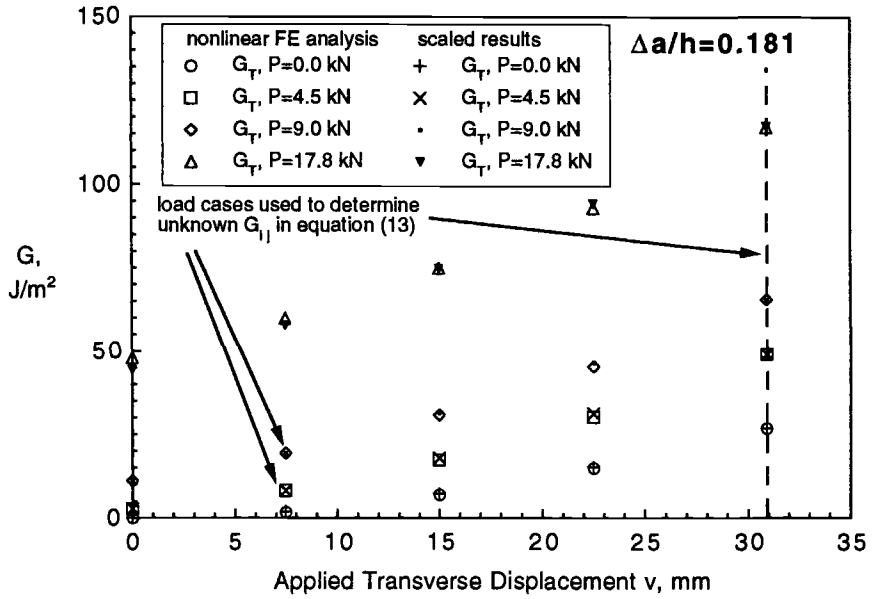


FIG. 13—*Comparison of computed total strain energy release rates with scaled values for combined tension and bending load cases.*

forces were replaced by internal force and moment resultants. The energy release rates calculated using this technique seemed sufficiently accurate for preliminary design studies. However, while external forces are known, force and moment resultants at the flange tip need to be calculated analytically or computed from finite-element analysis. For the current study of the combined axial tension and bending load case, nonlinear finite analyses were used to calculate the force and moment resultants at the flange tip as shown in Fig. 11. This requires about the same computational effort as directly computing the energy release rates from nonlinear analyses using the virtual crack closure technique. An additional effort is required to obtain the unknown parameters G_{IJ}. The use of the technique as given in Eq 11 may therefore become time consuming and less appealing for quickly calculating energy release rates for a large number of new load combinations from a set of known results. Furthermore, this process may have to be repeated for the simulation of delamination growth where for each new delamination length modeled mixed mode energy release rates need to be calculated to obtain the distribution of G_{I}, G_{II} and G_T as a function of delamination length. Consequently, another approach was developed for the simulation of delamination growth.

Simulation of Delamination Growth

The techniques developed in the previous sections focused on simple procedures to calculate the strain energy release rate for various combinations of loads from results previously computed for other load cases. A related problem is the simulation of delamination growth where mixed mode energy release rates need to be calculated as a function of delamination length, a. The shape of the G versus a curves for G_{I}, G_{II} and G_T yield information about stability of delamination growth and often dictate how these energy release rates are used to predict the onset of delamination [*17*]. During the nonlinear finite-element analyses, the delaminations are extended and strain energy release rates are computed at virtual delamination lengths using the virtual crack closure technique. For preliminary design studies with several load cases of interest, delamination positions and lengths need to be

checked continuously. Hence, the amount of computation time necessary may become excessive. Therefore fast and accurate alternatives need to be developed.

Review of Simulated Delamination Propagation Using a Series of Nonlinear FE Analyses

The schematics of the deformed geometries, the boundary conditions, and the loads examined in this part of the study are shown in Fig. 2 for all three load cases. The boundary conditions considered in the simulations were chosen to model the actual test from Refs *6* and *7* as closely as possible. For the tension and bending case, the mean loads reported for the point of damage initiation were applied. At this point, matrix cracks are likely to form. To be consistent with the combined axial tension and bending tests, a constant axial load, $P = 17.8$ kN, was applied in a first load step while transverse loads remained zero. In a second load step, the axial load was kept constant while the load orientation rotated with the specimen as it deformed under the transverse load. In the FE simulation, a prescribed displacement was applied which corresponded to the average of the transverse stroke ($v = 31$ mm) for which flange debond occurred [*6,7*].

The initial matrix crack was modeled on one flange tip perpendicular to the flange taper as suggested by the microscopic investigation and shown in Fig. 3. The model of the discrete matrix crack and delamination is shown in Fig. 4. During the nonlinear finite-element analyses, the delaminations were extended and strain energy release rate components were computed as a function of delamination length using the virtual crack closure technique. The delamination lengths, a, were measured from the end of the initial matrix crack as shown in Fig. 4. The delamination was extended in twelve increments up to about 0.6 mm ($a/h = 3.2$) which corresponds to a length where matrix crack branches were observed in the experiments as shown in Fig. *3b*. The simulated delamination propagation therefore required 12 nonlinear FE analyses for each load case, consequently 36 analyses for all three load cases. The results plotted in Figs. 14 through 16 show that G_{II} increases monotonically for all load cases while G_I begins to level off at the longest delamination lengths [*6,7*]. These results

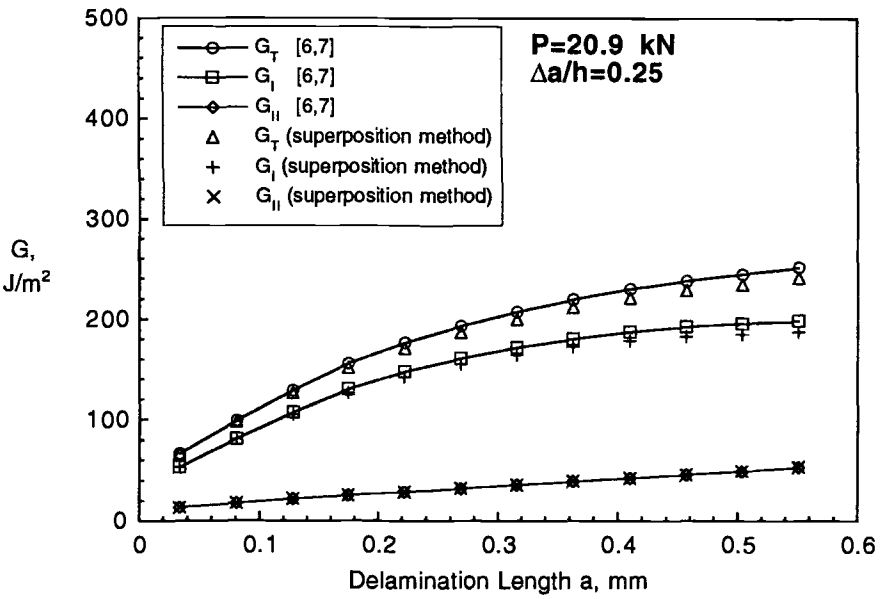


FIG. 14—*Computed strain energy release rates for delamination growth in a 90°/45° flange ply interface for tension load case.*

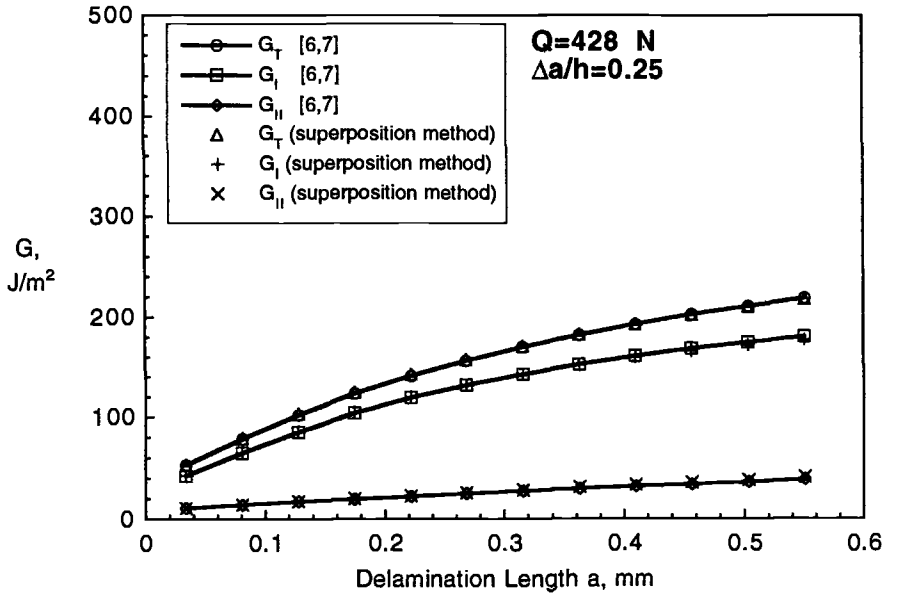


FIG. 15—*Computed strain energy release rates for delamination growth in a 90°/45° flange ply interface for three-point bending load case.*

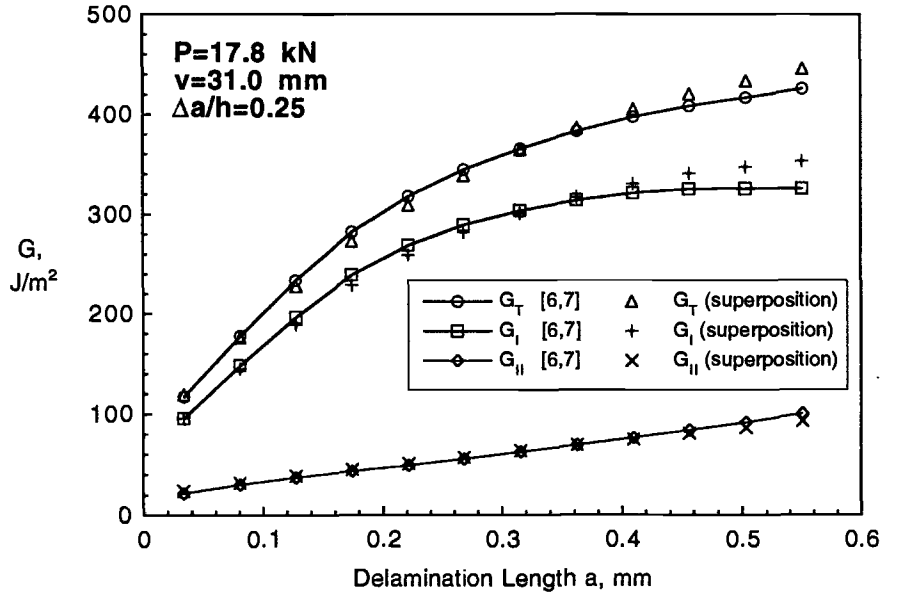


FIG. 16—*Computed strain energy release rates for delamination growth in a 90°/45° flange ply interface for combined tension and bending load case.*

were intended as reference solutions to be compared with results from the superposition method in the following section.

Superposition Technique for Simulated Delamination Growth

In the previous sections, simple quadratic expressions were developed which made it possible to calculate the strain energy release rate for various load combinations. In this part of the investigation a technique was developed where the forces and displacements at the crack tip (see Fig. 6) obtained from three linear analyses are superposed. The calculated energy release rates for one delamination length are matched with the corresponding results from one nonlinear finite element analysis and a correction factor is determined. This correction factor is then used to size the results obtained from linear analyses for all other delamination lengths.

Only one nonlinear finite-element analysis was performed for each load case using a full model of the damaged specimen as shown in Fig. 4. Loads measured at the onset of damage as shown in Fig. 2 and discussed in the previous paragraph were simulated. Mode I and Mode II energy release rates $G_{I,NL}$ and $G_{II,NL}$ were computed for a delamination length equal to the length of the first element ($a/h = 0.181$) as shown in Fig. 4. Local force and moment resultants N_{xx}, Q_{xy} and M_{xx} were calculated at the location where the end of the frame or stringer flange meets the skin as shown in Fig. 11. Resultants plotted in Fig. 17 show that the force resultant N_{xx} is zero for the three-point bending test as it is free of axial tension. Also as expected, there is a small transverse shear, which is nonzero. For the tension test, in addition to the membrane resultant, a bending moment is present due to the load eccentricity in the flange region and the asymmetric lay-up of the combined skin and flange laminate with respect to the neutral axis. The shear force resultant Q_{xy} is nearly zero, as expected. For the axial tension and bending test, calculated membrane and moment resultants lie between the computed pure tension and pure bending values [7]. Due to the high transverse load during the tests, the shear force resultant is significant for this load condition. It was assumed that these local force and moment resultants calculated at the flange tip vary only slightly when the delamination is extended.

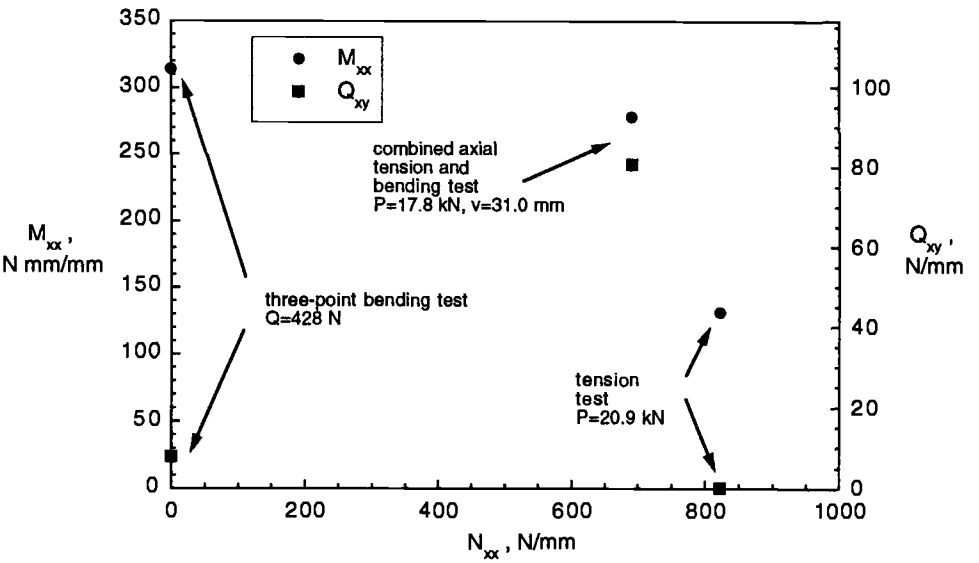


FIG. 17—*Computed force and moment resultants at flange tip.*

Three local submodels (shown in Fig. 18) were then developed to simulate delamination growth using a linear analysis. The local submodel consisted of a small section of the original model around the location where the end of the frame or stringer flange meets the skin. To avoid any disturbance associated with the load introduction, the length of the model to the left of the damage (d_1) was about three times the skin thickness and the length of the model to the right of the damage location (d_2) was about three times the skin plus flange thickness ($t_s + t_f$). The mesh used for the local submodel is the same as the mesh of the full model shown in Fig. 4. As shown in Fig.

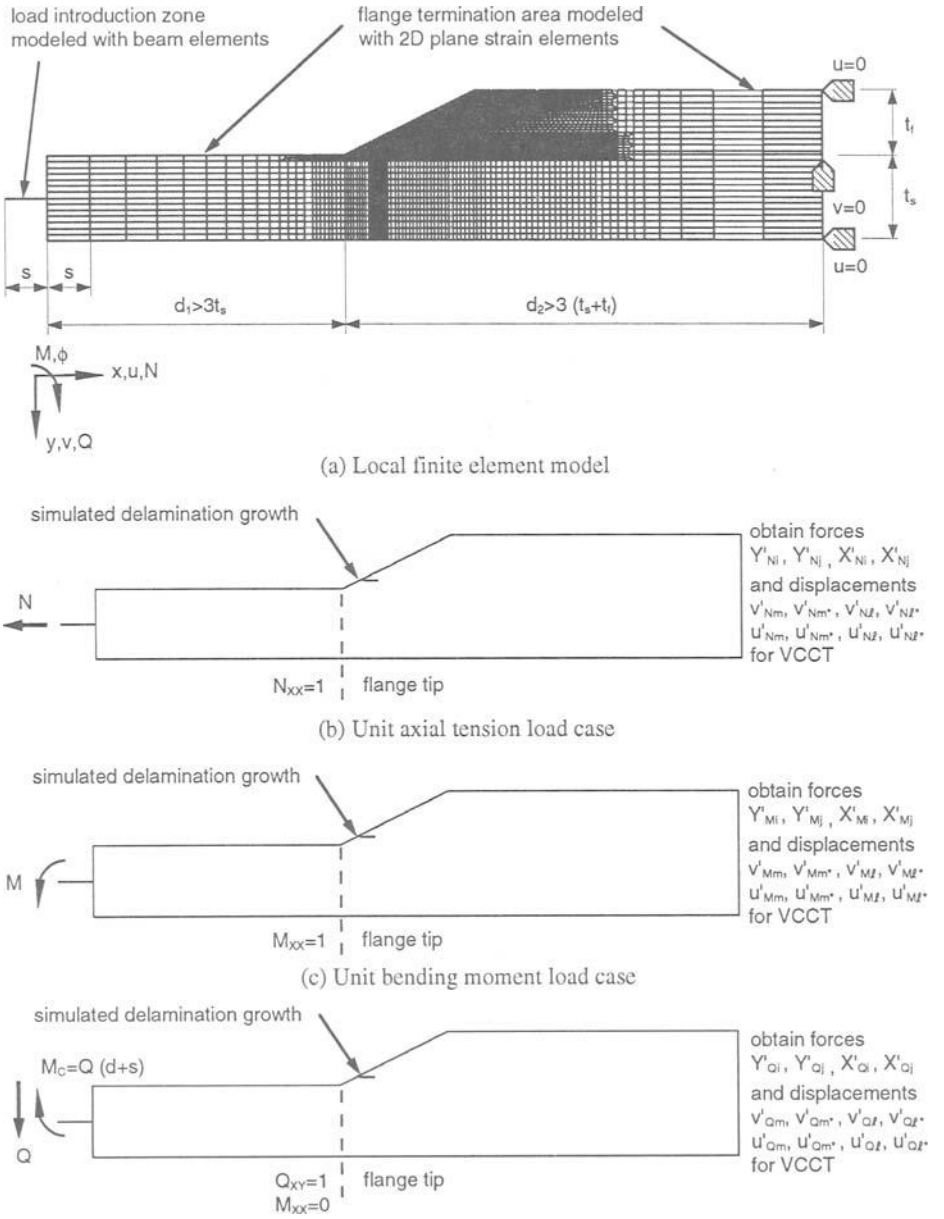


FIG. 18—*Local finite-element model for linear analyses and unit loads.*

18*a*, boundary conditions for all local submodels were selected to prevent the translations in the plane and rotation of the model. Three unit load cases were simulated as shown in Figs. 18*b* through *d* and the delamination was extended as explained in the paragraph above. External loads were chosen such that a unit force resultant N_{xx}, Q_{xy} or unit moment resultant M_{xx} exists at the reference station at the flange tip. For the unit transverse shear load case, a counter reacting moment, M_C, needs to be applied at the end of the model to assure a pure shear force resultant Q_{xy} at the flange tip. To facilitate the simulation of the external moment (Figs. 18*c* and *d*) three-noded quadratic beam elements with rotational degrees of freedom were used for the simulation of the load introduction zone, *s*, which had the same length as the adjacent plane strain elements (Fig. 18*a*). A rectangular beam cross section was selected to model the square cross section of the skin. The beams were connected to the two-dimensional plane strain model of the local section using multipoint constraints to enforce appropriate translations and rotations. This procedure was explained for the combined axial tension/bending load case and shown earlier in Fig. 5. For the beam model, smeared orthotropic material properties were calculated for the skin laminate and used as material input data.

For each unit load case (index N,M,Q), the delaminations were extended and a linear finite-element analysis was performed for each length *a*. For each simulation, forces $X'_{Ni}(a)$, $X'_{Mi}(a)$, $X'_{Qi}(a)$, and $Y'_{Ni}(a)$, $Y'_{Mi}(a)$, $Y'_{Qi}(a)$, at the delamination tip at node *i* and the relative displacements $\Delta u'_{Nm}(a)$, $\Delta u'_{Mm}(a)$, $\Delta u'_{Qm}(a)$, and $\Delta v'_{Nm}(a)$, $\Delta v'_{Mm}(a)$, $\Delta v'_{Qm}(a)$, at the corresponding node *m* behind the delamination tip were retrieved from the finite-element results (see Fig. 6). Forces at node *j* and relative displacements at node ℓ were also obtained. In a second step, forces and relative displacements for each of unit load cases were scaled by multiplying with the corresponding force and moment resultant N_{xx}, Q_{xy} and M_{xx} obtained from the nonlinear analysis of the full model. The scaled forces and displacements were then superposed yielding

$$
\begin{aligned}
Y'_i(a) &= N_{xx} \cdot Y'_{Ni}(a) + M_{xx} \cdot Y'_{Mi}(a) + Q_{xz} \cdot Y'_{Qi}(a) \\
Y'_j(a) &= N_{xx} \cdot Y'_{Nj}(a) + M_{xx} \cdot Y'_{Mj}(a) + Q_{xz} \cdot Y'_{Qj}(a) \\
\Delta v'_m(a) &= N_{xx} \cdot \Delta v'_{Nm}(a) + M_{xx} \cdot \Delta v'_{Mm}(a) + Q_{xz} \cdot \Delta v'_{Qm}(a) \\
\Delta v'_\ell(a) &= N_{xx} \cdot \Delta v'_{N\ell}(a) + M_{xx} \cdot \Delta v'_{M\ell}(a) + Q_{xz} \cdot \Delta v'_{Q\ell}(a)
\end{aligned}
\tag{14}
$$

Forces $X'_i(a)$ and $X'_j(a)$ as well as relative displacements $\Delta u'_m(a)$ and $\Delta u'_\ell(a)$, were obtained accordingly. All forces ($X'_i(a)$, $X'_j(a)$, and $Y'_i(a)$, $Y'_j(a)$), and relative displacements ($\Delta u'_m(a)$, $\Delta u'_\ell(a)$, and $\Delta v'_m(a)$, $\Delta v'_\ell(a)$) obtained, served as input for the virtual crack closure technique

$$
G_{\mathrm{I}}(a) = -\frac{c_{\mathrm{I}}}{2\Delta a} \cdot \left[Y'_j(a) \cdot \frac{(v'_m(a) - v'_m{}^*(a))}{\Delta v'_m(a)} + Y'_j(a) \cdot \frac{(v'_\ell(a) - v'_\ell{}^*(a))}{\Delta v'_\ell(a)} \right] \tag{15}
$$

$$
G_{\mathrm{II}}(a) = -\frac{c_{\mathrm{II}}}{2\Delta a} \left[X'_i(a) \cdot \frac{(u'_m(a) - u'_m{}^*(a))}{\Delta u'_m(a)} + X'_j(a) \cdot \frac{(u'_\ell(a) - u'_\ell \cdot (a))}{\Delta u'_\ell(a)} \right] \tag{16}
$$

The correction factors c_{I} and c_{II} for Mode I and Mode II, respectively, were introduced in order to size the results for G_{I} and G_{II} obtained from the superposition procedure (Eqs 15 and 16) along the delamination length. One set of correction factors c_{I} and c_{II} was determined for the entire study by matching the G_{I} and G_{II} results obtained for the initial crack ($a/h = 0.181$) with $G_{\mathrm{I,NL}}$ and $G_{\mathrm{II,NL}}$ computed from the initial nonlinear analysis. This is accomplished by calculating G_{I} ($a/h = 0.181$) and

G_{II} $(a/h = 0.181)$ first with the correction factors set to $c_I = c_{II} = 1$ and then solving for the correction factors

$$c_I = \frac{G_{I,NL}\,(a/h = 0.181)}{G_I\,(a/h = 0.181)} \quad \text{and} \quad c_{II} = \frac{G_{II,NL}\,(a/h = 0.181)}{G_{II}\,(a/h = 0.181)} \tag{17}$$

The correction factors obtained for the tension, three-point bending and combined axial tension/bending load case are given in Table 2. For the pure tension and the axial tension/bending load cases the correction factors are relatively large when compared with the factors calculated for the pure bending load case. This is most likely related to the distinct nonlinear load/deflection behavior of the specimens subjected to these loadings. Hence, large correction factors are required to match the results obtained from the three linear unit load cases with those obtained directly from nonlinear FE analysis using VCCT. Consequently, for a nearly linear load/deflection behavior—as observed during the bending test—a much smaller correction factor is required. The load/deformation behavior of the specimens for all three load cases is discussed in detail in Refs *6* and *7*.

For the tension, three-point bending and combined axial tension and bending load case, mixed mode energy release rates were calculated using the superposition technique described above and given in Eqs 14–17. The results were included in the plots of Figs. 14–16. For the initial matrix crack length $(a/h = 0.181)$ the results are identical, as this point was chosen to match the results and calculate the corrections factors (see Eq 17). The correction factors obtained were kept constant during the simulation of delamination growth. The obtained mixed mode energy release rates show that G_{II} increases monotonically for all load cases while G_I begins to level off at the longest delamination lengths. For the bending load case the results were in excellent agreement with energy release rates calculated directly from nonlinear finite-element results using VCCT along the entire delamination length. This may be attributed to the fact that the load/deflection behavior of the specimen under this load is nearly linear and therefore can closely be approximated by the linear analyses of the local submodels. Along the entire delamination length investigated, results were in good agreement for the other load cases as well. As the delamination length becomes longer, however, the results obtained from the superposition technique begin to deviate slightly from the values calculated directly from nonlinear finite-element analyses. For long delamination lengths it might therefore be advantageous to calculate several reference solutions for different delamination lengths from the full model using nonlinear analyses and updating the correction factors.

As mentioned in the previous paragraph, a total of 12 nonlinear analyses were necessary when using the conventional approach to obtain the results for one load case as shown in Figs. 14–16. The superposition technique described above required only one nonlinear analysis of the full model for each load case and 36 linear analyses of the local submodel. Even for one load case this means a considerable reduction in CPU time. Although additional modeling effort is required to create the local submodel, the results indicate that the proposed technique is very efficient for large parametric studies which may occur during preliminary design where multiple load combinations must be considered.

TABLE 2—*Correction factors for scaled energy release rates.*

Tension Load Case	Bending Load Case	Axial Tension/Bending Load Case
$c_I = 1.2657$	$c_I = 1.0036$	$c_I = 1.2791$
$c_{II} = 1.2484$	$c_{II} = 1.0646$	$c_{II} = 1.1720$

Concluding Remarks

Three simple procedures were developed to determine strain energy release rates, G, in composite skin/stringer specimens for various combinations of in-plane and out-of-plane loading conditions. These procedures may be used for parametric design studies in such a way that only a few finite-element computations will be necessary for a study of many load combinations. Since energy is a quadratic function of the applied loads, it was not possible to simply superpose and add the energy release rates from separate load cases. A simple quadratic expression was previously developed to calculate the strain energy release rate for any combination of loads. To validate the procedures, results obtained from the quadratic expressions were compared to Mode I and Mode II strain energy release rate contributions, which were calculated from nonlinear two-dimensional plane-strain finite-element analyses using the virtual crack closure technique.

For the first technique, the boundary conditions for the tension, bending and combined tension/bending load case were chosen in such a manner that the specimen deformation was assumed to be a linear function of the applied loads. Therefore, a linear finite-element solution was used to compute the strain energy release rate for various multi-axial load combinations. The technique involved solving three unknown parameters needed to determine the energy release rates from a simple tension, a simple bending, and one combined tension/bending load case. Excellent results were obtained when the external loads were used. This superposition technique, however, was only applicable if the structure exhibits a linear load/deflection behavior.

Consequently, a second modified technique was derived which was applicable also in the case of nonlinear load/deformation behavior. The expression derived for the linear case was modified such that terms of the external forces were replaced by internal force and moment resultants at the flange tip. The energy release rates calculated using this technique seemed sufficiently accurate for preliminary design studies. However, force and moment resultants at the flange tip need to be calculated and additional effort is required to obtain six unknown parameters from a set of six simultaneous linear equations to determine the energy release rates. This procedure, therefore, was not time efficient, and hence, less appealing.

Finally, a third procedure was developed to calculate mixed-mode energy release as a function of delamination lengths. This procedure required only one nonlinear finite-element analysis of the specimen with a single delamination length to obtain the force and moment resultants at the flange tip and a reference solution for the energy release rates. It was assumed that the local force and moment resultants calculated at the flange tip vary only slightly when the delamination is extended. Therefore, it is sufficient to calculate these resultants for one delamination length. The delamination was subsequently extended in three separate linear models of the local area in the vicinity of the delamination subjected to unit loads. Forces and displacements computed at the delamination tip for the unit load cases were superposed and used in the virtual crack closure technique to obtain the distribution of G with delamination length. Results were in good agreement with energy release rates calculated directly from nonlinear finite-element results using VCCT. Although additional modeling effort is required to create the local submodel, this superposition technique is very efficient for large parametric studies which may occur during preliminary design where multiple load combinations must be considered.

Acknowledgments

This work was performed as part of a Cooperative Research and Development Agreement (CRDA) between the U.S. Army Research Laboratory, Vehicle Technology Directorate, located at NASA Langley Research Center, and Boeing, Philadelphia.

References

[1] Minguet, P. J., Fedro, M. J., O'Brien, T. K., Martin, R. H., Ilcewicz, L. B., Awerbuch, J., and Wang, A., "Development of a Structural Test Simulating Pressure Pillowing Effects in a Bonded Skin/Stringer/Frame

Configuration," *Proceedings, Fourth NASA/DoD Advanced Composites Technology Conference,* Salt Lake City, UT, June 1993.

[2] Minguet, P. J. and O'Brien, T. K., "Analysis of Test Methods for Characterizing Skin/Stringer Debonding Failures in Reinforced Composite Panels," *Composite Materials: Testing and Design, Twelfth Volume, ASTM STP 1274,* August 1996, pp. 105–124.

[3] Minguet, P. J. and O'Brien, T. K., "Analysis of Composite Skin/Stringer Bond Failures Using a Strain Energy Release Rate Approach," *Proceedings of the Tenth International Conference on Composite Materials, Vol. I,* Woodhead Publishing Ltd., 1995, pp. 245–252.

[4] Minguet, P. J., "Analysis of the Strength of the Interface between Frame and Skin in a Bonded Composite Fuselage Panel," *Proceedings of the 38th AIAA/ASME/ASCE/AHS/ASC SDM Conference and Exhibit,* Kissimmee, FL, 1997, AIAA-97-1342, pp. 2783–2790.

[5] Cvitkovich, M. K., O'Brien, T. K., and Minguet, P. J., "Fatigue Debonding Characterization in Composite Skin/Stringer Configurations," *Composite Materials: Fatigue and Fracture, Seventh Volume, ASTM STP 1330,* 1998, pp. 97–121.

[6] Cvitkovich, M. K., Krueger, R., O'Brien, T. K., and Minguet, P. J., "Debonding in Composite Skin/Stringer Configurations under Multi-Axial Loading," *Proceedings of the American Society for Composites, 13th Technical Conference on Composite Materials,* ISBN 0-9667220-0-0 CD-ROM, 1998, pp. 1014–1048.

[7] Krueger, R., Cvitkovich, M. K., O'Brien, T. K., and Minguet, P. J., "Testing and Analysis of Composite Skin/Stringer Debonding under Multi-Axial Loading," NASA TM-209097, ARL-MR-439, Feb. 1999.

[8] Whitcomb, J. D., "Strain-Energy Release Rate Analysis of Cyclic Delamination Growth in Compressively Loaded Laminates," *Effects of Defects in Composite Materials, ASTM STP 836,* 1984, pp. 175–193.

[9] Rybicki, E. F. and Kanninen, M. F., "A Finite Element Calculation of Stress Intensity Factors by a Modified Crack Closure Integral," *Engineering Fracture Mechanics,* Vol. 9, 1977, pp. 931–938.

[10] Raju, I. S., "Calculation of Strain-Energy Release Rates with Higher Order and Singular Finite Elements," *Engineering Fracture Mechanics,* Vol. 28, 1987, pp. 251–274.

[11] ABAQUS/Standard, *User's Manual, Volume II,* Version 5.6, 1996.

[12] O'Brien, T. K., Murri, G. B., Hagemeier, R., and Rogers, C., "Combined Tension and Bending Testing of Tapered Composite Laminates," *Applied Composite Materials,* Vol. 1, 1995, pp. 401–413.

[13] Murri, G. B., O'Brien, T. K., and Rousseau, C. Q., "Fatigue Life Methodology for Tapered Composite Flexbeam Laminates," *Journal of the American Helicopter Society,* Vol. 43, No. 2, April 1998, pp. 146–155.

[14] Sun, C. T. and Manoharan, M. G., "Strain Energy Release Rates of an Interfacial Crack Between Two Orthotropic Solids," *Journal of Composite Materials,* Vol. 23, May 1989, pp. 460–478.

[15] Raju, I. S., Crews, J. H., and Aminpour, M. A., "Convergence of Strain Energy Release," *Engineering Fracture Mechanics,* Vol. 30, 1988, pp. 383–396.

[16] Broek, D., *Elementary Engineering Fracture Mechanics,* 4th revised ed., Kluwer Academic Publishers, ISBN 90-247-2656-5, 1991.

[17] Martin, R. H., "Incorporating Interlaminar Fracture Mechanics into Design," *International Conference on Designing Cost-Effective Composites, IMechE Conference Transactions,* London, 15–16 Sept. 1998, pp. 83–92.

Rotorcraft and Propeller Structural Qualification Issues

Leigh Killian Altman,[1] *D. J. Reddy,*[1] *and Heidi Moore*[2]

Fail-safe Approach for the V-22 Composite Proprotor Yoke

REFERENCE: Altman, L. K., Reddy, D. J., and Moore, H., **"Fail-safe Approach for the V-22 Composite Proprotor Yoke,"** *Composite Structures: Theory and Practice, ASTM STP 1383*, P. Grant and C. Q. Rousseau, Eds., American Society for Testing and Materials, West Conshohocken, PA, 2000, pp. 131–139.

ABSTRACT: The V-22 proprotor yoke is fabricated from filament-wound unidirectional glass/epoxy belts that react to centrifugal force (CF) loads and beam and chord bending loads. Fiberglass tape is laid up at off-axis orientation between the unidirectional belts to react shear loads. The structural criteria for both metallic and composite V-22 dynamically loaded rotor components specify that these components be fatigue tested and analyzed to show a "safe life" of 30 000 h. Based on the fatigue test results of prototype and production proprotor yokes, a safe life of 30 000 h for the composite proprotor yoke could not be substantiated. However, testing of the yoke was continued beyond delamination initiation. The V-22 proprotor yoke continued to carry load in the fatigue tests with significant delaminations within the composite structure. These results, in addition to similar test results produced by Bell Helicopter Textron on composite proprotor yokes for commercially produced aircraft, indicate that it will be possible to substantiate this component using a "fail-safe" methodology.

KEYWORDS: fail-safe testing, composite yoke, V-22, Navy

The V-22 proprotor yoke is a major composite component of the hub assembly (Fig. 1), which transmits torque to the rotor and reacts to blade loads. The qualification of the V-22 composite yoke was originally planned to achieve a safe life of 30 000 h. Historically, Bell Helicopter Textron, Inc. (BHTI), metallic and composite rotor system components have been structurally qualified using a safe life methodology based on an *S-N* (constant amplitude) test approach. Typically, four to six full-scale components are fatigue tested at various levels of elevated oscillatory loads to induce failures. These failures are used to define an average strength curve. A statistically reduced (3-sigma) strength curve is used with flight-measured loads in establishing the safe life of the component.

The V-22 specification defines several criteria for a test failure, including the initiation of a delamination, the dominant failure mode exhibited in the V-22 proprotor yoke testing. Evaluation of the composite proprotor yoke test results using the safe life methodology and the V-22 failure definition has resulted in a low calculated safe life for the proprotor yoke. However, the initial delaminations detected by either ultrasonic or visual inspections did not deteriorate the structural performance of the component in further testing.

Over the past 20 years, all of the failures seen in the fatigue tests of composite yokes at Bell Helicopter have been delaminations. The delaminations reflect a very shallow, or flat, *S-N* curve shape. Typical 3-sigma statistical strength reduction factors of 25% to 30% [*1*] for delamination failure modes result in undesirably low safe fatigue lives for these composite components. BHTI has begun using a fail-safe (damage tolerant) approach to qualify commercial composite rotor system parts.

[1] Engineering specialist and chief, Rotor Stress and Fatigue Fracture, respectively, Bell Helicoptor Textron Inc., P.O. Box 482, Fort Worth, TX 76101.

[2] Rotary wing strength engineer, Rotary Wing and Patrol/Support Strength Branch/NAVAIR Structures Division/Air 4.3.3.2, Building 2187, Suite 2340, NAVAIRSYSCOMHQ, 48110 Shaw Road, Unit 5, Patuxent River, MD 20670-1906.

Copyright© 2001by ASTM International www.astm.org

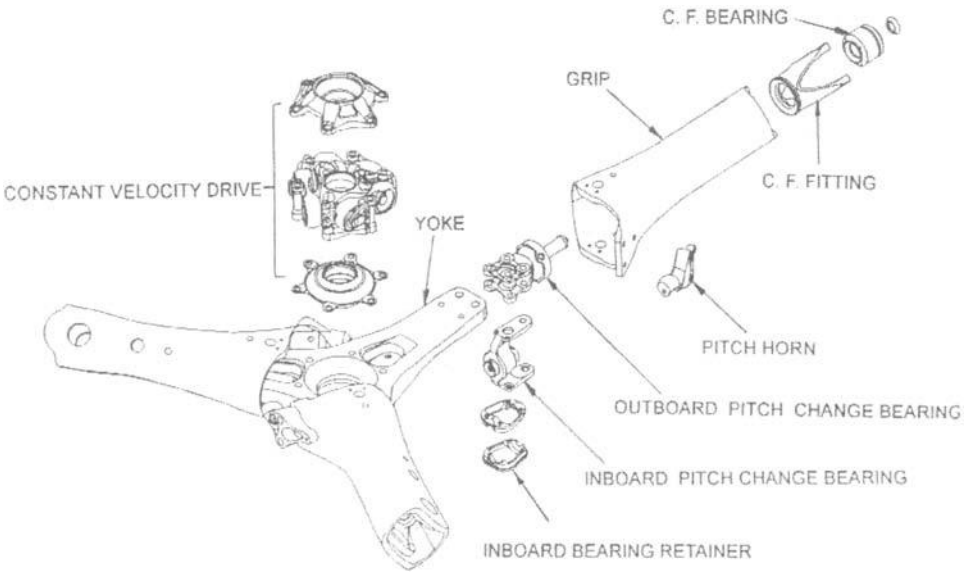


FIG. 1—*V-22 proprotor hub.*

Fail-safe qualification results in a component being replaced based on its condition instead of imposing a specific retirement life. This approach maximizes economic value without additional risk.

In a fail-safe qualification approach of critical structural components, the inspection techniques and frequency of inspections must be such that a detectable partial failure would not eventually become catastrophic and is certain to be found long before it can endanger the aircraft. To demonstrate the fail-safe criteria, it must be shown that a component with a detectable partial failure will be able to sustain flight loads for two inspection intervals, and will still be able to carry the limit load. Stiffness changes should be within acceptable limits determined from dynamic and aerodynamic considerations. Additionally, damage should not grow to the extent that maintenance action is required within two inspection intervals.

Although the U.S. Navy has not formally adopted a fail-safe qualification approach for all composite components, a revised approach for the qualification of the V-22 proprotor yoke using a fail-safe approach has been developed. The purpose of this paper is threefold: to discuss the history of the V-22 proprotor yoke testing and the life predictions resulting from these tests, to present the fail-safe qualification of composite yokes on other BHTI composite yokes as evidence of the "low risk" and "high reward" expected with a fail-safe qualification, and to outline the fail-safe qualification approach for the V-22 yoke.

Description of the V-22 Proprotor Yoke

The V-22 proprotor yoke transmits rotor torque from the drive hub into the grip and blade assemblies. Figure 2 presents an overview of the proprotor yoke. The yoke is stiff in-plane with three equally spaced coning flexure arms located 120 deg apart. These arms react to centrifugal force (CF), as well as shears and moments generated by dynamic and aerodynamic loads in the proprotor blades, while permitting feathering motion of the blade. The yoke tapers from 4.3 in. (110 mm) in the center to a minimum thickness of 1.7 in. (43 mm) in the flexure area and back up to 2.4 in. (61 mm) at the outboard end. The inboard flexure area of each arm contains a 6.7 in. (170 mm) by 4.4 in. (110 mm) hole for the attachment of the inboard pitch change bearing. The yoke is fabricated from filament-wound unidirectional S-glass belts with shear webs interspersed between the belts for shear continu-

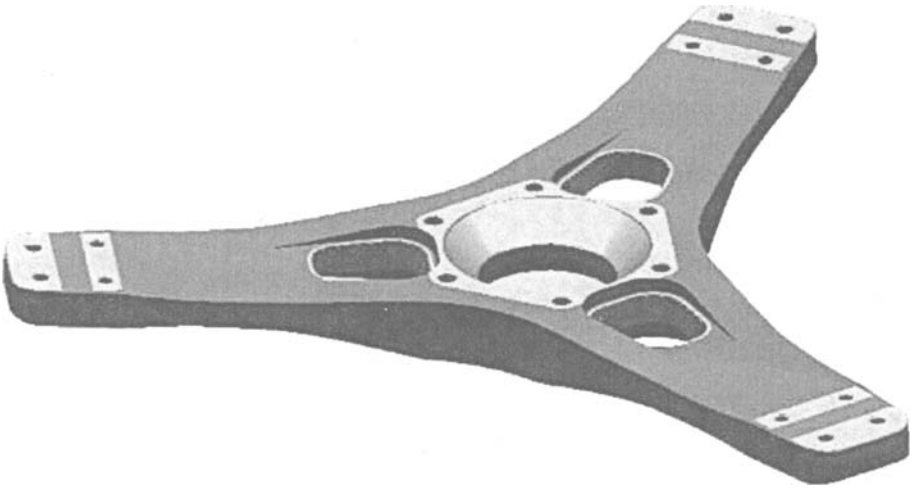


FIG. 2—*Overview of the V-22 proprotor yoke.*

ity. The precone angle of the production yoke configuration was modified slightly from the prototype design. The precone angle of the yoke arms in the prototype design was 2 deg. The precone angle in the production configuration was increased to 2.75 deg to optimize steady beam bending load on the yoke arm for various nacelle positions.

Fatigue Design Requirements

The V-22 tiltrotor is designed to operate as both a rotary-wing (nacelle incidence angles greater than 0 and less than or equal to 97.5 deg) and fixed-wing (nacelle incidence angle of 0 deg) aircraft. The V-22 specification required that the dynamic components shall have a minimum structural fatigue life of 30 000 h when substantiated for the design fatigue loading requirements in both of these operating modes. In addition, these components shall sustain no fatigue damage below certain thresholds in both rotary wing and fixed wing modes. The critical loading on the yoke is experienced when the rotor system is producing a majority of the lift to the aircraft. This occurs above nacelle incidence angles of 60 deg.

Prototype and Production Fatigue Testing Program Summary

The V-22 proprotor yokes were fatigue tested in a specially designed test fixture (Fig. 3). Steady and oscillatory bending moments and pitch link loads were applied to each specimen, as well as a steady load representative of the centrifugal force. Testing for both the prototype and the production configurations also included interspersed ground-air-ground (GAG) cycles. Reference oscillatory loads were accelerated, or increased by a factor, for performance of the fatigue tests. Since the intention of this type of testing is to identify failure modes and to define the fatigue strength of the test article, increased load levels are used to insure that failures do occur. The high-cycle fatigue strength is defined from this testing with a 3-sigma statistical scatter reduction from the mean curve to get a working curve for use in the fatigue analysis.

Prototype and early production yoke fatigue test results were used to determine an *S-N* curve for the primary failure mode, a delamination initiation at the inboard beam cutout. The delamination initiation *S-N* curve (Fig. 4) based on oscillatory beam bending and the production design loads were used to calculate a fatigue life for the proprotor yoke. This calculation resulted in a 1200 h fatigue life for the design loads spectrum.

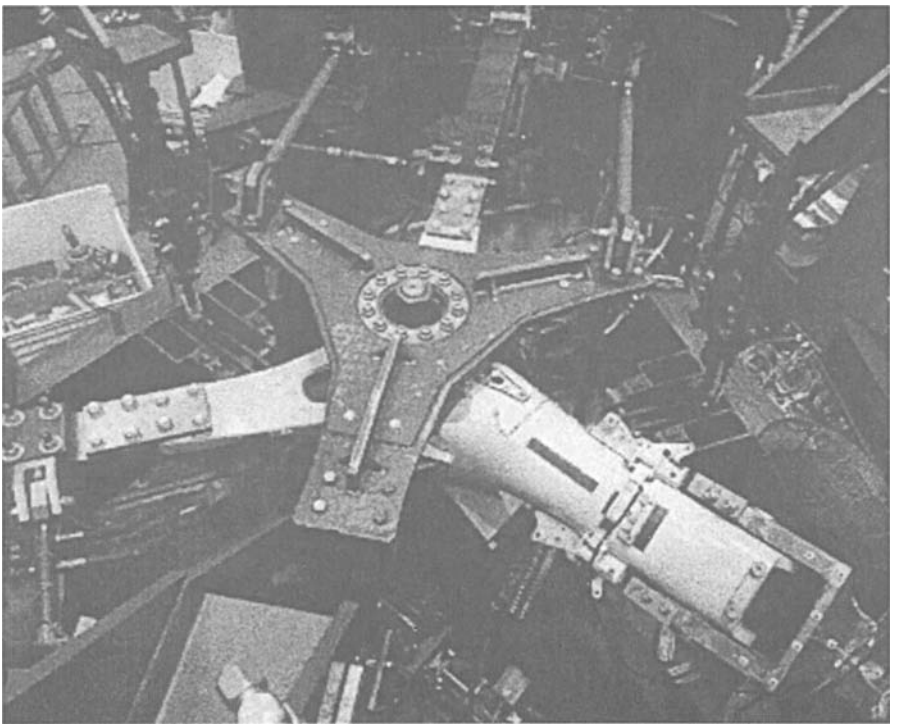


FIG. 3—V-22 *proprotor hub test fixture.*

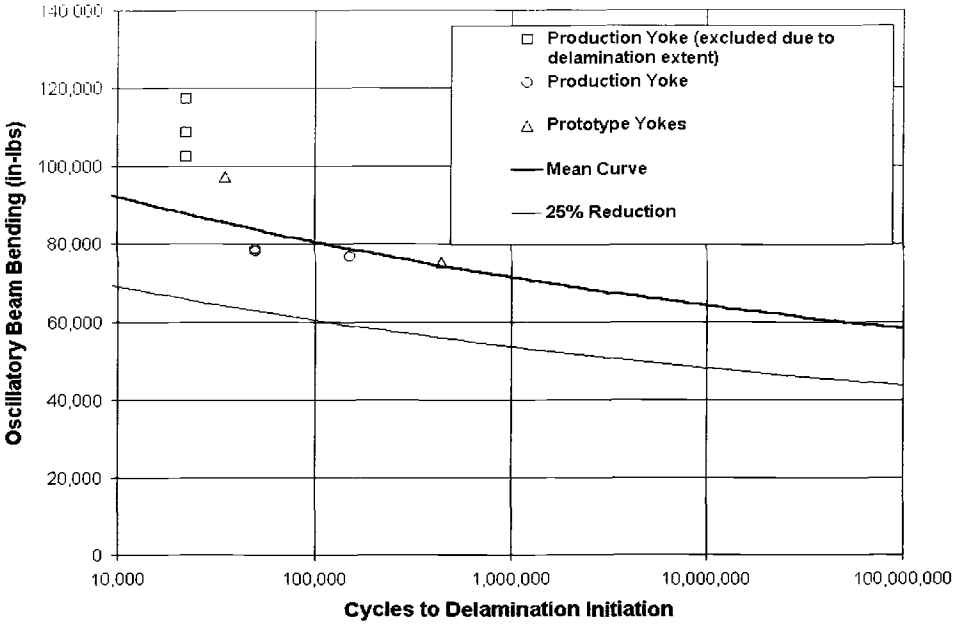


FIG. 4—S-N*curve for the V-22 proprotor yoke.*

In all of the V-22 yoke tests, testing was continued after initial delamination detection to investigate failure modes in the other hub components and to characterize delamination growth behavior. All of the prototype and production yokes were still capable of carrying applied loads when the tests were suspended. The failure mode exhibited by the V-22 proprotor yoke is a benign failure mode that does not result in loss of load-carrying capability or catastrophic failure of the component or the aircraft. One of the most important things to note in the V-22 rotor system hub components is that the components operate in a predominately tension field due to very high centrifugal force. Additionally, flight stresses are primarily in tension. This is in contrast to catastrophic failures in aircraft wing structures, which are usually due to compression-type failure modes such as buckling.

Prototype Fatigue Testing

The first prototype yoke was tested at elevated reference oscillatory *S-N* loads with interspersed GAG cycles. An 8 to 10 in. (20–25 cm) visible crack/delamination along the lower leading edge of the yoke was noted at 35 000 *S-N* cycles. The crack/delamination extended from the cutout for the inboard beam to the outboard end. Testing was continued for a total of 250 000 fatigue cycles without degradation of the load-carrying capability of the yoke. When testing was suspended, the crack had extended across half of the flexure span and extended from the centerline of the yoke almost all the way to the outboard end. The delamination origin was located in the inboard beam cutout area of the yoke as shown in Fig. 5. This delamination mode was typical for all prototype and production V-22 yoke testing.

Another prototype yoke was tested at lower elevated reference oscillatory loads. Small delaminations were found with ultrasonic inspection at the leading edge corners of the inboard beam bearing cutout at 440 800 fatigue cycles. Testing continued and was suspended at 963 600 total fatigue cycles. During that time, the delaminations had propagated out to the leading edge of the yoke, and extended approximately 10 in. (25 cm) along the leading edge.

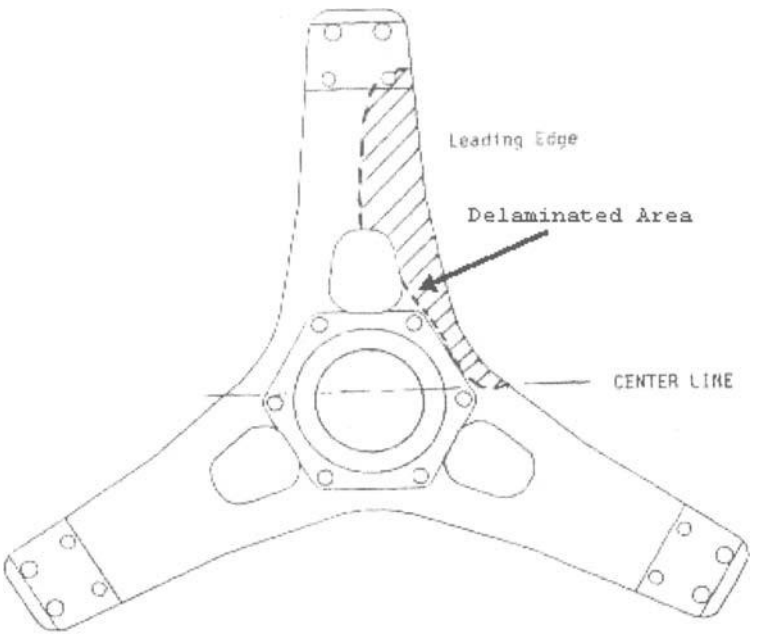


FIG. 5—*Typical delamination for the V-22 proprotor yoke.*

Production Fatigue Testing

Two production yokes have been tested with elevated *S-N* loads and interspersed GAG cycles. The first production yoke specimen had delamination indications in both the inboard beam cutout area and the center section of the yoke after 10 000 GAG cycles and 22 697 *S-N* test cycles. These delaminations were discovered with ultrasonic inspection. The test continued for 260 852 cycles (approximately 10 flight hours at elevated reference loads) after delamination detection. This yoke was also tested for another 1.1 million cycles (approximately 50 flight hours at elevated reference loads) in a subsequent hub test. On the second production yoke specimen tested at elevated load levels, two out of three arms showed delamination indications in the inboard beam cutout area after 50 000 test cycles. These delaminations were identified with ultrasonic testing. The third arm showed a delamination indication in this area after 150 000 total test cycles. The testing of the yoke was suspended after 355 000 total test cycles.

Static Testing

In addition to the fatigue testing, several yokes have been statically tested. All the static test yokes showed the similar delamination failure mode. The static test yokes were hot-wet conditioned and tested at 180°F. When delaminations were easily visible and significant, the static test yokes still demonstrated in excess of ultimate load capability. When the delamination occurred the load-carrying capability dropped slightly but still remained in excess of 150% of the limit load.

Fail-safe Qualification of Other BHTI Composite Yokes

The first BHTI composite yoke was fielded about 15 years ago on the Army OH-58D with a safe life qualification. The gross weight of the OH-58D aircraft has increased since it was first fielded and at the higher gross weights, the safe life of the OH-58D yoke was drastically reduced. Based on the known benign failure modes and demonstrated load-carrying capability with these failures present, BHTI proposed a fail-safe or "on-condition" retirement for the OH-58D yoke with visual inspections every 25 h. Through the end of 1997 the OH-58D fleet had accumulated approximately 400 000 flight hours. There has never been a report of a visible edge delamination.

The OH-58D yoke and all other composite yokes tested to date have shown delaminations as the only failure mode. There has never been a catastrophic failure in all of the fatigue and static testing of various BHTI composite yoke designs. All the test failures were delaminations in surface plies or mid-plane delamination failures which are readily detectable visually. All of the yokes demonstrated the capability of continuing to react to applied loads after visible delaminations.

The Model 407 helicopter was type certified in 1996. The Model 407 yoke is fielded with a 100 h visual inspection. There are currently more than 260 helicopters in service. The fleet had accumulated over 63 000 flight hours through the end of 1997. There has not been a single report of a main rotor yoke having a visible edge delamination during that time.

The Model 430 helicopter was certified in 1997. The fleet size is small and the total accumulated flight hours is not documented yet. The Model 430 yoke is currently certified with a 50 h visual inspection interval on the flapping flexure section and a 2500 h inspection for the torsion flexure.

The Bell commercial and military composite main rotor yokes all share a similar design feature in that they have a tapered flexure section to accommodate rotor coning and flapping motions. The main structural elements in the flexure are filament-wound S-2 unidirectional fiberglass belts. The belts react to the rotor centrifugal forces. The designs are tailored to provide the required beamwise and chordwise stiffness for each design. The taper is controlled by the use of partial length, off axis, shear plies of S-2 glass tape. Layers of ±45 deg material are used at the mid-plane and on the outside to provide in-plane shear reaction and to protect the unidirectional material on the upper and lower sur-

faces. All composite BHTI yokes designed to date including V-22 have very similar design limit strains in the range of 11 500 μin./in. to 13 000 μin./in.

Model 407 Yoke Fail-safe Fatigue Testing

The goal for certification of the Model 407 main rotor yoke was to retire the yoke on-condition. An inspection interval was to be established based on the results of flaw growth testing. First, the 407 yoke was fatigue tested at elevated *S-N* cycle loads to initiate a delamination. The delamination found on the trailing edge of one arm extended across the width of the arm inboard to the center section and around the corner toward the leading edge of the adjacent arm during subsequent testing. The delamination failure mode is typical of the failure exhibited by the OH-58D and 430 yokes which have similar designs in the flapping flexure sections. After the initial delamination was identified, the test loads were changed to an abbreviated spectrum of flight loads including the loads for ground-air-ground (GAG) cycles and testing was continued. After each 100 h block of test cycles, design limit loads were applied to each of the arms individually. After the equivalent of 600 flight hours of testing, the yoke was still capable of reacting design limit loads on all four arms. Since the test specimen was not preconditioned, a factor of six was used for the inspection interval. Another specimen was preconditioned to 10 years exposure to moisture absorption. The yoke was subjected to visible impact damage and was tested for an equivalent of 200 h.

Model 430 Fatigue Testing

Two main rotor yokes were tested at elevated flight loads with interspersed GAG cycles to evaluate the yoke design before proceeding with fail-safe (flaw growth) certification testing. Two different delamination failure modes were identified during the *S-N* testing. The delamination of the yoke center section originating in the area adjacent to the yoke-to-mast attachment holes at approximately mid-thickness was originally detected during scheduled contact ultrasonic inspections conducted during the test. In each specimen this delamination propagated to the edge of the yoke center section and was then easily detected visually. Another failure mode in the test was observed at the apex of the radial flanges of the feathering flexure. The initial visual indication was a white crazing under the outer layer of fiberglass and could be seen quite easily after the application of the first series of GAG cycles. The second specimen was painted on one end to aid in the detection of this delamination under simulated service conditions. As the test progressed this became a visible surface distress on the surface of the radial flange running in a span direction. In each case, the specimen continued to carry the applied loads and motions. The observations of these failure modes was subsequently used to aid in locating the seeded flaws and impact locations for the fail-safe (flaw and damage growth) testing of the third test yoke.

Fail-safe Test Results—Two specimens of the 430 main rotor yoke assembly were tested. Both specimens contained critically located flaws and were environmentally conditioned. After initiating a delamination on the leading edge of one of the yoke arms, the yoke was removed from the test fixture and impacted. The specimen was impact damaged at nine critical locations to a Barely Visible Indication of Damage (BVID) impact energy or to the maximum threat energy level. The maximum threat energy level is developed from probable damage that can occur during manufacturing, installation, and foreign object impact in-service. The yoke was then reinstalled in the fixture for multiple block spectrum testing of flight loads including the loads for ground-air-ground (GAG) cycles. The yoke specimen had been inadvertently overconditioned, and testing was discontinued after 100 flight hours of loading, supplemental GAG cycles, and a final static limit load. Using a safety factor of 2, an inspection interval of 50 flight hours was substantiated for the flapping and center section of the yoke, which may be visually inspected without disassembly of the hub. The torsional flexure outboard of the shear restraints is critical for GAG cycles and cannot be inspected without removing the

main rotor blade. Additional GAG cycles were applied to the portion of the yoke outboard of the shear restraints to demonstrate a longer inspection interval coinciding with the blade inspection interval. Assuming four GAG/hour and an inspection factor of two, the accumulated 19 200 GAG cycles qualify a 2400 h inspection interval.

Due to the overconditioning of the first yoke, the inspection intervals set during the fail-safe testing were shorter than desired. A second yoke specimen was conditioned to the expected 10 year moisture profile and tested to flaw tolerance criteria for a total of 450 equivalent flight hours. This was a painted specimen with implanted flaws which was environmentally conditioned and impacted at critical locations. The same load spectrum used to test the first flaw tolerance qualification specimen was applied to the second yoke specimen. As the test progressed, several minor delaminations were detected on this specimen. However, NDI inspections showed no significant growth of the delaminations after discovery. At the conclusion of the 450 h of spectrum testing, the yoke specimen was bagged and stored for later use.

A design change made to 430 hub configuration to incorporate fluid lead-lag dampers resulted in an increase in the yoke's oscillatory chord loads. Due to the increase in chord loads, the yoke's fail-safe qualification had to be resubstantiated. Conservatively, the yoke that was used in a previous fail-safe qualification test was also used for the qualification to the increased loads from the fluid dampers. The yoke was tested for a total of 450 equivalent flight hours at increased loads and for more than 40 000 GAG cycles. After finishing the spectrum testing, the static limit condition was applied. For the flapping flexure. a total of 450 equivalent flight hours were applied. Using an inspection factor of 2, an inspection interval of 225 h was substantiated. The inspection interval for the feathering flexure based on GAG cycles was set at 5000 h assuming 4 GAG/h and an inspection factor of 2.

Fail-safe Qualification Proposal for the V-22 Proprotor Yoke

Based on the promising results realized through fail-safe testing of Bell commercial composite yokes, and the limited testing with delaminated yokes in the V-22 program, a fail-safe qualification of the V-22 composite proprotor yoke is in progress. Three proprotor yokes will be tested as part of the fail-safe qualification. A stiffness check will be performed on each yoke tested at the beginning and end of each test. The stiffness checks are done to assure that the stiffness has not degraded below acceptable levels for dynamic and aerodynamic considerations. Limit load testing and residual strength testing will be performed at the end of each test.

The first yoke was tested at slightly elevated reference oscillatory loads to initiate delaminations in all three arms and testing continued until the delaminations became visible at the edges of the yoke arms. Additional cycles, equivalent to 420 flight hours of loading, are being applied to the yoke with periodic visual inspections. Successful conclusion of the stiffness check, limit load testing, and residual strength testing will result in a preliminary fail-safe qualification of the yoke.

The second yoke specimen will be subjected to 80 000 ground-air-ground cycles to substantiate the required GAG cycle requirement on the other hub components in the test. Then the reference oscillatory loads will be elevated high enough to obtain data on the composite grip and the metallic components of the hub assembly. Periodic NDI inspections of the grip and visual inspections of the yoke will be performed. Testing will be continued until it becomes impractical due to excessive delaminations in the yoke or until a failure of a metallic component occurs. The stiffness checks are done to assure that the stiffness has not degraded below acceptable levels for dynamic and aerodynamic considerations.

A third proprotor yoke specimen with seeded flaws will be environmentally conditioned and impact damaged. The load spectrum applied to the third yoke will incorporate updated flight load measurements. This specimen will provide the final fail-safe qualification of the proprotor yoke.

Risk Evaluation of Fail-safe Qualification

It is standard commercial practice at Bell to use a 3-sigma reduction in fatigue strength when performing a safe life calculation. This approach is also the standard for V-22 safe life calculations. A 1200 h safe life was calculated for the proprotor yoke based on the initiation of the delamination. This represents the possibility of a small delamination in one out of 1000 yokes fielded at 1200 flight hours. The failure mode of the V-22 yoke as demonstrated in the test is both benign and detectable. A small delamination initiates and grows until it becomes visible without affecting the load-carrying capability of the yoke. By retiring the V-22 yoke based on the condition of the yoke at regular inspection intervals, it is expected that at least 999 out of 1000 yokes will be in service beyond 1200 h.

Retiring yokes based on a regular inspection program will remove yokes from service before their load-carrying capability is affected. An inspection for a visible delamination allows each yoke to be easily evaluated based on its condition. This is preferable to retiring yokes at a safe life based on a 3-sigma reduction when only 1% would be expected to exhibit a delamination at retirement.

Conclusions

The fatigue and static testing accomplished to date on the V-22 yoke demonstrated very benign failure modes. The safe life approach to qualification of the V-22 yoke results in a low life and in a high life-cycle cost. Based on BHTI experience of qualifying similarly designed yokes on a fail-safe basis, the V-22 yoke was a good candidate for a fail-safe qualification. A disadvantage of fail-safe testing is that it is important to have the correct qualification load spectrum. If the qualification load spectrum changes, testing must be repeated. The advantage of fail-safe qualification is that the V-22 proprotor yoke will be retired based on the condition of the yoke as evaluated during periodic visual inspections. This will allow the yoke to remain in service beyond the retirement life selected in a safe life approach and will result in a lower life-cycle cost.

Reference

[1] Reddy. D. J.. "Qualification Program of the Composite Main Rotor Blade for the Model 214B Helicopter." Presented at the 35th Annual National Forum of the American Helicopter Society, Washington, DC, May 1979.

Alan Dobyns,[1] *Bruce Barr,*[1] *and John Adelmann*[1]

RAH-66 Comanche Building Block Structural Qualification Program

REFERENCE: Dobyns, A., Barr, B., and Adelmann, J., **"RAH-66 Comanche Building Block Structural Qualification Program,"** *Composite Structures: Theory and Practice, ASTM STP 1383*, P. Grant and C. Q. Rousseau, Eds., American Society for Testing and Materials, West Conshohocken, PA, 2000, pp. 140–157.

ABSTRACT: The paper discusses the RAH-66 Comanche airframe building block structural qualification program. The components of the building block program included: material selection and qualification tests (lamina properties); coupon level tests (static and fatigue laminate properties, including open hole and filled hole strength, bearing, and sandwich compression after impact strength), and element, subcomponent, and full-scale tests. Element tests included bolted and bonded joint strength tests, beaded shear panel tests, sandwich shear panel tests, crippling tests and bearing-bypass bolted joint tests. Subcomponent testing included fuselage section crush tests, hydraulic ram testing of fuel tanks, and numerous design specific joint tests. The building block program culminated in the full-scale static test of the airframe structure.

The interaction of the building block program testing with the Comanche detail design is described including specific examples where results from compression after impact, tub crush, and hydraulic ram testing caused changes in the structural configuration of the aircraft. This paper discusses only the Sikorsky Aircraft portion of the RAH-66 building block program. Boeing-Philadelphia also performed a related program to substantiate the design of their portion of the aircraft.

KEYWORDS: building block, structural qualification, structural certification, composites, carbon fiber, epoxy

The objectives of the RAH-66 Comanche building block program were to provide material properties and design values for use in design of the aircraft and to verify the accuracy of analysis methods used in the structural analysis of the airframe. The building block program consisted of material allowables coupons, structural elements, subcomponents, components, and a full aircraft structural test. The basic plan was to focus the analysis and testing effort on the simpler specimens to develop and verify the accuracy of analysis methods. Successful validation of the analysis methods permits fewer element and component tests to be performed for the structural qualification and simplifies the structural analysis of the aircraft. In addition, use of the statistical parameters from the different levels of testing makes possible the determination of load enhancement factors to be applied to subcomponent and full-scale tests to obtain a given reliability level [*1*].

During the design development process for RAH-66 Comanche airframe components, the need for materials with improved properties was identified. Although the list included many types of materials (paste and film adhesives, foaming adhesives, honeycomb cores, syntactics, glass reinforced prepregs, carbon fiber prepregs, aramid prepregs, and RTM systems), the material selection and allowables sections of this paper will only cover intermediate modulus carbon/epoxy tape and fabric prepregs. Following the selection of materials with improved properties, element, subcomponent, and component testing was performed to verify the translation of those improved properties into the full-

[1] Senior structures engineers and senior structural materials engineer, respectively, Sikorsky Aircraft Corporation, Stratford, CT 06615-9129.

Copyright© 2001by ASTM International www.astm.org

scale structure. The testing culminated in the full-scale airframe Static Test Article and in flight testing of the aircraft.

Material Selection

In 1986 requests for information (RFIs) were issued to composite material suppliers, soliciting data on new intermediate modulus carbon/epoxy prepreg tape systems. Prepreggers were asked to fabricate test panels from a single batch of material and conduct mechanical property testing in accordance with the test matrix shown in Table 1. This matrix is sufficient for comparing materials based on average lamina properties, sensitivity to notches and damage, and degradation of properties with environment, and is similar to the screening test matrix currently recommended in MIL-HDBK-17 [2].

Responses to the RFIs were received from six material suppliers for a total of seven material systems. Using the data provided by the suppliers, preliminary material allowables were estimated. These initial values were purposely aggressive in an effort to challenge the suppliers to formulate even better materials. Target B-basis values were generated by taking the best average property values from the limited data and reducing them by historical scatter factors. Environmental factors both from the screening data and from previous experience were also used. The estimated design values were used for preliminary sizing and structural analysis.

In order to rank the candidate systems, a set of criteria was needed based on structural requirements. A review of the proposed RAH-66 airframe elements indicated that about 38% of the weight of the composite structure was designed by stability and crippling, 29% was driven by ultimate strength and strain (mostly in compression), 27% was stiffness critical, and 6% was designed by minimum gage considerations. Based on this assessment, a weighted ranking system was devised, giving highest weight to compression after impact (CAI) (since barely visible impact damage (BVID) is assumed to be present in all RAH-66 composite structure), followed by 0° compression strength and modulus (for stability and crippling), and bearing strength. Other properties were given lower weight. Since cost differences between candidate materials were not deemed significant, cost was not considered in this evaluation. Table 2 shows the resulting rankings of the seven initial candidate materials.

With preliminary material allowables set and design drivers identified, a second RFI was issued, which included more focused material requirements and target specification values. Compression after impact (at multiple impact energies) was added to the initial screening matrix. Since it had been estimated that 75% of the airframe composite structure would be composed of fabric (25% composed

TABLE 1—*Generic screening matrix for carbon/epoxy prepreg tape.*

Property	Test Method	Number of Specimens			
		−65°F Amb.	RT Amb.	220°F Wet	Total
0° Tension on (S/M/P)	SRM 4 [*16*]	3	3	3	9
0° Compression (S)	D3410 B [*17*]	...	3	3	6
0° Compression (M)	SRM 1 [*18*]	...	3	3	6
In-plane shear (S/M)	SRM 7 [*19*]	...	3	3	6
QI open hole tens. (S/M/FS)	SRM 5 [*20*]	...	3	...	3
QI open hole compr. (S/M/FS)	SRM 3 [*21*]	...	3	...	3
Bolt bearing strength	MIL-17 [*22*]	...	3	...	3
Compr. after impact (S/M/FS)	SRM 2 [*23*]	...	3	...	3
Total					39

NOTE: S = Strength, M = Modulus, P = Poisson's ratio, FS = Failure strain, QI = Quasi-isotropic.

TABLE 2—*Generic screening matrix for carbon/epoxy prepreg tape.*

Material Supplier	Material System	Rank (1 = best)
Hercules (now Hexcel)	IM7/8551-7	1
Fiberite (now Cytec Fiberite)	IM7/977-2	2
American Cyanamid (now Cytec Fiberite)	IM7/1827	3
Ciba Geigy (now Hexcel)	T40/6376	4
Ciba Geigy (now Hexcel)	G40-700/6376	5
Dexter Hysol	Apollo-IM/HG9105-3	6
Hexcel	IM6/F584	7

of tape), suppliers were also asked to provide data on plain weave (PW) and/or eight harness satin (8HS) weave fabrics.

Data from this second round of screening showed that initial estimates of open hole compression capability for both tape and fabric were somewhat ambitious. Also, fill direction tensile strength for fabrics was lower than anticipated. All other properties were in fairly good agreement with earlier data and estimates. Based on the combined data from the two RFIs, IM7/8552 was selected as the primary intermediate modulus carbon/epoxy prepreg for both tape (160 g/m^2) and fabrics (196 g/m^2 plain weave and 370 g/m^2 eight-harness satin).

Material Properties and Design Values

Early in the program it was anticipated that the critical design environment would be 220°F (104°C) both wet and dry. As the program developed, it was determined from further assessment of the operating environment that the requirement should be 180°F (82°C) wet and 220°F (104°C) dry. Therefore, the first task for material allowables was to estimate 180°F (82°C) wet properties by interpolating between the RT ambient and 220°F (104°C) screening data estimates.

The next task was to fully qualify the IM7/8552 materials and develop final allowables based on multiple batch testing. The qualification test matrix shown in Table 3 was used to generate specification values and material allowables for ply (lamina) properties and for quasi-isotropic open hole

TABLE 3—*Qualification/allowables test matrix for carbon/epoxy prepreg tape and fabric.*

		No. of Specimens per Prepreg Batch				
Property	Test Method	−65°F Amb.	RT Amb.	RT Wet	180°F Wet	220°F Amb.
0°/Warp tension (S/M/P)	SRM 4 [*16*]	6	6	3	6	3
0°/Warp compression (S/M)	D 3410 B [*17*]	3	6	3	6	3
90°/Fill tension (S/M)	SRM 4 [*16*]	6	6	3	6	3
90°/Fill compression (S/M)	D 3410 B [*17*]	...	6	3	6	3
In-plane shear (S/M)	SRM 7 [*19*]	3	6	3	6	3
Interlaminar shear (S)	D 2344 [*24*]	...	6	3	6	3
0°/Warp flexure (S/M)	D 790 [*25*]	...	6	...	6	...
QI open hole tens. (S/M/FS)	SRM 5 [*20*]	6	6	...	...	...
QI open hole compr. (S/M/FS)	SRM 3 [*21*]	...	6	...	6	...
Compression after impact (S/M/FS)	SRM 2 [*23*]	...	6	.	6	...

NOTE: S = Strength, M = Modulus, P = Poisson's ratio, FS = Failure strain, QI = Quasi-isotropic.

tension (OHT), open hole compression (OHC), and CAI properties. Testing was shared between Sikorsky Aircraft and the material supplier. The same test specimen configurations and the same test methods were used at both locations. "Dry" condition testing was defined as the "as fabricated" condition (not oven dried), and the "wet" condition was defined as moisture equilibrium at 185°F (85°C) and 87% relative humidity. The largest numbers of specimens were concentrated at room temperature ambient (RTA) and elevated temperature wet (ETW—180°F/82°C). Smaller numbers of specimens were tested at other environments to verify that these were not more critical than 180°F (82°C) wet. Initially three batches of tape and each fabric were planned for testing. However, due to data scatter and some testing issues, testing of several additional batches was required for some properties and environments. In all, over 1100 tape specimens, over 600 8HS fabric specimens, and over 900 PW fabric specimens were tested.

Material allowables were calculated from the test data using statistical procedures and guidelines given in MIL-HDBK-17 [3]. The final B-basis strengths/strains and mean moduli were generally in good agreement with the original preliminary allowables (interpolated to 180°F (82°C)). Figure 1 shows this comparison for tape. None of the properties which were lower than initial estimates were significant enough to result in design changes.

In addition to the above tests, various bolted joint, sandwich, and interlaminar tension tests were conducted in a number of configurations to further quantify properties of specific design details. These are summarized in the following paragraphs.

Bolted Joint Tests

A number of tests were performed to verify the performance of specific laminates and configurations. These tests included open hole, filled hole, bearing, countersunk fasteners, and fasteners with lower than normal edge distance. Tests were conducted for RTA, ETW, ETD (elevated temperature dry), and CTD (cold temperature dry) conditions. Open hole tension and compression tests were conducted for several laminates: 25/50/25, 58.3/27.8/13.9, 20/60/20, and 12.5/75/12.5; where the numbers signify the percent of ply thickness in the 0, ±45, and 90 degree directions. The first laminate is quasi-isotropic with 25% 0°/50% ±45°/25% 90°. Three hole diameters were used—[$\frac{5}{32}$ in. (3.97 mm), $\frac{3}{16}$ in. (4.76 mm), and $\frac{1}{4}$ in. (6.35 mm)]. A *W/D* (specimen width/bolt diameter) of 6 was used for most of the tests. Some tests were done at *W/D* ratios of 4 and 8 to verify that there would be no discernible width effect. Filled hole tension tests were conducted for ETD and CTD environments. These tests are similar to open hole tests except that a standard bolt is inserted into a 0.003 in. (0.076 mm) oversize hole, with torque set to finger tight (25 in. · lb/2.83 N · m). Preliminary testing had shown that filled hole strengths in tension are normally lower than open hole strengths, so filled hole tension values were used for design.

Bearing tests were conducted for the four laminates and the three bolt diameters mentioned above, and for several values of bolt torque-up. The bolt torque used in testing can have a large influence on the bearing strength in composites due to the support the bolt head gives to the laminate. Increasing the bolt torque provides added clamp-up support at the contact points, creating a triaxial stress field. Tightening to just a finger tight torque can increase the bearing strength by 25% to 30% compared to the pin bearing or no bolt head restraint strength. Tests were conducted with specimens of varying width to show the effect on bearing strength.

Sandwich Compression After Impact (CAI) Tests

When a sandwich with composite face sheets is subjected to a low velocity impact by dropped tools, runway debris, or other low energy impacts, the compression strength is reduced due to the resulting delaminations, fiber breakage, matrix cracking, and core crushing. Typically the compression strength is reduced by around half by low velocity impact damage which produces damage at the threshold of visibility. Therefore the compression allowable strength used for design must assume

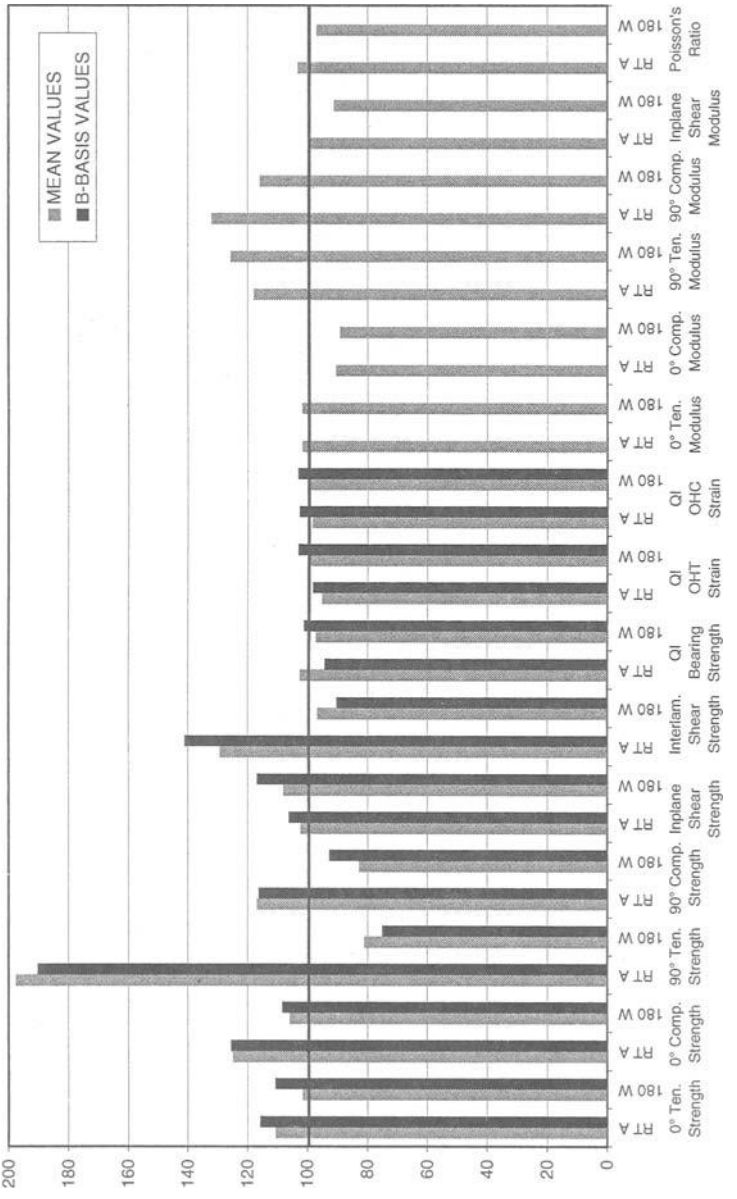


FIG. 1—*Final properties as percent of initial estimated properties, intermediate modulus carbon/epoxy tape.*

TABLE 4—*Sandwich compression and CAI static test matrix.*

Specimen ID	# Plies	Core	Core Density (PCF)	Cell Size (in.)	No Damage RTA	No Damage ETA	No Damage ETW	CAI Damage RTA	CAI Damage ETA	CAI Damage ETW
3NB	2	Nomex	3.0	1/8	3	...	5	...	...	...
1NB	3	Nomex	3.0	1/8	3	...	3	3	3	9
2NB	4	Nomex	3.0	1/8	6	3	3	12	6	9
2AB	4	5056	6.1	1/8	3	3	3	3	3	3
H3NB	2	HIFT	3.0	3/16	3	...	3	3	3	3
H1NB	3	HFT	3.0	3/16	3	3	3	3	3	3
H2NB	4	HFT	3.0	3/16	3	3	3	3	3	3
K1NB	3	Korex	3.0	1/8	3	...	4	3	.	5

that impact damage is present from the first day in service. To determine the BVID CAI strength a test program was performed to determine the impact energy required to produce barely visible impact damage, to impact specimens at this impact energy, and to perform compression strength tests on the impacted specimens. A number of facesheet laminate and honeycomb combinations were tested, as given in Table 4. Tests were conducted at RTA, ETW, and ETD environmental conditions. The test panels were constructed with 1 in. honeycomb core with potting compound inserted at the position of the loaded ends. 6 in. × 6 in. (152 mm × 152 mm) test specimens were then cut from the panel and the potted loaded ends were ground parallel. Each specimen was impact damaged and the specimen was compression tested in the fixture shown in Fig. 2 [*4*]. The test fixture was developed at Sikorsky after experiencing problems with sandwich beam tests.

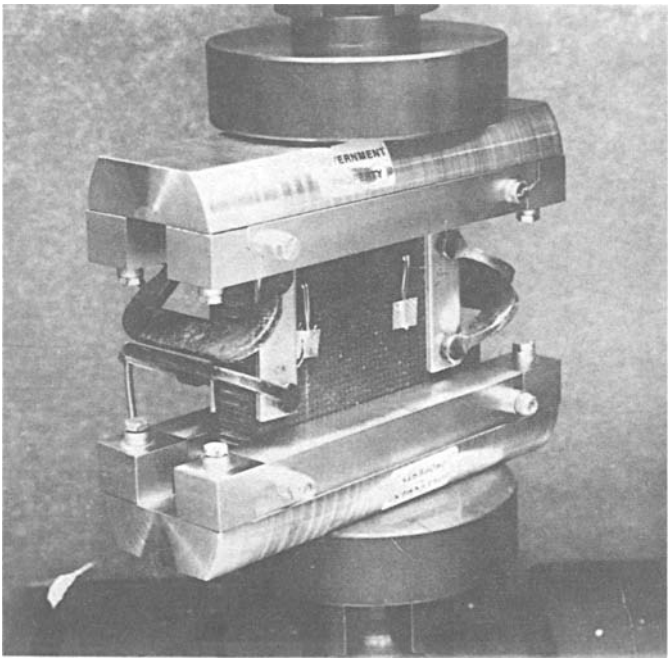


FIG. 2—*Sandwich compression test fixture.*

Interlaminar Tension Tests

Composite stiffeners and fittings can fail due to interlaminar tension stresses in curved members. For composite stiffeners and fittings this is a critical failure mode since the allowable interlaminar tension stress is so low. To determine the allowable stress for this mode curved beams were constructed and tested in bending as shown in Fig. 3, producing a delamination near the mid thickness in the corner. Closed form solutions [5] were used to determine the interlaminar tension stress for each test. Tests were conducted at RTA and ETW conditions to produce the required allowables.

Element Tests

A series of element tests was conducted to provide design values for use in design of the Comanche airframe. The element tests included: beaded shear panels, sandwich shear panels, crippling tests, and bearing bypass tests.

Beaded Shear Panels

Beaded shear panels are used in the aircraft as shear webs for lightly loaded areas such as bulkheads and some areas of the keel beam. Beaded shear webs have been used in metal aircraft since the 1940s but have not been used extensively in composites due to lack of test data on failure modes. A series of shear tests were performed with beaded shear webs in a picture frame apparatus, as shown

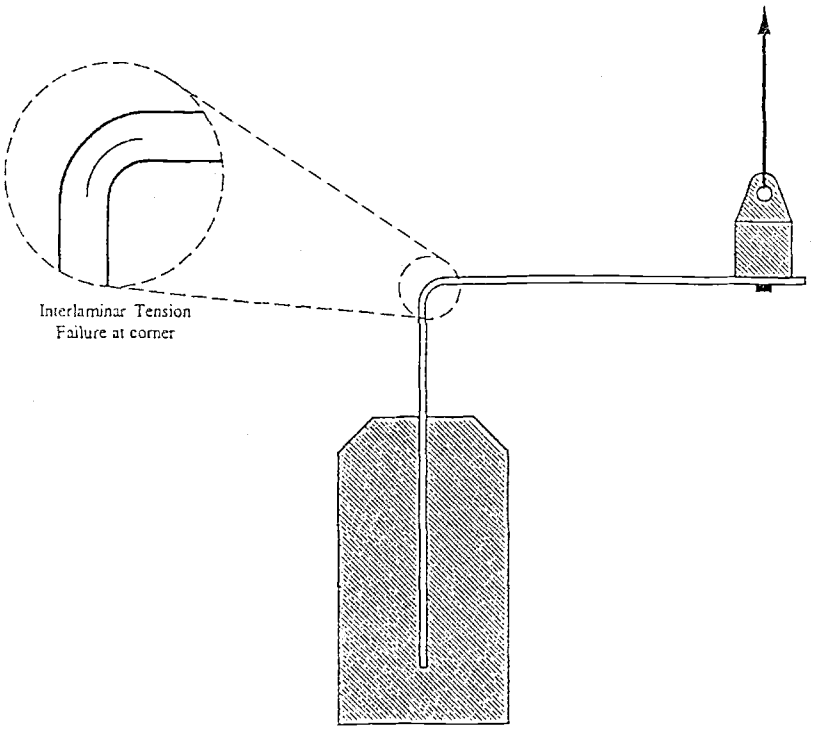


FIG. 3—*Curved beam interlaminar tension strength test.*

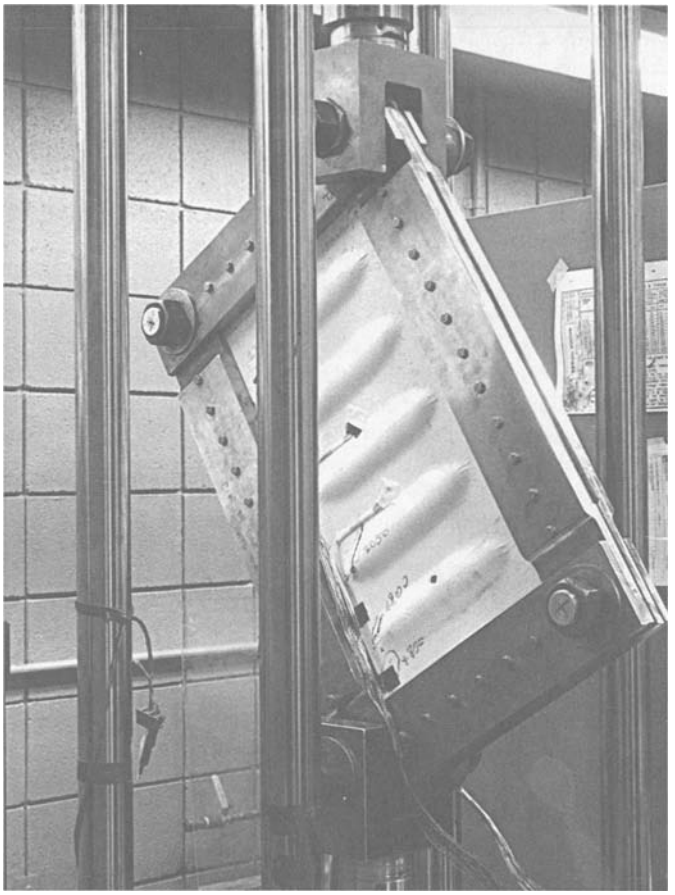


FIG. 4—*Beaded shear panel test.*

in Fig. 4. The test matrix included two panel thicknesses and two bead heights 0.375 in. (9.5 mm) and 0.50 in. (12.7 mm). Test panels were 15.5 in. × 25.5 in. (394 mm × 648 mm) between corner pins, with fiberglass doublers at the edges. Tests were performed on undamaged panels, on panels with impact damage, and with ballistic damage (12.7 mm bullet holes). Testing was done at both RTA and ETW conditions. The panels failed by snap through of the beads, with lower strengths at ETW, as would be expected due to the lower moduli at ETW. There were 29 undamaged, 30 impact damaged, and 21 ballistically damaged panels tested. The test results were correlated with equations used for metal panels [6] and with stiffened panel buckling equations, which assumed the bead acted like a transverse stiffener. Twenty-two undamaged solid laminate shear panels with circular cutouts were also tested in the same apparatus as the beaded shear panels. Impact and ballistically damaged panels with cutouts will be tested before the Comanche goes into production.

Sandwich Shear Panels

Sandwich shear panels may be used in the aircraft for areas that are too highly loaded for beaded panels to be used. Typical applications are bulkheads, keel beam webs, and the aircraft exterior skin. Nomex (aramid-fiber paper treated with phenolic resin), HFT (bias weave glass fabric), and Korex

honeycomb cores were used, depending on the load requirement. The honeycomb panels used a "pan-edged" design for the edge attachment region, where the honeycomb edges are ramped down at a 25 deg angle to a solid laminate at the edges. The edge attachments are reinforced locally to resist the moments and shears caused by the eccentric load introduction and to increase bearing area at the fasteners. The honeycomb shear panels were tested in a 26 in. (660 mm) square picture frame shear test frame, similar to the beaded shear panel test. The test program included RTA and ETW tests, with 20 undamaged specimens, 19 impact damaged specimens, and 9 ballistic damaged specimens. The test results were correlated with sandwich panel shear buckling equations [*7*] for overall panel buckling and with MSC/NASTRAN [*8*] for the stresses in the panned edge regions.

Crippling Specimens

Crippling specimens are used to determine the postbuckling compression strength of stiffeners. The stiffener will normally fail at a load greater than the initial buckling load with failure caused by the postbuckling deformations of the segments making up the stiffener. Tests are required to determine a crippling stress versus segment width/thickness (b/t) curve for use in design, since the theoretical buckling stress does not correlate with the crippling failure stress. An angle specimen was used to simulate the one-edge-free case, with a channel specimen for the no-edge-free case. The ends of the test specimen are potted and ground parallel before placing in the test machine. Figure 5 shows a

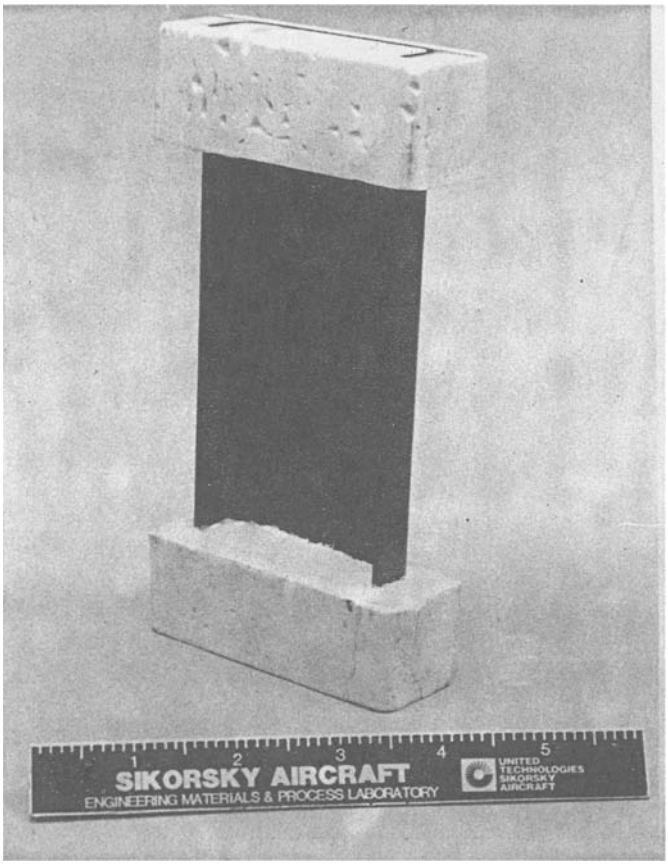


FIG. 5—*Channel crippling specimen.*

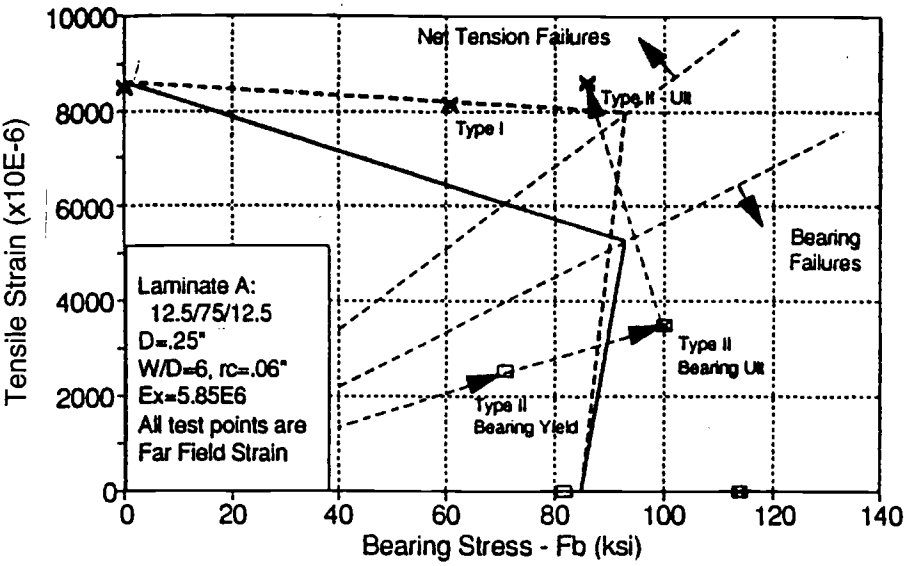


FIG. 6—*Typical bearing-bypass strength curve.*

typical channel specimen. The test program included three *b/t* ratios for the one-edge-free and no-edge-free cases, with both RTA and ETW environmental conditions, for a total of 36 specimens.

Bearing-Bypass Tests

In addition to the open hole, filled hole and bearing tests done to support design of single bolt joints, tests were done to determine the effect of varying the bearing stress and the far field (bypass) stress. Knowledge of the bearing-bypass interaction is needed to design the multiple bolt joints typical of fittings and splices, where each bolt will have a different bearing load. The bypass failure stress is reduced due to the interaction of the bearing stress with the bypass stress, as shown in Fig. 6. Analysis codes are available for predicting bearing bypass curves from analysis of the stress field around the joint (BJSFM [*9*]), and to determine the load for each bolt in the joint (A4EJ [*10*]). To obtain a bearing-bypass curve it is necessary to test specimens with different bearing/bypass ratios, which is a difficult task. The method used in the RAH-66 program was a bolted doubler arrangement as shown in Fig. 7, where the bearing load in the specimen is varied by changing the stiffness ratio between the specimen and the doubler. The only problem is that the ratio of bearing load to bypass load changes during the test. When the bearing load reaches its initial nonlinear yielding point the bolt hole starts elongating, which reduces the bearing/bypass ratio as the load is increased. At a given load, the doubler load is obtained as the applied load minus the bypass load in the laminate (which is given by the strain in the specimen times the modulus times the laminate area). The bolt load is then the doubler load, while the bypass strain is read from the strain gages on the laminate [*11*]. The data points are plotted as shown in Fig. 6 to find the point at which the bearing-bypass ratio starts to change.

Subcomponent Tests

A series of subcomponent tests were performed to validate design details and design analysis methodology. Subcomponent tests included: fuselage joint tests, fuselage tub crush tests, fuel tank

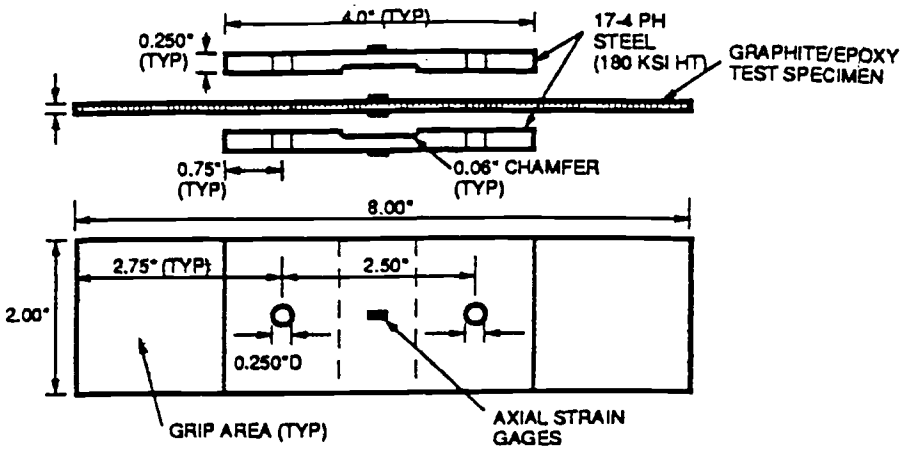


FIG. 7—*Bearing-bypass doubler test setup.*

hydraulic ram tests, hellfire missile exhaust plume effects tests, and main landing gear frangible tube tests. The subcomponent tests are described briefly below. Figure 8 displays the areas of the Comanche fuselage represented by the test specimens.

Fuselage Joint Tests

A number of fuselage joint concepts were tested to verify static and fatigue strength and validate the analytic sizing methodology, which was based on the material strength coupon testing and the bearing/bypass and crippling element testing described above. The joints typically consisted of a

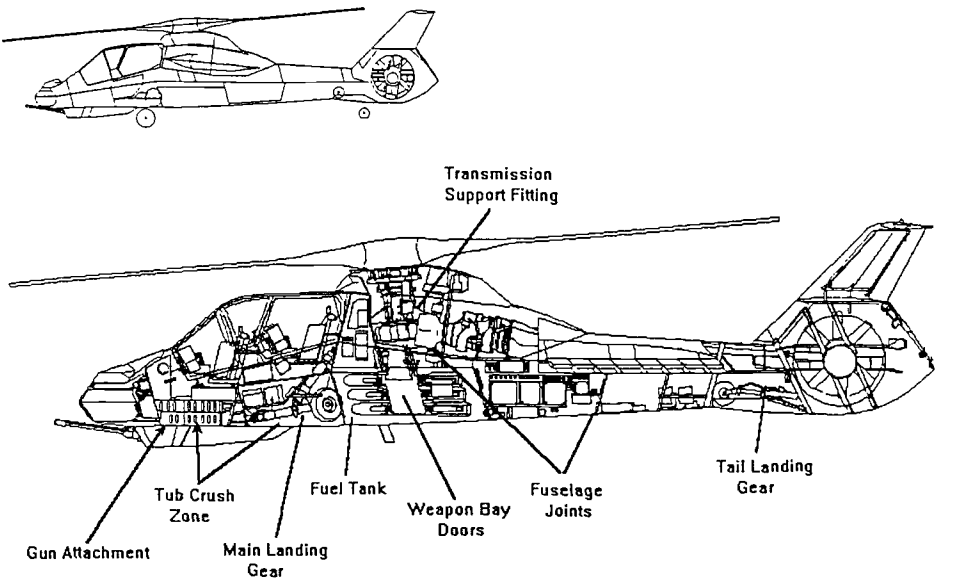


FIG. 8—*Areas covered by subcomponent and component testing.*

combination of metallic and graphite/epoxy elements, with load transfer either through tension bolts or through shear bolts. Parts were manufactured and assembled using production processes. Static testing was performed at both RTD and ETW conditions, while fatigue testing was performed at RTD conditions. BVID was not included in the specimens at this level, those effects being accounted for analytically based on the previous test results. Both static and fatigue performance of the joints was acceptable and the concepts were carried forward and refined in detail design.

Fuselage Tub Crush Tests

The purpose of the fuselage tub crush tests was to verify the crush and energy absorption characteristics of the lower "tub" section of the fuselage: the longitudinal keel beams, transverse bulkheads, and the side skins. During a crash, after the landing gear has fully stroked, the "tub" section of the fuselage will crush, absorbing additional energy, up to approximately 50% of the total crash energy attenuation at the design sink speed. Initial sizing and energy absorption predictions for beaded panels had been based on previous coupon work performed by Farley at AATD [*12*] and Sikorsky internal data from tests performed in the early 1980s for the All Composite Aircraft Program (ACAP) [*13*]. Initial sizing and energy absorption predictions for sandwich panels had been based on work previously published by Cronkhite at Bell Helicopter [*14*]. For both the beaded and sandwich panels, detail differences existed between the previously tested specimens and the Comanche configuration, primarily to improve the producibility of the Comanche. The tub crush tests were performed to verify the energy absorption performance of the Comanche configuration.

Test specimens were manufactured of two types: (1) graphite/epoxy monolithic panels with molded-in stiffening beads, and (2) graphite/epoxy faced sandwich panels. The test specimens were manufactured as four-sided boxes, representative of the size of the fuselage components, with variations in thickness and materials. Both static crushing and impact drop tests were performed, to determine the sensitivity of the energy absorption capability to variations in structural thickness and configuration. BVID was not included in these specimens as it was not expected to affect the crush energy absorption behavior of the overall specimen (see Fig. 9).

The performance desired of the specimens was to achieve as close as possible a rectangular load versus stroke curve, with load rapidly rising to a maximum load level which would not result in injurious deceleration of the aircraft, and sustain that load level to produce the maximum energy absorption. The initial testing revealed detail deficiencies which resulted in less energy absorption than desired. Details of the beaded panel closeout and the sandwich panel edge rampdown were modified and new specimens manufactured and tested, showing improved performance. The revised configurations were incorporated into the aircraft design. Good agreement was observed between the static crush tests and the drop tests with respect to peak load, mode of failure, and specific energy absorption for both the beaded and sandwich panels, except that the sandwich static crush specimens tended to fail in plate buckling, while the drop test specimens crushed at the panel ramp ends.

Additional tests performed with similar specimens incorporating hard points representing the gun attachment and the main landing gear attachment demonstrated that the attachments could be designed to prevent the hard points from causing undesirable high peak loads.

Data from the series of tub crush tests have since been incorporated into the Comanche KRASH 85 [*15*] model, a nonlinear crash impact analysis code, to verify the overall energy absorption of the fuselage and the survivability and crashworthiness of the aircraft.

Fuel Tank Hydraulic Ram Tests

Hydraulic ram occurs due to transfer of energy from a high speed projectile into an enclosed liquid, creating a shock wave that causes high peak pressure loads on the enclosing structure. In mili-

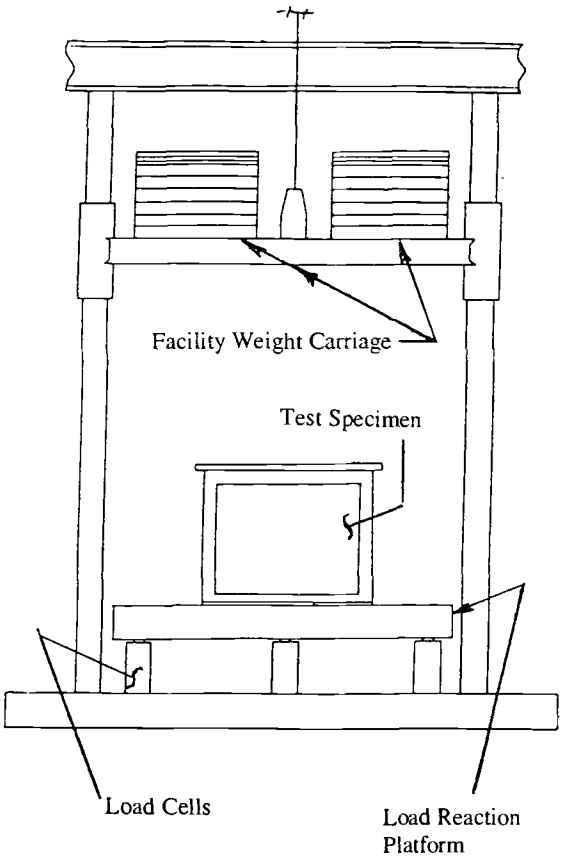


FIG. 9—*Tub crush drop test setup.*

tary aircraft, the primary concern is for the fuel tank, especially for integral fuel tanks which also serve as primary airframe load-bearing structure. Composite fuel tank structures are an additional concern, as composite structure is typically stiffer in bending and less ductile than typical aluminum structure, tending to aggravate the pressure loads. The Comanche fuel tank is formed, in part, by the structural keel beams, resulting in a tall narrow tank with support structure also required to carry aircraft primary structural loads. Several configurations of stiffened monolithic graphite/epoxy panels, corrugated graphite/epoxy panels, and graphite/epoxy faced honeycomb sandwich panels were proposed, however the analytical methodology was not capable of discriminating between the configurations. Therefore, ballistic impact tests were performed at Aberdeen Proving Ground on several configurations. A four-sided steel box was fabricated, representing the top, bottom, and ends of the fuel tank and forming the correct size and spacing of the aircraft keel beam. Bolted to the front and back openings of this box were test panels representative of the aircraft keel beam panels, through which the projectile was shot. The panel providing the best performance was a graphite/epoxy faced sandwich panel with aluminum honeycomb core and a grid of fiberglass damage-limiting strips co-cured in the sandwich face sheets.

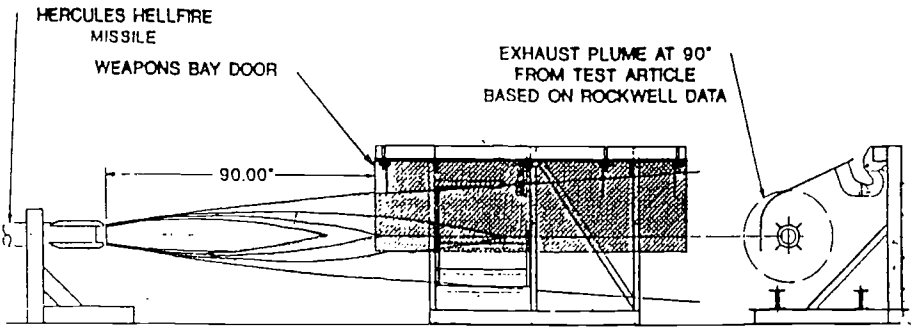


FIG. 10—*Weapons bay door Hellfire plume test setup.*

Hellfire Missile Exhaust Plume Effects Tests

A series of tests was performed with graphite/epoxy panels mounted in proximity to the plume of a Hellfire missile (see Fig. 10). The panels represented the side of the fuselage and the weapon support door. The Comanche mounts Hellfire missiles to the underside of a door which is operable during flight. Normal flight is performed with the doors closed and the missiles stored internally in the aircraft weapons bay. To fire the missiles, the doors are opened. The geometric constraints of this arrangement result in the Hellfire missile, and consequently the exhaust plume of the missile, being in relatively close proximity both to the fuselage side skins and the weapon support door. The panels were instrumented with strain gages and surface-mounted pressure transducers to measure overall bending and local pressure loads. Data measured during these tests verified the design of the skins and the weapon support door were adequate to react the pressure loads.

Main Landing Gear Frangible Tube Tests

The Comanche main landing gear has an air/oil shock strut for energy absorption during normal landings. For high-energy landings, such as during a crash, an additional energy absorption device is required to limit the peak loads reacted through the shock strut and to increase the efficiency of the energy absorption of the shock strut. The device used on the Comanche shock strut is a frangible aluminum tube, which, under compression loads, is forced onto a die which splits the tube longitudinally and forces the moving end outward. The energy absorbed due to this action results in a load which is fairly constant and insensitive to the relative speed of the tube. In the Comanche shock strut, the frangible tube is in series with the compression load path of the shock strut and normally serves as a static compression member. However, upon exceedence of the design load, a fusible link is severed, allowing motion of the frangible tube onto the die and the desired energy absorption. To determine the optimum diameter, wall thickness and die geometry, a series of tests on tube and die specimens were performed (see Fig. 11). These tests consisted of dropping a sufficient weight at the design impact speed to produce the desired energy absorption onto the tube and die specimen, causing the tube to stroke onto the die. The results of these tests were incorporated into the design of the Comanche main landing gear.

Component Tests

A series of component tests was performed to verify design capability. The component tests included: transmission support fitting fatigue test and the main and tail landing gear drop test. The component tests are briefly described below. Figure 8 displays the areas of the Comanche fuselage represented by the test specimens.

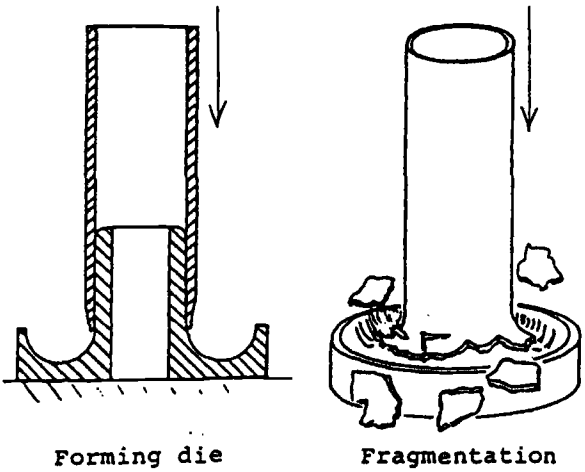


FIG. 11—*Frangible tube test, tested specimen.*

Transmission Support Fitting Fatigue Test

The transmission support fitting attaches the main rotor and transmission system to the airframe (see Fig. 12). The fitting consists of a central vertically oriented cylindrical structure, with flanges at the top and bottom and with four legs, two projecting forward and two aft. The main rotor mast, car-

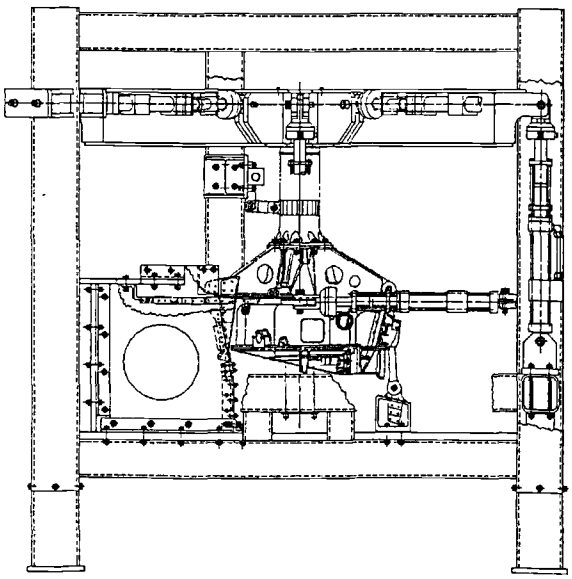


FIG. 12—*Transmission support fitting fatigue test facility.*

rying the main rotor flight loads, is bolted to the upper flange of the transmission support fitting, while the main rotor gearbox is bolted to the lower flange. The forward legs attach the fitting to the airframe structure. The fitting is machined from Titanium 10V-2Fe-3A1 (Ti-10-2-3) forging and is sized due to fatigue loads from the main rotor. Sizing of the fitting was based on a detailed NASTRAN finite-element model of the fitting used to calculate stress levels and standard Sikorsky fatigue analysis methodology, with Ti-10-2-3 fatigue allowables based on coupon test data developed for the Comanche program. A full-scale component of the transmission support fitting and its load interfaces was tested in fatigue. The test verified the overall fatigue performance of the fitting, while also identifying some shortcomings in the attachment to the airframe. Improvements in the attachment have been incorporated into the planned production design of the fitting and will be verified when production specimens are manufactured.

Main and Tail Landing Gear Drop Test

The main and tail landing gear have been subjected to drop tests up to the reserve energy sink speed of 11 ft/s (3.4 m/s) (see Fig. 13). The landing gears had been sized based on energy absorption and load predictions from detailed KRASH 85 models [*15*]. The drop tests have verified the energy absorption performance and structural capability of the landing gear up to that speed. Follow on testing up to full crash sink speed of 38 ft/s (11.6 m/s), which would verify the structural capability and the frangible tube energy absorption, is planned for the production program.

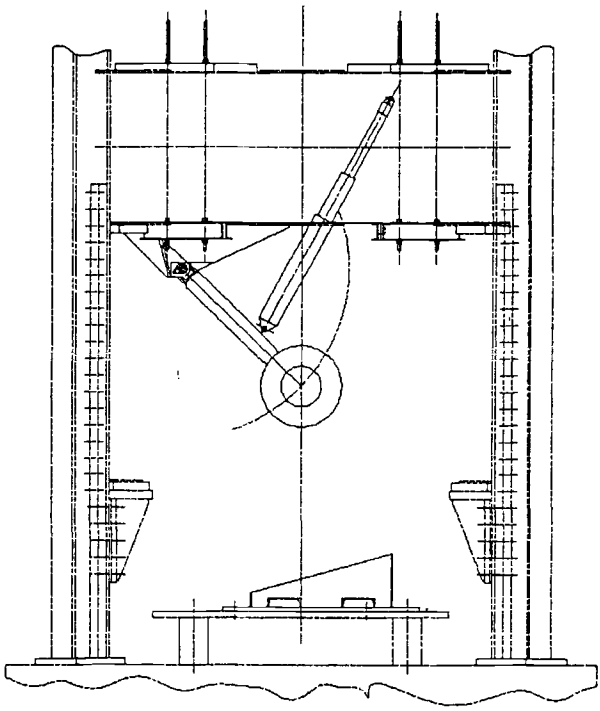


FIG. 13—*Landing gear drop test facility.*

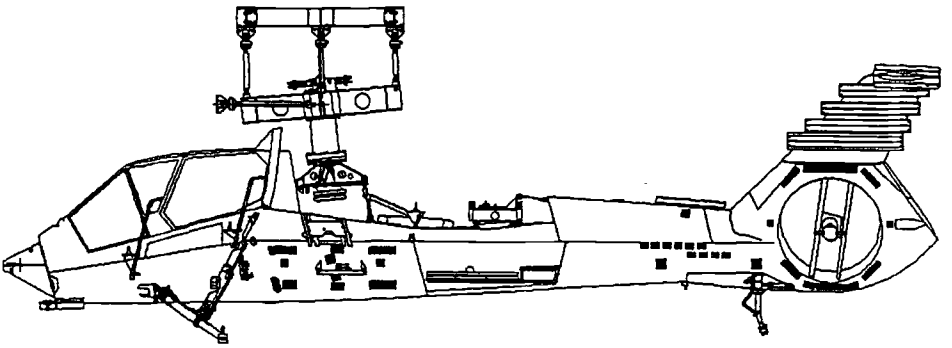


FIG. 14—*Comanche airframe full-scale static test article.*

Static Test Article

A full-scale static test article (STA) was manufactured to subject the airframe structure to simulated design flight and landing loads (see Fig. 14). The STA was manufactured on the same tooling and with the same processes as the flight aircraft. Additionally, intentional impact and delamination defects representing small manufacturing defects and BVID were included in critical areas to demonstrate flaw tolerance of the structure. In this test phase, loads were applied to a proof load of 115% of limit load to demonstrate the structural capability sufficient to clear the flight test aircraft for flight. Additional load enhancement factors to account for environmental effects were not applied at this phase due to the limited flight test period to be covered. Testing to substantiate the production aircraft to ultimate loads with full account of environmental and material variability effects is planned for a later phase of the program. Loads applied to the STA represented concentrated loads from the main and tail rotors and the landing gear, distributed aerodynamic loads on the control surfaces and fuselage, and concentrated and distributed inertia loads. A series of seven major test conditions, selected for criticality over a large section of the airframe, were performed, as well as seven locally critical minor conditions. As the structural components which build up into the flight aircraft as well as the STA had been sized using material and element allowables based on the testing described previously, the STA tests were the ultimate verification of the structural sizing methodology. The STA successfully completed this phase of its test program. During the course of the testing, several local areas were identified in which local load distribution was different than that assumed in the analysis, resulting in overloading of detail components. Structural modifications were implemented in the STA, retested to verify the improvement, and incorporated into the flight test aircraft. Additionally, data gathered on the flight test aircraft demonstrated higher than anticipated empennage aerodynamic loads. Following a revision to the load prediction, the STA empennage was subjected to additional testing to demonstrate the capability of the flight test aircraft for the higher loads.

Conclusions

The RAH-66 Comanche building block structural qualification program consisted of material selection and qualification tests, coupon level tests, element tests, subcomponent tests, and a full-scale static test of the airframe structure. The program provided data that validated our analysis methods and allowed for the reduction of the amount of testing needed. The test program provided data which permitted flight testing of the prototype. Before the Comanche can enter service, additional testing will be required to verify its ultimate strength, damage tolerance, crashworthiness, and its fatigue life.

References

[1] Whitehead, R. S., Kan, H. P., Cordero, R., and Sather, E. S., "Certification Testing Methodology for Composite Structure, Volume II—Methodology Development," NADC-87042-60, Northrop Corp., Oct. 1986.

[2] Military Handbook 17-1E, *Polymer Matrix Composites, Volume 1: Guidelines for Characterization of Structural Materials*, Jan. 1997, Section 2.3.1.1.

[3] Military Handbook 17-1E, *Polymer Matrix Composites, Volume 1: Guidelines for Characterization of Structural Materials*, Jan. 1997, Chapter 8.

[4] Dobyns, A. L., "Correlation of Sandwich Facesheet Wrinkling Test Results with Several Analysis Methods," 1995 AHS Forum, Fort Worth, TX, 9–11 May 1995.

[5] Martin, R. H., "Delamination Failure in a Unidirectional Curved Composite Laminate," NASA CR 182018, Analytical Services and Materials, April 1990.

[6] Bruhn, E. F., *Analysis and Design of Flight Vehicle Structures*, Tri-state Offset Co., Cincinnati, 1965.

[7] Davenport, O. B. and Bert, C. W., "Buckling of Orthotropic, Curved, Sandwich Panels Subjected to Edge Shear Loads," *Journal of Aircraft*, July 1972, pp. 477–480.

[8] *MSC/NASTRAN Quick Reference Guide Version 70.5*, The Macneal-Schwendler Corp., 1998.

[9] Garbo, S. P. and Ogonowski, J. M., "Effect of Variances and Manufacturing Tolerances on the Design Strength and Life of Mechanically Fastened Composite Joints," AFWAL-TR-78-179, 1978.

[10] Hart-Smith, L. J., "Design Methodology for Bonded-Bolted Composite Joints," AFWAL-TR-81-3154, Feb. 1982.

[11] Dobyns, A. L., Fantle, S. C., and Garbo, S. P., "Determination of Graphite/Epoxy Bearing-Bypass Strength Curves using a Bolted Doubler Test Specimen," *Proceedings, 10th DOD/NASA/FAA Composites Conference*, Nov. 1993.

[12] Farley, G. L., "A Method of Predicting the Energy-Absorption Capability of Composite Subfloor Beams," *Journal of the American Helicopter Society*, April 1989, pp. 63–67.

[13] Kay, B. F., "ACAP Structural Design," 1983 AHS Forum, Washington, DC, 9–11 May 1983.

[14] Cronkhite, J. D., Chung, Y. T., and Bark, L. W., "Crashworthy Composite Structures," USAAVSCOM TR-87-D-10, Dec. 1987.

[15] Gamon, M., Wittlin, G., and LaBarge, B., *KRASH 85 User's Guide-Input/Output Format*, DOT/FAA/CT-85/10, March 1986.

[16] SACMA Recommended Method (SRM) 4-88, "Tensile Properties of Oriented Fiber-Resin Composites," Suppliers of Advanced Composite Materials Association, Arlington, VA.

[17] ASTM Test Method D 3410-87, "Compressive Properties of Unidirectional or Crossply Fiber-Resin Composites," Method B, *Annual Book of ASTM Standards*, Vol. 15.03, American Society for Testing and Materials, West Conshohocken, PA.

[18] SACMA Recommended Method (SRM) 1-88, "Compressive Properties of Oriented Fiber-Resin Composites," Suppliers of Advanced Composite Materials Association, Arlington, VA.

[19] SACMA Recommended Method (SRM) 7-88, "Inplane Shear Stress-Strain Properties of Oriented Fiber-Resin Composites," Suppliers of Advanced Composite Materials Association, Arlington, VA.

[20] SACMA Recommended Method (SRM) 5-88, "Open-Hole Tensile Properties of Oriented Fiber-Resin Composites," Suppliers of Advanced Composite Materials Association, Arlington, VA.

[21] SACMA Recommended Method (SRM) 3-88, "Open-Hole Compression Properties of Oriented Fiber-Resin Composites," Suppliers of Advanced Composite Materials Association, Arlington, VA.

[22] Military Handbook 17-1E, *Polymer Matrix Composites, Volume 1: Guidelines for Characterization of Structural Materials*, Jan. 1997, Section 7.2.4.

[23] SACMA Recommended Method (SRM) 2-88, "Compression After Impact Properties of Oriented Fiber-Resin Composites," Suppliers of Advanced Composite Materials Association, Arlington, VA.

[24] ASTM Test Method D 2344-84 (89), "Apparent Interlaminar Shear Strength of Parallel Fiber Composites by Short-Beam Method," *Annual Book of ASTM Standards*, Vol. 15.03, American Society for Testing and Materials, West Conshohocken, PA.

[25] ASTM Test Method D 790-86, "Flexure Properties of Unreinforced and Reinforced Plastics and Electrical Insulating Materials," *Annual Book of ASTM Standards*, Vol. 8.01, American Society for Testing and Materials, West Conshohocken, PA.

Anthony Caiazzo,[1] *Michael Orlet,*[1] *Hank McShane,*[2] *Larry Strait,*[3] *and Chris Rachau*[3]

The Effects of Marcel Defects on Composite Structural Properties

REFERENCE: Caiazzo, A., Orlet, M., McShane, H., Strait, L., and Rachau, C., **"The Effects of Marcel Defects on Composite Structural Properties,"** *Composite Structures: Theory and Practice, ASTM STP 1383,* P. Grant and C. Q. Rousseau, Eds., American Society for Testing and Materials, West Conshohocken, PA, 2000, pp. 158–187.

ABSTRACT: This paper describes a method for predicting key structural properties of carbon fiber reinforced composite materials containing ply waviness several times the nominal ply thickness. These so-called marcelled regions have been observed in a number of highly loaded thick structural components. The origins of these defects are not fully understood, although several contributing factors have been identified. The goal of this work is to develop an analysis based disposition criterion for components where fabrication process changes cannot be readily implemented to eliminate marcel defects. Work to date has focused on developing a micro-mechanics-based procedure for modeling the strength and stiffness properties of a marcelled region given basic properties of the material and simple geometric parameters of the marcel that can be measured nondestructively. The result is a general constitutive model that can be used in global structural analysis packages to assess the effects marcel defects have on component performance. Analyses of test coupons containing marcelled regions have been carried out to illustrate the method and establish the validity of the modeling approach. Results indicate that the degree to which marcel defects affect structural properties depends not only on the maximum fiber misalignment angle, but also on the location and size of the marcelled region and nominal applied strain field.

KEYWORDS: marcel defect, ply waviness, accept/reject criteria, constitutive model, test data

Throughout this paper we will use the term marcel[4] to describe a deviation from the desired fiber (ply) orientation in a composite laminate which is relatively abrupt. Others have used terms like *fiber waviness* or *fiber wrinkles* to refer to these fabrication-induced defects. Marcels have been observed to occur in, or normal (through the thickness) to, the lamination plane. A typical through-the-thickness marcel defect is shown in Fig. 1. While the modeling approach described here is applicable to both types of marcels, analysis results and test data presented here are limited to through-the-thickness marcel defects.

It has been offered that processing parameters such as pressure application rate, pressure gradients, cure cycle, tool fit and mis-kitting of ply drop-off, are the source of marcel defects. The focus of our work is not how or why marcel defects appear in composite components. Rather, the goal is to develop an analysis-based criterion for determining the effects that marcel defects have on composite structural properties: stiffness (modulus), static strength (subcritical and ultimate), and residual strength after low-cycle fatigue loading. This objective was accomplished for the simple case of

[1] Technical director and engineer, respectively, Materials Science Corporation, Fort Washington, PA 19034.
[2] Polymers and Composites Branch, NAWCADPAX, Patuxent River, MD.
[3] Research associate and research assistant, respectively, Applied Research Laboratory, Penn State University, State College, PA.

[4] Per the American Heritage Dictionary—A hair style characterized by regular waves. Originated by Marcel Grateau.

Copyright© 2001by ASTM International www.astm.org

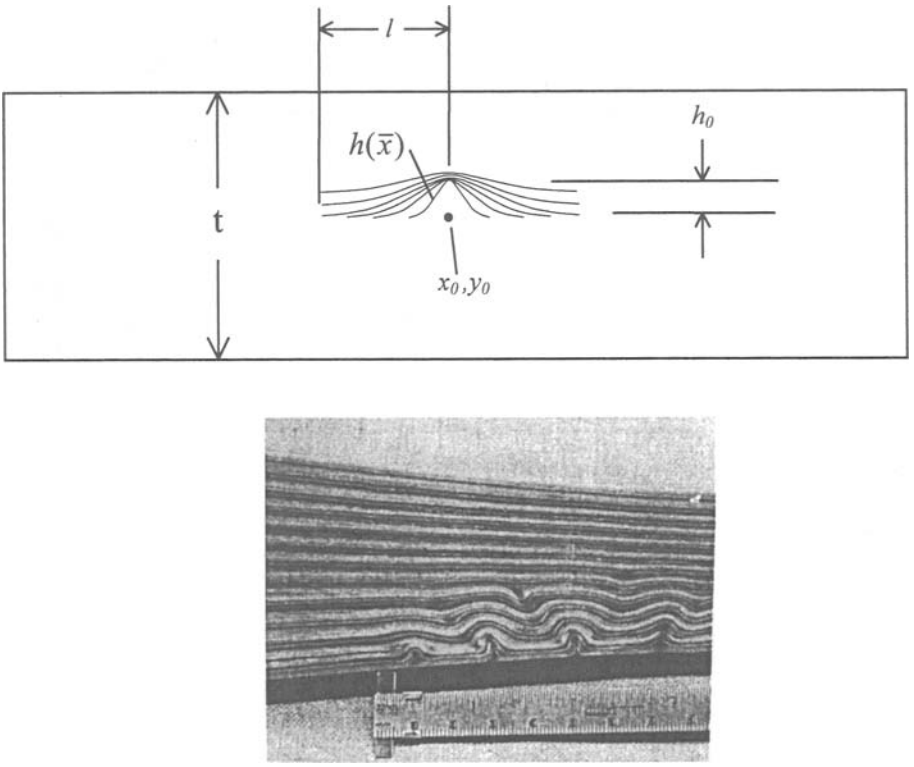


FIG. 1—*Schematic of marcel shape and photograph of actual marcels in a part.*

straight-sided test specimens by conducting analyses and experiments that: (1) establish load levels at which the defect produces subcritical (interlaminar or intralaminar) damage, and (2) track how damage progresses to ultimate failure. Each of these may be important in setting accept/reject criteria for composite components containing marcel defects.

This paper is structured as follows. Background on what a marcel defect is, why marcel defects warrant detailed study, and how micromechanics-based modeling techniques can be used to characterize how the marcel perturbs the local stress state is presented first. This is followed by results of an experimental program (coupon level tests) designed to illustrate the effects marcel defects have on key structural properties of composites. Discussion of test results and comparison of analyses of the experiments to the measured data are then presented. The relevance of this work to development of accept/reject criteria for composite parts containing marcel defects and a set of summary remarks conclude the paper.

Analysis Methods for the Effects of Marcel Defects on Structural Properties of Composite Materials

In this section, we present background on how a marcel defect can be characterized, how one can use micromechanics principles to assess the effects of marcel defects on structural properties, and why marcel defects warrant detailed study.

An underlying requirement to the modeling approach developed here is that it be suitable for use in flaw criticality analyses of complex composite structures which contain marcel defects. This im-

plies a certain level of computational efficiency be incorporated into the modeling strategy. It has been shown that one can include marcel defects in a 3-D continuum finite-element (FE) analysis by defining an element mesh that tracks along the wavy layers of the laminate [*1*]. However, it is not clear that such an approach can be readily adapted to the task at hand. An approach where marcel defects can be easily incorporated into a *standard* or *existing* structural analysis model is preferred. This would allow one to carry out a flaw criticality assessment by

1. Developing a FE model for a structure of sufficient detail to capture important stress (or strain) gradients assuming that the component is defect free.
2. Postulating that marcel defects exist in as many areas of the structure as one wishes by simply "placing a marcel" at discrete locations.
3. Comparing results of the analysis to experimental data to determine whether (or to what degree) the marcel defect affects structural reliability.

Carrying out Steps 2 and 3 above, for several different marcel defect *size and shapes*, would allow one to determine the maximum allowable marcel versus position in the structure which would be useful in setting nondestructive evaluation (NDE) requirements. Alternatively, if a marcel of a given *size and shape* is found via NDE, one could use Steps 2 and 3 to assess how margins of safety are affected by the defect. Thus, these analyses coupled with experimental data provide a mechanism for developing an accept/reject criteria for structural components.

Key Geometric Parameters

Before an assessment can be made whether a marcel defect is acceptable or rejectable, one must have a method for characterizing the anomaly. The geometric parameters chosen to describe the defect must be compatible with both nondestructive evaluation (NDE) techniques and the method by which the defect will be modeled in flaw criticality analyses.

A schematic of a marcel defect is shown in Fig. 1. The key parameters we have chosen to represent the defect are: the height of the marcel at its peak h_0, the span dimension 2ℓ, the shape of the marcel as defined as a function of spatial coordinates which may be rectangular, cylindrical, or spherical, and a set of coordinates which defines the spatial location of the *center* of the marcel. An additional function that defines the decay rate of the waviness is also required.

Micromechanics Based Analysis Method

An important aspect of the current work is the ability to include the effects of marcel defects in a structural analysis without explicitly modeling the wavy material layers (c.f., [*1*]). As indicated by Fig. 2, the spatial variation of material properties produced by the marcel defect can be included in the analysis through coordinate system transformations, i.e., via the 3×3 transformation matrix $[T]$

$$\begin{Bmatrix} u_X \\ u_Y \\ u_Z \end{Bmatrix} = \begin{bmatrix} T_{11} & T_{12} & T_{13} \\ T_{21} & T_{22} & T_{23} \\ T_{31} & T_{32} & T_{33} \end{bmatrix} \begin{Bmatrix} u_x \\ u_y \\ u_z \end{Bmatrix} \tag{1}$$

which relates quantities in the local coordinate system (viz., xyz) to the global system (viz., XYZ). The matrix $[T]$ must be defined for every integration point within the finite-element model. Away from the marcel defect, the local directions are aligned with the global axes giving the simple result, $T = \delta_{pq}$, the identity matrix. If, for example, the marcel geometry can be approximated by a simple polynomial or other analytical function of position (XYZ), $[T]$ for any integration point within the finite-element model can easily be computed by taking appropriate spatial derivatives. In the ABAQUS [*2*]

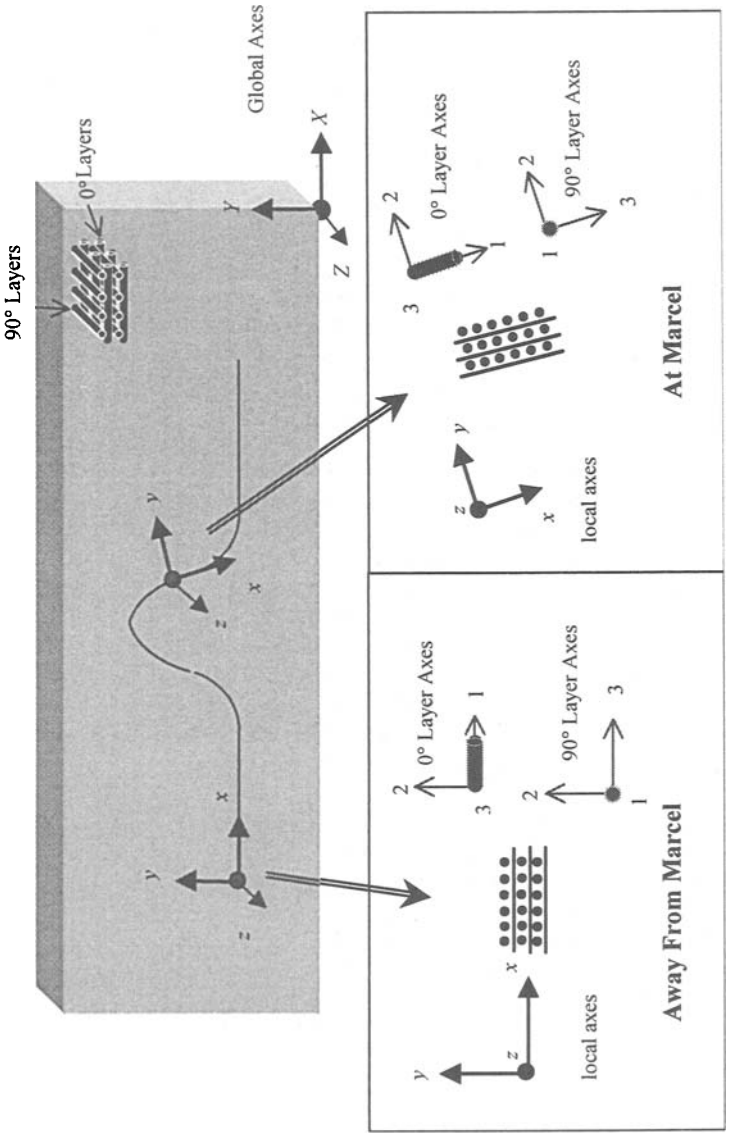


FIG. 2—*Fiber orientations near and away from marcel.*

finite-element analysis program, this task is automated by using a user written FORTRAN subroutine to perform the calculations.

For the marcel patterns investigated in this report, the marcel generator height h at any point $(\bar{x}, \bar{y})$ was represented by an equation of the form (for a two-dimensional marcel):

$$h(\bar{x}) = a + b\bar{x} + c\bar{x}^2 + d\bar{x}^3 + e\bar{x}^4 \ldots\ldots m\bar{x}^n \tag{2}$$

with boundary conditions of the type

$$h(-\ell) = 0, \quad h(+\ell) = 0, \quad h(0) = h_0, \quad \text{with} \quad h(\bar{x}_p) = \alpha_p \text{ and } h'(\bar{x}_p) = \beta_p \quad p = \ell, \ldots r \tag{3}$$

where $\bar{x}$ is the distance from the marcel center point (x_0, y_0), and the prime indicates derivative with respect to $\bar{x}$. In Eq 3, h_0 and ℓ can be considered as gross measures of the marcel defect size, while $h(\bullet) = \alpha$ and $h'(\bullet) = \beta$ are simply height and slope control points for the polynomial fit which may be defined by a detailed NDE map. An additional function $\psi(\bar{y})$ defines how the marcel wave *dies out* versus $\bar{y}$. For all work described here, we have assumed that the amplitude of the wave decays linearly over some distance $\hat{h}$. Clearly, more elaborate representations could be constructed, however, it is not clear that standard NDE techniques are capable of defining such a function. Other definitions (i.e., exponential functions) and three-dimensional shapes (i.e., bubble functions) have been implemented into ABAQUS without difficulty.

Once the local material directions have been defined, homogenization theory and micromechanics provides the mechanism for determining the effective constitutive relation of a representative volume element (RVE) of the composite. From a practical point of view, homogenization theory provides the properties of the material that allows one to conduct an analysis of a composite body as if it were a homogeneous continuum. For certain material architectures, the micromechanics problem can be solved in closed form, yielding an analytical model for the effective macroscopic behavior of the composite in terms of microstructural inputs [*3,4*]. The importance of the RVE concept and homogenization theory to the analysis of heterogeneous materials can not be overstated, for without it one would have to explicitly include details of the material microstructure in the constitutive relation making analyses of composite structures computationally prohibitive. The micromechanics analysis also provides what is commonly called a localization tensor, which defines the relationship between important field variables within the RVE (viz., spatially varying stress $\sigma(x)$ and strain $\varepsilon(x)$) and macroscopic averages (viz., Σ and E). This allows one to compute average layer (*xyz*) or unidirectional composite (UDC) (*123*) level stresses and strains from the macroscopic or continuum level (*XYZ*) stresses and strains produced by a finite-element analysis. As discussed later in this article, these layer or UDC level quantities are particularly useful in constructing physically based material failure models.

The composite material studied here is a $[0°/90°]_{ns}$ laminate, therefore, a typical RVE consists of two layers of material, one with fibers aligned with the local x axis and one with fiber aligned with local z. The stiffness tensor C^{RVE}_{ijkl} relating macroscopic composite stresses and strains in the xyz coordinate system, i.e.,

$$\Sigma_{ij} = C^{\text{RVE}}_{ijkl} E_{kl} \tag{4}$$

of this RVE can be constructed from unidirectional composite (UDC- or *123* coordinate system in Fig. 2) elastic constants using a method given by Rosen et al., [*5*].[5] The stress-strain relation C^{RVE}_{ijkl} for

[5] The method outlined by Rosen yields an analytical model that may be viewed as a three-dimensional version of classical laminated plate theory.

TABLE 1—*Unidirectional composite elastic properties.*

E_{11}	E_{22}, E_{33}	ν_{12}, ν_{13}	ν_{23}	G_{12}, G_{13}	G_{23}
19.4 Msi	1.1 Msi	0.3	0.4	0.60 Msi	0.38 Msi

a $[0°/90°]_{ns}$ laminate is of the reduced form:

$$\begin{Bmatrix} \Sigma_{xx} \\ \Sigma_{yy} \\ \Sigma_{zz} \\ \Sigma_{xy} \\ \Sigma_{xz} \\ \Sigma_{yz} \end{Bmatrix} = \begin{bmatrix} C_{xxxx} & C_{xxyy} & C_{xxzz} & 0 & 0 & 0 \\ & C_{yyyy} & C_{yyzz} & 0 & 0 & 0 \\ & & C_{zzzz} & 0 & 0 & 0 \\ & & & C_{xyxy} & 0 & 0 \\ & \text{SYM} & & & C_{xzxz} & 0 \\ & & & & & C_{yzyz} \end{bmatrix} \begin{Bmatrix} E_{xx} \\ E_{yy} \\ E_{zz} \\ E_{xy} \\ E_{xz} \\ E_{yz} \end{Bmatrix} \tag{5}$$

since this laminate is specially orthotropic in the local xyz coordinate system. Once C_{ijkl}^{RVE} and the transformation matrix $[T]$ have been defined, a continuum level finite-element analysis of a structure to establish how key structural properties are affected by the presence of a marcel defect can be carried out in the usual manner.

Linear Elastic Stress Fields Near a Marcel Defect

Before proceeding to a discussion of results of analyses that track damage progression in materials with marcel defects, results of elastic analyses that illustrate how a marcel defect perturbs the stress field in a uniformly loaded section of $[0°/90°]_{ns}$ IM7/8552 laminate will be presented. Both isolated and multiple marcel defects were considered, however, analysis results are only presented here for the case of a single isolated defect.[6] Two-dimensional plane strain analyses were performed using the ABAQUS code for several marcel geometries described by a polynomial of the form:

$$h(\bar{x}) = h_0 \left[1 - 3\left(\frac{\bar{x}}{\ell}\right)^2 + 2\left(\frac{\bar{x}}{\ell}\right)^3 \right] \tag{6}$$

assuming a linear die-out definition $\psi(\bar{y})$ over the height $\bar{y} \leq h_0$. Marcel geometries of various shapes (i.e., $0.2 \leq h_0/\ell \leq 1.0$), and extents (i.e., $0.2 \leq h_0/t \leq 0.8$) through the thickness were investigated. For all cases the marcel center (x_0, y_0) was located at the bottom laminate surface.

The material properties for the unidirectional carbon fiber toughened epoxy (IM7/8552) composite being studied are given in Table 1. If no marcel defect were present, the elastic constants would be as given in Table 2.

Contours of laminate level (xyz) stresses, normalized to the applied axial tensile stress, for the case $h_0/\ell = 0.5$, $h_0/t = 0.5$ with the marcel center located at the lower surface ($y_0 = -t/2$) and mid-thickness ($y_0 = 0$) are shown in Figs. 3 through 5. Maximum values of Σ_{xx} and Σ_{yy} for $y_0 = 0$ cases are summarized in Figs. 6 and 7. No plot is provided for the maximum interlaminar shear stress, since it did not vary significantly (i.e., the normalized $\Sigma_{xy} \cong 0.20$) for the cases studied. Note for each case $\Sigma_{xx} = 1$, and $\Sigma_{yy} = \Sigma_{xy} = 0$, if no marcel were present.

[6] The reasons for this are threefold: (1) it is easy to see that the method described here is sufficiently general to include multiple defects and, therefore, additional analysis results provide no unique information on the approach; (2) experimental data presented here are limited to single isolated defects; and (3) results show that the perturbation in the underlying stress field is highly localized so that most marcels may be termed isolated defects.

TABLE 2—*[0/90]$_{ns}$ composite laminate elastic properties.*

E_{xx}, E_{zz}	E_{yy}	ν_{xy}, ν_{zy}	ν_{xz}	G_{xy}, G_{zy}	G_{xz}
10.3 Msi	1.27 Msi	0.4	0.03	0.49 Msi	0.60 Msi

It is interesting to note that in the absence of damage, the apparent axial Young's modulus obtained from this analysis, i.e.,

$$E = \frac{\sigma_{avg}}{\varepsilon_{avg}} \tag{7}$$

where

$$\sigma_{avg} = \frac{\text{Total force}}{\text{Cross-sectional area}} \tag{8}$$

and

$$\varepsilon_{avg} = \frac{\text{End displacement}}{\text{Specimen length}} \tag{9}$$

is not significantly affected by what we would characterize as gross marcel defects (e.g., $h_0/\ell = 0.5$, $h_0/t = 0.5$), while a marcel defect of this size will certainly affect the failure process of composite laminates. These results show that significant interlaminar stresses are introduced for a far-field load that would normally produce a fiber dominated failure. These general observations have been made

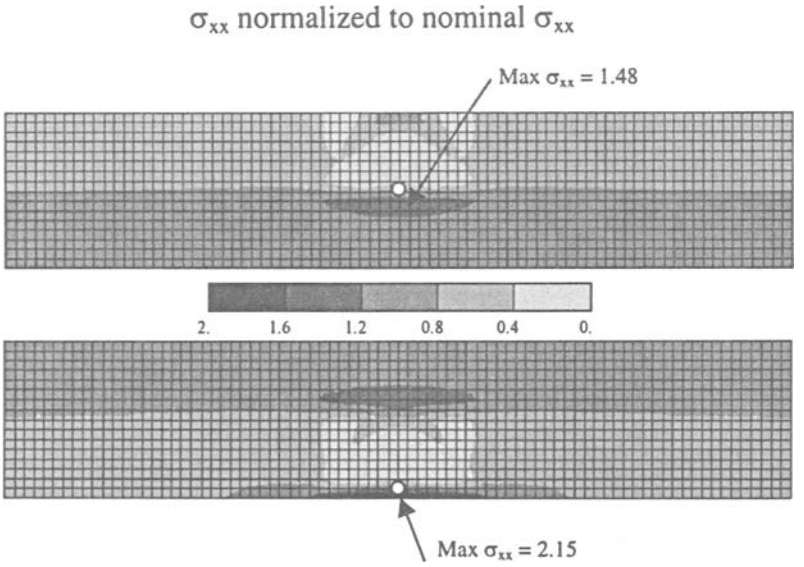


FIG. 3—*Normal stress in local x-direction normalized to nominal σ_{xx} for both marcel locations. The location of the marcel center is indicated.*

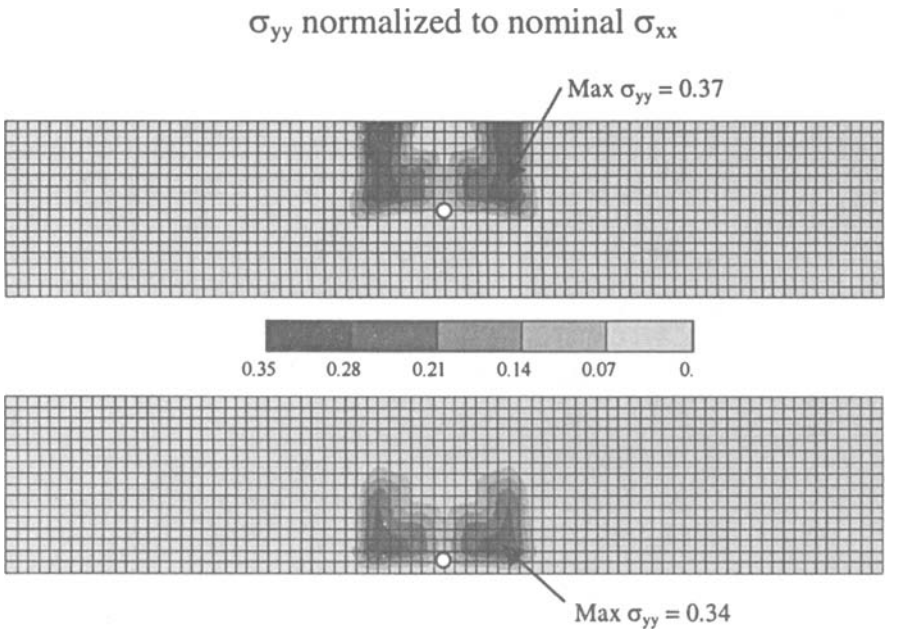


FIG. 4—*Normal stress in local* y*-direction normalized to nominal* σ_{xx} *for both marcel locations. The location of the marcel center is indicated.*

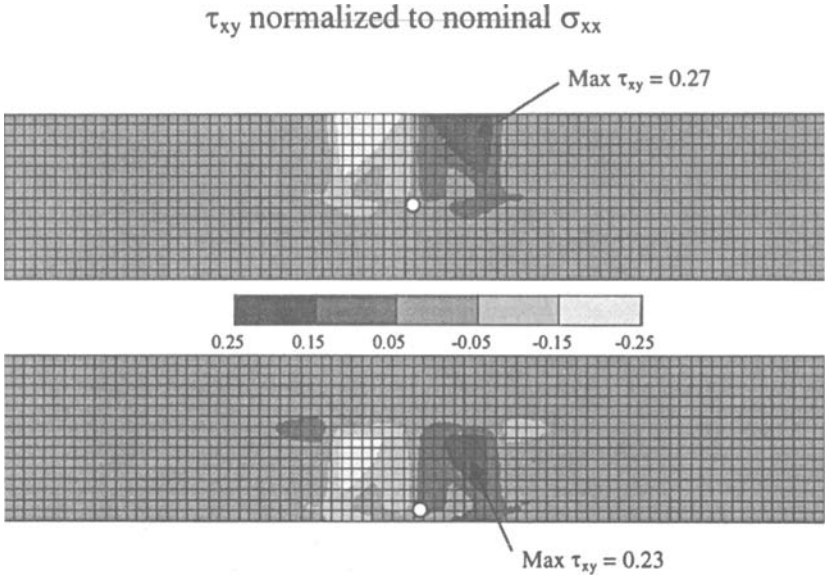


FIG. 5—*Local* xy*-direction shear stress normalized to nominal* σ_{xx} *for both marcel locations. The location of the marcel center is indicated.*

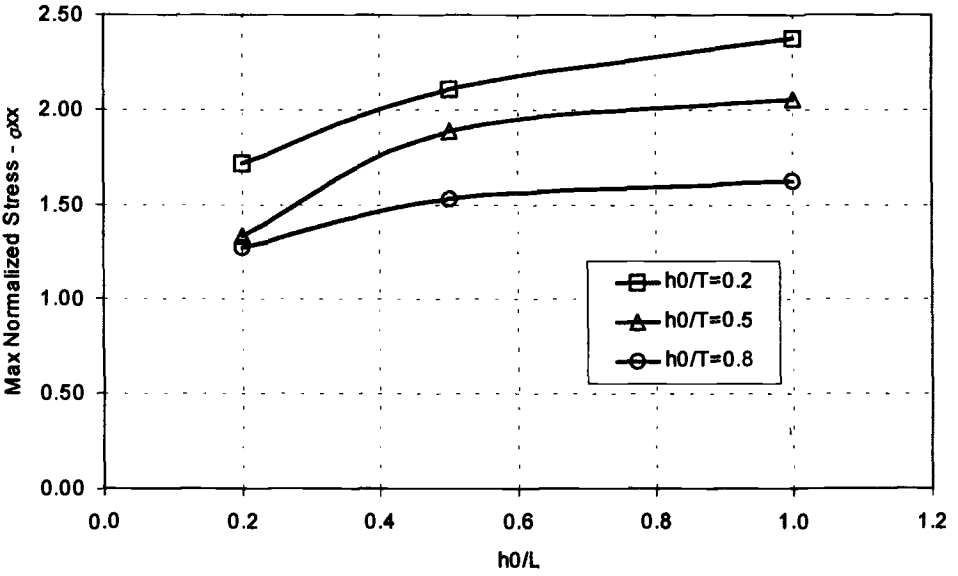


FIG. 6—*Results of linear elastic stress analyses for marcel at middle surface* (y = 0).

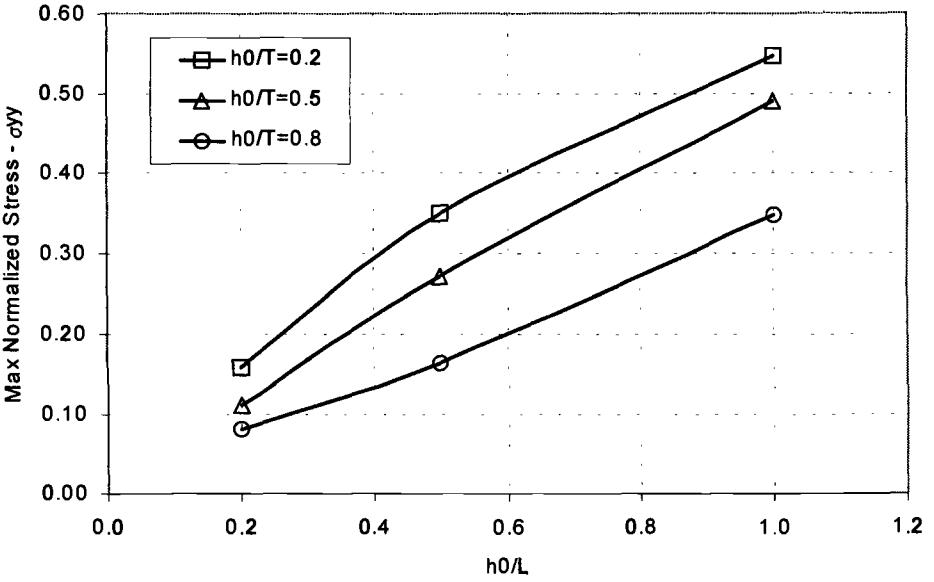


FIG. 7—*Results of linear elastic stress analyses for marcel at middle surface* (y = 0).

by others [*6–8*], although it is believed that this is the first work carried out using the general micromechanics based modeling method for the marcel defect presented in this article.

Physically Based Models for Damage Evolution in Composites

The results presented in the previous section show that a marcel defect produces a spatially varying multiaxial stress state in a material subjected to simple uniaxial far-field loads. Under repeated tensile loads, matrix microcracks caused by these inter- and intralaminar stresses can propagate, coalesce and form delaminations or ply separations that result in gross failure at load levels much lower than that of the monotonically loaded material. Furthermore, since load distribution depends on stiffness in an indeterminant, matrix-dominated interlaminar tension or shear (subcritical) failures may alter load paths and affect fiber-dominated (ultimate) failure strengths. Two physically based models for predicting the nonlinear response of the composite caused by subcritical damage initiation and growth are described next.

A model that approximates the UDC (*123*) material response before and after a brittle failure is illustrated by the one-dimensional stress-strain curve shown in Fig. 8. In this model, the stress-strain relation for the UDC is assumed to be bilinear and the modulus beyond initial failure is assumed to be small. The inelastic strain $\hat{\varepsilon}_{pq}$ defined as

$$\hat{\varepsilon}_{pq} \equiv \varepsilon_{pq} - \varepsilon'_{pq} \tag{10}$$

can be viewed as a damage variable which is loosely analogous to plastic strains in metals. Any physically based failure criterion can be used with the model. Extension to a general three-dimensional problem is straightforward; if failure occurs due to the nth direction strain component, all elements in the nth row and column of the layer stiffness tensor are reduced to a small fraction of their original value. The current or instantaneous inelastic composite stiffness C^{RVE}_{ijkl} is re-evaluated using the reduced UDC properties. The shaded areas in Fig. 8 can be used to calculate the strain energy stored and released (dissipated) during a load increment where failure occurs. Furthermore, for each increment, the total strain energy stored and the energy dissipated can be summed over the entire volume

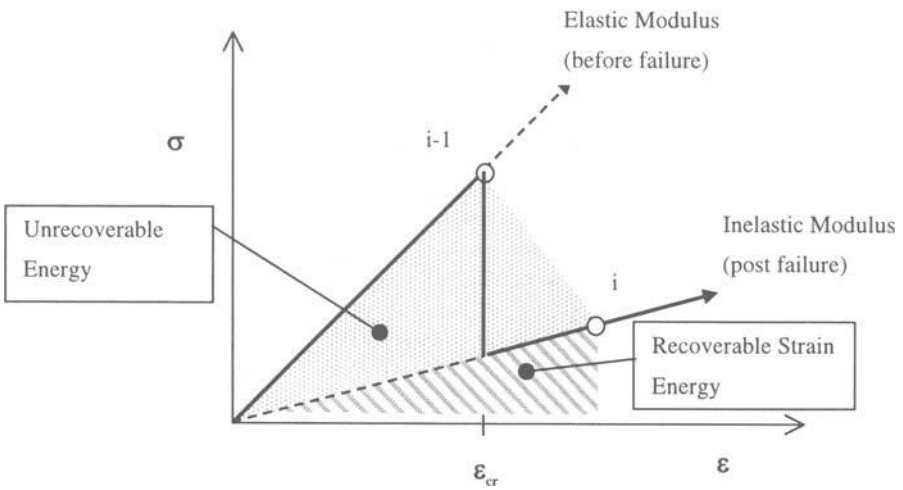


FIG. 8—*Schematic of one-dimensional, idealized, bilinear stress-strain curve before and after brittle failure occurring during load increment* i. *Shaded areas show strain energy quantities used to measure damage accumulation.*

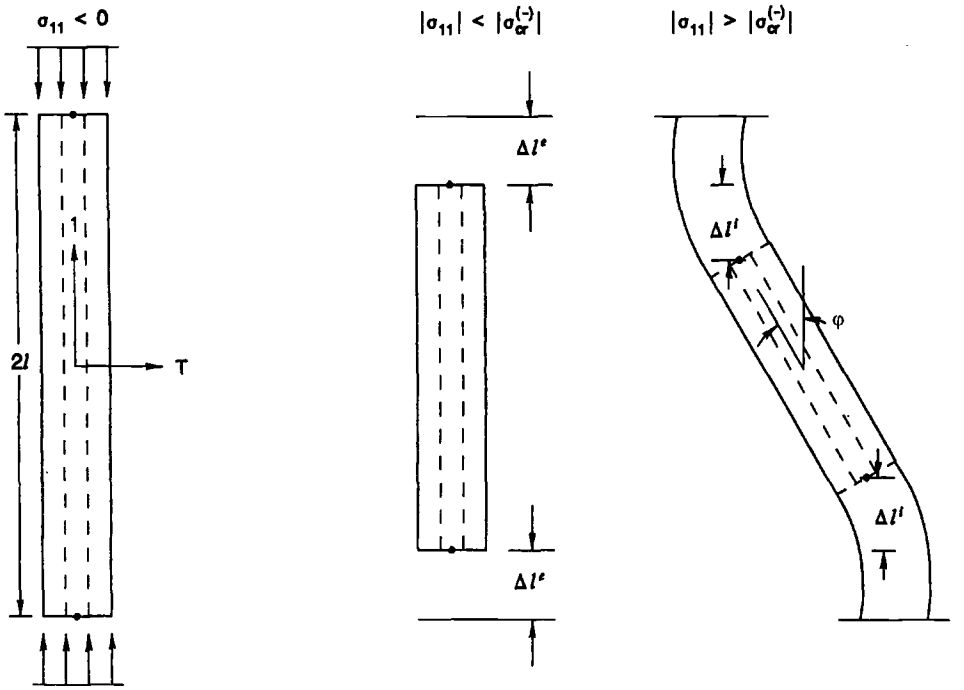


FIG. 9—*Microbuckling schematic.*

to provide an overall measure of damage within the material. Strain energy dissipated is a convenient damage measure, since this simple scalar quantity can easily be applied to more complex structures.

A model for tracking growth and initiation of microinstabilities in any UDC of a RVE is shown schematically in Fig. 9. In this model, it is assumed the UDC kinks which causes a loss in axial (*11* direction) stiffness defined by the rotation angle. The inelastic $\hat{\varepsilon}_{11}$ strain component can be defined by considering the kinematics of the rotation

$$\hat{\varepsilon}_{11} \cong (1 - \varepsilon_{11}^{cr}) \cdot (1 - \cos\varphi) \tag{11}$$

where ε_{11}^{cr} is the axial strain (fiber direction) at which microinstability initiates, and φ is the rotation angle from the axial direction. Knowing φ, C_{ijkl}^{RVE} can be updated to account for the rotation (kinking) of the UDC that have reached their compressive instability load. Therefore, microinstability failures produce a nonlinear (inelastic) stress-strain relation for the RVE. Note that the compressive strain required to initiate kinking (i.e., establishes ε_{11}^{cr}) depends on many factors, including fiber modulus, fiber volume fraction, and the in-situ nonlinear shear stress-strain of the UDC [*9*]. Effects of multiaxial stress states present near a marcel defect can be introduced assuming that the matrix behavior can be represented by J_2 deformation theory [*10*].

Either of the micromechanics based nonlinear constitutive relations described to this point can be used in a finite-element-based stress analysis as follows. For each load increment, the subroutine that defines material properties is called to get the current definition of the constitutive relation. Global (*XYZ*) equilibrium stresses and strains for each element are computed, and are then transformed to local element (*xyz*) coordinates. The local element quantities are passed back to the material subroutine where UDC (*123*) level stresses and strains at the material point are computed. The material subrou-

TABLE 3—*Unidirectional composite strengths used in sensitivity analyses.*

Strength	S_{11} (ksi)		S_{22} (ksi)		S_{12}, S_{13}	S_{23}
S1	+210	−140	+5.0	−12.0	9.0	8.0
S2	+210	−140	+9.0	−12.0	4.0	3.0

tine checks for failures within the RVE, and updates the constitutive relation accordingly. Residuals[7] arising from inelastic behavior are applied and global equilibrium is re-checked. The iterative process is repeated until all residuals are within an acceptable value. The ABAQUS code provides users with an easy to implement interface, called UMAT, for defining a general material constitutive relation that can be used with any elements in the stress analysis library.

Modeling Damage Evolution in Composite Elements Containing Marcel Defects

A series of analyses were conducted to predict, *prior* to conducting experiments, the response of simple test coupons containing marcel defects when loaded monotonically in tension beyond the elastic range. Two marcel sizes (M1; $h/\ell = 0.25$ and M2; $h/\ell = 1.0$) centered at the mid-thickness were investigated. Two sets of strength values for the composite were assumed; one with a relatively low transverse tensile strength (S1), and one with a low shear strength (S2). A range of material properties (given in Table 3) was investigated because we had no knowledge of how the individual matrix dominated failure strengths (tension and shear) might be affected by planned cyclic tensile tests. Note that fiber dominated strengths were held constant for all analyses. In the work reported in this article, the maximum strain failure criterion was used to determine if inelastic strains exist within an RVE, although this approach is easily implemented for any physically based failure criteria (i.e., maximum stress [*11*] or Hashin interaction [*12*]).

Figure 10 shows the average stress plotted versus average strain for the tension load cases studied. For each analysis, the end of the curve may not necessarily represent ultimate failure, but rather the highest applied displacement for which the solver obtained an equilibrium solution within the tolerance specified. The stress-strain curve for the composite with marcel M2 lies below that of marcel M1. This is due to more extensive matrix failure occurring earlier in the applied load history. At higher strains, specimens with strength S1 undergo a sudden drop in the average stress-strain response. These events have been labeled A and B on the plot. Event C represents less sudden but significant change in stress-strain response.

Ignoring Poisson effects, C_{xx} (dropping the RVE superscript for convenience) in Eq 4 relates stress to strain in the local x (0° laminate) direction. Significant degradation of C_{xx} would indicate fiber failure since the stiffness of the 90° layers is approximately 5% of the 0° layers for carbon fiber composite studied here. The C_{yy} term relates transverse stress to transverse strain (22-direction in both layers), while C_{xy} relates interlaminar shear stress to interlaminar shear strain (12- or 23-direction for the 0° and 90° layers, respectively). These terms are dominated by matrix (not fiber) properties. Figure 11 shows contour plots of C_{xx}, C_{yy}, and C_{xy} for the M2/S1 analysis case as the applied strain is increased from 0.56 to 0.58%. The most significant damage in the local x-direction occurs in the material with the higher shear strength (strength S1). This can be explained by considering that the load applied in the global X-direction must be transferred through shear around the locally more compliant marcel area. If the interlaminar shear strength is sufficiently high to support this shear stress, a stress concentration (similar to a notch effect) is created in the material directly above and below the marcel that can cause fiber failure. Conversely, if interlaminar shear failures occur at the marcel, the X-direction stress near the defect is spread over a larger area and no fiber failures result.

[7] The form of the residuals, i.e., forces or displacements, depends on the nonlinear solution algorithm used.

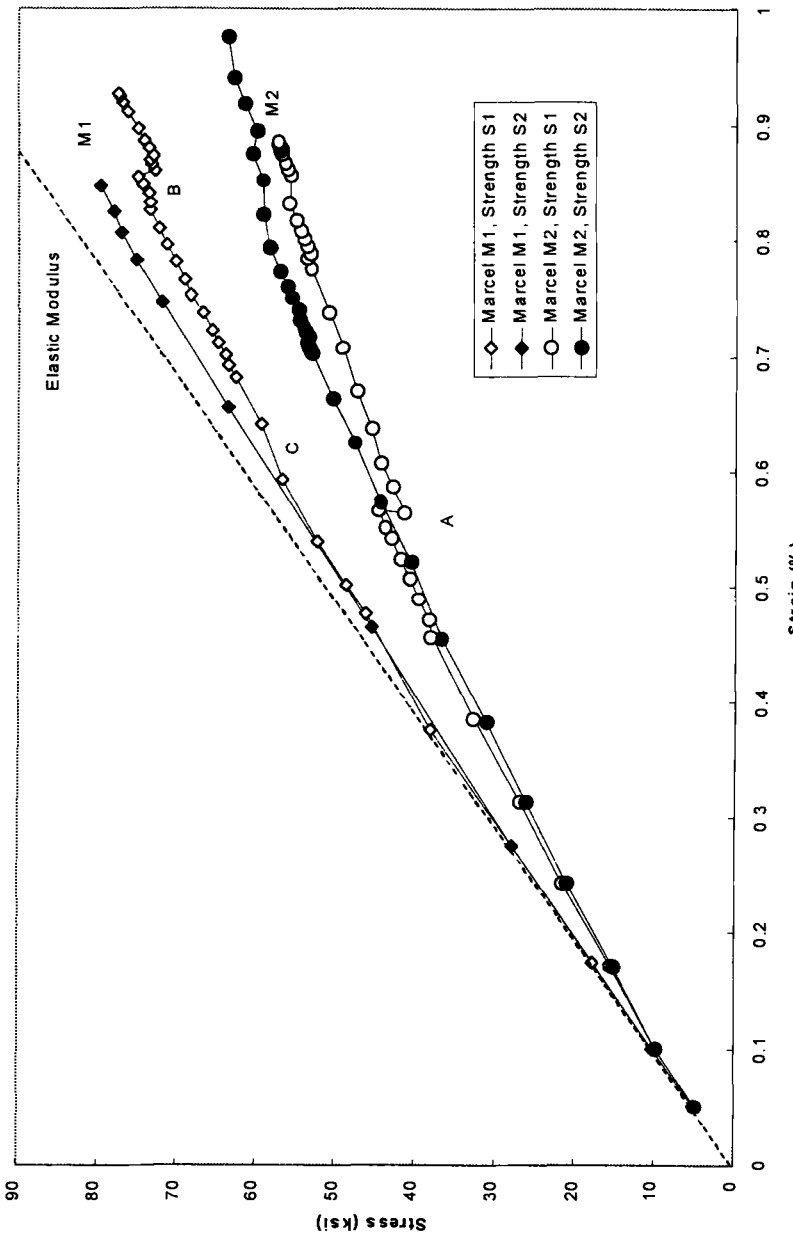


FIG. 10—*Analysis results for average stress vs. average strain for all four marcel patterns under displacement controlled tension.*

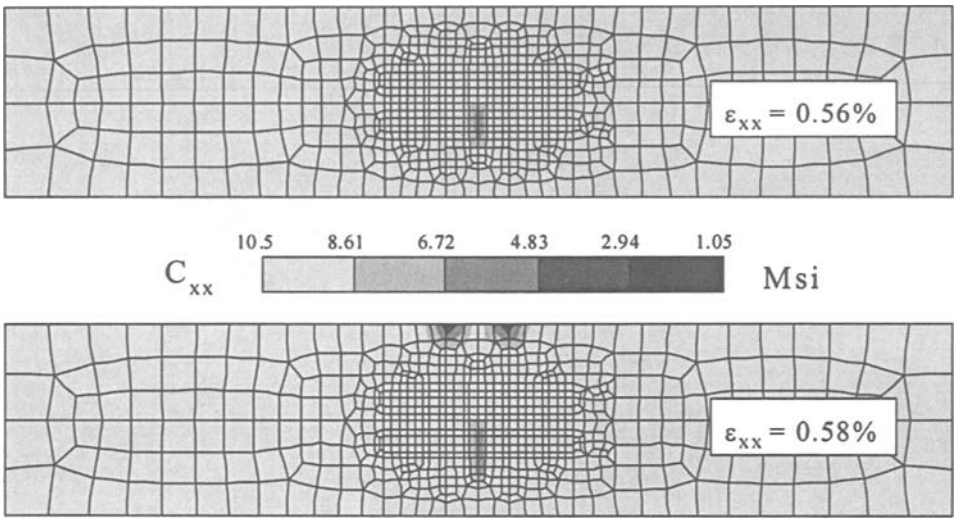


FIG. 11*a*—*Elastic constant* C_{xx} *before and after observed jump in dissipated energy. Darker regions indicate reduced stiffness.*

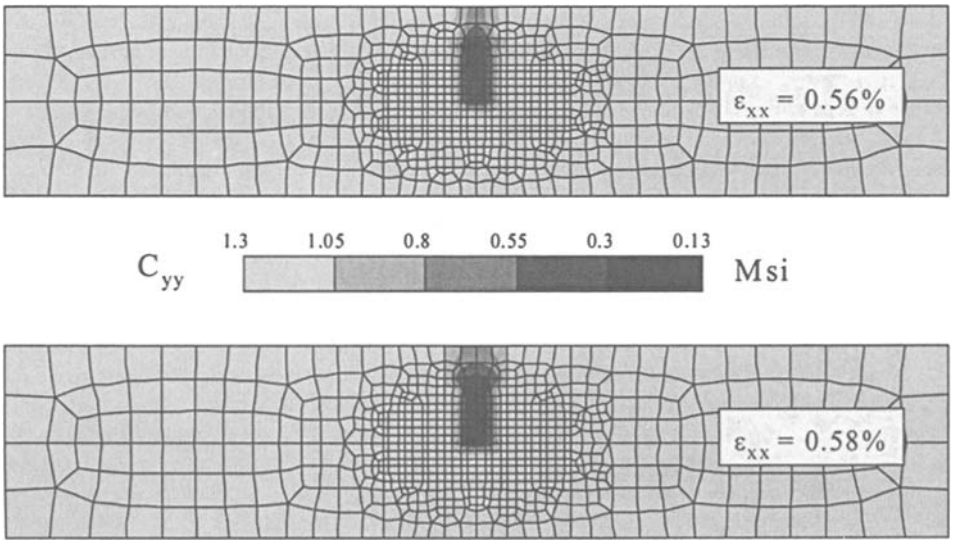


FIG. 11*b*—*Elastic constant* C_{yy} *before and after observed jump in dissipated energy. Darker regions indicate reduced stiffness.*

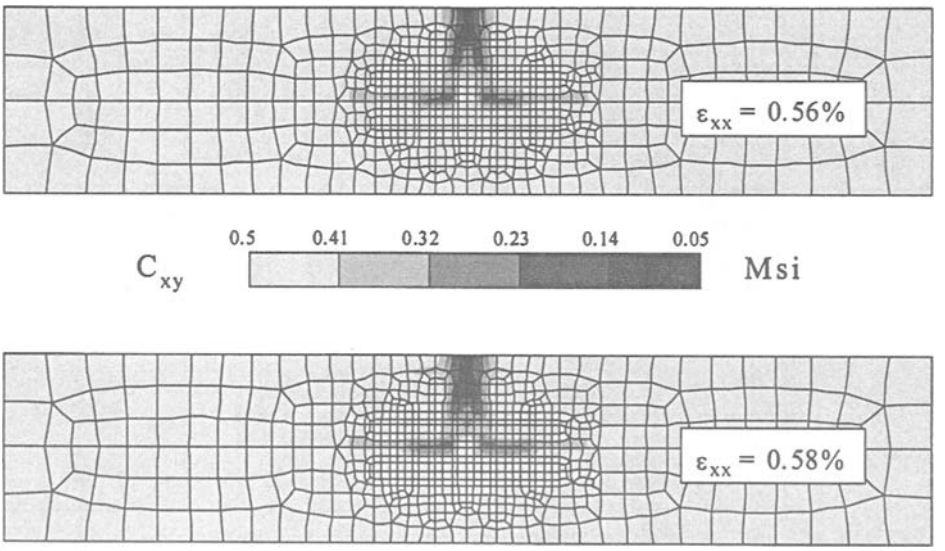


FIG. 11*c*—*Elastic constant* C_{xy} *before and after observed jump in dissipated energy. Darker regions indicate reduced stiffness.*

For each case studied, strain energies stored and dissipated during each load increment were computed using a computer program that is linked with the ABAQUS results database. These quantities are plotted versus load to identify two important load levels, viz. a value of load below which no significant matrix damage is expected and values below which no fiber dominated failure is expected. Figure 12 shows the ratio of total unrecoverable energy to recoverable strain energy versus applied strain. For lower strains, the composite with marcel M2 contain a higher fraction of dissipated energy than the composite with marcel M1. A more significant rise in this ratio is found for events labeled A and B in Fig. 10. This is exactly the result desired from a damage measure, because these events are associated with fiber failures that will significantly affect the residual strength and stiffness of the composite.

The analysis results indicate that significant subcritical[8] matrix damage is likely to occur in specimens with marcel defects under what would normally be considered low levels of tensile loading (<0.3% strain). As expected, matrix damage (*yy* and *xy* shear directions) is generally greater in the specimens with the more severe marcel (i.e., greater h_0/ℓ). The micromechanics based failure analyses yield physically intuitive results for the macroscopic behavior of the material; gradual changes in the stress-strain curves are due to matrix shear failure while sudden drops in load are due to fiber failure. Results of these analyses and basic interlaminar tension and shear strength data were used to set load levels that are expected to cause various levels of subcritical damage near marcel defects under tension-tension fatigue cycling. Subcritical matrix damage is expected to affect both the residual tension and compression strength, but to different degrees. Finally, these analyses also showed that the magnitude of energy released during an increment of loading depends on both the failure mode and volume of material failing. Each of these quantities depends upon both the marcel shape and inherent material strengths. This information suggests that recording acoustic emission during testing may be useful in defining load levels at which different types of subcritical damages occur.

[8] The term subcritical is used here to characterize a failure that causes damage to the material that may not be observable at the macroscopic level; i.e., the gross fiber-dominated stress-strain response is largely unaffected.

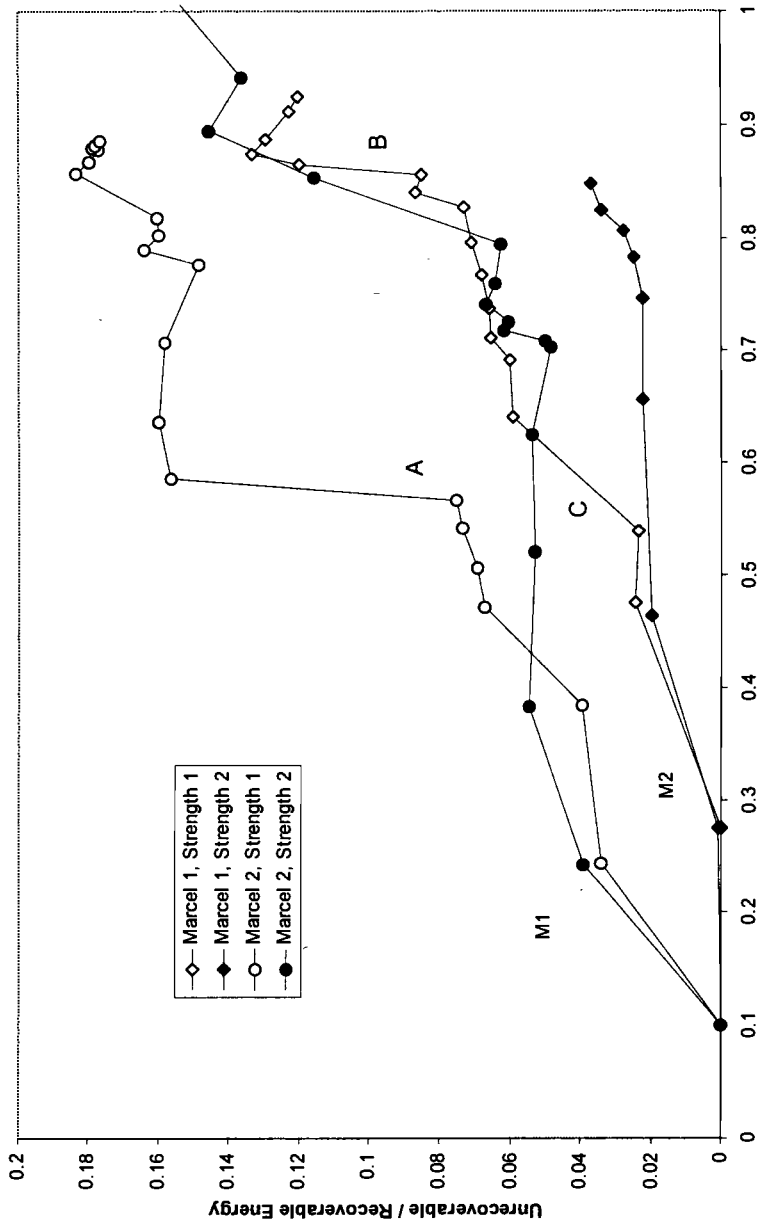


FIG. 12—*Analysis results for ratio of unrecoverable energy to recoverable strain energy for all four marcel patterns under displacement controlled tensile load.*

Experimental Program

Key elements of an experimental program to measure the effects marcel defects have on composite structural properties and provide critical data for validation of the modeling approach are summarized here. The primary material of interest in this study is Hexcel IM7/8552 unidirectional tape. This material consists of Hercules IM7 intermediate modulus carbon fibers in a 350°F cure, thermoplastic toughened epoxy resin designated 8552.

Compression Coupon Geometry Trade-Off Studies

Fabrication of samples containing marcels of the desired geometries required coupons with nonstandard thickness (t) and gage length (g) relative to SACMA 1R-94 [*13*] (t = 0.040 in. [0.1016 cm] nom., g = 0.188 in. [0.47752 cm]). In order to assess the effects of thickness and gage section on the compressive strength measurements, a series of trade-off studies was conducted. Due to the limited supply of IM7/8552 available, the trade-off studies were conducted using a similar unidirectional prepreg material (Fiberite IM7/977-2). Coupons with a constant gage length (0.188 in.) were fabricated with thicknesses of 0.057, 0.113, and 0.227 in. Coupons with a constant thickness (0.227 in.) were fabricated with gage lengths of 0.188, 0.350, and 0.500 in. None of the coupons contained marcel defects.

Results of the compression tests on the coupons with varying thickness are presented in Table 4. The results show increasing mean compression strength with decreasing thickness. However, the scatter in the data also increases with decreasing thickness, resulting in similar (within 5%) B-basis strengths for the full range of thicknesses considered. Results of the compression tests on the coupons with varying gage length are presented in Table 5. The results show minimal (less than 10%) effects of gage length on the mean compression strength for the range from 0.188 to 0.500 in. However, scatter is reduced significantly for the 0.188 in. gage length, resulting in a higher (approximately 10%) B-basis value. Based on the results of the trade-off studies, samples containing marcels were fabricated with a thickness of 0.227 in. and a gage length of 0.5 in. Details of fabrication of coupons containing marcel defects are provided in the next section.

Test Coupon Fabrication

Once the coupon geometry was finalized, five IM7/8552 panels measuring 6 × 12 in. were fabricated. The layup of the panels was $[(0_2/90_2)_4/0]_s$ with the 6 in. dimension oriented at 0°. Four panels contained marcels extending the full length of the panel (12 in. dimension) along the panel centerline. The fifth panel was fabricated without a marcel as a control. Of the four panels containing marcels, three contained "edge" marcels located two plies in from one surface, while the fourth contained a "center" marcel located ten plies in from one surface. Specific geometric parameters (length and height) are summarized in Table 6.

TABLE 4—*Effect of thickness on compressive strength. (Material: IM7/977-2T, Method: SACMA 1R-94, Gage Length: 0.188 in.).*

Thickness in.	Layup	Compressive Strength, ksi	
		Mean ± STD	B-Basis
0.227	$[(0_2/90_2)_4/0]_s$	112.33 ± 1.71	106.90
0.113	$[(0_2/90_2)_2/0/(90_2/0_2)_2]$	132.21 ± 7.36	112.37
0.057	$[(0/90)_2/0/(90/0)_2]$	154.99 ± 13.27	113.88

NOTE—Unless otherwise noted, all statistics are computed for normal distributions.

TABLE 5—*Effect of gage length on compressive strength. (Material: IM7/977-2T, Method: SACMA 1R-94, Thickness: 0.227 in.).*

Gage Length in.	Layup	Compressive Strength, ksi	
		Mean ± STD	B-Basis
0.188	$[(0_2/90_2)_4/0]_s$	112.33 ± 1.71	106.90
0.350	$[(0_2/90_2)_4/0]_s$	107.23 ± 3.48	97.40
0.500	$[(0_2/90_2)_4/0]_s$	104.12 ± 3.45	94.38

NOTE—Unless otherwise noted, all statistics are computed for normal distributions.

The general fabrication procedure for panels containing marcels is summarized in Fig. 13. The first 32 plies (for edge marcels) or 24 plies (for center marcels) are laid up on a flat surface. The plies are transferred to a tool with a 0.108 in. (small marcel) or 0.168 in. (large marcel) spar. The 0° orientation is aligned normal to the spar with two 0° plies on top and two 90° plies on the bottom (against the spar). A single layer of nonporous release film is placed between the plies and the tool. The plies are covered with a second layer of nonporous release film, followed by a 0.062-in.-thick silicone rubber flexible caul. A thermocouple is inserted in the edge of the laminate. The assembly is then placed in a laminating press and subjected to the following debulk cycle: (1) heat to 150°F (66°C) at contact pressure, (2) apply 50 psi (345 kPa) and hold for 10 min, (3) cool to 80°F (27°C), and (4) remove pressure. After debulk, the remaining plies (0_2 for edge marcels or $0_2/90_2/0_2/90_2/0_2$ for center marcels) are laid up over the depression formed in the debulked laminate by the spar. The depression is filled with small strips of prepreg oriented at 90° prior to applying the final plies. After application of the final plies, the panel is transferred to a flat tooling plate. Nonporous release film, two plies of 2.75 oz/yd^2 polyester bleeder, and porous Teflon™ (trifluoroethylene) release are laid up initially, followed by the panel, porous Teflon release, two more plies of 2.75 oz/yd^2 polyester bleeder and nonporous release film. Next, the edges of the panel are sealed with air dam (except for braided glass breather strands at the corners), an aluminum caul plate is placed over the assembly followed by a single layer of Super 10 heavy breather, and a vacuum bag is sealed to the tooling plate with bag tape. The panel is cured in an autoclave for 130 min at 355°F and 100 psi.

After cure, the panels were rough machined and prepared for tab bonding. Tabs were prepared using 0.110-in.-thick panels fabricated from T300/934 prepreg fabric with a $[0]_8$ layup. The tabs were bonded using Cytec FM-87 film adhesive autoclave cured for 2 h at 50 psi. This adhesive has been shown to provide bond strengths in excess of 5000 psi with T300/934 and IM7/977-2 adherends. During bonding, great care was taken to ensure that the marcel was located in the center of the gage section. A typical tabbed specimen is shown in Fig. 14.

TABLE 6—*Geometric parameters for marcel geometries.*

Designation	Height, in.	Length 21, in.
Small edge (SE)	0.060 ± 0.009	0.169 ± 0.007
Large edge #1 (LE1)	0.081 ± 0.005	0.223 ± 0.006
Large edge #2 (LE2)	0.077 ± 0.005	0.319 ± 0.021
Small center (SC1)	0.057 ± 0.007	0.235 ± 0.022

NOTE—Unless otherwise noted, all statistics are computed for normal distributions.

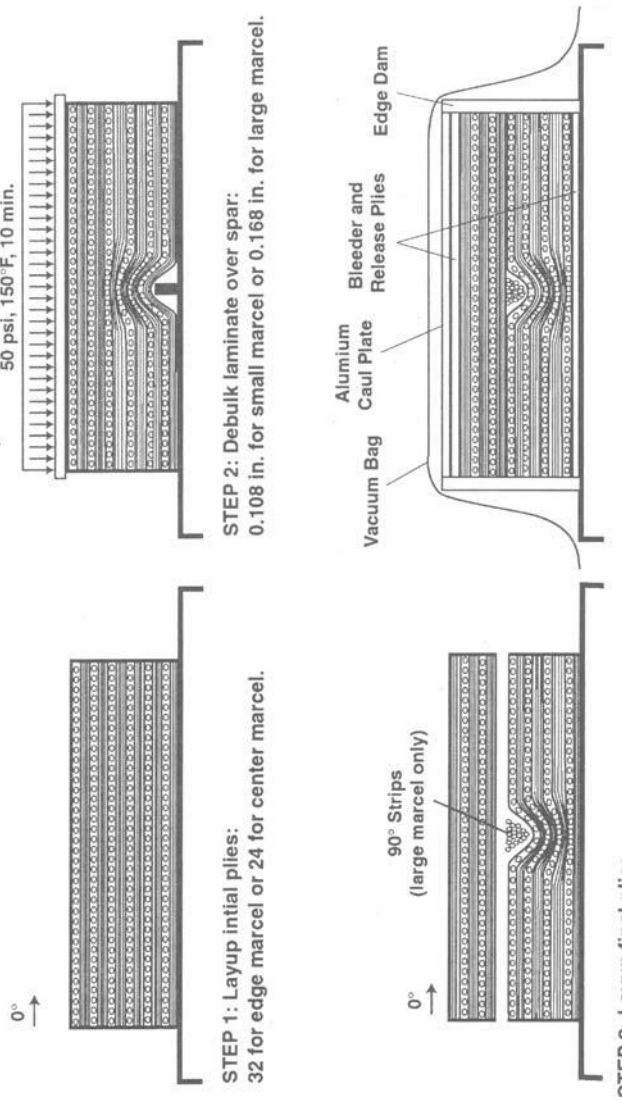


FIG. 13—*Fabrication procedure for panels containing marcel defects.*

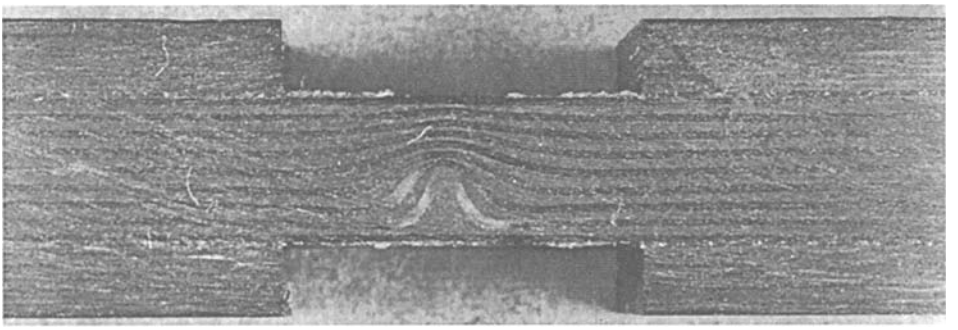


FIG. 14—*Typical tabbed test coupon with edge marcel.*

In addition to the 6 × 12 in., $[(0_2/90_2)_4/0]_s$ panels described above, a 24 × 24 in., $[(0_2/90_2)_2]_s$ panel (no marcels) was fabricated to permit generation of static tensile and tension-tension fatigue data for the IM7/8552 material. The panel was vacuum bagged and autoclave cured as described previously, however, a single bleeder ply was used on each face of the laminate during cure. Straight-sided, tabbed tensile specimens measuring 10 × 1 in. were prepared in accordance with SACMA 4R-94 [*13*] guidelines. Tab bonding was accomplished with FM-87 film adhesive as described previously.

Mechanical Testing and Results

Tensile strength and modulus measurements were performed on specimens without marcel defects using an Instron 4206 screw-actuated test frame. The tests were conducted in accordance with SACMA 4R-94 [*13*] guidelines for testing rate, procedures and data analysis. An axial bonded strain gage (Measurements Group CEA-06-500UW-350) was applied at the center of the gage section of each coupon using Measurements Group M-Bond 200 adhesive. A broad band (100 kHz–1 MHz) transducer was attached to each coupon to monitor acoustic emission. A typical tensile stress versus strain curve for IM7/8552 $[(0_2/90_2)_2]_s$ (no marcel) is provided in Fig. 15.

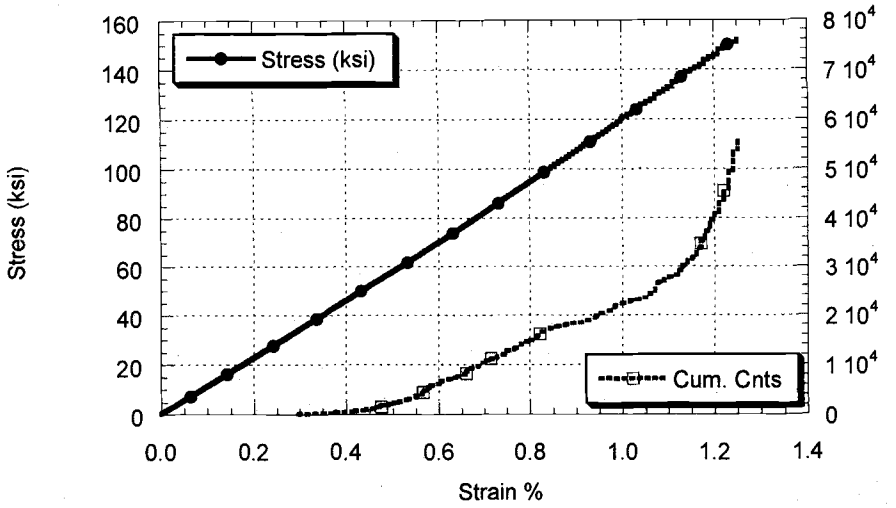


FIG. 15—*Typical static tensile stress-strain response and cumulative acoustic emission for specimen without a marcel.*

TABLE 7—*Static tensile data. (Material: IM7/8552 [$(0_2/90_2)_s$, Specimen: Tensile, Marcel: None)*

	Mean ± St. Dev.	B-Basis
Tensile strength, ksi	168.7 ± 8.8	135.8
Tensile modulus—chord: 0.1 to 0.3%, Msi	11.9 ± 0.4	N/A
Failure strain, %	1.292 ± 0.086	0.975

NOTE—Unless otherwise noted, all statistics are computed for Weibull distributions.

Cumulative acoustic emission versus strain is plotted on the same graph. This data was used to define the in-situ transverse tensile strength of the material. Static tensile data are summarized in Table 7.

Tension-tension fatigue tests were performed on selected tabbed compression coupons containing marcels to induce subcritical damage. The edges of all fatigue specimens were surface ground with a water-cooled 46 grit Al_2O_3 wheel to remove machining marks and inhibit initiation of edge delaminations. The fatigue tests were performed on an Instron 8500 servo-hydraulic test frame with Wavemaker software for monitoring load and displacement during the test. A broad band (100 kHz–1 MHz) transducer was attached to each coupon to monitor acoustic emission. The tests were conducted in load-control at an R-value ($\sigma_{min}/\sigma_{max}$) of 0.1 and a cyclic rate of 10 Hz. Forced air was directed at the center of the gage length to prevent hysteretic heating. Displacement amplitude and cumulative acoustic emission (AE) versus cycle count data for a typical tensile specimen with a large edge marcel is provided in Fig. 16. Both cumulative AE and dis-

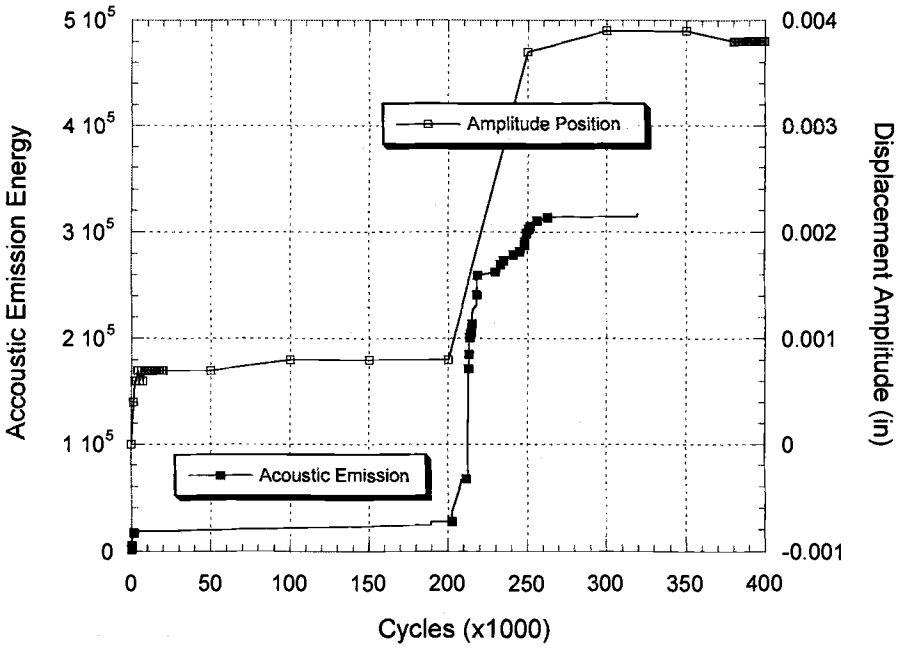


FIG. 16—*Stiffness and acoustic emission energy vs. cycle count for a large-edge marcel specimen subjected to 40 ksi tension-tension fatigue testing for 400 000 cycles.*

placement amplitudes increase at similar cycle counts. If it is assumed that displacement amplitude increase results from damage (stiffness reduction), this data indicates that AE can be a useful tool for monitoring damage initiation and growth when a simple stiffness measure is unavailable. Displacement amplitude changes under cyclic loading for three marcels are shown in Fig. 17. Note that the amount of stiffness degradation under load-control $R = 0.1$ tension cycling varies with marcel geometry.

Compression tests were conducted on IM7/8552 $[(0_2/90_2)_4/0]_s$ coupons with and without marcels. Residual compression tests were conducted on IM7/8552 $[(0_2/90_2)_4/0]_s$ coupons with marcels following tension-tension fatigue to prescribed cycle counts. Compressive strength measurements were performed on an Instron 4206 screw-actuated test frame using a Boeing-modified ASTM D 695 compression test fixture. The tests were conducted in accordance with SACMA 1R-94 guidelines for testing rate, procedures and data analysis. Back-to-back axial bonded strain gages (Measurements Group CEA-06-125UW-350) were applied using Measurements Group M-Bond 200 adhesive. For coupons containing a marcel, the strain gages were aligned with the apex of the marcel. A broad band (100 kHz - 1 MHz) transducer was attached to each coupon to monitor acoustic emission. Typical compressive stress versus strain curves for IM7/8552 $[(0_2/90_2)_4/0]_s$ coupons in the as-processed and post-fatigue condition with a large edge and small center marcel are provided in Figs. 18 and 19. The strain data from the back-to-back gages (i.e., at the apex and mouth of the marcel), and their averages, are plotted for each coupon. All compressive strength data are summarized in Table 8.

A limited number of residual tension tests were conducted on IM7/8552 $[(0_2/90_2)_4/0]_s$ coupons

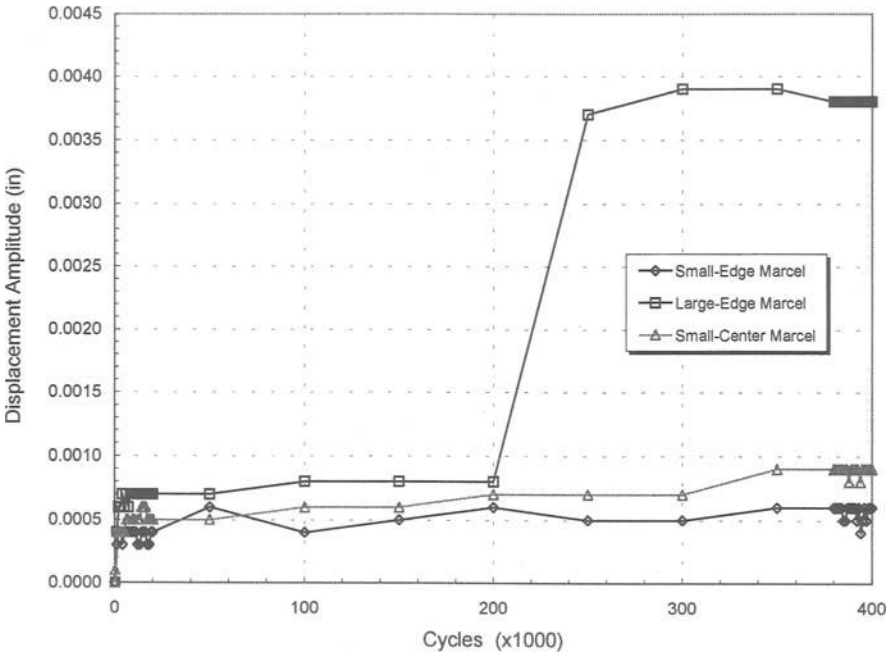


FIG. 17—*Stiffness degradation vs. cycle count for specimens with marcel sizes and locations subjected to 40 ksi tension-tension fatigue* (R = *0.1) testing.*

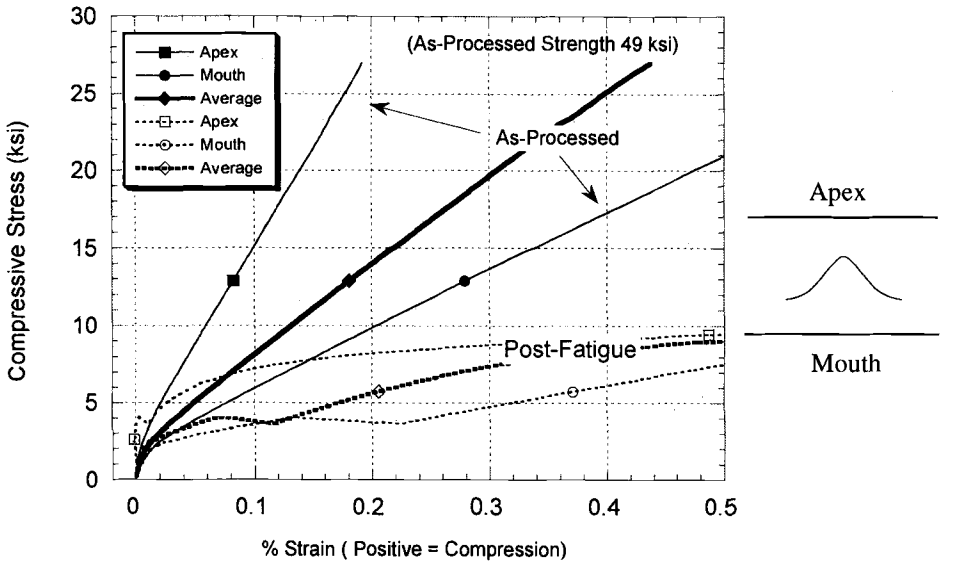


FIG. 18—*Stress vs. strain for specimens with a large-edge marcel comparing as-processed strength to post-fatigue strength following 400 000 cycles of 40 ksi tension-tension fatigue* (R = *0.1*) *loading.*

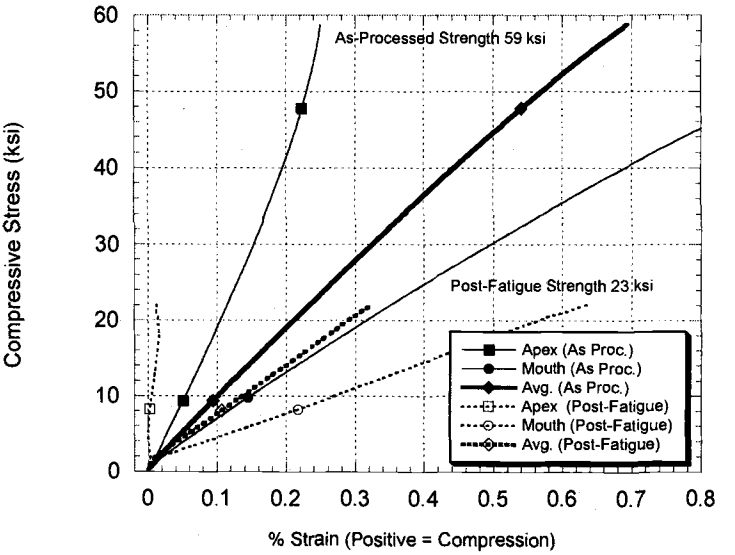


FIG. 19—*Stress vs. strain for specimens with a small-center marcel comparing as-processed strength to post-fatigue strength following 400 000 cycles of 40 ksi tension-tension fatigue* (R = *0.1*) *loading.*

TABLE 8—*Compressive strength data for IM7/8552 $[(0_2/90_2)_4/0]_s$ coupons containing marcels.*

Marcel Geometry	Compressive Strength, ksi				
	As-Processed	Post-Fatigue: Tension-Tension; $R = 0.1$; 400 000 Cycles			
		$\sigma_{max} = 60$ ksi	$\sigma_{max} = 40$ ksi	$\sigma_{max} = 30$ ksi	$\sigma_{max} = 20$ ksi
None	New Panel	...	...	...	...
Small edge (SE)	49.1 ± 2.7	$N_f = 1522$	20.0 ± 2.3	22.0 ± 2.0	41.0 ± 2.8
Large edge #1 (LE1)	49.8 ± 0.8	$N_f = 49$	15.5 ± 4.0	24.7 ± 3.4	40.4 ± 2.5
Large edge #2 (LE2)	48.0 ± 8.4	$N_f = 54$	23.1 ± 2.9	26.6 ± 4.1	41.0 ± 1.8
Small center (SC)	61.1 ± 5.3	16	24.8 ± 3.9	34.7 ± 6.5	55.3 ± 2.6

NOTES—(1) Unless otherwise noted, all statistics are computed for normal distributions.
(2) 60 ksi values represent a single coupon. All other data sets contain three coupons.
(3) N_f indicates cycles to failure during fatigue test.

with marcels following tension-tension fatigue to prescribed cycle counts. Typical tensile test data for a large edge and small center marcel are shown in Figs. 20 and 21. Compression results are shown for comparison. Examples of failed test specimens are shown in Fig. 22. All residual tensile strength data are summarized in Table 9.

Correlation of Analyses with Experimental Data and Discussion of Test Result

The analysis techniques described above were used to model the response of test specimens containing marcel defects. Due to space limitations, only a sampling of results is presented here.

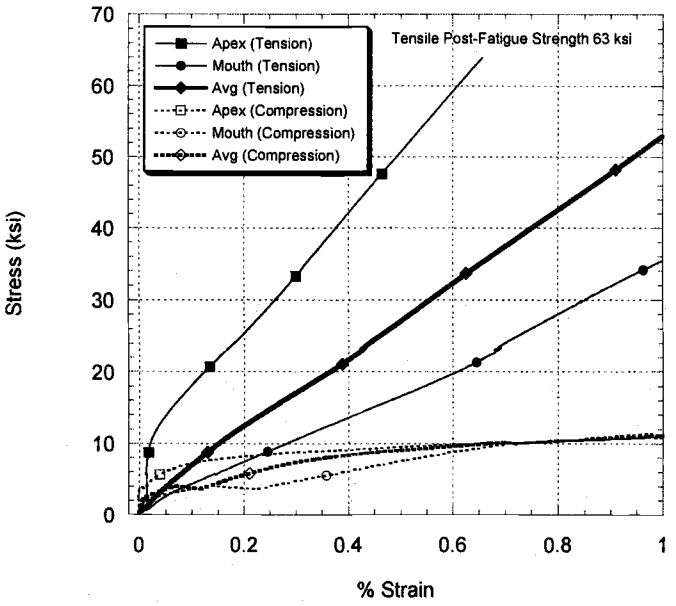


FIG. 20—*Stress vs. strain for specimens with a large-edge marcel comparing as-processed strength to post-fatigue strength following 400 000 cycles of 40 ksi tension-tension fatigue loading.*

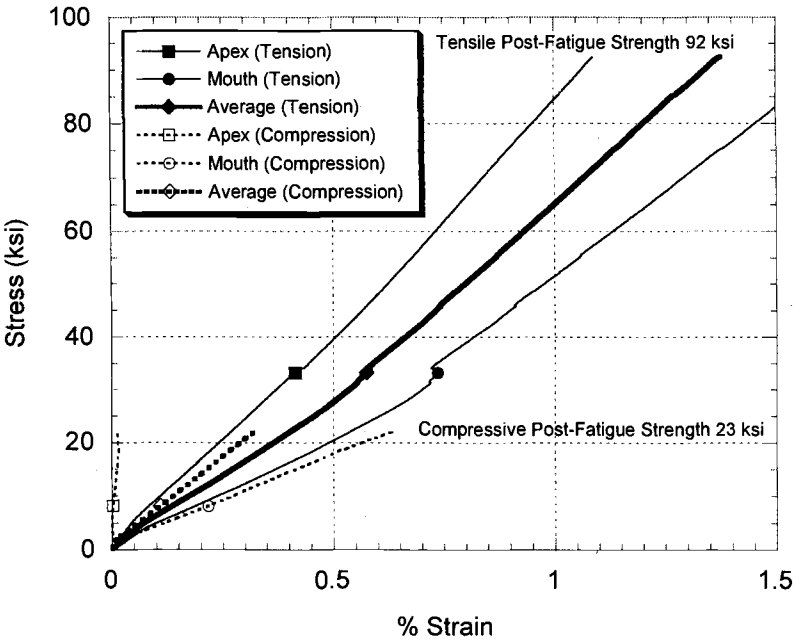


FIG. 21—*Stress vs. strain for post-fatigue tension and compressive strength testing on small-center marcel specimens that had been subjected to 40 ksi tension-tension fatigue (R = 0.1) loading for 400 000 cycles.*

Figure 23 shows average tensile stress (i.e., P/A) versus average strain (i.e., $\Delta L/L$) from analyses of the tabbed coupon specimen with the SC1 and LE2 marcel geometries listed in Table 6. The effects cyclic tensile loading has on residual properties were approximated in the analysis by reducing the "as-processed" interlaminar strengths by a factor of four, and the initial interlaminar moduli by a factor of two. The analysis indicates that the residual tensile strength of the coupon is almost unaffected

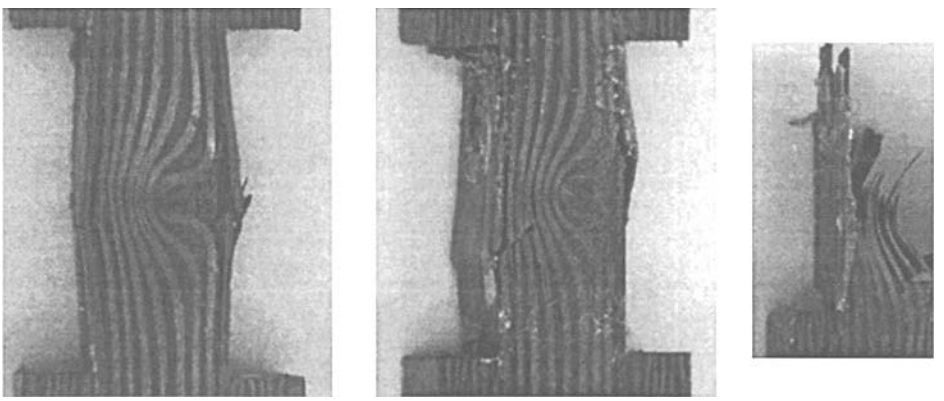


FIG. 22—*Typical failed compression specimens shown at left and middle, typical failed tensile specimen at right.*

TABLE 9—*Tensile strength data for IM7/8552 $[(0_2/90_2)_4/0]_s$ coupons containing marcels.*

Marcel Geometry	Tensile Strength, ksi				
	As-Processed	Post-Fatigue: Tension-Tension; $R = 0.1$; 400 000 Cycles			
		$\sigma_{max} = 60$ ksi	$\sigma_{max} = 40$ ksi	$\sigma_{max} = 30$ ksi	$\sigma_{max} = 20$ ksi
None	New Panel	...	...	...	...
Small edge (SE)	...	$N_f = 1522$	70.3 ± 4.2	...	...
Large edge #1 (LE1)	...	$N_f = 49$	66.4 ± 2.6	...	...
Large edge #2 (LE2)	...	$N_f = 54$	59.1 ± 5.4	...	...
Small center (SC)	...	...	93.2 ± 3.2	...	...

NOTES—(1) Unless otherwise noted, all statistics are computed for normal distributions.
(2) 60 ksi values represent a single coupon. All other data sets contain three coupons.
(3) N_f indicates cycles to failure during fatigue test.

by a fourfold reduction in interlaminar strength. The predicted ultimate residual strengths agree well (within 10%) with the mean measured values. Figure 24 shows average compressive stress versus strain for the same marcel defects. To approximate the effects subcritical damage induced by cyclic fatigue loading have on compressive strength, the matrix shear modulus and shear strength were reduced by a factor of four. The trend in the experimental data, i.e., that a marcel located at the midplane does not produce the same ultimate strength knockdown as a marcel located near the surface, is captured by the analysis. However, the analysis using the compression instability model described above overpredicts ultimate specimen failure by approximately 25%.

Initial (as-processed) and residual compressive strength after tension-tension fatigue cycling results were plotted versus key marcel geometry parameters (i.e., h_0, ℓ) in an attempt to identify trends in the data. Mean data, and the one standard deviation range, are shown in Figs. 25 through 27 for each of the cyclic stress levels tested. A clear trend as to which simple geometry descriptor (i.e., h_0/ℓ,

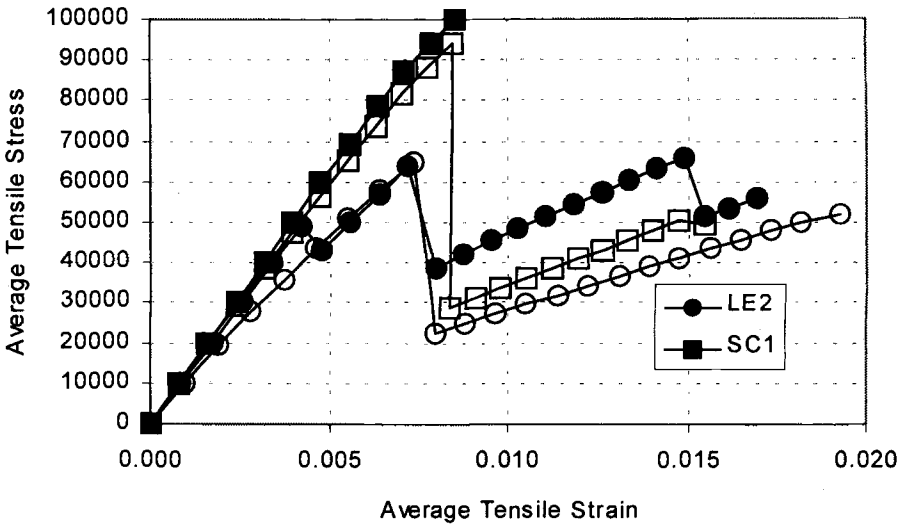


FIG. 23—*Analysis results for tabbed test specimens. Filled markers using as-processed properties, open markers using properties to approximate effects of cyclic tensile loading.*

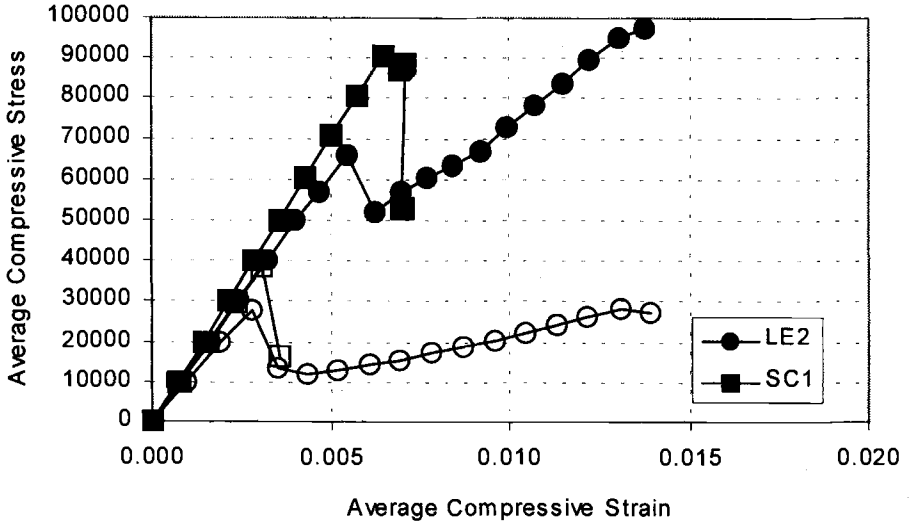


FIG. 24—*Analysis results for tabbed test specimens. Filled markers using as-processed properties, open markers using properties to approximate effects of cyclic tensile loading.*

h_0/t, $h_0 \cdot \ell$) can be used to identify a *worse case* defect was not found for the range of marcel sizes investigated. It is clear from these data that the residual strength decreased as the cyclic strain level increased. The limited data here clearly indicate that damage induced by cyclic tensile loading has a more significant affect on residual compressive strength than on residual tension strength. Note, however, that these data are for three replicates of each test only; therefore, no reliable statistical analysis can be conducted.

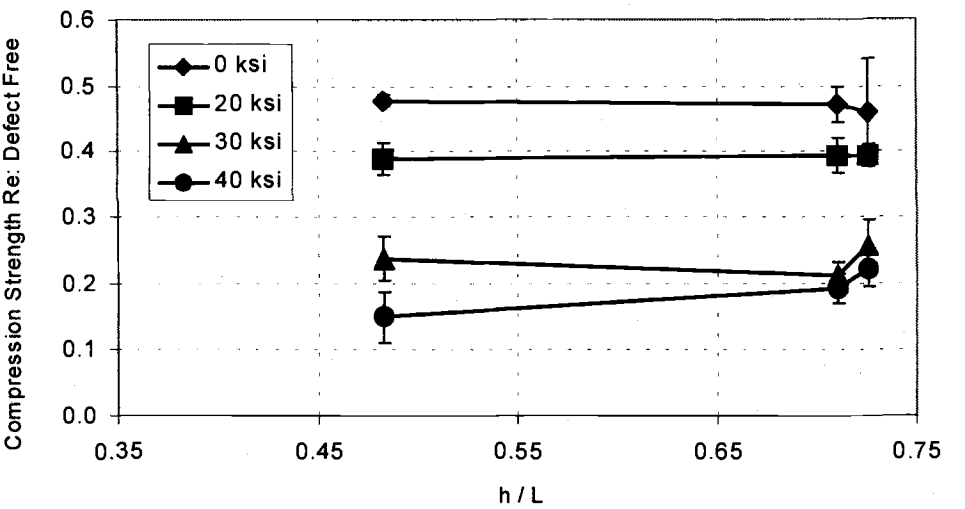


FIG. 25—*Measured compressive strength relative to the defect free compression strength after 400 000 cycles of* R = *0.1 tensile fatigue loading at indicated level plotted vs. marcel height relative to span length.*

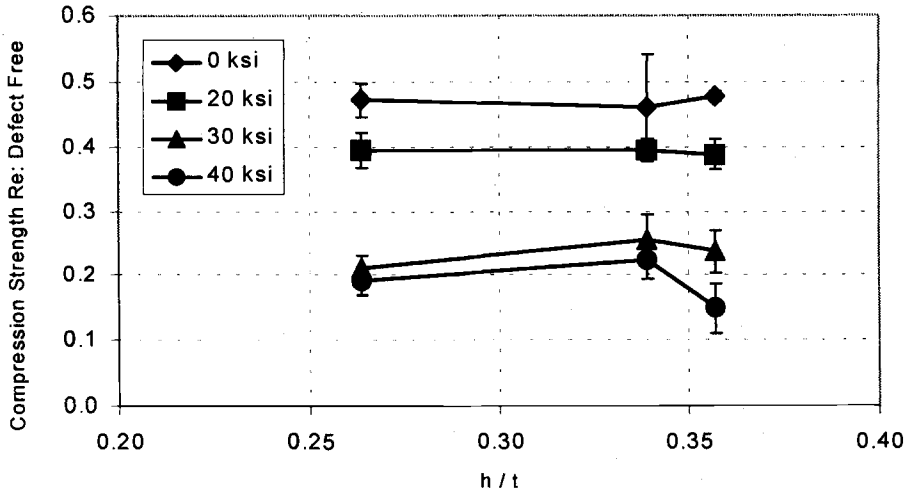


FIG. 26—*Measured compressive strength relative to the defect free compression strength after 400 000 cycles of* R = *0.1 tensile fatigue loading at indicated level plotted vs. marcel height relative to specimen thickness.*

Finally, the experimental data indicate that for a fixed value of load controlled tension-tension cycling, the amount of AE and displacement amplitude varied with marcel geometry. In a qualitative sense, this is consistent with the analyses that showed that the amount of material that sustains interlaminar damage depends on the magnitude of the applied load and marcel defect shape. No attempt was made to directly relate measured cumulative AE levels or displacement amplitude to predicted damage area or stiffness reduction. The predicted difference in the ratio of unrecoverable (i.e., dissipated) to recoverable strain energy in specimens exhibiting different failure modes suggests that this

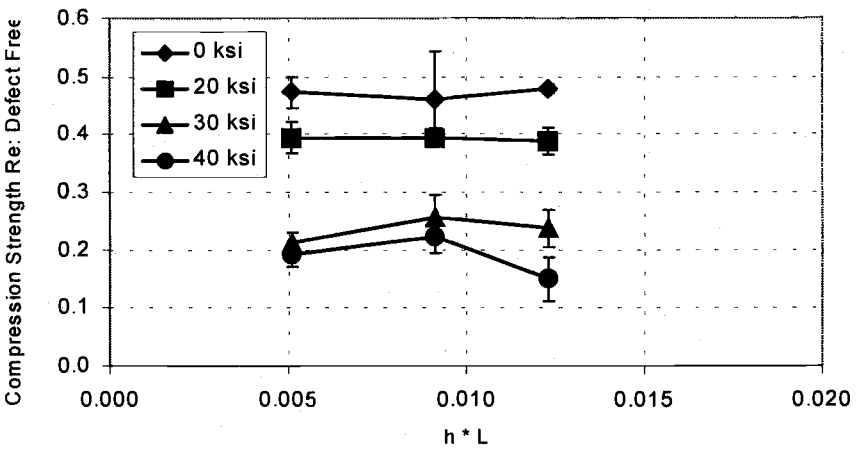


FIG. 27—*Measured compressive strength relative to the defect free compression strength after 400 000 cycles of* R = *0.1 tensile fatigue loading at indicated level plotted vs. volume of specimen with fiber waviness.*

measure may be useful to identify modes of unacceptable composite material damage. In future work, it would be useful to conduct a controlled study with the goal of correlating predictions of strain energy released as damage grows to measured acoustic emission and stiffness change.

Summary Remarks

The response of simple test specimens containing marcel defects and subjected to tension and compression loads has been modeled in this study. Analyses were conducted to predict the effects a marcel has on the local (elastic) stress state for a defect center positioned at the lower laminate surface and at the mid-thickness. Results indicate that the former produces the greatest interlaminar shear stress, while the latter produces higher fiber direction stresses but shear stress that are 20% lower than the surface marcel. Peak stresses were found to increase (not linearly) with increasing percentage of thickness that contains wavy layers.

Special purpose nonlinear constitutive models used to compare the predicted response of test specimens containing marcels of different severity have been compared. Analyses indicated that specimen stiffness degradation and the amount of strain energy stored and dissipated varies with marcel geometry. Results for two matrix strengths were compared to contrast the effect that different matrix failure modes have on average specimen response. Although a material with low interlaminar shear strength tends to accumulate more subcritical damage under monotonic loading, its ultimate tensile load carrying capacity and resistance to fiber failure is better than the matrix with low transverse tensile strength and higher shear strength. This is due to the fact that shear failure prohibits the load from being transferred to nearby fibers that are already highly stressed. The interlaminar failures serve to lessen the notch effect produced by the marcel, and more uniformly distribute the load throughout the cross section.

The experimental data and analysis results presented here show that important events observed at the macroscopic level (stiffness change and AE) can be related to different micro-failure modes. Sudden drops in stress during the monotonic tensile stress-strain history were predicted for marcel specimens with high interlaminar shear strength, while gradual stiffness degradation is predicted for specimens with low interlaminar strength. AE data taken during residual tension testing showed ranges of gradual accumulation and also discrete increases. Experimental results confirmed predictions that marcel defects will have little effect on the initial effective elastic modulus. This finding is important since it implies that a global analysis of the structure to identify high stress locations can be conducted without prior knowledge of defect locations.

For the range of marcel geometries studied, the measured static compression strength was reduced relative to the defect free strength by a factor of two. The data indicates that damage induced near the marcel by cyclic tensile loading has a more significant effect on residual compression strength than on residual tension strength. A marcel center located at the lower laminate surface produced a greater strength knock-down than a similar size defect at the laminate mid-plane.

Analyses also indicate that details of the marcel shape (i.e., polynomial fit order, exponential decay) need not be known to assess the affect a marcel defect has on ultimate strength (static or residual). Ultimate strength appears to be related to the fraction of thickness affected, and location of the marcel center through the thickness. This latter result is supported by experimental data. The defect shape plays a more important role in the amount of subcritical interlaminar damage produced by local stress field perturbation near the marcel. A marcel defect introduces interlaminar shear, and through-the-thickness normal stresses under in-plane loads. The sign (tension or compression) of the interlaminar normal stress, and therefore the amount of subcritical interlaminar damage and residual strength of the material, depends on the sign of the applied load. Clearly, then, any assessment of the severity of a marcel defect will depend on the defect-free stress state. Furthermore, these arguments lead to the conclusion that a marcel of a given size may be acceptable (i.e., not adversely effect structural performance) in an area where some combination of in-plane tension and interlaminar stresses

exist in the defect-free structure, while that same defect may be rejectable (i.e., require repair or part scrap) in an area of the structure subjected to pure compression loads.

References

[1] Adams, D. O. and Hyer, M. W., "Analysis of Layer Waviness in Flat Compression-Loaded Thermoplastic Composite Laminates," *Transactions of ASME—Journal of Engineering Materials and Technology* Vol. 118, January 1996, pp. 63–70.

[2] ABAQUS, A Finite Element Analysis Package, available from Hibbitt, Karlsson, and Sorensen, Inc., Pawtucket, RI.

[3] Hashin, Z. and Rosen, B., "The Elastic Moduli of Fiber Reinforced Materials," *Journal of Applied Mechanics,* Vol. 31, 1964, p. 223.

[4] Hashin, Z., "Theory of Fiber Reinforced Materials," NASA Contractor Report CR-1974, March 1972.

[5] Rosen, B. et al., "An Analysis Model for Spatially Oriented Fiber Composites," *Composite Materials: Testing and Design (Fourth Conference), ASTM STP 617,* 1977.

[6] Bradley, D. J., Adams, D. O., and Gascoigne, H. E., "Interlaminar Strains in Compression-loaded Composite Laminates Due to Layer Waviness," SEM, Spring Conference on Experimental Mechanics, Baltimore, MD, Society for Experimental Mechanics, Inc., Bethel, CT, 1994.

[7] Bogetti, T. A., Gillespie, J. W., and Lamontia, M. A., "Influence of Ply Waviness on the Stiffness and Strength Reduction on Composite Laminates," *Journal of Thermoplastic Composite Materials,* Vol. 5, No. 4, Oct. 1992, pp. 344–369.

[8] Telegadas, H. K. and Hyer, M. W., "The Influence of Layer Waviness on the Stress State and Failure in Composite Laminates," AIAA/ASME/ASCE/AHS/ASC Structures, 32nd Structural Dynamics and Materials Conference, Baltimore, MD, American Institute of Aeronautics and Astronautics, 1991, pp. 1204–1213.

[9] Rosen, B. W., "Mechanics of Composite Strengthening," *Fiber Composite Materials,* American Society for Metals, 1964.

[10] Rosen, B. W., "Failure of Fiber Composite Laminates," In: *Mechanics of Composite Materials—Recent Advances,* Zvi Hashin and Carl Herakovich, eds., Pergamon Press, New York, 1982.

[11] Christensen, R. M., *Mechanics of Composite Materials,* Wiley, New York, 1979.

[12] Hashin, Z., "Failure Criteria for Unidirectional Fiber Composites," *Journal of Applied Mechanics,* Vol. 47, 1980, pp. 329–334.

[13] Suppliers of Advanced Composite Materials Association.

Gretchen B. Murri[1]

Influence of Ply Waviness on Fatigue Life of Tapered Composite Flexbeam Laminates

REFERENCE: Murri, G. B., **"Influence of Ply Waviness on Fatigue Life of Tapered Composite Flexbeam Laminates,"** *Composite Structures: Theory and Practice, ASTM STP 1383,* P. Grant, and C. Q. Rousseau, Eds., American Society for Testing and Materials, West Conshohocken, PA, 2000. pp. 188–209.

ABSTRACT: Nonlinear tapered flexbeam laminates, with significant ply waviness, were cut from a full-size composite rotor hub flexbeam. The specimens were tested under combined axial tension and cyclic bending loads. All of the specimens had wavy plies through the center and near the surfaces (termed marcelled areas), although for some of the specimens the surface marcels were very obvious, and for others they were much smaller. The specimens failed by first developing cracks through the marcels at the surfaces, and then delaminations grew from those cracks, in both directions. Delamination failure occurred in these specimens at significantly shorter fatigue lives than similar specimens without waviness, tested in Ref *2*.

A 2-D finite-element model was developed which closely approximated the flexbeam geometry, boundary conditions, and loading. In addition, the FE model duplicated the waviness observed in one of the test specimens. The model was analyzed using a geometrically nonlinear FE code. Modifications were made to the original model to reduce the amplitude of the marcels near the surfaces. The analysis was repeated for each modification. Comparisons of the interlaminar normal stresses, σ_n, in the various models showed that under combined axial-tension and cyclic-bending loading, for marcels of the same aspect ratio, σ_n stresses increased as the distance along the taper, from thick to thin end, increased. For marcels of the same aspect ratio and at the same X-location along the taper, σ_n stresses decreased as the distance from the surface into the flexbeam interior increased. A technique was presented for determining the smallest acceptable marcel aspect ratio at various locations in the flexbeam.

KEYWORDS: marcel, ply waviness, delamination, finite element, flexbeam

Nomenclature

E_{11}, E_{22}	Young's moduli in the 1- and 2-directions, GPa
G_{12}	Shear modulus, GPa
L	Period of one marcel, mm
N	Number of loading cycles
P	Axial tension load, kN
$t(x)$	Flexbeam half-thickness at distance x from fixed end, mm
V	Transverse bending load, kN
v	Transverse displacement at tip of flexbeam, mm
$\bar{y}$	Vertical distance from flexbeam surface, mm
α	Waviness half-amplitude, mm
δ	Transverse stroke of ATB test machine, mm
ε	Flexbeam surface strain
ε_{max}	Maximum cyclic surface strain
σ_n	Interlaminar normal stress in FE model, MPa
ν_{12}	Poisson's ratio

[1] Research engineer, U.S. Army Research Laboratory, Vehicle Technology Directorate, MS 188E, NASA Langley Research Center, Hampton, VA 23681.

Copyright© 2001by ASTM International www.astm.org

Tapered laminated composite flexbeams are used in helicopter rotor hubs to reduce weight, drag, and the number of parts in the hub. The taper in these flexbeams is achieved by terminating internal plies along the length. However, the manufacturing procedures required by these flexbeams can sometimes cause significant ply waviness throughout the tapered section of the flexbeam.

In this paper the term *marcel* is used to describe an area where there is a sudden change in the ply direction, similar to a wrinkle in the ply. Because the manufacturing processes cannot always completely eliminate these marcels, the effect of this waviness on the flexbeam durability needs to be determined. Also, such a study on marcelling in flexbeams may be used to develop accept/reject criteria for these flexbeams.

In Ref *1*, the effect of ply waviness on pull-off loads in composite hat stringer specimens was studied using the finite-element method (FEM). Waviness was simulated in the FE model by an incline in the ply at the initial delamination location. Five different ply waviness angles were studied and the results showed that even mild amounts of waviness could result in significant reduction in stringer pull-off loads.

Reference *2* describes a method for determining the fatigue life of tapered composite flexbeam laminates. In that study, 25.4 mm (1 in.) wide coupon specimens were cut from a full-size flexbeam of S2/E7T1 glass/epoxy. The specimens were tested under combined axial tension and transverse bending loading in a servo-hydraulic load frame, called the axial-tension bending (ATB) machine [*2*], using a frequency of 3 Hz and fully-reversed loading ($R = -1$). Under fatigue loading, delaminations typically initiated in the areas around the ply-drop locations and grew in both directions along the length. Typical fatigue lives were 10^5 to 10^7 cycles.

In the current study, flexbeams of the same geometry, layup, and material, but with significant ply waviness, were tested in an identical manner to those in Ref *2*. The location of the delamination initiation and the fatigue lives of the wavy flexbeams were studied. A parametric study was also conducted using a finite-element (FE) model of the tapered laminate to examine the effect of the severity of the ply waviness at a given location, and the effect of marcels of the same severity at different locations along the taper or through-the-thickness.

Experiments

Specimen Configuration

Test specimens for this study were cut from a full-scale test flexbeam, which was manufactured in a closed-cavity tool. The full-scale test flexbeam and the cut coupon specimens are shown in Fig. 1. The full-scale flexbeam was cut in half crosswise and then each section was cut lengthwise into 25.4 mm-wide coupons, yielding six test specimens. The coupons were symmetric with respect to layup and geometry and were designed with a nonlinear taper. The total number of plies in the laminates varied from 145 at the thick end, to 41 plies at the thin end. An idealized view (no waviness) of the cross section of the upper half of the flexbeam is shown in Fig. 2. This figure shows that the laminate had a woven fabric layer on the surface, four continuous "belt" sections, each four plies thick,

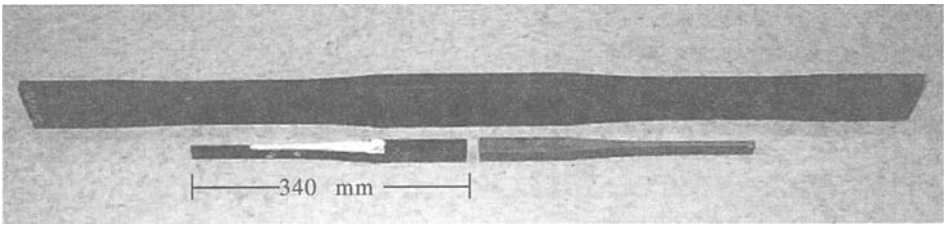


FIG. 1—*Full-scale flexbeam and coupon test specimens.*

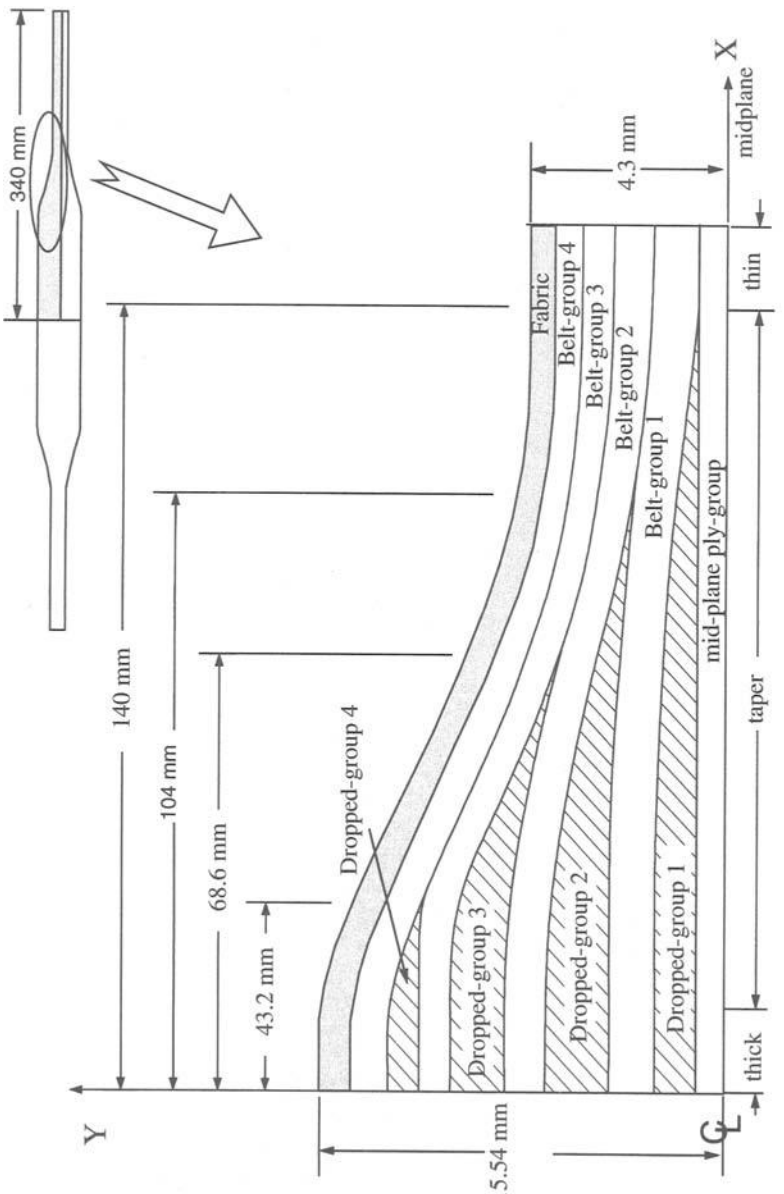


FIG. 2—*Schematic of flexbeam specimen with ply-group labels.*

TABLE 1—*Material properties.*

Material	E_{11}, GPa	E_{22}, GPa	G_{12}, GPa	ν_{12}
S2/E7T1 tape	47.6	12.6	4.81	0.28
E-glass/E7T1-2 fabric	25.3	24.1	4.56	0.153
Steel	201	201	77.3	0.30
Neat resin [2]	4.10	4.10	1.54	0.33

and four "dropped-ply" groups on each side of the midplane. At the midplane was a symmetric ply-group, which was five plies thick. Each dropped-ply group had a maximum thickness of 13 plies at the thick end. The dropped plies were arranged in a nonuniform, staggered manner. The woven fabric on the surface was E-glass/E7T1-2 and the interior plies were of S2/E7T1 tape. Properties for both materials are given in Table 1. The layups and material properties for each ply group shown in the figure are given in Table 2.

Although all six specimens were cut from the same full-size flexbeam, the degree of waviness, and locations of the wavy areas, varied from specimen to specimen. Specimens 1–3, cut from one side of the flexbeam, had considerably more waviness than specimens 4–6, cut from the other side. The ply waviness appeared as isolated areas of marcelling, and as waviness in the ply-groups at the center of the flexbeam. The waviness in the center ply-groups extended through most of the tapered region of the laminate, with the amplitude of the waves highest near the thick end, and gradually decreasing along the length. None of the specimens showed any waviness in the area of the laminate beyond the tip of dropped-group 2 in Fig. 2. An example of both types of wavy areas is shown in an edge view of specimen 1 in Fig. 3. The figure shows the waviness in the center ply-groups, and the enlarged photo shows two isolated areas of large amplitude marcels, one near each surface. The amount and type of waviness were fairly consistent on both sides of a given specimen, except for the large marcelled areas near the surfaces, which did not always appear on both sides.

Specimens 1–3, considered "severe" waviness, had waviness through the center ply-groups, as well as isolated areas near the surfaces where very large (high amplitude) marcels existed. Specimens 4–6, considered "moderate" waviness, had wavy plies through the center, but the waviness was of a lower amplitude than for specimens 1–3. Also, specimens 4–6 did not show the isolated areas of large marcels near the surfaces.

Figure 4 shows an edge view of specimen 2, which had several isolated areas of extreme waviness near the surface, shown in the enlarged photos, in addition to the waviness through the center ply-groups. (The circular white marks near the surfaces in the photos are paint marks that were used to position the strain gages.) Since specimen 2 had the most severe waviness of the six specimens, and since the waviness, including the isolated surface marcels, was identical on both sides, specimen 2 was chosen as the basis for the finite-element model. Specimen 3 was very similar to specimen 2, but did not have the marcel on the bottom surface in Fig. 4.

TABLE 2—*Ply-group layups and smeared properties.*

Ply Group	Layup	E_{xx}, GPa	E_{yy}, GPa	G_{xy}, GPa	ν_{xy}
Midplane	$[0_2/\overline{45}]_s$	41.1	13.7	6.32	0.34
Belt 1, 2, 4	$[0_4]$	47.6	12.6	4.81	0.28
Belt 3	$[\pm 45/0_2]$	31.6	15.6	9.19	0.33
Fabric	woven ± 45	25.3	24.1	4.56	0.153
Dropped 1–4	$[\pm 45]_n$	14.8	14.8	13.3	0.33

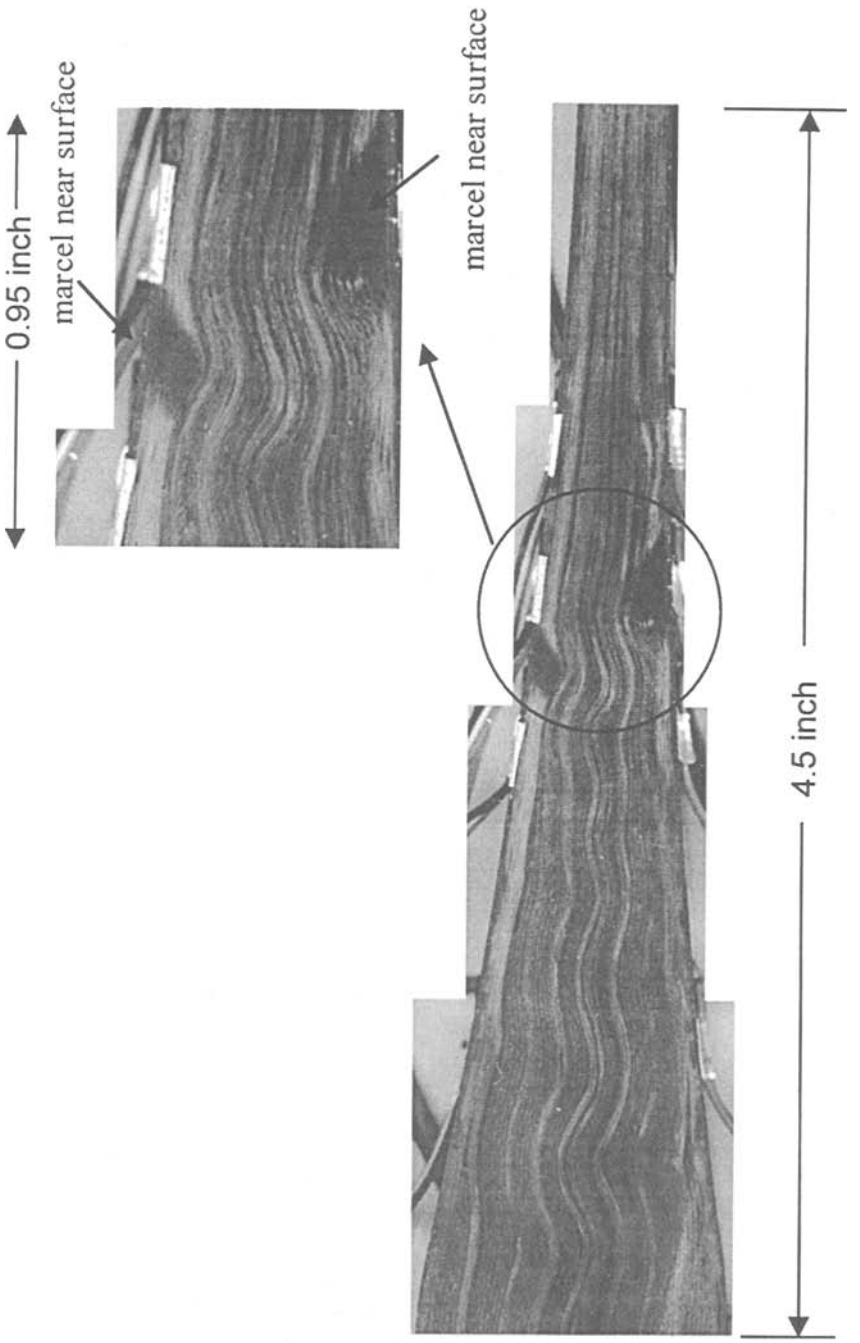


FIG. 3—*Specimen 1 with wavy plies.*

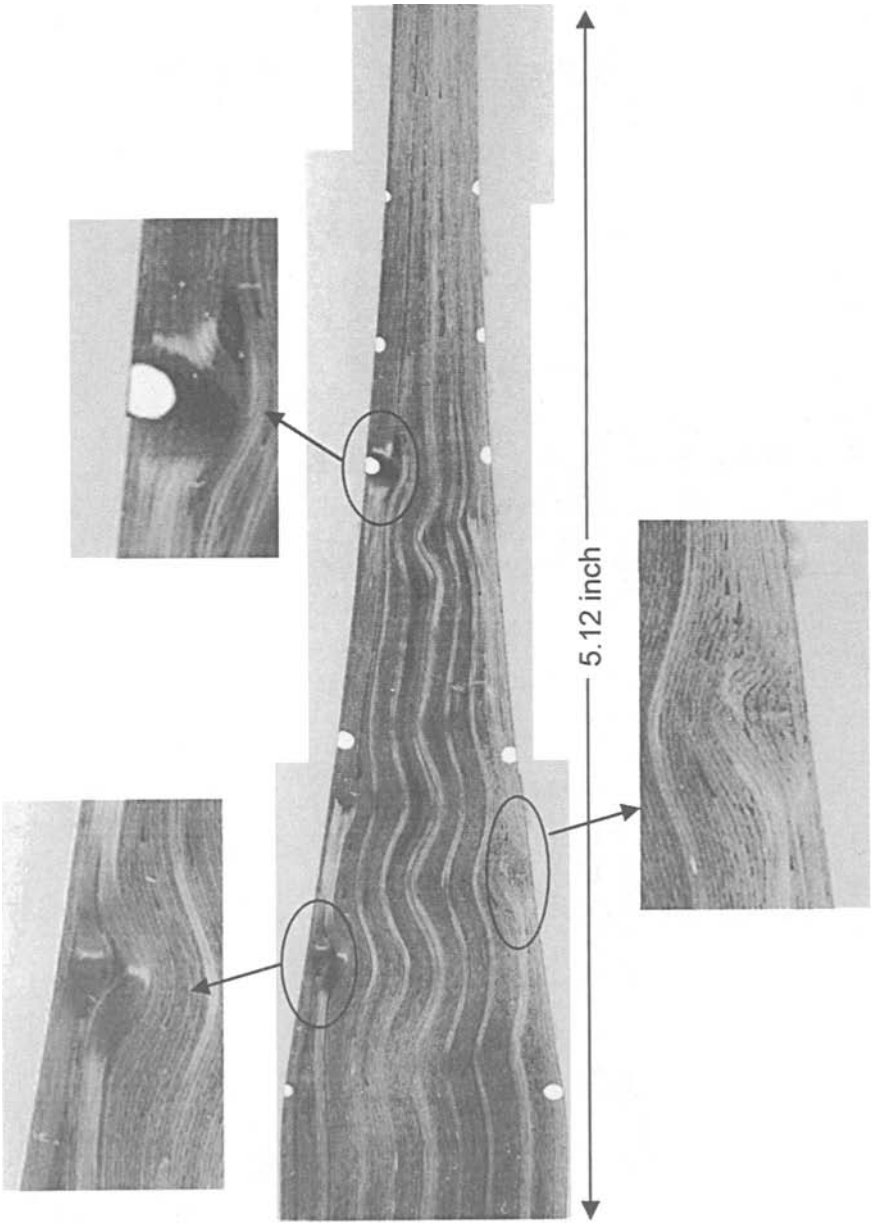


FIG. 4—*Specimen 2 with wavy plies.*

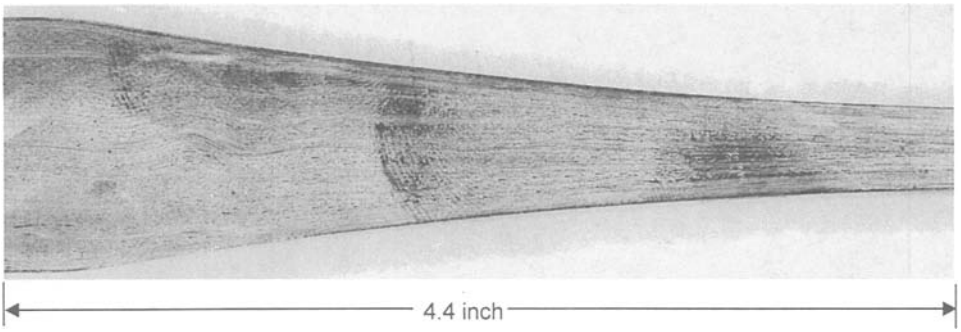
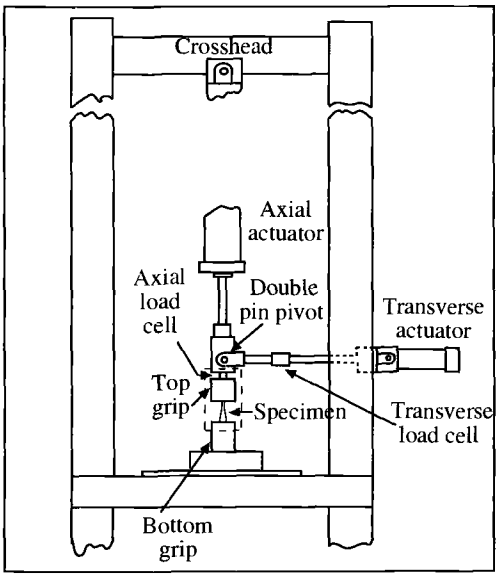


FIG. 5—*Specimen 4 with wavy plies.*

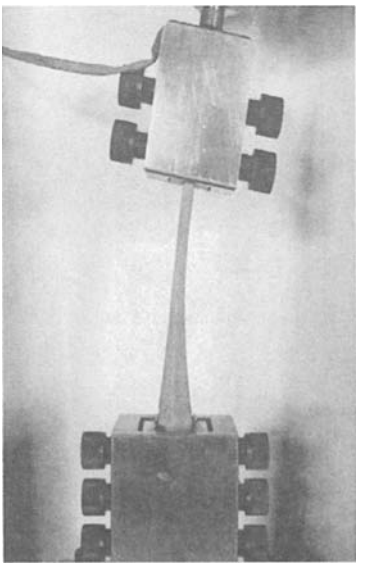
Figure 5 shows the edge of specimen 4. As the figure shows, the only evidence of ply-waviness in this specimen was in the center ply-groups near the thick end. Specimens 5 and 6 were similar to specimen 4.

Axial Tension Bending Machine

Specimens were tested under combined axial-tension and transverse-bending loading in the axial-tension bending (ATB) machine. The ATB, shown in Fig. 6, is a servo-hydraulic load frame, which produces combined tension-bending loading. As Fig. 6 shows, the axial load cell is located above the top grip, but below the pivot connecting the axial and transverse actuators. This allows the tension

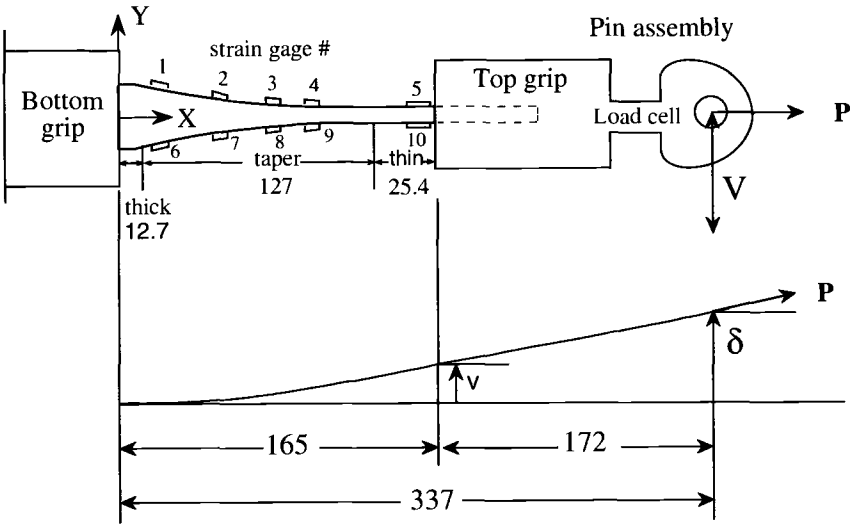


(a) schematic



(b) deformed specimen

FIG. 6—*Axial tension and bending test stand and deformed flexbeam.*



All dimensions in mm.

FIG. 7—*Test specimen and loading fixtures with combined loading.*

load to rotate with the specimen as the transverse load is applied. Hence, under axial load control, the magnitude of the tension load, P, remains constant as the specimen rotates under the transverse-bending displacement, δ. By controlling the axial tension actuator under load control and the transverse bending actuator under stroke control, a constant membrane load should be maintained throughout the loading cycle.

Static Tests

Initial static testing was conducted to determine the relationship between applied loads and the specimen deflection and surface strains. Specimens were first instrumented with strain gages at five locations along the length on each side: one near the junction of the thick and tapered regions (1 and 6), three along the tapered region (2–4 and 7–9), and one in the thin section (5 and 10). Figure 7 shows a schematic of the ATB and flexbeam, rotated 90° clockwise. The figure shows the numbered gages on each surface of the flexbeam and Table 3 lists their location in distance from the fixed end. The specimen was clamped in the grips with the thick end in the fixed bottom grip. The gage length between the grips was 165 mm (6.5 in.), and the specimen was placed in the grips so that within the gage section there was approximately a 12.7 mm (0.5 in.) thick region, a 127 mm (5 in.) tapered region and

TABLE 3—*Strain gage locations.*

Gage Number	Distance from Lower Grip, mm (in.)
1, 6	12.7 (0.5)
2, 7	53.3 (2.1)
3, 8	82.6 (3.25)
4, 9	98.5 (3.88)
5, 10	160.0 (6.3)

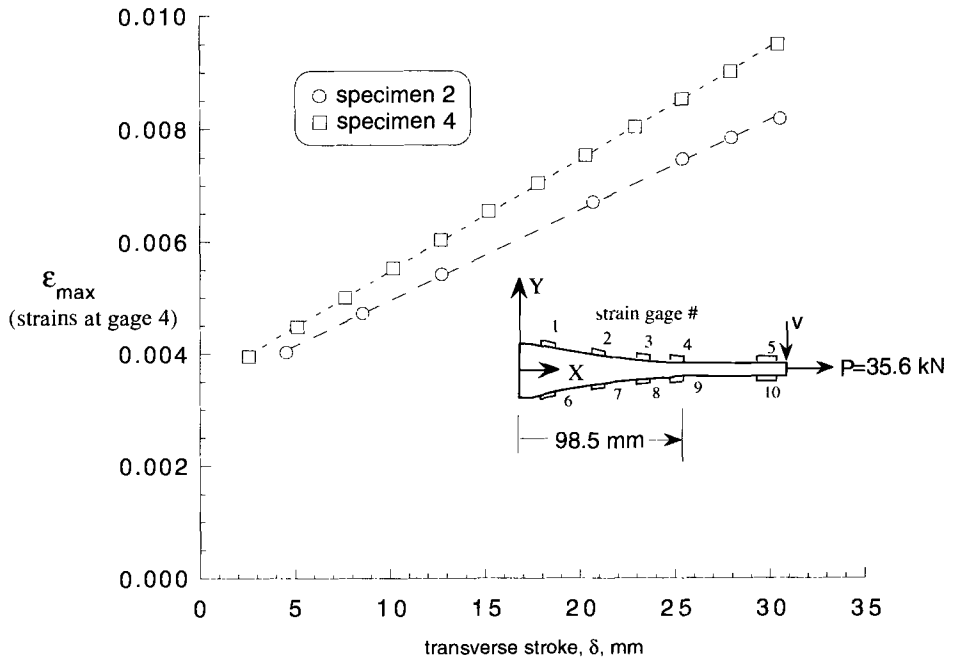


FIG. 8—*Maximum measured surface strain vs. applied transverse stroke.*

a 25.4 mm (1 in.) thin region, as shown in Fig. 7. Note also in Fig. 7 that the transverse bending load, V, was not applied at the top of the flexbeam, but was applied at the pivot point, which was 172 mm above the top grip.

For static excursion tests, a constant axial tension load, P, of approximately 35.6 kN (8000 lb) was applied first. Then the bending load, V, was applied in steps to produce a transverse stroke, δ, in increments of approximately 2.54 mm (0.1 in.), up to a maximum stroke of 25.4 mm (1.0 in.). At each transverse load step, the surface strains were recorded, as well as the transverse flexbeam tip-displacement, v. In order to measure the flexbeam tip-displacement, a spring-loaded direct-current differential tranformer (DCDT) was mounted to the side of the load frame. The DCDT detected the displacement of a bracket attached to the centerline of the top grip.

In Ref 2, the peak surface strains in an identical flexbeam without waviness were plotted as a function of applied transverse stroke, δ. The relationship was shown to be linear as long as the axial load is held constant. Similarly, for this study, the peak surface strains were measured at gage 4 in Fig. 7 (X = 98.5 mm). The maximum surface strains are plotted in Fig. 8 as a function of the transverse load with a constant axial load of P = 8000 lb. The results are shown to be linear for both specimens 2 and 4 (with severe and moderate waviness, respectively).

Fatigue Tests

Since the boundary conditions of the ATB differ from those of the full-scale flexbeam in the hub, it is more logical to control the fatigue tests to a desired maximum surface strain level rather than a prescribed transverse deflection. Hence, for each specimen, a maximum strain level for fatigue testing was chosen, and then results of the type shown in Fig. 8 were used to select the maximum cyclic transverse stroke, δ (see Fig. 7), to apply corresponding to the chosen strain level. The specimens

from Ref *2*, without wavy plies, were tested at transverse displacements of 27.9 mm or 30.5 mm, corresponding to maximum surface strains of 0.01 and 0.015 microstrain, respectively. However, because the static testing showed that the wavy specimens were susceptible to delamination at lower strain levels, the maximum strain levels (or maximum cyclic stroke) chosen for cyclic testing of these specimens were somewhat lower than those used for the specimens without ply waviness in Ref *2*. Specimens 2–6 were fatigue tested at maximum strain levels of 0.0075 to 0.01 microstrain.

In order to make the delamination damage easier to see, specimen edges were coated prior to testing with a thin layer of white paint. A constant tension load of 35.6 kN (8000 lb) was applied to the specimen, corresponding to the net axial stress due to the centrifugal force experienced by the full-scale flexbeam. The maximum cyclic transverse load, V, was applied by cycling sinusoidally to the desired maximum transverse stroke, at a frequency of 3 Hz, and using fully-reversed loading ($R = -1$). The specimens were cycled until they had extensive delamination damage along the length of the tapered region at one or more locations. Test results are discussed later in this report.

Analysis

Finite-Element Model

In order to duplicate the exact geometry of the wavy flexbeams, a software package known as MEGS (*M*odeling *E*xact *G*eometry from *S*canned *I*mages) was used [*4*]. With this software, a scanned image of the object to be modeled was used to create a wireframe image, incorporating as many "as manufactured" details as is desired. The wireframe data was then imported into a PATRAN file, to be used as the basis for developing a finite-element model of this configuration. Because specimen 2 appeared to have the most severe waviness at locations near the flexbeam surface, as well as wavy plies in the center of the laminate, specimen 2 was chosen for use in the analysis and FE model.

It was also necessary to apply the loads and boundary conditions to the model in a manner that duplicates the configuration of the ATB. A schematic of the configuration to be modeled by FE is shown in Fig. 9. Fixed conditions were applied at the thick end of the composite flexbeam. Beyond the thin end of the flexbeam, additional elements were created to represent the upper grip and steel fixture connecting to the pivot point where the transverse load is applied (see Fig. 7). The tension and bending loads are applied at the end of the model, rather than at the flexbeam tip. In this way, the loading conditions of the model duplicate the test conditions. Because the bending stiffness of the steel fixtures was two orders of magnitude greater than the flexbeam, the elements at the thin end that represent the steel loading fixtures were modeled with a rectangular cross section equal to the thin end of the composite flexbeam. A modulus was chosen so that the bending stiffness, EI, was equivalent to the bending stiffness of the actual ATB fixtures of 1.74×10^6 N·m^2 (6.05×10^8 lb·in.^{2}).

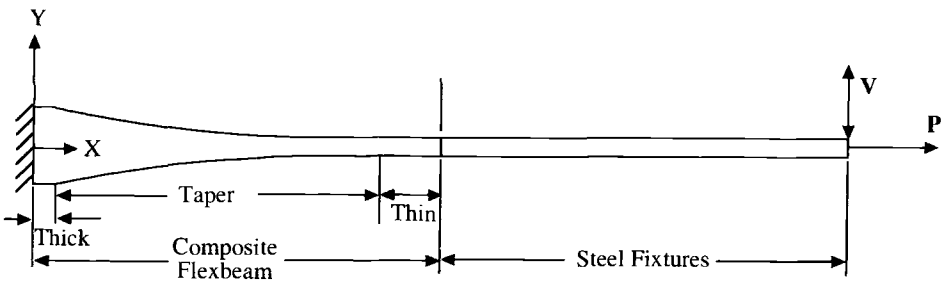


FIG. 9—*Schematic of flexbeam and fixtures subjected to combined loading.*

Finite Element Mesh and Boundary Conditions

A 2-D finite-element model of specimen 2 is shown in Fig. 10. The model had a total of 21,903 nodes and 6971 elements in the mesh. Eight-noded quadrilateral and six-noded triangular plane-strain elements were used. A fine mesh, using one element per ply-thickness, was used for the ply-groups closest to the surfaces, in the areas around the marcels nearest to the top and bottom surfaces. A coarser mesh was used in the interior of the model and in the thinner region of the flexbeam. In those areas, ply-groups were modeled, rather than individual plies, and smeared properties were used. The smeared moduli in the global X-Y coordinate system are presented in Table 2.

In order to assign appropriate material properties to the wavy plies, a local coordinate system was defined for each element in the model, with the 1-direction parallel to the element side from the local node i to local node $i + 1$, as shown in Fig. 10. The local t-n coordinate system was then used to define the material properties of each element. Figure 11 shows enlargements of three marcelled areas near the surface. These have been designated marcels 1–3, as shown. The shaded areas in the enlarged figures represent resin-rich regions. The elements in the resin-rich areas (not shown in Fig. 11) were assigned neat resin properties, as listed in Table 1.

The u- and v-displacements at the nodes at the thick end of the model were prescribed zero values to simulate clamped-end conditions. An axial tension load of 35.6 kN (8000 lb) was applied at the thin end (X = 337 mm) as a concentrated load (see Fig. 7). Transverse bending was produced by a point load of V = 4.45 kN (−1000 lb) applied at the thin end of the model, corresponding to the pivot point in the ATB load frame. To determine the effect of the bending load on each surface, the bending load was applied first in the negative Y-direction, and then in the positive Y-direction.

Computational Methods

The ABAQUS finite-element code was used in the analysis. Because the flexbeam undergoes large deflections, the geometric nonlinear solution option was used. Also, as with the ATB load frame, the axial load in the model was able to rotate with the flexbeam as it deformed under the transverse load. The ABAQUS program was used to calculate displacements and internal stresses and strains.

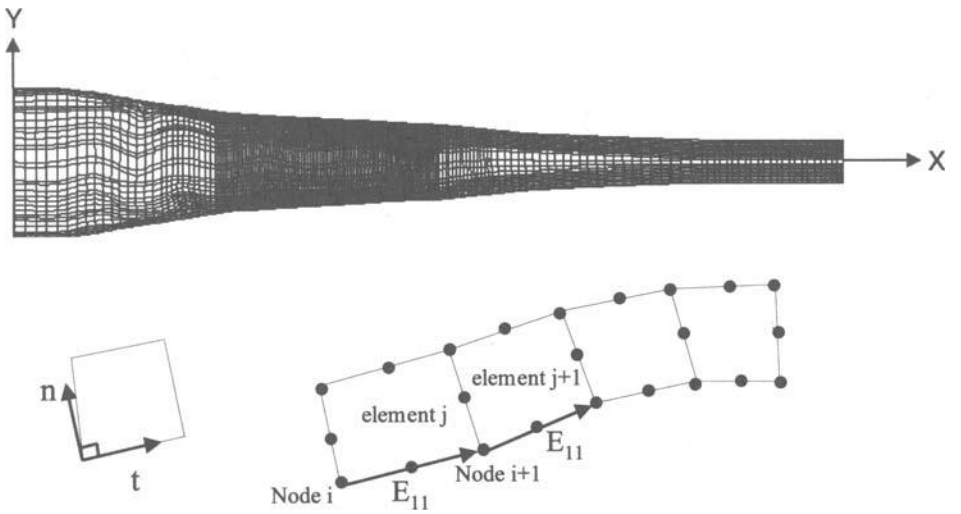


FIG. 10—*Finite-element mesh of tapered flexbeam with wavy plies and element property definition.*

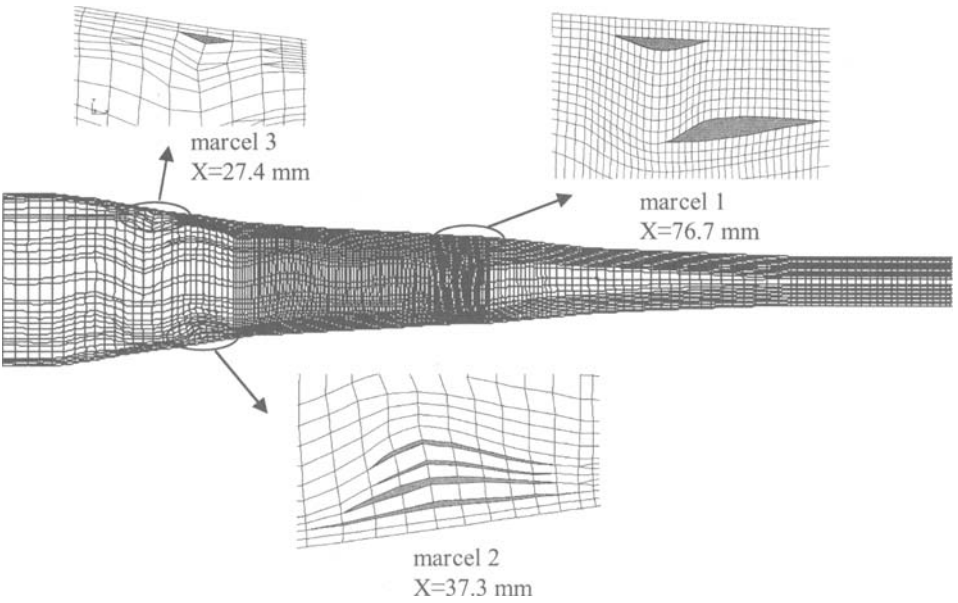


FIG. 11—*Finite-element mesh of tapered flexbeam with wavy plies and marcels near surfaces.*

To study the effects of changes in the ply-waviness, modifications were made to the original mesh. Using the PATRAN code, marcels 1, 2, and 3 were modified several times to reduce the amount of waviness at each location and the resin-rich areas were removed. The new models were analyzed with the same loading and boundary conditions, and the results were compared.

Results and Discussion

Global Response Comparison

Calculated values from the FE model for transverse displacements, v, at the flexbeam tip were compared with the test results to determine the accuracy of the FE model to reproduced the global behavior of the test specimens under the same loading conditions. Figure 12 compares the maximum surface strains versus flexbeam tip displacement, as measured by gages 4 and 9, in the static excursion tests, along with the calculated results from the ABAQUS FE model. The transverse displacement was varied while the axial load was held constant at 35.6 kN (8000 lb). The agreement is good throughout the range of tip-displacement, on both the tension and compression sides, although the calculated strains are slightly lower everywhere.

In Fig. 13, measured surface strains from the ten strain-gage locations are compared with the ABAQUS calculated strains along the flexbeam length. The calculated values are shown in the solid circles and test results are shown for a severely marcelled specimen (specimen 2, open circles) and a moderately marcelled specimen (specimen 4, open squares). The results shown are at $P = 35.6$ kN (8000 lb) and $\delta = 27.9$ mm (1.1 in.). Gages 1–5 were on the tension surface, and gages 6–10 were on the compression surface, as shown in the inset in Fig. 13. The agreement is reasonable for gages 1, 2, 4, and 5 on the tension surface. However, at the gage 3 location ($X = 85.8$ mm, 3.38 in.), the calculated strain is much higher than the measured strain from specimen 4. The FE model duplicated specimen 2, which has a large marcelled area near the surface at gage 3, which is not present in specimen 4. However, the data point for specimen 2 at the gage 3 location is shown with an upward arrow to

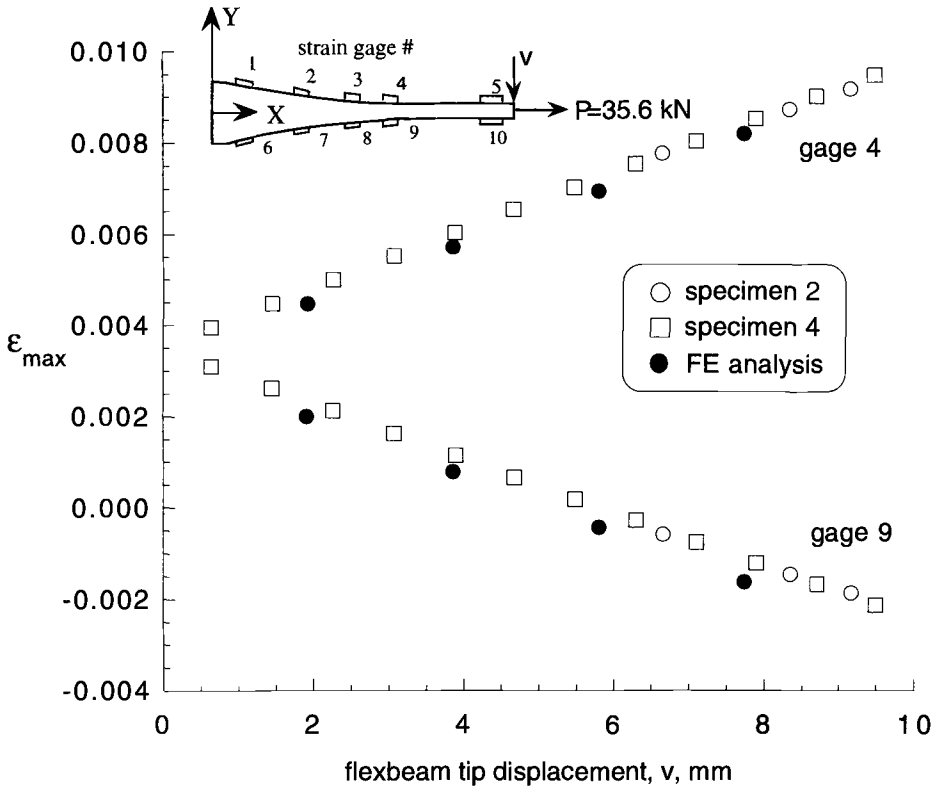


FIG. 12—*Maximum surface strains vs. flexbeam tip displacement.*

indicate that the strain reading had exceeded the limit of the gage (0.012 mm/mm). As the figure shows, the surface strains varied for the different specimens. Along the compression surface, FE results are not as accurate near $X = 0$, but are reasonably close at gage locations 8–10 and follow the trend of the data. Based on these results, the FE model appears to duplicate well the global response of the test specimens under loading in the ATB.

Static Test Results

During the static excursion tests of specimens 1, 2, and 3, all of which had severe waviness, some delamination damage occurred. This was first noticed as faint "clicking" noises as the transverse bending loads were applied. A visual check was made before increasing the load each time. In specimen 1, a crack formed first at the location corresponding to marcel 1 in Fig. 11, at a transverse displacement of $\delta = 12.7$ mm (0.5 in.). Several small delaminations were observed through-the-thickness at the same location. As static loading continued, more delaminations developed at other interfaces through-the-thickness. Figure 14 shows a photo of the coated surface with the delamination damage. Along with the internal delamination damage, there was significant surface ply splitting in the surface fabric above the surface marcel. Because of the large amount of delamination sustained in the static testing, specimen 1 was not fatigue tested. Specimens 2 and 3 each developed a small delamination at marcel 1 also, approximately one quarter of the thickness from the surface, when the transverse displacement reached $\delta = 20.3$ mm (0.8 in.). These specimens were fatigue tested with the

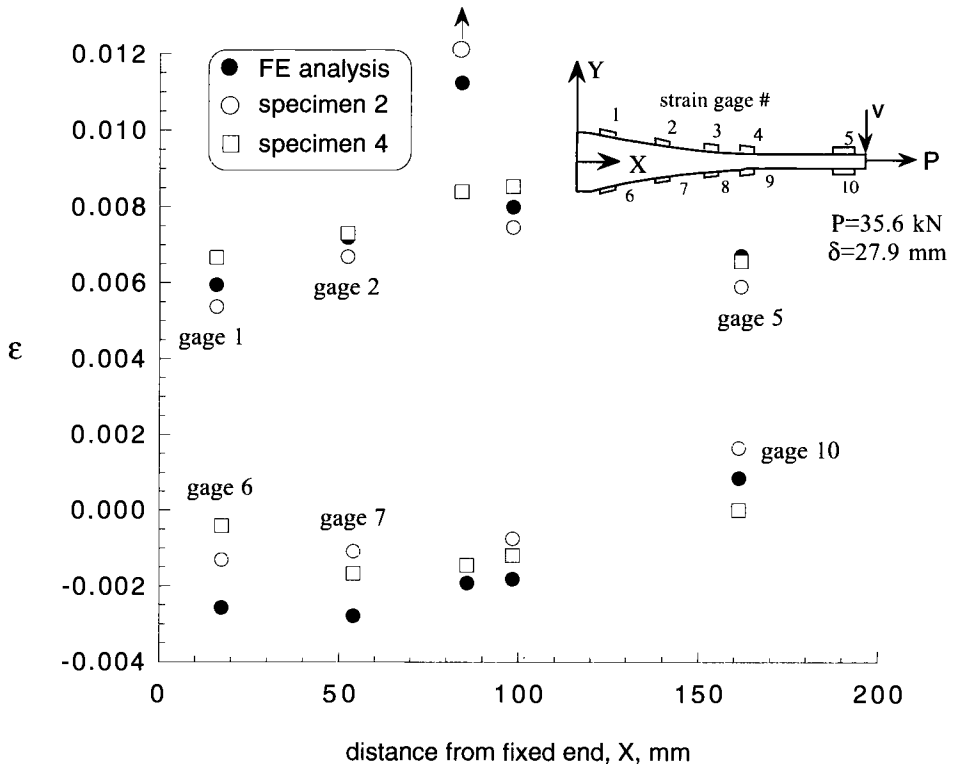


FIG. 13—*Surface strains in tapered flexbeam laminates under combined tension-bending loading.*

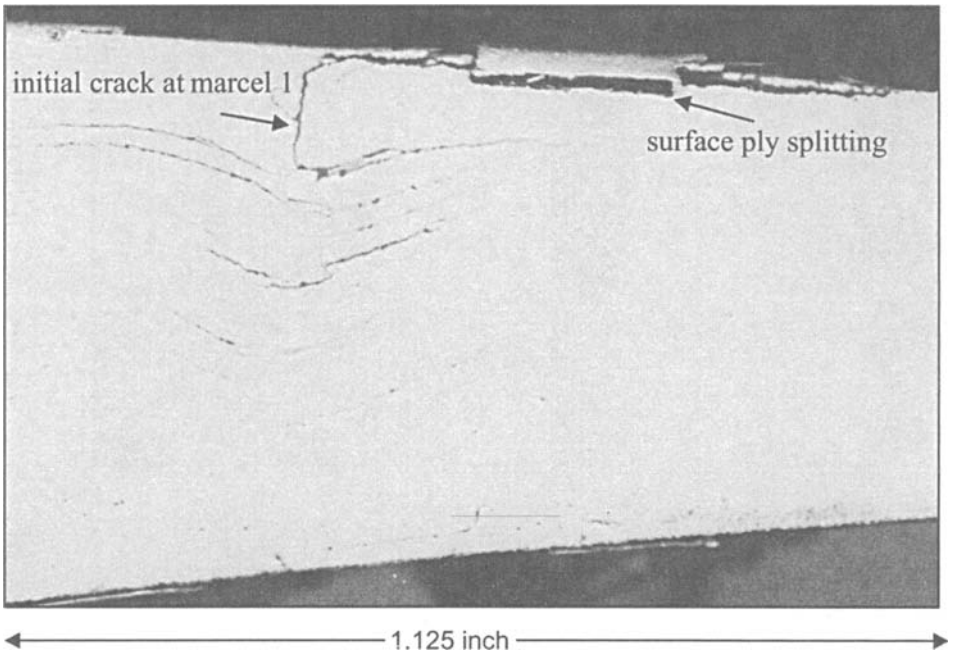


FIG. 14—*Multiple delaminations in wavy area of Specimen 1 after static testing.*

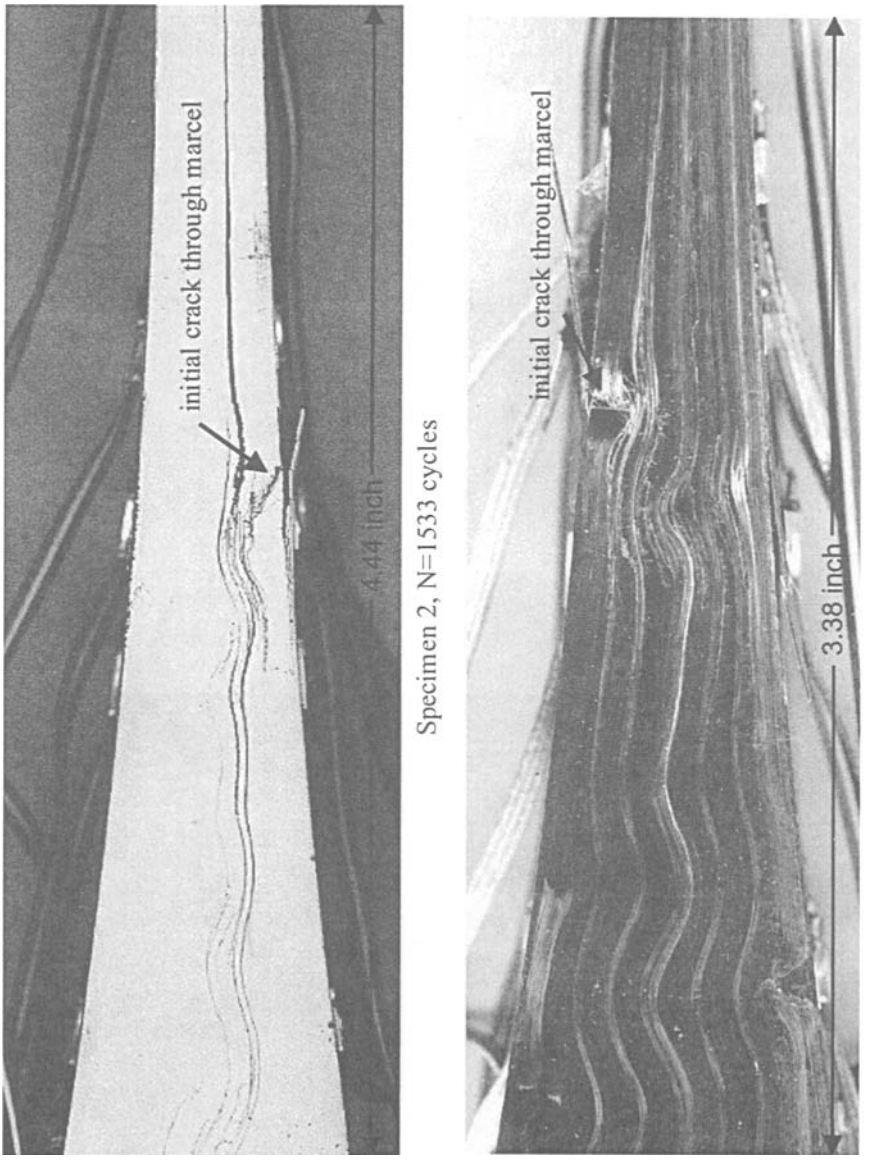


FIG. 15—*Fatigue delamination damage in Specimens 2 and 3.*

initial delamination damage. Specimens 4–6 had no apparent damage after static testing to a maximum transverse displacement of $\delta = 27.9$ mm (1.1 in.).

Fatigue Test Results

The specimens were visually monitored throughout the fatigue loading cycle. For specimens 2 and 3, which had a large marcel at the location "marcel 1" (see Fig. 11), damage began at that location, as a crack through the wavy area, followed by a delamination at the interface under the marcel. This initial crack formed almost immediately, i.e., at less than $N = 50$ cycles. As cycling continued, delaminations formed at neighboring interfaces, through the wavy areas. These delaminations grew in both directions with further loading. The internal delamination damage was always accompanied by splitting and peeling of the surface fabric ply at the location over the surface marcel. Continued fatigue loading caused delaminations to form and grow at interfaces in the wavy center ply-groups, near the thick end of the flexbeam. Figure 15 shows the delamination damage in specimens 2 and 3.

The first observed damage in specimens 4–6, which initially did not appear to have any marcels near the surfaces, appeared as a crack near the surface, similar to the initial damage in specimens 2 and 3. These cracks occurred soon after cyclic loading began, at approximately $N = 400$ cycles. Very small delaminations were observed at the cracks, although, unlike specimens 2 and 3, these delaminations grew very slowly and stably with continued loading. In specimens 4 and 6, delaminations first grew toward the thick end of the laminate, and then grew from the crack toward the thin end. In specimen 5, the delamination grew only toward the thick end. The fatigue loading was continued for these laminates until a delamination had grown from the onset location to the grip at the fixed (thick) end. This condition was considered final failure. Figure 16 shows the final failure of specimens 4 and 5. After testing, the original photographs of specimens 4–6 were re-examined. Surface marcels were found at the locations where the initial cracks formed, as in specimens 2 and 3, although these marcels were of much smaller magnitude.

Figure 17 compares the number of cycles to final delamination failure for specimens 2–6, with the results from Ref *2*, for identical specimens, but without any ply waviness. The solid circular symbols in Fig. 17 show the number of cycles to develop the initial crack through the wavy areas and the open circular symbols indicate the final failure. Even though the flexbeams in this study were tested at lower maximum strain levels than the flexbeams without waviness in Ref *2*, failures occurred at significantly shorter lives. The fatigue lives of specimens 2 and 3, with large amplitude marcels near the surface, were 1 to 2 orders of magnitude shorter than specimens 4–6, with smaller amplitude surface marcels.

Analytical Results

Ply-waviness was characterized in this paper by the aspect ratio of the marcel, defined as the half-amplitude, α, divided by the width of the period, L (see the inset in Fig. 18). In the FE model, the highest aspect ratios were found to be in the center ply-drop groups toward the thick end of the flexbeam and in the isolated marcels near the surfaces. All of those marcels had an α/L of 0.055 to 0.085. The aspect ratios of the marcels in the center plies decreased gradually along the length of the flexbeam.

Results of the FE model analysis were used to determine the peak interlaminar normal stresses, σ_n, in the model. The σ_n stresses reported are with reference to the element local (n-t) coordinate system, rather than the global coordinate system (Fig. 10). Several studies have shown that delamination failure in composites with similar geometry is predominantly due to opening mode failure (normal to the ply direction) [*2,4–6*], with a much smaller contribution from the interlaminar shear mode. In this study, therefore, delamination was also assumed to be controlled by the interlaminar tension, and only the interlaminar normal stresses were considered. Peak σ_n stresses occurred in the model at marcel 1, and another area of high σ_n stresses existed at marcel 3 (Fig. 11). When the transverse load direction

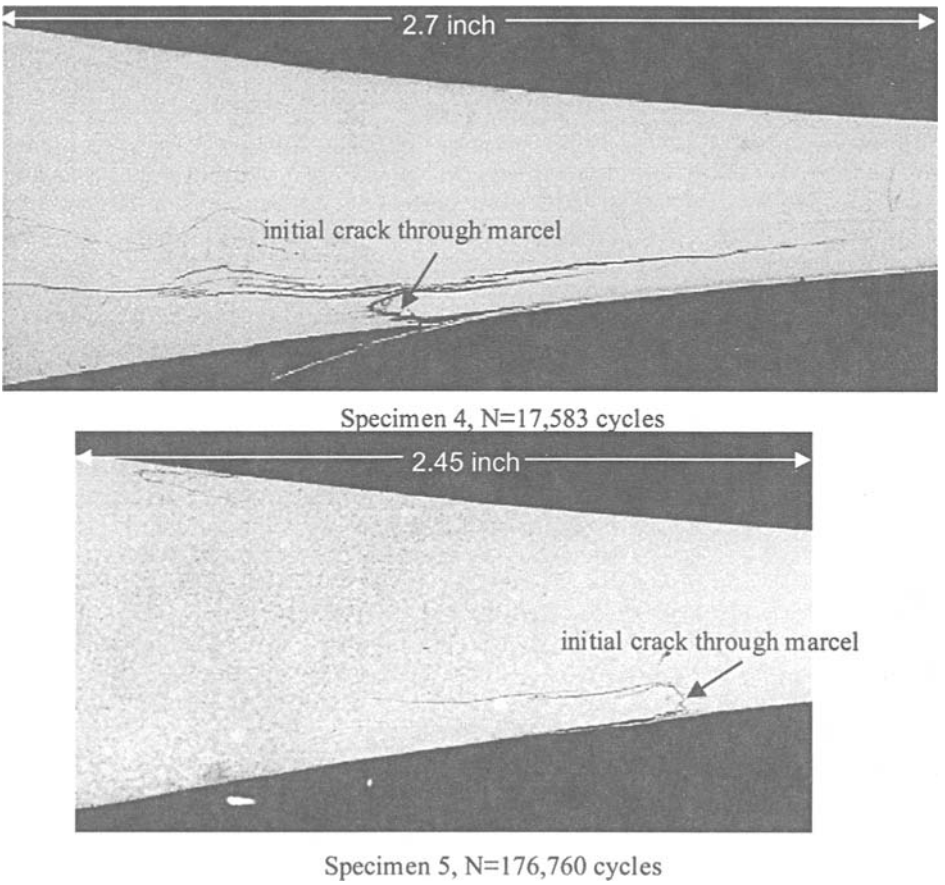


FIG. 16—*Fatigue delamination damage in Specimens 4 and 5.*

was reversed ($V = 4.45$ kN, 1000 lb), peak stresses occurred at marcel 2. In all cases, the peak stresses occurred at the most interior point of the marcel.

In order to determine the effect of marcel location on interlaminar normal stresses, the model was inspected to find marcels of the same aspect ratio, but at different X- or Y-locations. Figure 18 shows the effect of varying the X-location of a marcel, while keeping the aspect ratio and distance from the surface constant. The figure compares calculated interlaminar normal stresses, at marcelled areas of the model with aspect ratios of either 0.085 or 0.045, at approximately the same distance from the surface, but different X-locations. As the figure shows, for either aspect ratio, the stresses increase as the location of the marcel moves from the thick end toward the thin region.

In Fig. 19, the effect of the location of the marcel through-the-thickness is shown. For this case, stresses at different locations through-the-thickness are plotted for marcels with aspect ratios of 0.085 and 0.045, the same distances along the taper. The stresses are plotted as a function of the distance from the upper surface, $\bar{y}$, divided by the section half-thickness, $t(x)$. As Fig. 19 shows, stresses decrease sharply for both aspect ratios, as the marcel location moves from the surface toward the midplane of the flexbeam. Exponential curves were fitted to the data in Fig. 19.

To determine the effect of the marcel aspect ratio, the aspect ratios of marcels 1–3 in the original FE model were modified and the analyses were repeated. The aspect ratio of marcel 1 was reduced

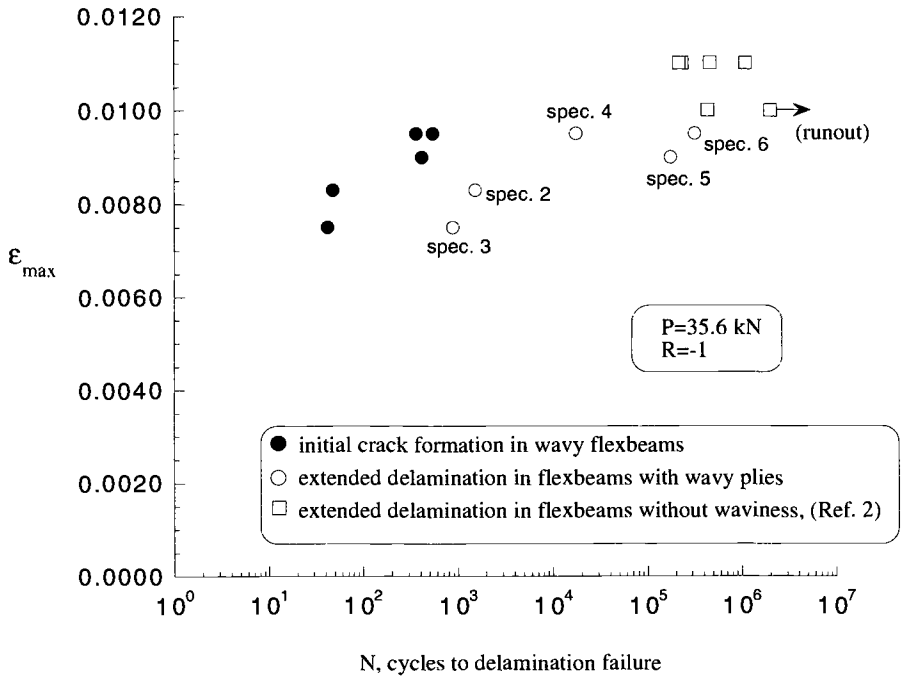


FIG. 17—*Fatigue delamination response of flexbeams with and without wavy plies.*

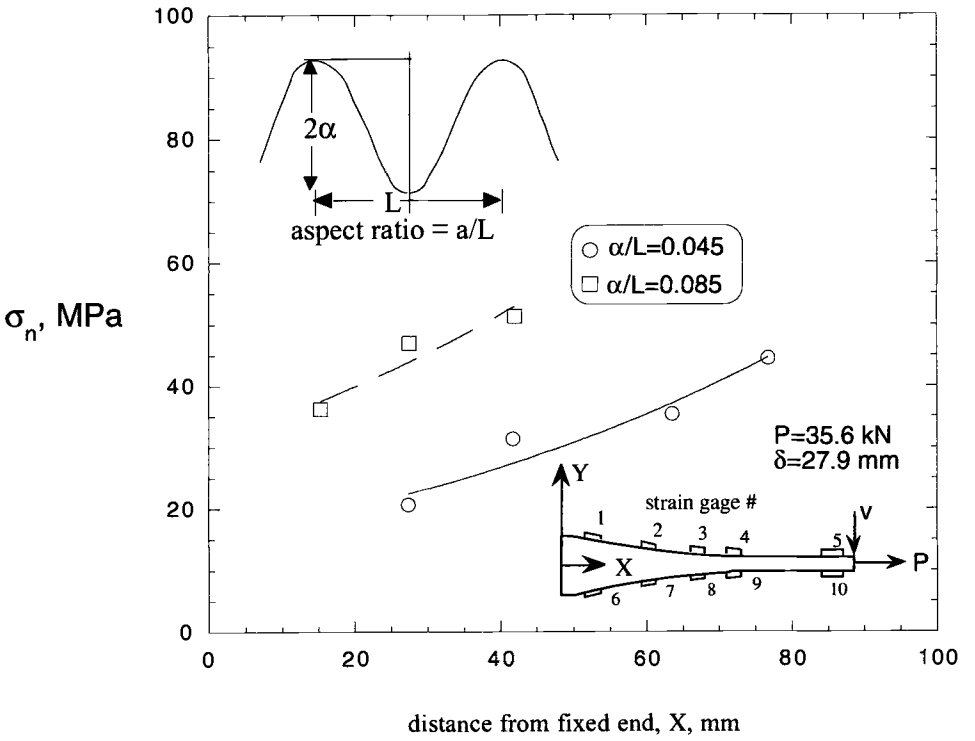


FIG. 18—*Interlaminar normal stresses along taper for marcels with identical aspect ratios.*

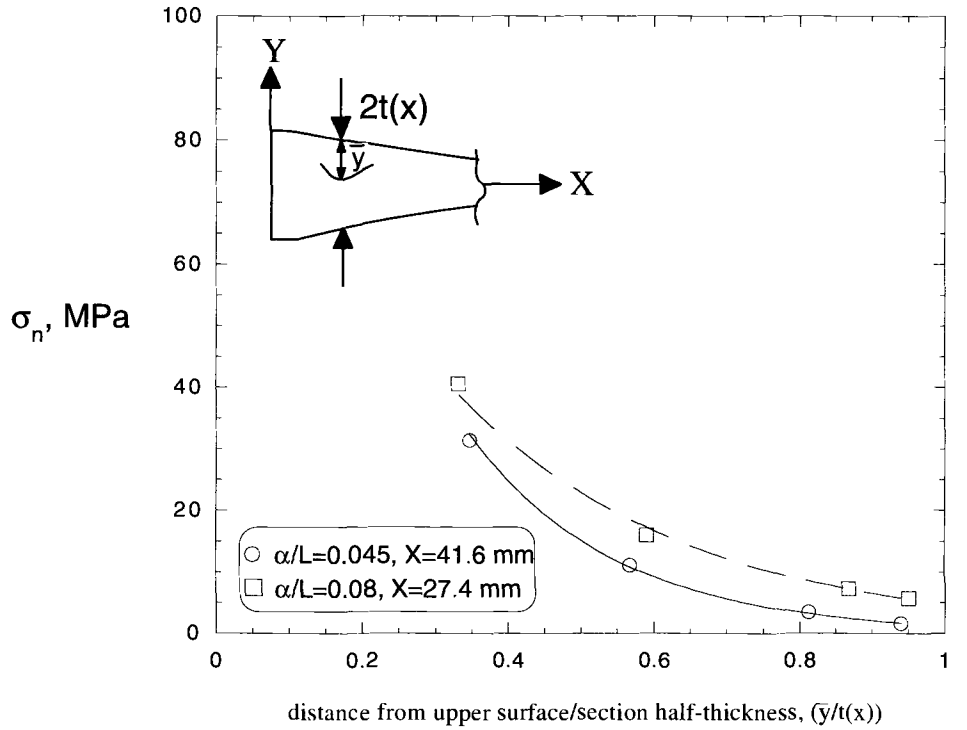


FIG. 19—*Interlaminar normal stresses at different locations through the thickness constant aspect ratio marcels.*

from the original, 0.085, to 0.055, 0.034, and 0.025. Marcel 2 was modified from the original aspect ratio of 0.05 to 0.028, 0.02, and then 0.014. The aspect ratio of marcel 3 was reduced from 0.085 to 0.08, 0.07, 0.06, and 0.03. Figure 20 shows a comparison of the σ_n stresses at marcel 1, 2, and 3 locations, as the aspect ratio was varied at each location. The peak interlaminar normal stresses increase exponentially as the aspect ratio increases. Again, the stresses are always highest for marcel 1, the marcel farthest from the fixed end. The curves for marcels 2 and 3, which are near the thick end, and at similar X-locations, appear to cross at an aspect ratio of about 0.03, but at higher aspect ratios, marcel 3, nearest the thick end, is the lower bound of the stresses.

The test results from Fig. 17 were used with the calculated curves from Fig. 20 to correlate the interlaminar normal stresses with the fatigue lives of the flexbeam test specimens. For each of the tested specimens, the aspect ratio was measured at the marcel where the delamination failure initiated. The corresponding interlaminar stress from the FE analysis was determined from the appropriate curve in Fig. 20. The curve for marcel 1 was used to determine the stresses for specimens 2 and 3, since for those specimens, delamination damage initiated there. For specimens 4–6, the curve for marcel 2 (at X = 37.3 mm) in Fig. 20 was used, since the X-location was closest to the actual location of the marcels where failure began. For specimen 4, damage initiated at a small marcel at X = 50.8 mm, and for specimens 5 and 6, at X = 48.26 mm. The resulting σ_n values were plotted against the number of loading cycles to failure for the test specimens in Fig. 21. As the interlaminar normal stresses decrease, the fatigue life increases. This figure also shows the data from the flexbeams without waviness from Ref 2. Finite-element results from Ref 2 showed that the maximum value of σ_n under com-

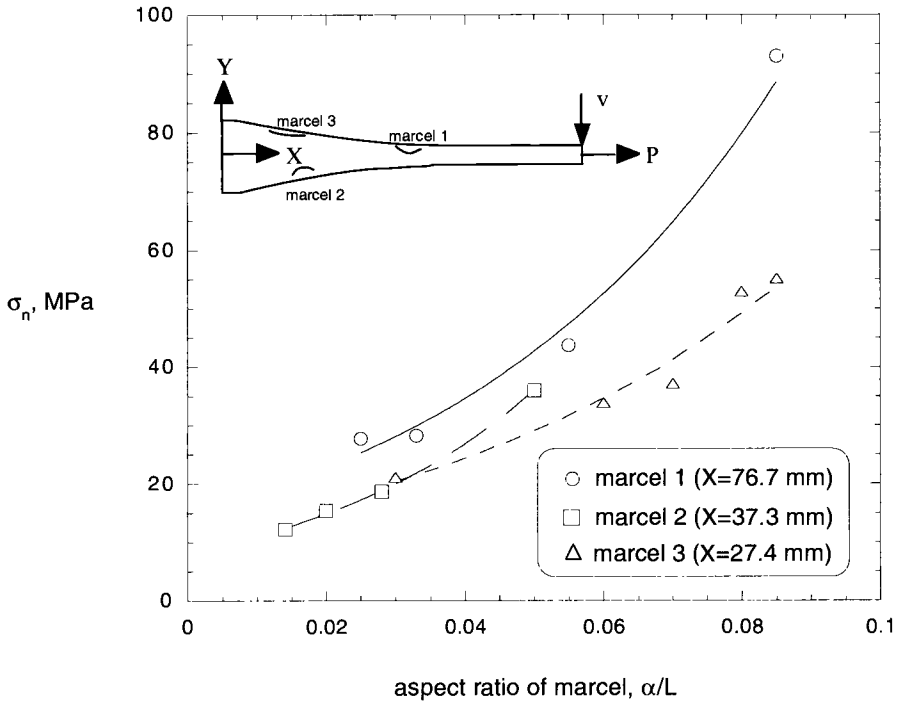


FIG. 20—*Interlaminar normal stresses at three locations, with varying aspect ratio marcels.*

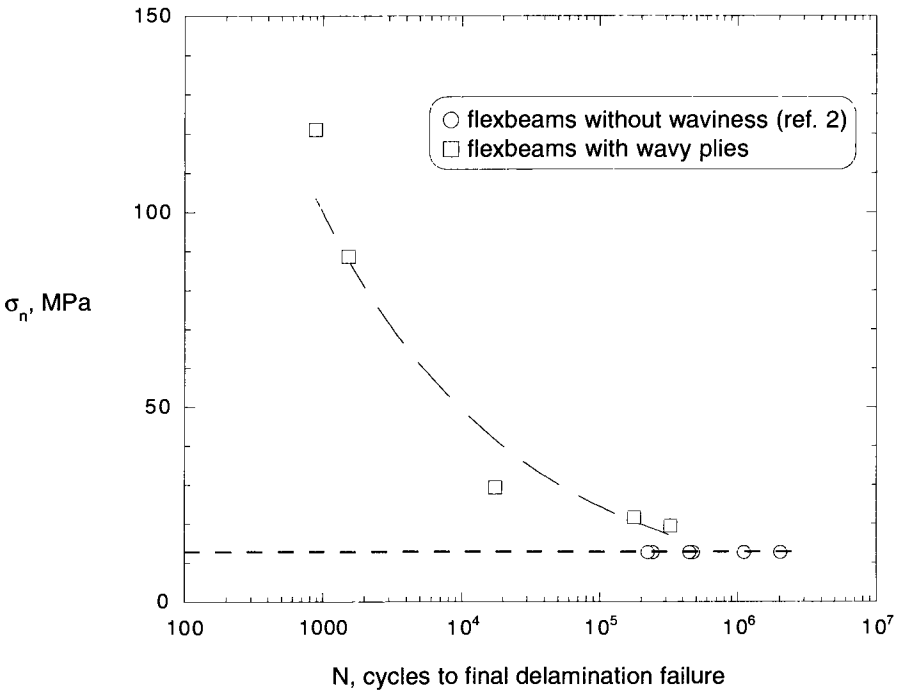


FIG. 21—*Calculated interlaminar normal stresses vs. cycles to delamination failure.*

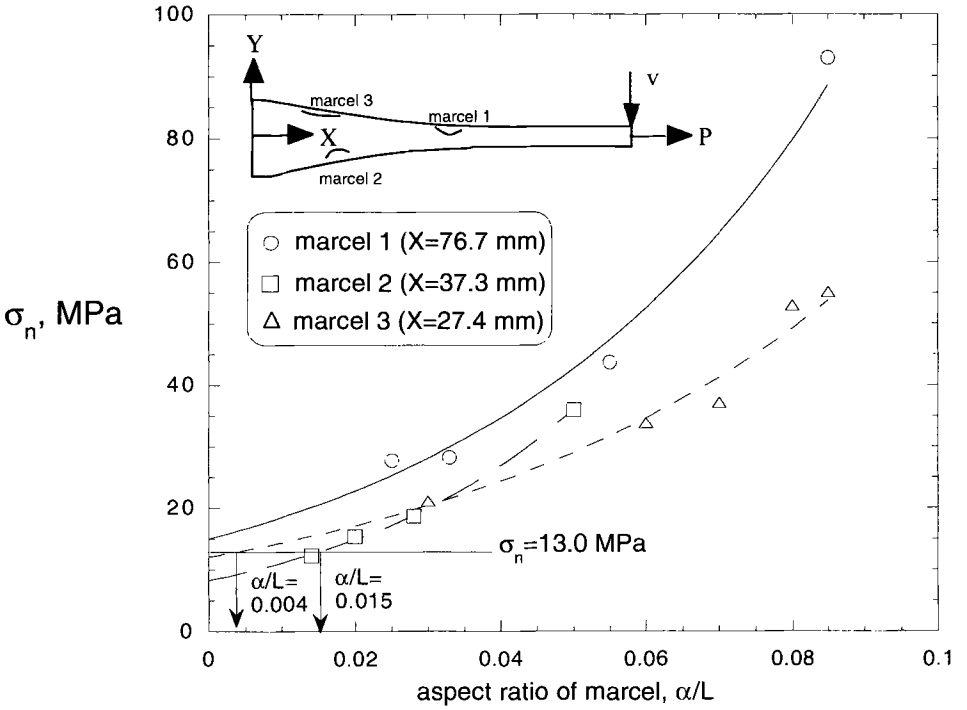


FIG. 22—*Marcel aspect ratio limits determined from test results and FE calculations.*

bined tension-bending loading was 12.5 MPa. Based on Fig. 21, σ_n = 13.0 MPa was chosen as the limit below which delamination failure will not occur at less than N = 200 000 cycles.

In Fig. 22, this lower limit is plotted with the curves and data from Fig. 20. The intersections of the curves show the maximum allowable α/L values for the corresponding X-locations in the flexbeam. Using the assumed lower limit, no marcel would be allowable at X = 76.7. At the X = 37.3 and X = 27.4 locations, marcels with aspect ratios of no more than 0.015 and 0.004, respectively, would be acceptable.

Discussion

Using this technique of combining test data with FE model results, a lower limit of interlaminar normal stress can be chosen for a desired fatigue life. That normal stress can then be used, as in Fig. 22, to determine the maximum allowable aspect ratio at various locations in the flexbeam.

The technique described above could be used as a first attempt at determining whether or not a given flexbeam should be used or discarded. However, the method has several limitations: e.g., an unlimited number of wavy ply configurations are possible, but it is not practical to model each case to determine the effect on the interlaminar stresses. Furthermore, varying the mesh size in the FE model may change the calculated stresses significantly. A mesh refinement study is required to verify this. A more complete picture of the delamination process in these flexbeams may be provided by an energy-based analysis, such as that used in Refs *1*, *2*, and *4*, in which simulated delamination growth is modeled at various locations and the associated strain energy release rates are calculated. However, considering the discussion in Fig. 17 and the considerably poorer performance of these flexbeams with marcels under the fatigue loading, the effort involved in such an analysis may not be justified.

Concluding Remarks

The effect of wavy plies on the durability of tapered laminated composite flexbeams was studied, for use in developing accept/reject criteria for these flexbeams. Tests were conducted on 25.4-mm-wide coupon specimens, which were cut from a full-size flexbeam of S2/E7T1 glass/epoxy. All of the specimens had significant ply waviness through the center of the flexbeam and isolated areas with varying amounts of waviness at locations near the surfaces. The specimens were tested under combined axial tension and transverse bending loading. For all of the tested laminates, damage started as a crack through a marcel near the surface. As the loading continued, delaminations grew from the crack in both directions along the length away from the marcel and multiple new delaminations formed at neighboring interfaces. Even though the flexbeams in this study were tested at lower maximum strain levels than identical specimens without ply-waviness from Ref *2*, failures occurred at significantly shorter lives. Fatigue lives for the tested laminates ranged from 10^3 to 10^5 cycles. In contrast, identical flexbeams without marcels had fatigue lives of 10^5 to 10^6 cycles at slightly higher bending loads.

A parametric study was conducted to determine the effects of ply-waviness along the taper and through-the-thickness. A (2-D) plane strain FE model was developed which modeled exactly the flexbeam layup and geometry of one of the test specimens, including the exact geometry of the wavy plies. The model was analyzed using the ABAQUS finite-element program to determine the interlaminar normal stresses, σ_n. For marcels of the same aspect ratio, and at the same depth from the surface, σ_n stresses increased with distance along the taper, from thick end to thin end. For marcels of the same aspect ratio, and at the same location along the taper, the σ_n stresses decreased from the surface inward toward the flexbeam midplane. The model was modified several times by decreasing the amplitude of the waviness in three marcels near the surfaces and the analysis was repeated. It was found that the σ_n stresses increased exponentially as the aspect ratio was increased in these surface marcels.

A technique was presented for determining the smallest acceptable marcel aspect ratio at various locations in the flexbeam. Test data were combined with calculated results for modeled marcels of different aspect ratios and at different locations, to determine a lower limit on the allowable interlaminar normal stresses. This limit was then related back to the calculated FE results to determine maximum allowable marcel aspect ratios to achieve a desired fatigue life.

References

[*1*] Li, J. and O'Brien, T. K., "Ply Waviness Effects on the Pull-off Loads in Composite Hat Stringer Specimens," *Proceedings of the 14th U.S. Army Symposium on Solid Mechanics,* Myrtle Beach, SC, Oct. 1996.

[*2*] Murri, G. B., O'Brien, T. K., and Rousseau, C. Q., "Fatigue Life Methodology for Tapered Composite Flexbeam Laminates," *Journal of the American Helicopter Society,* Vol. 43, No. 2, April 1998, pp. 146–155.

[*3*] Shivakumar, K. N. and Crews, J. H., Jr., "Bolt Clampup Relaxation in Graphite/Epoxy Laminate," *Long Term Behavior of Composites, ASTM STP 813,* T. K. O'Brien, Ed., American Society for Testing and Materials, West Conshohocken, PA, 1983, pp. 5–22.

[*4*] Li, J., O'Brien, T. K., and Rousseau, C. Q., "Test and Analysis of Composite Hat Stringer Pull-off Test Specimens," *Journal of the American Helicopter Society,* Vol. 42, No. 4, Oct. 1997, pp. 350–357.

[*5*] O'Brien, T. K., "Composite Interlaminar Shear Fracture Toughness, G_{IIc}: Shear Measurement or Sheer Myth?," *Composite Materials: Fatigue and Fracture, Seventh Volume, ASTM STP 1330,* American Society for Testing and Materials, West Conshohocken, PA, 1998, pp. 3–18. Also available as NASA TM-110280, ARL TM-1312, Feb. 1997.

[*6*] Krueger, R., Cvitkovich, M. K., O'Brien, T. K., and Minguet, P. J., "Testing and Analysis of Composite Skin/Stringer Debonding Under Multi-Axial Loading," NASA TM-1999-209097, ARL-TM-439, Feb. 1999.

Stephen L. Smith[1] *and Joseph L. Mattavi*[1]

Structural Qualification of Composite Propeller Blades Fabricated by the Resin Transfer Molding Process

REFERENCE: Smith, S. L. and Mattavi, J. L., **"Structural Qualification of Composite Propeller Blades Fabricated by the Resin Transfer Molding Process,"** *Composite Structures: Theory and Practice. ASTM STP 1383,* P. Grant and C. Q. Rousseau, Eds., American Society for Testing and Materials, West Conshohocken, PA, 2000. pp. 210–228.

ABSTRACT: The unique challenges for developing design allowables for a resin transfer molded propeller blade are discussed. Preliminary allowables were determined based on coupon tests for the initial blade design. Nonstandard specimen geometries were investigated in order to provide valid failure modes and associated strength values for the spar, shell and adhesive bond joint in terms of static and fatigue strengths out to 10^8 cycles. Full-size blade component tests were performed to verify or substantiate the preliminary allowables. Analyses of failure modes on the full-size specimens directed the structural qualification process. This included follow-up coupon fatigue tests and expansion of the full-size test matrix. The general conclusions are that coupon tests are necessary for determining elastic constants and for effects of batch variation, environment, and for shape of fatigue curves, but generally do not provide enough guidance to design a resin transfer molded (RTM) structure without some full-size test experience. This is due to the absence of edge, surface and width effects found in coupons and the inclusion of thermal, manufacturing and geometry effects found in the full-size specimens. These and other scale effect issues therefore dictate the need to test full-size specimens early on in the normal building block approach. The number of full-size tests is generally higher for an RTM blade or structure than for a metal blade or for a standard prepreg, thin composite structure, since statistical treatment of the full-size fatigue data is necessary for establishing final design allowables. This top-of-the-pyramid approach to structural qualification can make RTM unique from prepreg or metal structures.

KEYWORDS: resin transfer molding, design allowables, propeller blade, braided materials, bond joints, fatigue analysis

Nomenclature

Cv	Coefficient of variation (%)
E	Tensile modulus
G	Shear modulus
RTM	Resin transfer molding
RTA	Room temperature ambient
S-N	Stress life
SBS	Short beam shear
UTS	Ultimate tensile strength
USS	Ultimate shear strength
Vf	Fiber volume
τ	Shear stress
τ_{xz}	Shear stress in xz-plane, where x is longitudinal direction and z = through-the-thickness

[1] Senior materials engineer and chief of Materials Engineering, respectively, Hamilton Standard, Windsor Locks, CT 06096.

Copyright© 2001by ASTM International www.astm.org

τ_{yz} Shear stress in yz-plane, where y is circumferential direction
σ_z Normal stress in z-direction
μ Poisson's ratio

The approach for designing a primary structure with composite materials entails determining static "design allowables" using a building block approach [*1*]. The building block approach is an iterative process such that coupon tests are used to characterize composites and their attachments, which result in the definition of "preliminary allowables." The preliminary allowables are then validated with subelement and full-scale tests to address critical failure modes and correlation of design procedures using the preliminary allowables. This building block approach, described in Ref *1*, which incorporates various ASTM test standards for composite materials, is defined primarily for preimpregnated or prepreg composites and static loading. For the RTM composite propeller, adaptive procedures were required that were form-specific in nature and addressed vibratory load or fatigue environment. The ASTM Test Method for Tension-Tension Fatigue of Polymer Matrix Composite Materials (D 3479), which was adopted in 1996, has addressed fatigue testing. However, in 1989, a fatigue methodology was developed by Hamilton Standard to determine design allowables for a RTM composite propeller blade. This methodology has continued to evolve for new composite propeller blade applications, with varying flight profiles.

The generic RTM composite blade is fabricated with 2-D braided preforms, fabric broad goods and wound filaments, which are injected with resin. The blade is also comprised of polyurethane foam, film adhesives, prepreg materials and metal components. Hence, materials characterization to determine properties for composites and attachments was required to develop a database for design and certification. The burden of developing this database was minimized through selective testing to determine preliminary allowables. More emphasis was eventually placed on the subelement and full-scale test results since failure modes differed to some degree from the coupon level tests.

Blade Description

The generic RTM composite blade is fabricated in a five-step, patented process [*2*]. Figure 1 shows a schematic of the manufacturing process, beginning with a steel "tulip" retention which is peened and surface prepared for bonding (Step 1). A structural film adhesive is applied to the tulip and then layers of prepreg material are layed up on the outside and inside of the hollow tulip and subsequently press molded and cured to form a doubler (Step 1a). The purpose of the doubler is to produce an area for RTM attachment of the braided spar and to effectively produce a 360° double lap joint, which minimizes the tab end stress concentration effect at the end of the tulip realized by load transfer from the spar to the tulip. The doubler/tulip assembly is then placed in a spar core mold and foam is injected and cured (Step 2). The spar foam assembly has one layer of prepreg as a skin to produce an in situ mandrel for placement into a 144-carrier braiding machine (Step 3). The assembly is intermittently braided with T300, 6K carbon tows, which are manually interspersed with layers of an IM-7, 12K carbon uniweave fabric. The placement and orientation of the fibers are controlled to produce a satisfactory laminate for stiffness, stability and strength. The braid angle θ is controlled by mandrel velocity V, for a given perimeter P, and carrier circular speed ω, as follows

$$\theta = \tan^{-1}[\omega P/V] \tag{1}$$

Additionally, glass hoop wraps are filament wound into the laminate over the necked-down section of the tulip. The hoop filaments provide added stiffness and strength to the joint region in the event of a debond or delamination over the tulip, by developing a mechanical entrapment mechanism. With the dry spar fibers in place, the spar assembly is placed in a second foam mold, where the lead and trail edge foam is injected and cured (Step 4). The interior edges of the spar are sealed prior to injection to prevent foam accumulation in the dry preform. The face and camber sides of the spar remain

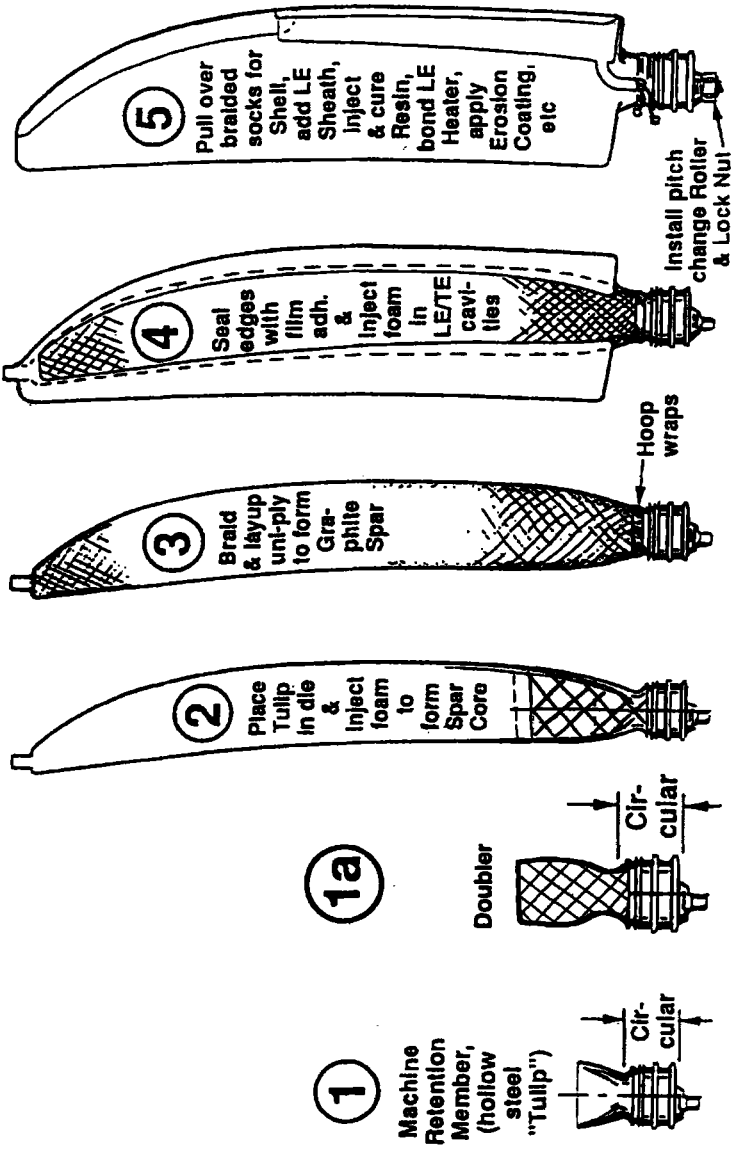


FIG. 1—*Schematic of the Hamilton Standard composite propeller blade manufacturing process.*

open to the air. The assembly is then fitted with two braided Kevlar™ sleeves, manufactured originally as free-braided tubes, and an aluminum lightning mesh and nickel sheath to form the airfoil shell structure. The entire assembly is placed in a RTM die and both the spar and shell are injected and co-cured with PR500 resin (Step 5). The PR500 resin was selected for its superior composite interlaminar fracture toughness properties. Later, erosion film and a deicing heater are added to the airfoil surface and a glass hoop compression wrap is filament wound and cured at room temperature over the blade root.

For structural qualification to produce a database, the blade was characterized in three main areas: (1) spar, (2) shell, and (3) the blade root tulip/spar bond joint. For this paper, only the spar and bond joint areas are discussed.

Coupon Tests

The coupon database produced properties for typical strength and elastic constants and evaluated the effect of material and processing variables, effect of environment and single/random batch scatter. The coupon database also included fatigue testing to establish cursory S-N curve shapes for construction of modified Goodman diagrams. The preliminary allowables were based on a "Three Sigma" approach as opposed to an A-Basis, five batch test type approach suggested in Ref *1*. The notion of using an average coefficient of variation = 10% for all material systems was adopted to minimize multiple batch testing. This $Cv = 10\%$ was considered conservative from past internal and external [*3*] materials characterization programs with notched and unnotched carbon/epoxy systems. Later, final coupon allowables either incorporated $Cv = 10\%$ as a minimum or actual Cv values if greater than 10%. This also assumed a minimum coupon test sample size of 14. Under these conditions, the typical Three Sigma allowable is consistent with a confidence level of 95% and a survival probability of 99% (equivalent to an A-Basis normal distribution value).

Batch-to-batch variation was implicitly considered during qualification of materials for procurement, where the supplier was instructed to perform three batch tests to meet a specification requirement. The three-batch testing was primarily for the RTM resin, carbon fiber and the film adhesives.

For a small sample size, the Three Sigma statistical approach generally produces a more conservative allowable than the A-Basis, five-batch approach and is more cost effective at the coupon level. Also, the benefit of conducting subelement and full-scale tests to establish the proper failure mode before conducting final material characterization testing was realized with the simple Three Sigma approach. Figure 2 shows a schematic of this approach. The final characterization included testing more samples at the blade limiting failure response for establishing definitive S-N curve shapes for the manipulation of full-scale test results to allow for life predictions and inspection requirements for

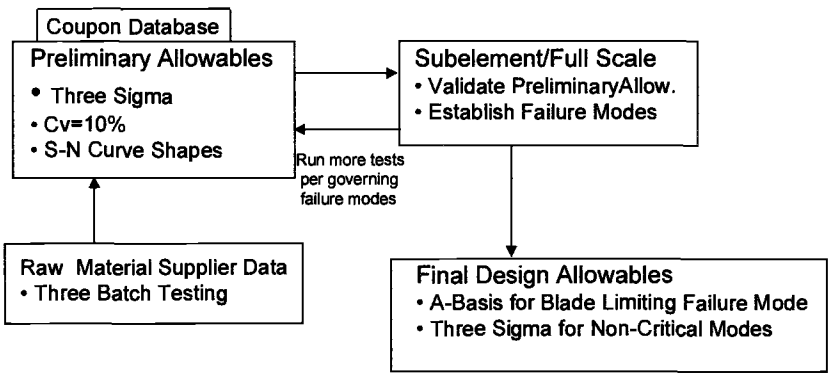


FIG. 2—*Design allowable methodology.*

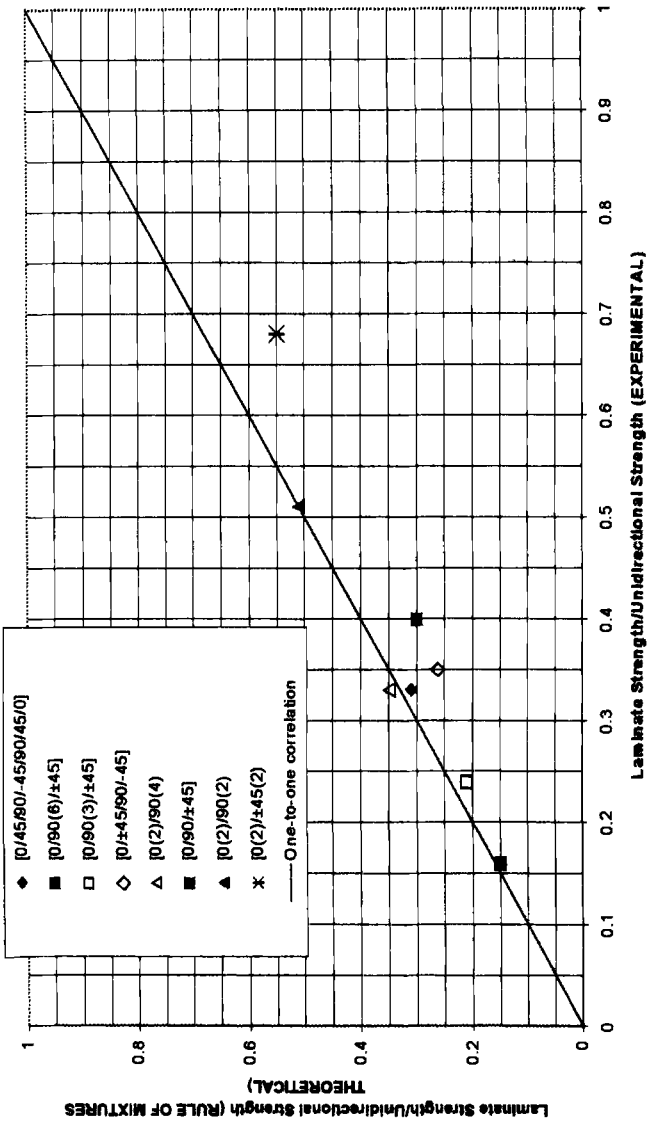


FIG. 3a—*Static comparison for T300/5208 carbon/epoxy.*

certification. A-Basis allowables were derived from full-scale results to take advantage of sample sizes greater than six.

Spar, In-plane Loading

The initial coupon test program for the spar was set up to characterize the braid and the uniweave materials separately and then together as a hybrid laminate. This was necessary to confirm a Rule-of-Mixtures strength approach for the combined 0° uniweave/$\pm\theta$° braid layup under in-plane loading. The basic equation is as follows:

$$\text{Hybrid laminate strength} = \frac{1}{T}\sum_{1}^{N}(S_i t_i) \tag{2}$$

where S_i is strength of individual layer, t_i is thickness of layer, N is layers of each t_i, and T is the total thickness

The simplified Rule-of-Mixtures strength approach was adopted since existing in-plane "weak link" strength failure criteria, i.e., maximum stress, maximum strain and Tsai-Hill, were deemed too conservative. Figure 3 shows a plot of static and fatigue data, from Refs *4–6* plotted as a function of laminate strength/unidirectional strength determined empirically versus theoretically by Rule-of-Mixtures. A reasonable one-to-one correlation between experiment and theory was realized and conservative for the [0/±45] family of laminates. For the braid contribution, it was still practical to investigate a "weak link" type failure criteria for the braid strength versus $\pm\theta$, since the braid would constitute a low percentage of the overall in-plane strength of the spar. Hence, the Tsai-Hill quadratic criteria was initially used for the braid characterization. The next challenge, after the failure criteria were selected, was to produce legitimate gage section, in-plane failures of the test coupons.

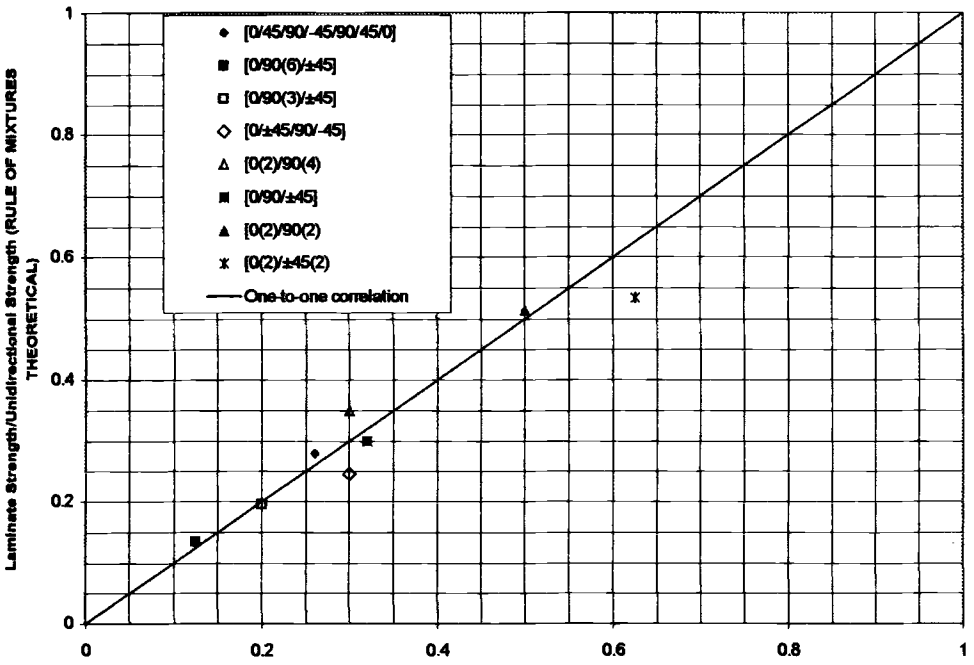
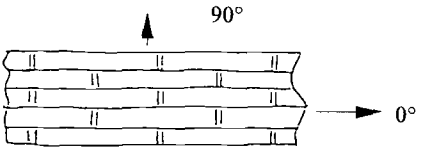
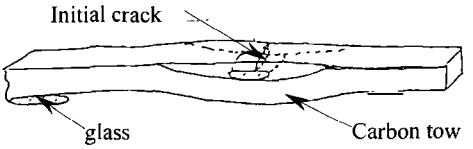


FIG. 3*b*—*Fatigue comparison for T300/5208 carbon/epoxy.*



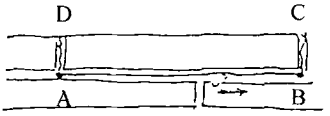
TPI 4375
95% IM-7, 12K
5% Glass

Resin cracks occur in 90° direction on surface plies over glass tows, see blow up.



Based on fracture toughness of graphite/epoxy, the stress to delaminate outer plies was determined.

$$\sigma_{del} = \frac{K_{IC}}{\beta} = \frac{22\ ksi\sqrt{inches}}{.2965} = 74 ksi \quad (510\ \text{MPa})$$



90° cracks produce 0° cracks or splits along adjacent graphite tows. When pt. A and B link up, Section ABCD pops up.

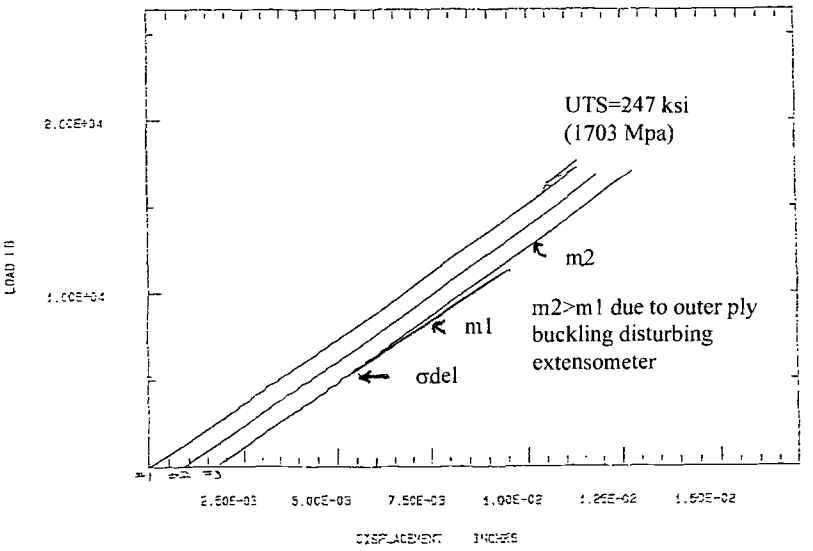


FIG. 4—*Mechanism of in-plane failure on uniweave carbon preform.*

For the uniweave material, the ASTM Test Method for Tensile Properties of Polymer Matrix Composite Materials (D 3039), 12.7 mm wide, 0° test coupon was first used. This broad good fabric consists of 95% 0° carbon tows and 5% 90° tackified glass filaments, which are spaced every 6.35 mm in a plain weave style to stabilize the dry uniplies. The ASTM D 3039 static and fatigue results were much lower than expected. This was due in part to the fiber undulation or crimp effects of the 95/5 uniweave material. The expected static strength without fiber undulation, based on prepreg data with the same fiber and resin was 2641 MPa at 60% fiber volume. Two failure modes were predominant for the ASTM D 3039 uniweave specimen: (1) off-axis fiber splitting, similar to Ref 7, and (2) resin/glass tow surface cracking and subsequent fiber splitting. The first anomalous failure scenario yielded a typical strength of 1524 MPa at 60% *Vf*. This was corrected by improving the coupon edge alignment with the fibers. The second failure scenario showed a static value of 1703 MPa. The latter scenario, where unsupported surface plies fail early and precipitate a complex failure, is explained in Fig. 4. The value for K_{Ic} for determining the stress to split and then delaminate a ligament between 90° filaments was estimated from Refs *8–10*. This additional resin on the surface in all uniweave coupons is an artifact of the layup in the RTM panel mold. In a layup where the 0° uniweave material is not on the surface, this phenomena is mitigated. This was demonstrated by testing a symmetric, balanced 0°/90° layup, i.e., $90/0_2/90_2/0_2/90$, and a 90° layup for determining indirectly the effective 0° strength. The result from these tests, where the 0° plies are sandwiched and supported between 90° plies, was a strength value of 2172 MPa. The 2172 MPa value was considered the true 0° in-plane strength of a 95/5 uniweave fabric, where the debit in strength is associated with fiber crimp instead of other artifacts. Additionally, a wider specimen can be tested in this indirect approach, reducing the potential for free edge delamination failures to occur. Nonetheless, for preliminary allowables, the lower typical value of 1524 MPa was conservatively used to produce the static allowable.

The ASTM D 3039 uniweave S-N data are shown in Fig. 5*a*. Failure modes were similar to the second scenario static tests and the slope of the *S-N* curve was steeper than anticipated when reflected against 0° carbon/epoxy prepreg data [*4*].

For the braid material, the specimen width was also a consideration due to the coarseness of the plain weave yarns. Initial tests were performed on 25.4 mm wide, tab-less coupons. Later tests were performed on 38.1-mm-wide coupons, similar to Refs *11* and *12*. The parameters for the failure criteria and elastic constants were determined by testing 0°/90° and ±45° coupons and estimating the 90° properties from micromechanics equations [*13*]. The panels were prepared from tubes braided at ±45° and flattened in the mold and resin injected. Braid angles were difficult to control in the mold

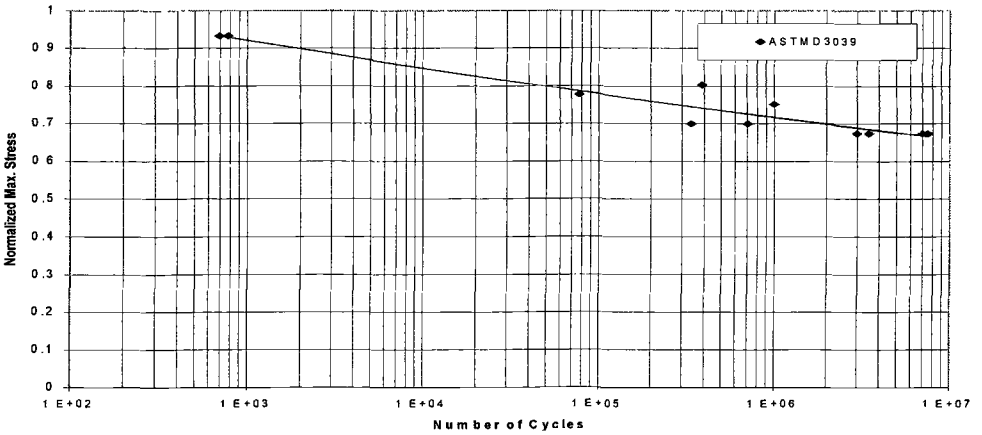


FIG. 5*a*—*0° 95/5 uniweave IM-7, 12K/PR500 fatigue results*, R = *0.1, RTA,* Vf = *55%.*

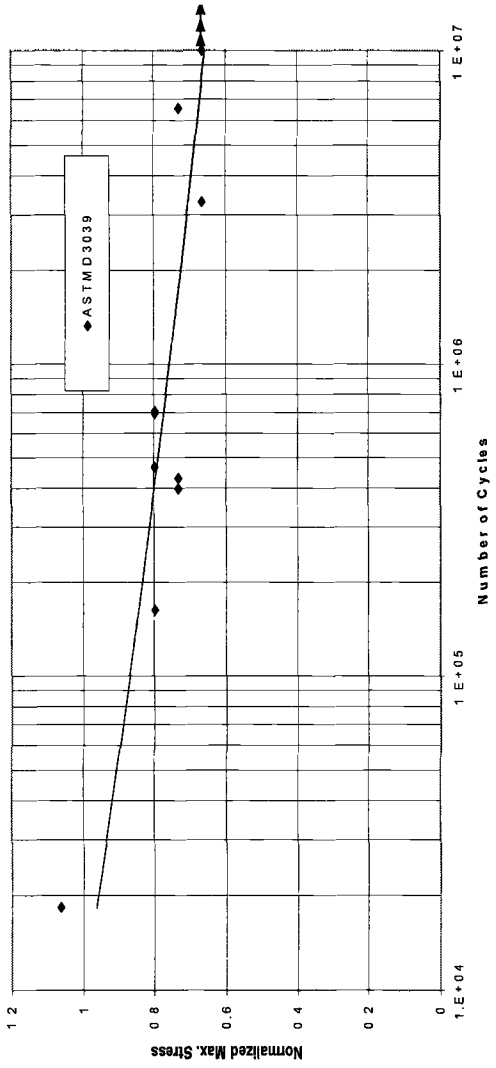


FIG. 5b—*±45° IM-7 braid/PR500 fatigue results,* R = *0.1, RTA,* Vf = *55%.*

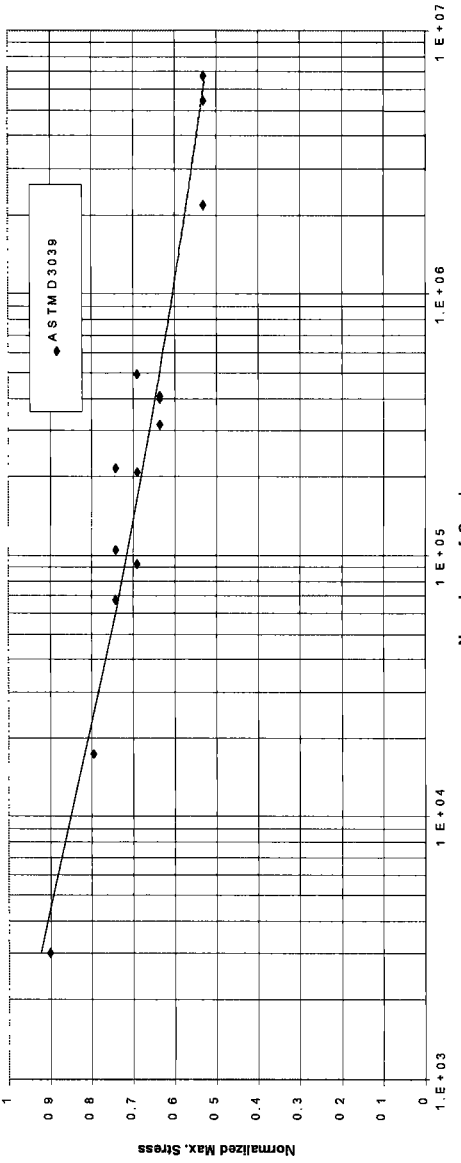


FIG. 5c—*80% ±45° IM-7 braid 0.20% 0 ± Unitape/PR500 fatigue results,* R = *0.1, RTA,* Vf = *63%.*

and later characterization tests used an averaging method to get the ±45° properties by removing specimens from panels in both orthogonal directions. With ASTM D 3518 as a guideline, braid elastic constants were obtained as follows by testing 0°/90° orientation coupons with extensometers and strain gages to get modulus and Poisson's ratio, respectively

$$G_{\pm 45^\circ} = \frac{E_{0^\circ - 90^\circ}}{2(1 + \mu_{0^\circ - 90^\circ})} \tag{3}$$

$$E_1 = 2(E_{0^\circ - 90^\circ}) - E_{2theo} \tag{4}$$

One can also estimate the effective UTS_{0° from the 0°/90° ultimate strength by

$$UTS_{0^\circ} = 2(UTS_{0^\circ - 90^\circ}) - UTS_{90^\circ theo} \tag{5}$$

From the ±45° coupons, shear modulus and strength were determined by

$$G_{0^\circ} = G_{0^\circ - 90^\circ} = \frac{E_{\pm 45^\circ}}{2(1 + \mu_{\pm 45^\circ})} \tag{6}$$

$$USS_{0^\circ} \approx \frac{USS_{\pm 45^\circ}}{2} \tag{7}$$

The initial tests were performed on an IM-7, 12K, two ends per yarn braid construction, which was then replaced by the Production T300J, 6K, three ends per yarn braid. The lower-cost T300J was acceptable since the T300J ±45° shear modulus from Eq 3 was equivalent to the IM-7 system. This equivalent shear modulus was realized by the fact that the T300 braid yarn aspect ratio afforded a lower apparent fiber waviness in the braid which offset the lower fiber modulus of T300 (234 GPa) compared with IM-7 (290 GPa). The shear modulus requirement was important to the design to assure the blade was free from torsional stall flutter. All the braid tensile results were compared with test data on a prepreg system [*14*], see Fig. 6. Good correlation was noted for T300/PR500 braid results when compared with the prepreg results, since the waviness ratio, as defined in Ref *15*, was nil for this braid system and due to the wider specimens tested.

The fatigue results are shown in Fig. 5*b*, for the IM-7 braid material. T300 braid fatigue data were produced but not included, since fiber angles were closer to ±40° than to ±45°. To verify the Rule-of-Mixtures assumption, ASTM D 3039, 25.4-mm-wide specimens were tested with a $[\pm 45_b/0_{2u}/\pm 45_b/0_{2u}/\pm 45_b]$ layup, where b = IM-7 braid and u = unidirectional prepreg. These 80% braid/20% unidirectional hybrid layup results, when normalized according to fiber volume, showed Rule-of-Mixtures strength to be 5% less than test value. Fatigue data are included in Fig. 5*c*, which shows a low dispersion in results (Cv = 6.3%). These results confirmed the adequacy of the Rule-of-Mixtures approach and the Cv = 10% rule for the preliminary in-plane allowables.

Spar, Out-of-Plane Loading and Bond Joint

For out-of-plane loading, associated with delamination in the root section of the blade during subelement and full-scale fatigue testing, it was necessary to invoke a biaxial interlaminar stress criteria for preliminary design allowables. The biaxial nature of stress was due in part to the thick composite laminate, the tab end geometry effects and the influence of the hoop and compression wrap regions. The tulip-to-spar bond joint adhesive layer was also influenced by these factors and a failure criteria was adopted from Ref *16*, which is based on an apparent shear strength as a function of the normal-shear stress interaction. For compressive or negative normal stresses, the appar-

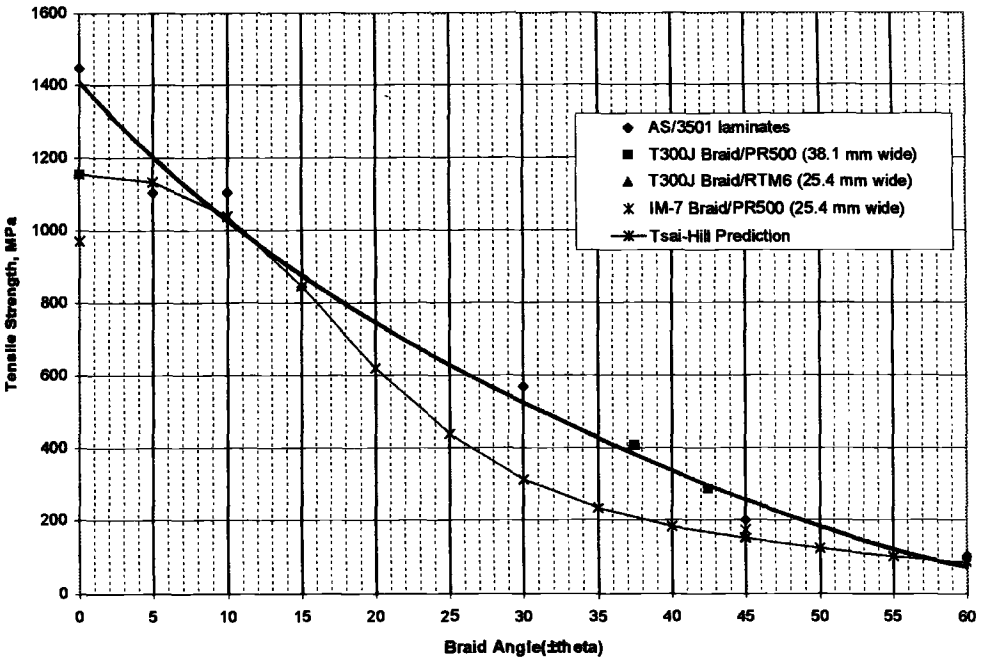


FIG. 6—*Tensile strength vs. braid angle.*

ent shear strength is proportionately greater than the shear strength with zero normal stress and proportionately less under the influence of tensile or positive normal stresses. This approach was adopted for the adhesive, as an equivalent von Mises shear stress and for the resin between laminate layers, for the interlaminar shear stresses (τ_{xz} or τ_{yz}) as a function of the normal/shear stress ratio (τ/σ_z).

For purpose of producing fatigue as well as static interlaminar shear allowables, a nonstandard short beam test coupon was selected for characterization, see Fig. 7*a*. This configuration was selected over ASTM Test Method for Apparent Interlaminar Shear Strength of Parallel Fiber Composites by Short Beam Method (D 2344) to mitigate fretting under the load nose, which had an increased radius. The span was also increased to accommodate the nose and the width was increased to minimize edge effects. An alternating $\pm 45_c/0_u$ layup was used, with c = T300J cloth (7 plies total) and u = uniweave (6 plies total). The failure modes were predominately single layer, midplane delaminations, with some specimens exhibiting multiple interlaminar failure. Several R-ratios were tested, with the most

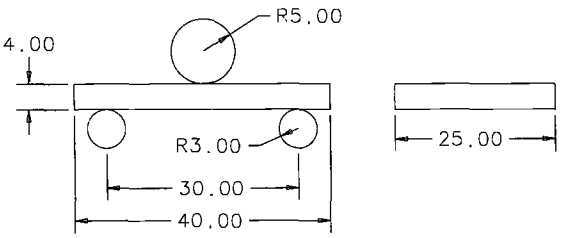


FIG. 7*a*—*Short beam shear fatigue test configuration.*

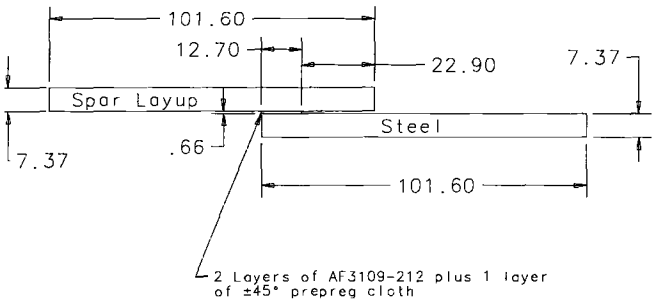


FIG. 7*b*—*Spar/tulip bond joint fatigue test configuration.*

specimens tested at $R = 0.1$. Figure 8*a* shows the *S-N* data. Unlike the in-plane loading tests, the scatter for short beam fatigue was greater than 10%. The data were plotted on a modified Goodman diagram to develop a relationship between cyclic and steady stress. The allowables were later calibrated with full-scale fatigue test results using finite-element analyses and showed reasonable results for predicting delamination initiation lives when comparing the cyclic shear stresses, at a given steady stress as a function of the maximum stress $\tau_{max}/\sigma_{z,max}$ ratio. This calibration of analysis to preliminary allowables is used to properly account for the thermal cure steady stress component in the blade.

The adhesive bond joint was also characterized to produce preliminary allowables. A variety of specimens was used in a separate building block approach to evolve both the process and the stress analysis. Many of the specimen configurations listed in the ASTM Standard Guide for Use of Adhesive-Bonded Single Lap-Joint Specimen Test Results (D 4896) were used. This included specimens to screen potential adhesives for hot-wet performance and to select candidates based on shear stress-strain behavior, as well as for surface preparation optimization, for batch variation, for correlating the von Mises peak stress criteria and finally for static and fatigue preliminary allowables. For static allowables, the ASTM Test Method for Measuring Strength and Shear Modulus of Nonrigid Adhesives by the Thick Adherend Tensile Lap Specimen (D 3983) was employed with aluminum adherends, i.e., the shear stress at the knee of the stress-strain curve was used to determine a static strength allowable. For fatigue, a more complex single overlap specimen with composite and steel adherends was used to fully represent the bonding constituents. A 2-D finite-element analysis was used to determine stress components in the adhesive and surrounding adherend layers for predicting influence of normal stresses. The specimen was designed to promote a failure either within the adhesive layer or at the resin bond layer between the prepreg and the spar laminate and not within the spar laminate. This was accomplished by the overhanging of the composite as shown in Fig. 7*b*. Both RTA and hot-wet (115°F/saturated) tests were performed. Failure mode for RTA environment was within the resin bond interface and for the hot-wet tests, the failure was cohesive in the adhesive layer. The RTA *S-N* results, Fig. 8*b*, show a fatigue slope similar to that of the SBS fatigue tests, but with scatter less than 10%. The slope similarity was important for setting test levels for subelement and full-scale testing.

Subelement and Full-Scale Tests

A brief summary of test experience is provided to tie together with coupon testing.

Spar In-Plane Loading

The spar preliminary design allowables were verified by two types of tests: (1) mean stress, and (2) zero mean stress. These types are resonant blade tests with strain gages placed on the

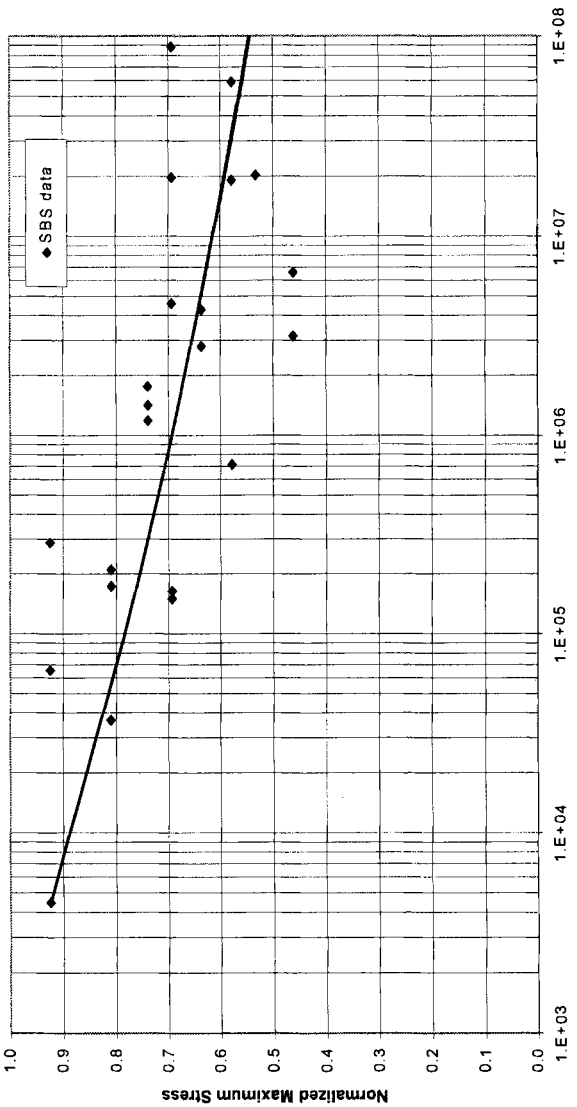


FIG. 8*a*—*0° IM–7 uniweave/145° T300J cloth/PR500 SBS results at* R = *0.1, RTA.*

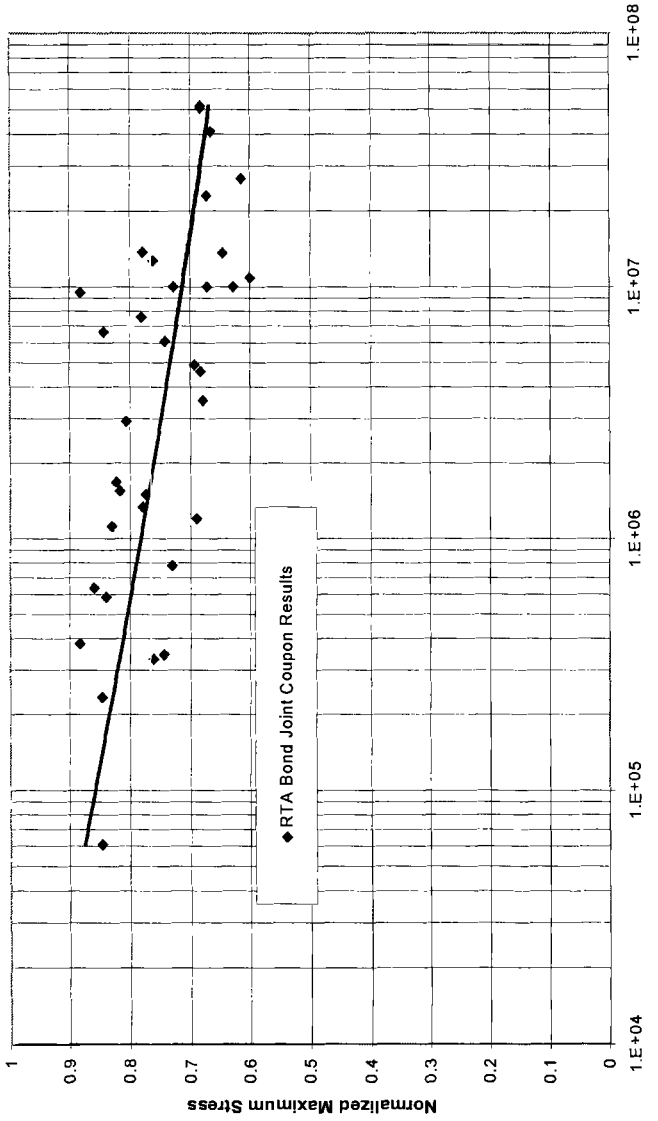


FIG. 8*b*—*Steel/spar bond joint single overlap shear stress cycles.*

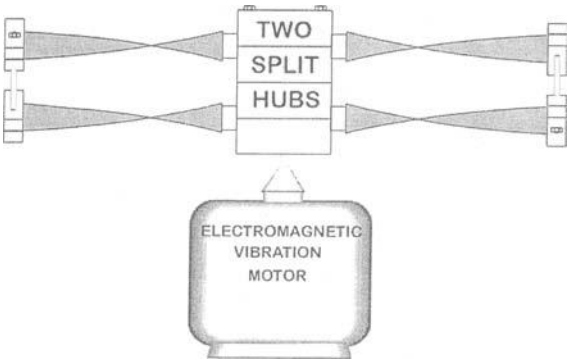


FIG. 9*a*—*Schematic of resonant mean stress fatigue test setup.*

outer airfoil surfaces to set test levels based on equivalent strain at the maximum strain, minimum margin areas of the structure. The inboard to mid-blade area was evaluated by the mean stress test in first flatwise mode in which four cropped blades are set up with the ends clamped together to provide a mean bending strain, see Fig. 9*a*. The mean bending strain takes into account the centrifugal load strain and the steady bending strain components matching the correct total strain on the tension side of the blade but not on the compression side. The cropping is established at a station that results in approximation of the full-length blade response to a 1P loading excitation. The outboard end of the blade was evaluated by zero mean stress in the second flatwise mode for paired full-length blades; see Fig. 9*b*. First-level certification testing was performed at various factors above the design limit strain. Subsequent test levels were conducted to produce fractures to determine margins of safety. Test were performed at RTA and at hot-wet conditions, where feasible, with production quality blades and with blades that had manufacturing defects, repairs and barely visible impact damage.

The modes of fracture for these tests have shown interesting results. For the mean stress tests, the blades fracture in the spar in a classic compression-compression fatigue failure mode. Hence, the desired tension-tension fractures were not attained, but runout levels of strain are much higher than the preliminary allowables would suggest. For the zero mean tests, the failures are associated with sheath cracks that propagated into the Kevlar shells, which occurred well above the design limits set for both materials. The operating stresses in the blade are below the design limits.

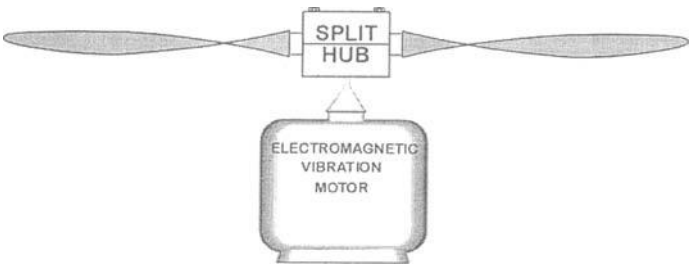


FIG. 9*b*—*Schematic of resonant zero mean fatigue test setup.*

Spar, Out-of-Plane Loading and Bond Joint

The root area of the blade was structurally evaluated several ways with subelement specimens, which represent full-size blades without the airfoil foam and shell, for each of several design concepts. To address the potential for a propeller overspeed condition, intentionally unbonded subelements were tested under static axial load. For certification, the samples must sustain a load level of twice the centrifugal load plus hot-wet factors for one hour. Tests are then continued to fracture for safety margin assessment. This approach evaluates the mechanical entrapment mechanism of the design. Failure modes for these tests were influenced by the braid hoop strain capability as the unbonded spar slides up the tulip wedge under axial load. Demonstrated strength levels exceeded the coupon test expectations in all cases, due in part to absence of edge effects.

To address the fatigue strength of the blade root, subelements were tested in various ways using servo-hydraulic actuators to apply loads. The low- and high-cycle fatigue tests, LCF and HCF, were

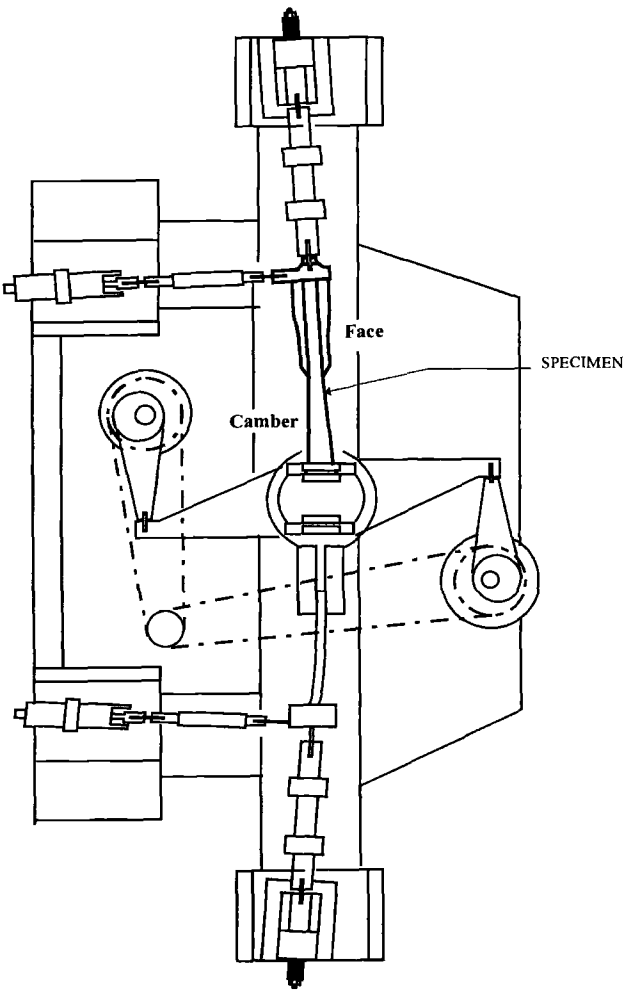


FIG. 10—*Axial/bending spectrum loading blade test setup.*

conducted with a combination of axial load, steady bending moment and cyclic bending moment. Factors were applied to the loads and cycles to account for material scatter, environmental effects and *S-N* curve shape. The results of the LCF and HCF tests were used to develop A-Basis allowables based on bending moment as opposed to strain. The failure mode of each test was verified to assure test factors were properly accounted for by the coupon characterization. These subsequent bending moment allowables were then interrogated by a series of spectrum load tests, Fig. 10, to assess a damage accumulation model for the blade root.

Conclusions

The ASTM test methods were used extensively but not solely for characterizing the properties required for the RTM composite propeller. Alternate specimen configurations were required to produce proper failure modes due to material geometry effects and fatigue issues. Development of the preliminary allowables for an RTM composite propeller blade was minimized at the coupon test level by a combination of: (1) testing more full-size specimens to develop the proper failure mechanism and safety margins for the blade, (2) usage of a Three Sigma approach and an average $Cv = 10\%$, (3) usage of the Rule-of-Mixture approach for in-plane allowables, (4) usage of a biaxial failure methodology for spar interlaminar shear and adhesive von Mises shear, and (5) having batch variation tests performed as part of material specification requirements. Verification of preliminary allowables showed higher strain capabilities for full-scale tests with in-plane failure modes. This was due in part to lack of edge effects. For out-of-plane failure modes, predicting failure was more complex due to presence of residual cure stresses and other geometric effects. Hence, final allowables were based on an equivalent bending moment approach under monotonic loading, which was later verified by spectrum testing.

Acknowledgments

Special thanks are extended to Mr. Patrice Brion, composite specialist at Ratier-Figeac, France, for his expertise on coupon testing and to Mr. Philippe Bailly, blade test specialist at Ratier-Figeac, France, for his fatigue test efforts. Sincere appreciation is also extended to Mr. John Kattler, chief technician of Hamilton Standard Structures Lab., for his contribution to the generation of the fatigue test data.

References

[1] MIL-HDBK-17-1E, Vol. 1, Chapter 2.1.
[2] Graff, J. M., Violette, J. A., et al., U.S. Patent No. 5,222,297, 29 June 1993.
[3] Sanger, K. B., Dill, H. D., and Kautz, E. F., "Certification Testing Methodology for Fighter Hybrid Structure," *Composite Materials: Testing and Design (Ninth Volume), ASTM STP 1059,* 1990.
[4] Hahn, H. T., "Fatigue Behavior and Life Prediction of Composite Laminates," *Composite Materials: Testing and Design (Fifth Volume), ASTM STP 674.* 1979.
[5] Salkind, M. J., *Composite Materials: Testing and Design (Second Volume), ASTM STP 497,* 1972.
[6] Whitney, J. M., "Fatigue Characterization of Composite Materials," AFWAL-TR-79-4111, Air Force Laboratory, Oct. 1979.
[7] Hart-Smith, J. "Some Observations about Test Specimens and Structural Analysis for Fibrous Composites," *ASTM STP 1059,* 1990.
[8] Thorat and Lakkad, "Fracture Toughness of Unidirectional Glass/Carbon Hybrid Composites," *Journal of Composite Materials,* Jan. 1983.
[9] Harris and Morris, "A Comparison of the Fracture Behavior of Thick Laminated Composites Utilizing Three Specimen Configurations," *Fracture Mechanics, ASTM STP 905,* 1986.
[10] Caprino and Halpin, "Fracture Mechanics in Composite Materials," *Composites,* 1979.
[11] Yang and Jones, "Statistical Fatigue of Graphite/Epoxy Angle-Ply Laminates in Shear," *Journal of Composite Materials,* Vol. 12, Oct. 1978.

[12] Curtis and Moore. "A Comparison of the Fatigue Performance of Woven and Nonwoven CFRP Laminates." *ICCM V,* 1987.
[13] Chamis, C. C., "Simplified Composite Micromechanics Equations for Strength, Fracture Toughness, Impact Resistance and Environmental Effects," NASA N84-27832.
[14] Kim, R. Y., "On the Off-Axis and Angle Ply Strength of Composites." *ASTM STP 734,* 1981.
[15] Whitcomb, J., "Three Dimensional Stress Analysis of Plain Weave Composites," NASA TM101672, Nov. 1989.
[16] Greszczuk, L. B., "Strength of Adhesives Under Combined Loading," *Proceedings, SAMPLE Conference,* Oct. 1987.

Bolted Joint Analysis

Endel V. Iarve[1] *and David H. Mollenhauer*[2]

Three-Dimensional Stress Analysis and Failure Prediction in Filled Hole Laminates

REFERENCE: Iarve, E. V. and Mollenhauer, D. H., **"Three-Dimensional Stress Analysis and Failure Prediction in Filled Hole Laminates,"** *Composite Structures: Theory and Practice, ASTM STP 1383*, P. Grant, and C. Q. Rousseau, Eds., American Society for Testing and Materials, West Conshohocken, PA, 2000, pp. 231–242.

ABSTRACT: An observed stacking sequence effect [*1*] on pin bearing strength was examined by three-dimensional modeling. A displacement spline approximation method was used to perform the stress analysis. The laminate and the fastener were assumed to be linear elastic. Processing residual stresses were included in the analysis. The contact region and stress were unknown a priori and resulted from the solution. A nonuniform contact region through the thickness was allowed. Undamaged thermoelastic moduli were employed in the model. A stacking sequence effect on bearing strength was investigated by comparing stress distributions in two quasi-isotropic laminates of $[0_2/90_2/45_2/-45_2]_s$ and $[0_2/45_2/90_2/-45_2]_s$ stacking sequence. Stress magnitudes were displayed relative to ply strength properties. It was observed that all stress components, including the in-plane stresses, were affected by the stacking sequence. In the vicinity of the bearing plane, very high transverse shear stresses were found. A qualitative agreement between predicted stress distributions and experimental damage investigation, performed in Ref *1*, was demonstrated. Using a point stress failure criterion, a prediction of failure onset was performed. The predicted failure initiation load for the $[0_2/90_2/45_2/-45_2]_s$ stacking sequence was approximately 40% higher than the predicted failure initiation load for the $[0_2/45_2/90_2/-45_2]_s$ stacking sequence.

KEYWORDS: composite, bolted joint, three-dimensional stress analysis, damage initiation prediction, stacking sequence effect

Bolted joining remains a primary joining method of load carrying composite structural elements in the modern aerospace industry. Significant attention in the literature has been given to practically all aspects of composite bolted joining, both in the analysis and experimental fields as described in a recent survey [*2*]. The need for a composite bolted joint design tool led to development of several composite bolted joint failure prediction programs, reviewed by Snyder et al. [*3*], and utilized in the industry. The common mechanical foundation for all of these tools reviewed is lamination theory combined with average or point stress failure criterion to predict final strength. A different failure prediction methodology, based on fracture mechanics, was developed in Refs *4* and *5* and is based on pseudo-crack propagation in the radial direction from the hole edge. Energy release rates for these cracks are obtained by utilizing the rule of mixtures and the number of plies of each orientations—0, ±45, and 90—in the laminate. In all of the above methods, the fastener-plate contact stress is assumed to vary as a cosine function over half the hole circumference with an amplitude of $-4/\pi$ times the nominal bearing stress. The advantage of these largely empirical approaches is that a broad spectrum of problems can be solved without significant computer resources. The disadvantage is the need for an extensive test database that is required for each new material system utilized. To develop new tools for composite bolted joint design and strength prediction based on measured ply properties, an

[1] Research engineer, University of Dayton Research Institute, Dayton, OH 45469.
[2] Materials research engineer, Air Force Research Laboratory, Wright-Patterson AFB, OH 45433-7750.

Copyright© 2001by ASTM International www.astm.org

in-depth understanding of the bearing failure mechanisms is important. Recent experimental works [*1,6,7*] dealing with graphite-epoxy laminates provide detailed investigation of the bearing failure process and show similar results. The specimens subjected to bearing loading were X-rayed and sectioned at different load levels lower or equal to the failure load. Microscopic studies of the bearing plane sections showed that bearing failure consists of a damage accumulation process initiated in the interior of the laminate at the hole edge. It consists of 45° transverse shear cracks propagating to the outer surfaces from the hole edge. According to Refs *6* and *7* in the case of a pin loaded hole, these cracks reach the outer surfaces at approximately a quarter of the laminate thickness away from the hole edge, resulting in final failure. In all cases, massive delamination was observed on the interior interfaces prior to failure. In the presence of clamping forces [*8*], the damage mechanism does not seem to change. The failure load significantly increases because the final failure does not occur until the damage accumulation region reaches the outer washer diameter, provided that the washer can carry the increasing plate expansion force. As concluded in Refs *1* and *6*, the bearing failure is a substantially three-dimensional process involving delamination and transverse shear; although in the sequel of works [*7,8*], the authors proposed a two-dimensional bearing strength prediction model, which was shown to provide good correlation with experimentally measured bearing strength. This model is based on nonlinear finite-element simulation with gradual property degradation algorithms.

Lamination theory, however, cannot account for stacking sequence effects on bearing strength. Hamada et al. [*1*] tested four symmetric laminates stacked with sequences of 0_2, $+45_2$, -45_2, and 90_2 ply groups. The material used was T300/2500. The bearing strength results obtained in Ref *1* are summarized in Table 1, and the specimen geometry used throughout this research is shown in Fig. 1. An approximately 13% difference was observed for specimens C and N, corresponding to stacking sequences $[0_2/90_2/45_2/-45_2]_s$ and $[0_2/45_2/90_2/-45_2]_s$, respectively. These specimens differ by an apparently minor alteration in stacking sequence only. The only difference is in exchanging the 90° and +45° plies while retaining the position of the 0° plies on the outside and −45° plies at the midsurface. The purpose of the present work is to perform three-dimensional stress analysis to explain the effect that such a small change of the stacking sequence can have on laminate pin bearing strength. Damage related stress redistribution was not considered in this research.

A previously developed fully three-dimensional stress analysis procedure [*9*] was used to examine the stress distributions occurring under bearing loading. The procedure is based on a cubic spline approximation of displacements along with a curvilinear transformation technique also based on the spline approximation. Due to the highly nonuniform stress-strain field through the thickness of the laminate, the contact zone becomes nonuniform through the thickness. An automated algorithm was developed for contact zone definition. Verification of the results of the interlaminar stress prediction was accomplished by comparison with the asymptotic solution.

Problem Definition

Consider a rectangular orthotropic plate containing a circular hole having a diameter D, as shown in Fig. 1. The plate consists of N plies of total thickness H in the z-direction and has a length L in the x-direction and width A in the y-direction. A circular isotropic elastic fastener of diameter d is situ-

TABLE 1—*Experimental bearing failure stresses obtained from Ref* 1.

Specimen Identification and Stacking Sequence	Bearing Stress, MPa
N—$[0_2/+45_2/90_2/-45_2]_s$	318
A—$[0_2/+45_2/-45_2/90_2]_s$	333
B—$[-45_2/0_2/+45_2/90_2]_s$	338
C—$[0_2/90_2/+45_2/-45_2]_s$	360

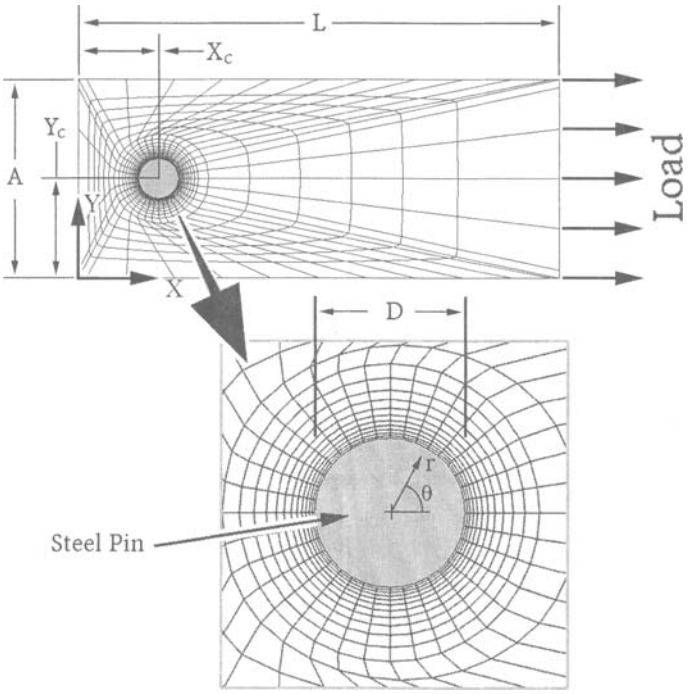


FIG. 1—*Specimen geometry.* L = *72 mm,* A = *30 mm,* D = *6 mm,* Xc = *12 mm,* Yc = *15 mm, and ply thickness ~0.25 mm.*

ated at the center of the hole. The length of the fastener in the z-direction is equal to the plate thickness H. We will consider the bearing loading case when the load is applied via displacement boundary conditions at $x = L$ while all other boundaries were kept free

$$u_x(L,y,z) = u_L,\ u_y(L,y,z) = u_z(L,y,z) = 0$$
$$\sigma_{xx}(0,y,z) = \sigma_{xy}(0,y,z) = \sigma_{xz}(0,y,z) = 0 \tag{1}$$

A cylindrical coordinate system is defined originating from the center of the hole

$$x = r\cos\theta + x_c, y = r\sin\theta + y_c, z = z \tag{2}$$

where x_c and y_c are the coordinates of the center of the hole. The fastener displacements will be denoted as v_r, v_θ, and v_z. The in-plane motion of the fastener is fixed at two points located at the center of the top and bottom fastener surfaces $z = 0$ and $z = H$, and the z displacement is fixed at the midsurface. In cylindrical coordinates, the boundary conditions are as follows

$$v_r(0,\theta,0) = v_\theta(0,\theta,0) = 0$$
$$v_r(0,\theta,H) = v_\theta(0,\theta,H) = 0 \tag{3}$$
$$v_z(0,\theta,H/2) = 0$$

For small deformations, the nonpenetration condition can be simplified as

$$u_r(D/2,\theta,z) - v_r(d/2,\theta,z) + \Delta R \geq 0 \tag{4}$$

where $\Delta R = D/2\text{-}d/2$ is the clearance between the hole and the fastener and u_r is the radial displacement of the composite plate.

The minimum potential energy principle along with the Lagrangian multiplier method was used to solve the problem. Frictionless contact is considered. The first variation of the following functional is required to vanish.

$$\delta\left(\Pi_p + \Pi_b + \int_{\Omega}\int_{(\theta,z)} \lambda(\theta,z)(u_r(D/2,\theta,z) - v_r(d/2,\theta,z) + \Delta R)dS\right) = 0 \tag{5}$$

The potential energy of the laminate is denoted as Π_p, and the potential energy of the elastic fastener as Π_b. $\Omega(\theta,z)$ is the contact zone on which relationship (4) becomes an equality. The size and location of this zone is unknown initially. Functional (5) suggests a simple interpretation for the Lagrangian multiplier as the value of the radial stress at the contact surface, i.e., $\sigma_{rr}^{(p)}(D/2,\theta,z) = \sigma_{rr}^{(b)}(d/2,\theta,z) = \lambda(\theta,z)$; $(\theta,z) \in \Omega(\theta,z)$.

In the following sections, the spline approximation of the functions included in Eq 5 will be constructed.

Spline Approximation

Curvilinear coordinates ρ and ϕ were introduced to map the plate with a cutout into a region $0 \leq \rho \leq 1$ and $0 \leq \phi \leq 2\pi$. Coordinate lines of this transformation are shown in Fig. 1. The transformation is built according to [*10*] so that the coordinate line $\rho = 0$ corresponds to the hole edge and $\rho = 1$ to the outer rectangular contour of the plate. The radial lines correspond to ϕ = constant. Sets of B-type cubic basis spline functions

$$\{R_i(\rho)\}_{i=1}^{m+3},\ \{\Phi_i(\phi)\}_{i=1}^{k+3},\ \{Z_i^{(s)}(z)\}_{i=1}^{n_s+3} \tag{6}$$

along each coordinate were built upon subdivisions $0 = \rho_0 < \rho_1 < \ldots < \rho_m = 1.0 = \phi_0 < \phi_1 < \ldots < \phi_k = 2\pi$, and $z^{(s-1)} = z_0 < z_1 < \ldots < z_{n_s} = z^{(s)}$ so that the sth ply occupies a region $z^{(s-1)} \leq z \leq z^{(s)}$ and n_s is the number of sublayers in each ply. The subdivision of the ρ coordinate is essentially nonuniform. The interval size increases in geometric progression beginning at the hole edge. The region $0 \leq \rho \leq \rho_{h}$ in which the curvilinear transformation is quasi-cylindrical is subdivided into m_0 intervals, so that $\rho_h = \rho_{m_0}$. The numbers of intervals of subdivision m, k, and n_s in each direction along with the mesh nonuniformity characteristics, such as m_0 and the consecutive interval ratio, determine the accuracy of the solution and the size of the problem.

The detailed solution procedure, including determination of the contact region, has been described in Ref *9*.

Failure Criteria

Bearing failure can be manifested by a combined effect of all individual failure modes: tensile fiber breakage, micro-buckling, delamination, matrix cracking, and compression/shear cracking. As a noncatastrophic failure mode [*6*], it can only be adequately described by taking into account the stress redistribution resulting from damage initiation and growth. As a result of the three-dimensional nature of the stress field in the bearing contact region, the modeling of bearing failure represents a challenging task. It has been accomplished so far in simplified two-dimensional models [*7,8*] that neglect delamination and stacking sequence effects. In the present work, a three-dimensional stress

analysis was performed instead to evaluate the magnitude of the interlaminar stress components and the effect of stacking sequence on bearing strength. No effect of stress redistribution due to damage was considered.

To put the stress values in perspective, they were compared to the respective ultimate strength. Six dimensionless functions s_i, $i = 1, \ldots, 6$, were introduced such that

$$ss_1 = \begin{cases} \dfrac{\sigma_{11}}{X_T}, & \sigma_{11} > 0 \\ \dfrac{\sigma_{11}}{X_c}, & \sigma_{11} < 0 \end{cases} \tag{7}$$

$$s_2 = \begin{cases} \dfrac{\sigma_{22}}{Y_T}, & \sigma_{22} > 0 \\ \dfrac{\sigma_{22}}{Y_c}, & \sigma_{22} < 0 \end{cases} \qquad s_3 = \begin{cases} \dfrac{\sigma_{33}}{Y_T}, & \sigma_{33} > 0 \\ \dfrac{\sigma_{33}}{Y_c}, & \sigma_{33} < 0 \end{cases} \tag{8}$$

$$s_4 = \left| \frac{\sigma_{23}}{S} \right| \qquad s_5 = \left| \frac{\sigma_{13}}{S} \right| \qquad s_6 = \left| \frac{\sigma_{12}}{S} \right| \tag{9}$$

The stress components σ_{ij}, $i, j = 1,2,3$ are in ply material coordinates and the x_1-axis coincides with the fiber direction. Parameters X_T and X_c are the tension and compression strength of the unidirectional laminate in the fiber direction, Y_T and Y_c are the tension and compression strength in the transverse direction, and S is the in-plane shear strength. The in-plane shear strength is also used for scaling the interlaminar shear stress components.

Bearing loading generates a three-dimensional state of stress in the vicinity of the hole edge. Comparison of the stress components to the respective ultimate material direction strengths neglects mode interaction. In the present work, the use of interactive failure criteria, such as Tsai-Wu [*11*] or Hashin [*12*], has been avoided because of a lack of experimental evidence supporting the reliability of strength prediction by these criteria in a three-dimensional state of stress as well as under stress gradients. All stress components in the present paper will be examined separately by using Eqs 7 to 9.

Three-dimensional ply level analysis performed in the present paper results in stress singularities at the ply interface and the hole edge intersections. In order to predict the onset of failure, a point stress criterion was applied. Failure initiation was predicted when one of the functions s_i, $i = 1, \ldots, 6$ has an absolute value greater than one at a distance of a ply-group (two plies) thickness away from the hole edge. The choice of a one-ply-group thickness characteristic distance was influenced by Kim and Soni [*13*] who used a one-ply thickness characteristic distance with an average stress failure criteria for prediction of delamination onset.

Numerical Results and Discussion

A schematic of the bearing specimen is shown in Fig. 1. To perform the three-dimensional stress analysis and to apply the failure criteria, a full set of thermoelastic and strength characteristics is needed. Because of a lack of sufficient data on the material tested in Ref *1*, a similar T300/5250 material was used for the analysis. The stiffness and strength parameters for T300/5250 are given in Table 2. The estimated temperature difference between the room temperature and the cure temperature, required for residual stress calculation, was $-100°C$. Bearing load was applied through the displacement boundary conditions (1). The applied bearing stress was calculated as

$$\sigma_B = \frac{1}{AD} \int_0^H \int_0^A \sigma_x(L,y,z)dydz \tag{10}$$

TABLE 2—*Material properties used in modeling.*

Elastic Constants	Failure Parameter
$E_1 = 181.0$ GPa	$X_T = 1500$ MPa
$E_2 = E_3 = 10.3$ GPa	$X_C = 1500$ MPa
$\nu_{12} = \nu_{13} = 0.28$	$Y_T = 40$ MPa
$\nu_{23} = 0.40$	$Y_C = 246$ MPa
$G_{12} = G_{13} = 7.17$ GPa	$S = 68$ MPa
$G_{23} = 3.68$ GPa	
$\alpha_1 = 0.02 \times 10^{-6}$/°C	
$\alpha_2 = 22.5 \times 10^{-6}$/°C	

The subdivisions in the circumferential and radial directions in the plate were $k = 36$ and $m = 18$, with $m_0 = 12$ intervals in the near hole region and the size ratio $q = 1.2$. The subdivisions in the radial and circumferential directions in the fastener were $k_b = 36$, $m_b = 8$, and $q_b = 1.2$. Two sublayers through the thickness of each ply were used. Only the upper half of the laminate was modeled because of symmetry.

First, the effect of stacking sequence on stress components was examined. The load level corresponding to failure of the weaker of the two specimens was chosen, so that $\sigma_B = 318$ MPa. The influence of stacking sequence on the in-plane stress components is illustrated in Fig. 2. The functions s_1, s_2, and s_6, introduced in Eqs 7 to 9, are shown on the bearing plane. This location was chosen due to available experimental evidence showing the bearing plane to be a critical damage area in the specimens. Both specimens had holes with a relatively small diameter (compared to specimen dimensions) and exhibited bearing-type failure. Five gray-scale color codes are used to display the results. The white regions correspond to $s_i < -1$ (i.e., compression failures) and the darkest regions correspond to $s_i > 1$ (i.e., tensile failures) for $i = 1,2,3$. In the case of the shear stresses, the functions s_i, $i = 4,5,6$, can only have positive values. The largest effect of the stacking sequence change on in-plane stress components can be seen for the transverse normal stresses. Figure 2*b* shows that the $s_2 > 1$ region (tensile matrix cracking) in the 0° ply is twice as large in specimen N compared with specimen C. This can be explained by the strong reinforcing effect of the 90° ply in specimen C compared with the weaker reinforcing effect of the 45° ply in specimen N. The fiber direction normal and in-plane shear stresses, Figs. 2*a* and 2*c*, do not show a significant stacking sequence effect. It should be mentioned that the function values should be compared in the same plies in the two specimens. For example, the difference in appearance of the shear stress function, s_6, in Fig. 2*c* is deceptive. The distribution of s_6 in the 45° and 90° plies in both specimens is quite similar.

Interlaminar stresses developed at the bearing plane were also examined. Of the three interlaminar components, the transverse shear stress, σ_{13}, was found to extend over the largest region where the ultimate value was exceeded. Figure 3*c* shows the contour plots of the function s_5 (Eq 9). For both specimens, σ_{13} exceeded its ultimate value in the vicinity of the hole edge. In the case of the stronger specimen, C, the area where $s_5 > 1$ is much smaller and consists of two isolated subregions at the 90/45 and 45/−45 interfaces. The other interlaminar shear stress component, σ_{23}, reflected in Fig. 3*b* by function s_4, exhibits lower values. The function s_3, related to the transverse normal stress, is shown on Fig. 3*a*. Compared to s_5 it also displays lower values; however, a significant difference in the distributions between the two laminates can be seen. The weaker laminate, N, displays significant tensile stresses throughout the laminate thickness, whereas laminate C has significant transverse normal tensile stress only in a small region in the 90° ply and at the 90/45 interface. This is in qualitative agreement with the cross-sectional micrographic studies of the failed specimens in Ref *1*. The cross section of specimen N shows significant expansion in z-direction with open delaminations in addition to transverse shear-induced 45° matrix cracking and fiber buckling bands. In the case of speci-

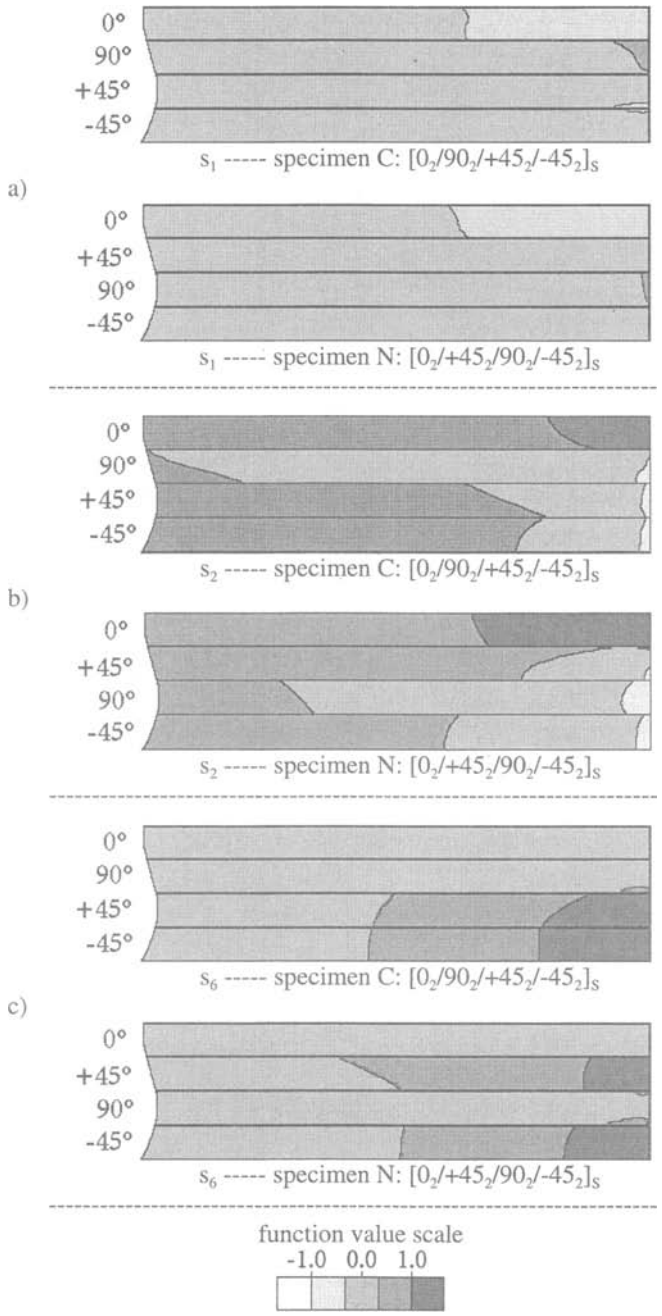


FIG. 2—*Stacking sequence effect on the in-plane stress components at the bearing plane for both specimens.*

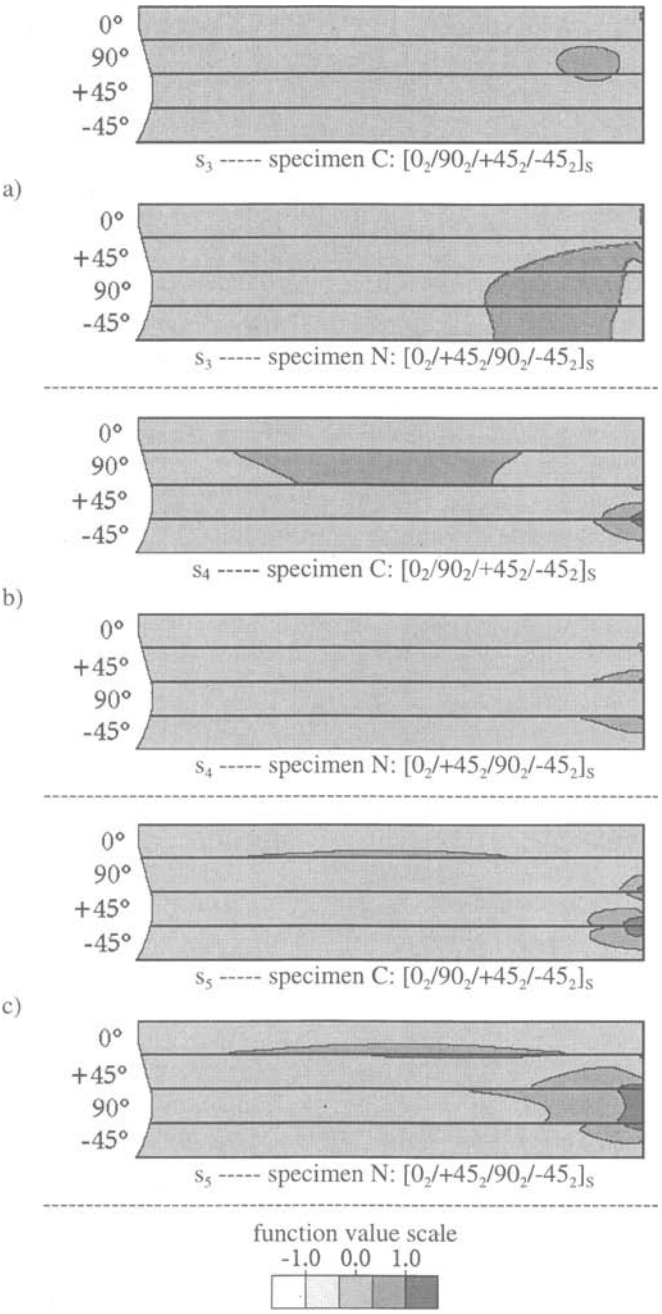


FIG. 3—*Stacking sequence effect on the interlaminar stress components at the bearing plane for both specimens.*

men C, the failed cross section is significantly less expanded in the transverse direction, with delamination clearly visible, but with much less opening. It must be noted that the correlation outlined above is qualitative because the stress state obtained under the assumption of a virgin specimen is not valid at the advanced stages of damage.

The X-rays of the two failed specimens, obtained from Ref *1*, show different patterns of 0° ply splits. The failure load was $\sigma_B = 318$ MPa and $\sigma_B = 360$ MPa for specimen N and specimen C, respectively. The functions s_2 and s_6 were analyzed at these load levels in the 0° ply in both specimens near the interface with the underlying ply. The observed matrix cracking can be produced both by the in-plane transverse tensile stress component and the in-plane shear stress component. Figure 4 displays superimposed gray-scale plots of the functions s_2 and s_6. Only two s_i value intervals, $s_i < 1$ and $s_i > 1$, are shown for each function. The white area corresponds to $s_i < 1$. The light gray corresponds to $s_6 > 1$, the dark gray to $s_2 > 1$, and the medium gray designates the area where both $s_i > 1$. Fig-

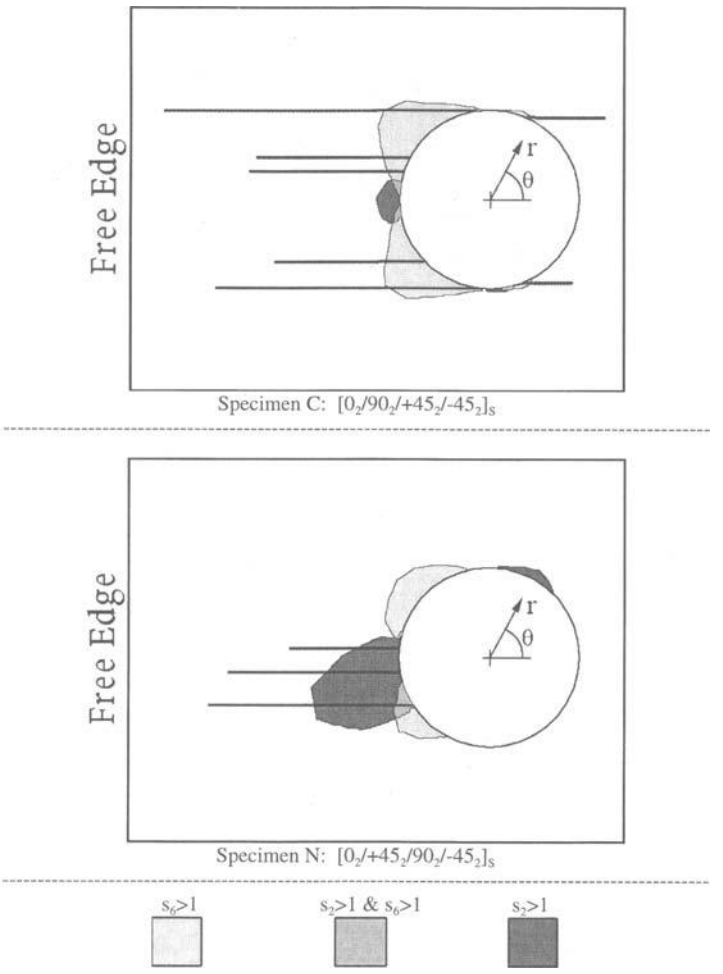


FIG. 4—*Comparison of* s_2 *and* s_6 *for 0° plies in both specimens at their respective failure loads. The straight solid lines represent the most clearly distinguishable 0° ply cracks obtained from X-rays published in Ref* 1.

ure 4 also displays the schematics of the matrix cracks in the 0° plies. They are distributed in a relatively symmetrical manner in laminate C and in a distinctly nonsymmetrical pattern in laminate N. These crack distributions agree well with distributions of the combined fields of $s_2 > 1$ and $s_6 > 1$ in each laminate displayed in Fig. 4. It is worth noting that the application of Hashin's [*12*] matrix cracking criteria, which combines the shear, transverse normal, and interlaminar normal stress components, also provides good agreement with the 0° ply splitting patterns in the two specimens.

Failure initiation prediction was performed by examining criteria 7 to 9 at one ply-group thickness away from the hole edge. The two specimens appeared to have the same initial damage mode—tensile matrix cracking in the 0° and 90° plies. Figure 5 shows the s_2 distribution in these plies at the load

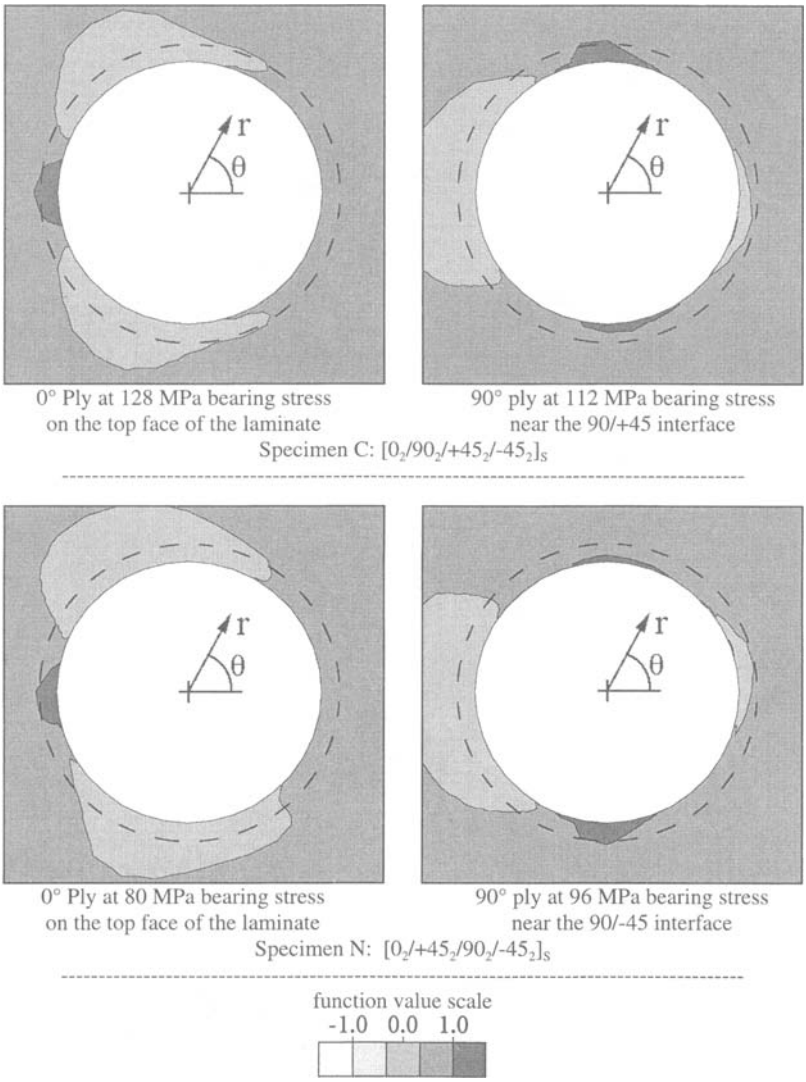


FIG. 5—*Initial damage prediction for both specimens (function* s_2. *The dashed lines represent a radius equal to the hole radius plus one ply-group thickness.*

levels when the $s_2 > 1$ region reached the dashed contour, which is a double ply thickness (one ply-group) away from the hole edge. This occurred in the 0° ply at 80 MPa and in the 90° ply at 96 MPa in specimen N and in the 0° ply at 128 MPa and in the 90° ply at 112 MPa in specimen C. In the 0° ply, this region is in the vicinity of the bearing plane; and in the 90° ply, there are two regions at opposite sides of the hole. Interestingly, the cracking of 0° and 90° plies is predicted in reverse order for the two laminates. The tensile transverse stress component is the dominating stress component at these locations.

Conclusions

1. Three-dimensional stress analysis in quasi-isotropic laminates under bearing loading was performed to explain the effect of stacking sequence on the pin bearing strength observed in Ref *1* by calculating accurate stress fields in undamaged plies.

2. A significant effect of stacking sequence was observed on the transverse normal in-plane stress component and predicted failure initiation loads. The specimen with the lower bearing strength exhibited lower damage initiation loads and a larger critical transverse normal tensile stress ratio area in plies with the same orientation. The 0° ply cracking patterns observed in experiments agree with superimposed in-plane shear and transverse normal stress maps.

3. Transverse shear and normal stresses were analyzed at the bearing plane of the specimens. A larger area of critical transverse shear stress ratio was found in the specimen with lower bearing strength. The transverse normal stress at the bearing plane of the weaker specimen had large areas of significant tensile values correlating with massive thickness expansion and delamination under bearing loading. The stronger specimen had smaller areas of significant tensile transverse normal stresses through the thickness of the bearing plane, which is consistent with the smaller thickness expansion and mostly compression shear failure pattern observed.

Acknowledgments

The first author acknowledges the support of the Materials and Manufacturing Directorate, Air Force Research Laboratory, Wright-Patterson AFB OH, under Contract No. F33615-95-D-5029. Both authors are deeply indebted to Dr. N. Pagano for fruitful discussions at all stages of the work.

References

[*1*] Hamada, H., Haruna, K., and Maekawa, Z., "Effects of Stacking Sequences on Mechanically Fastened Joint Strength in Quasi-Isotropic Carbon-Epoxy Laminates," *Journal of Composite Technology and Research,* Vol. 17, No. 3, 1995, pp. 249–259.

[*2*] Camanho, P. P. and Matthews, F. L., "Stress Analysis and Strength Prediction of Mechanically Fastened Joints in FRP: A Review," *Composites Part A,* Vol. 28A, 1997, pp. 529–547.

[*3*] Snyder, D. S., Burns, J. G., and Venkayya, V. B., "Composite Bolted Joints Analysis Programs," *Journal of Composite Technology & Research,* Spring, Vol. 12, No. 1, 1990, pp. 41–51.

[*4*] Eisenmann, J. R., "Bolted Joint Static Strength Model for Composites Materials," NASA TM_X-3377, *Third Conference on Fibrous Composite Materials in Flight Vehicle Design,* Part II, April 1976.

[*5*] Schulz, K. C., Packman, P. F., and Eisenman, J. R., "A Tension-Mode Fracture Model for Bolted Joints in Laminated Composites," *Journal of Composite Materials,* Vol. 29, No. 1, 1995.

[*6*] Camanho, P. P., Bowron, S., and Matthews, F. L., "Failure Mechanisms in Bolted CFRP," *Journal of Reinforced Plastics and Composites,* Vol. 17, No. 3, 1998, pp. 105–133.

[*7*] Wang, H. S., Hung, C. L., and Chang, F. K., "Bearing Failure of Composite Bolted Joints Part 1: Experimental Characterization," *Journal of Composite Materials,* Vol. 30, No. 12, 1996.

[*8*] Hung, C. L. and Chang, F. K., "Bearing Failure of Composite Bolted Joints Part 2: Model and Verification," *Journal of Composite Materials,* Vol. 30, No. 12, 1996.

[*9*] Iarve, E. V., "3-D Stress Analysis in Laminated Composites with Fasteners Based on the B-spline Approximation," *Composites Part A,* Vol. 28A, 1997, pp. 559–571.

[*10*] Iarve, E. V., "Spline Variational Three-Dimensional Stress Analysis of Laminated Composite Plates with Open Holes," *International Journal of Solids and Structures,* Vol. 33, No. 14, 1996, pp. 2095–2117.

[11] Tsai, S. W., "A Survey of Macroscopic Failure Criteria for Composite Materials," *Journal of Reinforced Plastics and Composites*, Vol. 3, pp. 40–62.

[12] Hashin, Z., "Failure Criteria for Unidirectional Fiber Composites," *Journal of Applied Mechanics*, Vol. 47, 1980, pp. 329–334.

[13] Soni, S. R. and Kim, R. Y., "Delamination of Composite Laminates Stimulated by Interlaminar Shear," *Composite Materials: Testing and Design (Seventh Conference), ASTM STP 893*, J. M. Whitney, Ed., American Society for Testing and Materials, West Conshohocken, PA, 1986, pp. 286–307.

Xinlin Qing,[1] *Hsien-Tang Sun,*[1] *Louis Dagba,*[1] *and Fu-Kuo Chang*[1]

Damage-Tolerance-Based Design of Bolted Composite Joints

REFERENCE: Qing, X., Sun, H.-T., Dagba, L., and Chang, F.-K., **"Damage-Tolerance-Based Design of Bolted Composite Joints,"** *Composite Structures: Theory and Practice, ASTM STP 1383,* P. Grant, and C. Q. Rousseau, Eds., American Society for Testing and Materials, West Conshohocken, PA, 2000, pp. 243–272.

ABSTRACT: An approach based on damage tolerance is proposed for the design of bolted composite joints. The approach requires knowledge of failure processes and damage accumulation in composites under physical loading. Based on experimental observation, a progressive damage model was developed for predicting the accumulated damage and failure modes in composite joints. In order to utilize the model for design, a computer code, 3DBOLT, has been developed. The code is based on the progressive damage model, and it interfaces with the commercial finite-element code ABAQUS to perform calculations of three-dimensional stresses, strains, and deformations of the joints for a given load. For a given joint configuration, ply orientation, and loading condition, the code can predict the response of the joint from the initial loading to final failure, estimate accumulated damage in the joint as a function of applied load, and predict the joint deformations.

In order to verify the proposed damage model, the data obtained from the experiments were compared with the predictions from the 3DBOLT/ABAQUS code. Based on the code, a parametric study was performed to characterize several important factors that can significantly influence the design of bolted composite joints.

KEYWORDS: Bolted composite joint, damage tolerance, progressive damage model, 3DBOLT

Joining by mechanical fasteners is a common technology for assembling structural components in aircraft. Since the integrity of mechanically fastened joints can directly affect the performance and safety of structural components, knowing the failure load and the response of bolted joints is critical for structural design. Optimal design of joints improves not only structural integrity and performance, but more important, it considerably minimizes the weight of the structures and, hence, can increase the load-carrying capability. Because of the complex failure modes of composite materials, the mechanical joining of structures made of composite materials demands much more rigorous design knowledge and techniques than those currently available to the traditional methodology for metallic joints.

Extensive analyses and experiments have been performed on bolted composite joints to evaluate the effect of material properties and ply orientation as well as layup on the joint response and failure [*1–23*]. There are three basic failure modes in composite joints: net-tension, shear-out, and bearing. Net-tension failure is associated with fiber and matrix tension failures, due to stress concentrations. However, shear-out and bearing failures result primarily from the shear and compression failures of fiber and matrix. The first two failure types tend to fail catastrophically. The bearing failure is more progressive and may not result in a total reduction of the load-carrying capability of the joints. A combination of any of the three modes may also occur in practice.

The properties and configuration of the bolts as well as the clamping effects, such as clamping area and initial clamping force, have been shown to significantly affect the response and strength of bolted

[1] Department of Aeronautics and Astronautics, Stanford University, Stanford, CA 94305.

Copyright© 2001by ASTM International www.astm.org

composite joints [*24–39*]. For the best performance, the initial clamping force recommended by manufacturers can be quite different for different types of bolts. Undoubtedly, the lateral constraining effect on a bolted composite joint is a 3-D problem. However, most of the existing analyses are based on a 2-D plane stress analysis, which cannot consider such effects. Very few studies characterizing these effects are found in the literature [*27,28,34–39*].

Three-dimensional stress analyses based on pin joints have been studied to model the through-the-thickness effect [*40–49*]. Investigations combining 3-D stress analyses and progressive damage models to predict the strength of mechanically fastened composite joints are not found in the literature.

The objective of this study is to develop a computational tool for analyzing the bolted composite joints by providing joint response, joint strength, failure mode, and damage progression.

Problem Statement

Consider a bolted joint made of laminated composites. The desire was to develop a computer code to determine the effects of lateral clamping force, washer size, loading condition, and joint configuration on the strength of bolted composite joints. The code shall provide the following information:

(1) Failure load of the joint.
(2) Failure mode of the joint.
(3) Joint response up to final failure.
(4) Effect of lateral clamping force on the response and failure of the joint.
(5) Effect of joint configuration on the response and failure of the joint.
(6) Effect of material and ply orientation on the response and failure of the joint.
(7) Damage accumulated in the joint as a function of load.

Methodology

Both experiments and analyses were conducted in order to achieve the objectives. Appropriate experiments were performed to characterize the failure mechanisms and failure modes for various joint configurations, loading conditions, and ply orientations. The details of the experiments can be found in Chang et al. [*73*]. Based on the experimental results, a computational method based on the progressive damage analysis was developed to predict the failure response and strength of bolted composite joints.

The computational method is implemented by the integration of the progressive damage analysis and the commercial finite-element code ABAQUS. The progressive damage model was originally developed by Chang and his associates [*57–59*] and was extended to three dimensions for analyzing bolted composite joints. The model is composed of two major parts:

(1) Constitutive modeling—A 3-D constitutive relationship was used on the ply level to calculate the laminate stiffness.
(2) Damage estimator—Failure criteria were selected to predict the damage accumulation in composites as a function of the applied load.

In order to facilitate the use of the proposed model with the ABAQUS code, an interface module 3DBOLT was developed. The module provides a user-friendly input deck, automatically generates a joint mesh, produces outputs and graphics for displaying the stresses, strains, and deformations of the joints, and predicts the failure progression in joints during loading. Detailed development of the progressive damage model and 3DBOLT code was previously given [*72,73*]. This paper only briefly summarizes the model development.

Prediction of Accumulated Damage

Accumulated Damage Prediction

A set of damage accumulation criteria for predicting damage accumulated in bolted composite joints was proposed by Hung and Chang [*59*]. Six failure modes were considered in the present study: matrix tension, fiber-matrix shearing, fiber tension, matrix compression, fiber-matrix compression, and fiber compression. Two-dimensional in-plane stresses were selected to predict damage and the corresponding failure mode:

(1) Matrix Tension $$\left(\frac{\sigma_2}{Y_t(\phi)}\right)^2 + \left(\frac{\sigma_6}{S(\phi)}\right)^2 \geq 1, \quad \sigma_2 > 0$$

(2) Fiber-Matrix Shearing $$\left(\frac{\sigma_1}{X_t}\right)^2 + \left(\frac{\sigma_6}{S(\phi)}\right)^2 \geq 1, \quad \sigma_1 > 0, \quad \sigma_2 + \sigma_3 > 0$$

(3) Fiber Tension $$\left(\frac{\sigma_1}{X_t}\right)^2 \geq 1, \quad \sigma_1 \geq 0$$

(4) Matrix Compression $$\left(\frac{\sigma_2}{Y_c}\right)^2 + \left(\frac{\sigma_6}{S(\phi)}\right)^2 \geq 1, \quad \sigma_2 < 0$$

(5) Fiber-Matrix Compression $$\left(\frac{\sigma_1}{X_c}\right)^2 + \left(\frac{\sigma_6}{S(\phi)}\right)^2 \geq 1, \quad \sigma_1 < 0$$

(6) Fiber Compression $$\left(\frac{\sigma_1}{X_c}\right)^2 \geq 1, \sigma_1 < 0$$

where σ_1 and σ_2 are the in-plane normal stresses parallel and normal to the fiber direction of the ply under consideration, respectively, σ_3 is the out-of-plane normal stress of the ply, and σ_6 is the in-plane shear stress of the ply. The corresponding on-axis coordinate system for a ply is shown in Fig. 1. X_t and X_c are the tensile and compressive strengths of the ply along the fiber direction, respectively. $Y_t(\phi)$, Y_c, and $S(\phi)$ are the transverse tensile strength, transverse compressive strength, and shear strength of the ply, respectively. Since compression does not create matrix cracks, except under shear loads, the transverse compressive strength, Y_c, is not a function of the matrix crack density ϕ.

It's important to point out that both $Y_t(\phi)$ and $S(\phi)$ are not constants and may vary from ply to ply in the laminate and depend on the crack density. Both $Y_t(\phi)$ and $S(\phi)$ could be determined based on the assumption of conservation of energy through fracture mechanics [*57*]. The expression of effective ply strengths $Y_t(\phi)$ and $S(\phi)$ can be found in Ref *58*.

Based on the experimental observation [*73*], the test results showed that the lateral compressive load could suppress the fiber-matrix splitting. Accordingly, it was postulated that the occurrence of fiber-matrix shearing would only occur when $\sigma_2 + \sigma_3 > 0$.

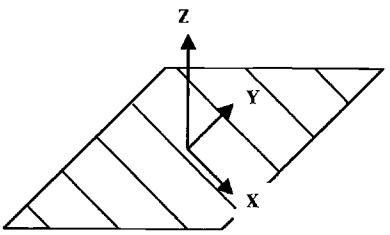


FIG. 1—*On-axis coordinate system used in damage analysis for composite material.*

For a given stress state, if the ply stresses satisfy any one of the criteria, the mode of failure and the state of accumulated damage are predicted on a ply-by-ply level. Consequently, the criterion can be used to monitor the damage progression in laminated composites if the corresponding constitutive equations for a ply are developed.

Constitutive Modeling

Once the damage and the corresponding failure mode are predicted, the resulting residual properties of the damaged material have to be determined in order to model the full response of bolted composite joints. Based on the degradation model developed by Shahid and Hung [*58,59*], a 3-D material degradation model was adopted here.

Matrix Tension—Under in-plane tensile and shear loads, matrix cracks are progressively generated in laminated composites [*52–56*], which degrades laminate properties. Based on the theory of elasticity and the concept of continuum damage mechanics, Shahid and Chang [*57,58*] derived the effective constitutive relationships that relate the stiffness of each lamina in a symmetric laminate as a function of the matrix crack density in its ply. These relationships can be extended to the 3-D on-axis coordinate system of the ply as follows

$$\{\sigma\} = [C(\phi)]\,\{\varepsilon\} \tag{1}$$

or

$$\begin{Bmatrix}\sigma_1\\ \sigma_2\\ \sigma_3\\ \sigma_4\\ \sigma_5\\ \sigma_6\end{Bmatrix} = \begin{bmatrix} C_{11}(\phi) & C_{12}(\phi)d_{mt} & C_{13}(\phi) & 0 & 0 & 0\\ C_{21}(\phi)d_{mt} & C_{22}(\phi)d_{mt} & C_{23}(\phi) & 0 & 0 & 0\\ C_{31}(\phi) & C_{32}(\phi) & C_{33}(\phi) & 0 & 0 & 0\\ 0 & 0 & 0 & C_{44}(\phi) & 0 & 0\\ 0 & 0 & 0 & 0 & C_{55}(\phi) & 0\\ 0 & 0 & 0 & 0 & 0 & C_{66}(\phi)\end{bmatrix} \begin{Bmatrix}\varepsilon_1\\ \varepsilon_2\\ \varepsilon_3\\ 2\varepsilon_4\\ 2\varepsilon_5\\ 2\varepsilon_6\end{Bmatrix} \tag{2}$$

where $[C(\phi)]$ is the effective degraded stiffness related to the matrix cracks.

When the matrix tension has occurred, the stiffness matrix is degraded as follows

$$[C(\phi)] = \begin{bmatrix} C_{11}(\phi) & C_{12}(\phi)d_{mt} & C_{13}(\phi) & 0 & 0 & 0\\ C_{21}(\phi)d_{mt} & C_{22}(\phi)d_{mt} & C_{23}(\phi) & 0 & 0 & 0\\ C_{31}(\phi) & C_{32}(\phi) & C_{33}(\phi) & 0 & 0 & 0\\ 0 & 0 & 0 & C_{44}(\phi) & 0 & 0\\ 0 & 0 & 0 & 0 & C_{55}(\phi) & 0\\ 0 & 0 & 0 & 0 & 0 & C_{66}(\phi)\end{bmatrix} \tag{3}$$

where d_{mt} is the matrix cracking failure degradation factor, and is defined as follows

$$d_{mt} = 1 \qquad \text{when} \qquad \varepsilon_2 < \varepsilon_2^0$$

$$d_{mt} = 0 \qquad \text{when} \qquad \varepsilon_2 \geq \varepsilon_2^0$$

where ε_2^0 is defined as the ply transverse tension failure strain corresponding to the saturated crack density ϕ_0 of a unidirectional ply in the laminate under consideration and is given by

$$\varepsilon_2^0 = \frac{Y_t(\phi_0)}{E_{22}}$$

where $Y_t(\phi_0)$ is the ply transverse tensile strength at saturated crack density and E_{22} is the ply transverse Young's modulus. ϕ is the matrix crack density in the ply.

Fiber-Matrix Shearing—For fiber-matrix shearing, the degraded on-axis ply stiffness matrix originally proposed by Hung and Chang [*35,59*] was adopted in the 3-D stiffness matrix as follows

$$[C(\phi)] = \begin{bmatrix} C_{11}(\phi)d_{fsp} & C_{12}(\phi) & C_{13}(\phi) & 0 & 0 & 0 \\ C_{21}(\phi) & C_{22}(\phi) & C_{23}(\phi) & 0 & 0 & 0 \\ C_{31}(\phi) & C_{32}(\phi) & C_{33}(\phi) & 0 & 0 & 0 \\ 0 & 0 & 0 & C_{44}(\phi) & 0 & 0 \\ 0 & 0 & 0 & 0 & C_{55}(\phi)d_{fs} & 0 \\ 0 & 0 & 0 & 0 & 0 & C_{66}(\phi)d_{fs} \end{bmatrix} \tag{4}$$

where d_{fs}, d_{fsp} are the fiber-matrix shearing failure degradation factors. d_{fs} is defined as follows

$$d_{fs} = 1 \quad \text{when} \quad \gamma_{12} < \gamma_{12}^0$$

$$d_{fs} = 0 \quad \text{when} \quad \gamma_{12} \geq \gamma_{12}^0$$

where γ_{12}^0 is defined as the ply shear failure strain corresponding to the saturated crack density ϕ_0 of a unidirectional ply in the laminate under consideration and is given by

$$\gamma_{12}^0 = \frac{S(\phi_0)}{G_{xy}}$$

where $S(\phi_0)$ is the ply shear strength at saturated crack density, G_{xy} is the ply shear modulus, and d_{fsp} is defined as follows

$$d_{fsp} = 1/n$$

where n is the number of plies in the ply group under consideration. d_{fsp} is used to describe the degradation of ply stiffness in the fiber direction due to the fiber-matrix splitting failure mode in the laminate. Based on the experimental observation [*73*], it was postulated that the reduction of fiber stiffness due to fiber-matrix splitting failure is inversely proportional to the thickness of the ply group under consideration.

Fiber Breakage—For fiber breakage, the degraded on-axis ply stiffness has the following form [*58*]

$$[C(\phi)] = \begin{bmatrix} C_{11}(\phi)d_f & C_{12}(\phi)d_f & C_{13}(\phi)d_f & 0 & 0 & 0 \\ C_{21}(\phi)d_f & C_{22}(\phi)d_f & C_{23}(\phi)d_f & 0 & 0 & 0 \\ C_{31}(\phi)d_f & C_{32}(\phi)d_f & C_{33}(\phi)d_f & 0 & 0 & 0 \\ 0 & 0 & 0 & C_{44}(\phi)d_f & 0 & 0 \\ 0 & 0 & 0 & 0 & C_{55}(\phi)d_f & 0 \\ 0 & 0 & 0 & 0 & 0 & C_{66}(\phi)d_f \end{bmatrix} \tag{5}$$

where d_f is defined as follows

$$d_f = 1 \quad \text{when} \quad A_f < \delta^2$$

$$d_f = 0 \quad \text{when} \quad A_f \geq \delta^2$$

where A_f is the accumulated fiber breakage area over which the stress is either equal to or higher than the fiber longitudinal strength X_t of the composite and δ is the criteria fiber interaction zone which is defined as an effective length of a fiber break on the surrounding fibers [*60*].

Matrix Compression—For matrix compression, the degraded on-axis ply stiffness takes the following form [*59*]

$$[C(\phi)] = \begin{bmatrix} C_{11} & C_{12}d_{mc} & C_{13} & 0 & 0 & 0 \\ C_{21}d_{mc} & C_{22}d_{mc} & C_{23} & 0 & 0 & 0 \\ C_{31} & C_{32} & C_{33} & 0 & 0 & 0 \\ 0 & 0 & 0 & C_{44} & 0 & 0 \\ 0 & 0 & 0 & 0 & C_{55}(\phi) & 0 \\ 0 & 0 & 0 & 0 & 0 & C_{66}(\phi) \end{bmatrix} \tag{6}$$

where d_{mc} is the matrix compression failure degradation factor, and is defined as follows

$$d_{mc} = 1 \quad \text{when} \quad \varepsilon_2 < \varepsilon_2^c$$

$$d_{mc} = 0 \quad \text{when} \quad \varepsilon_2 \geq \varepsilon_2^c$$

where ε_2^c is defined as the ply transverse compression failure and is given by

$$\varepsilon_2^c = \frac{Y_c}{E_{22}}$$

where Y_c is the ply transverse compressive strength and E_{22} is the ply transverse Young's modulus. Note that because compression creates no crack in the matrix except under shear loads, the material properties, except for the shear modulus, are not functions of the crack density ϕ.

Fiber-Matrix Compression—For fiber-matrix compression, the degraded on-axis ply stiffness has the following expression

$$[C(\phi)] = \begin{bmatrix} C_{11} & C_{12} & C_{13} & 0 & 0 & 0 \\ C_{21} & C_{22} & C_{23} & 0 & 0 & 0 \\ C_{31} & C_{32} & C_{33} & 0 & 0 & 0 \\ 0 & 0 & 0 & C_{44} & 0 & 0 \\ 0 & 0 & 0 & 0 & C_{55}(\phi)d_{fmc} & 0 \\ 0 & 0 & 0 & 0 & 0 & C_{66}(\phi)d_{fmc} \end{bmatrix} \tag{7}$$

where d_{fmc} is the fiber-matrix compression factor, and is defined as follows

$$d_{fmc} = 1 \quad \text{when} \quad \gamma_{12} < \gamma_{12}^0$$

$$d_{fmc} = 0 \quad \text{when} \quad \gamma_{12} \geq \gamma_{12}^0$$

where γ_{12}^0 is defined as the ply shear failure strain corresponding to the saturated crack density ϕ_0 of a unidirectional ply in the laminate under consideration and is given by

$$\gamma_{12}^0 = \frac{S(\phi_0)}{G_{xy}}$$

where $S(\phi_0)$ is the ply shear strength at saturated crack density and G_{xy} is the ply shear modulus.

Fiber Compression—For fiber compression, the degraded on-axis ply stiffness can be expressed as follows

$$[C(\phi)] = \begin{bmatrix} C_{11}d_{fc} & C_{12}d_{fc} & C_{13}d_{fc} & 0 & 0 & 0 \\ C_{21}d_{fc} & C_{22}d_{fc} & C_{23}d_{fc} & 0 & 0 & 0 \\ C_{31}d_{fc} & C_{32}d_{fc} & C_{33}d_{fc} & 0 & 0 & 0 \\ 0 & 0 & 0 & C_{44}d_{fc} & 0 & 0 \\ 0 & 0 & 0 & 0 & C_{55}(\phi)d_{fc} & 0 \\ 0 & 0 & 0 & 0 & 0 & C_{66}(\phi)d_{fc} \end{bmatrix} \tag{8}$$

where d_{fc} is the fiber compression factor, and is defined as follows

$$d_{fc} = 1 \qquad \text{when} \qquad \varepsilon_1 < \varepsilon_1^c$$

$$d_{fc} = 0 \qquad \text{when} \qquad \varepsilon_1 \geq \varepsilon_1^c$$

where ε_1^c is defined as the ultimate longitudinal compression strain and is given by

$$\varepsilon_1^c = \frac{X_c}{E_{11}}$$

where X_c is the longitudinal compression strength of composite and E_{11} is the longitudinal Young's modulus.

Notation:

$$\begin{bmatrix} \sigma_1 \\ \sigma_2 \\ \sigma_3 \\ \sigma_4 \\ \sigma_5 \\ \sigma_6 \end{bmatrix} = \begin{bmatrix} \sigma_{11} \\ \sigma_{22} \\ \sigma_{33} \\ \sigma_{23} \\ \sigma_{13} \\ \sigma_{12} \end{bmatrix} \qquad \begin{bmatrix} \varepsilon_1 \\ \varepsilon_2 \\ \varepsilon_3 \\ \varepsilon_4 \\ \varepsilon_5 \\ \varepsilon_6 \end{bmatrix} = \begin{bmatrix} \varepsilon_{11} \\ \varepsilon_{22} \\ \varepsilon_{33} \\ \varepsilon_{23} \\ \varepsilon_{13} \\ \varepsilon_{12} \end{bmatrix}$$

Three-Dimensional Bearing Effect

For bearing failure, experiments demonstrated that bearing damage was limited to a region underneath the bolt-hole contact area. Failure of bolted joints in a bearing mode results from the formation of shear cracks [*35*] associated with fiber compression failure in the bolted region.

It was observed that shear cracks greatly reduce the stiffness of composite materials in the area where bearing damage takes place, and are associated with fiber compression failure. Along the paths of the shear cracks, extensive fiber kinking takes place. Therefore, the fiber compression failure mode helps trigger the through-the-thickness shear cracks and results in significant stiffness loss in the damaged material.

However, the joint strength could be improved significantly by adding lateral supports, such as washers and side plates, to a bolted joint. Lateral supports offer constraints on the damaged material when the bearing damage occurs.

Hypothesis for Damaged Material Under Lateral Constraint—The reason why lateral clamping is so critical to the joint strength is the volume conserving behavior of the damaged material residing in the bearing area. Although the material has been damaged and has lost most of its stiffness under

compressive load, it is still constrained by the surrounding intact material and by the lateral support offered by the clamping and is thus capable of enduring considerable compressive stresses.

For composite material in the bolted region that failed in the fiber compression modes, it was assumed that the damaged material became incompressible due to the lateral clamping constraints. The incompressible condition assumed that the change of a unit volume due to compression from one strain state to another is zero, i.e.

$$^{n+1}V - {}^{n}V = \Delta V = 0 \tag{9}$$

and

$$\varepsilon_v = \frac{\Delta V}{{}^{n}V} = \varepsilon_1 + \varepsilon_2 + \varepsilon_3 \tag{10}$$

Equation 10 can also be written as follows

$$\varepsilon_v = \begin{bmatrix} 1 & 1 & 1 & 0 & 0 & 0 \end{bmatrix} \begin{Bmatrix} \varepsilon_{11} \\ \varepsilon_{22} \\ \varepsilon_{33} \\ \varepsilon_{23} \\ \varepsilon_{13} \\ \varepsilon_{12} \end{Bmatrix} \tag{11}$$

ε_v is the volumetric strain of composite material.

For an incompressible material, the change of volumetric strain ε_v is zero. This means that the material is not allowed to expand or shrink but is permitted to change its shape as long as its volume remains a constant.

Imposing Volumetric Constraint by Penalty Method—In order to model the volume conserving behavior of the bearing-damaged material under consideration, a 3-D penalty formulation [*69*] was incorporated in the current finite-element analysis.

Consider a motion of a continuum body that deforms from the known current configuration ${}^{n}V$ to the state of the next configuration ${}^{n+1}V$ due to the applied external loads. Following the method of the updated Lagrangian formulation [*67*], a variational form based on total potential energy of the body can be approximately written as [*72*]

$$\begin{aligned} \Pi = & \int_{{}^{n}V} {}_{n}\tilde{C}_{ijkl}\, {}^{n+1}_{n}\varepsilon_{kl}\delta^{n+1}_{n}\, \varepsilon_{ij} d^{n}\nu + \int_{{}^{n}V} {}^{n}\sigma_{ij}\, \delta^{n+1}_{n}\, \eta_{ij} d^{n}\nu \\ & + \int_{{}^{n}V} {}^{n}\sigma_{ij}\, \delta^{n+1}_{n}\, \varepsilon_{ij} d^{n}\nu - \int_{{}^{n}\Gamma_{\sigma}} {}^{n+1}\hat{T}_i \delta^{n+1}_{n}\, u_i d^{n}\Gamma \end{aligned} \tag{12}$$

where ${}_{n}\tilde{C}_{ijkl}$ is the tangent moduli of the material at current configuration ${}^{n}V$. ${}^{n+1}_{n}\varepsilon_{ij}$ is the incremental strain tensor associated with infinitesimal displacements and ${}^{n+1}_{n}\eta_{ij}$ is the rotational strain tensor associated with finite deformation at step $n+1$. ${}^{n+1}T_i$ is the surface traction at current configuration ${}^{n}V$. ${}^{n}\sigma_{ij}$ is the Cauchy stress tensor in the current configuration ${}^{n}V$.

By adding the constraining equation, Eq 10, the total potential energy Eq 12 associated with volumetric constraint $\overline{\Pi}$ can be written as follows

$$\overline{\Pi} = \Pi + \beta \int_{{}^{n}V} {}^{n+1}_{n}\varepsilon_{v}\delta^{n+1}_{n}\, \varepsilon_{v} d^{n}\nu = \Pi + \beta \int_{{}^{n}V} m_j\, {}^{n+1}_{n}\varepsilon_{ij}\, m_l \delta^{n+1}_{n}\, \varepsilon_{kl} d^{n}\nu \tag{13}$$

The quantity β is a "penalty number" required for solving the constrained equations.

Complete Damage Model with Addition of Volumetric Constraint—When bearing damage is predicted by the fiber compression criterion and the accumulated damage area is under lateral supports, by washers, side plates, etc., the volume conserving mode comes into play. By having the volume of the damaged material preserved under lateral supports, the mechanically fastened joints are able to carry higher bearing loads and thus achieve better performance.

As shown in Fig. 2, the volumetric constraint for bearing-damaged composite materials, once developed, was added to the existing progressive damage model described earlier to complete the material modeling in the failure analysis of composite bolted joints. Once a damage mode is predicted by failure criteria, the material properties are updated accordingly. If fiber compression happens and the damaged material is under constraint, the volume conserving technique is imposed upon the damaged material.

Numerical Prediction

Finite-element analysis was adopted to analyze the failure of bolted composite joints including open-hole and filled-hole laminates, double-lap bolted joints, and single-lap bolted joints. The com-

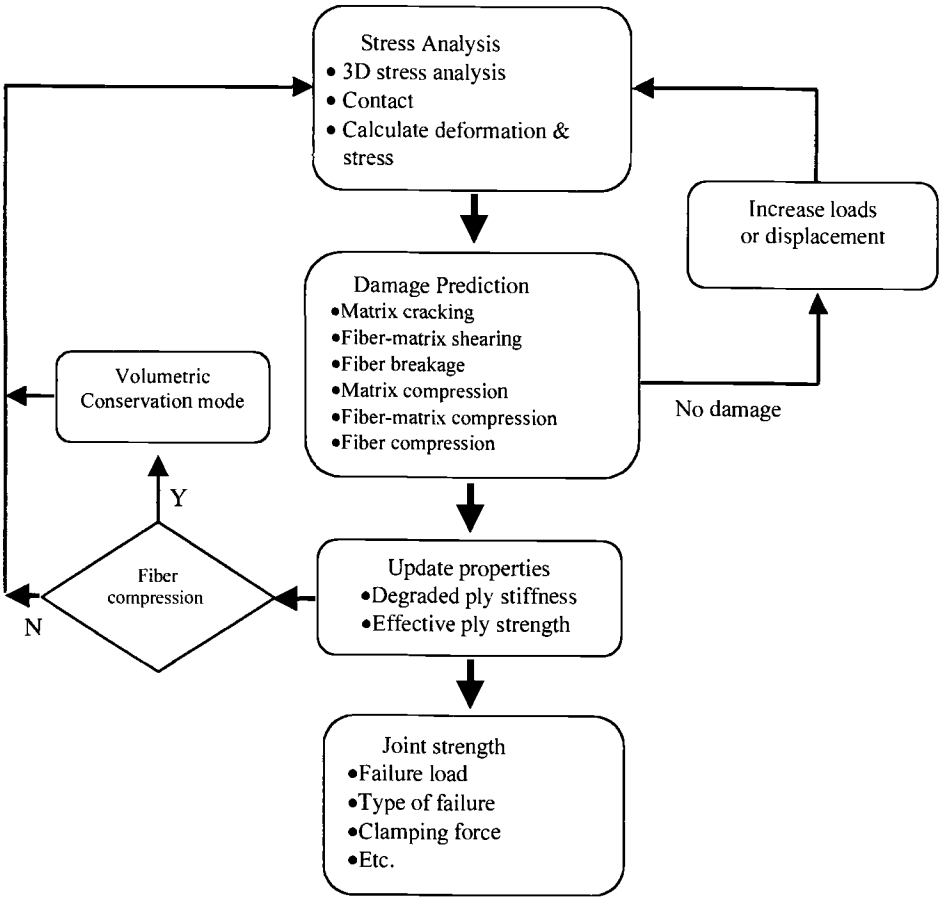


FIG. 2—*Flow chart of progressive damage analysis.*

mercial finite-element package ABAQUS was chosen to complete the task. The 3-D solid eight-node brick layered element [*72*] was utilized to avoid the lengthy computation process of modeling each ply with a single element through the laminate thickness. The package uses internal contact elements [*71*] developed to handle the contact between: (i) metal (washers, side plates) and composite, (ii) metal bolt and composite, (iii) composite and composite, and (iv) metal bolt and metal plates. Friction between these joint parts was also considered in the predictions [*72*].

The proposed progressive damage model was implemented in a computer code 3DBOLT to interface with ABAQUS/Standard [*70*]. During the calculations, ABAQUS passes information regarding strains distribution to the user's subroutine. The constitutive model in the user's subroutine then calculates the stress distribution based on the progressive damage analysis. The accumulated damage criteria estimates the state and extent of damage with given stresses. The constitutive model then degrades material properties according to the damage modes. Finally, the stresses are passed back to the finite-element solver in ABAQUS for the next load increment. Figure 3 shows the analysis scheme.

Two sequential steps were performed in the computer predictions of the bolted joint tests. In the first step, the metal bolt was prestrained in order to generate internal axial tension stress to simulate the clamping condition. This was necessary because as a bolt is tightened, it is essentially under tension while the washers and side plates are under out-of-plane compression. An artificial coefficient of axial thermal expansion in the bolt, α_{33}^T, was used to accomplish the task. The axial thermal strain ε_{33}^T in the bolt induced by the temperature change can be obtained as follows

$$\varepsilon_{33}^T = \alpha_{33}^T \Delta T \tag{14}$$

where ΔT is the temperature change in the bolt and should be negative in order to model the lateral clamping.

In the subsequent step, an incremental displacement was applied on the edge of the composite plate to simulate the loading condition.

The geometries of the composite plates for net-tension and bolt-bearing predictions are shown in Fig. 4. Figure 5 shows some typical 3-D meshes of different configurations of bolted joints used in the calculations to simulate the joint tests. For open-hole and filled-hole laminates, and double-lap bolted joint, only a quarter of the specimen was simulated due to symmetry. For single-lap bolted joint, a half of the specimen was simulated. In all cases, one element layer was used through half the thickness of the multi-directional laminate plates. The load cell mounted on the side of the fixture was also carefully simulated in some configurations.

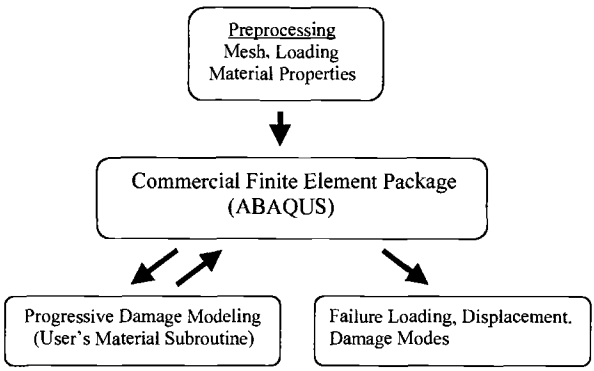


FIG. 3—*Interaction of user's material subroutine with ABAQUS.*

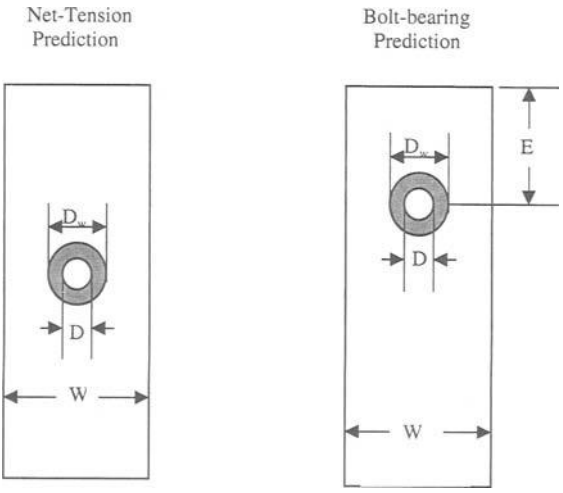


FIG. 4—*Geometries of composite plate for net-tension and bolt-bearing prediction.*

Verification and Comparison

In order to verify the proposed damage model, the data obtained from the experiments were compared with the predictions from the 3DBOLT/ABAQUS code. This paper summarizes only the comparison for the open-hole and filled-hole laminates, the metal-composite-metal(M/C/M) double-lap joints and the composite-composite (C/C) single-lap joints. Using the code, the damage progression and failure modes in composites during loading could also be generated, in addition to the load-deformation curve and the clamping force history. The visualization of damage progression and a complete joint response from the predictions could significantly assist engineers to optimally design bolted composite joints. The material properties used in the simulations for T800/3900-2 graphite/epoxy unidirectional prepreg tapes are listed in Table 1.

Open-Hole and Filled-Hole Laminates

Using the model, numerical predictions of tensile strengths of open-hole and filled-hole laminates were generated for T800/3900-2. Typical comparisons for the open-hole and filled-hole laminates between test data and numerical predictions are shown in Fig. 6 through Fig. 8. Figures 6 and 7 show the effect of washer size on the tensile strength of filled-hole laminates. Figure 8 shows the effect of clamping force on the tensile strength of filled-hole laminates. Test results were denoted as circles, and the predictions were represented by solid lines in the figures.

Overall, the results of the predictions showed that for the laminates (Group 1) which are not prone to fiber-matrix splitting and delamination, the model predictions agreed well with the data.

Figure 9 shows the X-radiograph of a tested open-hole laminate $[(0/\pm 45/90)_2]_s$ and its predicted image of accumulated damage. The predicted damage pattern resembled the X-radiograph well. The major dominated failure modes that were predicted were fiber breakage and matrix cracking.

However, for those laminates which are prone to fiber-matrix splitting and delamination, the predictions were not as accurate. The model could underestimate the notched strength by as much as 20% for some of the open-hole cases. However, the predictions became quite good for the loading conditions at which the strengths of the laminates were reduced by the lateral clamping force. Figure 10 shows the X-radiograph of a tested open-hole $[(45/0/0\text{-}45/0/0/90/0/0/90)]_s$ laminate and its pre-

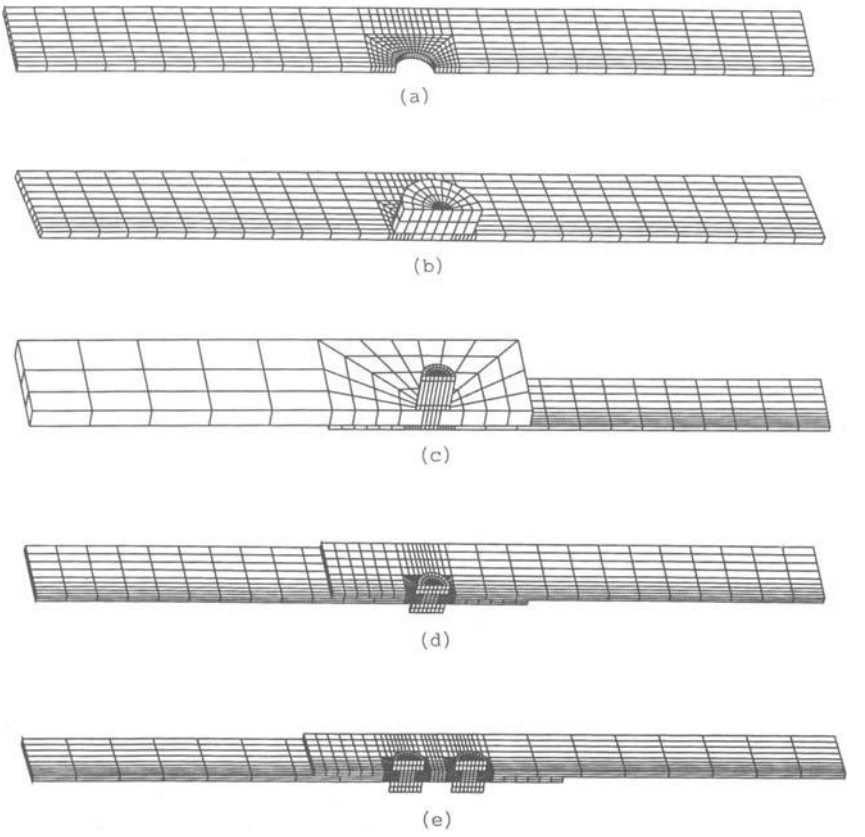


FIG. 5—*Finite element meshes for* (a) *open-hole laminate,* (b) *filled-hole laminate,* (c) *double-lap joint,* (d) *single-lap joint with one bolt, and* (e) *single-lap joint with two-bolts.*

TABLE 1—*Material properties used in numerical simulation for T800/3900-2 graphite/epoxy prepreg tapes.*

Material Properties	Symbol (units)	Value
Longitudinal Young's modulus	E_{11} (Msi)	23.2
Transverse Young's modulus	E_{22} (Msi)	1.30
Transverse Young's modulus	E_{23} (Msi)	1.30
Poisson's ratio	ν_{12}	0.28
Poisson's ratio	ν_{13}	0.28
Poisson's ratio	ν_{23}	0.36
In-plane shear modulus	G_{12} (Msi)	0.90
Out-of-plane shear modulus	G_{13} (Msi)	0.90
Out-of-plane shear modulus	G_{23} (Msi)	0.50
Shear nonlinearity	α	11664
Longitudinal tensile strength	X_t (ksi)	412
Longitudinal compressive strength	X_c (ksi)	225
Transverse compressive strength	Y_c (ksi)	24
Ply thickness	h (in.)	0.00645
Mode I fracture toughness	G_{IC} (in.-lb/in.^{2})	0.86
Mode II fracture toughness	G_{IIC} (in.-lb/in.^{2})	2.7
Fiber interactionzone	δ (in.)	0.055

[1] Msi = 6.9×10^9 Pa
[2] ksi = 6.9×10^6 Pa
[1] in. = 25.4 mm
[1] in.-lb/in.^{2} = 17.89 m-kg/m^2

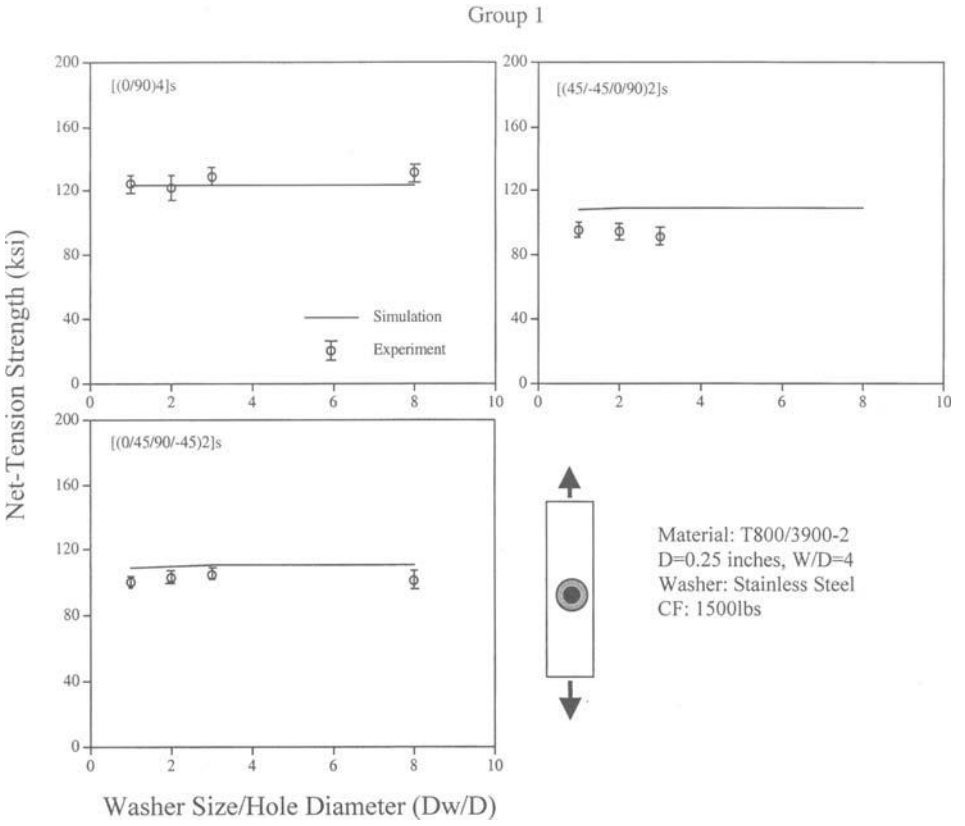


FIG. 6—*Effect of washer size on tensile strength of filled-hole laminates for Group 1.*

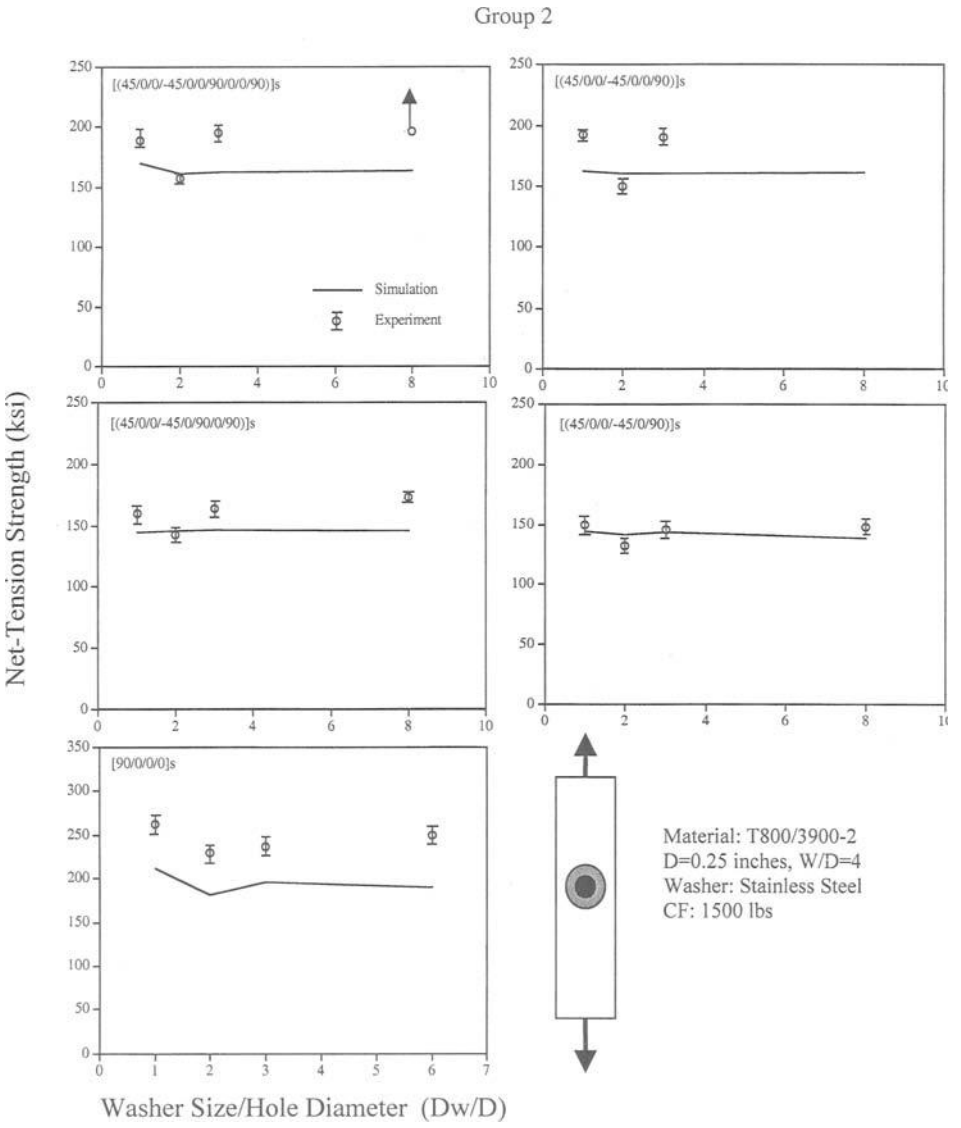


FIG. 7—*Effect of washer size on tensile strength of filled-hole laminates for Group 2.*

dicted image of accumulated damage by the code. It is worth noting that extensive fiber-matrix shearing and matrix cracking failures were predicted by the code before final failure as compared to the corresponding X-radiograph. Note that no delamination analysis was included in the model. It is believed that the localized fiber-matrix splitting failure around the hole could considerably reduce the stress concentration and, consequently, enhance the load-carrying capability of the laminates. Unfortunately, the proposed model, which was based on a continuum mechanics approach could not take into account the stress reductions due to localized cracking such as fiber-matrix splitting. A refined model or fracture model would be needed to address such a local phenomenon.

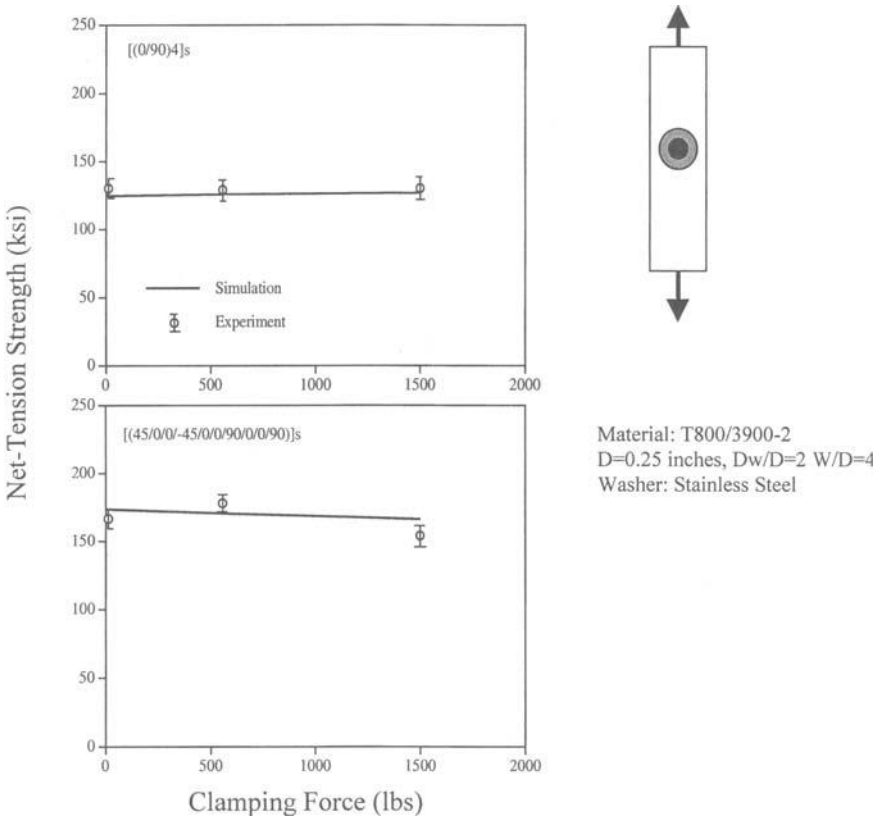


FIG. 8—*Effect of clamping force on tensile strength of filled-hole laminates.*

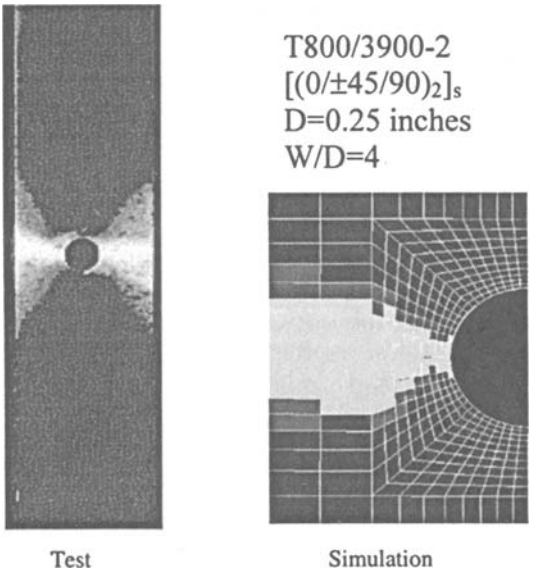


FIG. 9—*X-radiograph* (left) *and the predicted image of damage in the first 0° ply* (right) *for* $[(0/\pm 45/90)_2]_s$ *open-hole laminates,* D = *0.25 in. (0.635 cm),* W/D = *4.*

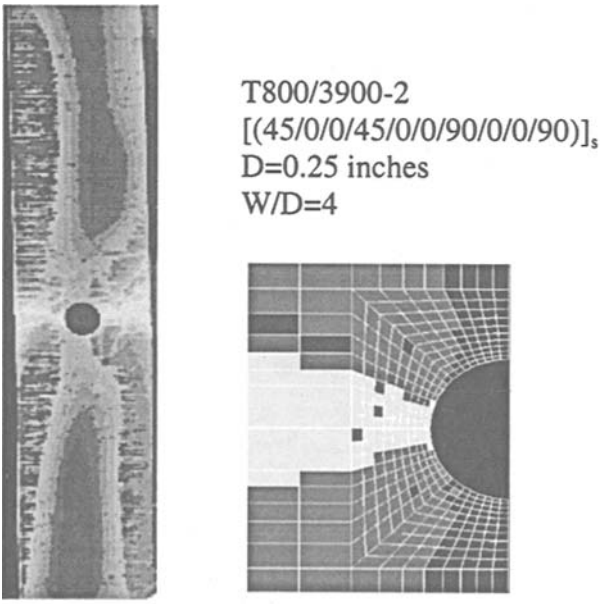


FIG. 10—*X-radiograph* (left) *and the predicted image of damage in the third 0° ply* (right) *for* $[(45/0/0/-45/0/0/90/0/0/90)_2]_s$ *open-hole laminates,* D = *0.25 in. (0.635 cm),* W/D = *4.*

As shown in Fig. 8, the clamp-up load can improve or reduce the notch strength of laminates, depending upon the failure modes and damage progression in the laminates. Based on the prediction, it was found that friction was the primary factor contributing to the increase in failure loads for those laminates which are not prone to fiber-matrix splitting. However, the tensile strength could be reduced, by adding clamp-up, to suppress the fiber-matrix splitting mode for those filled-hole laminates that are prone to delamination and fiber-matrix splitting.

Metal-Composite-Metal Double-Lap Joint

The comparison of load-deformation response between test data and numerical predictions for M/C/M double-lap joints under a fully clamped condition (no washers) is shown in Fig. 11. The circles indicate test data and the solid line represents the numerical prediction. No significant load drop was found. For the cross-ply laminate, the load reached a plateau after excessive deformation. However, the load continued gradually to increase for the $[(0/\pm 45/90)_3]_s$ laminate. The calculated clamping force history as a function of applied load for both joints is also presented in Fig. 12. The predicted clamping force agreed very well with test data.

Figure 13 shows the comparisons of failure load between test data and predictions for double-lap joints with different washer sizes. The failure load was determined by the first occurrence of either a significant load-drop or offset value at 8% of bolt diameter.

Composite-Composite Single-Lap Joint

Figure 14 shows the comparison of the load-deformation curves between the predictions and test data. The circles indicate test data. The solid line represents the numerical prediction where the bolt

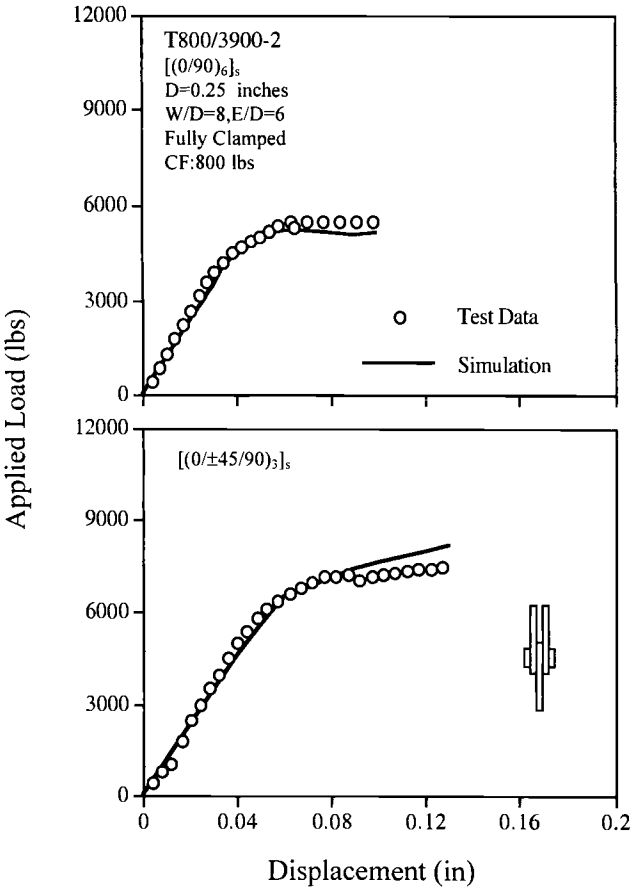


FIG. 11—*Comparisons of load-displacement curves for the* $[(0/90)_6]_s$ *and* $[(0/\pm45/90)_3]_s$ *composite double-lap joints under fully clamped condition (no washers).*

was considered to be elastic, and the dashed line represents the prediction, which considered the bolt to have an elastic-plastic behavior. The reason for consideration of the plastic deformation for bolts was because permanent bolt bending was found from some experiments upon unloading the single-lap joints. The constitutive equation of the elastic-plastic bolt was modeled based on the von Mises yield surface model and the isotropic hardening rules [*74*].

The prediction that considered plastic deformation of the bolt showed much better agreement with the experimental data than the simulation that considered only elastic deformation for the bolt. Figure 15 shows the comparisons of failure load between test data and predictions for single-lap joints with different initial clamping loads. The failure load was determined by the offset value at 8% of bolt diameter.

Parametric Study

Based on the 3DBOLT/ABAQUS code, a parametric study was performed to characterize several important factors that can significantly influence the design of bolted composite joints. The results

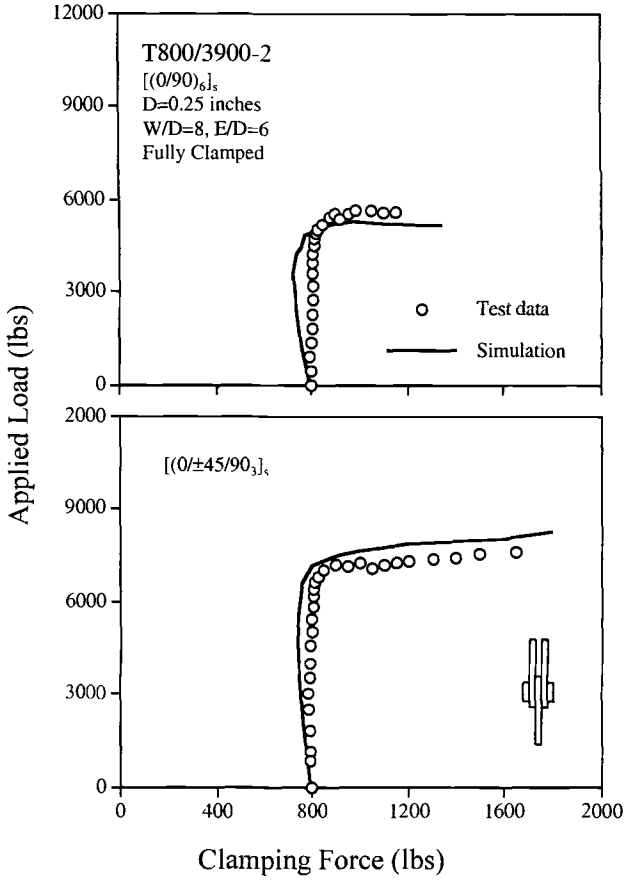


FIG. 12—*Comparisons of applied load-clamping force curves during the course of loading in the* $[(0/90)_6]_s$ *and* $[(0/\pm45/90)_3]_s$ *composite double-lap joints, fully clamped, the initial clamping force* f_c = *800 lb (363 kg).*

generated by the parametric study are utilized to show the typical procedures used to design bolted composite joints. This paper summarizes only the effect of clamping force, clamped area, joint geometry, and joint configuration on the failure load and response of bolted composite joints. Additional parametric study and procedures for design of bolted composite joints can be found in a previous study [*72*].

The material system used for this parametric study was T800H/3900-2 graphite/epoxy. The failure load was determined by the first occurrence of either a significant load-drop or offset value at 8% of bolt diameter.

Effect of the Clamping

As shown in the previous sections, lateral clamping can affect the strength of bolted composite joints. Both the clamped area and the clamping force were evaluated to determine the degree of their influence on the strength of bolted joints.

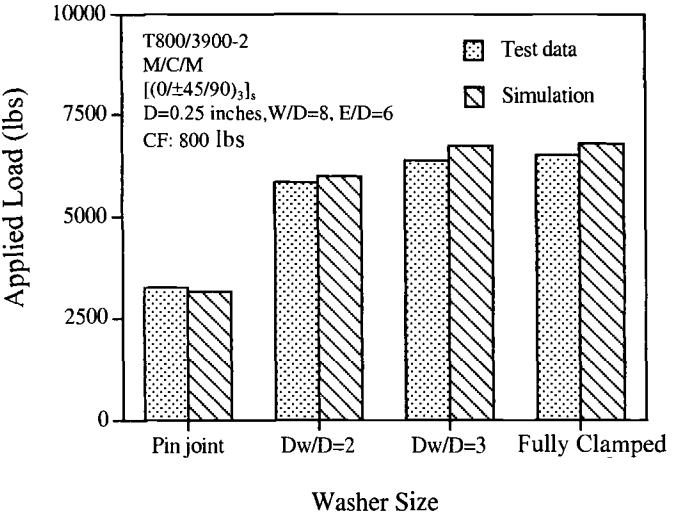


FIG. 13—*Comparisons of failure load between test data and simulations for double-lap joints with different washer sizes.*

Effect of Size of Clamped Area—Figure 16 shows the effect of washer size on the strength of M/C/M double-lap joints. The joint geometry was $D = 0.25$ in., $W/D = 8$, $E/D = 6$. The width of the joints was particularly selected to ensure that failure would occur in a pure bearing mode. Clearly, as the washer diameter-to-hole diameter (Dw/D) ratio was greater than or equal to 3, the joint strength reached a plateau for both the finger-tight and the 363 kg (800 lb) clamping force conditions. The

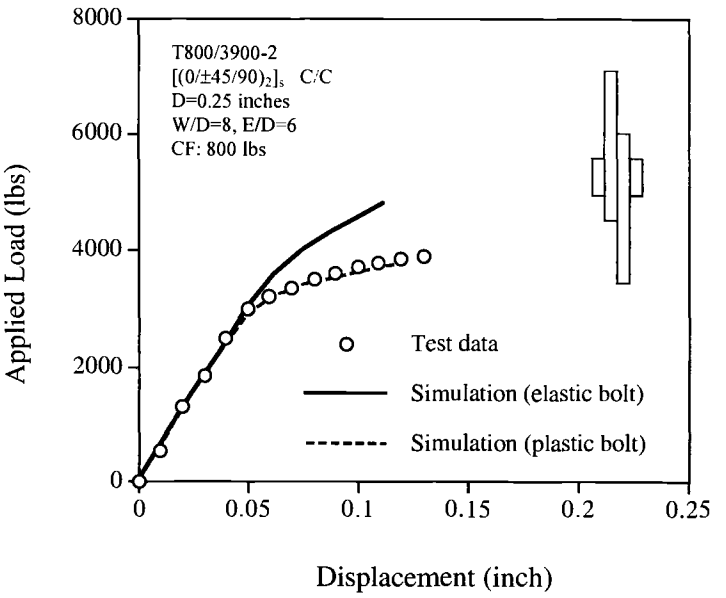


FIG. 14—*Load-deflection curves for $[(0/\pm 45/90)_2]_s$ single-lap bolted composite joints.*

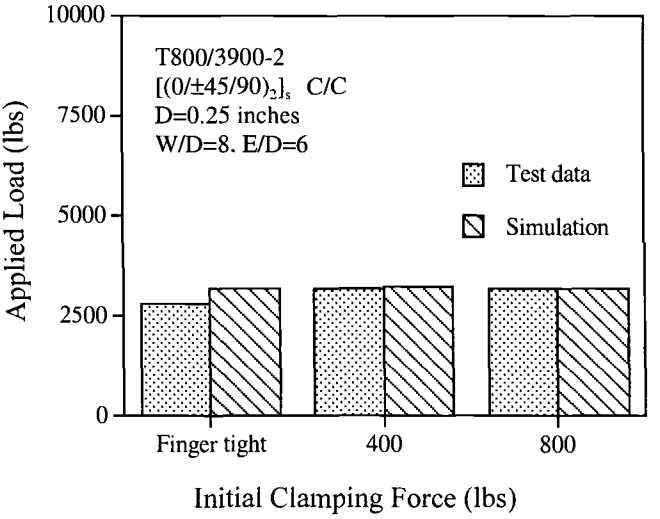


FIG. 15—*Comparisons of failure load between test data and simulations for single-lap joints with different initial clamping force.*

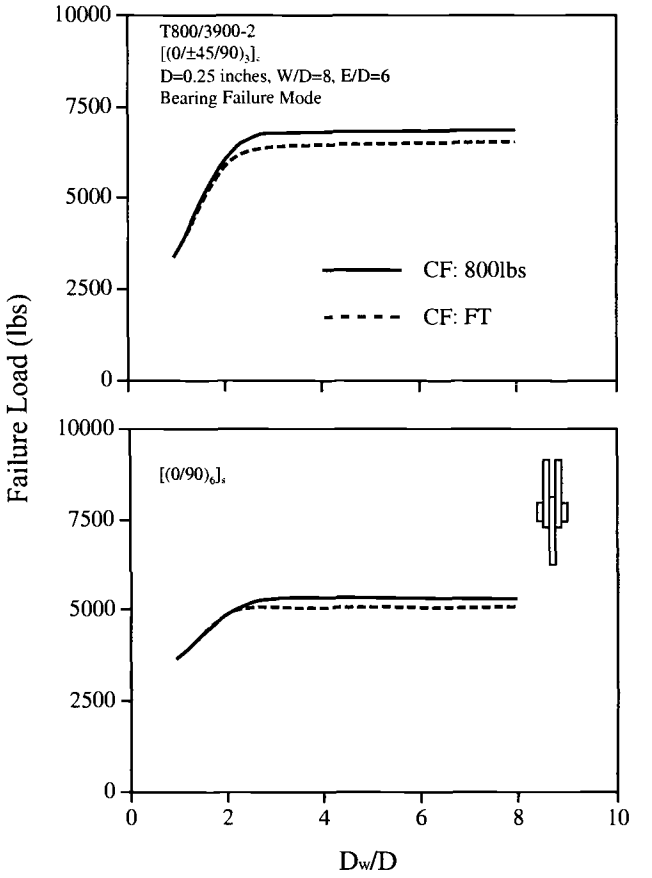


FIG. 16—*Simulations for effect of washer size on strength of double-lap joints (bearing is dominant failure mode).*

"finger-tight" condition was equivalent to a 23 kg (50 lb) clamping force. The results strongly suggest that a minimum value of *Dw/D* greater than 3 shall be recommended for bolted composite joints which may fail in a bearing mode.

As demonstrated in the previous sections, clamping can reduce the notch strength of filled-hole laminates under uniaxial tensile load. The filled-hole tension condition is normally referred to as the 100% bypass condition in bolted joint tests, while the bolted joint test that has been performed in the parametric study is typically referred to as the 0% bypass condition. Since bolted joints (at 0% bypass) could also fail in a tension mode similar to that of filled-hole laminates (100% bypass), the desire was to determine if the strength reduction in filled-hole laminates due to the clamp-up would also appear in bolted joints which fail in a tension mode.

Accordingly, numerical predictions were performed for both filled-hole laminates and bolted joints as shown in Fig. 17. The width of the joints was particularly selected to ensure the joints would fail in a tension mode. The geometry of both the double-lap joint and filled-hole laminate was $D = 0.25$ in., $W/D = 2.5$. Tension failure was the failure mode in both the double-lap joint and the filled-hole laminate.

The results of the study clearly showed that unlike filled-hole laminates, bolted joints (0% bypass) continue to benefit from the clamp-up in a tension mode, although filled-hole laminates produced

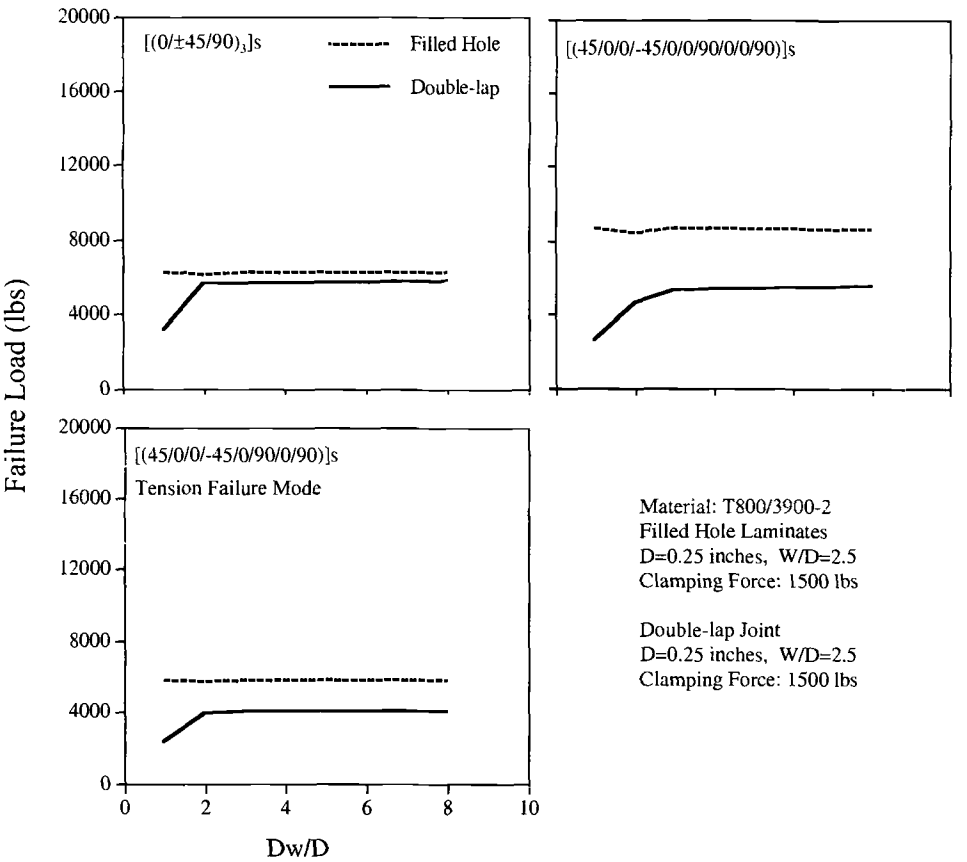


FIG. 17—*Simulations for effect of washer size on strength of double-lap joints and filled-hole laminates (fiber breakage is dominant failure mode).*

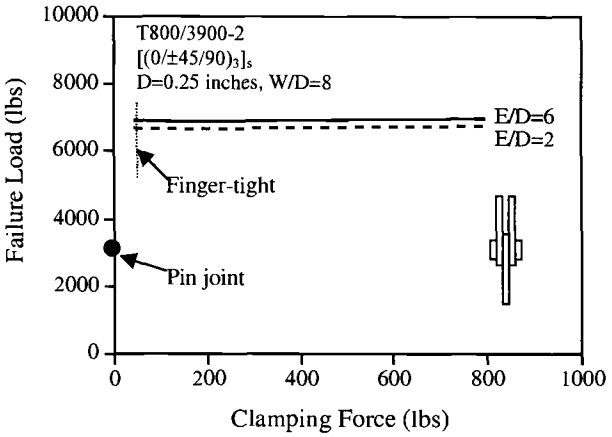


FIG. 18—*Simulations for effect of amount of initial clamping force on failure load of double-lap bolted composite joints.*

higher failure loads than bolted joints. At a *Dw/D* ratio greater than 3, the joint strength reached a plateau. Overall, it is recommended that a *Dw/D* ratio greater than or equal to 3 be used for bolted joint design.

Effect of the Initial Clamping Force—The effects of the initial clamping force were predicted for both $[(0/\pm 45/90)_3]_s$ double-lap joints and $[(0/\pm 45/90)_2]_s$ single-lap joints. The geometry of both double-lap and single-lap joints was $D = 0.25$ in., $W/D = 8$, $E/D = 6$. In the predictions of double-lap joints, no washers were inserted between the metal side plates and the center composite plate. Various levels of initial clamping force were applied. The "finger-tight" condition was equivalent to a 23 kg (50 lb) clamping force again. Based on experiments [*75*], a value of 0.13 was selected as the coefficient of friction between the composite and steel plates while a value of 0.36 was selected as the coefficient of friction between composite plates.

Figures 18 and 19 show the effect of the initial clamping force on the failure load of double-lap and

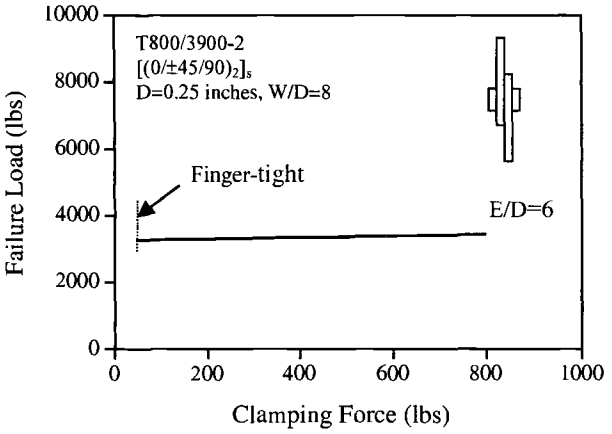


FIG. 19—*Simulation for effect of amount of initial clamping force on failure load of single-lap bolted composite joint.*

single-lap bolted composite joints, respectively. The failure load of the double-lap pin joint without lateral supports was also plotted for comparison. Clearly, the study showed that the initial clamping force had little effect on the failure load as long as at least a "finger-tight" initial clamping force was applied.

Effect of Joint Geometry

Effect of Panel Width—In order to study the effect of joint width W on the strength of composite joints, a large edge-distance (E) was selected to avoid any effect from edge-distance. A fixed E/D value equal to 6 was chosen in these simulations. Bolt diameter was selected to be 0.25 in. Figure 20 shows the effect of width on the strength of double-lap and single-lap joints. The bearing strength of double-lap and single-lap joints is defined as the failure load divided by the diameter of the hole and thickness of the plate. It's clearly evident that for both double-lap and single-lap joints, the failure load increased rapidly as width increased and reached a plateau as the width-to-hole diameter ratio W/D was greater than or equal to 4. When the width-to-hole diameter ratio W/D is less than or equal to 2.5, net-tension is the dominant and final failure mode for both double-lap and single-lap joints.

Figure 21 shows the predicted damage modes in 0-degree plies and the calculated load-displacement curve for a $[(0/\pm45/90)_2]_s$ single-lap bolted joint, where the width-to-hole diameter ratio W/D was equal to 2.5. In Fig. 21, due to bending effects, more damage accumulated in the third 0-deg ply group than the second 0-degree ply group in the single-lap bolted joint.

Figure 22 shows the progression of damage inside composites and the load-displacement curve for a $[(0/\pm45/90)_3]_s$ double-lap bolted joint, where the width-to-hole diameter ratio W/D was equal to 3. It is interesting to point out that, as shown in Fig. 22, bearing damage was the initial dominating failure mode in the bolted area, but the net-tension failure mode apparently accumulated faster than the bearing mode as the load increased. Finally, the joint failed in the net-tension mode.

Effect of Edge Distance—Simulations of the effect of edge distance on strength for double-lap and single-lap bolted composite joints are shown in Fig. 23. A fixed width-to-hole diameter ratio W/D =

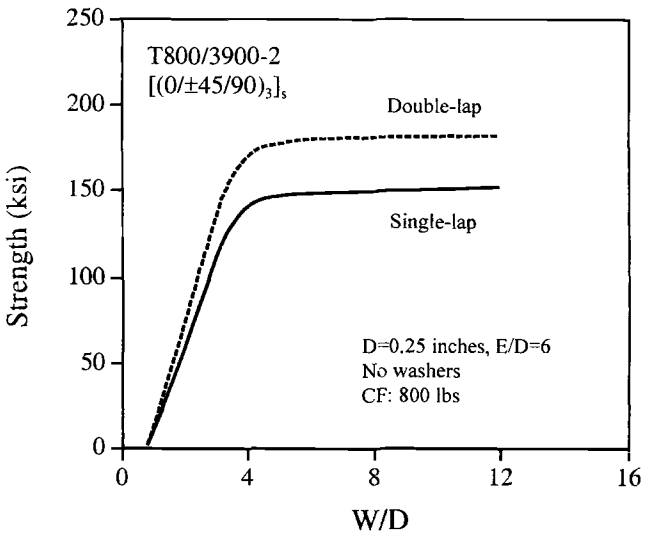
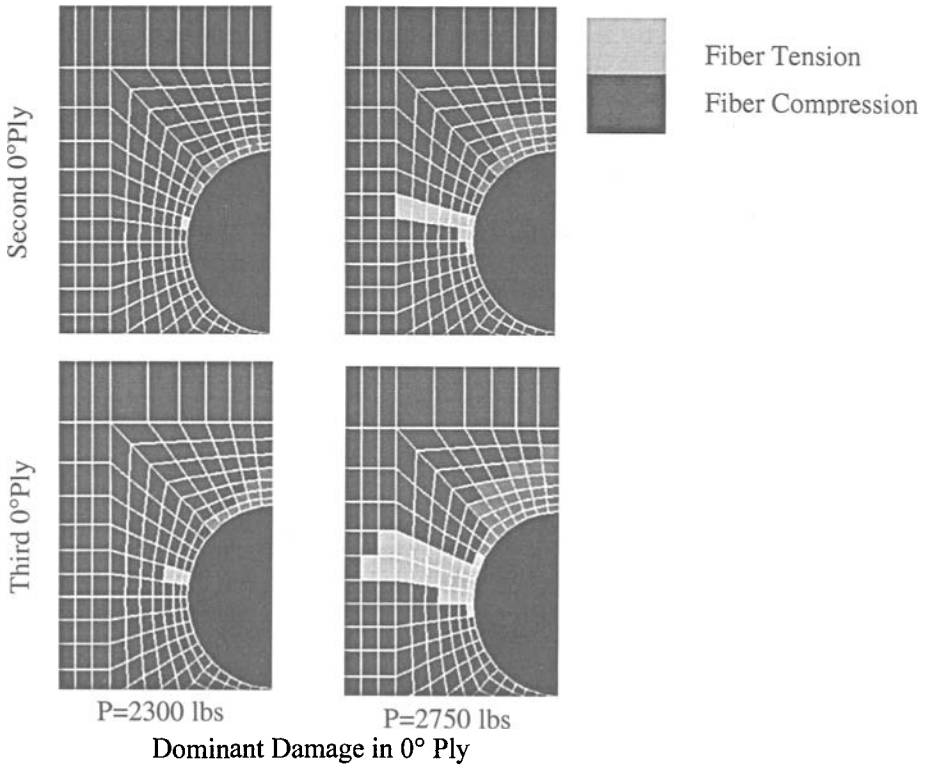


FIG. 20—*Simulations for effect of width on strength of double-lap and single-lap bolted composite joints.*



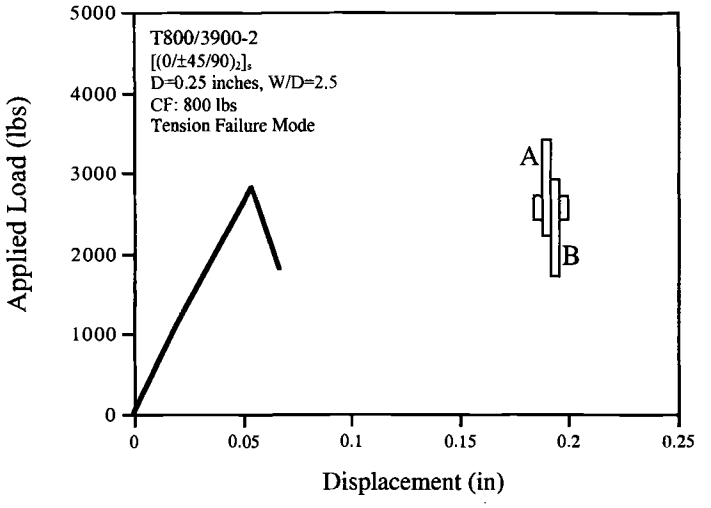


FIG. 21—*Dominant damage response and load-displacement curve of single-lap bolted composite joint.*

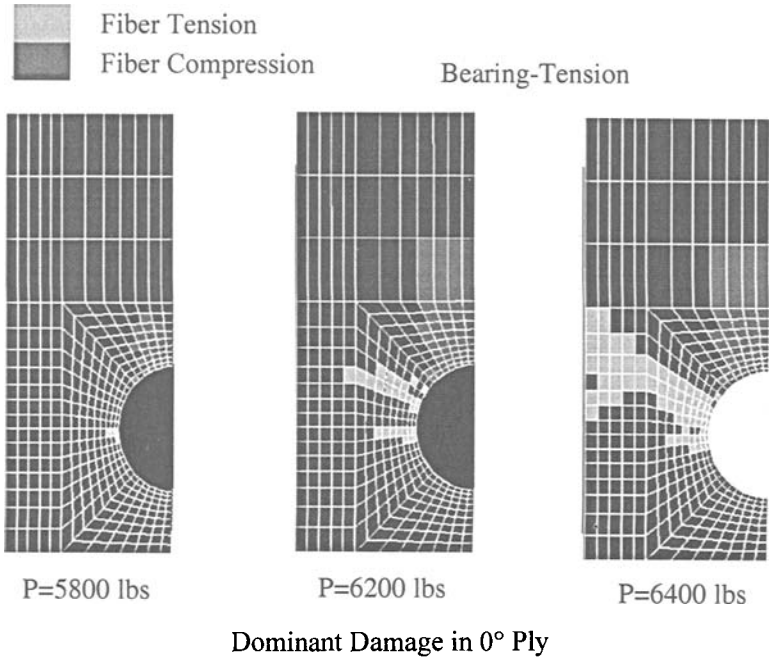


FIG. 22—*Dominant damage response and load-displacement curve of double-lap bolted composite joint.*

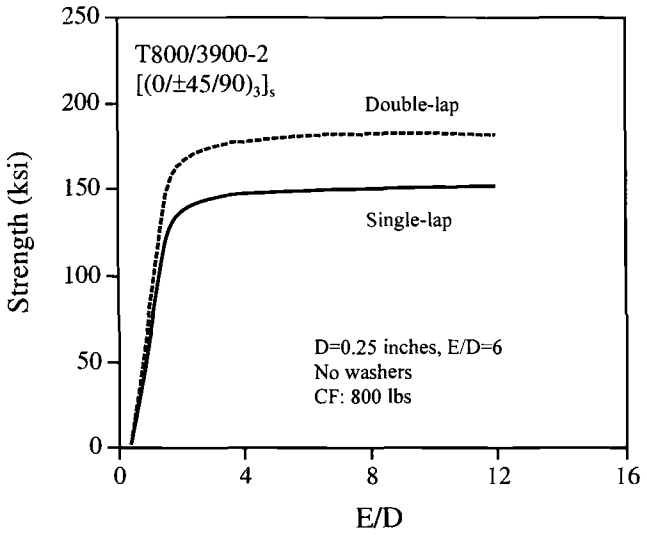


FIG. 23—*Simulations for effect of edge-distance on strength of double-lap and single-lap bolted composite joints.*

8 was chosen in the simulations. For an *E/D* value greater than or equal to 2, the edge distance has no effect on the failure load/strength of bolted joints.

Effect of Number of Holes

The load-displacement responses for $[(0/\pm 45/90)_2]_s$ single-lap joints with two bolts in series were also generated using the code. The results of the calculations were compared with the joints containing only a single hole but the same geometric dimension. Two joint widths (*W/D* = 8 and *W/D* = 2.5) were selected in the calculations. The selection of *W/D* = 8 was to ensure that the joints would fail in a bearing mode, while *W/D* = 2.5 was to make the joints fail in a tension mode.

As shown in Fig. 24, when the width-to-hole diameter ratio *W/D* was equal to 8, the failure load of the single-lap joint with two bolts was almost twice that of the single-lap joint with one bolt. Bearing was the failure mode for both joint configurations. However, when the width-to-hole diameter ratio *W/D* was equal to 2.5, the failure load of the single-lap joint with two bolts in series was almost the same as that of the single-lap joint with one bolt. Net tension was the failure mode for these joint types. Apparently, the failure mode strongly affects how the load is transferred from one bolt to another once damage starts to accumulate inside the joints.

Conclusion

A computer code 3DBOLT/ABAQUS has been developed for predicting the failure response and the strength of bolted composite joints. The constitutive model implemented in the code includes a progressive damage analysis for the damaged material and a volume conserving technique that accounts for the incompressible behavior of damaged material due to bearing failure inside the bolted joints. To verify the model and computer code 3DBOLT/ABAQUS, experimental data were compared with predictions from the code. Good agreement was found between the test data and numerical predictions. The code could be used for characterizing the response of the laminates for the fol-

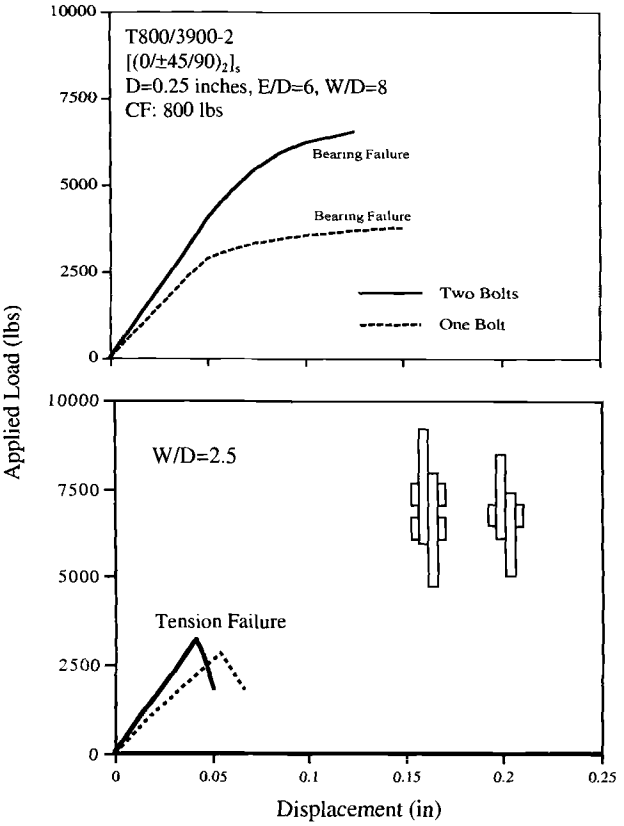


FIG. 24—*Comparison of simulations of single-lap joints with one and two bolts.*

lowing configurations: (i) open-hole tension, (ii) filled-hole tension, (iii) double-lap joints with and without lateral clamp-up loads, and (iv) single-lap joints with and without lateral clamp-up loads.

Acknowledgments

The support of the Boeing Commercial Airplane Group and the Federal Aviation Administration for this project is gratefully appreciated. Mr. John Aaron and Mr. Peter Shyprykevich are the program monitors.

References

[*1*] Agarwal, B. L., "Static Strength Prediction of Bolted Joints in Composite Material," *Proceedings, AIAA/ASME/ASCE/AHS. 20th Structure, Structural Dynamics and Material Conference,* St. Louis, MO, April 1979, pp. 303–309.

[*2*] Oplinger, D. W. and Gandhi, K. R., "Stresses in Mechanically Fastened Orthotropic Laminates," *Proceedings of the Conference on Fibrous Composites in Flight Vehicle Design,* Dayton, OH, 21–24 May 1974, Air Force Flight Dynamics Laboratory Report No. AFFDL-TR-74-103, pp. 811–842.

[*3*] Oplinger, D. W., "Analytical Studies of Structural Performance in Mechanically Fastened Fiber-reinforced Plates," *Proceedings of the Army Symposium on Solid Mechanics, 1974: The Role of Mechanics in Design—Structural Joints,* Army Materials and Mechanics Research Center, Watertown, MA, Report No. AMMRC MS 74-8, pp. 211–242.

[4] Garbo, S. P. and Gallo, R. L., "Strength of Laminates with Loaded Holes," presented at the 5th DOD/NASA Conference on Fibrous Composites in Structural Design, New Orleans, LA, January 1981.
[5] Matthews, F. L., *Joining Fiber-reinforced Plastics*, London, Elsevier Applied Science, 1987.
[6] Chang, F.-K., Scott, R. A., and Springer, G. S., "Failure of Composite Laminates Containing a Pin Loaded Holes—Method of Solution," *Journal of Composite Materials*, Vol. 18, 1984, pp. 255–278.
[7] Chang, F.-K., Scott, R. A., and Springer, G. S., "Failure Strength of Nonlinear Elastic Composite Laminates Containing a Pin Loaded Holes," *Journal of Composite Materials*, Vol. 18, 1984, pp. 467–477.
[8] Waszczak, J. P. and Cruse, T. A., "Failure Mode and Strength Predictions of an Isotropic Bolt-bearing Specimens," *Journal of Composite Materials*, Vol. 5, 1971, pp. 421–425.
[9] Soni, S. R., "Stress and Strength Analysis of Bolted Joints in Composite Laminates," *Composite Structures*, I. H. Marshall, Ed., Applied Science Publishers, NJ, 1981, pp. 50–62.
[10] Soni, S. R., "Failure Analysis of Composite Laminates with a Fastener Hole," *Joining of Composite Materials, Special Technical Publications 749*, Published by ASTM, Philadelphia, PA, pp. 145–164.
[11] Tsujimoto, Y. and Wilson, D., "Elasto-Plastic Failure Analysis of Composite Bolted Joints," *Journal of Composite Materials*, Vol. 20, 1986, pp. 236–252.
[12] Wilson, D. W. and Tsujimoto, Y., "On Phenomenological Failure Criteria for Composite Bolted Joint Analysis," *Composite Science and Technology*, Vol. 26, 1986, pp. 283–305.
[13] Lessard, L. B. and Shokrieh, M. M., "Two-dimensional Modeling of Composite Pinned-joint Failure," *Journal of Composite Materials*, Vol. 29, No. 5, 1995, pp. 671–697.
[14] Eriksson, L. I., "On the Bearing Strength of Bolted Graphite/Epoxy Laminates," *Journal of Composite Materials*, Vol. 24, 1990, pp. 1246–1269.
[15] Eriksson, L. I., "Contact Stresses in Bolted Joints of Composite Laminates," *Composite Structures*, Vol. 6, 1986, pp. 57–75.
[16] Chiang, Y. J. and R. E. Rowlands, "Finite Element Analysis of Mixed-mode Fracture of Bolted Composite Joints," *Journal of Composite Technology Research*, Vol. 13, No. 4, Winter 1990, pp. 227–235.
[17] Tsai, M. Y. and Morton, J., "Stress and Failure Analysis of a Pin-loaded Composite Plate: An Experimental Study," *Journal of Composite Materials*, Vol. 24, 1990, pp. 1101–1120.
[18] Chang, F.-K. and Chang, K.-Y., "Post-Failure Analysis of Bolted Composite Joints in Tension or Shear-out Mode Failure," *Journal of Composite Materials*, Vol. 21, 1987, pp. 809–827.
[19] Crews, J. H. and Naik, R. A., "Combined Bearing and Bypass Loading on a Graphite/Epoxy Laminate," *Composite Structures*, Vol. 6, 1986, pp. 21–40.
[20] Hart-Smith, L. J., "Mechanically-Fastened Joints for Advanced Composite-Phenomenological Considerations and Simple Analysis," *Douglas paper 6748*, 1978, pp. 1–32.
[21] Hart-Smith, L. J., "Bolted Joints in Graphite/Epoxy Composites," NASA Cr144899, National Aeronautics and Space Administration, Washington, DC, January 1977.
[22] Smith P. A., Pascoe K. J., Polak C., and Stroud D. O., "The Behavior of Single-lap Bolted Joints in CFRP Laminates," *Composite Structures*, Vol. 6, No. 1–3, 1986, pp. 41–55.
[23] Nekrasov, Yu. A., "A Study of the Strength of Bolted Joints Between Metal and Composite Plates," *Soviet Machine Science*, No. 3, 1985, pp. 87–91.
[24] Stockdale, J. H. and Matthews, F. L., "The Effect of Clamping Pressure of Bolt Bearing Loads in Glass Fiber-Reinforced Plastics," *Composites*, Vol. 7, 1971, pp. 34–38.
[25] Crews, J. H., "Bolt-Bearing Fatigue of a Graphite/Epoxy Laminates," *Joining of Composite Materials, ASTM STP 749*, K. T. Kedward, Ed., American Society for Testing and Materials, Philadelphia, PA, 1981, pp. 131–144.
[26] Matthews, F. L., Roshan, A. A., and Philips, L. N., "The Bolt Bearing Strength of Glass/Carbon Hybrid Composites," *Composites*, Vol. 13, 1982, pp. 225–227.
[27] Collings, T. A., "On the Bearing Strength of CFRP Laminates," *Composites*, Vol. 13, 1982, pp. 241–252.
[28] Collings, T. A. and Beauchamp M. J., "Bearing Deflection Behavior of a Loaded Hole in CFRP," *Composites*, Vol. 15, No. 1, 1984, pp. 33–38.
[29] Cooper, C. and Turvey, G. J., "Effects of Joint Geometry and Bolt Torque on the Structural Performance of Single Bolt Tension Joints in Pultruded GRP Sheet Material," *Composite Structures*, Vol. 32, 1995, pp. 217–226.
[30] Graham, U., Winsom, M. R., and Webber, P. H., "A Novel Finite Element Investigation of the Effects of Washer Friction in Composite Plates with Bolt-filled Holes," *Composite Structures*, Vol. 29, 1994, pp. 329–339.
[31] Balie, J. A., Duggan, M. F., and Bradshaw, N. C., "Design Data for Graphite Cloth Epoxy Bolted Joints at Temperatures Up to 450 K," *Joining of Composite Materials, ASTM STP 749*, K. T. Kedward, Ed., American Society for Testing and Materials, Philadelphia, PA, 1981, pp. 165–180.
[32] Herrington, P. D. and Sabbaghian, M., "Fatigue Failure of Composite Bolted Joints," *Journal of Composite Materials*, Vol. 27, No. 5, 1993, pp. 491–512.

[33] Akay, M., "Bearing Strength of As-cured and Hydrothermally Conditioned Carbon Fiber/Epoxy Composites Under Static and Dynamic Loading," *Composites*, Vol. 23, No. 2, March 1989, pp. 101–108.
[34] Wang, H.-S. Hung, C.-L., and Chang, F.-K., "Bearing Failure of Bolted Composite Joints. Part I: Experimental of Characterization," *Journal of Composite Materials*, Vol. 30, No. 12, 1996, pp. 1248–1313.
[35] Hung, C.-L. and Chang, F.-K., "Bearing Failure of Bolted Composite Joints. Part II: Model and Verification," *Journal of Composite Materials*, Vol. 30, No. 12, 1996, pp. 1359–1400.
[36] Sun, H.-T., Yan, Y., and Chang, F.-K., "Is Clamping Necessary for Bolted Composite Joints?," *Proceedings of the 11th DOD/NASA/FAA Conference on Fibrous Composite in Structural Design*, Fort Worth, TX, 26–28 Aug. 1996.
[37] Morgan, M. E. and Beckwith, S. W., "Bolt Torque Loading and Radial Gap Effects on Thick-wall Composite Joint Strength," *Proceedings of the 30th National SAMPE Symposium*, 19–21 March 1985, pp. 1321–1334.
[38] Horn, W. J. and Schmitt, R. R., "Influence of Clamp-up Force on the Strength of Bolted Composite Joints," *AIAA Journal*, Vol. 32, No. 3, 1993, pp. 665–667.
[39] Smith, P. A., Ashby, M. F., and Pascoe, K. J., "Modeling Clamp-up Effects in Composite Bolted Joints," *Journal of Composite Materials*, Vol. 21, No. 12, 1987, pp. 878–897.
[40] Camanho, P. P. and Matthews, F. L., "Stress Analysis and Strength Prediction of Mechanically Fastened Joints in FRP: A Review," *Composites Part A*, Vol. 28A, 1997, pp. 529–547.
[41] Matthews, F. L., Wong, C.-M., and Chryssafitis, S., "Stress Distribution Around a Single Bolt in Fiber-reinforced Plastic," *Composites*, Vol. 13, 1986, pp. 316–322.
[42] Chen, W.-H., Lee, S.-S., and Yeh, J.-T., "Three-dimensional Contact Stress Analysis of a Composite Laminate with Bolted Joint," *Composites Structures*, Vol. 30, 1995, pp. 287–297.
[43] Marshall, I. H., Arnold, W. S., and Wood, J., "Observations on Bolted Connections in Composite Structures," *Composites*, Vol. 13, 1989, pp. 133–151.
[44] Hyer, M. W. and Klang, E. C., "Contact Stresses in Pin-loaded Orthotropic Plates," *International Journal of Solids and Structures*, Vol. 21, 1985, pp. 957–975.
[45] Hyer, M. W., Klang, E. C., and Cooper, D. E., "The Effects of Pin Elasticity, Clearance and Friction on the Stresses in a Pin-loaded Orthotropic Plate," *Journal of Composite Materials*, Vol. 21, 1987, pp. 190–206.
[46] Barboni, R., Gandenzi, P., and Carlini, S., "A Three-dimensional Analysis of Edge Effects in Composite Laminates with Circular Holes," *Composite Structures*, Vol. 15, 1990, pp. 115–136.
[47] Iarve, E., "Stress Analysis in Laminated Composites with Fastener Holes," *Proceedings of the American Society for Composites 10th Technical Conference*, Technomic Publishing Co., Lancaster, PA, 1995, pp. 408–419.
[48] Iarve, E., "Three-dimensional Stress Analysis in Laminated Composites with Fasteners Based on the B-spline Approximation," *Composites Part A*, Vol. 28A, 1997, pp. 559–571.
[49] Hassen, N. K., Mohamedien, M. A., and Rizkalla, S. H., "Finite Element Analysis of Bolted Connections for PFRP Composites," *Composites Part B*, Vol. 27B, 1996, pp. 339–349.
[50] Lessard, L. B., "Compression Failure in Laminated Composites Containing an Open Hole," Ph.D. dissertation, Stanford University, 1989.
[51] Tan, S. C. and Perez, J., "Progressive Failure of Laminated Composites with a Hole Under Compressive Loading," *Journal of Reinforced Plastics and Composites*, Vol. 12, 1993, pp. 1043–1057.
[52] Hashin, Z., "Analysis of Orthogonally Cracked Laminates Under Tension," *Journal of Applied Mechanics*, Vol. 54, 1987, pp. 872–879.
[53] Nuismer, R. J. and Tan, S. C., "Constitutive Relations of a Cracked Composite Lamina," *Journal of Composite Materials*, Vol. 22, 1988, pp. 306–321.
[54] Tan, S. C. and Nuismer, R. J., "A Theory for Progressive Matrix Cracking in Composite Laminates," *Journal of Composite Materials*, Vol. 23, 1989, pp. 1029–1047.
[55] Sun, C. T. and Jen, K. C., "On the Effect of Matrix Cracks on Laminate Strength," *Journal of Reinforced Plastics and Composites*, Vol. 6, 1987, pp. 208–222.
[56] Tsai, C. L. and Daniel, I. M., "The Behavior of Cracked Cross-ply Composite Laminates Under Simple Shear Loading," *Composite Engineering*, Vol. 1, No. 1, 1991, pp. 3–11.
[57] Shahid, I. and Chang, F.-K., "Modeling of Progressive Failure of Cross-ply Composites Subjected to Combined In-Plane Loads," American Society of Composites Technical Conference, November 1992.
[58] Shahid, I., "Failure and Response of Laminated Composites Subjected to In-Plane Loads," Ph.D. dissertation, Stanford University, 1993.
[59] Hung, C.-L., "Composite Joints Subjected to Bypass Loads," Ph.D. dissertation, Stanford University, 1993.
[60] Hahn, H. T., "Nonlinear Behavior of Laminated Composites," *Journal of Composite Materials*, Vol. 7, 1973, pp. 257–271.
[61] Serabian, S. M., "The Effects of Nonlinear Intralaminar Shear Behavior on The Modeling Accuracy of

[(0/90),0]$_s$ and [$\pm$45]$_{3s}$ Pin-loaded Laminates," *Journal of Composite Technology & Research*, Vol. 13, No. 4, Winter 1991, pp. 236–248.

[62] Mallick, P. K., *Fiber reinforced Composites*, Marcel Dekker, New York, 1988, pp. 3–4.

[63] Crews, J. H., Jr, and Naik, R. A., "Failure Analysis of a Graphite/Epoxy Laminate Subjected to Bolt-Bearing Loads," *Composite Materials: Fatigue and Fracture, ASTM STP 907*, H. T. Hahn, Ed., American Society for Testing and Materials, Philadelphia, PA, 1986, pp. 131–144.

[64] Jurf, R. A. and Vinson, J. R., "Failure Analysis of Bolted Joints in Composite Laminates," *Composite Materials: Testing and Design (Ninth Volume), ASTM STP 1059*, S. P. Garbo, Ed., American Society for Testing and Materials, Philadelphia, PA, 1990, pp. 165–190.

[65] Eriksson, I., "On the Bearing Strength of Bolted Graphite/Epoxy Laminates," *Journal of Composite Materials*, Vol. 24, 1990, pp. 1246–1270.

[66] Serabian, S. M. and Oplinger, D. W., "An Experimental and Finite Element Investigation into the Mechanical Response of 0/90 Pin-Loaded Laminates," *Journal of Composite Materials*, Vol. 21, 1987, pp. 631–649.

[67] Bathe, K. J., *Finite Element Procedures in Engineering Analysis*, Prentice-Hall, Inc., NJ, 1982.

[68] Suh, J.-K., Spilker, R. L., and Holmes, M. H., "A Penalty Finite Element Analysis for Nonlinear Mechanics of Biphasic Hydrated Soft Tissue Under Large Deformation," *International Journal for Numerical Methods in Engineering*, Vol. 32, 1991, pp. 1411–1439.

[69] Zienkiewicz, O. C., *The Finite Element Method*, 4th ed., McGraw-Hill, 1989.

[70] Hibbit, Karlsson & Sorensen Inc., *Writing UMATs and Vumats, Volume II*, Hibbit, Karlsson & Sorensen Inc., Pawtucket, RI, 1995.

[71] Hibbit, Karlsson & Sorensen Inc., *ABAQUS/Standard Theory Manual*, Hibbit, Karlsson & Sorensen Inc., Pawtucket, RI, 1995.

[72] Sun, H. T., "Analysis of Composite-to-Metal Double-Lap Bolted Joints," Ph.D. dissertation, Stanford University, 1997.

[73] Chang, F.-K., Qing, X., Sun, H.-T., and Yan, Y., "Damage Tolerance-Based Design of Bolted Composite Joints," Final Report to the Boeing Commercial Airplane Groups and the Federal Aviation Administration, Aeronautics and Astronautics Department, Stanford University, 1999.

[74] Stouffer, D. C. and Dame, L.-T., *Inelastic Deformation of Metals, Models, Mechanical Properties and Metallurgy*, Wiley & Sons, Inc., 1996.

[75] Yan, Y., Wen, W.-D., Chang, F.-K., and Shyprykevich, P., "Experimental Study on Clamping Effects on the Tensile Strength of Composite Plats with a Bolt-Filled Hole," *Composite: Part A*, Vol. 30, 1999, pp. 1215–1229.

Hui Bau,[1] *D. M. Hoyt,*[1] *and Carl Q. Rousseau*[2]

Open Hole Compression Strength and Failure Characterization in Carbon/Epoxy Tape Laminates

REFERENCE: Bau, H., Hoyt, D. M., and Rousseau, C. Q., **"Open Hole Compression Strength and Failure Characterization in Carbon/Epoxy Tape Laminates,"** *Composite Structures: Theory and Practice, ASTM STP 1383*, P. Grant, and C. Q. Rousseau, Eds., American Society for Testing and Materials, West Conshohocken, PA, 2000, pp. 273–292.

ABSTRACT: Open hole compression (OHC) design criteria often size the thicknesses of composite aircraft skin structures. Therefore, there can be a significant payoff in improving OHC allowables through better characterization of OHC strength and behavior. This study, using progressive damage analysis and empirical methods, provides new insight into OHC strength and failure behavior.

OHC failure behavior was modeled using PDHOLEC, a progressive damage, 2-D finite-element code. Ultimate strength predictions were combined into carpet plots over a wide range of layups in three graphite composite material systems. A detailed evaluation of PDHOLEC progressive failure output resulted in the identification of several distinct predicted failure mechanisms. Predicted failure mechanisms and ultimate strengths are compared with OHC test data.

Two distinct failure mechanisms for OHC configurations were identified based on the PDHOLEC failure study and strength trend studies of test data: a 0° ply kinking/buckling failure mechanism and a matrix cracking mechanism. The PDHOLEC predictions and test data were grouped by the identified failure mechanisms. Then curve fit equations were generated to characterize the ultimate strength behavior for each failure mechanism.

KEYWORDS: composites, stress concentrations, compression, progressive damage, finite-element analysis, notches, open hole, strength, failure mechanisms

Nomenclature

(*a*/*b*/*c*) Layup description method for (0°/±45°/90°) laminates where:
- *a* = percentage of 0° plies
- *b* = percentage of ±45° plies
- *c* = percentage of 90° plies
- e.g., (62/29/9) is a layup with 62% 0° plies, 29% ±45° plies, and 9% 90° plies

AML Angle Minus Loaded-ply layup description method,
- AML = % ±45° plies − % 0° plies
- e.g., AML = −33 for (62/29/9)

Technical Terms

Allowables—Strength or strain values used for design
Carpet plot—Laminate strengths plotted as a failure surface over a range of layups
OHC—Open Hole Compression

[1] President and vice president, respectively, NSE Composites Stress Services, Seattle, WA 98103.
[2] Principal engineer, Research Structures, Bell Helicopter Textron, Fort Worth, TX 76101.

Copyright© 2001by ASTM International www.astm.org

ε_1^{cu}—Ultimate compression strain for unnotched coupon with all 0° plies
= Ultimate load/(coupon width × nominal thickness × uniaxial lamina modulus)
ε_{ohc}—OHC ultimate strain for coupon with centrally located open hole
= ultimate load/(coupon width × nominal thickness × laminate axial modulus)
NDI—Nondestructive inspection
Quasi-isotropic—A laminate with an equal number of fibers in at least three directions, the most common example having 25% of the plies in each of the 0°, +45°, −45°, and 90° directions
RTA—Room Temperature/Ambient moisture test environment
Soft layups or **laminates**—Layups with a low percentage of 0° plies

Open hole compression (OHC) design criteria are often used for composite structures in aircraft as a simple method to account for free edge effects, repair, and damage. As a result, a significant amount of skin thicknesses as well as bolted joint areas of composite skin structures in aircraft are often sized using OHC allowables. Improvements in OHC allowables may result in substantial weight savings in new composite aircraft designs, and may result in increased allowable damage or increased life in existing designs.

Currently, OHC strength allowables are generated either from notched stress field analyses with characteristic dimensions which are determined from tests [*1*], or by curve-fitting data from large test programs [*2,3*]. These methods may result in design allowables for certain conditions that are excessively conservative. Therefore, point design tests are often conducted in addition to the allowables testing, to either verify or improve the design strength allowables for critical locations. The testing and verification for OHC allowables by these methods is time consuming and expensive. By improving the understanding of OHC strength behavior, a significant payoff in both time and cost may be realized in the development of composites design allowables.

In this study, a parallel empirical/analytical approach with an emphasis on failure mechanisms was used to gain improved understanding of OHC strength behavior and to provide a strong basis for the validation of an analytical tool. OHC strength behavior was characterized by an approach where test data and progressive damage finite-element modeling results were separated by critical failure mechanisms. This approach is based on the premise that there are various mechanisms for failure in composites and that the strength behavior within each distinct failure mechanism should be consistent. Therefore, the strength behavior should be independently characterized for each distinct failure mechanism. For example, the strength behavior of a composite coupon with a 0° ply buckling dominated failure mechanism will be different from the strength behavior of a similar coupon with a ±45° ply matrix shear dominated failure mechanism, since the failure strengths will be sensitive to different composite and coupon parameters.

The OHC test data and analytical results both showed net section failure modes for all layups; however, in this approach, the results were further assessed to identify distinct critical ply-level failure mechanisms. Several techniques were used to identify the failure mechanisms, as discussed later. Using these techniques, the test data were grouped by critical failure mechanisms, then each mechanism was evaluated for its strength behavior. The analytical results were grouped and evaluated similarly, then compared to the test results. When good correlation was obtained, the strength behavior was characterized by curve fitting an equation to the test data and/or the analytical results. This curve fit was called the "characteristic equation" for the failure mechanism. Characteristic equations can be used directly to generate OHC design strength allowables and/or to validate OHC strength analysis models.

Test data and progressive damage finite-element analysis results were reviewed for Hexcel IM6/3501-6 graphite/epoxy [*2*], Hexcel IM7/8552 graphite/toughened epoxy [*4*], and Toray T800H/3900-2 graphite/toughened epoxy [*4*] tape material systems at room temperature ambient and/or 180°F/wet environments. The selected progressive damage finite-element analysis code, PDHOLEC [*5*], is a free-standing code that was developed exclusively for open hole compression. A progressive damage analysis model was chosen since it is desirable to track noncritical damage in order to accurately predict ultimate compression failure. PDHOLEC had not been through a compre-

hensive validation prior to this study. In this study, several techniques were used to evaluate the accuracy of PDHOLEC predicted strength as well as predicted failure mechanisms.

The tasks and techniques performed for this study of OHC behavior using the empirical/analytical separation by failure mechanisms approach are outlined below:

- Identify empirical strength behavior and failure mechanisms by studying ultimate strength trends in test data.
- Identify PDHOLEC predicted strength behavior and predicted failure mechanisms by studying:
  - —sensitivity studies of progressive damage analysis input parameters,
  - —predicted element damage progressions, and
  - —predicted first ply failures.
- Evaluate PDHOLEC analysis method through:
  - —comparison of predicted load/deflection plots with load/deflection plots from tests,
  - —comparison of ultimate strength predictions with test data,
  - —comparison of predicted trends with test data trends, and
- Quantify OHC strength behavior with characteristic equations for distinct failure mechanisms with carpet plots.

Test Data OHC Ultimate Strength Trend Study

Figure 1 is a plot showing OHC average test strains [*2,4*] plotted against the AML layup parameter for IM6/3501-6, IM7/8552, and T800H/3900-2 tape laminates at room temperature ambient (RTA) and 180°F/wet (~1.2% moisture content) test environments. All OHC specimens had centrally located 0.25 in. (0.635 cm) diameter holes and width/diameter ratios of 6. The Fig. 1 plot shows that the OHC ultimate strain behavior for these materials are similar. Most of these tested laminates fell within a narrow layup range with 90° plies between 8 and 11%, except for quasi-isotropic. However, similar strain behavior has been observed for OHC in other material systems over broader layup ranges [*6,7*]. Typical OHC behavior for carbon/epoxy laminates can be described as:

- Moderate to stiff laminates (AML $<$ ~20) tend have a relatively constant OHC ultimate strain behavior. A constant strain behavior would imply a failure mechanism which is dominated by the maximum compression strain capability of the 0° fibers.
- Intermediate (~20 $<$ AML $<$ ~40) to soft layups (AML $>$ ~50) have a trend of increasing ultimate strain with increasing % ±45° plies (increasing AML). A trend of increasing strain with increasing ±45° plies would imply a ±45° ply matrix dominated failure mechanism.

For the studied configurations, the change in failure mode occurs between ~0 $<$ AML $<$ ~50 depending upon material system and environment. A study of failed OHC test specimens would aid in the identification of the failure mechanism for each test specimen. However, failed specimens corresponding to the data used in this study were not available.

PDHOLEC Progressive Damage Models

PDHOLEC is a progressive damage finite-element code which was developed in 1989 to analyze open hole compression in composite materials [*5*]. PDHOLEC has an automatic mesh generator that creates 2-D plate, composite, nonlinear, finite-element models for OHC configurations. The code only allows uniaxial compression loading, and does not account for 3-D effects such as delaminations. PDHOLEC lacks a user-friendly post-processing routine for the progressive damage results, which resulted in significant difficulties in evaluating the progressive damage output. For a detailed discussion of PDHOLEC see Ref *5*.

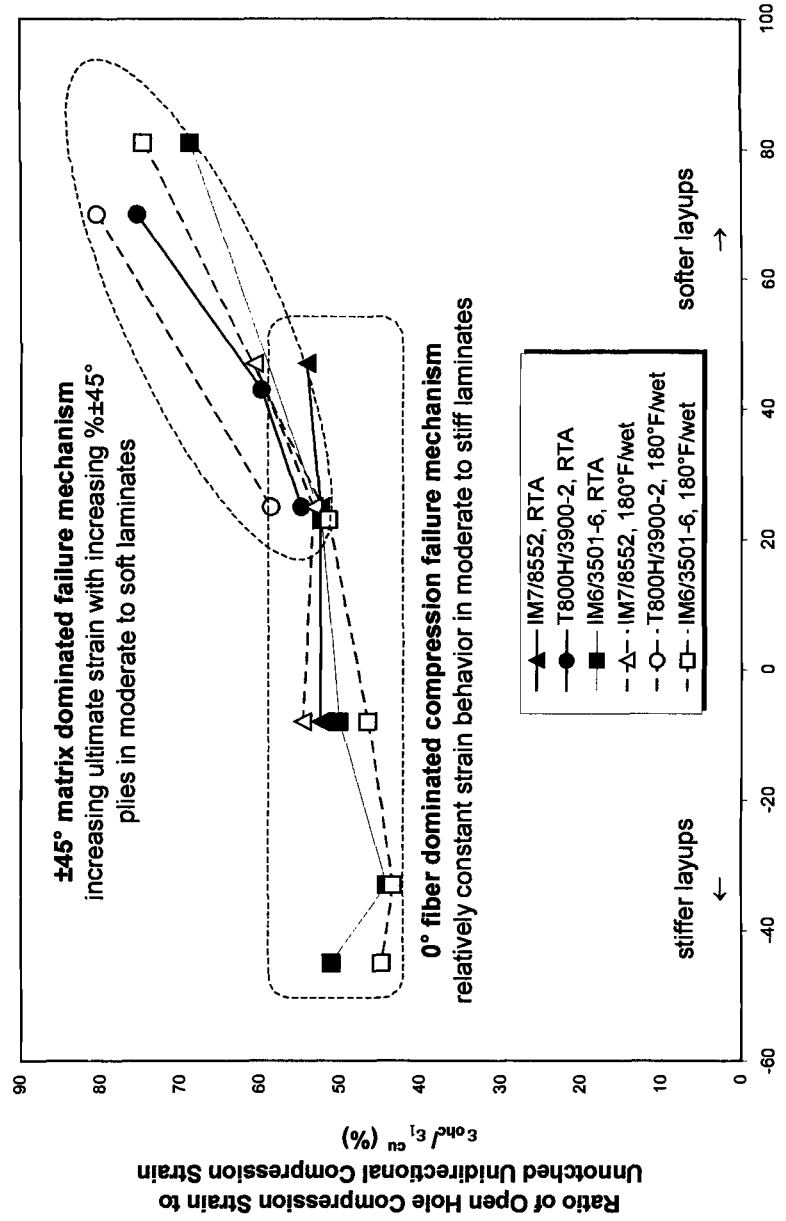


FIG. 1—*OHC test strain averages vs. layup, with identified failure mechanisms.*

PDHOLEC uses displacement steps in an iterative process to reduce ply properties based on predicted damage levels. PDHOLEC uses four-ply failure criteria: fiber kinking, fiber/matrix interface shear, matrix compression, and matrix tension. These failure criteria are applied to the element ply stresses. When ply failure is predicted in an element, the ply stiffnesses in the element is degraded based on the mode of failure predicted by the failure criteria. For example, fiber buckling is assumed to be a catastrophic failure mode for an element, so after fiber buckling is predicted in an element, all of the ply stiffnesses in that element are degraded to zero. For each displacement increment where damage is predicted, the code reformulates the model's stiffness matrix with the degraded element stiffnesses and applies the same displacement increment until no additional damage is predicted at that displacement. Higher displacement increments are then applied in this iterative process until ultimate failure is predicted. PDHOLEC predicts OHC ultimate load when the iterative routines were terminated in one of the following four ways:

- 10% load drop—A substantial load drop is the result of a severely degraded stiffness matrix, and indicates that additional increments will not result in any higher loads. Lesser predicted load drops which do not cause program termination are marked as "possible final failure load" in the output file.
- "Failure reached edge"—PDHOLEC checks the progress of damage across the width of the specimen and terminates when elements are failed to the edge.
- Negative Jacobian matrix—The negative Jacobian matrix signifies negative volume in a failure check, which indicates buckling [*5*]. This buckling usually occurs during the onset of ply level kinking at the hole edge.
- Nonconvergence—When a load step has an extraordinary number of iterations for its damage checks, it is assumed that there will be sustained damage growth progressing until global collapse is reached.

Due to the inherent problems with modeling stress concentrations with finite elements, PDHOLEC cannot accurately predict initial damage. PDHOLEC was developed to predict ultimate failures and assumes that the predicted progressive damage states are not highly dependent on initial damage. PDHOLEC analyses have been correlated to fiber, matrix, and interface damage mechanisms observed from NDI of test specimens of tape laminates.

As part of the assessment of PDHOLEC's robustness, sensitivity studies were conducted on many PDHOLEC input properties. In these studies, the value of one input parameter was varied, while the values for all other parameters were held constant. A few input parameters showed sensitivity problems such as inexplicable changes in predicted strength with small changes in input values. Sensitivity problems are typical to both progressive damage codes and buckling codes. The investigated parameters which appeared to have sensitivity problems were: incremental loading step size, end distance, coupon length, fiber volume ratio, and fiber diameter. An effort was made to avoid sensitive ranges for each of these parameters when appropriate. These parameters can be classified into three groups: progressive damage (load step size), finite-element model geometry (end distance and coupon length), and buckling (fiber volume ratio and fiber diameter).

More investigation is needed to resolve PDHOLEC's buckling-related sensitivity problems. PDHOLEC's sensitivity problems which are related to progressive damage and finite-element model geometry may be resolved by using a more robust progressive damage formulation and a more robust finite-element code, such as PDLAM2D and ABAQUS [*8*]. PDLAM2D uses PDHOLEC 2-D failure criteria for open hole compression analysis configurations, and is a laminated composites progressive damage module for the commercial finite-element code ABAQUS. A series of IM6/3501-6 incremental X-ray, open hole compression tests is being conducted to assess PDLAM2D damage progression predictions in a related program [*8*].

PDHOLEC Element Damage Progression

Element damage progression plots show the extent of predicted damage in the model. PDHOLEC element damage progression outputs were evaluated for several layups in each of the material systems. A post-processing routine is not available for assessing element damage progression. Three critical failure mechanisms were observed and evaluated.

0° Ply Kinking/Buckling Failure Mechanism

The PDHOLEC finite-element model illustration with damage progression for a (25/50/25), T800H/3900-2, RTA laminate is representative of the critical damage leading to ply kinking/global buckling failures (Fig. 2). PDHOLEC predicted similar damage at the side of the hole for all laminates having the kinking/buckling failure mode in all of the materials studied. For stiff laminates in all of the material systems, PDHOLEC also predicted matrix tension damage in 0° plies which initiated at the hole edge in the elements at the top and bottom of the hole prior to ultimate failure due to Poisson's ratio effects and low lamina transverse tension strengths. This 0° ply matrix tension damage did not spread to meet the damage at the critical failure locations at the side of the hole.

For each load iteration in which ply failures occur, PDHOLEC reapplies the same load to the model until no additional ply failures are predicted in any element. The element damage progressions indicate that damage initiated at the hole edge with fiber/matrix shear failures (Fig. 2). Prior to kinking, fiber/matrix shear failures generally only occurred within a few elements at the side of the hole near the hole edge. After the initiation of kinking, fiber/matrix shear damage continued and became more widespread, while kinking continued to progress laterally at the side of the hole. For this failure mechanism, PDHOLEC had negative Jacobian terminations after the kinking reached the sixth element away from the hole, indicating an instability condition.

±45° Ply Matrix Dominated Failure Mechanism

The element damage progression for the (5/86/9) layup IM6/3501-6 damage progression has a different failure pattern than in the 0° ply kinking/buckling failure mechanisms. Although a graphical output of this type of failure progression has not been produced, it appears from looking at the damaged element locations that the damage for this layup progresses toward the edge at approximately ±45° from the hole edge. This pattern was not observed for any of the other layups studied. This pattern indicates a ±45° dominated failure mechanism. The failure progression for this configuration is as follows: the first damage is fiber/matrix shear and matrix tension in the 0° plies at side of hole, followed by kinking (all plies at side of hole). A deflection jump in the load/deflection plot occurs along with kinking, but no load drop is predicted. Matrix damage continues to progress (fiber/matrix shear, matrix tension, and matrix compression) until fiber/matrix shear failures reach elements at the edge of the coupon.

0°/±45° Transition Failure Mechanism

The IM6/3501-6, (33/56/11) layup shows a slightly different failure progression than either the 0° ply kinking/buckling or the ±45° dominated failure mechanisms. The progression is very similar to 0° ply kinking/buckling failures in that ultimate failure is associated with the onset of kinking. However, the failure progression leading up to ultimate is different. In this case, the first damage is matrix tension in the 0° plies at side of hole. This is followed by fiber/matrix shear in the 0° plies at side of hole. Ultimate failure was interpreted in this case as a buckling mechanism, where a load drop is predicted at the onset of kinking.

PDHOLEC Ply Failure Progression

The ply failure progression study is used to evaluate the effectiveness of the ply failure criteria. The effects of damage progression on OHC ultimate strain were evaluated by tracking the first occurrence

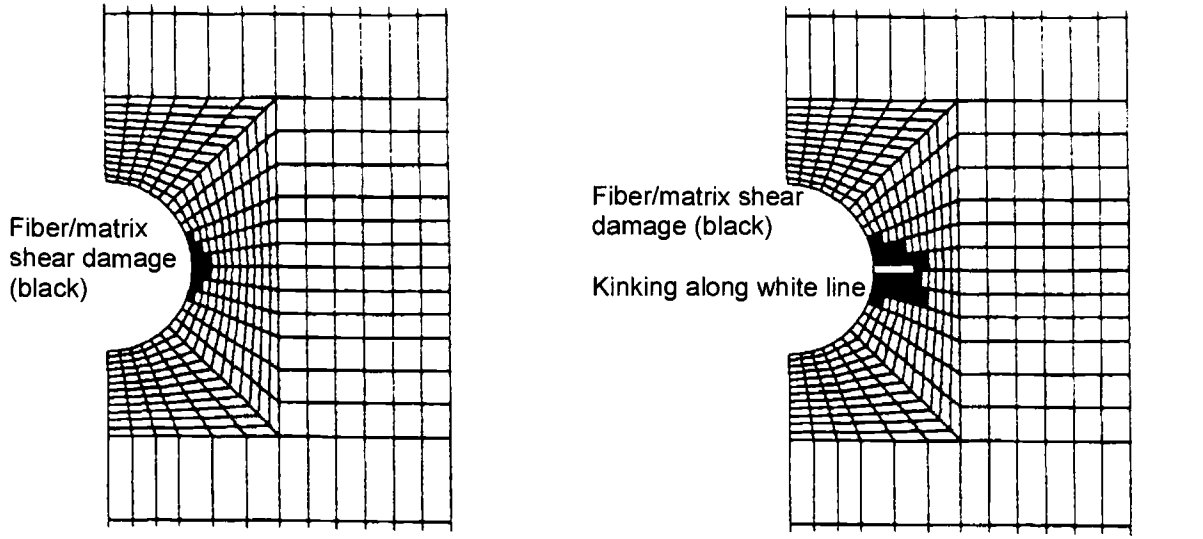


FIG. 2—*Element damage progression for T800H/3900-2 RTA, (25/50/25) layup.*

of each of the four possible ply failure mechanisms in each ply direction. This study was conducted for IM7/8552 and T800H/3900-2 laminates. Each laminate studied had at least one ply in each of the 0°, +45°, −45°, and 90° directions, which eliminated layups that had predicted failure modes other than 0° ply kinking/buckling. First ply failure loads are plotted on PDHOLEC OHC load/deflection plots for selected layups in Fig. 3.

The IM7/8552 predicted OHC strains for the first failure occurrences were calculated and plotted against AML (Fig. 4). The ply failure progression behavior for the T800H/3900-2 laminates is similar to the IM7/8552 laminates. PDHOLEC always predicts that 0° plies will experience fiber/matrix shear failures before kinking. This is due to the inclusion of the fiber kinking term in the quadratic axial/shear interaction for the fiber/matrix shear failure criteria [5]. PDHOLEC predicts a distinct difference between ply failure progression behavior for stiffer (low AML) and softer (high AML) laminates, as seen in Fig. 4 and described below.

- For soft laminates with high AMLs, PDHOLEC predicts a simple ply failure progression, with 0° ply fiber/matrix shear as the first ply failures, which occur at about 80% of ultimate failure.
- PDHOLE predicts more progressive failure complexity with decreasing AML (stiffer laminates). For these laminates, the onset of first ply failures appears to decrease linearly with AML. These first ply failures are still generally 0° fiber/matrix shear failures. In addition to the first ply failures at lower strains, PDHOLEC predicted more types of damage in stiff laminates prior to ultimate failure than for the soft laminates. This progressive damage behavior for stiff laminates was unexpected. Further study of this predicted phenomenon is recommended.

Load/Deflection Study

Load/stroke plots from OHC tests [*2.4*] and from PDHOLEC predictions were studied to evaluate noncritical damage. Strain gage, extensometer, or fractograph data are preferred over load/stroke data; however, OHC allowables specimens are typically not instrumented. Load/stroke data were the only potential indicator of noncritical damage for the evaluated test data. In the future, the authors will conduct additional comparisons between PDHOLEC and incremental X-ray data from an upcoming test program. All of the load/deflection plots reviewed from tests and from PDHOLEC were close to linear. Slight reductions in slope can be seen in most of the plots after initial damage. Some of the PDHOLEC and test plots for very soft laminates were slightly nonlinear throughout loading. This is due to the effect of nonlinear matrix shear stress/strain behavior on laminates with a high percentage of ±45° plies.

OHC load/stroke plots were reviewed for IM6/3501-6 laminates tested at 180°F (82°C)/wet with the goal of separating the data by failure mechanism. Each different failure mechanism should have a distinct behavior that may be reflected in load/deflection plots. Crosshead displacements (stroke) may include grip and fixture effects such as slippage, so the plots were evaluated primarily for curve shapes, slope changes, and load drops. Some of the curves from testing of stiffer layups are almost exactly linear to failure, implying that there was no significant damage prior to catastrophic failure. A first ply failure criterion which ignores noncritical damage may be adequate to predict the ultimate strength for these types of laminates. However, PDHOLEC predicted more damage prior to ultimate failure in these layups.

Subtle curve shapes were identified that may be used in separating the data by failure mechanism. Many of the plots (especially of the softer layups) show slight curvature that may indicate minor strain softening. Some layups show a bilinear or subtle piecewise linear behavior with distinct regions of slope change, indicating an event which reduces stiffness, for instance a ply failure. A few load/deflection curves had "events" such as load jumps or displacement jumps. These events either indicate that there is significant damage prior to ultimate failure, or testing factors such as grip slippage. For

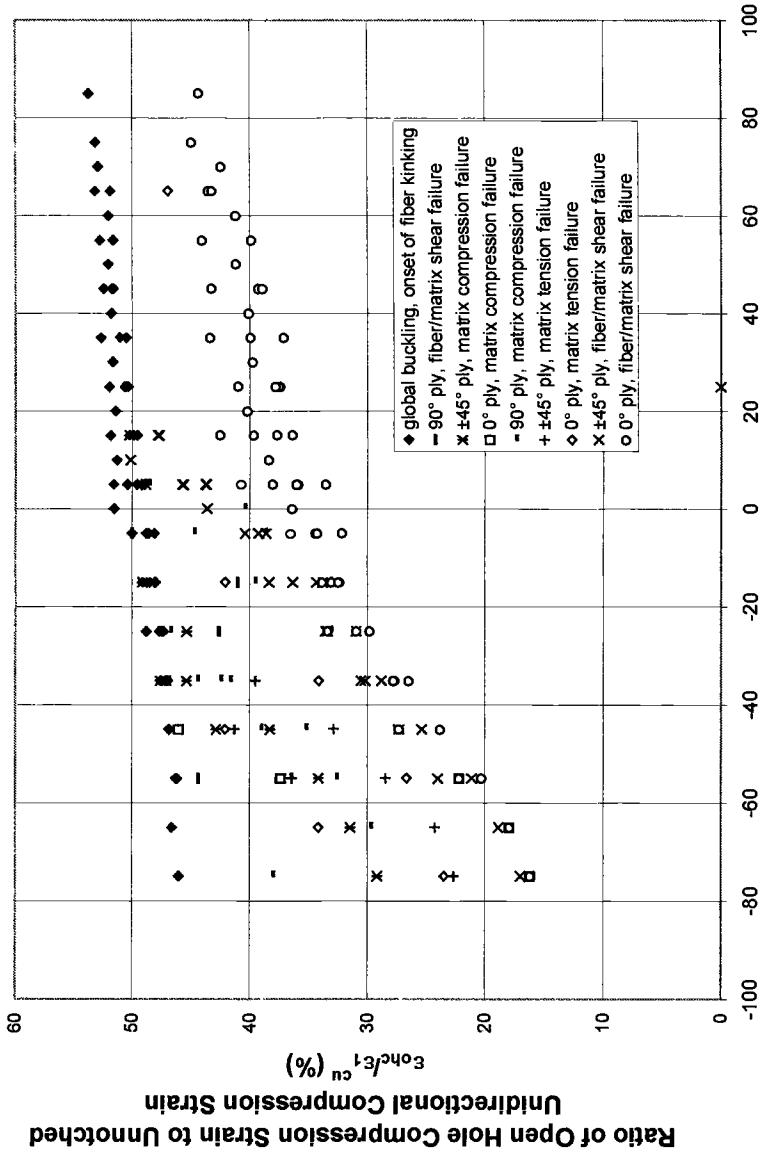


FIG. 3—*PDHOLEC ply failure progression—IM7/8552, 180°F (82°C)/wet.*

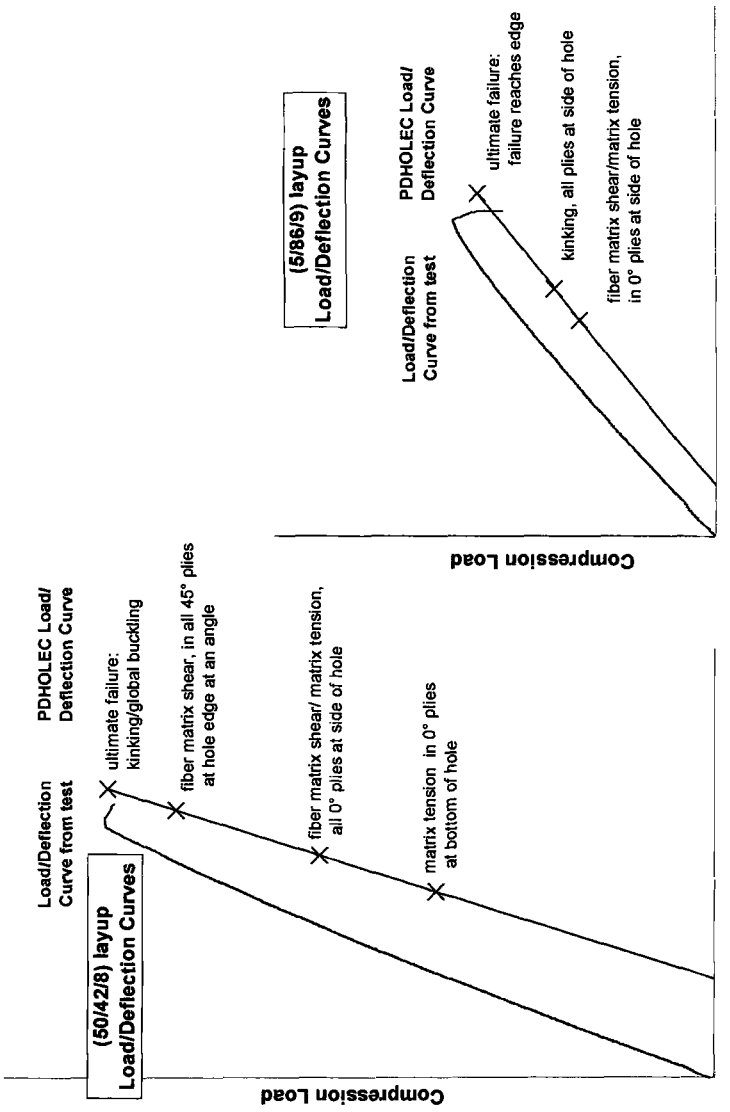


FIG. 4—*Qualitative comparison PDHOLEC vs. test—OHC IM6/3501-6 tape, 180°F (82°C)/wet.*

laminates with significant noncritical damage, first ply failure criteria are not likely to adequately predict ultimate strength.

OHC load/deflection plots from PDHOLEC were compared to load/crosshead deflection plots from V-22 test data (Fig. 4). Load/deflection plots from PDHOLEC output were generated for selected sets of layups, and ply failure progressions were noted on the plots. PDHOLEC ultimate loads, slopes, and ply failures events could then be directly compared to ultimate loads, slopes, slope changes, and/or load drop events on the load/deflection curves from actual OHC tests. Figure 4 shows curves for (50/42/8) and (5/86/9) layups, which have 0° kinking/buckling and ±45° ply dominated failure mechanisms, respectively, based on the results of the separation by failure modes study.

PDHOLEC Ultimate Strength Predictions versus Test Data

PDHOLEC predictions were compared to test data for IM6/3501-6, T800H/3900-2, and IM7/8552 tape laminates at room temperature ambient and/or 180°F/wet test conditions. For IM6/3501-6 laminates, PDHOLEC showed excellent correlation with the test data over the tested layup range, with predicted ultimate strains ranging from 91 to 107% of the test strains (Table 1). PDHOLEC predictions were compared with test data and three failure mechanisms that were observed in the PDHOLEC element damage progression study were identified (Fig. 5).

PDHOLEC also showed good correlation with test data for IM7/8552 and T800H/3900-2 quasi-isotropic laminates and the IM7/8552 (50/42/8) laminates. Since the OHC ultimate strain behavior for the 0° buckling mechanism is relatively flat in both test data and PDHOLEC predictions, the correlation between PDHOLEC predictions to test data for stiff and moderate layups is anticipated to be similarly reasonable. However, PDHOLEC did not predict ±45° dominated failure mechanisms in the IM7/8552 and T800H/3900-2 material systems, so PDHOLEC significantly underpredicted ultimate strengths in the softer laminates, especially in the (10/80/10) layups.

PDHOLEC Trend Study Plots

PDHOLEC predictions were generated for a series of layups which systematically covered the range of (0°/±45°/90°) laminates. For IM6/3501-6, PDHOLEC runs were conducted for the whole

TABLE 1—*PDHOLEC predicted vs. tested open hole compression strains.*

Material	Test Environment		Layup	Predicted/Test OHC Strains
	°F	Moisture		
IM6/3501-6	180	wet	(5/86/9)	91%
			(33/56/11)	95%
			(50/42/8)	102%
			(62/29/9)	105%
			(68/23/9)	107%
T800H/3900-2	70	ambient	(10/80/10)	62%*
			(23/67/10)	80%
			(25/50/25)	89%
T800H/3900-2	180	wet	(10/80/10)	62%*
			(25/50/25)	83%
IM7/8552	RTA	ambient	(50/42/8)	91%
			(25/50/25)	94%
			(20/67/13)	91%
IM7/8552	180	wet	(50/42/8)	89%
			(25/50/25)	95%
			(20/67/13)	84%

* PDHOLEC did not correctly predict the ±45° dominated failure mechanism for this laminate.

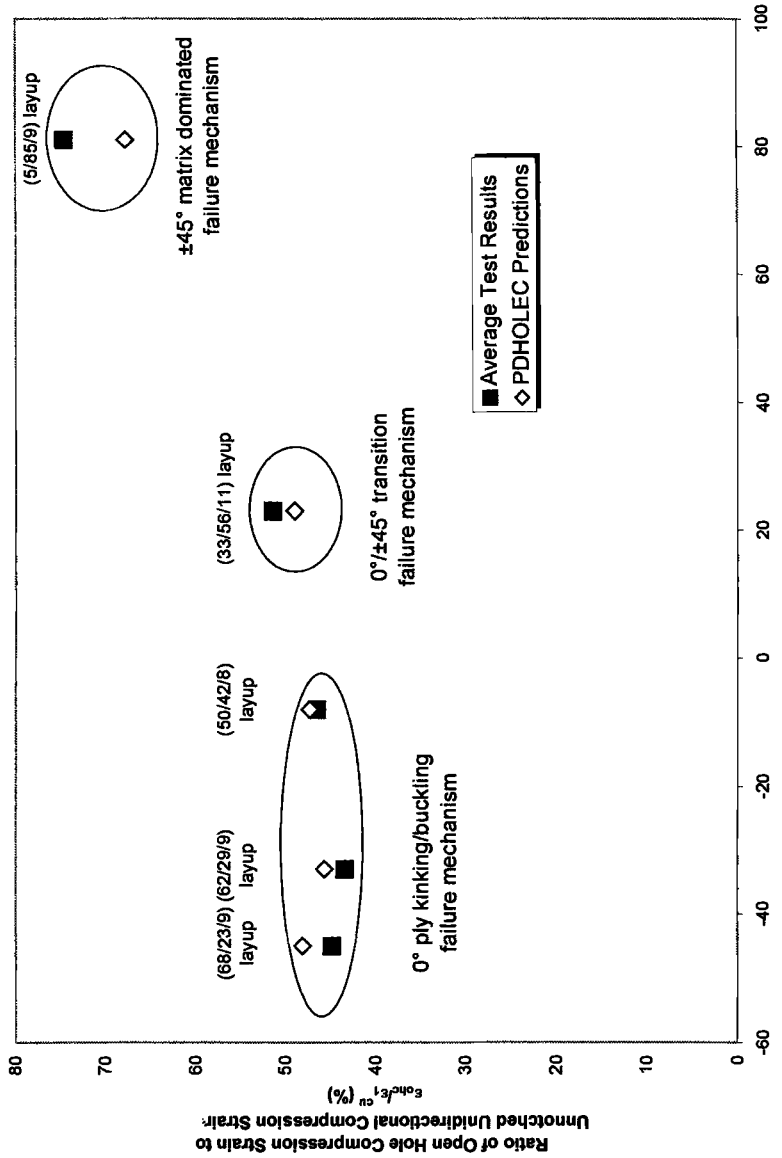


FIG. 5—*PDHOLEC vs. OHC test strain averages, IM6/3501-6 tape, 180°F (82°C)/wet.*

layup range, including extreme laminate such as (0/100/0), (100/0/0), and (0/0/100). For the IM7/8552 and T800H/3900-2 study, all of the studied laminates had at least one ply in each direction (5%), so PDHOLEC was not evaluated for extreme layups in those material systems.

Figures 6 and 7 show PDHOLEC predictions plotted against the AML layup parameter. These trend study plots were reviewed in terms of failure mechanisms along with PDHOLEC progressive failure output. PDHOLEC predicted a 0° ply kinking/global buckling failure mechanism for all of the analyzed laminates in the T800H/3900-2 and IM7/8552 material systems and for most of the IM6/3501-6 laminates. PDHOLEC predicted other failure mechanisms for some of the extreme IM6/3501-6 laminates. All of these failure mechanisms are described below.

0° Ply Kinking/Buckling

For all of the tape laminate systems, a nearly constant strain behavior was readily apparent for the majority of the layups. The near constant strain behavior is attributed to the 0° ply kinking/buckling critical mechanism described in the Element Damage Progression section. In PDHOLEC, the OHC ultimate strain in the ply kinking failure mechanism is a function of two competing and opposing factors: the stress concentration effect, and the effect of shear nonlinearity in the matrix. For the ply kinking/buckling mechanism in all of the material systems, the slightly increasing general trend in strain with AML is due to the rate of reduction in stress concentration with reduced laminate axial stiffness. Figure 6 shows a drop in OHC strain at AMLs > 60, which has not been observed in test data. Sensitivity studies indicated that this PDHOLEC predicted drop is a result of the increased effect of the shear nonlinearity factor for these laminates.

For the IM7/8552 and T800H/3900-2 layups studied, 0° kinking/buckling was the only ultimate failure mechanism predicted by PDHOLEC. A nearly constant strain behavior is typical in OHC test data for moderate to stiff laminates. However, typical OHC test data for aerospace graphite composite material systems show significantly higher ultimate strains for soft laminates. Therefore, PDHOLEC predicted behavior did not consistently correlate well with test data for soft laminates in these material systems.

Matrix Dominated Failures

PDHOLEC analyses for IM6/3501-6 laminates predicted high ultimate strains for laminates with few 0° plies, which indicates matrix dominated failure mechanisms (Fig. 7). Most of these IM6/3501-6 layups with the high ultimate strain matrix dominated failure mechanisms were extreme layups that did not contain any 0° plies. Sensitivity studies indicated that the high ultimate strains for layups with no 0° plies were a result of two different progressive failure mechanisms, a matrix cracking mechanism and a $\pm 45°$ ply dominated mechanism. Sensitivity studies were conducted to determine the effect of input parameters on PDHOLEC predicted matrix dominated failures. These sensitivity studies were not conclusive in determining PDHOLEC's inconsistency in correctly predicting $\pm 45°$ ply dominated failure mechanisms in soft laminates. The strains for several layups which had very few 0° plies, were somewhat higher than the relatively constant strains for the 0° ply kinking/buckling mechanism. These layups were identified to have an intermediate $0°/\pm 45°$ transition mode.

Matrix Cracking Mechanism—The failure strains were extremely high for these laminates with no 0° plies. For the majority of these soft layups, the ultimate loads were proportional to transverse compression strength. Failure in these layups did not appear to be dominated by a single ply group, so they were designated as the "Matrix Cracking" failure mechanism.

$\pm 45°$ Dominated Mechanism—For the remaining soft layups (with very high % 45° plies), load is not proportional to transverse compression strength, and therefore, these layups are not transverse

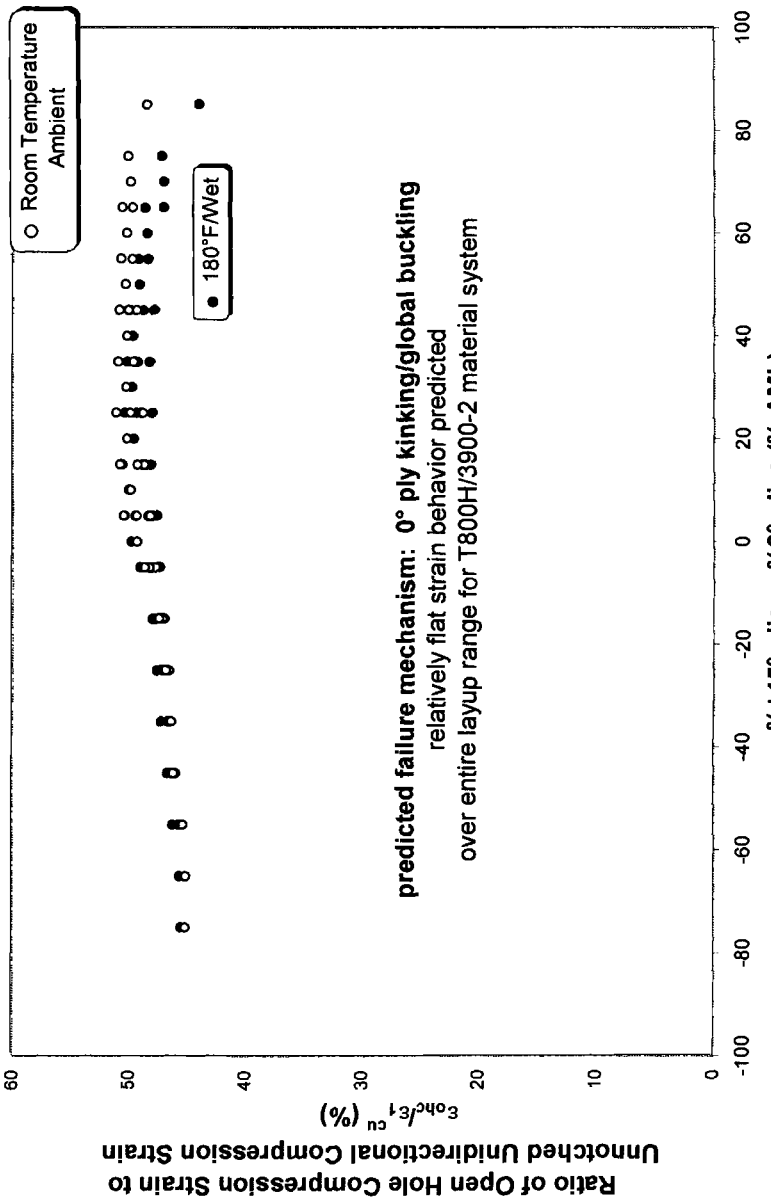


FIG. 6—*PDHOLEC predicted OHC ultimate strains: T800H/3900-2 laminates.*

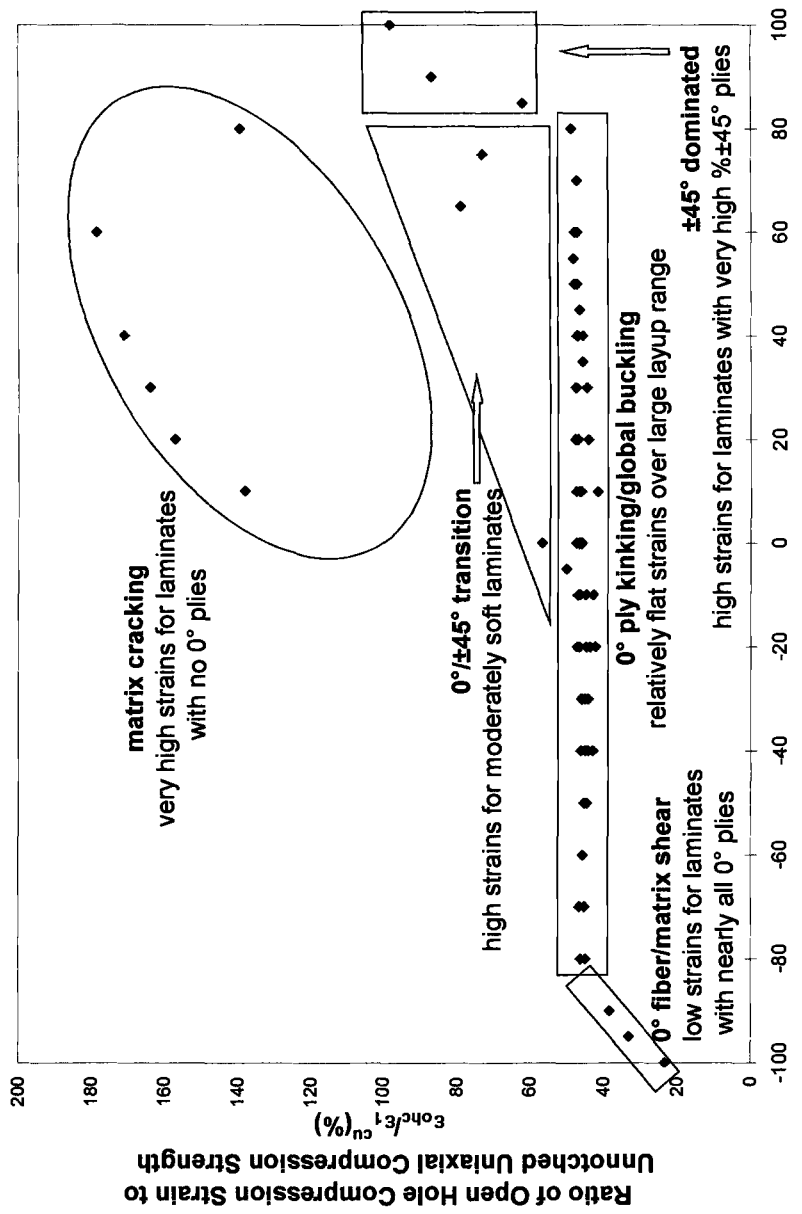


FIG. 7—*PDHOLEC OHC ultimate strains: IM6/3501-6 laminates @ 180°F (82°C)/wet.*

compression strength dominated. The failure mechanism was not readily apparent from the damage progression output file, so this mechanism was simply designated as "±45° Dominated."

0°/±45° Transition Mechanism—The layups with this failure mechanism are softer than adjacent layups which were identified with 0° ply kinking/buckling mechanism. This failure mechanism incorporates aspects of the 0° ply kinking/buckling and matrix dominated failure mechanisms as described in the PDHOLEC Element Damage Progression section.

0° Fiber/Matrix Shear

PDHOLEC predicted low compression strains for IM6/3501-6 layups with nearly all 0° plies (Fig. 7). A review of the damage progression output file for these layups indicated a "0° Fiber/Matrix Shear" dominated failure mechanism. This predicted behavior has not been correlated to tests since no OHC test data were available for layups with extremely high percentages of 0° fibers.

Characteristic Equations for Distinct Failure Mechanisms

The results from the different techniques described in this paper for separating by failure mechanism were reviewed together to identify distinct failure mechanisms. Using any one of these techniques alone would not be sufficient to convincingly identify the failure mechanism for a laminate. However, a strong argument for identifying a distinct failure mechanism can be made if several different methods concur and are consistent with theoretical predictions and/or generally accepted observations of composites failure. Future testing is necessary to conclusively identify the critical failure mechanisms and to track the noncritical progressive damage.

A detailed review of the results for IM6/3501-6 OHC tape data at the 180°F/wet environment indicated four distinct failure mechanisms and one transition failure mechanism (Table 2). Most of these failure mechanisms are associated with extreme layups and have not been adequately correlated to test data. These identified failure mechanisms are listed with the methods that support their identification.

Characteristic equations are curve fits of the relationship between strength and test parameters, and were generated for each distinct failure mechanism where possible. Linear regression was used for

TABLE 2—*Identified OHC failure mechanisms for IM6/3501-6 tape at 180°F(82°C)/wet.*

Identified Failure Mechanism	Supporting Evidence	Test Layups
0° ply kinking/buckling (layups with high % 0° plies)	Test data trend study plots Load/deflection plots from tests PDHOLEC element damage progression PDHOLEC load/deflection plots PDHOLEC trend study plots	(50/42/8) (62/29/9) (68/23/9)
±45° dominated (layups with very high % ± 45° plies)	Test data trend study plots Load/deflection plots from tests PDHOLEC load/deflection plots PDHOLEC damage progression PDHOLEC trend study plots	(5/86/9)
0°/±45 transition (between 0° kinking/buckling and ±45° dominated or matrix compression)	Test data trend study plots PDHOLEC damage progression	(33/56/12)
Matrix cracking (layups with no % 0° plies)	PDHOLEC trend study plots Yc (matrix comp. strength) sensitivity study	not available
0° fiber/matrix shear (layups with very high % 0° plies)	PDHOLEC trend study plots	not available

the curve fitting, except in the case of the 0° ply kinking/buckling constant strain behavior, where coefficient of variations are used to determine "goodness" of the curve fit. The PDHOLEC predictions for IM6/3501-6 tape at 180°/wet were grouped into four distinct failure mechanisms: 0° ply kinking/buckling, matrix compression, ±45° dominated, and 0° fiber/matrix shear. The predictions for the 0°/±45° transition mechanism were pooled with the matrix compression mechanism. A 3-D carpet plot of the failure surfaces for each of these failure mechanisms is shown in Fig. 8.

A characteristic equation based on test data and PDHOLEC results was generated for the 0° ply kinking/buckling mechanism. A preliminary characteristic equation for the matrix cracking mechanism was generated based on PDHOLEC results, without verification to test data. There were too few layups that had PDHOLEC predictions in the ±45° dominated and the 0° fiber/matrix shear mechanisms to adequately characterize their behavior, even though they are depicted in Fig. 8. The generated characteristic equations were not included in this report due to the proprietary nature of the test data. The characterization of the four failure mechanisms is described below.

0° Ply Kinking/Buckling Characteristic Equation

This failure mechanism showed a nearly constant strain trend in the test data and the PDHOLEC predictions. To validate using a constant strain trend, statistical screening for 95% outliers with the Grubbs method [*9*] was performed on PDHOLEC predictions (for a wide range of layups and for the tested layups) that were identified as having 0° ply kinking/buckling failures. Since no outliers were detected in either the pooled PDHOLEC predictions or the pooled test data and the coefficient of variation of the pooled data was small, it was reasonable to assume that the characteristic equation should have the form of a constant ultimate strain value. The subtle strain trends in the 0° kinking/buckling mechanism predicted by PDHOLEC were not incorporated in the characteristic equation due to the lack of supporting evidence from tested laminates. Although test data averages for this failure mechanism could be used as the constant in the characteristic equation, in Fig. 8 the average strain from PDHOLEC predictions for this failure mechanism was used as the constant since the other failure mechanisms plotted were based on PDHOLEC results.

0°/±45° Transition Failure Mechanism

There were not enough laminates in this study to generate a reasonable failure surface for the 0°/±45° transition failure mechanisms, so the transition failure laminates were grouped with another failure mechanism. The transition laminates were pooled with the matrix cracking laminates since they did not fit the 0° ply kinking/buckling or ±45° dominated failure mechanisms' trends. More PDHOLEC analyses are needed to verify whether the transition failure mechanism is distinct from the other failure mechanisms. Test data showing damage progression for this failure mechanism are expected to be available in October 1999 [*8*].

Matrix Cracking Preliminary Characteristic Equation

PDHOLEC predicted a matrix compression (cracking) mechanism for most layups with no 0° plies. A linear regression curve fit was applied to the predicted strains for the laminates that were identified to have matrix cracking and 0°/±45° transition failure mechanisms, to generate a characteristic equation. The curve fit resulted in a failure surface that was quadratic against layup parameters. The steep slope of the failure surface indicates a high sensitivity of the ultimate strain in this failure mechanism to small changes in layup. More study is required to verify this failure mechanism and its behavior.

±45° Dominated Failure Mechanism

PDHOLEC predicted a failure mechanism that was different from the matrix cracking mechanism for three layups with extremely high % 45° plies. To represent this failure mechanism in the 3-D car-

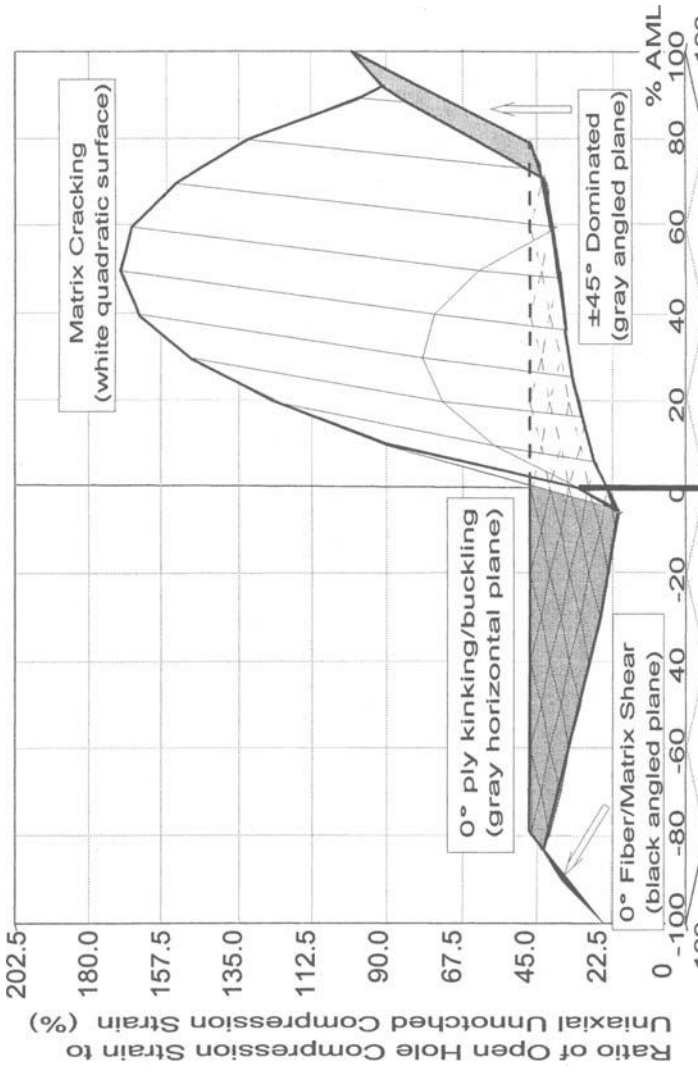


FIG. 8—*3-D failure mechanisms carpet plot for IM6/3501-6 at 180°F (82°C)/wet.*

pet plot, a plane was fit through the data for the three layups. Although there are aerospace structures that have all ±45° plies, not enough test data exist to verify this failure mechanism.

0° Fiber/Matrix Shear Failure Mechanism

PDHOLEC predicted a fiber/matrix shear failure mechanism for three layups with extremely high % 0° plies. To represent this failure mechanism in the 3-D carpet plot, a plane was fit through the three points. Aerospace structures are not designed in this layup range; therefore no OHC test data exist to verify this failure mechanism.

Conclusions

- Notched compression tests have distinct ply level failure mechanisms that can be determined using the methods described in this paper.
- The characteristic equations by separation of failure mechanisms approach used in this report is appropriate for notched compression configurations. However, additional analytical work and testing are needed to generate and validate the equations.
- The following failure mechanisms were identified:

0° Ply Kinking/Buckling—This mechanism was identified from test data and PDHOLEC predictions and characterized with a constant strain behavior over a large range of layups. This PDHOLEC predicted failure mechanism correlates well to test data based on trend studies, load/deflection plots, and PDHOLEC failure progression analysis.

Matrix Cracking—This mechanism was identified from PDHOLEC predictions for layups with very few or no 0° plies. A preliminary characteristic equation having a quadratic curve shape was generated for this mechanism. This preliminary characteristic equation has not been validated with test data.

Other Identified Failure Mechanisms—±45° dominated mechanism for laminates with very high % ±45° plies, 0°/±45° transition mechanism, and 0° fiber/matrix shear mechanism for laminates with very high % 0° plies. Characteristic equations were not developed for these mechanisms due to lack of test data.

- Finite-element progressive damage modeling has good potential for estimating OHC strength, but needs further development before use as practical analysis tools.

Strengths—PDHOLEC's kinking failure criteria provides reasonable predictions for OHC strength for 0° ply dominated failure mechanisms. PDHOLEC's ply kinking criterion is a reasonable model for fiber buckling. PDHOLEC is relatively easy to run. Material properties that have not been generated from test data can be estimated and produce good results. PDHOLEC is capable of predicting complex progressive damage and strength behavior. Distinct OHC strain behaviors can be traced to different parameters in the failure criteria, nonlinearity, stress distribution, etc.

Weaknesses—PDHOLEC needs further development in the areas of: (1) accurate prediction of matrix dominated ultimate failure mechanisms, (2) improved capability for analysis of through-the-thickness effects and delamination failures, (3) automated post-processing plotting, and (4) debugging to give robust results.

In summary, the combined empirical/analytical approach was successfully used in this program to identify and characterize failure mechanisms for OHC test configurations. This approach may also be applied to other test configurations. Improved design strength allowables may be achieved with this

approach, which would potentially reduce costs in generating allowables and reduce weight in new designs, and increase service life in existing aircraft.

Acknowledgments

This project was supported with shared funding by the U.S. rotorcraft industry and Government under RITA/NASA Cooperative Agreement No. NCCW-0076, Advanced Rotorcraft Technology, dated 15 August 1995.

References

[1] Ogonowski, J. M., "Effect of Variances and Manufacturing Tolerances on the Design Strength and Life of Mechanically Fastened Composite Joints." AFWAL-TR-81-3041, U.S. Air Force, 1981.

[2] "Material Substantiating Data and Analysis Report," Bell Helicopter V-22 Report No. 901-930-022, Contract No. N00019-85-C-0145, Bell Helicopter Textron, 1988.

[3] *BMA Stress Analysis Handbook. Advanced Composites.* Boeing B-2 Document D650-10316-2, 1993.

[4] Unpublished Bell internal data (1997, 1998).

[5] Chang, F. K. and Lessard, L. B., "Damage Tolerance of Laminated Composites Containing an Open Hole and Subjected to Compressive Loadings: Part I—Analysis and Part II—Experiment," *Journal of Composite Materials,* Vol. 25, 1990.

[6] *Structural Development Tests, Coupon Tests. Results and Evaluation (CDRL A196) Volume 05 Graphite Epoxy,* Report 5PPYA081-05, Lockheed/Boeing F-22 Contract F33656-91-C0006, 1994.

[7] *Structural Development Tests, Coupon Tests, Results and Evaluation (CDRL A196) Volume 06,* Report 5PPYA081-06, Lockheed/Boeing F-22 Contract F33656-91-C0006, 1994.

[8] Bau, H., "Global Approach to Characterizing Composites Strength with Empirical, Analytical and Progressive Damage Methods," AF96T009 STTR Phase II Proposal, U.S. Air Force, 1997.

[9] Neal, D. and Vangel, M., "Statistical Analysis of Mechanical Properties," *Engineered Materials Handbook. Volume 1.* Composites, ASM International, 1987, p. 303.

Adam J. Sawicki[1] *and Pierre J. Minguet*[1]

The Influence of Fastener Clearance Upon the Failure of Compression-Loaded Composite Bolted Joints

REFERENCE: Sawicki, A. J. and Minguet, P. J., **"The Influence of Fastener Clearance Upon the Failure of Compression-Loaded Composite Bolted Joints,"** *Composite Structures: Theory and Practice, ASTM STP 1383*. P. Grant and C. Q. Rousseau, Eds., American Society for Testing and Materials, West Conshohocken, PA, 2000, pp. 293–308.

ABSTRACT: The effects of fastener hole-filling and hole clearance upon the compressive strength of IM6/3501-6 tape composite bolted joints were investigated experimentally and analytically. Tests were conducted using coupon specimens loaded at several bearing-bypass loading ratios, with defined hole clearances spanning the range permitted in Class 1 structural holes (nominal bolt diameter +0.076/−0.000 mm). Bearing-bypass loads were applied using a dual actuator servo-hydraulic load frame augmented with bearing reaction supports. Three primary failure modes (net section compression, offset net section compression, and bearing) were observed. A linear relationship between bearing stress and bypass strain at failure was observed for specimens failing in the offset net section compression mode. Mean joint strengths were found to vary at most 7% due to variances in initial hole clearance. A semi-empirical strength prediction methodology, which uses 2-D finite-element analysis and ply-level quadratic failure theory, was used to interpret test results. Reasonable agreement between experimental data and predicted trends was demonstrated for IM6/3501-6 tape laminates. Incorporation of bolt elasticity effects and improved failure criteria within the methodology is necessary to improve the accuracy of strength predictions.

KEYWORDS: composites, bolted joints, compression loading, bearing-bypass interaction, hole tolerance, finite-element analysis, strength prediction

Composite bolted joints exhibit complex strength behavior arising from the interaction of bearing stresses (induced by load reacted at a hole) and bypass stresses (induced by net section loads not reacted at a hole). This is due to the variety of failure modes which arise under different applied load conditions. Historically, the complex strength behavior of composite joints has resulted in heavy reliance upon empirical data when generating design curves. Such design information can be developed more cost-effectively by first generating strength data at a limited number of bearing-bypass load ratios using coupon and element-level specimens, then using a semi-empirical analysis technique to interpolate strength values between the test points [*1*].

It has been demonstrated that bolted joint strength trends can be predicted accurately using analytical models which superpose bypass and bearing stress fields in the tension bypass-dominated regime. Numerous models (notably those of Ramkumar [*2*], Garbo [*3*], and Grimes [*4*]) have demonstrated the adequacy of simulating bearing loads using a "half-cosine" radial pressure distribution around the perimeter of the hole for tension-loaded joints. Conversely, models of this type have not been as successful in predicting failure modes and strengths for compression-loaded joints. As demonstrated by Crews and Naik [*5,6*], this results from the development of a through-fastener load path in the compression bypass-dominated regime.

[1] Engineer-scientists, Structures Research & Development, The Boeing Company, Philadelphia, PA 19142-0858.

Copyright© 2001by ASTM International www.astm.org

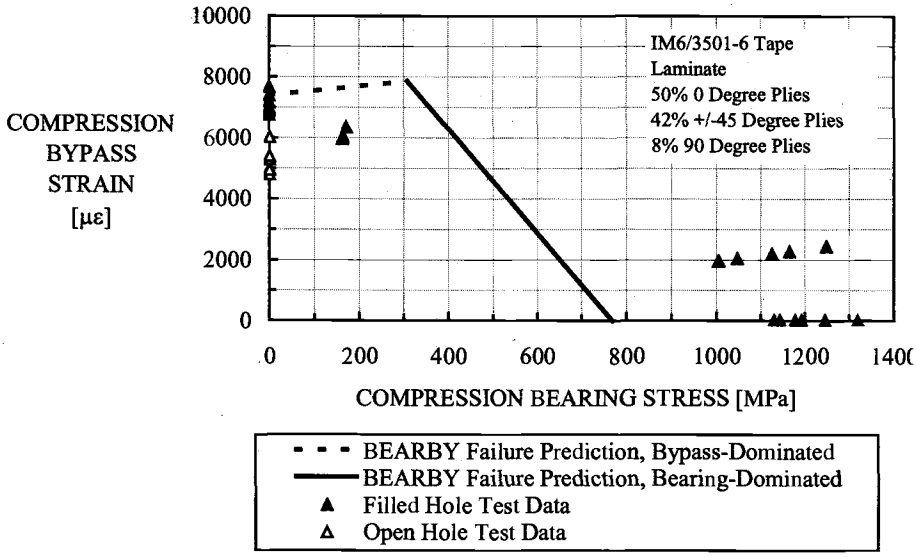


FIG. 1—*Comparison of bearing-compression bypass test data with BEARBY failure predictions.*

This effect is demonstrated in Fig. 1, in which strength interaction predictions generated using the Boeing-developed BEARBY analysis code are compared with test data obtained for an IM6/3501-6 tape laminate [*7*]. The BEARBY code consists of pre- and post-processors to the BJSFM stress analysis code [*3*], which utilizes a half-cosine bearing model in its closed-form analytic solution and does not account for through-fastener loading effects upon the state of stress [*8*]. As shown in the figure, BEARBY predicts compression bypass strain capability to initially increase as bearing stresses are applied, which contradicts the behavior of the test data.

The complexities of bearing-compression bypass failure and modeling have resulted in the use of conservative design values in this regime. Many allowables programs have used an open hole failure strain "cutoff" effectively to account for uncertainties regarding hole tolerance, elongation, etc. This approach resulted in incremental improvements in joint efficiency as basic material properties improved, until toughened resin systems and certain low cost manufacturing processes were introduced. Laminates fabricated using these materials and processes have been found to exhibit lower open hole compression strengths [*9*]. This reduces the open hole strain cutoff for these materials, effectively lowering their load-carrying capability when used in compression-loaded joints. To utilize new material forms and processes without adversely affecting joint efficiency, it may be necessary to change the criteria by which compression bearing-bypass design envelopes are defined. This requires eliminating the use of an open hole-based strain cutoff, in order to take full advantage of filled hole-based joint capability.

A research program was undertaken at Boeing-Philadelphia to better understand laminate failure in the presence of a filled hole under combined bearing and bypass loading, in order to develop appropriate allowables criteria. Experiments identified key parameters which influence the modes of failure and enhance strength relative to the open hole condition. Finite-element-based analytical models complemented the experimental data, such that states of stress and failure mechanisms could be better understood. The work expanded upon that conducted by Crews and Naik [*5,6*] and Chang [*10*] by examining failure modes and strengths of joints with hole diameters spanning traditional manufacturing tolerances, and emphasized improving our understanding of compression bypass-dominated failure.

Factors that Influence Compression Bypass-Dominated Strength

As shown in Fig. 2, the filled hole strength enhancement (relative to open hole strength) results from the addition of an alternate load path when dual-sided fastener-hole contact is achieved. This additional load path reduces the load carried by the laminate around the hole, and subsequently reduces the bypass stress concentration local to the hole edge. For the alternate load path to exist, the laminate must deform and eliminate any clearance between the fastener and the hole surfaces. The load share carried through the fastener, and subsequently the compression bypass strength, will vary depending upon both the initial hole clearance and the ability of the laminate to deform and eliminate this clearance.

Factors that influence the formation of a through-fastener load path include initial clearance, laminate stiffness, clamp-up torque, and bearing-bypass ratio. In a previous investigation, the authors examined the effects the first three factors upon pure filled hole compression bypass strength with no load transfer at the fastener [*11*]. The current investigation concentrated upon hole clearance and bearing-bypass ratio effects upon joint strength.

Initial clearance results from manufacturing tolerances and elongation resulting from repeated bearing loads. Clearance fit fastener holes used in composite primary structures are typically larger in diameter than the bolt diameter; for example, Class 1 holes of 6.35 mm (0.250 in.) nominal diameter may range in actual diameter between 6.35 mm to 6.43 mm (0.253 in.). Thus, Class 1 structural holes may be up to 1.2% larger in diameter than the fastener at installation. Filled hole-based bypass strain allowables for primary structures must account for hole clearances and/or elongation levels of this magnitude.

The bearing-bypass ratio affects fastener hole-filling due to the local deformation induced by the applied bearing load. Compression bypass-dominated joints tend to exhibit a through-fastener load path with dual-sided fastener-hole contact, shown in Fig. 2. As the ratio of bearing load to bypass load is increased, however, the fastener tends to contact the hole on one side only, and the through-fastener load path is lost. The initial clearance between the fastener and the hole edge influences the loading ratio at which dual contact is lost.

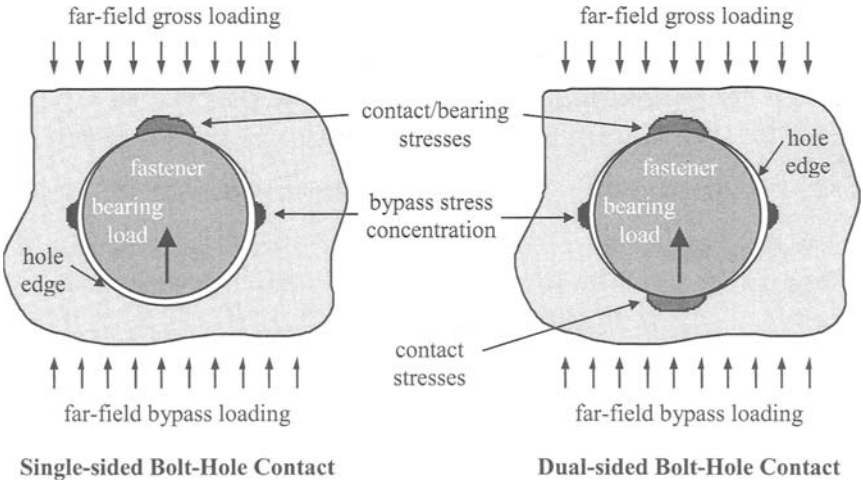


FIG. 2—*Single and dual-sided fastener contact in a loaded hole.*

TABLE 1—*Test matrix.*

Specimen Type	Nominal Hole Diameter	Number of Specimens per Bearing-Bypass Load Ratio*					
		0%	10%	15%	25%	50%	100%
Filled hole	6.350 mm (0.250 in.)	3	3	3	3	3	3
Filled hole	6.426 mm (0.253 in.)	3	3	3	3	3	3
Open hole	6.426 mm (0.253 in.)	3	...	...	...	...	...

* Bearing-bypass load ratio defined as ratio of bearing load to gross load (bearing load + bypass load).

Experimental Approach

Test Specimens

The influence of clearance upon strength was assessed using a matrix of 39 coupon-level open and filled hole bearing-bypass specimens. A summary of the test matrix, as well as hole conditions present for each test, is shown in Table 1. All tests were performed in room temperature, ambient humidity conditions. The bearing-bypass load ratio is defined as the ratio of bearing load to gross load (which equals the sum of bearing load plus bypass load, as defined in Fig. 2), and represents the percentage of load transferred at the fastener.

Test coupons were fabricated using IM6/3501-6 Grade 190 prepreg tape (manufactured by Hexcel Composites). The laminate stacking sequence is shown in Table 2. This stacking sequence has been used frequently in structural allowables test programs at Boeing-Philadelphia, as it is representative of longeron and stringer padups in tilt rotor fuselage and wing skins.

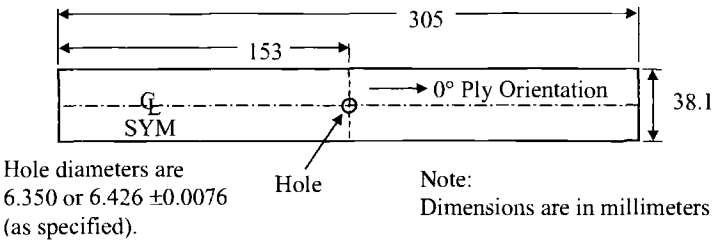
Test specimens, shown in Fig. 3, were 305 mm (12 in.) long and 38.1 mm (1.5 in.) wide. For the baseline hole diameter of 6.35 mm (0.250 in.), this provided a specimen width-to-diameter (w/D) ratio = 6 and an edge margin-to-diameter (e/D) ratio = 3. The specimens were manufactured using standard Boeing equipment and procedures, except that the holes were drilled to precise diameters using drill reamers. Hole diameters were nominally 6.350 mm (0.2500 in.) or 6.426 mm (0.2530 in.) with ±0.0076 mm (0.0003 in.) tolerance; the precise diameters permitted a meaningful examination of clearance effects. For fasteners of 6.350 mm diameter, this resulted in initial fastener-hole clearances of 0.000 mm and 0.076 mm (0.003 in.), which represent the range of clearances permitted for Class 1 holes.

Bolted joint failures can be classified as bearing-dominated and bypass-dominated, and the strength of each type is dependent upon fastener clamp-up provided through installation torque. It has been demonstrated that for bearing-dominated failures, high fastener clamp-up increases fastener-laminate friction, suppresses the onset of subcritical damage, and increases ultimate strength [7]. Conversely, previous work by the authors demonstrated that filled hole compression strength is relatively insensitive to clamp-up torque [11]. It was assumed, however, that bearing-induced subcritical damage could affect bypass-dominated failures to an extent not observed in the previous work. Thus,

TABLE 2—*Laminate configuration.*

Material	Stacking Sequence*	Nominal Thickness	% 0/45/90	Nominal Longitudinal Modulus
IM6/3501-6 Grade 190 Tape	$[45/90/-45/0_3/\pm 45/0_3/\overline{\pm 45}]_s$	4.51 mm (0.178 in.)	50/42/08	85.4 GPa (12.4 msi)

* Overscore indicates plies are not included in laminate symmetry.



Filled hole specimens use a BACB30VT8K pin (Fairchild VL10-8) and BACC30CC8 collar (Hi-Shear HST1571YN-8).

FIG. 3—*Open and filled hole specimen configurations.*

it was decided to conduct the tests with fasteners installed in a "finger-tight" condition, with a nominal installation torque of 0.3 to 0.7 N-m (3 to 6 in. · lb).

Test Apparatus and Procedure

Bearing-bypass loads were applied using the test system shown in Fig. 4. This apparatus was previously used in structural allowables testing for the Boeing 777 aircraft, and is similar to a device developed by Crews and Naik [*5,6*]. The system is composed of a 230 kN (50 kip) dual actuator servo-hydraulic load frame (with a load cell attached to each actuator), two bearing-reaction plates, fastener bushings, two bearing load cells and grip plates. Bearing loads are introduced to the specimen through the bearing-reaction plates by differentiating the deflection (and thus the loading) of the hydraulic actuators. Any difference between the applied actuator loads is reacted through a bolt attaching the specimen to the bearing-reaction plates.

To test a specimen under compression bearing-bypass loads, a production-representative titanium

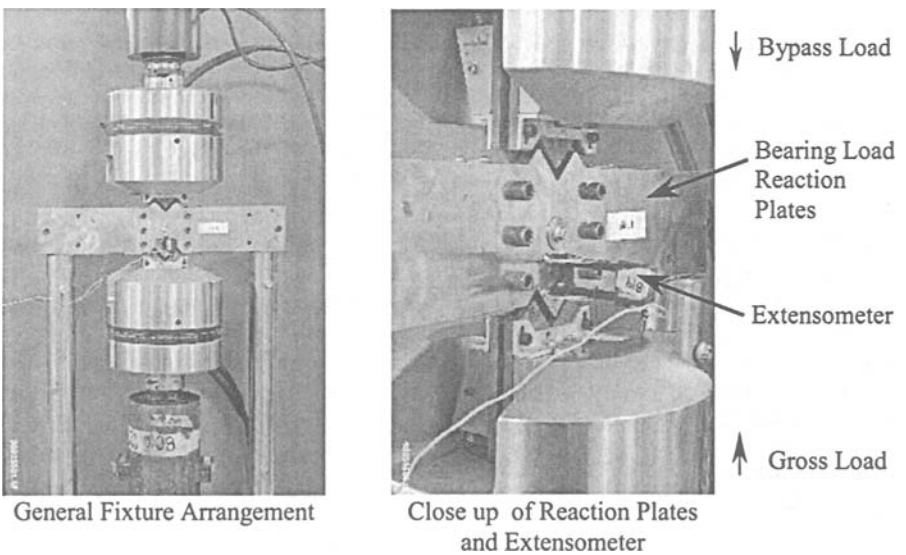


FIG. 4—*Bearing-bypass loading apparatus.*

fastener was installed though two 10.3 mm (0.44 in.) diameter bushings and the test specimen hole, then torqued to the required level. The use of bushings permitted clamp-up force to be transmitted to the specimen, and simulated the presence of a fastener head and collar against the specimen surface. The bushed specimen was then installed in the bearing-reaction plates, which were in turn secured to the load cells and load frame. The presence of the bearing-reaction plates stabilized the specimen under compression loads. Specimen ends were secured to the hydraulic actuators using grip plates. An extensometer was installed to differentiate bearing-induced deformation from overall specimen deformation. As shown in Fig. 4, deflection was measured between the bearing reaction plates and the specimen surface below the fastener, where the gross load is applied.

Once installed in the test apparatus, each specimen was loaded in longitudinal compression until final failure, under a constant bearing-bypass load ratio. A feedback control system provided input signals to the hydraulic actuators to induce the required deflections and maintain the required bearing-bypass load ratio (using load cell data) for each test. Actuator ramp rates were controlled such that for a given ultimate load and load ratio, three minutes were required for the specimen to reach the predicted ultimate load. Load-actuator displacement and load-extensometer deflection data were recorded at a rate of 1 reading per second.

The advantage of this bearing-bypass test system is that it permits constant bearing-bypass load ratios to be maintained throughout the test. This is especially important once bearing deformation becomes nonlinear with load; older deflection-controlled test systems tend to vary the bearing-bypass load ratio once bearing nonlinearity initiates [5]. Such capability made correlation of test results with analytical predictions much simpler.

Data Analysis

Bypass strains ε_{byp} and bearing stresses σ_{brg} at a given applied load P were calculated as follows

$$\varepsilon_{byp} = (1 - \beta)\frac{P}{w\,t\,E_{xx}} \tag{1}$$

$$\sigma_{brg} = \beta\frac{P}{dt} \tag{2}$$

where β is the bearing-bypass load ratio, w is the measured specimen width, t is the nominal laminate thickness, d is the nominal fastener diameter (6.350 mm) and E_{xx} is the laminate nominal modulus in the direction of loading. A β value of 0.0 represents the pure bypass condition (0% load transfer at the fastener) and a value of 1.0 represents the pure bearing condition (100% load transfer). No finite-width correction was used in bypass strain calculations.

In addition to obtaining failure load data, the load versus extensometer data were examined after each test. The vast majority of tests exhibited some degree of load-deflection nonlinearity, which may be indicative of subcritical damage formation. For this reason, initial nonlinearity loads were recorded for comparison with analytical predictions. The nature of the extensometer data made the application of a conventional offset criterion difficult. After examining several potential criteria, it was decided to define initial nonlinearity as the point at which the measured load for a given deflection was 5% lower than a projected load based upon the initial slope of the load-deflection curve. This definition is illustrated in Fig. 5.

Experimental Results

Failure Modes

Three primary catastrophic failure mechanisms were observed in the experiments. Zero percent load transfer open and filled hole specimens containing 6.426 mm holes failed in a net section com-

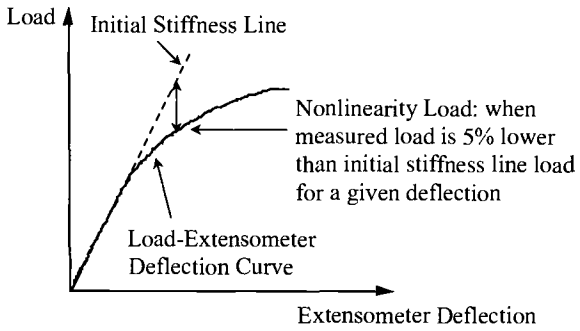


FIG. 5—*Definition of initial nonlinearity load using extensometer data.*

pression mode. This mode, shown in Fig. 6, is commonly observed in open hole compression testing, and is characterized by through-section fractures emanating from the hole at or near the location of peak bypass stress concentration. The filled hole specimens also exhibited surface bearing damage local to the bushings, which most likely was imparted after net section failure.

An offset net section compression mode, shown in Fig. 7, was observed in all other 0 to 25% load transfer filled hole specimens. First documented by Crews and Naik [*5.6*], this mode is characterized by through-section fractures emanating from the hole near the bearing-contact zones, as well as surface bearing damage local to the bushings.

The third failure mode, bearing, was observed in all of the 50% and 100% load transfer specimens. This mode, shown in Fig. 8, is characterized by extensive hole elongation and surface bearing damage local to the bushings; no through-section rupture was observed.

Load Versus Deformation Behavior

Representative load-extensometer deformation curves are shown for selected specimens in Fig. 9. Zero percent load transfer specimens exhibited little nonlinear behavior prior to final failure, although

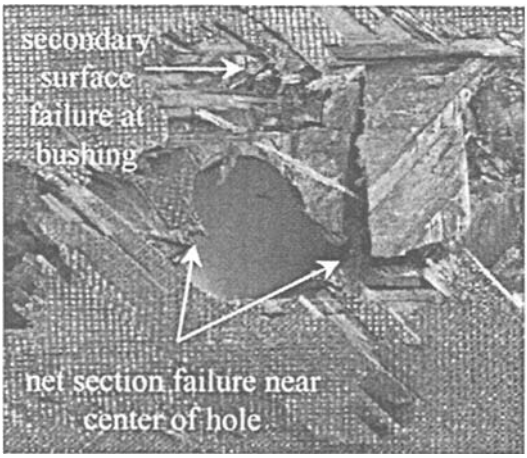


FIG. 6—*Photograph of representative net section compression failure (6.426 mm hole, 0% load transfer).*

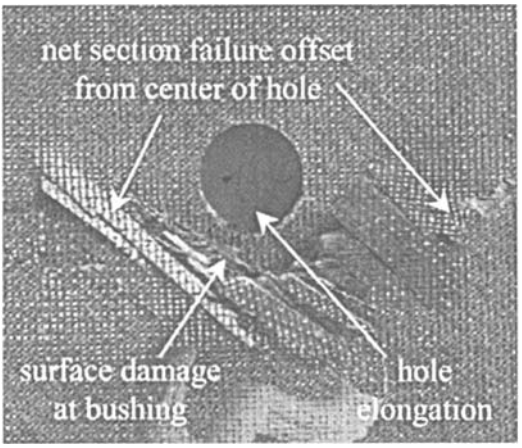


FIG. 7—*Photograph of representative offset net section compression failure (6.350 mm hole, 0% load transfer).*

some nonlinearity was observed upon the onset of loading in specimens with loose tolerance holes. As the percent load transfer increased, some slight nonlinear behavior was detected prior to final failure, indicating that catastrophic failure may have been preceded by subcritical damage formation. Extensive load-deformation nonlinearity was observed for specimens failing through bearing.

Strength Behavior

Individual bearing-bypass interaction test results are shown in Fig. 10, in which data for initial nonlinearity and final failure are plotted. A summary of mean bearing stresses and bypass strains at failure, as well as coefficients of variation, are provided in Table 3. Trend lines for the mean data are shown in Fig. 11.

A linear relationship between bearing stress and bypass strain at failure was observed for specimens loaded between 0 and 800 MPa (115 ksi) bearing stress. Similar behavior was observed for the

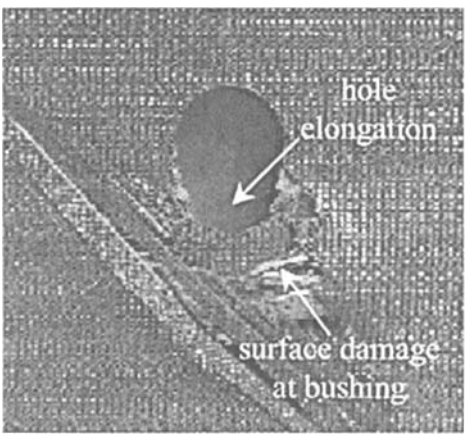
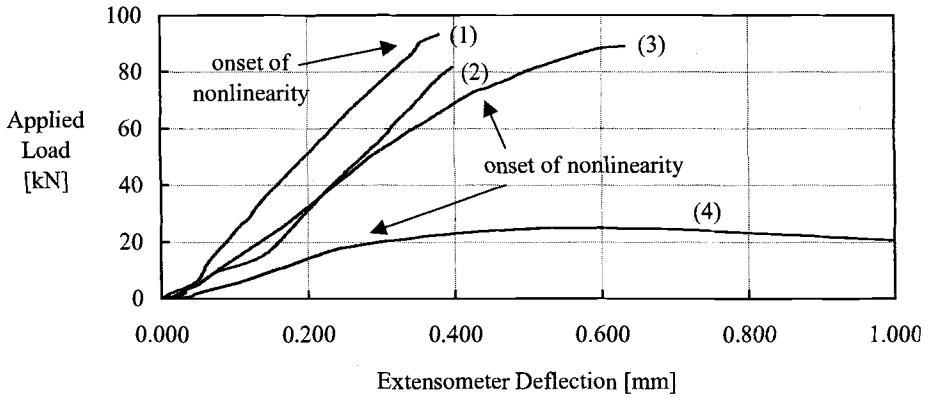


FIG. 8—*Photograph of representative bearing failure (6.426 mm hole, 100% load transfer).*

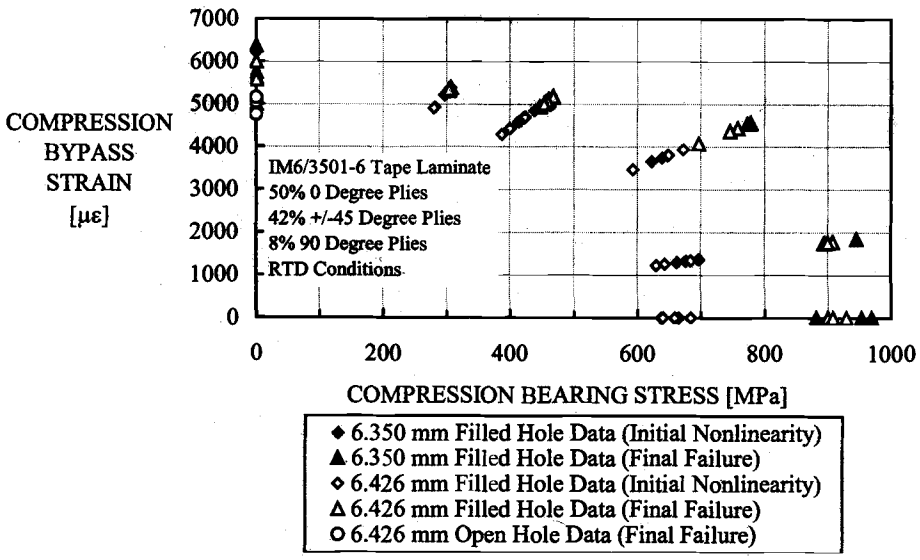


(1) 0% Load Transfer, 6.35 mm Hole, Offset Net Section Compression Failure
(2) 0% Load Transfer, 6.43 mm Hole, Net Section Compression Failure
(3) 25% Load Transfer, 6.35 mm Hole, Offset Net Section Compression Failure
(4) 100% Load Transfer, 6.35 mm Hole, Bearing Failure

FIG. 9—*Representative load versus extensometer deflection data plots.*

initial nonlinearity data in this range. These specimens, ranging between 0 and 25% load transfer at the fastener, generally failed through offset net section compression.

Specimens failing in the bearing mode (50 to 100% load transfer) exhibited much lower bypass strains for a given bearing stress level. The bearing-bypass interaction relationship for failure appears somewhat nonlinear in this range. Such behavior is in agreement with predictions reported by Crews and Naik [*5,6*] and Chang [*10*], and results from a variance in bearing contact area as bypass loading



◆ 6.350 mm Filled Hole Data (Initial Nonlinearity)
▲ 6.350 mm Filled Hole Data (Final Failure)
◇ 6.426 mm Filled Hole Data (Initial Nonlinearity)
△ 6.426 mm Filled Hole Data (Final Failure)
○ 6.426 mm Open Hole Data (Final Failure)

FIG. 10—*Compression bearing-bypass interaction test data.*

TABLE 3—*Summary of experimental strength results.*

Specimen Type	Nominal Hole Diameter	Bearing-Bypass Load Ratio (%)	Mean Compression Bearing Stress at Failure	Mean Comp. Bypass Strain at Failure ($\mu\varepsilon$)	Coefficient of Variation* (%)
Filled hole	6.350 mm (0.250 in.)	0	0 MPa (0.0 ksi)	5916	6.68
		10	304 MPa (44.1 ksi)	5342	0.70
		15	454 MPa (65.9 ksi)	5027	1.59
		25	777 MPa (113 ksi)	4550	0.35
		50	916 MPa (133 ksi)	1791	2.86
		100	934 MPa (136 ksi)	0	5.01
Filled hole	6.426 mm (0.253 in.)	0	0 MPa (0.0 ksi)	5524	8.96
		10	304 MPa (44.0 ksi)	5337	0.08
		15	459 MPa (66.6 ksi)	5081	1.62
		25	734 MPa (106 ksi)	4294	4.49
		50	901 MPa (131 ksi)	1759	0.82
		100	912 MPa (132 ksi)	0	1.64
Open hole	6.426 mm (0.253 in.)	0	0 MPa (0 ksi)	4986	4.10

* Maximum of bearing and bypass coefficients of variation.

is introduced. Conversely, bearing stresses at initial load-deflection nonlinearity were consistently in the 600 to 700 MPa (85 to 100 ksi) range, and were nearly invariant with applied bypass strain.

Failure data for specimens containing 6.350 and 6.426 mm holes are compared in Table 4. It is shown that bearing-bypass strengths did not vary drastically with initial hole diameter. The greatest variance in performance was observed in the pure bypass case (0% load transfer), in which the mean failure strain of specimens with 6.426 mm holes was 93% of that obtained for specimens with 6.350 mm holes. It is notable that this was the one load case in which different failure modes were observed

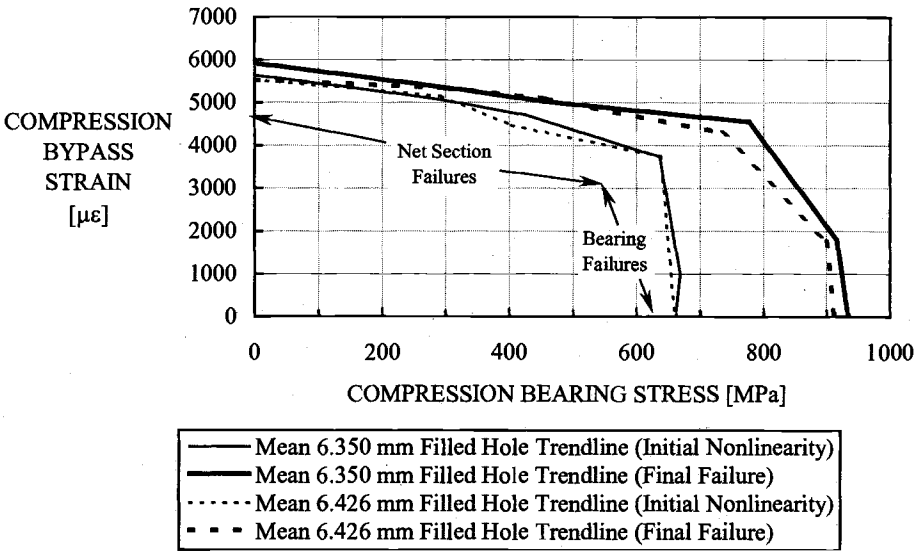


FIG. 11—*Mean failure trendlines for specimens of varying hole diameter.*

TABLE 4—*Examination of hole clearance effects upon mean joint strength.*

Bearing-Bypass Load Ratio (%)	Strength with 6.426 mm holes/ Strength with 6.350 mm holes	6.350 mm Bypass Strain at Failure/Open Hole Failre Strain	6.426 mm Bypass Strain at Failure/Open Hole Failure Strain
0	0.93	1.19	1.11
10	1.00	1.07	1.07
15	1.01	1.01	1.02
25	0.94	0.91	0.86
50	0.98	0.36	0.35
100	0.98	0.00	0.00

for specimens with different initial hole diameters. Strength variances due to initial clearance were typically less than 3% at other bearing-bypass load ratios.

Table 4 also compares mean bypass strains at failure to the mean open hole strain; these results are illustrated graphically in Fig. 12. Bolted joint bypass strains at failure were greater than or equal to the open hole compression failure strain between 0 and 500 MPa (70 ksi) applied bearing stress. Thus, joints with 0 to 15% load transfer were found to have bypass failure strains in excess of the open hole "cutoff" strain.

These results verify that the presence of a fastener in a Class 1 hole increases the pure compression bypass failure strain due to hole-filling and relief of the bypass stress concentration. Decreasing the initial clearance decreases the strain level at which dual-sided fastener-hole contact initiates, causing greater relief of the stress concentration at elevated strain levels. This subsequently increases the far-field failure strain and changes the failure mode to offset net section compression. Application of bearing stresses also changes the failure mode to offset net section compression, and diminishes the relative effect of initial clearance upon strength.

An additional finding of note is that total (gross) applied specimen loads at failure did not vary substantially until the applied bearing stress exceeded 800 MPa (115 ksi). This indicates that slight inaccuracies and variances in load transfer calculations should not significantly affect the total load-carrying capability of joints under compression bypass-dominated loading.

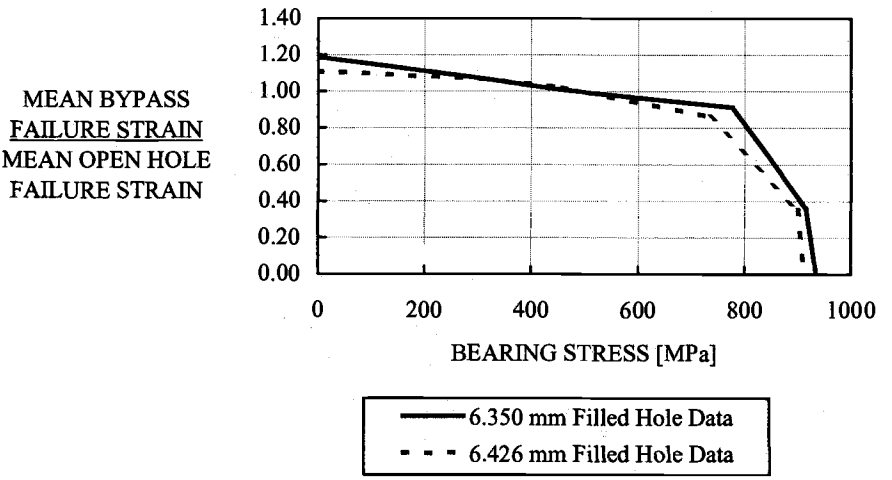


FIG. 12—*Comparison of filled hole bypass failure strains to open hole failure strain.*

Analytical Approach

The analysis methods and failure prediction methodologies used in this investigation are an extension of those used previously by the authors in developing a semi-empirical predictive capability for open and filled hole compression failure. The usefulness of similar finite-element models and progressive damage analysis of composite joints has been demonstrated by Crews and Naik [*5.6*] and Chang [*10*]. An extensive description of the methods used is provided in Ref *11*; only key assumptions, methods, and calibration results are provided herein.

The finite-element code used in this investigation was Samtech's SAMCEF-BOLT package [*12*], which consists of an automated finite-element mesher, a failure model, and material property degradation rules for progressive failure analysis. The finite-element model consists of a plate containing a hole, and a rigid, frictionless pin in the hole. The mesh is composed of 2-D isoparametric quadrilateral membrane elements. The analysis assumes that no through-thickness clamping pressure is applied, and does not account for stacking sequence effects. A key feature of the code is the ability to define the initial pin clearance by inputting separate hole and pin diameters. Contact is modeled using an iterative process, which restrains nodes encroaching within the pin boundary and releases restrained nodes found to have positive contact reactions. Typical stress field predictions are illustrated in Fig. 13.

Ply-level failure was assumed to occur when the following expression was satisfied:

$$F_1\sigma_{11} + F_{11}\sigma_{11}^2 + F_{66}\tau_{12}^2 = 1 \tag{3}$$

where σ_{11} and τ_{12} are in-plane extensional and shear stresses and F_1, F_{11}, and F_{66} are strength parameters based upon lamina tension, compression and shear strengths. This is a modified version of

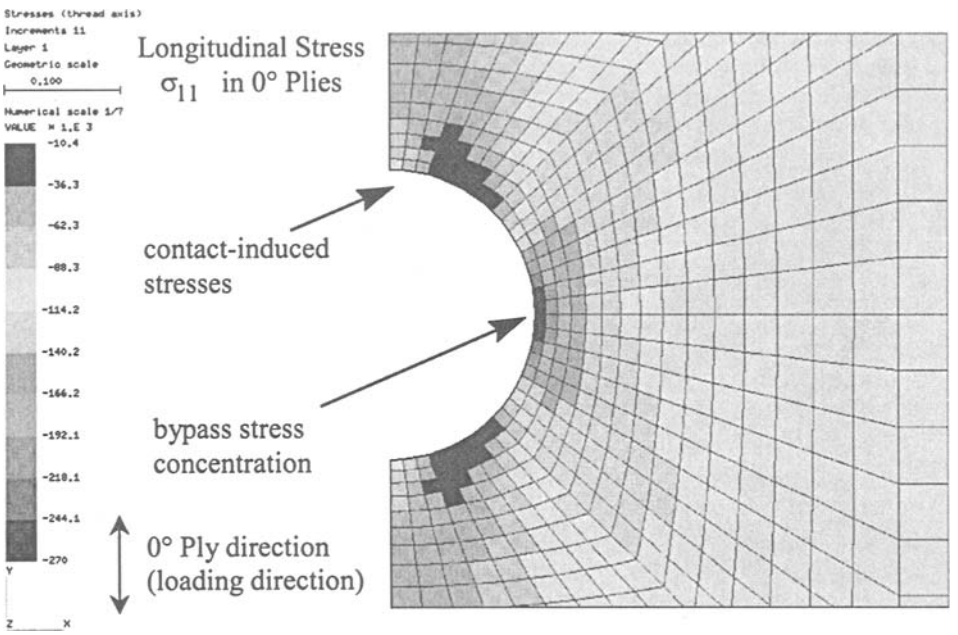


FIG. 13—*Typical stress distribution prediction (6.426 mm hole, 386 MPa, 0% load transfer), demonstrating onset of contact-induced bearing stresses.*

TABLE 5—*IM6/3501-6 tape lamina properties used in finite-element analysis.*

Stiffness or Geometric Property	Value	Strength Property	Value
E_{11}	145 MPa (21.0 msi)	σ_{1T}	2240 MPa (325 ksi)
E_{22}	9.7 MPa (1.4 msi)	σ_{1C}	2230 MPa (323 ksi) (calibrated analysis)
G_{12}	5.5 MPa (0.58 msi)	σ_{2T}	33 MPa (4.79 ksi)
ν_{12}	0.34	σ_{2C}	207 MPa (30 ksi)
t_{ply}	0.188 mm (0.0074 in.)	τ_{12}	100 MPa (14.5 ksi)

the Tsai-Wu ply-level quadratic failure criterion [*13*], which provides more representative interaction envelopes in the compression regime. The criterion is applied on an element-by-element basis, with average element stresses used in the expression. Lamina properties used in the analysis are provided in Table 5.

Progressive damage of a fiber-matrix element assembly was modeled by assuming the matrix fails first through shear while the fibers retain their load carrying capability. Total element failure occurs when the fibers subsequently break. Element stiffness properties were modified after matrix shear failure using a constant stress model.

As described in Ref *11*, the failure prediction methodology is based upon a semi-empirical calibration of ply-level longitudinal compression and shear strengths, the element length local to the hole, and far-field open hole compression strength. The ply-level longitudinal compression strength σ_{1C} used in the calibration varies when the element length is changed.

Using the open hole compression test results reported herein, the best compromise between predictive accuracy and computational efficiency was obtained when σ_{1C} = 2230 MPa (323 ksi) and a 0.179 mm (0.0076 in.) element length were used in the analysis. These values were used in subsequent analyses. Models using larger elements (lower mesh densities) were found to be less accurate in predicting notched compression strength trends as a function of laminate configuration. Denser meshes required longer computation time, yet provided no significant improvement in predictive accuracy.

Analytical-Experimental Correlation

Comparisons of bearing-bypass failure data with predictions for initial matrix and fiber failures are shown in Fig. 14. The predictions shown are for failure of specimens with 6.426 mm holes. Predictions for specimens with 6.350 mm holes are not shown, due to known analytical inaccuracies discussed in Ref *11*. Previous work by the authors found that the use of a rigid bolt in the analysis results in an overly stiff load path through the fastener once dual-sided contact initiates. This results in unconservative net section strength predictions for specimens with small initial clearance (tight tolerance holes). Net section strength predictions for specimens with 6.426 mm holes were found acceptable in Ref *11*, since dual-sided contact occurs at higher strain levels, and the resulting contribution to stress concentration relief is relatively small.

Two failure modes were predicted for specimens with 6.426 mm holes. From 0 to 350 MPa applied bearing stress at failure (corresponding to 0 to 10% load transfer), net section compression failure with dual-sided fastener-hole contact was predicted. Net section compression failure was also predicted from 350 to 500 MPa bearing stress (10 to 15% load transfer), but with single-sided fastener-hole contact. Bypass failure strains were predicted to increase in this range, since the bearing stresses relieve the bypass stress concentration in this situation. Above 500 MPa bearing stress (15 to 100% load transfer), bearing failure was predicted.

Predictions for initial fiber failure correspond reasonably well with the test data for pure bypass

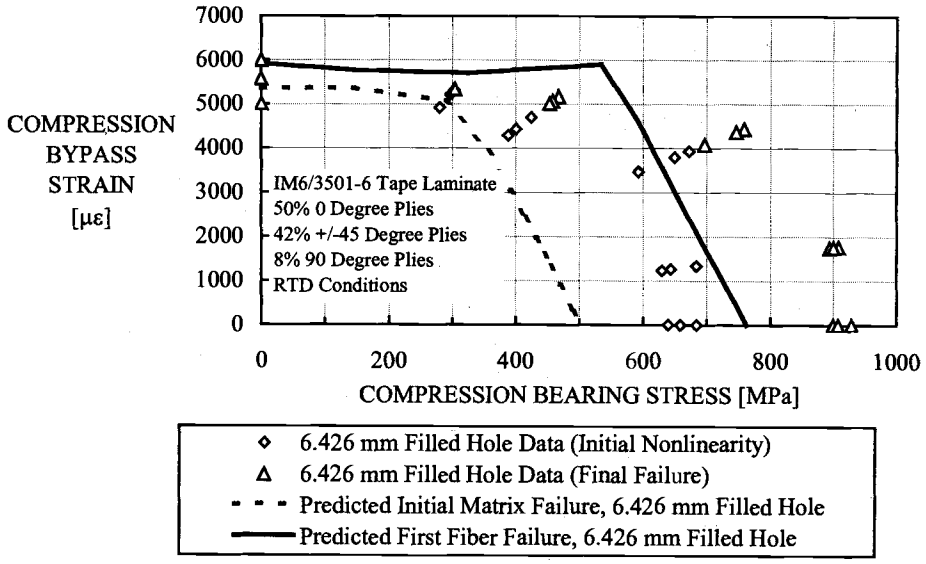


FIG. 14—*Comparison of failure predictions with bearing-bypass test data.*

failure, in which net section compression failures were observed for the 6.426 mm hole specimens. Predictions in the 100 to 500 MPa applied bearing stress range were less accurate, although the predicted bearing-bypass trend line is not that different from experimental behavior. The inaccuracy most likely results from the observed change in failure mode. It is also noteworthy that the slope of the failure data does not vary significantly in this range. This indicates that offset net section compression failure is consistently induced prior to the predicted change from dual-sided to single-sided fastener-hole contact.

Initial matrix and fiber failure predictions above 500 MPa were conservative relative to the bearing failure data. This is reasonable if bearing damage is not catastrophic, i.e., if progressive matrix and fiber damage occurs prior to attaining the failure stress. The transition from net section to bearing-dominated failures occurred at higher bearing stress levels than was predicted.

Examination of predicted stress and failure mode data indicated that a stronger interaction between longitudinal compression and shear stresses is required to predict initial failure at the offset location. The authors have observed this trend in another failure investigation [*9*], and believe the subject warrants additional research.

Conclusions

The investigation discussed herein resulted in an improved understanding of failure modes and strength properties observed in composite bolted joints loaded in compression. Three primary failure modes (net section compression, offset net section compression, and bearing) were observed. For low-load transfer joints, bypass failure strains were found to decrease linearly as bearing stresses were increased. The transition from net section to bearing-dominated failure was observed to occur above 800 MPa (115 ksi).

Relatively little variance in failure mode and strength were observed for specimens containing holes spanning the tolerance range used in primary structures (Class 1). The greatest variance in mean strength of this sort (7%) was observed for the pure bypass condition, and was associated with a change in failure mode. Analytical work demonstrated that fastener elasticity modeling and an im-

proved compression-shear failure criterion are necessary for accurate strength prediction of compression-loaded joints.

In regard to the allowables development process, it was demonstrated that joints loaded between 0 to 500 MPa (0 to 70 ksi) applied bearing stress may attain a performance enhancement by designing to filled hole-based failure strains, rather than to an open hole-based "cutoff" strain. Slight inaccuracies and variances in load transfer calculations should not significantly affect the total load-carrying capability of joints under compression bypass-dominated loading.

It should be noted that these conclusions are specific to the IM6/3501-6 tape material and the particular layup tested. Additional work is required to demonstrate the applicability of these conclusions to other materials and layups.

Future Work

Experiments examining the effects of material form (tape, fabric and hybrids), laminate stiffness, fastener countersink and environment upon failure mode and strength will be conducted to develop improved allowables criteria for compression-loaded bolted joints. Analytically, the influence of bolt elasticity upon load share, stress distributions about a filled hole, and failure predictions will be examined. An improved compression-shear failure criterion will be developed to permit accurate strength prediction of offset net section failures.

Acknowledgments

Technical tasks described in this paper include tasks supported with shared funding by the U.S. rotorcraft industry and Government under the RITA/NASA Cooperative Agreement No. NCCW-0076, Advanced Rotorcraft Technology, Aug. 15, 1995, under WBS No. 98-7.1.6(2) for Composite Life/Certification/Qualification. The efforts of R. Thompson of Boeing Commercial Airplane Group's Structural Materials Laboratory in conducting the bearing-bypass experiments were commendable and invaluable to this project. The contributions of Integrated Technologies Corporation in preparing the test specimens are also greatly appreciated. The authors also acknowledge Samtech S. A. for the development of the SAMCEF-BOLT code.

References

[1] MIL-HDBK-17-1E, *Polymer Matrix Composites, Volume 1—Guidelines for Characterization of Structural Materials*, Chapter 7, Feb. 1994, pp. 3–45.

[2] Ramkumar, R., "Bolted Joint Design, Test Methods and Design Analysis for Fibrous Composites," *ASTM STP 734*, 1981, pp. 376–395.

[3] Garbo, S., "Effects of Bearing/Bypass Load Interaction on Laminate Strength," AFWAL-TR-81-3114, Air Force Wright Aeronautical Laboratories, Sept. 1981.

[4] Grimes, G., et al., "Tape Composite Material Allowables Application in Airframe Design/Analysis," *Composites Engineering*, Vol. 3, Nos. 7–8, 1983, pp. 777–804.

[5] Crews, J. and Naik, R., "Effects of Bolt-Hole Contact on Bearing-Bypass Damage-Onset Strength," *Proceedings of the First NASA Advanced Composites Technology Conference*, Seattle, WA, Nov. 1990.

[6] Naik, R. and Crews, J., "Ply Level Failure Analysis of Graphite/Epoxy Laminates under Bearing-Bypass Loading," *ASTM STP 1059*, 1990, pp. 191–211.

[7] Grant, P. and Sawicki, A., "Relationship Between Failure Criteria, Allowables Development, and Qualification of Composite Structure," *Proceedings of the American Helicopter Society National Technical Specialist's Meeting on Rotorcraft Structures*, Williamsburg, VA, Oct. 1995.

[8] Sawicki, A., Grant, P., and Mabson, G., "Mechanical Assembly of Commercial Transport Fuselage Utilizing Tow-Placed and Textile Composites," *Proceedings of the 35th AIAA Structures, Structural Dynamics and Materials Conference*, Hilton Head, SC, April 1994.

[9] Sawicki, A. and Minguet, P., "The Effect of Intraply Overlaps and Gaps upon the Compression Strength of Composite Laminates," *Proceedings of the 39th AIAA Structures, Structural Dynamics and Materials Conference*, Long Beach, CA, April 1998.

[10] Hung, C. L. and Chang, F. K., "Strength Envelope of Bolted Composite Joints under Bypass Loads," *Journal of Composite Materials*, Vol. 30, No. 13, 1996, pp. 1402–1435.

[11] Sawicki, A. and Minguet, P., "Failure Mechanisms in Compression-Loaded Composite Laminates Containing Open and Filled Holes," *Proceedings of the American Society for Composites 13th Annual Technical Conference*, Baltimore, MD, Sept. 1998.

[12] Defourny, M. and Marechal, E., *Analyzing Composite Bolted Joints using SAMCEF-BOLT*, copyright © 1996 SAMTECH S. A., Liege, Belgium.

[13] Tsai, S. and Wu, E., "A General Theory of Strength for Anisotropic Materials," *Journal of Composite Materials*, Vol. 5, 1971, pp. 58–80.

Test Methods

Roderick H. Martin[1] *and Carl Q. Rousseau*[2]

Characterizing Delamination Growth in a 0°/45° Interface

REFERENCE: Martin, R. H. and Rousseau, C. Q., **"Characterizing Delamination Growth in a 0°/45° Interface,"** *Composite Structures: Theory and Practice, ASTM STP 1383,* P. Grant and C. Q. Rousseau, Eds., American Society for Testing and Materials, West Conshohocken, PA, 2000, pp. 311–323.

ABSTRACT: Structural configurations in helicopter rotor systems often contain plies of 0° and 45° to resist centrifugal and torsional loads. Delaminations in test specimens that are tested to failure often experience delaminations between a 0°/45° ply interface. However, the standard methods to characterize delamination utilize a unidirectional 0° specimen. The reasons for using a unidirectional layup are that multidirectional beams suffer from ply cracks in the nonzero plies, increased anticlastic bending and other effects. This work investigated the issues for testing a nonunidirectional double cantilever beam (DCB) specimen with a delamination in a 0°/45° interface. Several criteria were developed to minimize the effects noted above. These included reduction of bend twist coupling and residual thermal stresses, prevention of nonzero ply breakage, and minimized anticlastic bending. The resulting layup consisted of a 64-ply laminate of 0°, 45°, and −45° plies. Quasi-static and fatigue tests were conducted on unidirectional layups and the new configuration fabricated from S2/E773 glass/epoxy. For both the static and fatigue tests the delamination grew and remained in the 0°/45° interface for a significant portion of delamination growth. Crack branching was noted in some specimens as the delamination length became longer. The interlaminar fracture toughness, G_{Ic}, of the 0°/45° DCBs had more scatter and a 10% lower mean than the 0° DCB specimens. Both specimens experienced fiber bridging shown by an increase in G_{Ic} with delamination growth and observation of the delaminated surfaces. The influence of the fiber bridging was similar in the two specimen configurations. The fatigue delamination onset curves of the two specimen configurations were coincidentally not showing the scatter or lower values seen in the static tests. The static and fatigue results indicate that the use of 0° specimens for characterizing delamination in a 0°/45° interface is satisfactory for the materials tested in this work. However, the presence of fiber bridging in the 0°/45° specimens indicates that using the initiation value for predicting delamination growth may be overly conservative when fiber bridging is present. The same fiber bridging has also been observed in failure surfaces on structural components tested to failure. While the inclusion of fiber bridging in delamination growth predictive models is possible, further work should be conducted on the parameters that affect fiber bridging, such as thickness, processing and crack opening, to ensure that the properties from a DCB specimen are representative of that in the structures. Work on other material systems, other delamination modes and fatigue crack growth is also recommended.

KEYWORDS: delamination onset, double cantilever beam, fatigue, fiber bridging, interface, interlaminar fracture toughness, multidirectional

Nomenclature

- a Delamination length
- AS Antisymmetric layup
- b Width
- B_{ij} Coupling stiffnes matrix coefficients
- D_{ij} Bending and twisting stiffness matrix coefficients
- D_c Anticlastic bending parameter

[1] CEO and Head, Advanced Composites, Materials Engineering Research Laboratory Ltd., Hertford, UK.
[2] Conference chairman, Bell Helicopter Textron Inc., Fort Worth, TX 76101.

Copyright© 2001by ASTM International www.astm.org

E Young's modulus
G Strain energy release rate
G_{Ic}^{NL} Mode I interlaminar fracture toughness calculated at nonlinear point
$G_{Ic}^{5\%}$ Mode I interlaminar fracture toughness calculated at nonlinear point
G_{Imax} Maximum cyclic strain energy release rate
I Second moment of area
$N_{onset}^{5\%}$ Cycles to give a 5% increase in compliance
t Ply thickness
Δ Delamination length correction factor
σ_2 Transverse stress
σ_{2u} Transverse strength

The current standard test methods for characterizing interlaminar fracture toughness, e.g., ASTM Standard Test Method for Mode I Interlaminar Fracture Toughness of Unidirectional Fiber-Reinforced Polymer Matrix Composites (D 5528-94a) and ASTM Standard Test Method for Mode I Fatigue Delamination Growth Onset of Unidirectional Fiber-Reinforced Polymer Matrix Composites (D 6115-97), require the beams to be unidirectional. Most delaminations in structures occur between plies of a dissimilar orientation. In some instances, it is the different orientation that can initiate delaminations such as free edge delamination. However, the standard beams are unidirectional for several reasons, including:

- The unidirectional plies do not fail in plane during bending.
- The anticlastic beam bending effects are minimized.
- The residual thermal stresses do not cause a nonuniform energy release rate value along the delamination front.
- There are no off-axis plies to crack, causing the delamination to move from the centerline and invalidating the test.

When the layup of a DCB is non-unidirectional, a complex fracture behavior of crack jumping and fiber bridging may result. If this behavior is a function of the test rather than an intrinsic material property, clearly a test that does not experience this behavior is required. The unidirectional beam does not represent a typical structural layup, but it does not experience the above listed artifacts of a non-unidirectional beam. It is also generally thought to give a conservative value of G_{Ic}. Researchers, described below, have attempted to design a non-unidirectional DCB specimen to determine the interlaminar toughness values in more structural type layups. However, many of these works, as described below, have focused on angled ply layups or have concentrated on the realistic nature of the beams rather than the interface of interest. In dynamic components on rotorcraft, the layups are generally 0° and 45°, dominated to resist bending, twisting and centrifugal loads. Hence, one of the most likely delamination locations is at a 0°/45° interface. The purpose of this work is to design a DCB specimen that concentrates on the interlaminar toughness between such an interface under static and fatigue loads by minimizing the issues stated above. As a starting point, the key work in the literature was reviewed.

Previous Work on Non-Unidirectional DCBs

References dating back to 1982 were found on the subject of non-unidirectional DCBs, indicating its importance. However, only recent references (work over the past five years) reflect the developments in the understanding of the DCB test that is reflected in the included ASTM standards. Many of these references investigated delaminations between $\pm\theta$ plies [*1–3*]. The opposing arms of the DCB were kept similar by making each of them symmetric or antisymmetric and balanced. In all cases the cracks did not remain in the mid-plane of the specimen. It would branch along a matrix crack

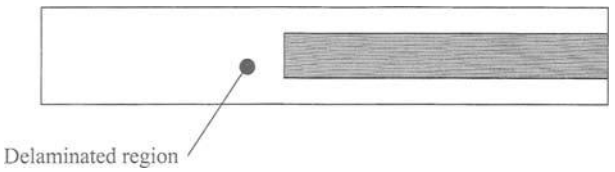


FIG. 1—*Plan view of DCB specimen with edge delamination.*

into another ply interface, resulting in significant fiber bridging. In one work [*4*], delamination between a 0°/45°, 0°/0° and other interfaces were investigated. This effort concluded that prior to the crack branching there was an area of consistent interlaminar growth from which G_{Ic} could be determined. The author concluded that G_{Ic} was similar for these layups. However, this work used a razor blade to initiate the delaminations and for the 0°/45° example, the delamination did not initiate at the mid-plane.

To overcome crack branching and fiber bridging, an edge delaminated DCB was developed [*5*], Fig. 1. The edge delamination was formed by using a Teflon™ (trifluoroethylene) insert that prevented the fibers from being pulled out at the edge of the specimen. The delamination was at 45/45 or 45/−45 interfaces and the individual arms of the DCB were balanced and antisymmetric. Although the edge delamination prevented the crack branching and fiber bridging for the carbon/epoxy (XAS/913) [*5*], it did not work for a T800/924 system [*6*]. In this latter work, delaminations between 0/30 and 0°/45° interfaces were investigated using the edge delaminated specimen. The reason that the edge delamination specimen did not work for the latter case was thought to be caused by the high transverse tensile stresses in the outer $\theta°$ plies. This was confirmed by the same specimen designs showing no signs of crack branching under mixed-mode loads where the transverse tensile stresses were reduced. Although the edge delaminated DCB specimen offers a means to evaluate delaminations between plies of different orientation, the practicality of accurately laying up each DCB specimens with symmetrically spaced edge inserts renders this specimen design unlikely to become part of a standard method.

Apart from the major problems of crack branching, additional problems include the nonuniform strain energy release rate, G, distribution along the delamination front caused by anticlastic bending. This can be further complicated by laminates that have large bend-twist coupling terms, D_{16}, further affecting the G distribution [*7,8*]. Five criteria were established for designing non-unidirectional DCBs to minimize these effects [*7*]. These are listed in Table 1 as 1–5. To meet Criterion 2, aluminum bars were adhesively bonded onto the backs of the composite layups in Ref *8*. Although this achieved Criterion 2, the complexities and potential problems of reinforcement bars becoming disbonded, as reported in Ref *8*, does not warrant this method being developed as the approach for this work.

TABLE 1—*Criteria for nonunidirectional DCB design* [7].

1	Delamination growth should initiate at the mid-plane between the ply pair of interest.
2	Values of D_{16} and D_{26} of the full and half thickness beams are at least three orders of magnitude less than the remaining flexural rigidities D_{11}, D_{22}, D_{12}, and D_{66} to prevent twisting.
3	The half-thickness beams were individually symmetric to prevent bend twist coupling.
4	The full thickness beams were either symmetric or antisymmetric to prevent warping from residual thermal stresses.
5	Within the limitations of the above constraints, the D_c ratio $D_c = \frac{D_{12}^2}{D_{11}D_{22}}$ of the cracked regions are minimized $D_c < 0.25$ to reduce anticlastic bending effects.

Specimen Design

Ply Layup Considerations

To prevent crack branching, the 45° ply at the interface should not experience transverse matrix cracking. The design of the specimen should be such that the transverse stress, σ_2, should be below the transverse strength, σ_{2u}, of the composite. However, this cannot be guaranteed because of the complex nature of the stresses at the crack tip. In this work the primary interest is for a delamination between a 0° and 45° ply. Thus, it is not possible to achieve Criterion 4 in Table 1 for the uncracked region. This criterion is included to allow the residual thermal stresses to be ignored. Hence, the effect of thermal stresses on the chosen laminate design should be minimized in place of Criterion 4 and the uncracked region should not warp. Further, because the upper and lower beams will be of a different layup, the total beam will be nonsymmetrical. To ensure a Mode I delamination, the bending stiffnesses of each beam should be similar. Thus, further criteria (6–8) are also required, Table 2.

If the beams are kept 0° dominant, Criteria 6 and 7 may be better met. To meet Criterion 2 and 8, the half laminates must have a layup of the form [X/−X] where X is a balanced symmetric layup and −X is identical to X except that each 45° ply is replaced with a −45° ply and vice versa. To meet Criterion 8, the D_{11}^{-1} values (the flexural rigidity) for both beams should be similar. Hence, the layups of individual beams should be largely similar in terms of the proportions of 0° and 45° plies.

Anticlastic curvature in the DCB specimen causes the values of G to be highest at the center of the specimen and lowest at the edge resulting in a curved delamination front [7]. The D_c ratio defined in Table 1 provides a measure of the maximum and minimum G value along the delamination front. The larger the value of D_c, the greater the nonuniformity in the G distribution across the delamination front and the greater the crack curvature. A limiting value of $D_c < 0.25$ was suggested in Ref 7. This value was used as a guide in Criterion 5. To minimize the effects of anticlastic curvature, the use of 90° plies within the laminate may prove beneficial and was investigated.

To determine if the outer 45° plies at or near the interface of the beam will crack, classical lamination theory was used with the maximum load that would be applied to the DCB specimen. The load was approximated from the beam theory expression for G, Eq 1, and the assumption that G_{Ic} was 430J/m^2. This value was arbitrarily three times the value from an all 0° DCB, as given in the Results section.

$$P = \sqrt{\frac{G_{Ic} E b^2 t^3}{12 a^2}} \tag{1}$$

Criterion 7 was evaluated by investigating the ratio of σ_2/σ_{2u} (transverse stress to transverse strength ratio) stress to cause matrix cracking in the outermost 45° ply.

Based on the above discussion and using the material properties in Table 3, the evaluation of different layups with respect to the various criterion are given in Table 4. The "AS" subscript in Table 4 indicates "antisymmetric," as discussed above. The top layup is one-half of the beam and the bot-

TABLE 2—*Additional design criteria.*

6	The residual thermal stresses from a beam that is not symmetric about its mid-plane should be minimized (replaces criterion 4) and the full thickness beam should not warp.
7	Loading of the 45° play at the delamination should not be sufficient to cause cracking from membrane stresses.
8	The bending stiffnesses of the upper and lower beam should be similar.

TABLE 3—*S2/E773 material properties supplied by BHTI.*

Property	E_{11} (GPa) (Msi)	E_{22} (GPa) (Msi)	G_{12} (GPa) (Msi)	ν_{12}	σ_{1u} (MPa) (psi)	σ_{2u} (MPa) (psi)	t (mm) (in.)
Value	47.92 6.95	15.72 2.28	4.51 0.654	0.34	2 206 263 000	34.5 7000	0.236 0.0093

tom layup is the other half. An example layup is

Layup notation	Full layup for DCB (// denotes delamination location)
$[-45/45/0_4/45/-45]_{AS}$	$[-45/45/0_4/45/-45/45/-45/0_4/-45/45//$
$[0/-45/45/0_2/45/-45/0]_{AS}$	$0/-45/45/0_2/45/-45/0/0/45/-45/0_2-45/45/0]$

For the DCB specimen it does not matter which is the upper or lower beam in the experimental work. Layups 1 and 2 illustrate the effects of increasing the number of 0° plies within the beam. Layup 3 investigates the effect of additional 90° plies on reducing effects such as anticlastic bending. Layups 4, 5, and 7 investigate the effect of adding further 0° plies away from the neutral axis of the individual beams. Layup 6 investigates the effect of adding 90° plies to these layups. Each criteria is evaluated as pass or fail (√ or x, respectively). Where a numerical value is available, it is given for comparison. The results for each criterion are given below.

Criterion 1—All of the layups chosen have the delamination at the mid-plane and hence all meet Criterion 1.

Criterion 2—By meeting Criterion 3, that the individual arms or half thickness laminates are all balanced and antisymmetric, D_{16} and D_{26} are zero and all layups also meet Criterion 2.

TABLE 4—*Suggested layups and criteria matches.*

	Layup	Criteria							
		1	2	3	4	5 (D_c)	6	7 (σ_2/σ_{2u})	8 $D_{11}^{Bot}/D_{11}^{Top}$
1	$[-45/45/0_4/45/-45]_{AS}$	√	√	√	×	× (0.17)	√	√ (0.34)	√ (0.92)
	$[0/-45/45/0_2/45/-45/0]_{AS}$	√	√	√	×	√ (0.13)	√	√ (0.32)	
2	$[-45/45/0_6/45/-45]_{AS}$	√	√	√	×	√ (0.14)	√	√ (0.35)	√ (0.94)
	$[0/-45/45/0_4/45/-45/0]_{AS}$	√	√	√	×	√ (0.12)	√	√ (0.30)	
3	$[-45/45/0_2/90_2/0_2/45/-45]_{AS}$	√	√	√	×	√ (0.13)	√	√ (0.44)*	√ (0.94)
	$[0/-45/45/0/90_2/0°/45°/-45/0]_{AS}$	√	√	√	×	√ (0.11)	√	√ (0.38)*	
4	$[-45/0°/45°/0_4/45/0/-45]_{AS}$	√	√	√	×	√ (0.13)	√	√ (0.34)	√ (0.97)
	$[0/-45/45/0_4/45/-45/0]_{AS}$	√	√	√	×	√ (0.12)	√	√ (0.30)	
5	$[-45/0_3/45_2/0_3/-45]_{AS}$	√	√	√	×	√ (0.12)	√	√ (0.34)	√ (0.97)
	$[0/-45/0_2/45_2/0_2/-45/0]_{AS}$	√	√	√	×	√ (0.11)	√	√ (0.30)	
6	$[-45/0_2/90°/45°_2/90/0_2/-45]_{AS}$	√	√	√	×	√ (0.10)	√	√ (0.37)*	√ (0.96)
	$[0/-45/0_2/45_2/0_2/-45/0]_{AS}$	√	√	√	×	√ (0.11)	√	√ (0.43)*	
7	$[-45/0_4/45/0_4/45/0_4/-45]_{AS}$	√	√	√	×	√ (0.08)	√	√ (0.27)	√ (0.99)
	$[0/-45/0_3/45/0_4/45/0_3/-45/0]_{AS}$	√	√	√	×	√ (0.08)	√	√ (0.25)	

Criterion 3—See Criterion 2.

Criterion 4—None of the layups can meet this criterion if they are to meet Criterion 1 and result in a delamination between a 0° and 45° ply, see Criterion 6.

Criterion 5—The values of D_c for all the layups are given in Table 4. In layup 2, more 0° plies have been used, thus reducing the 3-D effects of the 45° plies and reducing D_c. In layup 3, the use of 90° plies further reduces the 3-D effects by increasing the across width bending stiffness. However, this reduces the bending rigidity, see Criterion 7. The same reduction in 3-D effects may be achieved without 90° plies, by bringing the 45° plies towards the neutral axis of the upper and lower beams as seen in layups 4 and 5. In layup 6, again the use of 90° plies reduces the edge effects, but at the expense of the bending rigidity and Criterion 7. By further increasing the number of 0° plies (e.g., layup 5 to 7) the value of D_c is further reduced.

Criterion 6—By ensuring that the individual arms are balanced and symmetric, the residual thermal stresses do not affect the energy release rate in all of the layups. Although the resulting full thickness laminate is unsymmetric it should not warp because $[B_{ij}] = D_{16} = D_{26} = 0$. Therefore, all layups meet this criterion.

Criterion 7—The ratio of σ_2/σ_{2u} is shown in Table 4 for the upper and lower beams for each layup. The values of σ_2 were calculated from lamination theory with a moment applied to the laminate. The value of σ_2 quoted in Table 4 is for the uppermost tension loaded 45° ply. For the half beam with a 0° ply at the interface, the ratio is reported one ply in. For all cases the ratio is less than unity indicating that cracking in the 45° ply should not occur from membrane stresses. However, this analysis does not account for the interlaminar edge stresses nor the complex stresses at the crack tip. For layups 3 and 6 marked with an asterisk, the ratio of σ_2/σ_{2u} in the 90° ply was 0.86 and 0.91 in the upper beam. These values would indicate that cracking in the 90° plies is likely. Hence, the advantage of reducing D_c in Criterion 5 is outweighed by the possibility of 90° ply failure. By further increasing the flexural rigidity with 0° plies in layup 7, the likelihood of cracking in the outer plies is further reduced.

Criterion 8—The ratio of the D_{11} values for the upper and lower beams gives an indication of the bending stiffness of the beams or the quantity of Mode I. The lowest values for 20-ply beams, are for layups 2 and 3 with a 94% Mode I test. However, because of the increased proportion on 0° plies in layup 7, the mode ratio is increased to 99% Mode I.

From the evaluation of the above criteria, layups 4, 5 and 7 appear to be the preferential design. Although the various values of D_c, and σ_2/σ_{2u} in Table 4 may be lowered further by using more 0° plies it would not be cost effective. Layup 4 has the advantage over layup 5 of not having two adjacent 45° plies together and is therefore the preferred of the two. However, layup 7 is more predominantly Mode I with the lowest D_c. It is therefore layup 7 that was the preferential design. In full, this layup comprises 64 plies in the following sequence

$$[-45/0_4/45/0_4/45/0_4/-45/45/0_4/-45/0_4/-45/0_4/45//$$

$$0/-45/0_3/45/0_4/45/0_3/-45/0/0°/45°/0_3/-45/0_4/-45/03/45/0]$$

Sizing Requirements

The dimensions for a DCB of layup 7 must follow the basic rules given in ASTM D 5528. For the beam to be correctly designed, the delamination length must be sufficiently long with respect to the

specimen thickness to allow the cantilever beams to deform as slender beams. Hence, for each beam the length to thickness ratio should be greater than 10 for the effects of shear deformation to be ignored. Hence, the delamination length should be in excess of 75 mm. If the delamination length becomes too long with respect to the beam thickness, the cantilever beams will experience geometric nonlinearity. Assuming that the effects of geometric nonlinearity must remain under 2%, then the following expressions may be used to approximate the initial crack length of the beam (ASTM D 5528)

$$a = \sqrt{\frac{0.151EI}{bG_{\text{Ic}}}} \tag{2}$$

Therefore, for the beams used here typically the crack lengths should be less than 1.2 m; clearly this is not an issue.

Another consideration is the maximum load that the specimens may undergo. This is useful information to ensure the loads are within the capacity and accuracy of the test machine. The maximum load may be approximated by

$$P_{\text{max}} = \sqrt{\frac{bEIG_{\text{Ic}}}{8a^2}} \tag{3}$$

Using the design given above for a crack length of 75 mm and a width of 25 mm, the maximum load will be approximately 180 N.

Static and Fatigue Testing

Static Test Results

Static tests were conducted on six unidirectional (or 0°) S2/E773 DCB specimens and six DCB specimens with layup 7 (henceforth described as a 0°/45° DCB) using ASTM D 5528. The 0° specimens had 40 plies and were nominally 9.4 mm thick. Observation of the edge of the specimen during the tests on the 0°/45° DCBs revealed that the delamination remained between the 0° and the 45° ply as intended. In three of the six specimens tested, as the delamination grew longer the crack was observed to grow on either side of the 45° ply as illustrated in Fig. 2. However, the delamination had generally grown by at least 15 mm at this stage. A scan of the failure surfaces of the 0° and 0°/45°

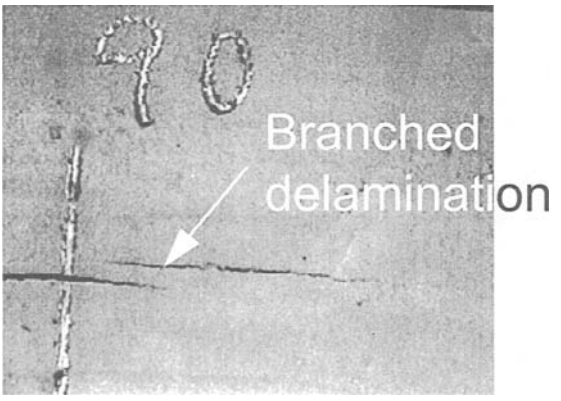


FIG. 2—*Micrograph of side of 0°/45° specimen.*

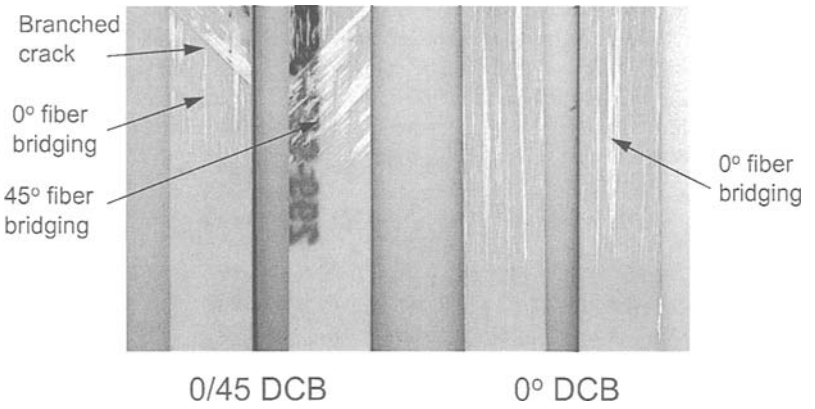


FIG. 3—*Scans of failure surfaces.*

DCB specimens is given in Fig. 3. For the 0°/45° specimen, the delamination is clearly seen to be within the 0°/45° interface.

Fiber bridging was observed in the 0° DCBs as seen by the lighter fibers in Fig. 3. However, in all cases of the 0°/45° specimens, there was also evidence of fiber bridging from both the 45° and the 0° plies as shown by the lighter color fibers in Fig. 3.

A typical load displacement curve for each specimen type is given in Fig. 4. Both curves show the consequence of fiber bridging with an increasing load as the delamination grows. The values of G_{Ic}^{NL}, $G_{Ic}^{5\%}$ and Δ are given in Table 5 for both configurations, see definitions in the Nomenclature section. The interlaminar fracture toughness values are plotted in Fig. 5. The bars are the mean of the data and the error bars one standard deviation. The 0°/45° data had a 10% lower mean value but much larger

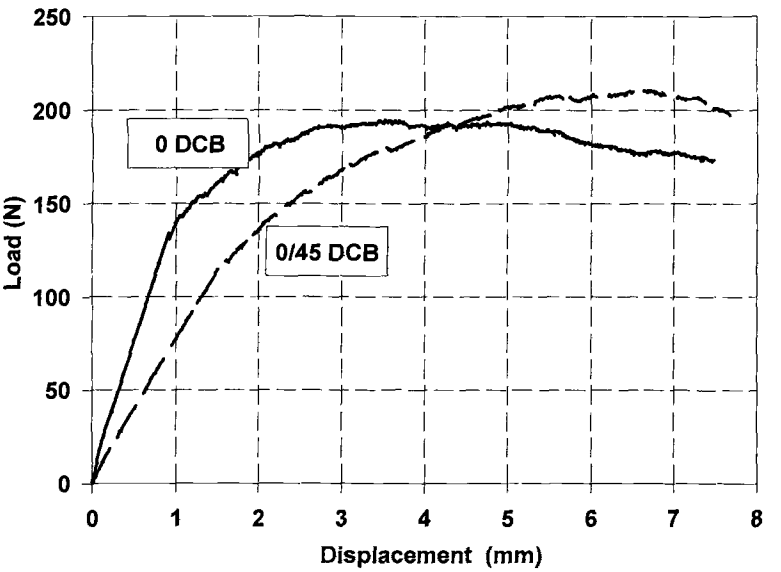


FIG. 4—*Typical load displacement curves.*

TABLE 5—*Quasi-static results.*

	0°			0°/45°		
	G_{Ic}^{NL} (J/m^2)	$G_{Ic}^{5\%}$ (J/m^2)	Δ (mm)	G_{Ic}^{NL} (J/m^2)	$G_{Ic}^{5\%}$ (J/m^2)	Δ (mm)
	129	153	25.0	173.8	181	22.2
	157	179	28.1	112.1	121	21.4
	134	151	17.9	130.3	137	25.3
	127	155	18.3	98.3	105	23.8
	136	132	16.0	92.9	97.0	29.0
	133	180	23.4		—invalid test—	
Mean s.d.	136 J/m^2	158 J/m^2	21.5 mm	122 J/m^2	128 J/m^2	24.4 mm
	11 J/m^2	18 J/m^2	4.8 mm	33 J/m^2	33 J/m^2	3.0 mm

scatter in the data (three times larger standard deviation). For both specimen configurations the G_{Ic}^{NL} values were lower than the $G_{Ic}^{5\%}$ values. An example R-curve for each specimen configuration is shown in Fig. 6. The increase in G_{Ic} for both specimens is a result of fiber bridging that was observed in both specimen configurations.

Fatigue Test Results

Fatigue delamination onset tests were conducted on eleven 0° S2/E773 DCB and twelve 0°/45° DCB specimens in accordance with ASTM D 6115. Observation of the edge of the specimen with a microscope did not show the delamination branching as in Fig. 2 but remaining in the 0°/45° inter-

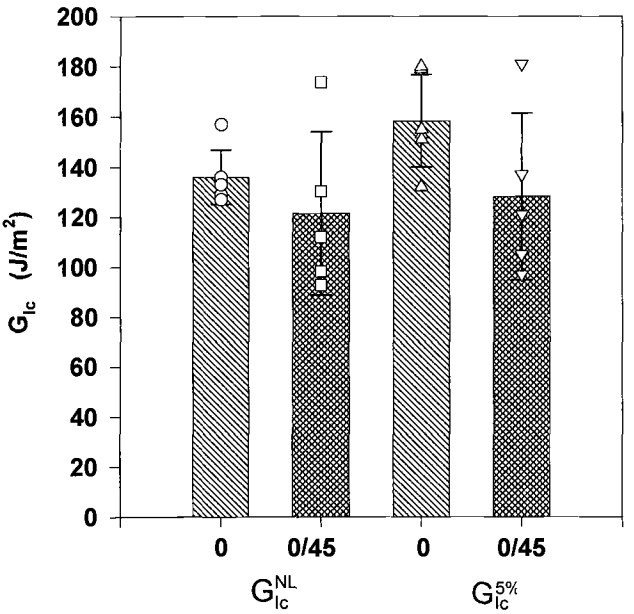


FIG. 5—*Comparison of interlaminar fracture toughness.*

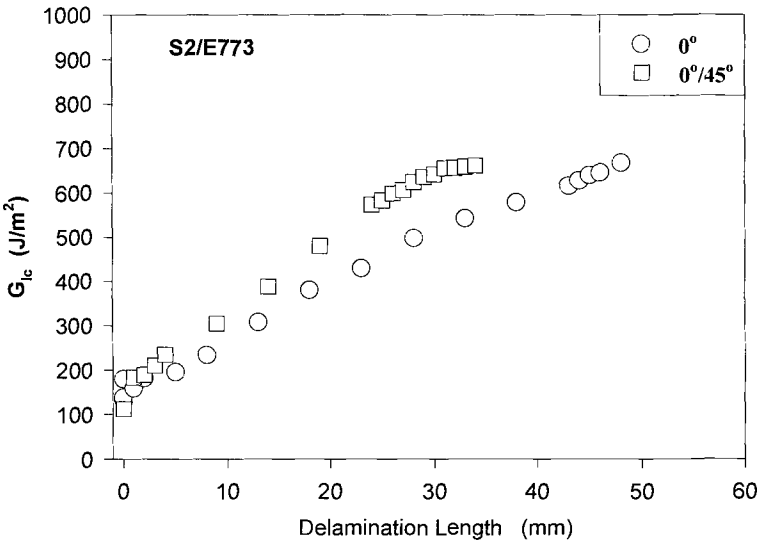


FIG. 6—*Typical R-curves.*

face. The values of the maximum cyclic strain energy release rate, G_{Imax}, and the corresponding $N_{\text{onset}}^{5\%}$ are given in Table 6. The fracture toughness and *G-N* data are shown in Fig. 7. The static fracture toughness data are plotted at $N = 1$ for comparison. As discussed above, the scatter from the 0°/45° static data is much larger than from the 0° specimens. However, this is not observed in the fatigue behavior where the *G-N* curves for the two configurations are very similar.

Discussion

Based on these results for this material system, layup and testing conditions characterization of delamination using a 0° DCB specimen is adequate to represent delamination in a 0°/45° interface. This

TABLE 6—*Fatigue results.*

0° DCB		0°/45° DCB	
$G_{T\text{max}}$ (J/m^2)	N_{onset}	$G_{T\text{max}}$ (J/m^2)	N_{onset}
95.8	4 100	67.9000	7 000
96.4	4 600	...	Hinge pin out
95.5	3 300	62.5000	29 000
68.3	17 100	67.9000	30 000
60.3	16 100	48.8000	300 000
48.5	86 700	50.6000	200 000
69.6	11 540	51.2000	135 000
45.3	1 510 000	47.1000	490 000
47.0	151 210	34.7000	2 450 000*
43.3	520 000	33.0000	2 450 000
43.6	1 130 000	28.6000	2 450 000
...	...	30.7000	2 450 000

* Underline indicates a runout.

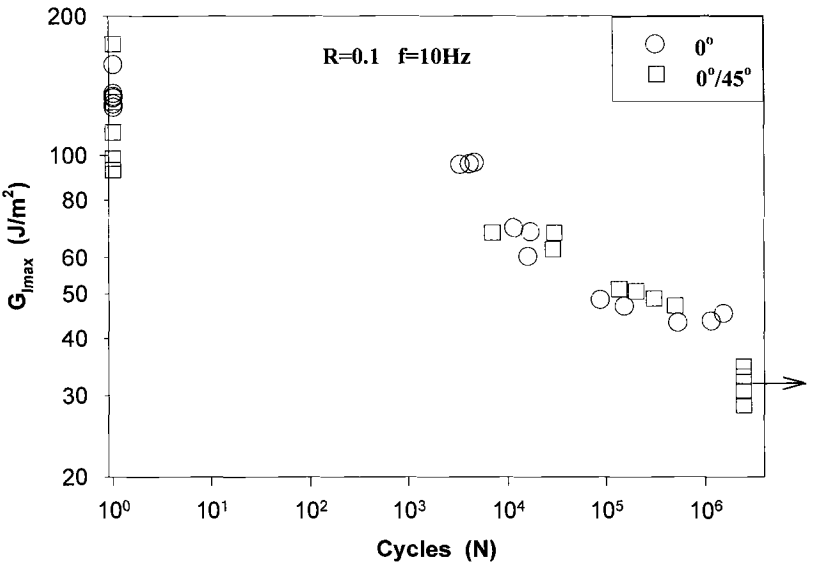


FIG. 7—G-N *curve for 0° and 0°/45° DCB specimens.*

applies to delamination initiation under quasi-static and fatigue loads. The issue of increased scatter in the static tests remains to be resolved. Although the nature of the fiber bridging is different in the two configurations (in that some 0° fibers and some 45° fibers bridged in the 0°/45° specimens) the R-curves appear very similar. There is some evidence that fiber bridging in unidirectional specimens is a function of thickness [*9*]. Therefore, either this system may not show such an effect or the similarities were coincidental. Further tests on specimens of different 0° thickness would resolve this issue.

The presence of fiber bridging in the 0°/45° specimens indicates for this material system and layup, under Mode I loading that fiber bridging may occur in structures delaminating in a similar fashion. There is evidence of this occurring as observed by the failure surface of a structural test element tested to destruction at Bell Helicopters, Fig. 8. Fibers from the 45° and 0° ply can be seen pulled out as evidence of fiber bridging. If this is so, then it is a beneficial effect because fiber bridging aids in resisting delamination growth. To relate any differences in fiber bridging from specimen thickness to structures of different thickness, investigations into crack opening displacements or rotations and their relation to fiber bridging may be required.

Most composite structures are being designed on a no-growth philosophy. This is based on the steepness of the fatigue delamination growth curve [*9,10*]. However, in systems such as the S2/E773, where there may be significant fiber bridging, the resulting increase in toughness may be sufficient to slow or arrest delamination growth once it has initiated. In these circumstances, the no-growth philosophy may be overly conservative. This is dependent on the structure and its loading and the resultant change of strain energy release rate with delamination growth.

Concluding Remarks

The work reported here developed a DCB specimen that allows the delamination between a 0° and 45° interface to be characterized. The specimen does not experience crack branching, bend-twist coupling, warping from residual thermal stresses, or excessive anticlastic effects, problems that have in-

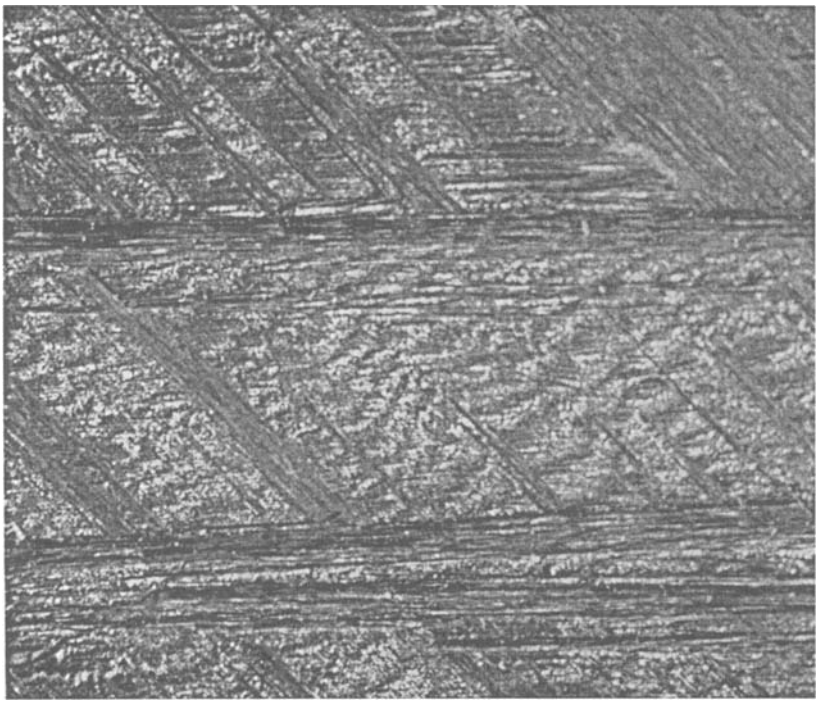


FIG. 8—*Failure surface of structural test element with 0° and 45° fiber bonding.*

validated tests from other researchers. The results from the tests illustrate that both the static and fatigue results are identical to that obtained from a traditional unidirectional beam. Thus, the traditional unidirectional beam is sufficient for characterizing Mode I delamination in a 0°/45° interface with this material. Using this approach it should be possible to design suitable specimens for other materials systems and also for Mode I and mixed Mode I/II loading to determine if the 0°/45° data are identical to the 0° data. The fatigue work reported here was for delamination onset. Comparison of the delamination growth data would also be useful to determine if the specimen design works for fatigue growth but also if the 0°/45° data are coincident with the 0° delamination growth data.

The 0°/45° specimens did experience fiber bridging where 0° fibers and 45° fibers bridged the delamination. It has generally been thought that fiber bridging does not occur between plies of different orientation. Delaminated parts should be examined to determine if evidence of fiber bridging can be seen. If so, then consideration should be given to using initiation and propagation values of G_{Ic} for predicting delamination growth.

References

[1] Russell, A. J. and Street, K. N., "Factors Affecting the Interlaminar Fracture of Graphite/Epoxy," *Proceedings, ICCM-IV,* 1982, pp. 279–286.

[2] Nicholls, D. J. and Gallagher, "Determination of G_{Ic} in Angle Ply Composites Using a Cantilever Beam," *Journal of Reinforced Plastics and Composites,* Vol. 2, 1983. pp. 2–17.

[3] Chou, I., Kimpara, I., Kageyama, K., and Ohsawa, I., "Mode I and Mode II Fracture Toughness Measured Between Differently Oriented Plies in Graphite/Epoxy," *Composite Materials, Fatigue and Fracture, 5th Volume. ASTM STP 1230,* pp. 132–151.

[4] Chai, H., "The Characterization of Mode I Delamination in Non-Woven Multi-directional Laminates," *Composites*, Vol. 15, No. 4, 1984, pp. 277–290.

[5] Robinson, P. and Song, D. Q., "A Modified DCB Specimen for Mode I Testing of Multidirectional Laminates," *Journal of Composite Materials*, Vol. 26, No. 11, 1992, pp. 1554–1577.

[6] Foster, S., Robinson, P., and Hodgkinson, J. M., "An Investigation of Interlaminar Fracture Toughness at $0°/\theta°$ Interfaces in Carbon-Epoxy," *Proceedings, 4th International Conference of Deformation and Fracture of Composites*. The Institute of Materials, Manchester, 24–26 March 1997, pp. 231–241.

[7] Polaha, J. J., Davidson, B. D., Hudson, R. C., and Pieracci, A., "Effects of Mode Ratio, Ply Orientation, and Precracking on the Delamination Toughness of a Laminated Composite," *Journal of Reinforced Plastics and Composites*, Vol. 15, Feb. 1996, pp. 141–173.

[8] Rubbrecht, P. and Verpoest, I., "The Development of Two New Test Methods to Determine the Mode I and Mode II Fracture Toughness for Varying Fiber Orientation at the Crack Interface," *Proceedings, International SAMPE Conference*, 11–13 May 1993, Anaheim, CA, pp. 875–887.

[9] Hojo, M. and Aoki, T., "Thickness Effect of Double Cantilever Beam Specimen on Interlaminar Fracture Toughness of AS4/PEEK and T800/Epoxy Laminates," *Composite Materials: Fatigue and Fracture, Fourth Volume, ASTM STP 1156*, pp. 281–298.

[10] Martin, R. H. and Murri, G. B., "Characterization of Mode I and Mode II Delamination Growth and Thresholds is AS4/PEEK Composites," *Composite Materials: Testing and Design (9th Volume), ASTM STP 1059*, S. P. Garbo, Ed., 1990, pp. 251–270.

M. R. Piggott,[1] *K. Liu,*[2] *and J. Wang*[1]

New Experiments Suggest that All Shear and Some Tensile Failure Processes are Inappropriate Subjects for ASTM Standards

REFERENCE: Piggott, M. R., Liu, K., and Wang, J., **"New Experiments Suggest that All Shear and Some Tensile Failure Processes are Inappropriate Subjects for ASTM Standards,"** *Composite Structures: Theory and Practice, ASTM STP 1383*, P. Grant, and C. Q. Rousseau, Eds., American Society for Testing and Materials, West Conshohocken, PA, 2000, pp. 324–333.

ABSTRACT: There are four ASTM standards which involve apparent shear failure of composites. These include the Iosipescu (D 5379), tube torsion (D 5448), the short beam test (D 2344), and two-rail and three-rail shear (D 4255). However, careful experiments in which polymers have been sheared show that failure is normally restricted to tensile failure with breaking of polymer chains and cross links. Moreover, it is already known that shear hackle is produced by a tensile process. In view of this, these standards should be reexamined to determine whether strengths should be reported at all. The same argument applies to the new standard being developed for mixed Mode I–Mode II interlaminar fracture toughness. Mode I is the only failure mode which is consistent with experimental observations.

In addition, the D 3039 standard for tensile strength has been revised to include balanced and symmetric laminates. Experiments have shown that, with angle ply laminates, much greater strengths can be obtained just by making the specimen wider and shorter. These latter tests agree very well with tests on pressurized filament wound tubes, with structures equivalent to the angle ply structures. This strongly indicates that the ASTM test can severely underestimate the strength. The ASTM standard also seriously underestimates the stiffness. There appears to be an "edge softening" effect, so that apparent properties are very dependent on the aspect ratio of the test sample. Thus, true material properties are not measured.

It is proposed that all ASTM D 30 mechanical tests be reexamined to determine (*a*) what purpose is served by having the test at all, and (*b*) whether it is measuring a true materials property.

KEYWORDS: strength, stiffness, tensile failure, shear failure, adequacy of standards

It is important that there be agreed upon methods of testing fiber composites, so that a known quality of product can be achieved. With the components of a composite, i.e., the fibers and the matrix, this is relatively straightforward. However, when these materials are combined in the composite, the resulting structure, consisting of at least two separate components, is much more difficult to assess.

For example, the structure is not described by simple models with parallel fibers, uniformly packed in hexagonal or square arrays, as assumed almost universally [*1*]. Instead there is what has been called the mesostructure [*2*]. This takes fiber bundling, resin-rich areas, and voids into account, i.e., packing mesostructures. Also included are fiber waviness and misalignment, which constitute orientation mesostructures. Packing mesostructures, such as fiber bundling, affect the compressive strength [*3*]

[1] Advanced Composites Physics & Chemistry Group, Department of Chemical Engineering & Applied Chemistry, University of Toronto, Toronto, Ontario M5S 3E5, Canada.

[2] Research associate, Building, Envelope & Structure Program, NRC, Montreal Road, Bldg. M-20, Ottawa K1A OR6, Canada.

Copyright© 2001by ASTM International www.astm.org

and translaminar fracture toughness [*4*]. Orientation mesostructures affect the compressive strength [*5*], probably contribute to the fiber bridging observed in Mode I interlaminar fracture toughness [*6*], and strongly affect the apparent shear strength [*7*].

Fiber waviness is dependent on the exact molding process used [*8*]. Thus it cannot be assumed that the packing mesostructures or orientation mesostructures will be the same in a specially made test sample, as in the same materials molded to produce a structure such as a wing section.

Further problems with developing standards include the need to appreciate that a test sample may not be able to yield materials properties, even in the absence of the mesostructure problem. Moreover, it is important that a real property is being measured. The objective of this paper is to discuss these latter problems and suggest solutions for them.

Shear Testing: ASTM D 2344, 4255, 5448, and 5379

Most of these methods purport to produce a number for shear modulus and for shear strength. However D 2344 has recently been revised, and now the maximum load is to be reported, and the method is designed to measure the "short beam strength." This is because the equation for shear strength S_H, i.e.

$$S_H = 3P_B/4bd \tag{1}$$

(where P_B is the breaking load, and b and d are, respectively, the width and thickness of the specimen) does not adequately represent the stress distribution or the failure modes often observed. Moreover, it is noted that "the occurrence of interlaminar shear as a catastrophic failure mode is not common."

In fact, our research supports the notion that shear failure is almost nonexistent. Instead, tensile failure occurs. This was first suggested some time ago for polymers [*9*]. In our study of apparent shear failure, there appeared to be a mesostructural effect, since the composite was stronger than the polymer, see Fig. 1*a*, and fibers crossed the crack plane (Fig. 1*b*). However, polymer shear strengths were often about equal to their tensile strengths, Fig. 2*a*, and in punch tests (ASTM D 332), although high shear strains (e.g., 80 000%) could be achieved with tough polymers, the failure process was normally tensile cracking; see Fig. 2*b*. The Iosipescu method was not suitable for polymers. Failure, if achieved at all, was tensile and transverse to the maximum tensile stress; see Fig. 3.

Further evidence comes from an *Encyclopedia of Composites* [*10*] and Fig. 4 reproduces the tensile cavitation process envisaged which produces "shear hackle." Moreover, tensile failure has been shown to be the most likely process occurring in axisymmetric single fiber tests to measure the bond strength between fibers and matrix. Shear stresses are applied in these tests, which include pull out, fragmentation, microtension, and microcompression [*11*]. However, the true failure process does not appear to involve shear failure. This is confirmed by a detailed examination of failure of polymers [*12*].

The standard shear test methods are directed towards measuring a property of a material which is homogeneous at the lamina level. As we have shown, it is not a true property. It originates from a different one, and so attempts to measure it are prone to error. The V-notch beam (D 5379) is especially subject to error on this account. It is well known that the 90° orientation shows evidence of failure because of transverse tensile stresses. However, a corrolary of this is that the 0° orientation will be subject to localized compressive stresses. Thus the 90° result appears to be too low and the 90° result may well be too high.

Thus, it is not advisable to report a strength in any of the above ASTM tests. Furthermore, it is hard to see what purpose is served by reporting the maximum load in the short beam test. The maximum load is a property of the geometry of the test. While it does apparently give some information about the microphenomena, it may not be at all indicative of a true materials property.

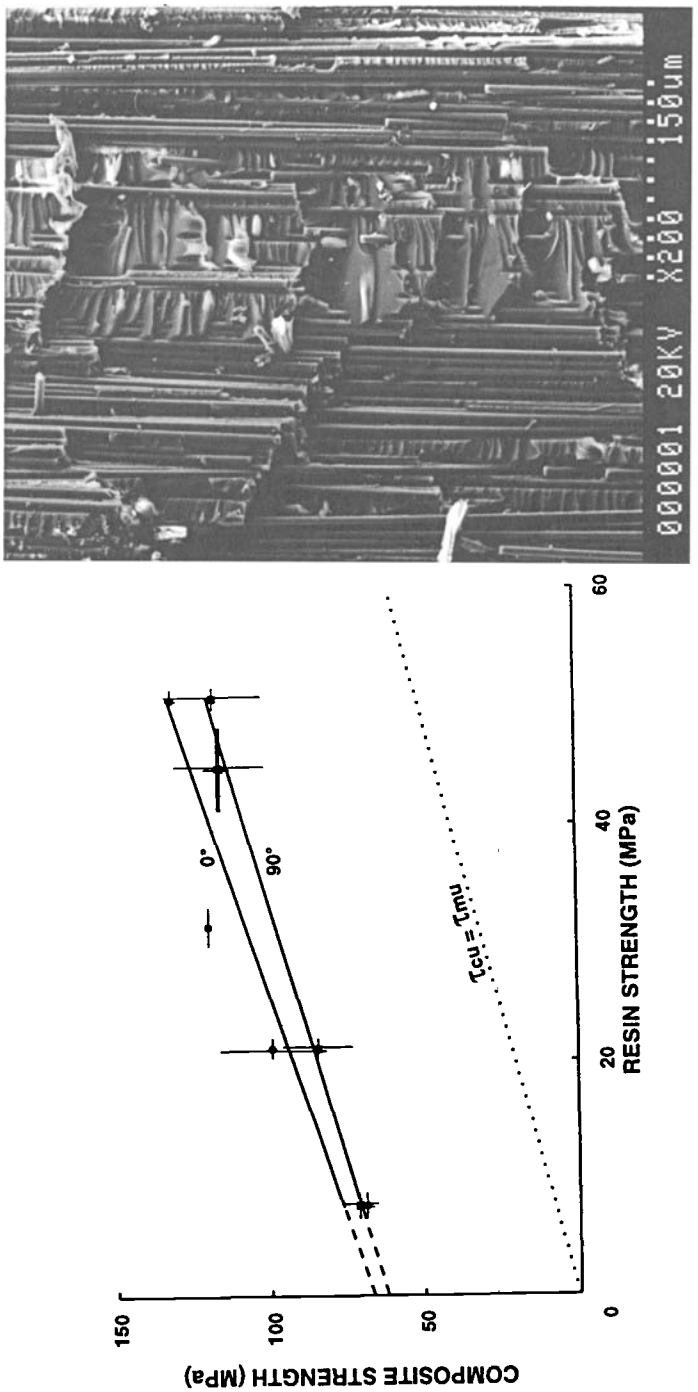
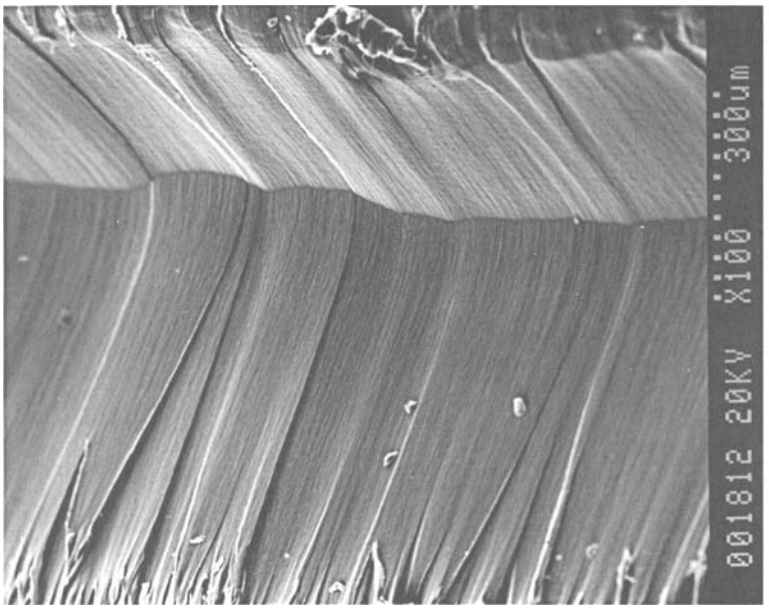


FIG. 1—(a) *Apparent Iosipescu shear strength of carbon-epoxy pultrusions and the epoxy matrix.* (b) *Iosipescu 90° fracture surface [7].*



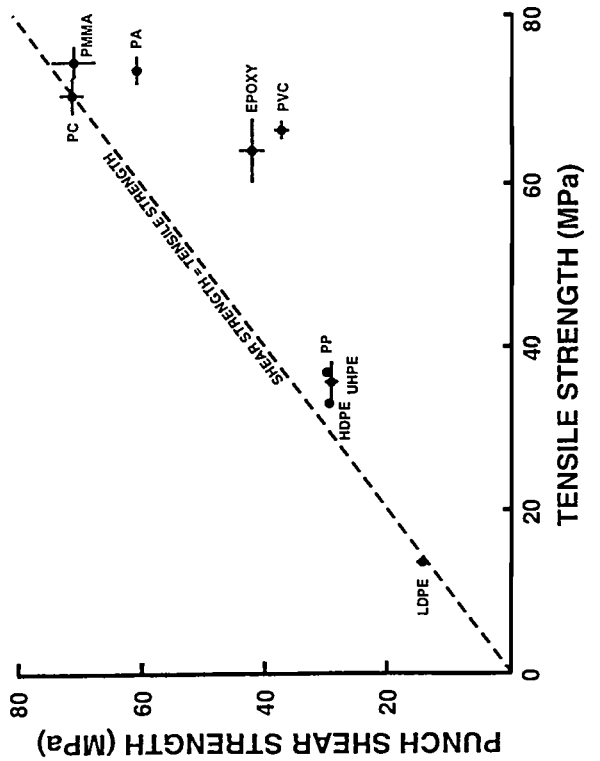
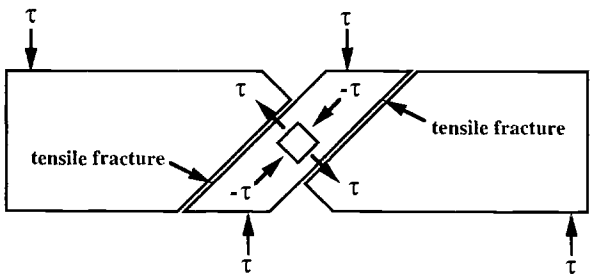


FIG. 2—(b) *Punch strength of polymers vs. tensile strength.* (b) *Tensile fracture in nylon sample sheared in punch test.*



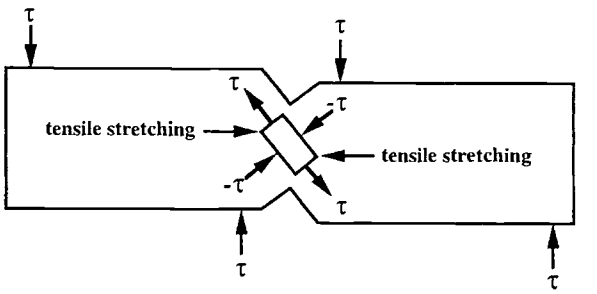


FIG. 3—*Failure modes for polymers in the Iosipescu test.*

Reporting shear modulus, G_{12}, may also be misleading in some cases. Consider the shear response test of a ± 45° laminate, D 3518. This uses the geometry specified for D 3039. Our tests (see Fig. 5) show that this geometry underestimates the tensile modulus, E_x, at least as compared with the laminated plate theory (LPT), which has been validated in tube tests to some degree at least (see tensile testing, below) and which is widely used for aircraft design. (It does however, produce a value for ν_{xy} which is close to LPT.) If we estimate G_{12} using the standard method we obtain 4.0 ± 0.4 GPa which is rather low compared with values reported from other methods on this type of material (T650 (Amoco) carbon-epoxy). For example, the Iosipescu method gives 4.8 ± 0.3 GPa and the tube methods gives 5.0 ± 0.4 [*13*]. Moreover, using our results from a wider and shorter sample give 5.3 ± 0.5. This could explain why a review of literature values G_{12} reveals such a wide diversity.

The best solution to these problems may be to restrict the standard to one straightforward method that makes few assumptions, i.e., the hoop wound tube method, D 5448, although this has the drawback of tubes being difficult to make. The V-notch beam, D 5379, is probably not suitable since there is a problem with disagreement between 0° and 90° orientations. In his round-robin review, Wilson [*14*] gives G_{12} = 6.3 ± 0.3 for the 0°, which is significantly different from 5.2 ± 0.5 which he gives for 90° for AS4-3501-6 carbon epoxy. Moreover, Lee and Munro [*15*] give D 5448 a score of 10 for

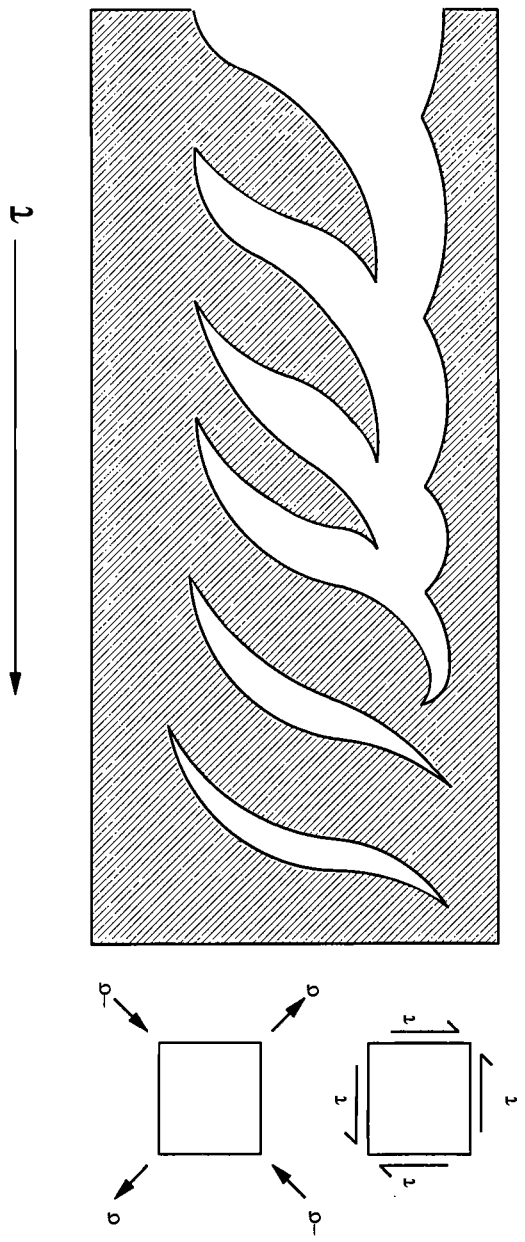


FIG. 4—*Process which produces "shear hackle" [10].*

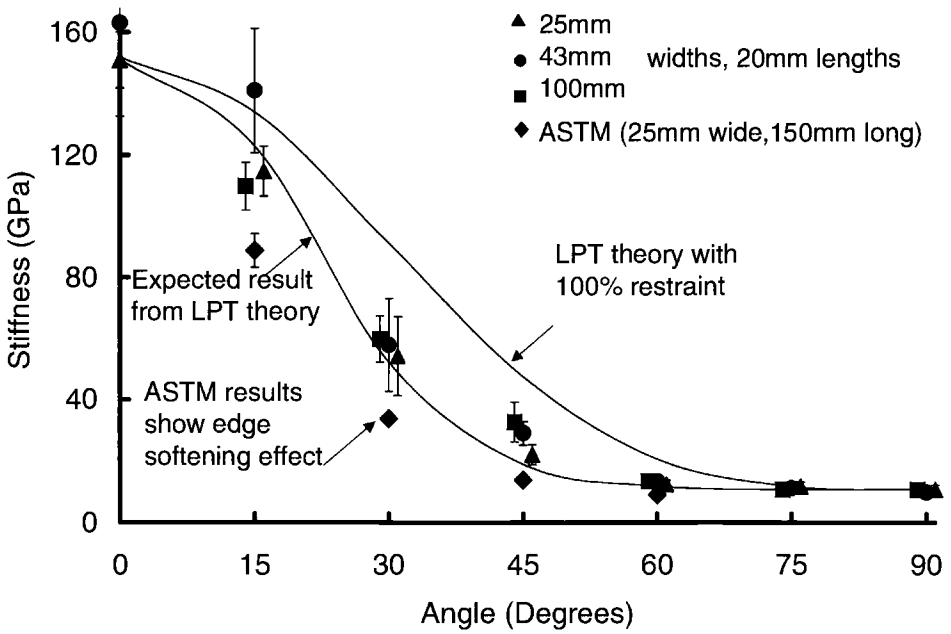


FIG. 5—*Stiffness,* E_x, *of angle-ply laminates tested with coupons having various aspect ratios compared with LPT with no grip constraint (*lower curve*) and full grip constraint (*upper curve*).*

accuracy of result and only 8 for the Iosipescu method. Thus it seems that G_{12} values should be reported and the other methods, i.e., D 2344 and D 4255, should probably be phased out. In addition, the shear-stress-strain response up to shear strains that are typically seen in practical structural laminates is useful to the industry and should be reported.

Since the apparent shear strength is truly a tensile strength with steric hindrance, and so not a reliable measure of any material property, the only standard which should be specified should be one that measures the transverse tensile strength of a laminate. Adopting D 3039 may be best for this, since the hoop wound tube (D 5450) cannot be expected to simulate a normal compression molded laminate. (Even if prepreg is used to make the tube, and it is cured according to standard lamination methods, there is a danger that the mesostructure may be different, since fiber waviness can develop in tubes.) Our experience with transverse testing, though, suggests that D 3039 can give low results for transverse strength unless the coupons have highly polished edges.

Tensile Testing: ASTM D 3039

The scope of this has recently been extended to include angle-ply laminates. However, it has been shown that laminate strength is dependent on the aspect ratio of the sample being tested [*16*]. Notched wide sample tests give strengths which can be up to ten times higher than those from long and narrow samples [*17*] and these results agree with Soden et al.'s from glass-epoxy tubes [*18*]. Furthermore, E_x estimated from wide sample tests and tubes agreed well with LPT, whereas long narrow samples gave results which were much too low for modulus as well as strength [*19*]. Tube tests give results which agree with LPT, however [*20*]. Moreover, they do not lend any support to the so called "standard" Tsai-Wu criterion [*21*].

Figure 5 contrasts ASTM D 3039 results with those from wide sample tests for carbon-epoxy angle ply compression moldings. (T650 (Amoco)) carbon-epoxy prepregs from Hexcel were used. They

were molded at 180°C for 2 h following recommended procedures and tested in a MTS servohydraulic machine at a crosshead rate of 2 mm/min.) There is apparently an edge softening effect. The long narrow D 3039 samples have a great deal of edge, with relatively few fibers going from grip to grip. Earlier work suggests that those fibers which emerge from the edges contribute only partially to modulus and strength: they are disabled. This is a problem for strength, σ_{xu}, as well; see Fig. 6. The wide samples constrain the Poisson's shrinkage, however, (Fig. 7) while the long narrow D 3039 samples give results that agree very well with LPT.

In view of this, ASTM D 3039 should not be used for laminates, except those with 0° and/or 90° plies only or with a preponderance of 0° plies so that the edge softening is negligible. Instead, tube tests are recommended. We are currently searching for simple methods of pressurizing tubes and at the same time having the ends free to contract so that we are not introducing constraints. This should give reliable values of ν_{xy}. However, for reliable values of E_x and σ_{xu} the tubes should probably be long and narrow. Even with lengths of ten diameters, the effective aspect ratio (s) is somewhat high at just under one third. Soden et al. used 100-mm-diameter, 320-mm-long tubes, i.e., with $s = 0.98$ while Swanson used 102-mm-diameter, 432-mm-long tubes with $s = 0.74$. Thus edge softening could still be a problem, and may be more serious for carbon than glass due to the higher stiffness of carbon. It is recommended that tubes, used for future validation of LPT, have lengths of at least ten diameters to avoid this problem.

Other Tests

Properties such as interlaminar fracture toughness, G_I, and compressive strength are very sensitive to misaligned fibers. To minimize this problem for the fracture toughness measurement, the G_I value at the point of initiation, i.e., before significant fiber bridging can occur, is taken as the appropriate

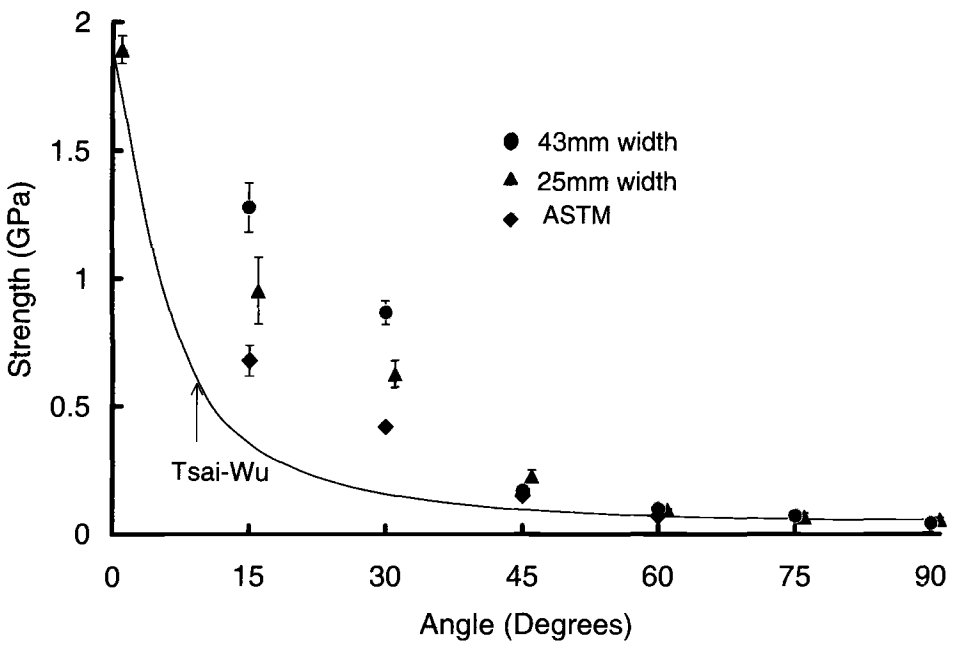


FIG. 6—*Strength of angle-ply laminates tested with coupons having various aspect ratios compared with "standard" criterion.*

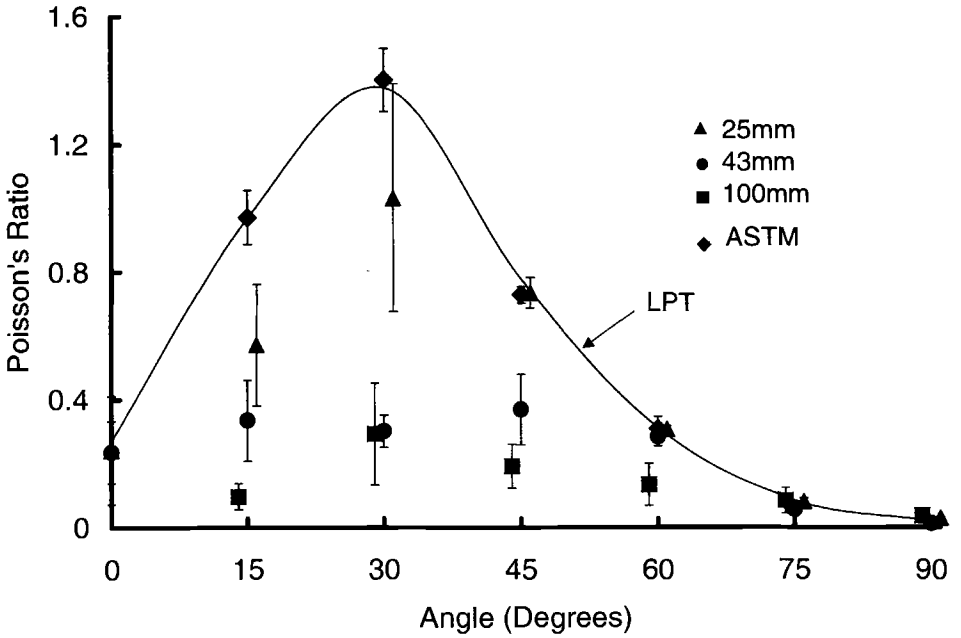


FIG. 7—*Poisson's ratio, ν_{xy}, tested with coupons having various aspect ratios compared with LPT.*

value. In this case, for a well-made composite with well adhering fibers, we expect $G_I = G_m$, i.e., the matrix fracture toughness [*22*] for the more brittle matrices, and some lower value determined by the thickness of the polymer between the fibers, for the tougher matrices [*23*]. A solution to this problem, therefore, is simply to test the matrix, using a standard method for polymers (e.g., D 5054) or perhaps the DCB adhesives test (D 3433) when a thickness effect is expected. If fiber-matrix adhesion is a problem, this may be assessed separately using the transverse test. Furthermore, in view of the problems with shear strength described above, the development of a standard for G_{II} and G_{III} is unlikely to be rewarding.

For compressive strength, there is the additional complication of the weakening effect of fiber bundling [*3*]. The fiber compressive strength can sometimes be evaluated using the Raman technique [*24*] so that the potential composite strength may be estimated from it using a Rule of Mixtures expression. However, since the compressive strength of a production molding is so dependent on the molding conditions, and the structure thus achieved, there appears to be no alternative to cutting a piece out of the structure and testing that using D 3410 or D 5467. It must be emphasized that compressive strength is a *structure* rather than a *materials* property for high-performance composite made with ceramic fibers.

With respect to fatigue tests, the same caveats apply as to the tensile and delamination tests. Thus D 3479 uses D 3039, so it should only be used for laminates with fibers in the 0° and 90° orientations. D 6115 (delamination fatigue) might perhaps as well be replaced by the DCB or other tests with the polymer alone, with separate tests to determine the endurance of the interface.

Conclusions

It has been shown that a number of tests are not performing adequately for reasons which were probably not apparent at the time of their inception.

The most serious problems are encountered with shear testing, where attempts are made to measure a property which normally does not exist (shear strength). Other problems arise where shear modulus is apparently being evaluated by an inaccurate method. The ASTM D 30 Committee should consider phasing out all but D 5448, and reporting only stress-strain response and shear modulus.

The next most serious is D 3039, which was recently extended to include materials with partly oblique fibers. Due to disabled fibers and consequent edge softening, it can give results which may be in error. The inclusion of laminates having only oblique fibers in this standard should be revoked as soon as possible.

Once these problems are resolved, there are still problems associated with structural irregularities, i.e., mesostructures. Here it may be worthwhile to transfer attention to the components (e.g., the polymer in the case of delamination tests) or to specify that the test only be carried out on a sample taken from the actual structure or a copy thereof, made exactly according to the same procedure.

The most important step needed is an appreciation that many standards are not measuring materials properties. Composites are structures with properties that vary according to the exact details of the manufacturing process, and with the aspect ratio of the specimen being tested. It is also important that the data which are really needed be identified, and that the tests and what is reported from them be tailored to that need.

Acknowledgments

The authors are grateful to NSERC (Canada) for financial support which made this work possible and to Hexcel for the generous supply of prepregs.

References

[1] Gibson, R. F., *Principles of Composite Material Mechanics,* McGraw-Hill, New York, 1994, Chapter 3.
[2] Piggott, M. R., *Proceeding of the 37th International SAMPE Symposium,* 1992, pp. 738–746.
[3] Piggott, M. R., *Journal of Material Science,* Vol. 16, 1981, pp. 2837–2845.
[4] Fila, M., Bredin, C., and Piggott, M. R., *Journal of Material Science,* Vol. 7, 1972, pp. 983–988.
[5] Mrse, A. and Piggott, M. R., *Composites Science & Technology,* Vol. 46, 1993, pp. 219–227.
[6] Piggott, M. R., *Composites Science & Technology,* Vol. 53, 1995, pp. 201–206.
[7] Liu, K. and Piggott, M. R., *Composites,* Vol. 26, 1995, pp. 829–840 and 841–848.
[8] Highsmith, A. L., Davies, J. J., and Helms, K. L. E., *ASTM STP 1120,* American Society for Testing and Materials, 1992, pp. 20–36.
[9] Puck, A. and Schneider, W., *Plastics and Polymers.* Vol. 37, 1969, pp. 33–41.
[10] Faliba, S. S. and Snider, J. A., *International Encyclopedia of Composites,* S. M. Lee, Ed., VCH Publishers, New York, Vol. 2, 1990, p. 268.
[11] Piggott, M. R., *Compositse Science & Technology,* Vol. 57, 1997, pp. 965–974.
[12] Liu, K. and Piggott, M. R., *Polymer Engineering Science,* Vol. 38, 1998, pp. 60–68 and 69–71.
[13] Broughton, W. R., Kumosa, M., and Hull, D., *Composite Science & Technology,* Vol. 38, 1990, pp. 299–326.
[14] Wilson, D. W., *Journal of Composites Technology & Research,* Vol. 12, 1990, pp. 131–138.
[15] Lee, S. and Munro, M., *Composites,* Vol. 17. 1986, pp. 13–22.
[16] Khatibzadeh, M. and Piggott, M. R., *Composites Science & Technology,* Vol. 58, 1998, pp. 497–504.
[17] Khatibzadeh, M. and Piggott, M. R., *Compositse Science & Technology,* Vol. 56, 1996, pp. 1443–1451.
[18] Soden, P. D., Kitching, R., Tse, P. C., and Tsavalas, Y., *Composites Science & Technology,* Vol. 46, 1993, pp. 363–378.
[19] Tsai, S. W., NASA CR 224, 1964.
[20] Swanson, and Toombes, G. R., *ASME Journal of Engineering Materials Technology,* Vol. 111, 1989, pp. 150–153.
[21] Kibler, J. J., *Engineered Materials Handbook, Vol. 1, Composites,* ASM International, Metals Park, OH, T. J. Reinhardt, Ed., 1987, p. 276.
[22] O'Brien, T. K., Personal Communication, 1997.
[23] Piggott, M. R., *Journal of Material Science,* Vol. 23, 1988, pp. 3778–3781.
[24] Wood, J. R., Huang, Y. L., Young, R. J., and Maron, G., *Compositse Science & Technology,* Vol. 55, 1995, pp. 223–229.

Clara Schuecker[1] *and Barry D. Davidson*[1]

Effect of Friction on the Perceived Mode II Delamination Toughness from Three- and Four-Point Bend End-Notched Flexure Tests

REFERENCE: Schuecker, C. and Davidson, B. D., **"Effect of Friction on the Perceived Mode II Delamination Toughness from Three- and Four-Point Bend End-Notched Flexure Tests,"** *Composite Structures: Theory and Practice, ASTM STP 1383*, P. Grant and C. Q. Rousseau, Eds., American Society for Testing and Materials, West Conshohocken, PA, 2000, pp. 334–344.

ABSTRACT: Results are presented from a study on the effect of friction on the Mode II delamination toughness as obtained by three- and four-point bend end-notched flexure tests. Finite-element analyses are used to assess the effect of friction on the compliance and energy release rate of the two types of test specimens. Energy release rates are first obtained by a virtual crack closure technique, which can be used to separate the energy lost by the system into that dissipated by friction and that used for crack advance. Energy release rates are then obtained by a simulated compliance calibration procedure. By modeling this commonly used method of data reduction and comparing results with those obtained by crack closure, the ratio of the material's intrinsic toughness to the toughness perceived by users of the tests can be assessed. For both tests, this assessment is made for physically realistic coefficients of friction and, for the four-point end-notched flexure test, as a function of the ratio of inner to outer span length. It is shown that frictional effects on the perceived toughness are considerably larger in the four-point than in the three-point bend end-notched flexure geometry, but that an appropriate choice of the four-point test geometry can make the influence of friction quite small.

KEYWORDS: energy release rate, Mode II, end notched flexure, delamination, toughness, friction

Recently, a four-point bend end-notched flexure (4ENF) test was proposed for Mode II delamination toughness testing of laminated composites [*1*]. The 4ENF test was postulated to have a few distinct advantages over the more commonly used three-point bend end-notched flexure (3ENF) test [*2,3*]. For example, crack advance is unstable in the 3ENF test, whereas it is stable in the 4ENF test [*1–5*]. Thus, several values of toughness per specimen can be obtained during a 4ENF test, whereas only a single value is obtained using the 3ENF. It follows that both non-precracked and precracked toughnesses can be obtained from the same specimen using the 4ENF. Here, "non-precracked" is used to denote growth directly from the preimplanted insert, and "precracked" is used to denote growth from a naturally created starter crack. In contrast, precracking is a difficult and time-consuming procedure in the 3ENF, and separate specimens need to be used to obtain non-precracked and precracked toughnesses [*2,3*].

The primary difficulty with the 4ENF test lies in the apparently large values of the Mode II toughness, G_{IIc}, that it produces. In Ref *1*, the 4ENF test was observed to produce values of G_{IIc} that were approximately 9% higher than those obtained by the 3ENF for non-precracked specimens, and approximately 21% higher than from the 3ENF for precracked specimens. However, there were some differences between the two batches of material used in these two test configurations, and there were difficulties with the 4ENF fixture that prevented a firm conclusion in this study. A more recent work

[1] Research scholar and associate professor, respectively, Department of Mechanical, Aerospace and Manufacturing Engineering, Syracuse University, Syracuse, NY 13244.

Copyright© 2001by ASTM International www.astm.org

[4] investigated this issue using a single batch of specimens. Specimens were tested in the 4ENF configuration with a fixed outer span and various inner span lengths, and it was found that the apparent toughness increased with increasing inner span length. At the shortest inner span length considered, precracked values of G_{IIc} from the 4ENF test were observed to be between 8 and 20% larger than those from the 3ENF, whereas at the largest inner span length the 4ENF values were 43 to 57% larger.

To understand the reasons for the preceding observed behaviors, in this work finite-element analyses are used to investigate the effect of friction on the perceived toughness in the 3ENF and 4ENF tests. Portions of this investigation are conducted using an approach similar to that developed in previous studies on the effects of friction on 3ENF test results [6,7]. A straightforward application of this approach to the 4ENF test allows for a direct comparison of frictional effects in the two test methods. In addition, a new approach for assessing the perceived toughness is developed that has direct application to the 3ENF and 4ENF tests methods as they are commonly used in practice. Here, the term "perceived toughness" is used to refer to the value that a user of the test will obtain by standard data reduction procedures, such as compliance calibration [1–5]. In both the 3ENF and 4ENF tests, this perceived toughness will differ from the true value, which can only be obtained if the energy lost by the system is separated into that dissipated by friction and that used to create newly delaminated surfaces. The amount by which the perceived and true values differ are related to the data reduction method and material coefficient of friction for both the 3ENF and 4ENF tests. Finally, these results are used to draw some conclusions on previously obtained experimental results.

Test Geometries

Figures 1*a* and 1*b* present schematic representations of the 3ENF and 4ENF test geometries, respectively. The 3ENF consists of a three-point bend configuration, with lower support rollers and a center loading pin [2,3]. The 4ENF uses a four-point bend configuration, where the support rollers comprise the outer span and the inner span consists of the loading rollers. The inner span is typically

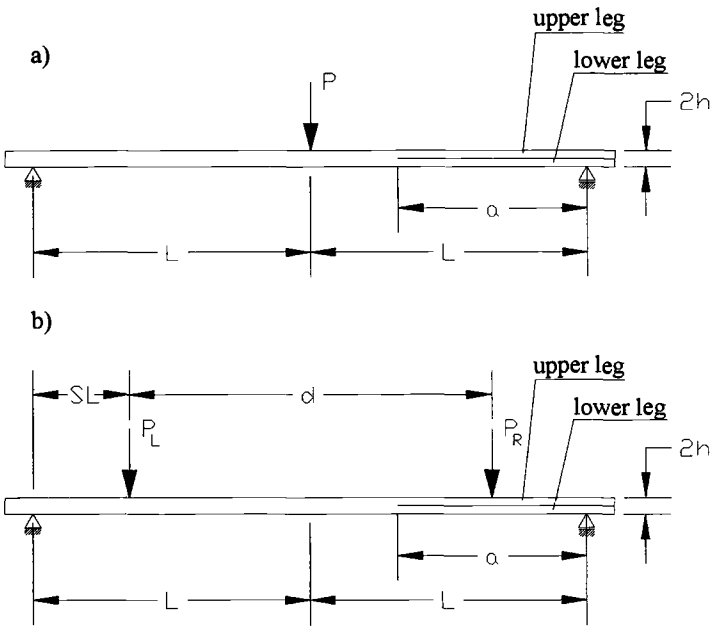


FIG. 1—*Schematic representations of* (a) *3ENF and* (b) *4ENF tests.*

centered between the outer support rollers (i.e., $S_L = L - d/2$), and the two loads, P_L and P_R, are equal. In the actual test configuration there is one load, $P = P_L + P_R$, introduced via bearings onto a loading platen to which the two loading pins are attached [*1,5*]. The bearing allows the loading platen to rotate freely about the axis normal to the specimen's length and ensures that $P_L = P_R$. To rule out the local influence of the compressive stress at the loading pin on the crack tip region, the initial crack length is chosen such that the crack tip is approximately 15 mm inside of the inner loading rollers [*1,5*]. The load is gradually increased, under displacement control, until crack growth occurs. A classical beam or plate theory analysis indicates that the energy release rate (ERR) is independent of crack length and that crack growth is stable under displacement control as long as the crack tip is in between the inner loading rollers [*1*]. Having a stable growth of delamination, the compliance versus crack length curve can be obtained during the test. It also eliminates the need for a precrack to determine propagation values of G_{IIc} and a complete R-curve can be generated from the data of just one test [*1,5*].

Finite-Element Models

There were two types of models used in this study. The dimensions of the models of "set 1" are given in Table 1*a*. The 3ENF models of this set were originally developed to validate our modeling procedure by comparing results to those of Ref *6*. The material properties for these models were chosen to match those of Ref *6* and are given as "material I" of Table 2. Model "set 2" was developed to perform a study to investigate whether frictional effects could fully account for the experimental results reported in Refs *1* and *4*. The dimensions of these models are presented in Table 1*b*. The material properties were chosen to correspond to those of unidirectional HTA/R6376 graphite/epoxy [*1,5*] and are given as "Material II" in Table 2. All models had the same thickness of $2h = 3$ mm (cf. Fig. 1) and the 4ENF models of both sets considered a centered inner span. All finite-element analyses were conducted using Abaqus Version 5.8, licensed from Hibbitt, Karlsson and Sorensen, Inc., and used eight-noded plane strain elements.

All finite-element models were discretized versions of Figs. 1*a* and 1*b*. The models of set 1 were considerably more refined than those of set 2; these former models were used to perform mesh refinement studies and to decide on the minimum mesh densities for various regions. The models of set 1 had eight elements through the thickness of the specimen and element aspect (length-to-height) ratios between 0.5 and 8.0. Figure 2 presents mesh plots of the models of set 2. As shown in Fig. 2*a*, remote from the crack tip these models also had eight uniform thickness elements through the specimen's thickness. All elements in these models had aspect ratios between 1.0 and 5.0 (this is not apparent in the figure, as the *y*-axis dimension has been scaled by a greater amount than the *x*-axis for

TABLE 1—*Model dimensions.*

	Model	Material	L (mm)	a (mm)	$d/2L$	B (mm)*
			(a) MODEL SET 1			
3 ENF	1	I	38.1	19.05	...	25.4
	2	I	50.8	19.05	...	25.4
4 ENF	1	I	50.8	50.8	0.6555	25.4
			(b) MODEL SET 2			
3 ENF	A	II	50	25†	...	1
4 ENF	A	II	50	30, 35, 40, 50, 60, 65, 70	0.6	1
	B	II	50	35, 40, 50, 60, 65	0.5	1
	C	II	50	40, 45, 50, 55, 60	0.4	1

* Out-of-plane width.

† Compliance taken at crack lengths of 15, 20, 25, 30, and 35 mm.

TABLE 2—*Material properties.*

Material	I	II
E_{11} (GPa)	131	145
E_{22} (GPa)	13	10.5
E_{33} (GPa)	13	10.5
G_{12} (GPa)	6.4	4.16
G_{13} (GPa)	6.4	4.16
G_{23} (GPa)	4.8	3.55
ν_{12}	0.34	0.293
ν_{13}	0.34	0.293
ν_{23}	0.35	0.48

ease of viewing). Remote from the crack tip, the element lengths in model set 2 were chosen to be 1.667 mm. This was done such that various inner span lengths and crack lengths, in 5 mm increments, could easily be specified (cf. Table 1). Also, our mesh refinement studies indicated these elements to be sufficiently small to capture the details of load transfer between the two crack faces in the areas of load application. For both the 3ENF and 4ENF models, it was found that this region of load transfer was confined to an area of approximately 1.7 mm to either side of the outer support point, i.e., over a total length of two elements for model set 2. Contact constraints, with a built-in small-scale sliding routine, were applied within this region that prevented crack face overlap and allowed for various values of the coefficients of static and dynamic friction to be specified. For the 4ENF, load transfer at the right side load, P_R, was also found to occur over a region approximately 1.7 mm on either side of the point of load application, and contact constraints were also applied at these points. Figure 2*b* shows the near-tip region that was used on all models. The mesh refinement technique used in the figure was extensively studied in Ref 8, and the recommendations of this work were therefore followed without modification.

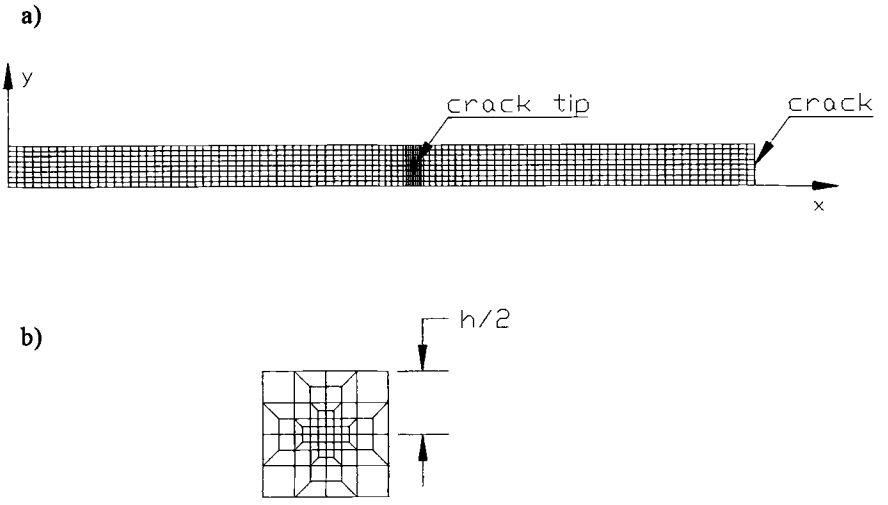


FIG. 2—*Finite-element mesh:* (a) *global view;* (b) *crack tip view.*

Methods of Modeling Friction

Two different methods were used to model friction between the crack faces. Initially, the approach of Ref *6* was followed. In this approach, frictional effects were assessed through a two-step procedure. In the first step, a geometrically linear finite-element (FE) analysis was performed using crack face contact constraints and frictionless sliding; i.e., the coefficient of friction was considered to be zero. Although the contact problem was solved incrementally, a geometrically linear formulation was used for this step. At each node of the delaminated interface that showed contact pressure, the frictional force F was calculated by $F = \mu N$, where N is the normal force at each node as found in the FE analysis and μ is the desired coefficient of friction. These computed frictional forces were then applied at the appropriate nodes along the delaminated interface and a second FE run was performed. For all cases, the normal forces from this second run were unchanged and the approach was assumed to have "converged" [*6*]. The ERR was calculated from the near-tip forces and displacements of this second run using the virtual crack closure technique [*9*]. For an ENF specimen (from model set 1) with $\mu = 0.5$, we compared our results to those of Ref *6* and obtained results that were within 2%. Since the results of this reference were presented in the form of graphs, much of this difference may have been due to interpolation.

To reduce the effort in modeling, a second method of assessing frictional effects was developed. To this end, the frictional interface contact formulation in Abaqus Version 5.8 was used directly, and ERRs were computed by the virtual crack closure technique from the near-tip nodal forces and displacements from this single FE run. A geometrically linear formulation was once again used, where the load was applied incrementally and the contact conditions were updated with each load increment. To assess the accuracy of this second approach, results were compared to those of the first approach described above. Rather than using the default penalty method formulation in Abaqus, which allows small sliding of "sticking nodes," it was found that the more computationally intensive LaGrange formulation was required. This formulation inhibits any relative motion when the surfaces are sticking. Typical comparisons between this new approach and the first approach are shown in Fig. 3. The figure presents ERRs as predicted by the two approaches for the 4ENF specimen, model set 2, geometry "A," for cases where $\mu = 0$ and $\mu = 0.5$. The crack tip is assumed to be within the inner span. Energy release rates in the figure are normalized by the classical beam theory prediction for this

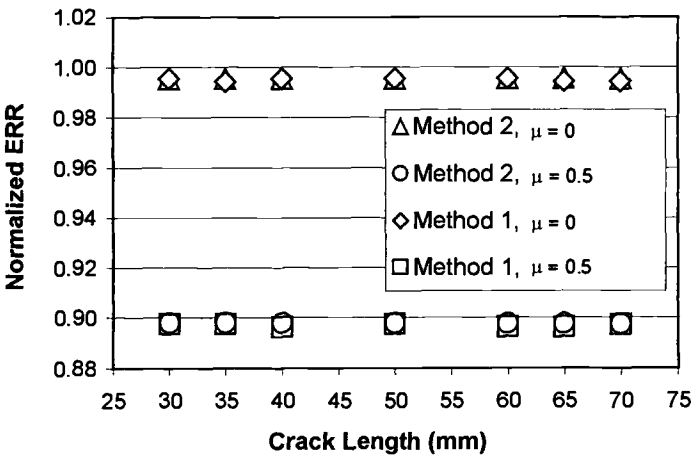


FIG. 3—*Comparison of methods for obtaining ERRs for 4ENF, geometry A, model set 2.*

geometry, given by [*1*]

$$G_{CBT}^{4ENF} = \frac{9P^2 S_L^2}{16B^2 Eh^3} \tag{1}$$

Here, P is the total applied load ($= P_L + P_R$), B is the specimen's width, E is the longitudinal Young's modulus, and S_L and h are as defined in Fig. 1. In Fig. 3, the results labeled "Method 1" refer to those where the modeling approach of Ref *6* was used, and those labeled "Method 2" refer to those where the contact algorithm in Abaqus Version 5.8 was used directly. It is clear that both methods give equivalent predictions of ERR. The results in Fig. 3 were obtained using a unit load. However, since this is a linear problem, the ERR will scale with the square of the load, and the absolute value of applied load is unimportant. For verification, we considered various values of applied loads with the both modeling approaches and found this to be the case. Thus, linear normalizations are used throughout this work, and all subsequent results are obtained using modeling method 2.

Frictional Effects on Perceived Toughness

Virtual Crack Closure Technique

Typically, when the ERR is determined by FE analyses and the virtual crack closure technique (VCCT), friction is not considered, i.e., in the FE model the coefficient of friction of the crack faces is set equal to zero. Let us momentarily assume that data reduction from a 4ENF test with geometry A is performed using this method and there is no modeling error. This approach would lead to the "perceived" toughness given by the "$\mu = 0$" results in Fig. 3. Suppose now that the material's coefficient of friction is equal to 0.5, and the FE model with friction is also exact. The results in Fig. 3 denoted as "$\mu = 0.5$" would provide the "true" toughness, as this approach separates the energy lost into that dissipated by friction and that used for crack advance. Thus, for the 4ENF, it can be seen that the ratio of "perceived" to "true" toughness is approximately 1.11; i.e., in this geometry, delamination face friction causes the toughness to appear 11% larger than its true value at all crack lengths. For the 3ENF, model set 2A, the ratio of perceived to true toughness was found to be 1.04, essentially the same ratio as reported in Refs *6* and *7*. This gives the first indication that frictional effects are significantly larger in the 4ENF than 3ENF configuration.

Compliance Calibration

The preceding approach is illustrative for assessing the influence of frictional effects and is similar to the way this issue has been examined in the past [*6,7*]. However, one does not generally use the VCCT for the reduction of test data, and this method is therefore not indicative of what one would obtain in practical applications. The most commonly used technique to reduce 3ENF and 4ENF data is compliance calibration [*1–5*]. The fundamental equation used for this method is given by [*10*]

$$G = \frac{P^2}{2B}\frac{\partial C}{\partial a} \tag{2}$$

where G is the total ERR, P is the total applied load, C is compliance and a is crack length. In deriving Eq 2, it is assumed that the system is linear and all energy lost goes into driving the crack [*10*]. Thus, this equation is not strictly valid for systems where frictional effects are present. To truly assess the effect of friction on the perceived toughness, it is therefore necessary to simulate the compliance calibration method of data reduction and compare these results to a method that is valid when frictional effects are present, such as the VCCT-based approach described previously.

To investigate the above issue, the models of set 2 were used to determine the compliance of the 3ENF and 4ENF specimens as a function of crack length. For 3ENF, the compliance was defined as

the centerpoint deflection divided by the applied load. For the 4ENF, compliance was defined as $C = \delta/P$, where P is the total applied load ($= P_L + P_R$) and

$$\delta = \frac{w_L + w_R}{2} \tag{3}$$

Here, w_L is the displacement below the left load, P_L, and w_R is the deflection beneath the right load, P_R [*1*]. In all cases, deflections were taken from either the center node, with respect to the FE model's thickness, or the bottom-most node. This was done to eliminate effects of the local contact deformation on compliance [*1*]. In all cases, deflections at a given x location were found to be the same at these two thickness locations. Once the compliance versus crack length data was obtained from a model, these data were fit with a polynomial expression, substituted into Eq 2, and used to determine the ERR as a function of crack length. For 3ENF, a third-order polynomial was used of the form [*3*]

$$C = C_o + C_1 a + C_2 a^2 + C_3 a^3 \tag{4}$$

Other curve fits, such as dropping the second-order term [*2*], were also investigated and found to have a negligible effect on results. For 4ENF, linear through fourth-order polynomials were considered. The linear expression gives ERRs that are independent of crack length. All other fits gave values that, at any crack length, differed from the results of the linear expression by less than 0.1%. In what follows, results from the linear curve fits are presented.

To check the simulated compliance calibration (CC) procedure, we initially did this with a coefficient of friction of zero and compared the CC results, at any crack length, to ERRs obtained by the VCCT (with $\mu = 0$). In all cases, these values differed by less than 0.2%. Next, all models were run with nonzero coefficients of friction. These results were reduced in two ways. The first was by simulated CC as described above, which is expected to correspond to the perceived toughness from a test where the CC method of data reduction is used. The second was by the VCCT. This approach is considered to yield the true toughness.

Figure 4 shows how the perceived toughness as obtained by compliance calibration compares to the VCCT results. As before, 3ENF and 4ENF configurations of model set 2, geometries A are con-

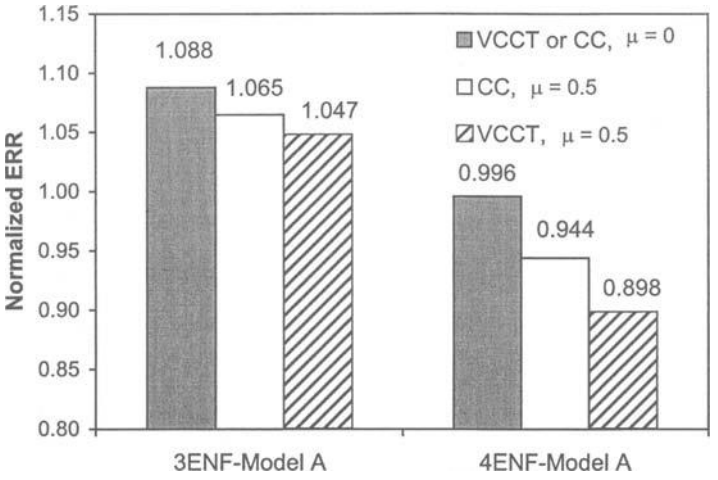


FIG. 4—*ERRs from various data reduction techniques.*

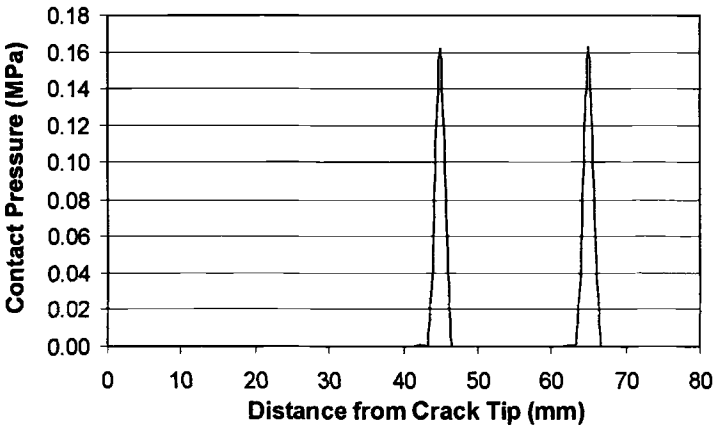


FIG. 5—*Pressure distribution for 4ENF, geometry A, model set 2,* a = *65 mm.*

sidered. All ERRs in Fig. 4 are normalized by the appropriate classical beam theory predictions. For 4ENF, Eq 1 is used; for 3ENF, the beam theory solution is given by [*2,3,6,7*]

$$G_{CBT}^{3ENF} = \frac{9P^2a^2}{16B^2Eh^3} \tag{5}$$

The results for 4ENF presented in Fig. 4 are independent of a for crack lengths between 35 and 65 mm.

Referring to Fig. 4, the bars labeled as "VCCT or CC, $\mu = 0$" are the results where friction is ignored and, as mentioned previously, are the same for the two analysis techniques. The bars labeled as "VCCT, $\mu = 0.5$" represent the "true" energy release rates at a coefficient of friction of 0.5. It is pointed out that the ratio of the ERR as found by the VCCT at $\mu = 0$ to that at $\mu = 0.5$ is the same as presented in Fig. 3: 1.04 for 3ENF and 1.11 for 4ENF. Next, consider the ERR obtained by the simulated CC procedure, denoted as "CC, $\mu = 0.5$." This represents the toughness that will be obtained by users of the two tests. Because compliance calibration comes from the models that have nonzero coefficients of friction, a certain amount of frictional effects show up in the ERR as obtained by this method. As might be expected, the CC, $\mu = 0.5$ results fall between those from the $\mu = 0$ values, where friction is totally ignored, and the VCCT, $\mu = 0.5$ results, where friction is fully accounted for. Thus, if data reduction for these geometries were performed by CC, the perceived toughness would be 2% higher for 3ENF and slightly over 5% higher for 4ENF as compared to the true value.

Note from Fig. 4 that the effect of transverse shear deformation on the ERR, as indicated by the difference between the $\mu = 0$ and beam theory predictions, is larger in the 3ENF than the 4ENF. This was one of the observations that led to the postulate [*1*] that friction would be less important in the 4ENF than the 3ENF test. To understand how crack face friction affects the results of the two tests, it is useful to examine the contact regions between the upper and lower leg of the test specimens. As described previously, it was observed that these regions extended approximately 1.7 mm to either side of the locations where forces were introduced, i.e., above the right side support for both specimens and, for 4ENF, additionally at the right loading point. Figure 5 shows a typical pressure distribution along the crack for a 4ENF specimen, model set 2, geometry A, at a crack length of 65 mm and 1 N of applied load. The contact pressure at 65 mm represents the right side support point, and the pressure at 45 mm represents the right load point. Integrating this contact pressure reveals that the force normal to the cracked surface equals approximately 0.25 N in each contact region. For a coefficient

of friction of $\mu = 0.5$, this leads to a frictional force of 0.125 N in each contact area and a total frictional force along the crack faces of 0.25 N. For the 3ENF geometry, the same contact pressure distribution is found at the right support point, i.e., 0.25 N of normal force and, for $\mu = 0.5$, 0.125 N of frictional force. Thus, the total frictional force present in the 4ENF is double that in the 3ENF, simply because there are two points in the 4ENF where load transfer occurs across the crack faces. This qualitatively explains the larger frictional effects in the 4ENF than the 3ENF observed in Fig. 4 and in previous experimental results [*1,4*].

Influence of Inner Span Length

In a recent work, the influence of the length of the inner span on toughness as found by the 4ENF and 3ENF tests was investigated [*4*]. Several experiments were performed, starting with the 4ENF test at a ratio of inner versus outer span $d/2L = 0.6$ (cf. Fig. 1), then decreasing this ratio until the specimen was finally tested in the 3ENF configuration ($d/2L = 0$). As described in the introduction, it was found that G_{IIc} monotonically decreased with decreasing inner span length. To investigate this effect, model set 2 was used to perform analyses for $d/2L = 0.6$, 0.5, 0.4, and 0.0. Coefficients of friction of 0.3 and 0.5 were considered. Based on experimental results reported in Ref *6*. it is expected that a graphite/epoxy specimen with a preimplanted delamination would have a true coefficient of friction within this range.

Figure 6 presents the results of the above study for a coefficient of friction equal to 0.3, and Fig. 7 presents results for $\mu = 0.5$. All results in both figures are normalized by the ERR obtained by the VCCT with frictional effects included, i.e., by the "true" toughness. Thus, the height of the bars in the figures represent the ratio of perceived to true toughness as obtained by the different data reduction techniques. In the legend, VCCT represents the toughness that would be obtained if data reduction were performed by the VCCT with standard FE analyses and $\mu = 0$. As before, it is assumed that there is no modeling error. The CC values represent results that would be obtained if data reduction were performed using compliance calibration. That is, the VCCT results have no frictional effects at all, and the CC results have frictional effects only as they would be accounted for through an actual CC procedure. The FE models used to generate the results in these figures are 3ENF-A and 4ENF-A, B, and C, which have $d/2L$ ratios equal to 0.6, 0.5 and 0.4, respectively (cf. Table 1*b*). The 4ENF results of Figs. 6 and 7 were found to be independent of crack length for crack lengths that are at least 10 mm inside of the loading rollers.

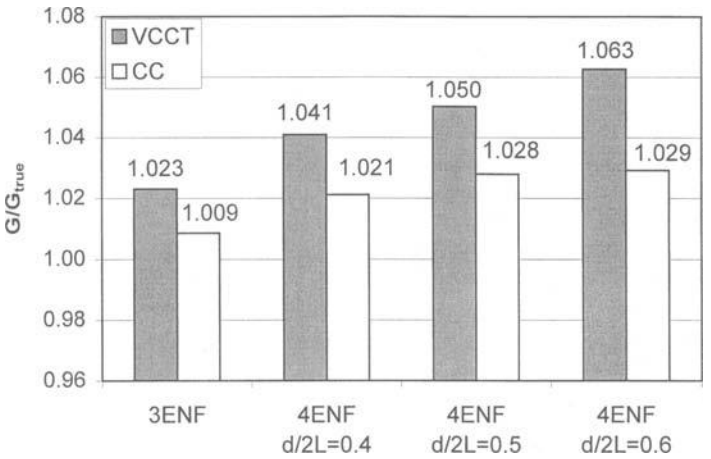


FIG. 6—*Perceived vs. true ERR for* $\mu = 0.3$.

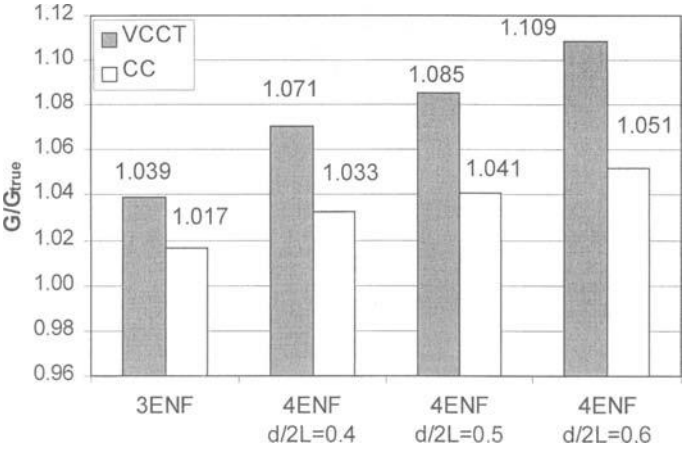


FIG. 7—*Perceived vs. true ERR for* $\mu = 0.5$.

Figures 6 and 7 qualitatively reflect the results of decreasing toughness with decreasing $d/2L$ that were obtained in Ref *4*. For $\mu = 0.3$ and the CC method of data reduction, it is seen from Fig. 6 that frictional effects are negligibly small for the 3ENF, and remain rather small for the 4ENF, increasing to only 2.9% for $d/2L = 0.6$. For $\mu = 0.5$ and the CC method of data reduction, frictional effects are still essentially negligible in the 3ENF and increase to 5.1% in the 4ENF. This is still quite small if one considers the spread of data in typical Mode II tests [*2,3*]; however, they are perhaps not sufficiently small to be ignored. Rather, it would be preferable to use the smallest possible inner span length in the 4ENF test.

Discussion

The finite-element results presented herein for the relative magnitudes of the perceived toughness from 3ENF and 4ENF tests, and for the effects of inner span length on the perceived toughness from the 4ENF test, agree qualitatively but not quantitatively with previously generated experimental results. That is, the FE results predict the differences in toughness should be smaller than what has been observed. We believe that other issues of concern in the 4ENF test procedure are likely responsible for reported experimental discrepancies. For example, one problem is the correct measurement of crack growth. Generally, the crack length is visually observed and measured on both sides of the specimen during the test [*1,4,5*]. However, in Mode II testing, it is extremely difficult to accurately observe the crack tip location. Also, the delamination front at various increments of crack growth will not necessarily be straight; this will affect the validity of the derivative $\partial C/\partial a$. Finally, in all previous studies on the 4ENF, the testing machine's actuator displacement was used to measure deflection. To get the precise deflection for CC in this test, the deflections beneath the left and right loading points should be independently measured and averaged [*1*]. Otherwise, fixture compliance enters into the expression for specimen compliance. Although this same procedure works well for the 3ENF test, the increased complexity of the 4ENF fixture likely means that there will be more "play" in a 4ENF fixture than a 3ENF, and therefore this effect will be more pronounced for 4ENF than 3ENF.

We have recently performed an experimental investigation into the above issues [*11*]. It was observed that there are considerable differences in the compliances obtained from the two measuring techniques described above, and in crack lengths measured visually versus those measured by ultrasonic inspection (c-scans). It was found that, when deflections and crack lengths were accurately measured, there was little difference in the Mode II fracture toughness as obtained by 3ENF and

4ENF tests, and there was little effect of inner span length on G_{IIc} as obtained by the 4ENF. Complete details and recommendations for conducting 4ENF tests are presented in Ref *11*.

Conclusions

Finite-element analyses of three- and four-point bend end-notched flexure specimens were conducted to assess the effect of friction on the perceived delamination toughness. This study was motivated by results in the literature showing different toughnesses for the same material as obtained from 3ENF and 4ENF tests, as well as an effect of test geometry on toughness in the 4ENF. It was found that frictional effects are quite a bit larger in the 4ENF than the 3ENF configuration, and that for 4ENF, frictional effects become more important with increasing inner span length. However, in all cases, the effect of friction was found to be small. Thus, it was concluded that other experimental issues were responsible for the differences in perceived toughness as obtained by 3ENF and 4ENF tests, and a careful study of these issues should be conducted with the aim of standardizing 4ENF test procedures. Many of these issues were examined in a companion experimental study [*11*].

One other interesting finding of this study was that, when the compliance calibration method of data reduction is utilized, frictional effects on the perceived toughness will not be as large as analyses solely by the VCCT would indicate [*6,7*]. Friction affects the specimen's compliance in a manner to reduce the value of $\partial C/\partial a$ in comparison to that which would be obtained from a specimen with a frictionless crack plane. Thus, the approach adopted herein, where the influence of friction is obtained by comparing results from the VCCT with friction present with those of a simulated compliance calibration procedure with friction present, would appear to be the most accurate means of assessing the effects of friction on perceived toughness.

References

[*1*] Martin, R. H. and Davidson, B. D., "Mode II Fracture Toughness Evaluation Using a Four Point Bend End Notched Flexure Test," Vol. 28, No. 8, 1999, pp. 401–406.

[*2*] O'Brien, T. K., Murri, G. B., and Salpekar, S. A., "Interlaminar Shear Fracture Toughness and Fatigue Thresholds for Composite Materials," *Composite Materials: Fatigue and Fracture, Second Volume, ASTM STP 1012*, P. A. Lagace, Ed., American Society for Testing and Materials, 1989, pp. 222–250.

[*3*] Polaha, J. J., Davidson, B. D., Hudson, R. C., and Pieracci, A., "Effects of Mode Ratio, Ply Orientation and Precracking on the Delamination Toughness of a Laminated Composite," *Journal of Reinforced Plastics and Composites*, Vol. 15, No. 2, 1996, pp. 141–173.

[*4*] Chin, R. J. M., "Fracture Testing of Composite Materials," BEng Project Report, Faculty of Engineering, University of Hertfordshire, U.K., May 1998.

[*5*] Martin, R. H., Elms, T., and Bowron, S., "Characterization of Mode II Delamination Using the 4ENF," Proceedings of the 4th European Conference on Composites: Testing and Standardization, Institute of Materials, London 1998, pp. 161–170.

[*6*] Mall, S. and Kochhar, N. K., "Finite-Element Analysis of End-Notch Flexure Specimens," *Journal of Composites Technology & Research*, Vol. 8, No. 2, Summer 1986, pp. 54–57.

[*7*] Gillespie, J. W., Jr., Carlsson, L. A., and Pipes, R. B., "Finite Element Analysis of the End Notched Flexure Specimen for Measuring Mode II Fracture Toughness," *Composites Science and Technology*, Vol. 27, 1986, pp. 177–197.

[*8*] Davidson, B. D., Hu, H., and Schapery, R. A., "An Analytical Crack Tip Element for Layered Elastic Structures," *Journal of Applied Mechanics*, Vol. 63, No. 6, 1995, pp. 243–253.

[*9*] Rybicki, E. F. and Kanninen, M. F., "A Finite Element Calculation of Stress Intensity Factors by a Modified Crack Closure Integral," *Engineering Fracture Mechanics*, Vol. 9, 1977, pp. 931–938.

[*10*] Broek, D., *Elementary Engineering Fracture Mechanics*, 4th revised ed., Kluwer Academic Publishers, Inc., 1986.

[*11*] Schuecker, C. and Davidson, B. D., "Evaluation of the Accuracy of the Four-Point Bend End-Notched Flexure Test for Mode II Delamination Toughness Determination," To Appear in *Composites Science and Technology*, 2000.

M. König,[1] *R. Krüger,*[1] *and S. Rinderknecht*[1]

Finite Element Analysis of Delamination Growth in a Multidirectional Composite ENF Specimen

REFERENCE: König, M., Krüger, R., and Rinderknecht, S., **"Finite Element Analysis of Delamination Growth in a Multidirectional Composite ENF Specimen,"** *Composite Structures: Theory and Practice, ASTM STP 1383,* P. Grant and C. Q. Rousseau, Eds., American Society for Testing and Materials, West Conshohocken, PA, 2000, pp. 345–365.

ABSTRACT: Two different finite element models have been applied to the analysis of delamination growth in a multidirectional graphite/epoxy ENF specimen, which has previously been investigated experimentally. For a more accurate computation of energy release rates along the delamination front, and particularly the individual mode contributions, a layered 3-D shell finite element has been used. A 2-D finite element, based on Reissner-Mindlin plate theory, has been employed for simulation of the delamination growth. This element incorporates a process layer in which the delamination can grow. The virtual crack closure method is employed in both models to compute the energy release rates along the delamination front. It is postulated that these energy release rates control the development of the shape of the delamination front, as well as the final unstable growth of the delamination, as observed in the experiment.

By a comparison between simulation and experiment it is found that in the present case of pure shear mode (combination of Modes II and III) the Griffith criterion predicts correctly the global delamination growth.

KEYWORDS: interlaminar fracture, mixed-mode failure, delamination growth, energy release rate, graphite/epoxy, ENF specimen, finite element analysis

Delamination is a prevalent state of damage in composite laminates. A survey [*1*] on problems concerning composite parts of civil aircraft shows that delamination, mainly caused by impact, amounts to 60% of all damage observed. In a 1991 *IATA* survey, air carriers reported that about 40% of all damages arise from ground handling and maintenance [*2*]. Up to now, failure caused by delamination is prevented by using empirically determined design criteria, usually based on maximum allowable strains. The common rule is not to exeed 0.3 to 0.4% strain, which is in fact not a convincing strategy for a material that is capable of withstanding 1% strain. Hence, for an optimal utilization of the potential offered by those materials and for being in the position to consider the concept of damage tolerance already in the design phase, it is essential that delamination growth in composite laminates can be predicted.

It is now commonly accepted that for prediction of delamination growth, fracture mechanics is an appropriate tool. For application of fracture mechanics, fracture toughnesses, i.e., critical energy release rates, and in the case of fatigue loading, threshold values of the energy release rates for delamination growth and Paris law parameters, have to be known. For the determination of these data, several simple test specimens and corresponding data reduction schemes have been developed. These include the double cantilever beam (DCB) specimen for Mode I [see ASTM Standard Test Method

[1] Institute for Statics and Dynamics of Aerospace Structures, University of Stuttgart, Pfaffenwaldring 27, 70550 Stuttgart, Germany.

Copyright© 2001by ASTM International www.astm.org

for Mode I Interlaminar Fracture Toughness of Unidirectional Fiber-Reinforced Polymer Matrix Composites (D 5528-94)], the end-notched flexure (ENF) specimen for Mode II [*3*] and the mixed mode bending (MMB) specimen for mixed Mode I and Mode II loading [*4,5*]. Mode III tests are also being developed, e.g., Ref *6*.

In general, these tests are performed with unidirectionally reinforced specimens, such that delamination growth occurs at a 0°/0° interface and the direction of crack propagation is parallel to the fibers. This kind of delamination growth, however, will rarely occur in real structures. Thus, it is of considerable importance to evaluate fracture toughnesses at interfaces with dissimilar ply orientations. Systematically investigating all possible angles $\Delta\theta$ between the fiber orientations of the plies bounding the delamination would be impractical. However, evaluating the energy release rates using a number of selected interfaces could provide a measure of the minimum value. This value would be appropriate for use in design in the sense of a conservative design philosophy.

Although delamination growth in $0°/\theta$ interfaces would be more appropriate to what happens in reality, it has been regarded as useful to design specimens with $\pm\theta$ interfaces for the measurement of Mode II fracture toughness, because in this case, it is easier to establish relatively simple data reduction procedures for obtaining critical energy release rates from the load-deflection test data [*7,8*].

In the present paper two different finite element models are applied for the analysis of an ENF specimen (Fig. 1) in which delamination growth occurs in a $\pm\theta$ interface with $\theta = 30°$. This specimen was investigated experimentally in Ref *8*. The first is a 3-D model that employs a layered 3-D shell element. This model can compute energy release rate distributions along arbitrarily shaped delamination fronts. Due to its three-dimensional nature, this model requires a considerable amount of modeling and computational effort. Therefore, a 2-D model has been developed that is based on Reissner-Mindlin plate theory. With this model, delamination growth can be simulated. However, the simulation is restricted to the Griffith criterion, i.e., the assumption that the development of the delamination front is controlled by the total energy release rate. This restriction exists due to the fact that—contrary to the 3-D model—the separation of the total energy release rate into the individual mode contributions is rather inaccurate. This is caused by the restricted plate kinematics on which the 2-D element is based.

The goal of the application of these two finite element models to the considered ENF specimen is to investigate the ability to predict delamination growth in angle-ply interfaces and to test the validity of the Griffith criterion for the pure shear case, i.e., the case where only Mode II and Mode III are present.

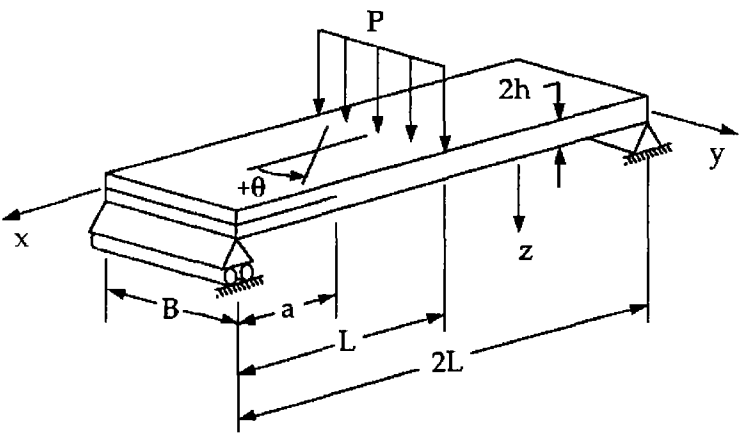


FIG. 1—*ENF specimen.*

Analytical Tools

The most significant step for the current approach is the computation of the distribution of the energy release rates along arbitrarily shaped delaminations fronts, which means that an analytical evaluation of energy release rates—as possible for geometrically simple cases—is not applicable. Computational methods based on finite element (FE) modeling are meaningful and efficient tools by which the energy release rate along the entire delamination front can be evaluated.

Continuum-Based 3-D Shell Element

Due to the extensive computation times already noticeable for 3-D models of simple DCB and ENF specimens [*9*], the development of a *layered volume element* using a continuum-based three-dimensional shell theory [*10*] has been found to be necessary since

- the computation of the complete load path in nonlinear computations using a layer of brick elements for each ply of the specimen will be extremely computer time consuming;
- the standard isoparametric eight- as well as twenty-noded volume elements have the tendency to lock for small element thickness to element length ratios, leading to an unnaturally stiff behavior of the structure during computation; and
- a volume-type element with eight nodes is necessary to assure complete compatibility with the contactor and target elements that are used to avoid structural overlapping in the vicinity of the crack front.

Several orthotropic layers of different orientations may be included in the developed layered 3-D shell element. An extended three-dimensional *ABD* matrix has to be supplied by the user as an input. The individual components of the matrix are calculated as from classical laminated plate theory [*11*] with

$$A = \sum_{i=1}^{m} Q'^{(i)} \cdot [z^{(i)} - z^{(i-1)}] \tag{1}$$

$$B = \frac{1}{2} \cdot \sum_{i=1}^{m} Q'^{(i)} \cdot [(z^{(i)})^2 - (z^{(i-1)})^2] \tag{2}$$

$$D = \frac{1}{3} \cdot \sum_{i=1}^{m} Q'^{(i)} \cdot [(z^{(i)})^3 - (z^{(i-1)})^3] \tag{3}$$

where A denotes the extended membrane stiffness matrix, D the extended flexural stiffness matrix, B the extended coupling stiffness matrix, $Q'^{(i)}$ the off-axis three-dimensional (6×6) stiffness matrix of the ith ply and $z^{(i)}$ and $z^{(i-1)}$ the distances of the surfaces of the ith ply from the element mid-plane as shown in Fig. 2. We thus obtain the relationship

$$\begin{bmatrix} N \\ M \end{bmatrix} = \begin{bmatrix} A & B \\ B & D \end{bmatrix} \cdot \begin{bmatrix} \varepsilon \\ \kappa \end{bmatrix} \tag{4}$$

where N and M denote the column matrices of the force and moment resultants, A, B and D the stiffness matrices, and ε and κ the column matrices of the strains and curvatures, respectively.

The first numerical tests of this element were performed using models of unidirectionally laminated DCB and ENF specimens. These were chosen for study as they had previously been investigated using FE-models consisting of brick elements with 20 nodes [*9*]. These analyses were repeated

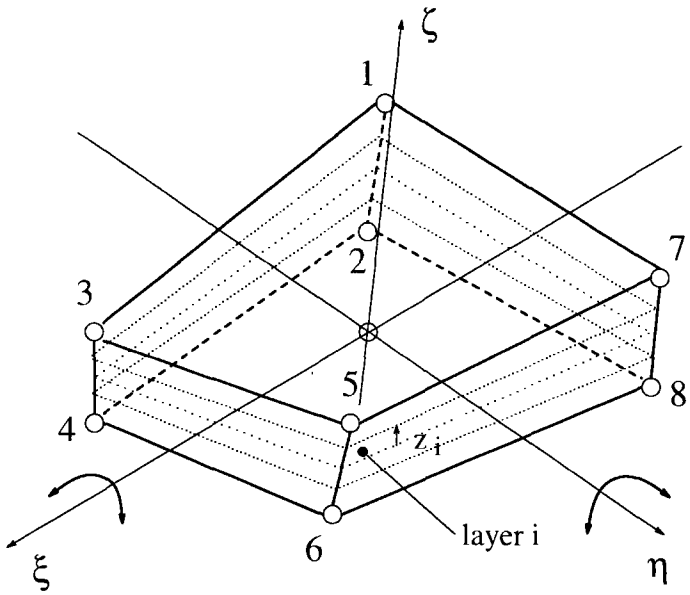


FIG. 2—*3-D shell element.*

using the layered 3-D shell element. This yielded the same results for the energy release rates but simultaneously reduced the computation time up to a factor of six. Additionally, energy release rates were computed for DCB and ENF specimens with a quasi-isotropic layup to validate the possibility of grouping several layers of different orientations in one element [*12*].

Virtual Crack Closure Method

It has been found that the virtual crack closure method is most favorable for the computation of energy release rates, because the separation of the total energy release rate into the contributions by the different crack opening modes is possible in a straightforward manner [*13,14*]. When using this method, only one FE computation is necessary for a given delamination front, which is beneficial especially when solving large, geometrically nonlinear problems.

When using eight-noded elements—such as the 3-D shell element described in the previous section—the procedure for the computation of the energy release rates can be illustrated by Figs. 3 and 4. The crack is virtually closed along the entire delamination front over the distance Δa_1. The energy release rate which is computed for the area ΔA is assigned to node 1′ on the crack front. This is mainly done to obtain the value at a nodal point of the FE mesh, which simplifies data management for postprocessing. For a specimen containing an arbitrarily shaped delamination contour, which is automatically meshed by commercially available software, however, it is not useful to assume an equal element area ΔA along the entire front. Therefore, in the most general case where the element widths b_i as well as the element lengths Δa_i may vary, the relative displacements Δu_1, Δv_1 and Δw_1 computed at node 1 behind the crack front for an element length Δa_1 have to be corrected to fit to the forces $X_{1'}$, $Y_{1'}$ and $Z_{1'}$ computed directly at the front (node 1′) for an element length Δa_2. This may be done by taking into account the shape functions of the elements. For volume elements with eight nodes, the displacements vary linearly along the edges and we obtain the desired values which correspond to the computed forces at point 1′ by linear interpolation ($\Delta a_1 > \Delta a_2$) or linear extrapolation ($\Delta a_1 < \Delta a_2$)

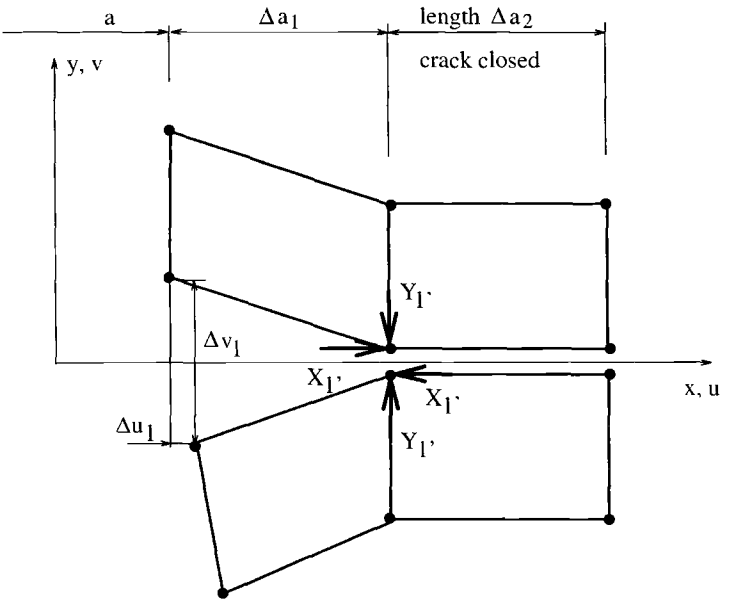


FIG. 3—*Virtual crack closure method, cut through plane of delamination.*

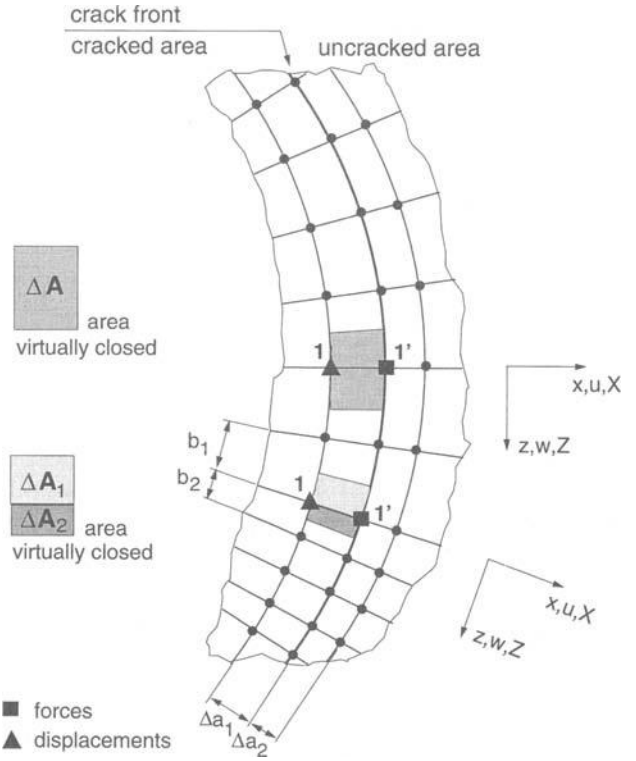


FIG. 4—*Virtual crack closure method, top view of the plane of delamination.*

of the computed displacements at point 1. Furthermore, allowing a variation of the element widths b_i requires an adjusted calculation of the adjacent element surfaces according to $\Delta A_i = \cdot \Delta a_1 \cdot b_i/2$

We thus obtain

$$G_{\mathrm{I}} = \frac{1}{2} \cdot \frac{1}{\Delta A_1 + \Delta A_2} Y_{1'} \cdot \Delta v_1 \cdot \frac{\Delta a_2}{\Delta a_1} \tag{5}$$

$$G_{\mathrm{II}} = \frac{1}{2} \cdot \frac{1}{\Delta A_1 + \Delta A_2} X_{1'} \cdot \Delta u_1 \cdot \frac{\Delta a_2}{\Delta a_1} \tag{6}$$

$$G_{\mathrm{III}} = \frac{1}{2} \cdot \frac{1}{\Delta A_1 + \Delta A_2} Z_{1'} \cdot \Delta w_1 \cdot \frac{\Delta a_2}{\Delta a_1} \tag{7}$$

Other techniques for virtually closing the crack along the crack front are mentioned in Refs *15* and *16*. The virtual crack closure length Δa_1, generally used by the authors, is between one and two times the ply thickness.

Mathematical solutions of the near crack tip field indicate that stresses start to oscillate in the immediate vicinity of the crack tip when crack growth occurs at interfaces between materials with dissimilar properties. These solutions, however, allow the crack surfaces to interpenetrate, which is physically not correct. A nonconvergence of the virtual crack closure method associated with the oscillatory singularity has been observed in previous investigations, e.g., Refs *17* and *18*. Convergence studies carried out on ENF and SLB specimens where crack propagation occurs between layers of different orientations did not show the reported nonconvergence [*12*]. This may be due to a very small bimaterial mismatch of the considered interfaces [*19*]. The issue will be investigated further.

Contact Processor to Avoid Interpenetration in the 3-D Model

Local contact occurring in the delaminated area is a phenomenon that has to be considered in each model used for investigating the delamination behavior. In the zone of contact the delaminated sublaminate is locally supported by the base laminate influencing the deformation behavior of the sublaminate. Using linear elastic finite element analysis, this phenomenon cannot be simulated because an interpenetration of the different layers may not be prevented. Therefore, a nonlinear analysis becomes necessary if the contact problem has to be taken into account.

The contact processor employed in the present study accounts for frictionless contact of deformable bodies by applying the penalty method [*20*]. One of the bodies serves as a so-called contactor, the other as the target, as shown in Fig. 5. The contact problem is described using two independent meshes, one applied to the surface of the three-dimensional mesh representing the body of the contactor, and the other to the surface of the corresponding mesh of the target. This is done to keep the description of the surfaces involved fairly simple. It should be mentioned that these surface elements are not structural elements in the common sense because they do not introduce additional degrees of freedom. Therefore, these surface elements are initialized and handled separately. The nodal points connected to the mesh of the contactor are called dependent nodes; those belonging to the mesh of the target are called guiding nodes. A dependent node can touch a target element that is defined by the guiding nodes along its edges. Using the penalty method, the amount of contact is directly controlled by the penalty factor.

Looking at Fig. 5, the kinematics of the problem is easily explained. Three dependent nodes have penetrated the target, violating the contact condition and thereby creating active contact elements during the finite element computation. An active element consists of the dependent node and the target element involved. The computed stiffness matrix provides the relationship between the contacting bodies and the resulting contact forces. It has to be considered that the contact elements should be kinematically compatible with those elements to which they are attached, thus transmitting the forces

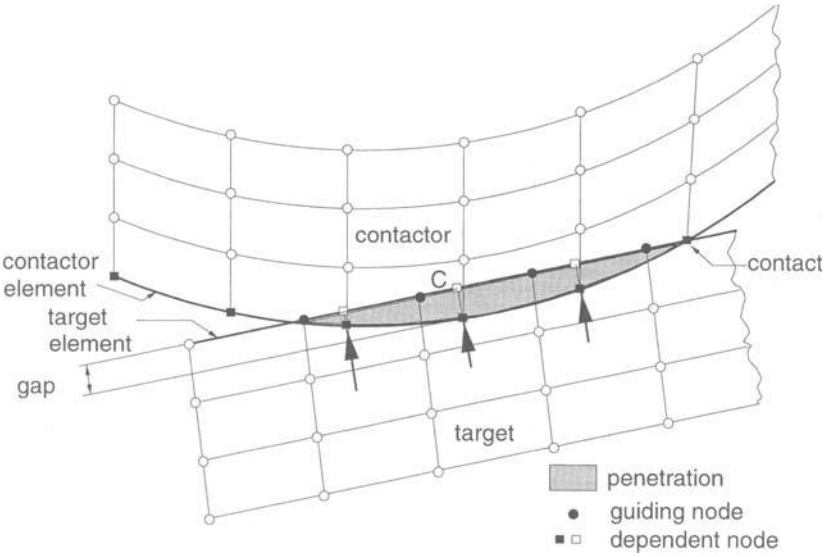


FIG. 5—*Contact analysis.*

of the base elements in a kinematically compatible manner. The algorithm used has to push the nodes onto the target surface following a vector normal to this surface. The intersection with the surface yields the physical location C of the contact. The length of the vector is equal to the distance. In a numerical analysis, contact with a surface can only be achieved within certain limits; the dependent node will always slightly penetrate even if equilibrium is reached. Therefore, the distance is important when checking for the contact conditions. Looking at Fig. 5, we notice that a dependent node is free if the distance is greater than zero and is in contact or penetrates once this distance becomes negative. Defining the maximum allowable penetration as *gap,* the kinematics of the contact problem can be described as follows:

- distance > 0: the dependent node is free;
- *gap* $<$ distance < 0: the dependent node is in contact; and
- distance $<$ *gap:* the dependent node has violated the contact condition and has penetrated. It therefore needs to be brought back to the target surface.

The maximal allowable penetration depth *gap* is a parameter, the value of which is to be set by the individual user. For the current study 1% of the ply thickness was chosen.

2-D Model for Simulation of Delamination Growth

Owing to the high computational effort using three-dimensional models, a finite element model based on the Reissner-Mindlin plate theory was developed in addition for simulation of delamination growth. The so-called delamination process element [*21*] incorporates both the sublaminate and the base laminate as well as a process layer to which the process of delamination growth is spatially restricted (Fig. 6). Owing to the possibility of specifying the damage state in the material law of the process layer,

$$\sigma_{ij} = (1 - \Psi) \cdot C_{ijkl} \cdot \varepsilon_{kl} \qquad \text{with} \qquad 0 \leq \Psi \leq 1 \tag{8}$$

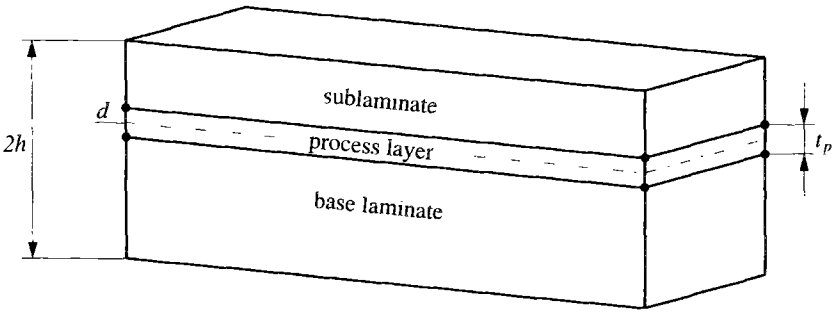


FIG. 6—*Delamination process element.*

the structure may be modeled with only one element over the laminate thickness. The process layer can be formulated as a three-dimensional continuum with finite thickness (Fig. 6) or alternatively as an infinitely thin interface. The latter approach is used in conjunction with the fracture mechanics calculations performed here. Furthermore, the element formulation allows the consideration of contact between sublaminate and base laminate, which is realized by a special control mechanism in the process layer [*21*].

The virtual crack closure method is again applied to this two-dimensional model in order to calculate energy release rates. However, the mode separation leads to unreliable results because the local kinematics in the immediate vicinity of the delamination front cannot be handled accurately by plate theory. However, good results are obtained for the total energy release rate G_T, which depends only on the global energy released by the entire structure and is thus not significantly affected by local errors along the delamination front.

For the simulation of delamination growth, the Griffith growth criterion, indicating that the total energy release rate G_T must exceed the fracture toughness G_c ($G_T > G_c$), is used. In this physically nonlinear calculation, this growth criterion must be checked along the delamination front and, thus, this front has to be traced during the iterative computation in each load step. Physically, it is assumed that a point on the delamination front starts to move if $G_T > G_c$ and stops again as soon as $G_T = G_c$ is reached. The moving delamination front is realized using a moving mesh technique, in which the mesh is geometrically adapted to the delamination front, after the delamination front nodes, moving on fictitious straight lines, are positioned (Fig. 7). The mesh topology, as well as the element node values of the damage parameter Ψ, does not change. Each delamination front node possesses only one motional degree of freedom and, thus, the solution procedure becomes very simple [*22*].

A delamination front with $G_T = const.$ may hence be calculated with this model when the delamination growth simulation is performed up to a state in which the entire front is growing. The iterated equilibrium conditions of each load step are then characterized by $G_T = G_c$ along the entire front.

Analysis of the Initial Straight Crack Front of the Specimen

The first step in the analysis of the considered specimen consisted in the computation of the energy release rate distribution along the initial straight crack front resulting from the foil insert. The layup of the specimen is:

$$[\pm 30°/(\mp 30°)_2/(\pm 30°)_2/\mp 30°/d/\mp 30°/(\pm 30°)_2/(\mp 30°)_2/\pm 30°]$$

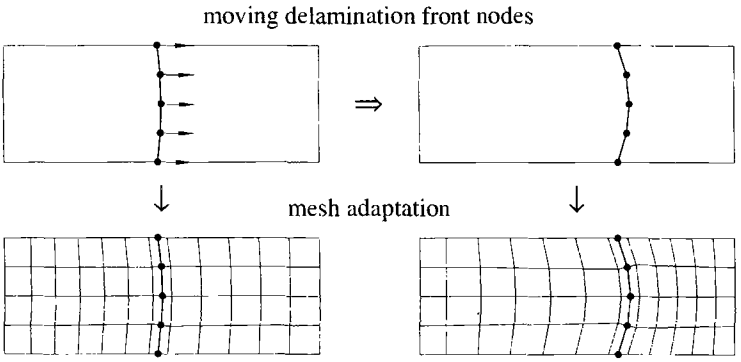


FIG. 7—*Moving mesh technique.*

The symbol d denotes the location of the delamination. The dimensions of the specimen are (see Fig. 1):

Thickness: $2h = 3.048$ mm
Length: $2L = 101.6$ mm
Width: $B = 25$ mm
Crack length: $a = 28.6$ mm

The following material data are assumed for the graphite/epoxy material Ciba Geigy (now Hexcel) C6000/R6376 (consisting of Celion fibers in 6376 resin) used in the experiment (notation according to Tsai [*11*] with subscript 1 denoting the fiber direction):

$$E_1 = 146\,860 \text{ N/mm}^2$$

$$E_2 = E_3 = 10\,620 \text{ N/mm}^2$$

$$E_5 = E_6 = G_{31} = G_{12} = 5450 \text{ N/mm}^2$$

$$\nu_{21} = 0.33$$

$$\nu_{23} = 0.33$$

The ply thickness is 0.127 mm.

The 3-D model has been utilized for the analysis of the initial straight crack front. Due to the existence of $\pm 30°$ plies, models extending across the entire width of the ENF specimen have to be used, as shown in Fig. 8. As shown in the cutout, eight elements were used over the thickness of the specimen, where the two plies above and the two plies below the plane of delamination were modeled with one element over the thickness of each ply, and the outer layers were modeled by grouping several plies together into one element. Across the width of the specimen, a 1.0 mm wide section on both edges was modeled using five elements, whereas the center part of the specimen (≈ 23 mm) was divided into twelve elements. Based on earlier investigations [*12*], penetration of the arms was prevented by introducing an artificial second support as shown schematically in Fig. 9, thus avoiding the contact analysis.

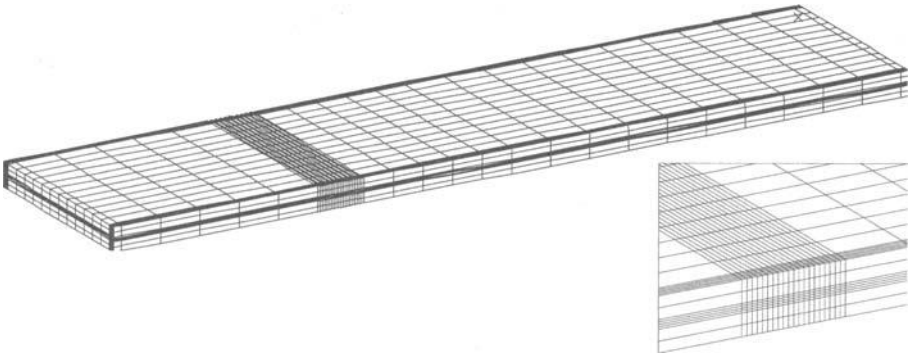


FIG. 8—*Full width model of ENF specimen.*

Looking at the distribution of the energy release rates G_{II} and G_{III} plotted versus the normalized width w of the specimen defined as (see Fig. 1)

$$w = \frac{B - y}{B} = 1 - \frac{y}{B} \tag{9}$$

we basically notice the same overall distribution (Fig. 10) as obtained for UD-layups [*9,12*]. The peaks at the edges of the specimen, however, are more pronounced than for UD-layups, causing the straight front to grow into a curved delamination front (see comparison with experiment in later section). It should be mentioned that the Mode I contribution has been found to be negligible, as expected, for the ENF specimen.

Simulation of Delamination Growth

The simulation of delamination growth in this section by applying the delamination process element is based on the Griffith criterion, with G_c assumed to be 1.4 kJ/m^2. This value was a first estimate of the Mode II fracture toughness of a $\pm 30°$ interface for the material considered. Measurements, performed later, resulted in values of 1.0 kJ/m^2 and 1.2 kJ/m^2, depending on the data reduction procedure that was applied for obtaining critical energy release rates from the load-deflection test data [*8*]. However, as long as geometrical nonlinearities are negligible, which is the case here, the computed delamination contours are independent of the assumed G_c value. Choosing a lower G_c value would only reduce the load levels and deflections corresponding to the different delamination front growth positions simulated.

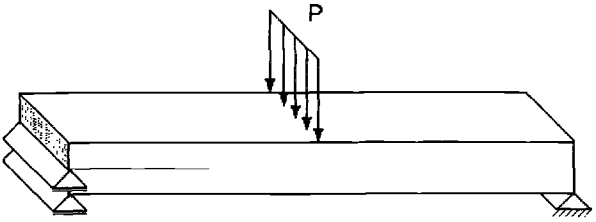


FIG. 9—*Modified boundary conditions for ENF specimen.*

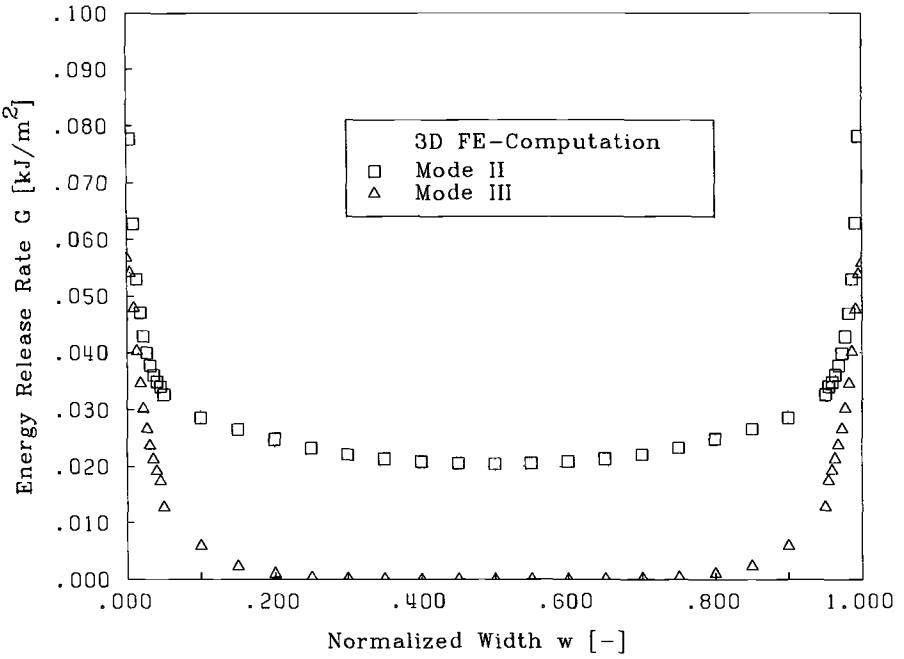


FIG. 10—*Variation of energy release rates across specimen width for external loading* P = *100 N.*

Firstly, delamination growth was analyzed using a rather coarse mesh with 11 equidistant nodes along the delamination front. Figures 11 and 12 show the calculated load-deflection behavior, the magnified structural deformation as well as the mesh movement. On the projected surfaces underneath the meshes, the dark gray shaded areas represent the growth of the delamination. In agreement with the experimental investigations (see comparison with experiment in later section), the application of the Griffith criterion leads to a curved front with increasing delamination growth from the center towards the edges of the specimen. Furthermore, stable delamination growth is observed up to growth position 2, where a sudden change to unstable growth occurs. As the load-growth behavior of Fig. 13 shows, this transition point is caused by the beginning of delamination growth at the front center, i.e., delamination growth occurring along the entire front.

A second simulation was performed using a fine mesh with 23 nodes along the delamination front, distributed with decreasing distances towards the edges (Fig. 14). Thus, a better discretization of a delamination front along which the total energy release rate is constant may be achieved. In this simulation, the converged delamination contour obtained with the coarse mesh for a load of 670 N (at the unstable growth path) was used as a start contour and a new contour was iterated for a load of 650 N. Comparing the results obtained with the coarse and the fine mesh (Fig. 15), we see a significant spatial deviation of the front positions calculated for the same load of up to about 1 mm, but a small difference (less than 3%) in the equilibrium load for fronts with approximately the same spatial position.

Furthermore, a high sensitivity of the energy release rate distribution with respect to the contour shape is observed. Although the two contours of Fig. 16 (both discretized with the fine mesh) show very small spatial deviations, the distributions of the total energy release rate differ significantly (Fig. 17). Hence, the analysis of experimentally measured individual contours will lead to a significant de-

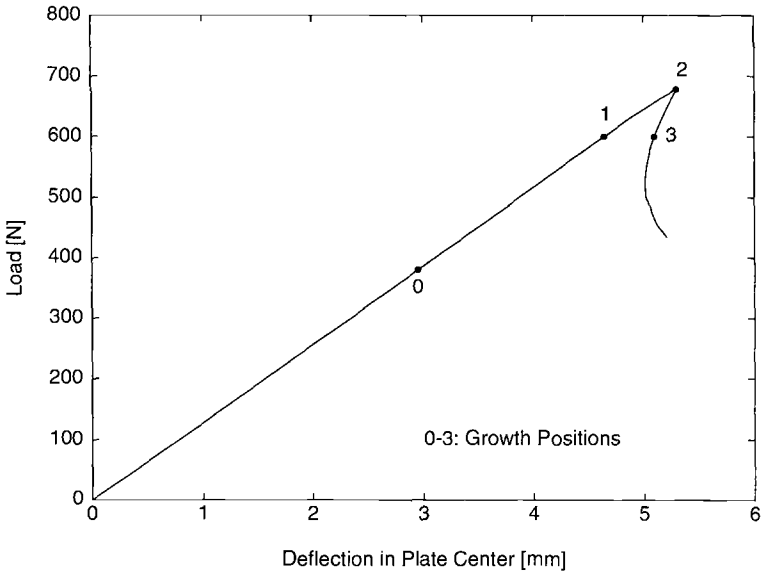


FIG. 11—*Load-deflection behavior for ENF specimen (coarse mesh).*

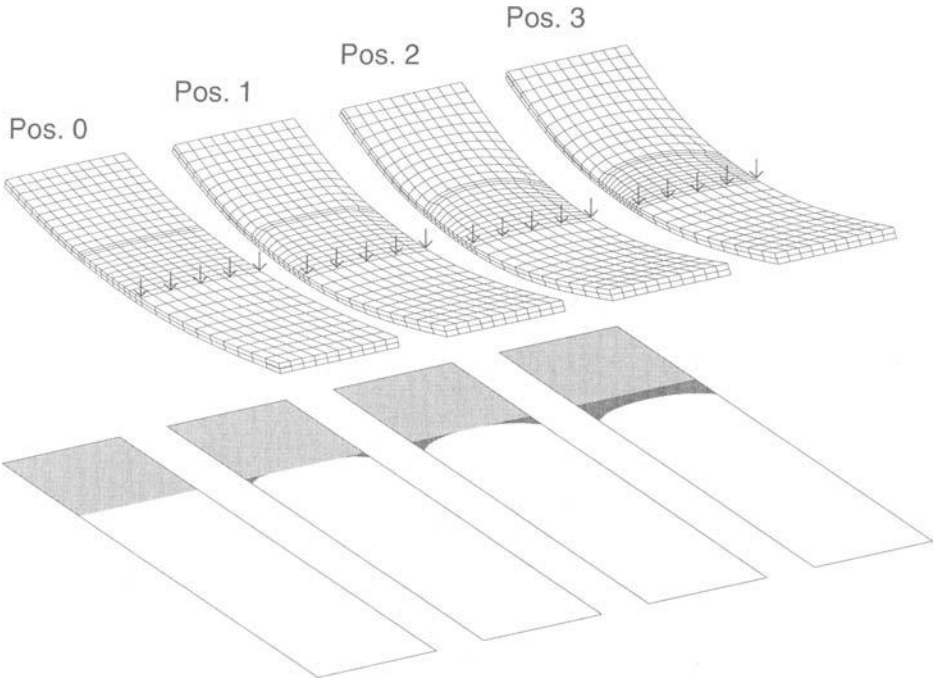


FIG. 12—*Structural deformation for different growth positions (coarse mesh).*

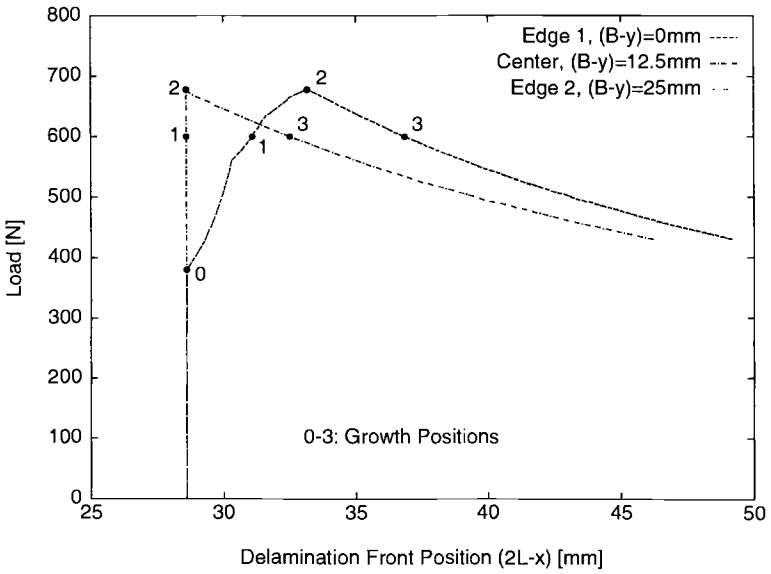


FIG. 13—*Load-growth behavior for ENF specimen (coarse mesh).*

viation from a constant energy release rate distribution, although the applied growth criterion might be well suited for simulation of the average delamination growth behavior.

3-D Computation of Energy Release Rates Along the Simulated Front

The analysis of the initial straight crack front showed, that for the initial straight crack front there exists a significant Mode III contribution to the total energy release rate. Hence, we must ask if for

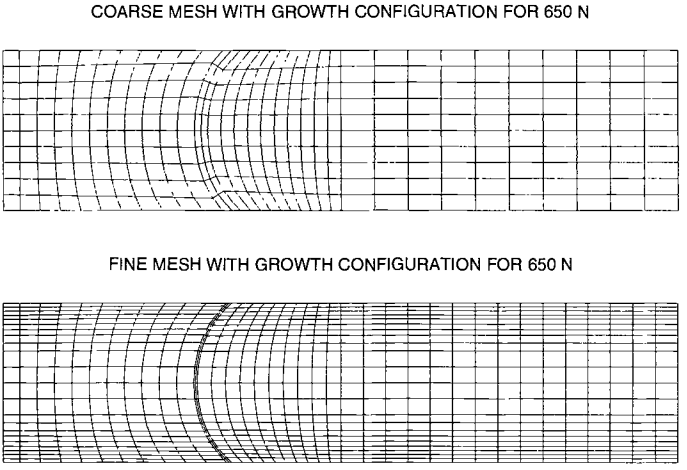


FIG. 14—*Finite element meshes used for 2-D simulation.*

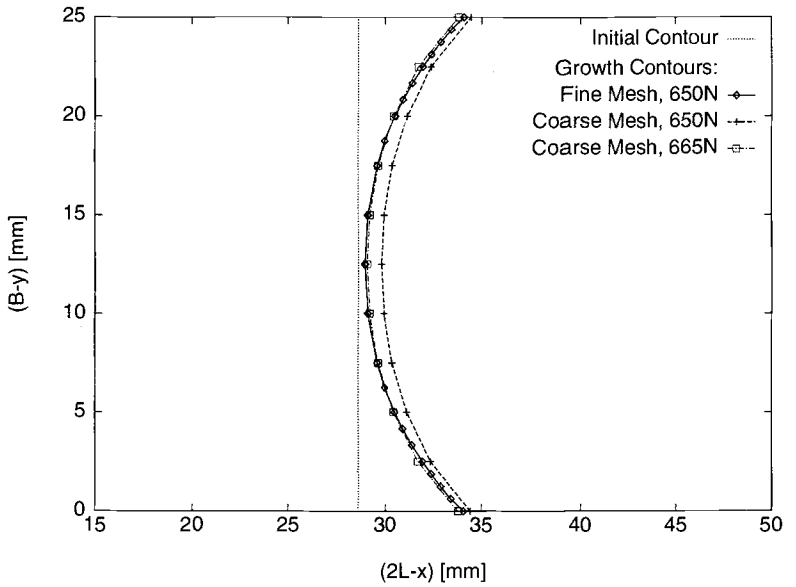


FIG. 15—*Delamination contours with coarse and fine mesh (unstable growth path).*

the delamination front that was iterated in the previous section for $G_T = const.$, G_{III} is also not zero and thus G_{II} is not constant and not equal to G_T. It was mentioned earlier that the 2-D model cannot perform a reliable separation of the total energy release rate into the individual mode contributions. Therefore, a computation employing the 3-D model has been performed. In this computation the ap-

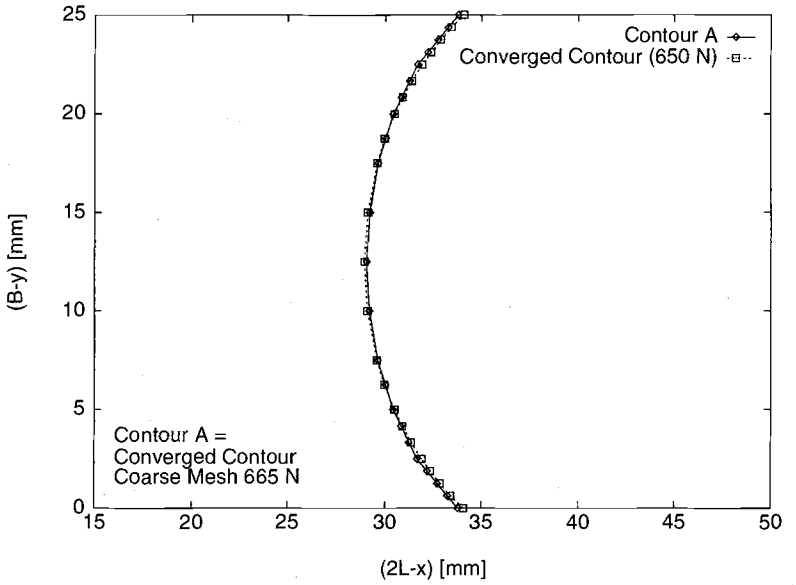


FIG. 16—*Different front contours for fine mesh.*

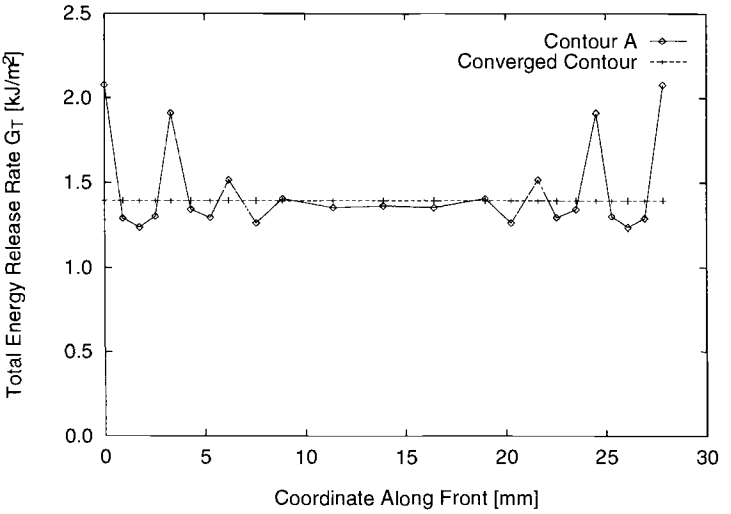


FIG. 17—*Energy release rates along different front contours (fine mesh,* P = *650 N).*

plied load was P_c = 601.2 N, which corresponds to 99.9% of the experimental peak load, i.e., the load observed in Ref *8* immediately before unstable delamination growth occurred.

A detail of the finite element mesh used is shown in Fig. 18. The computed energy release rates are plotted in Fig. 19. It is found that a fairly constant G_T distribution is observed along the front. The deviations from a perfectly straight line are caused by the input for the crack front coordinates. A total of 23 values, as obtained from the investigation in the previous section, was used as input; the contour itself was obtained by a fit. These minor deviations from the contour, as initially iterated, may significantly influence the computed energy release rates along the front (compare previous section). The discrepancy in the zones close to the free edges may, in addition, be caused by the basic difference between the two models. The 2-D model is not able to capture the local deformation in the thickness direction, especially near the free edges of the specimen. This may lead to the fluctuations in the computed energy release rate in this area. It should be mentioned that G_I is again negligible.

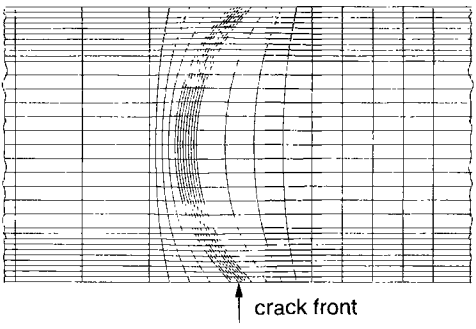


FIG. 18—*Detail of finite element model around computationally determined curved delamination front.*

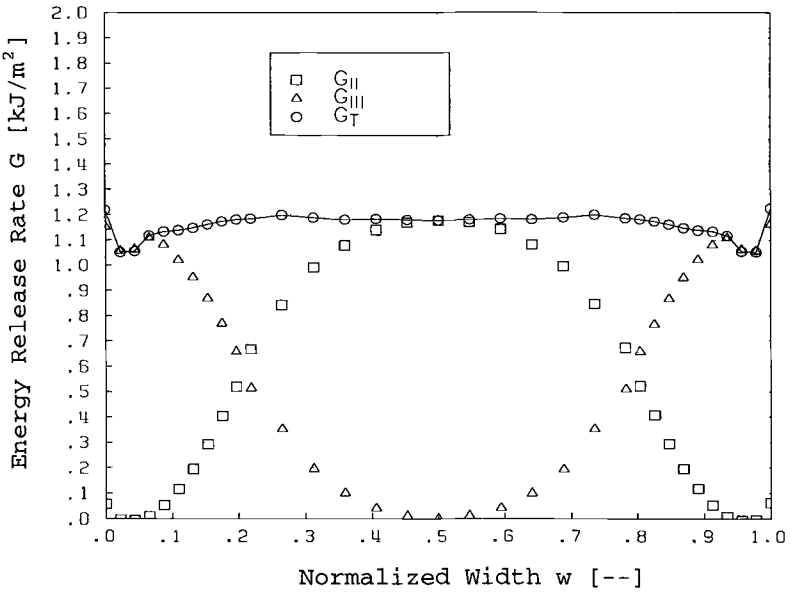


FIG. 19—*Variation of energy release rates across specimen width for specimen with simulated front* (P_c = *601.2 N*).

Regarding Fig. 19, it is evident that, while G_T is nearly constant along the delamination front, G_{II} and G_{III} vary and are equally significant. Hence, when the simulation coincides with experimental observations, it can be argued that the delamination growth is controlled by the total energy release rate, i.e., that the Griffith criterion is valid for the considered case in which G_I is negligible and only G_{II} and G_{III} are present.

Comparison of Observed with Simulated Delamination Growth

Figure 20 shows a sequence of ultrasonic C-scan images that have been obtained by loading the specimen "in stages" until unstable delamination growth occurs. The delamination is growing from the left to the right. The vertical and horizontal scales along the sides of the images are in inches. The light gray area on the right is the uncracked region, the medium gray area on the left is the mid-plane delamination. Figure 20*a* is at zero load, Fig. 20*b* at 96.2% of the critical load of this specimen, Fig. 20*c* is at 99.9% of the critical load, and Fig. 20*d* shows a scan of the specimen after unstable delamination growth had occurred. The dark gray triangles in Figs. 20*b* through 20*d* show that the delamination jumped through a transverse ply crack into the next ply interface and proceeded in that interface over the triangular area. This occurrence might be the reason that the delamination progression was not completely symmetrical with respect to the specimen width. Apart from this fact, the observed behavior compares well with the simulation. This is emphasized by Fig. 21, which shows a comparison of the observed delamination front with the computed delamination front at the stage of the beginning unstable delamination growth. Following the argument at the end of the previous section that the total energy release rate G_T controls delamination growth, i.e., that the Griffith criterion is valid, G_T should be constant along this delamination front, and it should be equal to the shear fracture toughness of the interface. In Ref *8* the fracture toughness of the ±30° interface has been measured employing ENF specimens that had been optimized to minimize Mode III effects. The fracture toughness obtained was 1.2 kJ/m^2 when a plate theory-based data reduction technique was employed,

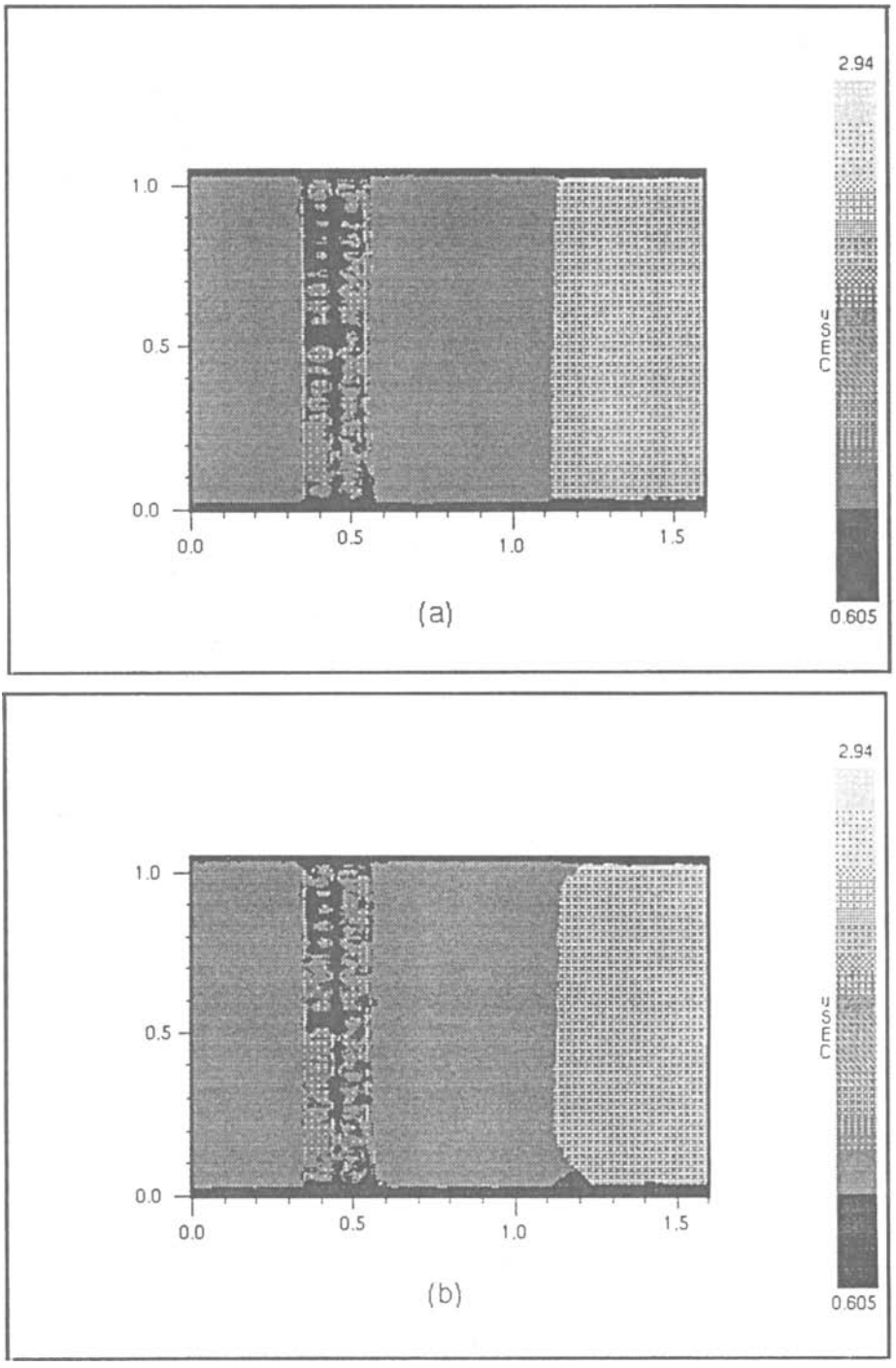


FIG. 20—*Ultrasonic C-scan images, showing various stages of delamination growth.*

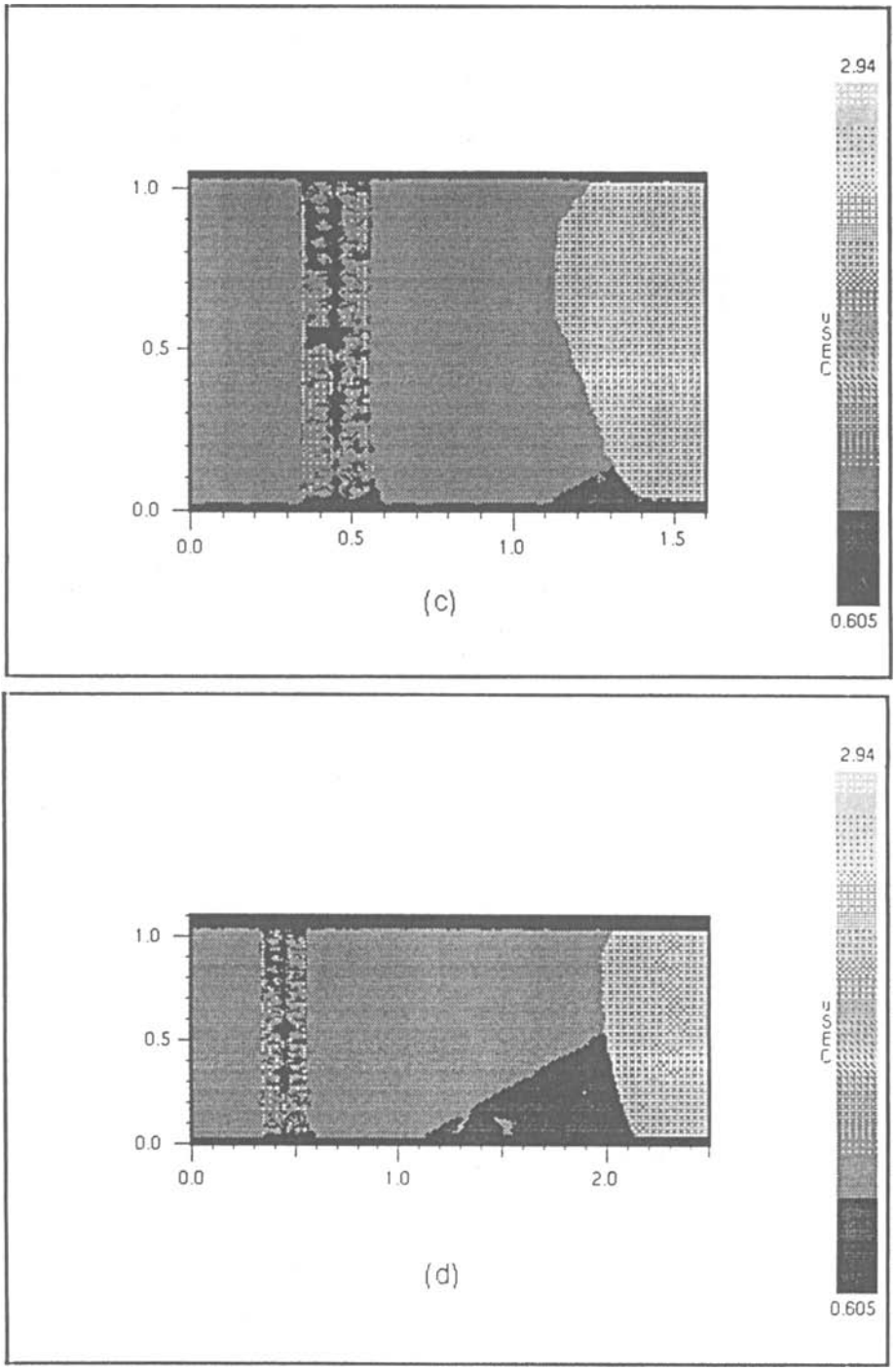


FIG. 20—*(Continued)*

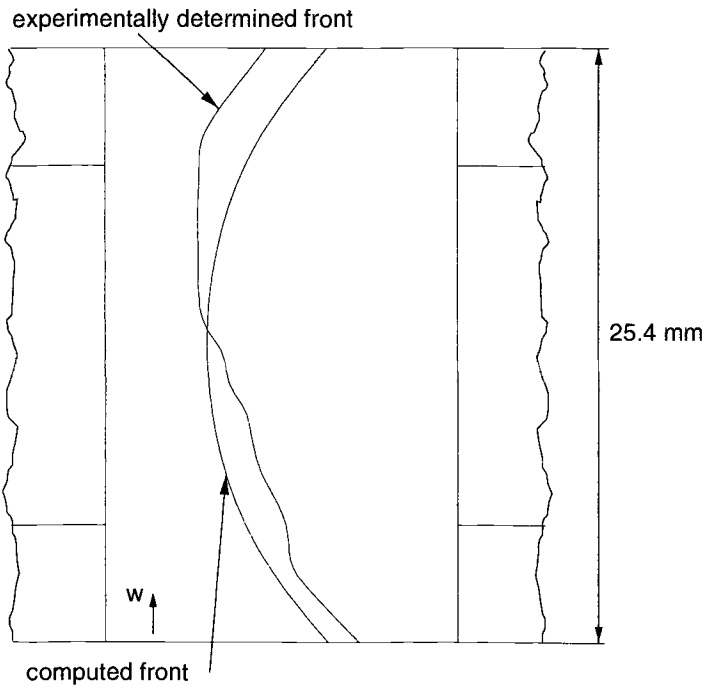


FIG. 21—*Comparison of experimentally and computationally determined delamination fronts at start of unstable delamination growth.*

and it was 1.0 kJ/m^2 when employing a compliance calibration procedure to deduce critical energy release rates from the load-deflection test data. Looking at Fig. 19, it can be seen that G_T is nearly constant along the simulated delamination front, and that the G_T values are in between the fracture toughness values that have been obtained in Ref *8* by the two data reduction methods.

Conclusions

From the adequate correspondence of the observed with the simulated delamination front, which has been obtained under the assumption of the Griffith criterion, the authors conclude that in the case of pure shear fracture, the Griffith criterion is applicable for the simulation of delamination growth. However, the irregular deviations from a smooth delamination front that are observed in the experiment cannot be explained by the energy release rates along the delamination front, because very small perturbations of the delamination front coordinates yield already considerable variations in the energy release rate distributions, as can be seen by comparing Figs. 16 and 17. The observed irregularities must result from a different, probably a micromechanical, mechanism. A micromechanical mechanism, e.g., connected with the fiber direction, could also be the reason for the unsymmetry of the observed delamination front with respect to the specimen width. A second possible reason for this unsymmetry, however, could be the observed ply crack and the associated jump of the delamination into the next ply interface, which were not included in the simulation.

In the present study, we had a case of pure shear fracture. It is evident that in the general case, in which in addition to Mode II and Mode III also Mode I fracture is present, the Griffith criterion cannot be valid, because for the considered material the Mode I fracture toughness is considerably

smaller than the Mode II and the Mode III fracture toughnesses [*6,23*]. However, based on the results of the present study, it seems a likely supposition that it is not necessary to separate the total energy release rate G_T into all three mode contributions for application of an interaction criterion for delamination growth. It should suffice to separate G_T into the Mode I contribution G_I and the total shear mode contribution,

$$G_s = (G_{II} + G_{III}) \tag{10}$$

and to apply an interaction criterion that expresses the critical energy release rate G_c as a function of G_I and G_s,

$$G_c = f(G_I, G_s) \tag{11}$$

Acknowledgments

The authors thank Prof. Barry D. Davidson of Syracuse University, New York, for providing the experimental data, Fig. 1, and the C-scan images presented in Fig. 20.

References

[*1*] Miller, A., Lovell, D., and Seferis, J., "The Evolution of an Aerospace Material: Influence of Design, Manufacturing and In-Service Performance," *Composite Structures*, Vol. 27, 1994, pp. 193–206.

[*2*] McConnel, V., "Getting a Fix on Repair," *High-Performance Composites*, May/June 1994, pp. 19–24.

[*3*] Carlsson, L., Gillespie, J., Jr., and Pipes, R., "On the Analysis and Design of the End Notched Flexure (ENF) Specimen for Mode II Testing," *Journal of Composite Materials*, Vol. 20, Nov. 1986, pp. 594–604.

[*4*] Reeder, J. and Crews, J., Jr., "Mixed Mode Bending Method for Delamination Testing," *AIAA Journal*, Vol. 28, No. 7, 1990, pp. 1270–1276.

[*5*] Reeder, J. and Crews, J., Jr, "Redesign of the Mixed-Mode Bending Delamination Test to Reduce Nonlinear Effects," *Journal of Composites Technology & Research*, JCTRER, Vol. 14, No. 1, 1992, pp. 12–19.

[*6*] Li, J., Lee, S., Lee, E., and O'Brien, T. K., "Evaluation of the Edge Crack Torsion (ECT) Test for Mode III Interlaminar Fracture Toughness of Laminated Composites," *Journal of Composites Technology & Research*, JCTRER, Vol. 19, No. 3, 1997, pp. 174–183.

[*7*] Davidson, B., Krüger, R., and König, M., "Three-Dimensional Analysis and Resulting Design Recommendations for Unidirectional and Multidirectional End-Notched Flexure Tests," *Journal of Composite Materials*, Vol. 29, No. 16, 1995, pp. 2108–2133.

[*8*] Davidson, B., Altonen, C., and Polaha, J., "Effect of Stacking Sequence on Delamination Toughness and Delamination Growth Behavior in Composite End-Notched Flexure Specimens," *Composite Materials: Testing and Design (Twelfth Volume), ASTM STP 1274*, 1996, pp. 393–413.

[*9*] Krüger, R., König, M., and Schneider, T., "Computation of Local Energy Release Rates Along Straight and Curved Delamination Fronts of Unidirectionally Laminated DCB- and ENF-Specimens," *Proceedings, AIAA-93-1457-CP, The 34th AIAA/ASME/ASCE/AHS/ASC Structures, Structural Dynamics and Materials Conference*, La Jolla, CA, 1993, pp. 1332–1342.

[*10*] Parisch, H., "A Continuum-Based Shell Theory for Non-Linear Applications," *International Journal for Numerical Methods in Engineering*, Vol. 38, 1995, pp. 1855–1883.

[*11*] Tsai, S., *Composite Design*, Think Composites, 4th ed., 1988, ISBN 0-9618090-2-7.

[*12*] Krüger, R., "Three-Dimensional Finite Element Analysis of Multidirectional Composite DCB, SLB and ENF Specimens," ISD-Report No. 94/2, Institute for Statics and Dynamics of Aerospace Structures, University of Stuttgart, 1994.

[*13*] Rybicki, E. and Kanninen, M., "A Finite Element Calculation of Stress Intensity Factors by a Modified Crack Closure Integral," *Engineering Fracture Mechanics*, Vol. 9, 1977, pp. 931–938.

[*14*] Buchholz, F., Grebner, H., Dreyer, K., and Krome, H., "2D- and 3D-Applications of the Improved and Generalized Modified Crack Closure Integral Method," *Computational Mechanics '88*, S. Atluri and G. Yagawa, Eds., Springer Verlag, 1988.

[*15*] Raju, I., Shivakumar, K., and Crews, J., Jr., "Three-Dimensional Elastic Analysis of a Composite Double Cantilever Beam Specimen," *AIAA J.*, Vol. 26, 1988, pp. 1493–1498.

[16] Shivakumar, K., Tan, P., and Newman, J., Jr., "A Virtual Crack-Closure Technique for Calculating Stress Intensity Factors for Cracked Three-Dimensional Bodies," *International Journal of Fracture*, Vol. 36, 1988, pp. R43–R50.

[17] Raju, I., Crews, J., Jr., and Aminpour, M., "Convergence of Strain Energy Release Rate Components for Edge-Delaminated Composite Laminates," *Engineering Fracture Mechanics*, Vol. 30, No. 3, 1988, pp. 383–396.

[18] Hwu, C. and Hu, J., "Stress Intensity Factors and Energy Release Rates of Delaminations in Composite Laminates," *Engineering Fracture Mechanics*, Vol. 42, No. 6, 1992, pp. 977–988.

[19] Gao, H., Abbudi, M., and Barnett, D., "Interfacial Crack-Tip Field in Anisotropic Elastic Solids," *Journal of Mechanics Physical Solids*, Vol. 40, No. 2, 1992, pp. 393–416.

[20] Parisch, H., "A Consistent Tangent Stiffness Matrix for Three-Dimensional Non-Linear Contact Analysis," *International Journal for Numerical Methods in Engineering*, Vol. 28, 1989, pp. 1803–1812.

[21] Rinderknecht, S. and Kröplin, B., "A Finite Element Model for Delamination in Composite Plates," *Mechanics of Composite Materials and Structures*, Vol. 2, 1995, pp. 19–47.

[22] Rinderknecht, S. and Kröplin, B., "Delamination Growth Simulation with a Moving Mesh Technique," *Advances in Non-Linear Finite Element Methods*, B. Topping and M. Papadrakakis, Eds., 1994, ISBN 0-048749-26-1, pp. 187–197.

[23] Trakas, K. and Kortschot, M., "The Relationship Between Critical Strain Energy Release Rate and Fracture Mode in Multidirectional Carbon-Fiber/Epoxy Laminates," *Composite Materials: Fatigue and Fracture (Sixth Volume), ASTM STP 1285*, 1997, pp. 283–304.

Andreas J. Brunner[1] *and Rolf Paradies*[1]

Comparison of Designs of CFRP-Sandwich T-Joints for Surface-Effect Ships Based on Acoustic Emission Analysis from Load Tests

REFERENCE: Brunner, A. J. and Paradies, R., **"Comparison of Designs of CFRP-Sandwich T-Joints for Surface-Effect Ships Based on Acoustic Emission Analysis from Load Tests,"** *Composite Structures: Theory and Practice, ASTM STP 1383*, P. Grant and C. Q. Rousseau, Eds., American Society for Testing and Materials, West Conshohocken, PA, 2000, pp. 366–381.

ABSTRACT: T-joints are typical structural elements in surface-effect ships. Seven different T-joint sandwich designs made of balsa wood cores and carbon fiber reinforced polymer (CFRP) facings have been compared under quasi-static tensile and compressive loading until failure. The T-joints differ in the details of the bond design between the horizontal and vertical plates. The performance of the designs is assessed based on failure loads and deformations, acoustic emission (AE) data and visual inspection. The design improvements yield an increase of the failure load from around 50 kN to at least 140 kN (corresponding to the failure of the horizontal plate). Preliminary results have been obtained for one repaired T-joint. AE monitoring indicates an early onset of damage and significant damage accumulation at loads around 70% of the ultimate failure load. For some T-joints there are indications for significant damage in zones outside that where final failure occurred.

KEYWORDS: composites, sandwich element, acoustic emission, failure, experiment

In the framework of a European BRITE-EURAM project a number of different designs for sandwich joints (T- and X-shape) have been developed and tested. The aim of the project was to design joints with specified static failure loads by comparing experimental data from full-size structural parts with theoretical simulation and finite-element modeling. Eight different T-joint designs with a balsa wood core and carbon fiber reinforced polymer (CFRP) facings (CF-epoxy) have been developed and built at the Institute for Construction and Building Processes (IKB) of the Swiss Federal Institute of Technology (ETH) in Zürich. A total of 13 T-joints were tested to failure at EMPA under quasi-static tensile, compressive and transverse loading. The design development at each stage was based on the results of the previous tests, all decisions on the designs were taken at ETH. The present paper focuses on the acoustic emission (AE) analysis of the tensile and compressive load tests of seven T-joint designs and compares AE behavior, failure loads and failure mechanisms of the different designs. The T-joints were investigated as part of a study of a modular hull for a surface-effect ship (SES) [*1*]. They represent one possible joint in a SES hull assembled of prefabricated elements. Studies on similar structures are reported, e.g., in Refs *2–5*.

T-Joint Design and Fabrication

The T-joints consisted of prefabricated sandwich elements at the three ends of the "T" and a wet laminated element in the center (Fig. 1). With the exception of the "simple" reference and framework

[1] Scientists, Polymers/Composites-Department, EMPA, Swiss Federal Laboratories for Materials Testing and Research, CH-8600 Dübendorf, Switzerland. The second author's present affiliation: Alusuisse Road & Rail AG, Structural Analysis and Testing CH-8048 Zuerich, Switzerland.

Copyright© 2001by ASTM International www.astm.org

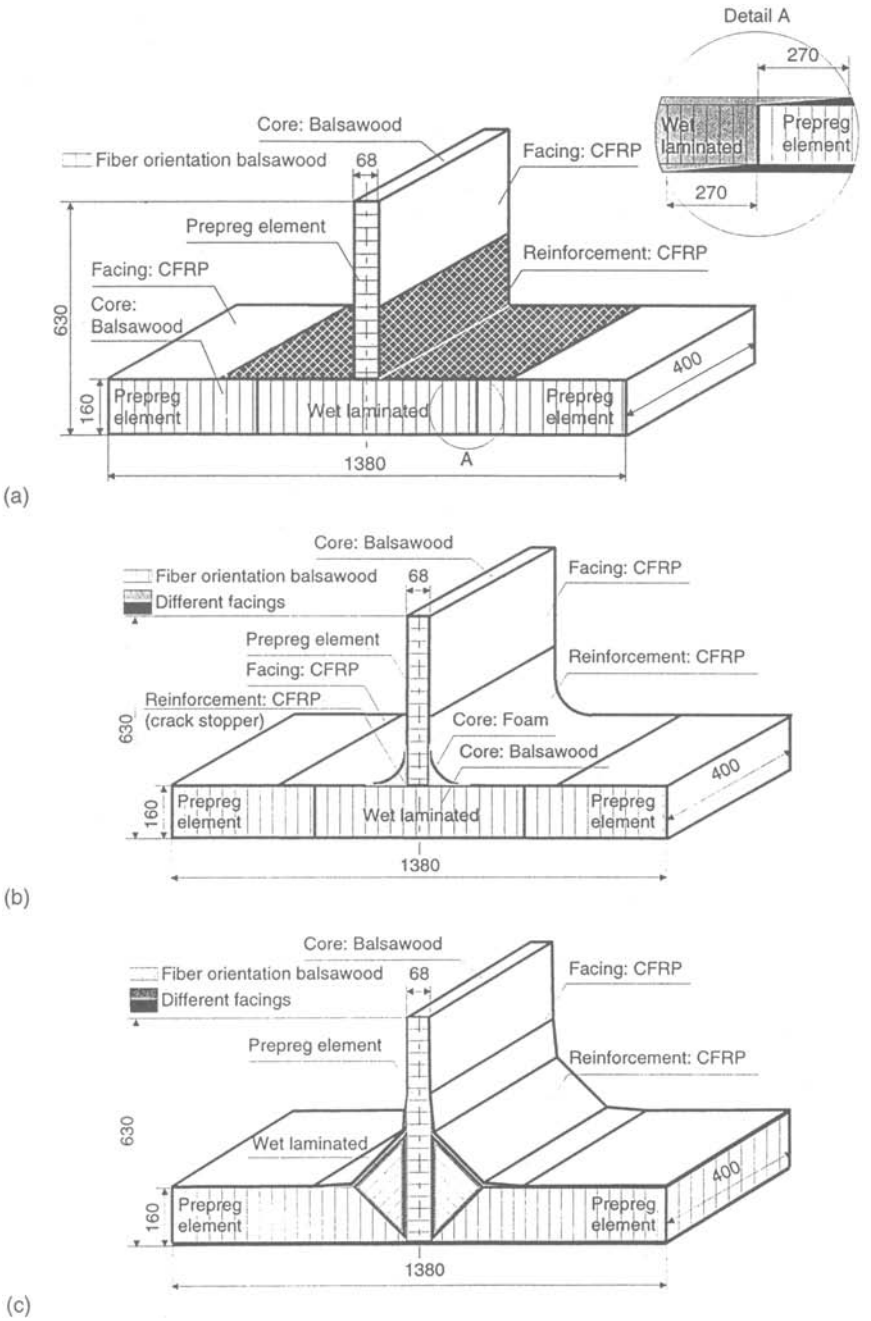


FIG. 1—*Schematic showing the basic design of the sandwich T-joints,* (a) *type A,* (b) *types B, C, D, E, G, and H, crack stopper only in designs E, G, and H,* (c) *type F (for details see Table 1), dimensions are given in mm.*

TABLE 1—*Main features of the different designs (Fig. 1).*

Design	Sandwich	Joint*	Remarks
A	balsa wood core/CFRP	"Simple" joint, no foam	reference part
B	balsa wood core/CFRP	PVC foam 75† with elastic filler‡	
C	balsa wood core/CFRP	PVC foam 200† with elastic filler‡	used for transverse loading only
D	balsa wood core/CFRP	PVC foam 200 spliced§	
E	balsa wood core/CFRP	PVC foam 200, with crack stopper§, ‖	
F	balsa wood core/CFRP	Framework	
G	balsa wood core/CFRP; core sections wrapped with CFRP¶	PVC foam 200, with crack stopper§, ‖	
H	balsa wood core/CFRP, core sections wrapped with CFRP¶	PVC foam 200, with crack stopper§, ‖	same as G, except for orientation of balsa wood in part of the vertical plate

* Refers to features of joint between base and vertical plates (Fig. 1).

† Number refers to nominal density of PVC foam in kg/m^3. The foam, together with CFRP facings, provides the joint between vertical and horizontal plate.

‡ An elastic filler was placed below the vertical plate to avoid single point load introduction [*1*].

§ The vertical and horizontal plate are bonded with a splice.

‖ The crack stopper is an L-shaped laminated bond angle on each side of the vertical plate joining it with the horizontal plate (Fig. 1*b*).

¶ Each of the three sections for the horizontal plate was wrapped with a layer of CFRP before joining, except the front and back side (orthogonal to the *z*-axis in Fig. 3).

designs (type A and F, Table 1) the joint was reinforced with a PVC foam fillet and a CFRP facing. The fabrication steps were: (1) positioning two prefabricated sandwich elements, joining them with the wet laminated sandwich element for the horizontal plate; (2) curing under vacuum and pressure; (3) positioning the prefabricated vertical plate on the horizontal plate; (4) joining of horizontal and vertical plates by either using a bonding filler, a so-called crack stopper (additional L-shaped laminated bond angle on each side of the vertical plate joining it with the horizontal plate (see Fig. 1*b*)) or splicing between the plates; and (5) covering the joining zone with a PVC foam fillet and an additional wet laminated bonding angle (all design types, except A and F). The CFRP facings consisted of a prepreg (2 × 2 twill, 660 g/m^2 areal density, nominal total thickness 9.1 mm for horizontal and 3.9 mm for vertical plate) for the prefabricated and a fabric (1 × 3 twill, 470 g/m^2 areal density) for the wet laminated elements. The taper ratio of the CFRP facings was 30:1 for all designs resulting in an overlap facing length of 270 mm for the horizontal sandwich element (Fig. 1*a*). No fillets were used for design A, and wedge-shaped balsa blocks with CFRP facings joined the plates in design F. T-joint No. F1 was repaired after tensile testing by injecting room-temperature cure resin into the delamination between the CFRP facing and balsa wood core on top of the horizontal plate. The resin was cured at room temperature under an applied load (four clamps near the edges of the horizontal plate) for about six days and the T-joint retested (tension test No. F2).

T-Joint Test Conditions

Table 2 shows the test matrix with design and load types. The tension and compression tests have been performed on a servohydraulic test machine (Instron type 1346) and both types of load were applied in a three-point bending configuration. The loading fixture for the tension tests is shown in Fig. 2, an analogous setup has been used for compression. The T-joints were instrumented with up to eight strain gages (type HBM LY 6/120) and up to three displacement transducers (type W20). The posi-

TABLE 2—*Test matrix with designs and load types.*

Design	Tensile	Compressive	Transverse*
A	1×	...	...
B	2×	2×	...
C	...	...	2×
D	1×	...	...
E	1×	...	...
F	3×†	2×‡	...
G	1×	...	...
H	1×	...	...

* The results of the transverse load tests will not be discussed in this paper.

† Including one T-joint tested a second time after repairs.

‡ T-joints tested under compression without repairs after tension tests.

tions of the strain gages were selected and they were mounted by ETH. Two displacement transducers were mounted on both sides of the vertical plate (Fig. 3), the position of the third (if used) changed from test to test. All tests were performed under displacement control at constant crosshead displacement (1 or 2 mm/min). Visual inspection provided information on the failure mechanisms. Failure location and type were documented and photographed.

Acoustic emission (AE) monitoring [*6*] was used to assess damage accumulation during the tests. Practices for assessing the integrity of composite structures with AE monitoring require a quasi-static load pattern. [ASTM Standard Practice for Acoustic Emission Monitoring of Structures During Controlled Stimulation (E 569), ASTM Standard Practice for Acoustic Emission Examination of Fiber-

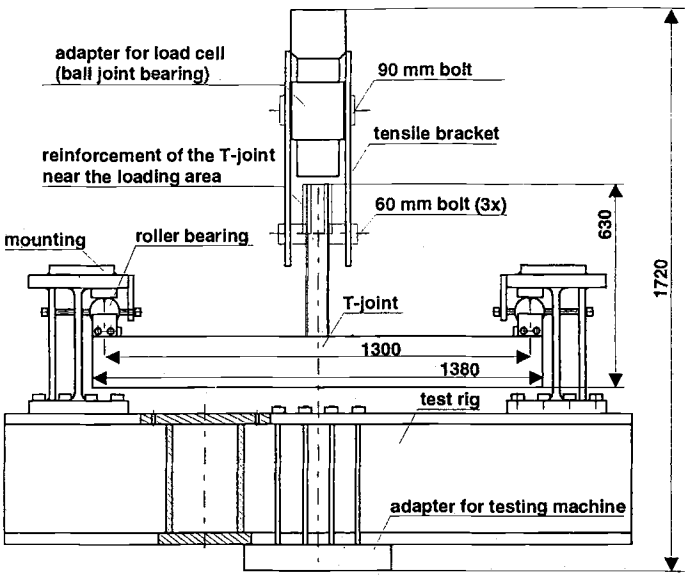


FIG. 2—*Schematic of the test support and load introductions for the tension tests (bolt spacing is roughly 140 mm from center to center, with the center bolt in the middle of the vertical plate).*

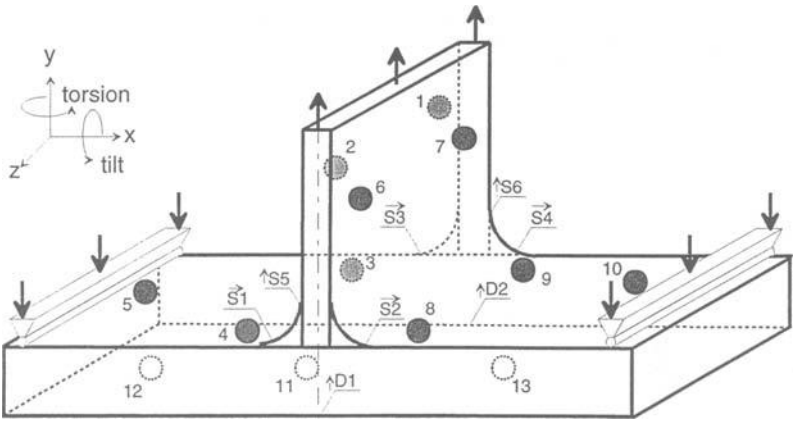


FIG. 3—*Positions of the strain gages (S), displacement transducers (D) and of the acoustic emission sensors (circles numbered 1 to 13) for the last two tension tests (No. G1, H1). The arrows near the S and D indicate the direction of the strain and displacement measurement, respectively.*

glass Reinforced Plastic Resin (FRP) Tanks/Vessels (E 1067)] Loading to failure consisted of subsequent cycles of loading (load step between 5 and 25 kN, Table 3), holding at constant load for 4 min, unloading to the previous hold load, holding for 1 min and reloading to the next higher load level (so-called "stair-step" pattern). In a few cases, holding at constant load has been extended beyond 4 min if high AE activity persisted (see Table 3). The AE signal parameters of between 11 and 15 resonant AE sensors (type SE-150M) were recorded during the tests. Five sensors each covered the top right and top left-hand side of the T-joints. The bottom was covered by one to three AE-sensors (Fig. 3) and for selected tests by two additional sensors with low resonance frequency (type SE 45-H). The threshold was set to 41 dB (referenced to 1 μV at the sensor output), the preamplifier gain to 34 dB, and the rearm time to 3.28 ms. Preliminary tests with simulated AE sources (pencil lead breaks) had shown that the sensitivity of the AE sensors was sufficient to cover the T-joint.

Overview of Test Results

The raw test data were: (1) load-signal as a function of time (test-machine), (2) crosshead displacement signal as a function of time (test machine), (3) strain gage signals as a function of time, (4) displacement transducer signals as a function of time, (5) AE signal parameter set as a function of time, (6) observations during the tests, and (7) visual inspection after testing. From the raw data, load-displacement plots (indicating failure loads, deformation at failure and permanent deformations after unloading), strain gage difference signals (indicating movement of the sandwich element and its parts in the fixture under load), AE activity and AE intensity as a function of load (information on damage growth, failure location and failure mechanisms) were derived. These were compared for each design with the observations during and after the test.

An example of a load displacement plot is shown in Fig. 4. Four features were noted: (1) a start-up range with a nonlinear load increase and then a roughly linear load increase, (2) a change in slope (above 130 kN), (3) a discontinuity in the slope around 140 kN, and (4) a nonlinear unloading curve and a permanent deformation after unloading. With the exception of the discontinuity in the slope, these features were observed in all tests. Where recorded, the permanent deformation amounted to 1 to 2 mm for tensile and to 0.5 to 1.5 mm for compression tests. The failure loads, the crosshead displacements at failure, the number of load cycles to failure and the load step per cycle are summarized

TABLE 3—*Failure loads and crosshead displacements at failure.*

Design, No. Load Type	Load Cycles*	Load Step,† kN	Failure Load,† kN	Displacement,† mm	Remarks
A1 Tensile⊗	2	5	6.7 (5)	7.3 (5)	Reference design, fails during load increase
B1 Compressive	3	50 (5, 5)‖	144 (100)	9.0 (6.1)	Fails during load increase
B2 Compressive	5	25 (5, 10, 10, 15)‖	111 (100, 76)	7.2 (6.2, 4.6)	Fails during load increase
B3 Tensile	2	25 (5, 5, 5, 5)‖	47 (25)	3.5 (2.1)	Fails during load increase
B4 Tensile	10	5 (5, 5, 5, 10)‖	51	3.7	Fails at reaching hold level
D1 Tensile	21	5	105‡ (95)	6.5 (5.9)	Fails after 150 s hold
E1 Tensile	13	10	130 (96)	8.7 (6.2)	Fails at reaching hold level
F1 Tensile	13	10 (2, 5, 6, 6, 6, 6, 6, 6, 8, 6, 6, 6)‖	131‡ (80)	6.1 (4)	Fails after 90 s hold
F2 Tensile	7	10 (2, 4, 4, 4, 4, 4)‖	70‡ (48, 38, 23)	3.4 (2.5, 2.1, 1.5)	Same as F 1 after repairs§, fails after 90 s hold
F3 Compressive	14	10	140 (130, 120, 110, 90, 80)	5.9 (5.4, 5, 4.6, 3.9, 3.5)	Same as F 2 after tension test, fails after 180 s hold
F4 Tensile	10	10	100‡ (90, 80)	5.7 (5.2, 4.8)	Fails after 15 s hold
F5 Compressive	14	10	140‡ (130, 118)	6.5 (6, 5.5)	Same as F 4 after tension test, fails after 120 s hold
G1 Tensile	8	20	160 (132, 148)	8.4 (6.9, 7.8)	Fails at reaching hold level
H1 Tensile	8	20	160 (140, 115)	7.8 (6.9, 5.7)	Fails at reaching hold level

* Number of load cycles until failure.

† Increase in load per load step, respectively.

† Values in parentheses indicate load and displacement levels, respectively, at which changes in the behavior of the structural elements were noted (e.g., audible cracking noise, drop in load, change in slope of load displacement plot).

⊗ A later, detailed analysis of the cross-head displacement, the strain gauge signals and of the bending elasticity of the reference design seems to indicate a larger failure load than that given by the test machine signal. The conclusions of the paper are not affected by these findings.

‖ In some cases, hold duration at constant load was extended beyond 4 min if high AE activity persisted (duration of extended hold in minutes for each step is shown in parentheses)

‡ Failure at constant load, during hold.

§ Room temperature cure, no thermal treatment.

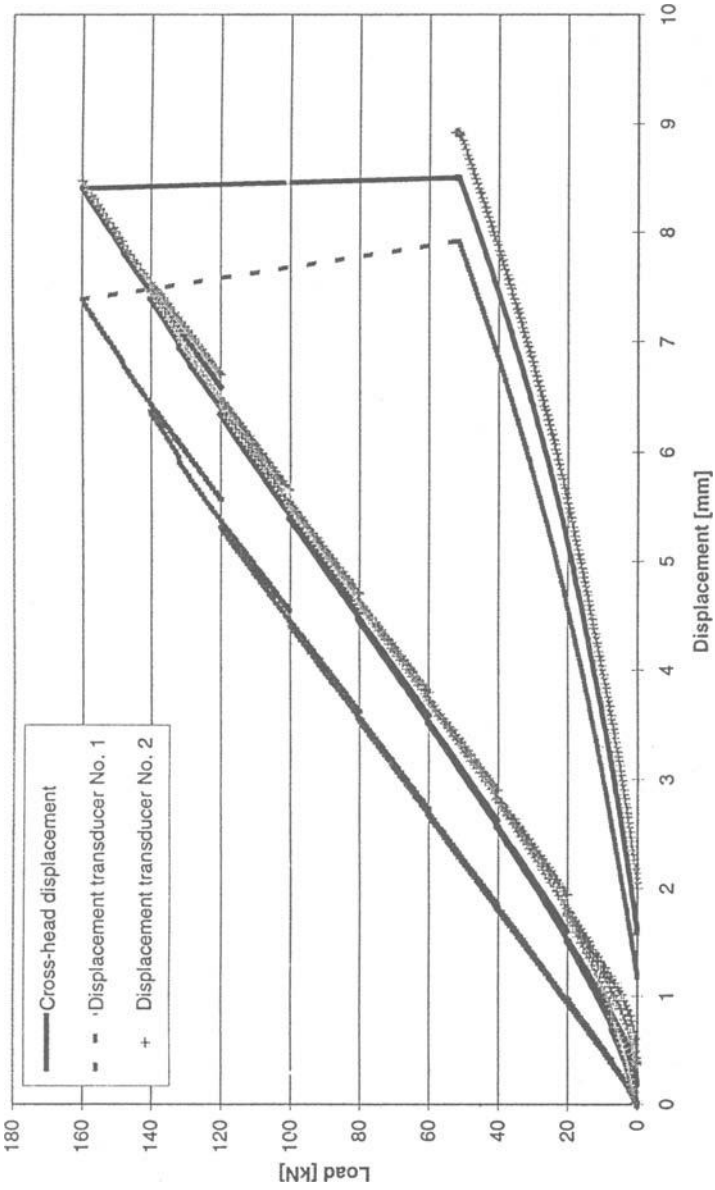


FIG. 4—*Load displacement plot (test machine and displacement transducer signals) from a tensile test (No. G1).*

in Table 3. Failure is defined as a distinct drop in load, either occurring during load increase or at constant load. After failure, the T-joints still sustained a certain load but show visible signs of damage, e.g., cracks or delaminations, often with large crack opening displacements.

Only the strain gage data from tensile test No. G1 are described here. Qualitatively, the strain gage signals follow the load pattern as a function of time. From the nominally symmetric arrangement of the strain gages (Fig. 3) the motion of the element relative to the support may be split into components by suitably calculating differences between the signals (Fig. 5). These components are (1) bending of the vertical plate, (2) bending of the horizontal plate, (3) tilting of the horizontal plate about the x-axis, and (4) torsion of the vertical plate about the y-axis (Fig. 3). As a function of load, these signals (Fig. 5) indicated that all four components were present to some extent.

The AE analysis investigated AE activity, AE intensity, the so-called Felicity ratio (FR) [*6*] and AE signal source location for predicting failure load, failure location and for analyzing failure mechanisms and damage accumulation. The measure used for AE activity is the cumulative number of "hits" (AE signals recorded by each individual sensor) as a function of time (Fig. 6). The ranking of the most active channel (MAC) in each zone of the T-joint indicated failure location (Table 4). Above a certain load level ("threshold load level"), the cumulative AE activity per load step increased significantly for each subsequent load step. A quantitative analysis showed that this threshold load level coincided with roughly 20% of the total cumulative AE activity until failure (Table 5). The FR analysis (Table 6) clearly indicated both failure load and location but cannot be performed fast enough for predictions during the test. Clustering of AE signal source locations was observed in the last load cycle(s) of some tests using a simple triangulation algorithm with a single value of the wave propagation speed. Typically, only 1 to 2% of all AE signal sources could be located for the different designs. AE intensity, measured by AE signal amplitudes, increased with increasing load. The majority of the AE signal amplitudes was between about 60 and 80 dB. Empirically, this amplitude range had been attributed to macrocrack or delamination growth in CFRP and glass fiber reinforced polymer (GFRP) specimens and parts [*7,8*].

During some of the tests, audible noise and changes in the slope of the load displacement plots were noted at certain loads (Table 3). No indication of visible damage was found immediately after these events. The load level during hold (nominally constant load but test machine under displacement control) decreased with increasing hold duration. The amount of this load decrease during hold (here termed "load relaxation") increased with increasing load (Table 7). Observations after failure are summarized in Table 8.

Discussion

The following results will be discussed: (1) load displacement plots, (2) strain gage signals, (3) failure location prediction from AE, (4) failure load prediction from AE, (5) failure mechanisms and damage accumulation, and (6) testing of repaired and damaged T-joints.

The continuous change in the slope of the load displacement plots (Fig. 4) indicated a corresponding change in stiffness. Discontinuities in the load displacement plot at loads below failure (Table 3) were attributed to irreversible changes, i.e., significant damage that could include macroscopic damage (e.g., macrocrack formation and growth). This interpretation is supported by the AE analysis and observations discussed below.

The strain gage signals of design No. G1 under tensile load yielded the signal differences shown in Fig. 5. The different sign and slope of the signals below 40 kN indicated that imperfections of the horizontal plate affected the initial loading. The imperfections resulted in a maximum gap between roller bearing and horizontal plate (Fig. 2) of 1.7 mm at the start of the test. The difference signals also indicated irreversible changes at loads of 120, 130, and 150 kN. Test No. H1 showed similar features at 140 and 150 kN. Due to the choice of the strain gage positions analogous signals were not obtained for the other tests.

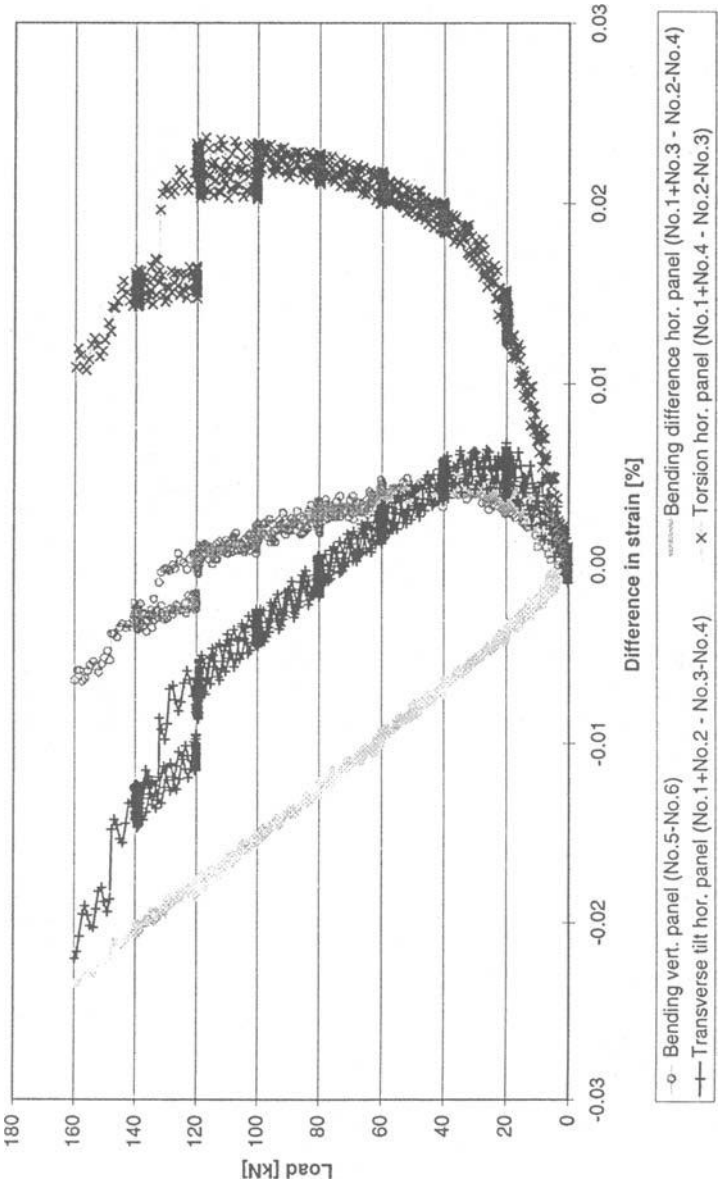


FIG. 5—*Difference of strain gage signals indicating modes of deformation from tensile load test No. G1 (see Fig. 3 for positions of the strain gages).*

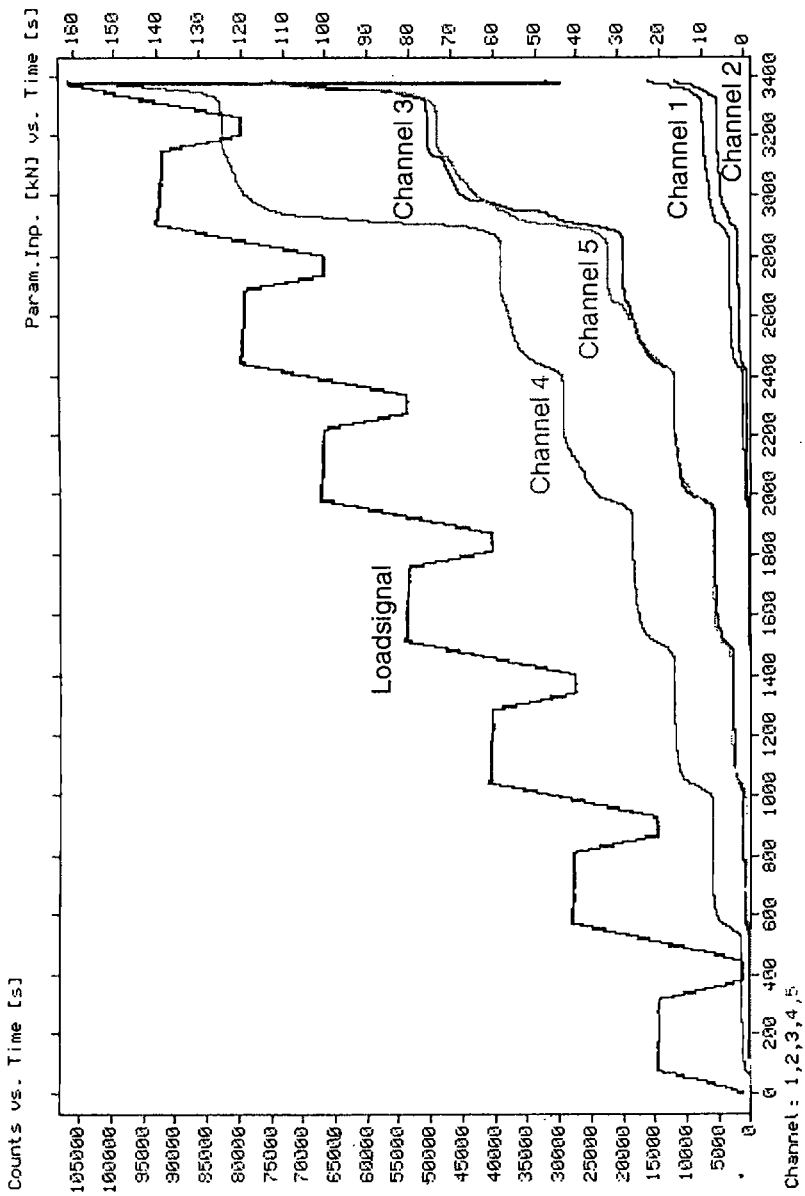


FIG. 6—*Cumulative number of AE signals ("hits") of AE sensors No. 1 to 5 (position "top right") and the stair-step load curve as a function of time for a tension test (No. H1). The most active channel is No. 4. Note the significant increase in the AE activity of all channels above about 70 kN.*

TABLE 4—*Most active AE channel (MAC, top left-hand side No. 1 to 5, top right-hand side No. 6 to 10 bottom No. 11 to 13) as a function of load cycles and location on sandwich element.*

Design No. Load Type	Load Level kN	MAC Top Left	MAC Top Right	MAC Bottom	Remarks (Ranking of Channels)*
B4, tensile	0–5	...	...	...	no activity
	0–10	2	6	13	13, 2, 6
	5–15	2	5	13	13, 5, 2, 6
	10–20	2	5	13	13, 2, 5, 6
	15–25	3	5	13	13, 5, 3, 6
	20–30	2	6	13	2, 6, 7, 13
	25–35	2	6	11	2, 6, 7, 11
	30–40	2	6	11	2, 6, 7, 11
	35–45	2	6	11	2, 6, 7, 1, 11
	40–50†	2	6	13	2, 6, 7, 1, 3, 4, 13
F 5, compressive	0–10	2	8	13	13, 8, 2
	0–20	2	8	13	13, 8, 2
	10–30	2	8	13	13, 8, 2
	20–40	2	8	13	13, 8, 9, 2
	30–50	2	9	13	13, 9, 8, 2
	40–60	2	9	13	13, 9, 8, 2
	50–70	2	9	13	13, 9, 8, 2
	60–80	2	9	13	13, 9, 8, 2
	70–90	2	9	13	13, 9, 8, 12, 2
	80–100	2	9	13	13, 9, 8, 2
	90–110	2	9	13	13, 9, 8, 2
	100–120	2	8	13	13, 8, 9, 12, 2
	110–130	2	9	13	13, 12, 8, 9, 2
	120–140‡	2	9	12	12, 13, 2, 9
G1, tensile	0–20	2	9	13	13, 9, 10, 6, 2
	0–40	2	9	13	13, 9, 10, 12, 2
	20–60	2	6	13	13, 6, 2, 9
	40–80	2	6	13	13, 6, 2, 1, 7, 9
	60–100	1	6	13	13, 6, 1
	80–120§	5	9	13	13, 9, 10, 12, 5
	100–140	5	9	12	12, 5, 9, 13
	120–160‖	5	9	12	12, 5, 9, 13

* Only the first few sensor numbers are listed in decreasing order of activity (measured in number of cumulative AE counts per load cycle, including hold time).

† Failure at 51 kN (reaching nominal hold level) by fracture of foam in joint area between vertical and horizontal plate on both left- and right-hand side.

‡ Failure at 140 kN (after 120 s hold time) by core fracture and delamination of top and bottom CFRP facings on left-hand side.

§ Audible noise from element at 118 kN and again during hold at 120 kN, change in slope of load displacement plot.

‖ Failure at 160 kN (reaching nominal hold level) by core fracture and delamination of top and bottom CFRP facings on left-hand side.

Post-test analysis (Table 6) showed the FR to be a consistent and reliable indicator of both failure location and failure load for all designs. For those elements failing during load increase, the indication of failure load and location from the FR was more pronounced than for elements that failed during hold at constant load. However, even there, the FR indicated that the element was reaching the critical load and which zone was becoming critical. During the test, the most active AE channel yielded reliable predictions of the failure zone (Table 4).

The quantitative analysis of the load relaxation effects (Table 7) that were observed for all designs showed that load relaxation increased with an increasing number of load cycles. Load relax-

TABLE 5—*Damage accumulation thresholds from AE analysis.*

Test No.	Load Level with Significant AE Activity Increase,* kN	Load Level at 20% Cumulative AE.* kN
A 1, tension	5 (71% of failure load)	5.5 (79% of failure load)
B 1, compression	105 (75% of failure load)	100 (70% of failure load)
B 2, compression	76 (69% of failure load)	75 (68% of failure load)
B 3, tension	13 (26% of failure load)†	9.7 (21% of failure load)†
B 4, tension	40 (78% of failure load)	31 (61% of failure load)
D 1, tension	70 (67% of failure load)	70 (67% of failure load)
E 1, tension	110 (85% of failure load)	110 (85% of failure load)
F 1, tension	100 (77% of failure load)	80 (62% of failure load)
F 2, tension	50 (71% of failure load)	60 (86% of failure load)
F 3, compression	110 (79% of failure load)	50 (36% of failure load)
F 4, compression	80 (80% of failure load)	70 (67% of failure load)
F 5, compression	120 (85% of failure load)	60 (43% of failure load)
G 1, tension‡	120 (75% of failure load)	120 (75% of failure load)
H 1, tension	120 (75% of failure load)	100 (63% of failure load)

* Significant AE is defined as significant increase in the cumulative AE activity curve.

† This load level varies depending on how the tangents are drawn. 13 kN is the lower limit, the upper limit is 42 kN (89% of the failure load). The relatively low load level at which 20% of the cumulative AE is reached is caused by significant AE during the first load increase.

‡ Test No. G1 showed changes in the slope of the load displacement plot and audible cracking noise around 120 kN at 20% of the total cumulative AE activity. These results are used to define an arbitrary AE activity criterion of 20%.

TABLE 6—*Felicity ratio (FR) as a function of zone of horizontal sandwich plate and load level for selected tests.*

Design No., Load Type	Load Level, kN	FR Top Left	FR Top Right	FR Bottom	Remarks‖
B2, compressive	0–50	1.04	1.04	1.06	
	25–75	1.04	1.02	1.01	
	50–100	0.98	0.98	0.98	all 3 critical
	75–125*	0.84	0.94	0.93	first drop <1
D1, tensile	50–60†	1.05	1.02	1.01	
	55-65	1.03	1.01	1.01	
	60–70	1.05	1.01	1.03	
	65–75	1.00	1.00	1.00	
	70–80	1.04	1.02	0.98	first drop <1
	75–85	1.03	1.01	1.00	
	80–90	1.03	0.99	0.99	
	85–95	1.02	1.02	1.02	
	90–100	0.98	0.98	1.00	
	95–105‡	1.02	0.97	1.00	
G1, tensile	0–40	1.28	1.18	1.05	
	20–60	1.14	1.15	1.06	
	40–80	1.03	1.03	0.97	first drop <1
	60–100	1.02	0.94	1.03	
	80–120	0.96	0.98	1.00	
	100–140	0.95	0.95	0.91	all 3 critical
	120–160§	0.89	0.91	0.89	

* Failure during load increase at 110 kN.

† At lower load levels, the AE activity was too low for determining FR.

‡ Failure at constant load of 105 kN after a hold time of about 150 s.

§ Failure during load increase at 160 kN (equal to nominal hold load).

‖ Criticality is based on the empirical FR value of 0.95 derived from pressure vessel tests [ASTM E 1067], experience indicates that similar FR values indicate the criticality of other structural elements from CFRP or GFRP.

TABLE 7—*Quantitative analysis of load relaxation effects at constant displacement (during hold).*

Design No., Load Type	Load at Start of Hold, kN	Load Minimum During Hold, kN	Load Relaxation During Hold,* kN/%	Remarks
F 5, compr.	80.4	80.0	0.4/0.50	
	89.9	89.6	0.3/0.33	
	100.3	99.5	0.8/0.80	
	110.4	109.6	0.8/0.72	
	120.2	119.3	0.9/0.75	
	130.4	128.8	1.6/1.23	Fails at 140 kN†
G 1, tensile	80.5	80.0	0.5/0.62	
	100.4	99.0	1.4/1.40	
	120.2	118.8	1.4/1.20	
	140.2	138.4	1.8/1.28	Fails at 160 kN
H 1, tensile	80.3	79.7	0.6/0.75	
	100.6	99.6	1.0/0.99	
	120.0	118.8	1.2/1.00	
	139.9	138.4	1.5/1.07	Fails at 160 kN

* The relative load relaxation is calculated with respect to the peak load during hold.
† Fails during hold at nominally 140 kN, after significant load relaxation to 137.5 kN (2.0%).

TABLE 8—*Failure mechanisms and failure location.*

Design No., Load Type	Failure Mechanism*	Failure Location†
A 1, tensile	fracture of balsa core in vertical plate, delamination of horizontal CFRP	near joint between vertical and horizontal plate
B 1, compressive	fracture of balsa core and delamination of both CFRP facings	between vertical plate and right-hand support
B 2, compressive	fracture of balsa core and delamination of both CFRP facings	between vertical plate and left-hand support
B 3, tensile	fracture of foam and delamination of CFRP reinforcement	between vertical and horizontal plate on left- and right-hand side
B 4, tensile	fracture of foam and delamination of CFRP reinforcement	between vertical and horizontal plate on left- and right-hand side
D 1, tensile	fracture of balsa core in vertical plate and of foam, delamination of CFRP bonding angle	near joint vertical and horizontal plate
E 1, tensile	fracture of balsa core, delamination of both CFRP facings and interlaminar delamination between prefabricated and wet laminated segment	on left-hand side
F 1, tensile	delamination of CFRP facing of framework joint	on left-hand side of framework
F 2, tensile	delamination of repaired zone	near joint between vertical and horizontal plate
F 3, compressive	fracture of balsa core and delamination of both CFRP facings	between vertical plate and left-hand support
F 4, tensile	delamination of CFRP facing of framework joint	on right-hand side of framework
F 5, compressive	fracture of balsa core and delamination of both CFRP facings	between vertical plate and left-hand support
G 1, tensile	fracture of balsa core and delamination of both CFRP facings	between vertical plate and left-hand support
H 1, tensile	fracture of balsa core and delamination of both CFRP facings	between vertical plate and left-hand support

* Macroscopic failure mechanism from visual inspection after test. Balsa core failure occurs in the horizontal sandwich except where noted.
† Left and right hand refer to the (arbitrary) orientation of the element on the test machine.

ation of between 1.07 and 1.28% of the peak cycle load was observed during the last hold period before failure for the tests listed in Table 7. The load relaxation at nominally constant load raised the following questions: (1) What is the "correct" value of the failure load for those elements that fail during hold? (2) Which mechanisms are responsible for the load relaxation? (3) Can "load relaxation" be used as an indicator for impending failure, i.e., as a measure to predict failure loads instead of the Felicity Ratio analysis that proved to be too slow? The failure loads (Table 3) are peak loads, i.e., neglecting relaxation effects. The mechanisms responsible for the load relaxation have not been identified yet. Tentatively, the results in this paper suggested that load relaxation may be a reliable indication for the failure load consistent with the results of the post-test AE FR analysis. Load relaxation may be analyzed during hold, sufficiently fast for predictions of the failure load. Load relaxation analysis is, therefore, proposed as a feasible alternative to the AE FR analysis for predicting failure loads. Prediction of failure location, even zonal location, was not possible from the load relaxation analysis.

Type classification of the AE signal amplitudes was consistent with a gradual transition of damage severity from microscopic (e.g., microcrack formation) to macrocrack or delamination growth with increasing load. In test No. G1, the AE signal amplitudes first reached saturation (100 dB) at 80 kN and again after each load increase. During hold, the AE signal amplitudes then decreased to about 60 and 80 dB. At loads above 50% of the failure load this behavior has been observed in most tests. Because of the statistical nature of the empirical correlation between AE signal amplitudes and failure mechanisms the identification of the failure mechanisms based on AE signal amplitudes was ambiguous.

In test No. G1, the cumulative number of AE counts increased sharply during the load increase to 120 kN and again during hold at 120 kN. The AE activity did not vanish during the hold time (maximum of 4 min). Similar sudden AE activity increases and persistent AE activity at constant load were observed in most tests.

The threshold load level for the significant AE activity increase was determined from the intersection of two tangents drawn on the cumulative AE activity curve. This is analogous to the AE "knee-point" for composite materials proposed by Mitchell [*9*]. The "knee-point" is interpreted as the border between two regimes with different failure mechanisms, e.g., microscopic damage growth switching to macrocrack and delamination growth. A single failure mechanism typically yields an exponential AE activity, e.g., in tensile tests of GFRP specimens; the relation between static tensile tests on material coupons and quasi-static ("stair-step" loading) tests on elements was further discussed in Ref *10*. Load displacement plot, AE activity and AE intensity thus indicated significant damage in element No. G1 around 75% of the failure load. This corresponds to about 20% of the total cumulative AE activity. Using the above tangent procedure the cumulative AE activity consistently showed a "knee-point" in most elements between 70 and 80% of the failure load (Table 5) that was interpreted as significant damage accumulation. The only exception was No. B3 where the AE activity was considerable during the first load increase and the element failed during the second load increase.

Similar damage thresholds (± 1 load step) as from the "knee-point" are obtained at 20% cumulative AE activity for tensile but lower thresholds for two compressive tests (No. F3, F5). This is probably caused by AE "noise," e.g., friction from damage accumulated during the preceding tensile test. The two compression tests (No. B1, B2) on "virgin" T-joints yielded damage thresholds around 70% as for the tension tests. It is interesting to note that the damage threshold for the tensile test on the repaired T-joint (No. F2) was not reduced. This can probably be explained by the Felicity effect [*6*], i.e., that no significant AE activity appeared until loads comparable to the previously applied load were reached. The 20% AE activity level was thus reached later, i.e., at loads comparable to those of a "virgin" sample.

The FR reached values close to 0.95 for several zones ("left," "right," "bottom") of the sandwich element, e.g., for No. B2, G1 (Table 6). This was observed in tests No. E1, F1, F2, G1, and H1 (ten-

sion) and B1, B2 and F5 (compression). The total cumulative AE activity of the most active channel in each zone was also comparable in several of those tests. These AE data are consistent with significant damage accumulation in zones that did not fail.

With the increasing use of sandwich elements their repairability and maintainability will increase in importance. The repair of one T-joint after tensile failure (delamination of the CFRP facing on top of the horizontal plate) was not state-of-the-art, e.g., as in a shipyard, but may represent a provisional effort performed at sea with limited resources and time. The reduced tensile strength after repair (failure load of 70 kN versus 130 kN in the first test) clearly shows that further research on repair procedures and their effectiveness is needed. On the other hand, T-joints tested under compressive load after having failed in tensile tests still reached close to 90% of the compressive failure load of comparable designs without any repairs. This was attributed to geometrical effects (bending induced by compression) that effectively "closed" existing delaminations and because of friction prevented relative surface motion and further delamination growth. This indicated that measures that limit or distribute the load and stresses of one load type may also be quite effective in ensuring the usability of damaged and repaired elements.

Besides T-joint No. G1, No. F4 also showed significant imperfections, quite likely due to manufacturing (thermal treatment). They resulted in a maximum gap between roller bearing and plate of 2.0 mm at the beginning of the test. Misalignment in the load introduction and support (e.g., position of the bolt holes) was estimated to contribute a few tenths of a mm to the uneven support. The imperfections were interpreted as indications of built-in stresses in the T-joints. This probably reduced the tensile failure load for No. F4 to 100 kN instead of about 130 kN as for other elements of design F, but not in the fillet design (No. G1, maximum gap of 1.7 mm). One explanation for this is that the joint area between vertical and horizontal plate is stiffer and hence less flexible under load in the framework design. Therefore, uneven support in the fixture led to larger stress concentrations in the joint between vertical and horizontal plate. T-joint No. F4 failed there, while No. G1 failed in the horizontal plate (as No. H1 with a much smaller maximum gap).

Comparison of the Tested T-joint Designs

For the comparison of the T-joint designs, three classes of the design and two load cases (tension and compression) were considered. Design classes were: (1) reference design with "simple" joint, (2) designs with foam fillet and wet laminate (with or without crack stopper and foams of different density), and (3) the framework design. The reference design had only been tested under tensile load and yielded the lowest failure load. Both, foam fillet and framework designs yielded considerable improvements in the tensile failure load over the reference design. For foam fillet designs it increased with increasing foam density, i.e., increasing foam strength and stiffness. The 200 kg/m^3 foam yielded maximum values around 100 kN without a crack stopper. With the crack stopper (additional L-shaped laminate bond angle on each side of the vertical plate joining it with the horizontal plate) the tensile load for tearing the horizontal and vertical plates apart became larger than that for fracturing the horizontal sandwich (about 160 kN). The change in the orientation of the balsa wood in the core of the vertical plate (Table 1) did not seem to affect the failure load. The more complex framework design failed at somewhat lower tensile loads (around 130 kN). Imperfections from manufacturing/processing that resulted in a gap between roller bearing and horizontal plate at the start of the test seemed to affect the framework design more than foam fillet designs. For compressive loading, failure loads around 140 kN were reached for foam fillet (low density foam) and framework designs (only tested after tensile failure without any repairs). The 140 kN load seemed to indicate the typical compressive strength of the horizontal sandwich and to be fairly independent from the design details. Therefore, the reference design is expected to yield comparable compressive failure loads. The design changes hence mainly increased the tensile failure load.

Conclusions

Experimental investigation of T-joint designs is a useful means for evaluation and comparison of different design types. T-joints with static tensile and compressive failure loads of at least 140 kN were built based on the the foam fillet design. The framework design yielded lower failure loads (around 130 kN), seemed to be more sensitive to imperfections from manufacturing, and involved a more complicated manufacturing process. AE monitoring yielded information on damage growth and accumulation as a function of load level and type and allowed prediction of the zone of failure and of the failure load.

Acknowledgments

This research has been funded in the framework of the European BRITE-EURAM project No. 7651BRE2-0582 MATSTRUTSES and of BWI-Project No. 93.0051. Technical support by D. Völki and comments from R. A. Nordstrom are gratefully acknowledged.

References

[1] Wallat, R., Weiblen, F., and Ziegmann, G., "Sandwich Design for High Thickness Balsa and Foam Cores with Facings from Advanced Composites," *Proceedings, 7th International Conference on Marine Applications of Composite Materials,* 1998, pp. C1–C10.

[2] Shenoi, R. A. and Violette, F. L. M., "A Study of Structural Composite Tee Joints in Small Boats," *Journal of Composite Materials,* Vol. 24, 1990, pp. 644–663.

[3] Kildegaard, C., "Experimental and Numerical Fracture Mechanical Studies of FRP-Sandwich T-Joints in Maritime Constructions," *Proceedings, 2nd International Conference on Sandwich Constructions, in "Sandwich Constructions 2, Vol. II.* D. Weissman-Berman and K-A. Olsson, Eds., EMAS Publishing, 1992, pp. 887–904.

[4] Theotokoglou, E. E. and Moan, T., "Experimental and Numerical Study of Composite T-Joints," *Journal of Composite Materils,* Vol. 30, 1996, pp. 190–209.

[5] Theotokoglou, E. E., "Analytical Determination of the Ultimate Strength of Sandwich Beams," *Applied Composite Materials,* Vol. 3, 1996, pp. 345–353.

[6] McIntire, P. and Miller, R. K., Eds., *Nondestructive Testing Handbook, Vol. 5, Acoustic Emission Testing,* 2nd ed., American Society for Nondestructive Testing, 1987.

[7] Hoa, S. V. and Li, L., "Acoustic Emission During Quasi-Static Loading/Hold/Unloading in Notched Reinforced Fiber Composite Materials," *Journal of Acoustic Emission,* Vol. 7, No. 4, 1988, pp. 145–160.

[8] Oyaizu, H., Yamaguchi, K., and Ida, M., "Features of Cracking and Friction AE in GFRP Low-Cycle Fatigue Tests by Multi-Parameter Analysis," *Proceedings, 4th World Meeting on Acoustic Emission (AEWG-35) and 1st International Conference on Acoustic Emission in Manufacturing,* S. Vahaviolos, Ed., American Society for Nondestructive Testing (ASNT), 1991, pp. 431–438.

[9] Mitchell, J. R., "Standard Test to Quantify the Knee in the AE vs. Load Curve as a Material Parameter for Composites," *Proceedings, 3rd International Conference on Acoustic Emission from Composites, AECM-3,* American Society for Nondestructive Testing, ASNT, 1989, pp. 207–217.

[10] Brunner, A. J., Nordstrom, R., and Flüeler, P., "A Study of Acoustic Emission-Rate Behavior in Glass Fiber-Reinforced Plastics," *Journal of Acoustic Emission,* Vol. 13, No. 3–4, 1995, pp. 67–77.

Ronald B. Bucinell[1] *and Brian Roy*[1]

Development of a Test Method for Closed-Cross-Section Composite Laminates Subjected to Compression Loading

REFERENCE: Bucinell, R. B. and Roy, B., **"Development of a Test Method for Closed-Cross-Section Composite Laminates Subjected to Compression Loading,"** *Composite Structures: Theory and Practice, ASTM STP 1383*, P. Grant and C. Q. Rousseau, Eds., American Society for Testing and Materials, West Conshohocken, PA, 2000, pp. 382–397.

ABSTRACT: A test method for evaluating the material properties of closed-cross-section composite laminates has been developed. A finite-element investigation of the first five eigenvalues for the specimen in buckling shows that the critical load is at least a factor of three higher than the failure load observed during testing. This same analysis shows that the highest stresses and strains occur in the gage section of the specimen.

The test specimens are 228.6 cm (9 in.) in length, 50.8 cm (2 in.) in diameter, and have fiberglass end tabs co-cured onto them. Several specimens were manufactured in a quasi-isotropic configuration ($[\pm 45/0/90]_s$ and $[\pm 45/90/0]_s$) in order to experimentally evaluate the robustness of the test method, observe typical failure modes, and to catalog the accumulation of damage in the specimens up to failure. Several of these tubes were outfitted with strain gages to detect the presence of buckling and bending in the specimens. Damage was observed by loading specimens to 45%, 60%, 75%, 90%, and 95% of the mean ultimate load. At each of these load levels specimens were cut along their length, a dye penetrate was applied, and then the tubes were X-rayed. The experimental investigation shows that the specimens did not buckle and that the mode of failure is a compressive material failure in the gage section of the tube.

KEYWORDS: composite materials, compression, tubes, experimental evaluation, graphite-epoxy

Structural challenges in aerospace, hydrospace, and infrastructure applications are forcing designers to carefully consider composite materials. Designing with composites requires that material design be performed simultaneously with structural design and the design of the manufacturing process. All these factors have a direct effect on the performance of the composite structure.

The success of the composite design process is contingent on the accurate characterization of the effects of the material, process, and structural form on the composite response. Because of the anisotropic heterogeneous nature of composite materials, tension, compression, and shear testing in multiple directions is needed to fully characterize composite materials. Of these, compression testing has proven to be one of the most challenging.

Traditionally, compression characterization is performed on flat coupons [*1,2*]. Critical issues for flat coupon compression testing include insuring valid failure modes, avoiding spurious failures or failures outside the gage region, and sensitivity of the test results to surface finish and alignment. Invalid failure modes typically are a result of buckling or severe stress concentrations in the load introduction region. Tabbed specimens tend to fail at the tab ends or inside the tabs. End loaded specimens tend to fail by brooming.

[1] Associate professor of Mechanical Engineering and student, respectively, Union College, Steinmetz Hall, Schenectady, NY 12308.

Copyright© 2001by ASTM International www.astm.org

In flat, finite-width coupons the stress state is exacerbated by the presence of stiffness and geometric discontinuities at the free edge. The exacerbated stress state has been shown to affect the damage accumulation in these specimens and to have an effect on the material characterization. Many aerospace, hydrospace, and infrastructure configurations incorporate closed cross-sectional geometry. Additionally, the processing of structures with closed cross sections (filament winding, tow placement, fiber placement, etc.) is a lot different than those for flat coupons (hand layup, hot press, etc.). Thus it can be concluded that the characterization of closed-cross-section composite structures using flat coupons can lead to error.

The need to develop separate compressive material characterization test methods for closed-cross-section composites has been recognized throughout the composite community. Swanson [*3*] developed a 102-mm-diameter (4 in.) tube that was capable of evaluating closed-cross section structures subject to biaxial loading. This tube has been shown to be effective for quasi-static loading; however, it has never been evaluated under fatigue loading. This specimen requires metal components to be bonded to the tube in order to transfer load into the gage section, which adds considerably to the cost of a data point. Bucinell et al. [*4*] developed a simplified 102-mm-diameter (4 in.) tube (ASTM Standard Test Method for Transverse Compressive Properties of Hoop Wound Polymer Matrix Composite Cylinders (D 5449/D 5449M-93). This test method, which was specifically designed to evaluate the transverse compressive properties of hoop wound tubes, has not been evaluated for angle-ply laminates. One of the major drawbacks to this method is removing the specimen from the fixture after testing is complete. Because the specimen is bonded to the fixture, it must be burned out to clean the fixtures for reuse. This process is both time-consuming and costly. This method was not intended for fatigue testing. Groves et al. [*5*] developed a 50.8-mm-diameter (2 in.) tube specifically for fatigue and biaxial loading. Their design incorporates a large tapered, built-up region to transfer the load from the fixture into the gage section. The taper on the buildup needs to match the taper on the fixture for proper load transfer to occur. Although the fixturing is expensive for this method, the method has been shown to produce very good results.

In a parallel effort, the closed-cross-section test method presented in this paper was developed. The design objectives were to develop a closed-cross section composite laminate test method that reliably predicts the compressive response, produces results that are both reproducible and repeatable, is relatively inexpensive, and easy to implement. The results of this effort are presented in the following sections. The discussion commences with a description of the specimen and fixture. This discussion includes the procedures for loading the specimen into the fixture. This section is followed by the introduction of the experimental program and results that were used to validate this test method. The finite-element model used to investigate the specimen response is then presented. This is followed by a discussion of the results and the validity of this test method. Finally, a summary of the work is presented along with conclusions and recommendations.

Closed-Cross-Section Specimen and Fixture

The development of a closed-cross-section composite material test method for compressive loading requires the development of both the specimen and fixturing needed to transfer the load into the specimen. The specimen needs to incorporate a load introduction region that will minimize the stress peaks, a transition region that will assist in forcing the failure in the gage section, and a gage section designed to produce proper failure modes in a repeatable and reproducible manner. The specimen design must also allow for multiple laminate geometries to be evaluated. The fixtures must be designed to efficiently transfer load into the specimen without causing failures in the gripping region, allow for easy specimen mounting and dismounting, and maintain specimen alignment.

The specimen geometry is illustrated in Fig. 1. The inside diameter of the specimen is 50.8 mm (2 in). The thickness of the composite is determined by the desired laminate geometry. For the evaluation of the test method in this study, specimens were fabricated using 0.254-mm thick (0.01 in.)

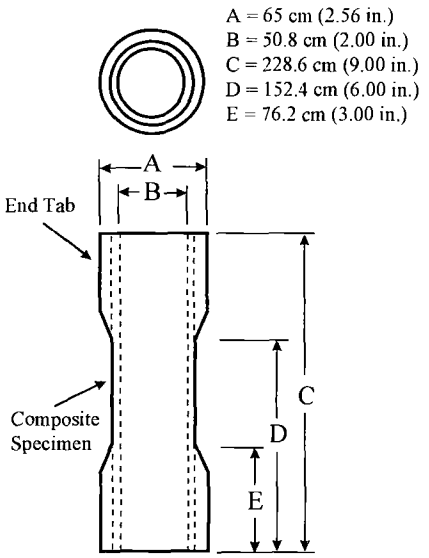


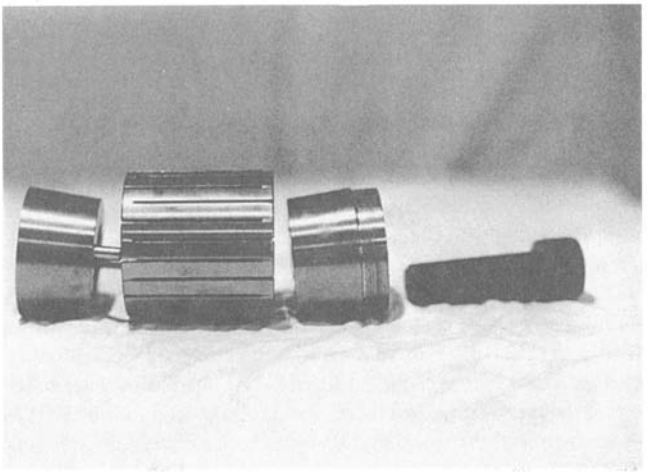
FIG. 1—*Illustration of the 5.08 cm (2 in.) diameter specimen's geometry.*

AS4/3501-6 towpreg tape supplied by Fiberite Corporation. Two quasi-isotropic laminate geometries were considered in this study, $[\pm 45/90/0]_s$ and $[\pm 45/0/90]_s$. The laminates were built up on a 1.83-m long (6 ft) aluminum mandrel with a 0.075 mm/m (0.001 in./ft) taper along the length. Fiberite MXB 7701/7781 strips, 76.2 mm (3.0 in.) wide, were wound at regular intervals along the length of the composite on the mandrel to form the end tabs. The composite and end tabs were co-cured and then the specimens were cut to length. Next the specimens were placed in a lathe and the end tabs were turned to their final shape of 65 mm (2.56 in.) outer diameter for 50.8 mm (2.0 in.). A 25.4 mm (1.0 in.) taper-down region was then cut down to the diameter of the composite. The end tabs are needed to protect the composite from the serrated grips used to shear in a portion of the compressive load and to prevent "brooming" at the end of the specimen where the remainder of the load is introduced through end loading. The taper allows the stress to normalize and reach a maximum in the gage length.

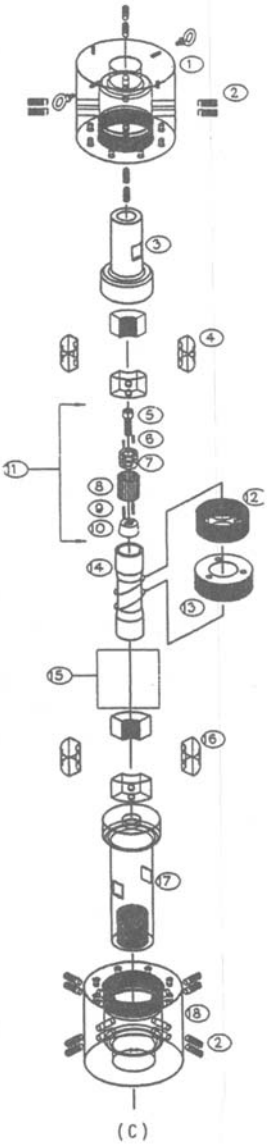
The fixtures for the closed-cross-section compression testing are illustrated in Fig. 2. A photo of the components of the fixture and specimens are shown in Fig. 2*a*, an enlarged view of the expanding collet in Fig. 2*b*, and an exploded assembly view of the specimen and fixture in Fig. 2*c*. The component designations seen in Fig. 2*c* are summarized in Table 1. The load stems (3 and 17) are slid through openings in the housings (1 and 18) and then attached to the crosshead and actuator of the load frame. The grip sets (4 and 16) are then positioned in the housing and held there by the capture plates (12 and 13). The expanding collet assembly (Fig. 2*b*) is then placed in the specimen as shown in Fig. 3 and expanded using the collet load bolt. The collet is needed to prevent failure of the composite when lateral grip pressure is applied. The upper and lower collet wedge both have raised shoulders that fit into the load stems. This assists in the alignment of the specimen in the test fixture. Once both collets are in place the specimen is placed in the lower housing as seen in Fig. 4. The upper housing is lowered onto the specimen and the lateral loading bolts (2) are then tightened in a star pattern in increments of 34 N·m (25 ft·lb) up to 136 N·m (100 ft·lb) torque. The load can now be applied and the specimen taken to failure. After the test is complete, the lateral loading bolts are backed off and the upper housing is raised. The specimen is removed and the expanding collet assembly is removed



(a)



(b)



(c)

FIG. 2—(a) *Components of the specimen and fixtures used in the testing program.* (b) *Components of the expanding collet used to support the inside of the 5.08 cm (2 in.) diameter tube.* (c) *Assembly drawing of the fixtures and specimen.*

from the specimen using the two collet pushout bolts (6). These are necessary because the taper on the collet wedges is designed to be self-locking.

The specimen and fixtures for this closed-cross-section compressive test method have been designed for both quasi-static and cyclic load. Only the quasi-static compression loading is discussed in this paper.

TABLE 1—*Fixture assembly drawing component designations used in Fig. 2.*

Number	Description
1	Upper housing
2	Lateral loading bolts
3	Upper load stem
4	Upper grip set
5	Collet load bolt
6	Collet push out bolts
7	Upper collet wedge
8	Expanding collet
9	Collet guide pins
10	Lower collet wedge
11 & 15	Expanding collet assembly
12	Upper housing capture plate
13	Lower housing capture plate
14	Specimen
16	Lower grip set
17	Lower load stem
18	Lower housing

Experimental Program

The experimental program had two major objectives. The first objective was to determine if the test specimen and fixture produced a valid compression failure. The second objective was to monitor the damage progression in the specimen up to failure. Both the $[\pm 45/90/0]_s$ and $[\pm 45/0/90]_s$ laminate tubes were used in the evaluation of both of these objectives.

All testing in this program was performed on a 100 kip servo-hydraulic MTS load frame. Figure 5 shows the fixtures and specimen mounted in the load frame. The load frame was adjusted to apply a quasi-static load at a rate of 0.130 mm/s (0.005 in./s) under stroke control. Prior to testing all specimens were measured to determine the inside diameter of the tube using inside micrometers and the outside diameter of the tube using calipers. Longitudinal markings were placed on the end tabs of each specimen at 90° increments and marked 0, 90, 180, and 270. Specimen designations were placed on the tapered portion of the end tabs. All of these markings are seen in Fig. 3. These markings helped to position the specimen in the fixture. The 0° tube direction was always facing directly out toward the front of the load frame and the specimen was positioned such that the specimen designation was right side up. This is illustrated in Fig. 4. This type of alignment helped to determine if there was an orientation bias in the damage formation or failure of the tube specimens.

A valid compression failure avoids bending failures resulting from specimen misalignment, Euler buckling, and failures in the transition or grip regions. The first part of the experimental program was designed to determine if any of these failure modes were present in the tubes when they were loaded to failure. Two sets of specimens were used in the evaluation of this objective. The first set of specimens was placed in the test fixtures and loaded to failure. This set of tests provides a statistically significant number of failure loads and identifies the location of the failure. The results of these experiments are summarized in Table 2. Almost without exception the failure for the specimens summarized in Table 2 is in the gage section. Figure 6 shows a typical specimen that was taken to failure.

The second set of experiments is designed to determine if buckling or bending occurs in the specimen during the quasi-static load to failure. These conditions are determined by monitoring strain

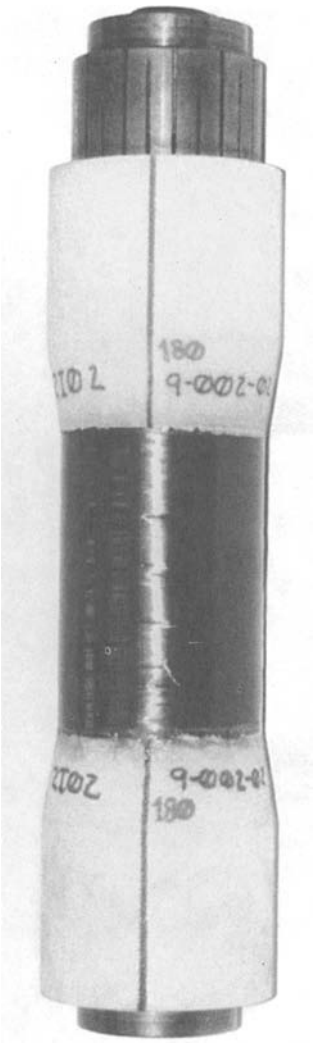


FIG. 3—*The 50.8 cm (2 in.) diameter specimen with expanding collet being inserted inside. Markings on specimen are used to identify the specimen and to orient the specimen in the fixture.*

gages during the loading of the specimen. The configuration for the strain gages on the specimen is illustrated in Fig. 7. At the 90° and 270° longitudinal positions, two 350 ohm uniaxial strain gages are positioned in the center of the specimen's gage section oriented in the axial direction (gages 4 and 8). At the 180° longitudinal position, three 350 ohm uniaxial strain gages are oriented in the axial direction positioned at the center of the gage length, 25.4 mm (1 in.) above the center gage, and 25.4 mm (1 in.) below the center (gages 5, 6, and 7). At the 0° longitudinal position a 120 ohm strain gage Rossette (0°:45°:90°) is placed at the center of the gage section (gages 1,2,3). The 0° Rossette gage is aligned with the axis of the specimen. During the quasi-static loading to failure, the strains from these gages are recorded at a rate of one sample per second. Three $[\pm 45/90/0]_s$ and two $[\pm 45/0/90]_s$ tube

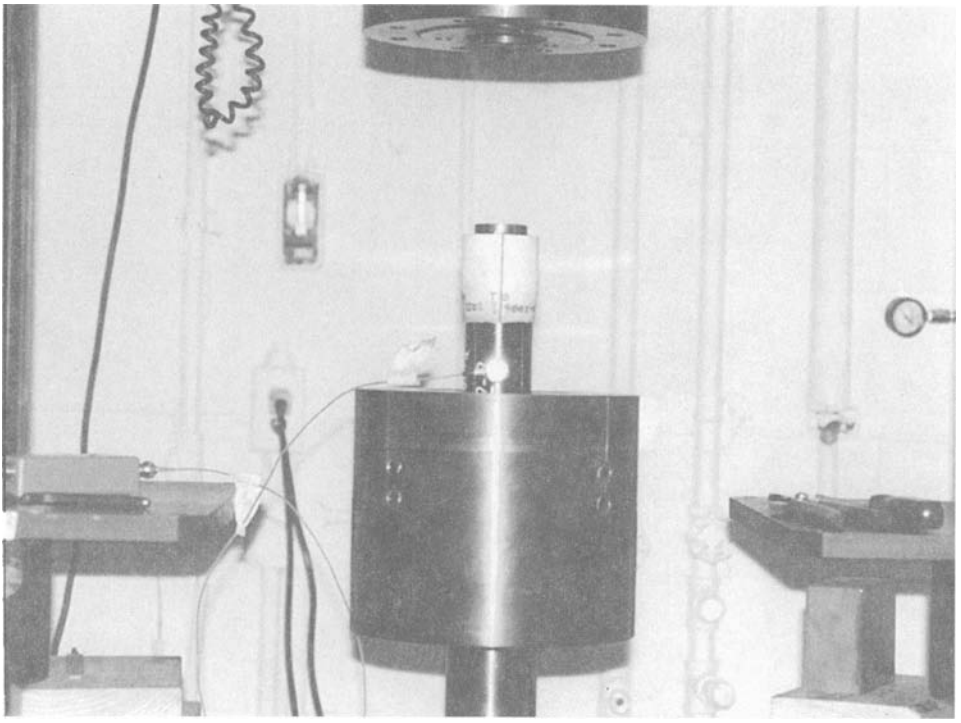


FIG. 4—*The 5.08 cm (2 in.) diameter specimen inserted into the lower fixture in preparation for testing.*

specimens are gaged to determine the presence of bending in the specimen. Figures 8 and 9 illustrate the stress-versus-strain behavior of the $[\pm 45/90/0]_s$ and $[\pm 45/0/90]_s$ specimens up to failure. The stress-strain curves do not indicate the presence of bending or buckling in the specimens. Table 3 summarizes the axial modulus of elasticity, for the gaged specimens, determined by a cord modulus between 1000 and 3000 μ-strain. The values in the table are the average of the five axial gages on the specimen (gages 4, 5, 6, 7, and 8). Due to technical difficulty, the Rossette gages (1, 2, and 3) did not function properly and are excluded from this discussion.

The second objective for this experimental program is to monitor the damage progression in the specimens up to failure. Typically, damage progression is monitored using an X-ray technique that includes placing a dye penetrant on the sides of the specimen to enhance the internal damage, acoustic emission, and/or ultrasonic inspection. Acoustic emission was not employed because it is not refined to the point where damage modes can be easily differentiated and, at the time of this testing, acoustic emission was not available in the lab. Ultrasonic inspection of the tubes also was not used because previous ultrasonic inspections of the tubes under other loading conditions did not yield the damage mode details being sought in this study. X-ray techniques have proved effective in locating transverse cracks, splits, and delaminations. In closed-cross-section structures the X-ray technique is difficult to implement due to the absence of free edges. It was decided to use the X-ray technique for this study because it provides the highest potential for detailed damage characterization.

The lack of free-edge/X-ray technique problems was resolved by loading specimens up to predetermined load levels and then removing them from the study so they could be cut in half, a penetrant applied, and X-rayed. Using the average strengths summarized in Table 2, three $[\pm 45/90/0]_s$ and $[\pm 45/0/90]_s$ tube specimens were selected to be loaded to 45%, 60%, 75%, 90%, and 95% of the ul-

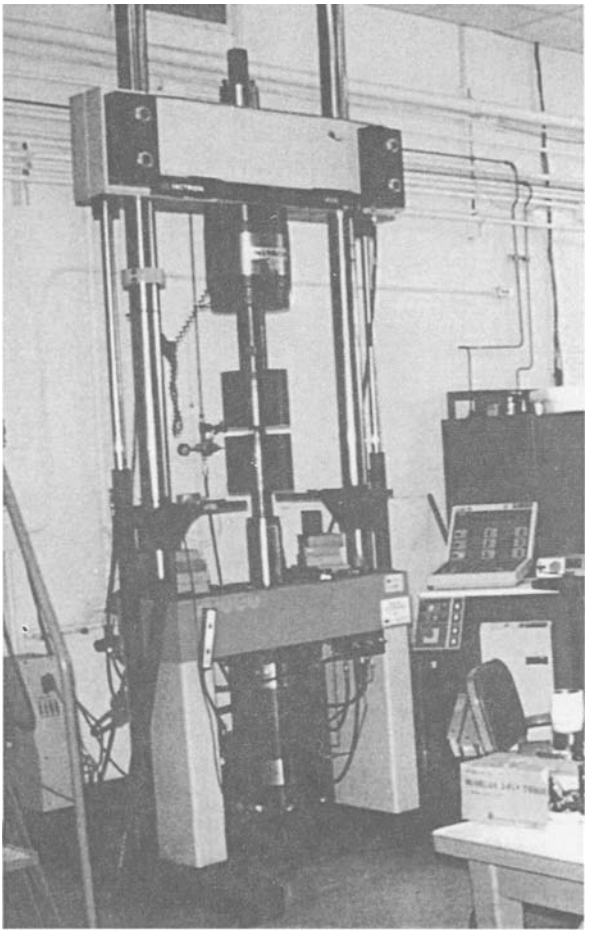


FIG. 5—*The 5.08 cm (2 in.) diameter specimen completely inserted into test fixtures.*

TABLE 2—*Results of quasi-static compression load to failure tests.*

$[\pm 45/0/90]_s$			$[\pm 45/90/0]_s$		
Failure Load kN (kip)	Area $mm^2(in.^2)$	Failure Stress MPa (ksi)	Failure Load kN (kip)	Area mm^2 $(in.^2)$	Failure Sress MPa (ksi)
243 (54.9)	359 (0.556)	680 (98.7)	241 (54.2)	356 (0.553)	676 (98.1)
244 (54.8)	354 (0.549)	687 (99.7)	271 (61.0)	352 (0.546)	772 (112)
219 (49.2)	354 (0.549)	618 (89.6)	225 (50.6)	350 (0.542)	643 (93.3)
255 (57.3)	354 (0.549)	717 (104)	245 (55.0)	359 (0.556)	682 (98.9)
255 (57.3)	354 (0.549)	717 (104)	262 (59.0)	352 (0.546)	744 (108)
250 (56.3)	354 (0.549)	703 (102)	246 (55.3)	345 (0.535)	710 (103)
			232 (52.1)	352 (0.546)	658 (95.5)
			251 (56.5)	372 (0.577)	674 (97.8)
Average			Average		
245 (55.0)	355 (0.550)	688 (99.8)	12.5 (55.5)	355 (0.550)	696 (101)

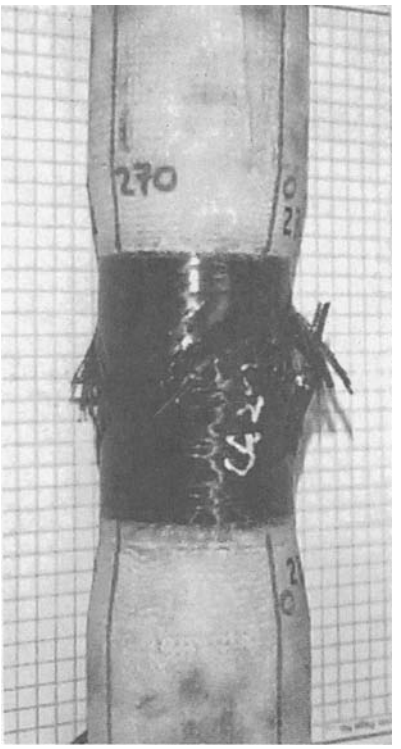


FIG. 6—*Typical failure of a 5.08 cm (2 in.) diameter specimen when subjected to compression loading.*

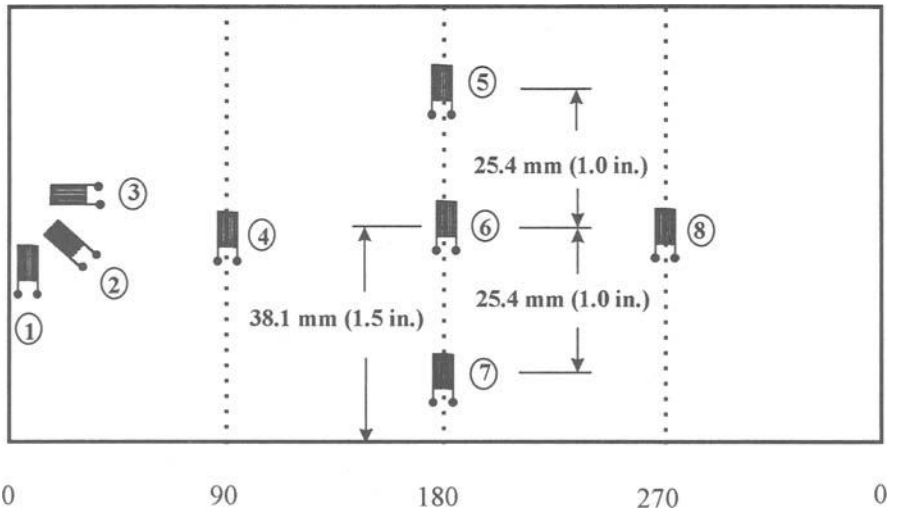


FIG. 7—*Positions of strain gages, strain gage orientation, and numbering scheme used to determine the presence of bending and/or buckling in the test specimens.*

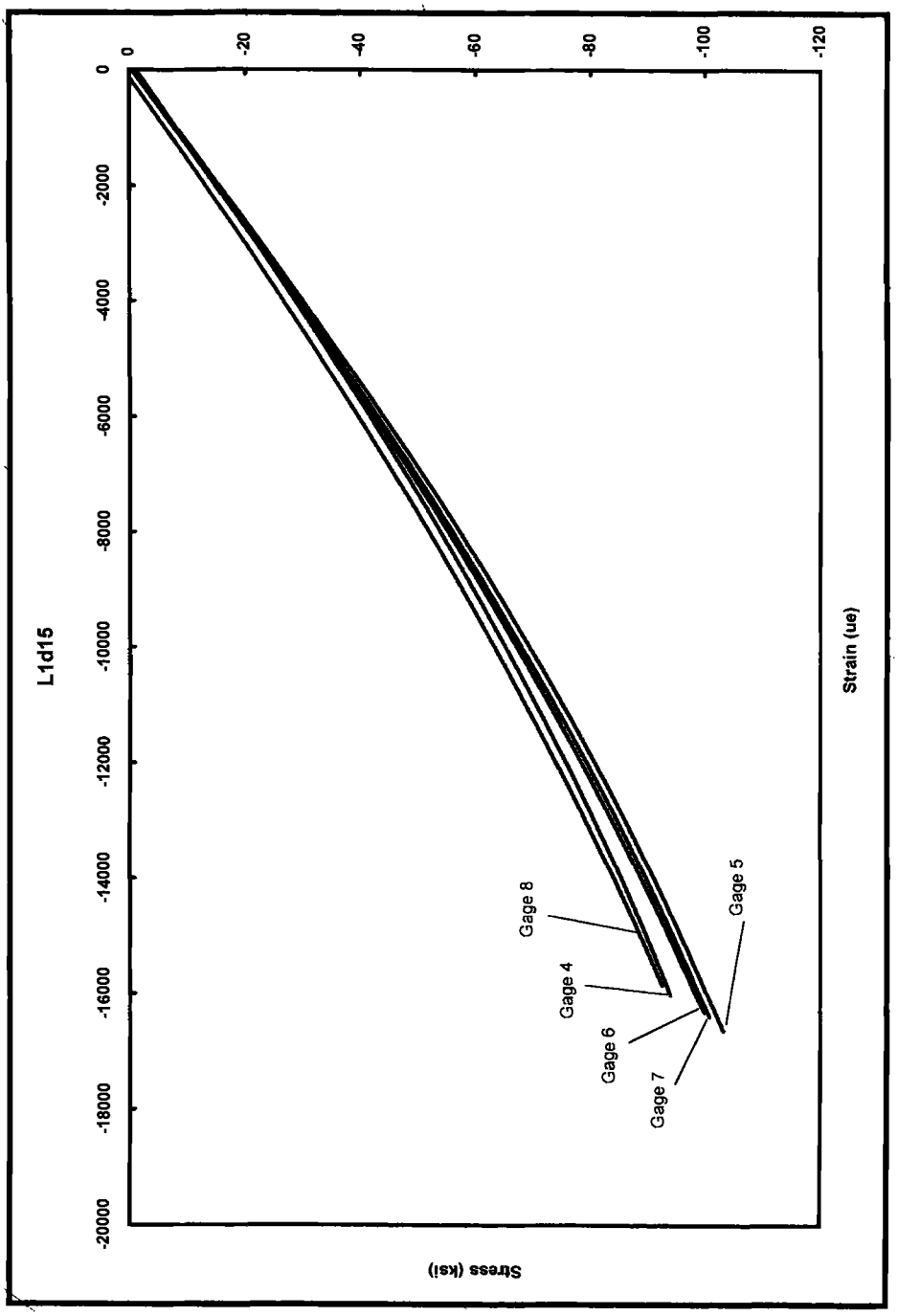


FIG. 8—*Stress-strain results for one of the [±45/0/90]$_s$ specimens that were strain gaged and subjected to quasi-static compression loading to failure.*

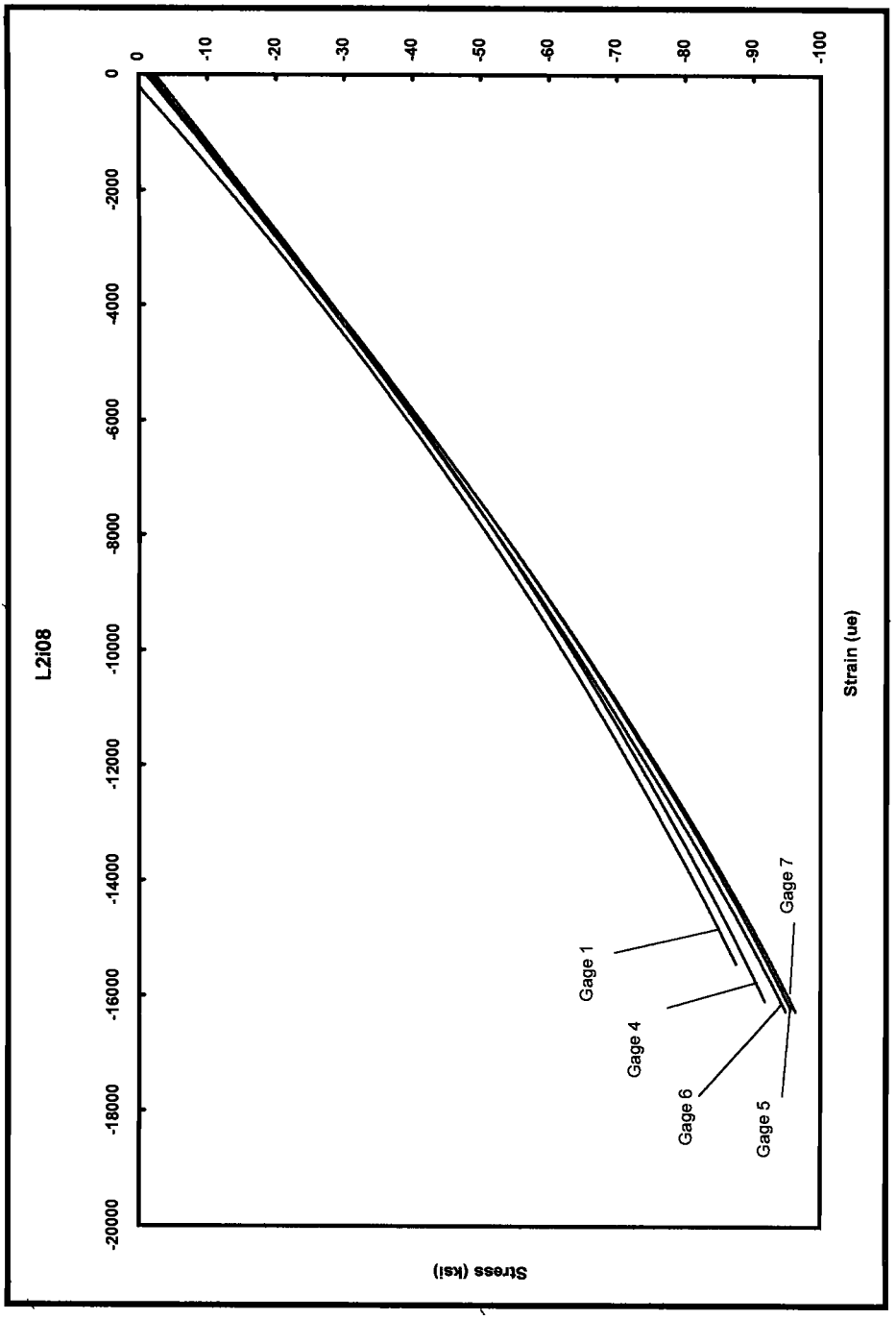


FIG. 9—*Stress-strain results for one of the [±45/90/0], specimens that were strain gaged and subjected to quasi-static compression loading to failure.*

TABLE 3—*Summary of the average modulus of elasticity for the gaged specimens.*

$[\pm 45/90/0]_s$ Axial Modulus GPa (Msi)	$[\pm 45/0/90]_s$ Axial Modulus GPa (Msi)
47.8 (6.94)	50.1 (7.27)
46.8 (6.79)	45.9 (6.66)
48.8 (7.08)	

timate compressive load. The specimens were then cut along the 0° and 180° longitudinal lines of the tubes. A zinc iodide penetrant was placed along the edges of the specimen and allowed to wick in overnight. Then the specimens were exposed to X-rays. Several exposure levels and times were tried; however, there was no indication of transverse cracking, splitting, or delamination in any of the tubes.

Finite-Element Evaluation of Specimen

The finite-element program COSMOS/M™ was used to build a model of the tube specimen. This model assists in evaluating if the specimen is prone to buckling and if the load in the gage section is both maximum and uniform. Element selection, material properties, boundary conditions, and loading were carefully considered and are discussed in the following paragraphs.

The finite-element model developed for the evaluation of the tube specimen is seen in Fig. 10. The model is made up of eight-node axisymmetric isoparametric quadrilateral elements. The

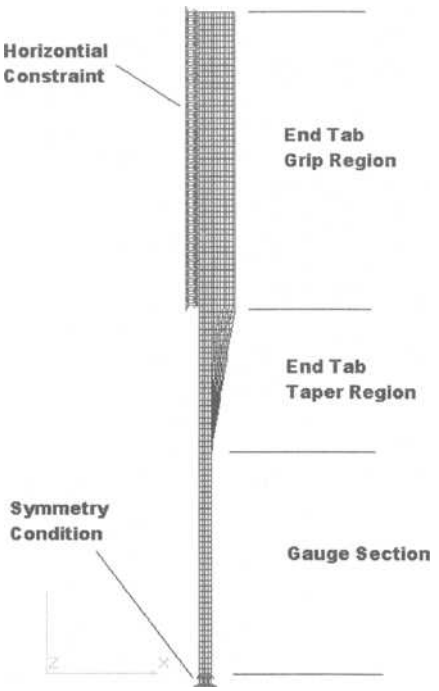


FIG. 10—*Mesh and boundary conditions used in the finite-element model of the 5.08 cm (2 in.) diameter tubes to determine the presence of buckling and how the load transitions from the end tabs into the gage section of the specimen.*

graphite/epoxy tube portion of the model is four elements thick and 115 elements long. Fifty of the composite elements are along the griping region of the end tab, 25 elements are along the taper region of the end tab, and 38 elements are along the gage section of the specimen. The end tab portion of the specimen is eight elements thick. The aspect ratios for the elements used in this model were kept below 3 to 1.

Orthotropic material properties are used as input to the finite-element model. The input orthotropic material properties were predicted using composite material mechanics and constituent properties supplied by the constituent manufacturers. Table 4 summarizes the constituent material properties (first four columns) and the predicted composite properties (last two columns). The last column summarizes the end tab material properties.

The tube specimen model is built with boundary conditions that take advantage of the symmetry of the specimen geometry. At the midplane of the specimen a symmetry boundary condition is applied. Vertical displacements and rotations about the horizontal axis are constrained. On the inside diameter of the specimen a horizontal displacement constraint is placed to simulate the expanding collet used to prevent buckling around the circumference when the grip pressure is applied.

A 222 kN (50 kip) normal load was applied to the specimen through the fixtures for the purposes of this analysis. Additionally, a 28 MPa (4 ksi) load was applied to the outside of the grip region of the end tabs in the horizontal direction to simulate the applied gripping pressure. It is not clear what percentage of the normal load is transferred to the specimen from the grips in shear loading and what percent through the load stem in end loading. Because of this a bounding procedure was used to evaluate the specimen. The bounding procedure first applies all of the 222 kN (50 kip) normal load through grip shear, and then, in a second analysis, applies the entire load through end loading. It is felt that looking at the extremes bounds the real loading condition.

The finite-element model was run in a quasi-static loading mode and in a buckling mode. The contours of the finite-element result seen in Fig. 11 indicate that bending is not present in the specimen and that the stress state was uniform and maximum in the gage section of the specimen. The gradient of stresses shown is minimum at the top of the model in the end tab region, gradually increases through the end tab region, and becomes maximum in the gage section. The finite-element investigation of the first five eigenvalues for the tubes in buckling shows that the critical load is at least a factor of three higher than the experimentally observed failure loads for the tubes.

TABLE 4—*Material properties used in the finite-element evaluation of the compression specimens.*

Material Property	AS4	3501-6	S-Glass	Epoxy	AS4/3501-6 $[\pm 45/90/0]_s$ $[\pm 45/0/90]_s$	S-G1/Ep $[\pm 45]$
E_{xx}, GPa	234	4.27	85.5	3.44	55.9	14.7
(Msi)	(34.0)	(0.62)	(12.4)	(0.50)	(8.10)	(2.14)
E_{yy}, GPa	22.4				55.9	14.7
(Msi)	(3.25)				(8.10)	(2.14)
E_{zz}, GPa	22.4				12.2	12.5
(Msi)	(3.25)				(1.77)	(1.81)
ν_{xy}	0.3	0.34	0.22	0.3	0.3045	0.5856
ν_{yz}	0.35				0.3059	0.1411
ν_{zx}	0.3				0.3059	0.1411
G_{xy}, GPa	9.01	1.59	35.0	13.3	21.4	1.49
(Msi)	(1.31)	(0.23)	5.082	1.923	(3.10)	(0.216)
G_{xz}, GPa					4.84	4.53
(Msi)					(0.702)	(0.657)
G_{zx}, GPa	9.01				4.84	4.53
(Msi)	(1.31)				(0.702)	(0.657)



FIG. 11—*Finite-element results of the axial stress when the load is sheared in through the end tabs.*

Discussion of Results and Effectiveness of Method

The results of this investigation into the validity of the 50.8-cm diameter (2 in.) closed-cross-section test specimen and fixture look very promising. The experimental and analytical investigations indicate that the specimen appears to avoid Euler buckling and develops a load that is both uniform and maximum in the gage section of the specimen. In the remainder of this section the results of this investigation are discussed in more detail.

One of the primary concerns upon entering this investigation was the potential for Euler buckling in the specimen. The finite-element results clearly indicate that Euler buckling will not occur in loads below 700 MPa (150 kips). This analysis only evaluated the structural response of the material and not the micromechanical response. The micromechanical evaluation of the damage site was hampered by the extent of the damage in the failure region. The lack of Euler buckling was experimentally verified by placing strain gages on the specimen, as shown in Fig. 7, and loading the specimen to failure. Figures 8 and 9 show the results of these experiments. Correcting for initial offsets, the gages are recording the same stress-strain behavior. If buckling were present, the stress-strain curves would diverge as a result of the bending caused by the elastic instability. This high level of buckling stability indicates that the specimen is much more robust than initially expected and can be used to evaluate laminates that have a higher proportion of 0° layers.

The finite-element axial stress state illustrated in Fig. 11 shows the load gradually being applied to the composite layer in the gage and transition sections of the tab region. At the end of the tab region, extending into the gage section, the load then becomes uniform and maximum. Both loading bounds, shear and end loading, produce the same result in the gage section as is expected from a St. Venant argument.

In the finite-element model the horizontal constraint applied in the gage section to simulate the inner collet and the horizontal load applied to the grip region of the end tabs need further consideration. Some may argue that horizontal constraint applied in the gage section artificially restricts the tube from deforming and thus biases the analytical results to be favorable. The expanding collet that is supporting the inner wall is made of steel and is significantly stiffer than the composite and end tab through the thickness. The 28 MPa (4 ksi) pressure applied by the grips will cause insignificant deformations in the expanding collet. Thus the constraint is considered a reasonable approximation to the actual boundary condition. The 28 MPa (4 ksi) load applied by the grips in the vertical direction was calculated by determining the force on the grips from the lateral loading bolts. This force was calculated from the torque applied to the bolts when the specimen was being set in place.

It is of interest to note that the experimentally determined axial moduli summarized in Table 3 compare very well to the axial moduli calculated from constituents that are summarized in Table 4. The constituent material properties used to predict the laminate properties for the finite-element model were values provided by the material suppliers. Micromechanical theory was used to then predict lamina properties. The lamina properties were then input to a laminate plate model to predict the laminate properties. The specimen finite-element model used "smeared" properties in the analysis. This is considered appropriate since the objective of the model was to determine the global response of the specimen to compressive loading. Using a lamina scale finite-element model would have complicated the model considerably and would not have provided a proportional amount of benefit.

The analytical and experimental results of this effort clearly indicate that the specimen and fixture configuration being presented can be used to reliably determine the compressive properties of closed-cross-section composite laminates. It is also of interest to note that the fixture is designed for ease of use. The self-aligning feature built into the expanding collet and load stem helps to raise the values of the repeatability and reproducibility for this test configuration. This configuration provides a relatively good cost-effective methodology for the characterization of closed-cross-section composite material laminates.

The experimental investigation under discussion in this paper did not evaluate flat coupons made using similar materials and fiber orientation. However, when this test method was first being considered, a preliminary study was carried out that did compare the same tubes with flat coupons [6].

In this preliminary study the tubes were tested without internal expanding collets and fixtures that gripped the end tabs. The tubes were placed between two compression platens, unsupported, and loaded to failure. The average failure load for the four $[\pm 45/90/0]_s$ specimens using this method was 622 MPa (90.2 ksi) and for the two $[\pm 45/0/90]_s$ specimens was 584 MPa (84.7 ksi). In the current

study, which supported the tubes with internal expanding collets and fixtures that gripped the end tabs, the average failure stress for the $[\pm 45/90/0]_s$ specimens was 696 MPa (101 ksi) and for the $[\pm 45/0/90]_s$ specimens was 688 MPa (100 ksi). The discrepancy between the results of the preliminary study and the current study can be attributed to the instability of the specimens in the preliminary study. It was very difficult to prevent specimen misalignment without support fixtures. The moduli determined in the preliminary study for the two geometries were very close to the moduli determined in the current study.

The flat coupons evaluated in the preliminary study were tested using the ASTM Test Method for Compressive Properties of Rigid Plastics (D 695-91) standard with a 3.81 cm (1.5 in.) width and 0.635 cm (0.5 in.) gage length. These tests resulted in a failure stress of 363 MPa (52.7 ksi) for the $[\pm 45/90/0]_s$ specimens and a failure stress of 426 MPa (61.9 ksi) for the $[\pm 45/0/90]_s$ specimens. The experimentally determined moduli for the flat coupons were similar to the tube specimens.

The large discrepancy between the flat coupons and the tubes appears to indicate the influence of free-edge damage modes. In Ref *6*, the authors point out that the average modulus reduction ratio for the flat coupons was 0.75 compared to 0.89 for the cylindrical specimens. They attribute the difference to the presence of free-edge induced damage such as delamination and transverse cracking. They also observed, using radiography and ultrasonics, that damage was not present in the tubes up to the time of final failure. These findings tend to support the assertion that flat coupons with free edges are not good material characterization analogs for closed-cross-section composite structures.

Summary, Conclusions, and Recommendations

The objective of this investigation was to determine if the specimen and fixture configuration presented was capable of accurately predicting the compressive properties of closed-cross-section composite material laminates. The resulting investigation evaluated the suitability of this configuration through both experimental and analytical means. Through this investigation this configuration was found to successfully prevent bending and buckling in the specimen, the maximum axial stress state was found to be uniformly distributed in the gage section, the configuration produced repeatable results, and it was relatively easy to use. An interesting side note to this investigation was the lack of transverse cracking, splitting, and delamination observed in these specimens up to failure.

To truly determine the robustness of this configuration additional investigations need to be conducted. Other specimen laminate geometries need to be evaluated. The ideal configuration would be capable of characterizing laminates that ranged from all axially oriented fibers to all transversely oriented fibers. The sensitivity of this specimen to laminate thickness and constituent materials needs to be investigated further. To get a sense of the true ease of use and reproducibility, a round robin needs to be conducted.

References

[*1*] Hsiao, H. M., Daniel, I. M., and Wooh, S. C., "A New Compression Test Method for Thick Composites," *Journal of Composite Materials,* Vol. 29, 1995, p. 1989.

[*2*] Chaterjee, S., Adams, D., and Oplinger, D. W., *Test Methods for Composites a Status Report Volume II: Compression Test Methods,* DOT/FAA/CT-93/17, 1993.

[*3*] Swanson, S. R., "Overview of Biaxial Test Results for Carbon Fiber Composites," *Composite Materials: Fatigue and Fracture, Seventh Volume, ASTM STP 1330,* R. B. Bucinell, Ed., American Society for Testing and Materials, 1998, p. 19.

[*4*] Bucinell, R. B., Moy, D., and Vandiver, T. L., "Transverse Tension, Transverse Compression, and Inplane Shear JANNAF Round Robin Test Methods Standardization Results," *Proceedings of the 1992 JANNAF Propulsion Meeting,* 27 February 1992, Indianapolis, IN.

[*5*] Groves, S. E., "Characterizing the Failure of Composite Structures," LLNL Thrust Area Annual Report, 1990.

[*6*] Andrews, K. B., Ochoa, O. O., and Roschke, P. N., "Damage Accumulation in Flat and Cylindrical Composite Specimens," Texas A&M internal report, College Station, TX, 1993.

Stephen D. Owens,[1] *Ronald P. Schmidt,*[1] *and John J. Davis*[1]

Tension Pull-off and Shear Test Methods to Characterize 3-D Textile Reinforced Bonded Composite Tee-Joints

REFERENCE: Owens, S. D., Schmidt, R. P., and Davis, J. J., **"Tension Pull-off and Shear Test Methods to Characterize 3-D Textile Reinforced Bonded Composite Tee-Joints,"** *Composite Structures: Theory and Practice, ASTM STP 1383,* P. Grant and C. Q. Rousseau, Eds., American Society for Testing and Materials, West Conshohocken, PA, 2000, pp. 398–409.

ABSTRACT: Test methods, data acquisition, and data reduction techniques used to generate design properties for skin-to-spar composite bonded joints that are reinforced using shaped 3-D textiles are presented. These methods represent the culmination of lessons learned after execution of government Small Business Innovative Research (SBIR), Contracted Research and Development (CRAD), and company Independent Research and Development (IRAD) projects. Industry recognition of the poor interlaminar properties of laminated composite materials has limited applications to structures that primarily react to in-plane loads. However, under company IRAD, CRAD, and SBIR-funded Z-fiber programs, revolutionary tension-loaded bonded joints that utilize 3-D woven textile preforms have demonstrated vastly improved strength and damage tolerance capabilities. Characterization of failure modes and the onset of permanent damage for these novel joints are described. Test procedures involving stepped and fatigue type loading have been developed in order to distinguish between ultimate failure loads that are typically reported versus the service load capability of a particular joint. Overviews of the procedures used to conduct two specific types of element tests are presented. The methods are described as (1) tension web pull-off or tee-pull, and (2) horizontal joint shear.

KEYWORDS: composites, test methods, bonded joints, 3-D, woven preforms

The application of composite materials to military airframe structures has been limited to members that primarily react to in-plane loads. Attachment of structural members is primarily accomplished with mechanical fasteners. In order to achieve a higher level of composite structural application and part integration, bonded joints capable of reliably carrying out-of-plane tension loads must be developed. To this end, Lockheed Martin initially demonstrated innovative joining concepts for composite materials that utilized 3-D woven-shaped preforms under the Robust Composite Sandwich Structures (ROCSS) program. These joint types were found to contain initial matrix failures and sustained substantial additional load before encountering significant, and finally, catastrophic failure. As a reference point, Fig. 1 illustrates one joint concept evaluated under the ROCSS program. Integration of individual sandwich panels was achieved using "pi"-shaped textile preforms. The textile preforms used for ROCSS were fabricated with IM7-6K fiber using a ply-to-ply angle interlock weave pattern. Details of joint designs and test results for the ROCSS Phase I program are documented in Ref *1*. In order to evaluate the performance and ultimately to provide design-to-property data for these types of 3-D textile reinforced bonded joints, tension pull-off and horizontal shear element tests were conducted. The purpose of this paper is to describe test objec-

[1] Engineering specialist senior, Structures Lead, engineering specialist senior, Design Lead, and engineering senior, Materials & Processes, respectively, Technology Integration, Lockheed Martin Tactical Aircraft Systems, Fort Worth, TX 76101.

Copyright© 2001by ASTM International www.astm.org

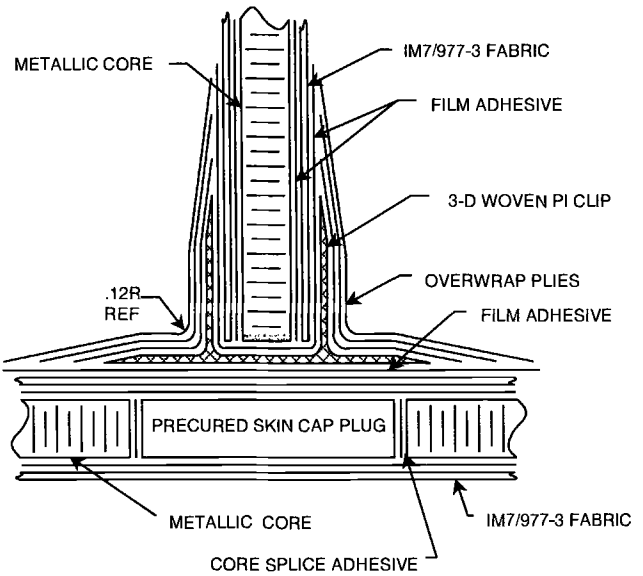


FIG. 1—*ROCSS 3-D reinforced bonded joint ply layup detail.*

tives, procedures, data, and failure modes commonly observed for pull-off and shear tests for 3-D preform reinforced bonded joints.

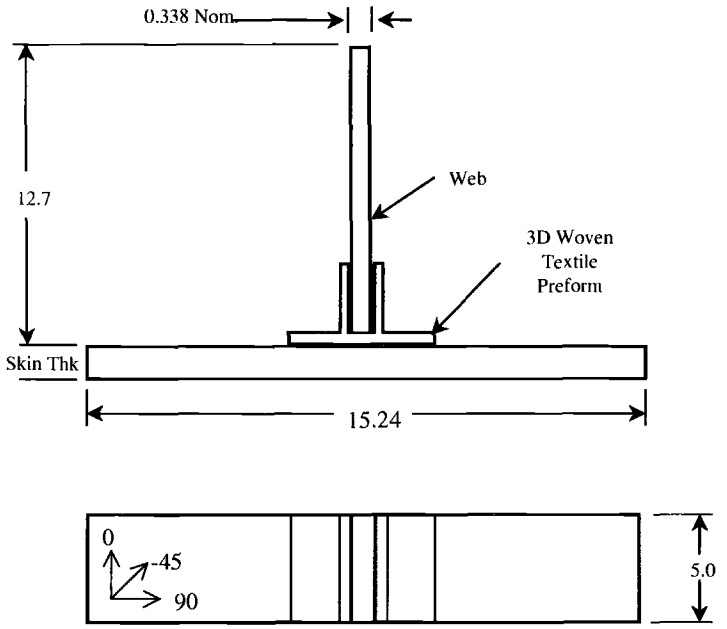
Tension pull-off loading has been used for many years to characterize the pull-off tension strength of hat, blade, and tee-stiffened bonded joint elements typical of helicopter and fixed-wing airframe structures [*2,3*]. While there is nothing unique about the pull-off test per se, what is unique and worthy of presentation here is the use of specific data acquisition and reduction techniques to characterize damage onset, damage attenuation, and ultimate failure of joints reinforced with 3-D textiles and/or Z-fiber reinforcements. This information is crucial to define the operational design limit load for composite bonded joints that exhibit progressive failure characteristics. In addition to characterization of joint pull-off load capability, shear strength is required for design. A simple test fixture and procedure was developed by Lockheed Martin to measure shear strength for 3-D textile-reinforced joints. The fixture, test procedures, typical results, and failure modes are described herein.

Work to date indicates that changes in joint compliance as determined from progressive step-loading and fatigue testing should be conducted to establish safe working load levels for joints that exhibit progressive damage growth and arrestment characteristics. The following test methods refer to an "initial crack" or "initial damage event" as detected via a clip gage measurement near the joint intersection. Other terms reference a visually detectable event and an ultimate failure event. Application of appropriate failure criteria based on these events leading to ultimate joint failure is critical for airframe design applications.

Experimental Methods

Tension Web Pull-off

The objective of this test is to measure the Z-direction (or out-of-plane) failing load of simple tee-section joined elements as illustrated in Fig. 2. This is typical of coupon geometry for tests conducted at Lockheed Martin. Specimen width is 5 cm while the length can be varied to accommodate different loading fixtures. Height of the web or upstanding leg is approximately 12.7 cm. A



Notes:

1. Sketch is not to scale
2. SI Dimensions (cm)

FIG. 2—*Tension pull-off coupon geometry.*

three-point flexure technique is typically used to introduce the pull-off load using simple supports. This test simulates critical out-of-plane loading conditions generated by fuel pressure and/or geometry-induced kick loads. The span and end fixity conditions can be modified to reflect conditions associated with a specific design configuration or set to specific values in order to compare different joint concepts.

Test Setup—A steel load reaction test frame is commonly employed to minimize undesirable "system" deflections during testing. An example is shown in Fig. 3. This fixture will accommodate specimen widths ranging from 3.8 to 6.4 cm. The end-fixity for this fixture approaches a pure clamped condition. Care is taken to locate and center each specimen to avoid introducing eccentric loading of the upstanding leg of the tee-section (typically simulating a web member). Specimens are first clamped into the upper grips of the load introduction machine to assure that it is centered in the test fixture. Then the specimen is checked for alignment of the vertical web by comparing relative gaps in the base laminate (typically representing a fuselage or wing skin) with the lower clamping block on the reaction fixture. If a gap exists, shims are installed. The upper clamps are then located and the four clamping bolts are secured in a stepped pattern to insure an even pressure distribution.

A standard MTS clip gage is used to measure local displacement between the web and skin. The primary function of the clip gage in this test setup is to acquire "local" load-displacement data necessary to determine initial failure and subsequent cracking events. The clip gage used for tee-pull testing has a "blade" contact on the web portion of the specimen and a "point" contact with the skin. The "point" contact is used on the skin to prevent erratic readings caused by extreme skin bending that

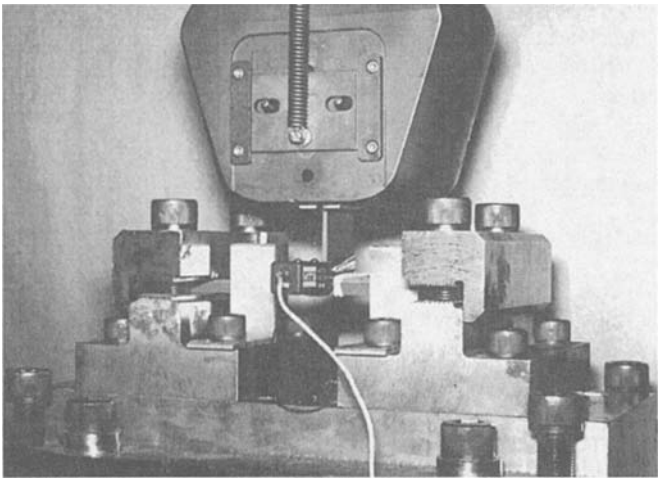


FIG. 3—*Tee pull-off load fixture.*

commonly occurs during this test. An approximate gage length of 1.0 cm is commonly employed. The clip gage is attached using elastic rubber bands for the room temperature (RTD) testing or metallic springs for hot/wet test conditions. Other techniques employ small bonded aluminum tabs to locate the gage. Data acquired during each test consists of a time stamp, crosshead deflection, clip gage deflection, and load.

Test Procedures—Static ramp to failure testing is performed to provide insight on first event (noncatastrophic damage) and ultimate load levels. Using the data obtained, an average first-event load level and an ultimate load level can be determined. This information then provides the setpoints for subsequent compliance and fatigue testing. The static ramp to failure test is conducted in stroke control—a specified rate of deflection is maintained by the test machine. A deflection rate of 0.5 mm/min (0.02 in./min) is used for most of the tests conducted at LMTAS. In order to effectively measure "initial" matrix cracking events, data acquisition sampling rates should equal or exceed 5 samples per second. However, when establishing the crosshead deflection rate, the span setting, specimen bending stiffness, and data sampling rate should be considered in order to optimize test performance. The applied deflection rate of 0.5 mm/min coupled with data sampling of 5 samples/s has proven to work well for crosshead deflections at failure ranging from 2.5 to 5.0 mm. If smaller deflections are anticipated, then either the sampling rate should be increased or the load rate decreased.

Stepwise loading tests are performed to generate a series of hysteresis loops. These loops are used to quantify changes in measured joint stiffness that can result from accumulation of damage events. These tests are conducted under load control. The loops are typically started at 40% of the average "first-event" value measured in the static test. Three to five hysteresis loops are measured at each load level. Subsequent load levels are incremented by 10% until failure occurs. Compliance loop data are then overlaid on a plot to determine changes in load-deflection behavior.

Finally, fatigue tests are performed to help confirm failure modes and establish safe operational load level for these types of bonded joints. Fatigue tests are conducted under load control using the same setup previously outlined. Cyclic load rate typically does not exceed 5 Hz. Simple blocked and constant amplitude loading profiles have been used successfully. Much of the work to date has been conducted using constant amplitude loading with a R-ratio of −0.05. Typically 20 K constant-am-

plitude cycles are applied followed by a static load to failure (if the joint survives). Application of 20 K cycles was selected to approximate application of the most damaging stresses found in two service lifetimes for a military tactical aircraft. Compliance loops are taken at intervals to determine if the cyclic loading introduces damage (and subsequent changes in joint stiffness). For fatigue testing, a specified percentage change in measured joint stiffness can be defined as failure. Thus, *S-N* curves can be generated based on a definition of failure that reflects either a permanent change in joint stiffness and/or two part failure.

Joint Horizontal Shear

Until recently, low pull-off strengths and the general lack of damage arrestment features of composite bonded joints precluded application on highly loaded airframe structures. Poor results from simple tension pull-off tests were usually sufficient to eliminate most composite bonded joint designs. Now, for the first time, ultimate pull-off load capabilities exceed typical design ultimate load requirements common to military airframe structural applications. Next, a technique to measure the shear strength of the 3-D textile preform with different fabric ply over-wrap configurations was required for design. A simple test fixture was developed at Lockheed Martin in Fort Worth as illustrated in Fig. 4 for this purpose. The fixture is designed to align the applied load axis with the joint

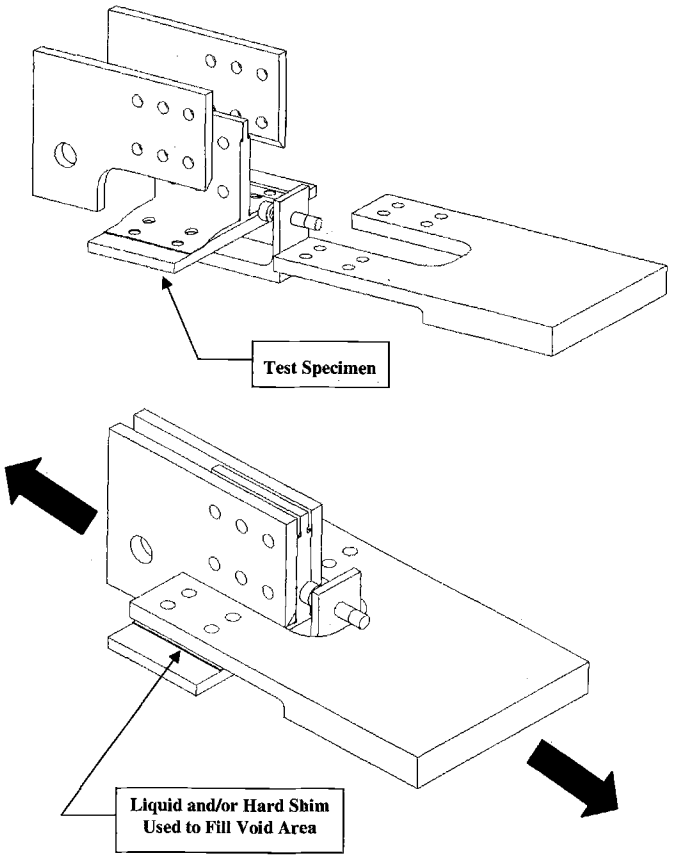


FIG. 4—*Horizontal joint shear test fixture.*

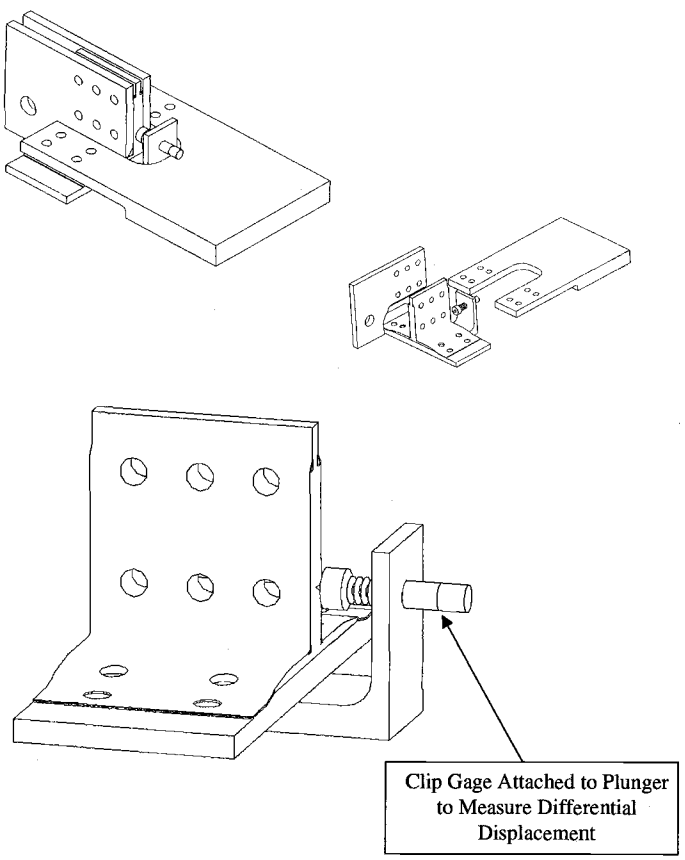


FIG. 5—*Clip gage plunger design and attachment for joint shear test.*

skin to web interface. This minimizes load eccentricity. Provisions are also included to mount a clip gage capable of measuring differential displacement of the base and upstanding leg members as previously described. Test setup, load application, and data acquisition methods for this test method are described in the following discussion. The primary differences between the two test methods are in the test setup. The coupon width is 5 cm as in the pull-off test, while length and height dimensions are not critical. Test procedures for the joint shear test are essentially the same as those previously outlined for the web tension pull-off, thus only the differences between the methods will be described.

Test Setup—The steel load introduction fixture illustrated in Fig. 5 was designed to align the load axis at the specimen joint interface. Coupons tested are approximately 5 cm wide and are drilled to match the test fixture using a drill template. The specimen is first attached to the "horseshoe" fixture. Shimming may be required if the specimen has a tapered transition from the web to skin. Then the two upper plates are bolted to the specimen. The fasteners are secured in a sequence that prevents eccentric loading on the coupon.

As with the tee-pull testing, the primary function of the clip gage in this test setup is to acquire local load-displacement data necessary to determine initial failure and subsequent cracking events,

as well as joint stiffness. A standard MTS clip gage is used to measure local displacement in the longitudinal axis between the web and the skin. A spring-loaded pin fixture is bonded to the specimen skin using double-back tape with the pin contacting the upstanding web member as shown in Fig. 5. The clip gage is attached to the spring-loaded fixture after the coupon is installed in the grips. Unlike the tee-pull clip gage, the shear clip gage uses blade contacts on both attach points since the gage is not directly attached to the specimen and skin bending is not an issue. An approximate gage length of 1.0 cm is commonly employed. In order to effectively measure "initial" matrix cracking events, data acquisition rates should equal or exceed 5 samples per second. The specimen/fixture is first installed in the lower grip of the test machine using the "horseshoe" bracket. Then the coupon is manually raised until the hole in the test fixture aligns with the hole in the machine grips. A pin is then installed which allows some freedom of rotation to prevent eccentric loading.

Test Procedures—Test procedures and equipment control settings for the joint shear test are essentially the same as for the tee pull-off test. A static ramp to failure is performed to provide insight on noncatastrophic damage and ultimate load levels. These values can then be used to provide set points for subsequent compliance and fatigue testing. Loading procedures have been developed to generate static ultimate strength, evaluate changes in joint stiffness via stepwise incremental loading, and assess the effects of cyclic loading.

Discussion of Results

Tension Web Pull-off

A typical load versus crosshead displacement curve from a static joint pull-off test is shown in Fig. 6*a*. The applied load as a function of local displacement, measured using the clip gage is provided as Fig. 6*b*. The fixture for this particular test used clamped end conditions with a span of 12 cm. Note a small, but discernible load drop on the crosshead deflection curve followed by essentially a linear load to ultimate failure. However, this seemingly insignificant "blip" in the curve actually corresponds to a first failure event as confirmed by the clip gage measured displacement shown in the lower panel of Fig. 6. This initial failure event is also commonly confirmed with both visual and audible cracking.

This particular specimen incorporated two additional wrap plies at the web to skin joint (as illustrated in Fig. 1) to improve shear strength. The sequence of failure events commonly observed is interlaminar tension-induced failure of the wrap plies in the radius, interlaminar shear and tension cracking of the textile preform in the radius, followed by interlaminar tension cracking of the 2-D skin laminate beneath the 3-D textile preform to skin interface. This sequence of failure events is illustrated in Fig. 7. The initial load drop at approximately 90 kN/m shown in Fig. 6 is typically associated with an interlaminar crack in the wrap plies. This repeatable event has been confirmed visually at approximately the same load and correlates with the large displacement event shown in the clip gage data. The magnitude of the clip gage displacement is generally ignored since the gage slips during some of the more energetic cracking events. The benefit of the 3-D textile is readily apparent as compared to results gathered from similar three-point flexure tests using hat sections [*2*]. The authors noted almost immediate failure after crack initiation [*4*] for an unreinforced joint design.

A potential failure criterion that is being explored is based on change in joint stiffness, or compliance. The incremental loading procedure (as previously outlined) was used to evaluate potential changes in joint compliance associated with increased load. Hysteresis curves (based on crosshead displacement) for one of these stepwise loading events is shown in Fig. 8. Unfortunately, total system compliance is reflected in these plots. In order to ease visualization, only one hysteresis loop is shown per load level. Remember that the test procedure calls for data collection of three to five

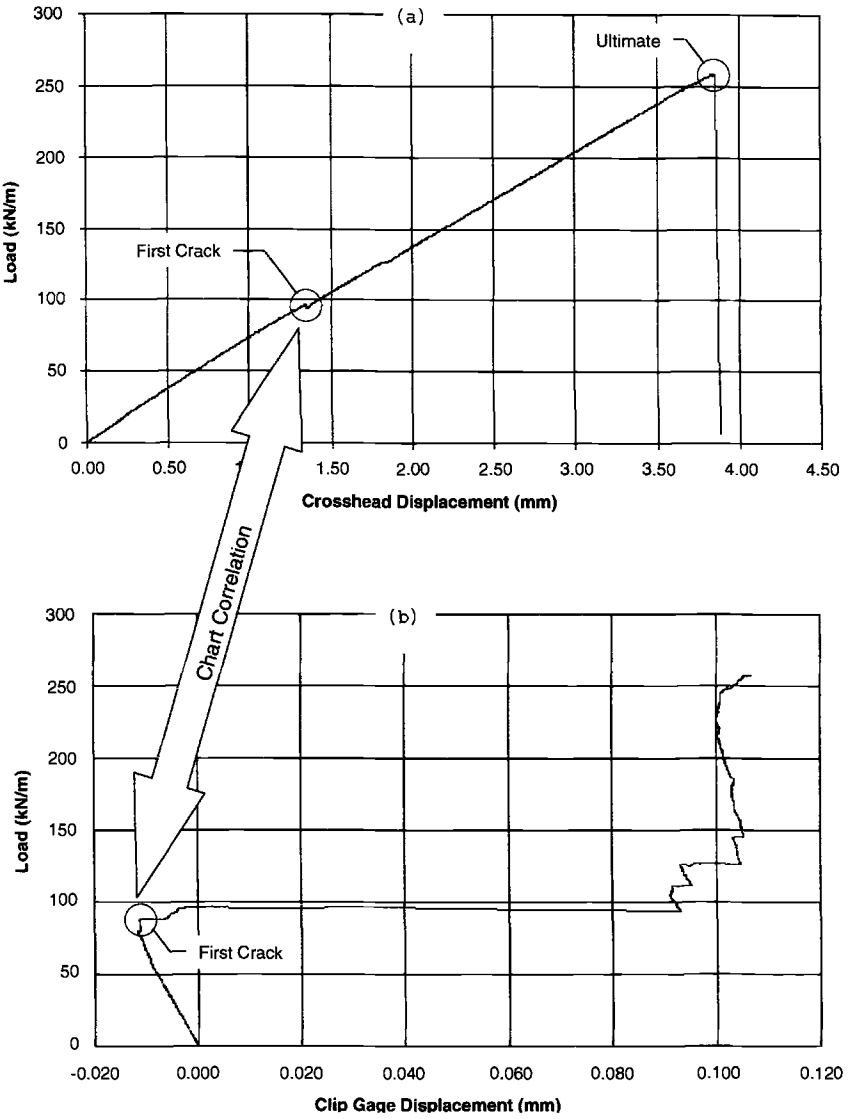


FIG. 6—*Tee pull-off crosshead and clip gage measured load—displacement plots.*

loops per load level. Once again, the useful data are collected via clip gage measurements located across the joint intersection. Clip gage based hysteresis loops for the same specimen are shown in Fig. 9. This particular specimen exhibited little change in joint stiffness despite development of initial interlaminar tension driven matrix cracks beneath the wrap plies in the radius area. Other configurations that have been evaluated exhibit up to 18% change in joint stiffness with increasing amounts of load. Measured changes in joint stiffness appear to coincide with the development of

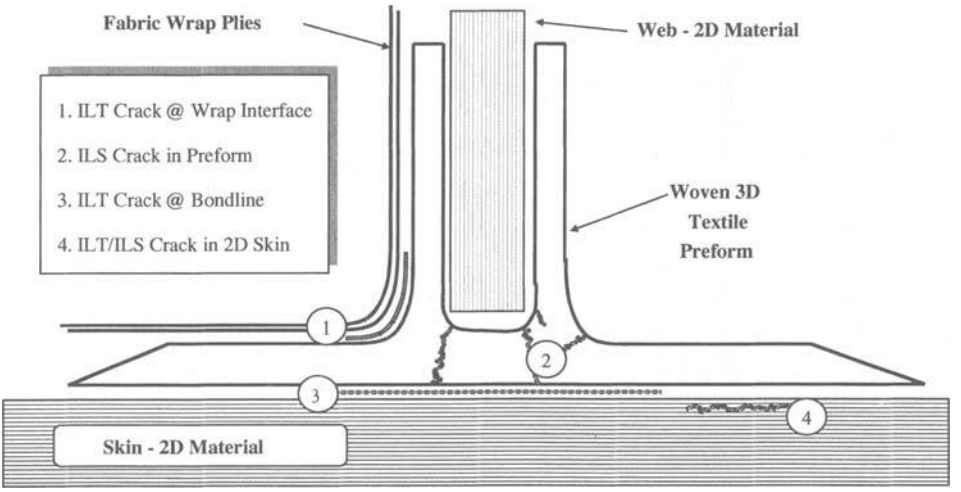


FIG. 7—*Experimentally observed failure modes for tension pull-off loading.*

interlaminar tension and shear driven matrix cracks that first occur in the radius area and then transition beneath the 3-D to 2-D material interface. A final set of pure fatigue tests can then be run to define an *S-N* curve. Fatigue testing is periodically halted to collect compliance loops. The definition of "failure" for tension loaded bonded reinforced with 3-D material is still being investigated. However, use of these procedures to collect data associated with changes in joint stiffness is considered useful for this purpose.

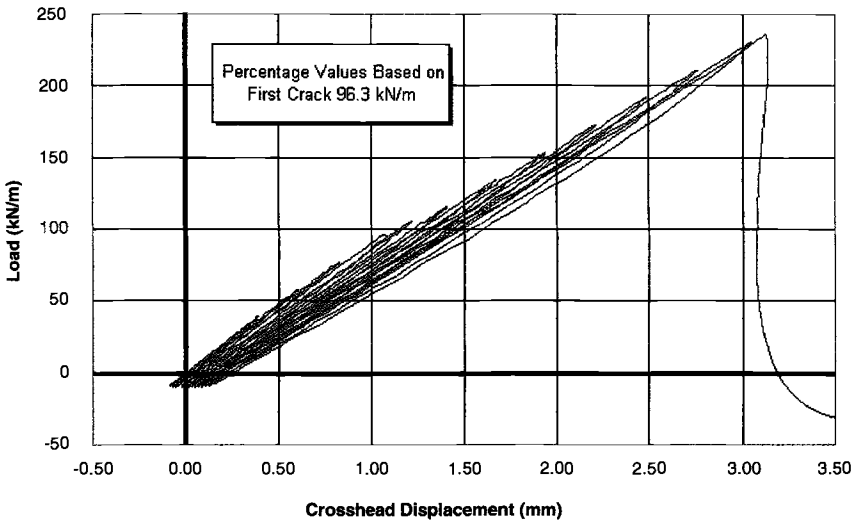


FIG. 8—*Hysteresis loops from stepwise loading test.*

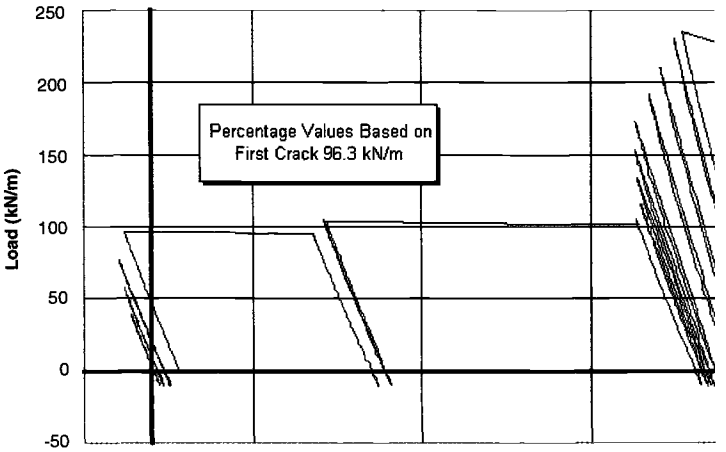


FIG. 9—*Clip gage measured joint stiffness loops from stepwise loading test.*

Joint Horizontal Shear

Typical sets of curves measured using this fixture are shown in Fig. 10. Displacements measured via the crosshead and clip gage are shown superimposed on the same plot. The typical failure mode is shear-induced fiber tension failure of any 45° fabric wrap plies, followed by shear-induced failure of the textile preform in the radius. Photographs of typical failed specimens are shown in Fig. 11. It is worth reiterating here—a different test configuration must be used to capture shear performance at the bondline between the web and legs of the 3-D preform. The shear test method described here is geared to examine the shear capability of the web-to-skin connection via the shaped 3-D textile preform.

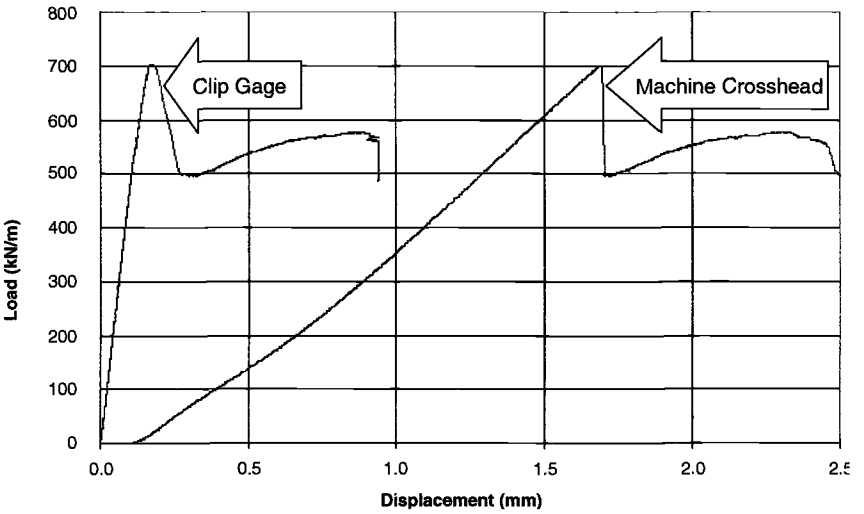


FIG. 10—*Joint shear crosshead and clip gage measured load—displacement plots.*

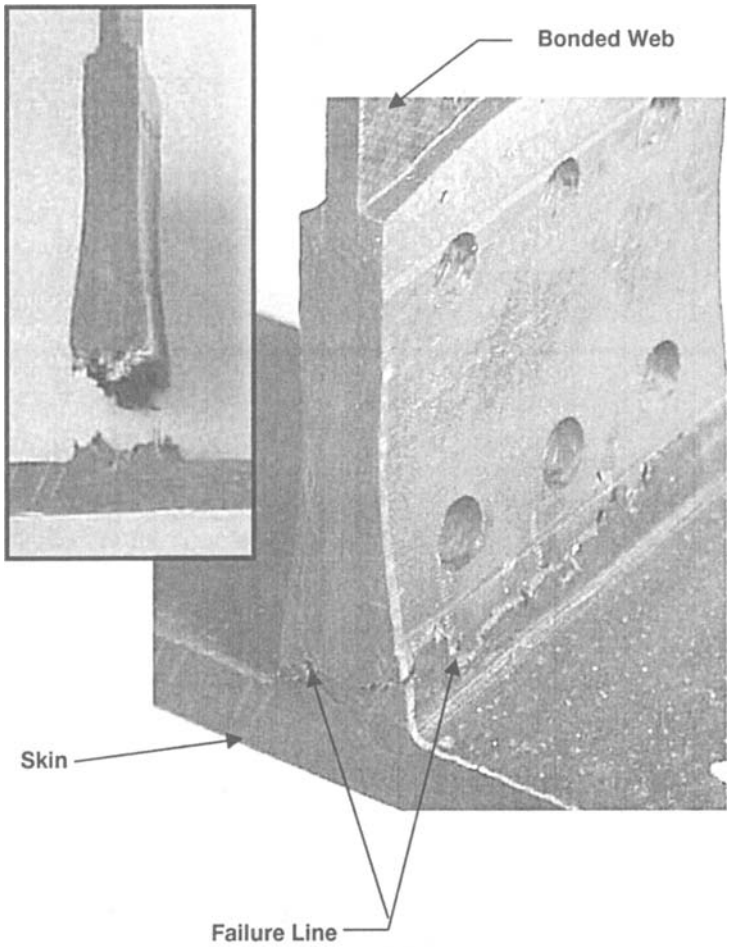


FIG. 11—*Failed joint shear test specimen.*

Conclusions

Test methods and data reduction techniques were devised under various contracted and internal R&D projects to capture the key performance characteristics that drive design of bonded joints which incorporate shaped 3-D textile preforms. Proper data acquisition and data reduction techniques were developed to capture highly localized initial failure events. These initial failure events may dictate that design service loads be set significantly less than the ultimate load. Observed failure modes and results in these joints have shown potential improvements in the use of shaped 3-D textiles over typical unreinforced co-cured joints. Additional tests are still necessary to quantify these improvements and to define process control characteristics.

References

[1] Sheahen, P., "ROCSS Preliminary Design Review," Robust Composite Sandwich Structures (ROCSS) Program Presentation, Dayton, OH AFRL, 6 May 1997.

[2] Li, J., O'Brien, T. K., and Rousseau, C., "Test and Analysis of Composite Hat Stringer Pull-off Test Specimens," NASA-TM-110263, June 1996.

[3] Minguet, P. J. and O'Brien, T. K., "Analysis of Test Methods for Characterizing Skin/Stringer Debonding Failures in Reinforced Composite Panels," *ASTM STP 1274*, American Society for Testing and Materials, 1996.

[4] Minguet, P. J. and O'Brien, T. K., "Analysis of Test Methods for Characterizing Skin/Stringer Debonding Failures in Reinforced Composite Panels," *ASTM STP 1274*, American Society for Testing and Materials, 1996, p. 111.

Strength Prediction

L. J. Hart-Smith[1]

What the Textbooks Won't Teach You About Interactive Composite Failure Criteria

REFERENCE: Hart-Smith, L. J., **"What the Textbooks Won't Teach You About Interactive Composite Failure Criteria,"** *Composite Structures: Theory and Practice, ASTM STP 1383*, P. Grant and C. Q. Rousseau, Eds., American Society for Testing and Materials, West Conshohocken, PA, 2000, pp. 413–436.

ABSTRACT: This paper exposes what really happens when interactive failure theories for fiber-polymer composites are combined with progressive-failure theories to justify discarding the predicted first-ply failure prediction in favor of a subsequent last-ply failure prediction. The procedure is shown to be far from the rational scientific process it is customarily presumed to be, even without any precise definition of the analytical procedure that is normally defined only in the associated computer codes, the source codes for which are not usually available. The paper shows how, and why, measured lamina properties are changed to others that cannot possibly be measured, and the theories changed, too, with no notice to that effect. The paper contains both qualitative and quantitative illustrations of the unacceptability of these theories, along with unresolved paradoxes that have bedeviled this process from the very start, but which have yet to be addressed. The never-justified simplifying assumptions made at the very first step of these analyses are explained, and a strong case is made that only mechanistic failure models, with separate equations for failures in the fibers, the matrix, and at the interface can be relied upon. An analogy can be drawn with reinforced concrete structures, the structural analysis of which requires the separate properties of steel and concrete, which are the "constituents" of this particular composite of materials. This does not imply that fiber-polymer composites can be characterized only at the micromechanical level: just that characterizations at the traditional macromechanical level must not be simplified (homogenized) to the point that they fail to adequately represent the dominant phenomena. Even for truly homogeneous materials, each mode of failure is completely defined by a single material reference property, be it a strength, a fracture toughness, or a modulus. It is noted that a need for multiple reference strengths should imply the presence of multiple independent failure mechanisms, not that there are interactions between them. A very strong recommendation is made that both the teaching and use of interactive composite failure theories cease forthwith, because the only applicability that any of these theories might have is to truly homogeneous anisotropic solids like rolled metallic plates and extrusions. Despite the fact that one of them, the Tsai-Wu theory, is the most widely taught theory for composites, not one of the many interactive theories for homogeneous anisotropic solids has ever been shown to have any relevance to inherently heterogeneous fiber-polymer composites. Progress towards simple reliable analysis tools for this task, to reduce the level of expensive testing that would be needed for entirely empirical characterizations, will not be achieved as long as these obstacles continue to stand in the way.

KEYWORDS: fiber-polymer composites, failure criteria

The ultimate reason for presenting this paper is to promote a long overdue open debate on the process of predicting the strength of unnotched fiber-polymer composites that has until now, in the USA at least, been largely ignored.

Two distinct approaches have been followed by the authors who published the many composite failure theories. In one, referred to as mechanistic, there are separate equations for each failure mode in each constituent in the composite of materials. A distinction is drawn between failures of the fibers, the matrix, and the interface between the two. This class of theories addresses mi-

[1] Phantom Works, The Boeing Company, Long Beach, CA.

Copyright© 2001by ASTM International www.astm.org

cromechanical effects, but has been formulated at both the micromechanical and macromechanical levels. In the other approach, most commonly referred to as interactive, the fibers and resin are homogenized into an "equivalent" anisotropic solid for each "ply" or lamina, which is permitted to have fibers in single or multiple directions, and no distinction is made between failures in the fibers or the matrix.

Fiber-polymer composites of materials are *not* homogeneous anisotropic solids. They consist of discrete constituents, and separate criteria are needed to characterize the failure (strength) of each constituent, fiber and resin matrix, as well as of the interface (see Fig. 1), just as steel and concrete properties are needed to analyze the strength of reinforced concrete structures. The only materials known to mankind for which some of these interactive theories for assumed homogeneous anisotropic materials might be applicable are rolled metallic plates, metallic extrusions, and the like. The very words "homogeneous composites" constitute an oxymoron.

It is the author's position that none of the interactive category have the slightest relevance to fiber-polymer composites, even though some of them are still the most widely taught, by academia and at workshops, still being prominent in even the latest textbooks. While incomplete, some of the mechanistic models have been of great use to the aerospace and other industries. The basic difference between the equations characterizing the two approaches is that within the usually single equation for interactive theories, the reference strengths in the denominator involve multiple modes of failure and/or both constituents of the fiber-polymer composite. Not all such theories involve only one equation. One, discussed in more detail later, contains four equations, intended to be noninteractive and specifically identified as such, but all four are coupled by the matrix-limited in-plane shear strength. In the mechanistic failure models, on the other hand, each equation refers to only one failure mode in one constituent, such as the longitudinal strength of a unidirectional lamina, a normalized fiber-dominated "lamina" property. Consequently, more than one equation is needed, each being independent of all others. The sequence of failure is established by evaluating each of these, on the lamina strain

SEPARATE **CHARACTERIZATIONS ARE NEEDED FOR** ***EACH*** **FAILURE MECHANISM IN** ***EACH*** **CONSTITUENT OF THE COMPOSITE** ***OF*** **MATERIALS**

INTERACTIONS **BETWEEN STRESSES AFFECTING THE** ***SAME*** **FAILURE MODE IN THE** ***SAME*** **CONSTITUENT OF THE COMPOSITE ARE PERMITTED**

INTERACTIONS BETWEEN ***DIFFERENT*** **FAILURE MODES ARE SCIENTIFICALLY INCORRECT**

TYPICAL FAILURE MECHANISMS FOR FIBER-POLYMER COMPOSITES:

- **FRACTURE OF FIBERS AT FLAWS AND DEFECTS, UNDER LONGITUDINAL TENSION**
- **FAILURE OF FIBERS REMOTE FROM ANY FLAWS OR DEFECTS, UNDER TENSILE LOADS**
- **MICRO-INSTABILITY, OR KINKING, OF FIBERS UNDER COMPRESSIVE LOADS**
- **SHEAR FAILURE OF WELL-STABILIZED FIBERS UNDER COMPRESSIVE LOADS**
- **DUCTILE FAILURE OF MATRIX, WITHOUT CRACKING, UNDER IN-PLANE LOADS**
- **CRACKING OF MATRIX BETWEEN THE FIBERS UNDER TRANSVERSE-TENSION LOADS, WHICH INVOLVES** ***BOTH*** **A MATERIAL PROPERTY** ***AND*** **A GEOMETRIC PARAMETER**
- **INTERFACIAL FAILURE BETWEEN THE FIBERS AND THE MATRIX**
- **INTERLAMINAR FAILURE OF MATRIX AT EDGES AND DISCONTINUITIES**
- **DELAMINATIONS BETWEEN THE PLIES UNDER IMPACT OR TRANSVERSE SHEAR LOADS**
- **DELAMINATIONS BETWEEN THICK PLIES INITIATING AT THROUGH-THICKNESS MATRIX CRACKS WITHIN A TRANSVERSE PLY**
- **FATIGUE FAILURES IN THIN PLIES CAUSED BY THROUGH-THICKNESS TRANSVERSE CRACKS IN ADJACENT THICK PLIES**

EACH **OF THESE POSSIBILITIES** ***REQUIRES*** **ITS** ***OWN*** **EQUATION, EVEN THOUGH NOT EVERY MODE CAN OCCUR FOR EVERY FIBER-POLYMER COMBINATION AND EVEN THOUGH SOME MODES CAN BE SUPPRESSED BY SKILLFUL SELECTION OF THE STACKING SEQUENCE**

FIG. 1—*Specification for fiber-polymer composite failure (strength) criteria.*

plane, superimposing all predictions for all plies, and identifying which events occur first, as a function of the biaxial strain state.

Interactive theories can be identified by the involvement of multiple reference strengths, for more than one failure mode, in what is usually (but not always) one single quadratic equation that interacts up to five stress components in defining a mathematical failure surface. The best known mechanistic model is the maximum-strain failure model [*1*], while the best known interactive theory is the tensor-polynomial theory referred to in America as the Tsai-Wu theory [*2*] and attributed to Goldenblat and Kopnov [*3*] in Russia and much of Europe. The most common form of interactive theory involves a single ellipse, or one ellipse per quadrant of the stress plane. The interactive failure envelope so defined is actually an abstract mathematical curve passed through unrelated data points, as discussed in Ref *4*. No scientific basis has ever been claimed for these theories. None has ever been validated experimentally. Indeed, their proponents openly acknowledge that they cannot be related to physical phenomena. In Ref *5*, Wu has stated that "composite failure criteria are like balloons. If you push them in one place, they bulge out somewhere else," while, on pp. 11–17 in Ref *6*, Tsai states that "failure criteria are empirical and phenomenological. They cannot be readily related to failure modes. The physical phenomena of the failure of composites are much too complicated to be described by any of the simple criteria mentioned in this section." (The criteria he was referring to included his own quadratic criterion.) While the author obviously agrees with these characterizations of their own interactive theory, he would question their claim that no other theories could be free from this limitation. Indeed, on pp. 11–5 in Ref *6*, when discussing the maximum-strain and maximum-stress failure models, Tsai states that "A failure *mode* is also implicitly assigned in each strain component. Interactions among the possible five *modes* are assumed to be nonexistent by this (maximum strain) and the maximum stress-criteria." Do not the italicized words, flagged by the author, refute the claims above that failure theories could not be related to physical phenomena? On pp. 11-1 in Ref *6*, Tsai even defines these five modes for each lamina as "longitudinal tensile strength, longitudinal compressive strength, transverse tensile strength, transverse compressive strength, and longitudinal shear strength." Aren't these measured strengths physical phenomena? The issue seems to be that only for mechanistic failure models can these meaningful strengths (or corresponding strains) be applied to biaxial stresses or strains off the reference axes. No physical meaning has yet been ascribed for failure under biaxial stresses or strains in association with interactive failure models.

There are innumerable inherent problems with the formulation of interactive failure theories and even more with their application. Some of these will be discussed here, because several of them are fatal. Some have been well documented in scholarly works by independent researchers [*7–9*] many years ago. Unfortunately, there has been no response from the proponents of interactive theories to these explanations that it is necessary to uncouple any failures of unidirectional laminae under tension loads transverse to the fibers from other failure modes under loads parallel to the fibers. Such separation is needed because matrix cracking is governed by fracture toughness, not by a universal failing stress, and because matrix cracking is influenced by the nature of the fibers in adjacent plies and even by the thickness of the ply under consideration. In other words, failure of the composite material under this mode cannot be predicted on the basis of a ply-by-ply assessment independent of the other plies. Of even more significance, one of the four reference strengths used to define elliptical failure envelopes has thereby been removed by this research. It is not possible to uniquely define an elliptical failure envelope using only the remaining three measured strengths; it should not have been possible in the past to do so without five such strengths, but the fifth term involved in predicting first-ply failures was merely the first of the many unmeasurable reference properties now needed to enable these theories to predict last-ply failure strengths. This problem arose because of the insistence by those who proposed interactive failure theories involving only one equation that the failure envelope had to be closed by that equation. But a failure envelope should be continuous in this manner only when there is no more than one failure mode involved, regardless of the state of biaxial stresses. This condition was satisfied by Hill, in proposing his yield criterion for anisotropic ductile metals

[*10*]. Tsai apparently failed to grasp the significance of this fact when he adapted Hill's theory for composites [*11*]. This problem does not arise with mechanistic failure models because there are multiple possible failure modes defining the perimeter of the failure envelope. Most do not define closed failure envelopes; this is particularly obvious in the case of failures under longitudinal loads in which fibers fail by brittle fracture under tension and some form of microinstability under axial compression. Only in interactive failure theories is there any prescribed interaction between these two physically unrelated measured reference strengths. The goal of creating a closed failure envelope with an interactive formula is the Achilles' heel of every such theory.

This goal is not even necessary, as can easily be seen by an assessment of the maximum-strain failure envelope. The constant longitudinal strains-to-failure, regardless of any transverse strains, uniquely define two sides of a box-shaped failure envelope, for both unidirectional laminae and laminates made from orthogonal fibers. The transverse cutoffs that complete the failure envelope may not be the same, however. For the unidirectional lamina, these transverse failures will be defined by matrix failures, one or both of which may be unique to the unidirectional lamina and have no relevance to any multidirectional laminate. For a 0°/90° laminate,[2] the transverse cutoffs of the failure envelope for the laminate will be defined by the orthogonal fibers under loads parallel to their fibers. For well-designed carbon-epoxy laminates, these fiber failures will precede any structurally significant matrix failures. In the case of glass-fiber-reinforced polymers, however, particularly under tensile loads, the laminate failure envelope for multidirectional laminates will be defined by real matrix failures that precede real fiber failures. However, these matrix failures bear no relation to the transverse strengths measured on unidirectional laminae, for many reasons, including the very different residual thermal stresses caused by curing the resin at temperatures far higher than those in which the structure operates. Mechanistic failure models would permit both the lamina and laminate failure envelopes to be closed, but not necessarily by a single universal equation. But, most importantly, with mechanistic failure models, any real progressive failures in the matrix would have absolutely no effect on the predicted tensile fiber longitudinal strengths, regardless of any transverse or inplane shear loads. They could, however, destabilize axially compressed fibers. One incurable problem with interactive failure theories is that any change in even one of the measured lamina reference strengths causes every predicted strength under bi-axial loads to be altered. For example, the Tsai-Wu theory would predict that the strongest submarine hulls, under biaxial compression, would be made by coating the fibers with a release agent before embedding them in the resin matrix, to decrease the transverse-tension strength of each lamina, as explained in Fig. 2.

Obviously unacceptable predictions based on models like this can occur only because of the use of interactive failure models. One objective of this paper is to open a debate on the question of whether or not any interactive failure models can be scientifically acceptable for fiber-polymer composites. The U.S. Navy submariners will not accept such projections; they truncate the predicted biaxial strengths to not exceed those predicted by the maximum-strain model. The military aircraft side of Daimler-Benz-Chrysler (ex DASA), in Germany, has a similar procedure whereby the compressive strength of the unidirectional lamina is restricted to not exceed the unidirectional tension strength, regardless of any transverse stresses. Curiously, neither group will abandon the theories used to make the predictions that they always reject. Most production groups in the aerospace industry stopped using these theories decades ago. When will academia stop teaching them?

Many researchers have adopted a position that the scientific pedigree of each of the many composite failure theories is unimportant. They feel that all that matters is the ability of each theory to match test data. There are two problems with trying to resolve the choice between failure criteria in

[2] Here, *any* multidirectional layer, or ply, is referred to as a laminate, even a *single* 0°/90° layer of woven fabric. This practice, although not universally adopted, leaves the word lamina to define unambiguously the highest possible level of "composite material" at which it is possible to formulate a macro-level model of strength that covers both fiber and matrix failures. A lamina is therefore a unidirectional 0° tape layer, which is the customary definition, or the equivalent decomposed component of a more complex form of "composite material."

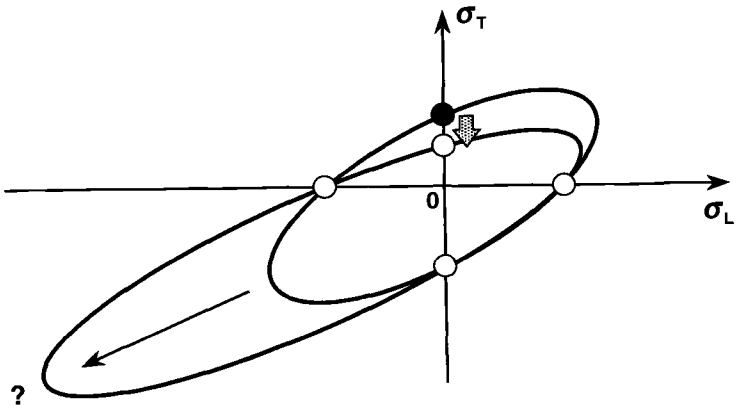


FIG. 2—*Prediction of "improved" submarine hull by coating fibers with release agents before impregnation, per typical interactive failure theory.*

this manner. Since all theories are automatically fitted to measured uniaxial lamina strengths, the only discriminating tests are those under biaxial loads. These have proved to be so difficult to execute that most such test results are even less representative of the strength of composite laminates than are most of the interactive failure theories. It took the organizers of a recent comparison [*12*] between composite failure theories over 18 months to find even three sets of biaxial test data which they felt were accurate enough to assess the different theories. Even so, most of the biaxial compression results were found to be premature, with respect to the intrinsic material strengths. The one equal biaxial strain test result in compression that matched the predictions of the maximum-strain failure theory was so much stronger than all other biaxial compression tests that it was clear that there had been a dominant influence of instability in the other sets of tests. Regrettably, the idea of using test data to validate, or discredit, composite failure theories has not been found to be decisive.

In any event, when major discrepancies, at the multidirectional laminate level, were identified between test results and the predictions of interactive theories early in the 1970s, the response was not to question the validity of such theories.[3] Instead, the proponents of interactive failure theories announced that the predicted failures at far lower tensile loads than measured by test were not real failures after all. Instead, they were henceforth called first-ply failures, in the matrix. This strategy might have had more credibility if it were not for the fact that the compression-dominated loads predicted by the same theories with the same lamina material properties were typically too high by a factor of 2. The premise of this denial of the obvious evidence was the seemingly plausible hypothesis that a sufficient density of cracks in the matrix between the fibers would decrease the transverse stiffness and increase the transverse strain-to-failure of the defined homogeneous unidirectional lamina. When the transverse lamina properties had been changed sufficiently, other fibers in other plies, orthogonal

[3] Tension-dominated strengths were about half what was predicted by the mechanistic and noninteractive maximum-strain failure model, while compression-dominated strengths were predicted to be about twice as high. Conversely, the proponents of mechanistic composite failure theories throughout most of the U.S. aerospace industry, at least, had already found that they could make predictions in reasonable agreement with test data at the laminate level merely by ignoring what they correctly deduced were false predictions of matrix failures. Based on observations that the matrix did not crack extensively before the fibers failed, at least not for carbon-epoxy laminates, they recognized that the lamina transverse-tension strength, so necessary to allow interactive failure theories to even be formulated, applied *only* to unidirectional laminae and should *not* be applied to multidirectional laminates. Once this was understood, the mechanistic maximum-strain and maximum-stress failure models could be used directly, in only one step, to make reasonable predictions of the ultimate strength of unnotched carbon-epoxy laminates.

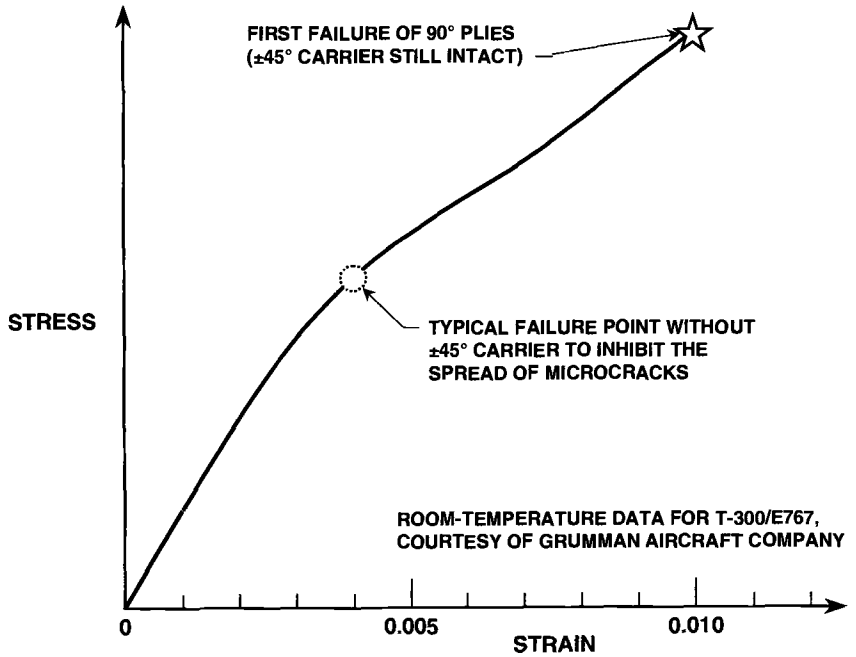


FIG. 3—*Extended stress-strain curve for 90° unidirectional plies when supported on ±45° carriers.*

to the matrix cracks, could attain the same strength as exhibited in uniaxial tests of unidirectional laminae. Curiously, no attempt has ever been made to verify that these "first-ply failures" predicted by the interactive theories on the basis of transverse strengths measured on isolated unidirectional laminae actually occurred when they were predicted to when the laminae were embedded in multi-directional laminates. Acoustic emission measurements published by researchers at Virginia Polytechnic Institute (Ref *13*, for example) show no abrupt increase in intensity at the typically 0.004 strain levels at which unidirectional carbon-epoxy laminates fail under transverse tension. Since the unloaded laminates already contain many microcracks, a visual inspection after loading to strain levels slightly greater than 0.004 would be inconclusive since there would be no way to establish when the cracks occurred. Nevertheless, this issue could be resolved visually, under a microscope, by comparing the matrix cracks at strain levels of 0.0035 and 0.0045, for example. A prediction of major matrix cracking at a strain of 0.004, for example, would require a step discontinuity in crack density and size between these two surrounding tests. In the absence of such verification, the advocates of interactive composite failure criteria have assumed the validity of their predictions in a curious context—that of an extremely selective "failure" of their presumed homogeneous anisotropic solid. Only certain strengths and stiffnesses are presumed to have been affected by the first-ply failures, leaving other properties unchanged. Worse, the reduction in transverse stiffness that is absolutely necessary in expanding the transverse strain to failure without increasing the transverse strength is contrary to measurements of the transverse lamina stiffness like those shown in Fig. 3.[4]

Here, the stress-strain curve to failure of a 90° carbon-epoxy ply has been extended by curing it with a ±45° carbon-epoxy carrier having almost exactly the same longitudinal (0°) stiffness.

[4] Source: Peter Shryprekevitch, FAA Tech Center, Atlantic City, formerly with Grumman Aerospace; private communication.

Whereas isolated 90° plies fail at a strain level of about 0.004 for typical carbon-epoxy laminates, when they are embedded in multidirectional laminates the same plies do not fail until they have attained almost the strain needed to fail 0° plies. Figure 3 makes it perfectly clear that there is no 3-fold or 100-fold reduction in transverse stiffness for strains beyond about 0.004, even though such reductions are customarily assumed to occur whenever interactive composite failure theories are converted from first-ply failure to last-ply failure models. Without such reductions in stiffness, it would be far more difficult to extend the 0° ply strains-to-failure appreciably without making it obvious that the failure envelope (on the lamina stress plane) was being altered too. The changes in failure envelope are usually apparent only on the lamina strain plane, but many interactive failure theories are formulated on the lamina stress plane.

In the absence of any possibility of making direct measurements of what these changes in "lamina" properties really are, at higher strain levels, the basis of changing the predicted strengths for last-ply failures has necessarily degenerated into the well-known technique of adjusting what are presumed to be matrix-dominated properties of the still-assumed-to-be-homogeneous anisotropic composite material to match measured laminate ultimate strengths. When these new properties are inserted into a suitably modified interactive failure theory, no modifications to which are ever acknowledged, it can be shown that the laminate strengths used to adjust the properties can then be "predicted" as last-ply failure laminate strengths. The more unmeasurable lamina properties are involved, the more opportunities there are to create such predictions. It is, at times, necessary to modify the changes made to the reference material properties differently for each of the various combinations of biaxial stress. The lowering of the predicted biaxial compression strengths requires a different stratagem. Cracks that are presumed to develop between the compressed fibers, even under pure monotonic axial compression loads, are assumed to destabilize the fibers and to allow them to fail at lower loads. This new failure characterization is not interacted with the original (but separately modified) interactive failure model for tension-dominated loads. So the single interactive failure envelope used at the first-ply failure level is replaced by two distinctly different criteria that do not interact with each other for the last-ply failure projections. This, in a nutshell, is how the rejected first-ply failure predictions from interactive failure theories are traditionally transformed into more acceptable last-ply failure predictions of the strength of multidirectional laminates. The process is described in the flow chart shown in Fig. 4.

Given the acknowledged difficulties in resolving these issues by comparisons between theories and test, and the demonstrated ability to "validate" each and every theory by matching any known test result through a reliance on arbitrarily adjustable unmeasurable input properties, a.k.a. disposable parameters, the author has attempted in the past [*4,14,15*] to expose the inadequacies of interactive theories by using the same theory to solve several different problems with the same material properties and revealing many obviously self-inconsistent predictions that do not arise with mechanistic failure theories [*16,17*]. Valid theories are identified by the absence of any obvious contradictory or physically impossible predictions emanating from each theory as it is evaluated in turn. This process does not involve comparisons between theories; only comparisons between predictions made with a single theory. In scientific terms, this long-forgotten but still scientifically valid technique is known as reductio ad absurdum. While all of the author's work has been ignored by the proponents and disciples of interactive composite failure theories, it seems significant that none of his criticisms has ever been rebutted.

The remainder of this paper is devoted to several specific individual issues that confirm the unsuitability of all interactive composite failure criteria for use with fiber-polymer composite laminates. Like the general issues raised above, any one of these should be sufficient to discourage any further use or teaching of these theories. As a minimum, it is hoped that these examples will cause the unwary to never again accept theories that cannot possibly be understood because they cannot be related to physical phenomena, to never again rely on computer codes without first identifying how they work and what phenomena they cover, and to perform sanity checks on any theory they do use.

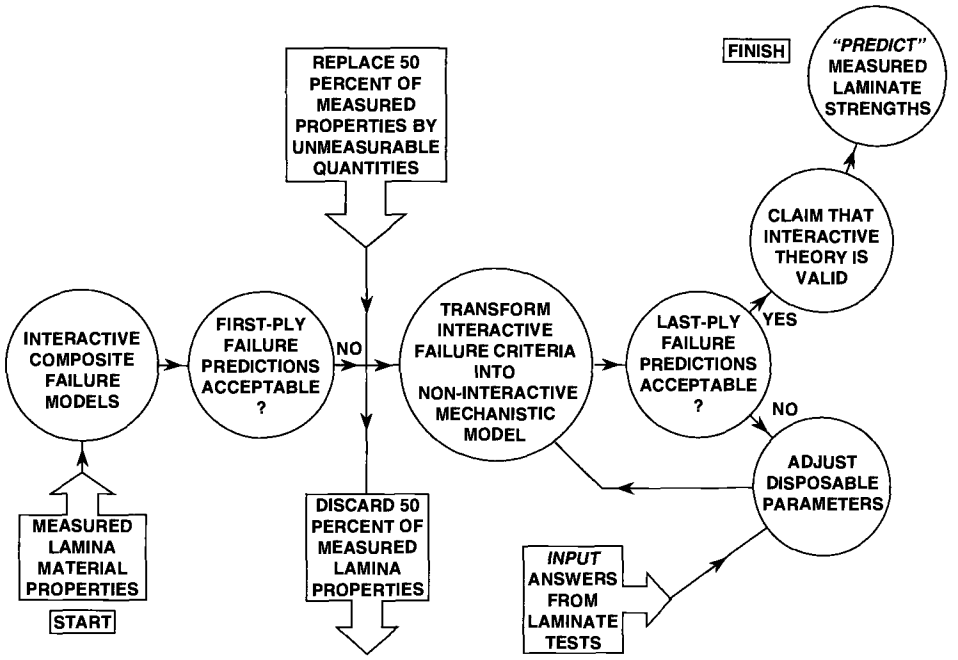


FIG. 4—*Flow chart characterizing the customary use of interactive composite failure criteria to produce first- and last-ply failure laminate strengths.*

The Perceived Differences Between a 0°/90° Laminate and a 0°/90° "Lamina"

The first of many fatal flaws in customary interactive composite failure criteria can be exposed by considering the very simple issue of how properly to characterize a simple 0°/90° woven cloth layer. Contemporary practice treats a 0°/90° laminate made by the combination of layers (plies) of 0° and 90° unidirectional tape laminae very differently from a 0°/90° laminate made from woven—or stitched—layers perceived as 0°/90° "laminae." This unjustifiable artificial distinction is absolutely critical in understanding the follies of interactive composite failure criteria. In the case of bi- (or multi-) directional laminates made from unidirectional laminae, each embedded lamina in the laminate can be predicted to fail under a fiber-dominated mechanism for loads dominated by the component parallel to the fiber directional and under a matrix-dominated mechanism for loads transverse to the fibers. On the other hand, laminates made from bidirectional laminae, whether or not there actually are any real matrix-dominated failures, are traditionally characterized by such a model so that it is not possible to predict any matrix failures. Each such "lamina" is characterized as being fiber-dominated in both directions; there is then no opportunity to predict matrix-dominated failures. Yet, in the case of uncrimped 0°/90° dry preforms to which resin is added later, there may be absolutely no difference between the dispersion of the fibers in the matrix from those in the corresponding laminate made from two orthogonal layers of unidirectional prepreg. The fibers in preforms can be located by tackifiers; there is no need for even the lightest of stitching. We see, therefore, that the same fibers in the same resin can be characterized by two very different mathematical models. This is true for both interactive and mechanistic composite failure criteria models. The difference is that the laminate strengths predicted for these identical laminates are *never* the same when the predictions are made by the interactive theories. They *are* the same when predicted by physically realistic mechanistic failure models. They should be the same, no matter whose failure model is used.

The reason why this situation has been allowed to develop is that bidirectional woven fabrics contain various degrees of fiber crimping, depending on the number of fibers in each tow, typically 3K, 6K, or 12K. There is virtually no crimping for some of the best 3K plain-weave cloths, but severe crimping for some of the least expensive 12K plain-weave fabrics. This effect would be lost if each layer of woven cloth were represented by the properties of two orthogonal layers of truly unidirectional tape. Nevertheless, this crimping effect would automatically be accounted for, in terms of both stiffness and compressive strength, if each such 0°/0° layer were characterized by the combination of two orthogonal sets of fibers with the matrix-dominated transverse properties established by appropriate tests of unidirectional tape laminae and with fiber-dominated longitudinal properties backed out from the customary tests on 0°/90° layers, as explained in Ref *18*. This recommended procedure would enable both fiber-dominated and matrix-dominated strengths to be predicted whenever 0°/90° cloth layers are embedded in multidirectional, or even in bidirectional, laminates. The obvious question is as to why is this not already being done. It is certainly not a difficult process, and has been well validated by the many tests referred to in Ref *19*. The author would suggest that the most plausible explanation is that, for the advocates of interactive failure theories, being unable to predict matrix failures has tremendous advantages. Specifically, if there are absolutely no unidirectional tape laminae in a laminate made entirely from 0°/90° layers oriented in various directions, the first predicted failures will always be in the fibers, so that there is no need to invoke progressive failure theories to produce a better last-ply failure answer.

However, the shortcomings of this approach can be revealed by actual analyses of identical quasi-isotropic laminates as a series of 0°, +45°, −45°, and 90° unidirectional tapes and as a combination of 0°/90° and ±45° bidirectional "laminae," using the computer code associated with Tsai's 1988 textbook [*5*]. Figure 5 compares various analyses of this same laminate, modeled in various guises, using this theory.

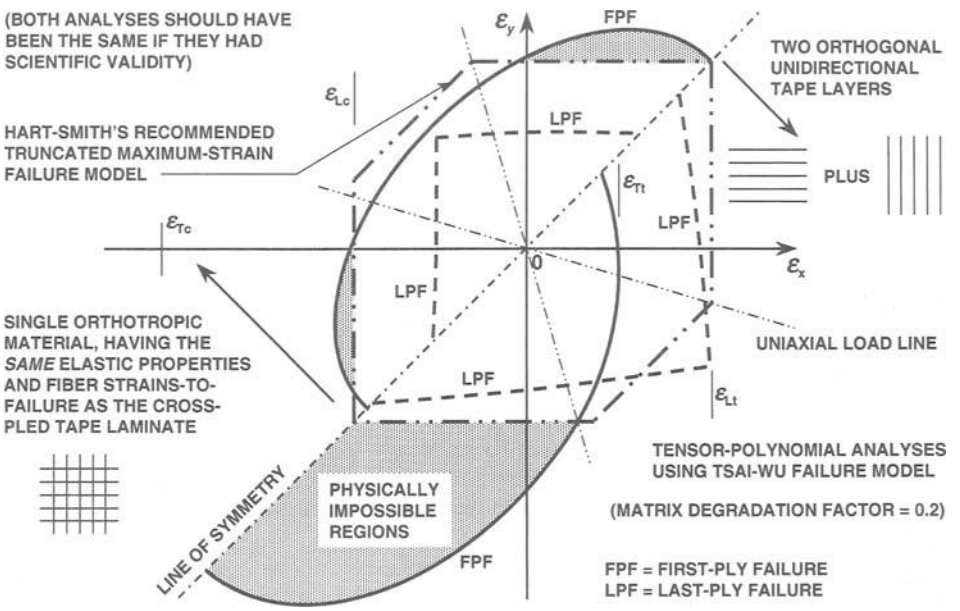


FIG. 5—*Different sets of first-ply and last-ply failure predictions of the same quasi-isotropic laminate made with the same computer code using apparently the same failure model but based on unidirectional and bidirectional basic laminae.*

All predicted failure envelopes under biaxial stresses are symmetric about the 45° diagonal running from the bottom-left to the top-right of the figure. Therefore, only half of each failure envelope is shown. Those in the lower-right corner refer to analyses based on unidirectional tape laminae, while those in the top-left refer to analyses based on bidirectional uncrimped "laminae." The failure envelopes created by using the same lamina properties with the mechanistic truncated maximum-strain failure model are included for comparison. Significantly, as stated earlier, both predictions from the mechanistic failure criteria are identical. Equally significantly, four very different predictions were made by use of the Tsai-Wu interactive failure criterion, using the material properties Tsai supplied in the back of his document. Starting first with the model of unidirectional tape laminae, the first-ply failure predictions are displaced way to the lower left of those given by the mechanistic model, being too low by about a factor two for tension-dominated loads and too high by a factor of two for compression-dominated loads. Using the automatic computer-provided default settings for a last-ply failure reanalysis of this same problem, the failure envelope is displaced up to the right, being nearly the same as predicted by the original (untruncated) maximum-strain failure model. It is also clear that the second failure predictions are made by two very different formulae, one for tension and another for compression, not by a single smooth ellipse. Nevertheless, even though these predictions had to be made with material properties of which half were totally unrelated to the measured lamina properties and with two failure criteria instead of one, the last-ply failure predictions are numerically reasonable, despite their ill-defined pedigree. The third step in the analyses involved taking the output from this second analysis and assuming that it represented the input to a further first-ply failure analysis based on homogenized 0°/90° and ±45° "laminae" with orthogonal fibers in each such "ply." As shown in the upper left portion of Fig. 5, this prediction is quite reasonable—in every respect except for the fact that it was not the same as for what should have been identical predictions in step two. It used the same "lamina" properties in ostensibly the same theory. Why was there a difference? Can this be blamed on anything but the failure model? Without being prompted, the computer code automatically generated a fourth solution, the last-ply failure envelope for the material formulated in terms of the multidirectional "laminae." Since the fibers were predicted to have failed first, their strengths and stiffnesses were "modified" automatically, leaving only a much weaker laminate, with matrix-dominated strengths and stiffnesses. A very small last-ply failure envelope was thus produced.

It is obvious to the reader, in this situation, that this final solution should be discarded and that the third solution from the interactive failure model matched the single prediction of the mechanistic model the best. But, in the context of a very large finite-element analysis, with thousands or more such predictions and no possibility of case-by case scrutiny by humans, how is the computer expected to know which of the four possibilities to select. In his text, Tsai recommended a combination of the first analysis for compression loads and the second one for tension loads. It would be dangerous to pick the largest of all four failure envelopes, even though that is effectively what he recommends. And one could never justify the use of laminates made from cloth layers on the basis of the fourth analysis. One would like to select the last-ply failure analysis for tape laminates and the first-ply analysis for the cloth laminates, but the author is unaware of even a single computer code that includes, in the input, a cue to differentiate between tape and fabric plies. In the middle of decomposing the results from a very large finite-element analysis, what is the poor befuddled computer expected to do? Precisely what it has been instructed to do, of course! No more, and no less. With the mechanistic model, it is possible to generate a single plausible failure envelope for the composite laminates. With the interactive models, one is faced with an undefined selection between four very different estimates, two of which are blatantly unacceptable even in this very simple case of an entirely fiber-dominated quasi-isotropic laminate. (Since the objective of this analysis was to portray the multiple solutions this particular interactive failure model predicted, and to compare them against the single mechanistic solution, the author was not able to identify which selection(s) the computer was coded to make. Obviously, it would be coded to reach a decision and proceed with the analysis. All that the author can guarantee is that it could not choose the best solution shown in Fig. 5, because there is no single best solution.)

What the analyses in Fig. 5 show is how unrealistic the first-ply failure predictions made with the best known of the interactive failure criteria are for laminates made from unidirectional tape laminae and how plausible are those made for cloth laminates with no unidirectional tape plies. The difference is that the matrix is predicted to fail first in the former case, while the fibers are predicted to fail first in the latter. But the input files contain no cue to differentiate between the two cases and designers are not apt to exclude tape plies from their designs and restrict their choice of laminates to various combinations of 0°/90° and 45° layers merely because the theories taught the most are incapable of making realistic analyses of their laminates unless they do so. Of course, none of this should even be apparent given that the composite of fibers and resin was homogenized to render all distinctions between fiber and matrix behavior impossible to make, but that is another matter.

The debate that the analyses in Fig. 5 are intended to encourage is whether or not it is ever permissible to model bidirectional layers as homogeneous laminae, which has the effect of precluding all possibility of predicting matrix failures from the analyses, or whether cloth layers and the like must be modeled as two co-located orthogonal equivalent "unidirectional tape" plies, with appropriate accounting of any crimping of the fibers due to the weaving process on the strength and stiffness of such fibers. Only the latter process can permit the prediction of any real matrix failures that may precede the failures of the fibers calculated here. Even then, not all such failures can be predicted by consideration of individual plies in isolation. The predicting of matrix cracking requires a fracture-mechanics analysis and necessarily involves an interaction with adjacent plies.

How is it Possible to Differentiate Between Fiber and Matrix Failures in *Homogeneous* Anisotropic Solids?

Given the fuss made about the legitimacy of transforming heterogeneous fiber-polymer composites into mathematically "equivalent" homogeneous anisotropic solids, to simplify the mathematics for first-ply failure predictions, the proponents of interactive theories should be faced with an insuperable challenge as to how to reverse the process for last-ply failure analyses. There are no separate terms characterizing fiber and matrix failures, no separate input properties for fiber and matrix failures—only half of each set needed to characterize the "composite material" at any stage of analysis, as explained in Fig. 6.

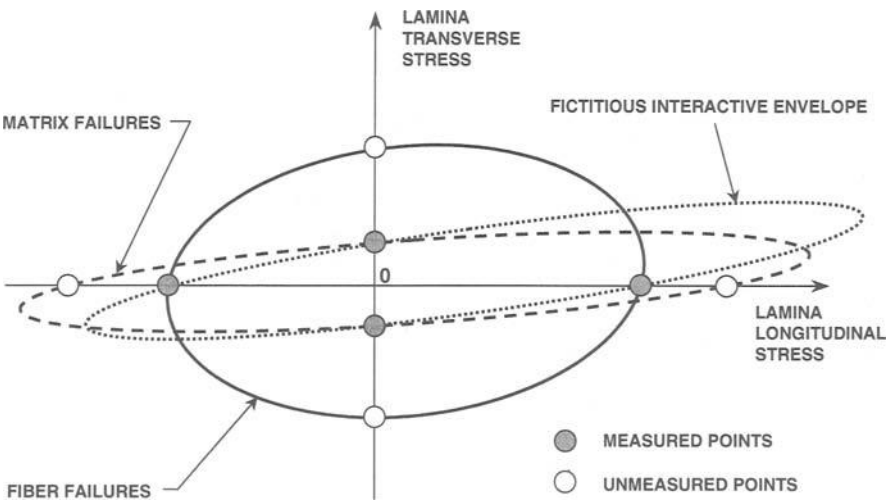


FIG. 6—*Separate characterizations of fiber and matrix failures on the lamina stress plane, in terms of lamina stresses.*

The fibers are characterized only by longitudinal strengths (normalized to account for their being embedded in low-modulus resin matrices); nothing is specified about their transverse strengths. The definition of matrix properties is restricted to transverse strengths alone. This is justified on the basis that the fibers prevent the matrix from failing under pure longitudinal tension, and the assumption that the matrix will always fail under pure transverse tension before the fibers in the ply under consideration could. But these omissions deprive the failure models of any opportunity to interact longitudinal and transverse stresses within each constituent of the composite. This would seem to be a serious omission from any theory claiming to be interactive.

But no matter what happens in the real world of physics, it is undeniably true that, in the virtual world of computer codes, a differentiation *is* made between fiber and matrix failures as part of the transition between first-ply- and last-ply-failure predictions. The "lamina" properties are changed selectively to make the overall laminate strengths more acceptable. The problem with this class of failure models is "Where, on the continuous single-valued failure surface does the failure mode change between fibers and the matrix?" (There is no such problem with mechanistic failure criteria, of course, since each distinct portion of the failure envelope is uniquely associated with one specific failure mechanism in one identified constituent of the composite.) The answer to this riddle is that, for interactive composite failure models, in almost every case, only the pure axial load along a fiber is regarded as a fiber failure. *Every* other point on the failure surface must be defined to be a matrix failure, even if the longitudinal component of these other strengths were greater than that of the fiber (normalized for resin content, of course). In other words, the final strength predictions are made on the basis of the measured longitudinal (normalized) fiber strengths *alone*! By then, the matrix is customarily analytically softened sufficiently that it is incapable of influencing the estimated strength for any laminate with fibers in a sufficient number of directions to be a structure rather than a mechanism. A cynic might well ask, "Of what value is the theory used to predict the invariably discarded first-ply-failure strengths?" The present author thinks this question deserves an answer too, and would encourage a debate on this very issue.

The most convincing proof that most computer codes restrict fiber failures to only two points of the failure envelope is provided by considering what happens if a finite portion (or at least an arc) were allowed to be defined as a fiber failure. The consequences of this procedure are described in Figs. 7 and 8. When the last-ply failure envelope is generated on each lamina strain plane, so that the sequence of failures can be identified, this failure surface *will contain discontinuities unless* the above restriction is enforced.

Only the transverse strains in the "softened but not failed" matrix can be expanded. Once a fiber is predicted to fail at the first-ply failure level, no strength enhancement is permitted for that ply. The same situation arises for matrix-shear failures. The "need" for this process, to enhance the predicted laminate strength to a level acceptable to the analyst, is to move the matrix-failure portions of the "lamina" failure surface further away from the origin, on the strain plane, so that all of the fibers will be predicted to fail first, at their full measured strength, in every ply, if suitable loads are applied. Given the existence of simple mechanistic failure models that proceed straight to this point without any intermediate steps, one might well question the value of interactive failure theories that do not. This, too, is a valid issue for debate.

The process of expanding the failure envelope fails whenever the "final" failure envelope on the strain plane has gaps[5] in it, as shown in Fig. 8. This is the basis for asserting that most progressive-failure analyses, as they are called, must restrict fiber failures to occur in the absence of transverse stress, but necessarily in the presence of transverse strain—in the lamina, if not in the fiber. Remarkably, all of this is usually accomplished without changing the lamina failure envelope on the stress

[5] The existence of the gaps in the failure envelopes for unidirectional laminae is not always evident at the laminate level. A gap in the envelope for one ply is often masked by a predicted failure in another ply, with fibers oriented in a different direction. Gaps in the latter ply's envelope are, in turn, obscured by predicted failures in the former ply.

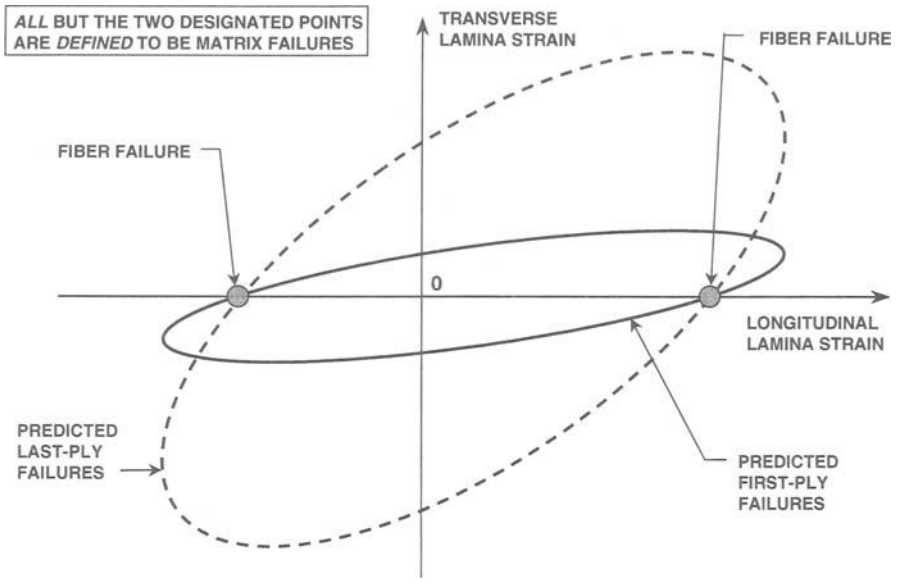


FIG. 7—*Expanded last-ply failure envelope, on the lamina strain plane, when first-ply fiber failures are restricted to only two points.*

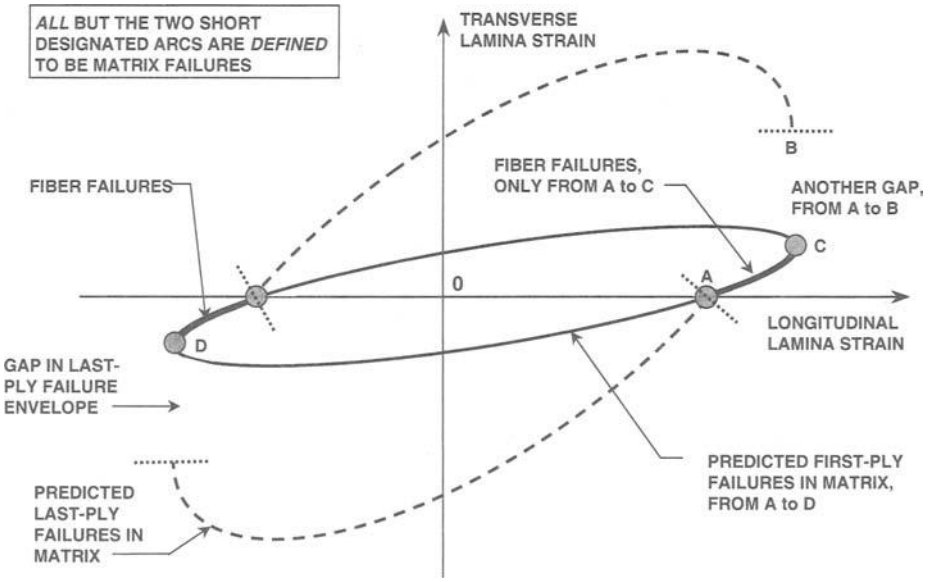


FIG. 8—*Expanded last-ply failure envelope containing gaps, on the lamina strain plane, whenever first-ply fiber failures are permitted to extend to arcs or areas.*

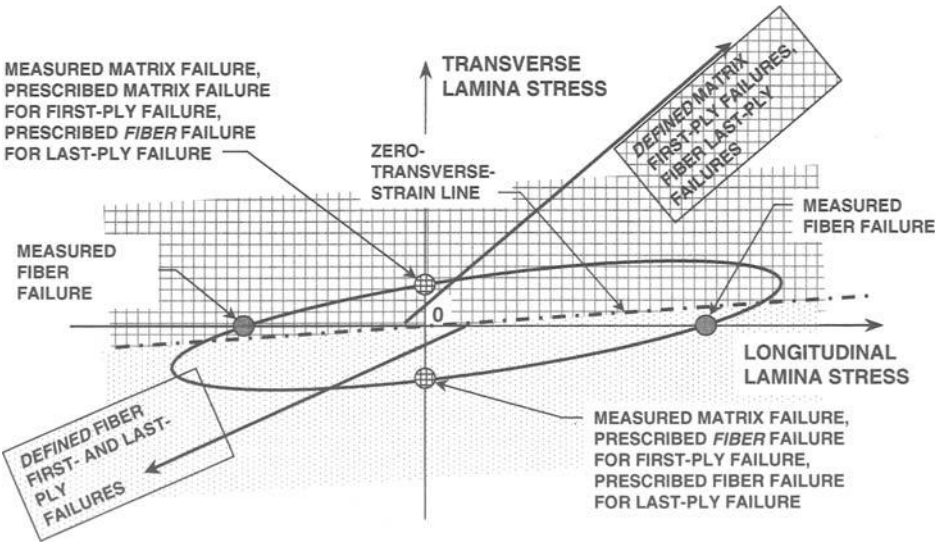


FIG. 9—*Tsai's latest progressive failure model for fiber-polymer composite laminae.*

plane, which is the basis of the pretense that the material "characterization" remains unchanged during the transition from first-ply to last-ply failure. Compatibility-of-deformations analyses, to identify the sequence of possible failures, are customarily performed on the laminate strain plane, however.

The problem of these gaps in the strain-based lamina failure envelopes is avoided for the Tsai-Wu failure criteria,[6] the latest form of use for which is illustrated in Ref *20,* by maintaining the fiction of the homogenized laminae until failure. Despite this, any first-ply failure occurring in the presence of tensile transverse tension stresses within the ply under consideration is defined to be a matrix failure, and the entire failure envelope is expanded on the strain plane by softening the matrix, since the formulation permits only one lamina transverse stiffness. The size of the fiber-failure domain for post-first-ply failure analyses is thereby expanded, too. A first-ply failure of the same lamina in the absence of tensile transverse stresses is defined to be a fiber failure, even if the state of stress were one of pure transverse compression in the absence of any axial stress in the fibers. These procedures are depicted in Fig. 9. Matrix failures under pure transverse compression are not permitted by this technique, despite the fact that the measurement of such a failure is used to locate one point on the lamina failure envelope. No enhancement of the failure envelope is permitted once fibers have been predicted to have "failed." Any subsequent prediction of failure in a ply that had previously suffered a first-ply failure is defined to be a fiber failure, even if the state of stress in the ply at the time of the second failure were one of pure transverse tension, with zero longitudinal stress in the fibers! Is this a credible way to predict the strength of fiber-polymer composites? The author would recommend that this, and similar procedures be debated openly.

[6] In this case, the gaps are avoided by restricting any transitions between matrix and fiber failures to occur only on the pure longitudinal stress axis for each unidirectional lamina. Bi-directional (cloth) laminae cannot be predicted to fail in the matrix under this criterion, so the problem of the gaps cannot then arise.

Other theories do not deny the possibility of matrix failures under transverse compression. In such cases, gaps will arise in the last-ply failure envelope for any transition between fiber and matrix failures not located directly on the unidirectional stress axis for the fibers in each lamina. First-ply failure predictions in fibers must then be restricted to the two points shown in Fig. 7.

Consider now the application of the procedure described in Fig. 9 to laminates in the family made from unidirectional plies in the 0°, ±45°, 90°. For simplicity, restrict attention to predominantly unidirectional tensile loads with only small increments of transverse and in-plane shear stresses, insufficient to cause predicted failures in the ±45° plies. The first failure to be predicted will be in the 90° plies, under transverse tension, at far too low a 0° laminate stress to be accepted as an ultimate strength. What is to be done about this? The transverse stiffness of the 90° plies will be reduced greatly, sufficiently to ensure that the next prediction of failure is not a further prediction of the same failure in the same plies, only at a higher 0° laminate strain (transverse strain in the 90° plies). If it were, this second failure would have to be declared a fiber failure, according to the procedures Tsai defined in Ref *20* that are cited above, provided that the procedure established in the computer code was followed strictly and was not available for tinkering by hand on a case-by-case basis. And that would be the end of the process. This would appear to explain why Sun et al. [*21*] chose to reduce the transverse stiffness by a factor of 100,[7] per pass, to be more certain that no subsequent matrix failures would be predicted than Tsai could be with a factor of only about 3. Neither Tsai nor Sun provides any experimental evidence to justify these reductions in matrix-dominated stiffnesses of the laminae.

Assuming that the reduction in transverse stiffness, for each ply of the quasi-isotropic laminate discussed above, was sufficient to achieve the objective of adequately expanding the failure envelope in the transverse direction, the next predicted failure would be in the 0° plies, at a far higher strain. If the high 0° strain in the laminate were combined with a small compressive transverse stress in the 0° plies, that would be the end of the procedure, and a last-ply failure would be declared in the 0° plies, according to Tsai's procedures in Ref *20*. However, if the transverse stress in the 0° plies were tensile, these same procedures would require that the failure be declared to be a second first-ply failure, this time in the 0° plies which had not previously been predicted to fail. This is why only the failure envelope for the 90° plies had been expanded previously, on the lamina strain plane, leaving the failure envelopes of the 0° and ±45° plies unaltered. So, in the presence of tensile transverse stress in the 0° plies, the failure envelope of the 0° plies would also be expanded in the transverse direction. Doing so would enhance the 0° strength of the embedded 0° plies under both predominantly longitudinal tension and compression loads. While the first enhancement is no more than dubious, the second is ludicrous. How can the compression strength of the fibers be increased by cracking the matrix between them and pulling the fibers apart to make absolutely sure that the matrix cannot possibly stabilize the fibers as well as it had before it had been cracked? Curiously, in Ref *5*, Tsai used a micromechanical model to reduce unacceptably high predicted first-ply-failure compression strengths using the logic that this same matrix cracking would lessen the ability of the resin matrix to support the fibers. However, we are dealing with a tensile longitudinal stress here, so it is possible to avoid consideration of this "problem." With the failure envelopes of the 0° plies expanded also, the third predicted laminate failure will be the second predicted for the 0° plies, so it can be declared the last-

[7] In the computer code listed in Appendix B of Ref *20*, subroutine ANALYS on p. B-39 contains a section near the bottom of p. B-40 entitled "Call Stiffness Reduction Model." This, in turn, calls for subroutines PSMA and/or PSMB, listed on p. B-51. These subroutines contain the self-evident instructions

$$e2(k) = 0.01 * e2(k) \qquad \text{and} \qquad g12(k) = 0.01 * g12(k)$$

to reduce the transverse stiffness and in-plane shear stiffness of each ply by arbitrary factors of 100. The author has found no restriction to prevent these subroutines being called more than once. Nowhere in the report is this factor tied to any measurements of reduction in stiffness of the matrix.

ply failure for the laminate. The process is very simple, isn't it? But isn't it more ritualistic than scientific? Why is no intermediate stage ever compared with experimental evidence? Shouldn't this have been necessary to validate the final prediction?

Even though the stress-based lamina failure envelope appears to be unchanged by progressive-failure analyses, it is effectively shrunk to the two longitudinal strength points on the longitudinal stress axis whenever the transverse stiffness is reduced to close to zero. On the lamina strain plane, the equivalent transformation is to two parallel constant-longitudinal-strength lines, as shown in Fig. 10. This leaves the transverse stress in that ply at zero, with no limit on the transverse strain.

The discourse above inspires the obvious question as to "How much transverse ply softening is needed to accomplish the desired transformation in predicted laminate strengths?" Factors of 3 and 100 hardly inspire the notion of unanimity amongst the advocates of this approach! It should also encourage those who advocate such procedures to present experimental evidence supporting their procedures, particularly in the light of contrary evidence shown in Fig. 3 and the fact that mechanistic failure models are known to be capable of providing acceptable predictions of laminate strength without recourse to such unsubstantiated manipulations.

Characterization of Matrix-Dominated Properties for Mechanistic Composite Failure Models

The astute reader will have observed that the inputs to mechanistic failure models do not match the initial tangent lamina moduli for transverse-tension and in-plane shear and may well see a similarity with the very procedures the author has criticized in the context of interactive failure models. There is a very big difference, however. The inputs for mechanistic failure models are typically in the form of a secant modulus that approximates the actual matrix-dominated stresses and the actual longitudinal strains in the fibers. In theory, the match could be precise, for every element included in a finite-element analysis, if sufficient iterations were employed. However, in practice, the transverse modulus E_T is customarily set by the transverse stress for which the transverse strain is equal to that needed to fail fibers in tension; the in-plane shear modulus G_{LT} is set by the stress at a shear strain equal to either twice the fiber strain to failure or $(1 + \nu_{LT})$ times that fiber strain, as in Fig. 11. (The factor of 2 derives from equal and opposite tension and compression; the lesser factor of about 1.3 is associated with a state of pure longitudinal tension.) These are not factors selected arbitrarily to make pre-

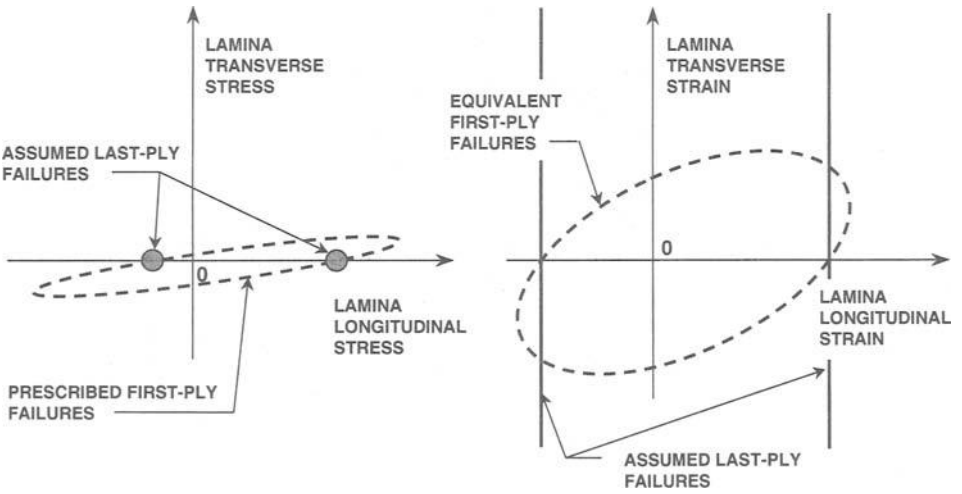


FIG. 10—*Lamina last-ply failure envelopes on stress and strain planes, starting from interactive elliptical failure envelope at first-ply failure level.*

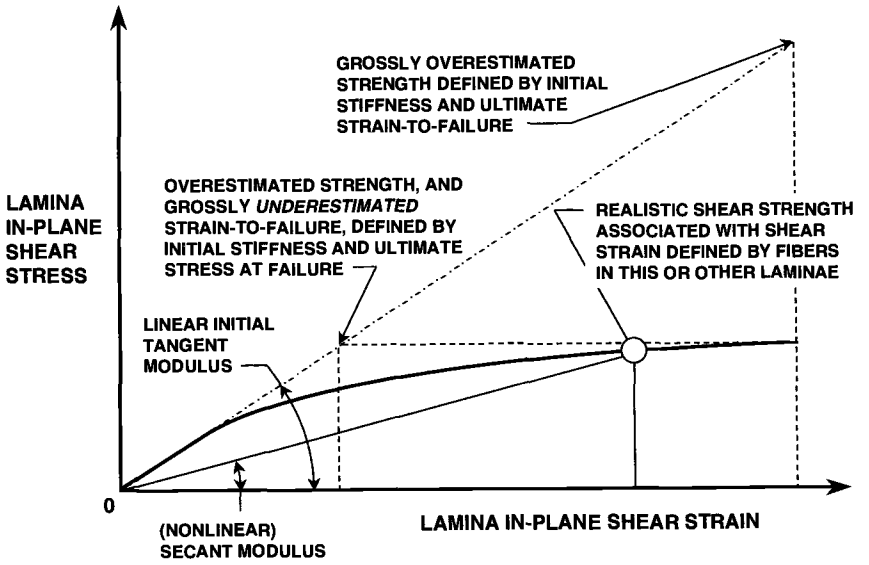


FIG. 11—*Mechanistic modeling of matrix-dominated lamina properties.*

dictions of matrix failures go away. They are attempts to match the actual material properties, for the states of strain involved, as precisely as practical analysis permits. This mechanistic modeling of the lamina properties did not originate with the introduction of carbon fibers; it can be traced back at least as far as to netting analysis for filament-wound fiberglass pressure vessels made in the 1950s.

There is no reason why this same mechanistic modeling of matrix-dominated lamina properties could not be equally applied to interactive failure models, too. Doing so would eliminate the great majority of the false predictions of first-ply failures. But one further major problem would remain—the interactive failure envelopes would still be of the wrong shape!

What Happens When the Fibers are Predicted to Fail First?

The whole intent of progressive-failure theories, other than when they are applied by purists, is to increase the predicted final laminate strength under predominantly tensile loads. This process has seemed plausible to many, whenever the matrix was actually observed to "fail" first in a noncatastrophic manner. But the fibers are sometimes predicted to fail first. What is to be done then? This happens most frequently when a cloth, rather than unidirectional tape, layer is mismodeled as a homogeneous anisotropic solid layer. Since both longitudinal and transverse strengths of this "ply" are now fiber-dominated, no predictions of matrix failures are possible, other than by in-plane shear. However, since the inputs to computer codes include no cue to differentiate between tape and cloth layers, every computer code programmed to generate both first- and last-ply failures will automatically reduce the transverse properties in the prescribed manner. Only, in this case, since the contribution to laminate strength of the transverse properties is far greater from stiff fibers than from soft matrices, the predicted last-ply strength will be far less than the predicted first-ply strength, as shown in the top half of Fig. 5. Such a calculation done by hand might easily be recognized as an aberration, but what of a very large finite-element analysis using automated pre-and post-processors? Which answer is it supposed to accept? And which one should it reject? The simple approach of taking the higher value will not work because that would fail to reject the excessive first-ply failure predictions under biaxial compression for laminates made from layers of unidirectional tape shown in the lower-left corner.

Curiously, the calculations shown in Fig. 5, based on Tsai's interactive failure model, would indicate that one laminate made from alternating layers of 0° and 90° prepreg tape would have twice the predicted biaxial compression strength of another laminate containing the same fibers in the same resin made from a dry preform of uncrimped 0°/90° collimated fibers into which resin was subsequently injected, merely because the matrix was predicted to fail first in the former analysis and the fibers were predicted to fail first in the latter. Only the mechanistic failure model predicted the same strengths. Doesn't this discrepancy warrant discussion of the causes of this large (2:1) discrepancy between predictions?

What Happens When the Failure Criteria Designate that Fiber Failures Occur at More Than Two Points on the Surface of the Failure Envelope?

It was shown earlier that most composite failure models that specify any more than two isolated points over the entire surface of the failure envelope to be fiber failures create unacceptable difficulties in regard to the application of post-first-ply-failure analyses. The entire remainder (i.e., all) of the failure surface for the defined homogeneous material must be defined to characterize matrix failures. These two points (or transitions between predicted fiber and matrix failures) must lie on the longitudinal stress axis for a unidirectional lamina. The last-ply failure envelope would otherwise contain gaps when necessarily expressed on the lamina strain plane to identify the sequence of failures. Most of those who have encoded composite failure have avoided this problem, but not all. The primary analysis model contained in MIL-HDBK-17 [*22*] for characterizing the composite "material" at the unidirectional lamina level serves ideally to show the consequences of mathematical, rather than physical, modeling of fiber-polymer composites. This supposedly mode-based model consists of four equations, one each for tension and compression of the fibers and two more for (transverse) tension and compression to characterize matrix failures. The origin of this model was a sincere attempt to point out that it was not necessary to use single-valued interactive failure criteria. Tragically, it is revealed by any attempt to actually apply these equations that this theory is the most interactive of all, since all four equations are coupled by the involvement in each of the in-plane-shear stress, and the associated reference strength. Figure 12 shows the defined demarcations between predicted fiber and matrix failures. (The author must confess to an inability to comprehend, and hence apply, the equation for compressive failure of the matrix and has used, instead, a mirror image of the predictions for tensile failures, but this has no substantial effect on the issues raised here.)

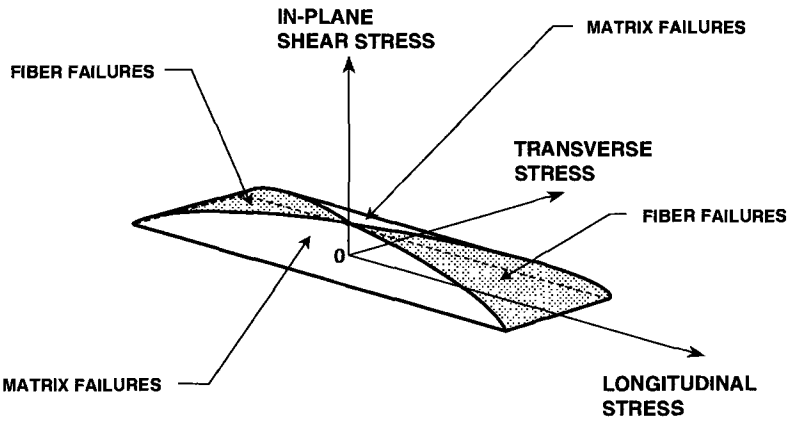


FIG. 12—*Demarcation between fiber and matrix predicted failures for unidirectional laminae, per the Hashin/Rosen composite failure theory in MIL-HDBK-17.*

It is immediately evident that 50% of the failure surface is defined to represent fiber failures, in a bow-tie-shaped area aligned along the axis representing the fiber direction. The remaining two triangular regions are likewise defined to represent matrix failures. The demarcations would be plausible, if this theory were proscribed to never be used in conjunction with progressive failure analyses. But this is not the case. The basic problem is that, throughout the area in which fibers are defined to fail first, it is not permissible to enhance the strength, as is possible with many other theories, by changing the input lamina reference strengths. (This does not inhibit advocates of this theory from doing so, of course, but it does lay them open to the question of how did the broken fibers heal themselves as a result of softening the matrix.) Only that portion of the envelope defining matrix failures may be expanded "legitimately," on the equivalent lamina strain plane. But the portion of this failure surface most frequently expanded by other theories, and the most effective in increasing the predicted last-ply failure laminate strengths, should be off limits here.

One obviously absurd consequence of this formulation of failure criteria is exposed by considering two immediately adjacent points on either side of the demarcation line. That in which the fiber is predicted to fail first is inviolate, but the immediately adjacent point can have its strength enhanced, by reducing the matrix-dominated stiffnesses by the usual large factor, as shown in Fig. 13. Indeed, all of the matrix-failure zones would be transformed into the two points denoting longitudinal failure under pure tension and under pure compression. One of the two immediately adjacent points on the failure envelope is not allowed to be changed, while the other is permitted to be enhanced to as close to the unidirectional fiber-dominated strength as the reduction in matrix stiffnesses permits. Is this distinction really credible? And what does this imply about the theory that created it?

Even the individual equations in this theory are highly interactive, as an assessment of the fiber-in-tension equation can attest. Figure 14 shows what happens when this equation is used to characterize the longitudinal strength of a glass fiber in the presence of only additional in-plane shear stresses. Consider a glass fiber embedded in an epoxy matrix. Because the glass fibers are isotropic, their transverse properties can be established without the difficulties associated with orthotropic carbon fibers, and the like. Let us assume that a unidirectional fiberglass-epoxy lamina has a longitudinal strength of 1720 MPa (250 ksi). This would correspond to a fiber strength on the order of 3103 MPa (450 ksi). Suppose, now, that the in-plane shear strength of the lamina is limited to 103 MPa (15 ksi) by the rel-

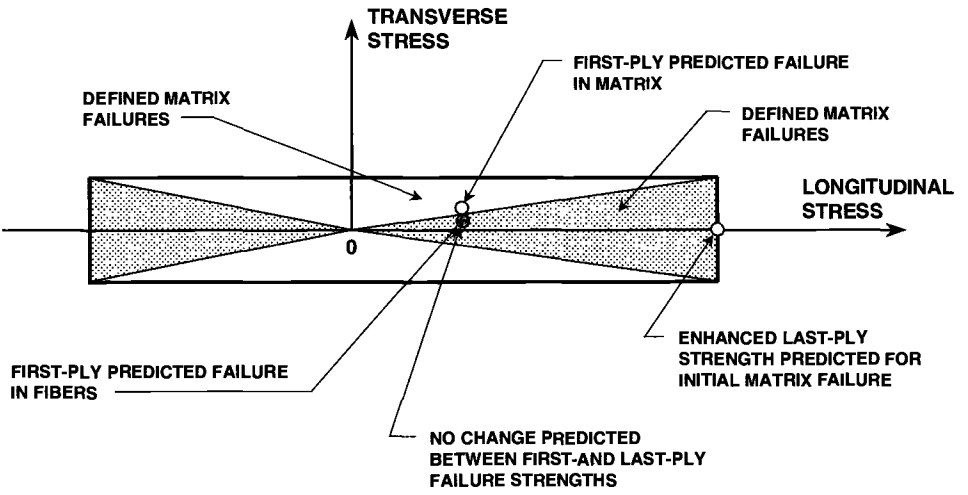


FIG. 13—*First- and last-ply failure predictions, per the Hashin/Rosen composite failure theory in MIL-HDBK-17.*

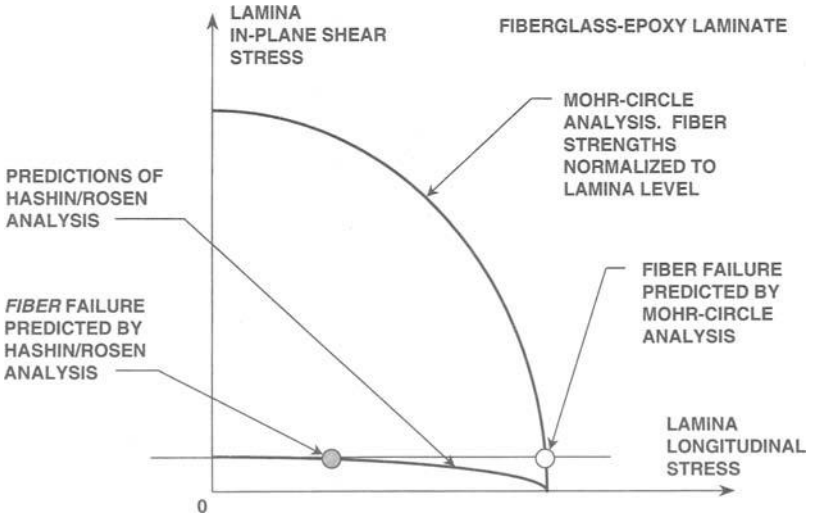


FIG. 14—*Longitudinal fiber-dominated strength in tension, in presence of added in-plane shear; comparison between Hashin/Rosen composite failure theory in MIL-HDBK-17 and Mohr circles.*

atively weak matrix, and that the lamina is subjected to an in-plane shear stress of 97 MPa (14 ksi), not quite sufficient to fail it under that load alone, in the absence of any transverse stress.

According to the third of the set of equations in the handbook, for the matrix mode under tension,

$$\left(\frac{\sigma_{22}}{F_2^{tu}}\right)^2 + \left(\frac{\sigma_{12}}{F_{12}^{su}}\right)^2 = 1$$

the lamina could not fail in the matrix but, according to the first of the equations, for the fiber mode under tension,

$$\left(\frac{\sigma_{11}}{F_1^{tu}}\right)^2 + \left(\frac{\sigma_{12}}{F_{12}^{su}}\right)^2 = 1$$

it could fail in the fiber if subjected simultaneously to a longitudinal lamina stress of 621 MPa (90 ksi), as shown in Fig. 14. The question is whether or not this reduction to 36% of the lamina tensile strength is a credible prediction. It is certainly not a misrepresentation of the equations. Because glass fibers are isotropic, it is permissible to use a Mohr circle analysis to assess the impact of this same 97 MPa (14 ksi) on the axial strength of the glass fibers. By this method of analysis, the fiber strength would be reduced to 3096 MPa (449 ksi). This same insignificant loss of axial strength, less than 0.2%, would be reflected proportionally at the lamina level also. This, too, is shown in Fig. 14, where it is apparent that these two components of stress should not have been interacted, at least not at the assumed homogeneous lamina level, for a composite of strong, stiff fibers in a soft, weak matrix. The real situation is characterized in Fig. 6. Within the confines of numerical accuracy, there isn't any interaction between the lamina longitudinal and in-plane shear strengths. In other words, the earlier estimate of a 64% loss of strength must be overridden or the theory used to compute it would be discredited. The problem facing the analyst is how can this be accomplished within the framework of the set of four equations, particularly when the associated terminology clearly states that, in this case, the fibers failed first! One is forced to conclude from Fig. 14 that either the classical theory of Mohr

circles is wrong or that the Hashin and Hashin/Rosen fiber-failure models for composite laminates are fatally flawed. Is this choice even worthy of a debate?

The obvious unacceptability of predictions made using this theory invite a request that, in future, no such theories be accepted for publication unless accompanied by worked examples, and that no such theories be submitted for publication until after they have been evaluated.

Quite obviously, the MIL-HDBK-17 model[8] [22] is grossly conservative for this combination of stresses, and unacceptably so. Figure 14 explains why. All reference strengths for fiber failures **must** be fiber properties, even if normalized to account for the presence of the resin matrix. None can be allowed to be measured via a matrix failure in the lamina, even if the transverse and in-plane shear strengths of the embedded fibers cannot be measured directly.

The simplicity of this two-variable elliptical interaction equation, and its obvious unsuitability for any fiber-polymer composite might make more obvious the fact that precisely the same problem exists, except that it is on a larger scale and less easy to visualize, with *every* interactive composite failure theory, whether four equations are involved or all of the terms are lumped together in a single equation.

Is it now clear, at last, that *only* mechanistic failure criteria have *any* relevance to the strength[9] of heterogeneous fiber-polymer composites?

Other Issues Needing to be Resolved About Fiber-Polymer Composite Failure Criteria

Limited space has permitted discussion of only a few of the many fundamental errors in interactive composite failure theory here. If an open debate is to take place about the merits of alternative methods for predicting the strength of fiber-polymer composites, many other issues need to be addressed. Among these are the following:

1. Omission of consideration of intralaminar residual thermal stresses in isolated unidirectional tape plies and woven fabric layers. No possible valid prediction of matrix failures can be made without the inclusion of these largest of all matrix stresses in the analysis.
2. The miraculous way in which standard analysis methods rely on matrix damage incurred under one load condition to have healed itself before the application of the next load case. If this were not done, and matrix damage was accumulated from case to case, the duration of the analysis process for large aircraft or missiles would run into decades or possibly centuries (even with the fastest of computers) because of the need to consider every possible sequence of application of these loads. If we suppose that there are 1000 aircraft in a given fleet, that they are expected to fly for 50 000 flights each, and that there are as few as 20 significant loads per flight, the number of analyses needing to be performed, keeping track of prior matrix damage, would be $1000 \times 1\,000\,000!$. The author has no grasp of the magnitude of factorial 1 000 000 but notes that the value of merely 100! is on the order of 10^{59}. There needs to be some acceptance of the notion that most such predicted failures never do happen,[10] which would invalidate the progressive-failure process as a "legitimate" means of con-

[8] The current revision of the "lamina-to-laminate" chapter of the handbook does include the original and truncated maximum-strain failure models, as well as that by Hashin and Rosen. However, they are followed by an implication that it is always necessary to invoke progressive-failure analyses to achieve numerically acceptable results, even though the intent of using secant moduli with the strain-based models is to avoid further analyses. But, more importantly, the entire chapter on "lamina characterization" is devoted to only the Hashin/Rosen model discussed here. It is hoped that future revisions will lead to the exclusive use of mechanistic failure models and warnings against the use of theories of elasticity for homogeneous anisotropic solids for anything more than the establishment of elastic constants for heterogeneous composite materials. (Of course, there is no reason to refrain from using some such theories to predict the strength of *truly homogeneous* anisotropic solids like rolled metallic plates and extrusions.)

[9] The homogenized model is perfectly adequate for calculating global laminate *stiffnesses*, and elastic constants, as it has for decades. But that is *all* that it is good for.

[10] The well-known Kevlar/Nomex water-accumulation problem in honeycomb secondary structures is not typical of composites. It was the result of the difficulty of the resin wetting Kevlar fibers in excessively large (12K) tow sizes. The author is unaware of any other widespread inspection program for cracks in fiber-polymer composites.

verting unacceptable first-ply failure predictions into more acceptable last-ply failure predictions. Alternatively, if such failures are real and structurally significant, there needs to be a search for new resins in which such failures do not occur, which would again proscribe the use of progressive failure theories in the customary manner. If they are real and cannot be avoided, there needs to be a recognition that real matrix failures, in complete structures rather than test coupons, constitute design ultimate strengths whenever, as is usual, many different loads may be applied in random order.

3. The belief that matrix cracking can be assessed on a ply-by-ply basis, without even invoking fracture mechanics. If this belief were valid, bonded composite crack patching could not possibly work. But it does! There are some 2000 bonded patches over cracks in metallic aircraft structure that have prolonged the service life of hundreds of aircraft for at least two decades in some cases, saving their operators (and the taxpayers) an enormous amount of money. Should these patches now be removed because analyses of their performance based on interactive composite failure criteria would show that they couldn't possibly work? Matrix failures under in-plane shear and transverse compression can be assessed without invoking interactions with adjacent plies, but cracking in the matrix between the fibers cannot. This phenomenon has been analyzed several times and is well documented in the literature. However, it appears to have been totally ignored by the advocates of interactive composite failure criteria because the only possible response to such wisdom is to admit that the theories they have defended are worthless. The very first casualty of an objective scientific assessment of this situation would be the highly questionable "first-ply failure" predictions that have historically served as the starting point of progressive-failure theories to generate more acceptable "last-ply failure" predictions. Every other mode of first-ply failure, apart from matrix cracking which cannot be predicted by any of the standard composite failure criteria, would instantly be recognized as catastrophic and would put an end to the analysis process and prevent any enhancement of the predicted laminate strength. It does seem curious that, in most cases, progressive-failure analyses are used not to decrease a predicted strength to account for a real loss of lamina strength or stiffness, but to increase a false prediction of failure rather than to admit to fatal errors in the theories used to make such predictions.

Concluding Remarks

There are many additional anomalies or fatal errors, depending on how one looks upon them, that the author could have cited in regard to the use and abuse of interactive composite failure criteria, particularly when they are used in conjunction with progressive failure theories. Some have been cited in his earlier papers on this subject, but there are many others. The strain-based lamina last-ply failure criteria for the Hashin/Rosen model, for example, are at times triple valued unless predicted first-ply failures in the fibers are overridden.

But the primary objective of this paper is to discourage further use, and teaching, of the great many highly questionable composite failure theories by revealing for others to debate precisely what they imply.

A further objective is to encourage the use of mechanistic failure models for all aspects of predicting the strength of composite laminates. They must include micromechanical effects, but may be modeled at the macro level, in equations that are even easier to use than single-function interactive models, because so many of the real criteria can be expressed as straight lines.

A standard rebuttal to the author's pleas for a change in how the strength of composite laminates is calculated is that his concerns affect only those neophyte analysts who have not yet learned not to stop at the first-ply-failure predictions. Everyone experienced enough to fiddle the process can add last-ply failure solutions and usually obtain an acceptable answer, even if he does have to switch to totally different failure criteria along the way. So what is the fuss about? This logic is true, but it does not detract from the author's message that going straight to a mechanistic failure (strength) model is both quicker and more reliable, and that the invariably discarded first-ply failure solution is just plain wrong, yet it does not come with a warning to that effect for the unwary.

In addition, any false prediction of a "first-ply failure" that does not actually occur leads to path-dependent predicted strengths and to enormous problems with certification of composite structures. Conversely, the gay abandon with which falsely predicted matrix failures are blithely ignored has obscured the need to treat real predictions of matrix failures as design ultimate strengths.

The author would suggest that the historical method of presentation of the interactive composite failure criteria to students has had much to do with their unthinking acceptance. At first, only the basic theories are taught, abstractly, without comparison with available test data. The need for supplementary progressive-failure analyses to make the predictions credible is not revealed until much later. By then, these theories are so deeply ingrained that there is a great reluctance to abandon them. Fiddling them to make them work then seems more acceptable, particularly in light of the easy availability of computer codes with which to facilitate that exercise.

However, the cost today of certifying composite aircraft structures primarily by extensive testing, because of acknowledged unreliabilities of the majority of available analysis codes, can be brought down only by improved failure theories that can be relied upon. The payoff from a rational approach to this subject is, therefore, of far more than academic interest. The concern is not only with unnotched laminate strengths; all failure models for "notched" laminates need unnotched reference strengths if they are not to be entirely dependent on expensive test data. This need is quite apparent for finite-element analyses of composite structures with large cutouts whenever the only available tests data are for laminates containing small holes. And any characterization of matrix failures, with or without notches, needs appropriate mechanistic failure models, including consideration of intralaminar residual thermal stresses.

This paper began with a plea for a serious debate about how best to characterize the properties of fiber-polymer composites in such a manner that structural analysts can reliably estimate at least the in-plane properties[11] of unnotched composite laminates. (Notched laminates will always require some further empirical data.) Some who developed composite failure theories have already joined in what is referred to as the "English Exercise," "World-Wide Failure Exercise," or the "Olympic Games," in which a number of problems have been analyzed using some of the more significant published failure models, with exactly the same input properties each time, so that the different predictions can be compared and assessed. (A second phase of the exercise includes a comparison of the predictions from these theories with test data that were not released during the first phase.) The intent had been for each of the "prominent" theories to be championed by its originator, to ensure that there were no misinterpretations. This was not always achieved, so there are still some well-known theories for which potential users have no means of assessing them, other than by applying them to the same problems, themselves.

Such an objective comparison of the capabilities and limitations of the many published failure theories for fiber-polymer composites is long overdue. Will there be a continuation of reliance on fiddling answers out of scientifically inappropriate failure models? Or will we, as an industry, develop and use only those theories that *do not need to be fiddled* to yield acceptable estimates of in-plane laminate strengths? And will the *users* of *all* theories for the strength of fibrous composite laminates, and the providers of computer codes, refrain at last from blindly accepting whatever theories they select and accept *their* responsibility first to thoroughly assess the capabilities and limitations inherent in them?

References

[1] Waddoups, M. E., "Characterization and Design of Composite Materials," In: *Composite Materials Workshop*, S. W. Tsai, J. C. Halpin, and N. J. Pagano, Eds., Technomic, CT, 1968, pp. 254–308.

[2] Tsai, S. W. and Wu, E. M., "A General Theory of Strength for Anisotropic Materials," *Journal of Composite Materials*, Vol. 5, 1971, pp. 58–80.

[11] Through-the-thickness effects are generally acknowledged as being an order of magnitude more difficult to cope with. But knowledgeable designers are aware that these laminates are inherently weak under such loads, and do their best to design structures in such a manner as to avoid such effects.

[3] Goldenblat, I. I. and Kopnov, V. A., *Anisotropy of Structural Materials,* Mashinostroenie, Moscow, 1968 (in Russian).

[4] Hart-Smith, L. J., "The Role of Biaxial Stresses in Discriminating Between Meaningful and Illusory Composite Failure Theories," McDonnell Douglas Paper MDC 91K0077, presented to 9th DoD/NASA/FAA Conference on Fibrous Composites in Structural Design, Lake Tahoe, NV, 4–7 November 4–7, 1991, in *Proceedings, DOT/FAA/CT-92-25, Part III,* pp. 1507–1528; also published in *Composite Structures,* Vol. 25, 1993, pp. 3–20.

[5] Wu, E. M., UCLA Extension Short Course on Advanced Analysis of Composites, L. B. Greszczuk coordinator, 1987–1998.

[6] Tsai, S. W., *Composites Design,* 4th ed., Think Composites, Dayton, OH, 1988.

[7] Bader, M. G., Bailey, J. E., Curtis, P. T., and Parvesi, A., "The Mechanisms of Initiation of Development of Damage in Multi-Axial Fiber-Reinforced Plastic Laminates," *Proceedings—Symposium on Mechanical Behavior of Materials,* Cambridge, UK, ICM-3, Vol. 3, 1979, p. 227.

[8] O'Brien, T. K., "Characterization of Delamination Onset and Growth in a Composite Laminate," NASA Langley Technical Memorandum 81940, January 1981.

[9] Wang, A. S. D., "Fracture Mechanics of Sublaminate Cracks in Composite Materials," *Composites Technology Review,* Vol. 6, No. 2, 1984, pp. 45–62.

[10] Hill, R., *The Mathematical Theory of Plasticity,* Oxford University Press, London, UK, 1971, pp. 317–340.

[11] Tsai, S. W., "Strength Characteristics of Composite Materials," NASA Report No. CR-224, April 1965.

[12] Soden, P. D., Hinton, M. J., and Kaddour, A.-S., "Lamina Properties and Lay-Up Configurations and Loading Conditions of a Range of Fibre Reinforced Composite Laminates," Special Issue of *Composites Science and Technology,* Vol. 58, No. 7, 1998, pp. 1011–1022.

[13] Williams, R. S. and Reifsneider, K. L., "Investigation of Acoustic Emission During Fatigue Loading of Composite Specimens," *Journal of Composite Materials,* Vol. 8, No. 4, 1974, pp. 8–17.

[14] Hart-Smith, L. J., "How to Calculate the In-Plane Strengths of Fiber-Polymer Composites," McDonnell Douglas Paper MDC 92K0023, presented to 25th MIL-HDBK-17 Meeting, Laughlin, Nevada, 31 March–2 April 1992; published in *SAMPLE Journal* Vol. 28, No. 6, Nov./Dec. 1992, pp. 25–35.

[15] Hart-Smith, L. J., "Fibrous Composite Failure Criteria—Fact and Fantasy," McDonnell Douglas Paper MDC 93K 0047, presented to Plenary Session of Seventh International Conference on Composite Structures, Paisley, Scotland, 5–7 July 1993; abridgement to be published in *Composites Part A: Applied Science and Manufacturing.*

[16] Hart-Smith, L. J., "Predictions of the Original and Truncated Maximum-Strain Failure Models for Certain Fibrous Composite Laminates," *Composites Science and Technology,* Vol. 58, July 1998, Special Issue on "Failure Criteria in Fibre-Reinforced-Polymer Composites," pp. 1151–1178.

[17] Hart-Smith, L. J., "Predictions of a Generalized Maximum Shear-Stress Failure Criterion for Certain Fibrous Composite Laminates," *Composites Science and Technology,* Vol. 58, July 1998, Special Issue on "Failure Criteria in Fibre-Reinforced-Polymer Composites," pp. 1179–1208.

[18] Hart-Smith, L. J., "Backing Out Equivalent Unidirectional Lamina Strengths from Tests on Cross-Plied Laminates," McDonnell Douglas Paper MDC 91K0078, presented to 37th International SAMPE Symposium and Exhibition, Anaheim, California, 9–12 March 1992; in *Proceedings,* pp. 977–990.

[19] Hart-Smith, L. I. "Generation of Higher Composite Material Allowables Using Improved Test Coupons," Douglas Paper 8557, presented to 36th International SAMPE Symposium and Exhibition, San Diego, California, 15–18 April 1991; in *Proceedings,* pp. 1029–1044; modified and republished in *Aerospace Composites & Materials,* Vol. 3, No. 3, May–June 1991, pp. 26–30, 58, and No. 4, July–Aug. 1991, pp. 13–16, 18.

[20] Liu, K.-S. and Tsai, S. W., "A Progressive Quadratic Failure Criterion for a Laminate," *Composites Science and Technology,* Vol. 58, July 1998, Special Issue on "Failure Criteria in Fibre-Reinforced-Polymer Composites," pp. 1023–1032.

[21] Sun, C. T., et al., "Comparative Evaluation of Failure Analysis Methods for Composite Laminates," FAA Technical Report DOT/FAA/AR-95/109, 1996.

[22] MIL-HDBK-17-1E, *Polymer Matrix Composites,* Vol. 1, Aug. 1996, Department of Defense, Washington, DC.

Scott O. Peck[1]

Curved Laminated Beams Subjected to Shear Loads, Moments, and Temperature Changes

REFERENCE: Peck, S. O., **"Curved Laminated Beams Subjected to Shear Loads, Moments, and Temperature Changes,"** *Composite Structures: Theory and Practice, ASTM STP 1383,* P. Grant and C. Q. Rousseau, Eds., American Society for Testing and Materials, West Conshohocken, PA, 2000, pp. 437–451.

ABSTRACT: Closed-form 2-D solutions for the displacements, strains, and stresses in curved, laminated orthotropic beams subjected to shear loads, moments, and temperature changes are developed. The solutions are exact and therefore equally applicable to sandwich structures as well as to ordinary laminates. The displacement solutions include rigid-body terms that are used to predict the contribution to spring-in of curved composite laminates due to differential thermal expansion in the radial and circumferential directions. Sample calculations for graphite/epoxy face-skinned aluminum honeycomb curved beams clearly predict anticipated failure modes.

KEYWORDS: curved beams, laminated composites, sandwich structures, spring-in, single-piece structures

Nomenclature

r, θ, z	Cylindrical coordinates
u_r, u_θ, u_z	Physical components of displacement
$\varepsilon_{rr}, \varepsilon_{\theta\theta}, \varepsilon_{zz}, \varepsilon_{rz}, \varepsilon_{\theta z}, \varepsilon_{r\theta}$	Physical components of strain
$\sigma_{rr}, \sigma_{\theta\theta}, \sigma_{zz}, \sigma_{rz}, \sigma_{\theta z}, \sigma_{r\theta}$	Physical components of stress
P	Applied shear load per unit width of beam
M	Applied moment per unit width of beam
ΔT	Uniform temperature difference from a reference temperature
a_i	Radial coordinate of ith ply interface
s_{ii}	Elastic compliances
E_r	Young's modulus in radial direction
E_θ	Young's modulus in tangential direction
$\nu_{\theta r}$	Poisson's ratio in r-θ plane
$G_{r\theta}$	Shear modulus in r-θ plane
α_r	Radial coefficient of thermal expansion
α_θ	Tangential coefficient of thermal expansion
$F(r, \theta)$	Stress function for shear load case
$Q(r, \theta)$	Stress function for moment and temperature load case
C_1, C_2, C_3, C_4	Constants to be determined from boundary conditions
D_1, D_2, D_3, D_4	Constants to be determined from boundary conditions
β, k	Constants determined from elastic compliances

[1] Principal engineer, Space Systems/Loral, 3825 Fabian Way, MS G-97, Palo Alto, CA 94303.

Copyright© 2001by ASTM International www.astm.org

The motivation for this paper is twofold: (*a*) Advanced spacecraft structures will be manufactured to the maximum extent possible as single-piece structures of complex geometry. Loads will be efficiently carried through corners by fibers, and manufacturing costs will be reduced due to the reduced part count. Thus, the behavior of corner regions subjected to end forces and moments is of interest. (*b*) It has been observed that laminates built on complex tools tend not to retain the exact tool shape after cure but permanently deform, a phenomenon known as spring-in. One of the suggested mechanisms for spring-in is the differential thermal expansion behavior of a ply between the through-thickness and in-plane directions. The formalism for studying the behavior of curved beams subjected to thermal loads turns out to be very similar to that due to moments. Solutions for spring-in require, in particular, exact expressions for displacements including rigid-body terms. Lekhnitskii [*1*] has developed a solution for a curved, orthotropic beam subjected to end forces and moments. Ko and Jackson [*2*] have developed that solution into a multilayered theory. Timoshenko and Goodier [*3*] find displacement solutions for isotropic beams. This paper builds on these works by developing the stress, strain, and complete displacement solutions for curved, laminated beams subjected to shear loads, moments and temperature changes.

Solutions such as the ones derived in this paper are of interest for a number of reasons: (*a*) The solutions are exact for the 2-D beam under consideration; higher-order shear deformation theories are unnecessary. (*b*) The computational power required to solve the problem is only that necessary to solve a linear system of equations once, where the number of equations is equal to three times the number of plies. Thus, even a very thick laminate problem can easily be solved on a personal computer in seconds. Finally, (*c*) the solution demonstrates some of the real limitations of laminated plate theory. As will be shown in one of the examples, the dominant mode of failure under "opening" conditions is due to tensile through-thickness stresses that develop, which are assumed to be zero in laminated plate theory.

Analysis

The following sections present the theoretical derivation of the stresses, strains, and displacements present in curved, laminated beams shown in Fig. 1 subjected to shear forces and moments [*2*] as well as temperature changes. Edge effects will be disregarded and the beam idealized as two-dimensional.

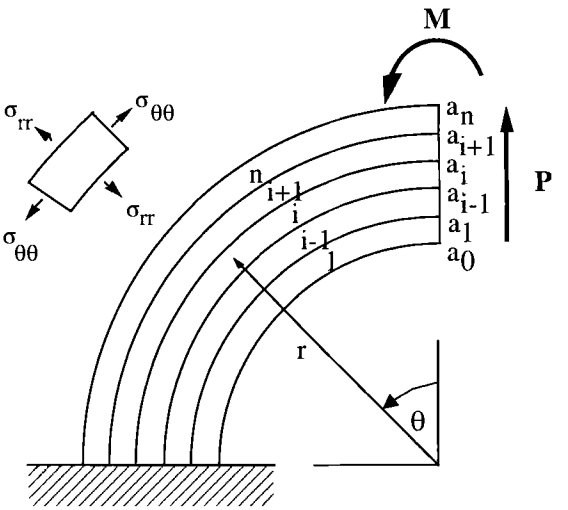


FIG. 1—*Laminated curved beam coordinates and nomenclature.*

The two-dimensional problem is most conveniently represented in cylindrical coordinates. The general equations for curved laminated beams will be presented first, followed by specific solutions for shear forces, moments, and temperature changes.

Anisotropic Curved Beams

Let u_r, u_θ, u_z represent the radial, tangential, and axial physical components of displacement. Let ε_{rr}, $\varepsilon_{\theta\theta}$, ε_{zz}, ε_{rz}, $\varepsilon_{\theta z}$, $\varepsilon_{r\theta}$ and σ_{rr}, $\sigma_{\theta\theta}$, σ_{zz}, σ_{rz}, $\sigma_{\theta z}$, $\sigma_{r\theta}$ represent the physical components of strain and stress, respectively. The beam is assumed to be in a state of plane stress such that

$$\sigma_{zz} = \sigma_{rz} = \sigma_{\theta z} = 0 \tag{1a,b,c}$$

The stress-strain relationships for an anisotropic material in plane stress are

$$\begin{aligned} \varepsilon_{rr} &= s_{11}\sigma_{rr} + s_{12}\sigma_{\theta\theta} + s_{16}\sigma_{r\theta} \\ \varepsilon_{\theta\theta} &= s_{12}\sigma_{rr} + s_{22}\sigma_{\theta\theta} + s_{26}\sigma_{r\theta} \\ 2\varepsilon_{r\theta} &= s_{16}\sigma_{rr} + s_{26}\sigma_{\theta\theta} + s_{66}\sigma_{r\theta} \end{aligned} \tag{2a,b,c}$$

where s_{11} through s_{66} are elastic constants. If the material axes of symmetry are coincident with radial and tangential generators, such as here, then $s_{16} = s_{26} = 0$ and the material is termed cylindrically orthotropic. In terms of engineering constants

$$s_{11} = \frac{1}{E_r} \quad s_{12} = -\frac{\nu_{\theta r}}{E_\theta} \quad s_{22} = \frac{1}{E_\theta} \quad s_{66} = \frac{1}{G_{r\theta}} \tag{3a,b,c,d}$$

where E_r and E_θ are the radial and tangential elastic moduli, $\nu_{\theta r}$ is Poisson's ratio, and $G_{r\theta}$ is the shear modulus. The strains are related to the displacements by

$$\begin{aligned} \varepsilon_{rr} &= \frac{\partial u_r}{\partial r} \\ \varepsilon_{\theta\theta} &= \frac{1}{r}\frac{\partial u_\theta}{\partial \theta} + \frac{u_r}{r} \\ \varepsilon_{r\theta} &= \frac{1}{2}\left(\frac{1}{r}\frac{\partial u_r}{\partial \theta} + \frac{\partial u_\theta}{\partial r} - \frac{u_\theta}{r}\right) \end{aligned} \tag{4a,b,c}$$

The equations of equilibrium are

$$\begin{aligned} \frac{1}{r}\frac{\partial}{\partial r}(r\,\sigma_{rr}) + \frac{1}{r}\frac{\partial \sigma_{r\theta}}{\partial \theta} - \frac{\sigma_{\theta\theta}}{r} &= 0 \\ \frac{1}{r^2}\frac{\partial}{\partial r}(r^2\,\sigma_{r\theta}) + \frac{1}{r}\frac{\partial \sigma_{\theta\theta}}{\partial \theta} &= 0 \end{aligned} \tag{5a,b}$$

The stresses may be derived from a stress function F as

$$\sigma_{rr} = \frac{1}{r}\frac{\partial F}{\partial r} + \frac{1}{r^2}\frac{\partial^2 F}{\partial \theta^2} \tag{6a}$$

$$\sigma_{\theta\theta} = \frac{\partial^2 F}{\partial r^2}$$

$$\sigma_{r\theta} = -\frac{\partial^2}{\partial r \partial \theta}\left(\frac{F}{r}\right) \tag{6b,c}$$

These stresses automatically satisfy the equations of equilibrium (Eq 5).

The following identity [*1*], known as the compatibility condition, may be verified by substitution of the strain-displacement relations (Eq 4)

$$\left(\frac{\partial^2}{\partial \theta^2} - r\frac{\partial}{\partial r}\right)\varepsilon_{rr} + r\frac{\partial^2}{\partial r^2}(r\varepsilon_{\theta\theta}) - \frac{\partial^2}{\partial r \partial \theta}(r2\varepsilon_{r\theta}) = 0 \tag{7}$$

Substituting the stress-strain relations for an anisotropic material (Eq 2) in the identity (Eq 7), and subsequently the stress function expressions for the stresses (Eq 6) yields the fundamental relationship for the anisotropic curved beam in terms of elastic constants s_{11} through s_{66} and the stress function F:

$$\begin{aligned}
&\left(\frac{\partial^2}{\partial \theta^2} - r\frac{\partial}{\partial r}\right)\left[s_{11}\left(\frac{1}{r}\frac{\partial F}{\partial r} + \frac{1}{r^2}\frac{\partial^2 F}{\partial \theta^2}\right) + s_{12}\frac{\partial^2 F}{\partial r^2} - s_{16}\frac{\partial^2}{\partial r \partial \theta}\left(\frac{F}{r}\right)\right] \\
&+ r\frac{\partial^2}{\partial r^2}\left[s_{12}\left(\frac{\partial F}{\partial r} + \frac{1}{r}\frac{\partial^2 F}{\partial \theta^2}\right) + s_{22}r\frac{\partial^2 F}{\partial r^2} - s_{26}r\frac{\partial^2}{\partial r \partial \theta}\left(\frac{F}{r}\right)\right] \\
&- \frac{\partial^2}{\partial r \partial \theta}\left[s_{16}\left(\frac{\partial F}{\partial r} + \frac{1}{r}\frac{\partial^2 F}{\partial \theta^2}\right) + s_{26}r\frac{\partial^2 F}{\partial r^2} - s_{66}r\frac{\partial^2}{\partial r \partial \theta}\left(\frac{F}{r}\right)\right] = 0
\end{aligned} \tag{8}$$

Solutions to Eq 8 will depend on the specific boundary conditions and applied loads. In addition, the requirements of a laminated beam must be addressed for the beams considered here.

Curved Laminated Beam Subjected to End Forces

The bending moment in a curved beam subjected to an end shear load is proportional to $\sin\theta$. Elementary beam theory predicts that the normal stress $\sigma_{\theta\theta}$ is proportional to the bending moment. It is therefore reasonable to assume that the stress function F is also proportional to $\sin\theta$ [*1*].

$$F(r, \theta) = f(r)\sin\theta \tag{9}$$

Substituting the assumed form of the stress function (Eq 9) into the governing partial differential equation (Eq 8) yields (assuming again that $s_{16} = s_{26} = 0$):

$$\begin{aligned}
&\left\{-(s_{11} + 2s_{12} + s_{66})f + (s_{11} + 2s_{12} + s_{66})r\frac{df}{dr}\right. \\
&\left. - (s_{11} + 2s_{12} + s_{66})r^2\frac{d^2 f}{dr^2} + 2s_{22}r^3\frac{d^3 f}{dr^3} + s_{22}r^4\frac{d^4 f}{dr^4}\right\}\sin\theta = 0
\end{aligned} \tag{10}$$

The solution to Eq 10 is

$$f(r) = C_1 r + C_2 r\log r + C_3 r^{1-\beta} + C_4 r^{1+\beta} \tag{11}$$

where C_1, C_2, C_3, and C_4 are constants to be determined from the boundary conditions, and the constant β is a function of material properties

$$\beta = \sqrt{1 + \frac{s_{11} + 2s_{12} + s_{66}}{s_{22}}} \tag{12}$$

The final expressions for the stresses are

$$\sigma_{rr}(r, \theta) = \left[C_4\beta r^{\beta-1} - C_3\beta r^{-\beta-1} + \frac{C_2}{r}\right] \sin\theta$$

$$\sigma_{\theta\theta}(r, \theta) = \left[C_4\beta(1 + \beta)r^{\beta-1} - C_3\beta(1 - \beta)r^{-\beta-1} + \frac{C_2}{r}\right] \sin\theta \tag{13a,b,c}$$

$$\sigma_{r\theta}(r, \theta) = -\left[C_4\beta r^{\beta-1} - C_3\beta r^{-\beta-1} + \frac{C_2}{r}\right] \cos\theta$$

Note that the shear stress and radial stress have the same magnitude but are out of phase.

Up to this point the relationships developed have implicitly referred to a single ply. From now on either the entire laminated beam or interfaces between lamina in the beam will be considered. The notation will remain the same except for a pre-superscript Latin letter or numeral indicating either a generic ply or a specific ply, respectively. The ply and interface numbering scheme is shown in Fig. 1.

Displacements

The displacements are found by integrating the strain-displacement equations (Eq 4) together with the stress-strain relation (Eq 2) [*3*].

$$^iu_r(r, \theta) = \int(^is_{11}\,^i\sigma_{rr} + {}^is_{12}\,^i\sigma_{\theta\theta})\,dr + {}^ih(\theta) \qquad i = 1,2, \ldots, n$$

$$^iu_\theta(r, \theta) = \int\{r(^is_{12}\,^i\sigma_{rr} + {}^is_{22}\,^i\sigma_{\theta\theta}) - {}^iu_r(r, \theta)\}\,d\theta + {}^ig(r)\; i = 1,2, \ldots, n \tag{14a,b}$$

where $^ih(\theta)$ and $^ig(r)$ for $i = 1,2, \ldots, n$ are as yet unknown functions of θ and r, respectively.

By substituting the solution to the stress function (Eq 11) into the defining relations for the stresses (Eq 6), then performing the integrations (Eq 14), expressions for the displacements can obtained which still contain the unknown functions $^ih(\theta)$ and $^ig(r)$. These displacement relations also need to satisfy the shear strain/shear stress relation (Eq 2) and shear strain/displacement relation (Eq 4).

$$^is_{66}\,^i\sigma_{r\theta} = \frac{1}{r}\frac{\partial^iu_r}{\partial\theta} + \frac{\partial^iu_\theta}{\partial r} - \frac{^iu_\theta}{r} \tag{15a}$$

which yields

$$^ih(\theta) = -\frac{1}{2}(^is_{11} + 2{}^is_{12} + {}^is_{22} + {}^is_{66})\,^iC_2\theta\cos\theta - {}^iK\sin\theta + {}^iL\cos\theta$$

$$^ig(r) = {}^iGr \tag{15b,c}$$

where ${}^iK$, ${}^iL$, and ${}^iG$ for $i = 1,2, \ldots, n$ are constants to be determined from the boundary and interface conditions.

Boundary Conditions at the Fixed End

The beam is assumed to be rigidly fixed at $\pi/2$ so that no rotation can occur. In addition, the displacements of the inner surface at $(a_0, \pi/2)$ are assumed to be zero. The appropriate boundary conditions are

$$\frac{\partial {}^iu_\theta}{\partial r}\left(r, \frac{\pi}{2}\right) = 0 \qquad i = 1,2, \ldots, n$$

$${}^iu_\theta\left(r, \frac{\pi}{2}\right) = 0 \qquad i = 1,2, \ldots, n \tag{16a,b,c}$$

$${}^1u_r\left(a_0, \frac{\pi}{2}\right) = 0$$

Notice that these conditions are the same as those considered in Ref *3*. The only difference is that Eqs 16*a*,*b* have to be satisfied for each layer. Application of these fixed-end boundary conditions yields

$${}^iG = 0 \qquad i = 1,2, \ldots, n$$

$${}^iL = -\frac{\pi}{4}{}^iC_2({}^is_{11} + 2{}^is_{12} + {}^is_{22} + {}^is_{66}) \qquad i = 1,2, \ldots, n \tag{17a,b}$$

The current expressions for the displacements, having used the stress results (Eqs 13), shear stress/shear strain results (Eqs 15), and fixed end boundary condition results (Eqs 17) in the original displacement expressions (Eqs 14), are

$$\begin{aligned} {}^iu_r(r, \theta) = &\left\{ \begin{array}{c} {}^iC_4r^{{}^i\beta}[{}^is_{11} + (1 + {}^i\beta)\,{}^is_{12}] + {}^iC_3r^{-{}^i\beta}[{}^is_{11} + (1 - {}^i\beta)\,{}^is_{12}] \\ + {}^iC_2 \log r({}^is_{11} + {}^is_{12}) - {}^iK \end{array} \right\} \sin\theta \\ &+ \left\{ \frac{{}^iC_2}{4}(\pi - 2\theta)({}^is_{11} + 2{}^is_{12} + {}^is_{22} + {}^is_{66}) \right\} \cos\theta \end{aligned} \tag{18a,b}$$

$$\begin{aligned} {}^iu_\theta(r, \theta) = &\left\{ \begin{array}{c} {}^iC_4r^{{}^i\beta}[{}^is_{11} - {}^i\beta(1 + {}^i\beta)\,{}^is_{22} + {}^is_{12}] + {}^iC_3r^{-{}^i\beta}[{}^is_{11} + {}^i\beta(1 - {}^i\beta)\,{}^is_{22} + {}^is_{12}] \\ + \frac{{}^iC_2}{2}[{}^is_{11} - {}^is_{22} + {}^is_{66} + 2 \log r({}^is_{11} + {}^is_{12})] - {}^iK \end{array} \right\} \cos\theta \\ &- \left\{ \frac{{}^iC_2}{4}(\pi - 2\theta)({}^is_{11} + 2{}^is_{12} + {}^is_{22} + {}^is_{66}) \right\} \sin\theta \end{aligned}$$

This leaves $4n$ constants (${}^iC_2$, ${}^iC_3$, ${}^iC_4$, and ${}^iK$) to be evaluated from boundary conditions on the exterior surfaces of the beam, at ply interfaces, and one remaining fixity condition (Eq 16*c*).

Free Surface and Ply Interface Boundary Conditions

The boundary condition at the free end of the beam is

$$\sum_{i=1}^{n} \int_{a_{i-1}}^{a_i} {}^i\sigma_{r\theta}\,dr = -P \tag{19}$$

where P is the shear load applied (see Fig. 1) per unit width of the beam. The inner and outer lateral surfaces of the beam are stress free. Thus, the boundary conditions at $r = a_0$ are

$$\begin{aligned} {}^{1}\sigma_{rr}(a_0, \theta) &= 0 \\ {}^{1}\sigma_{r\theta}(a_0, \theta) &= 0 \end{aligned} \tag{20a,b}$$

Likewise, the boundary conditions at $r = a_n$ are

$$\begin{aligned} {}^{n}\sigma_{rr}(a_n, \theta) &= 0 \\ {}^{n}\sigma_{r\theta}(a_n, \theta) &= 0 \end{aligned} \tag{21a,b}$$

Perfect bonding is assumed between plies. Therefore, the boundary conditions at ply interfaces are

$$\begin{aligned} {}^{i}\sigma_{rr}(a_i, \theta) &= {}^{i+1}\sigma_{rr}(a_i, \theta) \\ {}^{i}\sigma_{r\theta}(a_i, \theta) &= {}^{i+1}\sigma_{r\theta}(a_i, \theta) \\ {}^{i}u_r(a_i, \theta) &= {}^{i+1}u_r(a_i, \theta) \\ {}^{i}u_\theta(a_i, \theta) &= {}^{i+1}u_\theta(a_i, \theta) \end{aligned} \qquad i = 1,2, \ldots, n-1 \tag{22a,b,c,d}$$

Recall that the expressions for the radial stress and shear stress (Eqs 13a,c) differ only in the θ term. As a result, if Eq 20a is satisfied so is Eq 20b. The same is true for Eq 21a and Eq 21b, and for Eq 22a and Eq 22b, thus reducing the number of equations available.

Design Procedure

Application of the boundary conditions, Eq 19 through Eq 22, leads to a set of $4n$ equations for the $4n$ unknowns ${}^{i}C_2$, ${}^{i}C_3$, ${}^{i}C_4$, and ${}^{i}K$. The constants ${}^{i}C_1$ do not contribute to the stresses, strains or displacements. Notice that to satisfy displacement continuity for all values of θ, the displacement equations (Eqs 18a,b) and interface requirements (Eqs 22c,d) give rise to the three independent equations shown below. The third of these equations, Eq 23g, does not involve the radial coordinate, r. This implies that the product ${}^{i}C_2({}^{i}s_{11} + 2{}^{i}s_{12} + {}^{i}s_{22} + {}^{i}s_{66})$ equals a constant which is the same for every ply. The equations and their origins are:

Shear load (Eq 19)

$$\sum_{i=1}^{n} \{{}^{i}C_4(a_i^{{}^{i}\beta} - a_{i-1}^{{}^{i}\beta}) - {}^{i}C_3(a_i^{-{}^{i}\beta} - a_{i-1}^{-{}^{i}\beta}) + {}^{i}C_2(\ln a_i - \ln a_{i-1})\} = P \tag{23a}$$

Lateral surfaces (Eqs 20a, 21a)

$$\begin{aligned} {}^{1}C_4\,{}^{1}\beta a_0^{{}^{1}\beta-1} - {}^{1}C_3\,{}^{1}\beta a_0^{-{}^{1}\beta-1} + \frac{{}^{1}C_2}{a_0} &= 0 \\ {}^{n}C_4\,{}^{n}\beta a_n^{{}^{n}\beta-1} - {}^{n}C_3\,{}^{n}\beta a_n^{-{}^{n}\beta-1} + \frac{{}^{n}C_2}{a_n} &= 0 \end{aligned} \tag{23b,c}$$

Interface stresses (Eq 22*a*)

$$
\begin{aligned}
{}^{i}C_4\,{}^{i}\beta a_i^{{}^{i}\beta-1} - {}^{i}C_3\,{}^{i}\beta a_i^{-{}^{i}\beta-1} + \frac{{}^{i}C_2}{a_i} &= {}^{i+1}C_4\,{}^{i+1}\beta a_i^{{}^{i+1}\beta-1} \\
- {}^{i+1}C_3\,{}^{i+1}\beta a_i^{-{}^{i+1}\beta-1} + \frac{{}^{i+1}C_2}{a_i} &\qquad i = 1,2,\ldots,n-1
\end{aligned}
\tag{23d}
$$

Interface displacements (Eqs 22*c*,*d*)

$$
\begin{Bmatrix}
{}^{i}C_4 a_i^{{}^{i}\beta}[{}^{i}s_{11} + (1 + {}^{i}\beta)\,{}^{i}s_{12}] \\
+ {}^{i}C_3 a_i^{-{}^{i}\beta}[{}^{i}s_{11} + (1 - {}^{i}\beta)\,{}^{i}s_{12}] \\
+ {}^{i}C_2 \log a_i({}^{i}s_{11} + {}^{i}s_{12}) \\
- {}^{i}K
\end{Bmatrix}
=
\begin{Bmatrix}
{}^{i+1}C_4 a_i^{{}^{i+1}\beta}[{}^{i+1}s_{11} + (1 + {}^{i+1}\beta)\,{}^{i+1}s_{12}] \\
+ {}^{i+1}C_3 a_i^{-{}^{i+1}\beta}[{}^{i+1}s_{11} + (1 - {}^{i+1}\beta)\,{}^{i+1}s_{12}] \\
+ {}^{i+1}C_2 \log a_i({}^{i+1}s_{11} + {}^{i+1}s_{12}) \\
- {}^{i+1}K
\end{Bmatrix}
$$

$$i = 1,2,\ldots,n-1$$

$$
\begin{Bmatrix}
{}^{i}C_4 a_i^{{}^{i}\beta}[{}^{i}s_{11} - {}^{i}\beta(1 + {}^{i}\beta)\,{}^{i}s_{22} + {}^{i}s_{12}] \\
+ {}^{i}C_3 a_i^{-{}^{i}\beta}[{}^{i}s_{11} + {}^{i}\beta(1 - {}^{i}\beta)\,{}^{i}s_{22} + {}^{i}s_{12}] \\
+ \frac{{}^{i}C_2}{2}[{}^{i}s_{11} - {}^{i}s_{22} + {}^{i}s_{66} + 2\log a_i({}^{i}s_{11} + {}^{i}s_{12})] \\
- {}^{i}K
\end{Bmatrix}
\tag{23e,f,g}
$$

$$
=
\begin{Bmatrix}
{}^{i+1}C_4 a_i^{{}^{i+1}\beta}[{}^{i+1}s_{11} - {}^{i+1}\beta(1 + {}^{i+1}\beta)\,{}^{i+1}s_{22} + {}^{i+1}s_{12}] \\
+ {}^{i+1}C_3 a_i^{-{}^{i+1}\beta}[{}^{i+1}s_{11} + {}^{i+1}\beta(1 - {}^{i+1}\beta)\,{}^{i+1}s_{22} + {}^{i+1}s_{12}] \\
+ \frac{{}^{i+1}C_2}{2}[{}^{i+1}s_{11} - {}^{i+1}s_{22} + {}^{i+1}s_{66} + 2\log a_i({}^{i+1}s_{11} + {}^{i+1}s_{12})] \\
- {}^{i+1}K
\end{Bmatrix}
\qquad i = 1,2,\ldots,n-1
$$

$${}^{i}C_2({}^{i}s_{11} + 2{}^{i}s_{12} + {}^{i}s_{22} + {}^{i}s_{66}) = {}^{i+1}C_2({}^{i+1}s_{11} + 2{}^{i+1}s_{12} + {}^{i+1}s_{22} + {}^{i+1}s_{66})$$

$$i = 1,2,\ldots,n-1$$

Fixed displacement (Eq 16*c*)

$$
\begin{aligned}
{}^{1}K = {}^{1}C_4 a_0^{{}^{1}\beta}[{}^{1}s_{11} + (1 + {}^{1}\beta)\,{}^{1}s_{12}] \\
+ {}^{1}C_3 a_0^{-{}^{1}\beta}[{}^{1}s_{11} + (1 - {}^{1}\beta)\,{}^{1}s_{12}] + {}^{1}C_2 \log a_0({}^{1}s_{11} + {}^{1}s_{12})
\end{aligned}
\tag{23h}
$$

The system of equations is linear in the unknowns and can be formulated as a matrix problem [*5*]. Note that Eq 23*f* can be subtracted from Eq 23*e*, thereby eliminating ${}^{i}K$ and ${}^{i+1}K$. The $3n$ equations (Eqs 23*a*,*b*,*c*,*d*,*e*,*f*,*g*) can then be solved for the $3n$ unknowns ${}^{i}C_2$, ${}^{i}C_3$, ${}^{i}C_4$. Then, ${}^{1}K$ is calculated directly from Eq 23*h* and the remaining ${}^{i}K$ found recursively from either Eq 23*e* or Eq 23*f*. Once the constants are found, the stresses are calculated directly from Eq 13, the strains from the constitutive relations (Eq 2), and the displacements from Eqs 18*a*,*b*.

Curved Laminated Beam Subjected to an End Moment and Temperature Change

The following section discusses the behavior of a curved laminated beam subjected to an end moment and a temperature change from a reference stress free temperature. The assumption of plane stress, material properties, strain-displacement relations, equilibrium equations, and stress function (Eq 1 and Eq 3 through Eq 6) are the same as before. However, the Duhamel-Neumann form of the

stress-strain relations for a cylindrically orthotropic material is

$$\varepsilon_{rr} = s_{11}\sigma_{rr} + s_{12}\sigma_{\theta\theta} + \alpha_r \Delta T$$

$$\varepsilon_{\theta\theta} = s_{12}\sigma_{rr} + s_{22}\sigma_{\theta\theta} + \alpha_\theta \Delta T \qquad (24a,b,c)$$

$$2\varepsilon_{r\theta} = s_{66}\sigma_{r\theta}$$

Stress Function and Stresses

The solution procedure for a curved beam subjected to an end moment is similar to that for a shear force. The stress function for this case Q, is assumed to be independent of the angular position along the beam:

$$Q(r, \theta) = q(r) \qquad (25)$$

The temperature difference ΔT is assumed to be constant over the beam. The presumption is that differences in thermal expansion coefficients will have a greater effect on beam displacements than small differences in temperature. The governing equation (Eq 8) will have a different form if the temperature is assumed to vary with position. Substituting the assumed form of the stress function in Eq 8. which eliminates the θ dependence. and rearranging yields

$$s_{22}\frac{d^4q}{dr^4} + 2\frac{s_{22}}{r}\frac{d^3q}{dr^3} - \frac{s_{11}}{r^2}\frac{d^2q}{dr^2} + \frac{s_{11}}{r^3}\frac{dq}{dr} = 0 \qquad (26)$$

The solution to Eq 26 is

$$q(r) = D_1 + D_2 r^2 + D_3 r^{1+k} + D_4 r^{1-k}$$

$$k = \sqrt{\frac{s_{11}}{s_{22}}} \qquad (27a,b)$$

where D_1, D_2, D_3, and D_4 are constants to be determined from the boundary conditions. The final expressions for the stresses are

$$\sigma_{rr}(r, \theta) = 2D_2 + D_3(1 + k)r^{k-1} + D_4(1 - k)r^{-k-1}$$

$$\sigma_{\theta\theta}(r, \theta) = 2D_2 + D_3 k(1 + k)r^{k-1} - D_4 k(1 - k)r^{-k-1} \qquad (28a,b,c)$$

$$\sigma_{r\theta}(r, \theta) = 0$$

Displacements

The displacements are integrated from the strain-displacement relations [*4*]. Note again the explicit use of a superscript to indicate the properties of a particular ply.

$${}^i u_r(r, \theta) = \int \{{}^i s_{11}\,{}^i\sigma_{rr} + {}^i s_{12}\,{}^i\sigma_{\theta\theta} + {}^i\alpha_r \Delta T\}\, dr + {}^i m(\theta)$$

$$i = 1,2, \ldots, n \qquad (29a,b)$$

$${}^i u_\theta(r, \theta) = \int \{r({}^i s_{12}\,{}^i\sigma_{rr} + {}^i s_{22}\,{}^i\sigma_{\theta\theta} + {}^i\alpha_\theta \Delta T) - {}^i u_r(r, \theta)\} d\theta + {}^i n(r)$$

where ${}^{i}m(\theta)$ and ${}^{i}n(r)$ $i = 1,2, \ldots, n$ are as yet unknown functions of θ and r, respectively. Substituting Eqs 28*a,b* into Eqs 29*a,b* and integrating yields

$$
\begin{aligned}
{}^{i}u_r(r, \theta) &= {}^{i}D_2({}^{i}s_{11} + {}^{i}s_{12})\, 2r + {}^{i}D_3\,({}^{i}s_{11} + {}^{i}k\,{}^{i}s_{12})\left(\frac{1 + {}^{i}k}{{}^{i}k}\right)r^{ik} \\
&+ {}^{i}D_4(-{}^{i}s_{11} + {}^{i}k\,{}^{i}s_{12})\left(\frac{1 - {}^{i}k}{{}^{i}k}\right)r^{-ik} + {}^{i}\alpha_r \Delta T r + {}^{i}m(\theta) \qquad i = 1,2, \ldots, n \qquad (30a,b) \\
{}^{i}u_\theta(r, \theta) &= {}^{i}D_2({}^{i}s_{22} - {}^{i}s_{11})2r\theta + ({}^{i}\alpha_\theta - {}^{i}\alpha_r)\Delta T\, r\theta - \int {}^{i}m(\theta)d\theta + {}^{i}n(r)
\end{aligned}
$$

Substituting these expressions into the shear stress-shear strain relation (Eq 15*a*) as before, and noting that the shear stress is identically zero through the thickness, leads to

$$
\int {}^{i}m(\theta)d\theta + \frac{d}{d\theta}\,{}^{i}m(\theta) + r\frac{d}{dr}\,{}^{i}n(r) - {}^{i}n(r) = 0 \qquad i = 1,2, \ldots, n \qquad (31)
$$

Since Eq 31 is composed of functions of θ or r only, the solutions are

$$
\begin{aligned}
{}^{i}m(\theta) &= {}^{i}R \sin\theta + {}^{i}S \cos\theta \\
{}^{i}n(r) &= {}^{i}T\, r \qquad i = 1,2, \ldots, n
\end{aligned}
\qquad (32a,b)
$$

where ${}^{i}R$, ${}^{i}S$, and ${}^{i}T$ for $i = 1,2 \ldots, n$ are constants to be determined using the conditions of restraint at the fixed end. Applying Eqs 16*a,b* yields

$$
\begin{aligned}
{}^{i}T &= -({}^{i}s_{22} - {}^{i}s_{11})\,\pi\,{}^{i}D_2 - ({}^{i}\alpha_\theta - {}^{i}\alpha_r)\,\Delta T\,\frac{\pi}{2} \qquad i = 1,2, \ldots, n \\
{}^{i}S &= 0 \qquad i = 1,2, \ldots, n
\end{aligned}
\qquad (33a,b)
$$

Free Surface and Ply Interface Boundary Conditions

The boundary condition at the free end of the beam is

$$
\sum_{i=1}^{n} \int_{a_{i-1}}^{a_i} {}^{i}\sigma_{\theta\theta}\, r dr = -M \qquad (34)
$$

where M is the applied moment per unit width of the beam. The boundary conditions on the lateral surfaces and the ply interfaces are the same as for the shear force (Eqs 20 through 22). The current expressions for the displacements (Eqs 30*a,b*), using Eqs 32*a,b* and Eqs 33*a,b*, are

$$
\begin{aligned}
{}^{i}u_r(r, \theta) &= {}^{i}D_2({}^{i}s_{11} + {}^{i}s_{12})\, 2r + {}^{i}D_3\,({}^{i}s_{11} + {}^{i}k\,{}^{i}s_{12})\left(\frac{1 + {}^{i}k}{{}^{i}k}\right)r^{ik} \\
&+ {}^{i}D_4(-{}^{i}s_{11} + {}^{i}k\,{}^{i}s_{12})\left(\frac{1 - {}^{i}k}{{}^{i}k}\right)r^{-ik} + {}^{i}\alpha_r \Delta T\, r + {}^{i}R \sin\theta \qquad i = 1,2, \ldots, n \qquad (35a,b) \\
{}^{i}u_\theta(r, \theta) &= {}^{i}D_2 r({}^{i}s_{22} - {}^{i}s_{11})\,(2\theta - \pi) + 2r({}^{i}\alpha_\theta - {}^{i}\alpha_r)\,\Delta T(2\theta - \pi) + {}^{i}R \cos\theta
\end{aligned}
$$

Continuity of displacements for all values of θ demands that ${}^{i}R = {}^{i+1}R$. The final end-fixity condition (Eq 16*c*) provides the initial value of ${}^{1}R$.

$$
\begin{aligned}
{}^{1}R = &-a_0\,({}^{1}\alpha_r \Delta T + 2({}^{1}s_{11} + {}^{1}s_{12}))^{1}D_2 \\
&+ a_0^{-{}^{1}k}\,\frac{{}^{1}k - 1}{{}^{1}k}\,(-{}^{1}s_{11} + {}^{1}k\,{}^{1}s_{12})^{1}D_3 - a_0^{{}^{1}k}\,\frac{{}^{1}k + 1}{{}^{1}k}\,({}^{1}s_{11} + {}^{1}k\,{}^{1}s_{12})^{1}D_4
\end{aligned}
\tag{35c}
$$

Design Procedure

Application of the boundary conditions (Eq 34 and Eqs 20 through 22) leads to a set of $3n$ equations for the $3n$ unknowns ${}^{i}D_2$, ${}^{i}D_3$, and ${}^{i}D_4$ [2]. The constants ${}^{i}D_1$ do not contribute to the stresses, strains or displacements. The system of equations is again linear in the unknowns and can be formulated as matrix problem [5]. Note that the terms associated with a temperature change ΔT enter the equations on the right-hand side as a forcing term. The equations and their origins are

Moment and temperature (Eq 34)

$$
\sum_{i=1}^{n} \{{}^{i}D_2(a_i^2 - a_{i-1}^2) + {}^{i}D_3\,{}^{i}k(a_i^{{}^{i}k+1} - a_{i-1}^{{}^{i}k+1}) - {}^{i}D_4\,{}^{i}k(a_i^{-{}^{i}k+1} - a_{i-1}^{-{}^{i}k+1})\} = -M \tag{36a}
$$

Lateral surfaces (Eqs 20*a*, 21*a*)

$$
\begin{aligned}
2^{1}D_2 + {}^{1}D_3(1 + {}^{1}k)a_0^{{}^{1}k-1} + {}^{1}D_4(1 - {}^{1}k)a_0^{-{}^{1}k-1} &= 0 \\
2^{n}D_2 + {}^{n}D_3(1 + {}^{n}k)a_n^{{}^{n}k-1} + {}^{n}D_4(1 - {}^{n}k)a_n^{-{}^{n}k-1} &= 0
\end{aligned}
\tag{36b,c}
$$

Interface stresses (Eq 22*a*)

$$
\begin{aligned}
&2^{i}D_2 + {}^{i}D_3(1 + {}^{i}k)\,a_i^{{}^{i}k-1} + {}^{i}D_4(1 - {}^{i}k)\,a_i^{-{}^{i}k-1} \\
&\quad = 2^{i+1}D_2 + {}^{i+1}D_3(1 + {}^{i+1}k)\,a_i^{{}^{i+1}k-1} + {}^{i+1}D_4(1 - {}^{i+1}k)\,a_i^{-{}^{i+1}k-1} \qquad i = 1,2,\ldots,n-1
\end{aligned}
\tag{36d}
$$

Interface displacements (Eqs 22*c*,*d*)

$$
\begin{Bmatrix}
{}^{i}D_2({}^{i}s_{11} + {}^{i}s_{12})2a_i \\
+ {}^{i}D_3({}^{i}s_{11} + {}^{i}k\,{}^{i}s_{12})\left(\dfrac{1 + {}^{i}k}{{}^{i}k}\right)a_i^{{}^{i}k} \\
+ {}^{i}D_4(-{}^{i}s_{11} + {}^{i}k\,{}^{i}s_{12})\left(\dfrac{1 - {}^{i}k}{{}^{i}k}\right)a_i^{-{}^{i}k} \\
+ {}^{i}\alpha_r \Delta T a_i
\end{Bmatrix}
=
\begin{Bmatrix}
{}^{i+1}D_2({}^{i+1}s_{11} + {}^{i+1}s_{12})2a_i \\
+ {}^{i+1}D_3({}^{i+1}s_{11} + {}^{i+1}k\,{}^{i+1}s_{12})\left(\dfrac{1 + {}^{i+1}k}{{}^{i+1}k}\right)a_i^{{}^{i+1}k} \\
+ {}^{i+1}D_4(-{}^{i+1}s_{11} + {}^{i+1}k\,{}^{i+1}s_{12})\left(\dfrac{1 - {}^{i+1}k}{{}^{i+1}k}\right)a_i^{-{}^{i+1}k} \\
+ {}^{i+1}\alpha_r \Delta T a_i
\end{Bmatrix}
$$

$$
\begin{Bmatrix}
{}^{i}D_2 a_i({}^{i}s_{22} - {}^{i}s_{11})(2\theta - \pi) \\
+ 2a_i({}^{i}\alpha_\theta - {}^{i}\alpha_r)\Delta T(2\theta - \pi)
\end{Bmatrix}
=
\begin{Bmatrix}
{}^{i+1}D_2 a_i({}^{i+1}s_{22} - {}^{i+1}s_{11})(2\theta - \pi) \\
+ 2a_i({}^{i+1}\alpha_\theta - {}^{i+1}\alpha_r)\Delta T(2\theta - \pi)
\end{Bmatrix}
\qquad i = 1,2,\ldots,n \tag{36e,f}
$$

Once the constants are found, the stresses are calculated directly from Eqs 28, the strains from the constitutive relations Eq 24, and the displacements from Eqs 35.

TABLE 1—*Material properties for bending example.*

Property	P75/934	Al Honeycomb
Tangential modulus, E_θ	43.2 10^6 psi (298 MPa)	10 psi (69 kPa)
Radial modulus, E_r	1.2 10^6 psi (8.27 MPa)	0.097 10^6 psi (669 kPa)
Poisson's ratio, $\nu_{r\theta}$	0.29	0.0
Shear modulus, $G_{r\theta}$	0.48 10^6 psi (3.31 MPa)	0.045 10^6 psi (310 kPa)
Tensile strength, X_t	0.148 10^6 psi (1020 kPa)	na
Compression strength, X_c	0.59 10^6 psi (407 kPa)	na
Tangential thermal expansion, α_θ	$-0.75\ 10^{-6}$ in./in.-°F ($-1.35\ 10^{-6}$ m/m-K)	13.0 10^{-6} in./in.-°F (23.4 10^{-6} m/m-K)
Radial thermal expansion, α_r	21.0 10^{-6} in./in. - °F (37.8 10^{-6} m/m-K)	13.0 10^{-6} in./in.-°F (23.4 10^{-6} m/m-K)

Sample Cases

Two sample cases have been chosen to illustrate the solutions: (*a*) a curved sandwich beam subjected to a shear force and moment such as might occur in a one-piece structure, and (*b*) a solid laminate subjected to a temperature change demonstrating the deformation caused by differential thermal expansion spring-in.

Curved Sandwich Beam

A thick curved sandwich beam with dimensions and materials typical of tight corners in an aerospace structure was selected to demonstrate the deformation and stresses predicted by the model. The curved beam uses eight-ply $(0/+45/-45/90)_s$ P75/934 faceskins on 0.750 in. (19.1 mm) aluminum honeycomb core wrapped around an inner radius of 0.563 in. (14.2 mm). The skins are thus relatively thin, the overall beam thick with respect to the curvature, and the materials typical aerospace grade. The unidirectional material properties [*6*] used in the calculations are listed in Table 1. The materials properties were rotated into properties appropriate for each ply orientation by a standard laminate code. A unit shear load of 1 lbf/in. of beam width was assumed to act at a distance of 2.33 in. (59.2 mm) from the end of the beam, creating a shear load and moment at $\theta = 0$ as shown in the model (see Fig. 1). A tensile load is defined as one that tends to open the curved beam, whereas a compressive load tends to close the beam. The predicted deformed shape of the curved laminated beam under tensile loading is shown in Fig. 2.

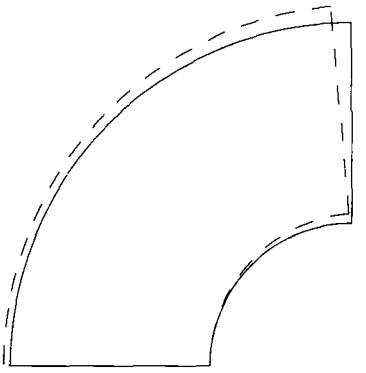


FIG. 2—*Deformed shape of a curved laminated sandwich beam under opening mode.*

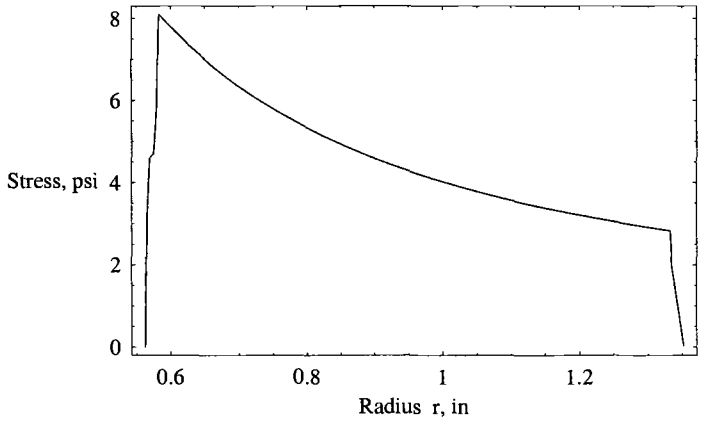


FIG. 3—*Radial stress per unit applied load at* $\theta = \pi/2$.

The radial stresses developed in the curved beam are shown in Fig. 3 as a function of distance through the thickness of the beam at an angular location of $\theta = \pi/2$. Notice that the stresses on the inner face skin plies are tensile. Flatwise tensile results for flat P75/934 honeycomb sandwiches range from 200 to 400 psi (1.38 to 2.76 kPa), suggesting that a load of 25 to 50 lbf/in. (4.4 to 8.8 kN/m) as applied in the example might be sufficient to fail the curved beam by delaminating the face skins from the core under opening mode.

The tangential stresses for the same case are shown in Fig. 4. The stresses are plotted versus the angle θ for the inner face skin ply. Note that the tangential stress reaches a maximum at $\theta = \pi/2$. The tangential stresses far exceed the magnitude of the radial stresses. However, the strength of the face skin P75 is also much greater in the tangential direction. The same 25 to 50 lbf/in. load would cause an 18 to 36 ksi (124 to 248 kPa) tensile stress in the inner face skin, insufficient to fail P75 which has a tensile strength of 148 ksi (1020 kPa).

If the sign of the applied shear load is reversed so that the beam is now in compression (tending to close), the signs of the stresses are reversed. In this case, a compressive radial stress does not con-

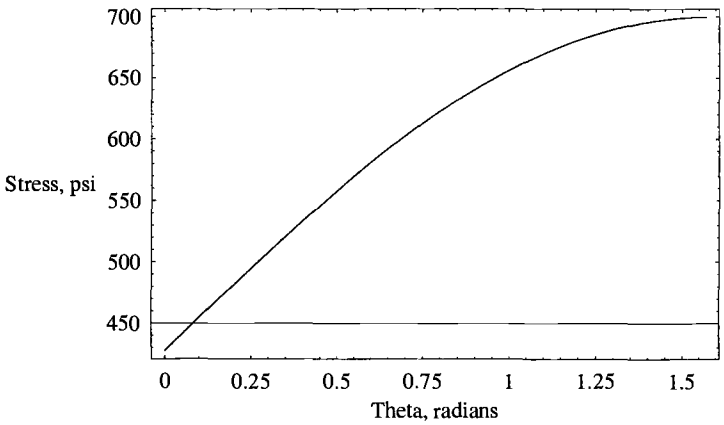


FIG. 4—*Tangential stress per unit applied load versus theta.*

TABLE 2—*Material properties for thermal example.*

Property	T300/934
Tangential modulus, E_θ	9.1 10^6 psi (62.7 MPa)
Radial modulus, E_r	1.0 10^6 psi (6.9 MPa)
Poisson's ratio, $\nu_{r\theta}$	0.30
Shear modulus, $G_{r\theta}$	0.48 10^6 psi (3.31 MPa)
Tangential thermal expansion, α_θ	$-0.40\ 10^{-6}$ in./in.-°F ($-0.72\ 10^{-6}$ m/m-K)
Radial thermal expansion, α_r	$21.0\ 10^{-6}$ in./in.-°F ($37.8\ 10^{-6}$ m/m-K)

tribute to the failure mode. Instead, the tangential stress dominates the failure of the P75 material, which is much weaker in compression. For example, the 59 ksi (407 kPa) compression strength of P75 corresponds to a predicted applied load at failure (closing) of 83 lbf/in. (14 N/m). Thus, the mode of failure depends on the direction of the applied load.

Differential Thermal Expansion

A relatively thin, eight-ply curved laminate formed around a tight 0.125 in. (3.18 mm) radius such as would be found in a hat section or bracket was selected to demonstrate the deformation in a beam due to differential thermal contraction between the radial and tangential directions. The curved beam consists of $(0)_8$ T300/934 woven fabric graphite/epoxy. The overall beam is thick with respect to the curvature. The unidirectional material properties [*6*] used in the calculations are listed in Table 2.

The reference temperature was chosen as 350°F (177°C), a typical cure temperature, and the current temperature 70°F (21°C). The predicted shape of the curved laminated beam is shown in Fig. 5. The displacements have been magnified by a factor of 10. The relatively large thermal contraction in the radial direction compared with a small expansion in the tangential direction causes the laminate to close, or spring-in, compared to the reference state. Note that in this particular case the laminate is essentially a homogeneous orthotropic material (no angles to the lay-up). Thus, no thermal stresses are developed and the resulting deformation is due solely to differential contraction. More generally, thermal stresses will also arise due to stiffness and expansion differences between plies.

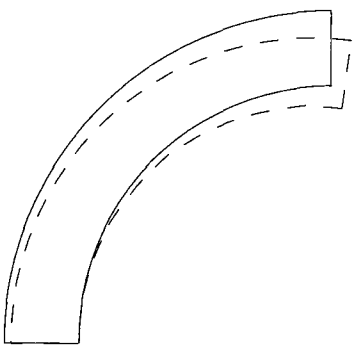


FIG. 5—*Spring-in of a hat section corner.*

Summary

Closed-form 2-D solutions for the displacements, strains, and stresses in curved, laminated orthotropic beams subjected to shear loads, moments, and temperature changes were developed. The solutions are exact and therefore equally applicable to sandwich structures as well as ordinary laminates. The displacement solutions include rigid-body terms that are used to predict the contribution to spring-in of curved composite laminates due to differential thermal expansion in the radial and circumferential directions.

Sample calculations for a graphite/epoxy face skinned aluminum honeycomb curved beam demonstrated the development of radial stresses in the laminate. Classical laminated plate theory assumes these stresses to be zero. For shear loads and moments tending to open the beam, the radial stresses are tensile. Although small with respect to the in-plane tangential stresses, the radial stresses may be sufficient to cause delamination. Deformation of a curved laminate due to differential thermal contraction from a reference temperature was demonstrated in a sample problem.

The computational power required to solve these problems is only that necessary to solve a linear system of equations once, where the number of equations is equal to three times the number of plies. Even a very thick laminate problem can easily be solved on a personal computer in seconds.

References

[1] Lekhnitskii, S. G., *Theory of Elasticity of an Anisotropic Body*, Mir Publishers, Moscow, 1981.
[2] Ko, W. L. and Jackson, R. H., "Multilayer Theory for Delamination Analysis of a Composite Curved Bar Subjected to End Forces and End Moments," NASA Technical Memorandum 4139, Sept. 1989.
[3] Timoshenko, S. P. and Goodier, J. N., *Theory of Elasticity*, McGraw-Hill Book Company, New York, 1970.
[4] Fung, Y. C., *Foundations of Solid Mechanics*, Prentice-Hall, Englewood Cliffs, NJ, 1965.
[5] Wolfram, S., *Mathematica, A System for Doing Mathematics by Computer*, Addison-Wesley Publishing Co., Inc., Reading, MA, 1988.
[6] Space Systems/Loral internal data.

Sailendra N. Chatterjee[1]

Damage, Stiffness Loss, and Failure in Composite Structures

REFERENCE: Chatterjee, S. N., **"Damage, Stiffness Loss, and Failure in Composite Structures,"** *Composite Structures: Theory and Practice, ASTM STP 1383,* P. Grant and C. Q. Rousseau, Eds., American Society for Testing and Materials, West Conshohocken, PA, 2000, pp. 452–469.

ABSTRACT: Laminated plate theory is widely used for elastic analysis and design of fiber composite structures. Use of the results for prediction of failure and for design of structures to avoid failure (with a margin of safety) is a more complex issue. Use of failure theories in terms of stresses or strains at a point can sometimes yield a very conservative estimate of the failure load. It is recognized that such theories, in conjunction with laminate analysis, yield an estimate of the point of damage onset (often in the matrix), but final failure usually requires progressive fiber breaks and significant load redistribution. Methods have been suggested to perform stress analyses beyond damage initiation, but they are very rarely used in practice (as compared to the use of plasticity theory for metal structures). Many progressive damage models make use of ad hoc assumptions for stiffness knockdowns. The objective of this paper is to demonstrate that damage mechanics (using a single or multiple damage parameters) can yield a set of constitutive laws, which are based on sound physical principles. It is shown that the dissipated energy density in a ply can be used as a damage parameter. Two structural problems are considered for demonstration. Results for the case of a pressure vessel are compared with those from netting analysis, a valid and widely accepted method for such designs. The second case is the problem of the "hole size effect," which is currently handled in practice by the use of semi-empirical methods and a series of tests.

KEYWORDS: damage mechanics, stiffness loss, nonlinear constitutive law, multiaxial straining, strain energy dissipation, stress analysis, failure

Experimental observations on composite laminates indicate various forms of damage in brittle matrix composites; namely, (i) ply cracks, (ii) delaminations, (iii) other matrix cracks, (iv) fiber breaks, (v) fiber/matrix debonds, and (vi) fiber microbuckling or kinking under compression, etc. In many cases, effects of these damages are obvious in the highly nonlinear load deformation or stress-strain responses. Various studies are reported in literature, which have attempted to obtain "in-situ" ply constitutive laws with appropriately chosen internal state variables (damage parameters, such as ply and matrix crack densities or spacings [*1–5*], delamination and debond densities [*4*], local fiber rotations due to kinking [*6*], etc.). Various material parameters, such as critical energy release rates for ply and matrix cracking as well as delamination growth are needed for such models. Some of these parameters are difficult to obtain directly from tests and are often calculated to fit specimen responses dominated by a particular form of damage.

Composite design engineers are aware that some types of laminate characterization specimens do show considerable damage growth and highly nonlinear responses under certain loading conditions. A $(\pm 45)_{ns}$ tension coupon used for characterizing the nonlinear shear response of the unidirectional material is an example. On the other hand, tension or compression response of high modulus unidirectional or cross ply coupons loaded in fiber dominated directions may not show any appreciable nonlinear response. Composite laminates used in aircraft structures are often fiber dominated, and for this reason aircraft engineers commonly use elastic theory for design purposes with due considera-

[1] Staff scientist, Materials Sciences Corporation, Fort Washington, PA 19034.

Copyright© 2001by ASTM International www.astm.org

tion to the nonlinear unidirectional response under shear and transverse tension. It may be noted that damages do occur in laminates under tension and/or compression loading in the fiber-dominated directions, but they are masked by the high-modulus fibers even up to the point of initial fiber failures, which quickly become catastrophic in coupon specimens. Near points of stress concentrations, such as holes, notches, or cutouts, a significant amount of load redistribution is expected before failure. Therefore, an inelastic stress analysis that uses nonlinear ply constitutive laws would yield a more realistic representation of local load redistributions between the plies and from damaged areas to neighboring undamaged regions in a structure.

Constitutive Law

Constitutive laws for modeling microcracking in a continuum are discussed in Ref 7. Such models have been found to be very successful representing the behavior of brittle materials and make use of a phenomenological approach and the internal variables ω^{α}, which represent damage variable α (such as average crack densities). One can write the formulation given in Ref 7 in the following form where $\underline{\sigma}$ and $\underline{\varepsilon}$ are vectors:

$$\underline{\sigma} \cdot d\underline{\varepsilon} - \rho d\psi = d\phi \geq 0; \text{ Clausius-Duhem inequality (see Fig. 1)} \tag{1a}$$

$$\rho = \text{mass density} \tag{1b}$$

$$\psi = \text{Helmholtz free energy} \tag{1c}$$

$$\sigma_i = \rho \frac{\partial \psi}{\partial \varepsilon_i} \tag{1d}$$

$$\underline{\sigma} = \text{stress vector} \tag{1e}$$

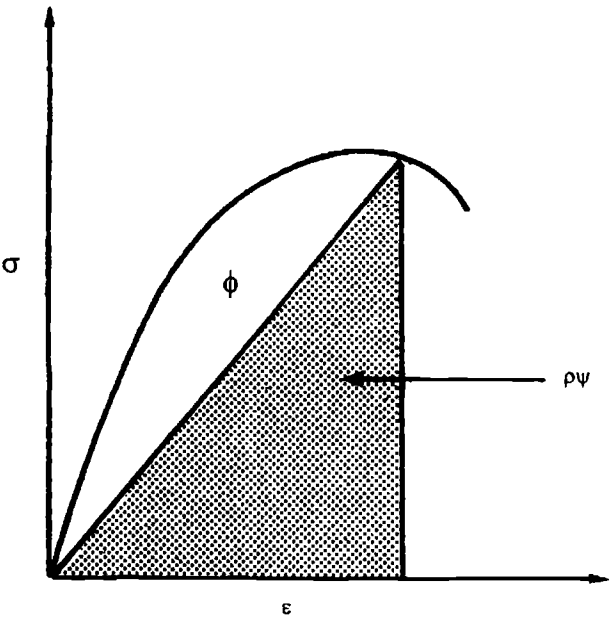


FIG. 1—*Helmholtz free energy $\rho\psi$ and dissipated energy ϕ.*

$$\underline{\varepsilon} = \text{strain vector} \tag{1f}$$

$$\phi = \text{dissipated energy density} \tag{1g}$$

$$d\phi = \sum_{\alpha} R^{\alpha} d\omega^{\alpha} \geq 0 \tag{1h}$$

$$R^{\alpha} = \text{conjugate thermodynamic force, an energy release rate} \tag{1i}$$

$$= -\rho \frac{\partial \psi}{\partial \omega^{\alpha}} = \frac{\partial \phi}{\partial \omega^{\alpha}}$$

In the strain energy dissipation (SED) formulation employed in Refs *8–11*, there is one damage variable—the dissipated energy density ϕ $(=\omega^1)$—and for this case one may choose the following form for the Helmholtz free energy

$$\rho\psi = \frac{1}{2} C_{ij}\varepsilon_i\varepsilon_j - \int_0^{\phi_c} R(\mathrm{E}_i, \phi) d\phi \tag{2}$$

where ϕ_c is the current value of ϕ and C_{ij} are the elastic stiffnesses. It follows from the expression for $R^1 = R$ in last part of Eq 1 that for damage growth to occur

$$R(\varepsilon_i, \phi) = 1 \tag{3}$$

and no damage growth is predicted when $R(\varepsilon_i, \phi) < 1$. In Refs *8–11*, it is also assumed that the dissipated energy is a function of the strain variables (independent of the loading path) and complete unloading (to zero stress level) will occur in a linear elastic manner when strains are reduced to zero. R may be chosen in various forms to match test data for different strain paths [*8–11*]. A simple form which can simulate the strain softening behavior for some selected paths including the softening under axial straining [*12*] is given below:

$$R = \frac{1}{2}[\varepsilon_1^2(a_{11}(\phi) + b_1(\phi)\,\mathrm{sgn}\,\varepsilon_1) + \varepsilon_2^2(a_{22}(\phi) + b_2(\phi)\,\mathrm{sgn}\,\varepsilon_2) + \varepsilon_3^2 a_{33}(\phi) + 2a_{12}(\phi)\varepsilon_1\varepsilon_2] \tag{4}$$

where $\varepsilon_1 = \varepsilon_{11}$, $\varepsilon_2 = \varepsilon_{22}$, $\varepsilon_3 = \gamma_{12}$ and sgn x is the sign of x (positive or negative).

Equations 3 and 4 yield the damage surfaces which are similar to the Tsai-Wu type polynomial failure criterion, but they are in terms of strains and the coefficients a_{ij} and b_i are functions of ϕ. The linear terms used in Tsai-Wu type criterion are not used here since they give a strong coupling between shear stress σ_3 and the extensional strains ε_1 and ε_2 in the resulting stress-strain relation discussed later. More complicated forms of R may be chosen [*13*] if desired, but the representation, Eq 4, is quite adequate to fit available test data and for the analog experiments described later. It may be noted that $a_{33}(\phi)$ can be obtained if the nonlinear shear stress-strain response is known and ϕ can be calculated for various values of shear strain ε_3. Similarly, if unidirectional strain-stress responses in fiber (1) and transverse (2) directions are known (for example, σ_1 is known for various ε_1, when $\varepsilon_2 = 0$), then $a_{11}(\phi)$, $b_1(\phi)$ and $a_{22}(\phi)$, $b_2(\phi)$ can be evaluated as functions of ϕ. Such an approach was adopted for obtaining initial estimates of these coefficients for AS-3501, which were later adjusted to fit available test data. Using the expression in Eq 1 for evaluation of σ_i as a derivative of $\rho\psi$ obtained by substituting Eq 4 in Eq 2, one obtains

$$\sigma_1 = (C_{11} - A_{11}^*)\varepsilon_1 + (C_{12} - A_{12})\varepsilon_2 \tag{5}$$

$$\sigma_2 = (C_{12} - A_{12})\varepsilon_1 + (C_{22} - A_{22}^*)\varepsilon_2 \tag{6}$$

$$\sigma_3 = (C_{33} - A_{33})\varepsilon_3 \tag{7}$$

$$A_{ii}^{*} = A_{ii} - B_i \operatorname{sgn}(\varepsilon_1);\ i = 1,2 \text{ (no sum)} \tag{8}$$

$$[A_{ij}(\phi), B_i(\phi)] = \int_0^{\phi} [a_{ij}(\phi), b_i(\phi)]d\phi \tag{9}$$

It is clear that A_{ij} and B_i define appropriate stiffness losses and a_{ij}, b_i are their derivatives with respect to ϕ. a_{ij}, b_i are needed for evaluation of ϕ for any loading path. The constitutive relations described above and the iterative procedures required for evaluation of current value of dissipated energy (using the condition $R = 1$) were incorporated in a subroutine, which is used with a finite-element code [*14*].

It is obvious that complete stiffness loss (describing full loss in load carrying capacity) will occur when the stiffness losses will equal the initial stiffnesses. Thus, for large values of ϕ, they should approach the corresponding initial elastic stiffnesses. Since the stiffnesses in directions other than the fiber direction (1) are much lower, the dissipated energy required for complete stiffness loss in those directions will be much lower than that for direction 1. Further, under transverse tension, stiffness loss is expected to occur at a much faster rate than that under transverse compression. This discussion should be useful in understanding the reasons for the choices of the coefficients $a_{ij}(\phi)$ and $b_i(\phi)$ described in the next section.

Damage Surfaces

These surfaces were estimated for a carbon epoxy composite (AS/3501) with elastic moduli and Poisson's ratio given in Table 1, which also gives the coefficients a_{ij} and b_i for various values of ϕ. As mentioned earlier, iterative procedures were used for determining the dissipated energy ϕ for increasing strains. The coefficients a_{33}, a_{22}, and b_2 were chosen so as to yield reasonable fit to average stress-strain response of $(\pm 45)_{ns}$, $(\pm 50)_s$, and $(\pm 30)_s$ tension coupons [*15–17*]. Analysis of results with chosen properties (Table 1) are compared in Figs. 2 and 3. The agreement is reasonable for low

TABLE 1—*Properties for a carbon/epoxy (AS/3501) material.* $E_1 = 130$ *GPa (18.85 Msi),* $E_2 = 10.5$ *GPa (1.52 Msi),* $\nu_{12} = 0.35$, $G_{12} = 6$ *GPa (0.87 Msi), Values of* a_{ii}, b_i.

ϕ, MPa (ksi)	a_{11}	a_{22}	a_{33}	a_{12}	b_1	b_2
0	0.5556E5	0.9028E5	0.4455E5	0.4863E5	0	0.3472E5
0.017 (0.0024)	0.2000E5	0.3602E5	0.2000E5	0.1339E5	0	0.1602E5
0.077 (0.011)	0.1285E5	0.1528E5	0.8889E4	0.4049E4	0.1545E3	0.8355E4
0.18 (0.026)	0.1051E5	0.8061E4	0.5000E4	0.2383E4	0.2436E3	0.3774E4
0.33 (0.047)	0.9969E4	0.5447E4	0.3200E4	0.1846E4	0.4569E3	0.2174E4
0.67 (0.097)	0.9339E4	0.2748E4	0.1633E4	0.1333E4	0.4143E3	0.2110E3
1.07 (0.155)	0.8749E4	0.1659E4	0.9877E3	0.886533	0.3815E3	−0.4089E3
2.07 (0.30)	0.7620E4	0.7620E3	0.5203E3	0.3485E3	0.2913E3	−0.5665E3
4.48 (0.65)	0.6001E4	0.3004E3	0.2148E3	0	0.3117E3	−0.3004E3
6.55 (0.95)	0.5009E4	0.1566E3	0.1533E2	0	0.2503E3	−0.1566E3
13.8 (2.0)	0.2871E4	0	0	0	0.6524E2	0
19.3 (2.8)	0.2036E4	0	0	0	0.4545E2	0
25.5 (3.7)	0.1477E4	0	0	0	0.2408E2	0
37.9 (5.5)	0.7500E3	0	0	0	0	0
51.7 (7.5)	0.3500E3	0	0	0	−0.5000E2	0
86.2 (12.5)	0.8355E2	0	0	0	−0.6045E2	0
137.9 (20.0)	0	0	0	0	0	0

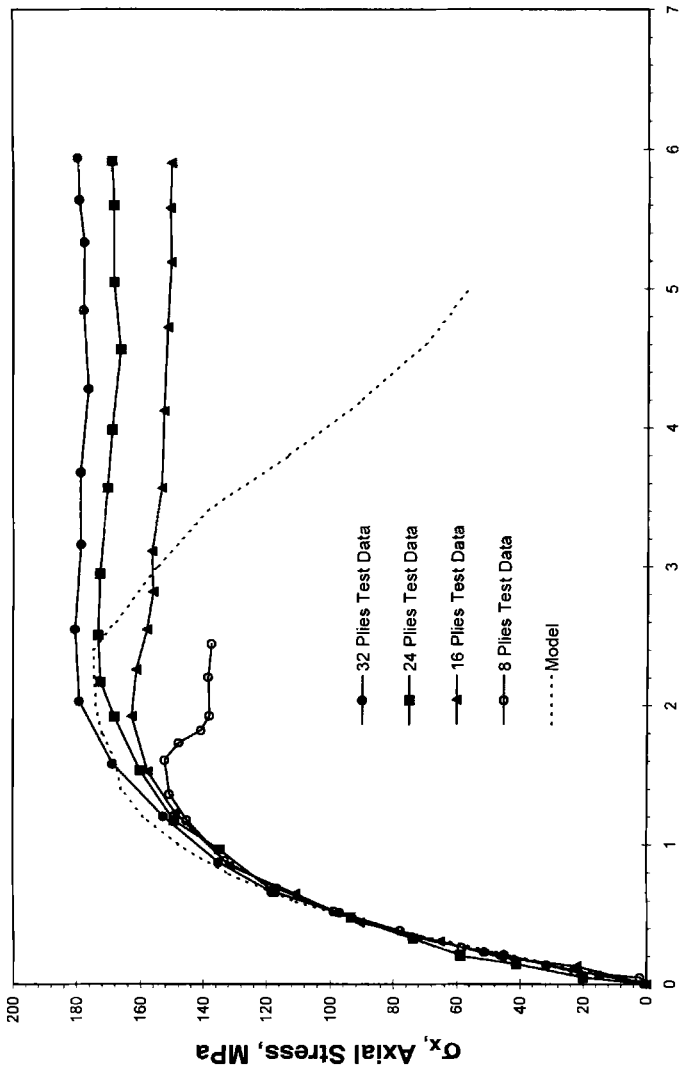


FIG. 2—*Axial stress vs. axial strain for* $(\pm 45)_{ns}$.

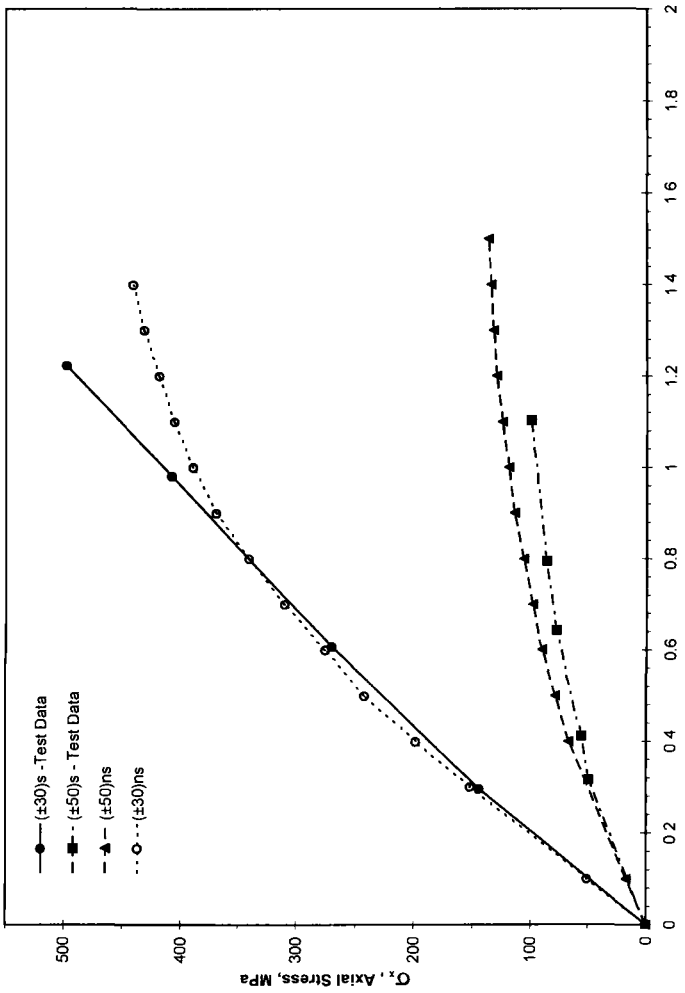


FIG. 3—*Axial stress vs. axial strain for* $(\pm 50)_{ns}$ *and* $(\pm 30)_{ns}$ *tension.*

axial strain levels in $(\pm 45)_{ns}$ coupons (Fig. 2) and up to experimental failure strains for $(\pm 50)_s$ specimens (Fig. 3). At high axial strain levels (above 2%) in $(\pm 45)_{ns}$ coupons, the values of assumed coefficients yield stresses which are lower than test data (Fig. 2) for thicker specimens ($\geq$ 16 plies). Geometry changes (scissoring) may occur after gradual development delaminations, which may cause some stiffening in thick specimens. (See Ref *15* for experimental evidence of such stiffening.) Thin specimens (8 plies) possibly fail quickly due to complete delamination before such stiffening can occur. Most likely scissoring also causes the differences in observed and predicted responses of $(\pm 30)_s$ tension coupons (Fig. 3). Detailed response of $(\pm\theta)_{ns}$ compression coupons of AS/3501 material are not known to the authors. Responses of $(\pm 60)_{ns}$, $(\pm 30)_{ns}$, and $(\pm 20)_{ns}$ coupons reported in Ref *18* for AS/3502 yield reasonable correlation with calculations.

The coefficients a_{12} were chosen so as to simulate the changes in transverse strain (Poisson strain) in cross ply $(0/90)_{ns}$ laminates loaded in axial tension reported in literature [*16,19*]. Load reduction and gradual softening in the fiber direction (as assumed in the model) can only be observed in very carefully conducted displacement controlled tests. It should be emphasized that the actual softening behavior is difficult to quantify directly. Attempts have been made for their indirect quantification through analyses and correlation of observed response of notched fiber dominated layups [*12*]. However, the analytical model used in [*12*] for that purpose is different from the one used here and, therefore, it is not possible to compare the softening pattern used in Ref *12* with the one employed here. Figure 4 shows the axial stress in the 0° layer in a $(0/\pm 45/90)_{ns}$ laminate subjected to axial strain (average transverse stress = 0) up to a strain level of 6%. This gives an idea of the softening pattern under axial straining. The dissipated energy in the 0° layer at 6% axial strain level is 49 MPa (7.1 ksi). Such high strain levels and energy loss are indicative of lots of progressive fiber breaks and fiber pull out before final separation. Therefore, it is necessary to perform calculations with different assumed

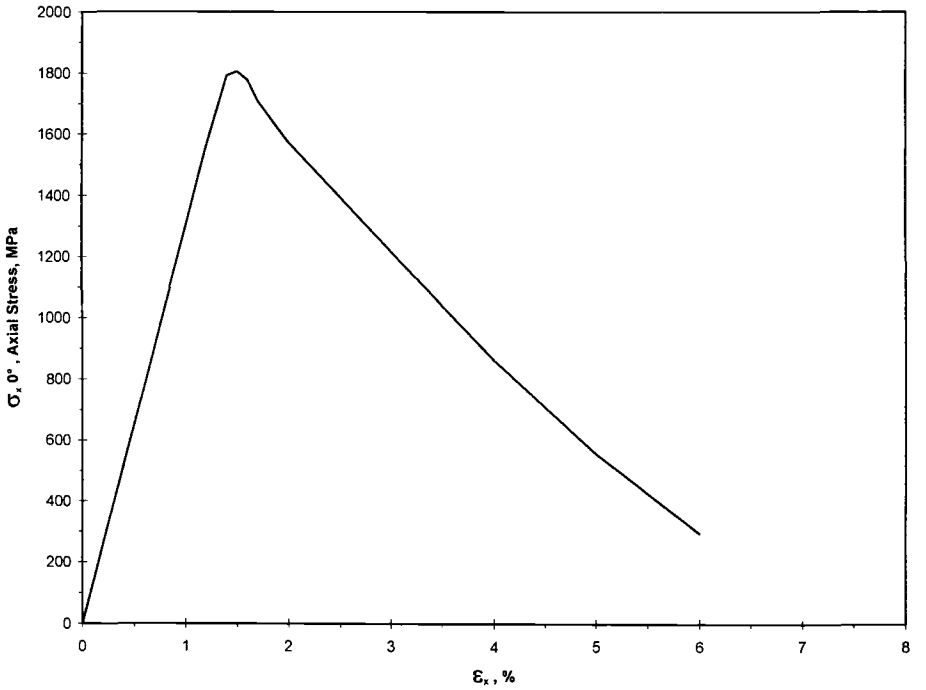


FIG. 4—*0° fiber direction stress vs. axial strain for* $(0/\pm 45/90)_{ns}$ *tension.*

softening behavior in terms of the assumed coefficients for high values of ϕ (see Table 1) to match data (notch opening displacements, notch tip strains versus load, failure load) from notched coupon tests with analysis results. Values of coefficients used here yield results which match notched quasi-isotropic coupon responses.

It should be noted that determination of damage surfaces as functions of ϕ by matching analysis results to test data for various laminate specimens is a complicated process, since the calculated fields depend on these surfaces. Use of elastic strain fields and an algorithm for minimizing errors suggested in Ref *8* will be adequate for small values of ϕ, i.e., when the actual fields are close to the elastic ones. In this study, we made use of several trials, starting with the values of the coefficients obtained from average stress-strain response of a ply for various uniaxial strain paths, which were estimated from test data. As discussed earlier, response of single rectangular laminate ($(\pm\theta)_s$ and $(0/90)_s$) elements were predicted and the values of a_{33}, a_{22}, b_2, and a_{12} were adjusted to obtain fits to test data. The coefficients a_{11} were then determined to match the response of one quasi-isotropic laminate coupon with a hole. Detailed finite-element analyses and several trials were needed for this purpose, since large stiffness losses occur and very high values of ϕ are attained near the edge of the hole. Performances of $(\pm\theta)_s$ and $(0/90)_s$ coupons were then predicted again, but no significant differences were observed. An automated procedure and an algorithm are under development.

Analysis of Structural Elements

To examine the usefulness of the concept, two types of elements were analyzed as described below.

1. *Elements showing some nonlinear response before failure*—Most possibly the simplest structural element in this category is a cylindrical pressure vessel (with closed ends) of $(\pm\theta)_{ns}$ construction commonly manufactured using the filament winding technique.
2. *Elements where the effects of nonlinearities are masked before peak loads are reached*—Possibly the most common element where a linear theory is not useful is a tension or compression coupon with a stress raiser, a notch, a hole, or a crack. In the composites industry, the load-carrying capacity of such an element is often predicted using the Whitney-Nuismer criterion [*20*], which was motivated by what is known as the hole-size effect. Parameters required in the model have to be determined by fitting the model predictions to test data for a specific laminate with various hole sizes. A review of various other criteria suggested for the problem can be found in Ref *21*. Tension coupons with two hole sizes were analyzed in this study to examine the usefulness of the SED concept in this problem. Most possibly this is a very severe test for the concept.

Results for the two types of elements are discussed next.

$(\pm\theta)_{ns}$ Cylindrical Pressure Vessel

In the cylindrical region of a closed end pressure vessel, the state of stress is known, i.e., the axial tensile stress σ_A is half of the hoop tension σ_H. It is a common design practice to optimize the fiber orientation θ using the concept of netting analysis, which assumes that at the point of failure the layers carry stresses σ_1 only in the fiber direction (load-carrying capacities in shear and transverse tension are destroyed), which yields

$$\sigma_H = \sigma_1 \cos^2 \theta \tag{10}$$

$$\sigma_A = \sigma_1 \sin^2 \theta \tag{11}$$

Since $\sigma_A = \sigma_H/2$, one obtains the optimum fiber angle

$$\tan \theta = \sqrt{2} \tag{12}$$

$$\theta = 54.7356° \tag{13}$$

For simplicity, a single element model was analyzed for various imposed σ_H and σ_A ($= \sigma_H/2$) till peak stresses were reached, which occurred at

$$\sigma_H = 1121 \text{ MPa } (162.6 \text{ ksi}) \tag{14}$$

$$\sigma_A = 560.5 \text{ MPa } (81.3 \text{ ksi}) \tag{15}$$

Beyond this level the stresses could not be increased because softening started in the fiber direction.

The stress in the fiber direction σ_1 and the dissipated energy density ϕ (DED) for various values of σ_H are plotted in Fig. 5. The stress σ_1 for high values of σ_H approaches the netting analysis solution. ϕ is found to increase rapidly for high values of σ_H reaching a value of 1.94 MPa (281 lb/in.^{2}), which implies that damages so far possibly do not involve fiber breakage, but some softening in the axial directions. Values of hoop strain ε_H and axial strain ε_A are plotted against σ_H in Fig. 6. The results show noticeable nonlinear responses for high values of σ_H. Use of netting analysis yields

$$\varepsilon_H = \varepsilon_A = \varepsilon_1 = \varepsilon_2 = 3\sigma_H/2E_1 \tag{16}$$

$$\gamma_{AH} = \varepsilon_3 (= \gamma_{12}) = 0 \tag{17}$$

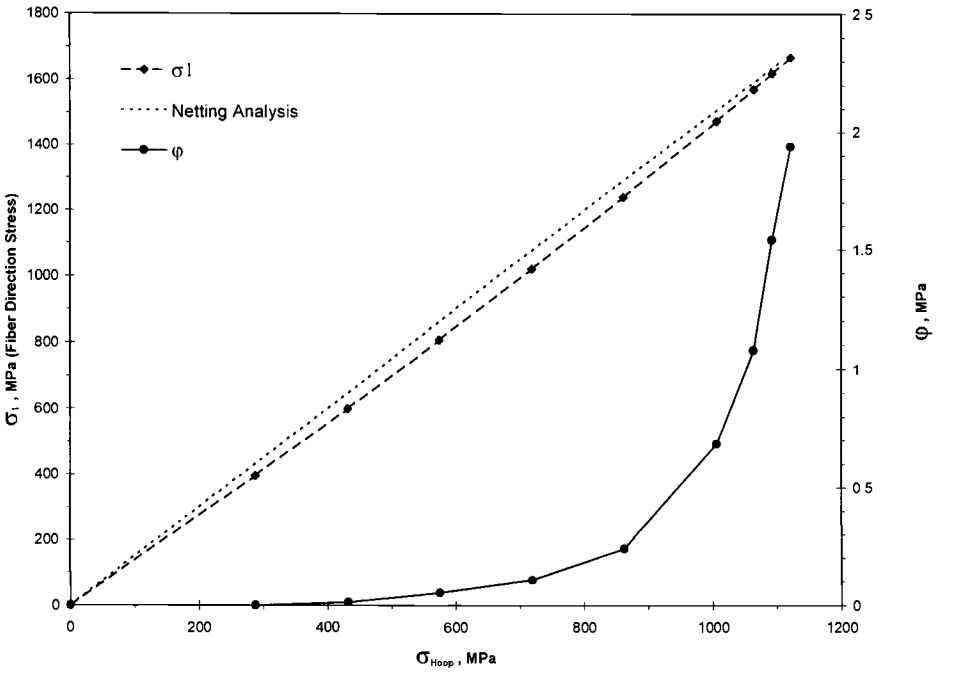


FIG. 5—*Fiber direction stress σ_1 and DED φ in each layer of a $(\pm 54.74°)_{ns}$ pressure vessel.*

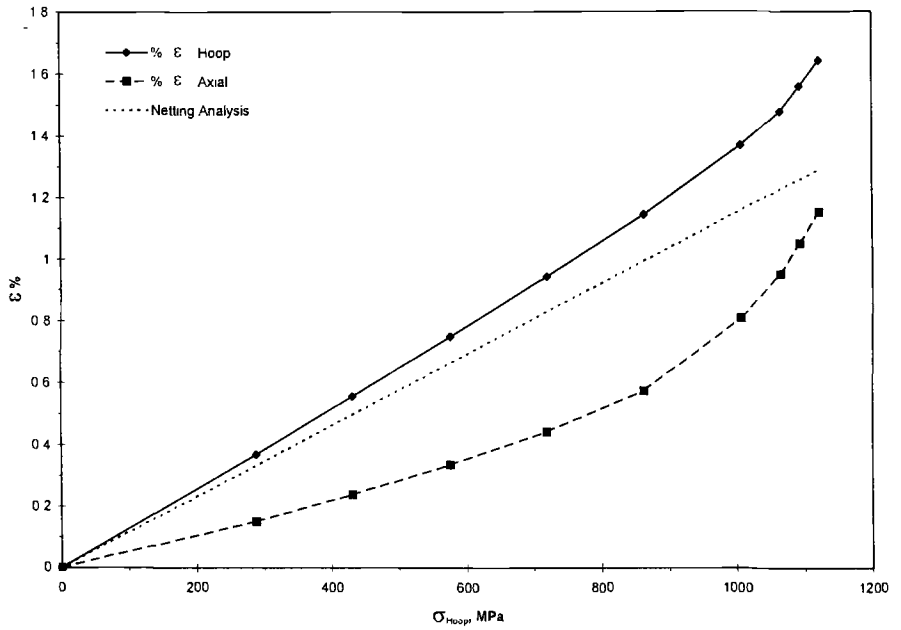


FIG. 6—*Hoop and axial strains vs. hoop tensile stress in a* $(\pm 54.74°)_{ns}$ *pressure vessel.*

The result is different from the calculated values (from nonlinear analysis) of ε_A and ε_H, which are quite different from each other (see Fig. 6). The layer stresses and strains at peak loads are as given below.

$$\sigma_1 = 1669 \text{ MPa (242 ksi)} \qquad \varepsilon_1 = 1.48\% \tag{18}$$

$$\sigma_2 = 13.2 \text{ MPa (1.92 ksi)} \qquad \varepsilon_2 = 1.32\% \tag{19}$$

$$\sigma_3 = \tau_{12} = \pm 4.69 \text{ MPa (0.68 ksi)} \qquad \varepsilon_3 = \gamma_{12} = \pm 0.46\% \tag{20}$$

For obvious reasons, the stresses are related to the strains by the constitutive laws (Eqs 5–9) for ϕ = 1.94 MPa. The fiber direction stress starts dropping rapidly beyond this value of ϕ and for this reason the pressure (or the stresses σ_H and $\sigma_A = \sigma_H/2$) cannot be increased any more.

Tension Coupons with Holes

Tension coupons 38.1 mm (1.5 in.) wide and 152.4 mm (6 in.) long were considered. Circular holes of diameter 6.35 mm ($^1/_4$ in.) and 3.18 mm ($^1/_8$ in.) at the center of the coupon (center of the hole is the origin $x = 0, y = 0$) were considered. Tensile load was applied by prescribing equal and opposite longitudinal displacements (u_x) at the two ends. The other displacement component u_y was assumed to be zero at these ends simulating clamping effects. The laminates were assumed to have a thickness of 1.016 mm (0.04 in.). Only a quarter of the coupon was analyzed because of symmetry about the planes $x = 0$ and $y = 0$. Finite-element meshes near the 6.35 mm ($^1/_4$ in.) hole are illustrated in

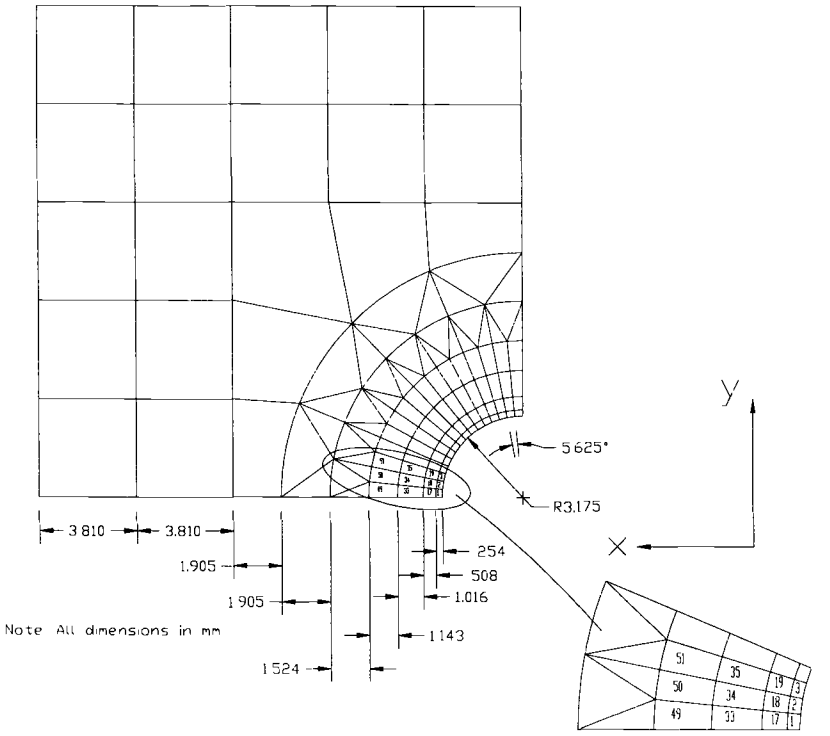


FIG. 7—*Finite-element mesh near a 6.35 mm diameter hole.*

Fig. 7. Two quasi-isotropic layups were analyzed, namely, $(0/\pm 45/90)_s$ and $(0/\pm 60)_s$. Loads were applied to a maximum value such that the dissipated energy density in a layer of the most critical element reached a value of 51.7 MPa (7500 lb/in.^{2}).

Total load deflection responses (Fig. 8) indicate that there are no appreciable nonlinearities even at the highest load level. However, the dissipated energy densities in various layers of some critical elements are of interest.

At maximum load for the $(0/\pm 45/90)_s$ layup with 6.35 mm ($^1/_4$ in.) hole, the DED (dissipated energy density) in the 0° layer in element 1 has a value of 51.7 MPa (7500 lb/in.^{2}) as shown in Fig. 9. In elements 17 and 33, the DED in 0° layers have not reached the maximum, but they are increasing at a fast rate. DED in the +45° and −45° layers of elements 1, 17, and 33 are also increasing rapidly (see, for example, Fig. 10), whereas DED in the 90° layers (not shown) have reached values of the order of 2.07 MPa (300 lb/in.^{2}), indicating nearly complete loss in transverse stiffness. The situation is analogous to a plane of separation developing through elements 1, 17, and 33, which are closest to the plane $x = 0$. DED in the elements above this set, 2, 18, and 34, on the other hand, do not show any increase with load (near the maximum load level) indicating the effect of separation below. It appears, therefore, that a catastrophic failure is expected very close to the load level reached. For all practical purposes, this level may be considered as the failure load. For the case of 3.18 mm ($^1/_8$ in.) hole (results not shown here), the situation is similar except for the fact that the elements 2, 18, and 34 show highest values of DED in 0°, 45°, and −45° layers and the values of DED in elements 1, 17, and 33 become fairly constant near the maximum load level. The strains ε_x in the most critical element for both hole diameters are of the order of 8%, which may be considered as rupture (separation in two parts).

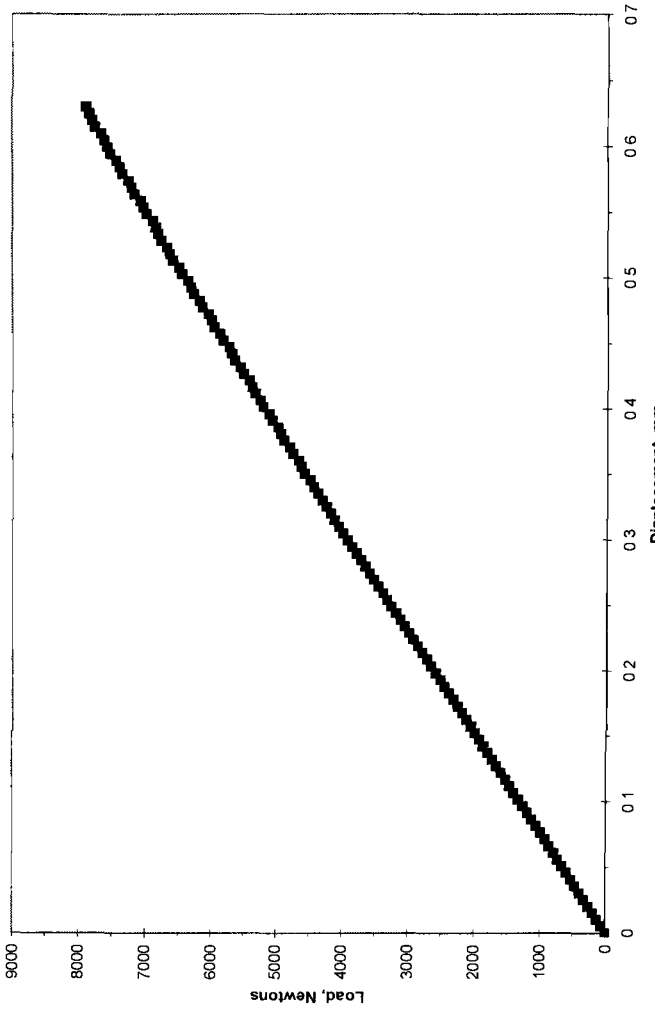


FIG. 8—*Load-displacement relation for* $[0/45/-45/90]_s$ *with a 6.35 mm hole.*

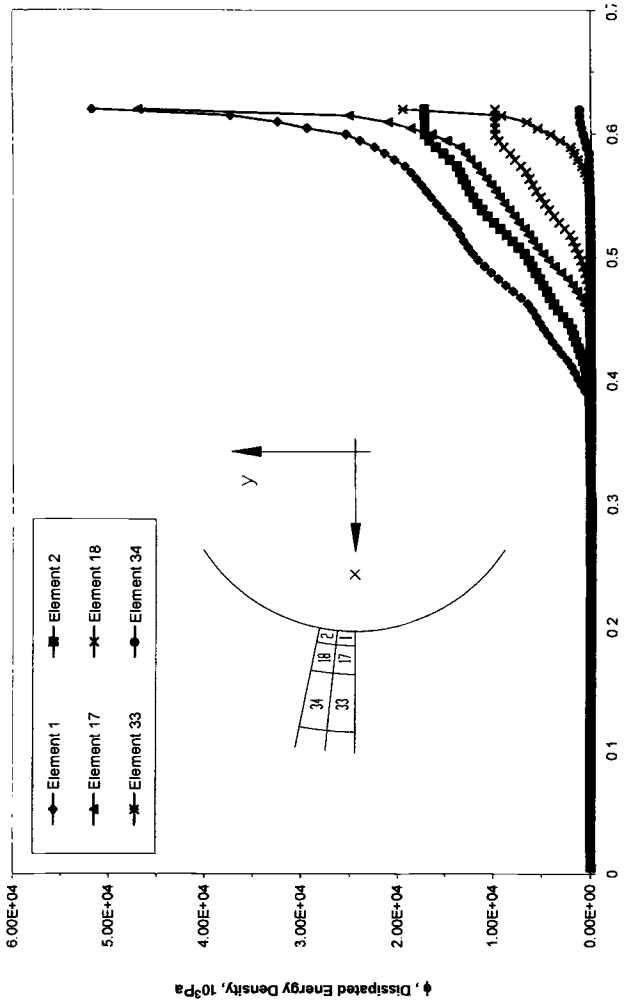


FIG. 9—*Dissipation energy vs. displacement for* $[0/45/-45/90]_s$ *with a 6.35 mm hole, 0-layer.*

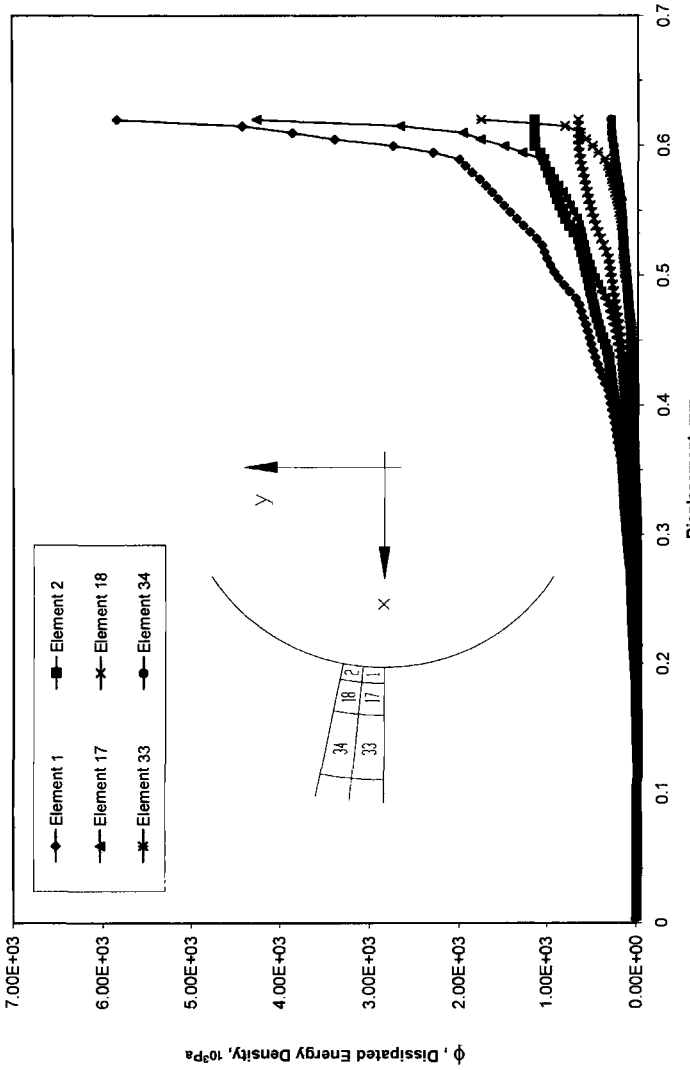


FIG. 10—*Dissipation energy vs. displacement [0/45/−45/90]$_s$ with a 6.35 mm hole, 45-layer.*

TABLE 2—*Failure stresses for coupons with and without holes.*

Laminate	Hole Diameter	Maximum Gross Stress, σ_N, MPa (ksi)	σ_N/σ_o
$(0/\pm 45/90)_s$	6.35 mm (1/4 in.)	400 (58.0)	0.592
	3.18 mm (1/8 in.)	455 (66.0)	0.673
	0	676 (98) (σ_o)*	1
$(0/\pm 60)_s$	6.35 mm (1/4 in.)	340 (49.3)	0.509
	3.18 mm (1/8 in.)	377 (54.7)	0.565
	0	667 (96.8) (σ_o)*	1

* From single element results.

For 6.35 mm (1/4 in.) as well as 3.18 mm (1/8 in.) hole in $(0/\pm 60)_s$ laminate (results not plotted here), the DED in the 0° layer of element 1 (as in the case $(0/\pm 45/90)_s$ with 6.35 mm (1/4 in.) hole) reaches a value of 51.7 MPa (7500 lb/in.^{2}) at maximum load and the 0° DED in element 17 is seen to increase rapidly. For +60 and −60 layers, the maximum values of DED are of the order of 4.14 MPa (600 lb/in.^{2}) indicating some softening in these layers too. The DED in various layers of elements 2 and 18 do not show any increase with load near the maximum load level indicating the effect of separation in a plane passing through elements 1 and 17.

Maximum average stresses based on the gross cross-sectional area for the cases studied are given in Table 2. The results (normalized gross section stresses, σ_N/σ_0) are also plotted in Fig. 11. σ_0, the unnotched strength, is taken as the peak stresses obtained from single element results. Also shown in Fig. 11 are the two bounds, one based on the assumptions of (i) no notch sensitivity (full ductility), and (ii) full notch sensitivity based on the stress concentration factor of 3.0. Usually test re-

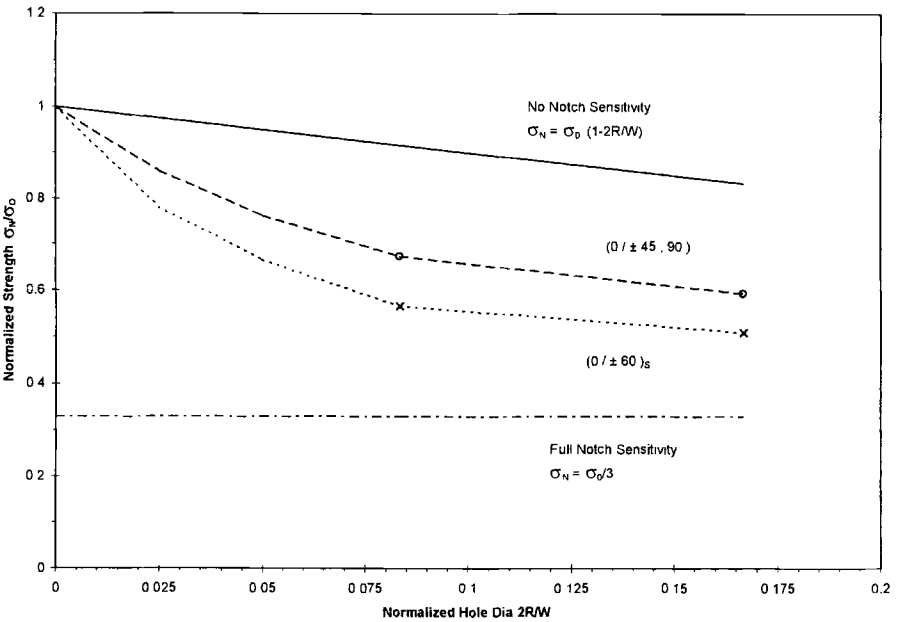


FIG. 11—*Calculated normalized gross section stress for open hole tension.*

sults for various hole sizes in such a figure are plotted after correcting the failure stress by the finite width correction factor based on elastic calculations. All results reported here are calculated for coupons of finite width. The results follow the trend of test data reported in literature. No systematic comparison with test results is reported here since the test data are also strongly influenced by development of delaminations (and hence the layup sequence) and through the thickness effects are not addressed here. However, we note that 38.1 mm (1.5 in.) wide AS4/3501-6 (bleed) $(0/+45/90/-45)_s$ laminates with 6.35 mm (¼ in.) holes typically yield [22] a mean gross section failure stress, σ_N of 427 MPa (62 ksi) with a standard deviation of 13.4 MPa (1.9 ksi) as compared to the calculated value of 400 MPa (58 ksi). The measured mean unnotched tensile strength σ_o [22] of the same laminate is 661 MPa (95.8 ksi) with a standard deviation of 39 MPa (5.7 ksi) as compared to 676 MPa (98 ksi) calculated here.

Discussions

The results for the filament wound pressure vessel problem indicates that the approach yields a good estimate of stiffness loss due to matrix mode damages (caused by transverse and shear strains). Also, the strain field at the point of failure is found to be quite different from those obtained from the elastic solution as well as netting analysis.

The second set of examples illustrates how the softening behavior in the axial direction influences the local field variables near a stress raiser and how rupture (separation after fiber breakage/pull out) can be simulated. Therefore, it is possible to estimate various knock down factors employed for design. One of the main assumptions in the approach (in its 2-D form) is that the laminate is not very thin and it contains dispersed layers arranged in a repeating pattern. Naturally it is not expected to simulate the three-dimensional effects which are generated due to sharp gradients of in-plane stresses. Improvements and modifications of the constitutive law and its application to 3-D problems are being explored in a recent work [*13*]. Use of finer mesh sizes near critical locations may alter the results to some extent. Effects of mesh sizes were not investigated for the open hole problem presented here. In a separate study [*23*] dealing with sharp cracks in a complex structural element, two mesh sizes of the order of 0.1 in. and 0.2 in. (the smaller value is about ten times the size used here) were utilized near the crack tips. The results indicate that the coarser mesh will yield a failure load which is about 15% lower than that for the finer mesh. Since the mesh size used here is much smaller ($\approx$0.01 in.), we believe that the results are quite accurate for the hole problem. It should be pointed out, however, that use of mesh sizes much smaller than ply thickness (0.13 mm $\approx$ 0.005 in.) may not be meaningful in modeling the effective response of a composite.

It has been demonstrated that material properties required to simulate matrix mode damages can be estimated from conventional test data (average stress versus measured strain) from a limited number of $(\pm\theta)_{ns}$ tension and compression coupons of moderate sizes. These tests are easy to conduct and yield a reliable measure of the properties, since the states of strain and stress are uniform almost over the entire specimen. An algorithm can be easily developed, if desired, to automate the process using the data for specimens with a finite number of values of θ to obtain the required damage surfaces. On the other hand, dissipated energy densities required to cause progressive fiber breaks and pull-outs are quite high. Most likely no specimen with uniform strain/stress state can be designed to characterize this softening behavior, which can occur under highly constrained conditions. One possible approach for characterization of such softening is to make use of center notched fiber-dominated layups such as $(0/90)_{ns}$, $(0/\pm45/90)_{ns}$, $(0/\pm60)_{ns}$ under tension and compression. These notches may be in the form of slits. It is known that a significant amount of nonlinearity is observed in the COD (crack opening/closing displacement) or NOD (notch opening/closing displacement) measured at the center of the notch. In contrast, there are no appreciable nonlinearities in the far-field load-displacementbehavior. The process can again be automated, if desired. However, the procedure will not be very simple and straightforward. It is not clear whether use of notched $(\pm\theta)_{ns}$ layups will yield the desired

information. Such specimens of small sizes have been used in NRL studies [*8–11*] using the in-plane loader. From data reported in Refs *8–11*, it is not clear whether the NRL database provides full information required for simulating rupture (significant softening in the fiber direction). If it does, they will obviously be useful. However, the reliability of such data generated from linear analysis may be questioned, unless their adequacies are demonstrated through additional tests and correlation studies.

Concluding Remarks

It has been shown that damage mechanics can provide a consistent set of constitutive laws for inelastic analyses of structural elements made of brittle laminated fiber composites. The SED approach for such analyses can easily be extended to consider the environmental effects if the formulation is made in terms of mechanical strains (instead of total strains) and if hygrothermal expansion properties are known. However, the damage surfaces must be treated as functions of temperature and moisture unless they are shown to be unaffected over the range of environment of interest. Available test data from $(\pm\theta)_{ns}$ coupons (± 45 data are often used for characterization of shear properties) at elevated temperatures show significant differences from room temperature data in the linear as well as nonlinear ranges. Open hole tension test data at elevated temperatures also show some differences from such data at room temperature. Therefore, although the approach can be used to address the issue of changing environment, appropriate material characterizations under such environments will be needed. It is hoped that such characterizations will be undertaken in the future and additional analytical studies will be performed with a variety of structural elements, so that the full potential of the approach can be explored and utilized by the composites industry.

Acknowledgment

The work was sponsored by Naval Air Systems Command, Contract No. N00019-96-C-2028.

References

[*1*] Chatterjee, S. N., Wung, E. C. J., and Yen, C. F., "Modeling Ply Crack Growth in Laminates Under Combined Stress-States," *ASTM STP 1156*, 1993, pp. 195–217.

[*2*] Hashin, Z., "Analysis of Cracked Laminates, A Variational Approach," *Mechanics of Materials*, Vol. 4, 1985, p. 121.

[*3*] Nairn, J. A., "The Strain Energy Release Rate of Composite Microcracking: A Variational Approach," *Journal of Composite Materials*, Vol. 23, 1989, p. 1009.

[*4*] Chatterjee, S. N., "Damage Growth Modeling in Ceramic Matrix Composites," MSC TFR 3402/LD02, for Pratt & Whitney NASA EPM Program, April 1994.

[*5*] Allen, D. H., Harris, C. E., and Graves, S. E., "A Thermo-Mechanical Constitutive Theory for Elastic Composites with Distributed Damage," *International Journal of Solids and Structures, Parts I and II*, Vol. 23, 1987, p. 1301.

[*6*] Chatterjee, S. N., Teti, G., and Sasdelli, M., "Development of Design Software and Material Failure Models for Fiber Reinforced Plastic Pressure Hulls, Parts 1 and 2," MSC TFR 3401/1437 and 3502/1437, NSWC Contract N00167-93-C-0022, May 1994 and March 1995.

[*7*] Illankamban, R. and Krajcinovic, D., "A Constitutive Theory for Progressively Deteriorating Solids," *International Journal of Solids and Structures*, Vol. 23, No. 11, 1987, p. 1521.

[*8*] Mast, P. W., et al., "Experimental Determination of Dissipated Energy Density as a Measure of Strain-Induced Damages in Composites," NRL/FR/6383-92-9369.

[*9*] Mast, P. W., et al., "Characterization of Strain-Induced Damage in Composites Based on the Dissipated Energy Density, Part I. Basic Scheme and Formulation," *Theoretical and Applied Fracture Mechanics*, Vol. 22, 1995, p. 71.

[*10*] Mast, P. W., et al., "Characterization of Strain-Induced Damage in Composites Based on the Dissipated Energy Density, Part II. Composite Specimens and Naval Structures," *Theoretical and Applied Fracture Mechanics*, Vol. 22, 1995, p. 97.

[*11*] Mast, P. W., et al., "Characterization of Strain-Induced Damage in Composites Based on the Dissipated Energy Density, Part III. General Material Constitutive Relations," *Theoretical and Applied Fracture Mechanics*, Vol. 22, 1995, p. 115.

[12] Walker, T., et al., "Damage Tolerance of Composite Fuselage Structure," *Proceedings, 6TH NASA/DoD Advanced Composites Technology Conference,* Anaheim, CA, August 1995, NASA Conference Publication 3326, Part 1, 30 June 1998. p. 481.

[13] Flanagan, G., Kollegal, M., and Chatterjee, S., "Stress Analysis and Damage Modeling of Textile Composites," Technical Progress Report, MSC TPR 3837/DA09, AFOSR Contract No. F49620-96-C-0018, Sept. 1998.

[14] Chatterjee, S. N., Yen, C. F., Ramnath, V., and Wung, E. C. J., "Development of a 3-Dimensional Stress Analysis to Examine Static and Fatigue Fracture," MSC TFR 2118/1111, NAWC Contract No. N62269-87-C-0238, Nov. 1990.

[15] Kellas, S., Morton, J., and Jackson, K. E., "Damage and Failure Mechanisms in Scaled Angle-Ply Laminates," ASTM *STP 1156, American Society for Testing and Materials* , 1993, p. 257.

[16] Kessler, J. and Adams, D. F., "Standardization of Test Methods for Laminated Composites, Vol. II. Experimental Efforts, Appendix: Stress Strain Curves and Photographs," MSC TFR 3313/1706-002, U.S. Army Research Lab., Contract No. DAAL04-89-C-0023, Oct. 1993.

[17] Lagace, P. A., "Nonlinear Stress-Strain Behavior of Graphite/Epoxy Laminates," *Proceedings, Part I, AIAA/ASME/ASCE/AHS 25th Structures, Structural Dynamics and Materials Conference,* AIAA, New York, 1984, p. 63.

[18] Shuart, M. J., "Failure of Compression Loaded Multidirectional Composite Laminates," *Proceedings, AIAA/ASME/ASCE/AHS 29th SDM Conference,* AIAA Paper No. 88-2293, Williamsburg, VA, April 1988.

[19] Kistner, M. D., Whitney, J. M., and Browning, C. R., "First-Ply Failure of Graphite/Epoxy Laminates," *ASTM STP 864,* 1985, pp. 44–61.

[20] Whitney, J. M. and Nuismer, R. J., "Stress Fracture Criteria for Laminated Composites Containing Stress Concentrations," *Journal of Composite Materials,* Vol. 8, 1974, p. 253.

[21] Awerbuch, J. and Madhukar, M., "Notched Strength of Composite Laminates: Predictions and Experiments—A Review," *Journal of Reinforced Plastics and Composites,* Vol. 4, 1985, p. 3.

[22] *Composite Materials Handbook,* MIL-HDBK-17-2E, Vol. 2, 24 May 1999.

[23] Chatterjee, S. N., Yen, C. F., and Mirto. D., "Failure and Damage Tolerance of Composite Materials," MSC TFR 3712/BD01, NASA Contract No. NAS1-97053, LaRC, Sept. 1997.

Ever J. Barbero[1] *and Edward A. Wen*[1]

Compressive Strength of Production Parts Without Compression Testing

REFERENCE: Barbero, E. J. and Wen, E. A., **"Compressive Strength of Production Parts Without Compression Testing,"** *Composite Structures: Theory and Practice, ASTM STP 1383,* P. Grant and C. Q. Rousseau, Eds., American Society for Testing and Materials, West Conshohocken, PA, 2000, pp. 470–489.

ABSTRACT: The purpose of this paper is to present a methodology to estimate the compressive strength of fiber-reinforced composite prototype and production parts. The procedure is based on test data that incorporate the effects of sample size and sample preparation but are simpler to obtain than compression test data. A simple formula is derived to relate the compressive strength to the shear stiffness, shear strength, and standard deviation of fiber misalignment. The formula is completely defined in terms of these three parameters, all of which can be measured by standard experimental procedures. It is proposed to use the shear stiffness and shear strength from coupon tests, usually available from the material supplier or from the characterization phase of the design/build project. Since these two parameters are relatively insensitive to part size and sample preparation, the coupon data are reliable and representative of the actual production part. Since fiber misalignment depends on the processing conditions, the third parameter used is the standard deviation of fiber misalignment, measured on samples from actual production parts. These three values characterize the compressive strength of the carbon/epoxy layups for which experimental data are found in the literature and those evaluated in this investigation. The predictions are then validated against data from a variety of specimens tested at high and low temperatures, as well as data from production prototype parts.

KEYWORDS: production parts, compression testing, compressive strength, fiber-reinforced composite prototype, shear stiffness, shear strength

Nomenclature

C_2	Stress-strain quadratic-term coefficient
Exp	Expected value
F	Cumulative folded probability
f	Folded probability density
F_{1c}	Longitudinal compressive strength
F_6	Composite shear strength
F_{xc}	Off-axis compressive strength of globally misaligned composite
G_{12}	Composite shear stiffness
n	Number of data points
p, q	Parameters in Eq 10
Sv	Standard deviation of sample variance
$t_{\alpha/2,n-1}$	t-distribution at $\alpha/2, n-1$
V	Sample variance
Ω	Standard deviation of fiber misalignment
α	Misalignment angle
α_G	Global misalignment angle

[1] West Virginia University, Morgantown, WV 26506-6106.

Copyright© 2001by ASTM International www.astm.org

χ Dimensionless number controlling compression behavior
γ In-plane shear stress
σ Bundle stress
σ_{app} Applied stress
σ_{eff} Effective stress
τ In-plane shear stress
ω 1/100 of percentage of buckled fibers

Compressive strength of PMC often controls the design, but yet it is very difficult to measure and very difficult to predict. Various test fixtures give different results (SACMA SRM-1R-94, ASTM D 5379, ASTM D 695, etc.) depending on sample preparation and sample size. Most of these fixtures measure the compressive strength of laboratory samples, which is often higher than that of production parts. But production parts cannot be tested because the specimens would be too thick for those fixtures. When prototype test specimens are tested, other problems such as buckling can mask the results. Additional problems, such as damage, appear when trying to machine samples out of prototype parts.

In the typical "Building Block" development process for large structures [*1*], design allowables are established from specimen tests. Structural elements are then tested to confirm design allowables. Larger elements, or subcomponents, are then tested to reconfirm design allowables and, finally, a full-scale test is performed to prove the entire design. Using the proposed methodology, compressive strength of structural elements can be predicted from available material data (shear stiffness and strength) and easily measured parameters (misalignment), thus reducing the number of structural tests required to substantiate the design process. Also, the proposed methodology can be used to perform failure analysis and postmortem diagnosis of failed composite structures that may be too damaged to be tested in compression.

Many models have been proposed to improve the prediction of compressive strength, the first introduced by Rosen [*2*]. The literature encompasses fiber buckling modes [*3*], kink-band models [*4*], and kink-bands induced by microbuckling [*5*]. In Ref *6*, an analytical formulation was introduced that used the standard deviation of the fiber misalignment to represent the misalignment distribution. An exact solution for microbuckling utilizing a continuum damage model was derived and simplified into an explicit equation for compression strength. In this work, a methodology is developed to predict compressive strength using this explicit equation at the specimen and structural element level.

Materials and Experimental Procedures

Two different carbon/epoxy prepregs were used in this study. The first material, Cytec Fiberite using 949-HYE epoxy and M30GC carbon fibers, has a standard modulus fiber with a tough resin. The second material, Cytec Fiberite using 948A1-HYE epoxy and M40J carbon fibers, has an intermediate modulus fiber and a relatively stiffer matrix.

The prepregs were laid up by hand and cured in an oven at 135°C for 90 min with approximately 27 in. Hg vacuum bag pressure. A 7-ply [0 deg] panel was made for the compression specimens and a 20-ply [0 deg] panel was used for the shear modulus and shear strength specimens. The 7-ply panel was cured with peel ply and caul plates on both sides of the panel so that the surface would have very little waviness and the thickness would be relatively uniform. To achieve low misalignment, great care was taken to align the 7 plies of the prepreg to the manufactured edge of the tape. The 20-ply panel was cured without caul plates or peel ply because the variations in thickness were judged to be small when compared to the total thickness.

Specimen Tests

The SACMA SRM-1R-94 procedure was selected for the longitudinal compression test because it typically provides compressive strengths 5% higher than the ASTM D 3410 "IITRI" method. In addition, the SACMA test would allow easier comparison with manufacturer's data because it is most commonly used by airframe manufacturers, prepreg producers, and so on.

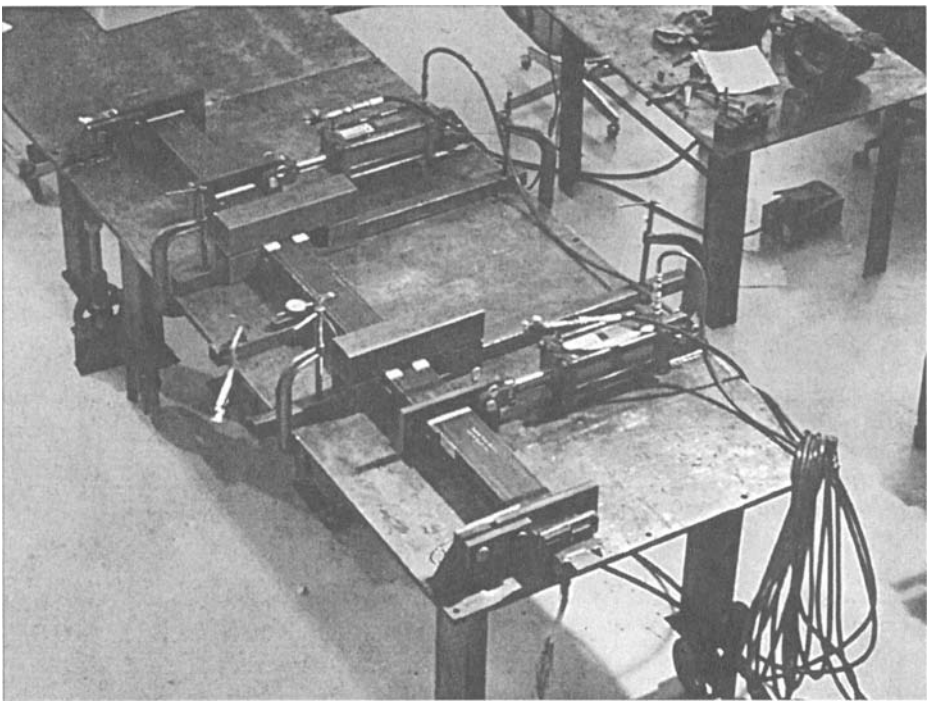


FIG. 1—*Four-point bending test.*

To measure shear strength and modulus, the ASTM D 5379 "Iosipescu" method was selected. MicroMeasurements shear gages were used since they average the shear strain between the entire region between the notches of the specimen. Modulus G_{12} data were taken between 1000 and 6000 microstrains from back-to-back shear gages and the results from each side were averaged together.

The in-plane shear strength, F_6, was taken where there was a significant change in the slope of the load-displacement plot. In the case of the specimens with the tougher resin 949-HYE there was no significant change, so F_6 was taken at the slight dip between the initial curved section and the linear section of the load-displacement plot (see Ref *13*).

The compression, shear strength, and shear modulus tests for the specimens were conducted at 82°C, room-temperature-ambient (RTA) and −87°C for both materials.

Beam Tests

Two C-section beams were tested in four-point bending at room temperature (Fig. 1). These beams were made of 949 HYE/M30GC and were relatively thick hand layups cured at 135°C with 27 in Hg vacuum pressure. In Beam 1, the gage section consisted of 60 ply of 0 deg and one ply ±45 deg on top and bottom. In Beam 2, the gage section had 56 ply with one ±45 deg ply every 8 ply of 0 deg.

Misalignment Characterization

The specimens were cut from panels with a diamond saw and ground to their final dimensions on a surface grinder. After the compression specimens were broken, the two halves of the specimens

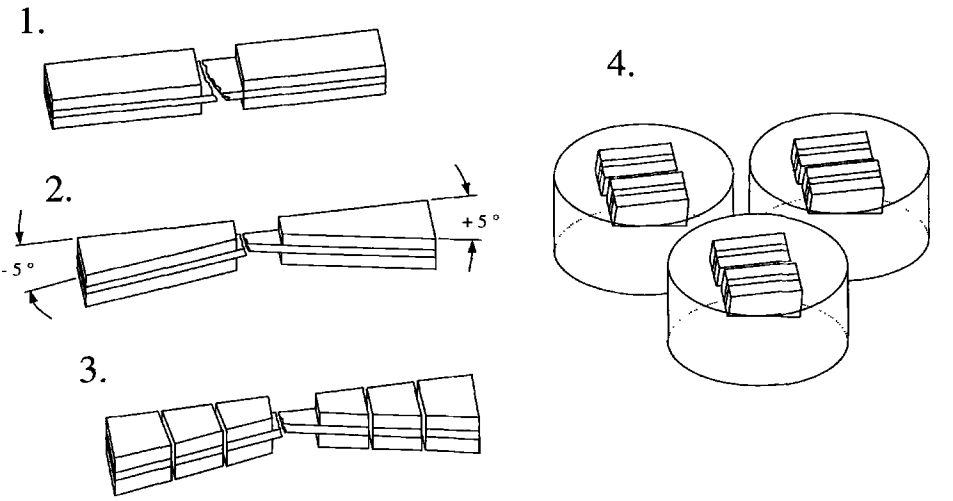


FIG. 2—*Specimen polishing procedure.*

were carefully ground to regain parallel edges. This is possible since the damage from the compression failure is around the gage section and the end of the specimen can still be used to establish a reference surface.

A 5 degree cut was made on each of the compression specimen halves so that one side would have +5 deg cut and the other side would have a −5 deg cut (Fig. 2). The specimen was then cut and potted in acrylic with the ±5 deg surfaces on top. These surfaces were then polished using the Buehler Ecomet 2 Polishing Machine at 240, 400, 600, 800 grit sandpaper and with 1 μm alumina polishing compound.

In the case of the beams, a piece was cut from the compression caps as near as possible to the location of the failure (Fig. 3). A piece cut in this manner had two faces that were against the tool and

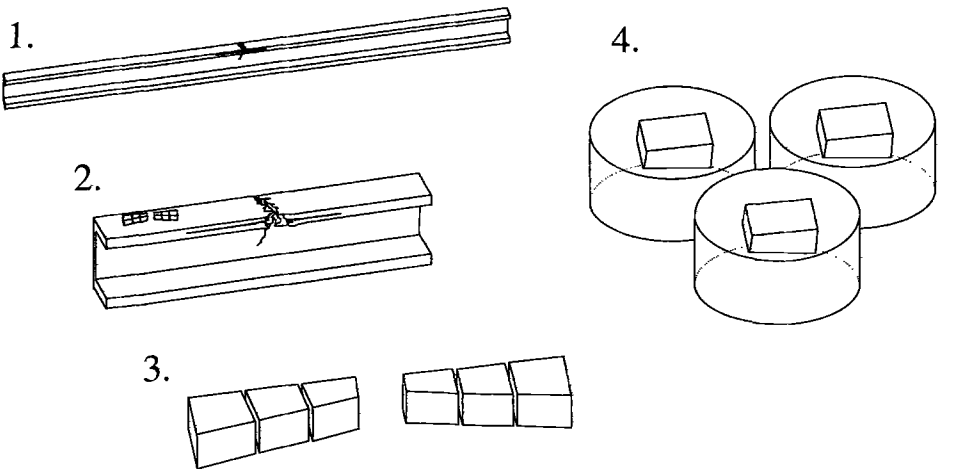


FIG. 3—*Beam specimen polishing procedure.*

therefore could be taken as reference surfaces when performing the subsequent grinding to square up the specimen. As previously, a +5 deg cut and −5 deg cut were made and then polished until the fibers could be viewed as complete ellipses.

To quantify fiber misalignment, the major and minor axes of the fiber ellipse were measured with a metallographic microscope and a video acquisition software [*13*]. The major axis was measured at ×200 magnification for 1512 fibers on each specimen and the minor axis of the fiber was measured at ×500 magnification for 40 points on each specimen.

As pointed out in Ref *7*, there is a tendency to pick the fibers with a major axis of smaller length and neglect the fibers with a longer length. To make the selection as random as possible, all fibers intersecting a line drawn on the screen were measured (Fig. 4). Data were taken starting from the top of the specimen and ending at the bottom. Additional lines of data were taken until the required number of points had been achieved.

The misalignment angle is computed from the major axis length, the fiber diameter and the angle of the cutting plane [*7,13*]. The distribution is shown to be Gaussian by using the cumulative distri-

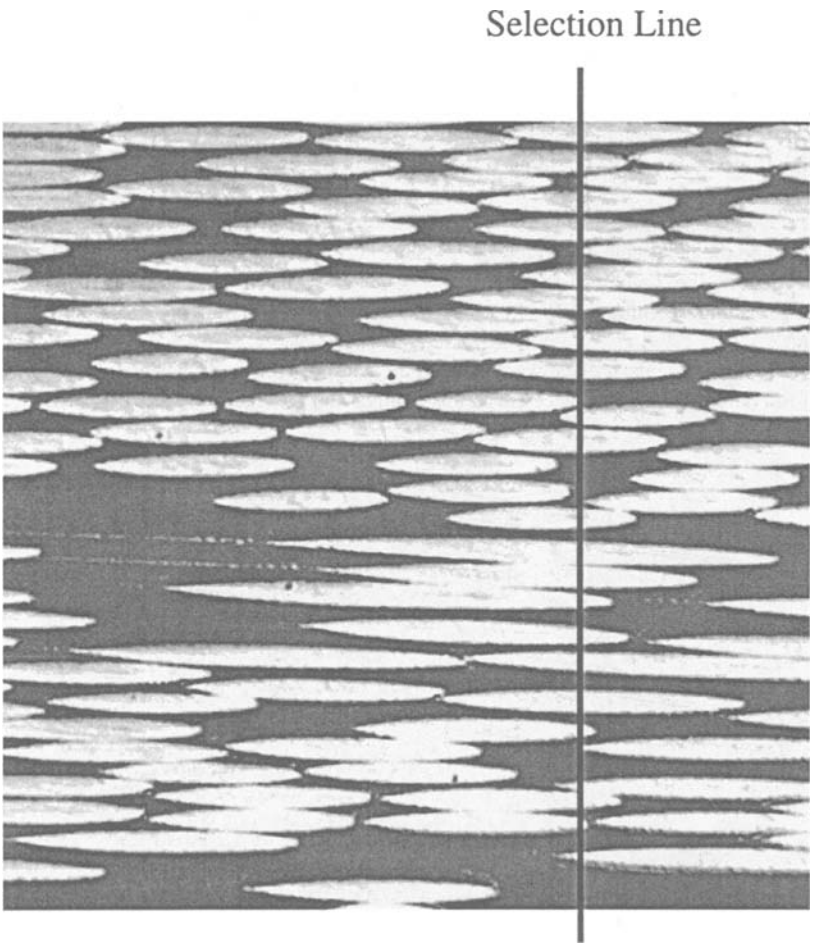


FIG. 4—*Selection of ellipses.*

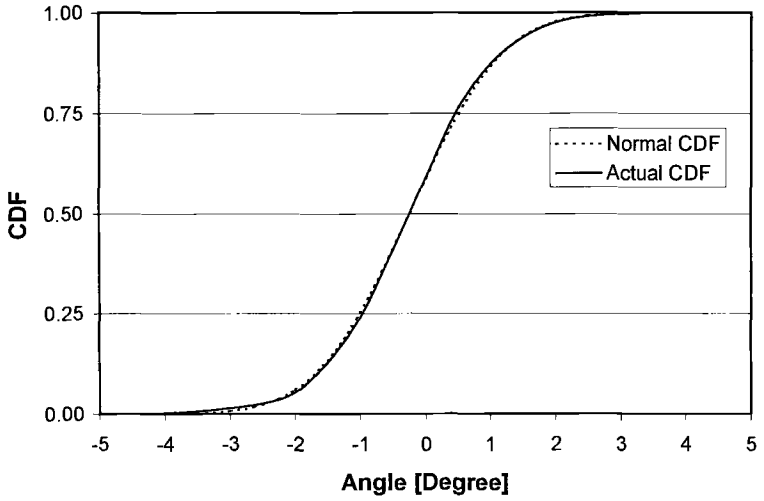


FIG. 5—*Cumulative distribution function of fiber misalignment for a specimen.*

bution function (CDF) in Fig. 5. When the mean of the distribution is zero, all the misalignment data are represented by just one parameter—the standard deviation of fiber misalignment Ω. Otherwise, the mean value is the global misalignment, its effect being considered here in the global misalignment section.

Compressive Strength Formula

The prediction of compression strength of composites was first introduced by Rosen [*2*], assuming that buckling of the fibers initiates a process that leads to the collapse of the material. The effect of initial shear stiffness on the compression strength has been studied experimentally [*8,9*], concluding that higher initial shear stiffness correlates with higher compression strength. The detrimental influence of fiber misalignment has been experimentally demonstrated [*8,10*]. The experimental evidence suggests that fiber buckling of perfectly aligned fibers (Rosen's model) is an imperfection sensitive problem if the shear response of the composite is nonlinear [*16*]. Rosen's model has been refined with the addition of initial fiber misalignment and nonlinear shear stiffness [*3*]. However, most existing models assume that all the fibers have the same value of misalignment α, which is taken as an empirical parameter. Then, the value of this empirical parameter is set so that the model predictions match experimental data. That is, experimental data must be available before the model can be used. Besides, it is well known that there is not a unique value for fiber misalignment for all the fibers but a Gaussian distribution of misalignment (Fig. 5) [*7*].

Although the standard deviation has been used as a single misalignment value in the theoretical models, the predicted compressive strength values did not compare well with experimental data [*12*]. Furthermore, the standard deviation is a measure of the dispersion, not of the expected value of a distribution. From a statistical point of view, a single value of misalignment that in the average represents the population is the expected value, or mean. However, the mean of the misalignment distribution is often equal to zero. Noting that fiber buckling occurs at the same load for positive or negative misalignment angle, the symmetric normal distribution can be converted to a half normal distribution. In the half normal distribution, the random variable is given as $x = \text{abs}|\alpha|$, where α is the random variable of the normal distribution. In other words, the half normal distribution represents

the normal distribution without the algebraic sign (negative side gets folded onto the positive side). The expected value of a half normal distribution is

$$\text{Exp} = \int_{x=0}^{x=\infty} \frac{1}{\Omega}\sqrt{\frac{2}{\pi}}\exp\left(\frac{-(x')^2}{2\Omega^2}\right)x'dx' = \sqrt{\frac{2}{\pi}}\Omega \tag{1}$$

However, using the expected value of the half-normal distribution as a single misalignment value did not lead to a good correlation with experimental data [*12*]. This means that the process of compression failure cannot be modeled by the mean of the absolute value of misalignment data. Since none of the statistical approaches described above give satisfactory predictions, a different procedure based on a combination of statistics and damage mechanics is introduced next. Basically, it is assumed that the fibers with large misalignment buckle first and the stress is redistributed to the remaining fibers [*11*]. This phenomenon continues until the remaining fibers are no longer capable of sustaining the load, thus defining the compressive strength of the material.

The bundle stress $\sigma(\alpha, \gamma)$ of a fiber bundle with all the fibers having the same misalignment α was derived by Barbero [*6*] following a method similar to Ref *3* and is shown in Fig. 6 for various values of α. For the bundle stress to have a maximum with respect to shear strain γ, a nonlinear shear stress-strain relationship must be used. According to Refs *11, 13,* and *14,* the equation

$$\tau = F_6 \tanh(G_{12}\gamma/F_6) \tag{2}$$

fits shear experimental data very well. However, a simpler equation

$$\tau = G_{12}\gamma + C_2\gamma^2 \tag{3}$$

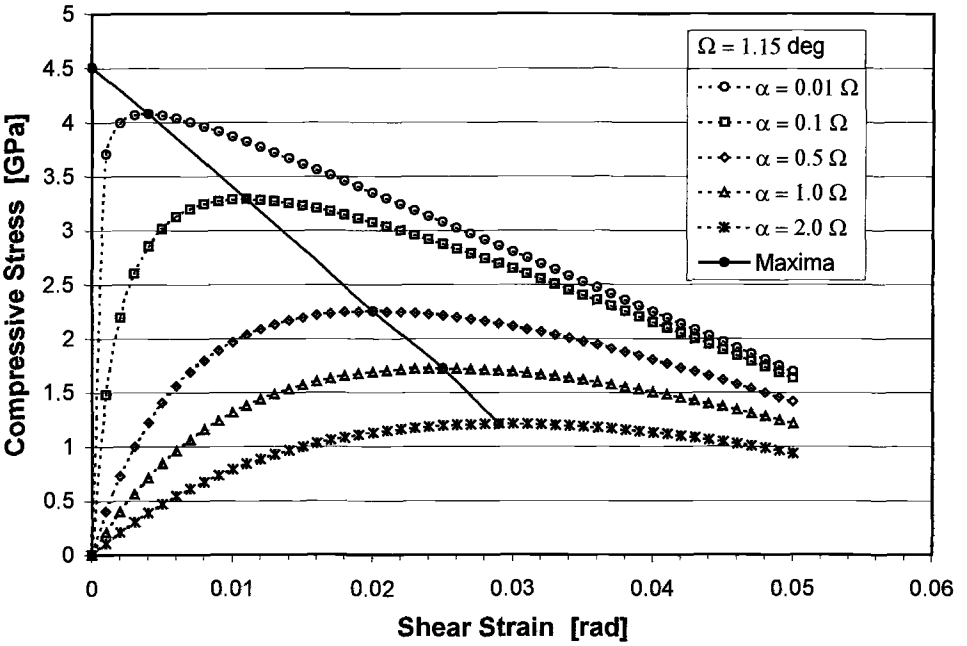


FIG. 6—*Bundle compressive stress vs. shear strain of 949/M30GC.*

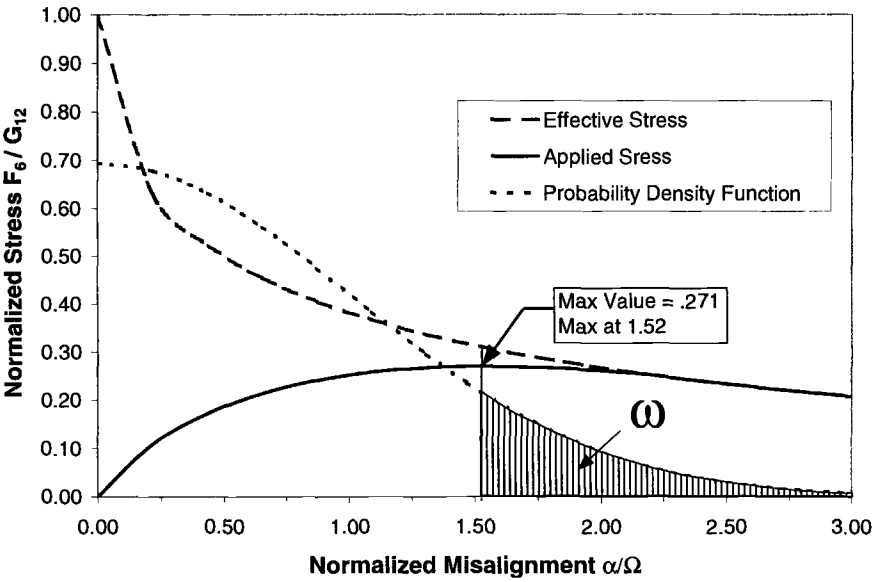


FIG. 7—*Combined buckling/misalignment of 949/M30GC.*

is accurate enough for the prediction of compressive strength provided C_2 is adjusted to fit the data in the interval of shear strain over which compression failure takes place. Taking this interval to be $0 < \gamma < 2F_6/G_{12}$, means that the shear strain will not exceed the point where the secant shear modulus is ½ of the original one. Most composites, including carbon-epoxy and glass-polyester, will fail in compression within this range. Then, the constant C_2 is found in terms of the parameters in Eq 2, taking into account that $\tanh(2) \approx 1$, as

$$C_2 = -\frac{G_{12}^2}{4F_6} \tag{4}$$

Following the procedure in Ref *6* but using Eq 3 instead of Eq 2, the bundle stress is obtained as

$$\sigma(\alpha, \gamma) = \frac{\gamma G_{12}}{\gamma + \alpha} + \frac{8}{3}\frac{C_2\gamma^2}{3(\gamma + \alpha)\pi} \tag{5}$$

The axial-stress versus shear-strain plot has a maximum for each misalignment value α, as shown in Fig. 6. The loci of maxima represent the bundle strength $\sigma_{\text{eff}}(\alpha)$ of a fiber bundle of a composite with all fibers equally misaligned at angle α, and it is shown by a dashed line in Fig. 7. Since such a composite does not exist, the Gaussian distribution of fiber misalignment must be brought in.

Continuous damage mechanics (CDM) was used [*6*] to combine the Gaussian distribution of misalignment with Eq 5. The misalignment distribution is Gaussian, and its probability density is given by

$$f(\alpha) = \frac{1}{\Omega\sqrt{2\pi}} e\left(\frac{-\alpha^2}{2\Omega^2}\right), \quad -\infty < \alpha < \infty \tag{6}$$

where Ω is the standard deviation of fiber misalignment. Therefore, the area fraction of composite that has fiber misalignment in excess of abs$|\alpha|$ is given by

$$\omega = \int_{\alpha}^{\infty} \frac{1}{\Omega} \sqrt{\frac{2}{\pi}} \exp\left(\frac{-(x')^2}{2\Omega^2}\right) x' dx' \quad ; \quad 0 \leq \omega \leq 1 \tag{7}$$

which corresponds to the shaded area under the folded probability density of fiber misalignment in Fig. 7. The folded distribution, $f(\text{abs}|\alpha|)$, is used because fiber microbuckling is indifferent to the sign of the misalignment. Since the integral above is transcendental, it is approximated by

$$F(\alpha) = 0.8341342 \frac{\alpha}{\Omega} - 0.1727790 \left(\frac{\alpha}{\Omega}\right)^2 \tag{8}$$

For a given value of applied stress σ_{app}, a number of fibers buckle because they have sufficiently high misalignment. The load is carried by the unbuckled fibers, having area $(1 - \omega)$. Therefore the applied stress is

$$\sigma_{\text{app}} = \sigma_{\text{eff}}(\alpha)[1 - \omega(\alpha)] \tag{9}$$

which is shown as a solid line in Fig. 7. The maximum of the applied stress is the compressive strength, given by

$$F_{1c} = G_{12}\left(\frac{\chi}{p} + 1\right)^q, p = 0.21, q = -0.69 \tag{10}$$

in terms of the dimensionless number

$$\chi = \frac{G_{12}\Omega}{F_6} \tag{11}$$

Equation 10 does not contain empirically adjustable factors and is simple enough to be used in practice. The parameters p and q are not set to fit any empirical data; they are obtained as the result of finding the maximum of Eq 9 using the procedure described in Ref *6*. It will be shown that predictions using Eq 10 compare well with compression strength data for a broad class of materials.

Statistical Analysis

Given that previous studies [*12*] used 1000 points of data for carbon fiber prepregs, 1512 points were taken for each specimen to provide a comfortable margin of accuracy. As many as 756 points of data were taken on the +5 deg side of the specimen and the same number on the −5 deg side.

Considering only one side of the specimen, the misalignment distributions are slightly skewed from a perfectly normal distribution because of a bias in the measurement technique [*13*]. For example, the +5 deg side (right side) usually has a distribution with more negative angles and therefore a negative skew (Fig. 8), while the −5 deg side has the opposite. In almost all of the cases, the fiber angles were between ±5 deg. If there were some points outside ±5 deg, these were discarded since they do not make a strong contribution to the compression strength of the laminate [*12*].

As discussed earlier, it is reasonable to expect that the distribution is normal and therefore the bias is attributed to the measurement technique. To cancel the bias, it is proposed to use the data from the

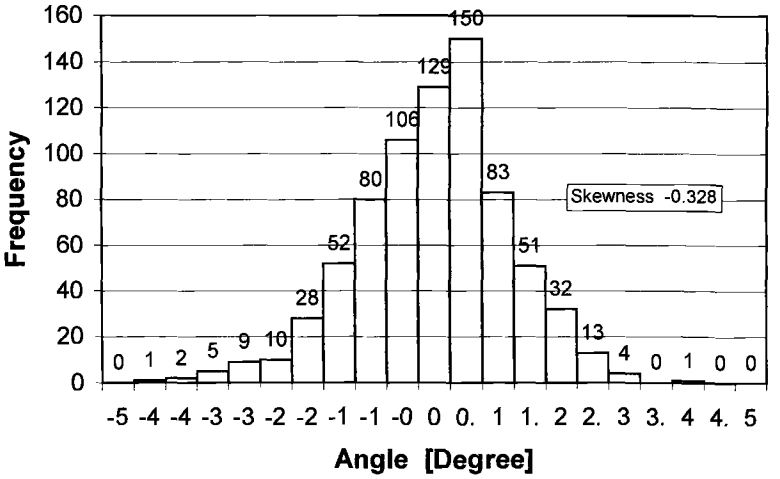


FIG. 8—*Distribution skew example. Sample NTP-15-86 right side angles.*

+5 and the −5 deg sides of the specimen and combine them together. The mean angle is shifted to zero before combining the results from both sides. This is reasonable because the average angle before shifting to zero was usually much less than ±0.5 deg, which is within ±0.5 deg tolerance due to cutting and polishing of the specimen. Once the plus and minus side data are combined, the data are normal (Gaussian) with negligible skew as shown in Fig. 5.

Standard deviation Ω was obtained from four 949 HYE/M30GC SACMA specimens, four 948A1 HYE/M40J SACMA specimens, four samples from beam 1 and four samples from beam 2. Confidence intervals at the 95% confidence level were constructed for each set using $n = 4$ and the t-distribution as given below

$$\sqrt{V - \frac{t_{\alpha/2,n-1}S_V}{\sqrt{n}}} \leq \Omega \leq \sqrt{V + \frac{t_{\alpha/2,n-1}S_V}{\sqrt{n}}} \tag{12}$$

where

Ω = population standard deviation
V = sample variance
S_v = standard deviation of sample variance
α = probability
n = number of data points
$t_{\alpha/2,n-1}$ = t-distribution at $\alpha/2$, $n - 1$.

The results are summarized in Tables 1 and 2. Since a very large number of fibers (1512) were used in the computation of each of the four Ω values, these can be considered to be exact, with very narrow individual confidence intervals, computed using the χ^2 distribution (Tables 1, 2).

The t-distribution was also used to establish the confidence intervals for the actual compression strengths, shear strengths, and shear moduli at the three test temperatures. Again, the confidence interval is at the 95% confidence level (Tables 3, 4).

TABLE 1—*949/M30GC confidence intervals on* Ω.

Type of Sample	I.D.	Specimen Standard Deviation, $n = 1512$ [deg]	95% Confidence Interval, (χ^2 dist.) [deg]	Population Standard Deviation Ω, $n = 4$ [deg]	95% Confidence Interval (t-dist). [deg]
949/M30GC SACMA compression specimen	NTP-15-1	1.236	+0.046 −0.043		
	NTP-15-84	1.123	+0.042 −0.039	1.150	+0.091 −0.099
	NTP-15-86	1.129	+0.042 −0.039		
	NTP-15-21	1.109	+0.041 −0.038		
949/M30GC Beam 1	B1-1	1.342	+0.0500 −0.046		
	B1-L1R1	1.328	+0.049 −0.046	1.313	+0.091 −0.097
	B1-L2R2	1.223	+0.045 −0.042		
	B1-L3R3	1.355	+0.050 −0.047		
949/M30GC Beam 2	B2-1	1.158	+0.043 −0.040		
	B2-L1R1	1.134	+0.042 −0.039	1.125	+0.055 −0.058
	B2-L2R2	1.074	+0.040 −0.370		
	B2-L3R3	1.133	+0.042 −0.039		

Predicted Results

Although Eq 10 predicts the experimental data from Refs *11* and *12* very well (Fig. 9), confidence intervals were not available in the literature to truly evaluate the merits of the proposed methodology. In this project, confidence intervals on the predicted compressive strength were obtained from the experimental confidence intervals on the parameters involved, namely G_{12}, F_6, and Ω. Values of the parameters and their experimental confidence intervals are shown in Tables 1 to 4. Those confidence intervals were obtained using the t-distribution (Eq 12) and the experimentally obtained sample variance from testing.

Because the three terms in the compression Eq 10 all have their own confidence interval, the predicted compression strength will have its associated confidence interval. By substitution in Eq 10, it can be shown that the highest value of F_{1C} occurs when G_{12} and F_6 are at their highest value and Ω is at its lowest. The lowest values of F_{1C} occur when the values take the opposite extremes, which is consistent with intuition.

Actual versus predicted compressive strengths of the SACMA specimens and four-point beam bending specimens are shown in Figs. 10 to 12. The formula predicts the compressive strength of the RTA and −87°C compression specimens very well. However, the 82°C specimen strength predictions were low even when using the full extent of the confidence interval. This is believed to be partly caused by the large changes in shear modulus that occur at high temperature. It can be inferred from

TABLE 2—*948A1/M40J confidence intervals on* Ω.

Type of Sample	I.D.	Specimen Standard Deviation, $n = 1512$ [deg]	95% Confidence Interval, (χ^2 dist.) [deg]	Population Standard Deviation Ω, $n = 4$ [deg]	95% Confidence Interval, (t - dist.) [deg]
948A1/M40J SACMA Compression Specimen	NTP-11-1	1.129	+0.040 −0.039	1.205	+0.157 −0.181
	NTP-17-7	1.164	+0.041 −0.040		
	NTP-16-5	1.163	+0.041 −0.040		
	NTP-11-21	1.352	+0.048 −0.047		

TABLE 3—*949/M30GC confidence intervals on* G_{12}, F_6, *Actual* F_{1C}.

Material	Temp. (C)	G_{12} (GPa)	95% Confidence Interval (*t*-dist.) (GPa)	F_6 (MPa)	95% Confidence Interval (*t*-dist.) (MPa)	F_{1c} Actual (GPa)	95% Confidence Interval (*t*-dist.) (GPa)
949/M30GC	82.2	2.86	+0.204	47.5	+3.21	1.03	+0.37
			−0.204		−3.21		−0.037
	23.0	4.51	+0.204	76.7	+4.86	+1.28	+0.148
			−0.204		−4.86		−0.148
	−87.2	4.91	+0.157	125.3	+7.09	+1.56	+0.080
			−0.157		−7.09		−0.080

TABLE 4—*948A1/M40J confidence intervals on* G_{12}, F_6, *actual* F_{1C}.

Material	Temp. (C)	G_{12} (GPa)	95% Confidence Interval (t-dist.) (GPa)	F_6 (MPa)	95% Confidence Interval (t-dist.) (MPa)	F_{1c} Actual (GPa)	95% Confidence Interval (t-dist.) (GPa)
948A1/M40J	82.2	3.46	+0.268	70.3	+0.976	1.34	+0.094
			−0.268		−0.976		−0.094
	23.0	4.92	+0.094	89.8	+1.76	1.43	+0.039
			−0.094		−1.76		−0.039
	−87.2	5.32	+0.307	112.6	+8.03	1.54	+0.128
			−0.307		−8.03		−0.128

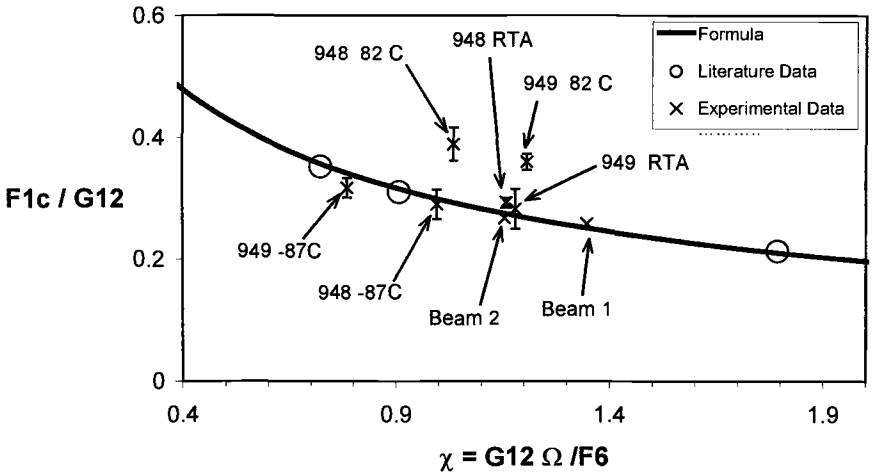


FIG. 9—*Formula vs. experimental data. Literature data from Refs* 11 *and* 12.

Tables 3 and 4 that shear strength is almost linear in the −87°C to 82°C temperature range while shear modulus has a large decrease between RTA and 82°C. Residual stresses may also play a role in the discrepancy.

Global Misalignment

When a layup has global misalignment α_G, but the misalignment of various layers is balanced and symmetric $[\pm\alpha_G]_s$, the laminate compressive strength can be found by stress transformation [*14*, p. 200]

$$F_{XC} = F_{1c} \cos^2(\alpha_G) \tag{13}$$

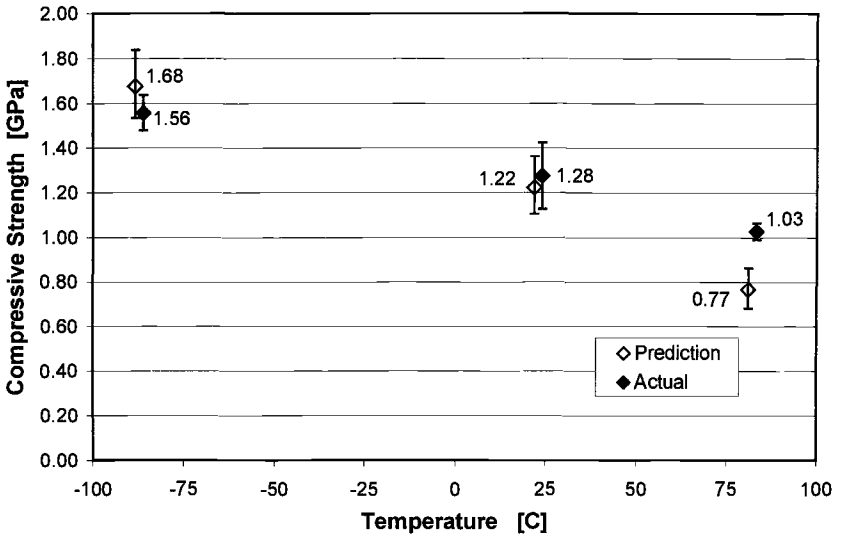


FIG. 10—*949/M30GC SACMA predicted vs. actual* F_{1c}.

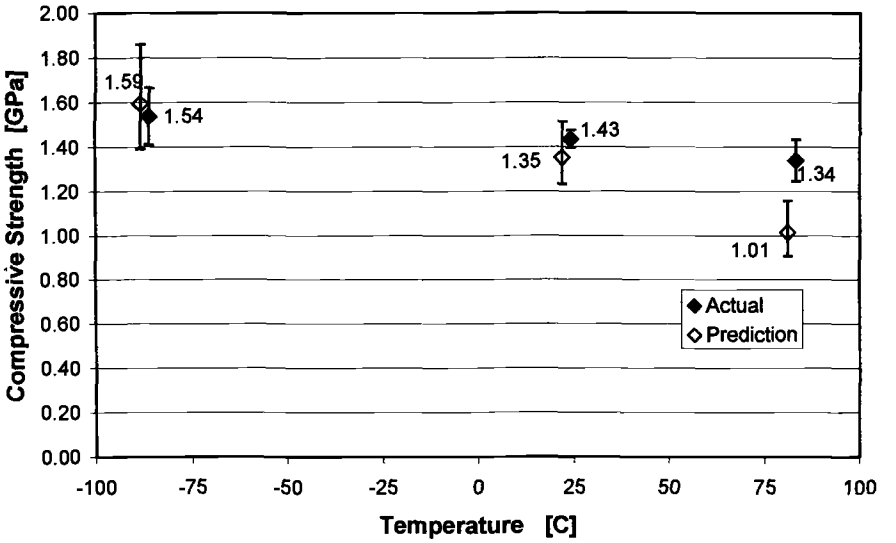


FIG. 11—*948A1/M40J SACMA predicted vs. actual* F_{1c}.

Using data from Ref *15*, it was found in this investigation that Eq 13 provides good agreement in the range $0 < \alpha_G < 10$ deg. However, there exists no known method for estimating the strength of laminates with unbalanced, global misalignment $[+\alpha_G]_n$ or $[-\alpha_G]_n$.

When there is unbalanced global misalignment, the equilibrium Eq 5 still applies but the distribution of fiber angles is shifted by the average angle α_G to

$$f(\alpha,\alpha_G) = \frac{1}{\Omega\sqrt{2\pi}}\, e\left(\frac{-(\alpha-\alpha_G)^2}{2\Omega^2}\right), \quad -\infty < \alpha < \infty \tag{14}$$

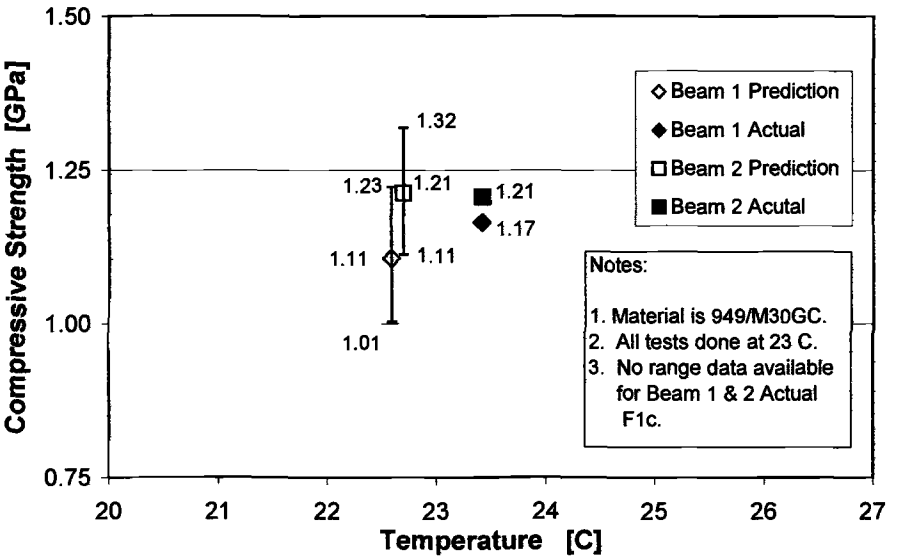


FIG. 12—*949/M30GC Beams 1 and 2 predicted vs. actual* F_{1c}.

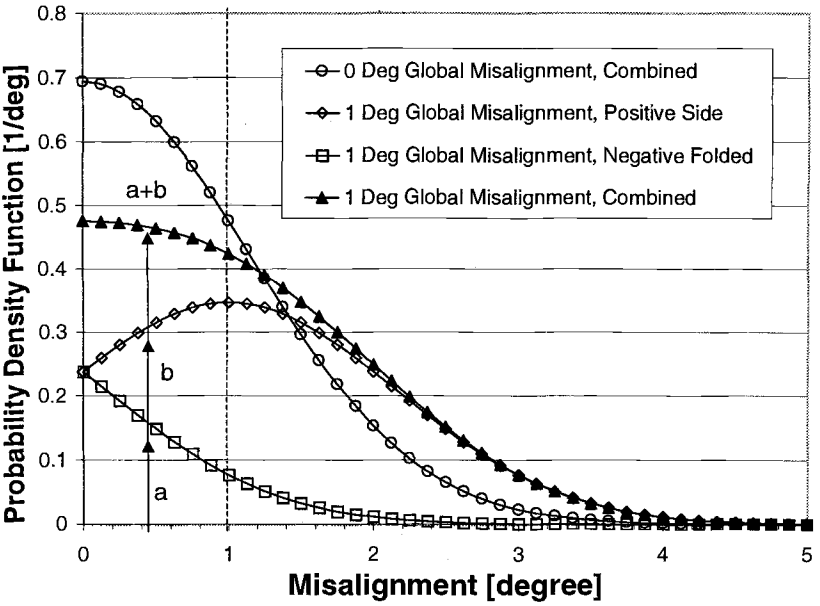


FIG. 13—*Shifted probability density function at 0, 1.0 global misalignment.*

The area fraction of composite with misalignment in excess of abs|α| is no longer given by Eq 5 because there is no symmetry about zero. Therefore, the quadratic polynomial approximation (Eq 8) cannot be used. Instead of using Eq 7, the integral

$$\omega = F(\alpha) = 2\int_{\alpha}^{\infty} f(\alpha',\alpha_G)d\alpha' \quad ; \quad 0 \le \omega \le 1 \tag{15}$$

must be integrated numerically. To illustrate the integration, the case of 1.0 degree global misalignment is shown in Fig. 13. The function is folded about zero and the two distributions are added together. For comparison, the probability density function for 0 deg global misalignment is shown also.

The integration of the combined shifted probability density used to obtain the cumulative distribution function at the given angles of global misalignment is shown in Fig. 14. When multiplied by the effective stress (dashed line in Fig. 7), the resulting applied stress curves are similar to the solid line in Fig. 7 [*13*]. The maximum of each curve represents the compressive strength at the given global misalignment angle. This technique is informally called the "Method of Shifted Distributions."

Note that Figs. 13 and 14 are for a fixed value of $\Omega = 1.15$ degrees. If taken at different values, it would produce a family of curves for F_{1C} as a function of Ω and α_G [*13*]. In this way, Fig. 15 was constructed to show the compressive strength F_{1C} as a function of global misalignment α_G when the standard deviation of fiber misalignment is fixed at various values. An individual curve represents a part fabricated with a prepreg layup that has a given value of Ω and is oriented with a global misalignment α_G with respect to the nominal direction (load direction).

Finally, it should be pointed out that laminate compressive strength is often controlled by the unidirectional layers [*15,17*]. Therefore, the proposed methodology applies not only to unidirectional composites but to laminated composites as well.

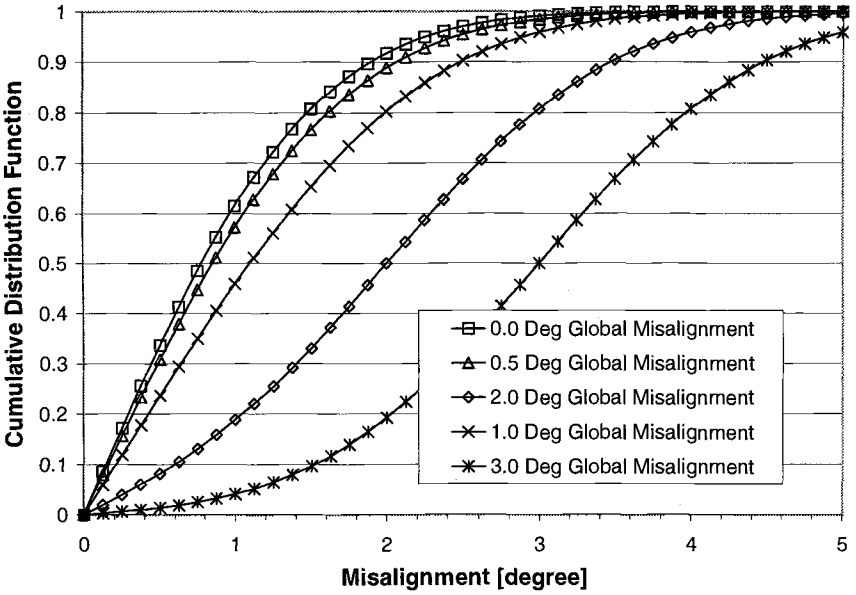


FIG. 14—*Cumulative distribution functions of the shifted probability density.*

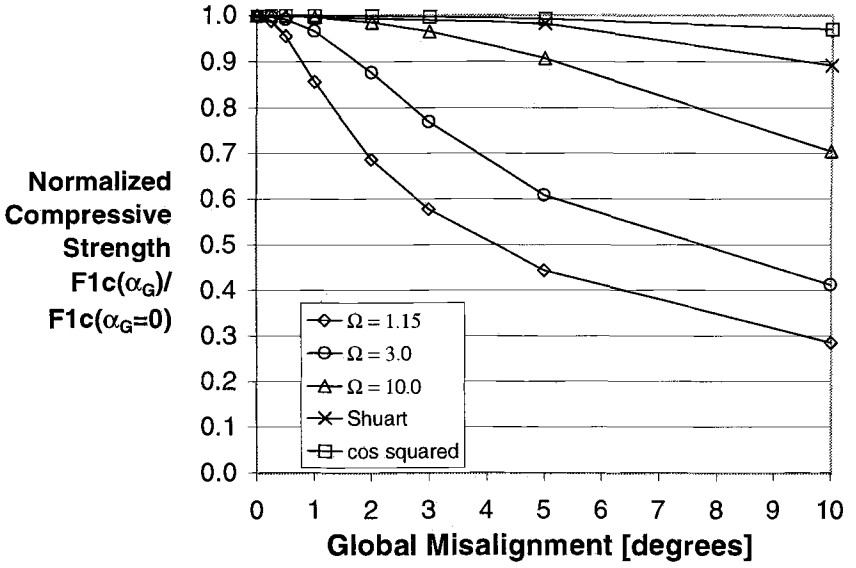


FIG. 15—*Normalized* F_{1C} *vs. global misalignment.*

Summary

The proposed methodology consists of the following:

a. Measure the global misalignment angle α_G and the standard deviation of fiber misalignment Ω on the actual part. This may be done on witness coupons or on the part itself during postmortem diagnosis.
b. Use the shear stiffness G_{12} and shear strength F_6 values from coupon data. Since these values are quite insensitive to sample size and preparation, they should be representative of the actual part. If in doubt, cut and test ASTM D 5379 coupons from the part itself.
c. Estimate the compressive strength of the material using Eq 10 in terms of the dimensionless number χ defined in Eq 11.
d. If the global misalignment is different from zero, use the procedure described in the foregoing global misalignment section to estimate the off-axis compressive strength.

Conclusions

When fiber misalignment data are combined with the shear stiffness and strength data of the material, the prediction formula presented in this paper accurately predicts the compressive strength of SACMA SRM-1R-94 compression specimens and beams in four-point bending at room temperature and at −87°C. At 82°C, the prediction is conservative by a 25% margin. It is clear that the proposed methodology can predict accurately the values of compressive strength, thus reducing the need for compression testing to substantiate the design process. In addition, this technique has application to "postmortem" analysis, where misalignment measurement on the failed structure combined with material shear data can be used to accurately estimate the compressive strength without compression testing. The technique proposed to predict compressive strength with global misalignment $[+\alpha_G]_n$ or $[-\alpha_G]_n$ also holds promise. From an experimental point of view, a procedure was presented to eliminate the skewness of the optical procedure used to measure fiber misalignment. Future work would include devising a means to verify the global misalignment predictions and to incorporate the effect of voids into the compressive strength model.

Acknowledgments

This project was partially sponsored by Aurora Flight Sciences under contract AWV97-2348. Our thanks go to Les Montford, Randy Tatman, Clint Church, and Alistar Wroe for providing the prototype data and guidance for the study.

References

[1] Dobyns, A., "RAH-66 Comanche Building Block Structural Qualification Program," ASTM Symposium on Composite Structures: Theory and Practice, *ASTM STP 1383,* 17–18 May 1999, Seattle, WA.
[2] Rosen, B. W., Chapter 3 in "Fiber Composite Materials," Metals Park, OH, American Society for Metals, 1965.
[3] Wang, A. S. D., "A Non-Linear Microbuckling Model Predicting the Compressive Strength of Unidirectional Composites," ASME Winter Annual Meeting, ASME Paper 78-WA/Aero-I, 1978.
[4] Lagoudas, D. C. and Saleh, A. M., "Compressive Failure Due to Kinking of Fibrous Composites," *Journal of Composite Materials,*" Vol. 27, 1993, pp. 83–106.
[5] Yin, W.-L., "A New Theory of Kink Band Formation," AIAA-92-2552-CP, 1992.
[6] Barbero, E. J., "Prediction of Compression Strength of Unidirectional Polymer Matrix Composites," *Journal of Composite Materials,* Vol. 32, No. 5, 1998, pp. 483–502.
[7] Yurgartis, S. W., "Measurement of Small Angle Fiber Misalignment in Continuous Fiber Composites," *Composite Science and Technology,* Vol. 30, 1987, pp. 279–293.
[8] Yurgartis, S. W. and Sternstein, S. S., "Experiments to Reveal the Role of Matrix Properties and Composite Microstructure in Longitudinal Compression Strength," ASTM Symposium on Compression Response of Composite Structures, 16–17 November 1992.

[9] Crasto, A. S. and Kim, R. Y., "The Effects of Constituent Properties on the Compression Strength of Advanced Composites," ASTM Symposium on Compression Response of Composite Structures. 16–17 November 1992.

[10] Mrse, A. and Piggott, "Relation between Fibre Divagation and Compressive Properties of Fibre Composites," *Proceedings, 35th International SAMPE Symposium*, 2–5 April 1990. pp. 2236–2244.

[11] Barbero, E. J. and Tomblin, J. S., "A Damage Mechanics Model for Compression Strength of Composites," *International Journal of Solid Structures*, Vol. 33, No. 29, 1996, pp. 4379–4393.

[12] Haberle, J. G., "Strength and Failure Mechanisms of Unidirectional Carbon Fibre-Reinforced Plastics Under Axial Compression," Ph.D. thesis, Imperial College, London, U.K., 1991.

[13] Wen, E., "Compressive Strength Prediction for Composite Unmanned Aerial Vehicles," thesis, West Virginia University, Morgantown, WV, 1999.

[14] Barbero, E. J., "Introduction to Composite Materials Design," Taylor and Francis, Philadelphia, PA, 1999.

[15] Shuart, M. J., "Failure of Compression-Loaded Multidirectional Composite Laminates," *AIAA Journal*, Vol. 27, 1989, pp. 1274–1279.

[16] Tomblin, J. S., Barbero, E. J., and Godoy, L. A., "Imperfection Sensitivity of Fiber Micro-Buckling in Elastic-Nonlinear Polymer-Matrix Composites," *International Journal of Solid Structures*, Vol. 34, No. 13, 1997, pp. 1667–1679.

[17] Barbero, E. J., Makkapati, S., and Tomblin, J. S., "Experimental Determination of Compressive Strength of Pultruded Structural Shapes," *Composite Science and Technology*, Vol. 59, 1999, pp. 2047–2054.

Environmental Effects

Kathleen A. Lubke,[1] *Lawrence M. Butkus,*[2] *and W. Steven Johnson*[1]

Environmental Effects on Bonded Graphite/Bismaleimide Structural Joints

REFERENCE: Lubke, K. A., Butkus, L. M., and Johnson, W. S., **"Environmental Effects on Bonded Graphite/Bismaleimide Structural Joints,"** *Composite Structures: Theory and Practice, ASTM STP 1383,* P. Grant and C. Q. Rousseau, Eds., American Society for Testing and Materials, West Conshohocken, PA, 2000, pp. 491–512.

ABSTRACT: There are many advantages to using adhesively bonded joints for aerospace applications, but their potential is not yet realized because not enough is known about the long-term durability of the polymeric adhesives. This paper focuses on the long-term durability of a toughened epoxy used to bond graphite/bismaleimide composites. Double cantilever beam (DCB), end-notched flexure (ENF), and cracked lap shear (CLS) tests were conducted to determine the fracture toughness of the adhesive system before and after environmental exposure. These specimens were exposed to either a hot/dry environment or thermal cycles between −54°C (−65°F) and 104°C (220°F). Unexposed and exposed specimens were tested at room temperature and it was found that the hot/dry environment lowered the fracture toughness of the joints. For the DCB and CLS geometry, unexposed specimens were tested at reduced and elevated temperatures. For some of the DCB and all of the CLS specimens, it was found that the cold temperature reduced the fracture toughness. In order to determine if the environment and temperature combined affect the toughness, the environmentally exposed DCB and CLS specimens were tested at the cold temperature. This combination of cold temperature and environmental exposure significantly lowered the fracture toughness of the material in all adhesive joints tested.

KEYWORDS: adhesive joints, double cantilever beam, end-notched flexure, cracked lap shear, environmental durability, composite bonding

Adhesives increasingly are being considered for many applications because of the advantages they offer over mechanical fasteners. These advantages include increased fatigue life, potentially lower costs, reduced weight, improved aerodynamics, fewer stress concentrations, and more effective thermal and electrical isolation properties [*1–3*]. One arena in which adhesive bonding is seen as being particularly attractive is the aerospace industry.

One such aerospace structural application of adhesive bonding occurs on the U.S. Air Force's F-22 "Raptor" fighter. Major performance goals of the F-22 include the ability to attain supersonic cruise without using afterburners, and to maintain low observability. In order to achieve these goals, the F-22's structure consists of approximately 24% composite material by weight, and adhesive bonding is crucial in attaching the external composite skins. These bonded skins are graphite fiber-reinforced bismaleimide composites [*4,5*]. The adhesive used for bonding is a toughened epoxy with a random mat scrim carrier cloth. The temperatures that the material will be exposed to will range from −65°F (−53°C) during high-altitude subsonic flight to 220°F (104°C) during supersonic cruise and high-speed maneuvers.

[1] Graduate student, Materials Engineering, and professor, Mechanical Engineering and Materials Engineering, respectively, Georgia Institute of Technology, Atlanta, GA 30332-0245.

[2] Former graduate student at Georgia Institute of Technology; currently, lead structures engineer for aging aircraft, Wright-Patterson AFB, OH.

Copyright© 2001by ASTM International www.astm.org

The objective of this research was to investigate the effects of extreme environments on the graphite/bismaleimide adhesively bonded joints used in the F-22. Research was conducted on joints employing either primarily unidirectional or near quasi-isotropic adherends. A variety of tests was conducted to investigate the energy release rate for different fracture modes. Double cantilever beam (DCB), end-notched flexure (ENF), and cracked lap shear (CLS) tests were employed to determine the Mode I, Mode II, and mixed Mode I/Mode II strain energy release rates, respectively. The strain energy release rates are a measurement of the amount of energy required to advance an existing crack tip. Since a tougher adhesive would require more energy to advance the crack tip, the strain energy release rate is a measurement related to the toughness of the adhesive. For this experiment, specimens were environmentally exposed and then tested at room temperature, cold temperature, or hot temperature. Some of the specimens were environmentally exposed to either hot/dry environments or a hot/wet environment followed by thermal cycles, which are described in detail later.

The fracture toughness varied for each test depending on the environmental exposure and the test temperature. The DCB and CLS were tested as-received (no exposure), and after exposure to thermal cycles and the hot/dry environment, to determine the effect of environmental exposure on the fracture toughness. Some of the as-received specimens were tested at cold temperature and hot temperature to determine the effect of test temperature. Finally, tests on environmentally exposed specimens were conducted at cold temperature to determine if the combination of test temperature and environmental exposure further affected the fracture toughness. All ENF tests were conducted at room temperature on specimens that were either as-received or environmentally exposed to hot/dry or thermal cycles.

Experimental Procedure

This section describes the experimental methods used to obtain the fracture toughness of the adhesive joints. Adherends consisted of IM7/5250-4 graphite/bismaleimide laminates. The adherend layups were either primarily unidirectional $[0_4/90]_s$ or quasi-isotropic $[\pm 45/0_2/\pm 45/90]_s$. Although these specimens are not true unidirectional or quasi-isotropic, for simplicity they will be referred to as such for the remainder of the paper. The adhesive used to bond the composite adherends was AF-191, a modified epoxy containing a nonwoven nylon scrim cloth.

Specimen Details

The specimens were fabricated by Lockheed Martin Aeronautical Systems Co. (Marietta, GA). Large panels of graphite/bismaleimide were cured before bonding. The surface of the composite was prepared for bonding by hand sanding with 180-grit abrasive paper followed by a methanol wipe. The composite panels were bonded with AF-191 in an autoclave held at 177°C (350°F) and 310 kPa (45 psi) for 60 min. Test specimens were cut from the large bonded panels. The final thickness of the specimen bond line was approximately 250 μm (9.8 mils).

The fracture toughness of the joints for different modes of failure was found using three different specimen geometries. The double cantilever beam (DCB) geometry was used to determine the Mode I ("opening" mode) fracture toughness. The DCB specimens consisted of two adherends of equal size bonded together except at one end where bonding was prevented by using a trifluoroethylene (Teflon™) insert. The insert was used to create a crack initiation site. Piano hinges were bonded to each face of the specimen on the debonded end. Tensile load was applied to the specimen from the hinges that pulled apart the two adherends.

The end-notched flexure (ENF) test was used to determine the Mode II ("shear" mode) fracture toughness. The ENF geometry was the same as the DCB geometry but without the piano hinges. As in the DCB specimens, a Teflon insert was used to create a crack initiation site. The ENF specimen was tested in bending rather than tension.

Since most adhesive bonds are not subjected to pure Mode I or pure Mode II, a test was needed to determine the mixed-mode fracture toughness. The cracked lap shear (CLS) test was used for this purpose. The CLS specimens consisted of two adherends of equal width, but different lengths, bonded together flush at one end. Again, a Teflon insert between the strap (long adherend) and lap (short adherend) was used to create a crack initiation site. The specimen was loaded in tension by gripping only the strap at one end and both the strap and lap at the opposite end. Figure 1 shows the DCB, ENF, and CLS specimen geometries.

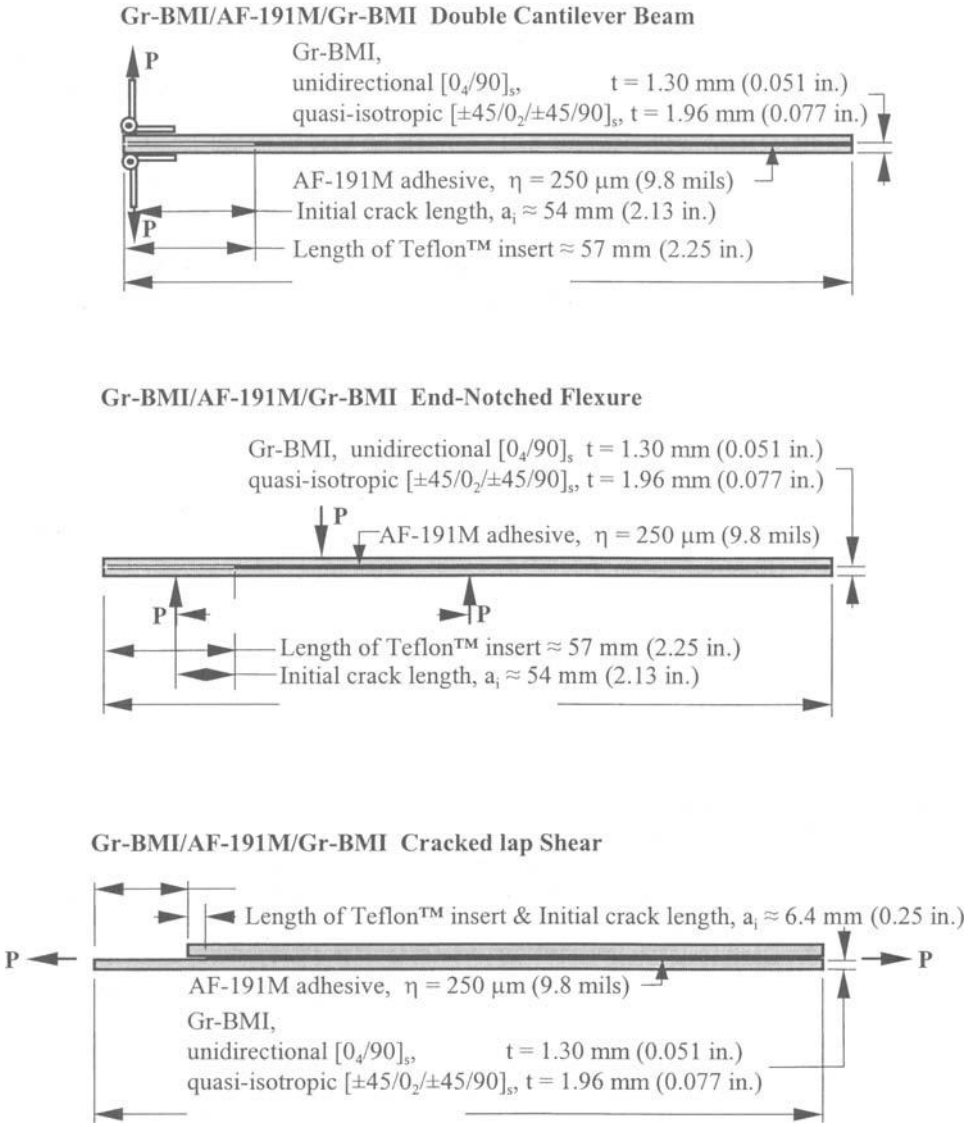


FIG. 1—*Specimen geometry for double cantilever beam, end-notched flexure, and cracked lap shear.* η = *thickness of bond line.*

Environmental Exposure

To determine the environmental durability of the adhesive bonds, selected specimens were exposed to simulated service conditions before testing and compared against specimens without any environmental exposure prior to testing.

Unidirectional specimens were exposed to "hot/dry" [220°F (104°C), 0% RH (relative humidity)] conditions for 5000 and 10 000 h. This exposure was conducted using a Thermotron circulating air oven in which the humidity was monitored by a humidistat. The "hot/dry" condition simulated what the F-22 is exposed to during high-performance maneuvers and has been determined to be the most severe environment for the F-22's bonded composite structures.

Both the primarily unidirectional and near quasi-isotropic specimens were exposed to an environment of hot/wet [140°F (71°C), >90% RH] conditions for 300 h followed by 100 thermal cycles between 104°C (220°F) and −54°C (−65°F). The "hot/wet" conditions were achieved by sealing the specimens in a humidity chamber and then placing the entire chamber in the Thermotron circulation air oven. The humidity chamber consisted of a 9.5 L (2.5 gal) glass jar laid on its side and partially filled with distilled water. In order to prevent the adhesive from coming into direct contact with the water, the specimens were supported above the water line by a plastic grating. The humidity was monitored by a humidistat in the chamber. Following the "hot/wet" exposure, the specimens were thermally cycled using a two-chamber apparatus at Warner Robins Air Logistics Center, GA. The bottom chamber was kept at −54°C (−65°F), while the top chamber was kept at 104°C (220°F). The specimens were then exchanged between chambers by an automatic trolley system for a total of 100 cycles. The average ramp rate of the specimens was 6°C(11°F)/min. Humidity levels were not controlled during the thermal cycles. However, the humidity of the lab was kept near 50% RH.

Storage

All specimens were carefully stored between the environmental exposure and testing. The hot/dry specimens were stored in a sealed container with desiccant in order to keep the bond line dry. The thermally cycled specimens were stored at room temperature and in laboratory air [72°F (22°C), 50% RH].

Testing Procedures

The following sections describe the testing procedures for the DCB, ENF, and CLS tests.

Double Cantilever Beam (DCB)—Testing of the DCB bonded joint specimens was carried out according to standard ASTM Standard Test Method for Mode I Interlaminar Fracture Toughness of Unidirectional Fiber-Reinforced Polymer Matrix Composites (D 5528-94a). The DCB specimens were loaded at the hinges at a constant crosshead displacement rate of 1 mm/min (0.04 in./min). This loading rate was based on the loading rates found in previous research [*6*]. The displacement and load applied to the specimen was recording during the test. When unstable crack growth occurred, the load versus displacement graph deviated from linearity. At this time, the crosshead was stopped, the length of the crack was measured, and the specimen was then unloaded. This procedure was repeated several times on each specimen.

End-Notched Flexure (ENF)—Since there is not a universal standard for the ENF test, the procedures used followed the guidelines established by Murri for round-robin testing [*7*]. The ENF specimens were tested using a 3-point bend fixture. The crack tip, which initially was the end of the debonded area, was placed halfway between the center and an outer loading point. The specimens were bent in displacement control at a rate of 0.5 mm/min (0.02 in./min). The load versus displace-

ment behavior was monitored during testing. When the crack tip advanced, the load versus displacement graph deviated from linearity. The crack length was measured on both sides of the specimen. After each test was conducted, the new crack tip was relocated to the halfway point between the center and an outer loading point. By using this method, several test runs could be conducted on a single specimen. By keeping the crack tip at the same location between the pins for each test, the initial crack length was kept constant.

Cracked Lap Shear (CLS)—The CLS test also does not have a universal standard, so test procedures were based on those used in previous research [*6,8*]. Prior to testing, a shim of with thickness equal to that of the strap (longer adherend) was attached to the lap (shorter adherend). This was done in order to keep the bond line completely vertical in the grips during testing so as to not induce any bending moments. The CLS test was conducted in load control at a rate of 100 N/s (22.5 lb/s). The loading rate was slower than that used by other researchers, but it allowed the crack growth to be visually observed. Unlike the DCB and ENF test, only one data point was collected for each sample because the crack tip grew into the ±45° layers of the composite adherend. Failures in the composite were expected based on research by Johnson and Mall [*9*]. The authors found that composite bonded specimens with ±45° plies closest to the adhesive had failed in the composite layers. Since failures in the composite were expected, unidirectional specimens were exposed and tested even thought they are less likely to be used in this application.

Analysis of Data

The following sections describe the equations that were used to analyze the DCB, CLS, and END specimens.

Analysis of DCB Specimen

A closed-form solution from the ASTM standard was used to determine the Mode I strain energy release rate, G_I, of the adhesive joint [*6,10*]. The strain energy release rate is the amount of energy required for crack growth, which determines the toughness of the specimens. The modified beam theory was selected for data reduction because it tends to calculate the most conservative strain rates [*11*]. Equation 1 may be used to determine the Mode I strain energy release rate based on the modified beam theory

$$G_I = \frac{3P\delta}{2b(a + |\Delta|)} \tag{1}$$

where

P = load (N)
b = specimen width (mm)
Δ = intercept of a-axis from compliance$^{1/3}$ versus a
δ = crosshead displacement (mm)
a = crack length (mm)

The load used in the calculation was taken at the point where the load versus displacement curve deviated from linearity, which is an indication of crack growth. The specimen width was measured in three places on the specimen, and the average was used as the width for the calculation. The crack length, a, was the final length of the crack measured from the loading point. Delta, Δ, was found from the graph of the cube root of compliance (C) versus crack length (a). The relationship between $C^{1/3}$ and a was a linear relationship, and Δ equaled the value of a, when $C^{1/3}$ was equal to zero. The com-

pliance of the specimen was found as the slope of P/δ. The Δ term is used to modify the calculation because it accounted for the uncracked end of the DCB being free rather than restricted [*10*].

Analysis of ENF Specimen

Since there was not a standard, the analysis for the ENF specimens was based on previous research [*8,12,13*]. The equation selected to determine the fracture toughness was the direct beam theory method that relies directly on experimental load and deflection data. The calculation can be seen in Eq 2.

$$G_{II} = \frac{9Pa^2\delta}{2b(2L^3 + 3a^3)} \tag{2}$$

where

P = load (N)
b = specimen width (mm)
L = half span between outer points of test fixture (mm)
δ = displacement (mm)
a = initial crack length (mm)

The load used in the calculation was taken at the point when the load versus displacement curve deviated from linearity indicating crack growth. As with the DCB specimens, the specimen width was measured in three places on the specimen, and the average was used as the width for the calculation. The crack tip was placed halfway between the center pin and an outer pin. After each test run, the specimen was relocated so that the new crack tip was located halfway between the center pin and an outer pin to keep the initial crack length, a, constant at 25.4 mm (1 in.). Since L was a constant of the test fixture, it remained 54.8 mm (2 in.).

Analysis of CLS Specimen

The CLS tests also did not have an accepted standard; therefore, the analysis was based on previous research [*6,8,12,13*]. The geometry and analysis selected for this research was developed by Brussat [*14*]. Equation 3 is the closed-form solution used to determine the total strain energy release rate, G_t

$$G_t = \frac{P^2}{2b^2}\left[\frac{1}{E_s t_s} - \frac{1}{E_s t_s + E_1 t_1}\right] \tag{3}$$

where

P = load (N)
E_s, E_1 = elastic modulus of strap and lap, respectively
t_s, t_1 = thickness of strap and lap, respectively
b = specimen width (mm)

The load used in the calculation was taken at the point when the crack growth was visually observed. As with the other tests, the specimen width was measured in three different locations on the specimen, and the average was used as the width for the calculations. The thickness was also measured in

three areas on the specimen, and the average was used as the thickness for the calculations. The elastic modulus of the composite adherends was supplied by Lockheed Martin as 137 GPa (19.9 Msi) for the primarily unidirectional adherends and 66 GPa (9.6 Msi) for the near quasi-isotropic adherends.

The closed-form solution used does not give the fracture toughness in terms of Mode I and Mode II, but rather the total fracture toughness of the adhesive bond. In order to determine the individual Mode I and Mode II components of the fracture toughness, a finite-element analysis developed by Valentin [*15*] was employed. This finite-element analysis determined a slightly more conservative value of fracture toughness than the closed-form solution. However, the FEA calculation was within 7% of the value of the closed-form solution for primarily unidirectional adherends and within 25% for the near quasi-isotropic specimens. The data presented in this report was calculated from the FEA model and the total strain energy release rate is equal to the sum of the Mode I and Mode II calculations.

Results and Discussion

The following sections discuss the results for the double cantilever beam, end-notched flexure, and crack lap shear tests.

DCB Specimens

Figure 2 compares the fracture toughness for different environmental exposures for DCB specimens with unidirectional and quasi-isotropic bonded adherends. Each bar on the graph represents a different environmental exposure, and the thin vertical bars on each data point represent the range of the 95% confidence interval. From the first four bars it can been seen that the specimens with primarily unidirectional adherends exposed to a hot/dry environment had a lower fracture toughness than the as-received specimens indicating that the hot/dry environment adversely affected the Mode I fracture toughness. For specimens with either unidirectional or quasi-isotropic adherends, the thermal cycles had little effect on the fracture toughness of the bonded joint [*16*].

Figure 3 shows the effect of the F-22's operating temperature range −54°C (−65°F) to 220°F (104°C) on the fracture toughness of the bonded graphite/bismaleimide system. These specimens were not environmentally exposed before testing, but were as-received. The fracture toughness of the bonds with primarily unidirectional adherends was not significantly reduced during testing at either the cold and hot temperature when compared with the toughness at room temperature. However, the cold temperature test had a larger degree of scatter in the data. The fracture toughness of the bonds with the near quasi-isotropic adherends was significantly reduced for only the cold temperature tests. The hot temperature did not seem to affect the Mode I fracture toughness for either the primarily unidirectional or the near quasi-isotropic [*17*].

Figure 2 shows a reduction in the fracture toughness for all specimens that were environmentally exposed and tested at room temperature. Figure 3 shows that for quasi-isotropic specimens, the specimens tested at cold temperature showed a reduction in toughness when compared to the room temperature specimens. Since the environmental exposure showed a loss of fracture toughness and for the unidirectional specimens and the cold temperature showed a reduction in toughness for the quasi-isotropic specimen, another set of tests was conducted to determine if a combination of environmental exposure and cold test temperature might further reduce fracture toughness. Figures 4 and 5 show the results of tests for the primarily unidirectional and near quasi-isotropic specimens that were environmentally exposed and tested at a cold temperature. Each graph compares the cold temperature test with the corresponding room temperature test. On both graphs, for every environmental exposure the tests conducted at cold temperature had a lower fracture toughness than the corresponding room temperature test even if the environmentally exposed specimen did not have a loss of toughness at room temperature.

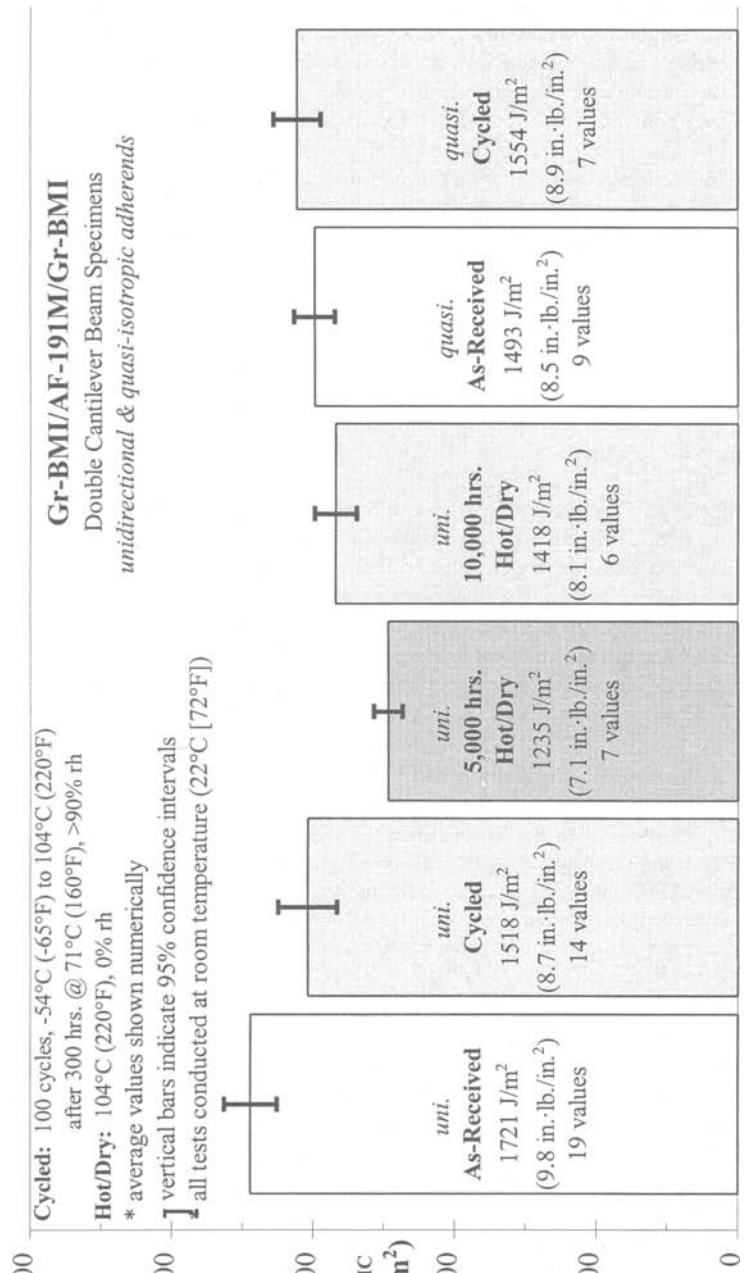


FIG. 2—*Effect of exposure on Mode I fracture toughness of Gr-BMI/AF-191M/Gr-BMI bonded system.*

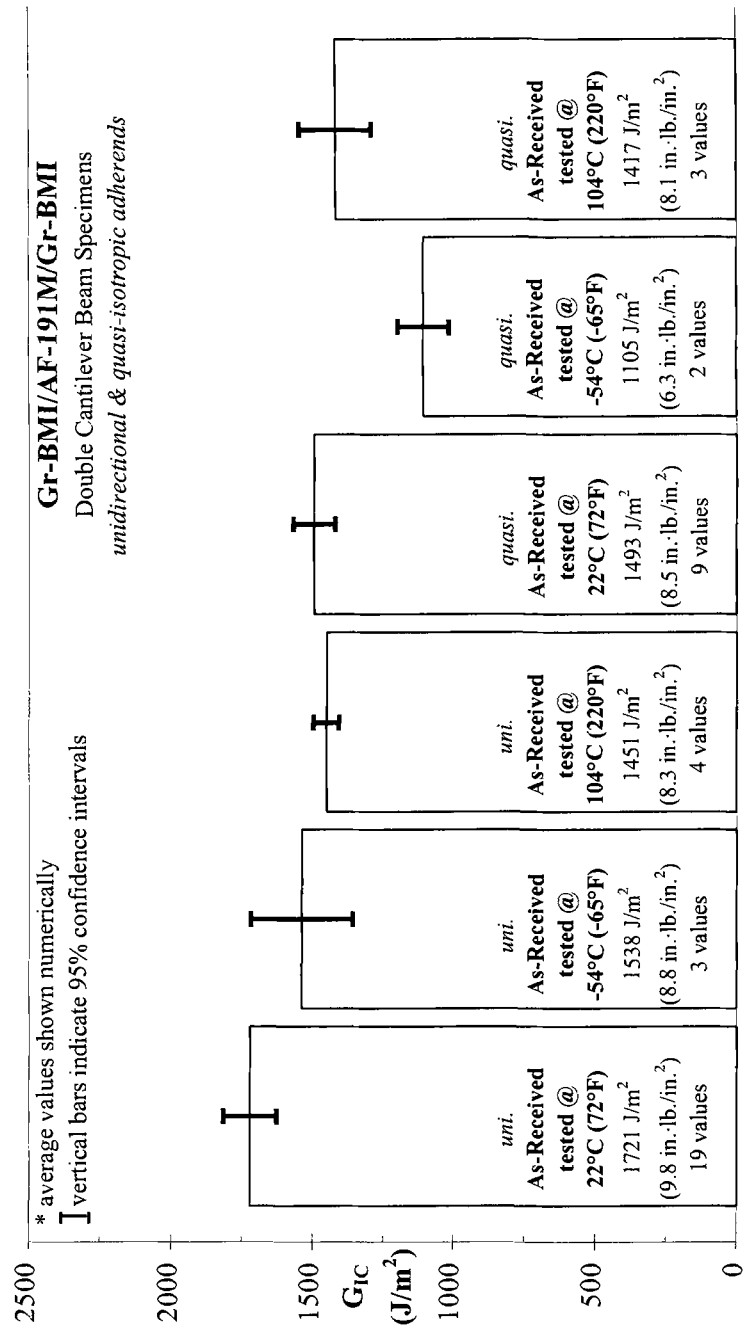


FIG. 3—*Effect of test temperature on Mode I fracture toughness of Gr-BMI/AF-191M/Gr-BMI bonded system.*

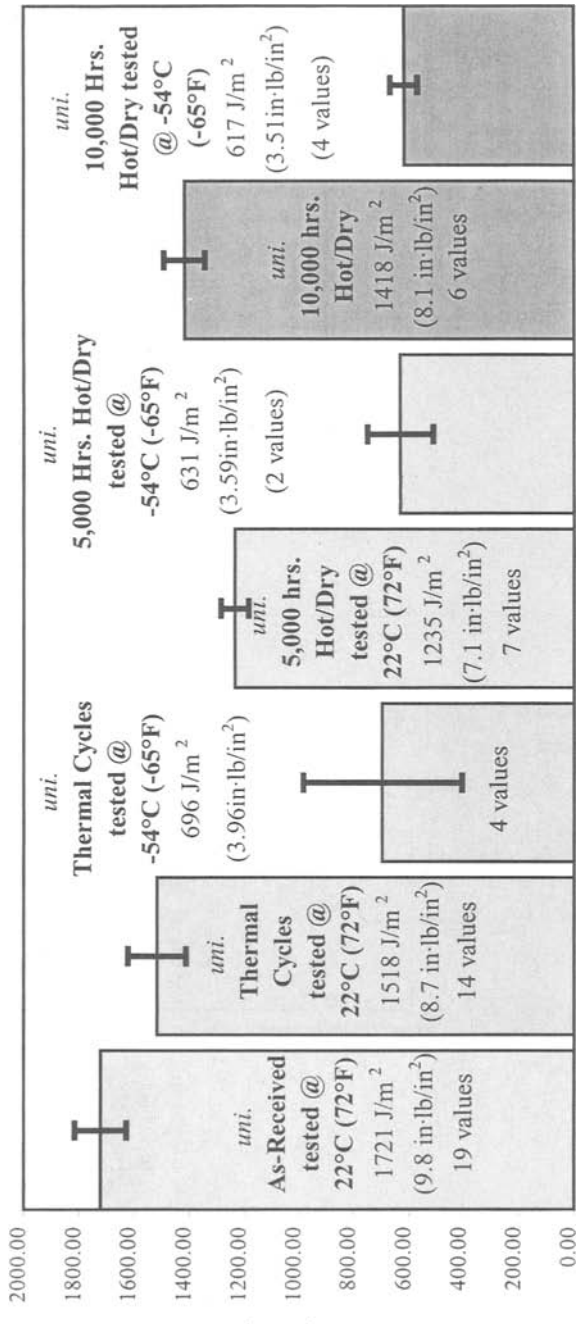


FIG. 4—*Effect of combination of environmental exposure and testing at cold temperature on unidirectional DCB Gr-BMI/AF-191/Gr-BMI.*

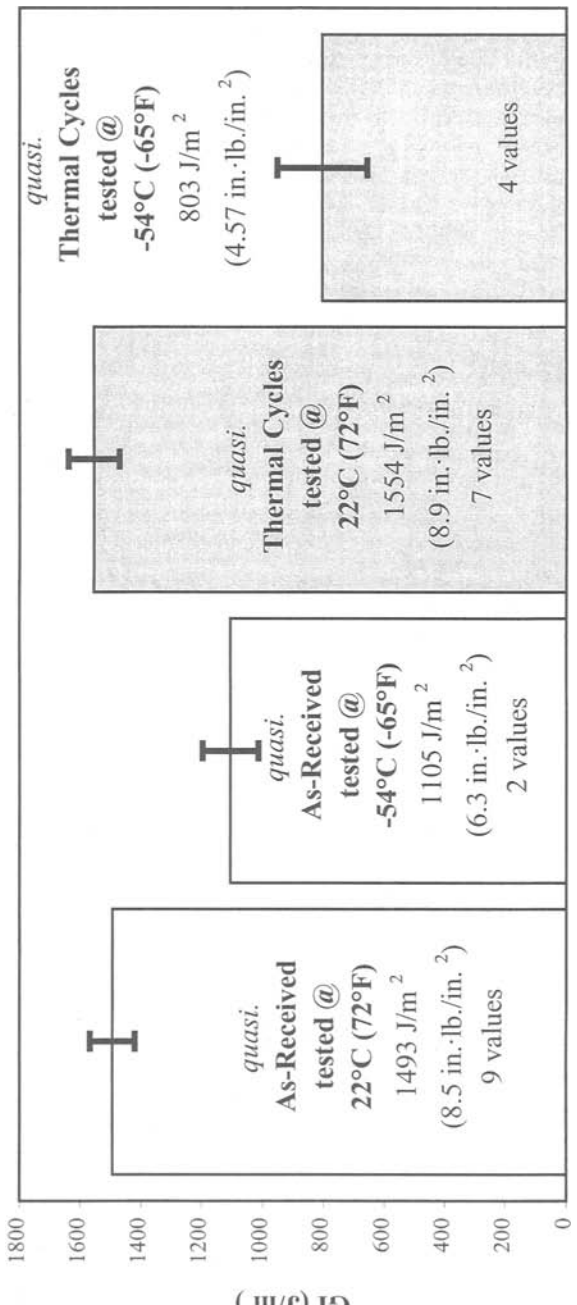


FIG. 5—*Effect of test temperature and environmental exposure on Mode I quasi-isotropic DCB Gr-BMI/AF-191/Gr-BMI specimens.*

Fracture Surface of DCB—The fracture surfaces of the primarily unidirectional adherends were different than the fracture surface of the near quasi-isotropic adherends. Figure 6 shows the fracture surface of both the unidirectional and quasi-isotropic adherends of the as-received specimens tested at room temperature. As seen in Fig. 6, the fracture path of the unidirectional adherends remained cohesive, mainly along the scrim cloth in the adhesive. This can be seen as the adhesive remaining on both adherends after testing. However, the fracture path of the quasi-isotropic specimens went into the $\pm 45°$ layers located adjacent to the bond line. This can be seen at the fibers are torn from one adherend and imbedded in the adhesive of the other adherend. The epoxy adhesive should be tougher than the bismaleimide used in the composite adherends. Therefore, a crack growing in the adhesive would require more energy to grow than a crack advancing in the composite. As a result, the difference in the fracture path may account for the fracture toughness of the unidirectional being higher than the fracture toughness of the quasi-isotropic.

ENF Specimens

The ENF specimens were used to determine the Mode II fracture toughness of the adhesive bonds. All of the ENF tests were carried out at room temperature. Figure 7 shows the results of the ENF tests for both the primarily unidirectional and near quasi-isotropic specimens. The Mode II fracture toughness for the unidirectional as-received specimen was 3057 J/m^2 (17.4 in. · lb/in.^{2}), which was significantly higher than the Mode I toughness of 1721 J/m^2 (9.8 in. · lb/in.^{2}) found from the DCB specimen. The Mode II toughness of the specimens with quasi-isotropic adherends was considered a lower-bound value. This is because during testing the adherends failed in compression at the pins. By comparing the exposed specimens with the as-received specimens in Fig. 7, the environmental exposure did not appear to have an effect on the Mode II fracture toughness of the system [*18*]. No tests were conducted at a cold or hot temperature on the ENF specimens due to equipment limitations.

CLS Specimens

Figures 8 and 9 show the results of the room temperature tests of the CLS specimens having primarily unidirectional and near quasi-isotropic adherends, respectively. The Mode I and Mode II components were determined using the finite element analysis developed by Valentin [*15*]. These values were lower than the values that were calculated with the closed-form solution. As seen in Fig. 8, specimens with unidirectional adherends that were exposed to thermal cycles and a hot/dry environment had significantly lower fracture toughness values than the as-received value. The unidirectional as-received value was 6026 J/m^2 (34.3 in. · lb/in.^{2}) whereas the specimen with an exposure for 10 000 h hot/dry had slightly more than half of the fracture toughness at 3363 J/m^2 (19.1 in. · lb/in.^{2}). As seen in Fig. 9, the quasi-isotropic specimens had a small reduction in fracture toughness from the as-received value for the specimens exposed to hot/wet plus thermal cycles. However, when the as-received values are compared from Fig. 8 to Fig. 9, the quasi-isotropic as-received specimen had less than half the fracture toughness of the unidirectional as-received specimen.

Figures 8 and 9 also show the results for tests conducted at a hot temperature and a cold temperature for the primarily unidirectional and near quasi-isotropic specimens, respectively. For both the primarily unidirectional and the near quasi-isotropic, the hot test temperature caused a failure in the strap before cracking was observed in the bond line. A lower bound was determined from the load at which the strap failed for both the unidirectional and quasi-isotropic specimens. As seen in Fig. 8, the cold test temperature severely reduced the as-received fracture toughness from 6026 J/m^2 (34.3 in. · lb/in.^{2}) at room temperature to 869 J/m^2 (4.9 in. · lb/in.^{2}) at a cold test temperature for the unidirectional specimens. For the quasi-isotropic specimens shown in Fig. 9, the cold test temperature reduced the fracture toughness more than half, from 2516 J/m^2 for as-received specimen tested at room temperature to 1366 J/m^2 (7.8 in. · lb/in.^{2}) for as-received specimen tested at cold temperature [*18*].

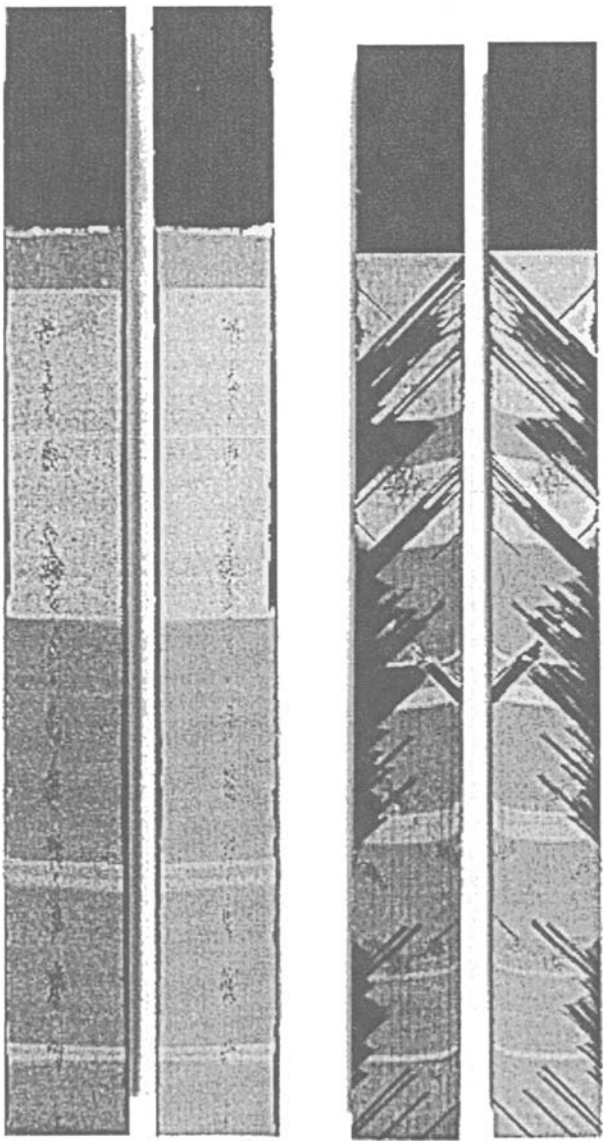


FIG. 6—(Top) *Fracture surface of primarily unidirectional DCB Gr-BMI/AF-191/Gr-BMI;* (bottom) *fracture surface of near quasi-isotropic DCB Gr-BMI/AF-191/Gr-BMI.*

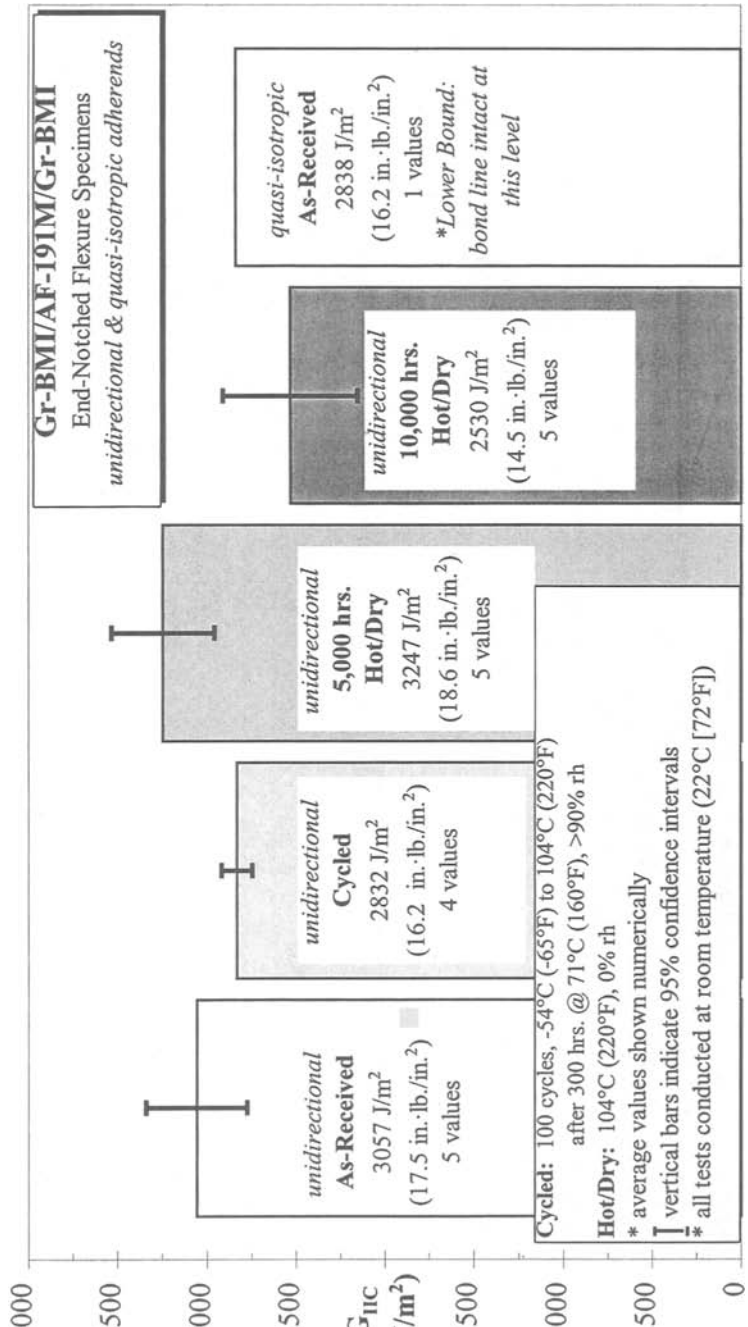


FIG. 7—*Effect of environmental exposure on Mode II fracture toughness for Gr-BMI/AF-191/Gr-BMI.*

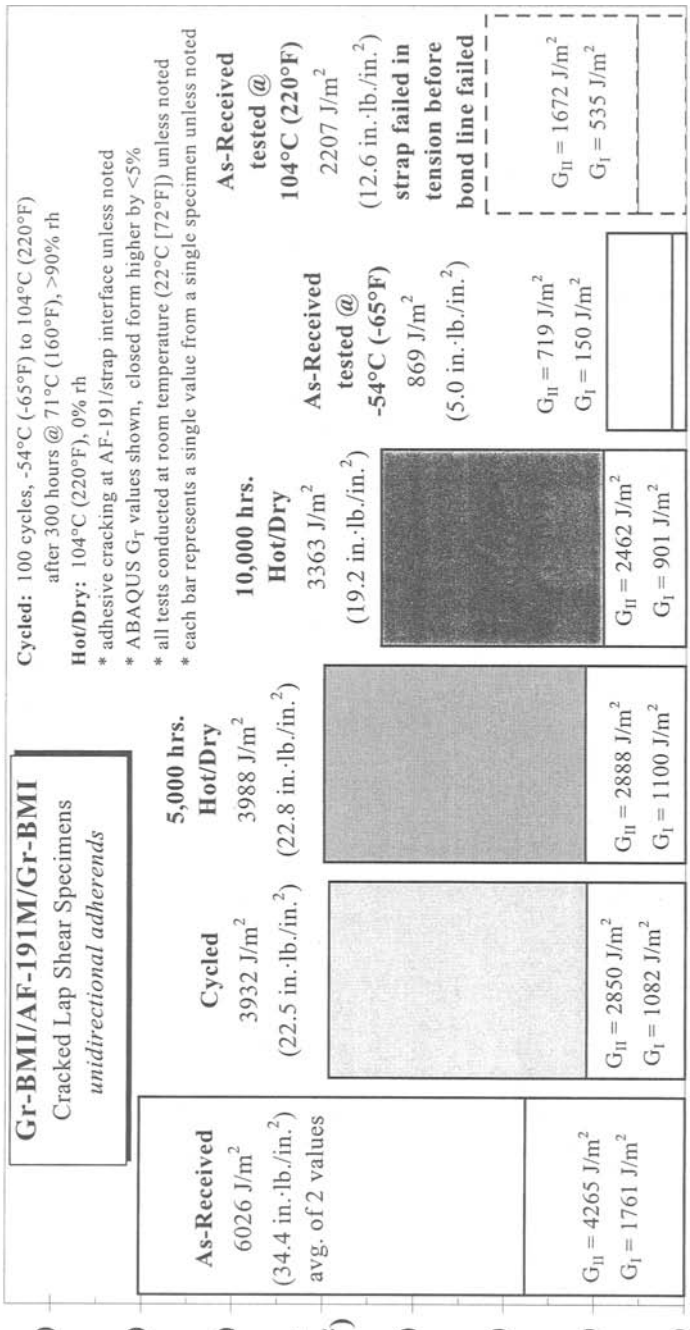


FIG. 8—*Effect of environmental exposure and test temperature on mixed-mode unidirectional Gr-BMI/AF-191/Gr-BMI.*

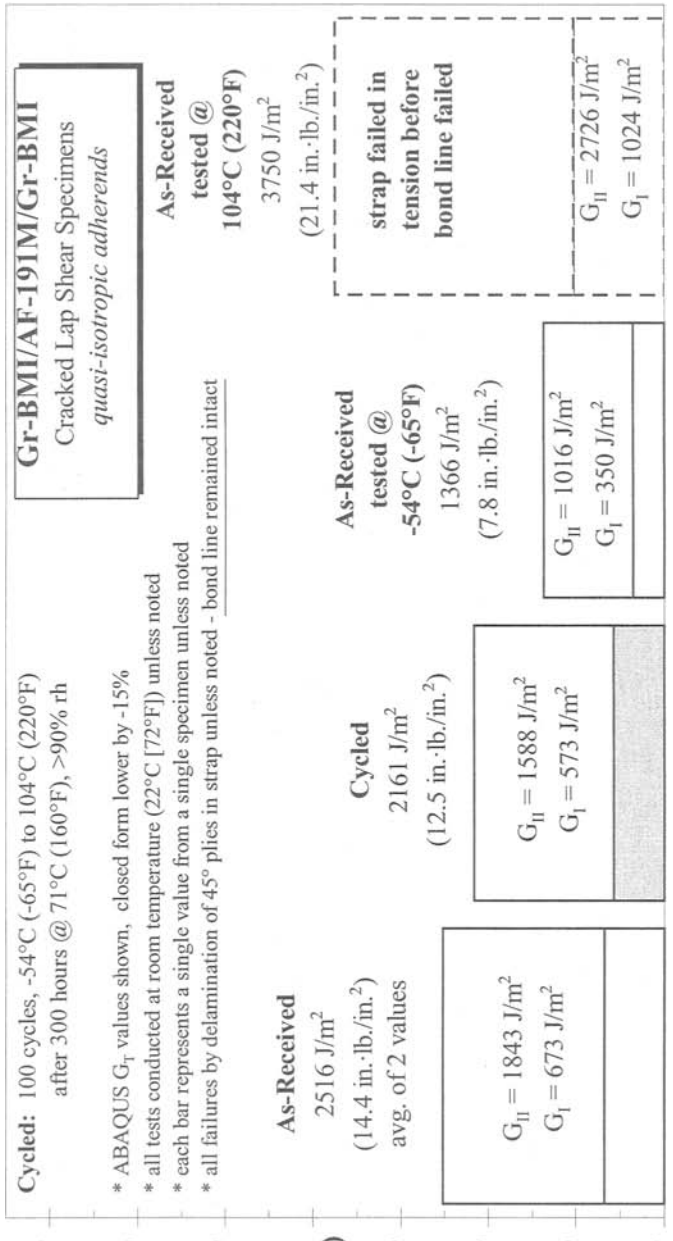


FIG. 9—*Effect of environment and test temperature on mixed-mode quasi-isotropic Gr-BMI/AF-191/Gr-BMI.*

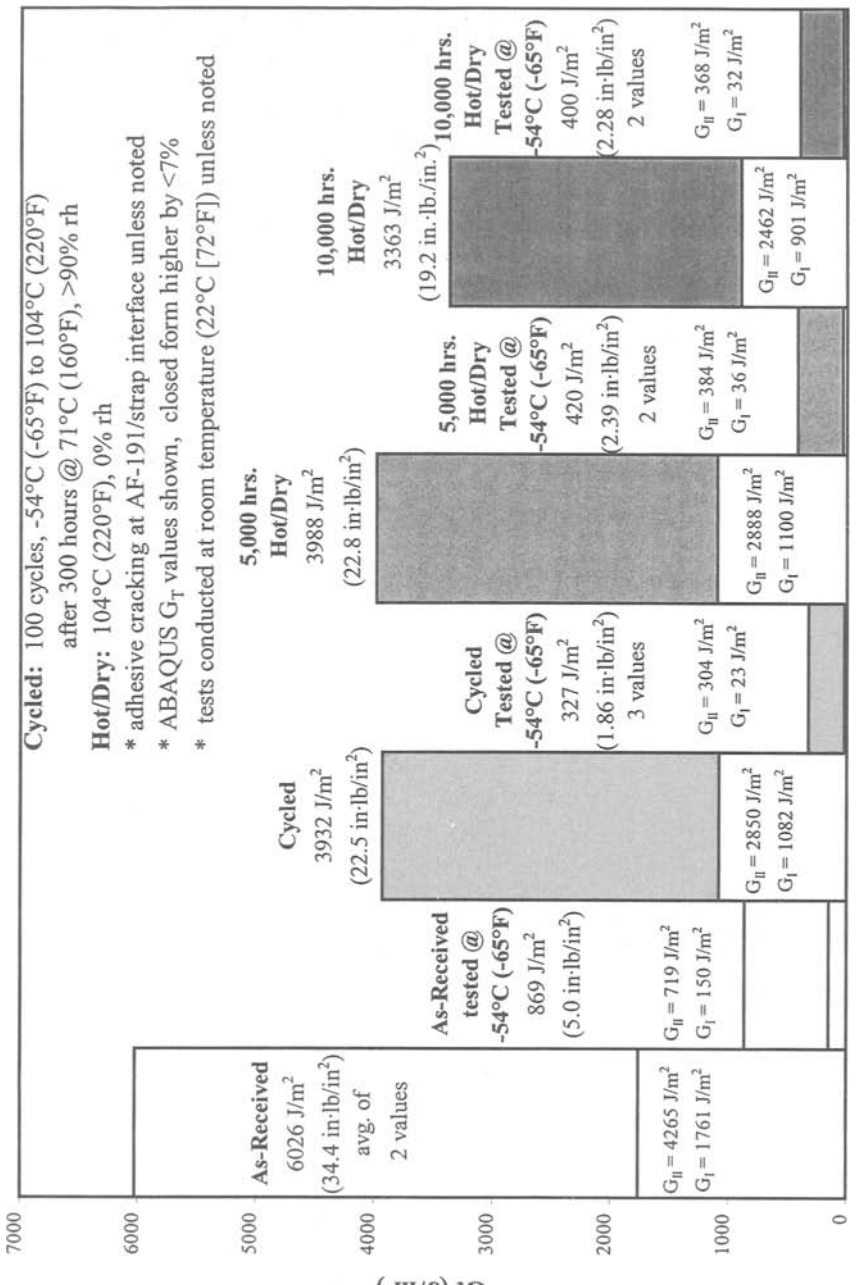


FIG. 10—*Effect of environmental exposure and cold test temperature on mixed-mode fracture toughness of unidirectional Gr-BMI/AF-191/Gr-BMI.*

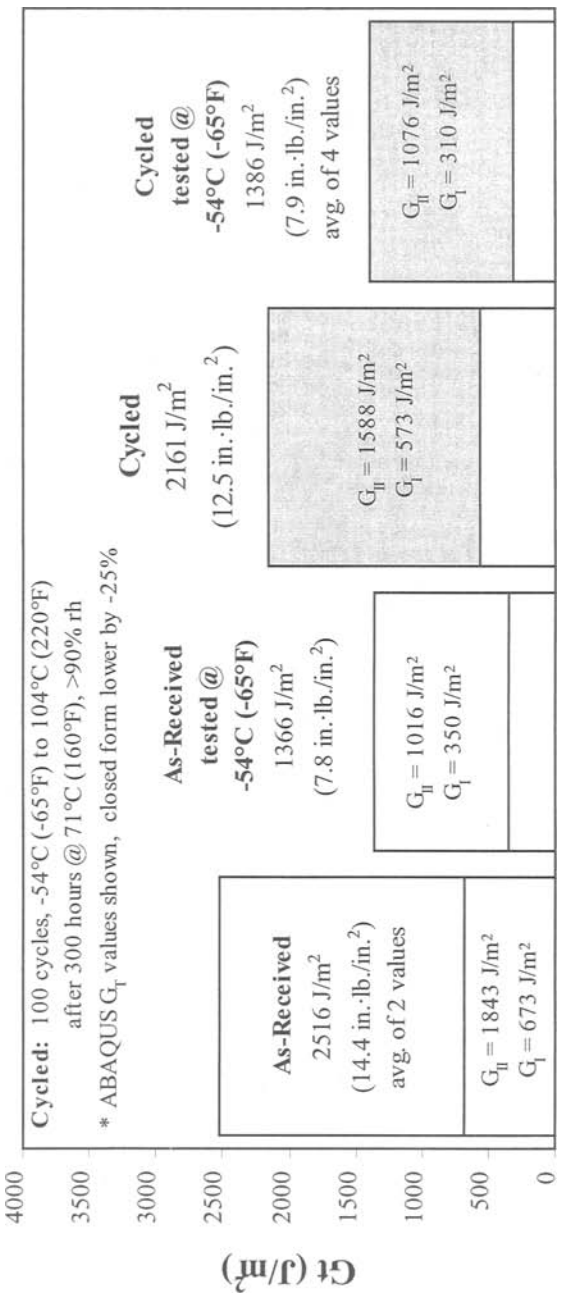


FIG. 11—*Effect of environmental exposure and cold test temperature on mixed-mode fracture toughness of quasi-isotropic Gr-BMI/AF-191/Gr-BMI.*

A reduction in fracture toughness was seen for both unidirectional and quasi-isotropic specimens that were environmentally exposed or tested at cold temperature. Tests were then conducted to see if the combination of environmental exposure and cold test temperature would combine to further reduce the fracture toughness. Specimens that were exposed to hot/dry or hot/wet plus thermal cycles were tested at cold temperatures to investigate the combination of exposure and test temperature for both unidirectional and quasi-isotropic. Figure 10 compares the results for the unidirectional adherends tested at room temperature and cold temperature for different environmental exposure. For every type of exposure, the fracture toughness of the cold temperature test was reduced to a fraction of the fracture toughness of the corresponding room temperature test. Figure 11 shows the results from the room temperature tests and cold temperature tests for the quasi-isotropic specimens. The cold test temperature had a similar effect on the fracture toughness of the as-received and hot/wet plus thermally cycled specimens. The reduction in fracture toughness of the hot/wet plus thermally cycled specimen from room temperature to cold temperature was approximately 35%, from 2161 J/m^2 (12.3 in. · lb/in.^{2}) to 1387 J/m^2 (7.9 in. · lb/in.^{2}).

As with the DCB specimens, the fracture toughness of the primarily unidirectional specimens was higher than the near quasi-isotropic specimens. The fracture surfaces of the CLS specimens were examined and it was found that near quasi-isotropic specimens failed almost completely in the composite rather than in the adhesive. As mentioned before, the adhesive is tougher than the bismaleimide in the composite. As a result, the primarily unidirectional specimens that failed in the adhesive required more energy to grow the crack, causing a higher strain energy release rate than the near quasi-isotropic specimens that failed in the composite layers.

Conclusions

The effect of environmental exposure on the adhesively bonded graphite/bismaleimide system was investigated for different modes of failure. The most significant finding of this research was that cold temperatures combined with environmental exposure are a significant factor in the fracture toughness of the adhesively bonded joint. For both DCB and CLS specimens as well as both primarily unidirectional and near quasi-isotropic specimens the combination of environmental exposure and cold test temperature severely reduced the fracture toughness of every specimen tested. This reduction was seen even in specimens where the environment alone or the cold temperature alone did not seem to affect the toughness of the adhesively bonded joint.

For the room temperature test, it was found that thermally cycled specimens either did not degrade the toughness as much as specimens exposed to hot/dry conditions (104°C, 220°F) for DCB and CLS specimens (Mode I and mixed Mode I/Mode II). This indicates that the hot/dry environment may have more effect on the adhesive that originally thought. Only the primarily unidirectional specimens were exposed to the hot/dry environment. Future testing should include the hot/dry environment on the near quasi-isotropic specimens. Due to the scatter in the data it could not be concluded that either environmental exposure had an effect on the ENF specimens (Mode II).

For the DCB and CLS specimens, cold and hot test temperatures were used to determine if the fracture toughness of the as-received specimens would be affected. Hot test temperature did not seem to have an effect on the fracture toughness of the specimens. However, CLS specimens tested at hot temperatures failed in the composite before the adhesive bond failed. The cold test temperature (−54°C, −65°F) reduced the fracture toughness of near quasi-isotopic DCB specimens and both the primarily unidirectional and near quasi-isotropic CLS specimens.

It was also found that the fracture surface of the quasi-isotropic specimen differed from the unidirectional specimen for the DCB and CLS tests. For the near quasi-isotropic specimens, the crack propagated in the composite ±45° plies rather than in the adhesive, needing less energy to propagate, whereas, the unidirectional specimens failed in the tough adhesive, usually along the scrim cloth. The difference in the fracture path may have caused a lower fracture toughness for the quasi-isotropic specimens since they failed in the weaker bismaleimide. To prevent the crack from growing into the composite adherends, unidirectional fibers should be placed closest to the adhesive rather than ±45° plies.

This research has shown that under certain conditions the fracture toughness of a modified epoxy adhesive used for composite bonding can be significantly degraded. The degradation has been shown here to occur under long-term isothermal conditions as well as at cold temperatures. Continued research into the fracture toughness of adhesively bonded materials is needed to identify a safe operating envelope in which they may be used effectively.

Acknowledgments

The authors would like to acknowledge the financial support of the FAA Technical Center (Grant 95G023) and the NASA sponsored HiPPAC Center at Clark Atlanta University. We would also like to thank Lockheed Martin Aeronautical Systems for manufacturing and supplying the bonded joint specimens.

References

[1] Hart-Smith, L. J., "Adhesive Bonding of Aircraft Primary Structures," *High Performance Adhesive Bonding,* G. DeFrayne, Ed., Society of Manufacturing Engineers, Dearborn, MI, 1983, pp. 99–113.

[2] Blomquist, R. F., "Adhesives—Past, Present, and Future," *Adhesion, ASTM STP 360,* American Society for Testing and Materials, 1964, pp. 179–212.

[3] Brenner, W., "Structural Adhesives Challenge Mechanical Fasteners," *Machine Design,* Vol. 57, Part 1, 24 Jan. 1985, pp. 61–64.

[4] Lockheed Martin Aeronautical Systems, "F-22 Raptor: Air Dominance for the 21st Century," *ASM Advanced Materials and Processes,* Vol. 153, No. 5, May 1998, pp. 23–26.

[5] Kandebo, S. W. and Hughes, D., "F-22 to Counter 21st Century Threats," *Aviation Week and Space Technology,* Vol. 143, 24 July 1995, pp. 38–47.

[6] Mall, S. and Johnson, W. S., "Characterization of Mode I and Mixed-Mode Failure of Adhesive Bonds Between Composite Adherends," *Composite Materials: Testing and Design, 7th Conference, ASTM STP 893,* J. M. Whitney, Ed., American Society for Testing and Materials, 1986, pp. 322–334.

[7] "Protocol for Interlaminar Fracture Testing-End-Notched Flexure," provided by G. Murri, NASA-Langley Research Center, July 1994.

[8] Johnson, W. S., "Stress Analysis of the Cracked Lap-Shear Specimen: An ASTM Round Robin," *Journal of Testing and Evaluation,* Vol. 15, No. 6, American Society for Testing and Materials, Nov. 1987, pp. 303–324.

[9] Johnson, W. S. and Mall, S., "Influence of Interface Ply Orientation on Fatigue Damage or Adhesively Composite Joints," *Journal of Composites Technology & Research,* Vol. 8, No. 1, Spring 1986, pp. 3–7.

[10] Hashemi, S., Kinloch, A. J., and Williams, J. G., "Corrections Needed in Double-Cantilever Beam Tests for Assessing the Interlaminar Failure of Fibre-Composites," *Journal of Materials Science Letters,* Vol. 8, No. 2, Feb. 1989.

[11] O'Brien, T. K. and Martin, R. H., "Round Robin Testing for Mode I Interlaminar Fracture Toughness of Composite Materials," *Journal of Composites Technology & Research,* JCTRER, Vol 15, No. 4, Winter 1993, pp. 269–281.

[12] Russell, A. J. and Street, K. N., "Moisture and Temperature Effects on the Mixed-Mode Delamination Fracture of Unidirectional Graphite/Epoxy," *Delamination and Debonding of Materials, ASTM STP 876,* W. S. Johnson, Ed., American Society for Testing and Materials, 1985, pp. 349–370.

[13] Johnson, W. S. and Mangalgiri, P. D., "Influence of the Resin on Interlaminar Mixed-Mode Fracture," *Toughened Composites ASTM STP 937,* N. J. Johnson, Ed., American Society for Testing and Materials, 1987, pp. 295–315.

[14] Brussat, T. R., Chiu, S. T., and Mostovoy, S., "Fracture Mechanics for Structural Adhesive Bonds—Final Report," Lockheed Co., Burbank, CA, for the USAF Materials Laboratory, AFML-TR-77-163, Oct. 1977.

[15] Valentin, R. V., "Finite Element Analysis of Adhesively Bonded Joints," Master's thesis, Georgia Institute of Technology, Atlanta, GA, July 1997.

[16] Butkus, L. M. and Johnson, W. S., "The Durability of Graphite-Bismaleimide Aerospace Composites Bonded Using a Modified Epoxy Adhesive," *Proceedings of the American Society of Composites 12th Annual Technical Conference,* Wayne State Univ., Detroit, MI, R. Gibson and G. Newaz, Eds., Technomic Publishing, Lancaster, PA, Oct. 1997.

[17] Butkus, L. M., Valentin, R. V., and Johnson, W. S., "Environmental Effects on the Mode I Fracture and Fatigue of Bonded Composites," *Progress in Durability Analysis of Composite Systems,* K. L. Reifsnider and A. H. Cardon, Eds., A.A. Balkema, Rotterdam, 1998, pp. 77–84.

[18] Butkus, L. M., "Environmental Durability of Adhesively Bonded Joints," Ph.D. thesis, Georgia Institute of Technology, Atlanta, GA, July 1997.

Tom G. Reynolds[1] *and Hugh L. McManus*[1]

Accelerated Tests of Environmental Degradation in Composite Materials

REFERENCE: Reynolds, T. G. and McManus, H. L., **"Accelerated Tests of Environmental Degradation in Composite Materials,"** *Composite Structures: Theory and Practice, ASTM STP 1383*, P. Grant and C. Q. Rousseau, Eds., American Society for Testing and Materials, West Conshohocken, PA, 2000, pp. 513–525.

ABSTRACT: Combined moisture cycling and thermal cycling environments are known to create damage, such as cracking of material near exposed surfaces and edges, in many new materials intended for high-temperature service. Material models suggest the damage mechanisms; these models are used to design tests to (1) isolate the effects of different damage mechanisms, and (2) accelerate them. Tests are carried out in the combined environment and in its individual components: time at moisture, moisture cycling, time at temperature, and thermal cycling. Accelerated moisture cycling and thermal cycling tests are also designed and carried out. Results are presented which suggest that, for the IM7/PETI-5 and IM7/PIXA-M materials tested, time at moisture is the most important cause of microcracking damage, with thermal cycling playing some role. Moisture cycling plays a role in the distribution of damage. The models are used to reduce laminate-specific microcracking data to general design data in the form of fracture toughness versus cycle ($G_{Ic}(N)$) curves.

KEYWORDS: accelerated aging, damage, degradation, design, durability, environmental effects, material properties, polyimides, polymer matrix composites, test methods

Nomenclature

G_{Ic}	Effective fracture toughness in microcracking (J/m^2)
n	Number of samples tested at a given condition
N	Number of cycles
t	Exposure time (hours)
ρ	Observed crack density (cracks/cm)
ρ'	Predicted crack density (cracks/cm)

The airframes of future supersonic aircraft are likely to make extensive use of advanced polymer matrix composite materials. In such applications, the materials are exposed to severe cyclic environments which include moisture, thermal, mechanical and chemical components. These environments are known to cause degradation of composite materials, so candidate materials for supersonic airframe applications need to be tested for their response to them. Typically, airframes have a service life of 20 000 or more cycles, each lasting several hours; it is therefore unrealistic to test the environmental response of candidate materials in real time. Accelerated test methods are required.

Environmental degradation takes many forms. Often the earliest to appear is visible cracking, including surface crazing and both edge and through-laminate microcracking. There are a number of different components of the environment that could be responsible for the different types of damage observed, including moisture cycling, thermal cycling, time at moisture, time at temperature, or interactions of any of these. Each has been shown to cause damage to composite materials, e.g., [*1–4*].

[1] Graduate student and principal research engineer, respectively, Department of Aeronautics and Astronautics, Massachusetts Institute of Technology, Cambridge, MA 02139.

Copyright© 2001by ASTM International www.astm.org

Here, specimens of two candidate materials and three candidate layups are subjected to five environments with different hygral, thermal, hygrothermal cycling, and/or thermal cycling components. Damage is observed in terms of cracks visible at the edges of specimens. In this paper, background leading up to the design of the test program is given, followed by a complete description of the tests. Both raw results (crack densities) and reduced results (in the form of degradation of material fracture toughness) are presented. Some observations on the likely mechanisms of material degradation under these environments are made based on the results.

Background

This primarily experimental work builds on the existing understanding of both experimentally observed damage effects and mechanism-based models of these effects. Here, only the literature directly relevant to the planning and understanding of this work is reviewed. The general philosophy behind most of the cited work has been to observed effects, propose mechanisms based on fundamental engineering principles, develop computational models based on these mechanisms, predict the behavior of material under test conditions, and correlate to real data, modifying the models where necessary. This approach has been used to understand and model thermal [*5–7*], thermal cycling [*2,8*], thermo-oxidative [*4,9,10*], moisture absorption [*11,12*], moisture degradation [*3*], and moisture cycling [*12,13*] effects, stresses and damage due to these effects [*14,15*], and combinations of all of the above [*16*].

Of particular relevance to this work is the understanding of microcracking damage. Microcracking damage usually refers to cracks that run parallel to the fibers of a unidirectional ply or ply group (group of identical plies running in the same direction). These cracks are as wide as the ply or ply group is thick, and run anywhere from short distances to the full width of the ply. They are easily observed on cut edges of composite laminates, especially in plies that have fibers perpendicular to the cut edge, referred to here as 90° plies (Fig. 1). The accumulation of observed microcracks is a useful measure of damage. Microcrack density is generally defined as the number of microcracks in a unit width of a ply or ply group. Unfortunately, it is found to be highly dependent on test-specific conditions such as layup and ply group thickness.

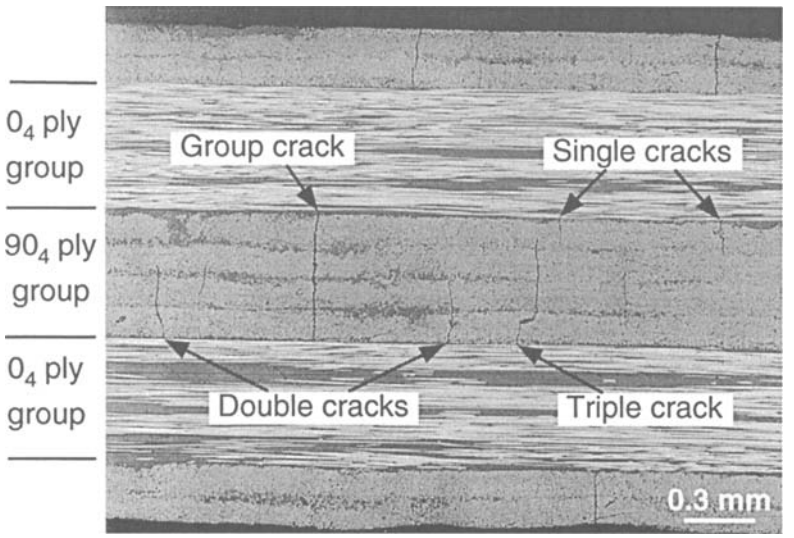


FIG. 1—*Microcracks of various widths visible at a cut edge of the "research" layup.*

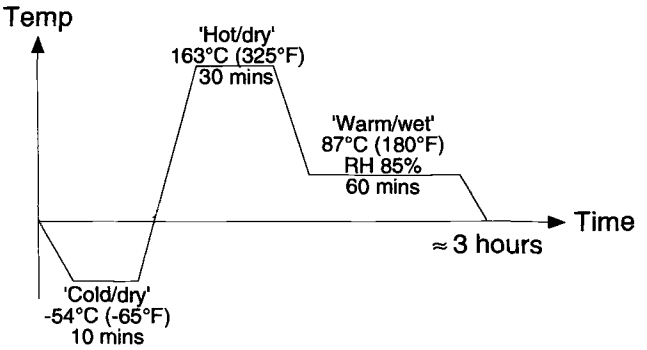


FIG. 2—*Baseline hygrothermal test cycle.*

Microcrack densities can, with the aid of appropriate models, be used to calculate an effective material fracture toughness that is independent of geometry. The modeling of this kind of damage generally involves a stress analysis of the cracked composite, and a Griffith-type failure criteria, in which it is assumed the crack will initiate and/or grow if the available strain energy is greater than the effective fracture toughness of the material. Stresses are present even in the absence of mechanical load due to stresses induced by thermal and moisture distributions. The stresses are highly dependent on layup, loading, and other test-specific factors (hence the test-specific nature of the observed microcracking), but the effective fracture toughness is a material property. Degradation of the material due to fatigue, environmental effects, etc., is captured in such models by assuming that the effective fracture toughness is reduced by the conditions [*2,3,8,17*]. This assumption can be used to reduce observed microcrack densities to effective fracture toughnesses as functions of the time in the environment and/or the number of cycles of the repeated condition. These relations are then plotted as $G_{Ic}(t)$ or $G_{Ic}(N)$ curves, where G_{Ic} is the effective fracture toughness in microcracking of the material, t is time, and N is the number of cycles of a cyclical environment or load. Data in this form can be used for design.

Environment of Interest

This work is part of an effort by the Boeing Company to understand material response to a supersonic-cruise environment. Boeing has developed a "baseline" test cycle shown in Fig. 2. The short "cold/dry" segment simulates subsonic cruise, followed by a longer "hot/dry" segment representative of supersonic flight. Moisture exposure is introduced via a "warm/wet" segment, representative of ground and low-altitude flight time. The baseline cycle is not meant to represent the exact conditions that any particular supersonic aircraft will encounter during a flight, but it captures the main elements of the environment.

The baseline environment has been observed to cause microcracking damage in a variety of candidate materials and layups [*1,18*]. A hygrothermal cycling analysis [*1,12*], using a Fickian diffusion model and an advanced solver for the cyclic conditions, has shown that this environment causes an interesting and unusual moisture and stress state in the materials and layups of interest. During warm-wet exposure, moisture diffuses into the material near the laminate surface; most of the moisture is driven out again during the next hot-dry exposure. Material in the laminate interior reaches a stable, low level of moisture after a few dozen cycles. Figure 3 shows the calculated absorbed moisture profiles in an initially dry IM7/PETI-5 laminate exposed to 100 baseline cycles. The interior of the specimen is stable and relatively dry, while a thin layer near the surface "thrashes" between wet and dry states. These predictions were partially verified by specimen weight measurements taken during hy-

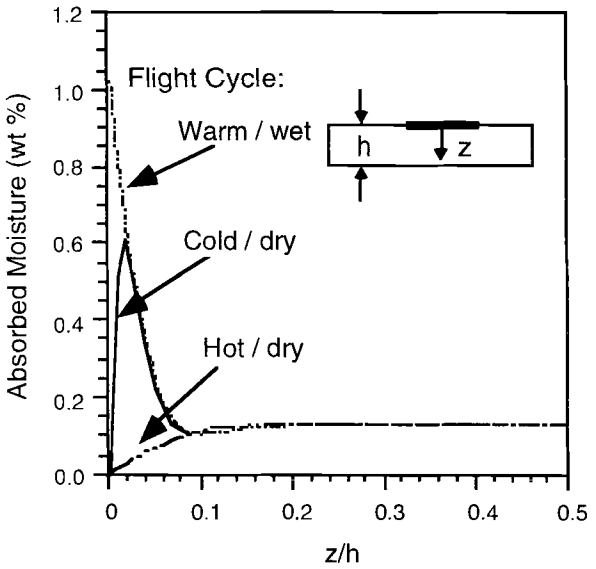


FIG. 3—*Absorbed moisture profiles at various points in the baseline cycle in IM7/PETI-5 composite (from Ref 1).*

grothermal exposure, which match the predicted total weight gains very well. The same analysis was used to show that an accelerated moisture cycling program could be used to produce very similar profiles of moisture concentration in less time (Fig. 4). An accelerated cycling program (defined in the next section) was designed to match the moisture profiles near the surface for a given number of cycles while taking less time per cycle [*1*].

Visible cracking was seen in many materials tested under this environment, generally increasing with cycling. A stress analysis [*12,15*] shows that neither the thermal residual stresses, nor the stresses

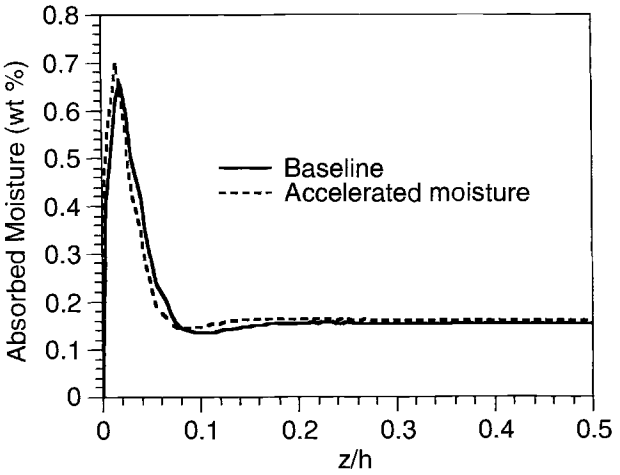


FIG. 4—*Absorbed moisture profiles from baseline and accelerated environments in IM7/PETI-5 composite (cold/dry segment after 100 cycles) (from Ref 1).*

created by the moisture distributions, are severe enough to cause cracking under these circumstances. Therefore, material degradation due to some component or combinations of components of the environment was hypothesized.

Problem Statement

In the work presented here, insights gained from mechanism-based models and prior exploratory testing are used to design tests to separate and accelerate the effects of different components of the baseline environment. The design of the tests is described, and the full test matrix and representative results are presented. A standardized method for interpreting edge microcrack data is developed and presented. Key results are reduced to design $G_{1c}(N)$ curves. Results from another study partly funded under the same program [*3*] are also considered. The combined results are used in observations of the relative contributions of the different components of environment to material degradation.

Experimental Procedures

The tests consisted of exposing samples to environmental conditions for varying times and/or numbers of cycles, and then checking them for microcracking damage by visual examination of edges and, in some cases, laminate interiors.

Test Matrix

The tests performed are summarized in Table 1. Two composite materials were considered—IM7/PETI-5 and IM7/PIXA-M. Standard 5 mil (0.127 mm) plies of these materials were used to build up laminates with three different layups. One was dubbed the "research" layup—its simple geometry, in particular the thick group of four 90° plies at the laminate centerline, was expected to exag-

TABLE 1—*Test matrix.*

Material*	Layup*	Test Type	No. of Cycles	Notes
PETI-5	"Research" $[90_2/0_4/90_2]_S$	Baseline	0, 50, 200, 500, 1000, 1500	Two different specimens at each cycle count
PIXA-M	"Crossply" $[0/90/0]_{2S}$	Accel. moisture	0, 288, 500, 1000, 1500, 1960	Two different specimens at each cycle count
	"Quasi" $[45/90/-45/0]_{2S}$	Isolate thermal	0, 50, 200, 500, 1000, 1500	Two different specimens at each cycle count
		Accel. thermal 1	0, 65, 100, 180, 300, 400, 540, 750	Same three specimens used throughout
		Accel. thermal 2	0, 80, 170, 280, 410, 560, 750	Same three specimens used throughout
		Isothermal	4250 h at 350°F (177°C) only	Research: 8 specimens Crossply: 4 specimens Quasi: 7 specimens
		Accel. thermal 1 (isothermal specimens)	0, 50, 150, 300, 400	Same three isothermal specimens used throughout

* All six combinations of material and layup used for every test type.

gerate damage and simplify modeling. The others were realistic layups typical of aircraft use. All laminates were vacuum bagged on a plate and autoclave cured. The PETI-5 laminates were cured at 750°F (399°C), and the PIXA-M at 700°F (371°C), both at 100 psi (690 kPa) pressure. Other processing parameters were proprietary. Samples, 2 in. × 1 in. (5.1 cm × 2.5 cm), were cut from cured plates with diamond saws, and all edges were polished.

The samples were exposed to a variety of environmental conditions. These included:

- Baseline cycle (Fig. 2): cold/dry (−54°C) for 10 min, hot/dry (163°C) for 30 min, warm/wet (87°C, 85% RH) for 60 min, heating rate 11°C/min, cooling rate 5.5°C/min, 160 min/cycle.
- Accelerated moisture cycle: cold/dry (−54°C) for 5 min, hot/dry (163°C) for 20 min, warm/wet (87°C, 85% RH) for 30 min, heating rate 11°C/min, cooling rate 14°C/min, 90 min/cycle.
- Accelerated thermal cycles: dry air, cycled from +163°C to −180°C (Accl. thermal 1) or +163°C to −150°C (Accelerated thermal 2), 14°C/min ramp rates
- Isothermal exposure: dry air at a constant 350°F (170°C). Some isothermal aging specimens were also subjected to the first accelerated thermal condition after their isothermal exposure.

In addition, isomoisture exposure tests of IM7/PETI-5 laminates (immersed in water at 80°C) were carried out by Nairn as part of a related program [*3*].

The baseline, accelerated moisture, and isothermal tests were performed in environmental chambers at Boeing without preconditioning the specimens; the accelerated thermal testing was carried out in a thermal cycling chamber at MIT after drying specimens for three days at 300°F (149°C).

As shown in Table 1, groups of samples were extracted after varying numbers of cycles. Most samples were then examined for damage as described below, and not returned to conditioning. The accelerated thermal cycling test samples were an exception. These samples were examined after each listed cycle, then returned to the conditioning chamber.

Damage Assessment Technique

The impact of the environment on the materials was measured by the amount of cracking damage that was visible on the edges of the specimens. The long edges of the 2 in. × 1 in. (5.1 cm × 2.5 cm) specimens were examined. In the research layup of $[90_2/0_4/90_2]_S$, the center 90_4 ply group was examined. A number of different crack configurations are possible, see Fig. 1. A "group" crack is defined as one which traverses the entire 90_4 ply group. "Triple," "double," and "single" cracks traverse three plies, two plies, and one ply in the group, respectively. In the other layups, the plies of interest were the single 90s, so the only damage seen was cracks spanning one ply.

The edge damage was measured through a microscope by counting the number of cracks on the entire length of each 2 in. (5.1 cm) side. For the research layup, the number of group, triple, double, and single cracks were recorded. For the crossply and quasi-isotropic layups, the number of cracks in each of the four 90° plies on each side was recorded. The 45° plies were checked, but very few cracks were observed. The internal damage states of some specimens were also examined by carefully grinding away material and visually examining the newly created surfaces.

Data Reduction

Most results will be presented in terms of observed crack densities and their standard deviations. The definitions of crack density, especially in the presence of multiple types of cracks or multiple

cracking layers, can become confusing, so they are explicitly defined here. For the research layups, the number of group cracks were counted in the 90_4 group on both long sides of all specimens at each condition. The average group crack density was calculated as

$$\text{Average group crack density (/cm)} = \frac{\sum_{\substack{\text{all sides and} \\ \text{specimens}}} (\text{Group crack count})}{n \text{ specimens} \times 2 \text{ sides} \times 5.08 \text{ cm/side}} \tag{1}$$

where n was the number of specimens tested (Table 1).

Counts of triple, double, and single cracks were also taken and averaged in the same way. An "aggregate" crack density was used as a measure of the overall level of cracking in these thick ply groups. The aggregate crack count in a given ply group was found from

$$\text{Aggregate crack count} = \begin{bmatrix} (4 \times \#\text{ of group cracks}) + (3 \times \#\text{ of triples}) \\ + (2 \times \#\text{ of doubles}) + (\#\text{ of singles}) \end{bmatrix} \tag{2}$$

The average aggregate crack density was then calculated using

$$\text{Average aggregate crack density (/cm)} = \frac{\sum_{\substack{\text{all sides and} \\ \text{specimens}}} (\text{Aggregate crack count})}{n \text{ specimens} \times 2 \text{ sides} \times 5.08 \text{ cm/side}} \tag{3}$$

Standard deviations for a given crack type were calculated using the equation

$$\text{Standard deviation} = \frac{\sum (\text{crack count} - \text{average})^2}{(\#\text{ of count values} - 1)} \tag{4}$$

where "crack count" is the number of cracks of a given type in each ply or ply group.

For crossply and quasi-isotropic layups, the number of ply cracks were recorded for all four 90° plies on each long side of all specimens at a given test condition. The average crack density was calculated using

$$\text{Average crack density (/cm)} = \frac{\sum_{\substack{\text{all plies, sides} \\ \text{and specimens}}} (\#\text{ of cracks in each ply})}{n \text{ specimens} \times 2 \text{ sides} \times 4 \text{ plies/side} \times 5.08 \text{ cm/side}} \tag{5}$$

Standard deviations were calculated as in Eq 4.

Crack densities were used to compute the effective fracture toughness of the material using models fully developed in Ref *6*. The models assume that new cracks will appear when the local strain energy available exceeds the fracture toughness of the material. This fracture toughness is assumed to be degraded by the environment as a function of time or cycles of a repeated condition. The fracture toughness as a function of cycles, $G_{Ic}(N)$, is found by the following procedure. For conditions where sufficient cracking took place as a function of cycling to interpolate a crack density function $\rho(N)$, a fracture toughness function $G_{Ic}(N)$ was assumed, typically starting at the virgin material value and dropping off when cracks first appear. This function was used by the model to predict a crack density function $\rho'(N)$, and the prediction compared to the data. By trial and error, the fracture toughness function $G_{Ic}(N)$ was altered until a best fit between the predicted and observed crack density functions was achieved.

Results

General Observations

Damage in all cases (bar only one specimen) was confined to material near surfaces and edges of specimens. The data taken from the interiors of specimens were used only to confirm this situation, and will not be further considered here. Surface damage was usually confined to the surface plies; data taken from these plies will not be considered. Edge damage was confined to a zone usually less than 2 mm in depth. Cracking was mainly seen in the 90° plies and only rarely in the 45° plies; this is consistent with prior observations [*5*].

There is a large amount of scatter in the data. This can be attributed to a number of different factors. Prior work [*19*] has shown that microcracking analyses will predict considerable data scatter if one considers factors such as material variations. The current study was also limited in the number of specimens available for testing at each condition. Only two or three specimens were used for most test conditions. The tests conducted at MIT tracked damage in the same specimens as they became progressively more damaged at each condition. In the Boeing tests, different specimens were used for each condition, introducing more variability. Overall, although the scatter is high, the trends in the data discussed here were all more significant than the data scatter. The scatter (in the form of ± one standard deviation error bars) is shown on all data presented here.

Hygrothermal Cycling Results

The baseline cycle produced extensive cracking in all laminates of both materials. The results can be seen in terms of observed group cracks (cracks that span all four plies of the center 90° layer) in the PETI-5 research layup (Fig. 5) and the PIXA-M research layup (Fig. 6). Smaller cracks were also observed in these laminates, e.g., Fig. 1.

The accelerated moisture cycle results are also shown in these figures. Accelerated cycles created much less damage per cycle than baseline cycles. These results were typical of all layups, materials, and crack types.

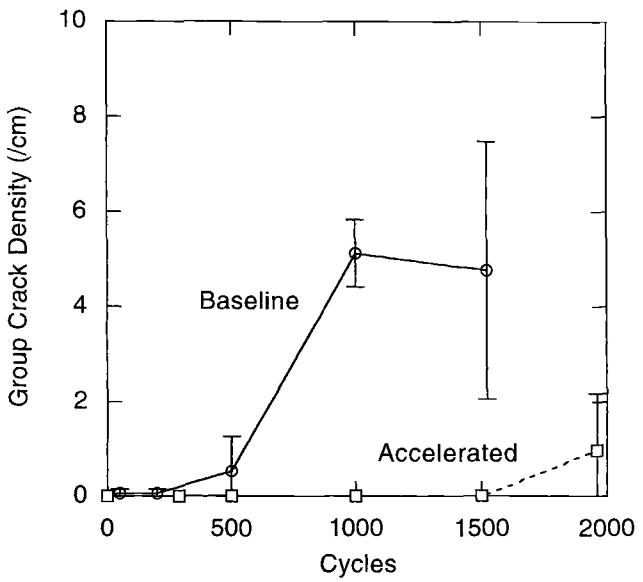


FIG. 5—*Group crack density in PETI-5 research layup under hygrothermal cycles.*

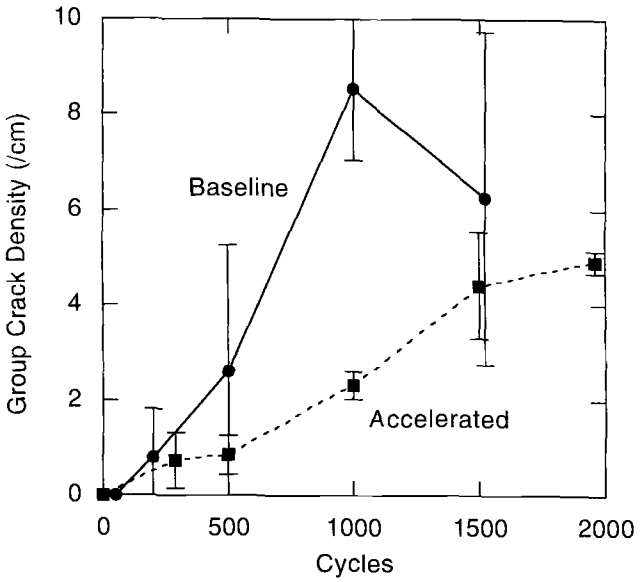


FIG. 6—*Group crack density in PIXA-M research layup under hygrothermal cycles.*

Thermal Cycling Results

The accelerated thermal cycling tests cause modest damage in the PIXA-M layups, and no damage in the PETI-5 ones. An illustrative result is shown in Fig. 7. Shown is the average crack density in the 90° plies of the quasi-isotropic specimens under baseline and accelerated thermal cycling. The 90° ply groups in the research layup, used in Figs. 5 and 6, developed only 1 or 2 cracks/cm in this case,

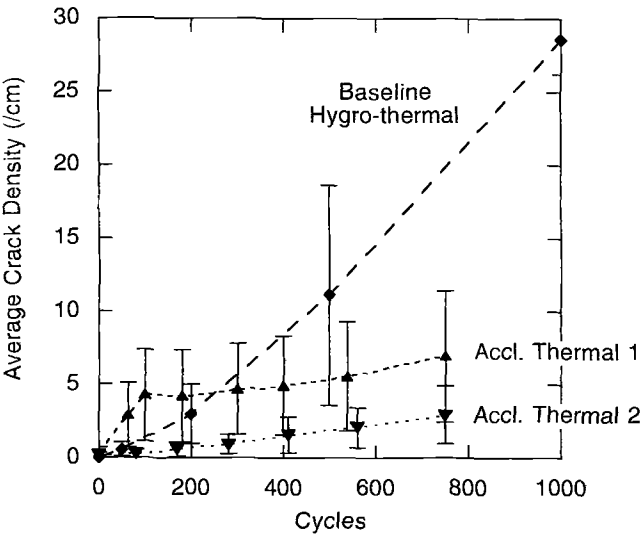


FIG. 7—*Average crack density in PIXA-M quasi-isotropic layup under thermal cycling.*

not significant enough to show a meaningful plot. Figure 7 shows higher crack densities than Figs. 5 and 6; this is an effect of layup and geometry, not the conditions [*2*]. The baseline hygrothermal cycling results for this layup are shown in Fig. 7 for comparison. Cracking is seen to increase with thermal cycles in a fashion consistent with prior studies [*2,8*]. The more severe "Accelerated thermal 1" condition caused more cracking, as expected.

Isothermal Test Results

The isothermal exposure caused no damage in any material. Isothermally exposed specimens were also subjected to the most severe accelerated thermal cycling condition. Damage levels were the same as, or less than, that seen in specimens exposed to the same thermal cycling without prior isothermal exposure.

Fracture Toughness Reduction

It is assumed that the components of the environment degrade the material, and in particular, lower its effective fracture toughness in microcracking G_{Ic}. Residual stresses then provide the strain energy necessary to crack the weakened material. With knowledge of elastic material properties, the microcrack density in any particular ply in any particular laminate can be predicted as a function of the fracture toughness. Iterative calculations are performed to fit a curve of $G_{Ic}(N)$ to the data using the CRACKOMATIC computer code [*6,8*]. A typical fit is shown in Fig. 8, which fits the group crack data from the PETI-5 research layup to a prediction using the $G_{Ic}(N)$ curve shown in Fig. 9.

Reduction of data to an effective fracture toughness allows comparison with data from other studies. In a related program, tests of material response to noncyclic moisture exposure were carried out by Nairn [*3*]. These tests used a different layup than any of the ones used here, so no direct comparison of microcrack densities is possible. Nairn's tests included conditioning in moist environments (assumed to degrade the material) followed by mechanical loading which provided the stress necessary to cause microcracks. The microcrack data were reduced in a fashion similar to the one used here to generate curves of fracture toughness versus time at moisture.

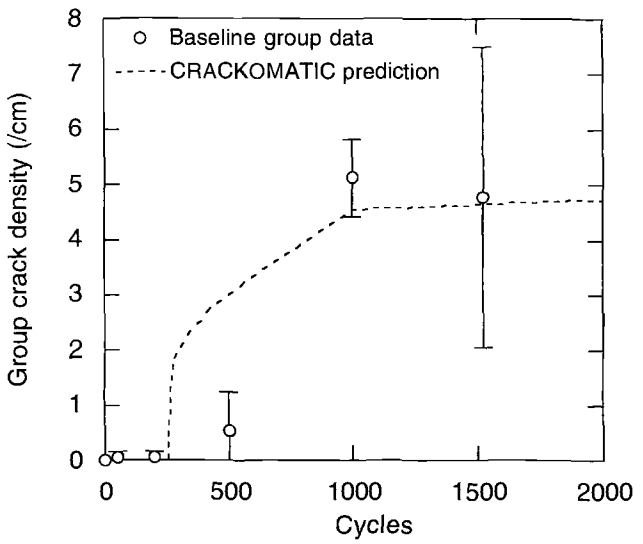


FIG. 8—*Fit of toughness-reduction model predictions to cracking data for PETI-5.*

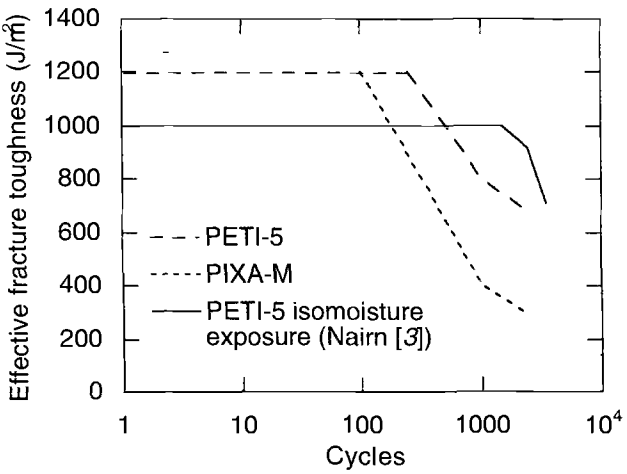


FIG. 9—*Comparison of reduced baseline data to isomoisture data of Nairn [3].*

Figure 9 compares the results from this study to Nairn's data for PETI-5 material, assuming that in each baseline cycle the material near the specimen edges spends approximately one hour in a moist condition. The group crack data from the research layup, exposed to the baseline environment, were used to produce the other $G_{Ic}(N)$ curves in Fig. 9.

Discussion

The hygrothermal cycling results suggest that moisture *cycling* is not the dominant damage mechanism. The accelerated cycles were intended to create the same moisture distributions near the edges of the specimens as the baseline cycles. The material was exposed to hot-wet conditions for only about half as long per cycle, however. Due to lags in the diffusion of this moisture into material any distance from the surface, most of the affected material spent much less than half as long per cycle in a wet condition. Thus the results are consistent with, but do not prove, a contention that *time in a moist condition* is the important parameter.

The accelerated thermal cycling results suggest that even severe thermal cycling is less damaging than the baseline environment (Fig. 7). However, at least in PIXA-M composites, thermal cycling could play some role in hygrothermal damage.

The isothermal test results suggest dry high temperature degradation (dominant in other applications [*4,9,10*]) does not play a role in damage under the conditions studied here.

The reduced fracture toughness results shown in Fig. 9 reinforce the thought that time at moisture is the dominant condition responsible for degradation. Given differing test methods, scatter, and the roughness of the fit in Fig. 8, the agreement between the baseline cycling results and the equivalent moisture exposure results from Nairn is reasonable. The PIXA-M results show earlier degradation of fracture toughness. This could be due to a combination of greater material vulnerability to moisture (PIXA-M was not studied by Nairn, so this is not independently quantified at this time) and the contribution of thermal cycling to the damage in this material.

Concluding Remarks

Results presented here clarify the mechanisms of observed microcracking damage in PETI-5 and PIXA-M composite materials exposed to realistic hygrothermal cycling environments. Time at mois-

ture appears to be the dominant factor in material degradation. This can be studied and accelerated using the techniques of Nairn [*3*]. Thermal cycling may also contribute to material damage, particularly in the PIXA-M composites. Its effects can be accelerated using the techniques presented in Refs *1* and *18* and used here. High temperature dry exposure is not important for the materials, conditions, and durations studied here.

Moisture *cycling* is not a major contributor to material damage, but plays a critical role in determining the *distribution* of moisture and, therefore, damage. Cyclic environments cause cycling levels of absorbed moisture near edges and surfaces of exposed laminates, but stable and often benign levels of absorbed moisture in the laminate interiors. The results of this study, showing damage limited to material near surfaces and edges, were consistent with prior work. This has important design implications; it also suggests that damage can be further restricted by design practices such as the use of sacrificial or barrier layers, coatings, and sealants.

For new materials or conditions, the set of tests presented here and in Ref *3* can form the basis for a standardized set of preliminary environmental durability tests. Such tests not only provide preliminary design data under the conditions of interests, but also provide the key insights necessary to understand the features of the environment that degrade the material. This insight can then be used to plan both accelerated tests for lifetime durability, and further detailed tests to provide statistically valid final design data for the key material properties under the critical environmental conditions.

Acknowledgments

This work was performed under contract PO#JN7675 from the Boeing Commercial Aircraft Company, as a subcontract to NASA Langley contract NAS1-20220. The authors would like to thank Ron Zabora and Eric Sager of the Boeing Company for their many contributions to this work.

References

[*1*] Reynolds, T. G. and McManus, H. L., "Understanding and Accelerating Environmentally-Induced Degradation and Microcracking," paper AIAA-98-1961, *Proceedings of the 39th AIAA/ASME/ASCE/AHS/ASC Structures, Structural Dynamics, and Materials Conference,* Long Beach, CA, April 1998.

[*2*] McManus, H. L., Bowles, D. E., and Tompkins, S. S., "Prediction of Thermal Cycling Induced Matrix Cracking," *Journal of Reinforced Plastics and Composites.* Vol. 15, No. 2, 1996, pp. 124–140.

[*3*] Nairn, J. A. and Han, M.-H., "Hygrothermal Aging of Polyimide Matrix Composite Laminates," *Proceedings of the 12th International Conference on Composite Materials (ICCM 12),* Paris, France, 1999.

[*4*] Bowles, K. J., Jayne, D., and Leonhardt, T. A., "Isothermal Aging Effects on PMR-15 Resin," *SAMPE Quarterly.* Vol. 24, No. 2, 1993, pp. 2–9.

[*5*] Park, C. H. and McManus, H. L., "Thermally Induced Damage in Composite Laminates: Predictive Methodology and Experimental Investigation," *Composites Science and Technology,* Vol. 56, No. 10, 1996, pp. 1209–1219.

[*6*] McManus, H. L. and Maddocks, J. R., "On Microcracking in Composite Laminates Under Thermal and Mechanical Loading," *Polymers and Polymer Composites,* Vol. 4, No. 5, 1996, pp. 304–314.

[*7*] Nairn, J. A., "Fracture Mechanics of Composites with Residual Thermal Stresses," *Journal of Applied Mechanics,* Vol. 64, 1997, p. 805.

[*8*] Bradai, M., "Microcracking in Composite Laminates Under Thermal Cycling," TELAC Report 97-9, Technology Laboratory for Advanced Composites, Massachusetts Institute of Technology, Cambridge, MA, 1997.

[*9*] Nam, J. D. and Seferis, J. C., "Anisotropic Thermo-oxidative Stability of Carbon Fiber Reinforced Polymeric Composites," *SAMPE Quarterly,* Vol. 24, No. 1, 1992, pp. 10–18.

[*10*] McManus, H. L. and Cunningham, R., "Coupled Materials and Mechanics Analyses of Durability Tests for High Temperature Polymer Matrix Composites," *High Temperature and Environmental Effects on Polymeric Composites, ASTM STP 1302,* American Society for Testing and Materials, 1997, pp. 1–17.

[*11*] Loos, A. C. and Springer, G. S., "Moisture Absorption of Graphite-Epoxy Composites Immersed in Liquids and in Humid Air," *Journal of Composite Materials,* Vol. 13, No. 2, 1979, pp. 131–140.

[*12*] Foch, B. and McManus, H. L., "Modeling of Environmentally-Induced Damage in Polymer Matrix Composites," *Proceedings of the 11th International Conference on Composite Materials,* Gold Coast, Australia, 1997, Vol. 5, pp. 432–443.

[13] Springer, G. S., "Moisture Content of Composites Under Transient Conditions," *Journal of Composite Materials,* Vol. 11, No. 1, 1977, pp. 107–122.

[14] Murthy, P. L. N., Ginty, C. A., and Sanfeliz, J. G., "Second Generation Integrated Composite Analyzer (ICAN) Computer Code," NASA TP-3290, Jan. 1993.

[15] McManus, H. L. and Chamis, C. C., "Stress and Damage in Polymer Matrix Composite Materials Due to Material Degradation at High Temperatures," NASA Technical Memorandum 4682, Jan. 1996.

[16] McManus, H. L., Foch, B., and Cunningham, R., "Mechanism-Based Modeling of Long-Term Degradation," in *Progress in Durability Analysis of Composite Systems, Proceedings of the 3rd International Conference on Progress in Durability Analysis of Composite Systems,* Blacksburg VA, Sept. 1997, pp. 63–70.

[17] Shiram, P., Khourchid, Y., Hooper, S., and Martin, R., "Experimental Development of a Mixed-Mode Fatigue Delamination Criterion," *Composite Materials: Fatigue and Fracture—Fifth Volume, ASTM STP 1230,* American Society for Testing and Materials, 1995, pp. 3–17.

[18] Reynolds, T. G., "Accelerated Tests of Environmental Degradation in Composite Materials," S.M. Thesis, Massachusetts Institute of Technology, Cambridge, MA, Sept. 1998.

[19] Michii, Y. and McManus, H. L., "Prediction of Microcracking Distributions in Composite Laminates using a Monte-Carlo Simulation Method," *Journal of Reinforced Plastics and Composites,* Vol. 16, No. 13, 1997, pp. 1220–1230.

Plenary Session

James H. Starnes, Jr.,[1] *Mark W. Hilburger,*[1] *and Michael P. Nemeth*[1]

The Effects of Initial Imperfections on the Buckling of Composite Cylindrical Shells

REFERENCE: Starnes, J. H., Jr., Hilburger, M. W., and Nemeth, M. P., **"The Effects of Initial Imperfections on the Buckling of Composite Cylindrical Shells,"** *Composite Structures: Theory and Practice, ASTM STP 1383,* P. Grant and C. Q. Rousseau, Eds., American Society for Testing and Materials, West Conshohocken, PA, 2000, pp. 529–550.

ABSTRACT: The results of an experimental and analytical study of the effects of initial imperfections on the buckling response of thin unstiffened graphite-epoxy cylindrical shells with and without a cutout, and with three different shell-wall laminates, are presented. Results that identify the individual and combined effects of traditional initial geometric shell-wall imperfections, and nontraditional shell-wall thickness variations, shell-end geometric imperfections, and variations in loads applied to the ends of the shells on the shell buckling and nonlinear responses, are included. The shells have been analyzed with a robust nonlinear finite-element analysis code for shells that accurately accounts for these effects on the buckling and nonlinear responses of the shells. The analysis results generally correlate well with the experimental results. The nonlinear analysis results are also compared with the results from a traditional linear bifurcation buckling analysis that is commonly used for shell design. The results suggest that the nonlinear analysis procedure can be used for determining accurate, high-fidelity, design knockdown factors for shell buckling and collapse. A discussion of how this high-fidelity nonlinear analysis procedure can be used to form the basis for a shell analysis and design approach that addresses some of the critical shell-buckling design criteria and design considerations for composite shell structures is included.

KEYWORDS: graphite-epoxy composite shells, buckling of composite shells, effects of imperfections on composite shell buckling, nonlinear analysis of composite shells

The traditional approach for designing compression-loaded thin-walled buckling-resistant metallic shell structures is to predict the buckling load of the shell with a deterministic analysis, and then to reduce this predicted buckling load with an empirical design or "knockdown" factor [*1*]. This empirical knockdown factor is intended to account for the difference in the predicted buckling load and the actual buckling load of the shell that is determined from tests. This knockdown factor is often overly conservative. The buckling load from a test of a compression-loaded shell can be significantly less than the predicted value. A linear bifurcation buckling or linear eigenvalue analysis is often used for this design-level buckling analysis, and this analysis is usually based on nominal dimensions of an idealized, geometrically perfect shell, nominal values of the material properties, and idealized boundary and loading conditions. These relatively simple analyses typically neglect nonlinear prebuckling deformations, and simply supported boundary conditions are often used to reduce the computational effort needed to conduct parametric or design studies. This linear bifurcation buckling analysis approach came into widespread use not only because of its computational efficiency, but also as the natural extension of the linear bifurcation buckling approach that has been used successfully for analyzing columns and plates.

[1] Senior engineer, Structures and Materials Competency, resident research associate, and senior research engineer, Mechanics and Durability Branch, respectively, NASA Langley Research Center, Mail Stop 190, Hampton, VA 23681-2199.

Copyright© 2001by ASTM International www.astm.org

The effects of initial geometric imperfections in the shell wall have been shown to influence strongly the buckling or collapse responses of compression-loaded metallic shells [*2–6*]. These initial geometric shell-wall imperfections are often associated with the fabrication process, and they are generally recognized as a major contributor to the unconservative nature of predicted shell buckling loads. The values of the shell buckling loads are sensitive to these initial imperfections because shells typically bifurcate from the stable primary prebuckling equilibrium path to an unstable equilibrium path. Even though a linear analysis is often used in the design process, the response of a thin-walled shell is geometrically nonlinear. The traditional knockdown-factor design approach based on a linear eigenvalue or bifurcation buckling analysis was developed before the widespread availability of modern high-fidelity nonlinear shell analysis procedures [*7*] and advanced computing capabilities. These modern nonlinear shell analysis procedures can account for the effects of initial geometric shell-wall imperfections by including measured shell-wall surface-shape data in the analysis if these data are available, or by approximating the imperfection shape with some approximate shape function if these data are not available. These high-fidelity nonlinear analysis procedures offer the opportunity to improve some of the engineering approximations that are used in the traditional knockdown-factor design approach. This traditional design approach was also developed before the introduction of advanced composite materials for aerospace structural applications.

The high strength-to-mass and high stiffness-to-mass attributes of composite materials make these materials a logical choice for high-performance aerospace structural applications. Designing minimum-mass composite shell structures that support compressive loads requires that the buckling behavior of these shell structures be well understood before these structures can be safely used in service. A minimum-mass requirement for the design of these shell structures is usually satisfied by making the shell wall as thin as possible to reduce the structural mass. Such a design can be overly conservative or unconservative, if the buckling load cannot be accurately predicted during the design process. The design would be overly conservative if the designer used a lower value of the knockdown factor than necessary, or it would be unconservative if the designer used a higher value of the design knockdown factor than necessary. Using the traditional metallic-shell-structure knockdown-factor design approach does not necessarily assure a conservative design for a given composite shell structure if the design knockdown factor used does not represent the physical behavior of the shell. Unfortunately, the traditional sources of design knockdown factors for predicting shell buckling loads [*1*] do not include data or information for composite shell structures. Recent studies [*8–10*] have shown that traditional initial geometric shell-wall imperfections, and other nontraditional forms of imperfections or variations in geometric and material parameters, loading conditions and boundary conditions can significantly affect the buckling load of a compression-loaded composite shell structure. The effects of these traditional and nontraditional classes of initial imperfections on composite shell buckling are generally not well understood by structural engineers and designers.

The present paper describes the results of an experimental and analytical study of the effects of traditional initial geometric shell-wall imperfections, and variations in other nontraditional geometric and material parameters, and loading conditions on the buckling response of unstiffened thin-walled graphite-epoxy cylindrical shells. The effects of initial geometric shell-wall imperfections, shell-wall thickness variations, shell-end imperfections and variations in loads applied to the ends of the shell, on the buckling response of these thin-walled shells are discussed. The effects of a cutout in the shell wall on the buckling and nonlinear responses of these thin-walled shells are discussed as an example of a major shell-wall discontinuity that dominates the shell response. The results of the study are used to isolate and illustrate the significance of these nontraditional initial imperfections. A nonlinear shell analysis procedure that is used to predict the buckling and nonlinear response of the shells is described, and the analysis results are correlated with the experimental results. The use of this nonlinear shell analysis procedure for determining accurate, high-fidelity design knockdown factors for shell buckling and collapse, and for determining the effects of uncertainties in shell geometric parameters on shell buckling is discussed. The results from this high-fidelity nonlinear analysis proce-

dure can be used to form the basis for a shell analysis and design approach that addresses some of the critical shell-buckling design criteria and design considerations for contemporary composite shell structures.

Test Specimens, Imperfection Measurements, and Test Apparatus and Tests

Test Specimens

The specimens tested in this investigation were fabricated from 0.13-mm-thick unidirectional graphite-epoxy tape material made from Hercules, Inc., AS4 graphite fibers preimpregnated with Hercules, Inc. 3502 epoxy resin. The nominal unidirectional lamina mechanical properties of a typical 0.13-mm-thick ply of this material system are as follows: longitudinal modulus $E_1 = 148.2$ GPa, transverse modulus $E_2 = 11.1$ GPa, in-plane shear modulus $G_{12} = 6.4$ GPa, and major Poisson's ratio $\nu_{12} = 0.295$. Unidirectional tape material was laid up on a mandrel to form six 8-ply-thick cylindrical shell specimens that are identified as specimens C1–C6 herein. Each specimen had either a quasi-isotropic $[\pm 45/0/90]_s$, an axially stiff orthotropic $[\pm 45/0_2]_s$, or a circumferentially stiff orthotropic $[\pm 45/90_2]_s$ laminate stacking sequence (see Table 1). Two shell specimens of each laminate stacking sequence were fabricated. The specimens had a nominal radius of 203.2 mm, a nominal length of 406.4 mm, and a nominal thickness of 1.02 mm. Both ends of each specimen were potted in an aluminum-filled epoxy resin to assure that the ends of the specimens remained circular and did not fail prematurely during the tests. The potting material extended approximately 25.4 mm along the length of the specimens at each end. The ends of the specimens were machined flat and parallel to assure proper load introduction during the tests, and the test section of the specimens was approximately 355.6 mm long. A 25.4-mm by 25.4-mm square cutout with 1.27-mm reentrant corner radii was machined at specimen mid-length in one specimen of each laminate stacking sequence. A typical specimen with a centrally located rectangular cutout is shown in Fig. 1, and the coordinate system used to

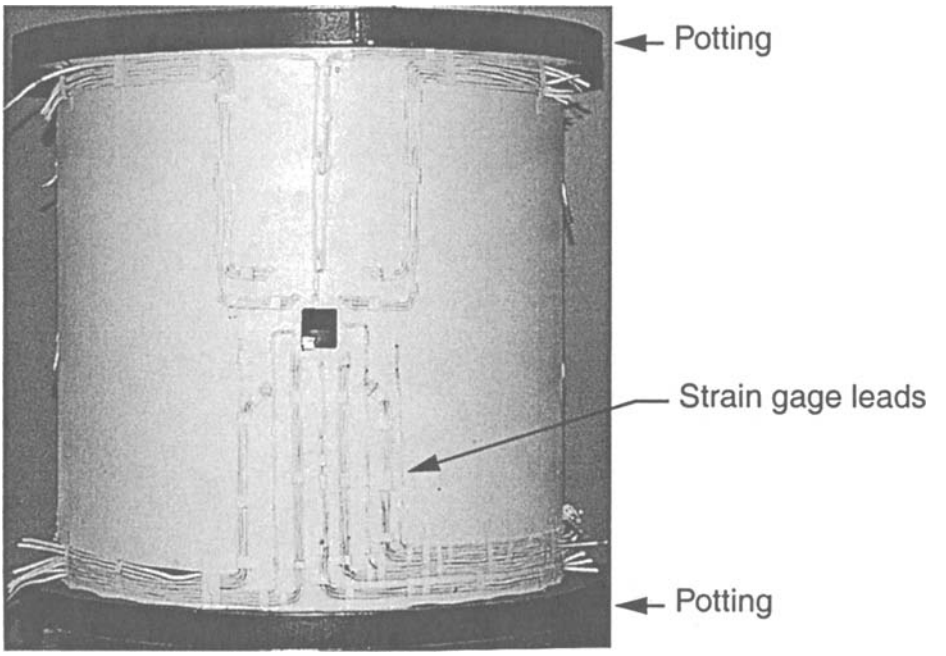


FIG. 1—*Typical test specimen and instrumentation.*

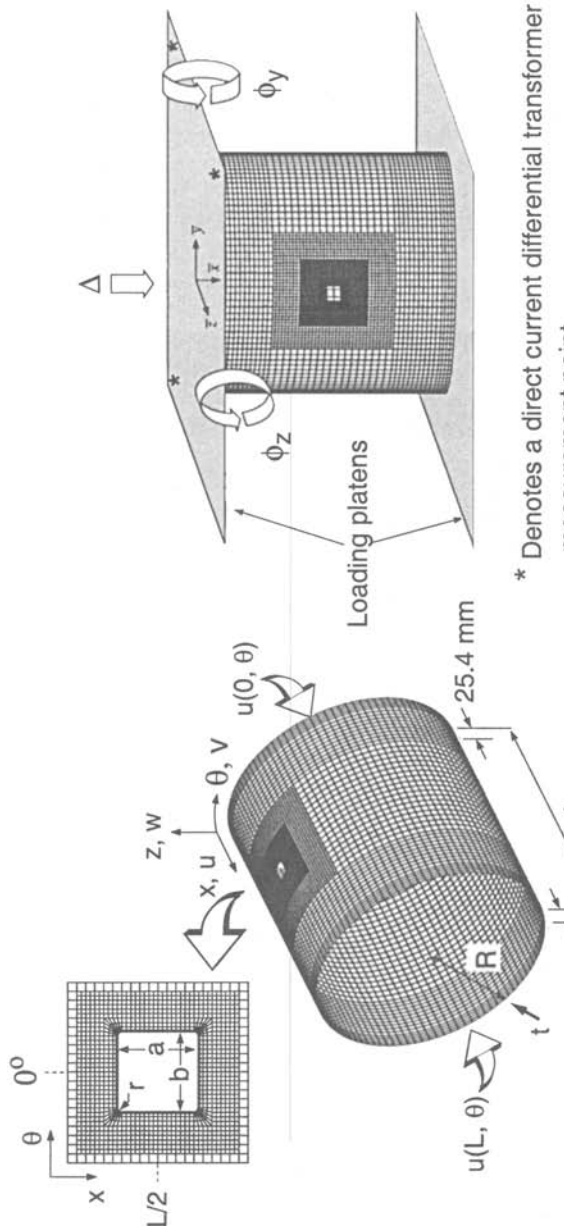


FIG. 2—*Typical finite-element model geometry and boundary conditions.*

represent the corresponding geometry is shown in Fig. 2. The cylinder length, radius and thickness are defined as L, R and t, respectively. The cutout axial length, arc-width, and reentrant corner radius are denoted by a, b and r, respectively. The cutout is centered on $\theta = 0°$ and $x = L/2$.

Imperfection Measurements

Three-dimensional surveys of the inner and outer shell-wall surfaces of each specimen were made prior to testing to determine the initial geometric shell-wall mid-surface imperfection shape and the shell-wall thickness distribution. Measurements were taken over a uniform grid with increments of 3.18 mm in the axial direction and 3.53 mm (1° of arc) in the circumferential direction over the exposed surfaces of the specimens. At each surface point the average of the measurements was used to determine the initial geometric shell-wall mid-surface imperfection shape, and the difference was used to determine the shell-wall thickness distribution. A typical contour plot of the nondimensionalized initial geometric shell-wall mid-surface imperfections $\overline{w_0}(x,\theta)$ for specimen C1 is shown in Fig. 3. The measured shell-wall mid-surface imperfection w_0 is nondimensionalized by the average measured shell-wall thickness $t_{ave} = 0.967$ mm (see Table 1). These results indicate that the initial geometric shell-wall imperfection is periodic in the circumferential direction and has slight deviations in the axial direction. The maximum amplitude of the imperfection is 0.724 t_{ave}. A typical contour plot of the nondimensionalized shell-wall thickness variation $t_0(x,\theta)$ for specimen C1 is shown in Fig. 4. The measured thickness value t is nondimensionalized by the average measured shell thickness t_{ave}. These results indicate that the shell-wall thickness, and hence the bending stiffnesses, varies significantly over a short distance. The darker angular pattern in the thickness distribution is caused by ply gaps generated during the lay-up and curing process, and the lighter angular pattern is caused by overlapped plies. The thickness varies from 0.942 to 1.060 times t_{ave}. The rule of mixtures was used to determine thickness-adjusted lamina properties that are based on the measured wall thickness values. The effective in-plane material property distribution for specimen C1 is similar to the inverse of the thickness distribution shown in Fig. 4 (a higher thickness corresponds to a lower modulus). The values of effective in-plane material properties vary significantly for specimen C1. For example, the effective longitudinal modulus E_x ranges from 64.7 to 88.0 GPa, the effective circumferential modulus E_θ ranges from 17.3 to 24.1 GPa, the effective in-plane shear modulus $G_{x\theta}$ ranges from 15.7 to 22.8 GPa, and the effective major Poisson's ratio $\nu_{x\theta}$ varies from 0.782 to 0.789.

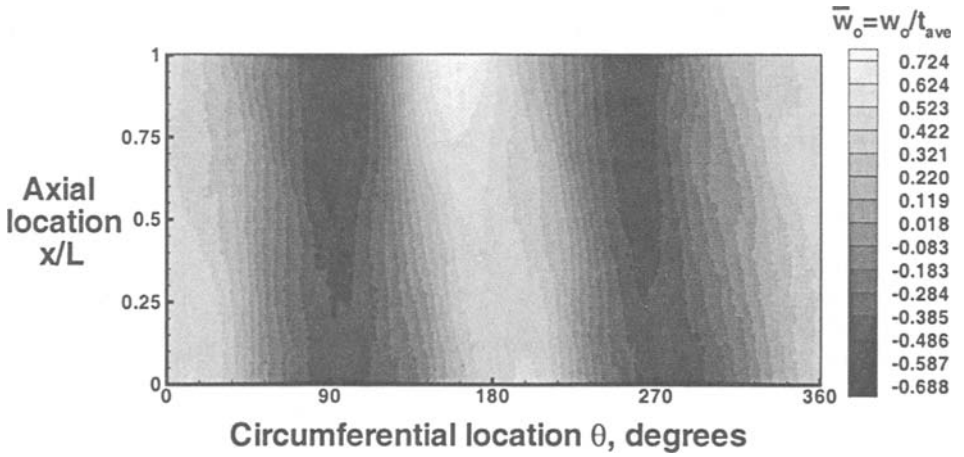


FIG. 3—*Measured mid-surface imperfection shape for specimen C1 ($[\pm 45/0_2]_s$ laminate).*

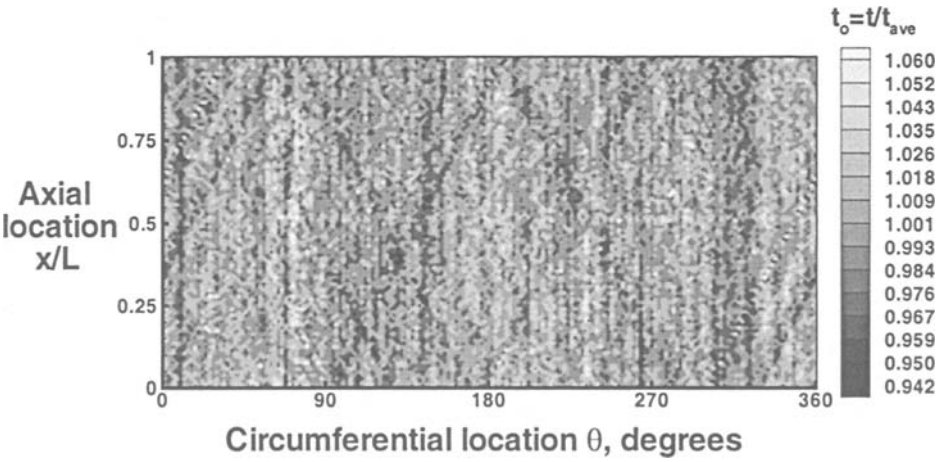


FIG. 4—*Measured wall thickness variation for specimen C1 ([±45/0₂], laminate).*

Measurements of the top and bottom loading surfaces of each specimen were made every degree around the circumference of the specimen to determine the variation in the shell-end or loading-surface geometry. Typical top and bottom shell-end or loading-surface geometry variations for specimen C1 are denoted by $\delta_{top}(\theta)$ and $\delta_{bot}(\theta)$, respectively, and are shown in Fig. 5. The maximum amplitude of this shell-end loading-surface variation is approximately 0.025 mm, which is approximately 2.6% of t_{ave}. The average measured specimen dimensions and average calculated thickness-adjusted effective in-plane material properties for all specimens are summarized in Tables 1 and 2, respectively.

Test Apparatus and Tests

All specimens were instrumented with electrical resistance strain gages and direct-current differential transducers were used to measure displacements. Three noncollinear direct-current differential

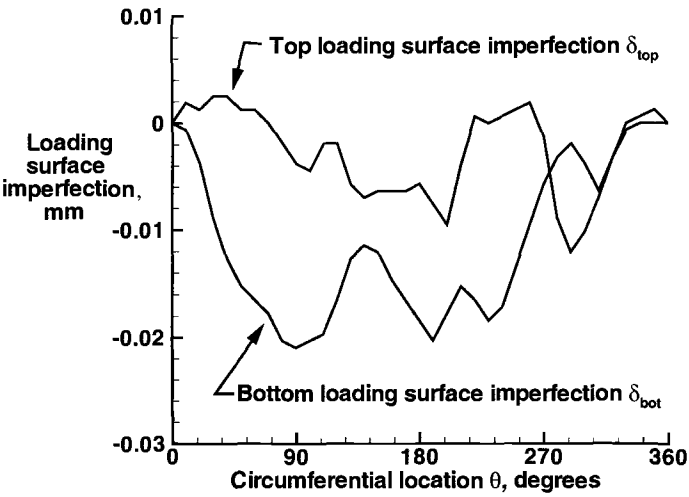


FIG. 5—*Measured loading surface imperfections for specimen C1 ([±45/0₂]ₛ laminate).*

TABLE 1—*Specimen laminate and average measured geometry.*

Specimen Number	Laminate	Cutout	Length L, mm	Radius R, mm	Thickness t, mm
C1	$[\mp 45/0_2]_s$	No	406.55	201.57	0.967
C2	$[\mp 45/0/90]_s$	No	406.78	201.65	0.983
C3	$[\mp 45/90_2]_s$	No	406.75	201.47	0.973
C4	$[\mp 45/0_2]_s$	Yes	406.60	201.48	0.955
C5	$[\mp 45/0/90]_s$	Yes	405.56	201.67	0.953
C6	$[\mp 45/90_2]_s$	Yes	406.40	202.00	1.031

transformers were positioned in three corners of the upper loading platen and used to measure the end-shortening displacement Δ and the rotations ϕ_y and ϕ_z of the loading platen as indicated in Fig. 2. A moiré interferometry procedure was used to observe the shell-wall prebuckling, buckling and postbuckling out-of-plane (perpendicular to the shells outer surface) deformation patterns. All data were recorded with a data acquisition system, and the moiré patterns corresponding to the response of the specimens were recorded photographically and on video tape.

The specimens were loaded in compression with a 1.33-MN hydraulic universal testing machine by applying an end-shortening displacement to the shell ends or loading surfaces of each specimen. To control the load introduction into the specimens, the upper loading platen was aligned with the shell end or loading surface of the specimens before each test by adjusting bolts in the corners of the upper loading platen until strains measured by selected strain gages indicated a uniform axial strain distribution in the shell wall. All specimens were loaded until general instability or global collapse of the shell occurred.

Finite-Element Models and Analyses

Nonlinear Analysis Procedure

All shells considered in this study were analyzed with the STAGS (STructural Analysis of General Shells) nonlinear shell analysis code [7]. STAGS is a finite-element code designed for the static and dynamic analysis of general shells, and includes the effects of geometric and material nonlinearities in the analysis. The code uses both the modified and full Newton methods for its nonlinear solution algorithms, and accounts for large rotations in a shell by using a co-rotational algorithm at the element level. STAGS has static and transient analysis capabilities that can be used to predict local in-

TABLE 2—*Average thickness-adjusted effective in-plane properties based on average specimen wall thicknesses in Table 1.*

Specimen Number	E_x, GPa	E_θ, GPa	$G_{x\theta}$, GPa	$\nu_{x\theta}$
C1	82.27	22.37	20.87	0.786
C2	54.97	54.97	20.57	0.336
C3	22.20	81.71	20.73	0.214
C4	83.45	22.72	21.18	0.786
C5	55.59	55.59	20.79	0.335
C6	20.83	76.84	19.49	0.214

stabilities and modal interactions that occur due to destabilizing mechanical loads, such as an applied compression or shear load. The Riks pseudo arc-length path-following method [*11*] is used to continue a solution past the limit points of a nonlinear response. With this strategy, the incrementally applied loading parameter is replaced by an arc-length along the solution path, which is then used as the independent loading parameter. The arc-length increments are automatically adjusted by the program as a function of the solution behavior. The transient analysis in STAGS uses proportional structural damping and a numerical time-integration method developed by Park [*12*].

The prebuckling, buckling and postbuckling responses of the shells were determined using the following analysis procedure. The prebuckling responses were determined using the geometrically nonlinear quasi-static analysis capability in STAGS. The Riks pseudo arc-length path-following method, described previously, was used to compute the initial shell response until just after buckling. The unstable postbuckling response of the shell was predicted using the nonlinear transient analysis option of the code. This option was also used to predict the response associated with mode shape changes that occur during the nonlinear buckling and postbuckling responses. The transient analysis was initiated from an unstable equilibrium state close to the limit point by incrementing the end displacement by a small amount. The transient analysis was continued until the kinetic energy in the shell was dissipated to a negligible level, which indicates that the transient response had attenuated. Once the transient analysis had attenuated to a near-steady-state solution, the load relaxation option of the code was used to establish a static equilibrium state. The subsequent stable postbuckling response of the shell was computed using the standard nonlinear, static analysis option in STAGS. Conventional linear bifurcation buckling analysis results were also determined with STAGS for comparison with the nonlinear response results.

Finite-Element Model

A typical finite-element model of a specimen with a square cutout is illustrated in Fig. 2. The finite-element mesh was defined by using user-written FORTRAN subroutines compatible with the STAGS finite-element code. These user-written subroutines facilitated the generation of models with various mesh densities and provided a convenient means for assessing the convergence of a given finite-element model. Convergence studies were conducted for all finite-element models. Both the standard 410 quadrilateral element and the 510 and 710 transition elements from the STAGS element library were used in the models. Idealizations of the end conditions with the potting material were used in the finite-element models. To simulate the constraints provided by the potting material, the circumferential and out-of-plane stiffness contributions of the potting material were calculated and applied to the edge regions of the shell indicated by the finer mesh at the ends of the model shown in Fig. 2. Multipoint constraints were used to enforce end-displacement constraints that correspond to the loading condition for each specimen.

Geometrically perfect and imperfect shells were analyzed in the present investigation. For each specimen, the average measured geometry, laminate thickness and thickness-adjusted lamina mechanical properties were used for the finite-element models for the geometrically perfect shells. These geometrically perfect finite-element models were modified to include the effects of the measured shell imperfections and to more closely simulate the response of the specimens. These modeling modifications include the measured initial geometric shell-wall mid-surface imperfections, shell-wall thickness variations, lamina property variations, shell-end geometric imperfections, and nonuniform end loads. The initial geometric shell-wall mid-surface imperfection $w_o(x, \theta)$ is included in the finite-element models by introducing an initial out-of-plane perturbation to each node of the mesh by using a user-written subroutine. The user-written subroutine uses a linear interpolation algorithm that calculates the value of the imperfection at each nodal coordinate which is based on the measured shell-wall data. The shell-wall thickness, t, and lamina material properties, E_1, E_2, G_{12}, and ν_{12}, are adjusted at each integration point of each element in the finite-element model. The lam-

ina properties are adjusted by using the rule of mixtures. In the rule-of-mixtures calculations, it is assumed that any variation in the shell wall thickness from the nominal thickness is due to a variation in resin volume only, and that the fiber volume remains constant for each ply. Nonuniform end loads for the specimens are attributed to initial specimen end or loading-surface imperfections and to upper loading platen rotations that are measured during the experiment. First, the measured upper and lower specimen end or loading-surface imperfections $\delta_{top}(\theta)$ and $\delta_{bot}(\theta)$, respectively, were included in the finite-element model by introducing an initial in-plane axial perturbation to the nodes at the loaded ends of the shell. Then, the compression load was introduced into the cylinder in two parts. The nonuniform specimen end imperfections, $-\delta_{top}(\theta)$ and $-\delta_{bot}(\theta)$, were applied to the upper and lower ends of the shell, respectively, as displacements at the beginning of the analysis to simulate a full contact condition between the shell ends or loading surfaces and the loading platens. Then, the experimentally measured end-shortening displacement Δ and upper loading-platen rotations ϕ_y and ϕ_z were applied to the upper shell end or loading surface while holding the lower loading surface fixed as illustrated in Fig. 2; that is, $u(0,\theta) = \Delta + R\cos\phi_y \cos\theta + R\cos\phi_z \sin\theta - \delta_{top}(\theta)$ and $u(L,\theta) = -\delta_{bot}(\theta)$. A typical converged finite-element model contained approximately 55 000 degrees of freedom and a typical nonlinear analysis required 8 CPU hours on an engineering workstation.

Results and Discussion

Analytically predicted and experimentally measured results for the compression-loaded graphite-epoxy cylindrical shells considered in this study are presented in this section. The predicted results were obtained from finite-element models that include initial geometric shell-wall mid-surface imperfections, shell-wall thickness variations and thickness-adjusted lamina properties, and nonuniform loading effects, unless otherwise indicated. These results are presented to illustrate the overall behavior of compression-loaded graphite-epoxy cylindrical shells, and the effects of a cutout and laminate properties on their response. The results include predicted and measured load-end-shortening response curves, measured load-end-rotation response curves, and initial postbuckling out-of-plane displacement patterns. Results from an analytical study of the effects of several types of measured imperfections on the compression response of the shells are also presented.

Predicted and Measured Response Comparisons

Traditional linear bifurcation buckling load analysis results for the six specimens tested in this study are given in Table 3. The measured buckling loads from the tests are also given in Table 3. The

TABLE 3—*Predicted and measured buckling load values.*

Specimen Number	Bifurcation Buckling Load P_{bif}, kN	Predicted Buckling Loads,* kN					Experimental Buckling Load Pcr_m, kN
		No Imperfection	Mid-surface Imperfection	Wall Thickness Variation	Nonuniform Load	All Imperfections	
C1	148.8	142.7	140.5	142.3	141.5	136.5	123.6
C2	215.4	200.3	182.6	199.3	195.9	184.9	152.0
C3	189.6	180.3	170.9	180.4	179.5	170.0	142.0
C4	108.9	105.4	108.9	106.1	74.9	75.3	74.8
C5	118.3	106.4	101.9	108.1	103.8	102.7	91.2
C6	106.8	105.4	106.9	105.4	105.4	105.0	95.7

* Predicted results obtained by using a nonlinear finite-element analysis.

effective global axial strains at buckling, Δ_{cr}/L, where Δ_{cr} is the end-shortening displacement at buckling, are 0.0011, 0.0021, 0.0042, 0.0007, 0.0013, and 0.0029 for specimens C1 through C6, respectively. In all cases, the measured buckling loads from the tests are significantly less than the predicted linear bifurcation buckling loads (20.0, 41.7, 33.5, 45.6, 29.7, and 11.6% less for specimens C1 through C6, respectively). These results indicate that the linear bifurcation buckling loads overpredict the measured buckling loads for all specimens regardless of the shell-wall laminate or whether or not there is a cutout in the shell wall.

To obtain improved buckling load predictions, nonlinear analyses were conducted for each specimen with and without all measured imperfections included in the models. The predicted buckling loads from the nonlinear analysis for each specimen with all measured imperfections included in the model are 136.5, 184.9, 170.0, 75.3, 102.7, and 105.0 kN for specimens C1 through C6, respectively (see Table 3). The measured buckling loads from the tests are still less than the predicted buckling loads from the nonlinear analyses, but not as much as for the predicted linear bifurcation buckling loads. The measured buckling loads are 9.5, 17.8, 16.5, 0.7, 11.2, and 8.8% less than the nonlinear buckling load predictions that include all imperfections for specimens C1 through C6, respectively. Predicted and measured load-shortening response curves for the six shells considered in this study are shown in Fig. 6. The solid curves correspond to the measured results and the dashed curves correspond to the predicted results from the nonlinear analyses. Buckling loads are indicated by filled squares and circles for the measured and predicted results, respectively, and global collapse loads are indicated by an X. Five of the specimens supported an applied load after global collapse, and these specimens had some residual postbuckling strength. The measured residual postbuckling strength of the specimens were 61.5, 51.1, 35.1, 62.6, and 59.6 kN for specimens C1 through C5, respectively. Specimen C6 had no residual postbuckling strength.

The measured load-shortening response curves shown in Fig. 6 correlate well with the corresponding predicted responses. The maximum difference between the measured and predicted initial prebuckling stiffnesses of the specimens is 3%. The results in the figure indicate that specimens C1

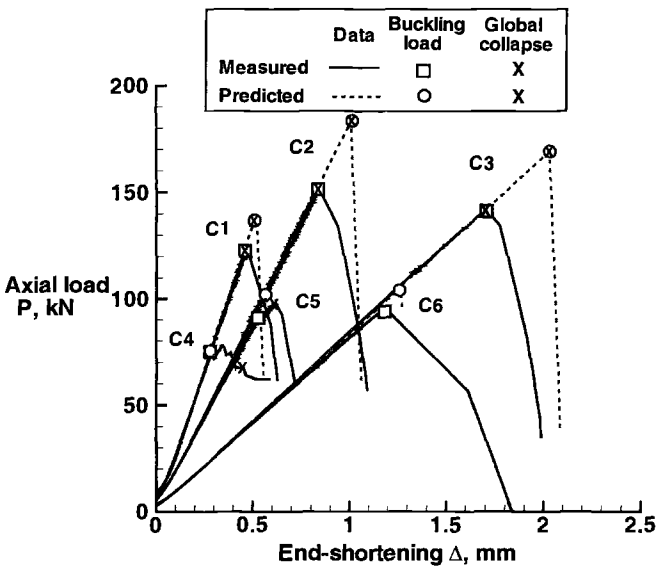


FIG. 6—*Numerically predicted and experimentally measured load-shortening response curves.*

and C4 with the $[\pm 45/0_2]_s$ laminate have the largest prebuckling stiffness magnitudes, followed by specimens C2 and C5 with the $[\pm 45/0/90]_s$ laminate, and finally by specimens C3 and C6 with the $[\pm 45/90_2]_s$ laminate. These results are consistent with the laminate stiffnesses for the shells. There are noticeable differences in the magnitudes of the predicted and measured buckling loads for all specimens except specimen C4 (see Table 3). Specimens C2 and C3 have the most significant differences in the measured and predicted buckling loads.

The measured and predicted results in Fig. 6 for specimens without cutouts (specimens C1–C3) indicate that the specimens have a linear prebuckling response and a distinct buckling load (indicated by the filled circles and squares in the figure). An unstable buckling response occurs when the buckling load is reached. This unstable response causes the global collapse of the specimens (indicated by an X in the figure) which is characterized by a significant reduction in the axial load supported by the specimen and a distinct change in the out-of-plane displacement field. After buckling occurs, these specimens have stable postbuckling equilibrium configurations with varying levels of residual postbuckling strength. Even though specimen C1 has the lowest buckling load value for the three specimens without a cutout, it has the highest value of residual postbuckling strength.

The results in Fig. 6 indicate that a cutout has a significant effect on the buckling and postbuckling responses of the specimens. The measured initial buckling loads of specimens with a cutout are an average of 37.3% less than the measured initial buckling loads of the specimens without a cutout. However, there are no noticeable differences in the prebuckling stiffnesses of the specimens with the same laminate regardless of whether there is a cutout or not. The results indicate that specimens with a cutout have a linear prebuckling response and a distinct initial buckling load. After initial buckling occurs, an unstable postbuckling response occurs. The initial unstable postbuckling response for specimens C4 and C5 is characterized by a local buckling response near the cutout that includes the development of rapidly varying local stress gradients and out-of-plane bending deformations near the cutout. These deformations are large relative to the shell-wall thickness. The first unstable buckling response for these specimens results in slight reductions in the axial load supported by the specimen. After initial buckling occurs, these specimens have a stable local postbuckling equilibrium configuration, and they can support additional applied load in this local postbuckling equilibrium state before global collapse occurs (indicated by an X in the figure). The measured results for specimen C4 indicate that several additional unstable local buckling responses occur before global collapse occurs as indicated by the discontinuities in the load-shortening response curve in the postbuckling response range. These additional unstable local buckling responses are associated with distinct local mode-shape changes that were observed during the experiment. In contrast, specimen C5 does not exhibit any additional unstable local buckling responses before global collapse occurs. The results indicate that the axial stiffness of each specimen is reduced after each local buckling response occurs as indicated by the reduction in the slope of each adjacent stable segment of the load-shortening response curve in the postbuckling response range. This stiffness reduction is caused by the large postbuckling deformations that develop near the cutout which cause a significant redistribution of the internal load away from the cutout. It has been shown by Hilburger et al. [*10*] that this local buckling response is caused by nonlinear coupling between the compressive in-plane biaxial stresses and the out-of-plane deformations that occur near the cutout. The measured postbuckling loads for specimens C4 and C5 after global collapse occurs are 2.1 and 1.4% greater than the corresponding postbuckling loads for specimens C1 and C2, respectively. These results indicate that the cutout has a relatively small effect on the postbuckling strength of these specimens. For specimen C6, however, the unstable local buckling response caused the catastrophic failure of the specimen and, as a result, there was no postbuckling strength for this specimen. This catastrophic failure appears to have been caused by local interlaminar shear failures that initiated near the large local bending deformations that occurred at the free edge of the cutout. Once failure was initiated, it propagated around the circumference of the specimen very rapidly.

The transient nature of the buckling response of the specimens is indicated by the typical predicted load-time response curve for the collapse response of specimen C1 shown in Fig 7. The inset figures in Fig. 7 represent the out-of-plane deformations of the shell wall at different stages in the collapse response, and illustrate the transient deformations that occur in the shell during collapse. At the onset of buckling, the shell-wall out-of-plane deformations change in a very short time from the uniform prebuckling deformation pattern indicated by Deformation Pattern A in the figure to a transient unstable deformation pattern indicated by Deformation Pattern B. The results indicated by Deformation Pattern B show that the deformations are characterized by a localized group of ellipse-like or diamond-shaped buckles near the ends of the shell. As the buckling process continues, there is a significant reduction in the axial load supported by the shell, and the local buckles in the deformation pattern increase in number and are redistributed around the circumference of the shell as indicated by Deformation Pattern C. After approximately 0.1 s have elapsed, the kinetic energy in the shell has dissipated to a negligible level, and the shell has deformed into a stable postbuckling mode-shape that consists of 14 half-waves around the circumference and two half-waves along the length, as indicated by Deformation Pattern D.

Typical predicted initial postbuckling out-of-plane displacement contours and the corresponding observed moiré fringe patterns for specimen C1 (without a cutout) are shown in Fig. 8. The dashed contour lines in the predicted displacement contours represent inward displacements and the solid lines represent outward displacements. The density of the contour lines indicates the severity of the displacement gradients in the specimen. The results indicate that the specimen collapses into a general-instability diamond-shaped buckling pattern with 14 half-waves around the circumference and two half-waves along the length, as predicted by the transient analysis. Typical predicted initial postbuckling out-of-plane displacement contours and the corresponding observed moiré fringe patterns

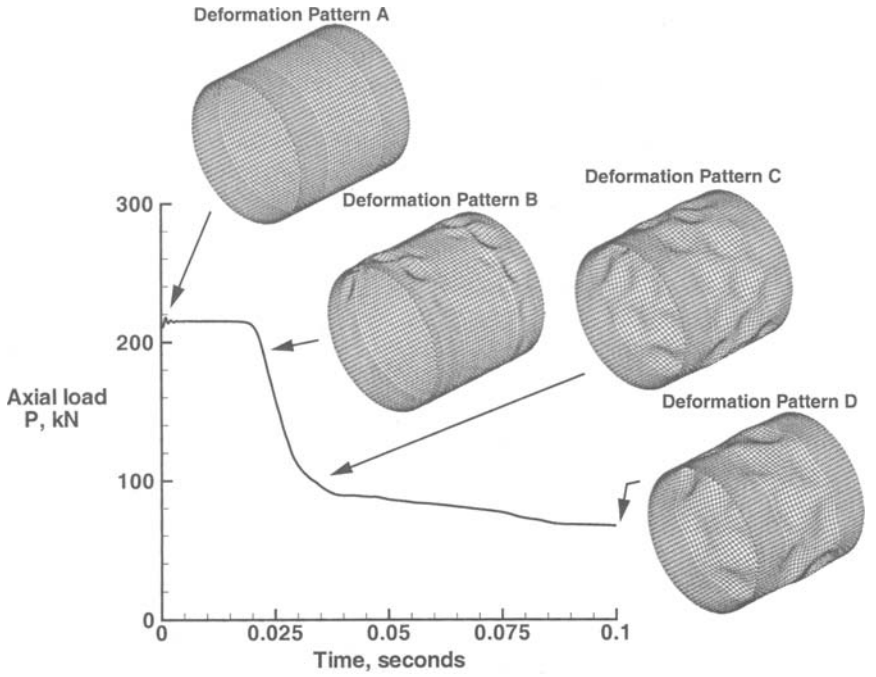
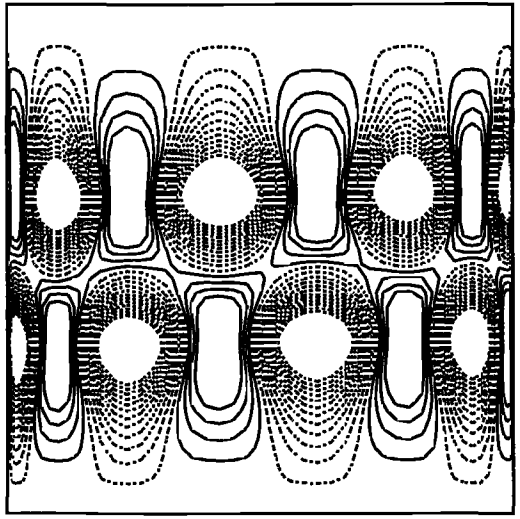
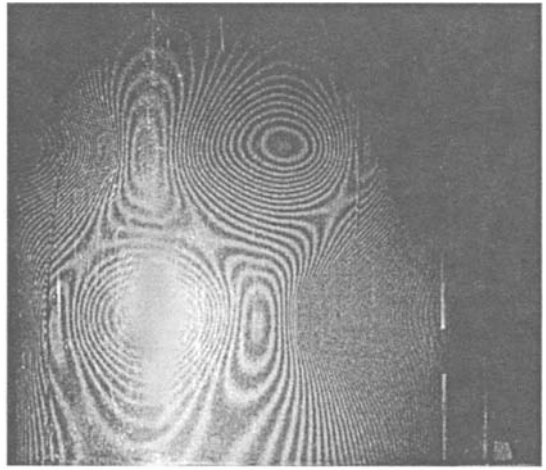


FIG. 7—*Typical transient global collapse response for specimen C1 ($[\pm 45/0_2]_s$ laminate).*

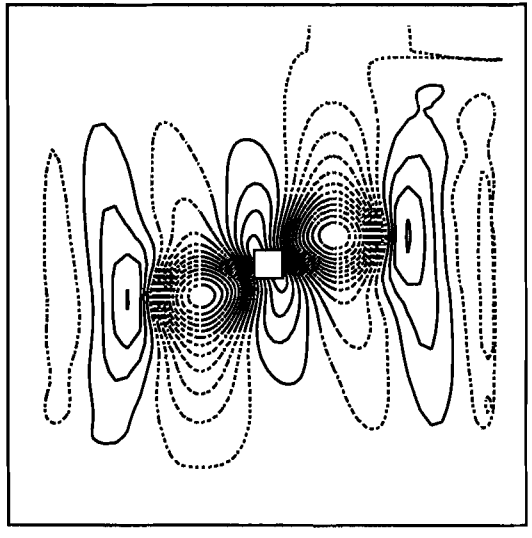


a) Predicted initial postbuckling out-of-plane displacement pattern.

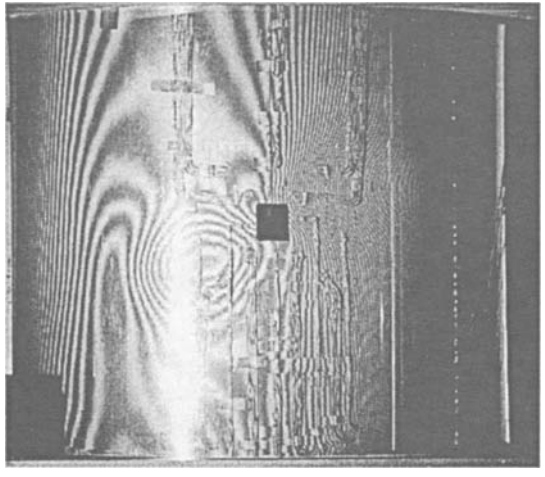


b) Observed initial postbuckling moiré fringe pattern.

FIG. 8—*Observed and predicted initial postbuckling out-of-plane displacements for specimen C1 ($[\pm 45/0_2]_s$ laminate).*



a) Predicted initial postbuckling out-of-plane displacement pattern.



b) Observed initial postbuckling moiré fringe pattern.

FIG. 9—*Observed and predicted initial postbuckling out-of-plane displacements for specimen C4 ($[\pm 45/0_2]_s$ laminate).*

for specimen C4 with a cutout are shown in Fig. 9. The deformation patterns consist of large ellipse-like or diamond-shaped buckles on either side of the cutout that appear to be in the form of a pattern with a central point of inversion symmetry (polar symmetry) at the center of the cutout. At global collapse, specimens C4 and C5 buckled into the general-instability mode-shape consisting of 14 half-waves around the circumference of the specimen and one half-wave along the length. Specimen C6 failed and did not have a stable general-instability postbuckling equilibrium configuration.

Experimentally measured upper loading platen rotations for specimens C1 and C4 are shown in Fig. 10. These results indicate that significant upper loading platen rotation occurs from the onset of loading up to a load level of approximately 31.1 kN. These rotations are due to initial misalignments between the loading frame and the specimen. The movable upper loading platen reaches an equilibrium state at a load level of approximately 31.1 kN, and the loading of the specimen, for the most part, continues without additional upper loading platen rotations from 31.1 kN up to the first buckling response. After the initial buckling response occurs, the upper loading platen undergoes an additional amount of rotation. In the case of specimen C4, the initial local buckling response in the specimen causes significant load redistribution away from the cutout and local stiffness reduction in the specimen. This local stiffness reduction results in a rotation (ϕ_y) of the upper loading platen towards the cutout during the buckling response. Additional erratic changes in the load-end-rotation curves for specimen C4 are associated with additional mode shape changes and material failures which cause additional rotation of the upper loading platen throughout the postbuckling response range.

Material Failures

Material failures were observed in all specimens at some point during their loading history. For the specimens without a cutout (specimens C1–C3), local material damage was not apparent immediately following the initial buckling response. However, as the applied end-shortening displacement was increased throughout the postbuckling response range, the magnitude of the out-of-plane bending gra-

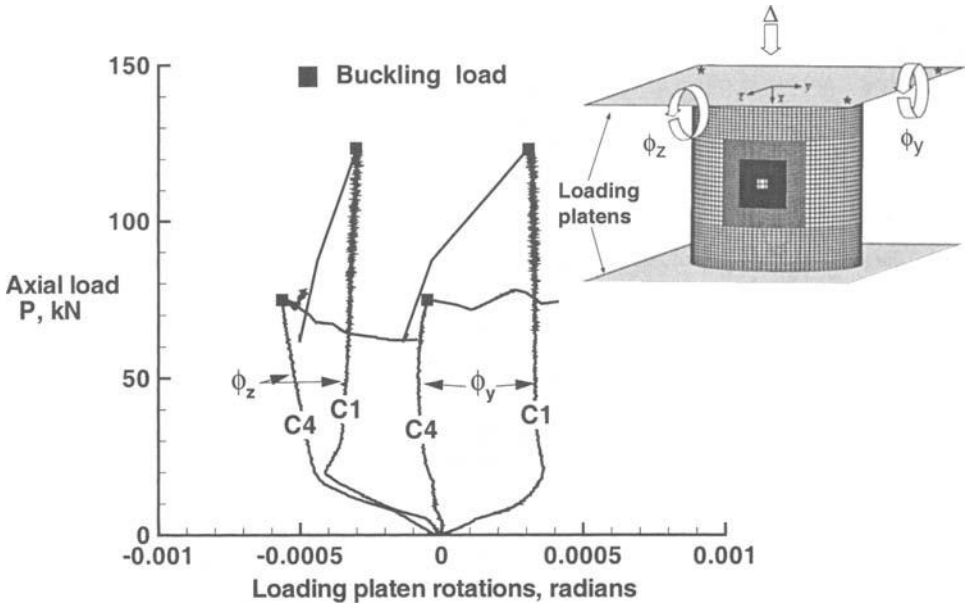


FIG. 10—*Experimentally measured loading platen rotations for specimens C1 and C4 ($[\pm 45/0_2]_s$ laminates).*

dients along the nodal lines of the postbuckling deformation pattern increased significantly, as indicated by the density of the moiré fringe patterns observed in the tests. Local interlaminar shear failures were observed along the nodal lines, and these local failures were accompanied by audible popping noises and slight reductions in the applied load. These local interlaminar shear failures near the nodal lines occurred in regions with large bending deformations that occurred over relatively short distances. For specimens with a cutout (specimens C4–C6), local interlaminar shear failures occurred near the corners of the cutout during the initial local buckling response. These interlaminar shear failures were caused by large out-of-plane bending gradients and high in-plane strain concentrations that occur in the local regions near the corners of the cutout during buckling. Specimens C4 and C5 supported additional applied load after the initial local failures occurred. However, the initial local failures that occurred near the cutout in specimen C6 propagated around the circumference of the specimen very rapidly and, as a result, this specimen had no postbuckling strength. In addition, analytical results for specimens C5 and C6 indicate that there may be additional failure mechanisms activated during the prebuckling response. Predicted in-plane compressive strains near the cutouts just before buckling can exceed 0.009. Compressive strain levels of 0.008 have been shown to cause microbuckling in the 0° fibers and to cause in-plane shear failures of the matrix in 45° plies. It is likely that local material failures occurred near the cutout in the specimens in the prebuckling response range. These material failures, and the ensuing internal load redistribution in the specimen, could provide enough of a lateral disturbance to the specimen at these applied load levels to cause the shell to buckle. Once the shell buckles locally, an interlaminar shear failure mechanism could be activated as discussed previously. These results suggest an explanation for some of the discrepancy between the predicted and measured buckling loads for the specimens.

Failures that initiate or occur near local regions of large out-of-plane bending gradients cannot be modeled with the two-dimensional shell elements in the STAGS element library. However, results from a nonlinear STAGS analysis can be used to identify regions of large local bending gradients in the shell wall, and these results can be used to calculate maximum induced shear stresses within the laminate. Failure will most likely initiate at locations where these maximum shear stresses reach a critical level within the laminate. A first-order engineering approximation was used to calculate the maximum shear stresses within the shell-wall laminate for each specimen model. A simple "strength of materials" approach, which assumes a parabolic shear stress distribution through the thickness of the laminate, was used to estimate the maximum shear stresses in the laminates. The failure was assumed to occur when the maximum shear stress in a laminate reached an assumed critical value of 41 MPa. For the specimens without a cutout (specimens C1–C3), this critical value occurred near the nodal lines of the postbuckling deformation pattern well into the postbuckling range for the specimens. In contrast, the critical stress value for the specimens with a cutout (specimen C4–C6) occurred in the corners of the cutouts after initial buckling occurred. These results are consistent with the experimentally observed failure modes for the specimens.

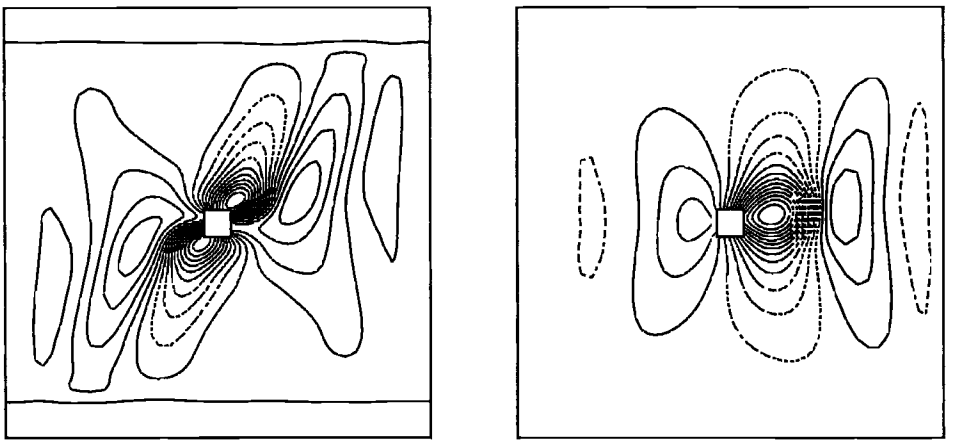
Effects of Imperfections on the Buckling Response

The results of an analytical study of the effects of different types of imperfections on the buckling response of the specimens considered herein are presented in this section. The imperfections studied include traditional initial geometric shell-wall mid-surface imperfections, other nontraditional shell-wall imperfections, and nonuniform loading effects. The nontraditional shell-wall imperfections included the combined effects of measured shell-wall thickness variations and thickness-adjusted lamina mechanical properties. The nonuniform loading conditions include the effects of shell-end geometric imperfections and the effects of small loading platen rotations. Each of these imperfections were independently introduced into the finite-element models to determine the relative sensitivity of the predicted response to each type of imperfection. The predicted nonlinear buckling loads for each geometrically perfect specimen without any measured imperfections included in the model are given

in Table 3. The results for the models with only the traditional initial geometric shell-wall mid-surface imperfections included in the model, with only the shell-wall thickness variations and the thickness-adjusted mechanical properties included in the model, and with only the nonuniform loading effects included in the model are also given in Table 3. These results indicate that the buckling load of the shell can be affected by each of these types of imperfections.

These results indicate that the measured imperfections, when considered independently, reduce the predicted buckling loads for the perfect specimens by an amount that ranges from 0.3 to 28.9%, depending on the specimen. In particular, the results indicate that the magnitude of the buckling loads for the specimens without a cutout (specimens C1, C2 and C3) and specimen C5, with a cutout, are most sensitive to traditional measured initial geometric shell-wall mid-surface imperfections. However, the traditional geometric imperfections result in only a 1.5, 8.8, 5.2, and 4.2% reduction in the buckling loads of these specimens, respectively, compared to the nonlinear results for the perfect specimens. In contrast, the traditional initial geometric imperfections result in a 3.3 and 1.4% increase in the buckling loads for specimens C4 and C6, respectively, compared to the nonlinear results for the perfect specimens. These results indicate that there are other effects that influence the buckling loads of these specimens. For the most part, all the other measured imperfections resulted in less than 2.5% reductions in the predicted nonlinear buckling load values. The results indicate that nonuniform loading effects have a small effect on the magnitude of the predicted buckling loads for all but one of the specimens. The relatively small effect of the nonuniform loading effects on the buckling loads is consistent with the observation that the amplitudes of the initial shell-end geometric or loading-surface imperfections were no greater than 2% of the magnitude of end-shortening displacement at buckling, and the magnitudes of the loading platen rotations were small in the prebuckling response range as illustrated in Fig. 10. However, the nonuniform loading effects for specimen C4 resulted in a 28.9% reduction in the buckling load, which was found to be caused by large amplitude shell-end geometric or loading-surface imperfections. The amplitude of the shell-end geometric imperfections for specimen C4 were approximately 60% of the magnitude of end-shortening displacement at buckling. In addition, the results indicate that the nontraditional shell-wall thickness imperfections have a relatively small effect on the magnitude of the buckling load (less than 2%) for the specimens considered herein.

The results presented previously suggest that the use of average wall properties and, in selected cases, the use of uniform applied displacements may be valid assumptions when predicting the buckling loads for these specimens. However, the combined effects of the traditional initial geometric shell-wall mid-surface imperfections, shell-wall thickness variations and thickness-adjusted lamina mechanical property variations, and nonuniform loading effects may have a significant influence on the predicted displacement response and on the strain and internal load distributions in the specimens. For example, the effects of the measured imperfections on the initial postbuckling deformations of specimen C5 are shown in Fig. 11. The results indicate that including the measured imperfections in the analysis can have a significant effect on the shape of the deformation pattern associated with the first local buckling response for specimen C5. The geometrically perfect shell has a deformation pattern with two ellipse-like or diamond-shaped buckles near the cutout, and the response pattern appears to have the form of a pattern with a central point of inversion symmetry at the center of the cutout. In contrast, the imperfect shell has a deformation response with one large elliptical-shaped buckle on one side of the cutout, without a central point of inversion symmetry. This deformation response predicted for the imperfect shell correlates well with the deformation response observed during the testing of this specimen. Predicted and measured axial strains near the top loaded edge of specimen C4 at buckling are shown in Fig. 12. The measured strain values from selected strain gages around the shell circumference are marked by filled squares, and the predicted strains for geometrically perfect and geometrically imperfect specimens (i.e., all imperfections included in the analysis) are represented by the dash and solid curves, respectively. The strains shown in the figure are nondimensionalized by the overall effective strain of the specimen at buckling; i.e., $\varepsilon_x^* = \varepsilon_x / (-\Delta_{cr}/L)$



a) geometrically perfect shell b) geometrically imperfect shell

FIG. 11—*Effects of measured imperfections on the predicted initial postbuckling out-of-plane displacement contours for specimen C5 ($[\pm 45/0/90]_s$ laminate).*

where Δ_{cr} is the end-shortening displacement at buckling. Compressive strains are positive for this nondimensionalization form. The results indicate that the measured imperfections can have a significant effect on the strain distribution in the shell. The predicted strain distribution for the geometrically perfect shell varies rapidly in the region of the shell from approximately −45° to 45° as shown in the figure. This variation in the strain distribution is caused by the cutout in the shell. The results

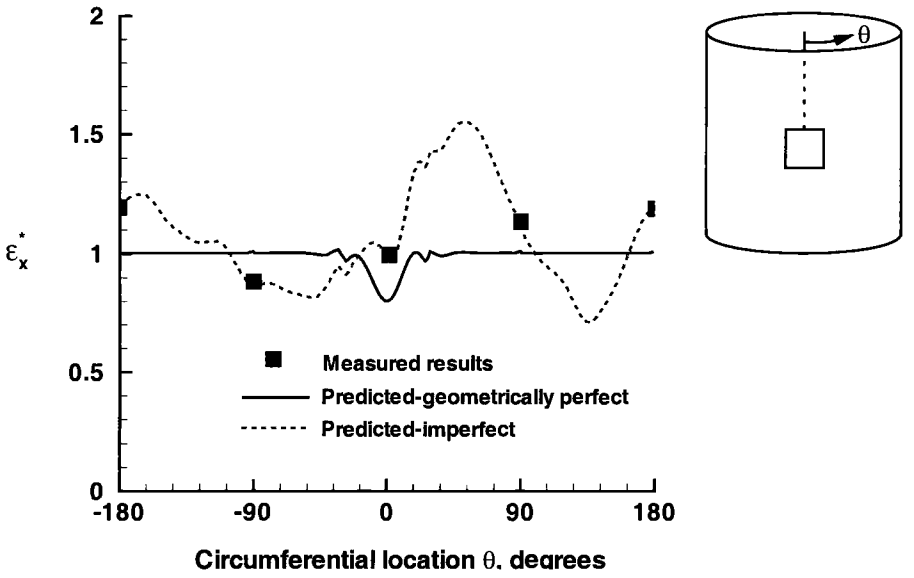


FIG. 12—*Effects of measured imperfections on the predicted strains near the loaded edge of specimen C4 ($[\pm 45/0_2]_s$ laminate).*

indicate that the predicted strain distribution for the imperfect shell is noticeably different from the predicted strain distribution for the perfect shell. The measured results correlate well with the predicted results for the geometrically imperfect model indicating that the measured imperfections are needed to model accurately the strains in the specimens.

For the most part, the results indicate that the effects of the measured imperfections on the buckling loads of the specimens cannot be added following the principle of superposition. Rather, the results suggest that the types of imperfections interact or couple in a nonlinear manner, which results in an overall reduction in the buckling load of the specimen. For example, the traditional initial geometric shell-wall mid-surface imperfections, the other nontraditional shell-wall thickness imperfections, and the loading imperfection effects of specimen C1 result in 1.5, 0.3 and 0.8% reductions in the buckling load of the specimen, respectively. However, the cumulative effect of all these imperfections causes a 4.3% reduction in the buckling load, which is 165% of the sum of the reductions caused by the individual imperfections.

Manufacturing Defects

For the most part, the predicted and measured buckling loads presented herein correlate to within approximately 10%. However, there are still significant differences in the results for some of the specimens. Most notably, the buckling loads for specimens C2 and C3 were overpredicted by approximately 16%. These specimens had visible manufacturing flaws in the form of gaps between adjacent strips of preimpregnated graphite-epoxy tape in some of the plys that were formed during the fabrication process. These manufacturing defects typically appear in the nondimensionalized thickness distribution contour (e.g., see Fig. 4) as distinct thin regions in the shell wall. In such a locally thin region, the shell wall is a 7-ply-thick laminate rather than the nominal 8-ply-thick laminate. Typically, a circumferential ply-gap constitutes a gap between two adjacent 90° plies in the laminate, a 45° or helical ply-gap constitutes a gap between two adjacent 45° plies, and an axial ply-gap constitutes a gap between two adjacent 0° plies.

A parametric study on the effects of lamina ply-gaps on the buckling response of the quasi-isotropic specimen C2 was conducted. Three ply-gap orientations were studied which included a circumferential ply-gap located at the cylinder mid-length, a 45° helical ply-gap and an axial ply-gap. Ply-gap widths of 1.15 and 2.30 mm were included in the models. The local shell walls associated with the circumferential, helical, and axial ply-gaps were modeled as unsymmetric laminates. The mid-surface of the local shell wall associated with the ply-gaps had an eccentricity of −0.0635 mm with respect to the nominal 8-ply-thick shell-wall mid-surface. The results of the study indicate that the circumferential ply-gap causes a 1.4 and 4.6% reduction in the buckling load of specimen C2 for the 1.15- and 2.30-mm-wide ply gaps, respectively, and the axial ply-gap causes a corresponding 2.0 and 5.3% reduction in the buckling load. However, the 45° helical ply-gap causes a 5.2 and 13.6% reduction in the buckling load for the 1.15- and 2.30-mm-wide ply gaps, respectively, which are significantly greater reductions than those caused by the other two ply-gap configurations. The results indicate that a ply-gap causes an abrupt change in the local stiffness of the shell wall, and an eccentricity in the local internal load path, which causes a significant amount of local bending that results in a reduction in the buckling load of the shell. Typical predicted out-of-plane deformations just prior to buckling for shells with the three ply-gap configurations are shown in Fig. 13. The results indicate that the orientation of the ply-gaps can have a significant effect on the distribution of the out-of-plane deformations in the shell. The shell with the circumferential ply-gap has an axisymmetric deformation shape as shown in Fig. 13*a*. The shell with a 45° helical ply-gap has a displacement response characterized by a local large inward deformation aligned with the helical gap as shown in Fig. 13*b*. The shell with the axially aligned ply-gap has a periodic deformation response with several half-waves along the length and several half-waves around the circumference as shown in Fig. 13*c*.

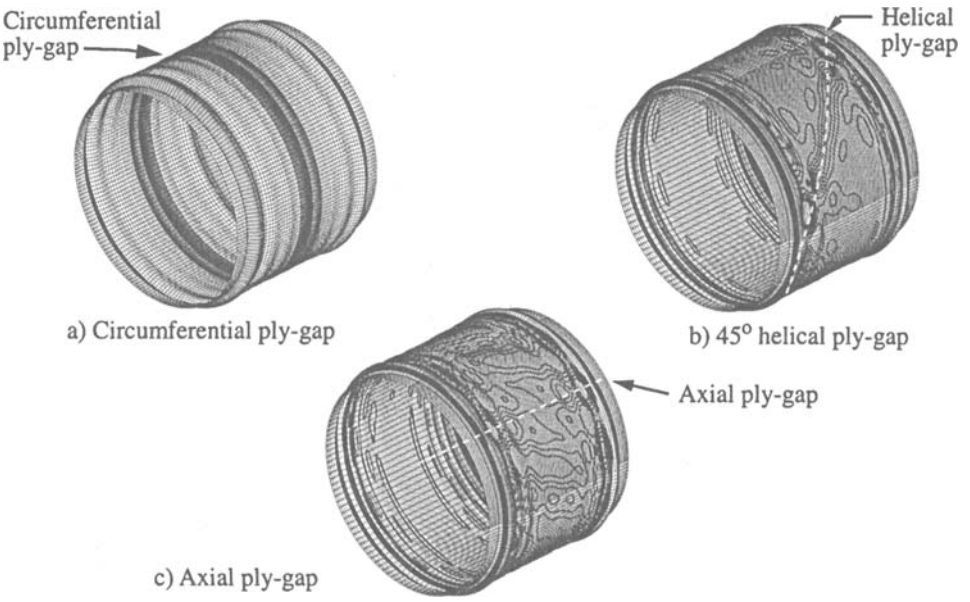


FIG. 13—*Effects of lamina ply-gaps on the predicted out-of-plane deformations of specimen C2 at the onset of buckling ([±45/0/90], laminate).*

Design Considerations

The nonlinear analysis procedure describe herein offers an accurate and robust approach for predicting the nonlinear response and stability characteristics of compression-loaded thin-wall graphite-epoxy shell structures. This nonlinear analysis procedure also offers a relatively affordable alternative to testing many replicates of a particular shell design of interest, or to relying on historical test data for shells that do not represent the configuration, material system, or fabrication procedure associated with the design of interest. This analysis procedure could be used as a parametric tool in the early stages of a design project to determine the sensitivity of a specific design to a number of different types of imperfections or differences in the mathematical design and the as-built shell structure. This analysis procedure should be used with a selected number of carefully conducted tests that would be used to verify the design and analysis results. A hierarchical approach to buckling load calculations [*9*] could also be used to converge on the design with more approximate and more computationally efficient analyses before using the nonlinear analysis procedure described herein.

The results of the present study indicate that designers need to be aware of nontraditional initial imperfections. The results show that it is now possible to represent geometric, material and manufacturing imperfections or variations of a nominal shell design by including these imperfections or variations in the nonlinear analysis for a shell design of interest. Traditional initial geometric shell-wall imperfections that are often associated with the tooling used in the fabrication process can easily be included in the analysis by measuring a typical specimen or by approximating their effects with eigenvectors from a linear bifurcation buckling analysis or some other relevant shape. Nontraditional shell-wall thickness variations associated with the fabrication processes typically used for graphite-epoxy structures can also easily be included in the analysis by recognizing that these local thickness variations affect the local shell-wall stiffnesses which can easily be represented in the analysis model. Other nontraditional imperfections, such as shell-end geometric imperfections and local gaps

between adjacent plies of tape in a given layer in the shell-wall laminate, can be included in the analysis by measuring the shell-end geometry or identifying acceptable manufacturing tolerances associated with the fabrication of the shell structure. Shell-end geometric imperfections can affect the strain in the shell enough to cause buckling to occur at a lower load than the load for a shell with perfect end geometries, and gaps between adjacent plies in a layer can cause local eccentricities and three-dimensional stress gradients that can buckle or fail the shell prematurely if these effects are not accounted for in the design. Accurately predicting the nonlinear response of shells with traditional and nontraditional imperfections is important for determining when a local failure mechanism might be activated in a laminated shell. A local failure would change the local stiffness of the shell wall and the internal load distribution in the shell, which could affect the stability characteristics of the shell. A local failure mechanism could also provide enough of a lateral disturbance in a highly stressed shell wall to initiate collapse at a load lower than the anticipated load.

The nonlinear analysis procedure described herein can be used to generate design curves that account for all of the types of imperfections described herein. Such design curves could be used as a scientifically based replacement to the traditional empirical design knockdown factors typically used in design today. A designer can determine which of the various types of imperfections described herein are representative of the manufacturing procedure or fabrication process that is appropriate for his or her design, and then use the relevant design curves to develop the design. If all of the parameters or imperfections are not well known, then the response results represented by the design curve could be bounded by judicious use of a hybrid of deterministic and nondeterministic analyses and models, and practical ranges of values of the parameters.

The tests used to validate the analyses and designs should be carefully conducted so that representative analysis results can be generated to correlate with the test results. Test boundary conditions can be accurately represented in the nonlinear analysis procedure described herein, and uncertainties about the effects of various types of shell boundary conditions can be resolved by conducting analyses. Test loading conditions and corresponding shell-end displacements and rotations should be measured during the tests and the results used as loading conditions in the analysis. The provenience and pedigree of each test specimen should be determined or measured to assure that the appropriate shell-wall geometry and thickness distribution, material properties, and fabrication process specific effects are included in the analysis used to develop the design of interest.

The nonlinear analysis procedure described herein can form the basis of a modern design approach and scientifically based design criteria for composite shell structures when the effects of all of the variations from the nominal dimensions and properties are properly included in the design process. These traditional and nontraditional imperfections can readily be included in the nonlinear analysis procedure and the results of the analyses should reduce the uncertainties associated with the use of empirical design knockdown factors that may not be representative of the design of interest. This nonlinear analysis procedure can determine the appropriate design knockdown factor by analyzing the design of interest and including the appropriate imperfections in the analysis. By using such a high-fidelity nonlinear analysis procedure in the design process, the design validation and verification tests can be used to qualify or evolve the design without having to rely on an excessive number of tests to develop design knockdown factors. These relatively affordable nonlinear analyses should be used in conjunction with a carefully designed test program to mature a design of interest.

Concluding Remarks

The results of an experimental and analytical study of the effects of initial imperfections on the buckling response of thin unstiffened graphite-epoxy cylindrical shells with and without a cutout, and with three different shell-wall laminates have been presented. The results identify the effects of traditional initial geometric shell-wall imperfections on the nonlinear response and buckling loads of these shells that are commonly discussed in the literature on shell buckling. Other results are pre-

sented that also identify the effects of several relatively unknown and nontraditional imperfections such as shell-end geometric imperfections, shell-wall thickness variations, and variations in loads applied to the ends of the shells on the shell buckling and nonlinear responses. A high-fidelity nonlinear shell analysis procedure has been used to predict the response of the shells, and this analysis procedure accurately accounts for the effects of these traditional and nontraditional imperfections on the buckling and nonlinear responses of the shells. The analysis results generally correlate well with the experimental results indicating that it is possible to predict the complex nonlinear response and buckling loads for composite shell structures. The analysis results also show that these nontraditional imperfections can be very important in some cases since they can significantly affect the buckling load. The nonlinear analysis results are also compared with the results from a traditional linear bifurcation buckling analysis. The results of this comparison suggest that the nonlinear analysis procedure can be used for determining accurate, high-fidelity design knockdown factors for predicting shell buckling and collapse in the design process. This high-fidelity nonlinear analysis procedure can be used to form the basis for a shell analysis and design approach that addresses some of the critical shell-buckling design criteria and design considerations for composite shell structures.

References

[1] Anon., "Buckling of Thin-Walled Circular Cylinders," NASA Space Vehicle Design Criteria, NASA SP-8007, Sept. 1965.

[2] Koiter, W. T., "On the Stability of Elastic Equilibrium," (in Dutch), H. J. Paris, Ed., Amsterdam, Holland, 1945; translation available as AFFDL-TR-70-25, Feb., 1970, Wright-Patterson Air Force Base.

[3] von Kármán, T. and Tsien, H-S., "The Buckling of Thin Cylindrical Shells Under Axial Compression," *Journal of the Aeronautical Science*, Vol. 8, No. 8, June 1941, pp. 303–312.

[4] Budiansky, B. and Hutchinson, J., "Dynamic Buckling of Imperfection Sensitive Structures," *Proceedings of the 11th IUTAM Congress*, H. Gortler, Ed., Springer-Verlag, Berlin, 1964, pp. 636–651.

[5] Árbocz, J. and Babcock, C. D., "The Effect of General Imperfections on the Buckling of Cylindrical Shells," *Journal of Applied Mechanics*, Vol. 36, Series E, No. 1, 1969, pp. 28–38.

[6] Sechler, E. E., "The Historical Development of Shell Research and Design," in *Thin-Shell Structures, Theory, Experiments and Design*, Y. C. Fung and E. E. Sechler, Eds., Prentice-Hall, Englewood Cliffs, NJ, 1974, pp. 3–25.

[7] Brogan, F. A., Rankin, C. C., and Cabiness, H. D., "STAGS Users Manual," Lockheed Palo Alto Research Laboratory, Report LMSC P032594, 1994.

[8] Árbocz, J., "The Effect of Imperfect Boundary Conditions on the Collapse Behavior of Anisotropic Shells," *Proceedings of the Joint Applied Mechanics and Materials ASME Summer Conference*, AMD-MD'95, Los Angeles, CA, 28–30 June 1995.

[9] Árbocz, J., Starnes, J. H., Jr., and Nemeth, M. P., "A Hierarchical Approach to Buckling Load Calculations," *Proceedings of the 40th AIAA/ASME/ASCE/AHS/ASC Structures, Structural Dynamics, and Materials Conference*, St. Louis, MO, 1999, AIAA Paper No. 99-1232.

[10] Hilburger, M. H., Waas, A. M., and Starnes, J. H., Jr., "Response of Composite Shells with Cutouts to Internal Pressure and Compression Loads," *AIAA Journal*, Vol. 37, No. 2, pp. 232–237.

[11] Riks, E., "Progress in Collapse Analysis," *Journal of Pressure Vessel Technology*, Vol. 109, 1987, pp. 27–41.

[12] Park, K. C., "An Improved Stiffly Stable Method for Direct Integration of Nonlinear Structural Dynamics," *Journal of Applied Mechanics*, Vol. 42, June 1975, pp. 464–470.

Author Index

A

Adelmann, John, 131
Altman, Leigh Killian, 131
Anderson, Timothy C., 29
Asp, Leif E., 12

B

Baker, Donald J., 72
Barbero, Ever J., 470
Barr, Bruce, 131
Bau, Hui, 273
Brunner, Andreas J., 366
Bucinell, Ronald B., 382

C

Caiazzo, Anthony, 158
Chang, Fu-Kuo, 243
Chatterjee, Sailendra N., 452

D

Dagba, Louis, 243
Davidson, Barry D., 334
Davis, John J., 398
Dobyns, Alan, 131

G

Grant, Peter, vii
Greenhalgh, Emile, 49

H

Hart-Smith, L. J., 413
Hethcock, J. Donn, 72
Hilburger, Mark W., 529
Hoyt, D. M., 273

I

Iarve, Endel V., 231

K

König, M., 345
Krüger, Ronald, 105, 345

L

Lincoln, John W., 3
Lui, K., 324

M

Martin, Roderick H., 311
Mattavi, Joseph L., 210
McManus, Hugh L., 513
McShane, Hank, 158
Minguet, Pierre J., 105, 293
Mollenhauer, David H., 231
Moore, Heidi, 131
Murri, Gretchen B., 188

N

Nemeth, Michael P., 529
Nilsson, Karl-Fredrik, 49
Nilsson, Soren, 12

O

O'Brien, T. Kevin, 105
Olsson, Robin, 12
Orlet, Michael, 158
Owens, Stephen D., 398

P

Paradies, Rolf, 366
Peck, Scott O., 437
Piggott, M. R., 324

Q

Qing, Xinlin, 243

Copyright© 2001by ASTM International

R

Rachau, Chris, 158
Reddy, D. J., 131
Reynolds, Tom G., 513
Rinderknecht, S., 345
Rousseau, Carl Q., vii, 72, 273, 311
Roy, Brian, 382

S

Sawicki, Adam J., 293
Schmidt, Ronald P., 398
Schuecker, Clara, 334
Singh, Sunil, 49
Sjögren, Anders, 12
Smith, Stephen L., 210
Starnes, James H., Jr., 529
Strait. Larry, 158
Sun, Hsien-Tang, 243

W

Wang, J., 324
Wen, Edward A., 470

Subject Index

A

ABAQUS, 243
Accelerated aging, 513
Accelerated tests, environmental degradation, 513
Accept/reject criteria, 158
Acoustic emission, 366
Adequacy of standards, 324
Aircraft, use of composite structures, 3
Allowables, 3, 29, 210
  open hole compression, 273
ASTM D 30, 324
ASTM D 2344, 324
ASTM D 3039, 324
ASTM D 4255, 324
ASTM D 5379, 324
ASTM D 5448, 324
ASTM standards, shear and tensile failure processes, 324

B

Bearing-bypass interaction, 293
Bolted joints
  damage-tolerance design, 243
  fastener clearance and, 293
  stress analysis and failure prediction, 231
Bonded joints
  propeller blades, 210
  tension pull-off and shear test methods, 398
Braided materials, 210
Buckling, 12, 72
  cylindrical shells, 529
Building block structural qualification program, 131

C

Carbon/epoxy tape laminates, 273
Carbon fiber, 12, 131
  predicting structural properties, 158
Carbon fiber reinforced polymer, 366
Carbon-fiber reinforced skin-stringer panels, 49
Certification, 131
  cost reduction, 29
Closed-cross-section laminates, 382
Composite tailboom, 29
Compression-after-impact strength, 72
Compression-after-impact testing, 29
Compression loading
  bolted joints, 293
  closed-cross-section laminates, 382
Compression strength, open hole, 273
Compression testing, compressive strength of production parts, 470
Compressive strength, parts without compression testing, 470
Constitutive model, 158
Curved beams, 437
Cylindrical shells, buckling, 529

D

Damage, environmental degradation, 513
Damage assessment, 12
Damage initiation prediction, 231
Damage mechanics, 452
Damage tolerance, 3
  design of bolted joints, 243
  three-stringer panel, 72
Delamination
  flexbeam laminates, 188
  as threat to structural integrity, 3
  under multiaxial loading, 105
Delamination growth, 12
  finite-element analysis, 345
  mechanisms, 49
  modeling, 49
  0°/45° interface, 311
Delamination onset, 311
Delamination toughness, friction effect, 334
Design
  development testing, 3
  environmental degradation, 513
Displacement spline approximation method, 231
Double cantilever beam, 311
Durability, 513

E

End notched flexure
  delamination growth, 345
  energy release rate, 334
Energy release rates, 105
  end notched flexure tests, 334
Environmental degradation, accelerated testing, 513
Epoxy, 131

F

Fail-safe testing, 131
Failure, 452
  interactive criteria, 413
  open hole, 273
Failure prediction, filled hole laminates, 231
Fastener clearance, effect on bolted joint failure, 293
Fatigue analysis, propeller blades, 210
Fatigue delamination, 0°/45° interface, 311
Fatigue tests, 0°/45° interface, 311
Fiber bridging, 311
Fiber misalignment, compressive strength and, 470
Fiber-polymer composites, interactive failure theories, 413
Filled hole laminates, stress analysis and failure prediction, 231
Finite-element analysis
  closed-cross-section laminates, 382
  debonding under multiaxial loading, 105
  end notched flexure tests, 334
  fastener clearance, 293
Finite-element modeling
  delamination, 49
  delamination growth, 345
  flexbeam laminates, 188
  open hole compression strength, 273
Flexbeam laminates, ply waviness, 188
Fractography, 49
Fracture mechanics, 105
Friction, effect on Mode II delamination toughness, 334
Full-scale testing, 3

G

Graphite-epoxy composite shells, 529
Graphite/epoxy end notched flexure specimen, 345

H

Hole size effect, 452
Hole tolerance, 293

I

Impact damage, 12
  barely visible, 29
  as threat to structural integrity, 3
Impact resistance, 12
Imperfections, initial, effects on buckling, 529
In-plane/out-of-plane loading conditions, 105
Integrally stiffened composite wing skins, 72
Interactive failure theories, 413
Interlaminar fracture, 345
  toughness, 311

L

Laminated composites, 437
Laminated plate theory, 452

M

Marcel defect, 158, 188
Material properties, environmental degradation, 513
Microcracking, 513
Mode II delamination toughness, friction effect, 334
Modified building block approach, 29
Moisture, as threat to structural integrity, 3
Moisture cycling, 513
Moving mesh, 49
Multiaxial straining, 452

N

Nonlinear analysis, composite shells, 529
Nonlinear constitutive law, 452

O

Open hole compression strength, 273

P

PDHOLEC, 273
Ply waviness, 158
  effect on fatigue life, 188
Polyimides, 513
Polymer matrix composites, 513
Progressive damage, 273
Propeller blade, structural qualification, 210
Proprotor yoke, 131

Q

Qualification of structures, 3
Quasi-static tests, 0°/45° interface, 311

R

RAH-66 Comanche, 131
Reissner-Mindlin plate theory, 345
Residual strength, 12
Resin transfer molding, 210

S

Sandwich element, 366
Sandwich structures, 437
Shear failure, ASTM standards, 324
Shear test method, 398
Single-piece structures, 437
Skin/flange interface, 105
Skin-stringer panels, delamination growth, 49
Small mass impact, 12
Spring-in, 437
Stacking sequence effect, 231

Stiffness, ASTM standards, 324
Stiffness loss, 452
Strain energy dissipation, 452
Strain energy release rates, under multiaxial loading, 105
Strength, ASTM standards, 324
Strength prediction, fastener clearance and, 293
Stress analysis, 452
  three-dimensional, 231, 243
Stress concentrations, 273
Stringer panel, compression-after-impact strength, 72
Structural failure, 49
Structural properties, marcel defect effects, 158
Structural qualification
  propeller blades, 210
  RAH-66 Comanche, 131
Surface-effect ships, 366

T

Tailboom, composite, 29
Tapererd composite flexbeam laminates, ply waviness, 188
Technology transition, 3
Temperature, as threat to structural integrity, 3
Tensile failure, ASTM standards, 324
Tension pull-off, 398
Test methods, reinforced bonded T-joints, 398
Thermal cycling, 513
T-joints
  sandwich designs, 366
  textile reinforced bonded, 398
3DBOLT, 243

U

U. S. Air Force, qualification of structures, 3

V

V-22, 131
Virtual crack closure technique, 105, 334

W

Woven preforms, 398

Y

Yoke, composite, 131

ISBN 0-8031-2862-2